Industria y Comercio
SUPERINTENDENCIA

Espacio reservado para el adhesivo de radicación

DIRECCIÓN DE NUEVAS CREACIONES
Procedimiento acelerado de exámenes de patente (PPH)

1	**NÚMERO DE SOLICITUD ANTE LA SIC** NC2019/0013707		
2	**GLOBAL - PPH** **X** PAÍS ESTADOS UNIDOS DE AMÉRICA	**3**	**PCT – PPH** ☐ PAÍS
4	**PROSUR** ☐ PAÍS	**5**	**Alianza del Pacifico (AdP)** ☐ PAÍS
6	**OFICINA DE PRIMERA PRESENTACIÓN (OPP)** ☐	**7**	**OFICINA DE EXAMEN ANTERIOR (OEA)** ☐
8	**NÚMERO DE SOLICITUD O PUBLICACIÓN DE LA SOLICITUD (OPP)** **X** **NÚMERO DE SOLICITUD EN OFICINA DE EXAMEN ANTERIOR (OEA):** ☐ **NÚMERO DE SOLICITUD PCT:** ☐		1. 16/184,466
9	☐ **REPRESENTANTE LEGAL** **X APODERADO**		

APELLIDOS	NOMBRES	IDENTIFICACIÓN
CASTELLANOS ABONDANO	MARGARITA	C.C . 39.779.654 T.P . 70.819

DIRECCIÓN	117 No. 5A-35	No. TELÉFONO	7560770
CIUDAD	BOGOTÁ D.C.	CORREO ELECTRÓNICO	patentessic@castellanosyco.co
PAÍS	COLOMBIA	No. RADICACIÓN O PROTOCOLO DE PODER GENERAL	

10 CONDICIONES PARA ACCEDER A ESTE PROCESO:

10.1. DATOS DE PRIORIDAD **X** SI ☐ NO

(33) PAÍS DE ORIGEN	CÓDIGO PAÍS	(31) NÚMERO	(32) FECHA (AAAA/MM/DD)
1.ESTADOS UNIDOS DE AMÉRICA	US	62/520,084	2017/06/15
2.ESTADOS UNIDOS DE AMÉRICA	US	62/554,155	2017/09/05

10.2. DATOS SOLICITUD INTERNACIONAL PCT **X** SI ☐ NO

Solicitud Internacional No.	PCT/US2018/037437	**Fecha**	2018/06/14
Publicación Internacional No.	WO/2018/232055	**Fecha**	2018/12/20

*El solicitante presenta una copia de la(s) reivindicación(es) patentable(s) u otorgable(s) de la solicitud de la Oficina de Primera Presentación que profirió el examen de patentabilidad, junto con una traducción al castellano. **X** SI ☐ NO

*El solicitante presenta los resultados de búsqueda de la Oficina de Examen Anterior, junto con una traducción al castellano **X** SI ☐ NO

REQUISITOS PARA EL RECONOCIMIENTO DE LOS RESULTADOS DE EXÁMENES DE PATENTABILIDAD EFECTUADOS A SOLICITUDES EXTRANJERAS

Para que la Superintendencia de Industria y Comercio pueda reconocer los resultados de exámenes de patentabilidad producidos por otras Oficinas de Propiedad Industrial se debe cumplir con las siguientes condiciones:

(a) Al momento de solicitar el examen de patentabilidad, si el solicitante pide que se reconozcan exámenes de patentabilidad de otras oficinas extranjeras, deberá aportar junto con el pago de la tasa correspondiente, los siguientes anexos:

(i) Copia de las resoluciones, fallos o decisiones que han sido relevantes para la determinación de la patentabilidad de la(s) solicitud(es) en la Oficina que haya proferido el examen de patentabilidad que contienen reivindicaciones patentables u otorgables que son la base de la petición, y si es del caso, su traducción al castellano. **X** SI ☐ NO

(ii) Copia de todas las reivindicaciones determinadas como patentables u otorgables en la Oficina que profirió el examen de patentabilidad y, si es del caso, su traducción al castellano. **X** SI ☐ NO

(iii) Copia de los antecedentes, información o documentos citados por el examinador de la Oficina de Primera Presentación del examen de patentabilidad, en las resoluciones, fallos o decisiones correspondientes, incluyendo la literatura no patente. Los documentos de patente deberán presentarse siempre y cuando no estén disponibles para la Superintendencia de Industria y Comercio mediante el simple acceso a bases de datos gratuitas. **X** SI ☐ NO

(iv) Una tabla de correspondencias de las reivindicaciones que han sido determinadas como patentables u otorgables en la solicitud de la Oficina que haya proferido el examen de patentabilidad. . **X** SI ☐ NO

11 FIRMA DEL SOLICITANTE, DEL APODERADO O DEL REPRESENTANTE LEGAL

Junto a cada firma, indicar el nombre del firmante y su calidad (si tal calidad no es obvia al leer el petitorio)



Margarita Castellanos Abondano

10 (iv)	**TABLA DE CORRESPONDENCIA DE REIVINDICACIONES**	
Reivindicaciones en la solicitud en Colombia	Reivindicaciones otorgables en la solicitud internacional	Explicación sobre la suficiente correspondencia ó Comentarios que explican la correspondencia
1. Un polinucleótido que comprende la SEQ ID NO: 979. *7. Un polinucleótido que consiste en la SEQ ID NO: 979.*	*31. Un polinucleótido que comprende la SEQ ID NO: 979.*	*Las reivindicaciones fueron modificadas voluntariamente para la solicitud en Colombia, el 02 de septiembre de 2020, con el ánimo de presentar la invención de forma más clara y para que la materia corresponda con la otorgada en EE. UU.* *Por esta razón se hace referencia a las reivindicaciones modificadas.*
2. Una partícula de virus adenoasociado (AAV) que comprende el polinucleótido de la reivindicación 1 y una cápside de AAV2. *6. Un método para producir una partícula de AAV de la reivindicación 2, que comprende:* *transfectar una célula con un constructo que comprende un polinucleótido que comprende la SEQ ID NO: 979 y un constructo que comprende un polinucleótido que codifica los genes rep y cap; y* *recolectar la partícula AAV a partir de la célula.* *8. Una partícula de AAV que comprende el polinucleótido de la reivindicación 7 y una cápside de AAV2.* *12. Un método para producir una partícula de AAV de la reivindicación 8, que comprende:* *transfectar una célula con un constructo que comprende un polinucleótido que comprende la SEQ ID NO: 979 y un constructo que comprende un polinucleótido que codifica los genes rep y cap; y* *recolectar la partícula AAV a partir de la célula.*	*32. Una partícula de virus adenoasociado (AAV) que comprende el polinucleótido de la reivindicación 31 y una cápside de AAV2.*	*Ídem.*

3. Una composición farmacéutica que comprende las partículas de AAV de la reivindicación 2 y excipientes farmacéuticamente aceptables. *9. Una composición farmacéutica que comprende las partículas de AAV de la reivindicación 8 y excipientes farmacéuticamente aceptables.*	*33. Una composición farmacéutica que comprende una o más de las partículas de AAV de la reivindicación 32.*	*Ídem.*
4. Una composición farmacéutica que comprende partículas de virus adenoasociado (AAV), en donde el 70-100% de las partículas de AAV contienen un polinucleótido que comprende la SEQ ID NO: 979. *5. La composición farmacéutica de la reivindicación 4, en donde el 90-100% de las partículas de AAV contienen un polinucleótido que comprende la SEQ ID NO: 979.* *10. Una composición farmacéutica que comprende partículas de AAV, en donde el 70-100% de las partículas de AAV contienen un polinucleótido que consiste en la SEQ ID NO: 979.* *11. La composición farmacéutica de la reivindicación 10, en donde el 90-100% de las partículas de AAV contienen un polinucleótido que consiste en la SEQ ID NO: 979.*	*34. La composición farmacéutica de la reivindicación 33, en la que por lo menos el 70% de las partículas de AAV contienen el polinucleótido que comprende la SEQ ID NO: 979.*	*Ídem.*

UNITED STATES PATENT AND TRADEMARK OFFICE

UNITED STATES DEPARTMENT OF COMMERCE
United States Patent and Trademark Office
Address: COMMISSIONER FOR PATENTS
P.O. Box 1450
Alexandria, Virginia 22313-1450
www.uspto.gov

APPLICATION NO.	FILING DATE	FIRST NAMED INVENTOR	ATTORNEY DOCKET NO.	CONFIRMATION NO.
16/184,466	11/08/2018	Maria Scheel	2057.1042USCON	6066

95854 7590 06/03/2019

DT Ward, PC
142A Main Street
Groton, MA 01450

EXAMINER
NOBLE, MARCIA STEPHENS

ART UNIT	PAPER NUMBER
1632	

NOTIFICATION DATE	DELIVERY MODE
06/03/2019	ELECTRONIC

Please find below and/or attached an Office communication concerning this application or proceeding.

The time period for reply, if any, is set in the attached communication.

Notice of the Office communication was sent electronically on above-indicated "Notification Date" to the following e-mail address(es):

docketing@dtwardlaw.com
dward@dtwardlaw.com
kcorbett@dtwardlaw.com

Corrected ***Notice of Allowability***	**Application No.** 16/184,466	**Applicant(s)** Scheel et al.	
	Examiner MARCIA S NOBLE	**Art Unit** 1632	**AIA (FITF) Status** Yes

-- The MAILING DATE of this communication appears on the cover sheet with the correspondence address--

All claims being allowable, PROSECUTION ON THE MERITS IS (OR REMAINS) CLOSED in this application. If not included herewith (or previously mailed), a Notice of Allowance (PTOL-85) or other appropriate communication will be mailed in due course. **THIS NOTICE OF ALLOWABILITY IS NOT A GRANT OF PATENT RIGHTS.** This application is subject to withdrawal from issue at the initiative of the Office or upon petition by the applicant. See 37 CFR 1.313 and MPEP 1308.

1. ☑ This communication is responsive to 5/1/2019.
   ☐ A declaration(s)/affidavit(s) under **37 CFR 1.130(b)** was/were filed on _____.

2. ☐ An election was made by the applicant in response to a restriction requirement set forth during the interview on _____; the restriction requirement and election have been incorporated into this action.

3. ☑ The allowed claim(s) is/are 1-4,6-11,13-15 and 17-37 . As a result of the allowed claim(s), you may be eligible to benefit from the **Patent Prosecution Highway** program at a participating intellectual property office for the corresponding application. For more information, please see **http://www.uspto.gov/patents/init_events/pph/index.jsp** or send an inquiry to **PPHfeedback@uspto.gov.**

4. ☐ Acknowledgment is made of a claim for foreign priority under 35 U.S.C. § 119(a)-(d) or (f).

   Certified copies:

   a) ☐ All b) ☐ Some *c) ☐ None of the:

   1. ☐ Certified copies of the priority documents have been received.
   2. ☐ Certified copies of the priority documents have been received in Application No. _____ .
   3. ☐ Copies of the certified copies of the priority documents have been received in this national stage application from the International Bureau (PCT Rule 17.2(a)).

   * Certified copies not received: _____ .

Applicant has THREE MONTHS FROM THE "MAILING DATE" of this communication to file areply complying with the requirements noted below. Failure to timely comply will result in ABANDONMENT of this application.
THIS THREE-MONTH PERIOD IS NOT EXTENDABLE.

5. ☐ CORRECTED DRAWINGS (as "replacement sheets") must be submitted.
   ☐ including changes required by the attached Examiner's Amendment / Comment or in the Office action of Paper No./Mail Date _____ .

   Identifying indicia such as the application number (see 37 CFR 1.84(c)) should be written on the drawings in the front (not the back) of each sheet. Replacement sheet(s) should be labeled as such in the header according to 37 CFR 1.121(d).

6. ☐ DEPOSIT OF and/or INFORMATION about the deposit of BIOLOGICAL MATERIAL must be submitted. Note the attached Examiner's comment regarding REQUIREMENT FOR THE DEPOSIT OF BIOLOGICAL MATERIAL.

Attachment(s)

1. ☐ Notice of References Cited (PTO-892)
2. ☐ Information Disclosure Statements (PTO/SB/08), Paper No./Mail Date _____.
3. ☐ Examiner's Comment Regarding Requirement for Deposit of Biological Material _____.
4. ☑ Interview Summary (PTO-413), Paper No./Mail Date. _____.
5. ☑ Examiner's Amendment/Comment
6. ☐ Examiner's Statement of Reasons for Allowance
7. ☐ Other _____.

/MARCIA S NOBLE/
Primary Examiner, Art Unit 1632

Notice of Pre-AIA or AIA Status

The present application, filed on or after March 16, 2013, is being examined under the first inventor to file provisions of the AIA.

EXAMINER'S AMENDMENT

An examiner's amendment to the record appears below. Should the changes and/or additions be unacceptable to applicant, an amendment may be filed as provided by 37 CFR 1.312. To ensure consideration of such an amendment, it MUST be submitted no later than the payment of the issue fee.

Authorization for this examiner's amendment was given in an interview with Mark Hanson on 5/29/2019.

The application has been amended as follows:

In the specification, rewrite the following claims as follows:

32. (Currently Amended) The pharmaceutical composition of claim 31, wherein the serotype of the AAV capsid is AAV2.

33. (Currently Amended) The pharmaceutical composition of claim 32, wherein at least 70% of the AAV particles contain a vector genome.

Any inquiry concerning this communication or earlier communications from the examiner should be directed to MARCIA STEPHENS NOBLE whose telephone number is (571)272-5545. The examiner can normally be reached on M-F 9-5:30.

Examiner interviews are available via telephone, in-person, and video conferencing using a USPTO supplied web-based collaboration tool. To schedule an interview, applicant is encouraged to use the USPTO Automated Interview Request (AIR) at http://www.uspto.gov/interviewpractice.

If attempts to reach the examiner by telephone are unsuccessful, the examiner's supervisor, Peter Paras can be reached on 571-272-4517. The fax phone number for the organization where this application or proceeding is assigned is 571-273-8300.

Information regarding the status of an application may be obtained from the Patent Application Information Retrieval (PAIR) system. Status information for published applications may be obtained from either Private PAIR or Public PAIR. Status information for unpublished applications is available through Private PAIR only. For more information about the PAIR system, see http://pair-direct.uspto.gov. Should you have questions on access to the Private PAIR system, contact the Electronic Business Center (EBC) at 866-217-9197 (toll-free). If you would like assistance from a USPTO Customer Service Representative or access to the automated information system, call 800-786-9199 (IN USA OR CANADA) or 571-272-1000.

MARCIA S. NOBLE
Primary Examiner
Art Unit 1632

/MARCIA S NOBLE/
Primary Examiner, Art Unit 1632

OFICINA DE PATENTES Y MARCAS DE ESTADOS UNIDOS

DEPARTAMENTO DE COMERCIO DE ESTADOS UNIDOS

Oficina de Patentes y Marcas de Estados Unidos

Dirección: COMISIONADO PARA PATENTES

P.O. Box 1450

Alexandria, Virginia 22313-1450

www.uspto.gov

SOLICITUD NO.	FECHA PRESENTACION	PRIMER INVENTOR	REFERENCIA ABOGADO	NO. CONFIRMACION
16/184,466	11/08/2018	Maria Scheel	2057-1042USCON	6066

DT Ward, PC

142A Main Street

Groton, MA 01450

EXAMINADOR	
NOBLE, MARCIA STEPHENS	
UNIDAD DE ARTE	NUMERO DE PAPEL
1632	
FECHA DE NOTIFICACION	MODO DE ENTREGA
06/03/2019	ELECTRONICO

Por favor encuentre a continuación y/o adjunto una comunicación de la Oficina relacionada con esta solicitud o procedimiento.

El periodo de tiempo para respuesta, si hay alguna, se define en la comunicación adjunta.

La Notificación de la comunicación de la Oficina fue enviada electrónicamente en la “Fecha de Notificación” indicada anteriormente a las siguientes direcciones de correo electrónico:

docketing@dtwardlaw.com

dward@dtwardlaw.com

kcorbett@dwardlaw.com

Notificación de Concesión Corregida	**Solicitud No.** 16/184,466	**Solicitante(s)** Scheel y otros	
	Examinador MARCIA S NOBLE	**Unidad de Arte** 1632	**Estado AIA (FITF)** Sí

-- La FECHA DE ENVIO de esta comunicación aparece en la hoja de cubierta con la dirección de correspondencia--

Todas las reivindicaciones son concedidas, TRÁMITE SOBRE EL FONDO ESTÁ (O PERMANECE) CERRADO en esta solicitud. Si no se incluye acá (o enviada previamente), una Notificación de Concesión (PTOL-85) u otra comunicación adecuada será enviada en su debido momento. **ESTA NOTIFICACION DE CONCESION NO ES UNA CONCESION DE DERECHOS DE PATENTE**. Esta solicitud está sujeta a retiro de emisión a la iniciativa de la Oficina o a petición del solicitante. Ver 37 CFR 1.313 y MPEP 1308.

1. ☒ Esta comunicación responde a 5/1/2019.

☐Una declaración bajo **37 CFR 1.130(b)** se presentó el_____.

2. ☐ Se hizo una elección por el solicitante en respuesta a un requerimiento de restricción definido durante la entrevista el ____; el requerimiento de restricción y la elección se han incorporado en esta acción.

3. ☒ Las reivindicaciones concedidas son 1-4,6-11,13-15 y 17-37. Como resultado de las reivindicaciones aceptadas, usted puede ser elegible del beneficio del programa de **Autopista de Trámite de Patente** en una oficina de propiedad intelectual participante para la correspondiente solicitud. Para más información, por favor ver http://www.uspto.gov/patents/init_events/pph/index.jsp o enviar una pregunta a PPHfeedback@uspto.gov.

4. ☐ Se reconoce una reivindicación de prioridad extranjera bajo 35 USC sección 119(a)-(d) o (f).

Copias certificadas:

a) ☐ Todas b) ☐ Algunas c) ☐ Ninguna de las:

1. ☐ Copias certificadas de los documentos de prioridad se han recibido.

2. ☐ Copias certificadas de los documentos de prioridad se han recibido en la Solicitud No. ____.

3. ☐ Copias de las copias certificadas de los documentos de prioridad se han recibido en esta solicitud de fase nacional de la Oficina Internacional (Regla PCT 17.2 (a)).

* Copias certificadas no recibidas: _____.

El Solicitante tiene TRES MESES A PARTIR DE LA “FECHA DE ENVIO” de esta comunicación para presentar una respuesta que cumpla con los requerimientos indicados anteriormente. Falla en cumplir a tiempo resultará en el ABANDONO de esta solicitud.

ESTE PERIODO DE TRES MESES NO ES EXTENSIBLE

5. ☐ Se deben presentar FIGURAS CORREGIDAS (como “hojas de reemplazo”).

☐ Incluyendo cambios requeridos por la Enmienda/Comentario del Examinador adjunto o en la Acción Oficial de Papel No./Fecha de Envío ____.

Los indicios de identificación tal como el número de solicitud (ver 37 CFR 1.84(c)) se deben escribir en las figuras en el frente (no atrás) de cada hoja. Las hojas de reemplazo deben estar etiquetadas como tal en el encabezado de acuerdo con 37 CFR 1.121(d).

6. ☐ Se debe presentar DEPOSITO DE y/o INFORMACIÓN acerca del depósito de MATERIAL BIOLOGICO. Note el comentario del Examinador adjunto con relación al REQUERIMIENTO PARA EL DEPOSITO DE MATERIAL BIOLOGICO.

Adjunto(s)

1. ☐ Notificación de Referencias Citadas (PTO-892)
2. ☐ Declaraciones de Divulgación de Información (PTO/SB/08), Papel No./Fecha Envío ____
3. ☐ Comentario del Examinador con Relación a Requerimiento para Depósito de Material Biológico
4. ☒ Resumen de Entrevista (PTO-413), Papel No./Fecha Envío ____.
5. ☐ Enmienda/Comentario del Examinador
6. ☐ Declaración del Examinador de Razones para Concesión.
7. ☐ Otro ____.

/MARCIA S NOBLE/ Examinador Principal, Unidad de Arte 1632	

Notificación de Estado Pre-AIA o AIA

La presente solicitud, presentada en o después del 16 de marzo de 2013, está siendo examinada bajo las disposiciones de primer inventor en presentar del AIA.

MODIFICACION DEL EXAMINADOR

Una modificación del examinador al registro se muestra a continuación. Si los cambios y/o adiciones son inaceptables para el solicitante, se puede presentar una modificación como se indica en 37 CFR 1.312. Para asegurar la consideración de dicha modificación, esta DEBE ser presentada no más tarde del pago de la tasa de emisión.

La autorización para esta modificación del examinador fue dada en una entrevista con Mark Hanson el 5/29/2019.

La solicitud ha sido modificada de la siguiente forma:

En la descripción, reescribir las siguientes reivindicaciones así:

32. (Actualmente Modificada) La composición farmacéutica de la reivindicación 31, en donde el serotipo de la cápside AAV es AAV2.

33. (Actualmente Modificada) La composición farmacéutica de la reivindicación 32, en donde por lo menos 70% de las partículas de AAV contienen un genoma de vector.

Cualquier inquietud relacionada con esta comunicación o comunicaciones anteriores del examinador debe ser dirigida a MARCIA STEPHENS NOBLE cuyo número telefónico es (571)272-5545. El examinador normalmente está disponible de L-V 9-5:30.

También hay disponibles entrevistas con el examinador vía teléfono, en persona, y video conferencia usando una herramienta de colaboración basada en web suministrada por la USPTO. Para agendar una entrevista, se invita al solicitante a utilizar la Solicitud Automática de Entrevistas de la USPTO (AIR) en http://www.uspto.gov/interviewpractice.

Si los intentos por comunicarse con el examinador por teléfono no son exitosos, el supervisor del examinador, Peter Paras puede ser contactado en 571-272-4517. El número de teléfono de fax para la organización donde esta solicitud o procedimiento es asignado es 571-273-8300.

Información relacionada con el estado de una solicitud puede ser obtenida del sistema de Recuperación de Información de Solicitud de Patente (PAIR). La información de estado para solicitudes publicadas puede ser obtenido del PAIR Privado o el PAIR Público. La información del estado para solicitudes no publicadas está disponible únicamente mediante el PAIR Privado. Para más información acerca del sistema PAIR, vea http://pair-direct.uspto.gov. Si tiene inquietudes sobre el acceso al sistema PAIR Privado, contacte el Centro de Negocios Electrónicos (EBC) en 866-217-9197 (totalmente gratis). Si desea ayuda de un Representante de Servicio al Cliente de la USPTO o acceso al sistema automático de información, llame al 800-786-9199 (EN EE.UU. O CANADA) o 571-272-1000.

MARCIA S. NOBLE

Examinador Principal

Unidad de Arte 1632

/MARCIA S NOBLE/

Examinador Principal, Unidad de Arte 1632

ALLOWED CLAIMS

1. An aromatic L-amino acid decarboxylase (AADC) polynucleotide comprising a nucleotide sequence which has at least 95% identity to SEQ ID NO: 979.

2. The AADC polynucleotide of claim 1, wherein the nucleotide sequence comprises a 5' inverted terminal repeat (ITR) region which has at least 95% identity to SEQ ID NO: 980.

3. The AADC polynucleotide of claim 1, wherein the nucleotide sequence comprises a 3' inverted terminal repeat (ITR) region which has at least 95% identity to SEQ ID NO: 991.

4. The AADC polynucleotide of claim 1, wherein the nucleotide sequence comprises a CMV enhancer region which has at least 95% identity to SEQ ID NO: 982 and CMV promoter region which has at least 95% identity to SEQ ID NO: 983.

5. The AADC polynucleotide of claim 1, wherein the nucleotide sequence comprises an immediate-early 1 (ie1) region, wherein the ie1 region comprises an ie1 exon 1 region which has 95% identity to SEQ ID NO: 984 and an ie1intron 1 region which has 95% identity to SEQ ID NO: 985.

6. The AADC polynucleotide of claim 1, wherein the nucleotide sequence comprises a human beta-globin (hBglobin) region, wherein the hBglobin region comprises a hBglobin intron 2 region which has 95% identity to SEQ ID NO: 986 and a hBglobin exon 3 region which has 95% identity to SEQ ID NO: 987.

7. The AADC polynucleotide of claim 1, wherein the nucleotide sequence comprises a poly(A) signal which is derived from human growth hormone and which has 95% identity to SEQ ID NO: 990.

8. The AADC polynucleotide of claim 1, wherein the nucleotide sequence consists of 3520-3530 nucleotides from the 5’ end of the 5’ ITR to the 3’ end of the 3’ ITR.

9. The AADC polynucleotide of claim 1, wherein the nucleotide sequence consists of 3526 nucleotides from the 5’ end of the 5’ ITR to the 3’ end of the 3’ ITR.

10. A recombinant adeno-associated virus (rAAV) comprising the AADC polynucleotide of claim 1, wherein the capsid serotype of the rAAV is AAV2.

11. The AADC polynucleotide of claim 1, wherein the nucleotide sequence has at least 99% identity to SEQ ID NO: 979.

12. The AADC polynucleotide of claim 11, wherein the nucleotide sequence consists of 3526 nucleotides from the 5’ end of the 5’ ITR to the 3’ end of the 3’ ITR.

13. A recombinant adeno-associated virus (rAAV) comprising the AADC polynucleotide of claim 11, wherein the capsid serotype of the rAAV is AAV2.

14. A pharmaceutical composition comprising one or more adeno-associated virus (AAV) particles, wherein the AAV particles comprise an AAV capsid and a vector genome, and wherein the vector genome comprises a nucleotide sequence which has at least 95% identity to SEQ ID NO: 979.

15. The pharmaceutical composition of claim 14, wherein the nucleotide sequence has at least 99% identity SEQ ID NO: 979.

16. The pharmaceutical composition of claim 15, wherein the serotype of the AAV capsid is AAV2.

17. The pharmaceutical composition of claim 16, wherein at least 70% of the AAV particles contain a vector genome.

18. An aromatic L-amino acid decarboxylase (AADC) polynucleotide comprising a nucleotide sequence which has at least 97% identity to SEQ ID NO: 979.

19. The AADC polynucleotide of claim 18, wherein the nucleotide sequence comprises a 5' inverted terminal repeat (ITR) region which has at least 97% identity to SEQ ID NO: 980.

20. The AADC polynucleotide of claim 18, wherein the nucleotide sequence comprises a 3' inverted terminal repeat (ITR) region which has at least 97% identity to SEQ ID NO: 991.

21. The AADC polynucleotide of claim 18, wherein the nucleotide sequence comprises a CMV enhancer region which has at least 97% identity to SEQ ID NO: 982, and wherein the nucleotide sequence comprises a CMV promoter region which has at least 97% identity to SEQ ID NO: 983.

22. The AADC polynucleotide of claim 18, wherein the nucleotide sequence comprises an immediate-early 1 (ie1) region, wherein the ie1 region comprises an ie1 exon 1 region which has 97% identity to SEQ ID NO: 984 and an ie1intron 1 region which has 97% identity to SEQ ID NO: 985.

23. The AADC polynucleotide of claim 18, wherein the nucleotide sequence comprises a human beta-globin (hBglobin) region, wherein the hBglobin region comprises a hBglobin intron 2 region which has 97% identity to SEQ ID NO: 986 and a hBglobin exon 3 region which has 97% identity to SEQ ID NO: 987.

24. The AADC polynucleotide of claim 18, wherein the nucleotide sequence comprises a poly(A) signal which is derived from human growth hormone and which has 97% identity to SEQ ID NO: 990.

25. The AADC polynucleotide of claim 18, wherein the nucleotide sequence consists of 3520-3530 nucleotides from the 5' end of the 5' ITR to the 3' end of the 3' ITR.

26. The AADC polynucleotide of claim 18, wherein the nucleotide sequence consists of 3526 nucleotides from the 5’ end of the 5’ ITR to the 3’ end of the 3’ ITR.

27. A recombinant adeno-associated virus (rAAV) comprising the AADC polynucleotide of claim 18, wherein the capsid serotype of the rAAV is AAV2.

28. A pharmaceutical composition comprising one or more adeno-associated virus (AAV) particles, wherein the AAV particles comprise an AAV capsid and a vector genome, and wherein the vector genome comprises a nucleotide sequence which has at least 97% identity to SEQ ID NO: 979.

29. The pharmaceutical composition of claim 28, wherein the serotype of the AAV capsid is AAV2.

30. The pharmaceutical composition of claim 29, wherein at least 70% of the AAV particles contain a vector genome.

31. A polynucleotide comprising SEQ ID NO: 979.

32. An adeno-associated virus (AAV) particle comprising the polynucleotide of claim 31 and an AAV2 capsid.

33. A pharmaceutical composition comprising one or more of the AAV particles of claim 32.

34. The pharmaceutical composition of claim 33, wherein at least 70% of the AAV particles contain the polynucleotide comprising SEQ ID NO: 979.

REIVINDICACIONES CONCEDIDAS

1. Un polinucleótido de descarboxilasa aromática de L-aminoácido (AADC) que comprende una secuencia de nucleótido que tiene por lo menos 95% de identidad con la SEQ ID NO: 979.
2. El polinucleótido AADC de la reivindicación 1, en donde la secuencia de nucleótidos comprende una región de repetición terminal invertida (ITR) 5' que tiene por lo menos un 95% de identidad con la SEQ ID NO: 980.
3. El polinucleótido AADC de la reivindicación 1, en donde la secuencia de nucleótidos comprende una región de repetición terminal invertida (ITR) 3' que tiene por lo menos un 95% de identidad con la SEQ ID NO: 991.
4. El polinucleótido AADC de la reivindicación 1, en donde la secuencia de nucleótidos comprende una región potenciadora de CMV que tiene por lo menos un 95% de identidad con SEQ ID NO: 982 y una región promotora de CMV que tiene por lo menos un 95% de identidad con SEQ ID NO: 983.
5. El polinucleótido AADC de la reivindicación 1, en donde la secuencia de nucleótidos comprende una región 1 (ie1) inmediata-temprana, en la que la región ie1 comprende una región del exón 1 que tiene una identidad del 95% con la SEQ ID NO: 984, y una región del intrón 1 ie1 que tiene el 95% de identidad con la SEQ ID NO: 985.
6. El polinucleótido AADC de la reivindicación 1, en donde la secuencia de nucleótidos comprende una región de beta-globina humana (hBglobina), en el que la región de hBglobina comprende una región del intrón 2 que tiene una identidad del 95% con la SEQ ID NO: 986 y una región del exón 3 de hBglobina que tiene una identidad del 95% con la SEQ ID NO: 987.

7. El polinucleótido AADC de la reivindicación 1, en donde la secuencia de nucleótidos comprende una señal de poli (A) que se deriva de la hormona del crecimiento humana y que tiene una identidad del 95% con la SEQ ID NO: 990.
8. El polinucleótido AADC de la reivindicación 1, en donde la secuencia de nucleótidos consta de 3520-3530 nucleótidos desde el extremo 5' de la ITR 5' hasta el extremo 3' de la ITR 3'.
9. El polinucleótido AADC de la reivindicación 1, en donde la secuencia de nucleótidos consta de 3526 nucleótidos desde el extremo 5' de la ITR 5' hasta el extremo 3' de la ITR 3'.
10. Un virus adenoasociado recombinante (rAAV) que comprende el polinucleótido AADC de la reivindicación 1, en el que el serotipo de la cápside del rAAV es AAV2.
11. El polinucleótido de AADC de la reivindicación 1, en donde la secuencia de nucleótidos tiene al menos un 99% de identidad con la SQE ID NO: 979.
12. El polinucleótido de AADC de la reivindicación 11, en donde la secuencia de nucleótidos consta de 3526 nucleótidos desde el extremo 5' de la ITR 5' hasta el extremo 3' de la ITR 3'.
13. Un virus adenoasociado recombinante (rAAV) que comprende el polinucleótido AADC de la reivindicación 11, en el que el serotipo de cápside del rAAV es AAV2.
14. Una composición farmacéutica que comprende una o más partículas de virus adenoasociado (AAV), en el que las partículas de AAV comprenden una cápside de AAV y un genoma de vector, y en la que el genoma de vector comprende una secuencia de nucleótidos que tiene por lo menos un 95% de identidad con la SEQ ID NO:979.
15. La composición farmacéutica de la reivindicación 14, en donde la secuencia de nucleótidos tiene por lo menos 99% de identidad con la SEQ ID NO: 979.

16. La composición farmacéutica de la reivindicación 15, en donde el serotipo de la cápside de AAV es AAV2.

17. La composición farmacéutica de la reivindicación 16, en donde al menos el 70% de las partículas de AAV contienen un genoma de vector.

18. Un polinucleótido aromático de L- aminoácido descarboxilasa (AADC) que comprende una secuencia de nucleótidos que tiene por lo menos un 97% de identidad con la SEQ ID NO: 979.

19. El polinucleótido AADC de la reivindicación 18, en donde la secuencia de nucleótidos comprende una región de repetición terminal invertida (ITR) 5' que tiene por lo menos un 97% de identidad con la SEQ ID NO: 980.

20. El polinucleótido AADC de la reivindicación 18, en donde la secuencia de nucleótidos comprende una región de repetición terminal invertida (ITR) 3' que tiene por lo menos un 97% de identidad con la SEQ ID NO: 991.

21. El polinucleótido AADC de la reivindicación 18, en donde la secuencia de nucleótidos comprende una región potenciadora del CMV que tiene por lo menos un 97% de identidad con la SEQ ID NO: 982, y en el que la secuencia de nucleótidos comprende una región promotora del CMV que tiene por lo menos un 97% de identidad con la SEQ ID NO: 983.

22. El polinucleótido AADC de la reivindicación 18, en donde la secuencia de nucleótidos comprende una región 1 (ie1) inmediata-temprana, en la que la región ie1 comprende una región del exón 1 ie1 que tiene una identidad del 97% con la SEQ ID NO: 984, y una región del intrón 1 ie1 que tiene 97% de identidad con la SEQ ID NO: 985.

23. El polinucleótido AADC de la reivindicación 18, en donde la secuencia de nucleótidos comprende una región de beta-globina humana (hBglobina),en la que la región de hBglobina comprende una región del intrón 2 de hBglobina

que tiene un 97% de identidad con la SEQ ID NO: 986, y una región del exón 3 de hBglobina que tiene una identidad del 97% con la SEQ ID NO: 987.

24. El polinucleótido AADC de la reivindicación 18, en donde la secuencia de nucleótidos comprende una señal de poli (A) que se deriva de la hormona de crecimiento humana y que tiene una identidad del 97% con la SEQ ID NO: 990.

25. El polinucleótido AADC de la reivindicación 18, en donde la secuencia de nucleótidos consta de 3520-3530 nucleótidos desde el extremo 5' de la ITR 5' hasta el extremo 3' de la ITR 3'.

26. El polinucleótido AADC de la reivindicación 18, en donde la secuencia de nucleótidos consta de 3526 nucleótidos desde el extremo 5' de la ITR 5' hasta el extremo 3' de la ITR 3'.

27. Un virus adenoasociado recombinante (rAAV) que comprende el polinucleótido AACD de la reivindicación 18, en el que el serotipo de la cápside del rAVV es AVV2.

28. Una composición farmacéutica que comprende una o más partículas de virus adenoasociado (AAV), en donde las partículas de AAV comprenden una cápside de AAV y un genoma de vector, y en la que el genoma de vector comprende una secuencia de nucleótidos que tiene por lo menos un 97% de identidad con la SEQ ID NO: 979.

29. La conformación farmacéutica de la reivindicación 18, en donde el serotipo de la cápside de AAV es AAV2.

30. La composición farmacéutica de la reivindicación 29, en donde por lo menos el 70% de las partículas de AAV contienen un genoma de vector.

31. Un polinucleótido que comprende la SEQ ID NO: 979.

32. Una partícula de virus adenoasociado (AAV) que comprende el polinucleótido de la reivindicación 31 y una cápside de AAV2.

33. Una composición farmacéutica que comprende una o más de las partículas de AAV de la reivindicación 32.

34. La composición farmacéutica de la reivindicación 33, en la que por lo menos el 70% de las partículas de AAV contienen el polinucleótido que comprende la SEQ ID NO: 979.

PTO/SB/08a (02-18)
Approved for use through 11/30/2020. OMB 0651-0031
U.S. Patent and Trademark Office; U.S. DEPARTMENT OF COMMERCE
Under the Paperwork Reduction Act of 1995, no persons are required to respond to a collection of information unless it contains a valid OMB control number.

INFORMATION DISCLOSURE STATEMENT BY APPLICANT

(Not for submission under 37 CFR 1.99)

Application Number	16184466
Filing Date	2018-11-08
First Named Inventor	Maria Scheel
Art Unit	1629
Examiner Name	
Attorney Docket Number	2057.1042USCON

U.S.PATENTS Remove

Examiner Initial*	Cite No	Patent Number	Kind Code[1]	Issue Date	Name of Patentee or Applicant of cited Document	Pages,Columns,Lines where Relevant Passages or Relevant Figures Appear
	1	9616090		2017-04-11	Anthony Conway	
	2	10041090		2018-08-07	GAO GUANGPING	

If you wish to add additional U.S. Patent citation information please click the Add button. Add

U.S.PATENT APPLICATION PUBLICATIONS Remove

Examiner Initial*	Cite No	Publication Number	Kind Code[1]	Publication Date	Name of Patentee or Applicant of cited Document	Pages,Columns,Lines where Relevant Passages or Relevant Figures Appear
	1	20160166709		2016-06-16	Beverly L. Davidson	
	2	20170022507		2017-01-26	Deepak Reyon	
	3	20160326524		2016-11-10	Terence Flotte	
	4	20170008939		2017-01-12	Rajesh Khanna	

If you wish to add additional U.S. Published Application citation information please click the Add button. Add

FOREIGN PATENT DOCUMENTS Remove

INFORMATION DISCLOSURE STATEMENT BY APPLICANT

(Not for submission under 37 CFR 1.99)

Application Number	16184466
Filing Date	2018-11-08
First Named Inventor	Maria Scheel
Art Unit	1629
Examiner Name	
Attorney Docket Number	2057.1042USCON

Examiner Initial*	Cite No	Foreign Document Number[3]	Country Code[2] i	Kind Code[4]	Publication Date	Name of Patentee or Applicant of cited Document	Pages,Columns,Lines where Relevant Passages or Relevant Figures Appear	T[5]
	1							

If you wish to add additional Foreign Patent Document citation information please click the Add button Add

NON-PATENT LITERATURE DOCUMENTS Remove

Examiner Initials*	Cite No	Include name of the author (in CAPITAL LETTERS), title of the article (when appropriate), title of the item (book, magazine, journal, serial, symposium, catalog, etc), date, pages(s), volume-issue number(s), publisher, city and/or country where published.	T[5]
	1	FERLA R, et al. Prevalence of anti-adeno-associated virus serotype 8 neutralizing antibodies and arylsulfatase B cross-reactive immunologic material in mucopolysaccharidosis VI patient candidates for a gene therapy trial. Hum Gene Ther. 2015 Mar;26(3):145-52.	
	2	HARRINGTON EA, et al. Neutralizing Antibodies Against Adeno-Associated Viral Capsids in Patients with mut Methylmalonic Acidemia. Hum Gene Ther. 2016 May;27(5):345-53.	
	3	KOTTERMAN MA, et al. Antibody neutralization poses a barrier to intravitreal adeno-associated viral vector gene delivery to non-human primates. Gene Ther. 2015 Feb;22(2):116-26.	
	4	HU JE, et al. Opposing effects of viral mediated brain expression of apolipoprotein E2 (apoE2) and apoE4 on apoE lipidation and A beta metabolism in apoE4-targeted replacement mice. Mol Neurodegener. 2015 March, 10:6	
	5	ZHAO L et al. Intracerebral adeno-associated virus gene delivery of apolipoprotein E2 markedly reduces brain amyloid pathology in Alzheimer's disease mouse models. Neurobiol Aging. 2016 Aug;44:159-72.	
	6	FOL R et al. Viral gene transfer of APPsα rescues synaptic failure in an Alzheimer's disease mouse model. Acta Neuropathol. 2016 Feb;131(2):247-66.	
	7	GANT JC, et al. Reversal of Aging-Related Neuronal Ca2+ Dysregulation and Cognitive Impairment by Delivery of a Transgene Encoding FK506-Binding Protein 12.6/1b to the Hippocampus. J Neurosci. 2015 July, 29;35(30):10878-87.	

INFORMATION DISCLOSURE STATEMENT BY APPLICANT (Not for submission under 37 CFR 1.99)		
	Application Number	16184466
	Filing Date	2018-11-08
	First Named Inventor	Maria Scheel
	Art Unit	1629
	Examiner Name	
	Attorney Docket Number	2057.1042USCON

	8	REN J, et al. Noninvasive tracking of gene transcript and neuroprotection after gene therapy. Gene Ther. 2016 Jan;23 (1):1-9.	
	9	VERHELLE A, et al. AAV9 delivered bispecific nanobody attenuates amyloid burden in the gelsolin amyloidosis mouse model. Hum Mol Genet. 2017 Apr;26(7):1353-1364.	
	10	Fan D-S, et al. Behavioral Recovery in 6-Hydroxydopamine-Lesioned Rats by Contransduction of Striatum with Tyrosine Hydroxylase and Aromatic L-Amino Acid Decarboxylase Genes Using Two Separate Adeno-Associated Virus Vectors. Human Gene Therapy. 1998 November 20; 9:2527-2535.	
	11	Herzog R, et al. Long-term correction of canine hemophilia B by gene transfer of blood coagulation factor IX mediated by adeno-associated viral vector. Nature Medicine. 1999 January; Volume 5 Number 1.	
	12	Jolesz F. Intraoperative Imaging in Neurosurgery: Where Will the Future Take Us?. Acta Nerochir Suppl. 2011:109:21-25.	
	13	MacLullich A, et al. Enlarged perivascular spaces are associated with cognitive function in healthy elderly men. J Neurol Neurosurg Psychiatry. 2004;75:1519-1523.	
	14	Potter G, et al. Cerebral Perivascular Spaces Visible on Magnetic Resonance Imaging: Development of a Qualitative Rating Scale and its Observer Reliability. Cerebrovascular Diseases. 2015 March 19;39:224-231.	
	15	Potter G, et al. Enlarged perivascular spaces (EPVS): a visual rating scale and user guide. Guide prepared by Gillian Potter, Zoe Morris and Prof Joanna Wardlaw (University of Edinburgh).	
	16	Racette B, et al. [18F]FDOPA PET as an Endophenotype for Parkinson's Disease Linkage Studies. Am J Med Genet B Neuropsychiatr Genet. 2006 April 5;141B(3):245-249.	
	17	Grimm D, et al. In Vitro and In Vivo Gene Therapy Vector Evolution via Multispecies Interbreeding and Retargeting of Adeno-Associated Viruses. Journal of Virology. 2008 Jun;5887-5911.	
	18	Kern A, et al. Identification of a Heparin-Binding Motif on Adeno-Associated Virus Type 2 Capsids. Journal of Virology. 2003 Oct;11072-11081.	

INFORMATION DISCLOSURE STATEMENT BY APPLICANT (Not for submission under 37 CFR 1.99)		
	Application Number	16184466
	Filing Date	2018-11-08
	First Named Inventor	Maria Scheel
	Art Unit	1629
	Examiner Name	
	Attorney Docket Number	2057.1042USCON

	19	VOYAGER THERAPEUTICS – INVESTORS & MEDIA – PRESS RELEASE, "Voyager Therapeutics Announces Positive Interim Results from Phase 1b Trial of VY-AADC01 for Advanced Parkinson's Disease, December 7, 2016, pages 1-6.	
	20	NAIDOO J, et al. Extensive Transduction and Enhanced Spread of a Modified AAV2 Capsid in the Non-human Primate CNS. Mol Ther. 2018 Jul 12 Epub ahead of print	
	21	VAN LIESHOUT LP, et al. A Novel Triple-Mutant AAV6 Capsid Induces Rapid and Potent Transgene Expression in the Muscle and Respiratory Tract of Mice. Mol Ther Meth Clin Dev 2018 Jun 15	
	22	JANKOVIC J, et al. Safety and Tolerability of Multiple Ascending Doses of PRX002/RG7935, an Anti-α-Synuclein Monoclonal Antibody, in Patients With Parkinson Disease: A Randomized Clinical Trial. JAMA Neurol. 2018 Jun 18 Epub ahead of print.	
	23	YUN SP, et al. Block of A1 astrocyte conversion by microglia is neuroprotective in models of Parkinson's disease. Nat Med 2018 Jun 11 Epub ahead of print.	
	24	HUDRY E, et al. Efficient gene transfer to the central nervous system by single stranded Anc80L65. Mol Ther Meth Clin Dev. 2018 Jul 15	
	25	DI MAIO R, et al. LRRK2 activation in idiopathic Parkinson's disease. Sci Transl Med. 2018 Jul 25;10(451).	
	26	MAN JHK, et al. Cell reprogramming approaches in gene- and cell-based therapies for Parkinson's disease. J Control Release 2018 Jul 17;286:114-124 Epub ahead of print.	
	27	STOKER TB, et al. Regenerative therapies for Parkinson's Disease: An Update	
	28	TSE LV, et al. Mapping and engineering function domains of the assembly-activating protein of adeno-associated viruses. J. Virol. 2018 Jun 29;92(14).	
	29	CHIEN YH, et al. Efficacy and safety of AAV2 gene therapy in children with aromatic L-amino acid decarboxylase deficiency: an open-label, phase 1/2 trial. Lancet Chil Adolesc Health 2017 Dec;1(4):265-273.	

INFORMATION DISCLOSURE STATEMENT BY APPLICANT (Not for submission under 37 CFR 1.99)		
	Application Number	16184466
	Filing Date	2018-11-08
	First Named Inventor	Maria Scheel
	Art Unit	1629
	Examiner Name	
	Attorney Docket Number	2057.1042USCON

	30	GOWANLOCK D, et al. A designer AAV variant permits efficient retrograde access to projection neurons. Neuron. (2016) Oct 19;92(2):372-382.

If you wish to add additional non-patent literature document citation information please click the Add button Add

EXAMINER SIGNATURE

Examiner Signature		Date Considered	

*EXAMINER: Initial if reference considered, whether or not citation is in conformance with MPEP 609. Draw line through a citation if not in conformance and not considered. Include copy of this form with next communication to applicant.

[1] See Kind Codes of USPTO Patent Documents at www.USPTO.GOV or MPEP 901.04. [2] Enter office that issued the document, by the two-letter code (WIPO Standard ST.3). [3] For Japanese patent documents, the indication of the year of the reign of the Emperor must precede the serial number of the patent document. [4] Kind of document by the appropriate symbols as indicated on the document under WIPO Standard ST.16 if possible. [5] Applicant is to place a check mark here if English language translation is attached.

INFORMATION DISCLOSURE STATEMENT BY APPLICANT (Not for submission under 37 CFR 1.99)		
	Application Number	16184466
	Filing Date	2018-11-08
	First Named Inventor	Maria Scheel
	Art Unit	1629
	Examiner Name	
	Attorney Docket Number	2057.1042USCON

CERTIFICATION STATEMENT

Please see 37 CFR 1.97 and 1.98 to make the appropriate selection(s):

That each item of information contained in the information disclosure statement was first cited in any communication from a foreign patent office in a counterpart foreign application not more than three months prior to the filing of the information disclosure statement. See 37 CFR 1.97(e)(1).

OR

☐ That no item of information contained in the information disclosure statement was cited in a communication from a foreign patent office in a counterpart foreign application, and, to the knowledge of the person signing the certification after making reasonable inquiry, no item of information contained in the information disclosure statement was known to any individual designated in 37 CFR 1.56(c) more than three months prior to the filing of the information disclosure statement. See 37 CFR 1.97(e)(2).

☒ See attached certification statement.

The fee set forth in 37 CFR 1.17 (p) has been submitted herewith.

A certification statement is not submitted herewith.

SIGNATURE

A signature of the applicant or representative is required in accordance with CFR 1.33, 10.18. Please see CFR 1.4(d) for the form of the signature.

Signature	/Mark J. Hanson/	Date (YYYY-MM-DD)	2019-02-08
Name/Print	Mark J. Hanson	Registration Number	62521

This collection of information is required by 37 CFR 1.97 and 1.98. The information is required to obtain or retain a benefit by the public which is to file (and by the USPTO to process) an application. Confidentiality is governed by 35 U.S.C. 122 and 37 CFR 1.14. This collection is estimated to take 1 hour to complete, including gathering, preparing and submitting the completed application form to the USPTO. Time will vary depending upon the individual case. Any comments on the amount of time you require to complete this form and/or suggestions for reducing this burden, should be sent to the Chief Information Officer, U.S. Patent and Trademark Office, U.S. Department of Commerce, P.O. Box 1450, Alexandria, VA 22313-1450. DO NOT SEND FEES OR COMPLETED FORMS TO THIS ADDRESS. **SEND TO: Commissioner for Patents, P.O. Box 1450, Alexandria, VA 22313-1450.**

Privacy Act Statement

The Privacy Act of 1974 (P.L. 93-579) requires that you be given certain information in connection with your submission of the attached form related to a patent application or patent. Accordingly, pursuant to the requirements of the Act, please be advised that: (1) the general authority for the collection of this information is 35 U.S.C. 2(b)(2); (2) furnishing of the information solicited is voluntary; and (3) the principal purpose for which the information is used by the U.S. Patent and Trademark Office is to process and/or examine your submission related to a patent application or patent. If you do not furnish the requested information, the U.S. Patent and Trademark Office may not be able to process and/or examine your submission, which may result in termination of proceedings or abandonment of the application or expiration of the patent.

The information provided by you in this form will be subject to the following routine uses:

1. The information on this form will be treated confidentially to the extent allowed under the Freedom of Information Act (5 U.S.C. 552) and the Privacy Act (5 U.S.C. 552a). Records from this system of records may be disclosed to the Department of Justice to determine whether the Freedom of Information Act requires disclosure of these record s.

2. A record from this system of records may be disclosed, as a routine use, in the course of presenting evidence to a court, magistrate, or administrative tribunal, including disclosures to opposing counsel in the course of settlement negotiations.

3. A record in this system of records may be disclosed, as a routine use, to a Member of Congress submitting a request involving an individual, to whom the record pertains, when the individual has requested assistance from the Member with respect to the subject matter of the record.

4. A record in this system of records may be disclosed, as a routine use, to a contractor of the Agency having need for the information in order to perform a contract. Recipients of information shall be required to comply with the requirements of the Privacy Act of 1974, as amended, pursuant to 5 U.S.C. 552a(m).

5. A record related to an International Application filed under the Patent Cooperation Treaty in this system of records may be disclosed, as a routine use, to the International Bureau of the World Intellectual Property Organization, pursuant to the Patent Cooperation Treaty.

6. A record in this system of records may be disclosed, as a routine use, to another federal agency for purposes of National Security review (35 U.S.C. 181) and for review pursuant to the Atomic Energy Act (42 U.S.C. 218(c)).

7. A record from this system of records may be disclosed, as a routine use, to the Administrator, General Services, or his/her designee, during an inspection of records conducted by GSA as part of that agency's responsibility to recommend improvements in records management practices and programs, under authority of 44 U.S.C. 2904 and 2906. Such disclosure shall be made in accordance with the GSA regulations governing inspection of records for this purpose, and any other relevant (i.e., GSA or Commerce) directive. Such disclosure shall not be used to make determinations about individuals.

8. A record from this system of records may be disclosed, as a routine use, to the public after either publication of the application pursuant to 35 U.S.C. 122(b) or issuance of a patent pursuant to 35 U.S.C. 151. Further, a record may be disclosed, subject to the limitations of 37 CFR 1.14, as a routine use, to the public if the record was filed in an application which became abandoned or in which the proceedings were terminated and which application is referenced by either a published application, an application open to public inspections or an issued patent.

9. A record from this system of records may be disclosed, as a routine use, to a Federal, State, or local law enforcement agency, if the USPTO becomes aware of a violation or potential violation of law or regulation.

DECLARACION DE DIVULGACION DE INFORMACION POR EL SOLICITANTE (No para presentación bajo 37 CFR 1.99)		
	Número de Solicitud	16184466
	Fecha de Presentación	2018-11-08
	Primer Inventor	Maria Scheel
	Unidad del Arte	1629
	Nombre del Examinador	
	Referencia de Abogado	2057-1042USCON

PATENTES DE EE.UU.						
Inicial del Examinador	**No. Cita**	**Número Patente**	**Código Tipo**	**Fecha Emisión**	**Nombre de Titular o Solicitante del Documento citado**	**Páginas, Columnas, Líneas donde Aparecen Pasajes Relevantes o Figuras Relevantes**
	1	9616090		2017-04-11	Anthony Conway	
	2	10041090		2018-08-07	GAO GUANGPING	
Si desea adicionar información de citación de Patentes de EE.UU. adicionales por favor haga clic en el botón adicionar						
PUBLICACIONES DE SOLICITUD PATENTE DE EE.UU.						
Inicial del Examinador	**No. Cita**	**Número Publicación**	**Código Tipo**	**Fecha Publicación**	**Nombre de Titular o Solicitante del Documento citado**	**Páginas, Columnas, Líneas donde Aparecen Pasajes Relevantes o Figuras Relevantes**
	1	20160166709		2016-06-16	Beverly L. Davidson	

	2	20170022507		2017-01-26	Deepak Reyon	
	3	20160326524		2016-11-10	Terence Flotte	
	4	20170008939		2017-01-12	Rajesh Khanna	

Si desea adicionar información de citación de Solicitudes Publicadas de EE.UU. adicionales por favor haga clic en el botón Adicionar

DOCUMENTOS DE PATENTE EXTRANJEROS

Inicial del Examinador*	**No. Cita**	**Número Documento Extranjero[3]**	**Código País[2]**	**Código Tipo[4]**	**Fecha Publicación**	**Nombre de Titular o Solicitante del Documento citado**	**Páginas, Columnas, Líneas donde Aparecen Pasajes Relevantes o Figuras Relevantes**
	1						

Si desea adicionar información de citación de Documentos de Patente Extranjeros adicionales por favor haga clic en el botón Adicionar

DOCUMENTOS DE LITERATURA NO PATENTE

Iniciales del Examinador*	No Cita	Incluir nombre del autor (en MAYUSCULAS), título del artículo (cuando sea adecuado), título del artículo (libro, revista, diario, serial, simposio, catálogo, etc.), fecha, página(s), número de volumen, editor, ciudad y/o país donde se publicó
	1	FERLA R, y otros. Predominio de anticuerpos de neutralización anti virus adenoasociado serotipo 8 y material inmunológico de reacción cruzada de arilsulfatasa B en candidatos pacientes con mucopolisacaridosis VI para un ensayo de terapia de gen. Hum Gene Ther. 2015 Mar;26(3):145-52
	2	HARRINGTON EA, y otros. Anticuerpos Neutralizadores Contra Cápsides Virales Adenoasociadas en Pacientes con Acidemia Metilmalónica mut. Hum Gene Ther. 2016 Mayo;27(5):345-53.

	3	KOTTERMAN MA, y otros. Neutralización de anticuerpo posee una barrera para entrega de gen de vector viral adenoasociado intravitreal en primates no humanos. Gen Ther. 2015 Feb;22(2):116-26
	4	HU JE, y otros. Efectos opuestos de expresión de cerebro mediada por virus de apolipoproteína E2 (apoE2) y apoE4 en lipidación apoE y metabolismo A beta en ratones de reemplazo con enfoque en apoE4. Mol. Neurodegener. 2015 Marzo, 10:6
	5	ZHAO L. y otros. Entrega de virus adenoasociado intracerebral de apolipoproteína E2 reduce notablemente patología amiloide cerebral en modelos de ratón con enfermedad de Alzheimer. Neurobiol Aging. 2016 Ago;44:159-72.
	6	FOL R, y otros. Transferencia de gen viral de APPsα rescata falla sináptica en un modelo de ratón con enfermedad de Alzheimer. Acta Neuropatol. 2016 Feb;131(2):247-66
	7	GANT JC, y otros. Reversión de Desregulación de Ca2+ Neuronal Relacionada con la Edad y Deterioro Cognitivo mediante Entrega de una Proteína de Unión a FK506 que Codifica Transgén 12.6/1b al Hipocampo. J. Neurosci. 2015 Julio, 29;35(30):10878-87
	8	REN J, y otros. Rastreo no invasivo de transcripción de gen y neuroprotección después de terapia de gen. Gen Ther. 2016 Ene;23(1):1-9.
	9	VERHELLE A, y otros. Nanocuerpo biespecífico con entrega AAV9 atenúa carga de amiloide en el modelo de ratón con amiloidosis de gelsolina. Hum Mol Genet. 2017 Abr;26(7):1353-1364
	10	Fan D-S, y otros. Recuperación de comportamiento en ratas con lesión de 6-hidroxidopamina mediante contransducción de estriado con hidroxilasa de tirosina y genes de decarboxilasa de aminoácido L usando dos vectores de virus adenoasociados separados. Terapia de Gen Humana. 1998 Noviembre 20; 9:2527-2535
	11	Herzog R, y otros. Corrección a largo plazo de hemofilia B canina por transferencia de gen de factor IX de coagulación sanguínea mediado por vector viral adenoasociado. Medicina de Naturaleza. 1999 Enero: Volumen 5, Número 1

	12	Jolesz F. Imagen Intraoperativa en Neurocirugía: A Dónde Nos Llevará el Futuro? Acta Nerochir Suppl. 2011:109:21-25
	13	MacLullich A, y otros. Espacios perivasculares ampliados están asociados con función cognitiva en hombres mayores saludables. J. Neurol Neurosurg Psychiatry. 2004;75:1519-1523
	14	Potter G, y otros. Espacios Perivasculares Cerebrales Visibles en Imagen de Resonancia Magnética: Desarrollo de una Escala de Valoración Cualitativa y su Confiabilidad del Observador. Enfermedades Cerebrovasculares. 2015 Marzo 19;39:224-231
	15	Potter G, y otros. Espacios perivasculares ampliados (EPVS): una escala de valoración visual y guía de usuario. Guía preparada por Gillian Potter, Zoe Morris y Prof. Joanna Wardlaw (Universidad de Edimburgo).
	16	Racette B, y otros. [18F]FDOPA PET como un Endofenotipo para Estudios Vinculados con Enfermedad de Parkinson. Am J Med Genet B Neuropsychiatr Genet. 2006 Abril 5;141B(3):245-249.
	17	Grimm D, y otros. Evolución de Vector de Terapia de Gen In Vitro e In Vivo por medio de cruza de múltiples especies y reorientación de Virus Adenoasociados. Diario de Virología. 2008 Jun;5887-5911.
	18	Kem A, y otros. Identificación de un Motivo de Unión a Heparina en Cápsides Tipo 2 de Virus Adenoasociados. Diario de Virología. 2003 Oct;11072-11081.
	19	VOYAGER THERAPEUTICS – INVESTORS & MEDIA – PRESS RELEASE, “Voyager Therapeutics Anuncia Resultados Interinos Positivos de Ensayo de Fase 1b de VY-AADC01 para Enfermedad de Parkinson Avanzada, Diciembre 6, 2016, páginas 1-6.
	20	NAIDOO J, y otros. Transducción Extensiva y Propagación Mejorada de una Cápside AAV2 Modificada en el CNS Primate no Humano. Mol Ther. 2018 Jul 12 Epub antes de impresión
	21	VAN LIESHOUT LP, y otros. Una Cápside AAV6 Mutante Triple Novedosa Induce Expresión Rápida y Potente de Transgén en el Músculo y Tracto Respiratorio de Ratones. Mol Ther Meth Clin Dev 2018 Junio 15.

	22	JANKOVIC J, y otros. Seguridad y Tolerabilidad de Múltiples Dosis Ascendentes de PRX002/RG7935, un Anticuerpo Monoclonal Anti-α-Sinucleína, en Pacientes con Enfermedad de Parkinson: Un Ensayo Clínico Aleatorio. JAMA Neurol. 2018 Jun 18 Epub antes de impresión.
	23	YUN SP, y otros. Bloque de conversión de astrocito A1 por microglía es neuroprotector en modelos de enfermedad de Parkinson: Nat Med 2018 Jun 11 Epub antes de impresión.
	24	HUDRY E, y otros. Transferencia de gen eficiente al sistema nervioso central por Anc80L65 monocatenario. Mol Ther Meth Clin Dev. 2018 Jul 15
	25	DI MAIO R, y otros. Activación de LRRK2 en enfermedad de Parkinson idiopática. Sci Transl Med. 2018 Jul 25;10(451)
	26	MAN JHK, y otros. Acercamientos de reprogramación celular en terapias a base de célula y gen para enfermedad de Parkinson. J Control Liberación 2018 Jul 17;286:114-124 Epub antes de impresión.
	27	STOKER TB, y otros. Terapias regenerativas para Enfermedad de Parkinson: Una Actualización
	28	TSE LV, y otros. Dominios de función de mapeo y modificación de la proteína de activación de ensamble de virus adenoasociados. J. Virol. 2018 Jun 29:92(14).
	29	CHIEN YH, y otros. Eficacia y seguridad de terapia de gen AAV2 en niños con deficiencia de descarboxilasa de aminoácido L aromático: un ensayo de fase ½ de etiqueta abierta. Lancet Chil Adolesc Health 2017 Dic;1(4):265-273.
	30	GOWANLOCK D, y otros, Una variante de AAV diseñador permite acceso retrogrado eficiente a neuronas de proyección. Neuron. (2016) Oct 19;92(2):372-382.

Si desea adicionar información de citación de documentos de literatura no patente adicionales por favor haga clic en el botón Adicionar

FIRMA DEL EXAMINADOR

Firma del Examinador		Fecha Considerada	

*EXAMINADOR: Inicial si la referencia es considerada, bien sea que la citación esté o no de acuerdo con MPEP 609. Dibuje una línea a través de una cita si no está de conformidad y si no es considerada. Incluya copia de este formulario con la siguiente comunicación al solicitante.

[1]Ver Códigos de Tipo de Documentos de Patente de USPTO en www.uspto.gov o MPEP 901.04. [2]Ingrese la oficina que emitió el documento, por el código de dos letras (Estándar OMPI ST.3). [3]Para documentos de patente japoneses, la indicación del año del reino del Emperador debe preceder el número de serie del documento de patente.[4] Tipo de documento por los símbolos adecuados como se indica en el documento bajo el Estándar OMPI ST.16 si es posible. [5]El solicitante debe poner una marca acá si se adjunta traducción al idioma inglés.

DECLARACION DE CERTIFICACION

Por favor ver 37 CDR 1.97 y 1.98 para hacer la selección adecuada:

Que cada artículo de información contenido en la declaración de divulgación de información fue citado primero en cualquier comunicación de una oficina de patentes extranjera en una solicitud extranjera correspondiente no más de tres meses antes de la presentación de la declaración de divulgación de información. Ver 37 CFR 1.97(e)(1).

O

Que ningún artículo de información contenido en la declaración de divulgación de información fue citado en una comunicación de una oficina de patentes extranjera en una solicitud extranjera correspondiente, y, al conocimiento de la persona que firma la certificación después de hacer investigación razonable, ningún artículo de información contenido en la declaración de divulgación de información era conocido a ningún individuo designado en 37 CFR 1.56(c) más de tres meses antes de la presentación de la declaración de divulgación de información. Ver 37 CFR 1.97(e)(2).

X Ver declaración de certificación adjunta.

La tasa definida en 37 CFR 1.17(p) ha sido presentada acá.

Una declaración de certificación no es presentada acá.

FIRMA

Se requiere una firma del solicitante o representante de acuerdo con CFR 1.33, 10.18. Por favor ver CFR 1.4(d) para la forma de la firma.

Firma	/Mark J. Hanson/	Fecha (AAAA-MM-DD)	2019-02-08
Nombre	Mark J. Hanson	Número de Registro	62521

Esta recolección de información es requerida por 37 CFR 1.76. La información es requerida para obtener o conservar un beneficio por parte del público que es el de presentar (y por la USPTO para procesar) una solicitud. La confidencialidad se rige por 35 USC 122 y 37 CFR 1.14. Esta colección está calculada a tardar 1 hora en completar, incluida la recogida, preparación y presentación de la forma de hoja de datos de la aplicación completa a la USPTO. El tiempo variará dependiendo de cada caso individual. Cualquier comentario sobre la cantidad de tiempo que necesita para completar este formulario y/o sugerencias para reducir esta carga, deben ser enviados al Jefe de Información, Oficina de Patentes y Marcas de Estados Unidos, Departamento de Comercio de Estados Unidos, P.O. Box 1450, Alexandria, VA 22313-1450. NO ENVIAR DINERO O LOS FORMULARIOS A ESTA DIRECCIÓN. **ENVIAR A: Comisario de Patentes, P.O. Box 1450, Alexandria, VA 22313-1450.**

Declaración de la Ley de Privacidad

La Ley de Privacidad de 1974 (P.L. 93-579) exige que se le proporcione a usted cierta información con respecto a su presentación del formulario adjunto en relación con una solicitud de patente o patente. Por lo tanto, de conformidad con los requisitos de la Ley, sírvase tomar conocimiento de: (1) que la norma jurídica general que rige la recolección de esta información es 35 U.S.C. 2(b)(2); (2) que es voluntario proporcionar la información solicitada; y (3) que el motivo principal para el que la Oficina de Patentes y Marcas de los Estados Unidos utilizará la información es procesar o examinar los documentos presentados en relación con una solicitud de patente o patente. Si no proporciona la información requerida, es posible que la Oficina de Patentes y Marcas de los Estados Unidos no pueda procesar o examinar los documentos presentados, lo que puede causar la terminación de las actuaciones o el abandono de la solicitud o la caducidad de la patente.

La información provista por usted en este formulario estará sujeta a los siguientes usos normales:

1. La información en este formulario se tratará de manera confidencial en la medida que lo permita la Ley de Libertad de Información (5 U.S.C. 552) y la Ley de Privacidad (5 U.S.C. 552a). Se pueden divulgar registros de este sistema de registros al Departamento de Justicia para determinar si la Ley de Libertad de Información exige la divulgación de estos registros.
2. Se puede divulgar, como un uso normal de la información, un registro de este sistema de registros durante la presentación de pruebas ante un tribunal, juez inferior o tribunal administrativo, e incluso al abogado de la parte contraria durante las negociaciones para llegar a un acuerdo extrajudicial.
3. Se puede divulgar, como un uso normal de la información, un registro de este sistema de registros a un Miembro del Congreso que presente un pedido que ataña a una persona, a quien corresponde el registro, cuando dicha persona

haya solicitado la ayuda del Miembro del Congreso con respecto al contenido del registro.

4. Se puede divulgar, como un uso normal de la información, un registro de este sistema de registros a un contratista del Organismo que necesite la información para ejecutar un contrato. Las personas que reciban la información deberán cumplir con los requisitos de la Ley de Privacidad de 1974, con sus enmiendas, de conformidad con 5 U.S.C. 552a(m).
5. Se puede divulgar un registro de este sistema de registros relacionado con una solicitud internacional presentada de conformidad con el Tratado de Cooperación en Materia de Patentes, como un uso normal de la información, a la Oficina Internacional de la Organización Mundial de la Propiedad Intelectual, de conformidad con el Tratado de Cooperación en Materia de Patentes.
6. Se puede divulgar, como un uso normal de la información, un registro de este sistema de registros a otro organismo federal para los fines de una revisión de Seguridad Nacional (35 U.S.C. 181) y para una revisión de conformidad con la Ley de Energía Atómica (42 U.S.C. 218(c)).
7. Se puede divulgar, como un uso normal de la información, un registro de este sistema de registros al Administrador de Servicios Generales, o a la persona que éste designe, durante una inspección de registros llevada a cabo por la GSA como parte de la responsabilidad de ese organismo de recomendar mejoras en las prácticas y programas de administración de registros, de conformidad con 44 U.S.C. 2904 y 2906. Dicha divulgación se realizará de acuerdo con los reglamentos de la GSA que rigen la inspección de registros para este fin, y con cualquier otra directiva pertinente (es decir, de la GSA o del Departamento de Comercio). No se debe utilizar dicha divulgación para hacer determinaciones acerca de individuos.

8. Se puede divulgar, como un uso normal de la información, un registro de este sistema de registros al público ya sea después de la publicación de la solicitud de conformidad con 35 U.S.C. 122(b) o el otorgamiento de una patente de conformidad con 35 U.S.C. 151. Además, se puede divulgar un registro, sujeto a las limitaciones de 37 CFR 1.14, como un uso normal, al público si el registro fue presentado en una solicitud que fue abandonada o con respecto a la cual se dio por finalizado el procedimiento cuando se hace referencia a dicha solicitud en una solicitud publicada, una solicitud abierta a la inspección del público o una patente otorgada.
9. Se puede divulgar, como un uso normal de la información, un registro de este sistema de registros a un organismo federal, estatal o local de aplicación de la ley, si la USPTO toma conocimiento de una violación o violación potencial de una ley o reglamento.

Efficacy and safety of AAV2 gene therapy in children with aromatic L-amino acid decarboxylase deficiency: an open-label, phase 1/2 trial

Yin-Hsiu Chien, Ni-Chung Lee, Sheng-Hong Tseng, Chun-Hwei Tai, Shin-ichi Muramatsu, Barry J Byrne, Wuh-Liang Hwu

Summary

Background Aromatic L-amino acid decarboxylase (AADC) deficiency is an inherited disease that causes depletion of neurotransmitters and severe motor dysfunction in infants and children. We previously reported compassionate use of an adeno-associated virus (AAV) vector containing the human AADC gene (AAV2-hAADC) in four children with AADC deficiency (aged 4–6 years). In this study, we aimed to establish the efficacy and safety of this treatment.

Methods We did an open-label, phase 1/2 trial at the National Taiwan University Hospital (Taipei, Taiwan). We included patients who had a definitive diagnosis and clinical symptoms of AADC deficiency (hypotonia, dystonia, and oculogyric crisis), who were older than 24 months or had skull bones suitable for stereotactic surgery, and who had an anti-AAV2 antibody titre lower than 1·0 optical density. All patients received bilateral intraputaminal injections of AAV2-hAADC ($1·81\times10^{11}$ vg in total) through stereotactic brain surgery. Primary efficacy outcomes were an increase in the Peabody Developmental Motor Scales (second edition; PDMS-2) score of greater than 10 points and an increase in homovanillic acid (HVA) or 5-hydroxyindoleacetic acid (5-HIAA) concentrations in the cerebrospinal fluid 12 months after gene therapy. We assessed patients at baseline and at 3, 6, 9, and 12 months after gene therapy, and every 6 months thereafter for one further year; all patients who received the treatment were included in the analysis. We assessed for surgical complications (cerebrospinal fluid leakage and intracerebral haemorrhage) at days 3–7 after AAV2 gene therapy, and we assessed adverse events during the follow-up evaluations for 12 months. This study is registered with ClinicalTrials.gov, number NCT01395641.

Findings Ten patients (median age 2·71 years, IQR 2·46–6·35) were enrolled from Oct 1, 2014, to Dec 2, 2015. All patients tolerated the surgeries and vector injections. One patient died from influenza B encephalitis during an endemic outbreak 10 months after treatment; therefore, 9 months of data were included in the analyses for this patient. All patients met the primary efficacy endpoint: 12 months after gene therapy, PDMS-2 scores were increased by a median of 62 points (IQR 39–93; p=0·005) and HVA concentrations by a median of 25 nmol/L (IQR 11–48; p=0·012); however, there was no significant change in 5-HIAA concentrations (median difference 0, IQR 0–5; p=0·20). In total, 101 adverse events were reported, with the most common being pyrexia (16 [16%] of 101 events) and orofacial dyskinesia (ten [10%]). 12 serious adverse events occurred in six patients, including one death (treatment-unrelated encephalitis due to influenza B infection), one life-threatening pyrexia, and ten events that led to hospital admission. Transient post-gene therapy dyskinesia occurred in all patients but was resolved with risperidone. Of 31 treatment-related adverse events, only one (patient 1) was severe in intensity, and none led to hospital admission or death.

Interpretation Our findings suggest that intraputaminal injection of AAV2-hAADC is well tolerated and might improve motor development in children with AADC deficiency.

Funding AADC Research Fund at National Taiwan University Hospital and the National Research Programme for Biopharmaceuticals.

Lancet Child Adolesc Health 2017; 1: 265–73

Published Online October 23, 2017 http://dx.doi.org/10.1016/S2352-4642(17)30125-6

See Comment page 250

Department of Pediatrics and Medical Genetics (Y-H Chien MD, N-C Lee MD, Prof W-L Hwu MD), **Department of Surgery** (S-H Tseng MD), **and Department of Neurology** (C-H Tai MD), **National Taiwan University Hospital and National Taiwan University College of Medicine, Taipei, Taiwan; Division of Neurology, Department of Medicine, Jichi Medical University, Shimotsuke, Japan** (Prof S Muramatsu MD); **Center for Gene & Cell Therapy, The Institute of Medical Science, The University of Tokyo, Tokyo, Japan** (Prof S Muramatsu); **and Powell Gene Therapy Center, Department of Molecular Genetics, Department of Microbiology, and Department of Pediatrics, University of Florida, Gainesville, FL, USA** (Prof B J Byrne MD)

Correspondence to: Prof Wuh-Liang Hwu, Department of Pediatrics, National Taiwan University Hospital, Taipei 10041, Taiwan **hwuwlntu@ntu.edu.tw**

Introduction

Aromatic L-amino acid decarboxylase (AADC) deficiency is an autosomal recessive disorder caused by mutations in the *DDC* gene, which lead to defective synthesis of the neurotransmitters dopamine and serotonin.[1] Clinical manifestations of AADC deficiency include motor dysfunction (hypotonia, hypokinesia, dystonia, and oculogyric crisis), behavioural problems (irritability, mood problems, and excessive crying), autonomic dysfunction, sleep problems, and developmental delay.[2–4] Current pharmacological treatments aim to increase dopamine concentrations through inhibition of monoamine oxidase and to directly stimulate dopamine receptors via dopamine agonists.[3] However, only a small proportion of patients who have mild forms of the disease respond to drugs, which offer partial relief from motor dysfunction and oculogyric crisis.[2,3] There is an increased incidence (1 in 32 000 children)[5] of AADC deficiency in the Chinese population because of the presence of the founder mutation 714+4A→T (intervening sequence [IVS]6+4A→T) in *DDC*.[2,6,7] Patients with the homozygous IVS6+4A→T mutation, or compound heterozygous

Research in context

Evidence before this study

In 2012, we reported the first compassionate use of an adeno-associated virus (AAV) gene therapy in four children (aged 4–6 years) with aromatic L-amino acid decarboxylase (AADC) deficiency. We searched PubMed using the term "AADC deficiency" and found 83 papers (in English) published from May, 1982, to April, 2017. With the exception of our studies on gene therapy, drug treatment did not improve motor development or change the outcome of patients with severe forms of AADC deficiency. We also searched ClinicalTrials.gov on Aug 21, 2017, using the terms "brain" AND "gene therapy", and obtained 51 trials. Excluding trials involving non-genetic conditions or transplantation of haemopoietic stem cells, most trials except ours did not consistently change the outcome of the disease.

Added value of this study

After our first report in 2012, we learned how to control the adverse events of gene therapy by medication and how to do stereotactic brain surgery in young children. In this phase 1/2 trial, we treated ten patients aged 1·7–8·4 years. Patients in this study mostly exhibited mild-to-moderate post-gene therapy dyskinesia, but all improved in motor development. Therefore, our results support the efficacy and safety of AAV2 gene therapy via intraputaminal injection for AADC deficiency in a larger population, which included young children.

Implications of all the available evidence

We showed that direct injection of AAV vectors to the brain can be effective. With the development of gene therapy for the brain, an organ poorly penetrated by drugs because of the blood–brain barrier, inherited neurological diseases that were untreatable in the past now have new hopes. Because an increasing number of inherited neurological diseases will be treated and because brain damage from these diseases can be irreversible, early diagnosis has become an important issue that needs to be resolved.

IVS6+4A→T and one severe mutation, present with hypotonia and hypokinesia at several months of age. In these patients, developmental milestones are never achieved and patients do not show head control, nor can they sit or stand. Such patients usually die before 5–6 years of age from respiratory complications.[4,8,9]

Adeno-associated virus (AAV) has emerged as an attractive vector for gene therapy of single-gene diseases,[10–12] including intraputaminal injections in Parkinson's disease,[13,14] a condition characterised by secondary dopamine deficiency. The benefits of using AAV for gene therapy include long-term gene expression, absence of autonomous replication, transduction of dividing and non-dividing cells, and no pathogenicity from wild-type infections.[15] We previously reported compassionate use of an intraputaminal injection gene therapy in four patients (aged 4–6 years) with AADC deficiency.[8] In this phase 1/2 trial, we aimed to establish the efficacy and safety of this treatment.

Methods

See Online for appendix

Study design and participants

We did an open-label, phase 1/2 trial at the National Taiwan University Hospital (Taipei, Taiwan). This study was approved by the Taiwan Food and Drug Administration and the Institutional Review Board at the National Taiwan University Hospital (NTUH 200802042D). The trial was monitored by an external monitoring board for safety.

We enrolled and recruited patients only by referral from doctors or families with AADC. We included patients if they had a definitive diagnosis of AADC deficiency, including decreased concentrations of homovanillic acid (HVA) and 5-hydroxyindoleacetic acid (5-HIAA) in the cerebrospinal fluid (CSF), and the presence of at least one *DDC* pathological mutation; had clinical symptoms of AADC deficiency, including hypotonia, dystonia, and oculogyric crisis; were older than 24 months or had skull bones suitable for stereotactic surgery; and had no serious medical or neurological conditions (other than AADC deficiency) that would create unacceptable operative risk. We excluded patients with an anti-AAV2 antibody titre higher than 1·0 optical density (OD), those with obvious change in brain structure, and those who were given drugs that might interfere with the trial. Medications specific for neurotransmitter deficiency were discontinued 2 weeks after gene therapy. We obtained written informed consent from the parents.

Procedures

After baseline assessments, all patients received stereotactic surgery for transduction of an AAV2 vector containing the human AADC gene (AAV2-hAADC; now named AGIL-AADC; figure 1) at two target points for each putamen (appendix).[8] Clinical grade AAV2-hAADC was manufactured at the Powell Gene Therapy Center (University of Florida, Gainesville, FL, USA). We prepared a vector-containing solution at a concentration of $5·67\times10^{11}$ vector genomes per mL, and injected 80 µL of the solution at a rate of 3 µL/min into each target; each patient received $1·81\times10^{11}$ vector genomes of AAV2-hAADC in total. The operation was derived from deep-brain stimulation surgery, which is more often done in adults than in children.[16] We improved the fixation of the Nextframe tower (Medtronics, MN, USA) to the skull so that it could be done in young children. Patients who had post-gene therapy dyskinesia, if it was expected to bother

swallowing, were treated with oral risperidone, a mild dopamine antagonist, at 0·1–0·2 mg twice a day (total dose) as needed. We assessed developmental milestones at baseline and at 3, 6, 9, and 12 months after gene therapy, and every 6 months thereafter for one further year (appendix). We also did brain MRI and PET scans, as well as CSF analyses at baseline and 12-month follow-up.

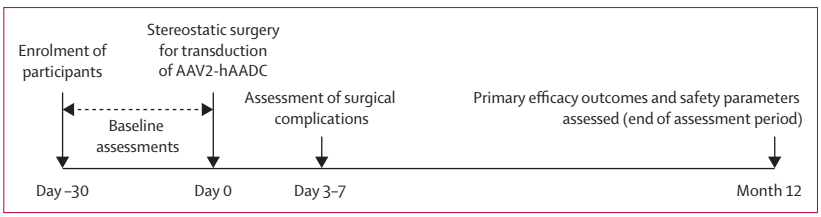


Figure 1: **Trial design**
After enrolment, we did baseline assessments over the course of 30 days. Patients were assessed at days 3–7 after surgery to monitor for surgical complications and at 12 months to evaluate efficacy and other safety parameters. AAV2-hAADC=adeno-associated virus serotype 2 vector encoding human aromatic L-amino acid decarboxylase.

Outcomes

The primary efficacy outcomes were an increase in the Peabody Developmental Motor Scales (second edition; PDMS-2) score of greater than 10 points and an increase in CSF HVA or 5-HIAA concentrations 12 months after therapy. In the PDMS-2, each item can be scored from 0 (cannot do) to 2 (does well); therefore, an increase of 10 points indicates an improvement of 5–10 items.

Secondary efficacy outcomes were bodyweight gain, increase in 6-[^{18}F]-fluoro-L-DOPA (FDOPA, a tracer for AADC) in the putamen (assessed by PET), and other developmental measurements, including the Alberta Infant Motor Scale (AIMS) and the cognitive and language subscales of the Bayley Scales of Infant and Toddler Development (third edition; Bayley-III).[17] Motor and developmental tests were done by a trained physical therapist, and the assessment process was videotaped. A second therapist scored one randomly selected video from each patient for PDMS-2. CSF HVA, 5-HIAA, and 3-*O*-methyldopa concentrations were measured by Medical Neurogenetics (Atlanta, GA, USA). Specific uptake of FDOPA indicates the conversion of L-DOPA into dopamine and therefore AADC activity. An increase in dopamine in the putamen, where dopamine acts, is considered functionally significant. We expressed as the ratio of radioactivity in the putamen to background activity using the formula (putamen-occipital lobe)/occipital lobe.

Blood and urine samples were collected for detection of anti-AAV2 antibodies and viral shedding. Serum levels of antibodies against AAV2 were determined as described.[18] For viral shedding, 150 ng of blood DNA or 1 µL of DNA extracted from urine, were assayed in triplicate by real-time polymerase chain reaction. We also asked parents to answer a questionnaire after the completion of the 12-month evaluations to evaluate (normal, slightly abnormal, or very abnormal) the current mood and the mood before gene therapy, sweating, body temperature, and oculogyric crisis of their children. This questionnaire has been used in our previous study[8] but has not been externally validated.

We assessed for surgical complications (CSF fluid leakage and intracerebral haemorrhage) at days 3–7 after AAV2 gene therapy, and we assessed adverse events during the follow-up evaluations for 12 months.

Statistical analysis

We included all participants who received the treatment in the efficacy and safety analyses. We presented results as medians with IQRs and as numbers with proportions. We analysed differences between baseline and the 12-month measurements using the Wilcoxon signed-rank test. Additionally, we analysed repeated measures of AIMS, PDMS-2, cognitive and language scores of Bayley-III, and bodyweight percentage at baseline (before surgery) and at 3, 6, 9, 12, 18, and 24 months after gene therapy using the Friedman test. We did post-hoc analysis of linear associations between treatment age and outcome using Spearman's ρ test. Additionally, we compared the data of patients in this study with natural history data of other patients with diagnosed AADC deficiency who had visited us previously (2004–16), although the comparators were not matched for age and sex.[9] We used SPSS (version 18.0) for all statistical analyses. We set the significance level for all tests at 0·05. There was no sample size calculation because of the exploratory nature of the study.

This study is registered with ClinicalTrials.gov, number NCT01395641.

Role of the funding source

The funders of the study had no role in study design, data collection, data analysis, data interpretation, or writing of the report. The corresponding author had full access to all data in the study and, with the support of the full author group, had final responsibility for the decision to submit for publication.

Results

Ten patients (five girls and five boys) were screened and enrolled from Oct 1, 2014, to Dec 2, 2015 (table 1). The median age at surgery was 2·71 years (IQR 2·46–6·35), and all participants had characteristic manifestations of AADC deficiency, including hypokinesia, dystonia, oculogyric crisis, unstable emotions and body temperature, and increased sputum. No participant had developed full head control or other more advanced gross motor skills during the observation period before enrolment (median 1·68 years, IQR 1·48–5·39). There was good correlation between the motor and developmental assessments done by the two physical therapists (n=10, r=0·90; p<0·001). All participants had very low CSF HVA (median 0 nmol/L, IQR 0–4) and 5-HIAA concentrations (0 nmol/L, 0–0), and increased

	Sex	Age at time of diagnosis (years)	Age at time of gene therapy (years)	Anti-AAV2 antibody (OD)		HVA* (nmol/L)		5-HIAA* (nmol/L)		3-O-methyldopa* (nmol/L)		PDMS-2		AIMS		Cognitive subscale of Bayley-III		Language subscale of Bayley-III	
				Baseline	Peak	Baseline	12 months	Baseline	12 months	Baseline	12 months	Baseline	12 months	Baseline	12 months	Baseline	12 months	Baseline	12 months
Patient 1	Female	0·91	6·17	0·091	1·749	5	16	0	0	432	715	12	60	1	17	14	16	14	19
Patient 2	Male	0·48	7·58	0·023	0·107	0	11	0	0	337	498	4	30	2	7	6	18	14	25
Patient 3	Female	0·85	8·42	0·088	0·833	0	10	0	0	596	660	8	51	1	10	6	11	14	26
Patient 4	Male	0·84	2·42	0·034	1·350	6	60	5	0	867	845	4	165	1	48	9	32	14	29
Patient 5	Male	0·87	2·58	0·035	0·743	0	22	0	0	617	734	15	52	1	11	14	18	16	25
Patient 6	Female	0·98	6·42	0·032	0·228	0	0	0	5	480	693	14	29	2	5	12	15	18	24
Patient 7	Male	1·98	2·58	0·021	1·411	28	ND	6	ND	680	ND	10	103†	2	27†	8	29†	17	25†
Patient 8	Female	2·72	2·83	0·019	0·783	0	48	0	0	761	803	6	114	1	23	10	25	18	26
Patient 9	Male	0·63	2·08	0·031	0·887	0	41	0	37	1149	990	10	103	1	25	9	29	16	26
Patient 10	Female	0·03	1·67	0·035	1·282	0	57	5	27	534	329	12	87	4	21	10	21	18	27

*Normal ranges of homovanillic acid for children aged 0·5–2 years are 294–1115 nmol/L, 2–5 years are 233–928 nmol/L, and 5–10 years are 218–852 nmol/L; 5-hydroxyindoleacetic acid for those aged 0·5–2 years are 129–520 nmol/L, 2–5 years are 74–345 nmol/L, and 5–10 years are 66–388 nmol/L; and 3-O-methyldopa for those aged 0–2 years are <300 nmol/L, 2–5 years are <150 nmol/L, and 5–10 years are <100 nmol/L. The detection limit of homovanillic acid and 5-hydroxyindoleacetic acid is 5 nmol/L. †Data from assessments at month 9. AAV2=adeno-associated virus serotype 2. OD=optical density. HVA=homovanillic acid. 5-HIAA=5-hydroxyindoleacetic acid. PDMS-2=Peabody Developmental Motor Scales (second edition). AIMS=Alberta Infant Motor Scale. Bayley-III=Bayley Scale of Infant and Toddler Development (third edition). ND=not done.

Table 1: **Patient demographics and outcome measurements**

dried blood spot 3-*O*-methyldopa and plasma prolactin concentrations (data not shown). *DDC* mutations included IVS6+4A→T in 16 chromosomes (80% of all mutations) and 1058T→C (Leu353Pro; patient 4), 1297dupA (Ile433Asn frame shift*60; patient 6), 179T→C (Val60Ala; patient 7), and 286G→A (Gly96Arg; patient 8) in one chromosome each. No participants had high anti-AAV2 antibody concentrations (median OD 0·033, IQR 0·025–0·035). Patient 7 died from influenza B encephalitis during an endemic outbreak 10 months after treatment, and only 9 months of follow-up data from this patient were included in the analyses.

All patients had very low PDMS-2 (≤15) and AIMS (≤4) raw scores before treatment. All surgeries were completed without complications or intracerebral haemorrhage, as examined by both immediate postoperative CT scans and follow-up MRIs 3–7 days after surgery. Patients stayed for a median of 8 days (IQR 6–10) in the hospital after surgery. All patients began to have transient uncoordinated movement in their mouth and extremities 2–3 weeks after gene therapy, which was classified as post-gene therapy transient dyskinesia or orofacial dyskinesia. Eight (80%) of ten patients received risperidone for 4–12 weeks after gene therapy, which relieved orofacial dyskinesia but did not decrease the extremity movements of patients. The other two patients only had mild dyskinesia and never received risperidone. All patients started to move their arms and mouths 2–3 weeks after gene therapy, and new motor skills were observed 2–3 months later.

Motor function continuously improved during the post-gene therapy follow-up period, and all patients met the primary efficacy outcome of an increase of greater than 10 points on the PDMS-2 at 12 months. Significant increases in PDMS-2 (median increase 62 points, IQR 39–93; p=0·005) and AIMS (17 points, 9–24; p=0·005) scores were observed 12 months after gene therapy (figure 2). All patients showed improvements on the cognitive (median 12 [IQR 4–19]; p=0·005) and language (9 [8–11]; p=0·005) subscales of Bayley-III. Analysis on the repeated measures at 3, 6, 9, 12, and 18 months showed significant differences compared with the baseline for AIMS, PDMS-2, cognitive, and language scales (p<0·001 in all four measures; appendix). Table 2 summarises the developmental milestones of the patients after gene therapy. However, the increases were partially driven by the substantial improvement in patient 4 (appendix).

Patient 4 had the largest gain in all four scales at 12 months after gene therapy: PDMS-2 increased from 4 to 165 points (equivalent to a change from 1 month to 14 months of developmental age in the stationary subscale and from 0 months to 8 months in the locomotor subscale), AIMS increased from 1 to 48 (ie, from 0 months to 10 months), cognitive scores from 9 to 32 (ie, from 2·3 months to 8 months), and language scores from 14 to 29 (ie, from 3·3 months to 13 months

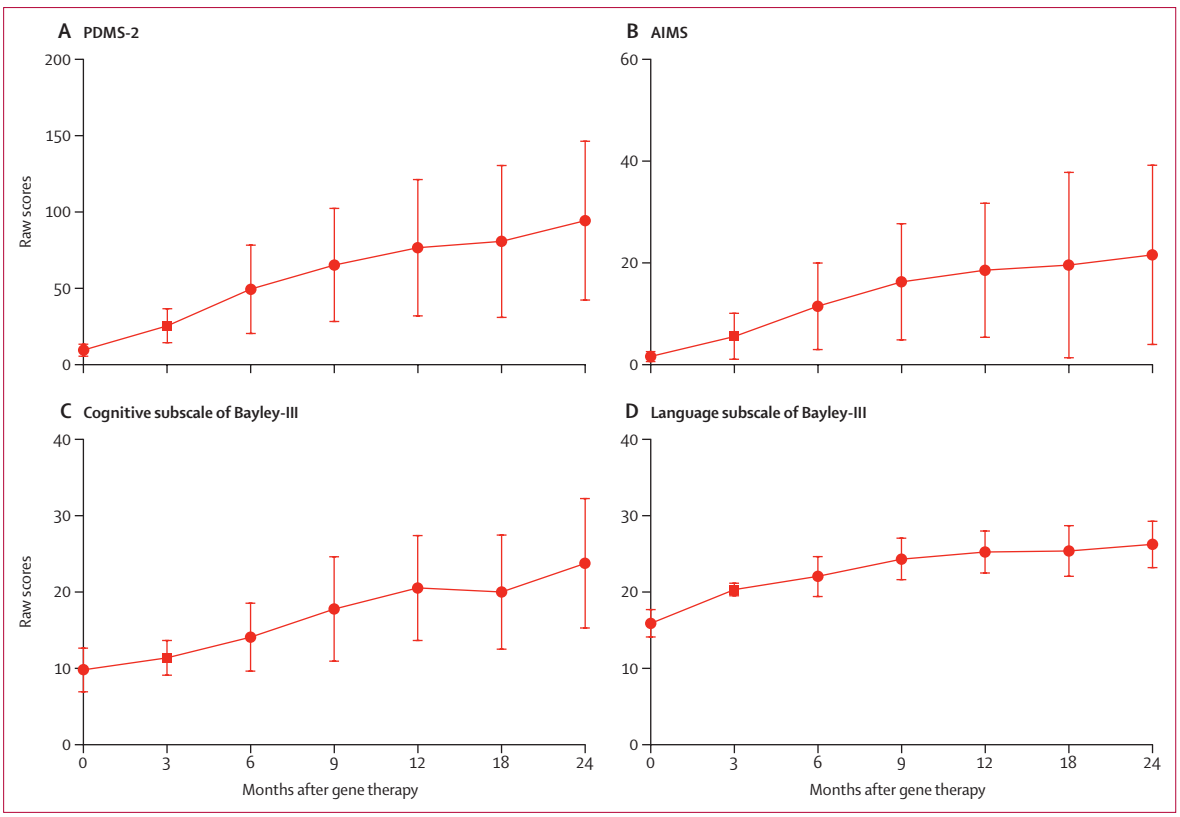


Figure 2: **Improvements in developmental scales after gene therapy**
Data are mean scores, and error bars are standard deviation. PDMS-2=Peabody Developmental Motor Scales (second edition). AIMS=Alberta Infant Motor Scale. Bayley-III=Bayley Scale of Infant and Toddler Development (third edition).

in receptive language and from 5 months to 12 months in expressive language; video 1). Additionally, patient 4 stood with support and moved around at the age of 5 years (2·58 years after gene therapy). Patient 7 showed the second best overall results but unfortunately died 10 months after gene therapy because of an incidental viral infection (video 2). The youngest patient (patient 10) was able to say a few words at 3·3 years of age, although with severe speech apraxia. Most of the parents thought their children had a better mood (six [60%] of ten), less sweating (nine [90%]), more stable body temperature (eight [80%]), and less severe oculogyric crisis (nine [90%]) after gene therapy.

In the comparator group of 27 patients (median age at last visit or before enrolment into past clinical trials 4·42 years, IQR 1·57–3·86), all had *DDC* mutations and IVS6+4A→T mutations represented 40 (74%) of 54 mutations. Most received medical care, and 26 (96%) of 27 had never developed full head control, nor were they able to sit or stand.

CSF analyses before and 12 months after gene therapy were available for nine patients (as patient 7 died before the second assessment). After gene therapy, eight (89%) of the nine patients (except patient 6) had an increase in CSF HVA concentrations (median difference 25 nmol/L, IQR 11–48; p=0·012; appendix). Six of ten patients received multiple CSF HVA analyses before gene therapy (eg, at the time of diagnosis), and all of these analyses revealed very low HVA concentrations (data not shown). There was no significant change in 5-HIAA (median difference 0, IQR 0–5; p=0·20) and 3-*O*-methyldoapa concentrations (64, –22 to 161; p=0·26) between baseline and 12 months after gene therapy for the nine patients.

See **Online** for videos

Before participation in this study, patients had poor or no weight gain. After gene therapy, all patients gained bodyweight (median gain 3 kg, IQR 1·7–3·9; p=0·005; figure 3). Analysis on the repeated measures at 3, 6, 9, and 12 months showed significant differences in bodyweight percentile compared with baseline (p=0·042; appendix). All but patient 6 ate via mouth, and all but patient 9 gained bodyweight to the normal value for their age.

At baseline, the PET scans of all patients revealed barely visible or completely absent uptake in the putamen. However, 12 months after gene therapy, signal uptake in the putamen could be clearly visualised for the nine patients who completed PET scans (figure 4; the appendix shows the full analysis). The median specific uptake of FDOPA increased from 0·20 (IQR 0·17–0·21) at baseline to 0·59 (0·44–0·61) after gene therapy (p=0·008; appendix).

	Age at time of gene therapy (years)	Baseline assessment	Assessment at 12 months after gene therapy	Latest assessment after gene therapy
Patient 1	6·17	No head control	Partial head control	Assessed at age 8·9 years; sits in stroller and reaches for toy with hands
Patient 2	7·58	No head control	Partial head control	Assessed at age 10·4 years; sits in stroller and reaches for toy with hands
Patient 3	8·42	No head control	Partial head control	Assessed at age 11·0 years; sits in stroller and reaches for toy with hands
Patient 4	2·42	No head control	Good head control, sit without support, stand with support	Assessed at age 5·0 years; stands with support and moves around, stands without support briefly, learning to walk, eats with hands
Patient 5	2·58	No head control	Good head control, sit with support briefly	Assessed at age 5·1 years; sits with support
Patient 6	6·42	No head control	Partial head control	Assessed at age 8·9 years; sits in stroller and reaches for toy with hands
Patient 7	2·58	No head control	Good head control, sit with support briefly*	..
Patient 8	2·83	No head control	Good head control, sit with support briefly	Assessed at age 5·1 years; sits well, stands with support, eats with hands
Patient 9	2·08	No head control	Good head control, sit with support briefly	Assessed at age 3·8 years; sits with support, eats with hands
Patient 10	1·67	No head control	Good head control, sit with support briefly	Assessed at age 3·3 years; sits well and moves around, learning to stand, eats with hands, can say up to 20 words

*Patient 7 died at age 3·4 years (10 months after gene therapy).

Table 2: **Developmental assessments**

Post-hoc analysis revealed that age at gene therapy was not correlated with the baseline AIMS score (r=–0·094; p=0·80), but was negatively correlated with 12-month AIMS (r=–0·72; p=0·02), PDMS-2 (r=–0·67; p=0·035), cognitive scores (r=–0·75; p=0·012), and HVA concentrations (r=–0·83; p=0·005; appendix). Only the six patients in the younger group (<3 years) showed significant improvement in PDMS-2, AIMS, cognitive, and language scores, as well as PET uptake, bodyweight, and HVA concentrations (appendix).

The viral genome was not detectable in the blood or urine of any patient at any time after gene therapy. Anti-AAV2 antibodies increased after gene therapy in all patients, peaking at 3–6 months and then decreased (appendix p 5). The median peak antibody OD at 3–6 months was 0·887 (IQR 0·753–1·333); in an exploratory analysis, anti-AAV2 antibody titre did not correlate with the increase in PDMS-2 (r=0·62; p=0·056) or cognitive scores (r=0·22; p=0·53).

In total, 101 adverse events were reported, with each patient having 3–16 events (median 12 events, IQR 7–12; table 3). 57 (56%) of 101 events were mild and 41 (41%) were moderate in intensity; however, 12 serious adverse events occurred in six patients: one event led to death, one was life threatening, and ten led to admissions to hospital. Patient 7 died of influenza B encephalopathy during an endemic outbreak of this infection; this event was not attributed to the gene therapy. The most common adverse event was pyrexia (16 [16%] of 101 events) followed by orofacial dyskinesia (ten [10%]). Transient post-gene therapy dyskinesia occurred in all patients but was resolved with risperidone. In total, 31 (31%) of 101 events were possibly related to gene therapy, but only one (patient 1) was classified as severe in intensity and none led to admission to hospital or death.

Discussion

Results from our phase 1/2 trial show that intraputaminal injection of AAV2-hAADC is well tolerated and might improve motor development in children with AADC deficiency. Compared with our previous report of compassionate use of AAV2-hAADC ($1·6\times10^{11}$ vg per patient) in four patients in 2012,[8] this trial has a larger patient population and included younger patients. Among the four patients (ie, CU-1 to CU-4) in our previous study, severe post-gene therapy dyskinesia occurred in two patients: CU-3 required nasogastric tube feeding for 3 months and CU-2 showed an increased frequency of apnoea episodes.[8] Efficacy was also variable: CU-1 (treated at age 4·25 years) was able to sit 12 months after gene therapy, and could stand with support and eat with their hands at age 11·7 years. By contrast, CU-3, who was treated at a similar age (4·50 years) as CU-1, could only sit in a stroller at age 11·9 years. In comparison, all 10 patients in this study mostly had mild-to-moderate post-gene therapy dyskinesia; all of them, especially the younger patients, had clinical benefits, as shown by functional measurements on several independent motor scales, PET imaging, assays of CSF neurochemical concentrations, and relief of symptoms. The highest post-gene therapy CSF HVA concentration (which reflects the average concentration in the whole brain) achieved in our study increased to 25% of the lower end of the normal range, and PET scans showed substantial dopamine production in the putamen. In a phase 1/2 trial of intracerebral injection gene therapy in mucopolysaccharidosis type IIIA,[12] 87 emergent adverse events were recorded in four patients. Therefore, compared with other direct brain-targeted gene therapies,[10,12–14] our gene therapy was well tolerated and had promising efficacy.

In our exploratory post-hoc analysis, patients younger than age 3 years showed higher CSF HVA concentrations and better functional recovery following gene therapy than older patients. In a phase 1 trial of *RPE65* gene therapy for Leber's congenital amaurosis, early treatment before retinal cell degeneration led better vision.[11] Neuronal plasticity might also decrease with age.[19] Therefore, gene therapy might have greater benefits if

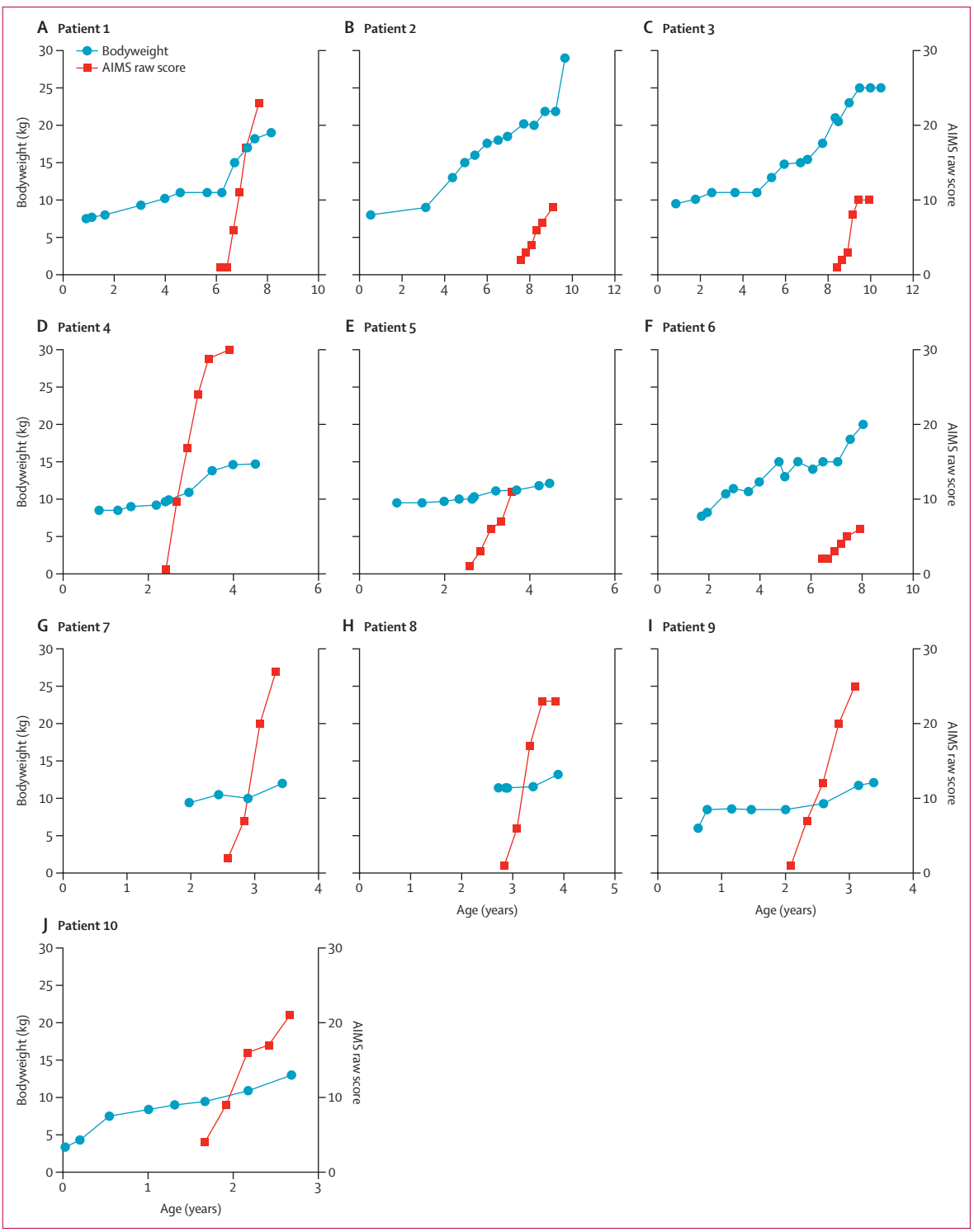


Figure 3: **Bodyweight and AIMS raw scores**
AIMS was done only after enrolment; therefore, the first datapoint of AIMS indicates the time of gene therapy. AIMS=Alberta Infant Motor Scale.

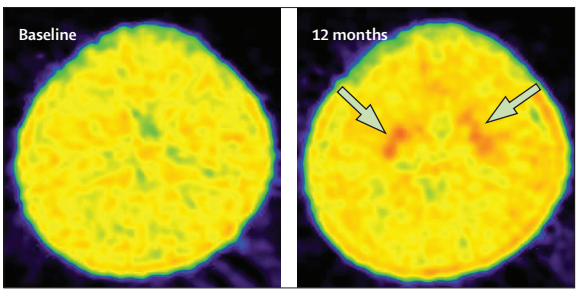


Figure 4: **FDOPA-PET images of patient 2**
FDOPA uptake in the bilateral putamen was barely visible at baseline (0 months) but was clearly visible (arrows) after gene therapy (12 months). See appendix for PET images of other patients. FDOPA=6-[^{18}F]-fluoro-L-DOPA.

	Number of patients	Event count
Adverse events*		
Pyrexia	8	16 (16%)
Orofacial dyskinesia†	9	10 (10%)‡
Diarrhoea	7	9 (9%)
Pneumonia or bronchopneumonia	7	9 (9%)‡
Dyskinesia†	8	8 (8%)
Insomnia†	4	5 (5%)
Upper gastrointestinal bleeding	3	5 (5%)
Hypotension	3	3 (3%)
Acute gastroenteritis	3	3 (3%)
Feeding difficulty†	3	3 (3%)
Increased saliva†	3	3 (3%)
Cerebral spinal fluid leakage†	2	2 (2%)
Hypoglycaemia†	1	1 (1%)
Encephalitis due to influenza B infection	1	1 (1%)‡
Total	10	101 (100%)
Serious adverse events		
Death by encephalitis due to influenza B infection	1	1 (8%)
Life-threatening pyrexia	1	1 (8%)
Admission to hospital	6	10 (84%)§
Total	6	12 (100%)

*Reported in three or more patients or a frequency >5%, or study-related or serious adverse event. †Study-related adverse event. ‡One event was classified as severe in intensity. All the other adverse events were mild to moderate in intensity. §Serious adverse event counts of bronchopneumonia or pneumonia (n=4), pyrexia (n=1), acute gastroenteritis (n=1), hypovolaemic shock (n=1), dehydration (n=1), pneumonia with respiratory failure (n=1), and diarrhoea (n=1).

Table 3: **Adverse events and treatment-emergent serious adverse events**

administered early. The gene therapy approach used in this study involved intraputaminal injection of the AAV2 vector. Because the substantia nigra dopaminergic cells send neural terminals to release dopamine in the putamen, direct replenishment of dopamine in the putamen has been shown to be safe and effective.[13,14] Injection in the substantia nigra, a brain stem structure, might have a higher risk than intraputaminal injection. Substantia nigra dopaminergic neurons might also be susceptible to protein overexpression.[20]

AAV vectors have a low risk of viral integration into the host genome,[21,22] and AAV2 is distinct from other serotypes: it shows substantial neuronal tropism, and the transduction of non-dividing neuronal cells further decreases the risk of vector-induced carcinogenesis.[23,24] In a primate model of Parkinson's disease, AAV2 vector delivered to the putamen yielded sustained behavioural recovery for 15 years.[25] Of the four patients we treated previously,[8] three (CU-1, CU-3, and CU-4) are still alive at present; they improved during the first 2 years after treatment and were stable thereafter, and PET scans done at 5 years after gene therapy confirmed the presence of AADC enzyme activity in the putamen (data not shown).

Our study has several limitations. First, the treatment was restricted to patients aged roughly 2 years because of limitations associated with surgical equipment. Second, because of the severity of this disease and the invasiveness of the procedure used, we did not use a randomised or placebo-controlled design. However, our patient cohort had similar genotypes to the historical comparator group,[9] enabling us to show gene therapy-induced changes in patient outcomes. Third, we did not do a dose-escalation investigation and simply used a dosage similar to the high-dose treatment in AAV2-hAADC gene therapy for Parkinson's disease.[13] In that study, high-dose treatment was more effective than low-dose treatment, and therefore we did not consider it necessary to study the low-dose treatment.[13] Transient orofacial dyskinesia after gene therapy, which was also seen in gene therapy for Parkinson's disease,[13] was probably due to hypersensitivity of dopamine receptors and might prevent further increase in dose. In the current trial, we expected a large variation in patient age, which made it difficult to further assess dose effect. Fourth, we targeted only the putamen. To replenish neurotransmitter production in other areas of the brain or in the body, the delivery method will need to be modified.[26] Fifth, the questionnaire we used to assess mood, sweating, temperature, and oculogyric crisis has not been externally validated.

In conclusion, our findings show the efficacy and safety of AAV2-hAADC for children with AADC deficiency. A phase 2b trial (NCT02926066) is ongoing to further assess the safety and efficacy of AAV2-hAADC in a larger patient population with dose escalation. We are also developing a systemic treatment to replenish neurotransmitter production in the whole brain and the autonomic nervous system in the body.[26] Although AADC deficiency is a rare disease, the gene therapy technology developed in this disease could be applicable to other conditions.

Contributors
Y-HC, N-CL, and W-LH designed and conducted the study. Y-HC did the data analysis. Y-HC and W-LH wrote the manuscript. S-HT operated the surgeries and C-HT designed the injection trajectory. SM and BJB contributed to vector production and technology support. All authors contributed to the interpretation of the results, reviewed and critically revised the article, and approved the final version of the article for submission.

Declaration of interests
SM has received grants and personal fees from Gene Therapy Research Institution, outside the submitted work. W-LH has received grants from the National Research Programme for Biopharmaceuticals and the AADC Research Fund at National Taiwan University Hospital (Taipei, Taiwan) during the conduct of the study; grants from gene therapy for AADC deficiency licensing to Agilis Biotherapeutics and grants from Agilis Biotherapeutics outside the submitted work. Additionally, W-LH has a pending patent for gene therapy for AADC deficiency. All other authors declare no competing interests.

Acknowledgments
This study was funded by the AADC Research Fund at National Taiwan University Hospital (MG364) and the National Research Programme for Biopharmaceuticals (MOST 103-2325-B-002-051). We thank the patients and their families for their participation in this study and the doctors who referred patients to us. We thank Toshiharu Nagatsu (Fujita Health University School of Medicine, Aichi, Japan) for providing *DDC* cDNA and Mika Ito and Naomi Takino (Jichi Medical University, Shimotsuke, Japan) for the antibody assay.

References

1 Hyland K, Clayton PT. Aromatic amino acid decarboxylase deficiency in twins. *J Inherit Metab Dis* 1990; **13:** 301–04.
2 Brun L, Ngu LH, Keng WT, et al. Clinical and biochemical features of aromatic L-amino acid decarboxylase deficiency. *Neurology* 2010; **75:** 64–71.
3 Pons R, Ford B, Chiriboga CA, et al. Aromatic L-amino acid decarboxylase deficiency: clinical features, treatment, and prognosis. *Neurology* 2004; **62:** 1058–65.
4 Wassenberg T, Molero-Luis M, Jeltsch K, et al. Consensus guideline for the diagnosis and treatment of aromatic L-amino acid decarboxylase (AADC) deficiency. *Orphanet J Rare Dis* 2017; **12:** 12.
5 Chien YH, Chen PW, Lee NC, et al. 3-*O*-methyldopa levels in newborns: result of newborn screening for aromatic L-amino-acid decarboxylase deficiency. *Mol Genet Metab* 2016; **118:** 259–63.
6 Lee HF, Tsai CR, Chi CS, Chang TM, Lee HJ. Aromatic L-amino acid decarboxylase deficiency in Taiwan. *Eur J Paediatr Neurol* 2009; **13:** 135–40.
7 Tay SK, Poh KS, Hyland K, et al. Unusually mild phenotype of AADC deficiency in 2 siblings. *Mol Genet Metab* 2007; **91:** 374–78.
8 Hwu WL, Muramatsu S, Tseng SH, et al. Gene therapy for aromatic L-amino acid decarboxylase deficiency. *Sci Transl Med* 2012; **4:** 134ra61.
9 Hwu WL, Chien YH, Lee NC, Li MH. Natural history of aromatic L-amino acid decarboxylase deficiency in Taiwan. *JIMD Rep* 2017; published online Aug 31. DOI:10.1007/8904_2017_54.
10 Leone P, Shera D, McPhee SW, et al. Long-term follow-up after gene therapy for Canavan disease. *Sci Transl Med* 2012; **4:** 165ra3.
11 Maguire AM, High KA, Auricchio A, et al. Age-dependent effects of *RPE65* gene therapy for Leber's congenital amaurosis: a phase 1 dose-escalation trial. *Lancet* 2009; **374:** 1597–605.
12 Tardieu M, Zerah M, Husson B, et al. Intracerebral administration of adeno-associated viral vector serotype rh.10 carrying human SGSH and SUMF1 cDNAs in children with mucopolysaccharidosis type IIIA disease: results of a phase I/II trial. *Hum Gene Ther* 2014; **25:** 506–16.
13 Mittermeyer G, Christine CW, Rosenbluth KH, et al. Long-term evaluation of a phase 1 study of AADC gene therapy for Parkinson's disease. *Hum Gene Ther* 2012; **23:** 377–81.
14 Muramatsu S, Fujimoto K, Kato S, et al. A phase I study of aromatic L-amino acid decarboxylase gene therapy for Parkinson's disease. *Mol Ther* 2010; **18:** 1731–35.
15 Grieger JC, Samulski RJ. Adeno-associated virus vectorology, manufacturing, and clinical applications. *Methods Enzymol* 2012; **507:** 229–54.
16 Air EL, Ostrem JL, Sanger TD, Starr PA. Deep brain stimulation in children: experience and technical pearls. *J Neurosurg Pediatr* 2011; **8:** 566–74.
17 Liao HF, Yao G, Wang TM. Concurrent validity in Taiwan of the Comprehensive Developmental Inventory for Infants and Toddlers who were full-term infants. *Percept Mot Skills* 2008; **107:** 29–44.
18 Ito T, Yamamoto S, Hayashi T, et al. A convenient enzyme-linked immunosorbent assay for rapid screening of anti-adeno-associated virus neutralizing antibodies. *Ann Clin Biochem* 2009; **46:** 508–10.
19 Soiza-Reilly M, Azcurra JM. Developmental striatal critical period of activity-dependent plasticity is also a window of susceptibility for haloperidol induced adult motor alterations. *Neurotoxicol Teratol* 2009; **31:** 191–97.
20 Albert K, Voutilainen MH, Domanskyi A, Airavaara M. AAV vector-mediated gene delivery to substantia nigra dopamine neurons: implications for gene therapy and disease models. *Genes* 2017; **8:** E63.
21 Gil-Farina I, Fronza R, Kaeppel C, et al. Recombinant AAV integration is not associated with hepatic genotoxicity in nonhuman primates and patients. *Mol Ther* 2016; **24:** 1100–05.
22 Nakai H, Yant SR, Storm TA, Fuess S, Meuse L, Kay MA. Extrachromosomal recombinant adeno-associated virus vector genomes are primarily responsible for stable liver transduction in vivo. *J Virol* 2001; **75:** 6969–76.
23 Watakabe A, Ohtsuka M, Kinoshita M, et al. Comparative analyses of adeno-associated viral vector serotypes 1, 2, 5, 8 and 9 in marmoset, mouse and macaque cerebral cortex. *Neurosci Res* 2015; **93:** 144–57.
24 Cearley CN, Vandenberghe LH, Parente MK, Carnish ER, Wilson JM, Wolfe JH. Expanded repertoire of AAV vector serotypes mediate unique patterns of transduction in mouse brain. *Mol Ther* 2008; **16:** 1710–18.
25 Sehara Y, Fujimoto KI, Ikeguchi K, et al. Persistent expression of dopamine-synthesizing enzymes 15 years after gene transfer in a primate model of Parkinson's disease. *Hum Gene Ther Clin Dev* 2017; **28:** 74–79.
26 Lee NC, Muramatsu S, Chien YH, et al. Benefits of Neuronal preferential systemic gene therapy for neurotransmitter deficiency. *Mol Ther* 2015; **23:** 1572–81.

Author Manuscript

Author Manuscript

Author Manuscript

Author Manuscript

HHS Public Access

Author manuscript

Sci Transl Med. Author manuscript; available in PMC 2019 January 24.

Published in final edited form as:

Sci Transl Med. 2018 July 25; 10(451): . doi:10.1126/scitranslmed.aar5429.

A Central Role for LRRK2 in Idiopathic Parkinson Disease

Roberto Di Maio[1,2,3], **Eric K. Hoffman**[1,2], **Emily M. Rocha**[1,2], **Matthew T. Keeney**[1,2], **Laurie H. Sanders**[1,2,4], **Briana R. De Miranda**[1,2], **Alevtina Zharikov**[1,2], **Amber Van Laar**[1,2], **Antonia Stepan**[5], **Thomas A. Lanz**[5], **Julia K. Kofler**[6], **Edward A. Burton**[1,2,7], **Dario R. Alessi**[8], **Teresa G. Hastings**[1,2], and **J. Timothy Greenamyre**[1,2,7,†]

[1]Pittsburgh Institute for Neurodegenerative Diseases, University of Pittsburgh, Pittsburgh, Pennsylvania. [2]Department of Neurology, University of Pittsburgh, Pittsburgh, Pennsylvania. [3]Ri.MED Foundation, Palermo, Italy. [4]Department of Neurology, Duke University, Durham, North Carolina. [5]Worldwide Medicinal Chemistry, Pfizer Worldwide Research and Development, Cambridge, Massachusetts. [6]Department of Pathology, University of Pittsburgh, Pittsburgh, Pennsylvania. [7]Geriatric Research, Education and Clinical Center, VA Pittsburgh Healthcare System, Pittsburgh, Pennsylvania. [8]MRC Protein Phosphorylation and Ubiquitylation Units, University of Dundee, Dundee, Scotland.

SUMMARY

Abnormally increased kinase activity due to mutations in the leucine rich repeat kinase 2 (LRRK2) gene is the cause of Parkinson disease (PD) in about 3–4% of people with the disease. We now show that, in the brains of individuals with idiopathic PD, LRRK2 kinase activity is aberrantly increased in vulnerable dopamine neurons by oxidative mechanisms involving α-synuclein and mitochondrial impairment – and this causes endolysosomal dysfunction and accumulation of phosphorylated α-synuclein. Thus, independent of mutation, activation of LRRK2 kinase activity contributes importantly to pathogenesis, suggesting inhibition of LRRK2 kinase activity will be useful for the majority of PD patients.

Abstract

Missense mutations in leucine-rich repeat kinase 2 (LRRK2) cause familial Parkinson disease (PD); however, the role of wildtype LRRK2 in idiopathic PD (iPD) is unclear. Here, we show that wildtype LRRK2 kinase activity is selectively enhanced in substantia nigra dopamine neurons in idiopathic PD and two different animal models of the disease. This occurs through ROS signaling, resulting in phosphorylation of the LRRK2 substrate Rab10 and other downstream consequences including abnormalities of mitochondrial protein import and lysosomal function. Overall, our work shows that, independent of mutations, wildtype LRRK2 plays a key role in idiopathic PD. LRRK2-directed therapeutics may therefore be useful for most people with PD.

[†]**Correspondence:** J. Timothy Greenamyre, University of Pittsburgh, 3501 Fifth Avenue, Suite 7039, Pittsburgh, PA 15260, Tel: 412-648-9793, Fax: 412-648-9766, jgreena@pitt.edu.

Competing interests: Greenamyre briefly held an advisory position at Pfizer. Otherwise, the authors declare that they have no competing financial interests.

Data and Materials Availability: JTG received the PF-360 compound from Pfizer and is not authorized to distribute it.

Author Manuscript Author Manuscript Author Manuscript Author Manuscript

INTRODUCTION

Parkinson's disease (PD) is a common neurodegenerative disease that results in motor impairment, cognitive and psychiatric symptoms and autonomic dysfunction (1). While numerous gene mutations are known to cause familial PD, about 90% of cases are "idiopathic" (iPD). LRRK2 missense mutations are the most common cause of autosomal dominant PD, and may account for about 3% of cases overall (2, 3). The *LRRK2* locus also contains a risk factor for iPD (4), but the role of LRRK2 in typical iPD is unknown. It is generally believed that the common missense mutations in LRRK2 confer a toxic gain-of-function and increased LRRK2 kinase activity has been strongly implicated in pathogenesis (5). Among the kinase substrates of LRRK2 are a subset of the Rab GTPases, including Rab10, which has been implicated in maintenance of endoplasmic reticulum, vesicle trafficking and autophagy (6). LRRK2-induced phosphorylation of Rab10 inhibits its function by preventing binding to Rab GDP-dissociation inhibitor factors necessary for membrane delivery and recycling. As such, aberrantly enhanced LRRK2 kinase activity is likely associated with reduced activity of Rab10 and its effectors.

Assessment of the kinase activity state of LRRK2 under various conditions has been somewhat cumbersome, although there appears to be a growing consensus that autophosphorylation at Ser1292 correlates with activity (7, 8). Phosphoserine1292 (pS1292) has generally been detected by western blotting rather than immunocytochemistry, which limits anatomical or cellular resolution. LRRK2 is believed to be a rather low-abundance protein, and efforts to detect it immunocytochemically sometimes rely on high antibody concentrations, which may reduce specificity. This problem may be compounded for pS1292 when only a fraction of the total (small) pool of LRRK2 is phosphorylated. The activity of LRRK2 is also regulated by its interaction with 14-3-3 proteins, whose binding to LRRK2 requires phosphorylation at LRRK2 serine residues 910 and 935 (9, 10), which are not autophosphorylation sites. Although the binding of LRRK2 to 14-3-3 protein is associated with reduced kinase activity (11), this interaction can be disrupted by oxidative stressors, including H_2O_2 (12). The interaction between LRRK2 and 14-3-3 has generally been assessed by co-immunoprecipitation. A critical barrier to understanding the role of LRRK2 in iPD has been the absence of a practical, sensitive, high-resolution assay for its activation state. We have developed and validated novel proximity ligation (PL) assays with excellent anatomical resolution that can rapidly provide information regarding activation state, cellular localization and physiological regulators of LRRK2. The assay is based on (i) S1292 phosphorylation and (ii) dissociation of 14-3-3 from LRRK2. Using this and other assays, we provide evidence that LRRK2 is activated oxidatively by mitochondrial impairment or α-synuclein overexpression and that it plays a central role in iPD pathogenesis by regulating autophagy and pSer129-α-synuclein levels.

RESULTS

Assay development and validation

As a LRRK2 autophosphorylation site, pSer1292 reflects the activity of LRRK2 *per se*. As such, we developed a proximity ligation assay to amplify the signal and increase the specificity of an antibody recognizing the pSer1292 epitope of the protein. For the PL assay,

Author Manuscript Author Manuscript Author Manuscript Author Manuscript

we paired the anti-pSer1292 antibody with a validated antibody directed against an epitope in the COR domain of the protein. In this way, the signal of the anti-pSer1292 antibody was amplified and detected only if it was in proximity to the anti-COR domain antibody (i.e., specific LRRK2 pSer1292 signals were amplified, whereas potential signals from non-specific or off-target antibody binding were filtered out by the PL assay). A second PL assay assessed the interaction between LRRK2 and 14-3-3, whose binding to LRRK2 is associated with reduced activity. Thus, the PL assays were designed such that LRRK2 activity should be associated with a strong pSer1292 signal and a weak 14-3-3 signal; conversely, when LRRK2 is inactive there should be little pSer1292 signal and a robust 14-3-3 signal.

To validate the assays, we used wildtype (WT), $LRRK2^{G2019S/G2019S}$ and $LRRK2^{-/-}$ human embryonic kidney- (HEK-) 293 cells, obtained by CRISPR/Cas9 gene editing. In WT cells, there was little pSer1292 signal and a strong 14-3-3 PL signal (figure 1A, B, D, E). The G2019S mutation is known to cause increased LRRK2 kinase activity (5, 6). Accordingly, in $LRRK2^{G2019S/G2019S}$ cells, there was a bright pSer1292 signal and loss of the 14-3-3 interaction. No signal in either PLA was seen in cells lacking LRRK2 (figure 1A, B, D, E), further establishing the specificity of the assays. The small GTPase, Rab10, has recently been shown to be directly phosphorylated at Thr73 by LRRK2 (6). Using a specific pThr73-Rab10 antibody, we found low levels of phosphorylated Rab10 in WT cells, and much higher levels in $LRRK2^{G2019S/G2019S}$ cells, in keeping with increased kinase activity of the mutant protein (figure 1A, C, D). After assay development, validation included blinded analysis and correct identification of all 3 cell lines with these assays alone. Using the selective LRRK2 kinase inhibitors, GNE-7915 and MLi-2 (13), in dose-response studies, we found that LRRK2 activation state, assessed by pSer1292 PL signal, correlated closely with phosphorylation of its substrate, Rab10 (figure 1F, G). We next looked at LRRK2 activation state in patient-derived lymphoblastoid cell lines. Relative to cells derived from a healthy age-matched control, in a LRRK2 G2019S mutation carrier, there was marked elevation of the pSer1292 signal and titration with the selective LRRK2 kinase inhibitor, GNE-7915, dose-dependently reduced the pSer1292 PL and pThr73-Rab10 signals in parallel (figure 1H).

To summarize, basal kinase activity of endogenous WT LRRK2, assessed by pSer1292 PL and pThr-Rab10 immunoreactivity was low. This was associated with a strong 14-3-3 PL signal, suggesting a significant interaction with 14-3-3 protein. In cells harboring the pathogenic G2019S mutation, LRRK2 was highly activated (strong pSer1292 PL signal and elevated levels of Rab10 phosphorylation) and there was loss of the 14-3-3 interaction. LRRK2 activation as evaluated by pSer1292 PL and pThr-Rab10 immunoreactivity, was reversed by the LRRK2 kinase inhibitors, GNE-7915 and MLi-2, at appropriate concentrations.

Endogenous, wildtype LRRK2 is activated in idiopathic PD

Conventional assays of LRRK2 activity often rely on overexpression, and they require substantial amounts of tissue, lack cellular/anatomical resolution, and cannot be performed in previously fixed tissue. In contrast, our assays can assess the activation state of endogenous LRRK2 on a cell-by-cell basis using fixed cells or tissue. In this context, we

Author Manuscript Author Manuscript Author Manuscript Author Manuscript

measured pSer1292 PL and pThr73-Rab10 by quantitative confocal immunofluorescence in sections of substantia nigra from 7 individuals dying with iPD and from 8 controls matched for age and postmortem interval. In nigrostriatal dopamine neurons from healthy controls, there were very low basal levels of pSer1292 PL and pThr73-Rab10 immunoreactivity signal and a strong 14-3-3 PL signal (figure 2). In contrast, the remaining dopamine neurons from the iPD cases showed about a 6-fold increase in pSer1292 PL ($p<0.0002$, two-tailed, unpaired t-test; $p<0.002$ with Welch's correction for unequal variances), and this was associated with a 4-fold increase in phosphorylation (pThr73) of the LRRK2 substrate Rab10 ($p<0.0002$). The increase in LRRK2 activation state in iPD dopamine neurons corresponded to a 5-fold decrease in the 14-3-3 PL signal ($p<0.0001$; $p<0.0004$ with Welch's correction). Thus, there is evidence that endogenous WT LRRK2 is activated in dopamine neurons in iPD, and this is associated with increased substrate phosphorylation.

In addition to neuronal expression, LRRK2 has also been associated with microglia (14). We found detectable levels of pS1292 PL signal in nigral microglia in controls (figure S1A, B), and the signal was more than doubled in microglia from iPD cases ($p<0.0005$, two-tailed, unpaired t-test).

WT LRRK2 activation is reproduced in mitochondrial and α-synuclein models of PD

Mitochondrial impairment and α-synuclein accumulation/aggregation have been strongly implicated in PD pathogenesis (15). Therefore, we tested whether LRRK2 is similarly activated in rat models based on these mechanisms. First, we used the rotenone model of PD, which has been shown to reproduce or even predict pathological and/or pathogenic features of the disease (16). Using substantia nigra sections from rotenone-treated rats that had reached behavioral endpoint (severe parkinsonism after 10–14 days), we found a 10-fold increase in pSer1292 PL signal in nigrostriatal dopamine neurons compared to vehicle-treated controls ($p<0.0001$, unpaired, 2-tail t-test) (figure 3A–C). In these animals, there was a dramatic loss of the 14-3-3 PL signal ($p<0.0001$, unpaired, 2-tail t-test) similar to the changes we observed in human brain. As in iPD brains, we found detectable pS1292 PL signal in control microglia (figure S1C,D), and the signal was more than doubled after rotenone treatment ($p<0.05$, unpaired, 2-tail t-test). To determine whether LRRK2 activation occurs prior to neurodegeneration, we examined tissue from animals that received only 1 or 5 days of rotenone, time points at which we detect no degeneration of the nigrostriatal neurons (figure S2). After a single dose of rotenone, pSer1292 PL signal was increased 5-fold relative to vehicle treatment ($p<0.0001$, ANOVA with Bonferroni correction), and after 5 daily doses, the PL signal was increased 6-fold ($p<0.0001$). These results indicate that mitochondrial impairment can lead to activation of LRRK2 well before there is any neurodegeneration.

α-Synuclein accumulation and Lewy pathology are hallmarks of PD. Elevated levels of WT α-synuclein may cause PD, and several groups have used viral vector-mediated overexpression of α-synuclein as a model of PD (17). Here, we used adeno-associated virus type 2 (AAV2)-mediated overexpression of wildtype human α-synuclein (*hSNCA*) injected unilaterally into substantia nigra pars compacta to induce slowly progressive neurodegeneration. Six weeks after vector injection, when degeneration is ongoing,

Author Manuscript Author Manuscript Author Manuscript Author Manuscript

remaining nigrostriatal neurons showed a marked 10-fold increase in pSer1292 PL signal compared to the contralateral, uninjected hemisphere ($p<0.0001$, paired 2-tail t-test) – and there was a concomitant loss of the 14-3-3 PL signal ($p<0.0001$) (figure 3D–F).

Both rotenone treatment and AAV2-mediated α-synuclein overexpression lead to oligomerization of α-synuclein, as well as accumulation of Ser129-phosphorylated α-synuclein (18, 19). We recently identified soluble oligomers and pSer129-α-synuclein as specific forms of α-synuclein that have deleterious effects on mitochondrial protein import machinery and which cause mitochondrial impairment (15). In analogous fashion, when *SNCA*$^{-/-}$ cells were treated with exogenous soluble oligomers of α-synuclein (400 nM monomer equivalent) for 24 hours, there was marked activation of endogenous WT LRRK2 with increased pSer1292 and loss of 14-3-3 PL signals (figure S3) ($p<0.0001$, ANOVA with Bonferroni correction). Treatment with monomeric α-synuclein did not activate LRRK2.

Both rotenone treatment and elevated α-synuclein increase formation of reactive oxygen species (ROS) and both insults activate WT LRRK2, which raises the possibility that it is secondary generation of ROS that actually activates LRRK2. To test directly whether ROS can activate LRRK2, we treated WT cells with H_2O_2 (figure 4A, B). Treatment with H_2O_2 dose-dependently (50 nM – 5 μM) activated the pSer1292 PL signal ($p<0.0001$ vs. control for all H_2O_2 doses; 1-way ANOVA with Bonferroni correction) and increased phosphorylation of its substrate, Rab10 ($p<0.0001$ for all doses above 50 nM H_2O_2). The antioxidant, α-tocopherol, blocked H_2O_2 activation of the pSer1292 signal ($p<0.0001$) and Rab10 phosphorylation ($p<0.0001$).

Further evidence of oxidative activation of LRRK2 resulted from study of endogenous NADPH oxidase 2 (NOX2). As *in vivo*, we found that rotenone treatment of WT HEK-293 cells caused an increased pSer1292 PL signal and Rab10 phosphorylation (figure 4C–E). Although rotenone may cause mitochondrial ROS formation, mitochondrially-derived ROS may also activate NOX2 in a process known as ROS-induced ROS release, which can feed forward to amplify ROS production (20, 21). We found that co-treatment with rotenone plus the specific NOX2 inhibitor peptide, Nox2ds-tat (22), blocked rotenone's effects on LRRK2 activation and phosphorylation of its substrate ($p<0.0001$, 1-way ANOVA with Bonferroni correction). Thus, NOX2-generated superoxide appears to be important in activating LRRK2.

In vivo treatment with a LRRK2 kinase inhibitor blocks rotenone-induced activation of nigrostriatal LRRK2 and has beneficial effects on pSer129-α-synuclein levels and markers of autophagy & lysosomes.

The rotenone model of PD reproduces many features of the human disease, including accumulation of pSer129-α-synuclein, impairment of autophagy, reduced mitochondrial protein import (15), and now, activation of endogenous WT LRRK2 in nigrostriatal dopamine neurons. To determine whether systemic treatment with a brain-penetrant LRRK2 inhibitor could block rotenone-induced LRRK2 activation, and to survey some of the potential downstream effects of LRRK2 activation, rats were treated for 5 days with rotenone (2.8 mg/kg/day, i.p.) with or without concomitant PF-360 (10 mg/kg p.o. twice daily), a highly selective LRRK2 kinase inhibitor (23, 24). This PF-360 dosing regimen

Author Manuscript Author Manuscript Author Manuscript Author Manuscript

results in a pharmacokinetic profile in which an IC_{90} concentration in brain is achieved for 15 hours daily and an IC_{50} concentration is achieved for a full 24 hours.

In a new cohort of rats treated with rotenone for 5 days, there was a marked increase in pSer1292 PL signal in nigrostriatal neurons, which was associated with an increase in phosphorylation of Rab10 (figure 5A–C). Co-treatment with PF-360 effectively blocked the rotenone-induced activation of LRRK2 ($p<0.0001$, two-way ANOVA, Sidak's correction) and phosphorylation of Rab10 ($p<0.0001$). Thus, the pSer1292 PL assay provided an *ex vivo* assay of target (LRRK2) engagement by PF-360, which was corroborated by measurement of pThr73-Rab10.

We reported previously that chronic rotenone treatment (10–14 days) leads to elevated levels of pSer129-α-synuclein (15). Here we found that the rats treated for only 5 days also accumulated pSer129-α-synuclein, and co-treatment with PF-360 prevented this accumulation (figure 5D, E). The mechanism by which pSer129-α-synuclein accrues in response to rotenone is uncertain, but it has been suggested that phosphorylation of α-synuclein at ser129 targets the protein for degradation by autophagy (25, 26). Both chaperone-mediated autophagy (CMA) and macroautophagy play roles in α-synuclein degradation (27, 28). Therefore, we assessed a marker for CMA, Lamp2A, which is located on lysosomes, and another marker, Lamp1, which may label late endosomes, autolysosomes or lysosomes. There were abundant Lamp2A and Lamp1 punctae in dopamine neurons from vehicle treated rats, which were dramatically lost after rotenone treatment, and preserved by co-treatment with PF-360 (figure 6A–E). Together, these results indicate that there is early profound impairment of CMA and lysosomal function which is downstream of LRRK2 kinase activity. Additionally, these results suggest that pSer129-α-synuclein accumulates in rotenone treated rats because of LRRK2-induced CMA and lysosomal dysfunction – and LRRK2 kinase inhibition prevents this. To complement these pharmacological studies, we examined the effects of rotenone on pSer129-α-synuclein in WT and $LRRK2^{-/-}$ HEK cells. As *in vivo*, we found that rotenone treatment caused accumulation of pSer129-α-synuclein in WT cells; however, there was no such accumulation in the LRRK2 null cells (Figure S4), thereby providing further evidence that buildup of pSer129-α-synuclein is LRRK2-dependent. Moreover, the rotenone-induced increase in pSer129-α-synuclein in WT cells was effectively blocked by PF-360 to the same extent as in $LRRK2^{-/-}$ cells, confirming the specificity of the PF-360 effect.

Similar to rotenone-treated rats, there was a dramatic loss of Lamp1 puncta in human brain specimens from individuals with iPD ($p<0.001$, unpaired 2-tail t-test) and this was accompanied by an accumulation of the autophagy cargo receptor, p62/SQSTM1 ($p<0.03$), into Lewy bodies, indicating autophagic and lysosomal dysfunction (figure 6F, G). As reported by many other groups, and as seen in rotenone-treated rats, there is accumulation of pSer129-α-synuclein in substantia nigra in iPD.

In vitro experiments have shown that pSer129-α-synuclein binds to TOM20 and inhibits mitochondrial protein import; however, this has not been examined directly in human brain or in the rotenone rat. Examination of human iPD brains (figure 7A,B) revealed a marked increase of pSer129-α-synuclein-TOM20 PL signal ($p<0.0001$, unpaired, 2-tail t-test),

Author Manuscript Author Manuscript Author Manuscript Author Manuscript

indicating that accumulation of this specific form of α-synuclein has toxic consequences in terms of mitochondrial protein import. Similarly, in the rotenone rats (figure 7C–E), the increased pSer129-α-synuclein we found at 5 days was associated with its binding to TOM20, measured as a strong pSer129-α-synuclein-TOM20 PL signal ($p<0.0001$, 2-way ANOVA with Bonferroni correction), as well as reduced levels and redistribution of the imported complex I subunit, Ndufs3, from mitochondria to cytosol ($P<0.0001$). Co-treatment with PF-360 prevented the elevation in pSer129-α-synuclein levels (figure 5E) and, as a result, there was little binding to TOM20 ($p<0.0001$ vs rotenone alone), and there was preservation of normal levels and mitochondrial localization of Ndufs3 (figure 7C,E). Thus, both the accumulation of pSer129-α-synuclein and its toxic consequences appear to be downstream of LRRK2 kinase activity.

DISCUSSION

Development of a new assay allowed us to show that endogenous WT LRRK2 is activated in nigrostriatal dopamine neurons in iPD – and this can be reproduced in rodent models of the disease. While our new assay does not measure activity *per se*, it provides a snapshot of relative LRRK2 activation state and does so with a cellular level of resolution (e.g., in dopamine neurons and microglia). The assay was validated (i) by using gene-edited cells, (ii) by demonstrating that the readout of LRRK2 activation state (pSer1292 PL signal) correlates with substrate (Rab10) phosphorylation levels, and (iii) by showing that both the pSer1292 PL and pThr73-Rab10 signals respond appropriately and in parallel to 3 structurally distinct LRRK2 kinase inhibitors (GNE-7915, MLi-2 and PF-360). Consistent with our results, others showed recently, by means of immunoblotting, that the phosphorylation state of LRRK2 (at Ser935) correlates with Rab10 phosphorylation in dose-response studies using PF-360 (23).

The finding that treatment of G2019S mutant engineered or patient-derived cells with kinase inhibitors blocks the pSer1292 PL signal indicates that this readout is readily reversible. Thus, the relative degree of LRRK2 activation detected reflects the physiological state of LRRK2 in the cell or tissue at the specific time of fixation. Additionally, the ease with which inhibitor dose-response relationships can be assessed suggests the assay can provide a quantitative measure of target (LRRK2) engagement.

Recent work from West and colleagues showed that genetic ablation or pharmacological kinase inhibition of endogenous WT LRRK2 reduced the toxicity of AAV2-*hSNCA* injected into substantia nigra, suggesting a possible role of LRRK2 in α-synuclein toxicity (29, 30). Implicit in such a conclusion is the assumption that WT LRRK2 kinase must be active in nigrostriatal neurons under these experimental conditions; however, this has been difficult to demonstrate with conventional assays. Consistent with this supposition, we found that AAV2-*hSNCA* (as used by West and colleagues) activates LRRK2 in nigrostriatal neurons. In this context, our findings indicate that LRRK2 is activated in the vulnerable dopamine neurons in human iPD and suggest that endogenous WT LRRK2 may play a role pathogenesis.

Author Manuscript Author Manuscript Author Manuscript Author Manuscript

Our assay allows relatively facile assessment of physiological regulators of LRRK2 activity. In cell culture, we showed that low concentrations of oligomeric, but not monomeric, α-synuclein activate LRRK2. We recently reported that oligomeric, but not monomeric, α-synuclein binds to TOM20, impairs mitochondrial protein import, and causes mitochondrial dysfunction and aberrant ROS production (15). Similarly, the mitochondrial toxin rotenone induces ROS production, and we showed that it caused LRRK2 activation and LRRK2 substrate phosphorylation. Interestingly, the rotenone-induced activation of LRRK2 was blocked by inhibition of NOX2, implicating ROS-induced ROS release and NOX2-derived superoxide in the phenomenon (20). To directly test whether ROS can activate LRRK2, cells were treated with physiological concentrations of H_2O_2, and this resulted in increased pSer1292 PL signal and concomitant Rab10 phosphorylation. These results suggest that oxidative stress, long implicated in PD pathogenesis, may up-regulate LRRK2 activity. Further, our results are consistent with the work of Mamais et al., which showed that H_2O_2 dissociates LRRK2 from 14-3-3 (12), and the study by Li et al., which found a small activation of LRRK2 by H_2O_2 (31). The molecular mechanisms by which ROS stimulate LRRK2 kinase activity are unknown; whether this activation results from direct effects on the LRRK2 protein or from effects on interacting proteins, such as protein phosphatases, remains to be explored.

The consistent finding that LRRK2 is activated in vulnerable dopaminergic neurons in human iPD raises the possibility that LRRK2 kinase activity may play a central role in pathogenesis of most PD cases. To investigate experimentally the possibility that LRRK2 activation may have downstream deleterious effects on putative pathogenic mechanisms, we treated rats for 5 days with rotenone – with or without co-treatment with the LRRK2 kinase inhibitor, PF-360. We found that rotenone (i) activated LRRK2 in nigrostriatal dopamine neurons; (ii) increased phosphorylation of a LRRK2 substrate, Rab10; (iii) increased levels pSer129-α-synuclein and binding to TOM20; and (iv) disrupted markers of autophagy. All these effects were blocked by PF-360, and we therefore conclude that these mechanisms are downstream of LRRK2 activity (figure 8).

Rab10 is a *bona fide* direct substrate of LRRK2 and has been implicated in maintenance of endoplasmic reticulum, vesicle trafficking and autophagy (32–34). LRRK2-induced phosphorylation of Rab10 inhibits its function by preventing binding to Rab GDP-dissociation inhibitor factors necessary for membrane delivery and recycling (6). Thus, LRRK2 activation leads to Rab10 phosphorylation (and inhibition) and this likely impairs autophagic and/or lysosomal function. Phospho-Rab10-induced autophagic dysfunction, in turn, may account for the early accumulation of pSer129-α-synuclein, which is normally degraded by CMA and macroautophagy. Consistent with our findings, Volpicelli and colleagues reported that the G2019S mutation was associated with accumulation of pSer129-α-synuclein-positive inclusions, which were prevented by LRRK2 kinase inhibitors, including MLi-2 (35). It is also noteworthy that pSer129-α-synuclein is one of the species of α-synuclein we reported that binds to TOM20 and impairs mitochondrial function (15). The fact that all these abnormalities are prevented by treatment with a LRRK2 kinase inhibitor strongly supports this hypothetical scheme (figure 8). Further, our experimental paradigm of surveying potential pathogenic mechanisms in a PD model, with and without concomitant

Author Manuscript Author Manuscript Author Manuscript Author Manuscript

treatment with a LRRK2 kinase inhibitor, will likely lead to new insights into how aberrant LRRK2 activity causes neurodegeneration.

Our study is not without limitations. As noted, the PL assays we employed do not measure activity *per se*; however, several convergent lines of evidence confirm that we measured reliable surrogates of LRRK2 activity: the pS1292 PL signal correlated with substrate (Rab10) phosphorylation and with loss of 14-3-3 binding signal – and both the 1292 PL signal and the pThr72-Rab10 signal were inhibited dose-dependently by selective LRRK2 kinase inhibitors of different chemical classes. In this context, we provided compelling evidence that wildtype LRRK2 is activated in nigrostriatal neurons in iPD and in rat models thereof. Nevertheless, while LRRK2 activation occurred very early in the course of rotenone-induced parkinsonism, and early intervention with a LRRK2 kinase inhibitor was beneficial, the time course of LRRK2 activation in the human brain is unknown and the clinical effects of LRRK2 inhibitors remain to be examined.

The fact that there are a variety of selective LRRK2 kinase inhibitors reflects the interest by the pharmaceutical industry in target-specific therapeutics for PD, even for the relatively small number of cases caused by LRRK2 mutations. The results presented here provide compelling evidence that WT LRRK2 is activated by PD-relevant relevant stimuli in dopamine neurons in iPD and that this, in turn, triggers a downstream pathological cascade of events culminating in neurodegeneration. As such, rather than being applicable for 3–4% of people with PD, LRRK2-targeted therapeutics may be useful for most, if not all, people with PD.

MATERIALS AND METHODS

Study Design.

This study was designed to assess the role of wildtype LRRK2 in iPD. To do so, we developed new PL assays to assess the phosphorylation state of the LRRK2 autophosphorylation site, Ser1292, and separately, the binding of LRRK2 to 14-3-3, which is associated with decreased LRRK2 kinase activity. These assays were validated using CRISPR/Cas9 genome-edited HEK293 cells and 3 chemically distinct LRRK2 kinase inhibitors. The validated assays were then used to assess LRRK2 activation state in iPD brains and rat models of PD. Additional studies examined the role of oxidative stress in activating LRRK2, as well as downstream consequences of LRRK2 activity *in vivo*.

CRISPR/Cas9 Genome Editing of HEK293 Cells to Produce LRRK2 Knockout and Knock-in Cell Lines.

To generate a LRRK2 knockout cell line, a CRISPR/Cas9 genome editing approach was used. A gRNA targeting exon 41 of the LRRK2 gene (5’-ATTGCAAAGATTGCTGACTAGTTTT- 3’) was cloned into the GeneArt CRISPR Nuclease vector (Invitrogen) as described by the manufacturer. HEK293 cells were transfected by nucleoporation using a Nucleoporater II device (Amaxa). Transfected cells were collected and enriched by FACS sorting. Sorted cells were grown and expanded for PCR and DNA sequencing analyses. To confirm gene editing of the LRRK2 gene, a region

Author Manuscript Author Manuscript Author Manuscript Author Manuscript

of exon 41 was PCR amplified using a forward primer (5'-TTTAAGGGACAAAGTGAGCA-3') and reverse primer (5'-CACAATGTGATGCTTGCATTT-3') and the resulting PCR product was sequenced. The LRRK2 G2019S knock-in cell line was generated using a similar approach but included transfection of a 120-mer single-stranded oligonucleotide containing a G to A substitution coding for a glycine to serine amino acid change.

A SNCA knockout cell line was generated using a similar approach but utilized a gRNA targeting exon 4 of the α-synuclein (SNCA) gene (5'-CTTTGTCAAAAAGGACCAGT-3') To confirm gene editing of the SNCA gene, a region of exon 4 was PCR amplified using a forward primer (5'- CCACCCTTTAATCTGTTGTTGC-3') and reverse primer (5'-ATATAAAGGTAGCACTTTTTCACAAGG-3') and the resulting PCR product was sequenced.

Proximity Ligation Assay.

PLA was performed as described previously in 4% PFA-fixed tissue or cells (15). Samples were incubated with specific primary antibodies to the proteins to be detected. Secondary antibodies conjugated with oligonucleotides were added to the reaction and incubated. Ligation solution, consisting of two oligonucleotides and ligase, was added. In this assay, the oligonucleotides hybridize to the two PLA probes and join to a closed loop if they are in close proximity. Amplification solution, consisting of nucleotides and fluorescently labeled oligonucleotides, was added together with polymerase. The oligonucleotide arm of one of the PLA probes acts as a primer for "rolling-circle amplification" using the ligated circle as a template, and this generates a concatemeric product. Fluorescently labeled oligonucleotides hybridize to the RCA product. The PL signal was visible as a distinct fluorescent spot and was analyzed by confocal microscopy (Duolink; Sigma Aldrich). Control experiments included routine immunofluorescence staining of the proteins of interest under identical experimental conditions.

Statistical analyses.

Each result presented here was derived from 3–6 independent experiments. For simple comparisons of 2 experimental conditions, 2-tailed, unpaired t-tests were used. Where variances were not equal, Welch's correction was used. When virus was injected into 1 hemisphere of the brain and the other hemisphere was used as a control, 2-tailed paired t-tests. For comparisons of multiple experimental conditions, 1-way or 2-way ANOVA was used, and if significant overall, post hoc corrections (Bonferroni or Sidak) for multiple pairwise comparisons were made. P-values less than 0.05 were considered significant.

Other methods are described in Supplemental Materials.

Supplementary Material

Refer to Web version on PubMed Central for supplementary material.

Author Manuscript Author Manuscript Author Manuscript Author Manuscript

Acknowledgements:

This work was supported by research grants from the National Institutes of Health (NS100744, R21ES027470, NS095387, AG005133), the Blechman Foundation, the American Parkinson Disease Association, and friends and family of Sean Logan. The brain bank has received support from the University of Pittsburgh Brain Institute. Work in the Alessi lab on LRRK2 is supported by the Michael J. Fox Foundation for Parkinson's research [grant number 6986]; the Medical Research Council [grant number MC_UU_12016/2] and the pharmaceutical companies supporting the Division of Signal Transduction Therapy Unit (Boehringer-Ingelheim, GlaxoSmithKline, and Merck KGaA, to D.R.A.).

REFERENCES

1. Kalia LV, Lang AE, Parkinson disease in 2015: Evolving basic, pathological and clinical concepts in PD. Nat Rev Neurol 12, 65–66 (2016). [PubMed: 26782330]
2. Paisan-Ruiz C, Jain S, Evans EW, Gilks WP, Simon J, van der Brug M, Lopez de Munain A, Aparicio S, Gil AM, Khan N, Johnson J, Martinez JR, Nicholl D, Carrera IM, Pena AS, de Silva R, Lees A, Marti-Masso JF, Perez-Tur J, Wood NW, Singleton AB, Cloning of the gene containing mutations that cause PARK8-linked Parkinson's disease. Neuron 44, 595–600 (2004). [PubMed: 15541308]
3. Zimprich A, Biskup S, Leitner P, Lichtner P, Farrer M, Lincoln S, Kachergus J, Hulihan M, Uitti RJ, Calne DB, Stoessl AJ, Pfeiffer RF, Patenge N, Carbajal IC, Vieregge P, Asmus F, Muller-Myhsok B, Dickson DW, Meitinger T, Strom TM, Wszolek ZK, Gasser T, Mutations in LRRK2 cause autosomal-dominant parkinsonism with pleomorphic pathology. Neuron 44, 601–607 (2004). [PubMed: 15541309]
4. Simon-Sanchez J, Schulte C, Bras JM, Sharma M, Gibbs JR, Berg D, Paisan-Ruiz C, Lichtner P, Scholz SW, Hernandez DG, Kruger R, Federoff M, Klein C, Goate A, Perlmutter J, Bonin M, Nalls MA, Illig T, Gieger C, Houlden H, Steffens M, Okun MS, Racette BA, Cookson MR, Foote KD, Fernandez HH, Traynor BJ, Schreiber S, Arepalli S, Zonozi R, Gwinn K, van der Brug M, Lopez G, Chanock SJ, Schatzkin A, Park Y, Hollenbeck A, Gao J, Huang X, Wood NW, Lorenz D, Deuschl G, Chen H, Riess O, Hardy JA, Singleton AB, Gasser T, Genome-wide association study reveals genetic risk underlying Parkinson's disease. Nat Genet 41, 1308–1312 (2009). [PubMed: 19915575]
5. Greggio E, Jain S, Kingsbury A, Bandopadhyay R, Lewis P, Kaganovich A, van der Brug MP, Beilina A, Blackinton J, Thomas KJ, Ahmad R, Miller DW, Kesavapany S, Singleton A, Lees A, Harvey RJ, Harvey K, Cookson MR, Kinase activity is required for the toxic effects of mutant LRRK2/dardarin. Neurobiol Dis 23, 329–341 (2006). [PubMed: 16750377]
6. Steger M, Tonelli F, Ito G, Davies P, Trost M, Vetter M, Wachter S, Lorentzen E, Duddy G, Wilson S, Baptista MA, Fiske BK, Fell MJ, Morrow JA, Reith AD, Alessi DR, Mann M, Phosphoproteomics reveals that Parkinson's disease kinase LRRK2 regulates a subset of Rab GTPases. eLife 5, (2016).
7. Fraser KB, Rawlins AB, Clark RG, Alcalay RN, Standaert DG, Liu N, Parkinson's C Disease Biomarker Program, A. B. West, Ser(P)-1292 LRRK2 in urinary exosomes is elevated in idiopathic Parkinson's disease. Mov Disord 31, 1543–1550 (2016). [PubMed: 27297049]
8. Sheng Z, Zhang S, Bustos D, Kleinheinz T, Le Pichon CE, Dominguez SL, Solanoy HO, Drummond J, Zhang X, Ding X, Cai F, Song Q, Li X, Yue Z, van der Brug MP, Burdick DJ, Gunzner-Toste J, Chen H, Liu X, Estrada AA, Sweeney ZK, Scearce-Levie K, Moffat JG, Kirkpatrick DS, Zhu H, Ser1292 autophosphorylation is an indicator of LRRK2 kinase activity and contributes to the cellular effects of PD mutations. Sci Transl Med 4, 164ra161 (2012).
9. Li X, Wang QJ, Pan N, Lee S, Zhao Y, Chait BT, Yue Z, Phosphorylation-dependent 14-3-3 binding to LRRK2 is impaired by common mutations of familial Parkinson's disease. PLoS One 6, e17153 (2011). [PubMed: 21390248]
10. Dzamko N, Deak M, Hentati F, Reith AD, Prescott AR, Alessi DR, Nichols RJ, Inhibition of LRRK2 kinase activity leads to dephosphorylation of Ser(910)/Ser(935), disruption of 14-3-3 binding and altered cytoplasmic localization. Biochem J 430, 405–413 (2010). [PubMed: 20659021]
11. Lavalley NJ, Slone SR, Ding H, West AB, Yacoubian TA, 14-3-3 Proteins regulate mutant LRRK2 kinase activity and neurite shortening. Hum Mol Genet 25, 109–122 (2016). [PubMed: 26546614]

Author Manuscript Author Manuscript Author Manuscript Author Manuscript

12. Mamais A, Chia R, Beilina A, Hauser DN, Hall C, Lewis PA, Cookson MR, Bandopadhyay R, Arsenite stress down-regulates phosphorylation and 14-3-3 binding of leucine-rich repeat kinase 2 (LRRK2), promoting self-association and cellular redistribution. J Biol Chem 289, 21386–21400 (2014). [PubMed: 24942733]
13. Fell MJ, Mirescu C, Basu K, Cheewatrakoolpong B, DeMong DE, Ellis JM, Hyde LA, Lin Y, Markgraf CG, Mei H, Miller M, Poulet FM, Scott JD, Smith MD, Yin Z, Zhou X, Parker EM, Kennedy ME, Morrow JA, MLi-2, a Potent, Selective, and Centrally Active Compound for Exploring the Therapeutic Potential and Safety of LRRK2 Kinase Inhibition. J Pharmacol Exp Ther 355, 397–409 (2015). [PubMed: 26407721]
14. Moehle MS, Webber PJ, Tse T, Sukar N, Standaert DG, DeSilva TM, Cowell RM, West AB, LRRK2 inhibition attenuates microglial inflammatory responses. J Neurosci 32, 1602–1611 (2012). [PubMed: 22302802]
15. Di Maio R, Barrett PJ, Hoffman EK, Barrett CW, Zharikov A, Borah A, Hu X, McCoy J, Chu CT, Burton EA, Hastings TG, Greenamyre JT, alpha-Synuclein binds to TOM20 and inhibits mitochondrial protein import in Parkinson's disease. Sci Transl Med 8, 342ra378 (2016).
16. Greenamyre JT, Cannon JR, Drolet R, Mastroberardino PG, Lessons from the rotenone model of Parkinson's disease. Trends Pharmacol Sci 31, 141–142; author reply 142–143 (2010). [PubMed: 20096940]
17. Ulusoy A, Decressac M, Kirik D, Bjorklund A, Viral vector-mediated overexpression of alpha-synuclein as a progressive model of Parkinson's disease. Prog Brain Res 184, 89–111 (2010). [PubMed: 20887871]
18. Dimant H, Kalia SK, Kalia LV, Zhu LN, Kibuuka L, Ebrahimi-Fakhari D, McFarland NR, Fan Z, Hyman BT, McLean PJ, Direct detection of alpha synuclein oligomers in vivo. Acta neuropathologica communications 1, 6 (2013). [PubMed: 24252244]
19. Betarbet R, Canet-Aviles RM, Sherer TB, Mastroberardino PG, McLendon C, Kim JH, Lund S, Na HM, Taylor G, Bence NF, Kopito R, Seo BB, Yagi T, Yagi A, Klinefelter G, Cookson MR, Greenamyre JT, Intersecting pathways to neurodegeneration in Parkinson's disease: effects of the pesticide rotenone on DJ-1, alpha-synuclein, and the ubiquitin-proteasome system. Neurobiol Dis 22, 404–420 (2006). [PubMed: 16439141]
20. Nazarewicz RR, Dikalova AE, Bikineyeva A, Dikalov SI, Nox2 as a potential target of mitochondrial superoxide and its role in endothelial oxidative stress. Am J Physiol Heart Circ Physiol 305, H1131–1140 (2013). [PubMed: 23955717]
21. Dikalov SI, Li W, Doughan AK, Blanco RR, Zafari AM, Mitochondrial reactive oxygen species and calcium uptake regulate activation of phagocytic NADPH oxidase. Am J Physiol Regul Integr Comp Physiol 302, R1134–1142 (2012). [PubMed: 22442197]
22. Csanyi G, Cifuentes-Pagano E, Al Ghouleh I, Ranayhossaini DJ, Egana L, Lopes LR, Jackson HM, Kelley EE, Pagano PJ, Nox2 B-loop peptide, Nox2ds, specifically inhibits the NADPH oxidase Nox2. Free Radic Biol Med 51, 1116–1125 (2011). [PubMed: 21586323]
23. Thirstrup K, Dachsel JC, Oppermann FS, Williamson DS, Smith GP, Fog K, Christensen KV, Selective LRRK2 kinase inhibition reduces phosphorylation of endogenous Rab10 and Rab12 in human peripheral mononuclear blood cells. Scientific reports 7, 10300 (2017). [PubMed: 28860483]
24. Baptista M, Merchant KM, Bharghava S, Bryce D, Ellis M, Estrada AA, Fell MJ, Fuji R, Galatsis P, Hill S, Hirst WD, Houle C, Kennedy M, Liu X, Maddess M, Markgraf CG, Mei H, Needle E, Steyn SJ, Yin Z, Yu H, Fiske B, Sherer TB, LRRK2 kinase inhibitors of different structural classes induce abnormal, but reversible, accumulation of lamellar bodies in type II pneumocytes in non-human primates. Program No. 763.02. 2015 Neuroscience Meeting Planner. Washington, DC: Society for Neuroscience, 2015. Online., (2015).
25. Kleinknecht A, Popova B, Lazaro DF, Pinho R, Valerius O, Outeiro TF, Braus GH, C-Terminal Tyrosine Residue Modifications Modulate the Protective Phosphorylation of Serine 129 of alpha-Synuclein in a Yeast Model of Parkinson's Disease. PLoS Genet 12, e1006098 (2016). [PubMed: 27341336]
26. Oueslati A, Schneider BL, Aebischer P, Lashuel HA, Polo-like kinase 2 regulates selective autophagic alpha-synuclein clearance and suppresses its toxicity in vivo. Proc Natl Acad Sci USA 110, E3945–3954 (2013). [PubMed: 23983262]

Author Manuscript Author Manuscript Author Manuscript Author Manuscript

27. Cuervo AM, Stefanis L, Fredenburg R, Lansbury PT, Sulzer D, Impaired degradation of mutant alpha-synuclein by chaperone-mediated autophagy. Science 305, 1292–1295 (2004). [PubMed: 15333840]

28. Webb JL, Ravikumar B, Atkins J, Skepper JN, Rubinsztein DC, Alpha-Synuclein is degraded by both autophagy and the proteasome. J Biol Chem 278, 25009–25013 (2003). [PubMed: 12719433]

29. Daher JP, Abdelmotilib HA, Hu X, Volpicelli-Daley LA, Moehle MS, Fraser KB, Needle E, Chen Y, Steyn SJ, Galatsis P, Hirst WD, West AB, Leucine-rich Repeat Kinase 2 (LRRK2) Pharmacological Inhibition Abates alpha-Synuclein Gene-induced Neurodegeneration. J Biol Chem 290, 19433–19444 (2015). [PubMed: 26078453]

30. Daher JP, Volpicelli-Daley LA, Blackburn JP, Moehle MS, West AB, Abrogation of alpha-synuclein-mediated dopaminergic neurodegeneration in LRRK2-deficient rats. Proc Natl Acad Sci U S A 111, 9289–9294 (2014). [PubMed: 24927544]

31. Li X, Moore DJ, Xiong Y, Dawson TM, Dawson VL, Reevaluation of phosphorylation sites in the Parkinson disease-associated leucine-rich repeat kinase 2. J Biol Chem 285, 29569–29576 (2010). [PubMed: 20595391]

32. Li Z, Schulze RJ, Weller SG, Krueger EW, Schott MB, Zhang X, Casey CA, Liu J, Stockli J, James DE, McNiven MA, A novel Rab10-EHBP1-EHD2 complex essential for the autophagic engulfment of lipid droplets. Sci Adv 2, e1601470 (2016). [PubMed: 28028537]

33. Vieira OV, Rab3a and Rab10 are regulators of lysosome exocytosis and plasma membrane repair. Small GTPases, 1–3 (2016).

34. English AR, Voeltz GK, Rab10 GTPase regulates ER dynamics and morphology. Nat Cell Biol 15, 169–178 (2013). [PubMed: 23263280]

35. Volpicelli-Daley LA, Abdelmotilib H, Liu Z, Stoyka L, Daher JP, Milnerwood AJ, Unni VK, Hirst WD, Yue Z, Zhao HT, Fraser K, Kennedy RE, West AB, G2019S-LRRK2 Expression Augments alpha-Synuclein Sequestration into Inclusions in Neurons. J Neurosci 36, 7415–7427 (2016). [PubMed: 27413152]

36. Sanders LH, McCoy J, Hu X, Mastroberardino PG, Dickinson BC, Chang CJ, Chu CT, Van Houten B, Greenamyre JT, Mitochondrial DNA damage: Molecular marker of vulnerable nigral neurons in Parkinson's disease. Neurobiol Dis 70, 214–223 (2014). [PubMed: 24981012]

37. Zharikov AD, Cannon JR, Tapias V, Bai Q, Horowitz MP, Shah V, El Ayadi A, Hastings TG, Greenamyre JT, Burton EA, shRNA targeting alpha-synuclein prevents neurodegeneration in a Parkinson's disease model. J Clin Invest 125, 2721–2735 (2015). [PubMed: 26075822]

38. Alafuzoff I, Ince PG, Arzberger T, Al-Sarraj S, Bell J, Bodi I, Bogdanovic N, Bugiani O, Ferrer I, Gelpi E, Gentleman S, Giaccone G, Ironside JW, Kavantzas N, King A, Korkolopoulou P, Kovacs GG, Meyronet D, Monoranu C, Parchi P, Parkkinen L, Patsouris E, Roggendorf W, Rozemuller A, Stadelmann-Nessler C, Streichenberger N, Thal DR, Kretzschmar H, Staging/typing of Lewy body related alpha-synuclein pathology: a study of the BrainNet Europe Consortium. Acta Neuropathol 117, 635–652 (2009). [PubMed: 19330340]

Author Manuscript
Author Manuscript
Author Manuscript
Author Manuscript

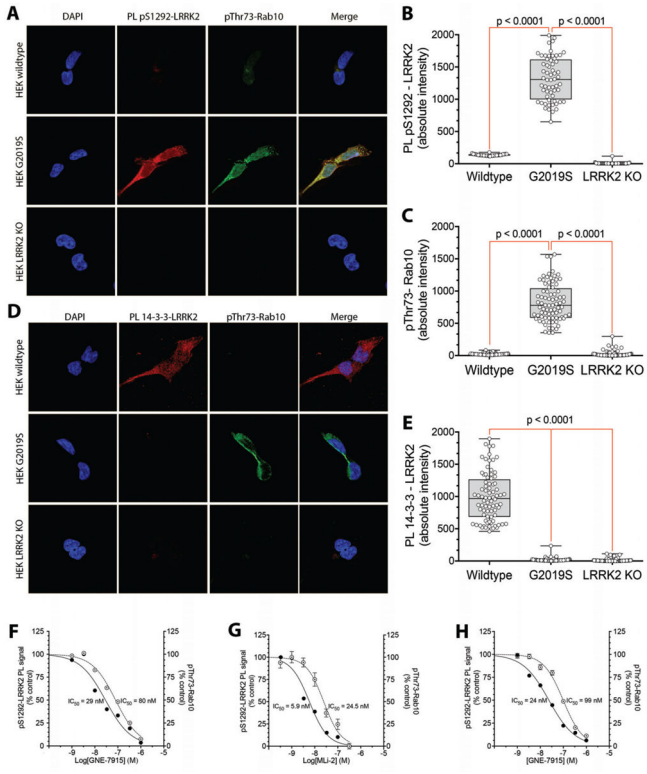


Figure 1.

Validation of assays using CRISPR/Cas9 gene-edited cells and selective LRRK2 kinase inhibitors. **(A)** PL assay showing LRRK2 kinase activation by means of phosphorylation of the autophosphorylation site, Ser1292 (red signal) and immunofluorescence of phosphorylation of the LRRK2 substrate Rab10 (green signal). In WT HEK cells (top row), there was little PL signal or pThr73-Rab10 immunofluorescence. In HEK$^{G2019S/G2019S}$ cells (2nd row) with elevated LRRK2 kinase activity, there was a bright pS1292 PL signal and strong pThr73-Rab immunofluorescence. In LRRK2 knockout HEK cells (bottom row) there was no pS1292 PL signal and very little pThr73-Rab signal. **(B)** Quantification of the pS1292 PL signal in WT, G2019S and knockout cells. Results reflect 3 independent experiments. Each symbol represents signal from a single cell. Statistical testing by ANOVA with post hoc Bonferroni correction. **(C)** Quantification of the pThr73-Rab10 signal in WT, G2019S and knockout cells. Results reflect 3 independent experiments. Each symbol represents signal from a single cell. Statistical testing by ANOVA with post hoc Bonferroni correction. **(D)** PL assay of 14-3-3 binding to LRRK2 and immunofluorescence of Rab10 phosphorylation at Thr73. In WT cells, there was a strong 14-3-3-LRRK2 PL signal (red) and little pThr73-Rab10 immunofluorescence (green). In HEK$^{G2019S/G2019S}$ cells, there was loss of 14-3-3 binding and a marked increase in pThr73-Rab10 signal. In LRRK2 knockout cells there was no 14-3-3-LRRK2 signal and little pThr73-Rab10 signal. **(E)** Quantification of the 14-3-3-LRRK2 PL signal in WT, G2019S and knockout cells. Results reflect 3 independent experiments. Each symbol represents signal from a single cell. Statistical testing by ANOVA with post hoc Bonferroni correction. **(F)** Dose-response curves of the LRRK2 kinase inhibitor GNE-7915 against the pS1292 PL signal (filled circles) and the pThr73-Rab10 signal (open circles) in HEK$^{G2019S/G2019S}$ cells. Cells were cultured for 24

Author Manuscript Author Manuscript Author Manuscript Author Manuscript

hours with various inhibitor concentrations. Results from 3 independent experiments. Symbols show mean ± SEM. IC_{50} values calculated by GraphPad Prism software. **(G)** Dose-response curves of the LRRK2 kinase inhibitor MLi-2 against the pS1292 PL signal (filled circles) and the pThr73-Rab10 signal (open circles) in $HEK^{G2019S/G2019S}$ cells. Cells were cultured for 24 hours with various inhibitor concentrations. **(H)** Dose-response curves of the LRRK2 kinase inhibitor GNE-7915 against the pS1292 PL signal (filled circles) and the pThr73-Rab10 signal (open circles) in LCLs derived from an individual carrying the G2019S mutation. Cells were cultured for 24 hours with various inhibitor concentrations.

Author Manuscript Author Manuscript Author Manuscript Author Manuscript

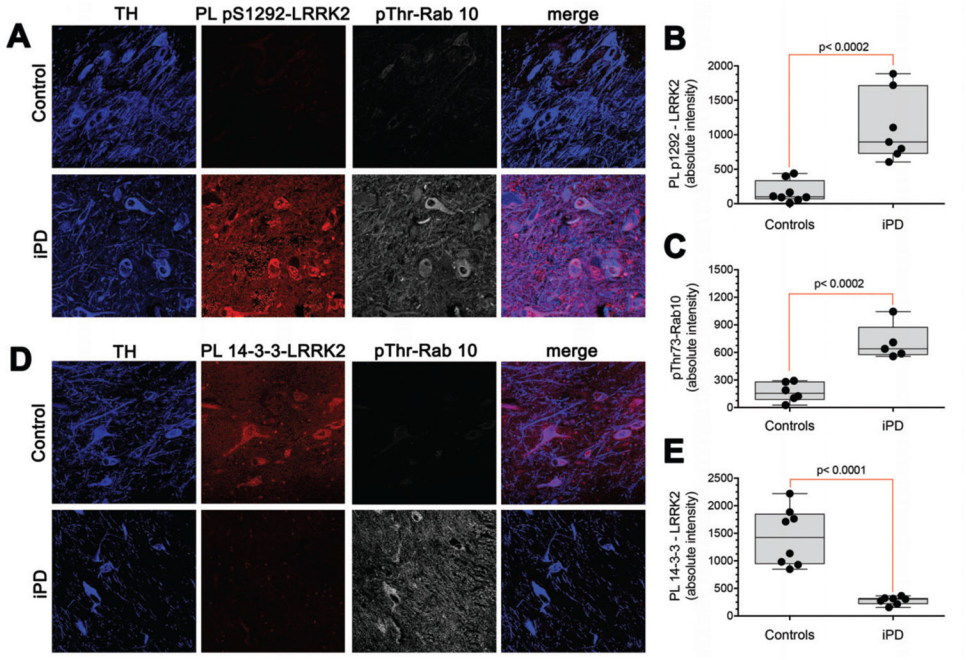


Figure 2.

Activation of LRRK2 kinase activity in nigrostriatal neurons in iPD. **(A)** pS1292 PL (red) and pThr73-Rab10 (gray) immunofluorescence signals in sections of substantia nigra from a control brain (top row) and a brain from an individual with iPD (bottom row). In the control brain, there was little pS1292 or pThr73-Rab10 signal, but in the iPD brain there were strong signals for both. **(B)** Quantification of pS1292 PL signal in 8 control brains and 7 iPD brains. Statistical comparison by unpaired 2-tail t-test. **(C)** Quantification of pThr73-Rab10 signal in 8 control brains and 7 iPD brains. Statistical comparison by unpaired 2-tail t-test. **(D)** 14-3-3-LRRK2 PL (red) and pThr73-Rab10 (gray) immunofluorescence signals in sections of substantia nigra from a control brain (top row) and a brain from an individual with iPD (bottom row). In the control brain, there was strong 14-3-3-LRRK2 PL signal and little pThr73-Rab10 signal, but in the iPD brain the opposite pattern was seen. **(E)** Quantification of 14-3-3-LRRK2 PL signal in 8 control brains and 7 iPD brains. Statistical comparison by unpaired 2-tail t-test.

Author Manuscript Author Manuscript Author Manuscript Author Manuscript

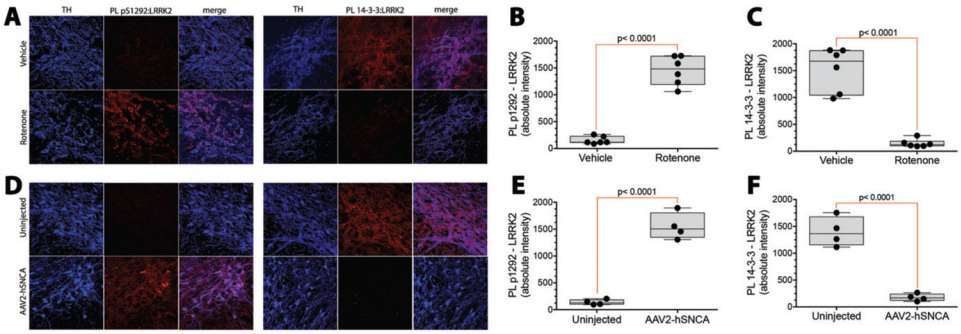


Figure 3.

Nigrostriatal LRRK2 activation is reproduced in 2 rat models of PD. **(A)** pS1292 PL and 14-3-3-LRRK2 PL signals in substantia nigra of control and rotenone treated rats. In the rotenone rats, there was increased pS1292 PL and loss of 14-3-3-LRRK2 PL signal indicating LRRK2 activation. **(B)** Quantification of pS1292 PL signal in nigrostriatal dopamine neurons from control and rotenone treated rats. Symbols represent individual animals. Statistical comparison by unpaired 2-tail t-test. **(C)** Quantification of 14-3-3-LRRK2 PL signal in nigrostriatal dopamine neurons from control and rotenone treated rats. Symbols represent individual animals. Statistical comparison by unpaired 2-tail t-test. **(D)** pS1292 PL and 14-3-3-LRRK2 PL signals in substantia nigra of rats that received a unilateral injection of AAV2-*hSNCA*. In the hemisphere overexpressing α-synuclein, there was increased pS1292 PL and loss of 14-3-3-LRRK2 PL signal indicating LRRK2 activation in nigrostriatal neurons. **(E)** Quantification of pS1292 PL signal in nigrostriatal dopamine neurons from the control and AAV-*hSNCA* injected hemispheres. Symbols represent mean values from each hemisphere. Statistical comparison by paired 2-tail t-test. **(F)** Quantification of 14-3-3-LRRK2 PL signal in nigrostriatal dopamine neurons from the control and AAV-hSNCA injected hemispheres. Symbols represent mean values from each hemisphere. Statistical comparison by paired 2-tail t-test.

Author Manuscript Author Manuscript Author Manuscript Author Manuscript

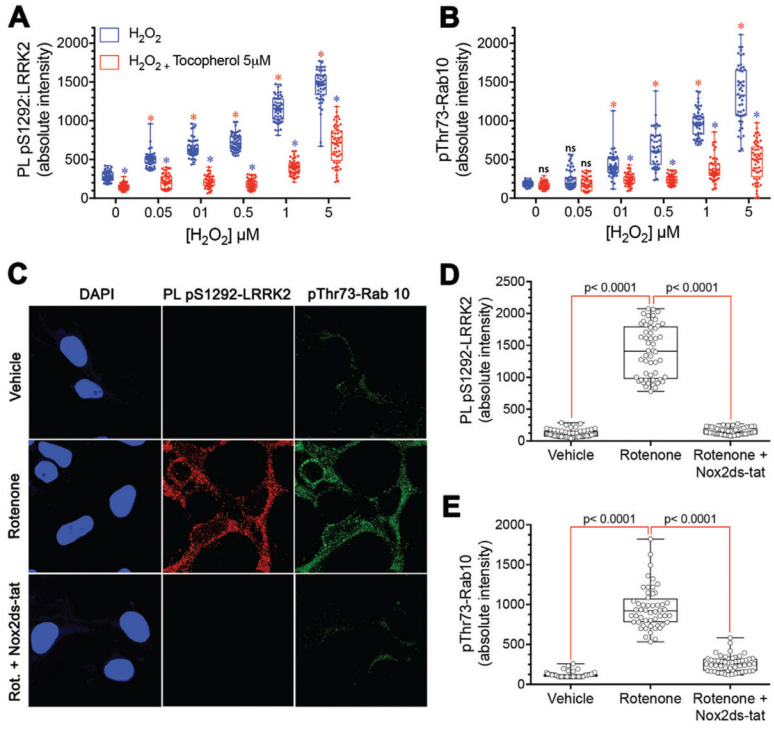


Figure 4.

LRRK2 is activated by reactive oxygen species. **(A)** pS1292 PL signal is increased dose-dependently by H_2O_2 (blue symbols), and the H_2O_2-induced increase is blocked by the antioxidant α-tocopherol (5 μM) (red symbols). Results represent 3 independent experiments. Symbols represent measurements from individual cells. Red asterisks = $p<0.0001$ vs no H_2O_2, ANOVA with Bonferroni correction; blue asterisks = $p<0.0001$ vs H_2O_2 alone at the same concentration. **(B)** pThr73-Rab10 signal is increased dose-dependently by H_2O_2 (blue symbols), and the H_2O_2-induced increase is blocked by the antioxidant α-tocopherol (5 μM) (red symbols). Results represent 3 independent experiments. Symbols represent measurements from individual cells. Red asterisks = $p<0.0001$ vs no H_2O_2, ANOVA with Bonferroni correction; blue asterisks = $p<0.0001$ vs H_2O_2 alone at the same concentration. ns = not significant. **(C)** In WT HEK cells rotenone treatment activates pS1292 signal and pThr73-Rab10 immunoreactivity. Both effects are blocked by the specific NOX2 inhibitor Nox2ds-tat. **(D)** Quantification of the pS1292 PL signal in vehicle- and rotenone-treated cells. Results represent 3 independent experiments. Symbols represent measurements from individual cells. Comparison by ANOVA with Bonferroni correction. **(E)** Quantification of the pThr73-Rab10 immunofluorescent signal in vehicle- and rotenone-treated cells. Results represent 3 independent experiments. Symbols represent measurements from individual cells. Comparison by ANOVA with Bonferroni correction.

Author Manuscript Author Manuscript Author Manuscript Author Manuscript

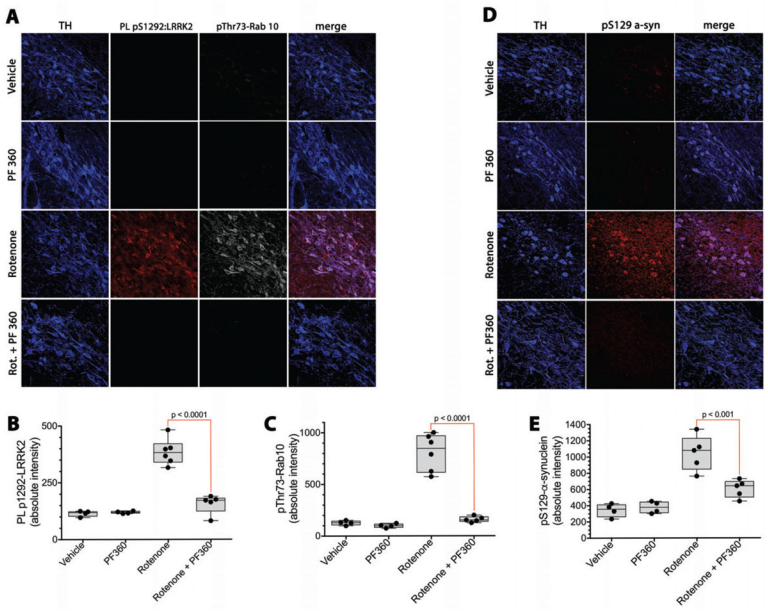


Figure 5.

Nigrostriatal LRRK2 activation and pSer129-α-synuclein accumulation can be blocked *in vivo* by a brain penetrant LRRK2 kinase inhibitor. **(A)** pS1292 PL and pThr73-Rab10 signals in rats treated with vehicle, PF-360 alone, rotenone alone and rotenone + PF-360. **(B)** Quantification of pS1292 PL signal in rats treated with vehicle, PF-360 alone, rotenone alone and rotenone + PF-360. Symbols represent individual rats. Comparison by ANOVA with Bonferroni correction. **(C)** Quantification of pThr73-Rab10 signal in rats treated with vehicle, PF-360 alone, rotenone alone and rotenone + PF-360. Symbols represent individual rats. Comparison by ANOVA with Bonferroni correction. **(D)** pSer129-α-Synuclein immunoreactivity in rats treated with vehicle, PF-360 alone, rotenone alone and rotenone + PF-360. **(E)** Quantification of pSer129-α-synuclein signal in rats treated with vehicle, PF-360 alone, rotenone alone and rotenone + PF-360. Symbols represent individual rats. Comparison by ANOVA with Bonferroni correction.

Author Manuscript Author Manuscript Author Manuscript Author Manuscript

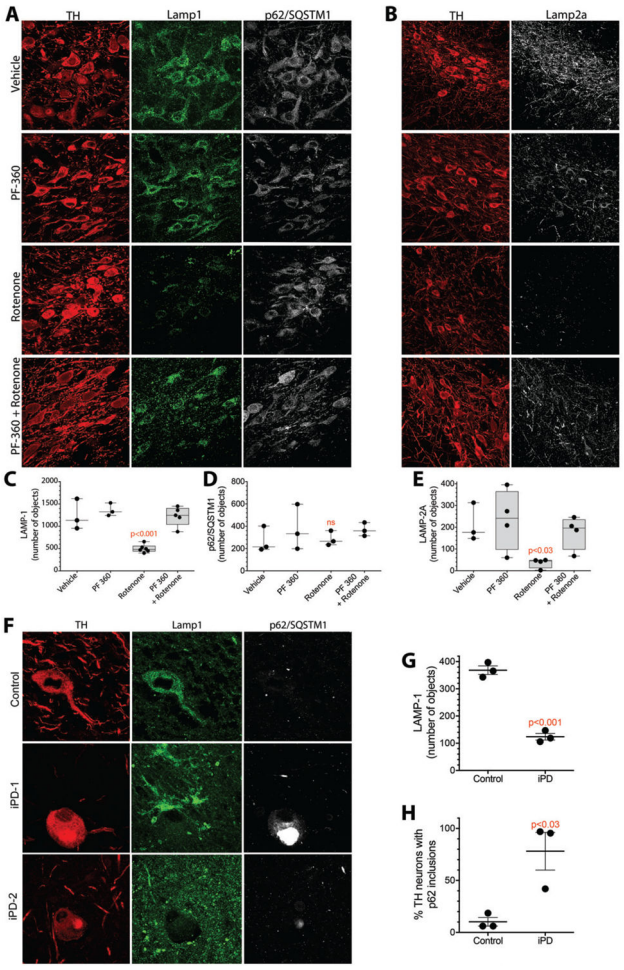


Figure 6.

Rotenone induces *in vivo* nigrostriatal lysosomal and CMA defects that are prevented by co-treatment with a LRRK2 kinase inhibitor. **(A)** Nigrostriatal Lamp1 and p62/SQSTM1 immunoreactivity in rats treated with vehicle, PF-360 alone, rotenone alone and rotenone + PF-360. **(B)** Nigrostriatal Lamp2A immunoreactivity in rats treated with vehicle, PF-360 alone, rotenone alone and rotenone + PF-360. **(C)** Quantification of Lamp1 signal in rats treated with vehicle, PF-360 alone, rotenone alone and rotenone + PF-360. Symbols represent individual rats. Comparison by ANOVA with Bonferroni correction. **(D)** Quantification of p62/SQSTM1 signal in rats treated with vehicle, PF-360 alone, rotenone alone and rotenone + PF-360. Symbols represent individual rats. Comparison by ANOVA with Bonferroni correction. **(E)** Quantification of Lamp2A signal in rats treated with vehicle, PF-360 alone, rotenone alone and rotenone + PF-360. Symbols represent individual rats. Comparison by ANOVA with Bonferroni correction. **(F)** Substantia nigra Lamp1 and p62/SQSTM1 immunoreactivity in a control brain and 2 iPD brains. In controls, dopamine neurons contain many small punctae of Lamp1 immunoreactivity and very little detectable p62/SQSTM1, presumably reflecting efficient autophagic flux. In iPD brains, note the marked loss of Lamp1 and accumulation of p62/SQSTM1 into large inclusions (Lewy bodies) in dopamine neurons in the iPD brains. **(G)** Quantification of Lamp1 in control vs

iPD dopamine neurons. Symbols represent individual brains. Comparison by unpaired 2-tail t-test. **(H)** Quantification of Lamp1 in control vs iPD dopamine neurons. Symbols represent individual brains. Comparison by unpaired 2-tail t-test.

Author Manuscript Author Manuscript Author Manuscript Author Manuscript

Author Manuscript Author Manuscript Author Manuscript Author Manuscript

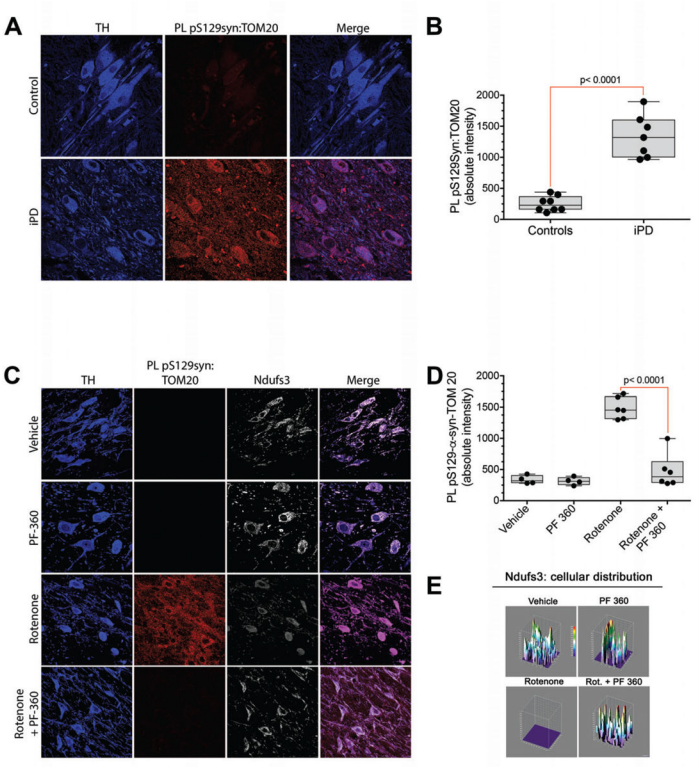


Figure 7.

Accumulated pSer129-α-synuclein binds to TOM20 in iPD and this is replicated in the rotenone rat model and is prevented by co-treatment with a LRRK2 kinase inhibitor. **(A)** pSer129-α-synuclein- (pS129syn)-TOM20 PL signal in human control and iPD substantia nigra brain sections. **(B)** Quantification of the pS129syn-TOM20 PL signal in 8 control brains and 7 iPD brains. Comparison by unpaired 2-tail t-test. **(C)** pS129syn-TOM20 PL signal and Ndufs3 immunoreactivity in substantia nigra of rats treated with vehicle, PF-360 alone, rotenone alone and rotenone + PF-360. In rotenone treated rats there is increased pS129syn-TOM20 PL signal and reduced levels and diffuse redistribution of the nuclear encoded and imported complex I subunit, Ndufs3. These abnormalities were prevented by treatment with PF-360. **(D)** Quantification of the pS129syn-TOM20 PL signal in substantia nigra of rats treated with vehicle, PF-360 alone, rotenone alone and rotenone + PF-360. Symbols represent individual rats. Comparison by ANOVA with Bonferroni correction. **(E)** Graphical representation of the distribution and fluorescence intensity levels of Ndufs3 in nigral dopamine neurons in rats treated with vehicle, PF-360 alone, rotenone alone and rotenone + PF-360. Note the loss of punctate, high intensity staining in the rotenone animals that is preserved by co-treatment with PF-360.

Author Manuscript Author Manuscript Author Manuscript Author Manuscript

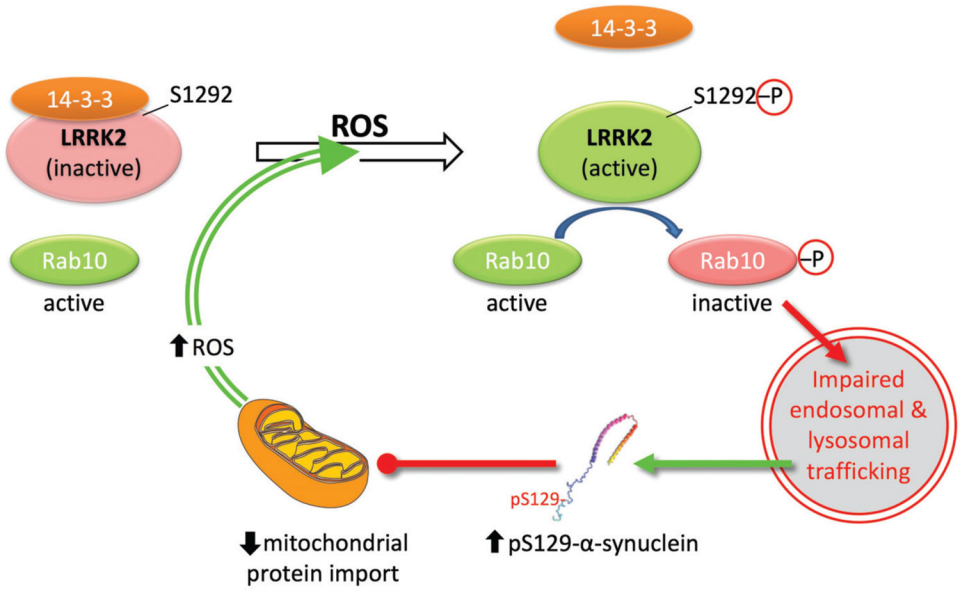


Figure 8.

Activation of LRRK2 kinase activity in iPD and its downstream consequences. Our data suggest that most wildtype endogenous LRRK2 is normally in an inactive state bound to 14-3-3 protein (although the specific isoform(s) of 14-3-3 have not been defined here). ROS signaling activates LRRK2 as indicated by phosphorylation of serine 1292 and dissociation from 14-3-3. In turn, LRRK2 kinase activity phosphorylates Rab10 at threonine 73 and inhibits its function by preventing binding to Rab GDP-dissociation inhibitor factors necessary for membrane delivery and recycling. As a result, there is impairment of endosomal and lysosomal function, which leads to accumulation of pSer129-α-synuclein, a known inhibitor of mitochondrial protein import. Blockade of mitochondrial protein import leads to senescent mitochondria that produce more ROS that can feed forward to amplify this cycle. LRRK2 kinase inhibitors block the downstream effects of LRRK2 activation.

HUMAN GENE THERAPY 9:2527–2535 (November 20, 1998)
Mary Ann Liebert, Inc.

Behavioral Recovery in 6-Hydroxydopamine-Lesioned Rats by Cotransduction of Striatum with Tyrosine Hydroxylase and Aromatic L-Amino Acid Decarboxylase Genes Using Two Separate Adeno-Associated Virus Vectors

DONG-SHEN FAN,[1,2] MATSUO OGAWA,[2] KEN-ICHI FUJIMOTO,[2] KUNIHIKO IKEGUCHI,[2] YOJI OGASAWARA,[1] MASASHI URABE,[1] MASATOYO NISHIZAWA,[2] IMAHARU NAKANO,[2] MITSUO YOSHIDA,[2] IKUKO NAGATSU,[3] HIROSHI ICHINOSE,[4] TOSHIHARU NAGATSU,[4] GARY J. KURTZMAN,[5] and KEIYA OZAWA[1]

ABSTRACT

Parkinson's disease (PD) is characterized by the progressive loss of the dopaminergic neurons in the substantia nigra and a severe decrease in dopamine in the striatum. A promising approach to the gene therapy of PD is intrastriatal expression of enzymes in the biosynthetic pathway for dopamine. Tyrosine hydroxylase (TH) catalyzes the synthesis of L-dopa, which must be converted to dopamine by aromatic L-amino acid decarboxylase (AADC). Since the endogenous AADC activity in the striatum is considered to be low, coexpression of both TH and AADC in the same striatal cells would increase the dopamine production and thereby augment the therapeutic effects. In the present study, the TH gene and also the AADC gene were simultaneously transduced into rat striatal cells, using two separate adeno-associated virus (AAV) vectors, AAV-TH and AAV-AADC. Immunostaining showed that TH and AADC were coexpressed efficiently in the same striatal cells *in vitro* and *in vivo*. Moreover, cotransduction with these two AAV vectors resulted in more effective dopamine production and more remarkable behavioral recovery in 6-hydroxydopamine (6-OHDA)-lesioned rats, compared with rats receiving AAV-TH alone ($p < 0.01$). These findings suggest an alternative strategy for gene therapy of PD and indicate that the simultaneous transduction with two AAV vectors can extend their utility for potential gene therapy applications.

OVERVIEW SUMMARY

In rodent models of Parkinson's disease (PD), the expression of tyrosine hydroxylase (TH), which catalyzes the synthesis of L-dopa, in the denervated striatum has been reported to induce behavioral recovery. L-Dopa is converted to dopamine by aromatic L-amino acid decarboxylase (AADC), but the endogenous AADC activity in the striatum is low. Therefore, both TH and AADC genes were cotransduced into rat striatal cells, using two separate adeno-associated virus (AAV) vectors, AAV-TH and AAV-AADC. More effective dopamine production, and more remarkable behavioral recovery, were observed in 6-hydroxydopamine (6-OHDA)-lesioned rats treated with both vectors compared with rats treated with AAV-TH alone.

INTRODUCTION

PARKINSON'S DISEASE (PD) is a common neurodegenerative disorder, causing cogwheel rigidity, resting tremor, and impairment in the initiation and speed of movements. The char-

[1]Division of Genetic Therapeutics, Center for Molecular Medicine, Jichi Medical School, Tochigi 329-0498, Japan.
[2]Department of Neurology, Jichi Medical School, Tochigi 329-0498, Japan.
[3]Department of Anatomy, School of Medicine, Fujita Health University, Aichi 470-1192, Japan.
[4]Institute for Comprehensive Medical Science, Fujita Health University, Aichi 470-1192, Japan.
[5]Avigen, Inc., Alameda, CA 94502.

acteristic pathological changes include a severe loss of dopamine cell bodies in the substantia nigra and a severe decrease in dopamine in the nerve endings of the striatum. The severity of PD is considered to be proportional to the loss of local dopamine. Oral administration of L-dopa, the precursor of dopamine, can restore a varying degree of motor function, since endogenous aromatic L-amino acid decarboxylase (AADC) can convert it to the neurotransmitter dopamine (Nagatsu, 1992). Unfortunately, systemic L-dopa therapy usually becomes less effective with progression of the disease and must often be discontinued owing to the numerous deleterious side effects. Local production of dopamine in the striatum can be obtained by intracerebral grafting of fetal mesencephalic cells (Freed *et al.*, 1992; Spencer *et al.*, 1992), but serious ethical issues are involved. Gene therapy represents a feasible alternative therapeutic approach. Using animal models, most of the gene therapy strategies for amelioration of PD have focused on intrastriatal grafting of cells genetically modified to express tyrosine hydroxylase (TH), which catalyzes the synthesis of L-dopa; the target cells used so far include fibroblasts, muscle cells, astrocytes, and even neurons (Jiao *et al.*, 1993; Lundberg *et al.*, 1996; Martinez-Serrano *et al.*, 1997). Direct gene transfer using TH-expressing vectors into the denervated striatum of lesioned rats has attracted considerable attention (During *et al.*, 1994; Kaplitt *et al.*, 1994). Among the vector systems for direct gene transfer into neurons, retrovirus vectors are not appropriate because they require active cell division for transduction. Adenovirus and herpes simplex virus vectors can efficiently transduce foreign genes into neurons (Le Gal La Salle *et al.*, 1993; During *et al.*, 1994), but both are cytotoxic to the recipient cells and induce immune responses against the transduced cells. A promising gene delivery vehicle for neurons is adeno-associated virus (AAV)-based vectors, because of the lack of any associated disease with wild-type virus and the ability to transduce nondividing cells as well as dividing cells (Kaplitt *et al.*, 1994; Flotte and Carter, 1995; Du *et al.*, 1996). In addition, AAV vectors do not contain viral genes, whose expression would elicit a host immune response against the transduced cells.

It is believed that L-dopa produced locally is converted to dopamine *in situ* (Kaplitt *et al.*, 1994). However, the source and the site of endogenous decarboxylase activity have yet to be identified. The AADC activity in the striatum is considered to be low (Jeager *et al.*, 1984; Tashiro *et al.*, 1989; Kang *et al.*, 1992). Therefore, one of the unsolved issues for gene therapy of PD is whether cells genetically engineered to produce L-dopa would suffice for dopamine production at the therapeutic level (Jinnah and Friedmann, 1995). Exogenous expression of both TH and AADC in striatal cells, which can supply dopamine locally, may be a more straightforward strategy. Some *in vitro* studies using nonneuronal cells have revealed that the coexpression of TH and AADC resulted in effective production of dopamine (Kang *et al.*, 1993). In the present study, we coexpressed TH and AADC in striatal cells using two separate AAV vectors, AAV-TH and AAV-AADC, since the capacity of AAV vectors for gene insertion is limited. Our main objectives in the present study were to examine whether two different genes can be efficiently transferred into the same target striatal cells by using two separate AAV vectors, and to determine whether cotransduction of the striatal cells with the TH and AADC genes would bring about better biochemical and behavioral changes than that with the TH gene alone.

MATERIALS AND METHODS

Plasmids and a 293 cell line

The AAV vector plasmids used in this study were derived from the parent vector plasmid pW1, which was constructed as follows. A 2.7-kb *Kas*I–*Ear*I fragment from a pUC119 was blunted and ligated to a multiple cloning sequence containing the following restriction enzyme sites (5′-*Not*I-*Mlu*I-*Sna*BI-*Age*I-*Bst*BI-*Bss*HII-*Nco*I-*Hpa*I-*Bsp*EI-*Pml*I-*Rsr*II-*Not*I-3′). The following fragments were successively cloned into the cloning sites: an *Spe*I–*Sac*II fragment containing the cytomegalovirus (CMV) immediate-early promoter was cloned into the *Sna*BI site, a *Bst*BI–*Bst*BI fragment from the human growth hormone first intron was inserted into the *Bst*BI site, the *lacZ* reporter gene was ligated into the *Bss*HII site, and *Hpa*I–*Bam*HI fragment of the simian virus 40 (SV40) polyadenylation signal sequence was cloned into the *Hpa*I site. The resulting *Not*I–*Not*I expression cassette was inserted between the AAV 145-bp inverted terminal repeats (ITRs) of a pUC-based plasmid. The pTH and pAADC vector plasmids were constructed by excising the *lacZ* reporter gene from the parent vector plasmid and replacing it with the 1.8-kb human TH (type 1) and 1.9-kb human AADC cDNAs, respectively (Kaneda *et al.*, 1987; Ichinose *et al.*, 1989; Nagatsu, 1991). pIM45 is a helper plasmid containing the AAV *rep* and *cap* genes, which are required for replication and capsid formation of AAV vectors, and has no overlapping AAV sequence compared with the vector plasmid. pladeno-1, a plasmid containing the E2A, E4, and VA genes of the adenovirus genome, was used in place of helper adenovirus for AAV vector production. Standard procedures were used for plasmid DNA construction. *Escherichia coli* DH5α was used for plasmid DNA amplification.

The 293 cells, a human embryonic kidney cell line, were grown in Dulbecco's modified Eagle's medium (DMEM)-F12 (GIBCO-BRL, New York, NY) culture medium containing 10% fetal bovine serum (FBS) and 2 m*M* L-glutamine at 37°C in 5% CO_2 in air.

AAV vector production

Subconfluent 239 cells were cotransfected by the calcium phosphate coprecipitation method with the vector plasmid (pW1, pTH, or pAADC), the helper plasmid (pIM45), and the pladeno-1 plasmid. After 72 hr, the cells were harvested and lysed in Tris buffer (10 m*M* Tris–150 m*M* NaCl, pH 8.0) by three cycles of freeze–thawing. The lysates were clarified of cell debris by centrifugation at 12,000 $\times$ *g* for 10 min, and the supernatants were used as the source of AAV vectors. The vector titer was determined by quantitative DNA dot-blot hybridization of the DNase-I-resistant fraction and was in the range of 10^{11}–10^{12} particles per milliliter. For some experiments, AAV vectors were purified by two rounds of CsCl density-gradient ultracentrifugation. A small amount of pseudo-wild-type recombinant virus was detectable in the vector preparations.

In vitro *transduction*

293 cells were seeded at 1.5×10^5 cells per 3.5-cm dish 1 day prior to transduction. The cells were transduced with AAV vectors by removing the growth medium and adding the indicated amount of vector stock diluted in DMEM-F12 to a final volume of 500 μl. After 1 hr of incubation, 1.5 ml of complete medium was added and the cells were grown for 24 hr. Primary cultures of rat striatal cells were obtained from day-20 Wistar rat embryos (Geller *et al.*, 1995). After 3 days of culture, three-quarters of the culture medium was replaced with fresh medium containing 40 μM cytosine arabinofuranoside (Sigma, St. Louis, MO) to suppress the growth of glial cells. About 10 days after plating, the cells were used for transduction as described above. LacZ expression by transduced cells was detected by 5-bromo-4-chloro-3-indolyl-β-D-galactopyranoside (X-Gal) staining. The TH and AADC expression was examined by dual-immunofluorescence staining. The cells were incubated with monoclonal anti-TH antibody (1:2000; Incstar, Stillwater, MN) and polyclonal anti-AADC antibody (1:2000) (Nagatsu *et al.*, 1988) at room temperature for 2 hr, washed with phosphate-buffered saline (PBS), and then incubated with rhodamine-conjugated goat anti-mouse IgG (1:50; Tago, Burlingame, CA) and fluorescein isothiocyanate (FITC)-conjugated goat anti-rabbit IgG (1:50; Tago) for 1 hr. After washing, the cells were examined under a fluorescence microscope.

L-Dopa and dopamine levels were assayed by high-performance liquid chromatography (HPLC) after incubation for 8 hr in a defined medium consisting of insulin (5 μg/ml), transferrin (100 μg/ml), 20 nM progesterone, 100 μM putrescine, 30 nM selenium, 0.5 mM methyltetrahydropterin, and 1 mM tyrosine (Sigma). The identification of peaks was carried out by comparison with standards. The amount of L-dopa or dopamine in each sample was quantitated by comparing the peak height relative to the standards with electrochemical detection (Matson *et al.*, 1987).

In vivo transduction of rat striatum

Thirty-three male albino rats of a Wistar-derived strain (200–250 g weight) were used, of which 21 rats were unilaterally lesioned at the left medial forebrain bundle with 6-hydroxydopamine (6-OHDA) before the intrastriatal transduction (Brecknell *et al.*, 1996). Vectors were stereotaxically injected into the striatum as follows. Rats were anesthetized with sodium pentobarbital (Nembutal, 20 mg/kg, intraperitoneally) and placed in a stereotaxic instrument (Narishige, Tokyo, Japan). The skull was exposed and three holes were drilled above the left striatum at the following Paxinos–Watson coordinates: anterior–posterior (AP) +1.8, lateral (L) 2.6, and AP +0.6, L 2.0 and L 3.2. AAV vector solution was injected slowly, using a Hamilton syringe, into each of the three sites at a dorsal–ventral depth of 5 mm. Each injection was 2 μl (5×10^8 vector particles per microliter, except for PBS) in volume, and was carried out over 5 min. The needle was left in place for a further 5 min before being withdrawn.

For X-Gal histochemical analysis, rats were perfused with 4% paraformaldehyde (PFA) containing 2 mM $MgCl_2$ and 5 mM ethylene glycol bis (β-aminoethylether)-*N,N,N′,N′*-tetraacetic acid, which could completely eliminate staining due to endogenous cellular enzymes (Kaplitt *et al.*, 1991). Brain was removed and placed in fixative for 1 hr, then submersed in 30% sucrose–2 mM $MgCl_2$ at 4°C overnight. Forty-micrometer sections were cut on a freezing microtome and floated briefly in PBS–2 mM $MgCl_2$ at 4°C as a wash. Sections were then transferred to substrate solution (X-Gal [1 mg/ml], 5 mM potassium ferricyanide, 5 mM potassium ferrocyanide, 2 mM $MgCl_2$, 0.01% sodium deoxycholate, 0.02% Nonidet P-40 in PBS, pH 7.2) and stained for 3 hr at 32°C.

For TH and AADC immunostaining, brain was fixed at 4°C with 4% PFA overnight and then with 15% sucrose overnight. Sections (30 μm) were cut on a freezing microtome and treated for 30 min with 0.3% hydrogen peroxide at room temperature. Nonspecific antibody binding was suppressed with an additional 30-min incubation in 2% FBS. The sections were incubated with polyclonal anti-TH (Nagatsu *et al.*, 1979) or anti-AADC antibody (1:10,000). The immunohistochemical labeling was visualized in brown by the avidin-biotinylated peroxidase complex procedure (Ogawa *et al.*, 1993). Dual-immunofluorescence staining of the sections (15 μm) for TH and AADC was conducted as described above.

In vivo striatal L-dopa and DOPAC (3,4-dihydroxyphenylacetic acid, one of the main dopamine metabolites) levels were assayed. Rats were killed and then decapitated 1 week after stereotaxic injection of AAV vectors. Brains were immediately dissected and placed on dry ice, and the striatum was isolated from both sides of the brain, respectively. The wet tissue weight was determined, and the tissues were then measured by HPLC as described above.

Behavioral testing

The 6-OHDA-lesioned rats were tested for rotational behavior at least three times before AAV vector intrastriatal injection. After the intraperitoneal administration of apomorphine (0.1 mg/kg), a dopamine receptor agonist, rats became unilaterally hyperactive and turned contralaterally. The total number of complete body turns was recorded. Six or more rotations per minute during the 15- to 20-min interval after the administration of apomorphine was used as the selection criterion of model rats, in which the rotation rate is consistent with a >90% reduction in the striatal dopamine level. Only the rats meeting this criterion were used for behavioral testing, and the rats were randomly assigned to each injection group. After the intrastriatal vector injection, the rats were periodically tested for rotational behavior. The data were statistically analyzed by repeated-measures analysis of variance (ANOVA).

RESULTS

AAV vector-mediated β-galactosidase expression in striatal cells

Primary cultured rat striatal cells were first transduced with the AAV-LacZ vector (ranging from 5×10^2 to 1×10^5 vector particles per cell) for 3 days, and then the β-galactosidase activity in the cells was determined by X-Gal staining. The transduction efficiency was dose dependent; the number of positive cells reached a plateau at 1×10^4 vector particles per cell and constituted nearly 30% of total cells (Fig. 1A). In addition, when the incubation time was prolonged from 1 to 14 days at

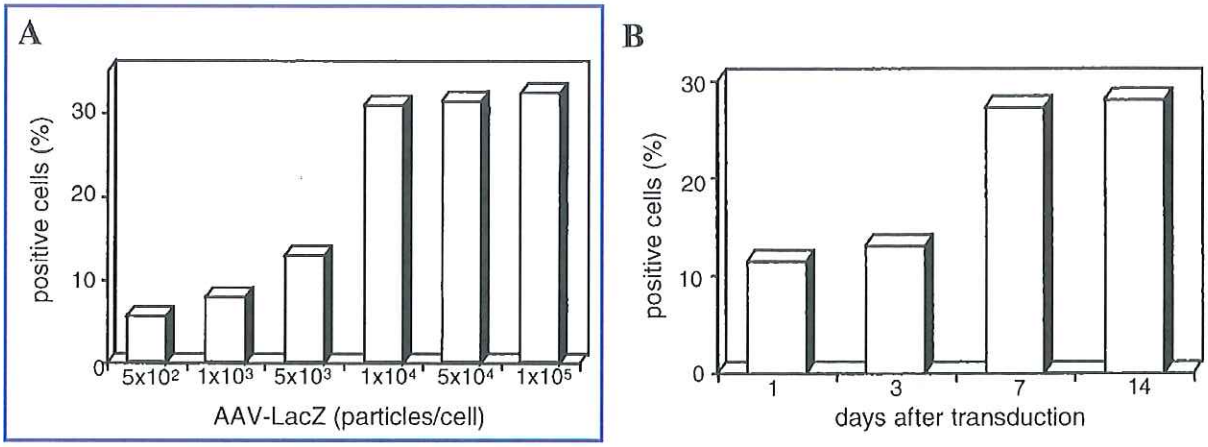


FIG. 1. Transduction efficiency of primary cultured rat striatal cells with AAV-LacZ. **(A)** The effect of vector dose on transduction efficiency. Three days after transduction with different amounts of AAV-LacZ, the cells were fixed and stained with X-Gal and subsequently with hematoxylin–eosin. **(B)** The effect of incubation period on transduction efficiency. At various time points after transduction with AAV-LacZ (5×10^3 vector particles per cell), the cells were fixed and stained with X-Gal.

5×10^3 vector particles per cell, a time-dependent increase in the number of positive cells was observed (Fig. 1B). About 1 week was required for maximum expression.

The purified AAV-LacZ was then stereotaxically injected into the normal adult rat striatum. When the rats were sacrificed at 1 week postinjection, β-galactosidase-positive cells were clearly identified at the injection site within the striatum without any background staining using X-Gal histochemistry (Color Plate 1). Most of the positive cells appeared to be neurons, on the basis of morphological criteria such as size, shape, dendritic patterns, cell body location, and placement in defined layers, although some of them were nonneuronal. No positive cell was observed on the contralateral, uninjected side of these sections (data not shown). All rats survived and appeared alert following vector injection. No pathological change was evident on microscopic examination in any animal.

AAV vector-mediated coexpression of TH and AADC in vitro

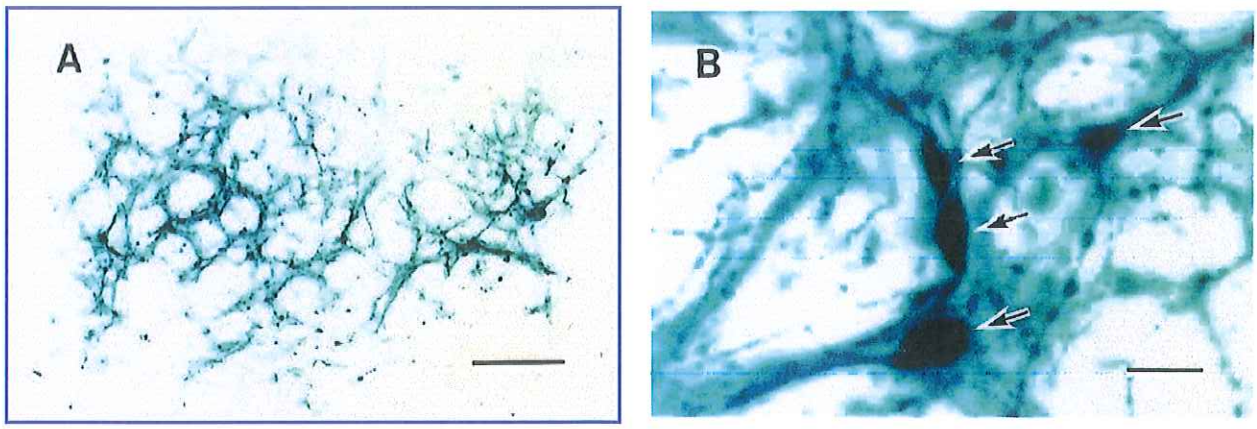
To test the AAV-TH and AAV-AADC vectors, 293 cells were transduced for Western blot analysis. As shown in Fig. 2, both TH and AADC were detected in the 293 cells cotransduced with an AAV-TH/AAV-AADC vector mixture. When transduced with AAV-TH or AAV-AADC alone, only TH or AADC expression was detected, respectively. No endogenous expression of TH or AADC was detected in untransduced 293 cells. To confirm that the coexpression of AADC with TH augments the dopamine production, the amount of AAV-AADC in the vector mixture was gradually increased while the amount of AAV-TH was kept fixed. One day after transduction, the amounts of L-dopa and dopamine in cell extracts were measured by HPLC. When the 293 cells were transduced with AAV-TH alone, the cells produced 23.35 fg of L-dopa per cell, but dopamine was not detected. A significant amount of dopamine was produced subsequent to cotransduction with both vectors, and the conversion from L-dopa to dopamine became more efficient with increasing amounts of AAV-AADC (Fig. 3). Neither L-dopa nor dopamine was detected in the untransduced or AAV-LacZ-transduced 293 cells.

Further, we examined the coexpression of TH and AADC in the primary cultured rat striatal cells after AAV vector-mediated gene transfer. One week after cotransduction, dual-immunofluorescence staining showed that TH and AADC were

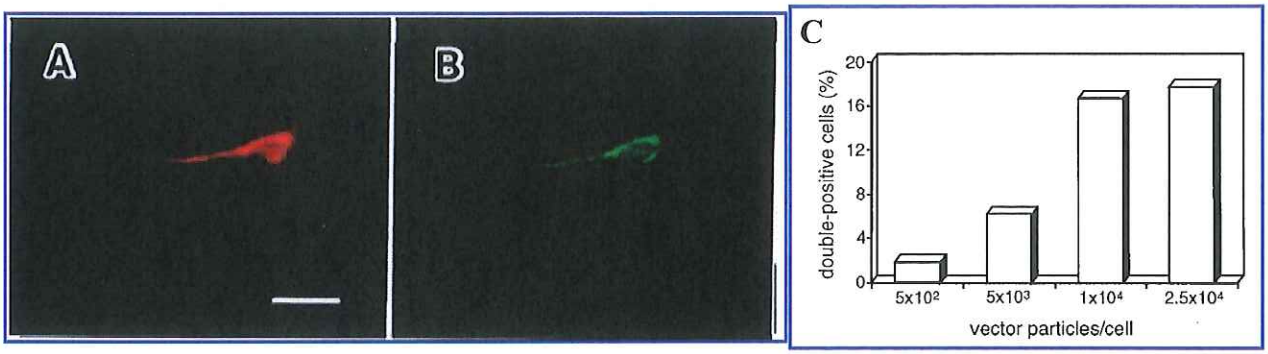
COLOR PLATE 1. LacZ expression in the rat striatum after stereotaxic injection of an AAV-LacZ. One week after intrastriatal injection, rats were sacrificed and brain sections were stained with X-Gal. All sections were 40 μm thick. Arrows in **(B)** indicate the X-Gal-positive neurons. Bar: **(A)** 200 μm; **(B)** 20 μm.

COLOR PLATE 2. Cotransduction of primary cultured rat striatal cells with AAV-TH and AAV-AADC. Coexpression of TH **(A)** and AADC **(B)** in the same striatal cell. One week after cotransduction with AAV-TH and AAV-AADC, the cultured striatal cells were fixed for dual-immunofluorescence staining with anti-TH and anti-AADC antibodies. Bar: 25 μm. **(C)**, Cotransduction efficiency. One week after cotransduction with various amounts of AAV-TH and AAV-AADC mixture (1:1), the percentage of cells double-positive for TH and AADC, relative to total stained cells, was estimated.

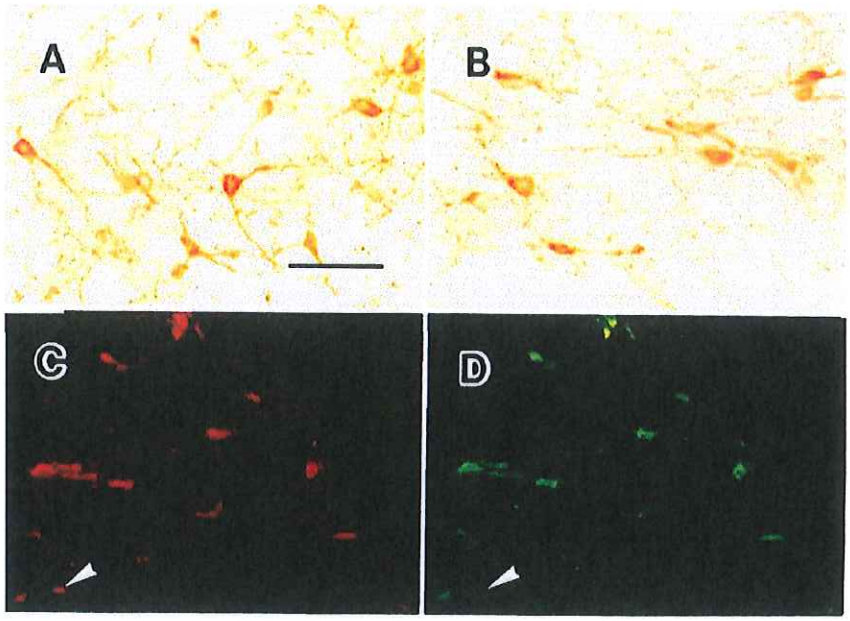
COLOR PLATE 3. Expression of TH and AADC in the denervated striatum of 6-OHDA-lesioned rats stereotaxically injected with AAV-TH and AAV-AADC mixture. Six weeks after intrastriatal injection, the rats were sacrificed and the brain sections were stained immunohistochemically. TH and AADC were detected with anti-TH **(A)** and anti-AADC **(B)** antibodies, respectively, by the avidin-biotinylated peroxidase complex procedure. Coexpression of TH **(C)** and AADC **(D)** was confirmed by dual-immunofluorescence staining. White arrowheads show that the indicated cell was positive for TH but negative for AADC. Bar: (**A** and **B**) 150 μm; (**C** and **D**) 200 μm.



COLOR PLATE 1.



COLOR PLATE 2.



COLOR PLATE 3.

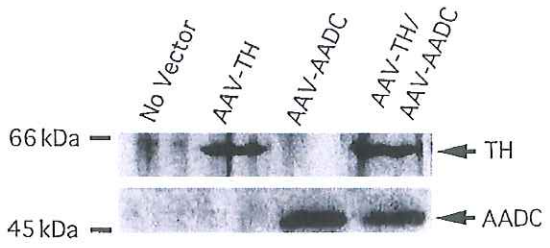


FIG. 2. Western analysis for TH and/or AADC expression in 293 cells transduced with AAV-TH and/or AAV-AADC.

coexpressed in the same striatal cells (Color Plate 2A and B). We quantified the cotransduction efficiency with increasing doses of the AAV-TH/AAV-AADC vector mixture (ranging from 5×10^2 to 2.5×10^4 vector particles per cell, each). The number of double-positive cells was dose dependent and increased to 18% of total stained cells (Color Plate 2C). To examine whether the striatal cells contransduced with the AAV-TH/AAV-AADC mixture can more efficiently synthesize dopamine than do cells transduced with AAV-TH alone, the intracellular L-dopa and dopamine levels were also measured by HPLC. Compared with those transduced with AAV-TH alone, the cultures cotransduced with the AAV-TH/AAV-AADC vector mixture (ratio, 1:1) showed a significant increase in dopamine level; vice versa, and apparent decrease in L-dopa level was observed, although it was not so remarkable as that in 293 cells (Table 1).

Stereotaxic injection of AAV-TH and/or AAV-AADC vectors in 6-OHDA-lesioned rats

The AAV-TH and/or AAV-AADC vectors were stereotaxically injected into the denervated striatum of 6-OHDA-lesioned rats. Apomorphine-induced asymmetrical body rotation, a behavioral test, was conducted every week following the injection to determine the effects of AAV-TH/AAV-AADC mixture, AAV-TH alone, AAV-AADC alone, AAV-LacZ, or PBS. As shown in Fig. 4, the rotational behavior of the rats injected with

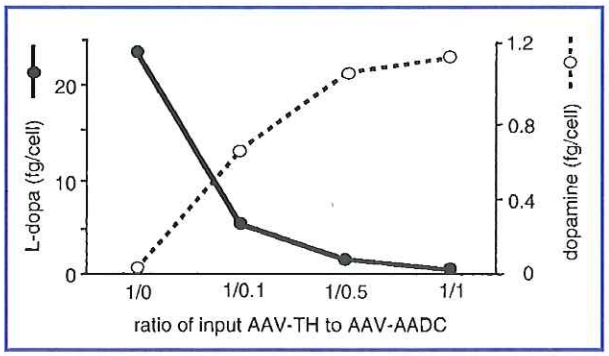


FIG. 3. L-Dopa and dopamine levels in 293 cells transduced with AAV-TH and AAV-AADC at various ratios. The cells were cotransduced with a fixed amount of AAV-TH (4500 vector particles per cell) and a variable amount of AAV-AADC (ranging from 0 to 4500 vector particles per cell). One day after transduction, L-dopa and dopamine levels in the cell extracts were measured by HPLC.

TABLE 1. PRODUCTION OF CATECHOLAMINES IN PRIMARY CULTURED RAT STRIATAL CELLS TRANSDUCED WITH AAV-TH/AAV-AADC OR AAV-TH ALONE[a]

	Catecholamine (fg/cell)	
Vector	*L-Dopa*[b]	*Dopamine*[b]
AAV-TH/AAV-AADC	0.91 ± 0.01	0.91 ± 0.03
AAV-TH	3.14 ± 0.02	<0.20
AAV-LacZ	ND	ND
PBS	ND	ND

[a]Primary cultured rat striatal cells were transduced with AAV vectors (1.4×10^4 vector particles per cell). Three weeks later, intracellular l-dopa and dopamine were assayed by HPLC.

[b]$p < 0.01$, compared between AAV-TH/AAV-AADC and AAV-TH alone, using Student's t test.

Abbreviation: ND, Not detected.

AAV-AADC alone ($n = 4$), AAV-LacZ ($n = 3$), or PBS ($n = 3$) was unaltered from baseline throughout the 6-week test period following the stereotaxic injection. However, significant decreases ($p < 0.01$) in the rotational rate were observed in both groups of rats treated with AAV-TH/AAV-AADC mixture ($n = 4$) and AAV-TH alone ($n = 4$). Moreover, the decrease was more remarkable in the rats injected with the AAV-TH/AAV-AADC mixture compared with those given AAV-TH alone ($p < 0.01$). Although these data were obtained by using crude preparations of AAV vectors, better behavioral recovery was also observed after stereotaxic injection with purified AAV-TH/AAV-AADC mixture in additional experiments (data not shown).

At 6 weeks postinjection, the expression of TH and AADC in the striatum was examined. In the denervated striatum of animals injected with AAV-TH/AAV-AADC mixture, both TH-immunoreactive (TH-IR) and AADC-immunoreactive (AADC-IR) cells were detected and clustered around the injection sites (Color Plate 3A and B). Furthermore, dual-immunofluorescence staining with anti-TH and anti-AADC antibodies showed that nearly all of the striatal TH-IR cells overlapped with AADC-IR cells; the percentage of double-positive cells was roughly estimated to be more than 95% of total transduced cells (Color Plate 3C and D). Neither TH-IR nor AADC-IR cells were observed on the contralateral, uninjected side of these sections as well as in the striata of PBS-injected or AAV-LacZ-injected control rats (data not shown).

To confirm that the behavioral recovery following AAV-TH/AAV-AADC cotransduction was caused by enhanced dopamine production *in vivo*, the striatal L-dopa and DOPAC levels were assayed by HPLC (Fig. 5A and B). In 6-OHDA-lesioned rats injected with AAV-TH alone, a large amount of L-dopa was detected in the lesioned striatum, but the DOPAC level was low. On the other hand, when coinjected with AAV-TH and AAV-AADC vectors, a significantly larger amount of DOPAC was detected in the lesioned striatum with low-level L-dopa, suggesting efficient conversion to dopamine. No significant difference in L-dopa and DOPAC levels was observed in the intact side of the striatum in all of the animals examined.

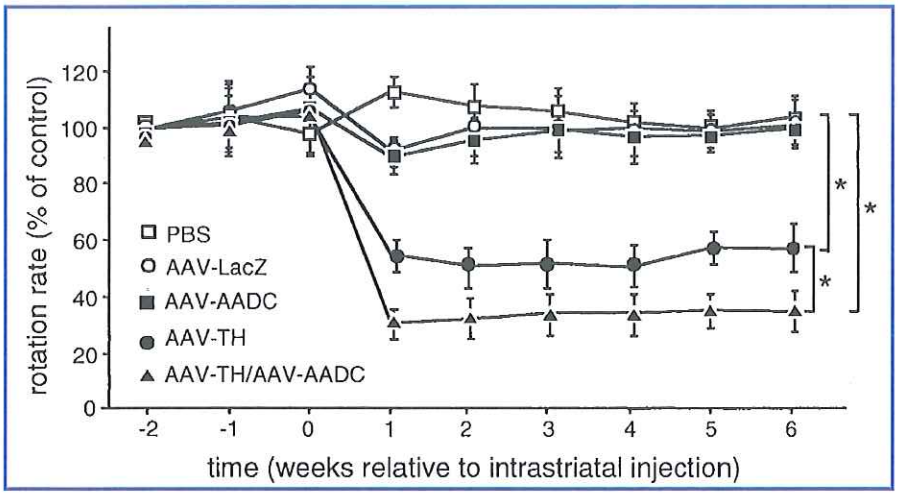


FIG. 4. Effects of intrastriatal injection of AAV-TH and/or AAV-AADC vectors on rotational behavior of 6-OHDA-lesioned rats. Apomorphine-induced asymmetrical rotation was evaluated every week before and after stereotaxic injection with PBS ($n = 3$), AAV-LacZ ($n = 3$), AAV-AADC ($n = 4$), AAV-TH ($n = 4$), or AAV-TH/AAV-AADC mixture ($n = 4$). Data were statistically analyzed by repeated-measures ANOVA ($^*p < 0.01$).

DISCUSSION

The present study showed the following: (1) AAV vectors efficiently transferred and expressed foreign genes in striatal cells *in vitro* and *in vivo*; (2) the use of two separate AAV vectors, AAV-TH and AAV-AADC, made it possible to coexpress TH and AADC in the same striatal cells; (3) cotransduction with these two AAV vectors resulted in more efficient dopamine production and more remarkable behavioral recovery in 6-OHDA-lesioned rats than with AAV-TH alone.

TH and AADC, as well as dopamine, have been immunocytochemically shown to be anterogradely transported from the substantia nigra to the striatum (Nagatsu *et al.*, 1990). In the striatum of PD and 6-OHDA-lesioned rats, not only dopamine but also TH and AADC were found to be decreased; this was caused by severe loss of dopaminergic nerve terminals in the local region (Hefti *et al.*, 1981; Nagatsu, 1993). Therefore, when gene therapy of PD is conducted with TH gene alone, one of the unsolved issues is how L-dopa is decarboxylated to dopamine in the striatum, since the endogenous AADC activity in the striatum is considered to be low (Jeager *et al.*, 1984; Tashiro *et al.*, 1989; Kang *et al.*, 1992). Evidence suggested that exogenous L-dopa decarboxylation does not occur in the striatum itself; that is, dopamine is formed in nearby areas and diffuses back into the striatum (Kang *et al.*, 1992). However, since it is believed that most of the L-dopa produced in the local region must be converted to dopamine *in situ* (Kaplitt *et al.*, 1994), a lack of substantial endogenous decarboxylase activity in the striatum may limit the therapeutic effect of the transfer of TH gene alone. In fact, it has been suggested that the reason why the intracerebral graft of mesencephalic fetal cells is effective is not because the graft provides dopamine directly but because it provides AADC (Melamed, 1988). This may explain why dopaminergic transplants to PD patients have reduced the L-dopa dose required, but have not been able to eliminate the need for medication entirely (Freed *et al.*, 1992; Spencer *et al.*,

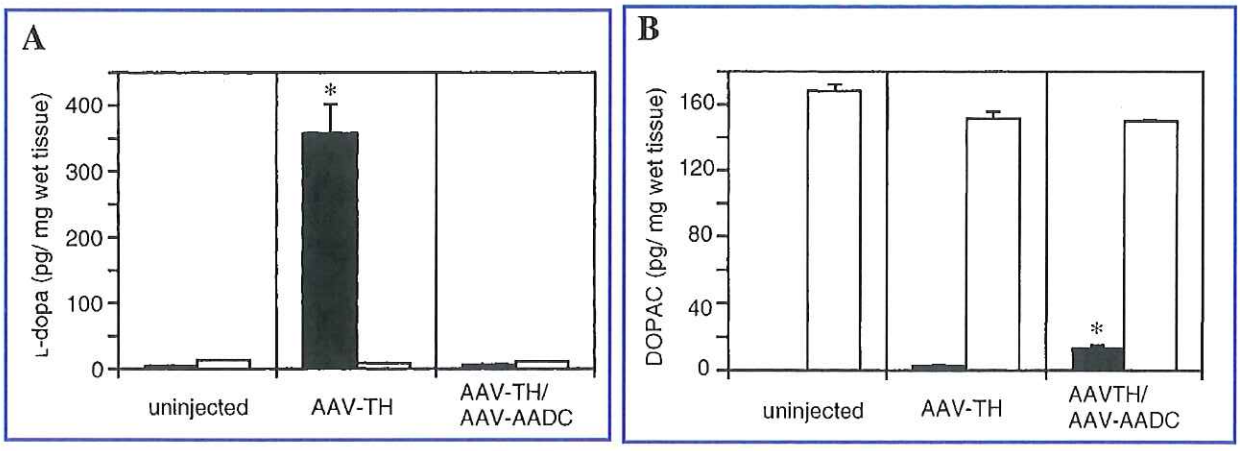


FIG. 5. L-Dopa **(A)** and DOPAC **(B)** levels in the 6-OHDA-lesioned striatum (solid bars) and intact striatum (open bars) of uninjected, AAV-TH-injected, and AAV-TH/AAV-AADC-injected rats. The striatal L-dopa and DOPAC levels were measured by HPLC 1 week after vector injection. No carbidopa was preadministered to inhibit peripheral AADC activity in capillary endothelium.

1992). Our study focused on the improvement in dopamine synthesis by the combined use of TH and AADC genes. On coexpression of TH and AADC, the striatal cells become autonomous dopamine-producing cells and, therefore, this is a more straightforward approach to gene therapy of PD. Dual-immunofluorescence staining showed that both TH and AADC were efficiently coexpressed in the same striatal cells, the majority of which appeared to be neurons morphologically.

Neurochemical research about intrastriatal grafting of AADC-expressing Cos cells showed that enhancing AADC activity in 6-OHDA-lesioned rat striatum can improve dopamine bioformation in response to systemically administered L-dopa (Kaddis *et al.*, 1997). In the present study, we showed that coexpression of TH and AADC with two separate AAV vectors resulted in a significant increase in the intracellular dopamine level in primary cultured rat striatal cells. Furthermore, better behavioral recovery was observed when 6-OHDA-lesioned rats were coinjected with AAV-TH and AAV-AADC rather than with AAV-TH alone. The improvement was probably caused by enhanced dopamine production, because biochemical analysis showed that effective L-dopa decarboxylation occurred in the lesioned striatum after coinjection with AAV-TH and AAV-AADC. We measured the striatal DOPAC level instead of dopamine. DOPAC is one of the main dopamine metabolites; it is converted from dopamine by striatal monoamine oxidase (MAO) and is proportional to the local dopamine bioformation. Since genetically produced dopamine is unlike primary dopamine in the nigrostriatal system—the latter can escape from MAO as it is stored in synaptic vesicles—the striatal DOPAC level is a reliable indicator of dopamine production through genetic intervention.

One of the possible sites of conversion of L-dopa to dopamine in the 6-OHDA-lesioned striatum has been previously postulated to be capillary endothelium (Duvoisin and Mytilineou, 1978; Hefti *et al.*, 1981). Interestingly, in the present study, a high concentration of the genetically produced L-dopa was detected in the lesioned striatum of rats injected with AAV-TH alone (carbidopa, an inhibitor of peripheral AADC activity, was not preadministered) (Fig. 5A). This finding suggests that AADC in endothelium is unlikely to be the site of local L-dopa decarboxylation, and confirmed that striatal AADC activity in 6-OHDA-lesioned rat model is insufficient as in PD, although it has been reported that the reduction in AADC activity is not as low as that of TH activity (Hefti *et al.*, 1981).

Long-term expression of transgenes can be expected when the genes are transferred into neurons *in vivo* using AAV vectors. Using the 6-OHDA-lesioned rat model, the TH expression in the striatum has been reported to persist for at least 4 months after intrastriatal AAV-TH injection (Kaplitt *et al.*, 1994). Therefore, the therapeutic effects of gene transfer into striatal cells, using AAV vectors, should persist for a fairly long time. In our vector preparations, a small amount of pseudo-wild-type recombinant virus was detected. Therefore, we cannot exclude the possibility of some effects of pseudo-wild-type virus on the level and duration of transgene expression. We are now developing a novel AAV helper plasmid that does not produce any pseudo-wild-type virus under any conditions.

It is worthy of note that multiple gene transfer into the same target cells is possible by cotransduction using separate AAV vectors. This method compensates for the restrictions concerning gene insertion into the small AAV vectors—their capacity is limited—and will be valuable in the development of a gene therapy strategy for diseases in which multiple gene transfer is required for better therapeutic effects. For instance, the addition of the gene encoding GTP cyclohydrolase I (GCH), an enzyme critical for the synthesis of the cofactor tetrahydrobiopterin (BH_4), would further improve the therapeutic effects of TH gene therapy in PD, because the limited success of the current TH expression strategy may also be related to insufficient availability of BH_4 (Nagatsu, 1993; Bencsics *et al.*, 1996). A triple transduction with AAV-TH, AAV-AADC, and AAV-GCH for gene therapy of PD is currently under investigation.

ACKNOWLEDGMENTS

We thank N. Shizuma, Y. Nagatsuka, and Y. Kubota for excellent technical assistance. We also thank K. Niijima and Y. Iwaki for helpful advice. This work was supported by a Grant-in-Aid for Scientific Research on Priority Areas from the Ministry of Education, Science, Sports and Culture of Japan; by grants from the Ministry of Health and Welfare of Japan; and by CREST (Core Research for Evolutional Science and Technology) of Japan Science and Technology Corporation (JST).

REFERENCES

BENCSICS, C., WACHTEL, S.R., MILSTIEN, S., HATAKEYAMA, K., BECKER, J.B., and KANG, U.J. (1996). Double transduction with GTP cyclohydrolase I and tyrosine hydroxylase is necessary for spontaneous synthesis of L-DOPA by primary fibroblasts. J. Neurosci. **16,** 4449–4456.

BRECKNELL, J.E., HAQUE, N.S.K., DU, J.-S., MUIR, E.M., FIDLER, P.S., HLAVIN, M.-L., FAWCETT, J.W., and DUNNETT, S.B. (1996). Functional and anatomical reconstruction of the 6-hydroxydopamine lesioned nigrostriatal system of the adult rat. Neuroscience **71,** 913–925.

DU, B., WU, P., BOLDT-HOULE, D.M., and TERWILLIGER, E.F. (1996). Efficient transduction of human neurons with an adeno-associated virus vector. Gene Ther. **3,** 254–261.

DURING, M.J., NAEGELE, J.R., O'MALLEY, K.L., and GELLER, A.I. (1994). Long-term behavioral recovery in Parkinson's rats by an HSV vector expressing tyrosine hydroxylase. Science **266,** 1399–1403.

DUVOISIN, R.C., and MYTILINEOU, C. (1978). Where is L-DOPA decarboxylated in the striatum after 6-hydroxydopamine nigrotomy? Brain Res. **152,** 369–373.

FLOTTE, T.R., and CARTER, B.J. (1995). Adeno-associated virus vectors for gene therapy. Gene Ther. **2,** 357–362.

FREED, C.R., BREEZE, R.E., ROSENBERG, N.L., SCHNECK, S.A., KRIEK, E., QI, J.-X., LONE, T., ZHANG, Y.-B., SNYDER, J.A., WELLS, T.H., RAMIG, L.O., THOMPSON, L., MAZZIOTTA, J.C., HUANG, S.C., GRAFTON, S.T., BROOKS, D., SAWIE, G., SCHROTER, G., and ANSARI, A.A. (1992). Survival of implanted fetal dopamine cells and neurologic improvement 12 to 46 months after transplantation for Parkinson's disease. N. Engl. J. Med. **327,** 1549–1555.

GELLER, A.I., DURING, M.J., OH, Y.J., FREESE, A., and O'MALLEY, K. (1995). An HSV-1 vector expressing tyrosine hydroxylase cause production and release of L-DOPA from cultured rat striatal cells. J. Neurochem. **64,** 487–496.

HEFTI, F., MELAMED, E., and WURTMAN, R.J. (1981). The site of

dopamine formation in rat striatum after L-DOPA administration. J. Pharmacol. Exp. Ther. **217,** 189–197.

ICHINOSE, H., KUROSAWA, Y., TITANI, K., FUJITA, K., and NAGATSU, T. (1989). Isolation and characterization of a cDNA clone encoding human aromatic L-amino acid decarboxylase. Biochem. Biophys. Res. Commun. **164,** 1024–1030.

JEAGER, C.B., RUGGIERO, D.A., ALBERT, V.R., JOH, T.H., and REIS, D.J. (1984). Immunocytochemical localization of aromatic L-amino acid decarboxylase. In *Handbook of Chemical Neuroanatomy,* Vol. 2. A. Bjorklund and T. Hokfelt, eds. (Elsevier, Amsterdam) pp. 384–408.

JIAO, S., GUREVICH, V., and WOLFF, J.A. (1993). Long-term correction of rat model of Parkinson's disease by gene therapy. Nature (London) **362,** 450–453.

JINNAH, H.A., and FRIEDMANN, T. (1995). Gene therapy and the brain. Br. Med. Bull. **51,** 138–148.

KADDIS, F.G., CLARKSON, E.D., WEBER, M.J., VANDENBERGH, D.J., DONOVAN, D.M., MALLET, J., HORELLOU, P., UHL, G.R., and FREED, C.R. (1997). Intrastriatal grafting of Cos cells stably expressing human aromatic L-amino acid decarboxylase: Neurochemical effects. J. Neurochem. **68,** 1520–1526.

KANEDA, N., KOBAYASHI, K., ICHINOSE, H., KISHI, F., NAKAZAWA, A., KUROSAWA, Y., FUJITA, K., and NAGATSU, T. (1987). Isolation of a novel cDNA clone for human tyrosine hydroxylase: Alternative RNA splicing produces four kinds of mRNA from a single gene. Biochem. Biophys. Res. Commun. **146,** 971–975.

KANG, U.J., PARK, D.H., WESSEL, T., BAKER, H., and JOH, T.H. (1992). DOPA-decarboxylation in the striata of rats with unilateral substantia nigra lesions. Neurosci. Lett. **147,** 53–57.

KANG, U.J., FISHER, L.J., JOH, T.H., O'MALLEY, K.L., and GAGE, F.H. (1993). Regulation of dopamine production by genetically modified primary fibroblasts. J. Neurosci. **13,** 5203–5211.

KAPLITT, M.G., PFAUS, J.G., KLEOPOULOS, S.P., HANLON, B.A., RABKIN, S.D., and PFAFF, D.W. (1991). Expression of a functional foreign gene in adult mammalian brain following *in vivo* transfer via a herpes simplex virus type 1 defective viral vector. Mol. Cell. Neurosci. **2,** 320–330.

KAPLITT, M.G., LEONE, P., SAMULSKI, R.J., XIAO, X., PFAFF, D.W., O'MALLEY, K.L., and DURING, M.J. (1994). Long-term gene expression and phenotypic correction using adeno-associated virus vectors in the mammalian brain. Nature Genet. **8,** 148–154.

LE GAL LA SALLE, G., ROBERT, J.J., BERNARD, S., RIDOUX, V., STRATFORD-PERRICAUDET, L.D., PERRICAUDET, M., and MALLET, J. (1993). An adenovirus vector for gene transfer into neurons and glia in the brain. Science **259,** 988–990.

LUNDBERG, C., HORELLOU, P., MALLET, J., and BJORKLUND, A. (1996). Generation of DOPA-producing astrocytes by retroviral transduction of the human tyrosine hydroxylase gene: *In vitro* characterization and *in vivo* effects in the rat Parkinson model. Exp. Neurol. **139,** 39–53.

MARTINEZ-SERRANO, A., LUNDBERG, C., and BJORKLUNG, A. (1997). Use of conditionally immortalized neural progenitors for transplantation and gene transfer to the CNS. In *Isolation, Characterization and Utilization of CNS Stem Cells.* F. Gage and Y. Christen, eds. (Springer-Verlag, Berlin) pp. 151–169.

MATSON, W.R., GAMACHE, P.G., BEAL, M.F., and BIRD, E.D. (1987). EC array sensor concepts and data. Life Sci. **41,** 905–908.

MELAMED, E. (1988). Brain grafting may reverse lose of responsiveness to levodopa therapy in Parkinson's disease. Clin. Neuropharmacol. **11,** 77–82.

NAGATSU, I., KONDO, Y., INAGAKI, S., KOJIMA, H., and NAGATSU, T. (1979). Immunofluorescent and biochemical studies on tyrosine hydroxylase and dopamine-beta-hydroxylase of the bullfrog sciatic nerves. Histochemistry **61,** 103–109.

NAGATSU, I., SAKAI, M., YOSHIDA, M., and NAGATSU, T. (1988). Aromatic L-amino acid decarboxylase immunoreactive neurons in and around the cerebrospinal fluid-contacting neurons of the central canal do not contain dopamine or serotonin in the mouse and rat spinal cord. Brain Res. **475,** 91–102.

NAGATSU, I., SAKAI, M., YOSHIDA, M., and NAGATSU, T. (1990). Dopamine immunocytochemistry in the nigrostriatal system of pre- and postnatal mice. In *Basic, Clinical, and Therapeutic Aspects of Alzheimer's and Parkinson's Disease.* T. Nagatsu, A. Fisher, and M. Yoshida, eds. (Plenum Press, New York) pp. 263–266.

NAGATSU, T. (1991). Genes for human catecholamine-synthesizing enzymes. Neurosci. Res. **12,** 315–345.

NAGATSU, T. (1992). Molecular biology of dopamine systems. In *Controversies in the Treatment of Parkinson's Disease.* U.K. Rinne and N. Yanagisawa, eds. (PMSI, Tokyo) pp. 15–26.

NAGATSU, T. (1993). Biochemical aspects of Parkinson's disease. In *Advances in Neurology,* Vol. 60: *Parkinson's Disease: From Basic Research to Treatment.* N. Yanagisawa and Y. Mizuno, eds. (Raven Press, New York) pp. 165–174.

OGAWA, M., ARAKI, M., NAITO, M., TAKEYA, M., TAKAHASHI, K., and YOSHIDA, M. (1993). Early changes of macrophage-like immunoreactivity in the rat inferior olive after intraperitoneal 3-acetylpyridine injection. Brain Res. **610,** 135–140.

SPENCER, D.D., ROBBINS, R.J., NAFTOLIN, F., MAREK, K.L., VOLLMER, T., LERANTH, C., ROTH, R.H., PRICE, L.H., GJEDDE, A., BUNNEY, B.S., SASS, K.J., ELSWORTH, J.D., KIER, E.L., MAKUCH, R., HORRER, P.B., and REDMONE, D.E., Jr. (1992). Unilateral transplantation of human fetal mesencephalic tissue into the caudate nucleus of patients with Parkinson's disease. N. Engl. J. Med. **327,** 1541–1548.

TASHIRO, T., KANEKO, T., SUGIMOTO, T., NAGATSU, I., KIKUCHI, H., and MIZUNO, N. (1989). Striatal neurons with aromatic L-amino acid decarboxylase-like immunoreactivity in the rat. Neurosci. Lett. **100,** 29–34.

Address reprint requests to:
Dr. Keiya Ozawa
Division of Genetic Therapeutics,
Center for Molecular Medicine
Jichi Medical School
3311-1, Yakushiji, Minamikawachi-machi
Kawachi-gun, Tochigi 329-0498, Japan

Received for publication December 28, 1997; accepted after revision August 31, 1998.

This article has been cited by:

1. Madhavi Rayapudi, Priya Rajavelu, Xiang Zhu, Ajay Kaul, Rituraj Niranjan, Scott Dynda, Akanksha Mishra, Jochen Mattner, Asifa Zaidi, Parmesh Dutt, Anil Mishra. 2014. Invariant natural killer T-cell neutralization is a possible novel therapy for human eosinophilic esophagitis. *Clinical & Translational Immunology* **3**, e9. [CrossRef]
2. Arpad Palfi, Naomi Chadderton, Alex G. McKee, Alfonso Blanco Fernandez, Peter Humphries, Paul F. Kenna, G. Jane Farrar. 2012. Efficacy of Codelivery of Dual AAV2/5 Vectors in the Murine Retina and Hippocampus. *Human Gene Therapy* **23**:8, 847-858. [Abstract] [Full Text HTML] [Full Text PDF] [Full Text PDF with Links] [Supplemental Material]
3. Sunyoung Kim, Zhaohui Peng, Yasufumi Kaneda. 2008. Current Status of Gene Therapy in Asia. *Molecular Therapy* **16**, 237-243. [CrossRef]
4. Keiya Ozawa. 2007. Gene therapy using AAV vectors. *Drug Delivery System* **22**, 643-650. [CrossRef]
5. Keiya OZAWA. 2007. Gene therapy using AAV. *Uirusu* **57**, 47-55. [CrossRef]
6. Hiroaki Mizukami, Jun Mimuro, Tsuyoshi Ogura, Takashi Okada, Masashi Urabe, Akihiro Kume, Yoichi Sakata, Keiya Ozawa. 2006. Adipose Tissue as a Novel Target for In Vivo Gene Transfer by Adeno-Associated Viral Vectors. *Human Gene Therapy* **0**:10.1089/hum.0.0.issue-0, 060913044654009. [CrossRef]
7. Hiroaki Mizukami, Jun Mimuro, Tsuyoshi Ogura, Takashi Okada, Masashi Urabe, Akihiro Kume, Yoichi Sakata, Keiya Ozawa. 2006. Adipose Tissue as a Novel Target for In Vivo Gene Transfer by Adeno-Associated Viral Vectors. *Human Gene Therapy* **0**:10.1089/hum.0.0.issue-0, 060815083008001. [CrossRef]
8. Marcel M. Daadi, Phillip Pivirotto, John Bringas, Janet Cunningham, John Forsayeth, Jamie Eberling, Krys S. Bankiewicz. 2006. Distribution of AAV2-hAADC-transduced cells after 3 years in Parkinsonian monkeys. *NeuroReport* **17**, 201-204. [CrossRef]
9. Corinna Burger, Kevin Nash, Ronald J. Mandel. 2005. Recombinant Adeno-Associated Viral Vectors in the Nervous System. *Human Gene Therapy* **0**:10.1089/hum.0.0.issue-0, 050701034702015. [CrossRef]
10. Shin-ichi Muramatsu, Hideo Tsukada, Imaharu Nakano, Keiya Ozawa. 2005. Gene therapy for Parkinson's disease using recombinant adeno-associated viral vectors. *Expert Opinion on Biological Therapy* **5**, 663-671. [CrossRef]
11. O. Eberhardt, J. B. Schulz. 2004. Gene therapy in Parkinson?s disease. *Cell and Tissue Research* **318**, 243-260. [CrossRef]
12. Keiya Ozawa. 2004. Development and Application of Gene Therapy Technologies. *Uirusu* **54**, 49-57. [CrossRef]
13. E. Antonio Chiocca. 2003. Gene Therapy: A Primer for Neurosurgeons. *Neurosurgery* 364. [CrossRef]
14. Ke-Qin Xin, Takaaki Ooki, Hiroaki Mizukami, Kenji Hamajima, Koji Okudela, Kumiko Hashimoto, Yoshitsugu Kojima, Nao Jounai, Yasuko Kumamoto, Shin Sasaki, Dennis Klinman, Keiya Ozawa, Kenji Okuda. 2002. Oral Administration of Recombinant Adeno-Associated Virus Elicits Human Immunodeficiency Virus-Specific Immune Responses. *Human Gene Therapy* **13**:13, 1571-1581. [Abstract] [Full Text PDF] [Full Text PDF with Links]
15. Gary Hsich, Miguel Sena-Esteves, Xandra O. Breakefield. 2002. Critical Issues in Gene Therapy for Neurologic Disease. *Human Gene Therapy* **13**:5, 579-604. [Abstract] [Full Text PDF] [Full Text PDF with Links]
16. Hoang N Le, David M Frim. 2002. Gene therapy for Parkinson's disease. *Expert Opinion on Biological Therapy* **2**, 151-161. [CrossRef]
17. T. Kawada, M. Nakazawa, S. Nakauchi, K. Yamazaki, R. Shimamoto, M. Urabe, J. Nakata, C. Hemmi, F. Masui, T. Nakajima, J.-I. Suzuki, J. Monahan, H. Sato, T. Masaki, K. Ozawa, T. Toyo-oka. 2002. Rescue of hereditary form of dilated cardiomyopathy by rAAV-mediated somatic gene therapy: Amelioration of morphological findings, sarcolemmal permeability, cardiac performances, and the prognosis of TO-2 hamsters. *Proceedings of the National Academy of Sciences* **99**, 901-906. [CrossRef]

18. T TOYOOKA, T KAWADA, H XI, M NAKAZAWA, F MASUI, C HEMMI, J NAKATA, A TEZUKA, K IWASAWA, M URABE. 2002. Gene therapy prevents disruption of dystrophin-related proteins in a model of hereditary dilated cardiomyopathy in hamsters. *Heart, Lung and Circulation* **11**, 174-181. [CrossRef]
19. Tomie KAWADA, Mikio NAKAZAWA, Teruhiko TOYO-OKA. 2002. Somatic gene therapy of dilated cardiomyopathy. *Folia Pharmacologica Japonica* **119**, 37-44. [CrossRef]
20. Yoshikazu Maeda, Uichi Ikeda, Masahisa Shimpo, Masabumi Shibuya, John Monahan, Masashi Urabe, Keiya Ozawa, Kazuyuki Shimada. 2000. Adeno-Associated Virus-Mediated Vascular Endothelial Growth Factor Gene Transfer into Cardiac Myocytes. *Journal of Cardiovascular Pharmacology* **36**, 438-443. [CrossRef]
21. Wolfgang Walther, Ulrike Stein. 2000. Viral Vectors for Gene Transfer. *Drugs* **60**, 249-271. [CrossRef]
22. Yang Shen, Shin-Ichi Muramatsu, Kunihiko Ikeguchi, Ken-Ichi Fujimoto, Dong-Sheng Fan, Matsuo Ogawa, Hiroaki Mizukami, Masashi Urabe, Akihiro Kume, Ikuko Nagatsu, Fumi Urano, Takahiro Suzuki, Hiroshi Ichinose, Toshiharu Nagatsu, John Monahan, Imaharu Nakano, Keiya Ozawa. 2000. Triple Transduction with Adeno-Associated Virus Vectors Expressing Tyrosine Hydroxylase, Aromatic-L-Amino-Acid Decarboxylase, and GTP Cyclohydrolase I for Gene Therapy of Parkinson's Disease. *Human Gene Therapy* **11**:11, 1509-1519. [Abstract] [Full Text PDF] [Full Text PDF with Links]
23. Thomas C. Chen, Gregory A. Helm. 2000. Introduction to gene therapy in neurological surgery. *Neurosurgical FOCUS* **8**, 1-5. [CrossRef]
24. B. L. Davidson, C. S. Stein, J. A. Heth, I. Martins, R. M. Kotin, T. A. Derksen, J. Zabner, A. Ghodsi, J. A. Chiorini. 2000. Recombinant adeno-associated virus type 2, 4, and 5 vectors: Transduction of variant cell types and regions in the mammalian central nervous system. *Proceedings of the National Academy of Sciences* **97**, 3428-3432. [CrossRef]
25. Emily J. Schwarz, Guillermo M. Alexander, Darwin J. Prockop, S. Ausim Azizi. 1999. Multipotential Marrow Stromal Cells Transduced to Produce L-DOPA: Engraftment in a Rat Model of Parkinson Disease. *Human Gene Therapy* **10**:15, 2539-2549. [Abstract] [Full Text PDF] [Full Text PDF with Links]
26. H. Büeler. 1999. Adeno-Associated Viral Vectors for Gene Transfer and Gene Therapy. *Biological Chemistry* **380**, 613-622. [CrossRef]

HUMAN GENE THERAPY 26:145–152 (March 2015)
Mary Ann Liebert, Inc.
DOI: 10.1089/hum.2014.109

Prevalence of Anti–Adeno-Associated Virus Serotype 8 Neutralizing Antibodies and Arylsulfatase B Cross-Reactive Immunologic Material in Mucopolysaccharidosis VI Patient Candidates for a Gene Therapy Trial

Rita Ferla,[1,2,*] Pamela Claudiani,[1,2,*] Marco Savarese,[1,3] Karen Kozarsky,[4] Rossella Parini,[5] Maurizio Scarpa,[6,7] Maria Alice Donati,[8] Giovanni Sorge,[9] John J. Hopwood,[10] Giancarlo Parenti,[1,11] Simona Fecarotta,[11] Vincenzo Nigro,[1,3] Hatice Serap Sivri,[12] Ans Van Der Ploeg,[13] Generoso Andria,[11] Nicola Brunetti-Pierri,[1,11] and Alberto Auricchio[1,2]

Abstract

Recombinant vectors based on adeno-associated virus serotype 8 (AAV8) have been successfully used in the clinic and hold great promise for liver-directed gene therapy. Preexisting immunity against AAV8 or the development of antibodies against the therapeutic transgene product might negatively affect the outcomes of gene therapy. In the prospect of an AAV8-mediated, liver-directed gene therapy clinical trial for mucopolysaccharidosis VI (MPS VI), a lysosomal storage disorder caused by arylsulfatase B (ARSB) deficiency, we investigated in a multiethnic cohort of MPS VI patients the prevalence of neutralizing antibodies (Nab) to AAV8 and the presence of ARSB cross-reactive immunologic material (CRIM), which will either affect the efficacy of gene transfer or the duration of phenotypic correction. Thirty-six MPS VI subjects included in the study harbored 45 (62.5%) missense, 13 (18%) nonsense, 9 (12.5%) frameshift (2 insertions and 7 deletions), and 5 (7%) splicing *ARSB* mutations. The detection of ARSB protein in 24 patients out of 34 (71%) was predicted by the type of mutations. Preexisting Nab to AAV8 were undetectable in 19/33 (58%) analyzed patients. Twelve out of 31 patients (39%) tested were both negative for Nab to AAV8 and CRIM-positive. In conclusion, this study allows estimating the number of MPS VI patients eligible for a gene therapy trial by intravenous injections of AAV8.

Introduction

Mucopolysaccharidosis VI (MPS VI) or Maroteaux–Lamy syndrome is an autosomal recessive disorder caused by deficiency of the enzyme arylsulfatase B (ARSB), which results in lysosomal storage of the glycosaminoglycan (GAG) dermatan sulfate (DS). Clinical features of the disease include growth retardation, skeletal dysplasia, joint stiffness, organomegaly, heart valve disease, and corneal clouding without primary involvement of the central nervous system.[1]

[1]Telethon Institute of Genetics and Medicine, 80078 Pozzuoli, Naples, Italy.
[2]Medical Genetics and [11]Section of Pediatrics, Department of Translational Medicine, ''Federico II'' University, 80131 Naples, Italy.
[3]Department of Biophysics and Pathology, Second University of Naples, 80138 Naples, Italy.
[4]REGENXBIO, Washington, DC 20006.
[5]Rare Metabolic Diseases Unit and Neonatal Intensive Care Unit, Fondazione MBBM, A.O. San Gerardo, 20900 Monza, Italy.
[6]Department of Pediatrics, University of Padova, 35128 Padua, Italy.
[7]Horst Schmidt Klinik Rare Disease Center, 65199 Wiesbaden, Germany.
[8]Section of Psychology, Department of Neuroscience, Psychology, Drug, and Child's Health, University of Florence, 50135 Florence, Italy.
[9]Department of Pediatrics, University of Catania, 95123 Catania, Italy.
[10]Lysosomal Diseases Research Unit, South Australian Health and Medical Research Institute, 5001 Adelaide, Australia.
[12]Section of Metabolic Disorders, Department of Pediatrics, Hacettepe University Faculty of Medicine, 06100 Ankara, Turkey.
[13]Department of Pediatrics, Center for Lysosomal and Metabolic Diseases, Erasmus Medical Center, University Hospital, 3015 Rotterdam, The Netherlands.
*These two authors have contributed equally to this work.

© Rita Ferla et al. 2015; Published by Mary Ann Liebert, Inc. This Open Access article is distributed under the terms of the Creative Commons License Attribution-Non-Commercial Share Alike (http://creativecommons.org/licenses/by-nc-sa/4.0/).

Enzyme replacement therapy (ERT) is currently the standard of care for MPS VI.[2] However, despite amelioration of both visceral phenotype and endurance, ERT has limited efficacy on several MPS VI complications such as ocular, cardiac, and skeletal abnormalities. In addition, ERT requires inconvenient weekly infusions of costly recombinant enzyme[2,3] that are associated with increased risks of adverse reactions such as hypersensitivity reactions.[4] Alternative strategies with similar or better therapeutic efficacy without the inconvenience and risks of multiple infusions are desirable.

We have recently demonstrated that a single intravenous administration of a recombinant vector based on adeno-associated virus serotype 8 (AAV2/8), which efficiently transduces liver,[5–8] results in long-term therapeutic efficacy in rodent and feline models of MPS VI.[9–13] Levels of serum ARSB activity falling within the normal range were detected in MPS VI cats up to 6 years postinjection, which was the last time-point of observation (Ferla and Auricchio, unpublished results). Based on these promising results, translation from bench to bedside of this therapeutic strategy is now ongoing.

The outcome of *in vivo* gene transfer may be influenced by several factors. Preexisting neutralizing antibodies (Nab) to wild-type AAV8 even at low titers are sufficient to prevent liver transduction by AAV2/8 vectors, and thus significantly reduce the efficacy of gene therapy,[14–17] as shown also in MPS VI cats.[11] Gene therapy efficacy may also be limited by the development of humoral immunity to the therapeutic transgene product. The immune response is more likely to occur in patients or animal models that carry bi-allelic null mutations in the disease-causative gene because of lack of cross-reactive immunologic material (CRIM). Liver-directed gene transfer with either AAV or lentiviral vectors has been shown to either prevent[18] or eradicate[19,20] humoral immunity to the transgene product. However, immune tolerization was not observed in MPS VI rats that are homozygous for a null *ARSB* mutation.[9,13]

In the prospect of determining patients' eligibility for a clinical trial for MPS VI involving intravenous administrations of AAV2/8 vectors, a multiethnic unselected cohort of MPS VI patients from multiple metabolic clinics has been evaluated for the presence of both Nab to AAV8 and CRIM that will dictate eligibility and will likely affect the outcomes of the clinical trial.

Patients, Materials, and Methods

Patients

The participants in the study were all MPS VI patients diagnosed and followed-up at multiple metabolic clinics in Italy (Catania, Florence, Naples, Monza, and Padua), in the Netherlands (Rotterdam), and in Turkey (Ankara). The clinical research protocol was approved by the Institutional Review Board (IRB) of each participating metabolic clinic. All patients signed an informed consent to be included in the study. The study included the following assessments: (1) clinical and instrumental (height or length; endurance through the 6 min walk test and 3 min stair climb; forced vital capacity; forced expiratory volume at 1 min; joint stiffness and pain, grip, and pinch scores; Childhood Health Assessment Questionnaire scores; visual acuity and ocular abnormalities by full ocular examination; and magnetic resonance imaging of hand, wrist, and knee joints performed in cooperative subjects); (2) biochemical (urinary GAGs, ARSB levels in serum, leucocytes and/or fibroblasts, dosage of Nab to AAV8, clinical chemistry and hematology, and HBV and HCV tests); and (3) molecular (DNA sequencing of the *ARSB* gene; see below for details).

The molecular and clinical findings of these patients are summarized in Tables 1 and 2. The involvement of the main tissue/organs affected by the disease at the age of last evaluation was graded by the referring clinicians as absent (0), mild (1), moderate (2), or severe (3). A disease severity score ranging from 0 (least severe) to 21 (most severe) was assigned based on the degree of severity of each affected tissue/organ ($n = 7$ tissues/organs).

Cell culture

Cultured skin fibroblasts from MPS VI patients obtained for diagnostic purposes were maintained in Dulbecco's modified Eagle's medium (Gibco–Life Invitrogen, Paisley, UK) containing 20% fetal bovine serum (Gibco, Invitrogen Corporation, Carlsbad, CA), 1% of Glutamine (Sigma-Aldrich, Steinheim, Germany), and 1% antibiotic–antimycotic (Gibco, Invitrogen Corporation).

Mutational analysis of the ARSB *gene*

Genomic DNA was extracted from cultured skin fibroblasts by phenol/chloroform extraction. All *ARSB* exons were amplified by PCR, using M13-tailed primers. Sanger sequencing was performed with an ABI PRISM 3130 XL automatic DNA Sequencer Genetic Analyzer (Applied Biosystems, Foster City, CA). Primer sequences and PCR conditions are described in Supplementary Table S1 (Supplementary Data are available online at www.liebertpub.com/hum).

ARSB cross-reactive immunologic material analysis

The presence of ARSB cross-reactive immunologic material was evaluated by Western blot analysis of cultured skin fibroblast lysates. Cells were lysed in RIPA buffer (50 m*M* NaCl, 25 m*M* Tris-HCl pH 8.0, 0.5% NP40, 0.1% SDS, and 10 mg/ml leupeptin–aprotinin–pepstatin A). Seventy micrograms of proteins were separated by SDS-PAGE on a 10% polyacrylamide gel, transferred to a polyvinylidene difluoride membrane (Roche, Basel, Switzerland), and incubated with the following antibodies: (1) sheep polyclonal anti-ARSB antibody, diluted to 1:500 in 5% milk, prepared as previously described,[21] and (2) mouse monoclonal anti-beta actin antibody (A5441; Sigma-Aldrich, Milan, Italy), diluted to 1:3000 in 5% nonfat dried milk (Euroclone, Milan, Italy).

Nab to AAV assay

MPS VI patients were screened for preexisting Nab to AAV8 using an *in vitro* transduction inhibition assay with Huh7 cells, as previously described.[22] The detection limit of the assay is a 1:5 serum dilution.

Results

ARSB *mutations and ARSB cross-reactive immunologic material in MPS VI patients*

Serum and skin fibroblasts from 36 patients with a clinical diagnosis of MPS VI confirmed by ARSB deficiency on

Table 1. Arylsulfatase B Mutations in Mucopolysaccharidosis VI Patients

Patient	*Ethnicity*	*Allele 1 nucleotide/ protein change*	*Allele 2 nucleotide/ protein change*	*Mutations previously reported by*
1	Turkish	c.962T > C/p.L321P	c.962T > C/p.L321P	Isbrandt et al.[41]
2	Turkish	c.908G > A/p.G303E	c.908G > A/p.G303E	Lin et al.[42]
3	Turkish	c.962T > C/p.L321P	c.962T > C/p.L321P	Isbrandt et al.[41]
4	Guinean	c.971G > T/p.G324V	c.971G > T/p.G324V	Karageorgos et al.[37]
5	Turkish	c.962T > C/p.L321P	c.962T > C/p.L321P	Isbrandt et al.[41]
6	Turkish	c.962T > C/p.L321P	c.962T > C/p.L321P	Isbrandt et al.[41]
7	Moroccan	c.883-884dupTT/ p.F295FfsX42	c.883-884dupTT/ p.F295FfsX42	Novel
8	Turkish	c.903C > G/p.N301K	c.903C > G/p.N301K	Brands et al.[23]
9	Azerbaijan	c.1036delG/p.E346SfsX11	c.1178A > G/p.H393R	Novel
10	Turkish	c.962T > C/p.L321P	c.962T > C/p.L321P	Isbrandt et al.[41]
11	Turkish	c.571C > T/p.R191X	c.571C > T/p.R191X	Karageorgos et al.[37]
12	Italian	del exon 5	del exon 5	[a]
13	Moroccan	c.995T > G/p.V332G	c.995T > G/p.V332G	Brands et al.[23]
14	Turkish	c.962T > C/p.L321P	c.962T > C/p.L321P	Isbrandt et al.[41]
15	Turkish	c.962T > C/p.L321P	c.962T > C/p.L321P	Isbrandt et al.[41]
16	Turkish	c.962T > C/p.L321P	c.962T > C/p.L321P	Isbrandt et al.[41]
17	Turkish	c.571C > T/p.R191X	c.571C > T/p.R191X	Karageorgos et al.[37]
18	Turkish	c.571C > T/p.R191X	c.571C > T/p.R191X	Karageorgos et al.[37]
19	Turkish	c.962T > C/p.L321P	c.962T > C/p.L321P	Isbrandt et al.[41]
20	Venezuelan	c.979C > T/p.R327X	c.979C > T/p.R327X	Karageorgos et al.[43]
21	Dutch	c.629A > G/p.Y210C	c.979C > T/p.R327X	Litjens et al.[26] and Karageorgos et al.[43]
22	Italian	c.943C > T/p.R315X	c.1475delC/pP492LfsX80	Voskoboeva et al.[44] Di Natale et al.
23	Italian	c.943C > T/p.R315X	c.899-1142del	Arlt et al.[45] and Voskoboeva et al.[44]
24	Turkish	c.962T > C/p.L321P	c.962T > C/p.L321P	Isbrandt et al.[41]
25	Dutch	c.629A > G/p.Y210C	c.979C > T/p.R327X	Litjens et al.[26] and Karageorgos et al.[43]
26	Dutch	c.629A > G/p.Y210C	c.979C > T/p.R327X	Litjens et al.[26] and Karageorgos et al.[43]
27	Pakistani	c.1142 + 2T > C	c.1142 + 2T > C	Brands et al.[23]
28	Turkish	c.454C > T/p.R152W	c.454C > T/p.R152W	Voskoboeva et al.[46]
29	Turkish	c.454C > T/p.R152W	c.454C > T/p.R152W	Voskoboeva et al.[46]
30	Dutch	c.629A > G/p.Y210C	c.937C > G/p.P313A	Litjens et al.[26] and Brooks et al.[47]
31	Italian	c.1213 + 6T > C	c.725A > C/p.H242P	Di Natale et al.[24]
32	Turkish	c.1168G > A/p.E390K	c.1168G > A/p.E390K	Kantaputra et al.[48]
33	Turkish	c.1036delG/p.E346SfsX11	c.1036delG/p.E346SfsX11	Novel
34	Italian	c.1213 + 6T > C	c.1213 + 6T > C	Di Natale et al.[24]
35	Turkish	c.454C > T/p.R152W	c.454C > T/p.R152W	Voskoboeva et al.[46]
36	Turkish	c.1168G > A/p.E390K	c.1168G > A/p.E390K	Kantaputra et al.[48]

[a]Patient 12 (BA1196) carries a genomic deletion of exon 5 on both *arylsulfatase B (ARSB) alleles*; the breakpoints of the deletion were not defined at the nucleotide levels.

enzyme assay were collected from referral metabolic clinic centers in Italy, the Netherlands, and Turkey, which provided samples from 7, 11, and 18 MPS VI patients, respectively (Tables 1 and 2). The age of patients ranged from 5 to 25 years (age 5–10, $n = 15$; age 11–18, $n = 18$; age 19–25, $n = 3$; Table 1) and their severity varied significantly (Table 2).

At the time of this study, molecular diagnoses of MPS VI were already available for 18 out of the 36 patients.[23–25] In the remaining 18 patients, PCR amplification and Sanger sequencing of all *ARSB* exons and intron–exon boundaries were carried out. Collectively, we observed 45/72 (62.5%) missense, 13/72 (18%) nonsense, 9/72 (12.5%) frameshift (2 insertions and 7 deletions), and 5/72 (7%) splicing *ARSB* mutations (Table 1). To the best of our knowledge, three mutations had not been previously described. These were one missense (c.1178 A > G p.H393R), not reported in dbSNP or in exome server databases, resulting in the change of a highly conserved histidine residue (Supplementary Fig. S1) that had already been found to be mutated in MPS VI,[26] and two frameshift mutations (883-884duplTT [p.F295FfsX42], c.1036delG [p.E346SfsX11], Table 1) predicted to result in truncated proteins.

Genotypes of MPS VI patients were correlated with the presence of ARSB CRIM by Western blot analysis with anti-ARSB antibody of lysates from cultured skin fibroblasts (Fig. 1). In 24/34 (71%) of analyzed patients, 43 and 57 kDa bands corresponding to ARSB mature and precursor proteins, respectively, were detected (Fig. 1). Based on this observation, these MPS VI patients were deemed CRIM positive. Importantly, the CRIM status could be predicted based on *ARSB* mutations; all patients bearing missense mutations were consistently found to be CRIM positive, whereas patients bearing null mutations in both alleles were CRIM negative (Tables 1 and 2). No correlation between clinical severity and CRIM status was observed (Fisher exact test p-value = 0.2). However, the power of the test was low (0.03) because of the small sample size, and thus definitive conclusions on this aspect cannot be drawn.

Table 2. Clinical Severity, Cross-Reactive Immunologic Material Status, and Anti–Adeno-Associated Virus Serotype 8 Antibody Titers in Mucopolysaccharidosis VI Patients

				Involvement									
Patient	*Age at the last evaluation (years)/gender*	*Age at diagnosis (years)*	*Age at start of ERT (years)*	*Eye*	*ENT*	*Heart*	*Growth*	*Bone and joints*	*Spinal cord*	*Motor*	*Clinical score (0–24)*	*CRIM*	*Nab anti-AAV8*
1	5/M	1.0	1.0	2	0	2	0	2	0	2	8	+	n.a.
2	5/M	1.0	2.0	1	0	2	1	2	0	2	8	+	<5
3	5/F	4.0	4.0	1	2	2	1	1	0	1	8	n.a	<5
4	6/M	1.9	2.3	2	1	1	1	2	0	1	8	+	160
5	7/M	2.5	3.0	1	1	1	2	2	0	2	9	+	5
6	7/F	4.0	4.0	1	2	3	2	2	0	2	12	+	40
7	7/M	1.7	2.5	1	2	2	1	1	0	1	8	−	<5
8	7/F	1.8	2.1	2	1	2	3	2	0	2	12	+	<5
9	8/F	4.5	n.a	1	2	2	2	1	0	2	10	+	n.a
10	8/M	3.0	3.0	1	2	2	2	1	0	1	9	+	<5
11	8/M	2.0	4.0	2	2	2	2	2	0	2	12	−	10
12	8/M	0.6	2.0	1	3	1	3	3	2	2	15	−	<5
13	9/F	2.8	2.9	2	0	2	2	2	1	2	11	+	<5
14	10/F	2.0	3.5	2	1	2	2	3	3	2	15	+	<5
15	10/M	1.0	4.0	2	1	2	2	3	2	2	14	+	<5
16	12/M	2.0	5.0	3	1	2	2	2	0	2	12	+	10
17	12/M	7.5	7.5	2	2	2	2	2	0	2	12	−	20
18	12/M	8.0	8.0	2	1	2	2	3	0	2	12	−	20
19	12/F	5.0	6.0	2	1	2	2	1	0	2	10	+	n.a
20	12/M	5.0	5.4	2	2	1	3	3	3	3	17	−	<5
21	12/M	5.8	6.1	1	0	0	0	2	0	2	5	+	20
22	12/M	1.2	6.1	2	2	2	3	3	3	3	18	n.a	<5
23	12/M	1.6	4.0	2	2	2	2	2	1	2	13	−	<5
24	13/F	4.0	7.0	3	2	2	2	1	2	2	14	+	5
25	13/M	5.1	5.9	0	0	1	2	2	0	3	8	+	<5
26	13/F	7.4	7.8	0	0	0	2	2	0	2	6	+	640
27	13.5/F	3.4	6.8	2	2	3	3	3	0	3	16	−	<5
28	14/F	7.8	8.3	1	1	1	2	2	0	1	8	+	<5
29	14/M	0.7	7.6	0	0	1	0	2	0	2	5	+	<5
30	14/M	10.2	10.6	0	0	1	1	2	0	3	7	+	<5
31	14/F	4.0	6.0	1	0	1	1	1	1	0	5	+	<5
32	17/M	12	13.0	0	1	2	2	3	3	2	13	+	20
33	17/M	3.5	11.5	2	3	2	2	3	2	2	16	−	160
34	21/F	4.5	10.0	2	2	3	3	3	1	2	16	−	320
35	23/M	10.1	18.3	0	1	1	2	2	0	3	9	+	<5
36	25/F	23	24	0	1	2	2	3	2	2	12	+	20

CRIM, cross-reactive ARSB immunologic material; ENT, ear, nose, and throat; ERT, enzyme replacement therapy; F, female; M, male; n.a, not available.

Involvement was graded as absent (0), mild (1), moderate (2), or severe (3).

Evaluation of Nab to AAV8 in MPS VI patients

Sera from MPS VI patients were analyzed using an *in vitro* AAV2/8 transduction inhibition assay[22] to detect Nab to AAV8. Nab to AAV8 were undetectable in the sera of 19/33 of analyzed patients (58%), whereas sera from the remaining 14 patients (42%) showed a titer of Nab $\geq$1:5, which is the detection limit of the assay (Table 2). The seroprevalence was 31%, 47%, and 67% in patients whose age ranged between 5 and 10, 11 and 18, and 19 and 25 years, respectively (Fig. 2a and b). The highest seroprevalence (67%) was found in patients from the referral center in Turkey, followed by patients from the Dutch (27%) and Italian (14%) referral centers (Fig. 2c). Statistical analysis (Fisher exact test) suggested no association between Nab and age ($p=0.5$), and, conversely, a significant difference between Nab and referral centers ($p=0.05$). However, the power of the test was low (0.2 and 0.5, respectively) because of the small sample size. Hence, definitive conclusions on these aspects cannot be inferred.

Discussion

Gene therapy is emerging as a successful strategy for treatment of inherited diseases.[27] *In vivo* gene transfer with AAV2/8 vectors is regarded as a possible approach to convert the liver into a factory organ for systemic release of therapeutic proteins. A recent clinical trial using intravenous administrations of AAV2/8 in patients with hemophilia B has supported this paradigm in humans; some treated patients exhibited multiyear stable factor IX levels following a single administration of vector.[15,28] By a similar approach, we have recently demonstrated that a single systemic administration of AAV2/8 encoding ARSB is able to convert the liver into a

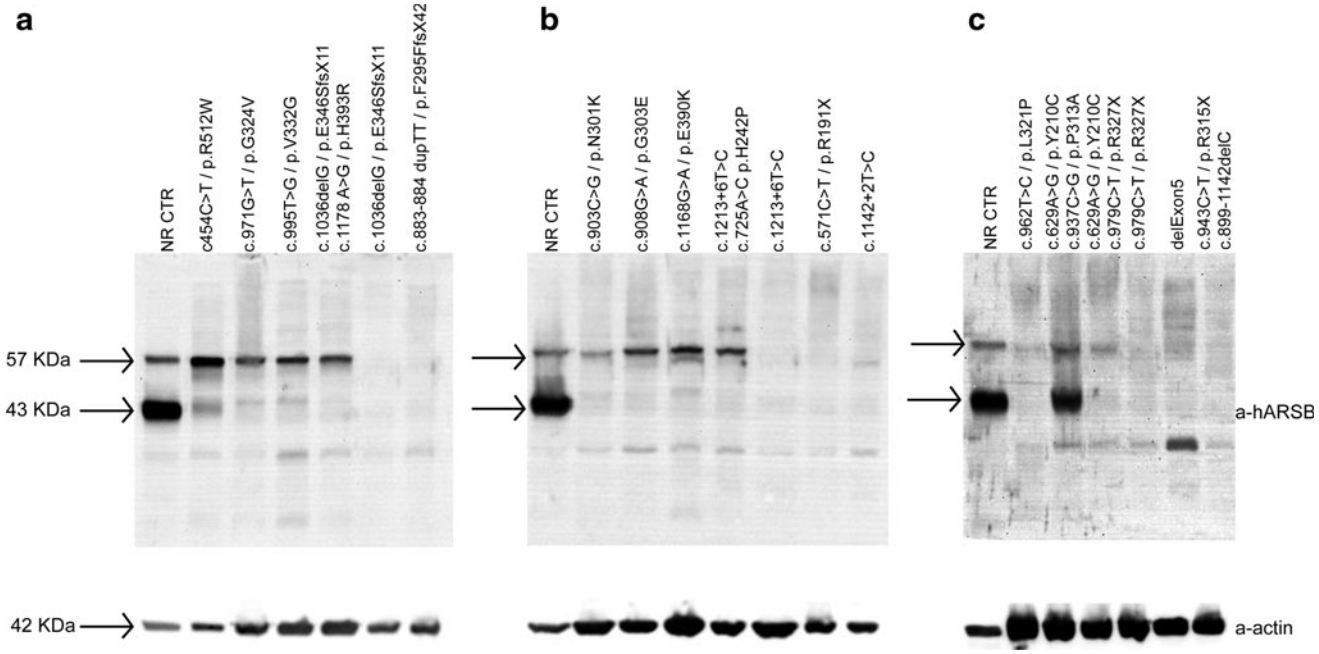


FIG. 1. ARSB CRIM in MPS VI patients. The presence of ARSB CRIM was evaluated by Western blot analysis of lysates of cultured skin fibroblasts, as described in the Patients, Materials, and Methods section. Samples corresponding to each ARSB genotype have been loaded in **(a–c)**. Bands of 43 and 57 kDa corresponding to ARSB mature and precursor proteins, respectively, are indicated by the arrows. ARSB, arylsulfatase B; CRIM, cross-reactive immunologic material; MPS, mucopolysaccharidosis; NR CTR, normal control. The following mutations have not been described before: c.1178 A > G (p.H393R), 883-884duplTT (p.F295FfsX42), and c.1036delG (p.E346SfsX11).

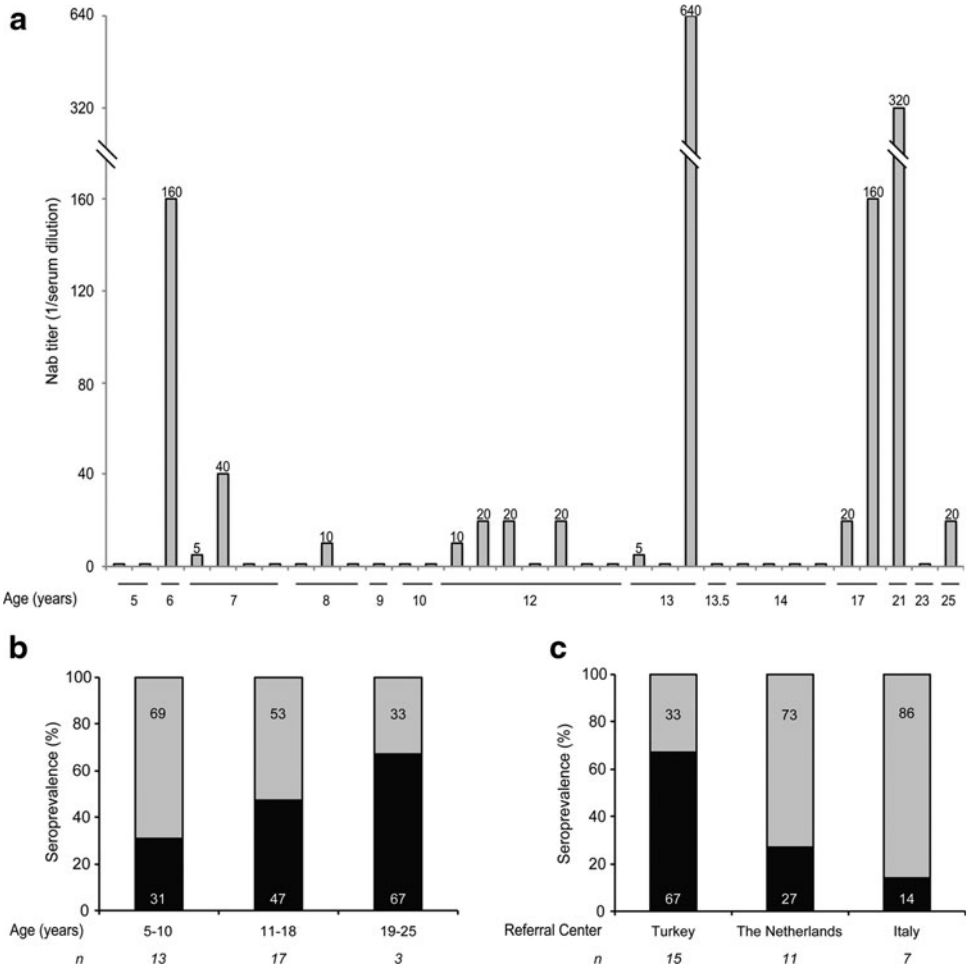


FIG. 2. Seroprevalence of Nab to AAV8 by age and referral centers. The Nab titer of each patient is reported in **(a)**. Data relative to Nab to AAV8 in MPS VI patients were additionally stratified by age **(b)** and referral center **(c).** The percentage of samples positive (Nab +, black bar) and negative (Nab −, gray bar) for Nab to AAV8 is reported in **(b)** and **(c)**, and the corresponding values are inside each bar. The number (*n*) of patients in each group is indicated under each bar. AAV8, adeno-associated virus serotype 8; Nab, neutralizing antibodies.

factory organ, providing stable secretion of ARSB. This results in long-term therapeutic efficacy in rodent and feline models of MPS VI.[9–13] Gene therapy was at least as effective as weekly infusions of recombinant human ARSB (rhARSB) in a mouse model of MPS VI,[12] suggesting that it may be preferable to ERT, especially because it potentially requires a single intravenous administration. This bodes well for further investigating the safety and efficacy of intravenous administrations of AAV2/8 in patients with MPS VI.

Immune responses to the vector have been shown to limit both efficacy and longevity of gene transfer.[27,29] Very low levels of Nab to AAV8 are sufficient to strongly reduce liver transduction and thus therapeutic efficacy.[11,14,16,17] Decoy capsids that inhibit circulating Nab without interfering with endogenous AAV receptors and AAV preparations with empty capsids are two potential strategies to overcome the barrier of preexisting anti-AAV antibodies.[30] However, until these strategies are demonstrated to be safe and efficient in humans, the presence of circulating Nab to AAV8 is better considered an exclusion criterion in trials in which systemic administrations of AAV2/8 vectors are used. Therefore, we screened MPS VI patients for Nab to AAV8, which were undetectable in 58% of subjects. Among the MPS VI patients tested for Nab to AAV8, the titer was $>1{:}20$ in 15% and $>1{:}80$ in 12% of subjects. These results are consistent with previously published data showing that the seroprevalence of Nab to AAV8 at serum dilution of $>1{:}20$ and $>1{:}80$ is about 20% and 15%, respectively, in samples from healthy European individuals.[22,31] The seroprevalence of Nab to AAV8 observed in our cohort is slightly lower than that (33%) reported in both healthy subjects and hemophilic patients from Japan.[32]

No definitive conclusions can be drawn from the analyses of AAV8 seroprevalence stratified by referral centers, age, or clinical severity because of the small sample size. However, we have observed that AAV8 seroprevalence varies between samples collected from different referral centers and is highest in patients of Asiatic origin (50%) followed by patients of European and African origins (33% each). These observations support previous studies in which AAV seroprevalence was shown to vary depending on the geographical origin of the studied population; this was probably at least partially attributed to living conditions or population density.[22,33] In line with a previous study showing that seroprevalence to AAV8 significantly increases through the childhood and the adolescence in healthy subjects,[34] the seroprevalence to AAV8 we have measured is higher in adolescents than in children and does not correlate with the clinical severity of the disease (Fisher exact test p-value $= 0.95$; power 0.06), which may account for an increased exposure because of more frequent clinic or hospital admissions.

Gene therapy efficacy may be additionally limited by T-cell-mediated and humoral immunity to the therapeutic transgene product. T-cell-mediated responses to rhARSB have not been reported in MPS VI patients treated with ERT.[2,35] On the other hand, recent results from phase I/II liver gene therapy clinical trials for hemophilia B and acute intermittent porphyria showed no T-cell-mediated immune responses to the therapeutic transgene product,[15,36] suggesting that this might not be a major limitation for liver gene therapy.

The risk of humoral immunity to the transgene product correlates with the presence of CRIM.[9,13] Here, we show that the CRIM positivity of MPS VI patients could be precisely predicted by the presence of at least one *ARSB* allele carrying a missense mutation. To the best of our knowledge, this is the first example of analysis, which correlates the genotype of MPS VI patients with ARSB CRIM, clearly showing that the CRIM status could be predicted based on *ARSB* mutations. On the contrary, there was no correlation between CRIM status and disease severity. The frequencies of *ARSB* missense and null mutations that we found in our series of MPS VI patients (62.5% and 37.5%, respectively) are similar to those previously found in a larger patient cohort.[37]

While even low levels of Nab to AAV8 should be viewed as an exclusion criterion for a trial with AAV2/8 infusions, exclusion of ARSB CRIM-negative MPS VI patients is debatable. First, almost all MPS VI patients treated with ERT develop antibodies to rhARSB independently of their genotypes or disease severity.[4,23,38–40] Nevertheless, they experience clinical benefits under ERT.[4,38–40] In addition, liver-directed gene therapy has been demonstrated to either prevent the generation of humoral immunity[18] or to eradicate it, if already present,[19,20] which makes the impact of preexisting humoral immunity to the transgene product on gene therapy efficacy difficult to predict. Therefore, there is a good argument for not excluding neither patients with preexisting immunity to rhARSB nor ARSB CRIM-negative patients from the trial.

Although CRIM-negative status would not be an exclusion criterion, CRIM-positive patients may be preferred in a gene therapy trial as they have lower possibility to generate humoral immunity to the newly synthesized transgene product secreted by transduced hepatocytes.[9,13] The current study has revealed that 12 of 19 patients negative for Nab to AAV8 were also CRIM positive. These 12 patients correspond to 39% of the patients analyzed for both markers. Although using both criteria will likely result in a significant reduction of eligible MPS VI subjects, based on the estimated number from this study, a phase I/II, open-label, dose-escalation (2 patients treated at a low, 3 at an intermediate, and 3 at a high dose of vector) safety study would still be feasible.

Acknowledgments

We gratefully acknowledge Lucia Perone (Cell Culture and Cytogenetics Core, Telethon Institute of Genetics and Medicine [TIGEM], Pozzuoli, Naples) for culturing of MPS VI fibroblasts; Annamaria Carissimo and Luisa Cutillo (Bioinformatics core, TIGEM, Pozzuoli, Naples) for statistical analysis; Alexis Burton (Scientific Office, TIGEM, Pozzuoli, Naples) for critical reading of this article; Roberto Calcedo (Gene Therapy Program, University of Pennsylvania) for Nab analysis; and Bianca Fontanella (Scientific and Regulatory Office, TIGEM, Pozzuoli, Naples) and Valentina Pecorella (Clinical Trial Office, Section of Pediatrics, Department of Translational Medicine, ''Federico II'' University, Naples) for data collection from referral centers.

This work was supported by the European Community's Seventh Framework Programme (FP7/2007–2013)—MeuSIX [304999] and by the Isaac Foundation.

Author Disclosure Statement

Rita Ferla, Pamela Claudiani, Marco Savarese, Giancarlo Parenti, Simona Fecarotta, Vincenzo Nigro, Ans Van Der Ploeg, Hatice Serap Sivri, Generoso Andria, Nicola Brunetti-Pierri, and Alberto Auricchio declare that no competing financial interests exist.

Karen Kozarsky has no conflicts of interest beyond being an employee of REGENXBIO.

References

1. Neufeld E, Muenzer J. The mucopolysaccharidoses. In: The Online Metabolic and Molecular Bases of Inherited Disease. R Scriver, ed. (McGraw Hill, New York). 2010; pp. 1–73.
2. Giugliani R, Lampe C, Guffon N, et al. Natural history and galsulfase treatment in mucopolysaccharidosis VI (MPS VI, Maroteaux-Lamy syndrome)-10-year follow-up of patients who previously participated in an MPS VI survey study. Am J Med Genet A 2014;164A:1953–1964.
3. Wyatt K, Henley W, Anderson L, et al. The effectiveness and cost-effectiveness of enzyme and substrate replacement therapies: a longitudinal cohort study of people with lysosomal storage disorders. Health Technol Assess 2012;16: 1–543.
4. Harmatz P, Giugliani R, Schwartz I, et al. Enzyme replacement therapy for mucopolysaccharidosis VI: a phase 3, randomized, double-blind, placebo-controlled, multinational study of recombinant human N-acetylgalactosamine 4-sulfatase (recombinant human arylsulfatase B or rhASB) and follow-on, open-label extension study. J Pediatr 2006; 148:533–539.
5. Cotugno G, Annunziata P, Barone MV, et al. Impact of age at administration, lysosomal storage, and transgene regulatory elements on AAV2/8-mediated rat liver transduction. PLoS One 2012;7:e33286.
6. Gao GP, Alvira MR, Wang L, et al. Novel adeno-associated viruses from rhesus monkeys as vectors for human gene therapy. Proc Natl Acad Sci USA 2002;99:11854–11859.
7. Nathwani AC, Rosales C, McIntosh J, et al. Long-term safety and efficacy following systemic administration of a self-complementary AAV vector encoding human FIX pseudotyped with serotype 5 and 8 capsid proteins. Mol Ther 2011;19:876–885.
8. Wang L, Wang H, Bell P, et al. Systematic evaluation of AAV vectors for liver directed gene transfer in murine models. Mol Ther 2010;18:118–125.
9. Cotugno G, Tessitore A, Capalbo A, et al. Different serum enzyme levels are required to rescue the various systemic features of the mucopolysaccharidoses. Hum Gene Ther 2010;21:555–569.
10. Cotugno G, Annunziata P, Tessitore A, et al. Long-term amelioration of feline Mucopolysaccharidosis VI after AAV-mediated liver gene transfer. Mol Ther 2011;19:461–469.
11. Ferla R, O'Malley T, Calcedo R, et al. Gene therapy for mucopolysaccharidosis type VI is effective in cats without pre-existing immunity to AAV8. Hum Gene Ther 2013;24:163–169.
12. Ferla R, Claudiani P, Cotugno G, et al. Similar therapeutic efficacy between a single administration of gene therapy and multiple administrations of recombinant enzyme in a mouse model of lysosomal storage disease. Hum Gene Ther 2014;25:609–618.
13. Tessitore A, Faella A, O'Malley T, et al. Biochemical, pathological, and skeletal improvement of mucopolysaccharidosis VI after gene transfer to liver but not to muscle. Mol Ther 2008;16:30–37.
14. Manno CS, Pierce GF, Arruda VR, et al. Successful transduction of liver in hemophilia by AAV-factor IX and limitations imposed by the host immune response. Nat Med 2006;12:342–347.
15. Nathwani AC, Tuddenham EG, Rangarajan S, et al. Adenovirus-associated virus vector-mediated gene transfer in hemophilia B. N Engl J Med 2011;365:2357–2365.
16. Wang L, Calcedo R, Wang H, et al. The pleiotropic effects of natural AAV infections on liver-directed gene transfer in macaques. Mol Ther 2010;18:126–134.
17. Wang L, Calcedo R, Bell P, et al. Impact of pre-existing immunity on gene transfer to nonhuman primate liver with adeno-associated virus 8 vectors. Hum Gene Ther 2011;22: 1389–1401.
18. LoDuca PA, Hoffman BE, Herzog RW. Hepatic gene transfer as a means of tolerance induction to transgene products. Curr Gene Ther 2009;9:104–114.
19. Annoni A, Cantore A, Della Valle P, et al. Liver gene therapy by lentiviral vectors reverses anti-factor IX pre-existing immunity in haemophilic mice. EMBO Mol Med 2013;5:1684–1697.
20. Markusic DM, Hoffman BE, Perrin GQ, et al. Effective gene therapy for haemophilic mice with pathogenic factor IX antibodies. EMBO Mol Med 2013;5:1698–1709.
21. Meikle PJ, Grasby DJ, Dean CJ, et al. Newborn screening for lysosomal storage disorders. Mol Genet Metab 2006;88: 307–314.
22. Calcedo R, Vandenberghe LH, Gao G, et al. Worldwide epidemiology of neutralizing antibodies to adeno-associated viruses. J Infect Dis 2009;199:381–390.
23. Brands MM, Hoogeveen-Westerveld M, Kroos MA, et al. Mucopolysaccharidosis type VI phenotypes-genotypes and antibody response to galsulfase. Orphanet J Rare Dis 2013;8:51.
24. Di Natale P, Villani GR, Parini R, et al. Molecular markers for the follow-up of enzyme-replacement therapy in mucopolysaccharidosis type VI disease. Biotechnol Appl Biochem 2008;49:219–223.
25. Villani GR, Grosso M, Pontarelli G, et al. Large deletion involving exon 5 of the arylsulfatase B gene caused apparent homozygosity in a mucopolysaccharidosis type VI patient. Genet Test Mol Biomarkers 2010;14:113–120.
26. Litjens T, Brooks DA, Peters C, et al. Identification, expression, and biochemical characterization of N-acetylgalactosamine-4-sulfatase mutations and relationship with clinical phenotype in MPS-VI patients. Am J Hum Genet 1996;58:1127–1134.
27. Mingozzi F, High KA. Therapeutic *in vivo* gene transfer for genetic disease using AAV: progress and challenges. Nat Rev Genet 2011;12:341–355.
28. Davidoff AM. AAV-8 Mediated Gene Therapy for Hemophilia B—Oral Communication. American Society of Cell and Gene Therapy, Washington, DC, 2014.
29. Mingozzi F, High KA. Immune responses to AAV vectors: overcoming barriers to successful gene therapy. Blood 2013;122:23–36.
30. Mingozzi F, Anguela XM, Pavani G, et al. Overcoming preexisting humoral immunity to AAV using capsid decoys. Sci Transl Med 2013;5:194ra92.
31. Boutin S, Monteilhet V, Veron P, et al. Prevalence of serum IgG and neutralizing factors against adeno-associated virus

(AAV) types 1, 2, 5, 6, 8, and 9 in the healthy population: implications for gene therapy using AAV vectors. Hum Gene Ther 2010;21:704–712.
32. Mimuro J, Mizukami H, Shima M, et al. The prevalence of neutralizing antibodies against adeno-associated virus capsids is reduced in young Japanese individuals. J Med Virol 2014;86:1990–1997.
33. Calcedo R, Wilson JM. Humoral immune response to AAV. Front Immunol 2013;4:341.
34. Calcedo R, Morizono H, Wang L, et al. Adeno-associated virus antibody profiles in newborns, children, and adolescents. Clin Vaccine Immunol 2011;18:1586–1588.
35. Harmatz P, Giugliani R, Schwartz IV, et al. Long-term follow-up of endurance and safety outcomes during enzyme replacement therapy for mucopolysaccharidosis VI: final results of three clinical studies of recombinant human N-acetylgalactosamine 4-sulfatase. Mol Genet Metab 2008; 94:469–475.
36. D'Avola D, Lopez-Franco E, Harper P, et al. Phase I clinical trial of liver directed gene therapy with rAAV5/2-PBGD in acute intermittent porphyria: safety data. European Society of Cell and Gene Therapy Abstract OR036, 2014.
37. Karageorgos L, Brooks DA, Pollard A, et al. Mutational analysis of 105 mucopolysaccharidosis type VI patients. Hum Mutat 2007;28:897–903.
38. Harmatz P, Whitley CB, Waber L, et al. Enzyme replacement therapy in mucopolysaccharidosis VI (Maroteaux-Lamy syndrome). J Pediatr 2004;144:574–580.
39. Harmatz P, Ketteridge D, Giugliani R, et al. Direct comparison of measures of endurance, mobility, and joint function during enzyme-replacement therapy of mucopolysaccharidosis VI (Maroteaux-Lamy syndrome): results after 48 weeks in a phase 2 open-label clinical study of recombinant human N-acetylgalactosamine 4-sulfatase. Pediatrics 2005;115:e681–e689.
40. Harmatz P, Kramer WG, Hopwood JJ, et al. Pharmacokinetic profile of recombinant human N-acetylgalactosamine 4-sulphatase enzyme replacement therapy in patients with mucopolysaccharidosis VI (Maroteaux-Lamy syndrome): a phase I/II study. Acta Paediatr 2005;94:61–68; discussion 57.
41. Isbrandt D, Arlt G, Brooks DA, Hopwood JJ, et al. Mucopolysaccharidosis VI (Maroteaux-Lamy syndrome): six unique arylsulfatase B gene alleles causing variable disease phenotypes. Am J Hum Genet 1994;54:454–463.
42. Lin WD, Lin SP, Wang CH, Hwu WL, et al. Genetic analysis of mucopolysaccharidosis type VI in Taiwanese patients. Clin Chim Acta 2008;394:89–93.
43. Karageorgos L, Harmatz P, Simon J, Pollard A, et al. Mutational analysis of mucopolysaccharidosis type VI patients undergoing a trial of enzyme replacement therapy. Hum Mutat 2004;23:229–233.
44. Voskoboeva E, Krasnopol'skaia KD, Peters K, von Figura K. [Identification of mutations in the arylsulfatase B gene in Russian mucopolysaccharidosis type VI patients]. Genetika 2000;36:837–843.
45. Arlt G, Brooks DA, Isbrandt D, Hopwood JJ, et al. Juvenile form of mucopolysaccharidosis VI (Maroteaux-Lamy syndrome). A C-terminal extension causes instability but increases catalytic efficiency of arylsulfatase B. J Biol Chem 1994;269:9638–9643.
46. Voskoboeva E, Isbrandt D, von Figura K, Krasnopolskaya X, et al. Four novel mutant alleles of the arylsulfatase B gene in two patients with intermediate form of mucopolysaccharidosis VI (Maroteaux-Lamy syndrome). Hum Genet 1994;93:259–264.
47. Brooks DA, Gibson GJ, Karageorgos L, Hein LK, et al. An index case for the attenuated end of the mucopolysaccharidosis type VI clinical spectrum. Mol Genet Metab 2005;85:236–238.
48. Kantaputra PN, Kayserili H, Guven Y, Kantaputra W, et al. Clinical manifestations of 17 patients affected with mucopolysaccharidosis type VI and eight novel ARSB mutations. Am J Med Genet A 2014;164A:1443–1453.

Address correspondence to:
Prof. Alberto Auricchio
Telethon Institute of Genetics and Medicine (TIGEM)
Via Campi Flegrei 34
80078 Pozzuoli
Naples
Italy

E-mail: auricchio@tigem.it

Received for publication September 2, 2014;
accepted after revision January 13, 2015.

Published online: February 4, 2015.

Acta Neuropathol (2016) 131:247–266
DOI 10.1007/s00401-015-1498-9

ORIGINAL PAPER

Viral gene transfer of APPsα rescues synaptic failure in an Alzheimer's disease mouse model

Romain Fol[1,2,3] · Jerome Braudeau[1,2] · Susann Ludewig[7] · Tobias Abel[6] · Sascha W. Weyer[9] · Jan-Peter Roederer[9] · Florian Brod[6] · Mickael Audrain[1,2,3] · Alexis-Pierre Bemelmans[2,4,5] · Christian J. Buchholz[6] · Martin Korte[7,8] · Nathalie Cartier[1,2] · Ulrike C. Müller[9]

Received: 18 May 2015 / Revised: 7 October 2015 / Accepted: 15 October 2015 / Published online: 4 November 2015
© Springer-Verlag Berlin Heidelberg 2015

Abstract Alzheimer's disease (AD) is characterized by synaptic failure, dendritic and axonal atrophy, neuronal death and progressive loss of cognitive functions. It is commonly assumed that these deficits arise due to β-amyloid accumulation and plaque deposition. However, increasing evidence indicates that loss of physiological APP functions mediated predominantly by neurotrophic APPsα produced in the non-amyloidogenic α-secretase pathway may contribute to AD pathogenesis. Upregulation of APPsα production via induction of α-secretase might, however, be problematic as this may also affect substrates implicated in tumorigenesis. Here, we used a gene therapy approach to directly overexpress APPsα in the brain using AAV-mediated gene transfer and explored its potential to rescue structural, electrophysiological and behavioral deficits in APP/PS1ΔE9 AD model mice. Sustained APPsα overexpression in aged mice with already preexisting pathology and amyloidosis restored synaptic plasticity and partially rescued spine density deficits. Importantly, AAV-APPsα treatment also resulted in a functional rescue of spatial reference memory in the Morris water maze. Moreover, we demonstrate a significant reduction of soluble Aβ species and plaque load. In addition, APPsα induced the recruitment of microglia with a ramified morphology into the vicinity of plaques and upregulated IDE and TREM2 expression suggesting enhanced plaque clearance. Collectively, these data indicate that APPsα can mitigate synaptic and cognitive deficits, despite established pathology. Increasing APPsα may therefore be of therapeutic relevance for AD.

R. Fol and J. Braudeau are joint first authors.

N. Cartier and U. C. Müller are joint senior authors.

Electronic supplementary material The online version of this article (doi:10.1007/s00401-015-1498-9) contains supplementary material, which is available to authorized users.

✉ Nathalie Cartier
nathalie.cartier@inserm.fr

✉ Ulrike C. Müller
u.mueller@urz.uni-heidelberg.de

[1] INSERM U1169/MIRCen CEA, 92265 Fontenay aux Roses, France

[2] University Paris Sud, University Paris-Saclay, 91400 Orsay, France

[3] Université Paris Descartes, 75006 Paris, France

[4] Commissariat à l'Energie Atomique et aux Energies Alternatives (CEA), Département des Sciences du Vivant (DSV), Institut d'Imagerie Biomédicale (I2BM), Molecular Imaging Research Center (MIRCen), 92260 Fontenay aux Roses, France

[5] Centre National de la Recherche Scientifique (CNRS), UMR 9199, Neurodegenerative Diseases Laboratory, 92260 Fontenay aux Roses, France

[6] Molecular Biotechnology and Gene Therapy, Paul-Ehrlich-Institut, 63225 Langen, Germany

[7] Division of Cellular Neurobiology, Zoological Institute, TU Braunschweig, Brunswick, Germany

[8] Helmholtz Centre for Infection Research, AG NIND, Inhoffenstr. 7, 38124 Brunswick, Germany

[9] Department of Bioinformatics and Functional Genomics, Institute of Pharmacy and Molecular Biotechnology, Heidelberg University, Im Neuenheimer Feld 364, 69120 Heidelberg, Germany

Keywords Alzheimer · Gene therapy · Amyloid precursor protein · APPsα · Synaptic plasticity · Spines · Behavior · Microglia · AAV

Introduction

Synaptic dysfunction, cognitive decline, and excessive accumulation of neurotoxic β-amyloid peptides (Aβ) are hallmark features of Alzheimer's disease (AD). Aβ is generated by sequential cleavage of the amyloid precursor protein (APP) by β- and γ-secretase. In the competing and physiologically predominant non-amyloidogenic pathway, α-secretase cleaves APP within the Aβ region [50, 63] thus precluding the formation of Aβ peptides. This also leads to the secretion of the neuroprotective ectodomain APPsα into the extracellular space in a process that can be stimulated by neuronal and synaptic activity [34, 35].

AD is characterized by upregulation of β-secretase (BACE-1) resulting in a shift towards amyloidogenic APP processing [2, 36]. Increasing evidence suggests that the concomitant reduction in APPsα and the loss of its physiological functions contribute to AD pathogenesis. Reduced levels of APPsα or ADAM10 were reported in patients with mild cognitive impairment and AD [22, 44] (see also review by [25]). Lowered levels of CSF APPsα were also correlated with poor memory performance in aged rats [4, 25] and moreover, in a Swedish family with AD, a strong correlation was found between low APPsα levels and poor performance in cognitive tests, whereas no association was reported for amyloid β-peptide [3]. In addition, α-secretase attenuating mutations have been associated with hereditary late-onset AD [74].

Previously, a number of in vitro studies indicated that APP and APPsα may protect cell lines and cultured neurons against various forms of stress, including growth factor withdrawal [55], apoptotic stimuli [18] and excitotoxicity [43, 48, 58, 64, 79]. In contrast, so far only few studies have addressed a protective role of APPsα in vivo and these were limited to acute forms of experimental brain injury. APPsα had beneficial effects when infused as a protein shortly after mechanical head trauma [19, 78] or after induction of ischemia in adult rats [72]. From these studies, however, it is difficult to extrapolate to the situation in neurodegenerative diseases such as AD, characterized by chronic production and accumulation of neurotoxic molecules including Aβ. Another challenge is the need for sustained expression of neurotrophic/neuroprotective factors that calls for a gene therapy approach.

Loss of function studies in APP knockout mice had indicated diverse physiological functions of APP in the PNS and CNS for neuronal morphology, synaptogenesis, adult neurogenesis, synaptic plasticity and hippocampus-dependent behavior [1, 7, 15, 33, 42, 76, 83–85]. However, it remained unclear whether deficits of mice lacking APP family members may arise due to defects (such as impaired synaptogenesis) originating in development [85]. To delineate the specific role of APPsα, we previously generated APPsα knockin (KI) mice that lack Aβ production and expresses solely the secreted APPsα ectodomain due to a stop codon insertion into the mouse APP locus behind the α-secretase cleavage site. APPsα-KI mice showed a wild-type-like phenotype lacking the LTP impairment of APP-KO mice [65]. While these early studies suggested an important role of endogenous APPsα for normal LTP, it remained unclear whether APPsα may also be of therapeutic relevance. Recently, we generated conditional double knockout (cDKO) mice lacking APP and the related APLP2 [33]. These cDKO mice revealed reduced spine density and impaired synaptic plasticity that was associated with deficits in hippocampus-dependent behaviors [33]. Interestingly, the impairment of LTP found in cDKO mice could be rescued by acute application of nanomolar amounts of recombinant APPsα, indicating a crucial role for APPsα to support synaptic plasticity in the adult brain [33]. Despite this, the question remained whether these beneficial acute effects of APPsα observed in vitro for a relatively short time of recording may also prove relevant in vivo including AD model mice.

Here, we intended to test the concept of enhancing/restoring APPsα levels using a gene therapy approach as a potential AD treatment strategy. To this end, we used direct overexpression of APPsα by AAV-mediated gene transfer into the brain to explore its potential to ameliorate or rescue structural, electrophysiological and behavioral deficits of AD model mice. We show that overexpression of APPsα in aged transgenic APP/PS1ΔE9 mice with well-established plaque pathology improves synaptic plasticity and partially rescues spine density deficits. Restoration of synaptic plasticity and increased spine density is also accompanied by a rescue of spatial reference memory. Moreover, we demonstrate that AAV-APPsα expression leads to moderately reduced Aβ levels and significantly ameliorated plaque pathology. Interestingly, in AAV-APPsα injected mice, we observed an increased number of microglia with ramified morphology in the vicinity of plaques that was associated with increased IDE and TREM2 expression which may have led to increased plaque clearance. Collectively, our data suggest that even at stages with advanced plaque deposition APPsα may mitigate Aβ induced synaptotoxic effects and improve cognitive function.

Materials and methods

AAV plasmid design and vector production

The mouse APPsα coding sequence (derived from Uniprot: P12023-2) was codon optimized (Geneart, Regensburg) and then cloned under control of the synapsin promoter into the single-stranded rAAV2-based shuttle vector pAAVSynMCS-2A-Venus [75] via NheI-HindII restriction sites. For easy detection, an N-terminal double HA-tag was inserted downstream of the APP signal peptide at the N-terminus of APPsα. The control vector (pAAV-Venus) encodes the yellow fluorescent protein Venus fused to a C-terminal farnesylation signal for membrane anchoring. All constructs were packaged into AAV9 by the MIRCen viral production platform as described [10]. Briefly, viral particles were produced by transient co-transfection of HEK-293 cells with an adenovirus helper plasmid (pXX6-80), an AAV packaging plasmid carrying the rep2 and cap9 genes, and the AAV2 transfer vector containing the above-mentioned expression cassettes. 72 h following transfection, virions were purified and concentrated from cell lysate and supernatant by ultracentrifugation on a iodixanol density gradient followed by buffer exchange to PBS, 0.01 % Pluronic via a 100kd Amicon Centrifugal filter unit (Merck-Millipore, Darmstadt, Germany). Concentration of the vector stocks was estimated by quantitative PCR according to the method described by [5]) and expressed as viral genomes per ml of concentrated stocks (vg/ml).

Animals

Sixteen APPswe/PS1ΔE9 mice (referred to as APP/PS1ΔE9; The Jackson Laboratory, Bar Harbor, USA) and seven age-matched littermate control mice were used for behavior, pathology and biochemistry. Eleven APP/PS1ΔE9 and five littermates were used for electrophysiology and spine density analysis. APP/PS1ΔE9 mice express the human APP gene carrying the *Swedish* double mutation (K595N/M596L). In addition, they express the human PS1ΔE9 variant lacking exon 9 [13, 38, 87]. Only male mice were used throughout the study. APP knockout mice have been described previously [49]. For age at AAV injection and age at analysis/sacrifice, see results section. All experiments were conducted in accordance with the ethical standards of French, German and European regulations (European Communities Council Directive of 24 November 1986).

Stereotactic injection of AAV

Mice were anesthetized by intraperitoneal injection of ketamine/xylazine (0.1/0.05 g/kg body weight) and positioned on a stereotactic frame (Stoelting, Wood Dale, USA). Vectors (either AAV-Venus or AAV-APPsα) were bilaterally injected into the hippocampus using 2 µl of viral preparation (10^{10} vg/hippocampus) at a rate of 0.2 µl/min. Two injection sites per hippocampus were used to optimize virus spreading. Stereotactic coordinates of injection sites from bregma were: anteroposterior −2 mm; mediolateral ±1 mm; dorsoventral −2.25 mm and anteroposterior −2 mm; mediolateral ±1 mm; dorsoventral −1.75 mm.

Brain samples

APP/PS1ΔE9 mice were sacrificed 5 months post-injection at 17 months of age. Following anesthesia, mice were transcardially perfused with 0.1 M phosphate-buffered saline (PBS) before dissection. For immunohistochemistry, the left cerebral hemisphere was dissected and post-fixed in 4 % paraformaldehyde (PFA) for 1 week and cryoprotected in 30 % sucrose for 24 h. 40 µm sections were cut using a freezing microtome (Leica, Wetzlar, Germany), collected in a cryoprotective solution and stored at −20 °C. The right hemisphere was dissected to segregate hippocampus and cortex for biochemical analysis. Samples were then homogenized in lysis buffer (TBS, NaCl 150 mM and Triton 1 %) containing phosphatase and protease inhibitors. After centrifugation (20 min, 13,000 rpm, 4 °C), the supernatant was collected and the protein concentration was quantified by BCA Assay (Thermo Fisher Scientific, Waltham, USA). Lysate aliquots (3 mg of protein/ml) were stored at −80 °C.

Immunostaining

Slices were washed with 0.1 M PBS and permeabilized in 0.25 % PBS-Triton before blocking in PBS-Triton 0.25 % containing 5 % goat serum for 60 min. For vector encoded HA-APPsα immunolabeling, slices were incubated with an anti-HA antibody (Covance, Princeton, USA, 1/250) overnight at 4 °C. After successive washes (PBS-Triton 0.25 %, PBS and PB 0.1 M), incubation with a biotinylated anti-mouse antibody was performed for 1 h at room temperature. For signal amplification, samples were incubated using the ABC kit (Vector laboratories, Burlingame, USA) for 1 h at room temperature. Finally, slices were incubated in Cy3-coupled streptavidin. HA-APPsα was co-immunostained overnight with the following primary antibodies: Rabbit anti-Iba1, 1/500, Wako, Richmond, USA;

Mouse-GFAP Cy3 conjugate, 1/500, Sigma-Aldrich, Saint-Louis, USA. For immunofluorescent staining of plaques, slices were stained using a 30 min incubation in 1 % thioflavin S solution, rinsed twice (1 min each) in 50 % EtOH and mounted in Vectashield fluorescent mounting media (Vector laboratories). Images were taken with a Nikon Eclipse T*i* microscope (Nikon, Tokyo, Japan) and a Leica SP8 confocal microscope (Leica). For plaque quantification, slices were incubated in 88 % formic acid solution for 15 min (antigen retrieval). To inactivate endogenous peroxidase, samples were incubated in hydrogen peroxide (30 min) before blocking and incubation with the primary antibody (4G8, Covance, 1/1000). Incubation with a horseradish-coupled secondary antibody was done at RT, developed using the DAB kit (Vector laboratories) and mounted in Eukit mounting media (Sigma-Aldrich). Images were taken with a Z6 APO macroscope (Leica). Plaques, GFAP and Iba1 immunoreactivity were quantified using ImageJ (NIH, Bethesda, USA) or Icy (Institut Pasteur, Paris, France). Laser power, numeric gain and magnification were kept constant between animals to avoid potential technical artifacts. Images were first converted to 8-bit gray scale and binary thresholded to highlight a positive staining. At least 2 sections per mouse (between −1.7 and −2.3 mm caudal to bregma) were quantified for either hippocampus or cortex. The average value per structure was calculated for each mouse. For quantification of Iba1 and GFAP immunoreactivity around plaques, a region of interest (ROI) was drawn around the center of the plaque. The diameter of the circular ROI was set as three times the diameter of the plaque. Mean fluorescence intensity values were measured for either Iba1 or GFAP immunoreactivity and were processed via Icy software (Institut Pasteur, Paris, France). Experiments and data analysis were performed blind with respect to treatments and genotypes.

Western blot analysis

Proteins were separated by SDS-PAGE using 4–12 % Bis–Tris gels (NuPAGE, Life Technologies, Carlsbad, USA) in MES SDS running buffer (NuPAGE, Life Technologies) and transferred to nitrocellulose membranes (iBlot, Life Technologies). For CTF analysis, proteins were separated using 10–20 % Tris–Tricine gradient gels (Novex, Life Technologies) and electroblotted onto 0.22 µm PVDF membrane (BioRad, Hercules, USA). After blocking in 5 % milk-PBS 0.1 M for 60 min, membranes were incubated with the primary antibodies overnight at 4 °C. The following antibodies were used: HA, 1/2000, Covance; β-actin, 1/5000, Merck Millipore; Venus (GFP), 1/1000, Vector laboratories; GAPDH, 1/4000, Abcam, Cambridge, UK; Iba1, 1/2000, Wako, Richmond, USA; GFAP, 1/4000 Dako, Glostrup, Denmark; IDE, 1/200, Santa Cruz Biotechnology, Dallas, USA; TREM2, 1/500, R&D Systems, Minneapolis, USA; APP: mouse monoclonal m3.2 and c1/6.1, 1/1000; kind gift from Paul Mathews; Y188, 1/1000, Abcam; see also Fig. S1 for a summary of anti-APP epitopes recognized by these antibodies. Membranes were then washed with TBS-T (with 0.1 % Tween), incubated with a horseradish peroxidase coupled secondary antibody and developed using enhanced chemiluminescence (ECL, GE Healthcare, Little Chalfont, UK and Super Signal, Thermo Fisher Scientific). Signals were detected with Fusion FX7 (Vilber Lourmat, Marne-la-Vallée, France) and analyzed and quantified using ImageJ.

Biochemical separation of soluble APPsα

Hippocampi were homogenized in tissue homogenization buffer (THB, 20 mM Tris–HCl, pH 7.4; 250 mM Sucrose; 1 mM EDTA; 1 mM EGTA) including phosphatase and protease inhibitors (Roche, Basel, Switzerland)) using a Potter homogenizer. After homogenization, a brief low-speed spin (5000 g, 5 min) was performed to remove remaining tissue fragments. For the detection of the soluble fragments APPsα and APPsβ, a high-speed centrifugation step (60 min at 100,000*g*) was performed and membrane-free supernatant was used for further analysis. Total brain homogenate or supernatant (20 µg protein) was used for SDS-PAGE using 12 % Tris–Tricine gels and electroblotted onto PVDF membrane (BioRad). Western blot signals were detected by enhanced chemiluminescence (Super Signal West Pico; Pierce, Rockford, USA) and imaged using the ChemiDoc Imaging System (BioRad). For quantification, all images were analyzed with the ImageLab software (BioRad).

Elisa

For quantification of APP processing products in brain samples, the following ELISA kits were employed: Human-specific APP β-CTF Assay Kit (IBL, Hamburg, Germany, JP27776), huAPP$_{SWE}$-specific ELISA (IBL, JP27733), V-PLEX Plus Aβ Peptide Panel 1 (6E10) Kit (Meso Scale Discovery, Rockville, USA) detecting at the same time huAβ$_{38}$, huAβ$_{40}$, huAβ$_{42}$, and V-PLEX Plus Aβ Peptide Panel 1 (4G8) Kit (Meso Scale Discovery) detecting hu/muAβ$_{38}$, hu/muAβ$_{40}$, and hu/muAβ$_{42}$. The procedures were performed according to the respective supplier instructions.

Morris water maze

Experiments were performed in a 120-cm-diameter, 50-cm-deep tank filled with opacified water kept at 21 °C and equipped with a 10-cm-diameter platform submerged 1 cm under the water surface. Visual clues

were disposed around the pool as spatial landmarks for the mouse and luminosity was kept at 430 lux. Training consisted of daily sessions (three trials per session) during 5 consecutive days. Start positions varied pseudo-randomly among the four cardinal points. Mean inter-trial interval was 15 min. Each trial ended when the animal reached the platform. A 60-s cutoff was used, after which mice were gently guided to the platform. Once on the platform, animals were given a 30-s rest before being returned to their cage. 72 h after the last training trial (day 8), retention was assessed during probe trial in which the platform was no longer present. Animals were video tracked using Ethovision software (Noldus, Wageningen, the Netherlands) and behavioral parameters (swim speed, traveled distance, latency, percentage of time spent in each quadrant) were automatically calculated. Experiments and statistical evaluation of data were performed by an experimentator blind to genotype and treatment group.

Statistics

Statistical analyses were performed as indicated for the respective experiments. Outliers were detected and rejected using maximum normed residual test (Grubbs' test). In most cases, data were analyzed using non-parametric Mann–Whitney *U* tests excepted for behavioral experiments. Two-way ANOVA with repeated measures were carried out when required by the experimental plan to assess statistical effects. Correlation matrices were generated using non-parametric Spearman rank correlation coefficient. For all analysis, statistical significance was set to a p value <0.05. All analyses were performed using Statistica (StatSoft Inc., Tulsa, USA) or Prism (GraphPad Software, La Jolla, USA).

Electrophysiology

In vitro extracellular recordings were performed on acute hippocampal slices of WT littermates stereotactically injected with AAV-Venus ($N = 5$), APP/PS1ΔE9 mice injected either with AAV-Venus ($N = 4$) or AAV-APPsα virus ($N = 6$) at 8 months of age. Electrophysiological recordings were performed 4–5 months later at an age of 12–13 months. In-between animals were housed in a temperature- and humidity-controlled room with a 12-h light–dark cycle and had access to food and water ad libitum.

Slice preparation

Acute hippocampal transversal slices were prepared from individuals at an age of 12–13 months. Mice were anesthetized with isoflurane and decapitated. The brain was removed and quickly transferred into ice-cold carbogenated (95 % O_2, 5 % CO_2) artificial cerebrospinal fluid (ACSF) containing 125 mM NaCl, 2 mM KCl, 1.25 mM NaH_2PO_4, 2 mM $MgCl_2$, 26 mM $NaHCO_3$, 25 mM glucose. After dissection of the two hemispheres, one was used for Golgi–Cox staining and the other for electrophysiology. The hippocampus was sectioned into 400-µm-thick transversal slices with a vibrating microtome (Leica, VT1200S). Slices were maintained in carbogenated ACSF (125 mM NaCl, 2.mM KCl, 1.25 mM NaH_2PO_4, 2 mM $MgCl_2$, 26 mM $NaHCO_3$, 2 mM $CaCl_2$, 25 mM glucose) at room temperature for at least 1.5 h before transferred into a submerged recording chamber. Before recording, each slice of the AAV-Venus injected animals was proofed for fluorescence expression of Venus in area CA1 and CA3 (Axiovert 35, Zeiss, Oberkochen, Germany). Slices absent of the fluorescence protein in the recording areas were excluded from further analysis.

Extracellular field recordings

Slices were placed in a submerged recording chamber and perfused with carbogenated ACSF (32 °C; 125 mM NaCl, 2 mM KCl, 1.25 mM NaH_2PO_4, 1 mM $MgCl_2$, 26 mM $NaHCO_3$, 2 mM $CaCl_2$, 25 mM glucose) at a rate of 1.2–1.5 ml/min. Field excitatory postsynaptic potentials (fEPSPs) were recorded in stratum radiatum of CA1 region with a borosilicate glass micropipette (resistance 2–4 MΩ) filled with 3 M NaCl at a depth of ~150–200 µm. Monopolar tungsten electrodes were used for stimulating the Schaffer collaterals at a frequency of 0.1 Hz. Stimulation intensity was adjusted to 40 % of maximum fEPSP slope for 20 min baseline recording. LTP was induced by applying theta-burst stimulation (TBS: 10 trains of 4 pulses at 100 Hz in an 200 ms interval, repeated 3 times). Basal synaptic transmission properties were analyzed via input–output (IO) measurements and short-term plasticity was examined via paired pulse facilitation (PPF). The IO measurements were performed either by application of defined current values (25–175 µA) or by adjusting the stimulus intensity to certain fiber volley (FV) amplitudes (0.1–0.7 mV). PPF was performed by applying a pair of two closely spaced stimuli in different inter-stimulus intervals (ISI) ranging from 10 to 160 ms. After completion of electrophysiological measurements, we performed anti-HA staining to monitor HA-APPsα expression or Venus expression (blind to genotype). Only well-transduced sections as evidenced by either Venus immunofluorescence or HA staining were included in the electrophysiological data analysis.

Dendrite and spine analysis

Golgi–Cox staining

Golgi staining was done using the Rapid Golgi Staining Kit (FD NeuroTechnologies, Columbia, USA) according to the manufacturer's instructions. All procedures were performed under dark conditions. One hemisphere of each mouse was used for electrophysiology and the other one for Golgi–Cox staining. Hemispheres were immersed in 2 ml mixtures of equal parts of kit solutions A and B and stored at RT for 2 weeks. Afterwards, brain tissues were stored in solution C at 4 °C for at least 48 h and up to 7 days before sectioning. Solutions AB and C were renewed within the first 24 h. Coronal sections of 200 µm were cut with a vibrating microtome (Leica, VT1200S) while embedded in 2 % Agar in 0.1 M PBS. Each section was mounted with Solution C on an adhesive microscope slide pre-coated with 1 % gelatin/0.1 % chromalaun on both sides and stained according to the manufacturer´s protocol with the exception that ApliClear (AppliChem) was used instead of xylene. Finally, slices were cover-slipped with Permount (Thermo Fisher Scientific).

Imaging and analysis of spine density in Golgi–Cox stained slices

Imaging of second- or third-order dendritic branches of hippocampal pyramidal neurons of area CA3 and CA1 was done with an Axioplan 2 imaging microscope (Zeiss) using a 63× oil objective and a z-stack thickness of 0.5 µm under reflected light. The number of spines was determined per micrometer of dendritic length (in total 100 µm) at apical and basal compartments using ImageJ (1.48v, National Instruments of Health, USA). At minimum four animals per genotype and four neurons per animal were analyzed blinded to genotype and injected virus.

Data analysis

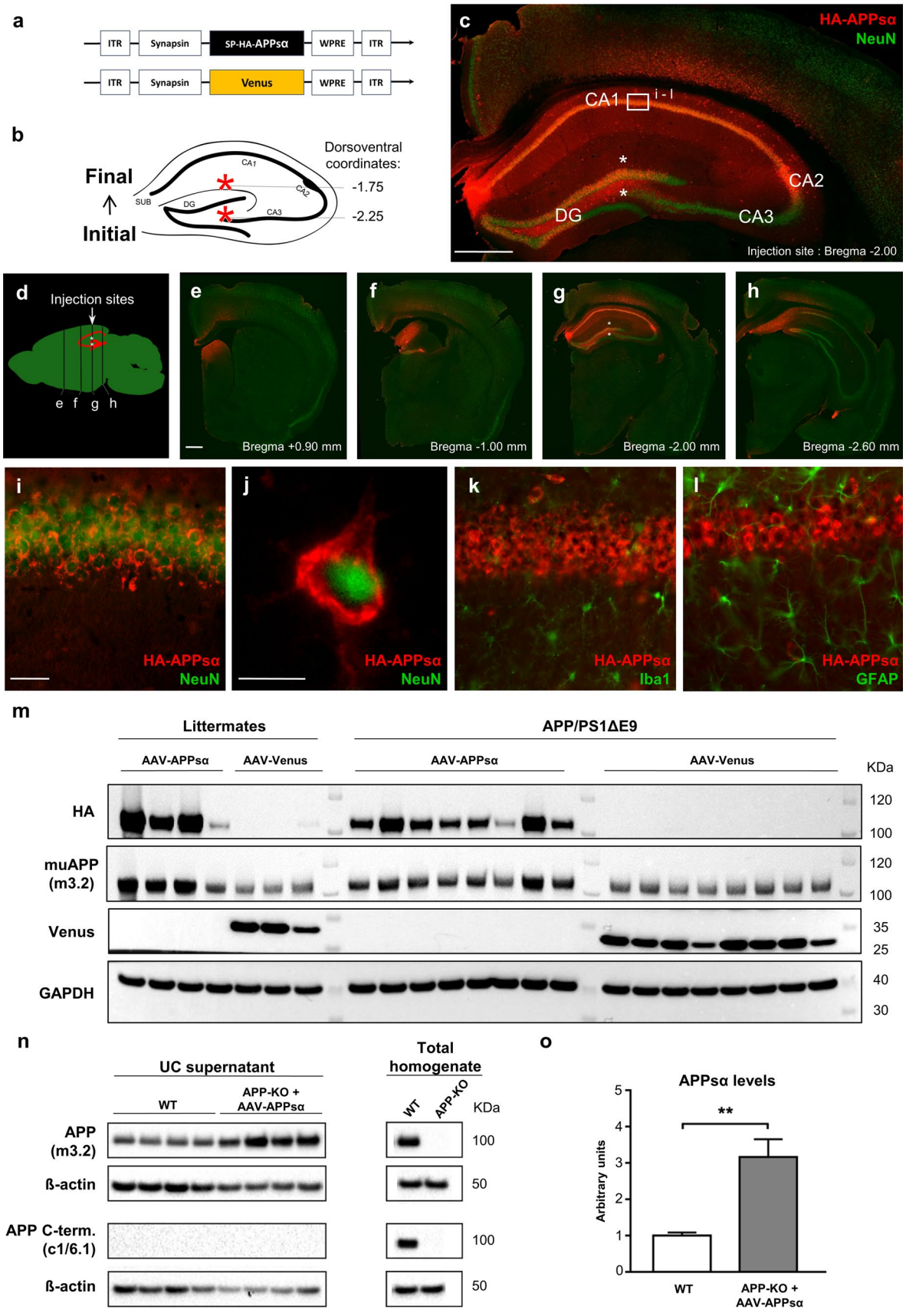
Data of electrophysiological recordings were collected, stored and analyzed with LABVIEW software (National Instruments, Austin, USA). The initial slope of fEPSPs elicited by stimulation of the Schaffer collaterals was measured over time, normalized to baseline and plotted as average ± SEM. Analysis of the PPF data was performed by calculating the ratio of the slope of the second fEPSP divided by the slope of the first one and multiplied by 100. Data of Golgi–Cox staining were analyzed using GraphPad Prism (Version, 5.01) software. Spine density is expressed as mean ± SEM. Differences between genotypes were detected with one-way analysis of variance (ANOVA) followed by Bonferroni's post hoc test using IBM SPSS Statistics 21.

Fig. 1 Widespread expression of APPsα throughout the hippocampus and in parahippocampal cortex in AAV-APPsα injected APP/PS1ΔE9 mice. APP/PS1ΔE9 and non-transgenic littermate control mice (LM) were injected either with AAV-Venus or AAV-APPsα at 12 months of age and sacrificed at 17 months of age. (LM: AAV-Venus $n = 3$, AAV-APPsα $n = 4$; APP/PS1ΔE9 mice: AAV-Venus $n = 8$, AAV-APPsα $n = 8$; all males). **a** Schematic representation of AAV9 constructs enabling the neuron-specific expression of Venus (Control) and HA-tagged APPsα. ITR: inverted terminal repeat; SP: APP signal peptide; HA: Human influenza hemagglutinin tag; WPRE: Woodchuck hepatitis virus posttranscriptional regulatory element. **b** Scheme of the hippocampus with coordinates of the two injection sites (*red stars*). **c** High magnification of the hippocampus of an APP/PS1ΔE9 mouse injected with the AAV-APPsα. APPsα is detectable throughout the hippocampus and the proximal cortex. *Scale bar*, 500 µm. Injection sites indicated by *white stars*. **d** Scheme representing anteroposterior coordinates of coronal sections depicted in **e–h**. **e–h** Immunostaining of APPsα (anti-HA tag, *red*) and NeuN (*green*) at different anteroposterior coordinates. *Scale bar*, 500 µm. **i–l** Double immunostaining of CA1 pyramidal cells from the area boxed in **c** expressing APPsα (anti-HA tag, *red*) and specific neuronal (NeuN, *green*, **i**, **j**), microglial (Iba1, *green*, **k**) or astrocytic (GFAP, *green*, **l**) markers. *Scale bar*, 50 µm (**i**, **k**, **l**), 20 µm (**j**). Note that AAV-mediated APPsα expression is restricted to neurons. **m** Western blot analysis of Venus, muAPP and HA-muAPPsα expression in APP/PS1ΔE9 and LM hippocampi of mice injected with AAV-Venus or AAV-APPsα vectors. Note that antibody m3.2 is specific for muAPP and recognizes endogenous muAPP and HA-muAPPsα (see also Fig. S1 for antibody epitopes) **n** Analysis of extracellular muAPPsα in APP-KO mice injected with AAV-APPsα ($n = 4$) in comparison to endogenous muAPPsα produced in non-injected WT mice ($n = 4$). *Left panels* Homogenates of hippocampi were subjected to ultracentrifugation (UC) to separate soluble proteins. The C-terminal anti-APP antibody (c1/6.1) was used to confirm the separation of soluble APPsα from membrane bound full-length APP. **o** Quantification of muAPPsα (m3.2 immuoreactivity) normalized to β-actin. Data represent mean ± SEM, Student's *t* test, $^{**}p < 0.01$

Results

AAV-APPsα injection mediates efficient and long-lasting neuronal expression of APPsα in the hippocampus of APP/PS1ΔE9 mice

To assess the therapeutic potential of APPsα, we used AAV-mediated overexpression of APPsα in the brain of aged (12-month-old) APP/PS1ΔE9 mice. APP/PS1ΔE9 mice show progressive plaque deposition starting at about 5–6 months of age and highly abundant plaques are observed at 12 months of age [38, 87]. AAV9 vectors expressing either Venus or codon-optimized HA-tagged murine APPsα (HA-APPsα) under the control of the neuronal synapsin promoter (further referred to as AAV-Venus and AAV-APPsα, Fig. 1a) were bilaterally injected into the stratum lacunosum moleculare region of the dorsal hippocampus and into

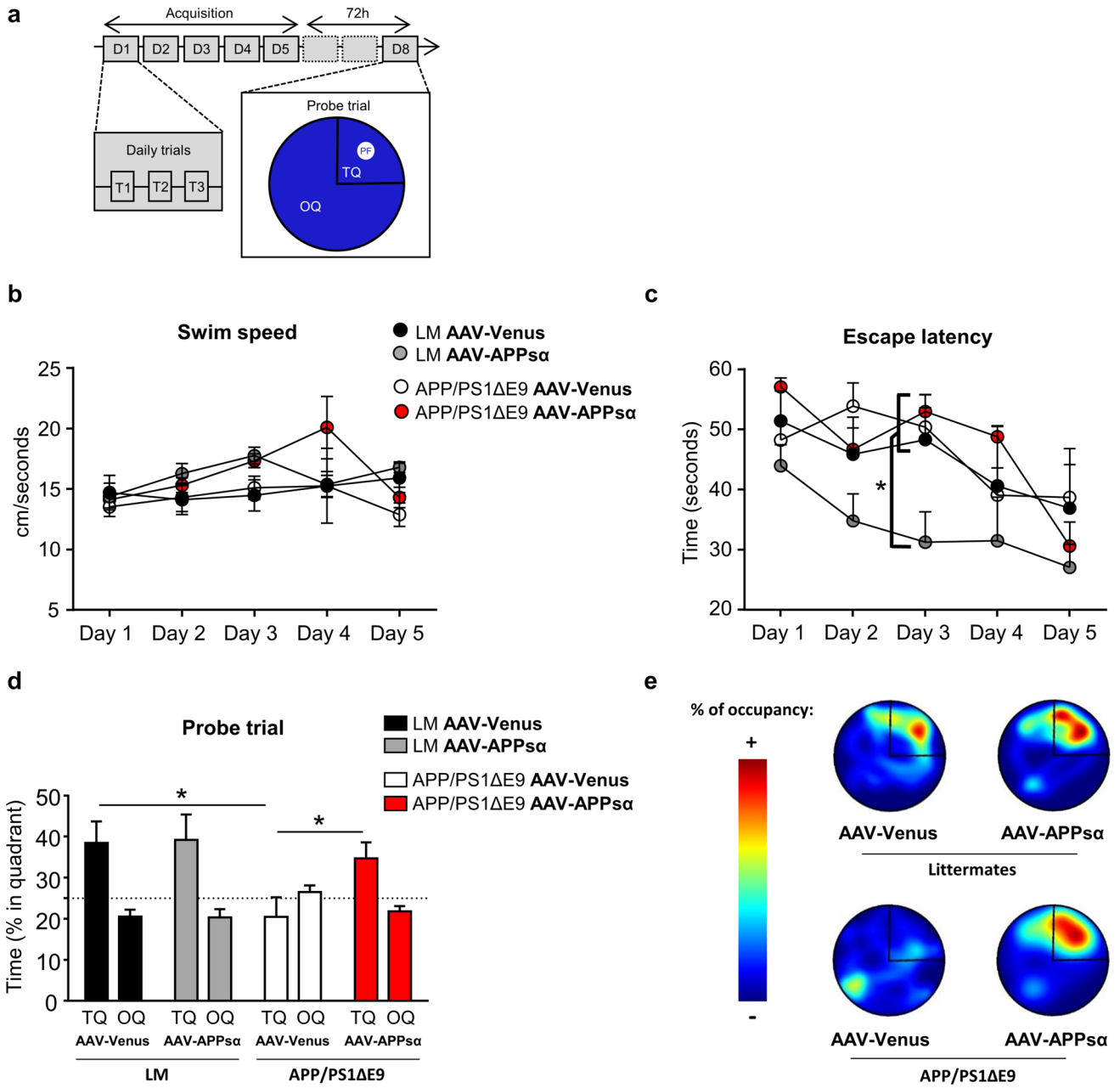

a
ITR
Synapsin
SP-HA-APPsα
WPRE
ITR
ITR
Synapsin
Venus
WPRE
ITR
b
Final
Initial
SUB
DG
CA1
CA2
CA3
Dorsoventral coordinates:
-1.75
-2.25
c
HA-APPsα
NeuN
CA1
i - l
CA2
DG
CA3
Injection site : Bregma -2.00
d
Injection sites
e f g h
e
Bregma +0.90 mm
f
Bregma -1.00 mm
g
Bregma -2.00 mm
h
Bregma -2.60 mm
i
HA-APPsα
NeuN
j
HA-APPsα
NeuN
k
HA-APPsα
Iba1
l
HA-APPsα
GFAP
m
Littermates
APP/PS1ΔE9
AAV-APPsα
AAV-Venus
AAV-APPsα
AAV-Venus
KDa
HA
muAPP (m3.2)
Venus
GAPDH
120
100
120
100
35
25
40
30
n
UC supernatant
Total homogenate
WT
APP-KO + AAV-APPsα
WT
APP-KO
KDa
APP (m3.2)
ß-actin
APP C-term. (c1/6.1)
ß-actin
100
50
100
50
o
APPsα levels
**
Arbitrary units
0
1
2
3
4
5
WT
APP-KO + AAV-APPsα

the dentate gyrus (Fig. 1b) of 12-month-old male APP/PSΔE9 mice. To monitor vector-mediated Venus and APPsα expression, mice were sacrificed 5 months after injection. Immunohistochemistry using an HA-tag-specific antibody revealed widespread expression of HA-APPsα not only in the hippocampus, but also in the cortical layers above the injected hippocampus (Fig. 1c). Analysis of serial anteroposterior coronal sections demonstrated widespread HA-APPsα immunoreactivity (over 3.5 mm) in the hippocampus from −2.6 mm posterior to +0.9 mm anterior from the injection site (Fig. 1d–h) and in the adjacent cortex. More detailed analysis showed prominent expression of vector-mediated HA-APPsα in the pyramidal cells of the subiculum, in the CA1, CA2 regions and in granular neurons of dentate gyrus (Fig. 1c). Within the CA3 subfield HA-APPsα expression was detectable but considerably lower. As APPsα expression was driven by the neuron-specific synapsin promoter, HA-APPsα expression was restricted to neuronal cells as revealed by double immunostaining against NeuN (Fig. 1i, j). Consistently, no expression was detectable in microglia (Iba1, Fig. 1k) or in astrocytes (GFAP, Fig. 1l). The AAV-Venus expression pattern was largely similar to that of AAV-APPsα. Western blot analysis of hippocampal extracts confirmed vector-mediated HA-APPsα protein expression in all injected animals. Comparable levels of either HA-APPsα or Venus were detected in hippocampi of injected APP/PS1ΔE9 mice or non-transgenic littermates, respectively (Fig. 1m). To quantify vector-mediated muAPPsα overexpression blots were also probed with an antibody (m3.2) directed against a mouse-specific APP epitope located between the β- and α-secretase site (see middle panel in Fig. 1m; see also Fig. S1 for antibody epitopes) that detects endogenous full-length muAPP, endogenously secreted muAPPsα and vector-derived AAV-muAPPsα. This analysis indicated an increase in muAPP species (m3.2 immunoreactivity) of about 1.73 ± 0.13 fold ($p < 0.0001$, t test) in AAV-APPsα injected mice ($n = 12$) as compared to the control group receiving AAV-Venus ($n = 11$). This analysis does, however, not allow to distinguish between soluble extracellular APPsα and cell bound muAPP species (including transmembrane muAPP and muAPPsα still present in compartments of the secretory machinery). To specifically determine the amount of soluble muAPPsα that is produced by AAV-APPsα injection, we employed APP knockout mice. Four weeks after injection hippocampi of injected APP-KO and non-injected WT mice were dissected, homogenized and ultracentrifugation was used to separate AAV encoded secreted, soluble APPsα from cell bound APPsα. Comparison to wild-type mice indicated that AAV-mediated soluble APPsα expression is increased by about 3.1-fold ($p < 0.01$, t test) in hippocampi of AAV-vector injected mice as compared to endogenous soluble muAPPsα (Fig. 1o) in wild-type mice. In summary, we demonstrate that our AAV-based approach leads to efficient and long-lasting APPsα expression in the hippocampus and adjacent cortex.

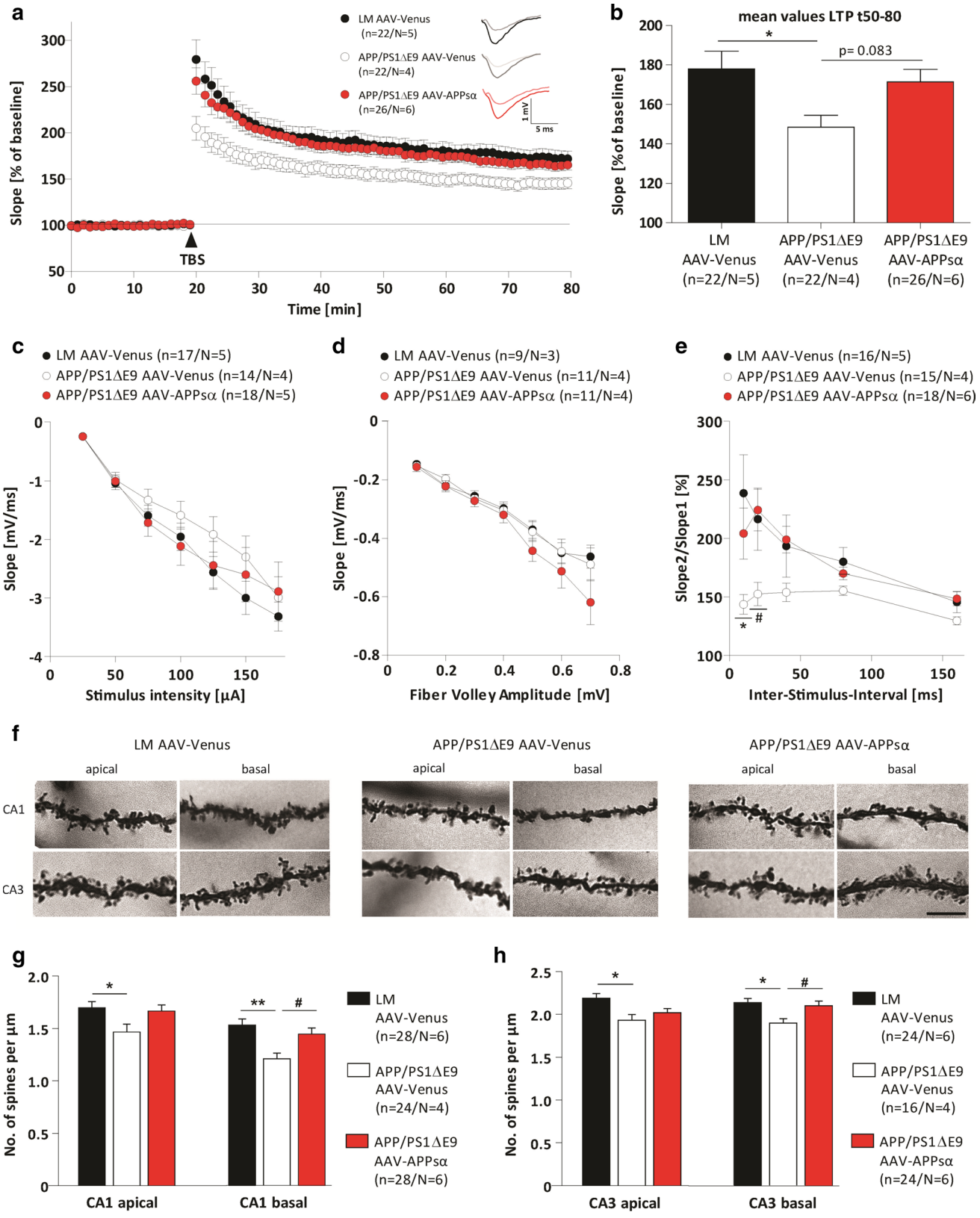
Fig. 2 APPsα overexpression enhances Morris water maze performance in WT mice and rescues the spatial memory deficit of APP/PS1ΔE9 mice. Transgenic APP/PS1ΔE9 mice ($n = 8$ per group) or littermate (LM) controls ($n = 3$–4 per group) were either injected with AAV-Venus or AAV-APPsα vectors at 12 months of age and tested 2 months later at 14 months of age. **a** Training phase consisted of daily sessions (three trials per session: T1, T2 and T3) during five consecutive days (D1–D5). 72 h (D8) after the last trial the platform was removed and memory retention was assessed during the probe trial. *Insert* water maze configuration during training sessions. PF: platform (*white*); TQ: target quadrant (*small segment*); OQ: other quadrants (*large segment*). **b** Swim speed and **c** escape latency of littermate controls or APP/PS1ΔE9 mice injected either with AAV-Venus or AAV-APPsα. Swim speed was similar between the different groups (2-way ANOVA: group effect: $F_{3,100} = 2.40$; ns; time effect: $F_{4,100} = 1.41$; ns; group × time interaction: $F_{12,100} < 1$; ns). **c** Littermates injected with AAV-APPsα showed improved performance, as indicated by reduced escape latency (2-way ANOVA: time effect: $F_{4,100} = 7.138$; $p < 0.0001$; group effect: $F_{3,100} = 7.247$; $p = 0.0002$, followed by Tukey post hoc test: APP/PS1ΔE9 mice injected with AAV-APPsα versus each of the other groups, $p < 0.013$). **d** Probe trial performance at 72 h. 2-way ANOVA, group effect: $F_{3,17} = 3.356$; $p < 0.04$; quadrant effect: $F_{1,17} = 23.54$; $p < 0.007$; group × quadrant interaction effect: $F_{3,17} = 3.356$; $p < 0.04$. APP/PS1ΔE9 mice injected with AAV-Venus were impaired in comparison to littermate mice injected with AAV-Venus (Tukey post hoc test: $p = 0.023$) confirmed by no preference for the trained target quadrant. Strikingly, AAV-APPsα treated APP/PS1ΔE9 mice spent more time in the target quadrant compared to APP/PS1ΔE9 mice injected with AAV-Venus (Tukey post hoc test: $p = 0.017$). Data represent mean ± SEM and were analyzed by 2-way ANOVA (genotype and group as factors) with repeated measures followed by Tukey post hoc test. $^*p < 0.05$ **e** Representative occupancy plots during the probe trial show a more random search strategy for AAV-Venus injected APP/PS1ΔE9 mice. Note that AAV-APPsα injected transgenic mice show directionality towards the platform (indicated by *segment*) similar to littermate controls. Values represent mean ± SEM

AAV-APPsα treatment rescues the spatial memory impairment of APP/PS1ΔE9 mice

To analyze the consequences of AAV-APPsα or AAV-Venus injection for spatial learning and memory, mice were tested in the Morris water maze place navigation task (Fig. 2). To this end, transgenic APP/PS1ΔE9 mice ($n = 8$ per group) or non-transgenic littermate controls ($n = 3$–4 per group) were injected either with AAV-Venus or AAV-APPsα vectors at 12 months of age and tested 2 months later at 14 months of age. Swim speed was comparable in all groups of animals (Fig. 2b) over the 5 days of training, thus excluding impairments in motor performance. While all four groups of mice did show learning, as evidenced by reduced latency to reach the platform over the 5 days of training, we observed a group effect resulting from an overall significantly increased performance in non-transgenic littermates that had received AAV-APPsα (Fig. 2c). Injection of AAV-APPsα did not, however, improve the performance of



APP/PS1ΔE9 mice (Fig. 2c). Similar results were obtained when analyzing the path length to reach the platform (data not shown). During the probe trial that assesses spatial reference memory and was conducted 72 h after the last trial of training APP/PS1ΔE9 mice injected with AAV-Venus were strongly impaired (Fig. 2d) in comparison to littermate mice injected with AAV-Venus and showed no preference for the trained target quadrant (Fig. 2d; paired *t* test: $t_7 = 0.96$; $p = 0.37$). Strikingly, APP/PS1ΔE9 mice that had been injected with AAV-APPsα showed a clear preference for the trained target quadrant (Fig. 2d; paired *t* test: $t_7 = 2.516$; $p = 0.045$), that was statistically indistinguishable from the performance of littermate controls (Fig. 2d; $p > 0.84$, 2-way ANOVA followed by Tukey's post hoc test). To get further insight into the search strategy of individual mice we also analyzed spatial occupancy plots of individual mice during the probe trial (Fig. 2e). Transgenic APP/PS1ΔE9 mice injected with control vector frequently showed a rather random occupancy of the swimming arena and no preference for the trained target quadrant, indicating an impaired spatial reference memory 3 days after training. In contrast, occupancy plots of AAV-APPsα injected transgenic mice revealed clear directionality towards the trained platform similar to non-transgenic littermates injected with AAV-Venus or AAV-APPsα (Fig. 2e). Thus, vector-mediated APPsα expression rescued the spatial memory


a
LM AAV-Venus (n=22/N=5)
APP/PS1ΔE9 AAV-Venus (n=22/N=4)
APP/PS1ΔE9 AAV-APPsα (n=26/N=6)
1 mV
5 ms
Slope [% of baseline]
TBS
Time [min]
b
mean values LTP t50-80
Slope [%of baseline]
p= 0.083
LM AAV-Venus (n=22/N=5)
APP/PS1ΔE9 AAV-Venus (n=22/N=4)
APP/PS1ΔE9 AAV-APPsα (n=26/N=6)
c
LM AAV-Venus (n=17/N=5)
APP/PS1ΔE9 AAV-Venus (n=14/N=4)
APP/PS1ΔE9 AAV-APPsα (n=18/N=5)
Slope [mV/ms]
Stimulus intensity [µA]
d
LM AAV-Venus (n=9/N=3)
APP/PS1ΔE9 AAV-Venus (n=11/N=4)
APP/PS1ΔE9 AAV-APPsα (n=11/N=4)
Slope [mV/ms]
Fiber Volley Amplitude [mV]
e
LM AAV-Venus (n=16/N=5)
APP/PS1ΔE9 AAV-Venus (n=15/N=4)
APP/PS1ΔE9 AAV-APPsα (n=18/N=6)
Slope2/Slope1 [%]
Inter-Stimulus-Interval [ms]
f
LM AAV-Venus
APP/PS1ΔE9 AAV-Venus
APP/PS1ΔE9 AAV-APPsα
apical
basal
CA1
CA3
g
No. of spines per µm
CA1 apical
CA1 basal
LM AAV-Venus (n=28/N=6)
APP/PS1ΔE9 AAV-Venus (n=24/N=4)
APP/PS1ΔE9 AAV-APPsα (n=28/N=6)
h
No. of spines per µm
CA3 apical
CA3 basal
LM AAV-Venus (n=24/N=6)
APP/PS1ΔE9 AAV-Venus (n=16/N=4)
APP/PS1ΔE9 AAV-APPsα (n=24/N=6)

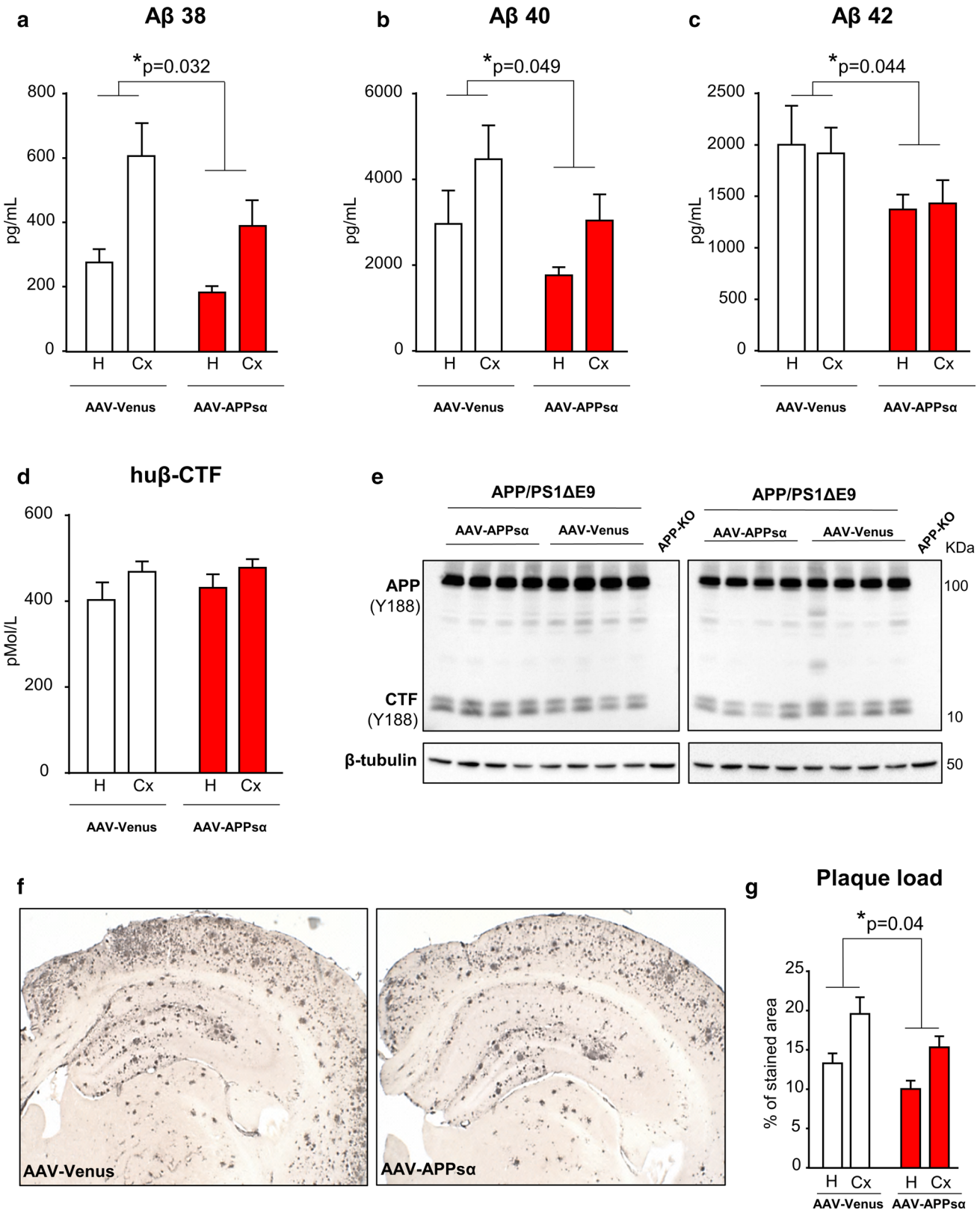
◀**Fig. 3** APP/PS1ΔE9 mice reveal structural and functional synaptic impairments that are ameliorated by APPsα expression. **a**, **b** LTP was induced by TBS at hippocampal CA3-CA1 synapses after 20 min baseline recordings (*arrowhead*). Acute slices of AAV-Venus injected APP/PS1ΔE9 animals (*open circles*) exhibited significant lower induction and maintenance of LTP compared to littermate controls (LM, black circles) showing similar expression of Venus (averaged potentiation minutes t50–80: 148.47 ± 6.04 % vs. 178.01 ± 8.98 %, $p = 0.021$). Viral expression of APPsα (*red circles*) restored potentiation after TBS (171.48 ± 6.29 %) in transgenic animals and resulted in an LTP curve progression comparable to that of LM controls. The LTP induction rate is shown as percentage % of mean baseline slope, n = number of slices, N = number of mice. **c**, **d** Input–Output strength of all AAV-injected mice showed no alterations between genotypes at any fiber volley (FV) amplitude or stimulus intensity tested. **e** Altered PPF at the 10 ms ISI revealed a significant impairment in the pre-synapse of APP/PS1ΔE9 mice injected with AAV-Venus in comparison to LM controls ($^{*}p = 0.030$) that was restored after AAV-APPsα injection ($^{\#}p = 0.047$). **f** Detailed segments of 2nd or 3rd order dendritic branches of apical and basal dendrites of CA1 and CA3 neurons after Golgi–Cox staining, *scale bar* 8 µm. **g** APP/PS1ΔE9 Venus injected mice had significantly less spines at apical ($p = 0.043$) and basal ($p = 0.002$) dendrites in comparison to their littermate controls. APPsα overexpression partially restored the spine density deficit at apical and completely at basal compartments ($p = 0.019$). **h** Reduced spine density at CA3 apical ($p = 0.014$) and basal ($p = 0.011$) dendritic segments of APP/PS1ΔE9 AAV-Venus injected mice that is partially rescued at apical and completely at basal dendrites ($p = 0.039$) by APPsα. N = number of animals, n = number of neurons, Data represent mean ± SEM and were analyzed by one-way ANOVA followed by Bonferroni's post hoc test. Significant differences between littermates and APP/PS1ΔE9 animals injected with AAV-Venus are indicated by *asterisk*; *ash* indicates comparison between APP/PS1ΔE9 animals injected by AAV-Venus or AAV-APPsα

impairment in aged APP/PS1ΔE9 mice despite established plaque deposition.

Impaired synaptic plasticity and reduced spine density of APP/PS1ΔE9 mice are rescued by AAV-APPsα expression

Having established that AAV-APPsα expression restored the spatial memory deficits of APP/PS1ΔE9 mice we evaluated whether these improvements were also reflected at the functional neuronal network level. We analyzed synaptic plasticity which is considered to represent the basis of newly formed declarative memory, 4–5 months after AAV injection at an age of 12–13 months. To this end, we induced long-term potentiation (LTP) at the Schaffer collateral to CA1 pathway by theta-burst stimulation (TBS) after baseline recording (Fig. 3a). Consistent with our previous results in non-injected APP/PS1ΔE9 mice [32], AAV-Venus injected APP/PS1ΔE9 mice exhibited significantly lower induction and maintenance of LTP ($n = 22$ slices), as compared to AAV-Venus injected littermate controls ($n = 22$, Fig. 3a). Non-transgenic control slices showed at the stable phase of LTP (t50–80 min after TBS) a potentiation of 178.01 ± 8.98 %, that was significantly reduced to only 148.47 ± 6.04 % in AAV-Venus injected APP/PS1ΔE9 mice (Fig. 3b; $p = 0.021$, 1-way ANOVA followed by Bonferroni's post hoc test). In contrast, the LTP curve recorded from AAV-APPsα injected APP/PS1ΔE9 slices ($n = 26$) closely overlapped with and was statistically indistinguishable (1-way ANOVA for t50–80, $p > 1$) from that of non-transgenic littermate controls (Fig. 3a). AAV-mediated expression of APPsα largely ameliorated LTP deficits of APP/PS1ΔE9 mice as evidenced by nearly identical average potentiation at t50–80 in AAV-APPsα treated APP/PS1ΔE9 mice (171.48 ± 6.29 %) and littermate controls (178.01 ± 8.98 %) receiving AAV-Venus control virus (Fig. 3b). While basal synaptic transmission was comparable in all groups (Fig. 3c, d), short-term synaptic plasticity evaluated by paired pulse facilitation (PPF, Fig. 3e) was significantly impaired in APP/PS1ΔE9 mice. Transgenic animals injected with AAV-Venus showed an overall lowered response towards the second stimulus in the PPF paradigm, reaching significance at an inter-stimulus interval (ISI) of 10 ms compared to littermate controls ($p = 0.03$; 1-way ANOVA followed by Bonferroni's post hoc test). Strikingly, AAV-APPsα treatment completely rescued presynaptic functionality in APP/PS1ΔE9 animals, as evidenced by PPF values statistically indistinguishable from littermate controls and significantly different from that of AAV-Venus injected transgenic animals [$p(ISI_{20ms}) = 0.047$; Fig. 3e].

Next, we evaluated spine density as a correlate of excitatory synapses in the same set of animals as used for electrophysiology. Previous studies had indicated reduced spine density in various AD mouse models, presumably due to Aβ-mediated toxic effects (reviewed in [73]). Spine density of basal and mid-apical dendritic segments of hippocampal CA1 and CA3 pyramidal cells was assessed using Golgi staining (Fig. 3f). Consistent with the literature, we found an overall reduction in spine density of APP/PS1ΔE9 mice at both dendritic compartments of CA1 and CA3 neurons in comparison to littermate controls similarly injected with AAV-Venus. At CA1 neurons, the effect was even more pronounced in the basal ($p = 0.002$, 1-way ANOVA followed by Bonferroni´s post hoc test) than in the apical ($p = 0.04$) dendritic segment (Fig. 3g). Analysis of CA3 neurons revealed significantly fewer spines in both basal ($p = 0.01$) and apical ($p = 0.014$) dendritic segments when comparing AAV-Venus expressing APP/PS1ΔE9 mice and non-transgenic littermates controls. Importantly, AAV-APPsα overexpression partially restored spine density in apical compartments of CA1 ($n = 28$) and CA3 segments ($n = 24$). A complete rescue of the spine density deficit was achieved in basal dendrites of CA1 ($p = 0.019$, Fig. 3g) and CA3 dendrites ($p = 0.039$, Fig. 3h) of APP/PS1ΔE9 mice. Together, these data indicate that APPsα expression


a
Aβ 38
*p=0.032
pg/mL
800
600
400
200
0
H
Cx
H
Cx
AAV-Venus
AAV-APPsα
b
Aβ 40
*p=0.049
pg/mL
6000
4000
2000
0
H
Cx
H
Cx
AAV-Venus
AAV-APPsα
c
Aβ 42
*p=0.044
pg/mL
2500
2000
1500
1000
500
0
H
Cx
H
Cx
AAV-Venus
AAV-APPsα
d
huβ-CTF
pMol/L
600
400
200
0
H
Cx
H
Cx
AAV-Venus
AAV-APPsα
e
APP/PS1ΔE9
APP/PS1ΔE9
AAV-APPsα
AAV-Venus
APP-KO
AAV-APPsα
AAV-Venus
APP-KO
KDa
APP
(Y188)
CTF
(Y188)
β-tubulin
100
10
50
f
AAV-Venus
AAV-APPsα
g
Plaque load
*p=0.04
% of stained area
25
20
15
10
5
0
H
Cx
H
Cx
AAV-Venus
AAV-APPsα

◀ **Fig. 4** AAV-APPsα injection decreases Aβ and plaques load. **a–c** Quantification (4G8 based MSD immunoassay detecting both mu/huAβ species) of TBS soluble Aβ38 (group effect: $F_{1,14} = 5.110$, $p = 0.032$ (−35 %), Aβ40 [group effect: $F_{1,14} = 4215$, $p = 0.049$ (−36 %)] and Aβ42 (group effect: $F_{1,14} = 4.461$, $p = 0.044$ (−28 %); region effect: Aβ38 $F_{1,14} = 15.22$, $p = 0.0005$, Aβ40 $F_{1,14} = 4.760$, $p = 0.0377$, Aβ40 $F_{1,14} < 1$, ns; group × region interaction effect: $F_{1,14} < 1$, ns) in hippocampus and cortex of APP/PS1ΔE9 mice. Note that AAV-APPsα injected animals show significantly reduced levels of Aβ in both anatomical regions analyzed (hippocampus and cortex). **d** ELISA quantification of huβ-CTF in hippocampus (H) and cortex (Cx) of APP/PS1ΔE9 mice. No difference was detectable between AAV-Venus and AAV-APPsα injected animals. **e** Western blot analysis showing unaltered CTF level in the hippocampus of AAV-APPsα or AAV-Venus injected APP/PS1ΔE9 mice. For quantification CTF signal intensities (C-terminal antibody Y188, see also Fig. S1 for epitope) were normalized to β-tubulin ($p > 0.05$, ns, $n = 8$/group, t test). **f** Representative images of hippocampus and cortex of APP/PS1ΔE9 mice injected either with AAV-Venus or AAV-APPsα. **g** Quantification of 4G8 immunolabeled area in hippocampus and cortex [2-way ANOVA: group effect: $F_{1,13} = 5.50$, $p = 0.04$ (−24 %); region effect: $F_{1,13} = 22.89$, $p = 0.0004$; group × region interaction effect: $F_{1,13} < 1$, ns]. Note that 4G8 immunoreactive plaque area is significantly reduced in AAV-APPsα treated animals. Number of animals $n = 8$/group. Data represent mean ± SEM and were analyzed by 2-way ANOVA (Genotype, group and region as factors) with repeated measures followed by Tukey post hoc test. *$p < 0.05$

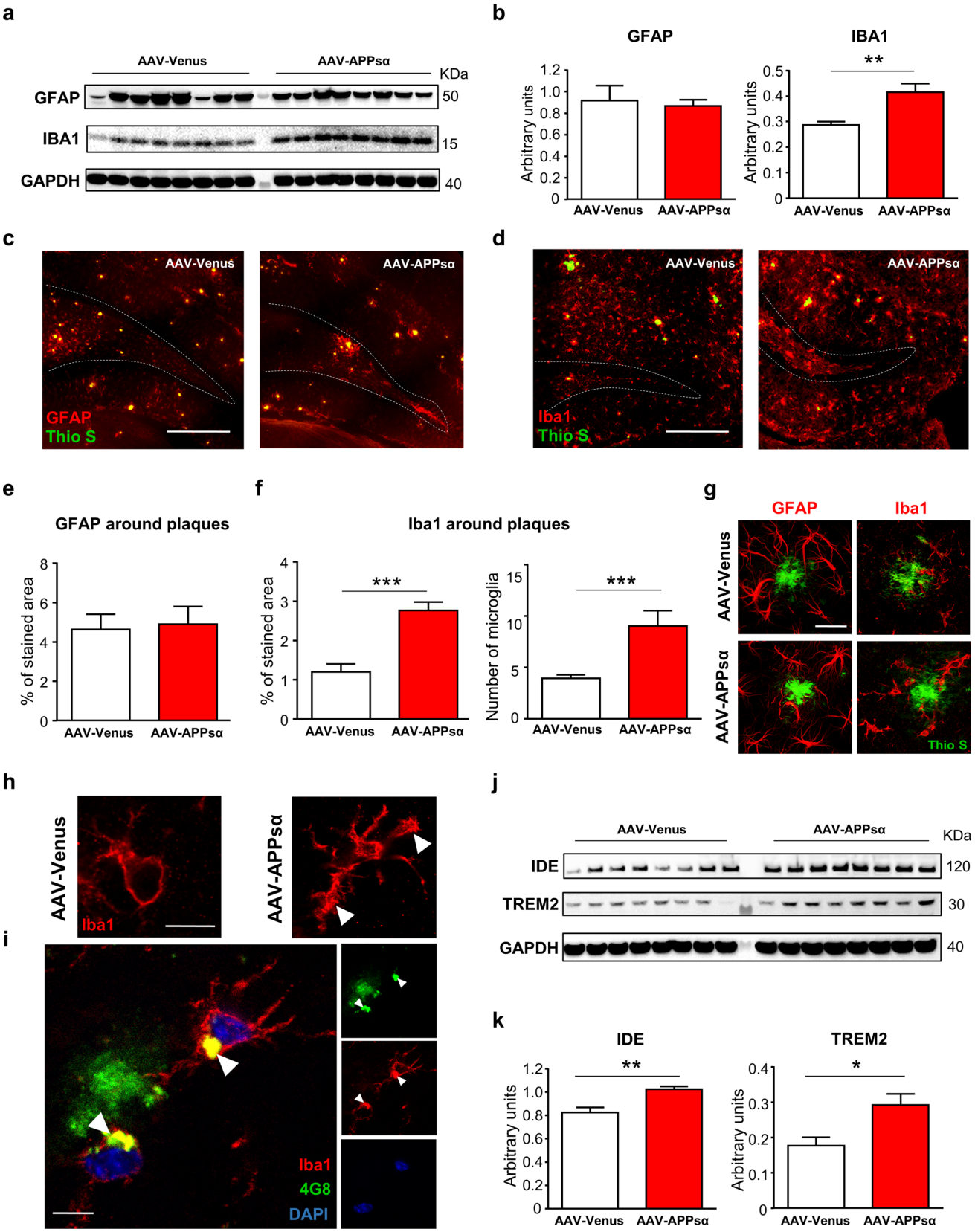
substantially ameliorates both structural and functional synaptic impairments of aged AD model mice.

AAV-APPsα expression decreases Aβ levels and plaque deposition in aged APP/PS1dE9 mice

APPsα had previously been reported to bind to BACE-1 and thereby reduce Aβ production [60]. We therefore evaluated if beneficial effects of AAV-APPsα overexpression on synaptic plasticity and cognitive function were associated with reduced amyloidogenic processing of APP. Employing a sensitive electrochemiluminescence ELISA, we quantified the products of amyloidogenic metabolism Aβ, secreted APPsβ and β-CTF (APP C-terminal fragment produced by β-secretase cleavage) in the cortex (Cx) and hippocampus (H) of 17 months old APP/PS1ΔE9 mice ($n = 8$/group), 5 months after viral vector injection. Using an (4G8 based) ELISA that detects both human and mouse Aβ species, we observed a significant decrease in soluble Aβ40 (reduced by about 36 % vs control, $p = 0.049$, 2-way ANOVA followed by Tukey's post hoc test, Fig. 4b) and, Aβ42 (−28 %, $p = 0.044$, Fig. 4c) in both cortex and hippocampus of APP/PS1ΔE9 mice injected with AAV-APPsα vector, as compared to AAV-Venus control injections (Fig. 4a–c). In addition, we also assessed specifically human Aβ species in transgenic mice employing a (6E10 based) human-specific ELISA (Fig. S2). We found a comparable reduction of huAβ42 (−33 %, $p = 0.04$, Fig. S2c) in both cortex and hippocampus of APP/PS1ΔE9 mice injected with AAV-APPsα vector, as compared to AAV-Venus control injections. Similarly, we found a trend towards decreased amounts of huAβ38 and huAβ40 that did, however, not reach statistical significance (Fig. S2a, b). Consistent with previous data [65] endogenous Aβ levels in non-transgenic littermates were much lower (Fig. S2). Upon AAV-APPsα injection, muAβ40 and muAβ42 were decreased, but not significantly different from Aβ levels of AAV-Venus injected littermate controls (Fig. S2d–f). In contrast to the reduction of Aβ, the amount of secreted transgene derived huAPPsβ-$_{SWE}$ that was assessed by ELISA was not significantly different in APP/PS1ΔE9 mice injected with AAV-APPsα vector, as compared to control injected mice (Fig. S2g). Similarly, we found no significant alterations in human β-CTF levels measured by ELISA (Fig. 4d) or CTFs measured by Western blot analysis (Fig. 4e) in APP/PS1ΔE9 mice injected with AAV-APPsα or control vector. To assess the impact of APPsα overexpression on amyloid deposition, we used 4G8 immunostaining to quantify the area covered by plaques both in the hippocampus and cortex of 17-month-old APP/PS1ΔE9 mice injected with viral vectors (Fig. 4f, g). Interestingly, AAV-APPsα injection ($n = 8$) resulted in a significantly reduced plaque area both in cortex and hippocampus as compared to AAV-Venus injected controls ($p = 0.04$, 2-way ANOVA followed by Tukey's post hoc test, Fig. 4g). Together, these results indicate that AAV-mediated APPsα overexpression moderately reduces both Aβ generation and amyloid plaque load in APP/PS1ΔE9 mice not only in the AAV-injected hippocampus but also in distant cortical areas.

AAV-APPsα induces microglia recruitment and activation in the vicinity of amyloid plaques

Accumulation of amyloid plaques in APP/PS1ΔE9 mice has previously been shown to be accompanied by microgliosis and astrocytosis notably at advanced stages of plaque pathology [41, 62]. Here, we evaluated the expression of GFAP (as an astrocyte-specific marker) and Iba1 (as a microglial marker) by Western blot analysis (Fig. 5a, b) and IHC (Fig. 5c–h) in the hippocampus of 17-month-old APP/PS1ΔE9 mice treated either with AAV-APPsα or control vector. While no significant difference was detectable for the astroglial marker GFAP, AAV-APPsα treatment lead to a significant increase in Iba1 expression (about +44 %; t test, $p = 0.003$; Fig. 5a, b), as compared to AAV-Venus control injections. Staining of brain sections further confirmed these data (Fig. 5c, d) at the cellular level. We went on and quantified GFAP and Iba1 immunoreactivity around amyloid plaques in the hippocampus. Consistent with Western blot analysis, GFAP immunoreactivity was not affected by AAV-APPsα injection (Fig. 5c, e). In contrast, the reduction of amyloid deposits observed after injection


a
AAV-Venus
AAV-APPsα
KDa
GFAP
IBA1
GAPDH
50
15
40
b
GFAP
IBA1
Arbitrary units
AAV-Venus
AAV-APPsα
**
c
GFAP
Thio S
d
Iba1
Thio S
e
GFAP around plaques
% of stained area
f
Iba1 around plaques
***
Number of microglia
g
GFAP
Iba1
Thio S
h
Iba1
i
4G8
DAPI
j
IDE
TREM2
120
30
k
*

◀**Fig. 5** AAV-APPsα promotes microglia recruitment around plaques in APP/PS1ΔE9 mice. **a**, **b** Western blot analysis showing the expression of GFAP and Iba1 in the hippocampus of AAV-Venus or AAV-APPsα injected APP/PS1ΔE9 mice ($n = 8$/group). **b** For quantification signal intensities were normalized to GAPDH used as a loading control. AAV-APPsα treatment specifically increased Iba1 (microglial marker) expression (*t* test: $t_{14} = 3.586$; $p = 0.003$), whereas the astrocyte marker GFAP was not affected. **c**, **d** Co-staining of amyloid plaques (Thioflavin S, *green*) and GFAP (**c**, *red*) or Iba1 (**d**, *red*) in hippocampus (DG subfield) of APP/PS1ΔE9 transgenic mice. *Dotted line* indicates the granular layer of the DG. *Scale bar*, 500 µm. **e**, **f** Whereas the distribution of GFAP positive astrocytes is unaltered, increased recruitment of Iba1 positive microglia is observed in the vicinity of amyloid plaques. **f** Significant increase was found for the Iba1 stained area (*t* test, $p < 0.0001$) and the number of Iba1 + microglia (*t* test, $p < 0.0002$) in the vicinity of plaques. **g** Higher magnification of co-staining depicting amyloid plaques (Thioflavin S, *green*) and astrocytes (GFAP, *red*) or microglia (Iba1, *red*). *Scale bar*, 20 µm. **h** Morphology of microglia in the hippocampus of AAV-injected APP/PS1ΔE9 mice. Increased ramified profile is observed in microglia of AAV-APPsα injected mice (*right*, indicated by *arrow heads*). *Scale bar*, 10 µm. **i** Co-immunostaining of Iba1 (*red*) and 4G8 (β amyloid, *green*) in AAV-APPsα injected APP/PS1ΔE9 mice indicating the uptake of Aβ (*arrow heads*) in plaque-associated microglia. *Scale bar*, 10 µm. **j**, **k** Western blot analysis showing the expression of IDE and TREM2 in the hippocampus of AAV-Venus or AAV-APPsα injected APP/PS1ΔE9 mice. Both Aβ clearance related proteins are significantly upregulated (IDE: *t* test, $p = 0.0014$; TREM2: *t* test, $p = 0.010$) following AAV-APPsα treatment. Values represent mean ± SEM. ***$p < 0.001$, **$p < 0.01$, *$p < 0.05$

of the AAV-APPsα vector in APP/PS1ΔE9 mice was paralleled by a 2.3-fold increase in Iba1 immunoreactivity and a similar increase in the number of microglia in the vicinity of plaques (Fig. 5d, f, g). Moreover, we observed an altered morphology of microglia in AAV-APPsα treated mice characterized by increased ramifications in AAV-APPsα versus control vector injected APP/PS1ΔE9 mice (Fig. 5g, h). Previously, it had been reported that AAV-mediated delivery of Aβ42 or β-CTF to the hippocampus lead to significant leakiness of the blood–brain barrier (BBB) [24], as evidenced by increased mouse IgG immunoreactivity. We therefore incubated sections of AAV-APPsα or AAV-Venus injected transgenic APP/PS1ΔE9 mice with DAPI to stain for nuclei or NeuN (to reveal neuronal cell bodies) and in addition with secondary anti-mouse IgG antibody. Overall, only very few stained cells were detectable and there was no increase in sections of AAV-APPsα injected mice (Fig. S3) indicating that AAV-APPsα injection did not result in a major BBB breakdown. We therefore conclude that microglia activation in the vicinity of plaques is not secondary to AAV-APPsα induced BBB leakiness.

Microglia contribute to Aβ clearance and are thought to play a protective role at least during early stages of AD [62], while they may acquire a senescence-like stage during disease progression [62]. Indeed, plaque-associated microglia (from both AAV-APPsα and AAV-Venus treated mice) were also engaged in Aβ uptake as evidenced by Iba1/4G8 double staining (Figs. 5i, S4). Recently, genetic variants of TREM2 (Triggering Receptor Expressed on Myeloid cells) have been associated with an increased risk for AD [31, 40]. Although the precise role of TREM2 for AD pathogenesis and Aβ pathology is still controversial [39, 82] TREM2 expression has been consistently detected in plaque-associated Iba1$^+$ cells in AD model mice [26, 39]. Consistent with an increase in plaque-associated microglia, we detected a significant increase of TREM2 expression (about 60 % vs control, *t* test, $p < 0.01$) by Western blot analysis in hippocampi of APP/PS1ΔE9 mice injected with AAV-APPsα versus controls (Fig. 5j, k, $n = 8$ per group). We also determined the expression of neprilysin (NEP) and insulin-degrading enzyme (IDE) that are proteases produced by microglia that contribute to Aβ clearance [56]. Expression of NEP was identical in APP/PS1ΔE9 mice injected with AAV-APPsα versus control (not shown). However, a significant increase (of about +20 %, *t* test, $p < 0.0014$) in IDE expression was observed after AAV-HA-APPsα vector injection (Fig. 5j, k). Together, these data suggest that AAV-mediated APPsα expression induces microglia recruitment, activation and possibly also phagocytic function which may lead to enhanced Aβ and plaque clearance.

Discussion

Despite a recent shift of research efforts towards preventive strategies, there is still an urgent lack of an effective treatment of patients with clinically established AD. So far, many therapeutic approaches targeted the secretases processing APP. However, since all secretases act on many different substrates besides APP [63, 80], these strategies have major drawbacks for clinical application. γ-secretase is physiologically essential and current clinical trials to develop γ-secretase inhibitors have been abrogated due to serious side effects, likely resulting from impaired Notch signaling [23]. Also systemic upregulation of the major α-secretase ADAM10 to boost APPsα production is problematic, as this may enhance cleavage of substrates implicated in tumorigenesis (reviewed by [59, 63]). Thus, direct overexpression of APPsα in the brain may be more promising than pharmacological upregulation of α-secretase.

Here, we explored a gene therapy approach and used AAV-based gene transfer to overexpress APPsα in the brain of transgenic APP/PS1ΔE9 mice, that have been widely used in experimental studies assessing the efficacy of AD therapies. Bigenic APP_{SWE}/PS1ΔE9 mice express a chimeric mouse/human APP (with Swedish double mutation) and a mutant human PS1 gene (PS1ΔE9) both associated with familial forms of AD. They produce high amounts of huAβ leading to amyloid deposition starting at 5–6 months

and pronounced progression of plaque pathology with age [68] that is associated with impairments in cognitive behavior [68]. Using bilateral injection of AAV-APPsα vector particles, we achieved highly efficient and widespread expression of APPsα throughout the whole hippocampus and also in adjacent cortical areas. We attribute this on one hand to the well-established spreading/diffusion of small AAV particles, particularly along the injection needle track [16] and on the other hand to the secretion of APPsα that may diffuse in the brain parenchyma. In this study, a single bilateral injection of AAV-APPsα particles was sufficient to mediate long-lasting APPsα expression over 5 months that was well tolerated without apparent adverse effects. This was a crucial prerequisite to study potential therapeutic efficacy of AAV-APPsα overexpression. To this end, we used aged (12-month-old) APP/PS1ΔE9 mice with preexisting amyloidosis to mimic the situation in AD patients that are usually clinically diagnosed many years after the onset of pathology [81].

Taken together, we demonstrate that in aged APP/PS1ΔE9 AD model mice AAV-APPsα could rescue or ameliorate key aspects of AD pathology: (1) defective synaptic plasticity (LTP and PPF), (2) reduced synaptic density and most importantly (3) impaired spatial reference memory.

There is a strong correlation between synapse loss and cognitive decline in AD and synaptic dysfunction is thought to underlay early stages of the disease [69, 77]. The ability of synapses to undergo long-term potentiation and thus increase their synaptic strength is considered as a cellular mechanism underlying learning and memory. Indeed, defects in LTP have not only been reported in several AD mouse models with Aβ overexpression (see, e.g., review by [73]) but also upon application of synthetic or native Aβ oligomers from AD patients to hippocampal slices (e.g. [70, 71]). Interestingly, we observed that deficits of 12- to 13-month-old APP/PS1ΔE9 mice in the induction and maintenance phase of LTP were largely rescued upon AAV-APPsα overexpression despite the presence of high amounts of soluble Aβ and extensive Aβ deposition (see Fig. 4, see also Fig. 3 regarding LTP) at this age. Given that AAV-APPsα did not affect basal synaptic transmission, but completely rescued the defects in paired pulse facilitation of APP/PS1ΔE9 mice this suggests that restoration of presynaptic function may contribute to the LTP rescue. In this regard, it is noteworthy that APP has been localized to synaptic sites, including the presynaptic active zone [45, 86]. Our present findings are perfectly in line and further extend the previously demonstrated physiological role of APP and APPsα in synaptic plasticity. Consistent with a presynaptic role of APP, we previously found a reduction in quantal content and readily releasable pool at neuromuscular synapses of APP/APLP2 mutant mice [84]. In the CNS, APP-KO mice showed altered GABAergic short-term plasticity and disturbed Ca^{2+}-homeostasis [88]. In addition, APPsα knockin mice that lack transmembrane APP and express solely secreted APPsα completely rescued the LTP impairment of APP-KO mice [65].

Previously, indirect evidence suggested that APPsα may have synaptotrophic properties not only under physiological, but also under pathological conditions. Studies involving transgenic mice with moderate overexpression of human WT APP [57], or indirect upregulation of APPsα by transgenic expression of the α-secretase ADAM10 [9], that is enriched at synaptic contacts [52], all led to increased synaptic density. In Tg2576 mice expression of mutant huAPP decreased spine density in aged animals, whereas an increase in spine density was observed in young mice prior to plaque deposition pointing towards a possibly trophic effect of APPsα [46]. Here, we now directly demonstrate that in addition to its beneficial effects on synaptic plasticity, AAV-APPsα overexpression ameliorates spine density defects associated with Aβ accumulation in aged APP/PS1ΔE9 mice, and restores normal spine density in basal dendritic segments of CA1 and CA3 neurons. Most importantly, increases in spine counts and restored synaptic plasticity were also reflected in significantly improved behavior. Although, we detected no positive effects during the acquisition phase of Morris water maze (MWM) spatial navigation AAV-APPsα treatment completely rescued the impaired probe trial performance of transgenic mice as evidenced by a significant increase in the time spent in the target quadrant that was statistically indistinguishable from AAV-Venus injected littermate controls. Moreover, AAV-APPsα injected transgenic mice showed clear directionality towards the trained platform. Together, this further supports the notion that AVV-APPsα expression improved the cognitive performance of mice and restored spatial reference memory in APP/PS1ΔE9 mice. A similar phenotype with no difference in MWM acquisition, but significant difference in probe trial performance has previously been reported for several other AD mouse models, including homozygous 3 × TG mice (APP_{SWE} × P301L × PS1M146 V) that developed early cognitive deficits in probe trial performance while MWM acquisition learning was unaffected [11]. Also, TauP301L overexpressing mice tested at 6 months of age showed impaired probe trail performance while both MWM acquisition learning and reversal learning were normal, consistent with normal working memory, as assessed by the Y-maze [61]. In addition, our results are also in agreement with findings in rats with experimentally induced lesion of the hippocampal CA3 subfield that resulted in deficits in memory retrieval [67]. Of note, the CA3 area is not only affected by plaque deposition in our APP/PS1ΔE9 mice but this was also associated with deficits in spine density which might thus lead to compromised properties of the

hippocampal network. Together, it is possible that spatial working memory is conserved longer than spatial reference memory. Of note, we also observed reduced escape latency during acquisition learning in wild-type controls injected with AAV-APPsα. These data suggest that APPsα could not only play a role in behaviorally impaired AD model mice, but might also enhance learning in normal WT mice. Future studies with larger cohorts of mice are needed to further substantiate these findings.

Although the precise role of APPsα at the synapse is still unknown, there is a large body of evidence that APPsα affects several pathways that likely contribute to its beneficial effects in APP/PS1ΔE9 mice. In vitro studies using WT rats showed that exogenous APPsα application can shift the frequency dependence of LTD and enhance LTP [37]. Moreover, intra-hippocampal infusion of recombinant APPsα (rec APPsα) increased in vivo LTP recorded at the dentate gyrus of adult rats [76] and infusion of APPsα or peptides derived from it enhances memory in mice, chicks and rats [14, 53, 54, 66]. Mechanistically, the effects on LTP may involve modulation of NMDA receptor function as recAPPsα was shown to facilitate tetanically evoked NMDA receptor-mediated currents in vitro [76]. Immunoprecipitation studies indicated that transmembrane APP interacts with GluN1/GluN2 NMDARs and enhances their cell surface expression in vitro [20, 21], but it is presently unclear whether this also holds true for extracellular APPsα. Moreover, recAPPsα has been shown to increase synaptodendritic de novo protein synthesis, an important mechanism for normal plasticity [17].

Although in this study we did not investigate neuronal death, it is noteworthy that in vitro studies had implicated APPsα in neuroprotective signaling relevant to AD pathogenesis, including protection against excitotoxic stress resulting from glutamate receptor overactivation [28] and notably also Aβ induced toxicity [27, 29, 30]. Intriguingly, a recent study identified cell surface holo-APP as the receptor that binds APPsα and confers neuroprotection via G protein-coupled activation of the Akt stress signaling pathway [55]. While these data established holo-APP as a receptor mediating prosurvial/antiapoptotic signaling, it is also clear, however, that the very rapid effects of APP on synaptic plasticity must be mediated by a receptor distinct from APP. In this respect, we recently showed that the LTP impairments of conditional DKO mice, lacking both APP and APLP2 can be rescued by a brief (30 min) pre-incubation with nanomolar amounts of APPsα [33].

In addition to beneficial effects on synaptic morphology and function, we also detected significantly reduced levels of soluble Aβ species and a significant (about 25 %) decrease in plaque load upon AAV-APPsα treatment that may contribute to the rescue of synaptic failure. Our results of reduced Aβ levels following AAV-APPsα treatment are further supported by a recent study indicating that APPsα may bind to BACE-1 and thereby reduce Aβ production [60]. In that study, classical germline APPsα transgenic (TgAPPsα) mice were generated and APP processing was investigated after crossing to APP/PS1ΔE9 mice [60]. Whereas TgAPPsα/APP/PS1ΔE9 mice revealed a reduction in both huAβ and in huβ-CTFs (consistent with BACE inhibition), we were unable to detect besides reduced Aβ levels significant alterations of other proteolytic fragments of the amyloidogenic pathway such as huAPPsβ-$_{SWE}$ and β-CTFs. These apparent differences might be related to the more variable AAV-mediated APPsα overexpression (see Fig. 1) and the fact that in TgAPPsα mice, APPsα was expressed from early development onwards (as opposed to expression in aged mice in this study). In addition, Obregon et al. assessed APP processing much earlier (at 8 months of age), when huAβ build up is considerably lower [60]. Importantly, and in contrast to our study, the functional consequences of APPsα overexpression on neuronal morphology, synaptic function and behavior had, however, not been assessed in that study [60]. In addition, we now provide evidence suggesting that AAV-APPsα may also improve pathology in a mechanism unrelated to BACE inhibition. While previous co-culture studies of neurons with microglial cell lines or primary microglia indicated that secreted APPsβ and APPsα can activate microglia and may thus indirectly affect neuronal metabolism and survival in vitro (e.g., [6, 8, 12]), the consequences of selective APPsα expression in vivo have not been studied so far. Here, we observed that AAV-APPsα treatment lead to the recruitment of microglia with ramified morphology, believed to indicate an activated state [62] towards plaques. This was paralleled by an increase in TREM2 expression. TREM2 receptor was recently shown to sustain the microglial response to Aβ and suggested to function as a sensor for anionic lipids exposed during Aβ deposition and on damaged neurons [82]. In addition, we demonstrate an upregulation of the proteolytic enzyme IDE that is produced by microglia and was previously shown to enhance Aβ and plaques clearance [32, 47]. Together, our data strongly suggest that APPsα-mediated activation and recruitment of microglia may contribute to the ameliorated Aβ pathology in APP/PS1ΔE9 mice.

AD pathogenesis is complex, still incompletely understood and multiple factors contribute to pathogenesis. Therefore, the concept of synaptic repair has recently been put forward, e.g., to tackle/ameliorate pathophysiology and improve clinical outcome as an alternative to eliminating toxic factors [51]. Notably, due to the highly plastic nature of synapses, synaptic dysfunction and synapse loss are reversible processes. Here, we provide several converging lines of evidence that viral vector-mediated APPsα expression rescues synaptic failure in AD model mice with established Aβ deposition, indicating its potential as a novel

therapeutic strategy even in the presence of pathogenic factors.

Acknowledgments This work was supported by the Deutsche Forschungsgemeinschaft Grants (MU 1457/9-1, 9-2 to UCM; KO 1674/3-1, 3-2 to MK), the ERA-Net Neuron (01EW1305A to CJB, NC and UCM), and the LOEWE Center for Cell and Gene Therapy Frankfurt funded by Hessisches Ministerium für Wissenschaft und Kunst (III L 4- 518/17.004 (2010)) to CJB.

Compliance with ethical standards

Conflict of interest The authors declare no conflict of interest.

References

1. Abramov E, Dolev I, Fogel H, Ciccotosto GD, Ruff E, Slutsky I (2009) Amyloid-beta as a positive endogenous regulator of release probability at hippocampal synapses. Nat Neurosci 12:1567–1576. doi:10.1038/nn.2433
2. Ahmed RR, Holler CJ, Webb RL, Li F, Beckett TL, Murphy MP (2010) BACE1 and BACE2 enzymatic activities in Alzheimer's disease. J Neurochem 112:1045–1053. doi:10.1111/j.1471-4159.2009.06528.x
3. Almkvist O, Basun H, Wagner SL, Rowe BA, Wahlund LO, Lannfelt L (1997) Cerebrospinal fluid levels of alpha-secretase-cleaved soluble amyloid precursor protein mirror cognition in a Swedish family with Alzheimer disease and a gene mutation. Arch Neurol 54:641–644
4. Anderson JJ, Holtz G, Baskin PP et al (1999) Reduced cerebrospinal fluid levels of alpha-secretase-cleaved amyloid precursor protein in aged rats: correlation with spatial memory deficits. Neuroscience 93:1409–1420 **(pii: S0306-4522(99)00244-4)**
5. Aurnhammer C, Haase M, Muether N et al (2012) Universal real-time PCR for the detection and quantification of adeno-associated virus serotype 2-derived inverted terminal repeat sequences. Human Gene Therapy Methods 23:18–28. doi:10.1089/hgtb.2011.034
6. Austin SA, Combs CK (2008) Mechanisms of microglial activation by amyloid precursor protein and its proteolytic fragments. In: Lane TE, Carson M, Bergmann C, Wyss-Coray T (eds) Central nervous system diseases and inflammation. Springer US, New York, pp 13–32
7. Aydin D, Weyer SW, Muller UC (2012) Functions of the APP gene family in the nervous system: insights from mouse models. Exp Brain Res 217:423–434. doi:10.1007/s00221-011-2861-2
8. Barger SW, Harmon AD (1997) Microglial activation by Alzheimer amyloid precursor protein and modulation by apolipoprotein E. Nature 388:878–881. doi:10.1038/42257
9. Bell KF, Zheng L, Fahrenholz F, Cuello AC (2008) ADAM-10 over-expression increases cortical synaptogenesis. Neurobiol Aging 29:554–565. doi:10.1016/j.neurobiolaging.2006.11.004
10. Berger A, Lorain S, Josephine C et al (2015) Repair of rhodopsin mRNA by spliceosome-mediated RNA trans-splicing: a new approach for autosomal dominant retinitis pigmentosa. Mol Ther. doi:10.1038/mt.2015.11
11. Billings LM, Oddo S, Green KN, McGaugh JL, LaFerla FM (2005) Intraneuronal Abeta causes the onset of early Alzheimer's disease-related cognitive deficits in transgenic mice. Neuron 45:675–688. doi:10.1016/j.neuron.2005.01.040
12. Bodles AM, Barger SW (2005) Secreted beta-amyloid precursor protein activates microglia via JNK and p38-MAPK. Neurobiol Aging 26:9–16. doi:10.1016/j.neurobiolaging.2004.02.022
13. Borchelt DR, Ratovitski T, van Lare J et al (1997) Accelerated amyloid deposition in the brains of transgenic mice coexpressing mutant presenilin 1 and amyloid precursor proteins. Neuron 19:939–945
14. Bour A, Little S, Dodart JC, Kelche C, Mathis C (2004) A secreted form of the beta-amyloid precursor protein (sAPP695) improves spatial recognition memory in OF1 mice. Neurobiol Learn Mem 81:27–38 **(pii: S1074742703000716)**
15. Caille I, Allinquant B, Dupont E et al (2004) Soluble form of amyloid precursor protein regulates proliferation of progenitors in the adult subventricular zone. Development 131:2173–2181
16. Casanova F, Carney PR, Sarntinoranont M (2014) Effect of needle insertion speed on tissue injury, stress, and backflow distribution for convection-enhanced delivery in the rat brain. PLoS One 9:e94919. doi:10.1371/journal.pone.0094919
17. Claasen AM, Guevremont D, Mason-Parker SE et al (2009) Secreted amyloid precursor protein-alpha upregulates synaptic protein synthesis by a protein kinase G-dependent mechanism. Neurosci Lett 460:92–96. doi:10.1016/j.neulet.2009.05.040
18. Copanaki E, Chang S, Vlachos A et al (2010) sAPPalpha antagonizes dendritic degeneration and neuron death triggered by proteasomal stress. Mol Cell Neurosci 44:386–393. doi:10.1016/j.mcn.2010.04.007
19. Corrigan F, Vink R, Blumbergs PC, Masters CL, Cappai R, van den Heuvel C (2012) sAPPalpha rescues deficits in amyloid precursor protein knockout mice following focal traumatic brain injury. J Neurochem 122:208–220. doi:10.1111/j.1471-4159.2012.07761.x
20. Cousins SL, Hoey SE, Anne Stephenson F, Perkinton MS (2009) Amyloid precursor protein 695 associates with assembled NR2A- and NR2B-containing NMDA receptors to result in the enhancement of their cell surface delivery. J Neurochem 111:1501–1513. doi:10.1111/j.1471-4159.2009.06424.x
21. Cousins SL, Innocent N, Stephenson FA (2013) Neto1 associates with the NMDA receptor/amyloid precursor protein complex. J Neurochem 126:554–564. doi:10.1111/jnc.12280
22. Dobrowolska JA, Kasten T, Huang Y et al (2014) Diurnal patterns of soluble amyloid precursor protein metabolites in the human central nervous system. PLoS One 9:e89998. doi:10.1371/journal.pone.0089998
23. Doody RS, Raman R, Farlow M et al (2013) A phase 3 trial of semagacestat for treatment of Alzheimer's disease. N Engl J Med 369:341–350. doi:10.1056/NEJMoa1210951
24. Drummond ES, Muhling J, Martins RN, Wijaya LK, Ehlert EM, Harvey AR (2013) Pathology associated with AAV mediated expression of beta amyloid or C100 in adult mouse hippocampus and cerebellum. PLoS One 8:e59166. doi:10.1371/journal.pone.0059166
25. Endres K, Fahrenholz F (2012) Regulation of alpha-secretase ADAM10 expression and activity. Exp Brain Res 217:343–352. doi:10.1007/s00221-011-2885-7
26. Frank S, Burbach GJ, Bonin M et al (2008) TREM2 is upregulated in amyloid plaque-associated microglia in aged APP23 transgenic mice. Glia 56:1438–1447. doi:10.1002/glia.20710
27. Furukawa K, Barger SW, Blalock EM, Mattson MP (1996) Activation of K + channels and suppression of neuronal activity by secreted beta-amyloid-precursor protein. Nature 379:74–78. doi:10.1038/379074a0
28. Furukawa K, Mattson MP (1998) Secreted amyloid precursor protein alpha selectively suppresses *N*-methyl-D-aspartate currents in hippocampal neurons: involvement of cyclic GMP. Neuroscience 83:429–438 **(pii: S0306452297003989)**
29. Furukawa K, Sopher BL, Rydel RE et al (1996) Increased activity-regulating and neuroprotective efficacy of alpha-secretase-derived secreted amyloid precursor protein conferred by a C-terminal heparin-binding domain. J Neurochem 67:1882–1896

30. Goodman Y, Mattson MP (1994) Secreted forms of beta-amyloid precursor protein protect hippocampal neurons against amyloid beta-peptide-induced oxidative injury. Exp Neurol 128:1–12. doi:10.1006/exnr.1994.1107
31. Guerreiro R, Wojtas A, Bras J et al (2013) TREM2 variants in Alzheimer's disease. N Engl J Med 368:117–127. doi:10.1056/NEJMoa1211851
32. Heneka MT, Kummer MP, Stutz A et al (2013) NLRP3 is activated in Alzheimer's disease and contributes to pathology in APP/PS1 mice. Nature 493:674–678. doi:10.1038/nature11729
33. Hick M, Herrmann U, Weyer SW et al (2015) Acute function of secreted amyloid precursor protein fragment APPsalpha in synaptic plasticity. Acta Neuropathol 129:21–37. doi:10.1007/s00401-014-1368-x
34. Hoe HS, Lee HK, Pak DT (2012) The upside of APP at synapses. CNS Neurosci Ther 18:47–56. doi:10.1111/j.1755-5949.2010.00221.x
35. Hoey SE, Williams RJ, Perkinton MS (2009) Synaptic NMDA receptor activation stimulates alpha-secretase amyloid precursor protein processing and inhibits amyloid-beta production. J Neurosci 29:4442–4460. doi:10.1523/JNEUROSCI.6017-08.2009
36. Holsinger RM, McLean CA, Beyreuther K, Masters CL, Evin G (2002) Increased expression of the amyloid precursor beta-secretase in Alzheimer's disease. Ann Neurol 51:783–786. doi:10.1002/ana.10208
37. Ishida A, Furukawa K, Keller JN, Mattson MP (1997) Secreted form of beta-amyloid precursor protein shifts the frequency dependency for induction of LTD, and enhances LTP in hippocampal slices. NeuroReport 8:2133–2137
38. Jankowsky JL, Fadale DJ, Anderson J et al (2004) Mutant presenilins specifically elevate the levels of the 42 residue beta-amyloid peptide in vivo: evidence for augmentation of a 42-specific gamma secretase. Hum Mol Genet 13:159–170. doi:10.1093/hmg/ddh019
39. Jay TR, Miller CM, Cheng PJ et al (2015) TREM2 deficiency eliminates TREM2+ inflammatory macrophages and ameliorates pathology in Alzheimer's disease mouse models. J Exp Med 212:287–295. doi:10.1084/jem.20142322
40. Jonsson T, Stefansson H, Steinberg S et al (2013) Variant of TREM2 associated with the risk of Alzheimer's disease. N Engl J Med 368:107–116. doi:10.1056/NEJMoa1211103
41. Kamphuis W, Mamber C, Moeton M et al (2012) GFAP isoforms in adult mouse brain with a focus on neurogenic astrocytes and reactive astrogliosis in mouse models of Alzheimer disease. PLoS One 7:e42823. doi:10.1371/journal.pone.0042823
42. Klevanski M, Saar M, Baumkotter F, Weyer SW, Kins S, Muller UC (2014) Differential role of APP and APLPs for neuromuscular synaptic morphology and function. Mol Cell Neurosci 61C:201–210. doi:10.1016/j.mcn.2014.06.004
43. Kogel D, Deller T, Behl C (2012) Roles of amyloid precursor protein family members in neuroprotection, stress signaling and aging. Exp Brain Res 217:471–479. doi:10.1007/s00221-011-2932-4
44. Lannfelt L, Basun H, Wahlund LO, Rowe BA, Wagner SL (1995) Decreased alpha-secretase-cleaved amyloid precursor protein as a diagnostic marker for Alzheimer's disease. Nat Med 1:829–832
45. Lassek M, Weingarten J, Einsfelder U, Brendel P, Muller U, Volknandt W (2013) Amyloid precursor proteins are constituents of the presynaptic active zone. J Neurochem 127:48–56. doi:10.1111/jnc.12358
46. Lee KJ, Moussa CE, Lee Y et al (2010) Beta amyloid-independent role of amyloid precursor protein in generation and maintenance of dendritic spines. Neuroscience 169:344–356. doi:10.1016/j.neuroscience.2010.04.078
47. Leissring MA, Farris W, Chang AY et al (2003) Enhanced proteolysis of beta-amyloid in APP transgenic mice prevents plaque formation, secondary pathology, and premature death. Neuron 40:1087–1093
48. Leyssen M, Ayaz D, Hebert SS, Reeve S, De Strooper B, Hassan BA (2005) Amyloid precursor protein promotes post-developmental neurite arborization in the Drosophila brain. EMBO J 24:2944–2955. doi:10.1038/sj.emboj.7600757
49. Li ZW, Stark G, Gotz J et al (1996) Generation of mice with a 200-kb amyloid precursor protein gene deletion by Cre recombinase-mediated site-specific recombination in embryonic stem cells. Proc Natl Acad Sci USA 93:6158–6162
50. Lichtenthaler SF, Haass C, Steiner H (2011) Regulated intramembrane proteolysis–lessons from amyloid precursor protein processing. J Neurochem 117:779–796. doi:10.1111/j.1471-4159.2011.07248.x
51. Lu B, Nagappan G, Guan X, Nathan PJ, Wren P (2013) BDNF-based synaptic repair as a disease-modifying strategy for neurodegenerative diseases. Nat Rev Neurosci 14:401–416. doi:10.1038/nrn3505
52. Marcello E, Gardoni F, Mauceri D et al (2007) Synapse-associated protein-97 mediates alpha-secretase ADAM10 trafficking and promotes its activity. J Neurosci 27:1682–1691. doi:10.1523/JNEUROSCI.3439-06.2007
53. Meziane H, Dodart JC, Mathis C et al (1998) Memory-enhancing effects of secreted forms of the beta-amyloid precursor protein in normal and amnestic mice. Proc Natl Acad Sci USA 95:12683–12688
54. Mileusnic R, Lancashire CL, Rose SP (2004) The peptide sequence Arg-Glu-Arg, present in the amyloid precursor protein, protects against memory loss caused by A beta and acts as a cognitive enhancer. Eur J Neurosci 19:1933–1938. doi:10.1111/j.1460-9568.2004.03276.x
55. Milosch N, Tanriover G, Kundu A et al (2014) Holo-APP and G-protein-mediated signaling are required for sAPPalpha-induced activation of the Akt survival pathway. Cell Death Dis 5:e1391. doi:10.1038/cddis.2014.352
56. Miners JS, Barua N, Kehoe PG, Gill S, Love S (2011) Abeta-degrading enzymes: potential for treatment of Alzheimer disease. J Neuropathol Exp Neurol 70:944–959. doi:10.1097/NEN.0b013e3182345e46
57. Mucke L, Abraham CR, Masliah E (1996) Neurotrophic and neuroprotective effects of hAPP in transgenic mice. Ann N Y Acad Sci 777:82–88
58. Murakami N, Yamaki T, Iwamoto Y et al (1998) Experimental brain injury induces expression of amyloid precursor protein, which may be related to neuronal loss in the hippocampus. J Neurotrauma 15:993–1003
59. Nhan HS, Chiang K, Koo EH (2015) The multifaceted nature of amyloid precursor protein and its proteolytic fragments: friends and foes. Acta Neuropathol 129:1–19. doi:10.1007/s00401-014-1347-2
60. Obregon D, Hou H, Deng J et al (2012) Soluble amyloid precursor protein-alpha modulates beta-secretase activity and amyloid-beta generation. Nat Commun 3:777. doi:10.1038/ncomms1781ncomms1781
61. Pennanen L, Wolfer DP, Nitsch RM, Gotz J (2006) Impaired spatial reference memory and increased exploratory behavior in P301L tau transgenic mice. Genes Brain Behav 5:369–379. doi:10.1111/j.1601-183X.2005.00165.x
62. Prokop S, Miller KR, Heppner FL (2013) Microglia actions in Alzheimer's disease. Acta Neuropathol 126:461–477
63. Prox J, Rittger A, Saftig P (2012) Physiological functions of the amyloid precursor protein secretases ADAM10, BACE1, and Presenilin. Exp Brain Res 217:331–341. doi:10.1007/s00221-011-2952-0
64. Ramirez MJ, Heslop KE, Francis PT, Rattray M (2001) Expression of amyloid precursor protein, tau and presenilin RNAs in

rat hippocampus following deafferentation lesions. Brain Res 907:222–232
65. Ring S, Weyer SW, Kilian SB et al (2007) The secreted beta-amyloid precursor protein ectodomain APPs alpha is sufficient to rescue the anatomical, behavioral, and electrophysiological abnormalities of APP-deficient mice. J Neurosci 27:7817–7826. doi:10.1523/JNEUROSCI.1026-07.2007
66. Roch JM, Masliah E, Roch-Levecq AC et al (1994) Increase of synaptic density and memory retention by a peptide representing the trophic domain of the amyloid beta/A4 protein precursor. Proc Natl Acad Sci USA 91:7450–7454
67. Roozendaal B, Phillips RG, Power AE, Brooke SM, Sapolsky RM, McGaugh JL (2001) Memory retrieval impairment induced by hippocampal CA3 lesions is blocked by adrenocortical suppression. Nat Neurosci 4:1169–1171. doi:10.1038/nn766
68. Savonenko A, Xu GM, Melnikova T et al (2005) Episodic-like memory deficits in the APPswe/PS1dE9 mouse model of Alzheimer's disease: relationships to beta-amyloid deposition and neurotransmitter abnormalities. Neurobiol Dis 18:602–617. doi:10.1016/j.nbd.2004.10.022
69. Selkoe DJ (2002) Alzheimer's disease is a synaptic failure. Science 298:789–791. doi:10.1126/science.1074069
70. Shankar GM, Bloodgood BL, Townsend M, Walsh DM, Selkoe DJ, Sabatini BL (2007) Natural oligomers of the Alzheimer amyloid-beta protein induce reversible synapse loss by modulating an NMDA-type glutamate receptor-dependent signaling pathway. J Neurosci 27:2866–2875. doi:10.1523/JNEUROSCI.4970-06.2007
71. Shankar GM, Li S, Mehta TH et al (2008) Amyloid-beta protein dimers isolated directly from Alzheimer's brains impair synaptic plasticity and memory. Nat Med 14:837–842. doi:10.1038/nm1782
72. Smith-Swintosky VL, Pettigrew LC, Craddock SD, Culwell AR, Rydel RE, Mattson MP (1994) Secreted forms of beta-amyloid precursor protein protect against ischemic brain injury. J Neurochem 63:781–784
73. Spires-Jones T, Knafo S (2012) Spines, plasticity, and cognition in Alzheimer's model mice. Neural Plast 2012:319836. doi:10.1155/2012/319836
74. Suh J, Choi SH, Romano DM et al (2013) ADAM10 missense mutations potentiate beta-amyloid accumulation by impairing prodomain chaperone function. Neuron 80:385–401. doi:10.1016/j.neuron.2013.08.035
75. Tang W, Ehrlich I, Wolff SB et al (2009) Faithful expression of multiple proteins via 2A-peptide self-processing: a versatile and reliable method for manipulating brain circuits. J Neurosci 29:8621–8629. doi:10.1523/JNEUROSCI.0359-09.2009
76. Taylor CJ, Ireland DR, Ballagh I et al (2008) Endogenous secreted amyloid precursor protein-alpha regulates hippocampal NMDA receptor function, long-term potentiation and spatial memory. Neurobiol Dis 31:250–260. doi:10.1016/j.nbd.2008.04.011
77. Terry RD, Masliah E, Salmon DP et al (1991) Physical basis of cognitive alterations in Alzheimer's disease: synapse loss is the major correlate of cognitive impairment. Ann Neurol 30:572–580. doi:10.1002/ana.410300410
78. Thornton E, Vink R, Blumbergs PC, Van Den Heuvel C (2006) Soluble amyloid precursor protein alpha reduces neuronal injury and improves functional outcome following diffuse traumatic brain injury in rats. Brain Res 1094:38–46. doi:10.1016/j.brainres.2006.03.107
79. Van den Heuvel C, Blumbergs PC, Finnie JW et al (1999) Upregulation of amyloid precursor protein messenger RNA in response to traumatic brain injury: an ovine head impact model. Exp Neurol 159:441–450. doi:10.1006/exnr.1999.7150
80. Vassar R, Kuhn PH, Haass C et al (2014) Function, therapeutic potential and cell biology of BACE proteases: current status and future prospects. J Neurochem 130:4–28. doi:10.1111/jnc.12715
81. Villemagne VL, Burnham S, Bourgeat P et al (2013) Amyloid beta deposition, neurodegeneration, and cognitive decline in sporadic Alzheimer's disease: a prospective cohort study. Lancet Neurol 12:357–367. doi:10.1016/S1474-4422(13)70044-9
82. Wang Y, Cella M, Mallinson K et al (2015) TREM2 lipid sensing sustains the microglial response in an Alzheimer's disease model. Cell 160:1061–1071. doi:10.1016/j.cell.2015.01.049
83. Wang Z, Wang B, Yang L et al (2009) Presynaptic and postsynaptic interaction of the amyloid precursor protein promotes peripheral and central synaptogenesis. J Neurosci 29:10788–10801. doi:10.1523/JNEUROSCI.2132-09.2009
84. Weyer SW, Klevanski M, Delekate A et al (2011) APP and APLP2 are essential at PNS and CNS synapses for transmission, spatial learning and LTP. EMBO J 30:2266–2280. doi:10.1038/emboj.2011.119
85. Weyer SW, Zagrebelsky M, Herrmann U et al (2014) Comparative analysis of single and combined APP/APLP knockouts reveals reduced spine density in APP-KO mice that is prevented by APPsalpha expression. Acta Neuropathol Commun 2:36. doi:10.1186/2051-5960-2-36
86. Wilhelm BG, Mandad S, Truckenbrodt S et al (2014) Composition of isolated synaptic boutons reveals the amounts of vesicle trafficking proteins. Science 344:1023–1028. doi:10.1126/science.1252884
87. Xiong H, Callaghan D, Wodzinska J et al (2011) Biochemical and behavioral characterization of the double transgenic mouse model (APPswe/PS1dE9) of Alzheimer's disease. Neurosci Bull 27:221–232. doi:10.1007/s12264-011-1015-7
88. Yang L, Wang Z, Wang B, Justice NJ, Zheng H (2009) Amyloid precursor protein regulates Cav1.2 L-type calcium channel levels and function to influence GABAergic short-term plasticity. J Neurosci 29:15660–15668. doi:10.1523/JNEUROSCI.4104-09.2009

Development/Plasticity/Repair

Reversal of Aging-Related Neuronal Ca^{2+} Dysregulation and Cognitive Impairment by Delivery of a Transgene Encoding FK506-Binding Protein 12.6/1b to the Hippocampus

John C. Gant,[1] Kuey-Chu Chen,[1] Inga Kadish,[2] Eric M. Blalock,[1] Olivier Thibault,[1] Nada M. Porter,[1] and Philip W. Landfield[1]

[1]Department of Pharmacology and Nutritional Sciences, University of Kentucky, Lexington, Kentucky 40536 and [2]Department of Cell, Developmental, and Integrative Biology, University of Alabama at Birmingham, Birmingham, Alabama 35294

Brain Ca^{2+} regulatory processes are altered during aging, disrupting neuronal, and cognitive functions. In hippocampal pyramidal neurons, the Ca^{2+}-dependent slow afterhyperpolarization (sAHP) exhibits an increase with aging, which correlates with memory impairment. The increased sAHP results from elevated L-type Ca^{2+} channel activity and ryanodine receptor (RyR)-mediated Ca^{2+} release, but underlying molecular mechanisms are poorly understood. Previously, we found that expression of the gene encoding FK506-binding protein 12.6/1b (FKBP1b), a small immunophilin that stabilizes RyR-mediated Ca^{2+} release in cardiomyocytes, declines in hippocampus of aged rats and Alzheimer's disease subjects. Additionally, knockdown/disruption of hippocampal FKBP1b in young rats augments neuronal Ca^{2+} responses. Here, we test the hypothesis that declining FKBP1b underlies aging-related hippocampal Ca^{2+} dysregulation. Using microinjection of adeno-associated viral vector bearing a transgene encoding FKBP1b into the hippocampus of aged male rats, we assessed the critical prediction that overexpressing FKBP1b should reverse Ca^{2+}-mediated manifestations of brain aging. Immunohistochemistry and qRT-PCR confirmed hippocampal FKBP1b overexpression 4–6 weeks after injection. Compared to aged vector controls, aged rats overexpressing FKBP1b showed dramatic enhancement of spatial memory, which correlated with marked reduction of sAHP magnitude. Furthermore, simultaneous electrophysiological recording and Ca^{2+} imaging in hippocampal neurons revealed that the sAHP reduction was associated with a decrease in parallel RyR-mediated Ca^{2+} transients. Thus, hippocampal FKBP1b overexpression reversed key aspects of Ca^{2+} dysregulation and cognitive impairment in aging rats, supporting the novel hypothesis that declining FKBP1b is a molecular mechanism underlying aging-related Ca^{2+} dysregulation and unhealthy brain aging and pointing to FKBP1b as a potential therapeutic target.

Key words: Alzheimer's disease; aging; calcium; FKBP; memory; ryanodine receptor

Significance Statement

This paper reports critical tests of a novel hypothesis that proposes a molecular mechanism of unhealthy brain aging and possibly, Alzheimer's disease. For more than 30 years, evidence has been accumulating that brain aging is associated with dysregulation of calcium in neurons. Recently, we found that FK506-binding protein 12.6/1b (FKBP1b), a small protein that regulates calcium, declines with aging in the hippocampus, a brain region important for memory. Here we used gene therapy approaches and found that raising FKBP1b reversed calcium dysregulation and memory impairment in aging rats, allowing them to perform a memory task as well as young rats. These studies identify a potential molecular mechanism of brain aging and may also have implications for treatment of Alzheimer's disease.

Introduction

The population of developed nations is projected to age significantly over the next several decades. Because advanced age is the leading risk factor for Alzheimer's disease (AD) and other cognitive disorders, a corollary of this increase in population age will be a substantial rise in the prevalence of cognitively impaired individuals and a resulting enormous socioeconomic burden (Reitz

Received March 31, 2015; revised June 15, 2015; accepted June 23, 2015.

Author contributions: J.C.G., K.-C.C., and P.W.L. designed research; J.C.G., K.-C.C., and I.K. performed research; J.C.G. and E.M.B. analyzed data; J.C.G., K.-C.C., E.M.B., O.T., N.M.P., and P.W.L. wrote the paper.

This work was supported by Grant R37-AG004542 from the National Institute on Aging.

This article is freely available online through the *J Neurosci* Author Open Choice option.

Correspondence should be addressed to either John C. Gant or Philip W. Landfield at the above address. E-mail: cgant@uky.edu or pwland@uky.edu.

DOI:10.1523/JNEUROSCI.1248-15.2015

Copyright © 2015 Gant et al.

This is an Open Access article distributed under the terms of the Creative Commons Attribution License Creative Commons Attribution 4.0 International, which permits unrestricted use, distribution and reproduction in any medium provided that the original work is properly attributed.

et al., 2011; Hebert et al., 2013). Discovery of new therapeutic approaches that can delay cognitive impairment would significantly mitigate this burden, but such discovery will likely be difficult without improved understanding of the molecular mechanisms underlying unhealthy brain aging and aging-related susceptibility to Alzheimer's disease. In this regard, accumulating evidence suggests that mechanisms of deleterious brain aging can be elucidated in part by investigation of the molecular machinery regulating neuronal Ca^{2+} homeostasis.

Numerous studies have found that Ca^{2+}-dependent neuronal processes are dysregulated during brain aging, generally in a cell type- and region-specific manner (Gibson and Peterson, 1987; Landfield, 1987; Khachaturian, 1989; Disterhoft et al., 1996; Foster and Norris, 1997; Lynch et al., 2006; Murchison and Griffith, 2007; Thibault et al., 2007; Toescu and Verkhratsky, 2007). In CA1 pyramidal neurons of the dorsal hippocampus, a region important for learning and memory (Moser et al., 1995; Buzsáki and Moser, 2013), one of the most consistent manifestations of aging is an increased magnitude of the Ca^{2+}-dependent, K^+-mediated slow afterhyperpolarization (sAHP; Landfield and Pitler, 1984; Moyer et al., 1992; Disterhoft and Oh, 2006; Gant et al., 2006). The sAHP is generated by hyperpolarizing Ca^{2+}-sensitive K^+ channels that are activated by action potential-induced Ca^{2+} influx and resulting Ca^{2+} release from intracellular ryanodine receptors (RyRs; Madison and Nicoll, 1984; Sah and Bekkers, 1996; Lancaster et al., 2001; Andrade et al., 2012). The aging-related increases in the hippocampal sAHP and other Ca^{2+}-mediated processes, which act to dampen neuronal excitability, have been found to correlate with impaired learning in several species (Disterhoft et al., 1996; Thibault and Landfield, 1996; Tombaugh et al., 2005; Luebke and Amatrudo, 2012), suggesting that the mechanisms underlying Ca^{2+} dysregulation may be directly relevant to brain dysfunction with aging. Although aging-related augmentation of the hippocampal sAHP appears to be driven primarily by elevations in voltage-gated L-type Ca^{2+} channel (LTCC) activity (Moyer et al., 1992; Disterhoft et al., 1996; Thibault and Landfield, 1996; Murphy et al., 2006) and Ca^{2+}-induced Ca^{2+} release (CICR) from intracellular RyRs (Kumar and Foster, 2005; Gant et al., 2006; Thibault et al., 2007), the elevated activity is not associated with upregulation of LTCC expression (Rowe et al., 2007). Thus, the molecular bases for these increases in Ca^{2+} sources remain unclear.

However, in microarray studies of gene expression in the rat hippocampus (Kadish et al., 2009), we found aging-related downregulation of the gene encoding FK506-binding protein 12.6/1b (FKBP1b), a small immunophilin that inhibits Ca^{2+} release from sarcoplasmic reticulum RyRs in cardiomyocytes (Zalk et al., 2007). Moreover, in electrophysiological and Ca^{2+} imaging studies, we found that knockdown/disruption of FKBP1b in rat hippocampal neurons augments Ca^{2+} transients generated by RyR-mediated Ca^{2+} release or LTCC activation (Gant et al., 2011). Those findings suggest the hypothesis that aging-related decline or dysfunction of FKBP1b is a molecular mechanism of hippocampal Ca^{2+} dyshomeostasis and consequent cognitive impairment. Here, using viral-mediated delivery of a transgene encoding FKBP1b, we tested a key prediction of this hypothesis, namely, that selectively counteracting the FKBP1b deficit in aged hippocampus should reduce/reverse Ca^{2+} dysregulation and impaired cognition. The results clearly show that overexpressing FKBP1b in hippocampal neurons is sufficient to reverse major manifestations of Ca^{2+}-mediated brain aging.

Materials and Methods

Animals. Young mature (4–5 months old) and aged (20–22 months old) male Fischer 344 (F344) rats were obtained from the aging rodent colony maintained by the National Institute on Aging. The present study comprises experiments using four cohorts of F344 male rats. The size, composition, treatments, and measures used for each cohort are described in the corresponding Results section. All protocols and procedures were performed in accordance with institutional guidelines and were approved by the Animal Care and Use Committee.

Adeno-associated viral vector constructs and microinjection. We induced FKBP1b overexpression in the hippocampus of male F344 rats using one-time microinjection of a recombinant adeno-associated viral (AAV) vector construct containing the transgene for rat FKBP1b under the control of the largely neuron-specific Ca^{2+}-calmodulin kinase II (CaMKII) promoter. Because of their safety, efficacy, and long-lasting effects, AAV vector approaches are widely used for brain gene transfer studies in animal models and humans (Broekman et al., 2006; Kaplitt et al., 2007; McCown, 2010; Salegio et al., 2012; Bosch et al., 2014). Before the FKBP1b overexpression experiments, we used a reporter gene, enhanced green florescent protein (EGFP), and the FKBP1b transgene to conduct extensive pilot studies and compare transduction efficiency, tropism, and expression of three AAV serotypes (1, 8, and 9) and three promoters (CB7, CaMKII, and Synapsin) under our specific experimental conditions. These serotypes have been shown to exhibit high transduction efficiency in principal neurons of the brain (Broekman et al., 2006; Aschauer et al., 2013; Bosch et al., 2014), and in our studies all three serotypes showed good *in vivo* transduction of hippocampal pyramidal neurons in adult rats 4–6 weeks after microinjection into the hippocampus (see Results, below). For the FKBP1b overexpression experiments, we selected AAV serotype 9 and the CaMKII promoter, as this combination exhibited slightly higher transduction and expression in pyramidal neurons of the dorsal hippocampus with minimal spread beyond the ipsilateral hippocampus. Vectors were delivered via microsyringe under stereotaxic guidance to the apical dendrites (stratum radiatum), below the mediolateral peak of the CA1 pyramidal cell body layer (stratum pyramidale) in dorsal hippocampus. Under isoflurane anesthesia, the microsyringe tip was stereotaxically guided to the target coordinates in CA1 stratum radiatum (3.8 mm caudal, 2.8 mm lateral from bregma, and 1.7–1.8 mm ventral from the top of the cortex). For each injection, 2 μl of AAV vector were infused into the hippocampus at a rate of 0.2 μl/min using a 10 μl Hamilton syringe with a custom 30 gauge needle (Hamilton Company) and a Stoelting QSI microinjection pump. Following surgery, animals were treated with analgesics and monitored closely under the supervision of veterinary staff. The design of the AAV-FKBP1b vector was AAV2/9.CAMKII0.4.ratFKBP1b.rBG (titer, 1.99e13 genome copies per milliliter (GC/ml) or 1.99e12 GC/ml). The design of the AAV-EGFP control vector was the same except that the EGFP transgene was substituted for the FKBP1b transgene: AAV2/9.CAMKII0.4.EGFP.rBG (titer, 1.86e13 GC/ml). AAV vectors were constructed and amplified by the Penn Vector Core (Philadelphia, PA).

Morris water maze test of spatial memory. Cognitive function was tested using the Morris water maze (MWM), with procedures similar to those described previously (Rowe et al., 2007; Kadish et al., 2009). Multiple groups have found deficient spatial learning in the MWM to be a highly sensitive and reliable index of aging-related cognitive impairment in rodents (Gallagher and Rapp, 1997; Markowska, 1999; Tombaugh et al., 2005; Kadish et al., 2009). The MWM used here consisted of a 190-cm-diameter black round tub filled with water (26°C). A 15-cm-diameter escape platform was placed in one of four pool quadrants 1 cm below the water surface and remained in this position until the memory retention probe trial, during which it was removed. The pool was surrounded by circular black curtains with three high-contrast geometric images hung on the inner side of the curtains. Tracking was achieved through contrast imaging using water maze acquisition software (Columbus Instruments). The spatial learning protocol consisted of 4 d of training (learning phase) followed by a memory retention probe trial on the fifth day and a visual acuity/motor function test (cued trial, sixth day). On each training day, subjects were given three trials in which they were placed

into the pool from a different quadrant location on each trial and allowed up to 60 s to find and climb onto the escape platform. After a rat found the platform, it was left on the platform for an additional 30 s. Those animals that did not find the platform were gently guided to the platform and allowed to remain there for 30 s before being returned to their cage. Intertrial interval was 2 min. On the fifth day (retention test probe), the platform was removed, and the subjects were placed into the pool from a different location and allowed to swim for 60 s. On the sixth day, a cued trial was performed with a white contrasting marker placed 6 inches above the platform location. Performance on all trials was assessed by path length and latency to reach the platform or former location of the platform.

For the maze learning experiment, 15 aged rats (20 months old) received bilateral injections of AAV-FKBP1b, 7 rats at the original titer (1.99e13 GC/ml) and 8 rats at a 10-fold lower titer (1.99e12 GC/ml), and 10 aged control animals received bilateral injections of AAV-EGFP (1.86e13 GC/ml). Ten young control rats received bilateral injections of AAV-EGFP (1.86e13 GC/ml, $n = 5$) or bilateral sham surgeries ($n = 5$) in which the microsyringe was lowered into the hippocampus, but no injection administered. Because the two AAV-FKBP1b titer subgroups did not differ on any performance measure, they were combined into a single group, Aged-FKBP1b, for the statistical analyses. Similarly, the young control EGFP and young control sham subgroups did not differ from one another on any measure and were treated statistically as a single group, Young-Control.

Intracellular recording in hippocampal slice pyramidal neurons. Our sharp-electrode electrophysiological methods have been described previously (Thibault et al., 2001; Gant et al., 2006, 2011). Briefly, rats were anesthetized in a CO_2 chamber before rapid decapitation. Intracellular recordings were obtained from CA1 pyramidal neuron cell bodies in 350-μm-thick dorsal hippocampal transverse slices maintained in oxygenated artificial CSF [containing (in mM) 128 NaCl, 1.25 KH_2PO_4, 10 glucose, 26 $NaHCO_3$, 3 KCl, 2 $CaCl_2$, and 2 $MgCl_2$] using sharp glass pipettes filled with HEPES (10 mM) and $KMeSO_4$ (2 M). Electrophysiological data were acquired and analyzed using pClamp 8, a sharp-electrode amplifier in current-clamp mode (Axoclamp 2B; Molecular Devices), and a DigiData 1320 board (Molecular Devices). Voltage records were digitized at 2–20 kHz and low-pass filtered at 1 kHz. The sAHPs were triggered at 0.1 Hz by depolarizing current injection steps (200 ms duration) set at an intensity in each cell that consistently elicited a burst of four action potentials. The amplitude of the sAHP was measured at 800 ms following the end of the depolarizing step, and sAHP duration was determined as the interval from the end of the current step to the time point at which the membrane potential returned to prestimulus baseline. The integrated area under the curve (AUC; millivolts by milliseconds) of the sAHP was determined following stimulating current termination.

Ca^{2+} imaging. Intracellular Ca^{2+} responses were recorded simultaneously with electrophysiological responses in neurons from a separate cohort of10 aged rats injected with AAV-FKBP1b in the right (ipsilateral) hippocampus and with AAV-EGFP in the contralateral hippocampus. Imaging methods used were similar to those described previously by several groups, including ours (Magee and Johnston, 1997; Thibault et al., 2001; Hemond and Jaffe, 2005; Gant et al., 2011; Oh et al., 2013). Individual hippocampal slice neurons were impaled with sharp pipettes containing the single-wavelength Ca^{2+} indicator Calcium Orange (5 mM). Pyramidal neurons with acceptable baseline electrophysiological characteristics (Table 1) that were also sufficiently close to the slice surface to permit simultaneous visualization of Ca^{2+} responses (9 AAV-FKBP1b- and 6 AAV-EGFP-treated neurons) were imaged on the stage of a Nikon E600 microscope equipped with a 40× water-immersion objective and a CCD camera (Princeton Instruments). Calcium Orange was allowed to diffuse into the cell for at least 10 min before Ca^{2+} fluorescence measures were obtained. Calcium Orange was excited using a wavelength switcher (Lambda DG-4; Sutter Instrument Company) and software control (Axon Imaging Workbench; Molecular Devices, version 2.2.1.54). The 575 nm wavelength was monitored through a dichroic mirror centered at 570 nm during excitation with the 550 nm wavelength. The Ca^{2+} response elicited during activation of the sAHP was recorded in each neuron simultaneously with electrophysiological recordings of the sAHP. In addition, in each cell we recorded the Ca^{2+} response elicited by 10 s of 7 Hz repetitive synaptic stimulation (RSS) delivered via a bipolar stimulating electrode on the Schaffer collaterals, which synapse on CA1 pyramidal cells. Stimulation intensity during RSS was set at action potential threshold, which at 7 Hz generates an action potential on essentially each pulse (Thibault et al., 2001). The rise time of this RSS-induced Ca^{2+} response is markedly accelerated with aging because of increased RYR-mediated Ca^{2+} release (Gant et al., 2006). Ca^{2+} responses were measured in the visible outline of the cell soma, excluding surrounding low-intensity diffracted light. Following background subtraction from an area devoid of cells, the percentage change in fluorescence during RSS was determined relative to baseline (%$\Delta F/F$). The AUC (percentage of fluorescence change times seconds) of the Ca^{2+} response was determined for the first 5 s of the sAHP-associated Ca^{2+} responses and the first 5 s of the RSS-generated responses. The RSS-induced Ca^{2+} levels during the rise to peak Ca^{2+} concentration were fit with an exponential curve (confidence interval, >93%) to calculate the rising time constant (τ, time to ~63.7% of the peak) for each cell.

Table 1. Baseline electrophysiological measures for neurons from behaviorally characterized rats (means ± SEM)

	Aged-FKBP1b	Aged-Control	Young	*F* value	*p* value
N animals	7	6	5		
n neurons	17	16	13		
Resting potential (mV)	−59.88 ± 0.74	−59.44 ± 0.75	−59.39 ± 0.70	0.14	0.87
Input resistance (MΩ)	56.29 ± 2.02	53.81 ± 2.65	53.85 ± 3.92	0.27	0.76
AP height (mV)	83.91 ± 1.34	86.28 ± 1.47	87.94 ± 2.24	1.50	0.24

Quantitative real-time polymerase chain reaction. mRNA amplification was performed as described previously (Gant et al., 2011) using an ABI prism 7700 sequence detection system (Applied Biosystems) and Taqman One Step RT-PCR reagents (Applied Biosystems). All samples were run in duplicate in a final volume of 30 μl containing 50 ng of cellular RNA and a Taqman probe (5 μM) and primers (10 nM each), with an amplicon spanning the rat *Fkbp1b* cDNA region from nucleotides 155 to 259. Cycling parameters for all assays were as follows: 30 min at 48°C, 10 min at 95°C, followed by 40 cycles of 15 s at 95°C and 1 min at 60°C. Primers were designed using Primer Express software (version 1.5, Applied Biosystems) and chemically synthesized by Applied Biosystems (forward primer, 5′-GCAAGCAGGA AGTCATCAAAGG-3′; reverse primer, 5′-CAGTAGCTCCATATGCCA-CATCA-3′; Taqman probe, 5′-AGCTCATCTGGGCAGCGCCTTCTT-3′). The RNA levels of glyceraldehyde-3-phosphate dehydrogenase (Gapdh) were used as normalization controls for Fkbp1b RNA quantification. Reported values (Fig. 1*C*) are log10 transforms of the Fkbp1b/Gapdh ratio.

Immunohistochemistry. Our immunohistochemistry (IHC) methods have been described previously (Kadish et al., 2009). Animals were deeply anesthetized with sodium pentobarbital (100 mg/kg, i.p.) and perfused transcardially with cold saline. Brains were placed in 4% paraformaldehyde overnight and then transferred to 15% sucrose for cryoprotection. Before staining, 30-μm-thick sections were rinsed in TBS-T and incubated in the primary FKBP1b antibody (1:500; sc-98742; Santa Cruz Biotechnology) at room temperature for 18 h. The tissues were rinsed and incubated with appropriate secondary antibody for 2 h at room temperature, followed by incubation for 2 h in avidin-peroxidase. Staining was visualized using a metal-enhanced diaminobenzidine (DAB) solution. For tissue from animals receiving AAV-EGFP injections, 30 μm sections were mounted directly on slides and coverslipped. Imaging was performed using a Nikon Eclipse TE200 and CRi Nuance Multispectral Imaging System (Cambridge Research and Instrumentation). A wavelength of 480 nM was used to visualize EGFP. Gray scale analysis of DAB immunoreactivity was accomplished using Scion software and reported as optical density (average gray value/pixel).

Statistical analysis. Data analyses were performed with Clampfit8 (Molecular Devices) or Sigma Plot (Systat Software), and statistical analyses performed with StatView (SAS Institute). Multigroup results were analyzed using ANOVA across all groups. Fisher's protected least significant

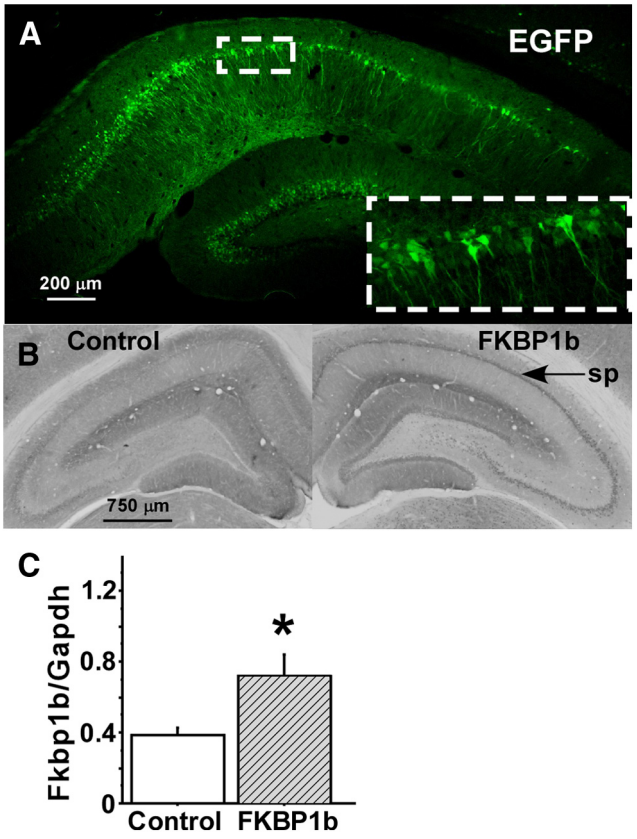


Figure 1. Hippocampal expression of EGFP and FKBP1b following microinjection of AAV vectors harboring the encoding transgenes. ***A***, AAV-EGFP microinjection into field CA1 of dorsal hippocampus resulted in extensive EGFP expression (green fluorescence) in CA1 pyramidal cell bodies of the stratum pyramidale. Inset, Higher magnification of CA1 pyramidal cell bodies and dendrites expressing EGFP. ***B***, FKBP1b immunostaining in AAV-EGFP control (left) and AAV-FKBP1b-injected (right) hippocampi, showing more intense immunostaining in the FKBP1b hippocampus, particularly in CA1 pyramidal cell bodies of the stratum pyramidale (sp, arrow). ***C***, qRT-PCR measures of *Fkbp1b* mRNA expression normalized to *Gapdh* mRNA. Shown is a comparison of right (FKBP1b) versus the left (control) hippocampus of aging rats ($n = 6$) 4–5 weeks following injection of AAV-FKBP1b into right hippocampus of each animal. *$p < 0.05$ (paired *t* test).

difference test was used for *post hoc* group comparisons. Correlations were calculated using the Pearson product-moment correlation coefficient. *P* values <0.05 were considered significant. All results are expressed as mean ± SEM.

Results

Localization of overexpression

We performed extensive pilot studies with unilateral injection of AAV-EGFP or AAV-FKBP1b into the hippocampal field CA1. Fluorescence microscopy of EGFP and immunostaining of FKBP1b showed that by 4–6 weeks after injection, there was pronounced expression of EGFP (Fig. 1*A*) or FKBP1b (*B*) in stratum pyramidale neuronal cell bodies of the CA1, CA2, and, to a lesser extent, CA3 fields of the ipsilateral dorsal hippocampus. Expression was less intense in dendrites. The AAV vectors did not significantly transduce cells in the contralateral hippocampus. Granule cells in the dentate gyrus were also often transduced (Fig. 1*A*), likely because of AAV retrograde/anterograde spread along axonal pathways such as the mossy fibers (Cearley and Wolfe, 2006; Betley and Sternson, 2011; Castle et al., 2014). Consequently, although FKBP1b expression in the hippocampus appears to underlie the behavioral effects reported below, contributions from hippocampal cell types other than CA1 neurons cannot be excluded. In another group of six aging rats, FKBP1b overexpression 5–6 weeks following delivery of the transgene was confirmed by qRT-PCR analyses in dorsal hippocampal tissue. These analyses showed a significant increase in Fkbp1b mRNA expression in the hippocampus injected with AAV-FKBP1b compared with the contralateral control hippocampus ($p < 0.05$, paired *t* test; Fig. 1*C*).

In hippocampal pyramidal cells, the sAHP is generated largely in the proximal dendrites (Andreasen and Lambert, 1995; Sah and Bekkers, 1996; Lancaster et al., 2001) and possibly the cell bodies (Lima and Marrion, 2007). To confirm that FKBP1b expression declines with aging and is rescued by AAV-FKBP1b transduction in the hippocampal CA1 neurons, we measured FKBP1b immunostaining optical density in the CA1 neuronal cell body layer of a separate cohort of 16 rats (five Young-Control rats, five Aged-Control rats, six Aged-FKBP1b rats). Effects of AAV-FKBP1b microinjection on FKBP1b expression in stratum pyramidale were visibly apparent (Figs. 2*A–C*), and semiquantitative optical density analyses revealed a main effect of age/treatment group ($F_{(2,12)} = 4.24$; $p < 0.05$). *Post hoc* comparisons showed that density of FKBP1b immunostaining was significantly lower ($p < 0.05$) in Aged-Control (134.30 ± 4.29; $n = 5$) relative to Young-Control (150.90 ± 3.58; $n = 5$) or AAV-FKBP1b-treated aged animals (Aged-FKBP1b; 150.40 ± 4.64; $n = 6$).

Cognitive performance

To test whether overexpression of FKBP1b could reverse established indicators of aging-related cognitive decline, we assessed MWM spatial memory in another cohort of young and aged F344 rats ($n = 35$ animals total). Aged animals were divided into two groups: the Aged-Control group ($n = 10$) received bilateral injections of AAV-EGFP, and Aged-FKBP1b rats ($n = 15$) received bilateral injections of AAV-FKBP1b. Additionally, a Young-Control group ($n = 10$; five bilateral EGFP plus five bilateral Sham) was included to determine the normal young baseline under our conditions. Behavioral testing was initiated 5–6 weeks after bilateral AAV injections. Animals were given 4 d of training (three trials per day) to learn the fixed location of a submerged escape platform. The platform was removed on the fifth day, and animals were tested for memory (retention probe trial) of the platform's former location. On the sixth day (cued trial), sensorimotor function was evaluated in a trial during which the platform's location was visually cued. All groups exhibited a significant improvement in water maze performance over the 4 d course of training (Fig. 3*A*), as reflected in main effects across trials (repeated measures ANOVA across all trials) for latency and path length to platform location ($F_{(11,352)} = 16.74$, $p < 0.0001$ and $F_{(11,352)} = 6.28$, $p < 0.01$, respectively; for illustrative clarity, only path length values are shown in Figure 3*A*). No consistent group differences were seen across training, although by the last training day there was a trend for the Young-Control and Aged-FKBP1b groups to outperform the Aged-Control group (Fig. 3*A*).

The memory retention probe trial, performed 24 h after the last training session (Day 5), revealed a highly significant main effect of treatment group on both path length and latency to the platform's former location ($F_{(2,32)} = 11.15$, $p < 0.001$ and $F_{(2,32)} = 4.92$, $p < 0.01$ respectively). *Post hoc* analyses showed that the Aged-FKBP1b group and the Young-Control group both performed significantly better than the Aged-Control group on path length and latency to platform ($p < 0.001$ and $p < 0.01$, respectively; Fig. 3*B*), but did not differ from each other. No group

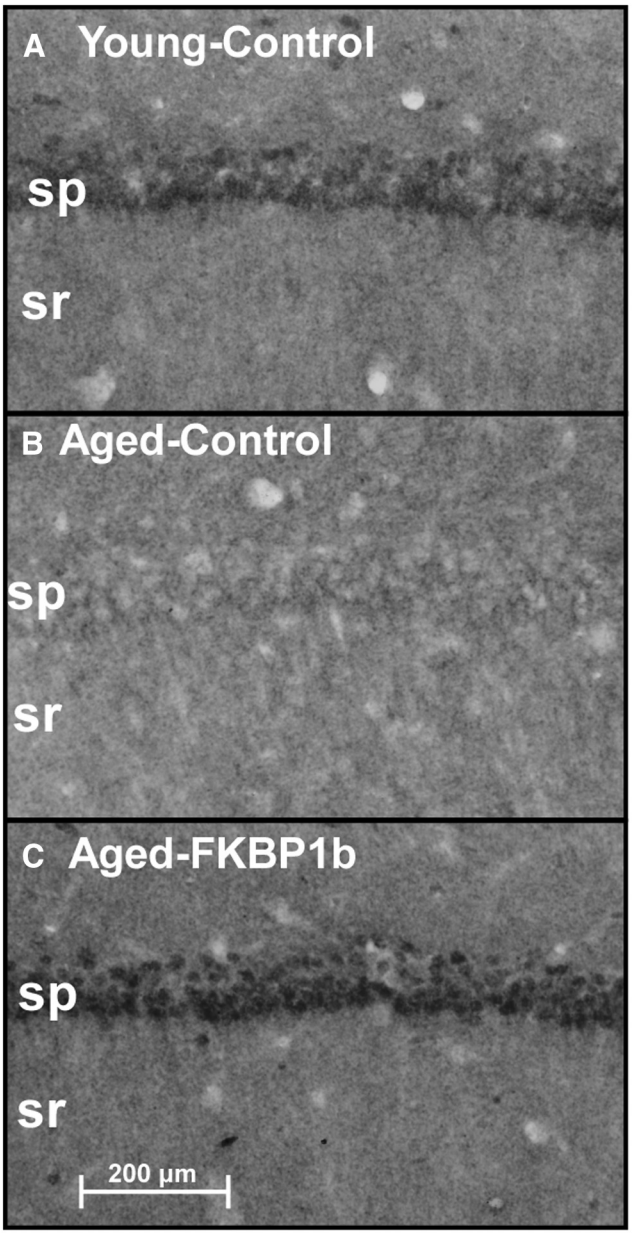


Figure 2. Aging-related decline in FKBP1b expression in CA1 pyramidal cell bodies is counteracted by AAV-mediated FKBP1b overexpression. ***A–C***, Representative examples of FKBP1b immunostaining in the CA1 pyramidal cell body layer (stratum pyramidale) of Young-Control (***A***), Aged-Control (***B***), and AAV-FKBP1b-treated (***C***) rats, illustrating age-related decline of FKBP1b expression and rescue in aged rats by AAV-FKBP1b microinjection. sp, Stratum pyramidale; sr, stratum radiatum.

differences were found in the cued test (Day 6). All groups performed at a high level (Fig. 3*C*), indicating that aging-related sensorimotor deficits did not account for the differences in MWM retention performance.

Effects of FKBP1b overexpression on the Ca^{2+}-dependent sAHP

We then determined whether the AAV-FKBP1b intervention also reversed age-related changes in the sAHP in a behaviorally correlated manner. Following completion of the MWM testing, we used a subset of the same animals described above for electrophysiological studies in hippocampal slices. We obtained high-quality intracellular recordings of sAHPs in CA1 pyramidal cells

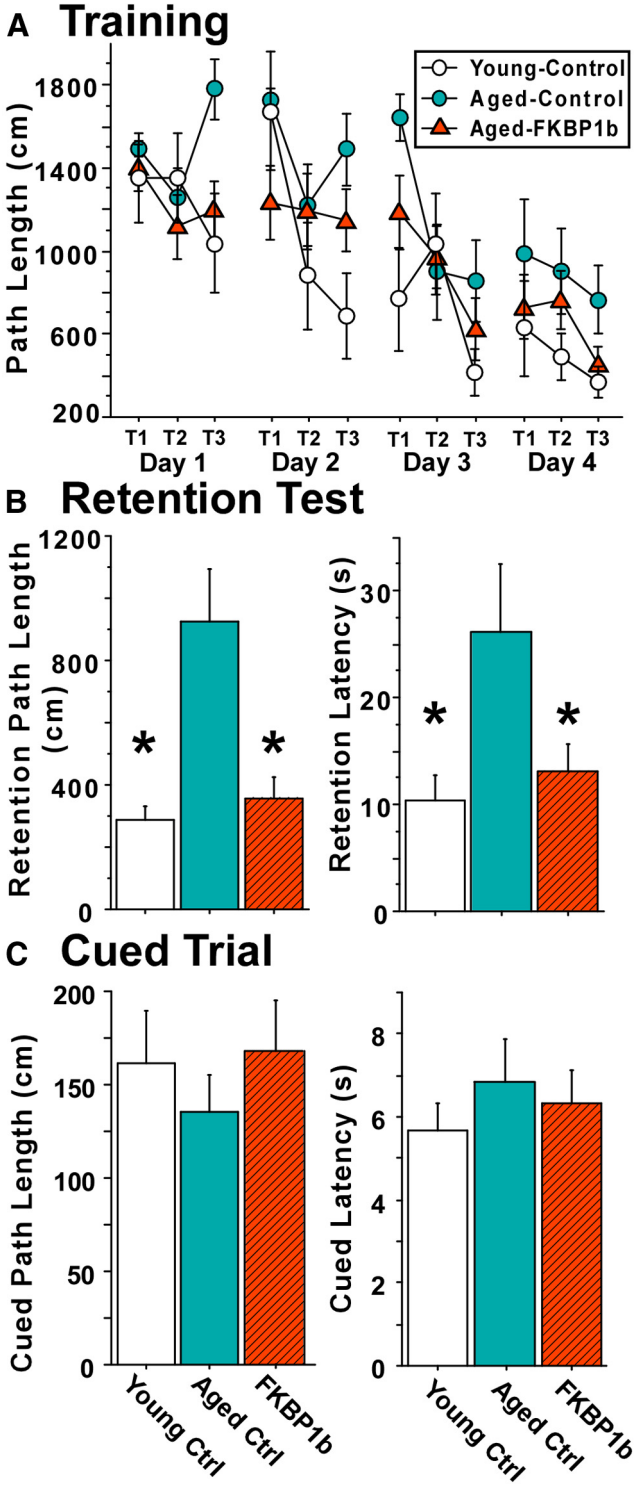


Figure 3. FKBP1b overexpression in hippocampal neurons reversed spatial memory deficits in aged F344 rats. ***A***, Path length values for the training trials (T1–T3) on each day across 4 training days. Young-Control, Aged-Control (bilateral AAV-EGFP), and Aged-FKBP1b (bilateral AAV-FKBP1b) rats all improved across training trials, although there was a trend for Aged-Control rats to perform more poorly. ***B***, On the retention probe trial (Day 5, platform removed), Aged-FKBP1b animals exhibited enhanced memory relative to Aged-Control animals, as indicated by shorter path length ($p < 0.001$) and latency ($p < 0.01$) to reach the platform's former location; Aged-FKBP1b rats did not differ from Young-Controls on the retention test. Asterisks denote a significant difference from Aged-Control. ***C***, No group differences in path length or latency were observed during the visually cued trial (Day 6), indicating that deficits in sensorimotor function did not account for the differences in retention performance.

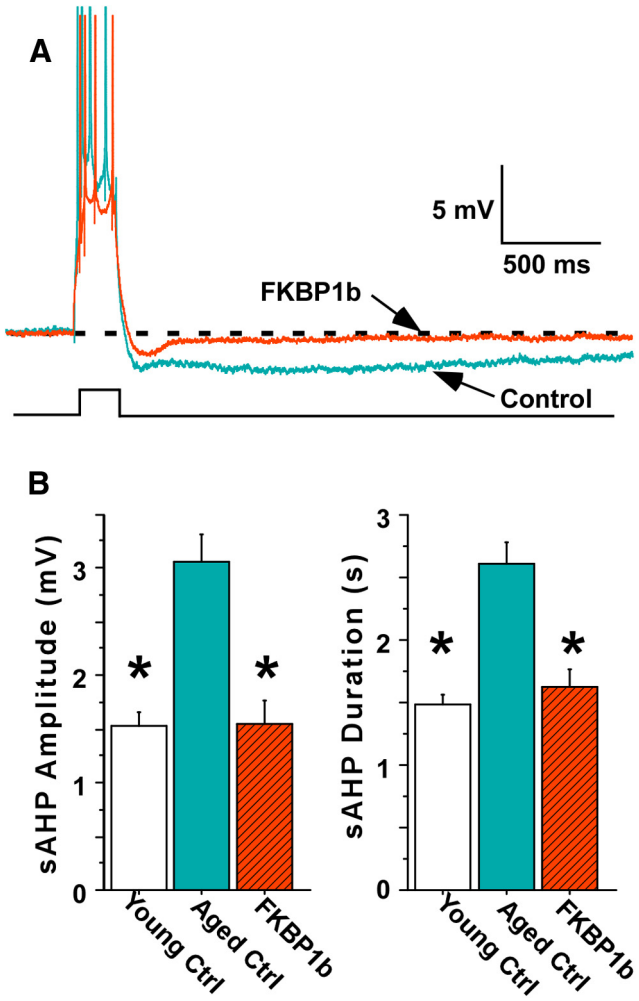


Figure 4. FKBP1b overexpression reversed the age-related augmentation of the sAHP in hippocampal neurons from the MWM-tested aged animals. ***A***, Representative traces of the sAHP following a burst of four action potentials elicited by an intracellular current pulse (lower trace) in hippocampal neurons of an Aged-Control rat (blue) and an Aged-FKBP1b rat (red). ***B***, sAHP amplitude and duration were substantially greater in neurons from Aged-Control rats than neurons from Young-Control rats ($p < 0.0001$) or Aged-FKBP1b ($p < 0.0001$) rats, but did not differ between Aged-FKBP1b and Young-Control rats. Asterisks denote a significant difference from Aged-Control.

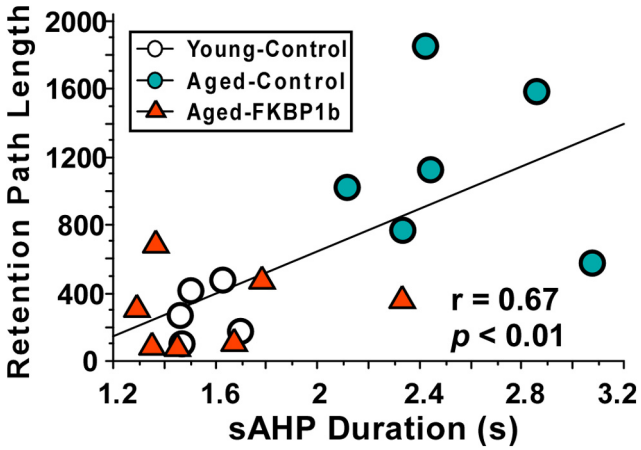


Figure 5. Correlation of sAHP duration with impaired spatial memory in the MWM. Pearson correlation analysis between MWM performance and averaged sAHPs for individual animals showed that enhanced spatial memory performance (shorter retention trial path length) was correlated with reduced sAHP duration and sAHP amplitude (data not shown). Note that there was very little overlap in sAHP duration between the Aged-FKBP1b group and the Aged-Control group.

(Fig. 4*A*) from 18 of the behaviorally characterized animals (13 neurons from five Young-Control rats; 16 neurons from six Aged-Control rats; and 17 neurons from seven Aged-FKBP1b rats). These recording studies began 7 d after behavioral testing ended and continued for ~9 weeks, alternating animals from the different groups.

All cells recorded met standard criteria for healthy neurons, and no group differences were seen in baseline electrophysiological parameters (Table 1). However, highly significant group differences were found for sAHP amplitude and duration, regardless of whether individual cells ($F_{(2,43)} = 16.64$; $p < 0.0001$) or averaged values per animal ($F_{(2,15)} = 12.89$; $p < 0.01$) were used as the statistical population. The sAHPs from Aged-FKBP1b rats were similar to those from Young-Control rats and substantially smaller than those from Aged-Control rats (Fig. 4*A*,*B*). This effect was dramatic, as there was little overlap of sAHP magnitudes between the Aged-Control and Aged-FKBP1b groups. The electrophysiological effects of FKBP1b overexpression were highly stable across the 9 week recording period, as there was no difference ($p = 0.41$) in sAHP amplitudes between FKBP1b-transduced cells recorded during earlier (1.66 ± 0.29 mV; $n = 9$) versus later (1.34 ± 0.24 mV; $n = 8$) phases of the recording period.

Furthermore, across individual animals, we found significant positive correlations between the degree of impairment of water maze memory performance and both sAHP amplitude ($r = 0.51$; $p < 0.05$) and sAHP duration ($r = 0.67$; $p < 0.01$; Fig. 5). Thus, the FKBP1b intervention shifted both Ca^{2+}-dependent electrophysiology and cognitive performance in aged rats to levels similar to those in young rats, in a correlated manner. This correlation remained even when the Young-Control group was omitted from analysis to remove age as a confounding factor (e.g., without the Young-Control group, correlation of MWM path length with sAHP duration was $r = 0.62$; $p < 0.05$).

Simultaneous Ca^{2+} imaging and electrophysiological recording

We then imaged intracellular Ca^{2+} responses simultaneously with electrophysiological recordings in a separate cohort of aged animals ($n = 10$) to test the prediction that FKBP1b overexpression should induce effects on coincident Ca^{2+} transients that covaried with its effects on Ca^{2+}-dependent sAHPs. In addition, we measured Ca^{2+} responses elicited during trains of postsynaptic action potentials generated by 7 Hz RSS of the Schaffer collaterals. With aging, the rise time of this Ca^{2+} response is substantially accelerated because of increased RyR-mediated Ca^{2+} release from the endoplasmic reticulum (Gant et al., 2006, 2011).

In 10 aged rats, AAV-FKBP1b was injected into one hippocampus and AAV-EGFP into the contralateral hippocampus, and intracellular responses were measured in hippocampal slices over a 3 week period beginning ~6 weeks after AAV injection. We obtained concurrent electrophysiology and optical Ca^{2+} imaging in nine neurons from the AAV-FKBP1b-injected hippocampi and six neurons from the AAV-EGFP control hippocampi. sAHPs were substantially smaller in the FKBP1b-treated neurons (Fig. 6*A*; amplitude and duration, $p < 0.01$; mean values not shown), essentially replicating the preceding

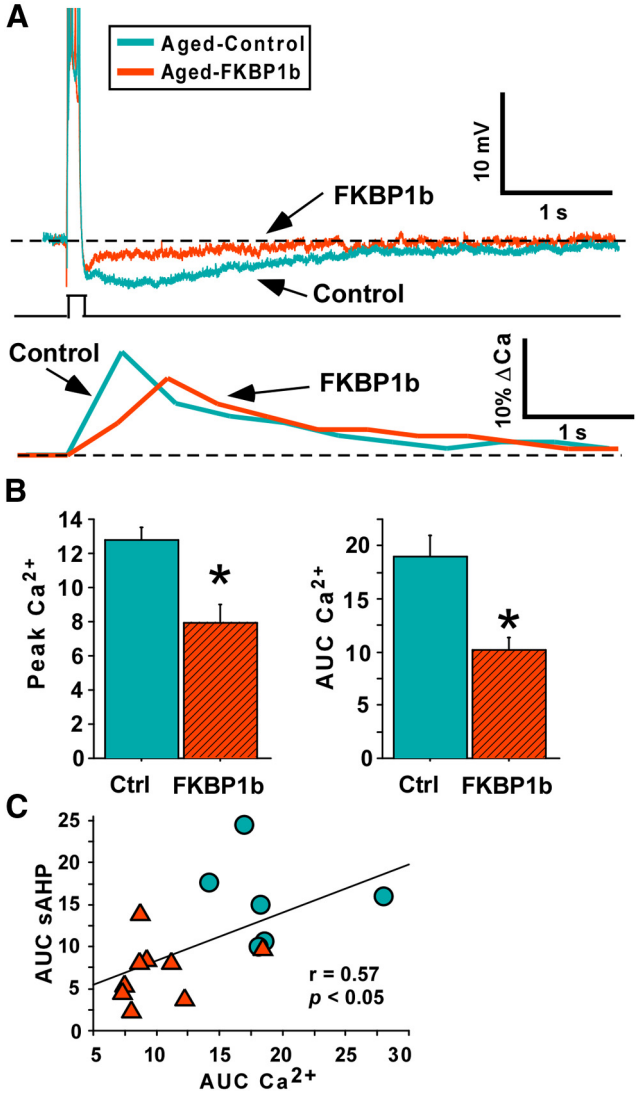


Figure 6. FKBP1b overexpression in aged rat neurons reduced Ca^{2+} transients imaged simultaneously with the sAHP. ***A***, Representative examples of the sAHPs (top traces) and simultaneously imaged Ca^{2+} transients (bottom traces) in an Aged-Control neuron and an Aged-FKBP1b neuron illustrating that FKBP1b induced a decrease in both responses. Middle trace, Intracellular current pulse triggering the action potential burst. ***B***, FKBP1b overexpression significantly reduced PeakΔCa^{2+} ($p < 0.05$) and the area under the curve ($p < 0.001$) of the Ca^{2+} response during the sAHP. Asterisks indicate a significant difference from Aged-Control. ***C***, Across individual neurons, the FKBP1b-induced AUC Ca^{2+} reduction was correlated with the reduction in the AUC of the sAHP. Red triangles, Aged-FKBP1b; blue circles, Aged-Controls; AUC Ca^{2+}, $\%\Delta F$ times seconds; AUC sAHP, millivolts times milliseconds).

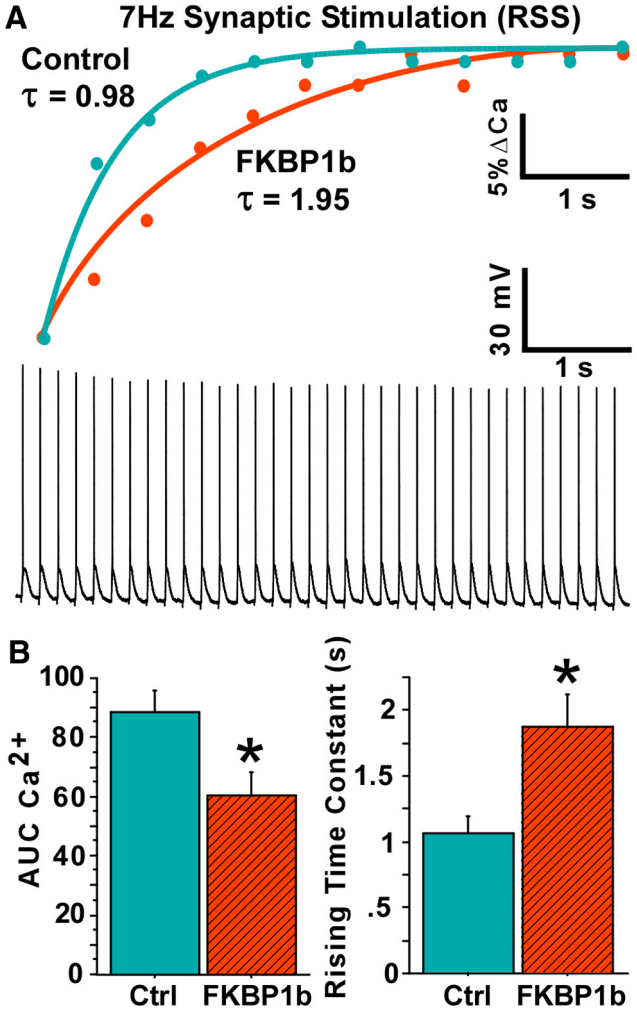


Figure 7. FKBP1b overexpression in aged rat neurons slowed the Ca^{2+} rise associated with RSS. ***A***, Examples of Ca^{2+} responses during the first 5 s of RSS of the Schaffer collaterals in neurons from an Aged-Control and an Aged-FKBP1b rat, illustrating the difference in the rising time constant (τ), but not the peak of the response. The bottom trace is a representative intracellular recording showing the train of action potentials elicited by the 7 Hz synaptic stimulation protocol. ***B***, FKBP1b overexpression significantly reduced the AUC of the RSS Ca^{2+} response and significantly increased the rising time constant. AUC units of the Ca^{2+} responses, $\%\Delta F$ times seconds. *$p < 0.05$ (significant difference from Aged-Control.

sAHP experiment (Fig. 4). Additionally, AAV-FKBP1b significantly reduced the area under the curve of the sAHP ($p < 0.01$).

Optical imaging of the Ca^{2+} transients coinciding with the sAHPs showed that AAV-FKBP1b injection significantly reduced the peak amplitude ($\%\Delta F/F$) and AUC of the Ca^{2+} transients compared with AAV-EGFP-injected cells (Fig. 6*B*; $p < 0.05$ and $p < 0.01$, respectively). Moreover, correlation analysis showed that the AUCs of the Ca^{2+} responses and sAHPs covaried across individual neurons (Fig. 6*C*; $r = 0.57$; $p < 0.05$).

In addition, the 7 Hz RSS-induced Ca^{2+} response, the rise time of which is strongly accelerated by RyR-mediated Ca^{2+} release (Gant et al., 2006), reached peak levels more slowly in neurons from aged AAV-FKBP1b-injected hippocampi (much as in neurons from young rats) compared with aged AAV-EGFP control neurons (increased τ, $p < 0.05$; Fig. 7*A*,*B*). No differences were observed in peak $\%\Delta Ca^{2+}$ during RSS, although the AUC of the RSS stimulated Ca^{2+} response was reduced in AAV-FKBP1b-treated hippocampal neurons ($p < 0.05$) because of the slower rise time to peak (Fig. 7*B*).

Discussion

The present study combines gene transfer approaches, behavioral assessment, intracellular electrophysiology and simultaneous Ca^{2+} imaging to elucidate mechanisms of brain aging-related neuronal Ca^{2+} dysregulation and cognitive impairment. We show, for the first time, that in aged rats in which hippocampal RyR-mediated Ca^{2+} transients and the Ca^{2+}-dependent sAHP are normally increased, hippocampal overexpression of FKBP1b dramatically reduced these responses, restoring them to levels found in young rats. Furthermore, this reduction of the sAHP was significantly correlated with reversal of the spatial memory impairment characteristically present in aged animals (Fig. 5).

These data strongly support the novel hypothesis that the deficit in hippocampal CA1 FKBP1b expression/function observed previously in aging rats (Kadish et al., 2009; Gant et al., 2014) is an underlying molecular mechanism of brain aging-related Ca^{2+} dysregulation and cognitive dysfunction. Specifically, our present results satisfy the critical prediction of a mechanistic molecular hypothesis (Falkow, 2004) that selectively counteracting the proposed pathogenic mechanism (FKBP1b deficit) should substantially lessen or reverse pathologic manifestations. Thus, together with our prior study on the effects of hippocampal FKBP1b knockdown (Gant et al., 2011), the findings here with FKBP1b overexpression indicate that FKBP1b is a key regulator of neuronal Ca^{2+} homeostasis and provide strong support for an FKBP1b-deficiency mechanistic hypothesis of unhealthy brain aging.

Relationship of cognitive impairment to Ca^{2+} dysregulation

FKBP1b overexpression reversed both cognitive impairment and Ca^{2+} dysregulation, raising the question of whether the reversal of Ca^{2+} dysregulation played a causal role in the enhanced cognition. As noted, several prior studies have found close associations between aging-related impairment of cognition/plasticity and increased sAHP magnitude or LTCC activity in hippocampal or cortical pyramidal neurons of rabbits, rats, and monkeys (Disterhoft et al., 1996; Thibault and Landfield, 1996; Tombaugh et al., 2005; Disterhoft and Oh, 2007; Luebke and Amatrudo, 2012). In addition to those correlational data, it has been shown that L-type Ca^{2+} channel blockers and other agents that reduce the sAHP can improve learning (Disterhoft and Oh, 2006). Furthermore, in the present work, we show that memory performance remained inversely correlated with sAHP magnitude following a molecular intervention (FKBP1b overexpression) that significantly reduced the sAHP (Fig. 5) and parallel Ca^{2+} transients (Fig. 6). The persistence of this association despite strong modification of the sAHP appears to substantially increase the likelihood of a causal influence of hippocampal Ca^{2+} responses on cognitive function.

However, reduction of the sAHP is clearly not the only pathway through which restoration of Ca^{2+} regulation could have enhanced learning. Presumably, multiple Ca^{2+}-related processes in addition to the sAHP were rescued by FKBP1b overexpression, and normalization of one or more of those might have contributed to enhanced spatial learning. For example, long-term potentiation, a lasting form of synaptic plasticity associated with learning, is a Ca^{2+}-dependent process shown to be impaired at some pyramidal cell synapses with aging (Lynch et al., 2006). Because it depends on dendritic spine cytoskeletal reorganization mediated by the Ca^{2+}-activated protease calpain (Lynch and Baudry, 1987; Lynch et al., 2006), excessive Ca^{2+} transients with aging could seemingly disrupt finely tuned spine calpain activation, resulting in impaired LTP. Accordingly, one pathway through which restoration of Ca^{2+} regulation by FKBP1b might have enhanced learning is via LTP rescue.

FKBP1b actions on Ca^{2+} regulation

FKBPs are immunophilins that bind the immunosuppressant drugs FK506 and rapamycin and mediate inhibition of immune response pathways. In addition, FKBPs are characterized by peptidylprolyl isomerase activity and are present in many cell types of the body. Although FKBPs have diverse functions, including protein folding, protein chaperoning and transcriptional regulation (Kang et al., 2008), only FKBP1b and its closely related isoform, FKBP1a/FKBP12, the smallest members of the FKBP protein family, are known to importantly regulate Ca^{2+} in excitable cells. In myocytes, FKBP1b and FKBP1a bind to and stabilize RyRs in the closed state, thereby inhibiting Ca^{2+}-induced Ca^{2+} release from the sarcoplasmic reticulum. Deletion of FKBP1b in cardiac cells (or FKBP1a in other myocytes) results in aberrant excitation–contraction coupling and "leaky" RyRs (Zalk et al., 2007; MacMillan, 2013). Although it has not been known whether the small FKBPs regulate Ca^{2+} release in neurons, we found previously that FKBP1b knockdown/disruption in pyramidal neurons results in an increased sAHP magnitude, faster rise time of the RSS-induced Ca^{2+} response, and an increase in plasma membrane LTCC activity (Gant et al., 2011). Conversely, we show here that FKBP1b overexpression had the opposite effects on these responses, reducing the sAHP and its parallel Ca^{2+} transient and slowing the rise of the RSS-activated Ca^{2+} response. Since sAHP magnitude and RSS-response rise time are highly dependent on RyR-mediated Ca^{2+} release (i.e., are suppressed by ryanodine; Gant et al., 2006), our data show that, as in myocytes, FKBP1b in neurons inhibits CICR from RyRs. Additionally, in neurons, FKBP1b inhibits membrane LTCC activity. Thus, FKBP1b appears to exert substantial regulatory control over Ca^{2+}-dependent signaling in neurons.

Small FKBPs also inhibit the mammalian target of rapamycin (mTOR) (Hoeffer et al., 2008; Hausch et al., 2013), an important regulator of growth and plasticity pathways (Hoeffer and Klann, 2010). In the brain, mTOR is a target of BDNF, which plays major roles in neural plasticity, neurite outgrowth, and neuroprotection (Lynch et al., 2006; Scharfman and MacLusky, 2006). Although mTOR can apparently modulate Ca^{2+} release from IP3 receptors in smooth muscle, it is not known to participate in RyR-mediated Ca^{2+} release (MacMillan and McCarron, 2009). Therefore, it appears unlikely that the FKBP–mTOR pathway contributed significantly to the FKBP1b-induced reductions in RyR-mediated Ca^{2+} responses seen in the present study.

Reversibility of Ca^{2+} dysregulation and cognitive aging

A particularly striking finding in this study is that major aging-related changes in hippocampal Ca^{2+} regulation and spatial memory could be fully reversed by FKBP1b overexpression at >20 months of age. In rats, detectable alterations in hippocampal Ca^{2+}-dependent processes (Gant et al., 2006; Lynch et al., 2006) and MWM memory performance (Markowska, 1999; Kadish et al., 2009) normally emerge by midlife (~12 months old) and are well established by 20 months of age. Reversibility of learning deficits in aging animals has also been seen previously in studies of Ca^{2+} channel antagonists (Disterhoft and Oh, 2006) and antioxidants (Cartford et al., 2002), among other treatments. This reversibility of cognitive deficits at late ages seems surprising considering the numerous reports of aging-related structural changes in brain synapses, axons, and dendrites, many of which have been correlated with declining cognitive functions (Peters et al., 1996; Rosenzweig and Barnes, 2003; Masliah et al., 2006; Morrison and Hof, 2007; Scheff et al., 2007). One possible explanation for reversibility despite morphological alterations may be that the aging brain compensates for some localized anatomical changes, but is unable to compensate for a widely acting and fundamental deficit such as Ca^{2+} dysregulation. Alternatively, morphological alterations may be more reversible than is generally recognized (Morrison and Hof, 2007). Regardless of the reasons, however, the observations on reversibility may have important translational implications.

Potential relevance to Alzheimer's disease

Advanced age is essentially the leading risk factor for AD (Reitz et al., 2011), suggesting that some processes seen in normal brain aging increase susceptibility to neurodegeneration and AD. Considerable evidence indicates that one of those processes may be neuronal Ca^{2+} dysregulation. Elevated intracellular [Ca^{2+}] induces electrophysiological deterioration of hippocampal neurons (Scharfman and Schwartzkroin, 1989), and elevated Ca^{2+} release from RyRs is toxic to neurons (Verkhratsky, 2005; Bezprozvanny and Mattson, 2008). Importantly, significant Ca^{2+} dysregulation is also present in AD, as evidenced by altered calcineurin and calpain activation, modified Ca^{2+} release, and disturbance of Ca^{2+} signaling by AD-related pathology (Nixon et al., 1994; Gibson et al., 1996; Rozkalne et al., 2011; Hudry et al., 2012; Overk et al., 2014). Furthermore, mouse models of AD exhibit dysregulated Ca^{2+} release from RyRs and IP3 receptors, as well as altered Ca^{2+} channel activity (Disterhoft and Oh, 2006; Stutzmann et al., 2006; Thibault et al., 2012; Wang and Mattson, 2014). *In vivo* Ca^{2+} imaging in AD model mice also has revealed elevation of Ca^{2+} in cortical neuron dendrites, which is more pronounced in locations proximal to β amyloid plaques (Kuchibhotla et al., 2008).

In previous microarray studies, we found that hippocampal FKBP1b gene expression is downregulated in human subjects with incipient or advanced AD (Blalock et al., 2004) as well as in normally aging rats (Kadish et al., 2009; Gant et al., 2014). Together with the present results, those findings raise the intriguing possibility that declining expression of the gene encoding FKBP1b during normal brain aging might act synergistically or additively with other sources of pathology to exacerbate Ca^{2+} dysregulation and increase susceptibility to and/or progression of AD. Thus, if supported by further studies, the present findings suggest that cell-specific elevation of FKBP1b expression may be a feasible new approach for modifying the course of deleterious brain aging and, possibly, early stage Alzheimer's disease.

References

Andrade R, Foehring RC, Tzingounis AV (2012) The calcium-activated slow AHP: cutting through the Gordian knot. Front Cell Neurosci 6:47. Medline

Andreasen M, Lambert JD (1995) The excitability of CA1 pyramidal cell dendrites is modulated by a local Ca(2+)-dependent K(+)-conductance. Brain Res 698:193–203. CrossRef Medline

Aschauer DF, Kreuz S, Rumpel S (2013) Analysis of transduction efficiency, tropism and axonal transport of AAV serotypes 1, 2, 5, 6, 8 and 9 in the mouse brain. PLoS One 8:e76310. CrossRef Medline

Betley JN, Sternson SM (2011) Adeno-associated viral vectors for mapping, monitoring, and manipulating neural circuits. Hum Gene Ther 22:669–677. CrossRef Medline

Bezprozvanny I, Mattson MP (2008) Neuronal calcium mishandling and the pathogenesis of Alzheimer's disease. Trends Neurosci 31:454–463. CrossRef Medline

Blalock EM, Geddes JW, Chen KC, Porter NM, Markesbery WR, Landfield PW (2004) Incipient Alzheimer's disease: microarray correlation analyses reveal major transcriptional and tumor suppressor responses. Proc Natl Acad Sci U S A 101:2173–2178. CrossRef Medline

Bosch MK, Nerbonne JM, Ornitz DM (2014) Dual transgene expression in murine cerebellar Purkinje neurons by viral transduction *in vivo*. PLoS One 9:e104062. CrossRef Medline

Broekman ML, Comer LA, Hyman BT, Sena-Esteves M (2006) Adeno-associated virus vectors serotyped with AAV8 capsid are more efficient than AAV-1 or -2 serotypes for widespread gene delivery to the neonatal mouse brain. Neuroscience 138:501–510. CrossRef Medline

Buzsáki G, Moser EI (2013) Memory, navigation and theta rhythm in the hippocampal-entorhinal system. Nat Neurosci 16:130–138. CrossRef Medline

Cartford MC, Gemma C, Bickford PC (2002) Eighteen-month-old Fischer 344 rats fed a spinach-enriched diet show improved delay classical eyeblink conditioning and reduced expression of tumor necrosis factor alpha (TNFalpha) and TNFbeta in the cerebellum. J Neurosci 22:5813–5816. Medline

Castle MJ, Gershenson ZT, Giles AR, Holzbaur EL, Wolfe JH (2014) Adeno-associated virus serotypes 1, 8, and 9 share conserved mechanisms for anterograde and retrograde axonal transport. Hum Gene Ther 25:705–720. CrossRef Medline

Cearley CN, Wolfe JH (2006) Transduction characteristics of adeno-associated virus vectors expressing cap serotypes 7, 8, 9, and Rh10 in the mouse brain. Mol Ther 13:528–537. CrossRef Medline

Disterhoft JF, Oh MM (2006) Pharmacological and molecular enhancement of learning in aging and Alzheimer's disease. J Physiol Paris 99:180–192. CrossRef Medline

Disterhoft JF, Oh MM (2007) Alterations in intrinsic neuronal excitability during normal aging. Aging Cell 6:327–336. CrossRef Medline

Disterhoft JF, Thompson LT, Moyer JR Jr, Mogul DJ (1996) Calcium-dependent afterhyperpolarization and learning in young and aging hippocampus. Life Sci 59:413–420. CrossRef Medline

Falkow S (2004) Molecular Koch's postulates applied to bacterial pathogenicity–a personal recollection 15 years later. Nat Rev Microbiol 2:67–72. CrossRef Medline

Foster TC, Norris CM (1997) Age-associated changes in Ca(2+)-dependent processes: relation to hippocampal synaptic plasticity. Hippocampus 7:602–612. CrossRef Medline

Gallagher M, Rapp PR (1997) The use of animal models to study the effects of aging on cognition. Annu Rev Psychol 48:339–370. CrossRef Medline

Gant JC, Sama MM, Landfield PW, Thibault O (2006) Early and simultaneous emergence of multiple hippocampal biomarkers of aging is mediated by Ca2+-induced Ca2+ release. J Neurosci 26:3482–3490. CrossRef Medline

Gant JC, Chen KC, Norris CM, Kadish I, Thibault O, Blalock EM, Porter NM, Landfield PW (2011) Disrupting function of FK506-binding protein 1b/12.6 induces the Ca(2)+-dysregulation aging phenotype in hippocampal neurons. J Neurosci 31:1693–1703. CrossRef Medline

Gant JC, Blalock EM, Chen KC, Kadish I, Porter NM, Norris CM, Thibault O, Landfield PW (2014) FK506-binding protein 1b/12.6: a key to aging-related hippocampal Ca2+ dysregulation? Eur J Pharmacol 739:74–82. CrossRef Medline

Gibson GE, Peterson C (1987) Calcium and the aging nervous system. Neurobiol Aging 8:329–343. CrossRef Medline

Gibson GE, Zhang H, Toral-Barza L, Szolosi S, Tofel-Grehl B (1996) Calcium stores in cultured fibroblasts and their changes with Alzheimer's disease. Biochim Biophys Acta 1316:71–77. CrossRef Medline

Hausch F, Kozany C, Theodoropoulou M, Fabian AK (2013) FKBPs and the Akt/mTOR pathway. Cell Cycle 12:2366–2370. CrossRef Medline

Hebert LE, Weuve J, Scherr PA, Evans DA (2013) Alzheimer disease in the United States (2010–2050) estimated using the 2010 census. Neurology 80:1778–1783. CrossRef Medline

Hemond P, Jaffe DB (2005) Caloric restriction prevents aging-associated changes in spike-mediated Ca2+ accumulation and the slow afterhyperpolarization in hippocampal CA1 pyramidal neurons. Neuroscience 135:413–420. CrossRef Medline

Hoeffer CA, Klann E (2010) mTOR signaling: at the crossroads of plasticity, memory and disease. Trends Neurosci 33:67–75. CrossRef Medline

Hoeffer CA, Tang W, Wong H, Santillan A, Patterson RJ, Martinez LA, Tejada-Simon MV, Paylor R, Hamilton SL, Klann E (2008) Removal of FKBP12 enhances mTOR-Raptor interactions, LTP, memory, and perseverative/repetitive behavior. Neuron 60:832–845. CrossRef Medline

Hudry E, Wu HY, Arbel-Ornath M, Hashimoto T, Matsouaka R, Fan Z, Spires-Jones TL, Betensky RA, Bacskai BJ, Hyman BT (2012) Inhibition of the NFAT pathway alleviates amyloid beta neurotoxicity in a mouse model of Alzheimer's disease. J Neurosci 32:3176–3192. CrossRef Medline

Kadish I, Thibault O, Blalock EM, Chen KC, Gant JC, Porter NM, Landfield PW (2009) Hippocampal and cognitive aging across the lifespan: a bioenergetic shift precedes and increased cholesterol trafficking parallels memory impairment. J Neurosci 29:1805–1816. CrossRef Medline

Kang CM, Hong Y, Dhe-Paganon S, Yoon HS (2008) FKBP family proteins: immunophilins with versatile biological functions. Neurosignals 16:318–325. CrossRef Medline

Kaplitt MG, Feigin A, Tang C, Fitzsimons HL, Mattis P, Lawlor PA, Bland RJ,

Young D, Strybing K, Eidelberg D, During MJ (2007) Safety and tolerability of gene therapy with an adeno-associated virus (AAV) borne GAD gene for Parkinson's disease: an open label, phase I trial. Lancet 369:2097–2105. CrossRef Medline

Khachaturian ZS (1989) The role of calcium regulation in brain aging: reexamination of a hypothesis. Aging (Milano) 1:17–34.

Kuchibhotla KV, Goldman ST, Lattarulo CR, Wu HY, Hyman BT, Bacskai BJ (2008) Aβ plaques lead to aberrant regulation of calcium homeostasis *in vivo* resulting in structural and functional disruption of neuronal networks. Neuron 59:214–225. CrossRef Medline

Kumar A, Foster TC (2005) Intracellular calcium stores contribute to increased susceptibility to LTD induction during aging. Brain Res 1031:125–128. CrossRef Medline

Lancaster B, Hu H, Ramakers GM, Storm JF (2001) Interaction between synaptic excitation and slow afterhyperpolarization current in rat hippocampal pyramidal cells. J Physiol 536:809–823. CrossRef Medline

Landfield PW (1987) "Increased calcium-current" hypothesis of brain aging. Neurobiol Aging 8:346–347. CrossRef Medline

Landfield PW, Pitler TA (1984) Prolonged Ca2+-dependent afterhyperpolarizations in hippocampal neurons of aged rats. Science 226:1089–1092. CrossRef Medline

Lima PA, Marrion NV (2007) Mechanisms underlying activation of the slow AHP in rat hippocampal neurons. Brain Res 1150:74–82. CrossRef Medline

Luebke JI, Amatrudo JM (2012) Age-related increase of sI(AHP) in prefrontal pyramidal cells of monkeys: relationship to cognition. Neurobiol Aging 33:1085–1095. CrossRef Medline

Lynch G, Baudry M (1987) Brain spectrin, calpain and long-term changes in synaptic efficacy. Brain Res Bull 18:809–815. CrossRef Medline

Lynch G, Rex CS, Gall CM (2006) Synaptic plasticity in early aging. Ageing Res Rev 5:255–280. CrossRef Medline

MacMillan D (2013) FK506 binding proteins: cellular regulators of intracellular Ca2+ signalling. Eur J Pharmacol 700:181–193. CrossRef Medline

MacMillan D, McCarron JG (2009) Regulation by FK506 and rapamycin of Ca2+ release from the sarcoplasmic reticulum in vascular smooth muscle: the role of FK506 binding proteins and mTOR. Br J Pharmacol 158:1112–1120. CrossRef Medline

Madison DV, Nicoll RA (1984) Control of the repetitive discharge of rat CA 1 pyramidal neurones *in vitro*. J Physiol 354:319–331. CrossRef Medline

Magee JC, Johnston D (1997) A synaptically controlled, associative signal for Hebbian plasticity in hippocampal neurons. Science 275:209–213. CrossRef Medline

Markowska AL (1999) Sex dimorphisms in the rate of age-related decline in spatial memory: relevance to alterations in the estrous cycle. J Neurosci 19:8122–8133. Medline

Masliah E, Crews L, Hansen L (2006) Synaptic remodeling during aging and in Alzheimer's disease. J Alzheimers Dis 9:91–99. Medline

McCown TJ (2010) The future of epilepsy treatment: focus on adeno-associated virus vector gene therapy. Drug News Perspect 23:281–286. CrossRef Medline

Morrison JH, Hof PR (2007) Life and death of neurons in the aging cerebral cortex. Int Rev Neurobiol 81:41–57. CrossRef Medline

Moser MB, Moser EI, Forrest E, Andersen P, Morris RG (1995) Spatial learning with a minislab in the dorsal hippocampus. Proc Natl Acad Sci U S A 92:9697–9701. CrossRef Medline

Moyer JR Jr, Thompson LT, Black JP, Disterhoft JF (1992) Nimodipine increases excitability of rabbit CA1 pyramidal neurons in an age- and concentration-dependent manner. J Neurophysiol 68:2100–2109. Medline

Murchison D, Griffith WH (2007) Calcium buffering systems and calcium signaling in aged rat basal forebrain neurons. Aging Cell 6:297–305. CrossRef Medline

Murphy GG, Shah V, Hell JW, Silva AJ (2006) Investigation of age-related cognitive decline using mice as a model system: neurophysiological correlates. Am J Geriatr Psychiatry 14:1012–1021. CrossRef Medline

Nixon RA, Saito KI, Grynspan F, Griffin WR, Katayama S, Honda T, Mohan PS, Shea TB, Beermann M (1994) Calcium-activated neutral proteinase (calpain) system in aging and Alzheimer's disease. Ann N Y Acad Sci 747:77–91. Medline

Oh MM, Oliveira FA, Waters J, Disterhoft JF (2013) Altered calcium metabolism in aging CA1 hippocampal pyramidal neurons. J Neurosci 33:7905–7911. CrossRef Medline

Overk CR, Cartier A, Shaked G, Rockenstein E, Ubhi K, Spencer B, Price DL, Patrick C, Desplats P, Masliah E (2014) Hippocampal neuronal cells that accumulate alpha-synuclein fragments are more vulnerable to Aβ oligomer toxicity via mGluR5–implications for dementia with Lewy bodies. Mol Neurodegener 9:18. CrossRef Medline

Peters A, Rosene DL, Moss MB, Kemper TL, Abraham CR, Tigges J, Albert MS (1996) Neurobiological bases of age-related cognitive decline in the rhesus monkey. J Neuropathol Exp Neurol 55:861–874. CrossRef Medline

Reitz C, Brayne C, Mayeux R (2011) Epidemiology of Alzheimer disease. Nat Rev Neurol 7:137–152. CrossRef Medline

Rosenzweig ES, Barnes CA (2003) Impact of aging on hippocampal function: plasticity, network dynamics, and cognition. Prog Neurobiol 69:143–179. CrossRef Medline

Rowe WB, Blalock EM, Chen KC, Kadish I, Wang D, Barrett JE, Thibault O, Porter NM, Rose GM, Landfield PW (2007) Hippocampal expression analyses reveal selective association of immediate-early, neuroenergetic, and myelinogenic pathways with cognitive impairment in aged rats. J Neurosci 27:3098–3110. CrossRef Medline

Rozkalne A, Hyman BT, Spires-Jones TL (2011) Calcineurin inhibition with FK506 ameliorates dendritic spine density deficits in plaque-bearing Alzheimer model mice. Neurobiol Dis 41:650–654. CrossRef Medline

Sah P, Bekkers JM (1996) Apical dendritic location of slow afterhyperpolarization current in hippocampal pyramidal neurons: implications for the integration of long-term potentiation. J Neurosci 16:4537–4542. Medline

Salegio EA, Samaranch L, Kells AP, Forsayeth J, Bankiewicz K (2012) Guided delivery of adeno-associated viral vectors into the primate brain. Adv Drug Deliv Rev 64:598–604. CrossRef Medline

Scharfman HE, MacLusky NJ (2006) Estrogen and brain-derived neurotrophic factor (BDNF) in hippocampus: complexity of steroid hormone-growth factor interactions in the adult CNS. Front Neuroendocrinol 27:415–435. CrossRef Medline

Scharfman HE, Schwartzkroin PA (1989) Protection of dentate hilar cells from prolonged stimulation by intracellular calcium chelation. Science 246:257–260. CrossRef Medline

Scheff SW, Price DA, Schmitt FA, DeKosky ST, Mufson EJ (2007) Synaptic alterations in CA1 in mild Alzheimer disease and mild cognitive impairment. Neurology 68:1501–1508. CrossRef Medline

Stutzmann GE, Smith I, Caccamo A, Oddo S, Laferla FM, Parker I (2006) Enhanced ryanodine receptor recruitment contributes to Ca2+ disruptions in young, adult, and aged Alzheimer's disease mice. J Neurosci 26:5180–5189. CrossRef Medline

Thibault O, Landfield PW (1996) Increase in single L-type calcium channels in hippocampal neurons during aging. Science 272:1017–1020. CrossRef Medline

Thibault O, Hadley R, Landfield PW (2001) Elevated postsynaptic [Ca2+]i and L-type calcium channel activity in aged hippocampal neurons: relationship to impaired synaptic plasticity. J Neurosci 21:9744–9756. Medline

Thibault O, Gant JC, Landfield PW (2007) Expansion of the calcium hypothesis of brain aging and Alzheimer's disease: minding the store. Aging Cell 6:307–317. CrossRef Medline

Thibault O, Pancani T, Landfield PW, Norris CM (2012) Reduction in neuronal L-type calcium channel activity in a double knock-in mouse model of Alzheimer's disease. Biochim Biophys Acta 1822:546–549. CrossRef Medline

Toescu EC, Verkhratsky A (2007) The importance of being subtle: small changes in calcium homeostasis control cognitive decline in normal aging. Aging Cell 6:267–273. CrossRef Medline

Tombaugh GC, Rowe WB, Rose GM (2005) The slow afterhyperpolarization in hippocampal CA1 neurons covaries with spatial learning ability in aged Fisher 344 rats. J Neurosci 25:2609–2616. CrossRef Medline

Verkhratsky A (2005) Physiology and pathophysiology of the calcium store in the endoplasmic reticulum of neurons. Physiol Rev 85:201–279. CrossRef Medline

Wang Y, Mattson MP (2014) L-type Ca2+ currents at CA1 synapses, but not CA3 or dentate granule neuron synapses, are increased in 3xTgAD mice in an age-dependent manner. Neurobiol Aging 35:88–95. CrossRef Medline

Zalk R, Lehnart SE, Marks AR (2007) Modulation of the ryanodine receptor and intracellular calcium. Annu Rev Biochem 76:367–385. CrossRef Medline

Author Manuscript

Author Manuscript

Author Manuscript

Author Manuscript

HHS Public Access

Author manuscript

Neuron. Author manuscript; available in PMC 2018 March 28.

Published in final edited form as:

Neuron. 2016 October 19; 92(2): 372–382. doi:10.1016/j.neuron.2016.09.021.

A designer AAV variant permits efficient retrograde access to projection neurons

D. Gowanlock R. Tervo[1], **Bum-Yeol Huang**[2,#], **Sarada Viswanathan**[1], **Thomas Gaj**[2], **Maria Lavzin**[1,3], **Kimberly D. Ritola**[1], **Sarah Lindo**[1], **Susan Michael**[1], **Elena Kuleshova**[1,5], **David Ojala**[2], **Cheng-Chiu Huang**[1,¥], **Charles R. Gerfen**[1,4], **Jackie Schiller**[1,3], **Joshua T. Dudman**[1], **Adam W. Hantman**[1], **Loren L. Looger**[1], **David V. Schaffer**[2], and **Alla Y. Karpova**[1]

[1]Janelia Research Campus, Howard Hughes Medical Institute, Ashburn, VA, USA

[2]Department of Chemical Engineering and Helen Wills Neuroscience Institute, University of California, Berkeley, CA, USA

[3]Department of Physiology, Technion Medical School, Bat-Galim, Haifa, Israel

[4]Laboratory of Systems Neuroscience, National Institute of Mental Health, Bethesda, MD, USA

[5]Institute of Higher Nervous Activity and Neurophysiology of the Russian Academy of Sciences, Moscow, Russia

Summary

Efficient retrograde access to projection neurons for the delivery of sensors and effectors constitutes an important and enabling capability for neural circuit dissection. Such an approach would also be useful for gene therapy, including the treatment of neurodegenerative disorders characterized by pathological spread through functionally connected and highly distributed networks. Viral vectors, in particular, are powerful gene delivery vehicles for the nervous system, but all available tools suffer from inefficient retrograde transport or limited clinical potential. To address this need, we applied *in vivo* directed evolution to engineer potent retrograde functionality into the capsid of adeno-associated virus (AAV) — a vector that has shown promise in neuroscience research and the clinic. A newly evolved variant, rAAV2-retro, permits robust retrograde access to projection neurons with efficiency comparable to classical synthetic retrograde tracers, and enables sufficient sensor/effector expression for functional circuit interrogation and *in vivo* genome editing in targeted neuronal populations.

Correspondence to AYK – alla@janelia.hhmi.org, DVS – schaffer@berkeley.edu.
[#]Present address: 4D Molecular Therapeutics, Emeryville, CA
[¥]Present address: TLC Biopharmaceuticals, Inc., South San Francisco, CA

Author Contributions: L.L.L, D.V.S, and A.Y.K. conceived the project; D.G.R.T., B-Y.H., J.T.D., A.W.H., L.L.L., D.V.S. and A.Y.K. designed and oversaw the molecular evolution process; B-Y.H. performed library packaging, amplifications, and sequencing; K.D.R. designed and oversaw viral production and quality control process; D.G.R.T., S. V., T. G., M.L., S. L., S.M., E.K., D.O. and C-C.H. performed experiments; D.G.R.T. wrote custom analysis code, D.G.R.T., S.V., T.G., and D.O. analyzed the data; D.G.R.T., L.L.L., D.V.S, and A.Y.K. wrote the manuscript. C.R.G. and J.S. provided essential reagents, expertise, and input to the manuscript.

Author Manuscript Author Manuscript Author Manuscript Author Manuscript

Introduction

Brain functions such as perception, cognition, and the control of movement depend on the coordinated action of large-scale neuronal networks, local circuit modules linked together by long-range connections (Miller and Vogt, 1984; Tomioka et al., 2005; Ramón y Cajol, 1911). Such long-range connections are formed by projection neurons that often comprise several intermingled classes, each projecting to a distinct constellation of downstream targets. Projection neurons have also been implicated in the spread of several neurodegenerative diseases from spatially localized sites of onset (Guo and Lee, 2014; Seeley et al., 2009). Thus, the ability to selectively target specific classes of projection neurons for transgene delivery (*e.g.* for activity monitoring or manipulation, or genome editing for targeted gene knock-outs or repair of pathological mutations) will be important both for gaining insights into how large-scale networks contribute to brain function and, in the long-run, for therapeutic intervention in neurodegenerative diseases.

Viral vectors constitute an important class of tools for introducing transgenes into specific neuronal populations and are by far the best option for genetic access to target projection neurons through entry at axonal terminals and retrograde transport of their payload to the cell nuclei. A number of naturally evolved neurotropic viruses exhibit retrograde spread as part of their lifecycle, including rabies (Baer et al., 1965; Callaway and Luo, 2015; Wickersham et al., 2007), poliovirus (Ohka et al., 1998) and herpes simplex virus (HSV) (Ugolini et al., 1987) among others. Of these, rabies virus is particularly neuro-invasive (Coulon et al., 1989) and quickly propagates through the nervous system through trans-cellular transfer (Kelly and Strick, 2000). However, its potential for both biological investigation and gene therapy is hampered by excessive virulence (Schnell et al., 2010), though progress is being made to reduce its toxicity (Reardon et al., 2016). In addition to naturally neurotropic strains, many other viruses can infect neurons when administered directly to the nervous system, with “pseudorabies” (SuHV1, actually a herpesvirus), adenoviruses and lentiviruses used most commonly in animal research. Canine adenovirus-2 (CAV-2) displays the best infectivity and retrograde transport of this class of viruses (Soudais et al., 2001) and has increasingly become the reagent of choice for accessing projection neurons (Junyent and Kremer, 2015). However, CAV-2 permits only modest levels of transgene expression, displays some toxicity (Piersanti et al., 2013; Simão et al., 2015) and is currently not easily compatible with scalable, robust production for the generation of clinical-grade or even large animal studies (Kremer et al., 2000). Thus, the development of a non-toxic, readily manufactured viral vector that affords flexible packaging of different transgenes, is robustly internalized and retrogradely transported by axons, and supports long-term, high-level payload expression remains a pressing need.

Recombinant adeno-associated viruses (rAAVs) have emerged as an effective platform for *in vivo* gene therapy, as they mediate high-level transgene expression, are non-toxic, and evoke minimal immune responses (Kaplitt et al., 2007). These properties were at the core of the decision to grant the first full regulatory approval of any gene therapy treatment to rAAV-mediated restoration of lipoprotein lipase deficiency (Gaudet et al., 2010). rAAVs hold great promise in clinical trials for a range of neurological disorders (Ojala et al., 2014), and they constitute some of the most widespread vectors in neuroscience research (Murlidharan et al.,

Author Manuscript Author Manuscript Author Manuscript Author Manuscript

2014). Since the original discovery that AAV can undergo retrograde transport (Kaspar et al., 2002), rAAVs have afforded some degree of retrograde access to projection neurons in select circuits (Castle et al., 2014; Hollis Ii et al., 2008; Kaspar et al., 2002; Kaspar et al., 2003; Rothermel et al., 2013; Taymans et al., 2007; Towne et al., 2010), but their natural propensity for retrograde transport is low, hampering efforts to address the role of projection neurons in circuit computations or disease progression. Here we describe the *in vivo* directed evolution (Kotterman and Schaffer, 2014) of a new rAAV variant (rAAV2-retro) that – in addition to its regular ability to infect neuronal cell bodies at the site of exposure – is robustly internalized by axons and mediates retrograde access to projection neurons with efficiency comparable to classical retrograde labeling reagents such as synthetic dyes. The rAAV2-retro gene delivery system can be used on its own or in conjunction with Cre recombinase driver lines to achieve long-term, high-level transgene expression that is sufficient for effective functional interrogation of neural circuit function, as well as for genome editing in targeted neuronal populations.

Results

Directed evolution of rAAV2-retro

To engineer novel rAAVs with enhanced retrograde transport, we designed an *in vivo* directed-evolution approach to enrich for rAAV capsid variants that were efficiently transported to cell bodies of neurons sending long-range projections to the site of virus injection in the mouse brain (Figure 1A and Experimental Procedures). To maximize the likelihood of recovering a variant with the desired properties, we started with a diverse mixture of previously described libraries of rAAV *cap* variants (Koerber et al., 2008; Koerber et al., 2009; Koerber et al., 2006; Müller et al., 2003). Viral particles were packaged in a way that linked each capsid variant to the AAV genome containing the corresponding *cap* gene, and the final pool of capsid variants included point mutants, variants with a random 7-mer (plus 3 constant flanking residues) peptide insertion into the region AAV2 utilizes to bind its co-receptor heparin (Kern et al., 2003), and random chimeras of capsid gene sequences from seven parental serotypes (Figure 1A and Experimental Procedures). To identify variants with broad retrograde tropism, we targeted two independent populations of projection neurons: striatal GABAergic neurons projecting to substantia nigra pars reticulata (SNr) and glutamatergic hindbrain neurons projecting to the cerebellar cortex. Three weeks following injection of the entire pool of rAAV variants into the SNr or cerebellum (one injection per animal), striatal or hindbrain tissue, respectively, was removed, the *cap* sequences were recovered by PCR, and virus was repackaged (Figure 1B). After two more selection steps, error-prone PCR was performed to further diversify the library, followed by two final *in vivo* selection steps.

We sequenced 30 *cap* variants after the fourth round of evolution, and the majority originated from the insertion library and contained exogenous 10-mer peptides between N587 and R588 of the wild-type AAV2 VP1 capsid gene (Müller et al., 2003) (see Experimental Procedures). Intriguingly, all of the recovered inserts were of the form **LA**xxDxTKx**A** or **LA**xDxTKxx**A**; mutations elsewhere in the sequence were also enriched (Table S1). We sequenced a further 22 clones after the fifth round of evolution, and with this

Author Manuscript Author Manuscript Author Manuscript Author Manuscript

additional round of evolution, all sequences were AAV2 mutants with **LA**xxDxTKx**A/ LA**xDxTKxx**A** insertions (Table S1), demonstrating a marked degree of further convergence. Such convergence suggested that specific peptide insertions into the heparin-binding loop were largely responsible for the retrograde functionality, with potential secondary contributions from the other sites (see Discussion).

We next focused a secondary screen (not shown) on seventeen isolated variants possessing different combinations of peptide insertions and point mutations in the capsid sequence. To apply a high level of stringency, the chosen variants were packaged with enhanced green fluorescent protein (EGFP) transgene driven by the *CMV* promoter, which is typically weak in neurons. For each capsid variant, we evaluated its ability to deliver sufficient payload to cell bodies in key afferent regions to permit the detection of non-antibody-amplified EGFP signal three weeks after injection. The clone (insert **LA**DQDYTKT**A**+ V708I + N382D) that displayed the strongest retrograde transport in two independent circuits in this secondary screen (cortex to globus pallidus and inferior olive/basal pontine nuclei (BPN) to cerebellum) was chosen for further analysis and named rAAV2-retro. When we assessed two additional promoters more commonly used in rodent *in vivo* studies (*CAG* – Figure 1B, or human *Synapsin-1*, data not shown), we observed remarkable retrograde labeling efficiency with this rAAV variant in a range of different circuits in mice and rats (Figure 1B, Figure S1, Movie S1 and see below). Swapping the 7-mer insertion to one of the other recovered sequences or adding additional point mutations identified in the screen did not lead to further increases in retrograde transport (data not shown).

Efficient retrograde access to projection neurons

The corticopontine tract is a remarkably convergent descending motor pathway, contributing more than95% of the afferents to the basal pontine nuclei (BPN) (Brodal and Bjaalie, 1992). This pathway is therefore particularly advantageous for quantifying the efficiency of viral uptake and retrograde transport by axonal terminals of projection neurons. Indeed, injection of rAAV2-retro into the BPN resulted in dense labeling of layer V neurons (Figure 2A), consistent with past tracing studies (Legg et al., 1989).

We therefore next compared the efficacy of retrograde transport in the corticopontine circuit for rAAV2-retrovs. several commonly used AAV serotypes, under identical infection and processing conditions (Figure 2B–D, Experimental Procedures). To ensure quantification accuracy and to eliminate the possible confound of cell-to-cell variability in transgene expression level, we used the AAV to deliver Cre recombinase to Rosa26-Lox-STOP-Lox-H2B-EGFP (histone-fused EGFP) transgenic mice (He et al., 2012). Even a low concentration of the Cre enzyme is sufficient to turn on the expression of such a Cre-dependent cassette (Nagy, 2000), and the stringent nuclear localization of the histone-fused reporter affords unambiguous identification of infected cells, without confounding neuropil signal.

We used a semi-automated analysis procedure to calculate the linear density of infected cortical projection neurons in imaged sagittal sections from mouse brains harvested three weeks after local virus injection in the BPN (Figure 2C, Experimental Procedures). For animals infected with rAAV2, we observed minimal cortical GFP expression (linear density

Author Manuscript Author Manuscript Author Manuscript Author Manuscript

0.98 ± 0.20 neurons/mm, mean ± S.E.M., n=5; Figures 2B, middle panel). In contrast, and in agreement with the earlier observation (Figure 2A), a dense layer of GFP-positive layer V projection neurons could be observed throughout the rostro-caudal axis of the cortex in rAAV2-retro-injected animals (linear density 130.11±11.08 neurons/mm, n=4; Figure 2B, lower panel). None of the other commonly used AAV serotypes, nor the canine adenovirus-2,matched the retrograde efficiency of the engineered rAAV2-retro variant (linear density AAV1: 0.05 ± 0.04, AAV2: 0.98 ± 0.2, AAV5: 2.38 ± 1.24, AAV8: 1.43 ± 1.43, AAV9: 1.98 ± 0.86, DJ: 24.82 ± 14.32, CAV-2: 5.56 ± 4.13, n=3 to 5 each; Figure 2D, Figure S2). The poor performance by the common AAV serotypes could not have arisen simply as a result of differences in infectivity since even the serotypes displaying similar labeling efficiency at the injection site to that of rAAV2-retro (rAAV2, rAAV9) did not permit efficient retrograde access to corticopontine neurons (Figure S3). Strikingly, the density of cortical projection neurons labeled by rAAV2-retro was comparable to that achieved with Fluoro-Gold (Schmued and Fallon, 1986), a robust synthetic retrograde tracer (linear density 81.03 ± 11.08 neurons/mm, n=3). Thus, rAAV2-retro exhibits up to two orders of magnitude enhancement over existing serotypes in retrograde access to corticopontine projection neurons, and rivals the efficacy of synthetic retrograde tracers.

Generality of retrograde functionality

We next examined whether the retrograde functionality of rAAV2-retro extended to other circuits, specifically by characterizing the extent to which it labeled various afferents to the dorsomedial striatum (DMS) – a part of the basal ganglia that receives long-range inputs from a variety of cortical and subcortical areas (Pan et al., 2010). We found that the efficacy of rAAV2-retro-mediated retrograde access to the strongest afferent inputs into DMS—cortex, thalamus and amygdala—was comparable to that of fluorescent beads classically used for retrograde tracing (Figure 3A). To provide an unbiased estimate for the number of retrogradely labeled neurons in all brain areas known to provide significant long-range input to the DMS, we next assigned any detected fluorescent label in an imaged section of the mouse brain to specific brain areas by aligning the section to the annotated Allen Brain Atlas (Figure 3B–C). Quantitative analysis (Figure 3B-C) revealed that strong retrograde labeling was found in the vast majority of regions that have been previously reported to send prominent projections to the striatum (Pan et al., 2010). In one noticeable exception, only modest labeling was observed in the substantia nigra pars compacta (SNc), despite it being the source of a strong dopaminergic input to the DMS (Figure 3C, arrow at cell count for SNc). A small subset of projection neuron classes was found to be similarly refractory to retrograde access by rAAV2-retro in some of the other circuits tested (Table S2; note that all other AAV serotypes tested also failed to label these projections). Despite these exceptions, rAAV2-retro is broadly applicable for retrograde access to projection neurons within the central nervous system. We note that no rAAV2-retro-mediated labeling of unexpected pathways has been reported to date (Table S2), however additional studies will be necessary to fully rule out its ability to infect axons of passage.

Retrograde access to genetically defined neuronal populations

We also determined whether the retrograde functionality of rAAV2-retro could be combined with the specificity of Cre transgenic lines to enable the interrogation of specific classes of

Author Manuscript Author Manuscript Author Manuscript Author Manuscript

projection neurons. Specifically, we asked whether we could combine rAAV2-retro and Cre transgenic lines to segregate two functionally distinct long-range connections that run in parallel between two brain areas. Projections from cerebral cortex to the striatum arise primarily from neurons in layer V but some neurons in layers II and III also provide striatal inputs. It has been suggested that inputs to the striatum from different cortical layers constitute separate pathways, with neurons in layer V projecting to the patch compartment of the striatum, and neurons in layers II and III to the matrix (Gerfen, 1989). The interdigitated nature of patch and matrix micro-compartments makes it difficult to selectively target these pathways for functional interrogation with the rAAV2-retro system alone. We therefore explored whether we could segregate the two inputs by combining rAAV2-retro with a transgenic line that expresses Cre recombinase in most layer V neurons (Gerfen et al., 2013), but not in neurons in layers II and III (Figure 4A).

To highlight both pathways in the same experiment, we chose a Cre-dependent color-flipping payload, which expresses tdTomato in the absence of Cre, but inverts to drive the expression of EGFP in Cre-positive cells (Saunders et al., 2012). When rAAV2-retro carrying this payload was injected into the dorsomedial striatum of a layer V-specific Cre driver line, *Rbp4*_KL100 Cre (Gerfen et al., 2013), layer V, but not layer II/III, neurons projecting to the striatum were robustly labeled with EGFP. Furthermore, the corticostriatal pathway originating in layer II/III was clearly distinguishable by the expression of tdTomato (Figure 4B). In accordance with the topographic nature of the corticostriatal projection, highly localized injections of the virus into the dorsomedial striatum led to a labeling of correspondingly small sections of the cortex. Cortical regions with selective layer II/III labeling were not observed, however, suggesting that the two pathways from the same cortical area traverse through the neighboring matrix and patch micro-compartments within striatum.

While this experiment highlighted both pathways, choosing a “Cre-on” or a “Cre-off” payload will permit selective interrogation of one at the exclusion of the other. This example, therefore, highlights the added specificity of circuit interrogation that can be achieved by combining a highly efficient retrograde virus with available Cre (or Flp) driver lines.

UsingrAAV2-retro for circuit interrogation and gene manipulation

The utility of rAAV2-retro for circuit interrogation will depend on its ability to mediate high levels of expression of genetically encoded indicators and effectors. We first assessed the ability to monitor neural activity in defined classes of projection neurons, through rAAV2-retro-mediated expression of GCaMP6f (Chen et al., 2013) (Figure 5A-C). Using *in vivo* two-photon Ca^{2+} imaging, we detected dendritic and somatic Ca^{2+} transients in the primary motor cortex as early as 7 days after viral delivery to the BPN (Figure 5D). The temporal profile of Ca^{2+} signals reflected the structure of a cued reaching task, with the signal in many corticopontine neurons being tightly linked to the “go” cue (Figure 5E–F) (Li et al., 2015). Repeated recordings from identified neurons were possible both across trials within a session early in the expression time course (Figure 5E, F), and across many behavioral sessions for over two months post-infection. Thus, rAAV2-retro confers the ability to express sensors in projection neurons at levels sufficient for imaging, creating many new

Author Manuscript Author Manuscript Author Manuscript Author Manuscript

opportunities for deciphering the contributions of specific projections to neural circuit computations.

Finally, we evaluated the utility of rAAV2-retro for delivery of effectors, such as the CRISPR/Cas9 gene editing system, to projection neurons (Figure 6). Specifically, we packaged into rAAV2-retro the *Staphylococcus aureus* Cas9 (SaCas9, (Slaymaker et al., 2016)) and a single guide RNA designed to ablate the expression of tdTomato (Experimental Procedures). Delivery of rAAV2-retro-SaCas9-anti-tdTomato to the BPN of animals expressing tdTomato in cortical layer V excitatory neurons resulted in suppression of tdTomato expression in 88.6 ± 0.7% of SaCas9-expressing layer V neurons (Figure 6B, bottom panel and Figure 6C, n=3). In contrast, delivery of a non-targeted SaCas9 did not lead to any discernible changes, with only 4.4 ± 3.2% of cells displaying potential reduction in tdTomato expression (Figure 6B, top panel, and Figure 6C, n=3). Furthermore, tdTomato expression remained unaffected in layer V neurons that were inaccessible *via* pontine injection. The rAAV2-retro system thus permits efficient gene modification selectively in neurons projecting to specific areas of interest.

Collectively, these observations establish rAAV2-retro as an effective reagent to genetically access projection neurons for functional interrogation of neural circuits and, in the long run, for possible therapeutics.

Discussion

Recombinant adeno-associated viruses (rAAVs) can greatly facilitate the functional dissection of mammalian neural circuits, and hold promise for therapeutic intervention in disorders of the nervous system. We have used directed evolution to endow the AAV capsid with the additional capacity for efficient retrograde access to projection neurons in many neural circuits. The newly engineered rAAV2-retro offers up to two orders of magnitude enhancement in retrograde transport compared to commonly used AAV serotypes, matching the efficacy of synthetic retrograde tracers in many circuits. The level of transgene expression achieved with rAAV2-retro *via* retrograde access is ample for interrogating neural circuit function, as well as for targeted manipulations of the neuronal genome. Thus, by enabling selective monitoring and manipulation of projection neurons connecting different brain areas, rAAV2-retro based tools are poised to provide insights into how large-scale networks enable brain function, and may form the basis for future therapeutic intervention in diseases characterized by progressive large-scale network dysfunction.

The markedly increased efficacy of retrograde access afforded by rAAV2-retro compared to its parental serotype AAV2 might have been enabled through an insertion-mediated disruption of the native binding site for heparin and/or through the creation of a new binding surface that incorporates the inserted peptide. This variant does have reduced heparin affinity (Figure S4), which could decrease virus sequestration in the extracellular matrix of the synaptic cleft and enhance local vector spread, as has been observed with rAAV1 and rAAV6 (Arnett et al., 2013). However, the resulting increase in vector spread alone cannot explain the efficacy of retrograde transport, as other inserted 7-mer sequences disrupt heparin binding similarly but do not affect retrograde transport (Dalkara et al., 2013).

Author Manuscript Author Manuscript Author Manuscript Author Manuscript

Furthermore, rAAV5 and rAAV9 do not bind heparin, yet their retrograde transport efficiency is similar to that of rAAV2. In support of the alternative explanation, the peptide insertions selected in the original selection (**LA**xxDxTKx**A/LA**xDxTKxx**A**) share the same overall composition, differing simply in the register of the conserved motif. The engineered peptide insertion might support enhanced binding to an existing cellular co-factor in the AAV pathway (*e.g.* the recently identified common AAV receptor (Pillay et al., 2016)), or it might create a novel interaction with the cellular machinery such as a cell surface receptor and/or a component of the vesicular trafficking or nuclear entry pathway. Further experiments will be required to elucidate the mechanism of the profound enhancement in the efficacy of retrograde transport.

Despite the multiple orders of magnitude improvement in retrograde transport that rAAV2-retro offers over existing serotypes, a small set of projection neuron classes appears refractory to efficient retrograde infection by this newly evolved rAAV variant (Table S2). It should be noted, however, that other AAV serotypes fail to label these projections as well. Whether the expression level of the critical cellular factor that interfaces with this novel AAV variant in these neurons is just extremely low—a conclusion supported for the corticothalamic and corticocollicular projections, for instance, by the observation that rAAV2-retro could still deliver sufficient Cre recombinase to cell bodies to direct high-level of expression for locally delivered Cre-dependent payloads (Table S2, highlighted entries)—or whether the factor is missing entirely, remains to be determined in each case. Other viral reagents with retrograde functionality (such as HSV1 (Enquist et al., 1998) or Hi-Ret lentivirus (Kato et al., 2010)) might prove useful for targeting some of these projection neuron classes. Alternatively, additional AAV capsid engineering could extend retrograde transduction to all neurons.

Since gaining access to individual classes of projection neurons will be a critical enabling step in elucidating how local circuit dynamics and large-scale network function are coordinated, the rAAV2-retro vector system provides an important addition to the genetic toolkit for dissecting neural circuit function. Local circuit computations are increasingly thought to depend on the dynamics of the entire neuronal population within a particular local circuit module (Fusi et al., 2016). How these dynamics map onto the different classes of projection neurons—and thus what information is passed on to the different downstream targets—remains unresolved for most circuits. rAAV2-retro based vectors, alone or in combination with specific Cre transgenic lines, permit genetic access to specific populations of projections neurons. In turn, rAAV2-retro carrying rabies G glycoprotein can be used to trans-complement conditional rabies vectors (*e.g.* the newly developed, less toxic version described by Reardon et al., 2016) for access to presynaptic microcircuits impinging on particular classes of projection neurons (Brown and Hestrin, 2009). The resulting ability to selectively monitor and manipulate activity of individual projection neuron classes and their local microcircuits should provide insight into how projection neurons translate local circuit dynamics for their respective large-scale networks.

rAAV2-retro also holds promise for therapeutic intervention, with several possible applications. For example, in situations where pathology impacts large volumes of neural tissue—such as Alzheimer's or lysosomal storage diseases—multiple injections pose a safety

Author Manuscript Author Manuscript Author Manuscript Author Manuscript

risk and may be insufficient to achieve the needed levels of transduction. However, a small number of injections in strategic locations can enable vector dispersal over large volumes (*e.g.* corticopontine tract from the point of convergence in the BPN), or difficult-to-access tissue (*e.g.* spinal motor neurons from the muscle (Kaspar et al., 2003)). Furthermore, large-scale functional networks have been implicated in the spread of many neurodegenerative disorders from their spatially localized onset. A prominent emerging view posits that deposition of abnormal protein assemblies in vulnerable neuronal populations triggers a pathological cascade of aberrant neuronal activity within, and disintegration of, large-scale functional networks, ultimately leading to failure of neurological functions (for a recent review see (Brettschneider et al., 2015)). Intriguingly, the affected neural networks appear capable of transiently overcoming the aberrant dynamics early in the disease, as patients with many neurodegenerative diseases often display periods of dramatic improvement. Thus, early intervention aimed at slowing down the spread of aggregates from the cortical origin of pathology might be sufficient to stabilize, or even restore, cognitive function. From this perspective, subcortically-projecting neurons in the mesocortical regions where pathological protein aggregates first appear, in both Alzheimer's (Braak and Braak, 1996) and Parkinson's (Braak et al., 2003) disorders, constitute an attractive intervention target. Accessing those projection neurons with rAAV2-retro-based tools designed, for instance, to introduce a mutation that is capable of arresting further aggregation in *cis* (Gregoire et al., 2014) or to deliver chaperones capable of dissembling the aggregates (Jackrel et al., 2014) thus has the potential to slow down the progression of the most debilitating, cognitive, symptoms. Evaluating the efficiency and long-term safety of rAAV2-retro reagents in non-human primates will pave the path to their eventual consideration for these, and other, gene therapy approaches.

Experimental Procedures

All procedures were in accordance with protocols approved by the Janelia Research Campus and the University of California Berkeley Institutional Animal Care and Use Committees.

Library generation and viral production

Four previously generated virus libraries were used at the start of the directed evolution procedure: 1) a random mutagenesis library, generated by subjecting the AAV2 *cap* gene (encoding virus proteins VP1-3 and Assembly-Activating Protein, AAP) to error prone PCR (Maheshri et al., 2006); 2) library of AAV2 *cap* gene variants containing 7-mer randomized peptide within a 10-mer insert of the form **LA**XXXXXXX**A** between N587 and R588 (Müller et al., 2003); 3) library of AAV2 *cap* gene variants containing randomized loop regions (Koerber et al., 2009); and 4) a DNA shuffling library generated from wild-type AAV1, AAV2, AAV4, AAV5, AAV6, AAV8 and AAV9 *cap* gene sequences (Koerber et al., 2008). Each pool of mutant DNA had been originally sub-cloned into the replication-competent AAV packaging plasmid to create a viral plasmid library that, when packaged into AAV virions, can be selected for any new property or function. The replication-competent AAV system incorporates the mutant *cap* gene into the viral payload, and thus the genotype of each variant is linked to its phenotype. Capsid sequences of the desired property can then be recovered by DNA sequence analysis of the encapsulated AAV genome.

Author Manuscript Author Manuscript Author Manuscript Author Manuscript

The four replication-competent AAV libraries were packaged by calcium phosphate transient transfection of HEK293-T cells followed by virus harvest, iodixanol gradient centrifugation, and Amicon filtration (Maheshri et al., 2006).

In vivo virus or tracer injections

For virusinjections, ~50-100 nl (mice) or ~250-500nl (rats) of virus-containing solution was slowly injected at each depth into the tissue. For tracer injections, 50 nl of 5% Fluoro-Gold (Fluorochrome, Denver, CO) in 0.9% NaCl, or 100 nl of retrobeads (LumaFluor, Durham, NC) diluted 1:1 in 0.9% NaCl were injected at the same set of sites for each injection target.

Library selection and evolution

The four mutant virus libraries were pooled and injected either into the SNr or into the cerebellum of adult (6-8 week old) wild-type C57/Bl6J mice (either sex; Charles River). Three weeks following injections, striatal or hindbrain tissue was accordingly removed, DNA was extracted, and virions that had successfully reached the remote retrograde target tissue were PCR-amplified and recloned into an rcAAV packaging plasmid to create a new replication competent AAV library for the next round of selection. After three selection steps, the rescued *cap* genes were randomly mutated by error prone PCR using 5′-ACGCGGAAGCTTCGATCAACTACGCAG-3′ and 5′-AGACCAAAGTTCAACTGAAACGAATTAAACGG-3′ as forward and reverse primers, respectively. Two additional *in vivo* selection rounds were then performed. Individual isolates were sequenced after rounds 4 and 5 to evaluate the degree of library enrichment (Table S1). Seventeen variants were chosen for secondary screening at the end of round five, and the corresponding *cap* gene sequences were re-cloned into an rAAV helper plasmid. Individual high-titer preps of the parental wild type AAV2 and of each of the seventeen chosen mutant variants carrying a *CMV*-EGFP payload were then performed by Vector BioLabs, Inc (Philadelphia, PA). The *CMV* promoter is typically weak in neurons, and thus this secondary screen provided a stringent test of the efficiency of retrograde transport. The individual AAV variants were injected either into the cerebellum or into the globus pallidus. After three weeks, endogenous, unamplified EGFP fluorescence was visualized in the regions expected to be labeled if retrograde transport was efficient. Mutant r5H6 (insert **LA**DQDYTKT**A** + V708I + N382D) displayed the strongest retrograde transport in both circuits, and was thus chosen for further analysis and named rAAV2-retro (see Supplemental Information for the complete gene sequence).

Payloads and promoters used in the study

For all subsequent experiments, the *CMV* promoter was replaced with a promoter known to be more robust in adult neurons. Cre recombinase and the GCaMP6f calcium sensor were driven by the human *Synapsin-1* (*hSyn1*) promoter; all of the fluorophores were driven by the *CAG* promoter; and the color-flipping construct was driven by the *EF1α* promoter.

Virus production for the quantification of retrograde efficiency

hSyn-Cre payload was packaged using rAAV1, rAAV2, rAAV5, rAAV8, rAAV9, DJ and rAAV2-retro capsids at the Janelia Virus Shared Resource. All seven virus preparations were

Author Manuscript Author Manuscript Author Manuscript Author Manuscript

processed in parallel, and were titer matched before *in vivo* injections. All lots were diluted to the lowest measured titer (1.3 E12 GC/ml), and each virus was injected into the right pontine nucleus of three to five adult *Rosa26*-Lox-STOP-Lox-H2B-EGFP mice (He et al., 2012).

Histology

Animals were sacrificed two-three weeks following virus injections, at which point the brains were harvested and the right hemisphere was sagittally sectioned at a thickness of 50 μm. In the triple labeling experiment in Figure 1B and Movie S1, the fluorphores were antibody-amplified; otherwise, unstained sections were used. The sections were mounted in VECTASHIELD Antifade Mounting Medium containing DAPI (Vector Laboratories), and imaged using a P-E Pannoramic slide scanner (3D Histech) using a 20× objective and FITC and DAPI filters.

Retrograde transport quantification

To quantify retrograde transport, the extent of corticopontine labeling was assessed in sagittal sections lateral to the injection tract (~1 mm lateral with respect to midline) taken from *Rosa26*-Lox-STOP-Lox-H2B-EGFP animals injected in the basal pons with various AAV serotypes carrying a Cre recombinase transgene. Images obtained with the Pannoramic slide scanner were stitched together and then analyzed using custom software written in Matlab (Mathworks) to detect the GFP-labeled nuclei across the cortex.

For each chosen sagittal section, a region of interest (ROI) was manually drawn around the cortex to isolate the area in the image for automated cell counting. To enhance the detection of nuclei, the image was then convolved with a “Mexican Hat” kernel comprising the difference of two Gaussians (26.00 μm variance and 3.25 μm variance). Image noise was reduced using a median filter, and peak detection was then performed. Linear density was computed as the number of labeled nuclei per mm of the total length of a line drawn manually to trace the outline of cortical layer V.

Quantification of infection efficiency at the injection site

For rAAV2, rAAV9 and rAAV2-retro, additional analysis of infection efficiency at the injection site was performed. A single sagittal section spanning the middle of the injection site—as judged by the presence of extensive labeling along the injection tract—was chosen for each of the injected brains. The green channel was convolved with the “Mexican Hat” kernel (see above), and peaks were then detected as local maxima on these threshold images using custom functions written in Matlab. An ROI was drawn over the midbrain area containing the basal pontine nuclei but excluding the injection tract, and the total number of labeled nuclei within the ROI was tabulated.

Analysis of the generality of retrograde transport

Rosa26-Lox-STOP-Lox-H2B-EGFP mice were injected with 25 nl of rAAV2-retro *hSyn1*-Cre (1.3E12 GC/ml) in the dorsal striatum. Three weeks after injection, coronally-sectioned brains were imaged using a Pannoramic Scanner to visualize DAPI stained nuclei and green fluorescence from H2B-GFP expressing nuclei. The green channel was similarly used for

Author Manuscript Author Manuscript Author Manuscript Author Manuscript

the detection of labeled nuclei (see above). The blue channel of each section was aligned to the Nissl images from the Allen Brain Institute's standardized mouse brain atlas using custom analysis routines written with the help of the Matlab Image Processing Toolbox. The annotated regions from the Allen Brain Institute's mouse brain atlas were then used to assign detected neurons in aligned sections to specific brain regions (Kuan et al., 2015).

We note that finite precision of the reference atlas together with anatomical variability of individual brains limit the robustness of this semi-automated process to prominent afferent inputs.

Imaging of neuronal population activity *in vivo* following retrograde delivery of GCaMP6f

Seven adult mice were implanted with custom-made headposts as previously described (Osborne and Dudman, 2014). rAAV2-retro carrying a *hSyn1*-GCaMP6f (1.0E13 GC/ml) payload was injected into the BPN using a Nanoliter 2010 injector (World Precision Instruments). A cranial window was placed over the primary motor cortex. All animals had visually identifiable GCaMP6f expressing cells in layer V of M1 one-week post injection. Then the animals were habituated to head fixation in a custom-built apparatus, trained to retrieve a food pellet as previously described (Guo et al., 2015). Calcium transients during behavior were imaged by exciting GCaMP6f at 920 nm. Emission light passed through a 565 DCXR dichroic filter (Chroma Technology) and an ET525/70m-2p filter (Chroma Technology) and was detected by a GaAsP photomultiplier tube (10770PB-40, Hamamatsu). Images (512 × 512 pixels) were acquired at ~30 Hz with resonating scanners using ScanImage software.

CRISPR/Cas9 genome editing

The *CMV* promoter in pAAV-*CMV*-SaCas9-empty (Slaymaker et al., 2016) was replaced with *hSyn1* to generate pAAV-*hSyn1*-SaCas9-empty. Oligonucleotides encoding sgRNA protospacer sequences were custom ordered, phosphorylated, hybridized and ligated into the *Bsa*I restriction sites of pAAV-*hSyn1*-SaCas9-emtpy to generate pAAV-*hSyn1*-SaCas9-tdTomato-1 to -10 (see Supplemental Information for oligonucleotide sequences tested and details of the *in vitro* selection procedure). sgRNA 7—one of two that appeared to direct two cleavage events within the tdTomato sequence *in vitro*—was packaged into AAV2-retro and used for *in vivo* genome editing.

Approximately 100 nl of rAAV2-retro-*hSyn1*-SaCas9-tdTomato (5.0 E13 GC/ml) or rAAV2-retro-*hSyn1*-SaCas9-empty was then injected into the BPN of *Rbp4*_KL100 Cre × tdTomato mice as described above. Six weeks after injections, brains were harvested and 40 μm-thick coronal sections were cut, stained against the HA-tagged Cas9 and imaged using a Zeiss Axio Observer A1 inverted microscope. Quantification of immunostaining was performed using ImageJ analysis software (NIH).

Supplementary Material

Refer to Web version on PubMed Central for supplementary material.

Author Manuscript Author Manuscript Author Manuscript Author Manuscript

Acknowledgments

We are indebted to K. Svoboda for suggesting the use of Rosa26-lox-STOP-lox-H2B-EGFP mice. We thank H. Adesnik for providing the Rbp4_KL 100Cre × tdTomato mouse line, J. Brousseau for invaluable assistance with the pilot experiments, M. Proskurin for help with the rat experiments, and J. Santiago-Ortiz for help with the CRISPR/Cas9 experiments. We are grateful to the members of the Dudman, Hantman, Jessell, Ji, Karpova, Petreanu, Sabatini, Spruston, Svoboda and Zuker labs for beta-testing rAAV2-retro and contributing their findings to the knowledge base summarized in Table S2.

T. Jessell, N. Spruston and K. Svoboda offered useful discussions and comments on the manuscript. D.V.S. is supported by NIH R01EY022975, T.G. by F32GM113446. This work was supported by the Howard Hughes Medical Institute.

References

Arnett AL, Beutler LR, Quintana A, Allen J, Finn E, Palmiter RD, Chamberlain JS. Heparin-binding correlates with increased efficiency of AAV1-and AAV6-mediated transduction of striated muscle, but negatively impacts CNS transduction. Gene therapy. 2013; 20:497–503. [PubMed: 22855092]

Baer GM, Shanthaveerappa TR, Bourne GH. Studies on the pathogenesis of fixed rabies virus in rats. Bull World Health Organ. 1965; 33:783–794. [PubMed: 5295402]

Braak H, Braak E. Development of Alzheimer-related neurofibrillary changes in the neocortex inversely recapitulates cortical myelogenesis. Acta neuropathologica. 1996; 92:197–201. [PubMed: 8841666]

Braak H, Rüb U, Gai W, Del Tredici K. Idiopathic Parkinson's disease: possible routes by which vulnerable neuronal types may be subject to neuroinvasion by an unknown pathogen. Journal of neural transmission. 2003; 110:517–536. [PubMed: 12721813]

Brettschneider J, Del Tredici K, Lee VMY, Trojanowski JQ. Spreading of pathology in neurodegenerative diseases: a focus on human studies. Nature Reviews Neuroscience. 2015; 16:109–120. [PubMed: 25588378]

Brodal P, Bjaalie JG. Organization of the pontine nuclei. Neurosci Res. 1992; 13:83–118. [PubMed: 1374872]

Brown SP, Hestrin S. Intracortical circuits of pyramidal neurons reflect their long-range axonal targets. Nature. 2009; 457:1133–1136. [PubMed: 19151698]

Callaway EM, Luo L. Monosynaptic Circuit Tracing with Glycoprotein-Deleted Rabies Viruses. J Neurosci. 2015; 35:8979–8985. [PubMed: 26085623]

Castle MJ, Gershenson ZT, Giles AR, Holzbaur EL, Wolfe JH. Adeno-associated virus serotypes 1, 8, and 9 share conserved mechanisms for anterograde and retrograde axonal transport. Human gene therapy. 2014; 25:705–720. [PubMed: 24694006]

Chen TW, Wardill TJ, Sun Y, Pulver SR, Renninger SL, Baohan A, Schreiter ER, Kerr RA, Orger MB, Jayaraman V. Ultrasensitive fluorescent proteins for imaging neuronal activity. Nature. 2013; 499:295–300. [PubMed: 23868258]

Cong L, Ran FA, Cox D, Lin S, Barretto R, Habib N, Hsu PD, Wu X, Jiang W, Marraffini LA. Multiplex genome engineering using CRISPR/Cas systems. Science. 2013; 339:819–823. [PubMed: 23287718]

Coulon P, Derbin C, Kucera P, Lafay F, Prehaud C, Flamand A. Invasion of the peripheral nervous systems of adult mice by the CVS strain of rabies virus and its avirulent derivative AvO1. Journal of virology. 1989; 63:3550–3554. [PubMed: 2664219]

Dalkara D, Byrne LC, Klimczak RR, Visel M, Yin L, Merigan WH, Flannery JG, Schaffer DV. In vivo–directed evolution of a new adeno-associated virus for therapeutic outer retinal gene delivery from the vitreous. Science translational medicine. 2013; 5:189ra176–189ra176.

Enquist L, Husak PJ, Banfield BW, Smith GA. Infection and spread of alphaherpesviruses in the nervous system. Advances in virus research. 1998; 51:237–347. [PubMed: 9891589]

Fusi S, Miller EK, Rigotti M. Why neurons mix: high dimensionality for higher cognition. Current Opinion in Neurobiology. 2016; 37:66–74. [PubMed: 26851755]

Author Manuscript Author Manuscript Author Manuscript Author Manuscript

Gaudet D, de Wal J, Tremblay K, Déry S, van Deventer S, Freidig A, Brisson D, Méthot J. Review of the clinical development of alipogene tiparvovec gene therapy for lipoprotein lipase deficiency. Atherosclerosis Supplements. 2010; 11:55–60. [PubMed: 20427244]

Gerfen CR. The neostriatal mosaic: striatal patch-matrix organization is related to cortical lamination. Science. 1989; 246:385–388. [PubMed: 2799392]

Gerfen CR, Paletzki R, Heintz N. GENSAT BAC cre-recombinase driver lines to study the functional organization of cerebral cortical and basal ganglia circuits. Neuron. 2013; 80:1368–1383. [PubMed: 24360541]

Gregoire S, Zhang S, Costanzo J, Wilson K, Fernandez EJ, Kwon I. Cis-suppression to arrest protein aggregation in mammalian cells. Biotechnology and bioengineering. 2014; 111:462–474. [PubMed: 24114411]

Guo JL, Lee VM. Cell-to-cell transmission of pathogenic proteins in neurodegenerative diseases. Nature medicine. 2014; 20:130–138.

He M, Liu Y, Wang X, Zhang MQ, Hannon GJ, Huang ZJ. Cell-type-based analysis of microRNA profiles in the mouse brain. Neuron. 2012; 73:35–48. [PubMed: 22243745]

Hollis ER Ii, Kadoya K, Hirsch M, Samulski RJ, Tuszynski MH. Efficient retrograde neuronal transduction utilizing self-complementary AAV1. Molecular Therapy. 2008; 16:296–301.

Jackrel ME, DeSantis ME, Martinez BA, Castellano LM, Stewart RM, Caldwell KA, Caldwell GA, Shorter J. Potentiated Hsp104 variants antagonize diverse proteotoxic misfolding events. Cell. 2014; 156:170–182. [PubMed: 24439375]

Jang JH, Koerber JT, Kim JS, Asuri P, Vazin T, Bartel M, Keung A, Kwon I, Park KI, Schaffer DV. An evolved adeno-associated viral variant enhances gene delivery and gene targeting in neural stem cells. Molecular Therapy. 2011; 19:667–675. [PubMed: 21224831]

Junyent F, Kremer EJ. CAV-2—why a canine virus is a neurobiologist's best friend. Current opinion in pharmacology. 2015; 24:86–93. [PubMed: 26298516]

Kaplitt MG, Feigin A, Tang C, Fitzsimons HL, Mattis P, Lawlor PA, Bland RJ, Young D, Strybing K, Eidelberg D, et al. Safety and tolerability of gene therapy with an adeno-associated virus (AAV) borne GAD gene for Parkinson's disease: an open label, phase I trial. Lancet. 2007; 369:2097–2105. [PubMed: 17586305]

Kaspar BK, Erickson D, Schaffer D, Hinh L, Gage FH, Peterson DA. Targeted retrograde gene delivery for neuronal protection. Molecular Therapy. 2002; 5:50–56. [PubMed: 11786045]

Kaspar BK, Llado J, Sherkat N, Rothstein JD, Gage FH. Retrograde viral delivery of IGF-1 prolongs survival in a mouse ALS model. Science. 2003; 301:839–842. [PubMed: 12907804]

Kato S, Kobayashi K, Inoue Ki, Kuramochi M, Okada T, Yaginuma H, Morimoto K, Shimada T, Takada M, Kobayashi K. A lentiviral strategy for highly efficient retrograde gene transfer by pseudotyping with fusion envelope glycoprotein. Human gene therapy. 2010; 22:197–206.

Kelly RM, Strick PL. Rabies as a transneuronal tracer of circuits in the central nervous system. Journal of neuroscience methods. 2000; 103:63–71. [PubMed: 11074096]

Kern A, Schmidt K, Leder C, Müller O, Wobus C, Bettinger K, Von der Lieth C, King J, Kleinschmidt J. Identification of a heparin-binding motif on adeno-associated virus type 2 capsids. Journal of virology. 2003; 77:11072–11081. [PubMed: 14512555]

Koerber JT, Jang JH, Schaffer DV. DNA shuffling of adeno-associated virus yields functionally diverse viral progeny. Molecular Therapy. 2008; 16:1703–1709. [PubMed: 18728640]

Koerber JT, Klimczak R, Jang JH, Dalkara D, Flannery JG, Schaffer DV. Molecular evolution of adeno-associated virus for enhanced glial gene delivery. Molecular Therapy. 2009; 17:2088–2095. [PubMed: 19672246]

Koerber JT, Maheshri N, Kaspar BK, Schaffer DV. Construction of diverse adeno-associated viral libraries for directed evolution of enhanced gene delivery vehicles. Nature protocols. 2006; 1:701–706. [PubMed: 17406299]

Kotterman MA, Schaffer DV. Engineering adeno-associated viruses for clinical gene therapy. Nat Rev Genet. 2014; 15:445–451. [PubMed: 24840552]

Kremer EJ, Boutin S, Chillon M, Danos O. Canine adenovirus vectors: an alternative for adenovirus-mediated gene transfer. J Virol. 2000; 74:505–512. [PubMed: 10590140]

Author Manuscript Author Manuscript Author Manuscript Author Manuscript

Kuan L, Li Y, Lau C, Feng D, Bernard A, Sunkin SM, Zeng H, Dang C, Hawrylycz M, Ng L. Neuroinformatics of the allen mouse brain connectivity atlas. Methods. 2015; 73:4–17. [PubMed: 25536338]

Legg C, Mercier B, Glickstein M. Corticopontine projection in the rat: the distribution of labelled cortical cells after large injections of horseradish peroxidase in the pontine nuclei. Journal of Comparative Neurology. 1989; 286:427–441. [PubMed: 2778100]

Li N, Chen TW, Guo ZV, Gerfen CR, Svoboda K. A motor cortex circuit for motor planning and movement. Nature. 2015; 519:51–56. [PubMed: 25731172]

Maheshri N, Koerber JT, Kaspar BK, Schaffer DV. Directed evolution of adeno-associated virus yields enhanced gene delivery vectors. Nature biotechnology. 2006; 24:198–204.

Miller MW, Vogt BA. Direct connections of rat visual cortex with sensory, motor, and association cortices. J Comp Neurol. 1984; 226:184–202. [PubMed: 6736299]

Müller OJ, Kaul F, Weitzman MD, Pasqualini R, Arap W, Kleinschmidt JA, Trepel M. Random peptide libraries displayed on adeno-associated virus to select for targeted gene therapy vectors. Nature biotechnology. 2003; 21:1040–1046.

Murlidharan G, Samulski RJ, Asokan A. Biology of adeno-associated viral vectors in the central nervous system. Frontiers in molecular neuroscience. 2014; 7

Nagy A. Cre recombinase: the universal reagent for genome tailoring. Genesis. 2000; 26:99–109. [PubMed: 10686599]

Ohka S, Yang WX, Terada E, Iwasaki K, Nomoto A. Retrograde transport of intact poliovirus through the axon via the fast transport system. Virology. 1998; 250:67–75. [PubMed: 9770421]

Ojala DS, Amara DP, Schaffer DV. Adeno-associated virus vectors and neurological gene therapy. The Neuroscientist. 2014:1073858414521870.

Pan WX, Mao T, Dudman JT. Inputs to the dorsal striatum of the mouse reflect the parallel circuit architecture of the forebrain. Front Neuroanat. 2010; 4:147. [PubMed: 21212837]

Piersanti S, Astrologo L, Licursi V, Costa R, Roncaglia E, Gennetier A, Ibanes S, Chillon M, Negri R, Tagliafico E. Differentiated neuroprogenitor cells incubated with human or canine adenovirus, or lentiviral vectors have distinct transcriptome profiles. PloS one. 2013; 8:e69808. [PubMed: 23922808]

Pillay S, Meyer N, Puschnik A, Davulcu O, Diep J, Ishikawa Y, Jae L, Wosen J, Nagamine C, Chapman M. An essential receptor for adeno-associated virus infection. Nature. 2016

Ramón y Cajol, S. Histologie du système nerveux de l'homme et des vertébrés. Vol. 2. Paris: Maloine; 1911.

Reardon TR, Murray AJ, Turi GF, Wirblich C, Croce KR, Schnell MJ, Jessell TM, Losonczy A. Rabies Virus CVS-N2c ΔG Strain Enhances Retrograde Synaptic Transfer and Neuronal Viability. Neuron. 2016

Rothermel M, Brunert D, Zabawa C, Díaz-Quesada M, Wachowiak M. Transgene expression in target-defined neuron populations mediated by retrograde infection with adeno-associated viral vectors. The Journal of neuroscience. 2013; 33:15195–15206. [PubMed: 24048849]

Saunders AB, Johnson C, Sabatini BL. Novel recombinant adeno-associated viruses for Cre activated and inactivated transgene expression in neurons. 2012

Schmued LC, Fallon JH. Fluoro-Gold: a new fluorescent retrograde axonal tracer with numerous unique properties. Brain Res. 1986; 377:147–154. [PubMed: 2425899]

Schnell MJ, McGettigan JP, Wirblich C, Papaneri A. The cell biology of rabies virus: using stealth to reach the brain. Nature Reviews Microbiology. 2010; 8:51–61. [PubMed: 19946287]

Seeley WW, Crawford RK, Zhou J, Miller BL, Greicius MD. Neurodegenerative diseases target large-scale human brain networks. Neuron. 2009; 62:42–52. [PubMed: 19376066]

Simão D, Pinto C, Fernandes P, Peddie C, Piersanti S, Collinson L, Salinas S, Saggio I, Schiavo G, Kremer E. Evaluation of helper-dependent canine adenovirus vectors in a 3D human CNS model. Gene therapy. 2015

Slaymaker IM, Gao L, Zetsche B, Scott DA, Yan WX, Zhang F. Rationally engineered Cas9 nucleases with improved specificity. Science. 2016; 351:84–88. [PubMed: 26628643]

Author Manuscript Author Manuscript Author Manuscript Author Manuscript

Soudais C, Laplace-Builhe C, Kissa K, Kremer EJ. Preferential transduction of neurons by canine adenovirus vectors and their efficient retrograde transport in vivo. The FASEB Journal. 2001; 15:2283–2285. [PubMed: 11511531]

Taymans JM, Vandenberghe LH, Haute CVD, Thiry I, Deroose CM, Mortelmans L, Wilson JM, Debyser Z, Baekelandt V. Comparative analysis of adeno-associated viral vector serotypes 1, 2, 5, 7, and 8 in mouse brain. Human gene therapy. 2007; 18:195–206. [PubMed: 17343566]

Tomioka R, Okamoto K, Furuta T, Fujiyama F, Iwasato T, Yanagawa Y, Obata K, Kaneko T, Tamamaki N. Demonstration of long-range GABAergic connections distributed throughout the mouse neocortex. European Journal of Neuroscience. 2005; 21:1587–1600. [PubMed: 15845086]

Towne C, Schneider B, Kieran D, Redmond D, Aebischer P. Efficient transduction of non-human primate motor neurons after intramuscular delivery of recombinant AAV serotype 6. Gene therapy. 2010; 17:141–146. [PubMed: 19727139]

Ugolini G, Kuypers HG, Simmons A. Retrograde transneuronal transfer of herpes simplex virus type 1 (HSV 1) from motoneurones. Brain Res. 1987; 422:242–256. [PubMed: 2445438]

Wickersham IR, Finke S, Conzelmann KK, Callaway EM. Retrograde neuronal tracing with a deletion-mutant rabies virus. Nat Methods. 2007; 4:47–49. [PubMed: 17179932]

Author Manuscript Author Manuscript Author Manuscript Author Manuscript

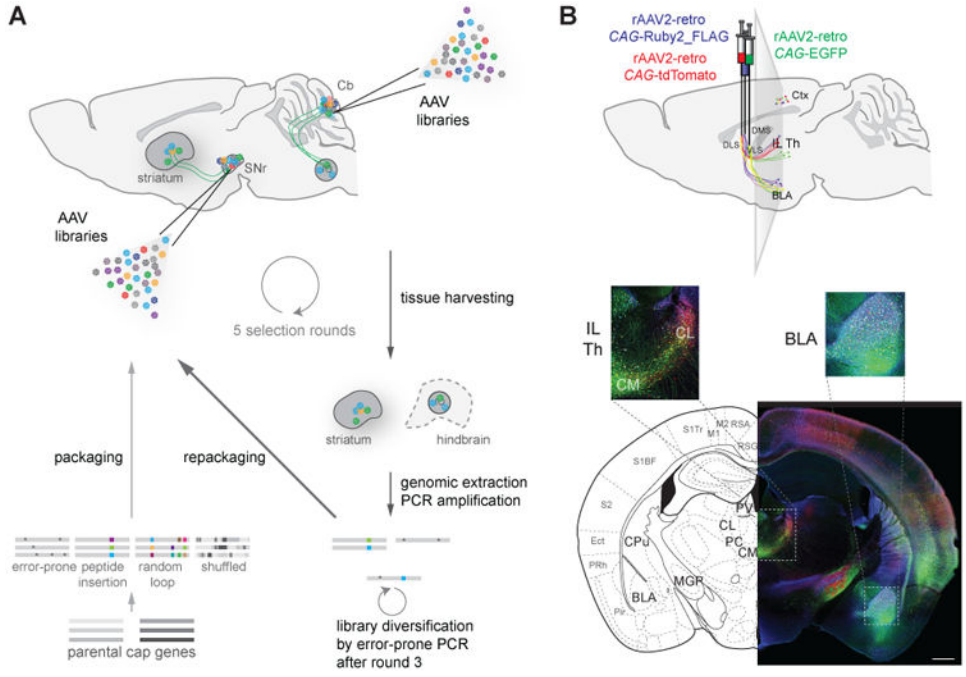


Figure 1. Directed evolution of rAAV2-retro

(**A**) Schematic of the directed evolution procedure. Plasmid libraries containing variant AAV *cap* genes previously generated by error prone PCR, peptide insertion, randomization of loop regions, and DNA shuffling were packaged, and the resulting viral vector libraries were injected into substantia nigra or cerebellar cortex. Three weeks later, striatal or hindbrain, respectively, tissues were removed, viral genomes isolated, and selected *cap* genes amplified and packaged for the next round of selection.(**B**) Example retrograde labeling of projection neurons with the final chosen variant, rAAV2-retro. Retrograde access to intermingled sub-populations of neurons in various brain regions projecting to three striatal compartments was assessed two weeks after delivery of rAAV2-retro carrying different fluorescent proteins into the corresponding axonal fields. rAAV2-retro-tdTomato was injected into dorsolateral striatum (DLS), rAAV2-retro Ruby2_FLAG into dorsomedial striatum (DMS), and rAAV2-retro EGFP into ventrolateral striatum (VLS). Unlike in subsequent experiments (see Figures 2-6), the three probes were visualized by immunohistochemistry to ensure robust detection of retrograde transport at this early time point. Ctx: cortex; BLA: basolateral amygdala; IL TH: intralaminar thalamic nuclei; CL: centrolateral thalamic nucleus; CM: centromedial thalamic nucleus. Scale bar: 1mm. See also Figures S1 and S4, and Movie S1.

Author Manuscript Author Manuscript Author Manuscript Author Manuscript

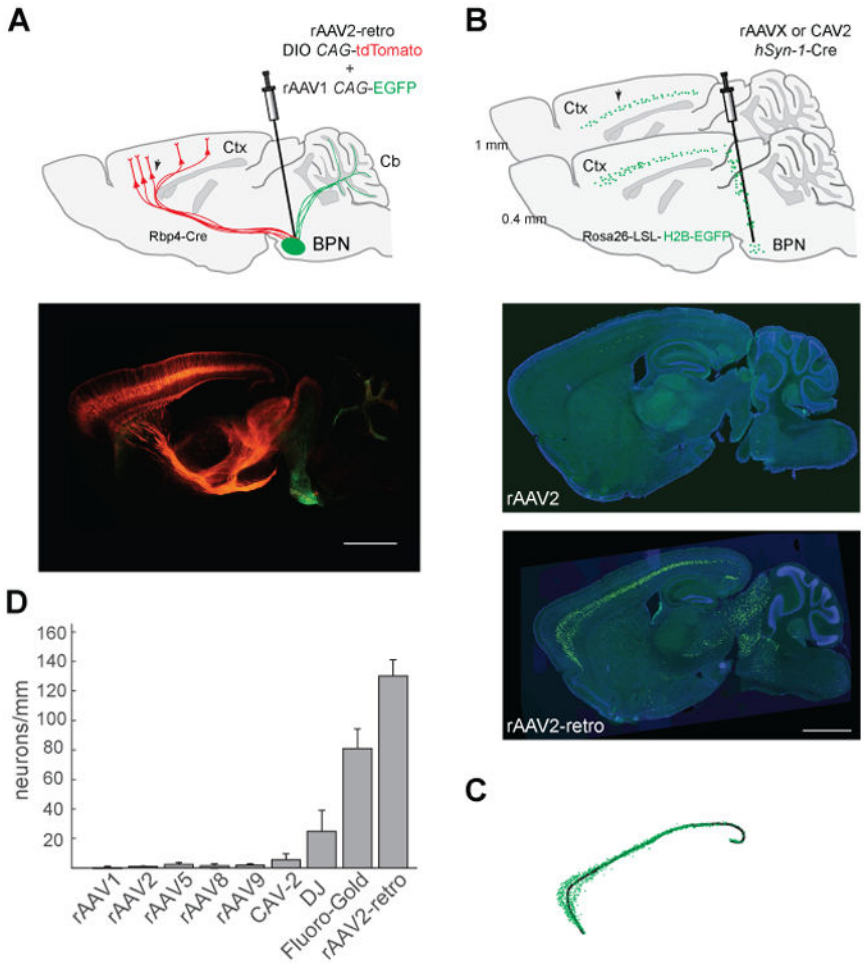


Figure 2. Quantification of retrograde transport efficiency

(**A**) Efficient labeling of the corticopontine tract throughout the rostro-caudal axis *via* basal pontine injection of rAAV2-retro-DIO-CAG-tdTomato in a layer V-specific Cre mouse line (*Rbp4*_KL100 Cre). Top panel: schematic of the experiment. Injection site was marked by co-injecting rAAV1-CAG-EGFP. BPN: Basal pontine nuclei. Bottom panel: unamplified tdTomato and EGFP expression three weeks after injection. Scale bar: 1 mm. (**B**) Quantification assay design. Top panel: schematic of the experiment. Corticopontine labeling was assessed in sagittal sections lateral to the injection tract (~1 mm lateral with respect to midline) taken from Rosa26-Lox-STOP-Lox-H2B-EGFP animals injected in the BPN with various AAV serotypes carrying Cre recombinase transgene. Arrow indicates expected nuclear GFP labeling in cortical neurons of the corticopontine tract. Middle panel: representative image of an rAAV2-injected brain. Bottom panel: representative image of rAAV2-retro-injected brain. Scale bar for both the panels: 1 mm. (**C**) Schematic of the semi-automated quantification procedure. Fluorescent nuclei (green) were automatically detected and counted along a manually drawn line that traced the length of cortical layer V (black). (**D**) Retrograde transport efficiency for different AAV serotypes and for canine adenovirus type 2 (CAV-2) (See Experimental Procedures). Error bars represent the S.E.M. See also Figures S2 and S3.

Author Manuscript Author Manuscript Author Manuscript Author Manuscript

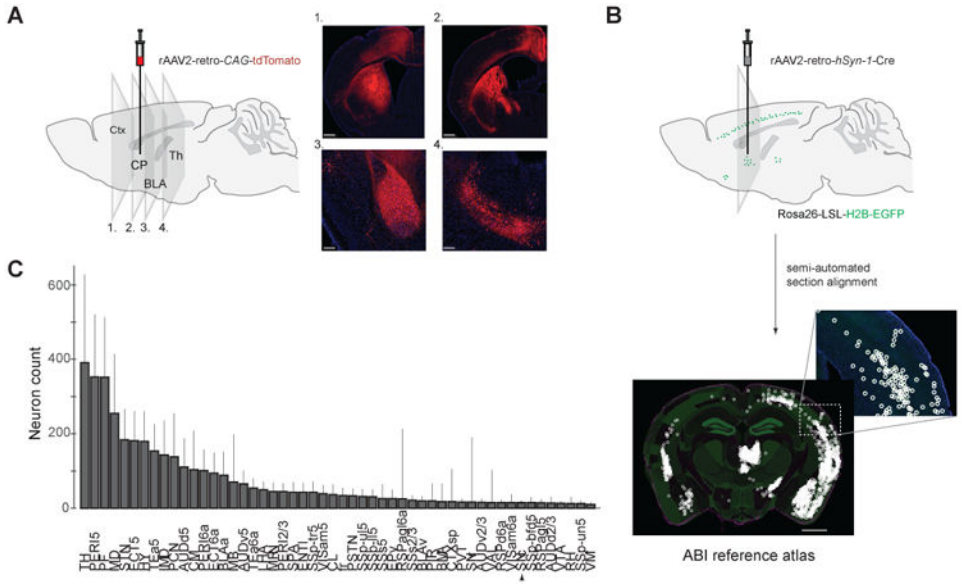


Figure 3. Generality of retrograde transport afforded by rAAV2-retro

(**A**) Representative images showing extensive labeling in the main input structures to the dorsal striatum including cortex (panel 1), amygdala (panel 3), and thalamus (panel 4). Scale bars: 800 micrometers for panels 1 and 2,200 micrometers for panels 3 and 4.Ctx: cortex; CP: caudate/putamen; BLA: basolateral amygdala; Th: thalamus; (**B**) Schematic of automated whole-brain quantification of retrograde labeling. Brains of *Rosa26*-LSL-H2B-EGFP injected with rAAV2-retro-*hSyn1*-Cre were imaged to visualize DAPI stained nuclei and green fluorescence from H2B-GFP expressing nuclei. The green channel was used to detect labeled neurons; the blue channel was aligned to the Nissl images from the Allen Brain Institute's standard mouse brain (see Experimental Procedures). The alignment permitted detected neurons to be assigned to different regions using the annotation provided by the brain atlas. Scale bar: 1.25 mm. (**C**) Whole-brain quantification of retrograde labeling out of a small region of the dorsomedial striatum. Abbreviations for the different brain areas are given according to the Allen Brain Atlas. Arrow highlights the SNc. Error bars represent the S.E.M.

Author Manuscript Author Manuscript Author Manuscript Author Manuscript

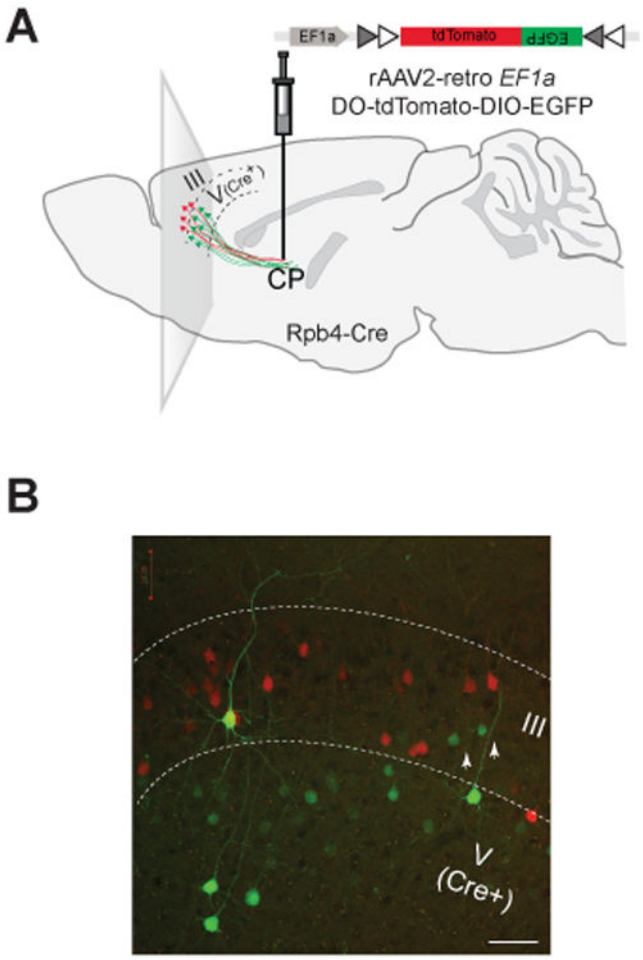


Figure 4. Combining rAAV2-retro system with Cre driver lines for selective access to parallel corticostriatal pathways

(**A**) Schematic of the experiment. rAAV2-retro carrying a Cre-dependent color flipping fluorescent reporter was injected into the striatum of a cortical layer V-specific Cre line. (**B**) Two corticostriatal pathways differentially labeled through a Cre-dependent inversion of the reporter in one (layer V), but not the other (layer II/III), pathway. A presumed Cre-independent inversion— typical for all AAV vectors—was observed in a small fraction of corticostriatal neurons in layer II/III (white arrows). Scale bar: 50 micrometers.

Author Manuscript Author Manuscript Author Manuscript Author Manuscript

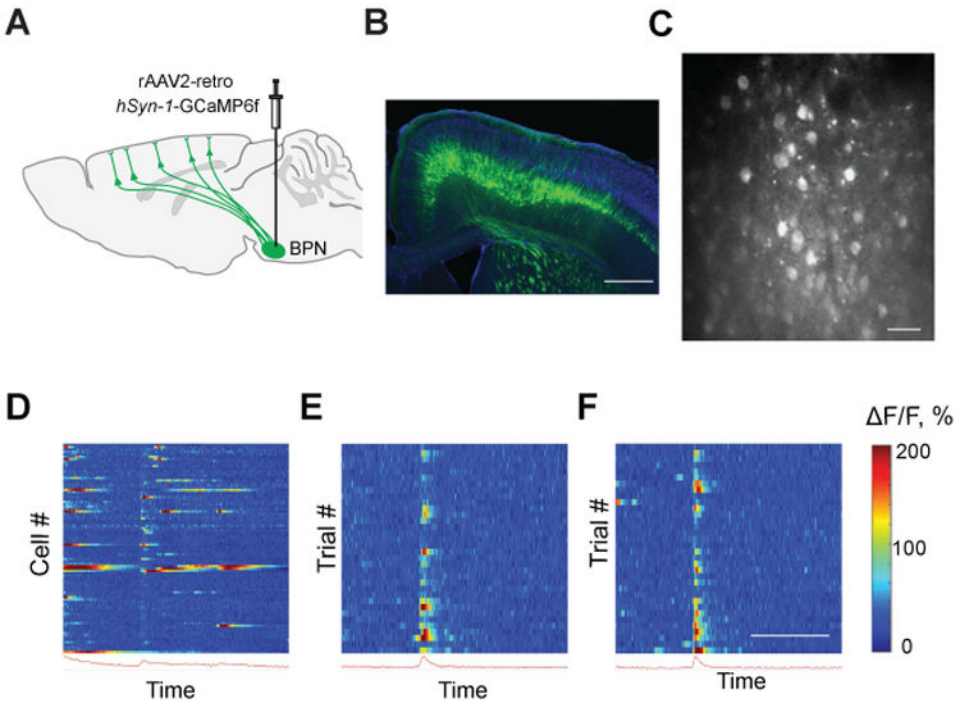


Figure 5. rAAV2-retro supports sufficient transgene expression for functional circuit interrogation

(**A**) Schematic of the experiment. Expression of calcium indicator GCaMP6f is restricted to corticopontine neurons using localized injection of rAAV2-retro into the BPN. (**B**) Cross section of the mouse brain showing GCaMP6f expression throughout the corticopontine tract. Scale bar: 50 micrometers. (**C**) Maximum projection of an *in vivo* two-photon calcium image taken during a single reach showing layer V-pyramidal tract somas and apical dendrites. Scale bar: 50 micrometers. (**D**) Activity of 89 ROIs during a single paw reach repetition (broken line denotes the tone “go” signal). (**E-F**) Two examples of single corticopontine neurons during 40 consecutive trials (same animal as in B-D). Scale bar: 4 seconds.

Author Manuscript Author Manuscript Author Manuscript Author Manuscript

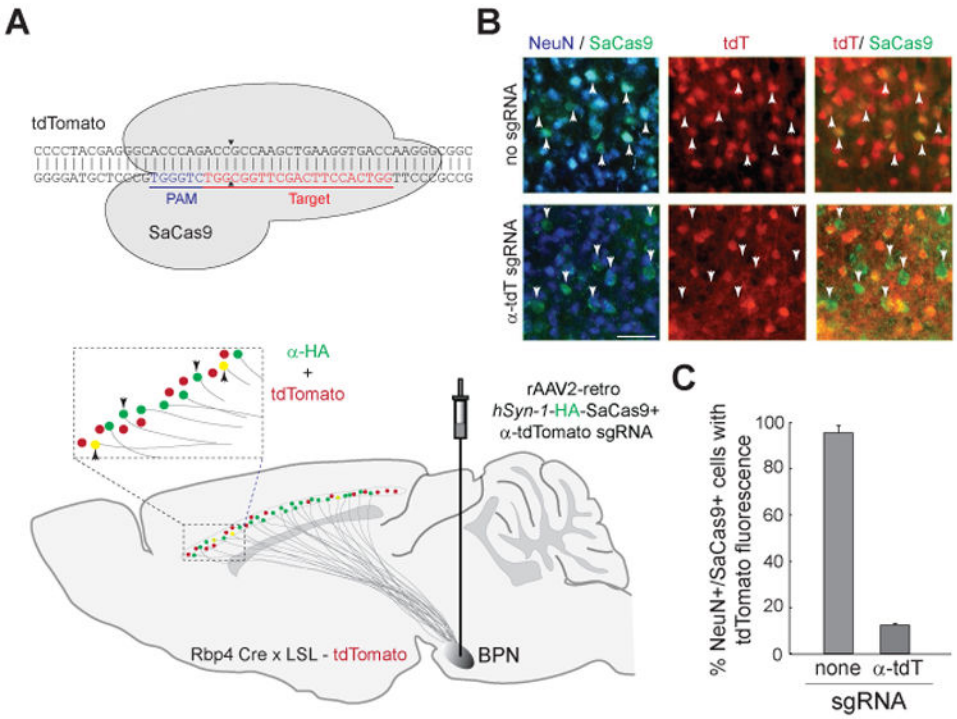


Figure 6. rAAV2-retro system enables *in vivo* genome editing using CRISPR/Cas9

(**A**) Schematic of the experiment. Top panel: The rAAV2-retro system was used to deliver Staphylococcus aureus Cas9 (SaCas9) single guide RNA combination engineered to ablate expression of tdTomato. Bottom panel: rAAV2-retro carrying the SaCas9-anti-tdTomato payload was injected into the BPN of mice expressing tdTomato from a single genomic locus in layer V neurons. SaCas9 was epitope tagged, permitting identification of retrogradely labeled neurons (green channel). Upward arrows: expected labeling following successful ablation of tdTomato. Downward arrows: expected labeling if tdTomato expression is unaffected. (**B**) Representative images from brain sections of animals that received the CRISPR/Cas9 system targeted against tdTomato or carrying a non-targeted guide. tdT: tdTomato. Scale bar: 50 micrometers. (**C**) Efficiency of ablation. Error bars represent the S.E.M.

JOURNAL OF VIROLOGY, June 2008, p. 5887–5911 Vol. 82, No. 12
0022-538X/08/$08.00+0 doi:10.1128/JVI.00254-08
Copyright © 2008, American Society for Microbiology. All Rights Reserved.

In Vitro and In Vivo Gene Therapy Vector Evolution via Multispecies Interbreeding and Retargeting of Adeno-Associated Viruses▽†

Dirk Grimm,[1]‡ Joyce S. Lee,[1] Lora Wang,[1] Tushar Desai,[2] Bassel Akache,[1] Theresa A. Storm,[1] and Mark A. Kay[1]*

Departments of Pediatrics and Genetics, 300 Pasteur Drive,[1] and Department of Biochemistry, 279 Campus Drive,[2] School of Medicine, Stanford University, Stanford, California 94305

Received 4 February 2008/Accepted 2 April 2008

Adeno-associated virus (AAV) serotypes differ broadly in transduction efficacies and tissue tropisms and thus hold enormous potential as vectors for human gene therapy. In reality, however, their use in patients is restricted by prevalent anti-AAV immunity or by their inadequate performance in specific targets, exemplified by the AAV type 2 (AAV-2) prototype in the liver. Here, we attempted to merge desirable qualities of multiple natural AAV isolates by an adapted DNA family shuffling technology to create a complex library of hybrid capsids from eight different wild-type viruses. Selection on primary or transformed human hepatocytes yielded pools of hybrids from five of the starting serotypes: 2, 4, 5, 8, and 9. More stringent selection with pooled human antisera (intravenous immunoglobulin [IVIG]) then led to the selection of a single type 2/type 8/type 9 chimera, AAV-DJ, distinguished from its closest natural relative (AAV-2) by 60 capsid amino acids. Recombinant AAV-DJ vectors outperformed eight standard AAV serotypes in culture and greatly surpassed AAV-2 in livers of naïve and IVIG-immunized mice. A heparin binding domain in AAV-DJ was found to limit biodistribution to the liver (and a few other tissues) and to affect vector dose response and antibody neutralization. Moreover, we report the first successful in vivo biopanning of AAV capsids by using a new AAV-DJ-derived viral peptide display library. Two peptides enriched after serial passaging in mouse lungs mediated the retargeting of AAV-DJ vectors to distinct alveolar cells. Our study validates DNA family shuffling and viral peptide display as two powerful and compatible approaches to the molecular evolution of novel AAV vectors for human gene therapy applications.

A large number of inherited or acquired diseases remain promising targets for human gene therapy. One vector that has shown outstanding potential thus far in numerous preclinical and clinical evaluations is based on nonpathogenic adeno-associated virus (AAV). A unique asset among various properties that make AAV especially attractive over its competitors, such as adenoviral or lentiviral vectors, is the availability of a vast number of natural isolates which differ significantly in their properties (24). We and others have shown previously that the function of an AAV vector particle is determined mainly by the capsid protein and that viral Rep proteins and genomic packaging elements are largely interchangeable (24, 27, 85). Paradoxically, the ever-increasing repertoire of naturally occurring and synthetically generated AAV capsid sequences (>300 to date) is currently creating a dilemma for the rational selection of the optimal serotype for a given application. The importance of finding the ideal capsid for efficient and safe gene transfer has been exemplified in many preclinical studies, as well as in a clinical trial using the AAV type 2 (AAV-2) prototype in human liver tissue (36, 47). In one previous study, the treatment of patients with severe hemophilia B with recombinant AAV-2 expressing human factor IX (hFIX) resulted in mildly elevated, yet therapeutic, levels of this blood coagulation factor. However, expression was short lived, and the hFIX decline was accompanied by a transient asymptomatic increase of liver transaminases, due to a T-cell immune response against the AAV-2 capsid (47). Also, preexisting neutralizing anti-AAV-2 antibodies (frequent in humans) in these individuals likely inhibited the linear vector dose response previously observed in animals.

We and others have suggested previously that the use of novel AAV serotypes, in particular, nonhuman isolates, will help to overcome some of these problems (19, 24, 63). Important examples are AAV-8 and AAV-9, which can transduce mouse liver far better than AAV-2, albeit the difference in dogs or primates is less clear (17, 52, 54, 75). The potential for the complete transduction of liver tissue and perhaps other tissues makes these two non-AAV-2 serotypes also particularly interesting for therapeutic RNA interference (RNAi) (28). We recently demonstrated the feasibility of efficiently and persistently suppressing hepatitis B virus with RNAi from a double-stranded AAV-8 vector (28). On the other hand, a potential drawback of AAV-8 and AAV-9 is their lack of specific tissue tropism (34, 52). The resulting frequent vector dissemination into all organs, including the brain, even from low peripheral doses in mice or monkeys (52, 54) is a particular concern for RNAi therapies in which control over vector biodistribution and the limitation of off-target effects will be imperative for the success of the approach (28).

In order to overcome the constraints of wild-type AAV

* Corresponding author. Mailing address: Departments of Pediatrics and Genetics, School of Medicine, Stanford University, 300 Pasteur Dr., Stanford, CA 94305. Phone: (650) 498-6531. Fax: (650) 498-6540. E-mail: markay@stanford.edu.

† Supplemental material for this article may be found at http://jvi.asm.org/.

‡ Present address: University of Heidelberg, Cluster of Excellence CellNetworks, BIOQUANT, Im Neuenheimer Feld 267, D-69120 Heidelberg, Germany.

▽ Published ahead of print on 9 April 2008.

serotypes, numerous groups have recently begun to develop novel strategies to engineer "designer" AAVs tailored for the therapeutic transduction of clinically relevant organs (reviewed in detail in references 9, 12, 35, 41, 51, and 85). Briefly, the variety of strategies can be grouped into indirect or chemical approaches and direct physical modification strategies. In the indirect approaches, specific molecules (e.g., bispecific antibodies [6] or avidin-coupled ligands [4]) are allowed to react with the viral surface (biotinylated in the case of avidin [4]), as well as a cellular receptor, forming a conjugate ideally able to retarget the capsid to a refractory cell type. Yet, numerous pharmacological problems, such as concerns about in vivo complex stability and difficulties in upscaling complex manufacturing, continue to prevent the broad adaptation of these approaches. Alternative, more powerful strategies rely on the direct physical modification of the AAV capsid protein and gene. Early examples include the generation of mosaic AAV capsids via the mixing of helper plasmids carrying capsid genes from distinct serotypes, such as AAV-1 and AAV-2 (30) and pairwise combinations of AAV-1 through AAV-5 (62). Similar mosaics were generated previously via a marker rescue approach, yielding AAV-2/AAV-3 recombinants with unique properties (8). A related strategy is the rational creation of chimeric virions via domain swapping among multiple parental serotypes, involving either entire capsid loops or parts thereof or individual residues. Notable examples include AAV-1/AAV-2 chimeras with improved tropism in muscle tissue (31), with one of these chimeras presently being studied in a phase I clinical trial for the treatment of Duchenne muscular dystrophy (85). Most recently, our own group described a battery of unique chimeras comprising elements from serotypes 2 and 8, which were exploited to identify capsid subdomains responsible for efficient AAV transduction in murine liver tissue in vivo (64).

A special type of chimeric capsids are those containing foreign proteins or peptides inserted into various positions of the virion shell. The methods and strategies used are widely diverse, and again, we refer to comprehensive reviews (12, 35, 41). Noteworthy here are approaches to fuse targeting ligands to the N termini of AAV capsid proteins (ideally, VP2 [45, 83]), or more powerful, to insert short peptides (up to 14 amino acids [21], typically 7) into exposed regions of the assembled virion. This strategy is referred to as viral display, in analogy to phage display, and has already been used extensively to retarget AAV-2 virions to a multitude of refractory or hard-to-infect cell types, such as vascular endothelial, smooth muscle, and pancreatic islet cells (43, 55, 77, 81, 82) and various tumor lines (22, 58, 65, 66). It has particularly benefited from comprehensive mutational analyses by various groups (e.g., references 21, 33, 56, and 83) that have resulted in the identification of prominent locations within the AAV-2 capsid tolerating peptide insertion. Most notable is the heparin binding domain (HBD), consisting of a total of four arginine (R) residues and one lysine residue, with R585 and R588 representing the most crucial components (37, 56). Numerous groups have now consistently shown that the insertion of 7-mer peptides into this region not only is frequently well tolerated and efficiently mediates virus retargeting, but also provides the extra benefit that the endogenous AAV-2 tropism can be abolished, thus enhancing target specificity (e.g., reference 21).

In addition to identifying sites for vector engineering, some of the mutational AAV studies directly yielded novel capsid variants with potential benefits for clinical use. A remarkable case was a recent study by Lochrie et al. (42) in which a set of 127 AAV-2 variants with point or insertion mutations were generated and screened for multiple properties. Several capsids were isolated which differed from the wild-type AAV-2 capsid in having better in vitro transduction efficiencies (albeit being equally efficient in vivo) or, clinically most relevant, higher-level resistance to individual or pooled human antisera. Nonetheless, the limitations of the approach also became clear, most notably, the extreme effort required to generate and manually screen a large number of mutants, which in fact prevented the interesting analyses of all possible combinations of beneficial point mutations in further capsids.

Indeed, the factors of time and labor are the main reasons why an increasing number of groups have recently begun to develop novel means for AAV vector evolution that no longer rely on the rational modification of the AAV-2 capsid. Instead, the new combinatorial methodologies allow for the far more efficient creation and selection of interesting candidates in a library-based high-throughput format. Thus far, two different strategies have been reported, both principally expanding on previously developed techniques. One is the use of viral display libraries, in which random 7-mer peptides are inserted into the AAV-2 HBD (at amino acid 587 or 588), yielding between 4×10^6 and 1.7×10^8 capsids potentially exposing new ligands on their surfaces (50, 58, 76). Subsequent iterative selection on diverse cell types refractory to the wild type, e.g., coronary artery endothelial cells, cardiomyoblasts, and carcinoma, leukemia, and megakaryocytic cell lines, led to enrichment with peptide mutants with increased target specificities and efficacies (48, 50, 58, 76). The second library type, independently described by two groups in 2006, relies on error-prone PCR amplification of the AAV-2 capsid gene (46, 59). Similar to the methods in earlier mutational studies, this approach resulted in the identification of AAV-2 point mutations (usually up to two per capsid) which yielded mutants that differed from the wild type in having mildly enhanced efficacies in vitro and/or improved transduction efficiencies in the presence of neutralizing anti-AAV-2 antibodies either generated in rabbits or preexisting in individual human sera.

Here, for the first time, we introduce the technology of DNA family shuffling into the realm of AAV vector evolution. The basic concept of this technology is the in vitro recombination of related parental genes with >50% homology, which are first fragmented and then reassembled based on partial homology, resulting in libraries of chimeric genes. Iterative amplification under pressure can then yield hybrids not only combining parental assets, but also ideally exhibiting novel and synergistic properties (70, 71). DNA family shuffling has been used extensively in recent years to evolve and improve all types of proteins, from markers and enzymes to vaccines (e.g., references 10, 13–15, and 39). Importantly, a set of reports also suggested its power to enhance viral gene therapy vectors by creating retro- or lentiviruses with improved stability or efficacy compared to that of the parental wild types (57, 61, 69). Here, we describe the novel use of DNA family shuffling for the highly efficient molecular interbreeding of eight multispecies AAVs to create chimeric capsids and, moreover, document its com-

patibility and synergism with existing AAV vector evolution technology.

MATERIALS AND METHODS

Plasmids for generation of shuffled AAV capsid library. Plasmids containing full-length capsid genes (*cap*) of seven different AAV serotypes were present in the lab (for AAV-2, AAV-4, and AAV-5) or kindly provided by James Wilson (for AAV-8 and AAV-9) or Jay Chiorini and Rob Kotin (for avian and bovine AAV). Goat AAV was not available as a molecular clone early in our study and was therefore partly synthesized (GeneArt, Regensburg, Germany) as an 888-nucleotide (nt) fragment (nt 1023 to 1910). This subclone corresponds to the entire right half of the goat AAV capsid protein, which comprises all 42 reported (3) differences between goat AAV and AAV-5. The other seven *cap* genes were initially amplified via PCR and subcloned into pBluescript II SK (Stratagene). The purpose was to flank all *cap* genes with sites for the unique restriction enzyme PacI (5′) or AscI (3′) to facilitate the later cloning of shuffled *cap* genes into a wild-type AAV plasmid (see below). All primers also contained either a HindIII (5′) or a SpeI (3′) site to allow directed cloning into pBluescript (none of the four restriction enzymes cut in any parental *cap* gene). A 20-nt signature region was inserted between the two restriction sites in each primer to provide conserved primer binding sites for the later PCR amplification of shuffled genes. The resulting sequence of the forward primer was 5′ GGACTC **AAGCTT** GTC TGAGTGACTAGCATTCG ***TTAATTAA*** CAGGT ATG N_{22} 3′ (the HindIII site is in bold, the PacI site is in bold italics, the signature region is underlined, and N_{22} denotes the first 22 nt of each *cap* gene following the ATG start codon). Likewise, the reverse primer was 5′ CGTGAG **ACTAGT** GCTTACTGAAGCT CACTGAG ***GGCGCGCC*** TTA N_{22} 3′ (the SpeI site is in bold, the AcsI site is in bold italics, the signature region is underlined, and N_{22} denotes the last 22 nt of each *cap* gene up to the TAA stop codon).

In parallel, a wild-type *cap* recipient plasmid was engineered to contain the AAV-2 packaging elements (inverted terminal repeats [ITRs]) flanking the AAV-2 *rep* gene (encoding AAV replication proteins), together with PacI and AscI sites for *cap* cloning and the AAV-2 polyadenylation site. Therefore, AAV-2 *rep* (nt 191 to 2189) was PCR amplified using primers containing BglII sites and then subcloned into pTRUF3 (carrying AAV-2 ITRs with adjacent BglII sites) (88). The forward primer used was 5′ CGAACC **AGATCT** GTCCT GTATTAGAGGTCACGTGAG 3′ (the BglII site is in bold, and AAV-2 nt 191 is underlined), and the reverse primer was 5′ GGTAGC **AGATCT** GTTCGAC CGCAGCCTTTCGAATGTCCGG TTTATT GATTA ***GGCGCGCC*** CTGG ACTC ***TTAATTAA*** CAT*TTA*TTGTTCAAAGATGC 3′ (the BglII site is in bold, the polyadenylation signal is underlined, the AscI site is in bold italics, the PacI site is underlined and shown in bold italics, and the AAV-2 *rep* stop codon is underlined and shown in italics). Note that this procedure changed the AAV-2 SwaI site (downstream of the *rep* stop codon) into a PacI site.

DNA family shuffling of AAV capsid genes. For DNA family shuffling, we basically utilized a two-step protocol in which the parental genes were first fragmented using DNase I enzyme and then reassembled into a full-length gene via primerless PCR (69, 71). This PCR was followed by a second PCR including primers binding outside of the *cap* genes, allowing the subcloning of the products into the wild-type recipient ITR-*rep* plasmid (see above and Fig. 1B). Initially, we isolated all *cap* genes from our subclones via HindIII/SpeI digestion (EcoRI digestion for goat AAV) and then optimized the reaction conditions as follows. We tested various DNase I concentrations and incubation times, aiming to obtain a pool of fragments between 0.2 and 1.0 kb in size (which gave the best results in later steps). The optimal conditions were found to be 1 μg of each *cap* gene, 1 μl of 1:200-prediluted DNase I (10 U/μl; Roche), 50 mM Tris-Cl (pH 7.4), and 1 mM $MgCl_2$ in a total volume of 50 μl. The reaction mixture was incubated for 2 min at room temperature, and then the reaction was stopped by heat inactivation at 75°C for 10 min. Fragments of the desired sizes were isolated by running the entire reaction mixture on a 1% agarose gel (total final mixture volume, ~60 μl). We next optimized the reassembly PCR by testing various DNA polymerases (Platinum Pfx [Invitrogen], DeepVent [NEB], and *Taq* [Amersham]) and respective conditions. Best results were obtained using PuReTaq ready-to-go PCR beads (Amersham) and the following conditions: 25 μl of purified *cap* fragments and a program of 4 min at 95°C; 40 cycles of 1 min at 95°C, 1 min at 50°C, and 3 min at 72°C; 10 min at 72°C; and 10 min at 4°C. Agarose gel (1%) analysis of 1 μl from this reaction mixture typically showed a smear in the area up to the 5-kb marker and no distinct bands. The same three polymerases listed above were then evaluated for the primer-containing second PCR mixture, and the following conditions were found to be optimal: 1 μl of Platinum Pfx, 2 μl of the product from the first PCR, 1 mM $MgSO_4$, 1 μg of each primer (see below), and 0.3 mM (each) deoxynucleoside triphosphates in a total volume of 50 μl and a program of 5 min at 94°C; 40 cycles of 30 s at 94°C, 1 min at 55°C, and 3 min at 68°C; 10 min at 68°C; and 10 min at 4°C. The primers used bound to the 20-nt signature regions described above. This reaction gave a distinct ~2.2-kb full-length *cap* band (on 1% agarose gel), which was purified (60 μl total) and cloned (4 μl) by using the Zero Blunt TOPO PCR cloning kit (with electrocompetent *Escherichia coli* TOP10 cells; Invitrogen, Carlsbad, CA). This intermediate cloning step significantly enhanced the yield of shuffled *cap* genes compared to that of efforts to clone the PCR product directly via conventional means (data not shown). The shuffled *cap* genes were then released from the TOPO plasmid via PacI and AscI double digestion and cloned into the appropriately digested ITR-*rep* recipient plasmid.

Performing all these reactions under minimal conditions (with respect to volumes and amounts), we obtained a library of approximately 3×10^4 bacterial colonies. The upscaling of each step (including final plating onto 100 15-cm plates) resulted in a final library of $\sim 7 \times 10^5$ plasmid clones. The integrity, genetic diversity, and functionality of the library were confirmed by DNA sequencing and small-scale expression studies (see Fig. 1C and Fig. S1 and S2 in the supplemental material).

Selective in vitro amplification of the shuffled capsid library. We prepared a viral library by transfecting 293 cells in 50 T225 flasks ($\sim 10^9$ cells) with 50 μg of plasmid from the bacterial library per flask, together with 25 μg of an adenoviral helper plasmid (23). The resulting hybrid viruses were concentrated, purified, and titrated as described previously for recombinant AAV (23, 53). The final library used in this study had a particle titer (viral genome concentration) of 8.2×10^{11}/ml (total volume, 3 ml). Various amounts of purified shuffled AAV were then incubated with the different cell lines (in 6-cm dishes), together with various amounts of helper adenovirus type 5. Ideally, the adenovirus would lyse the cells within 3 days, giving the AAV sufficient time to replicate. The AAV amounts were adjusted empirically so that we obtained minimal signals in Western blot analyses of cell extracts. This strategy helped to optimize the stringency of our library in each amplification round by ensuring that (ideally) a single viral genome was delivered to each cell and subsequently packaged into the capsid expressed from this particular viral genome. In one set of experiments, the library was additionally subjected to intravenous immunoglobulin (IVIG) pressure during amplification. Therefore, various volumes of the library and IVIG (GamimuneN [10%]; Bayer, Elkhart, IN) were mixed (see Fig. S3 in the supplemental material for examples), and the mixtures were incubated for 1 h at 37°C and then added to the cells. After overnight incubation, the cells were washed and superinfected with adenovirus. The wash step was included to avoid helper virus inactivation by the IVIG. As before, AAV amplification was controlled by Western blotting after each round, and only supernatants giving minimal expression were used for subsequent infections. The increasing IVIG resistance of the library during consecutive passages allowed us to continuously escalate the IVIG doses (see Fig. S3 in the supplemental material). All amplification experiments comprised five infection cycles (adenovirus was heat inactivated between each and then added fresh, to avoid uncontrolled amplification). Finally, viral DNA was purified from the supernatant by using a DNA extractor kit (Wako, Japan), and AAV *cap* genes were PCR amplified by using DeepVent polymerase and primers 5′ GATCTGGTCAATGTGGATTTGGATG 3′ (binding in AAV-2 *rep* upstream of the PacI site used for *cap* cloning) and 5′ GACCGCAGCCTTTC GAATGTCCG 3′ (binding downstream of the AscI site and the polyadenylation signal). The resulting blunt-ended *cap* genes were subcloned using the Zero Blunt TOPO PCR cloning kit for sequencing (Invitrogen), and DNA from individual clones (96 per cell line per amplification round) was prepared. To assemble full-length *cap* sequences, we first used T3 and T7 primers to obtain the 5′ and 3′ ends of each clone and then designed individual primers (data not shown) to acquire the remaining sequence. Alignments (DNA and protein) with the sequences of the eight parental viruses were performed using BLAST and VectorNTI 10/AlignX software (Invitrogen).

Helper plasmid cloning and vector particle production. Helper plasmids expressing wild-type AAV-2, AAV-8, or AAV-9 *cap* together with AAV-2 *rep* genes, as well as AAV-2-based vector plasmids expressing the hFIX gene from a liver-specific promoter or the elongation factor 1α promoter, *lacZ* from a cytomegalovirus (CMV) promoter, or the luciferase gene from a simian virus 40 promoter, have all been described previously (18, 19, 28, 52). The generation of two self-complementary vector plasmids expressing either the *gfp* gene from a CMV promoter or the human alpha-1 antitrypsin (hAAT) gene from a Rous sarcoma virus promoter will be described in detail elsewhere (D. Grimm, L. Wang, J. S. Lee, T. A. Storm, and M. A. Kay, unpublished data). For the cloning of helper plasmids expressing shuffled *cap* genes, the entire AAV-8 *cap* gene was removed from the AAV-8 helper construct by cutting with SwaI and PmeI (both create blunt ends; SwaI cuts 9 nt upstream of the VP1 gene start codon, and PmeI cuts 53 nt downstream of the polyadenylation signal). The novel *cap* genes

were amplified from the respective TOPO constructs (see above) via PCR using the forward primer 5′ AAAT CAGGT N_{25} 3′ (the underlined nucleotide sequence restored the SwaI site to maintain correct reading frames, and N_{25} denotes the first 25 nt of each *cap* gene, ATGGCTGCCGATGGTTATCTT CCAG for AAV-DJ, AAV-2, AAV-8, and AAV-9). The reverse primer was 5′ AAAC GAATTCGCCCTTCGCAGAGACCAAAGTTCAACTGAAACGAA TCAACCGG **TTTATT** GATTAACAGGCAA N_{23} 3′ (the nucleotides restoring the PmeI site are underlined, the polyadenylation signal is shown in bold, and N_{23} denotes the last [3′] 23 nt of the shuffled capsid genes, TTACAGATTAC GGGTGAGGTAAC for AAV-DJ [3′-to-5′ orientation]). PCRs were performed using DeepVent DNA polymerase (NEB), creating blunt ends allowing straightforward insertion into the linearized AAV-8 helper plasmid. Insert junctions and correct orientation were confirmed via DNA sequencing (Biotech Core). Vector production and particle titration (by dot blotting) were performed as described previously (53); yields for all vectors including AAV-DJ and the HBD mutants typically exceeded 6×10^{13} total physical particles per 50 T225 flasks (2×10^9 cells). HBD mutant plasmids (see Fig. 6A) were generated by A585X and B588Y site-directed mutagenesis using a QuikChange II kit (Stratagene), with A and B representing the native residues and X and Y representing the new residues. The gain or loss of heparin binding ability was confirmed via a standard heparin binding assay using type I heparin agarose (Sigma) (data not shown). Due to an unknown deficiency, the AAV-9/AAV-2 chimeric mutant (AAV-9/2) could not be produced in sufficient amounts for in vivo evaluation.

Helper plasmids for peptide display. Prior to the generation of AAV peptide display libraries, we mutated the AAV-DJ helper plasmid to permit the insertion of oligonucleotides encoding seven amino acids after residue R588. In parallel, we created (using the cloning strategy for *cap* described above) and also mutated an AAV-2 helper. We basically adapted a multistep mutagenesis strategy first described for AAV-2 by Müller and colleagues (50), with the exception that we additionally mutated R585 into a glutamine (as in AAV-8). Accordingly, our mutagenesis primers were identical to those described above, except for the final (third) primer pair, which was 5′ CAACCTCCAG**CA**AGGCCAGAGAGGCC AAGGCCCAGGCGGCCACCGCAG 3′ (nucleotides changing R585 to Q585 are underlined and shown in bold) and 5′ CTGCGGTGGCCGCCTGGGCCT TGGCCTCTCTGGCCTTGCTGGAGGTTG 3′. The resulting AAV-2/AAV-DJ helper plasmids carried two unique SfiI sites permitting the straightforward insertion of 21-mer oligonucleotides encoding specific peptides. Notably, another SfiI site normally present in the AAV-2 *rep* gene was absent in the helper plasmid backbone used here (it had to be mutated in the original cloning strategy [50]; see also below). The oligonucleotides corresponding to the two lead peptides in this study were as follows: for the peptide NSSRDLG, 5′ AGGC**AACTCAAGCCGAGAC CTAGGA**GCCCAGG 3′ and 5′ GGGCTCCTAGGTCTCGGCTTGAGTTGCC TCTC 3′, and for MVNNFEW, 5′ AGGC**ATGGTCAACAATTTTGAGTGG**GC CCAGG 3′ and 5′ GGGCCCACTCAAAATTGTTGACCATGCCTCTC 3′ (nucleotides encoding the respective seven amino acids are underlined and shown in bold). Each oligonucleotide pair was annealed and then ligated into the SfiI-cut AAV-DJ helper plasmid. The presence of the correct inserts was confirmed upon sequencing with the HBD primer 5′ GTCATGATTACAGACGA AGAGGAAATC 3′ (binding upstream of the HBD-encoding sequences in the AAV-2 and AAV-DJ *cap* genes).

Creation of viral peptide display libraries based on AAV-2 and AAV-DJ. The actual libraries of infectious AAV plasmids carrying random 21-mer oligonucleotides were again created in a multistep approach, similar to the generation of our shuffled library. First, we destroyed the SfiI site in wild-type AAV-2 *rep* in the context of the pΔTR18 plasmid (carrying AAV-2 *rep* and *cap*) (27). Primers used were 5′ GTGAGTAAGGC**A**CCGGAGGCCC 3′ and 5′ GGGCCTCCGGTGC CTTACTCAC 3′ (the nucleotide change disrupting the SfiI site is underlined and shown in bold). The mutated *rep* gene was then PCR amplified using the same BglII site-containing forward primer described above and, as the reverse primer, 5′ GGTAGC **AGATCT *GTTTAAAC*** CAT*TTA*TTGTTCAAAGATGC AGTC 3′ (the BglII site is in bold, the PmeI site is underlined and shown in bold italics, and the AAV-2 *rep* stop codon is underlined and shown in italics). This fragment was inserted into BglII-cut pTRUF3 to become flanked by AAV-2 ITRs. The resulting construct was linearized by cutting with HindIII and PmeI, and the mutated AAV-2 and AAV-DJ *cap* genes (containing two adjacent SfiI sites but lacking any insert) were inserted as HindIII/PmeI fragments. In a final step, we then cloned a library of 21-mer oligonucleotides encoding random peptides into the two plasmids. The 21-mers were flanked by sequences comprising BglI sites, so that after cleavage they would be compatible with the SfiI-cut AAV *rep-cap* plasmids. The full sequence of the forward primer was 5′ CAGTCG**GCC**AGAGA**GGC** $(NNB)_7$ **GCC**CAGGC**GGC**TGACGAG 3′ (BglI sites are underlined and shown in bold), with B representing the nucleotide T, C, or G (see Results). To create a double-stranded oligonucleotide for actual BglI cleavage and cloning, primer 5′ CTCGTCAGCCGCCTGG 3′ was used in a second-strand synthesis reaction as described previously (50). The presence of random 21-mer inserts or of 21-mer inserts selected after biopanning (see below) in individual clones was confirmed using the HBD sequencing primer.

AAV protein analyses. Western blot and immunofluorescence analyses were carried out as reported previously (29) by using the monoclonal B1 antibody (useful because its 8-amino-acid epitope [see Fig. 2D and Fig. S4 in the supplemental material] is largely conserved across known AAV serotypes) for the detection of immobilized AAV capsid proteins. For immunofluorescence studies, polyclonal antisera were diluted 1:200 in 1× phosphate-buffered saline (PBS) while monoclonal antibodies (B1, A20, and 303.9) were used undiluted. Atomic structure models were created using DeepView Swiss-PdbViewer software version 3.7 (www.expasy.org/spdbv) and VIPER (viperdb.scripps.edu/oligomer_multi.php).

In vitro transduction, binding, and cleavage assays. All transformed cell lines were maintained in Dulbecco's modified Eagle's medium (Gibco) containing 10% fetal calf serum, 2 mM L-glutamine, and 50 IU each of penicillin and streptomycin/ml at 37°C in 5% CO_2. Fresh primary human hepatocytes (in 6-well plates without Matrigel) were obtained from Admet (Durham, NC) and maintained in hepatocyte basal medium (Cambrex, Walkersville, MD) with recommended supplements. The titration of *gfp*-expressing recombinant AAV particles was performed in 96-well plates (27), following the normalization of each virus stock to 2×10^9 particles/ml. For in vitro neutralization studies, 50-μl aliquots of each vector preparation were incubated with serial 10-fold dilutions of IVIG or mouse sera (following a 1-h heat inactivation step at 56°C) for 1 h at 37°C prior to titration on cells. Titers of neutralizing antibodies were calculated as reported previously (29). Details of the cell binding and cathepsin B digestion were reported recently (2).

In vivo biopanning. Wild-type FVB mice (6 to 8 weeks old; Jackson Laboratory, Bar Harbor, ME) were inoculated with the shuffled or peptide-displaying libraries at the doses indicated below. The mice also received different volumes (see Results) of wild-type adenovirus stocks purchased from the American Type Culture Collection (ATCC; Manassas, VA): human adenovirus C deposited as adenovirus 5 (catalog number VR-5) and mouse adenovirus (catalog number VR-550). Total inoculum volumes were 300 μl of 1× PBS for liver panning (injected via the tail vein) and 50 μl of 1× PBS for lung panning. For the latter, the mice were briefly anesthesized using an isoflurane vaporizer and placed on their backs. The virus suspension was then carefully pipetted directly onto both nostrils, resulting in the rapid aspiration of the suspension within a few seconds. Typically, 7 days postinfection, the mice were sacrificed and the organs were harvested, minced, and frozen in aliquots in liquid nitrogen. Total genomic DNA was prepared (as reported in reference 27) from one aliquot for subsequent PCR amplification of AAV DNA by using Platinum Pfx polymerase (Invitrogen) and specific primers flanking the entire capsid gene. For the shuffled *cap* genes, the primers were identical to those used before for in vitro biopanning. For the peptide-encoding *cap* genes, we used the same forward primer but a serotype-specific reverse primer: for AAV-2, 5′ TTACAGATTACGAGTCA GGTATC 3′, and for AAV-DJ, 5′ TTACAGATTACGGGTGAGGTAAC 3′. As before, the *cap* genes were then cloned using the Zero Blunt TOPO PCR cloning kit and sequenced using either T3 and T7 primers for the shuffled genes or the HBD sequencing primer for the peptide-expressing clones. Another aliquot was freeze-thawed three times in liquid nitrogen in 200 μl of 1× PBS and additionally homogenized to release intact AAV particles. Tissue debris was spun down (16,000 × *g* for 5 min), and the supernatant was heat inactivated (30 min at 65°C to kill amplified adenovirus) and then used for reinoculation into new mice (for liver tissue, up to 100 μl, and for lung tissue, 25 μl), together with freshly added helper adenovirus. In some cases (see below), the supernatant (50 μl) was depleted of murine immunoglobulin G (IgG) prior to reinfection by using a commercial kit (ProteoPrep immunoaffinity albumin and IgG depletion kit) according to the instructions provided by the manufacturer (Sigma, St. Louis, MO).

Expression studies with mice. Wild-type female C57BL/6 mice (6 to 8 weeks old) were purchased from the Jackson Laboratory (Bar Harbor, ME). Recombinant AAVs expressing the hFIX or hAAT genes in 300 μl of 1× PBS were administered via tail vein infusion. Blood was collected at the indicated time points via retroorbital bleeding, and plasma hFIX or hAAT levels were determined via an enzyme-linked immunosorbent assay as described previously (28, 52). Recombinant AAVs expressing the firefly luciferase gene in 300 μl of 1× PBS were infused via the tail vein for liver transduction or administered nasally in 50 μl of 1× PBS for lung transduction. Luciferase experiments were conducted with wild-type female FVB/NJ mice (6 to 8 weeks old) from the Jackson Laboratory (Bar Harbor, ME), and expression in live animals was monitored as described previously (28). Recombinant AAV-DJ variants expressing the *lacZ* gene were also given nasally. Two weeks later, animals were euthanized, the tracheas were cannulated, and lungs were inflated with 2% low-melting-point agarose and then sectioned with a Vibratome sectioning

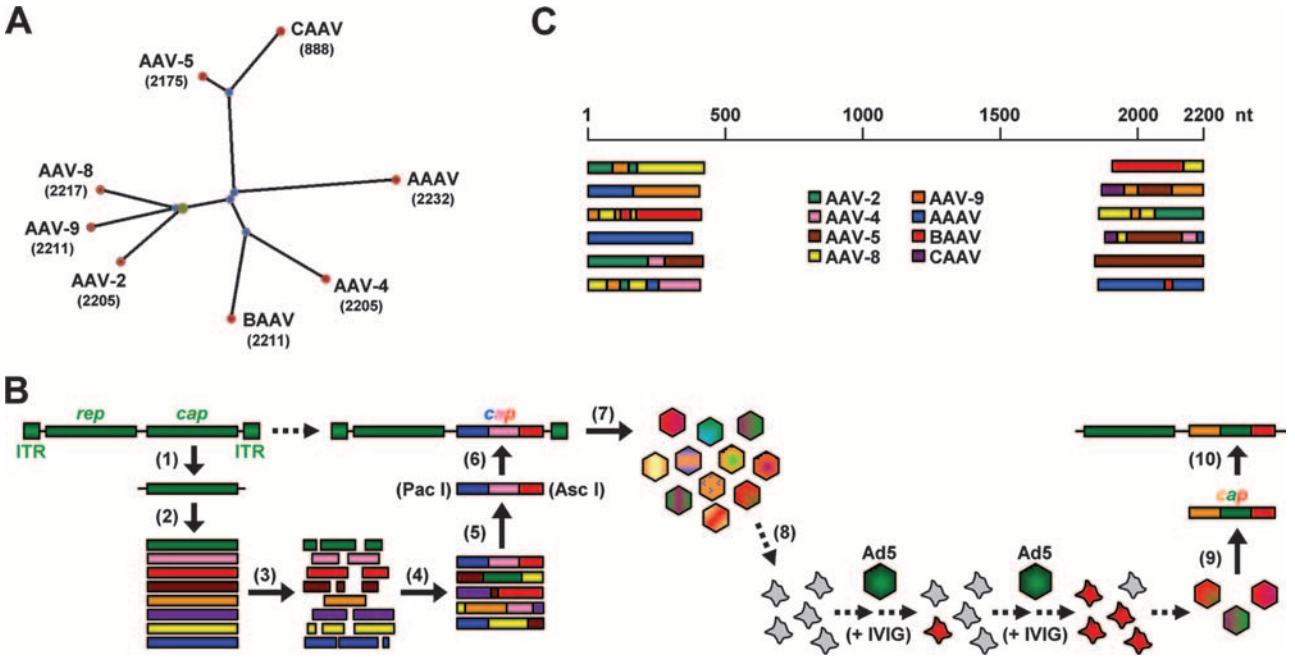


FIG. 1. Generation of an AAV capsid library via DNA family shuffling. (A) Phylogram tree (created using PhyloDraw [http://pearl.cs.pusan.ac.kr/phylodraw/#test]) showing the eight AAV serotypes used as parents for DNA family shuffling (numbers denote lengths of capsid genes, in nucleotides). Branch lengths are proportional to the amounts of evolutionary change, calculated in ClustalW (http://www.ebi.ac.uk/clustalw/#). CAAV, AAAV, and BAAV, caprine, avian, and bovine AAVs, respectively. (B) Individual steps for generation of the library (scheme). Full-length *cap* genes were PCR amplified and subcloned for further amplification (1) and then isolated (2) and DNase I digested (3). Two consecutive PCRs without (4) or with (5) conserved primers were performed to reassemble shuffled full-length *cap* genes. These genes were inserted (6) into a plasmid carrying AAV-2 ITRs and a *rep* gene. The transfection of 293 cells with the resulting plasmid library (7) together with an adenoviral helper resulted in a viral library. One possible selection scheme used in this study was the coinfection of cultured liver cells (8) with the library and helper adenovirus under stringent conditions, resulting in the amplification of specific AAV capsids. Viral DNA can then be isolated (9) and cloned into an AAV helper plasmid carrying the AAV-2 *rep* gene without ITRs (10) for subsequent vector production. Ad5, helper adenovirus type 5. (C) Examples of shuffled *cap* genes in an initial small-scale library. DNA was extracted from 24 randomly chosen clones, and 5′ and 3′ ends of the individual *cap* genes were sequenced (using T3/T7 primers binding in the plasmid backbone). Shown, per end, are six representative alignments with the eight parents.

system into 100-μm slices, which were fixed overnight at 4°C in 4% paraformaldehyde. For β-galactosidase detection, lung slices were washed three times for 5 min each time in a solution of 1× PBS, 2 mM $MgCl_2$, 0.02% NP-40, and 0.01% sodium deoxycholate and then incubated overnight at room temperature in the dark in a solution containing the β-galactosidase substrate X-Gal (5-bromo-4-chloro-3-indolyl-β-D-galactopyranoside). Lungs were postfixed in 4% paraformaldehyde and stored at 4°C in 1× PBS. All procedures were approved by the Animal Care Committee at Stanford University. Genomic DNA was extracted from mouse tissues and analyzed via Southern blotting using hFIX gene-specific probes as reported previously (53).

Immunologic in vivo assays. For passive immunization studies, mice were injected intravenously (via the tail vein) with 40 μl (low dose) or 200 μl (high dose) of IVIG (100 mg/ml) diluted in 1× PBS in a total volume of 300 μl and, 24 h later, infused (via the tail vein) with 2×10^{11} recombinant hFIX gene-expressing AAV particles. For cross-neutralization studies, mice were immunized against individual AAV serotypes by the peripheral infusion of 10^{11} recombinant hAAT gene-expressing particles. Three weeks later, mouse sera were collected for in vitro neutralization assays before the mice were reinfused with 10^{11} (or 5×10^{11} for AAV-2) (see below) recombinant hFIX gene-expressing AAV particles. In an experiment for which the data are not shown, the two AAV injections were carried out in the reverse order (first hFIX-expressing particles and then hAAT-expressing particles); the conclusions substantiated those presented below (see Fig. 9C).

RESULTS

Generation of an AAV capsid library via DNA family shuffling. A chimeric AAV capsid library was generated from eight parental wild-type viruses of human, primate, or nonprimate origin (Fig. 1A). In line with our primary goal, to evolve novel AAV capsids on liver cells in vitro, they were chosen based on performance in culture (AAV-2) or in liver tissue (AAV-8 and AAV-9), their substantial sequence divergence from AAV-2 (AAV-4, AAV-5, and avian, bovine, and caprine AAVs), or their low prevalence in the human population (all but AAV-2 and AAV-5). The conditions for AAV DNA family shuffling were established in small-scale studies (schematically depicted in Fig. 1B and C) in order to optimize parameters, including the choice of DNA polymerases for the PCRs and the lengths of the subgenomic capsid fragments (see Materials and Methods for details). The best conditions were then upscaled to yield a hybrid capsid-encoding plasmid library with a complexity of $\sim 7 \times 10^5$ distinct sequences. Packaging via the cotransfection of 293 cells with an adenoviral helper plasmid resulted in the final viral library, with a particle titer of $\sim 8.2 \times 10^{11}$ genomes/ml (total volume, 4 ml from $\sim 10^9$ cells, i.e., ~3,300 particles per cell).

The isolation and sequencing of 48 randomly chosen clones confirmed extensive genetic diversity and validated the presence of all eight parental viruses in the final pool (see Fig. S1 and S2 in the supplemental material). Importantly, there was no apparent bias toward particular serotypes or combinations thereof in our library, nor did we obtain evidence for preferred

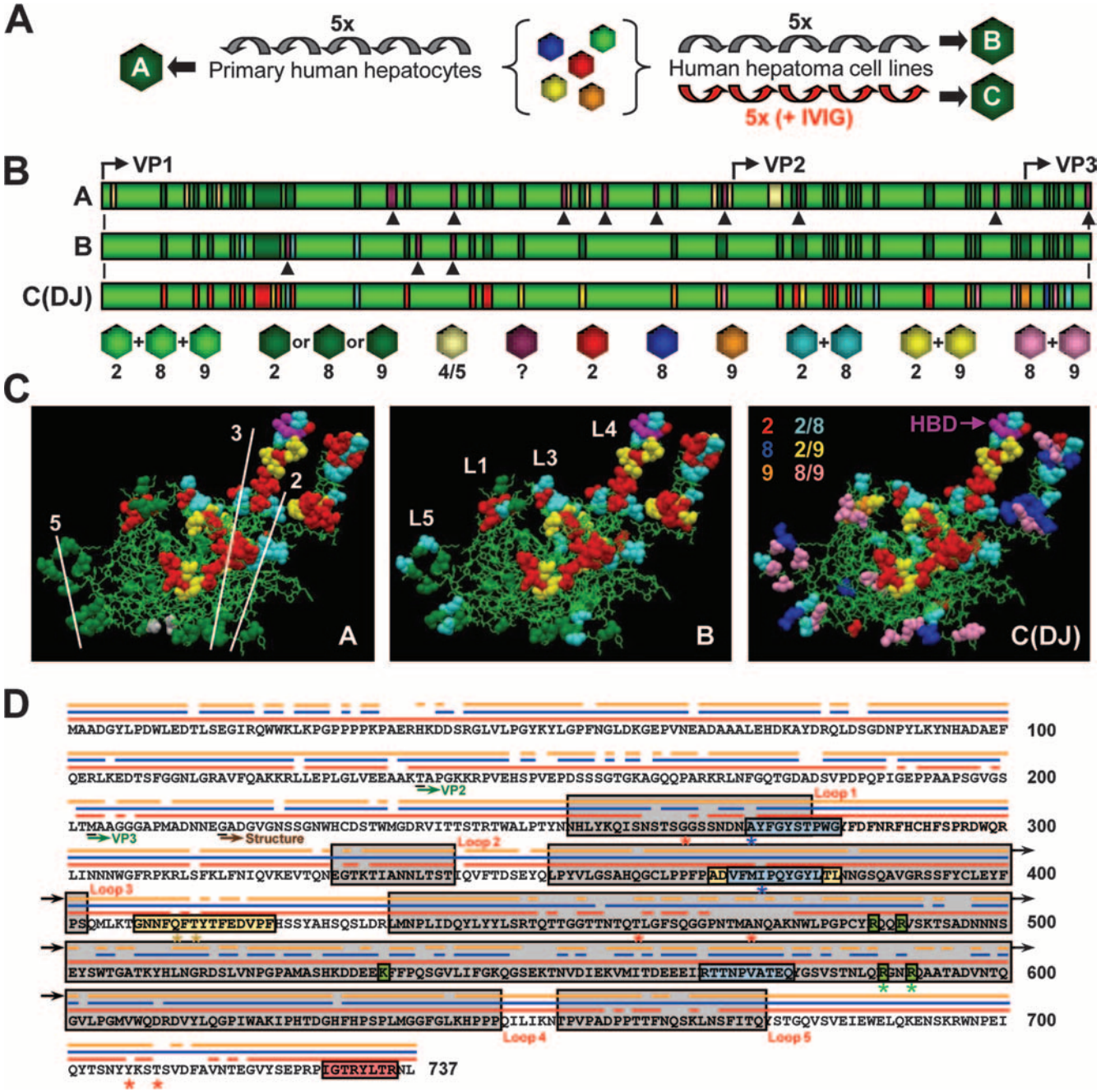


FIG. 2. Molecular evolution of AAV vectors via DNA family shuffling. (A) The AAV capsid library was serially amplified on primary or transformed human liver cells. Purified human Igs (IVIG) were added to increase the selection pressure and to force vector evolution. Each scheme yielded a distinct pool of viral capsids (pools A to C). The alignment of ≥96 clones per pool with the sequences of the eight parental viruses confirmed the enrichment with specific sequences in association with increasing selection pressure. 5x, five times. (B) First 217 amino acids of the VP1 capsid protein for each pool. Colors represent the relationships to the parental strains (serotypes 2, 4, 5, 8, and 9), as also shown and detailed in Fig. S3 in the supplemental material. Arrowheads represent point mutations. Start codons for all three capsid proteins are shown. Pool C contained a single clone, designated AAV-DJ. (C) Putative atomic structure for each pool (the previously reported AAV-2 structure [Protein Data Bank file 1LP3 {http://www.rcsb.org}] was used as the basis for modeling; this structure lacks the residues represented in panel B). Thin green lines indicate sequence homology among the AAV-2, AAV-8, and AAV-9 parents. Residues shown as colored balls were derived from a subset of parental strains (see panel B for color codes; note that beige symbolizes AAV-5 in pool A here). AAV capsid symmetry axes (pool A) and four of the five loops (pool B) are shown. The location of two arginines as part of the conserved HBD (37) at the tip of loop IV is shown for AAV-DJ (pool C). (D) Capsid protein sequence of AAV-DJ. The three parental viruses are shown as thin lines above the sequence (AAV-2, red; AAV-8, blue; AAV-9, orange). Locations of the capsid loops, VP start codons, and the first residue of the atomic structure are indicated. A20 and B1 epitopes are boxed in blue and red, respectively (two mutations in the A20 epitope are shown by blue asterisks). Two recently identified immunogenic AAV-2 peptides (47) are boxed in yellow (AAV-DJ carries three point mutations, indicated by asterisks). Residues in green boxes form the conserved AAV-2 HBD (asterisks denote two arginines mutagenized in this study). Red asterisks denote residues previously discovered using other methods and believed to determine AAV-2 immunogenicity (see the text).

hot spots for recombination. Instead, all eight parents were found in a random pattern, which is the ideal result. We were especially pleased to find recombinants with elements from very diverse serotypes, such as AAV-4 and AAV-5 (see data for clone S8 in Fig. S1 in the supplemental material), as it confirmed the potential of DNA family shuffling to create hybrids from parents differing by as much as ~50%. As a result, the capsids in our library reflected and recapitulated the diversity of natural AAVs, exemplified by the fact that the levels of clonal homology to the AAV-2 prototype ranged anywhere from 46 to 93% (see Fig. S1 and S2 in the supplemental material). This wide sequence diversity positively distinguishes our methodology from previous AAV libraries, in which all resulting particles remained over 99% identical to the single parental virus, usually AAV-2 (46, 50, 58, 59, 76) (see also Discussion). Last but not least, we observed several point mutations in individual clones but found no evidence for lethal mutations or frameshifts. This outcome was in line with our expectations, as a hallmark of DNA family shuffling is the in-frame recombination of related functional sequences. This result further distinguishes our methodology from prior AAV evolution approaches, particularly those based on error-prone PCR, in which the offspring were frequently not viable (46, 59).

Stringent selection of AAV variants on human liver cells. To screen for capsids with enhanced efficiency in liver cells, we serially (five times) amplified our library on human primary hepatocytes (Fig. 2A, pool A) or hepatoma cells (Huh-7 and HepG2) (Fig. 2A, pools B and C) as detailed in Materials and Methods. The extraction and sequencing of viral DNA from up to 192 clones per cell type (384 clones total) yielded 369 full-length capsid genes, whose compositions are shown in Fig. 2B and C. Strikingly, all clones showed predominant homology to five of the eight starting viruses, serotypes 2, 4, 5, 8, and 9, and had retained an HBD from the AAV-2 parent. Notably, this domain, whose function is binding to the primary AAV-2 receptor heparan sulfate proteoglycan (72), was clearly underrepresented in the unselected library, where it was found in only 3 of 48 clones (~6%) (see, e.g., data for clone S8 in Fig. S2 in the supplemental material), in line with the random presence of AAV-2 sequences. The enrichment with and conservation of the HBD during selection on cultured cells suggested its crucial role for in vitro transduction. Indeed, vectors made from 10 individual capsids gave infectious titers similar to those of wild-type AAV-2 and exceeding those of HBD-deficient serotypes 8 and 9 (data not shown).

Despite the similarity of pools A (primary cells) and B (cell lines), we recovered only a single capsid sequence twice (Fig. 3, lane A), while all other 367 clones differed from each other by at least three amino acids (defined as our redundancy cutoff). In a direct comparison of the two pools, we noted the increased accumulation of serotype-specific residues, together with a reduction of random point mutations, in the capsids from the hepatocyte cell lines (Fig. 2B and C). This finding likely reflected the fact that HepG2 and Huh-7 cell lines are substantially more homogenous than primary human hepatocytes, which often vary among batches and donors. Nonetheless, the clonal heterogeneity even in the more evolved pool B prevented the reasonable selection and study of single sequences. To further force the evolution of individual capsids, we thus applied additional strong negative selection pressure to our

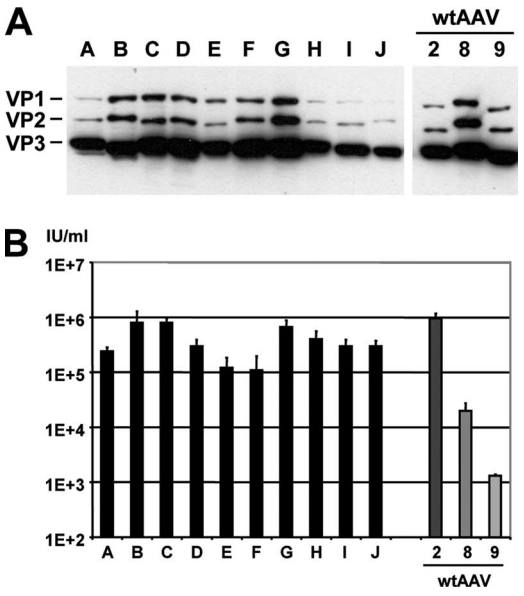


FIG. 3. In vitro analysis of selected shuffled capsids. Following five consecutive amplifications of the AAV library on primary human hepatocytes, viral DNA was extracted from 10 randomly chosen clones (with the exception of the clone corresponding to lanes A, which was recovered twice from pool A), and the *cap* genes were subcloned into an AAV helper plasmid. (A) Western blot (using B1 antibody) showing differences in the expression levels and sizes of the individual VP proteins compared to those of wild-type AAVs (wtAAV). (B) Results from titration of infectious *gfp*-expressing particles. The helper plasmids described above were used to package a *gfp*-expressing AAV vector plasmid, and titers of recombinant particles in crude cell extracts were determined ($n = 3$) as detailed in Materials and Methods. All shuffled clones gave higher titers than the AAV-8 or AAV-9 helpers. No linear correlation between VP protein expression levels (A) and titers (B) could be made, suggesting that the various chimeras differed in their packaging efficacy, infectivity, and/or other parameters.

library via incubation with pooled human antisera (IVIG) prior to reamplification (see Fig. S3 in the supplemental material). The high-level neutralizing activity of our particular IVIG batch (GamimuneN [10%]; Bayer) against multiple serotypes, especially AAV-2, implied its potential to eliminate capsids displaying prevalent epitopes from the library. Any surviving capsids were deemed to be useful in humans, with regard to the high frequency of neutralizing anti-AAV-2 antibodies in the population (63).

The sequencing of 96 clones after five passages under IVIG pressure revealed successful enrichment with a single chimera. This clone, termed AAV-DJ, displayed predominant sequence homology to serotypes 2, 8, and 9 (Fig. 2B and D) at levels (85 to 92%) similar to those of the homology of these wild types to one another (Table 1). Notably, AAV-DJ was distinguished from its closest natural relative, AAV-2, by a total of 60 amino acids (>8% of the VP1 capsid protein). It was thus substantially more divergent than, and compared highly favorably to, the bulk of previously evolved capsids, which typically differed from their single parent by only up to seven residues (depending on the library type, but in all cases corresponding to <1% of the capsid protein). AAV-DJ also showed ~60% identity to the other five parental viruses, explained by the fact that all eight wild-type AAVs used in our study were at least ~50%

TABLE 1. Sequence homology of AAV-DJ and wild-type AAV capsid proteins[a]

Vector	% Homology of capsid protein of indicated vector to capsid protein of:								
	DJ (737)	2 (735)	8 (738)	9 (736)	4 (734)	5 (724)	A (743)	B (736)	C (296)
DJ	100								
2	92	100							
8	88	82	100						
9	85	81	85	100					
4	61	60	63	62	100				
5	57	57	58	57	53	100			
A	57	57	57	58	54	54	100		
B	58	59	58	59	76	55	54	100	
C	47	46	49	45	42	86	44	43	100

[a] Shown are percentages of homology between the capsid protein of AAV-DJ and those of the eight parental wild-type AAVs. Numbers in parentheses indicate overall lengths of the various capsid proteins (in amino acids). AAV-DJ showed the highest levels of homology to wild types 2, 8, and 9 but also ~50 to 60% homology to the other five parents. High degrees of homology of 81 to 85% were also evident for the three most efficient (in vitro and/or in murine liver) wild types, AAV-2, AAV-8, and AAV-9. Not surprisingly, these three serotypes were the predominant AAV-DJ parents (see the text). Notably, all five other wild types showed ~40 to 60% homology to one another or to the AAV-2-AAV-8-AAV-9 group, exemplifying the overall close relationship of all naturally occurring AAVs. The levels of homology were higher for the even more closely related AAV-4 and bovine AAV, as well as for AAV-5 and goat AAV, as reported before. Note that only a subfragment (888 bp) of goat AAV which covered the diverse loops III and IV was used in this study, explaining the seemingly lower degrees of homology of other isolates to this serotype. A, avian AAV; B, bovine AAV; C, caprine (goat) AAV; 2, 8, 9, 4, and 5, wild-type AAV serotypes.

homologous to one another (Table 1). As a result, many individual residues in the AAV-DJ sequence could not be assigned to a particular parent.

Clearly, AAV-DJ was more evolved than the clones obtained in the absence of IVIG, as was already evident from the data in Fig. 2B and C and as was further confirmed by sequence homology comparisons to pool A (from primary human hepatocytes). Indeed, the 10 clones in pool A displayed higher relative similarities to AAV-2, while AAV-DJ was more homologous to AAV-8 (Table 2). This finding validated our initial assumption that IVIG pressure would lead to an elimination of AAV-2 epitopes from our library. Concurrently, AAV-DJ was only ~88 to 90% homologous to pool A, which further highlights its divergence from capsids evolved under less stringent conditions (the use of heterogeneous primary cells and the lack of IVIG pressure for pool A).

Molecular evolution affects mostly exposed capsid regions. AAV capsids are complex three-dimensional protein structures, suggesting that the majority of amino acid changes resulting from our evolution process would occur on the exterior of the virion, at positions accessible to the selection pressure. Indeed, the bulk of the 60 non-AAV-2 residues in AAV-DJ were located in the loops extruding from the particle, especially in the major loop IV (Fig. 2C and D and also see Fig. S4 in the supplemental material). Consequently, the overall identity of AAV-DJ to its eight parents dropped from ~31% (for the total VP1 protein) to only ~18% in this exposed capsid region. Importantly, the AAV capsid loops contain most of the residues critical for natural receptor binding or for antibody recognition or escape. This arrangement explains the observed lack of AAV-DJ detection by the AAV-2-specific A20 antibody, as the conformational epitope of the A20 antibody (80) was dispersed over three of the five capsid loops and disrupted by two point mutations in AAV-DJ (Fig. 4). In contrast, the highly conserved residues constituting the capsid core remained mostly unchanged in AAV-DJ, as their inaccessible location on the inside of the assembled particle protected them from synthetic (or natural) AAV evolution. This arrangement also explains why all eight parental AAVs in our study (and perhaps all naturally occurring AAVs) showed ~31% overall identity and at least 50% homology in pairwise comparisons (see Fig. S4 in the supplemental material and Table 1).

The critical roles of the residues in the capsid loops were further apparent upon alignments of AAV-DJ sequences with

TABLE 2. Homology of pool A and C and wild-type AAV capsid genes and proteins[a]

Vector	% Homology of capsid gene/protein of indicated vector to gene/protein of:										
	DJ (2,214/737)	A4 (2,211/736)	A11 (2,208/735)	D4 (2,208/735)	C8 (2,211/736)	G6 (2,208/735)	G5 (2,217/738)	B3 (2,211/736)	B4 (2,208/735)	G12 (2,208/735)	C3 (2,211/736)
DJ	100/100	89/90	89/91	89/91	87/88	89/91	88/91	88/90	91/93	88/88	88/89
2	90/92	92/94	90/93	94/96	88/90	96/96	93/94	90/93	91/94	92/93	94/95
8	87/88	82/84	81/84	82/83	82/85	81/84	85/87	83/87	84/85	81/83	81/84
9	81/85	81/83	87/88	83/85	85/85	81/84	80/84	84/86	82/86	82/84	80/83

[a] Shown are the percentages of homology between pairs of full-length AAV capsid genes (first numbers) and proteins (second numbers). The designations in the column heads indicate 10 individual clones from pool A (selected on primary human hepatocytes in the absence of IVIG) (Fig. 2A). The numbers in parentheses show the total lengths of each capsid gene (first number, in nucleotides) and protein (second number, in amino acids). Clone A4 was independently recovered twice from pool A. Data for AAV-DJ are included for comparison. With the exception of clone C8, all clones from pool A showed higher levels of homology to wild-type AAV-2 (underlined values) than did AAV-DJ. In contrast, of all the clones, AAV-DJ showed the highest degree of homology to wild-type AAV-8 (underlined values). Both findings together suggest that stringent selection under IVIG pressure (i.e., that in the case of AAV-DJ) led to the elimination of AAV-2 sequences from the library and to a concurrent accumulation of AAV-8 residues. Also note that pool A (10 clones) and pool C (AAV-DJ) are on average only ~88 to 90% homologous (first row), which is lower than the degree of homology of pool A clones to wild-type AAV-2 (~92 to 94%) (second row). This result further highlights the divergence of AAV-DJ not only from wild-type AAVs but also from capsids evolved under less stringent conditions. 2, 8, and 9, wild-type AAV serotypes.

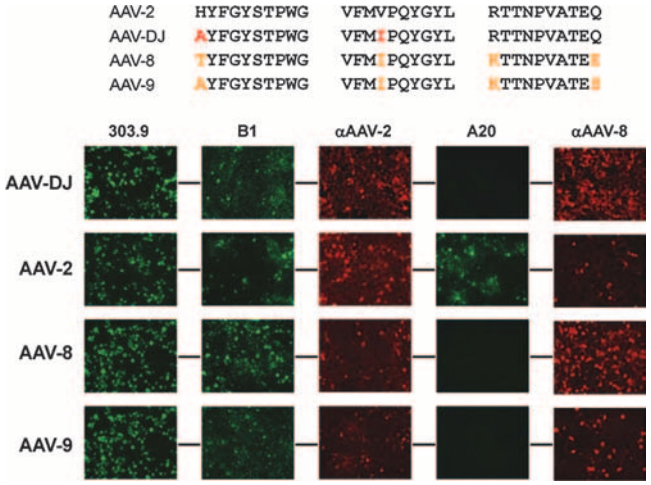


FIG. 4. Presentation of epitopes on the AAV-DJ capsid. Shown at the top are the putative AAV-2 epitope for the monoclonal antibody A20 (a conformational epitope comprising three distinct peptides [see also Fig. 2D]) and the corresponding sequences in AAV-DJ, AAV-8, and AAV-9 (amino acid changes compared to the sequence of AAV-2 are highlighted in red [AAV-DJ] or orange [AAV-8 and AAV-9]). The bottom panels show results from immunofluorescence studies of cells cotransfected with the various helper constructs and an adenoviral helper plasmid (to boost gene expression from the AAV plasmids). The two amino acid changes in AAV-DJ were already sufficient to abolish the binding of the A20 antibody, validating and narrowing down the A20 epitope (80) and thus exemplifying the potential of DNA family shuffling as a reverse-genetics tool. AAV-DJ cross-reacted with both the polyclonal anti-AAV-2 and anti-AAV-8 sera, as expected from its chimeric structure. Similar cross-reactivity with these sera was also observed for wild types 2, 8, and 9. The fact that AAV-DJ, AAV-8, and AAV-9 were detected by the B1 antibody (initially raised against AAV-2 capsid proteins) was not surprising considering the high degree of conservation of its epitope in natural AAVs (see Fig. S4 in the supplemental material). All mono- and polyclonal anti-AAV antibodies were described previously (78, 79), except for the polyclonal rabbit anti-AAV-8 antiserum. 303.9, anti-Rep; B1, anti-VP; αAAV-2, anti-AAV-2 VP serum; A20, anti-AAV-2 capsids; αAAV-8, anti-AAV-8 VP serum.

those of the 10 clones from pool A (Fig. 5). As mentioned above (Table 2), most clones from pool A had preserved AAV-2 sequences, while AAV-DJ was more related to serotypes 8 and 9 than the pool A clones were. In analogy to the results of the previous wild-type comparison, we noted that the greatest sequence diversity occurred in the exposed regions, with many of the changes clustered within loops I, IV, and V. Intriguingly, our alignments confirmed 6 of the 12 previously reported hypervariable regions (HVRs) in the AAV capsid gene (11, 16) but, moreover, identified several further hot spots of sequence diversity (Fig. 5 and also see Fig. S4 in the supplemental material). Most of them were located in the N termini of VP1 and VP2, while others were dispersed among the areas corresponding to HVRs 2 to 5. Our observation of multiple differences between the N termini of AAV-DJ and pool A was not surprising, as the N-terminal region is temporarily exposed during the AAV life cycle (7, 40, 68) and thus potentially subject to evolution pressure.

Notably, the phospholipase 2A domain in the VP1 N terminus, critical for particle infectivity (7, 86), remained highly conserved, with the single exception of clone C8 from pool A. In striking contrast to the N termini of the rest of the capsids, the AAV-DJ capsid N terminus was almost entirely derived from AAV-2, while the clones in pool A carried multiple dispersed residues from AAV-8 or AAV-9. These amino acids, especially the new clusters identified by our alignments, and their roles in the infection cycle should be very interesting targets for future AAV studies. These findings and considerations highlight the vast potential of DNA family shuffling, not only as a means to evolve viral vectors, but also as a functional genomics tool, useful to unravel basic virus biology.

In summary, we have cloned, sequenced (fully or partially), and compared a total of 513 candidates from our library before and after various selection schemes. Of the 465 clones from pools A to C, one was recovered twice (from pool A), while the 96 clones from pool C were completely identical (AAV-DJ). All other clones differed from one another by at least three amino acids and were not identified among the 48 clones from the unselected library. Likewise, AAV-DJ was found neither in pools A and B nor in the original library, confirming its specific evolution under stringent IVIG selection.

Recombinant AAV-DJ vectors mediate superior in vitro transduction. We next generated *gfp*-expressing vectors from the AAV-DJ capsid gene and compared their in vitro infectivities to those of the eight most commonly used wild-type AAVs (serotypes 1 through 6, 8, and 9), including five of the AAV-DJ parents (serotypes 2, 4, 5, 8, and 9). Impressively, titration on 14 cell types from different species and tissues, including primary human hepatocytes, melanoma cells, and embryonic stem cells, showed that AAV-DJ vectors were not only superior to all HBD-negative wild-type viruses (up to 100,000-fold better than AAV-8 or AAV-9), but also substantially better than AAV-2 (Table 3 and data not shown). Ratios of total to infectious particles were frequently far below 500, highlighting the extreme efficiency of AAV-DJ in vitro and suggesting its particular usefulness for ex vivo gene transfer applications. The only exceptions on which AAV-DJ was not most efficient were human monocytes and dendritic cells (Table 3). On these cells, AAV-1 and AAV-6 outperformed the other vectors, albeit AAV-DJ was among the most efficient capsids. Our data for AAV-1 confirm and extend the findings of a recent study in which this serotype also surpassed AAV-2 to AAV-5 on murine hematopoietic stem cells (87). As expected, AAV-DJ transduction was largely unaffected by IVIG (similar to AAV-8 and AAV-9 transduction) (data not shown).

To investigate the role of the AAV-DJ HBD, we mutated two crucial arginines (37, 56) into the respective residues in AAV-8 or AAV-9 (Fig. 6A and B). Green fluorescent protein expression from the resulting mutants was reduced by several orders of magnitude and was as low as that from serotypes 8 and 9 (Fig. 6C and Table 3) (results for mutants DJ/8 and DJ/9 were identical). The drop in infectivity correlated well with reduced binding to cells (Fig. 6D). However, cell attachment alone cannot explain the unusual infectivity of AAV-DJ, as AAV-2 actually bound 10-fold more efficiently. We rather assume a synergistic or additive effect from sharing beneficial properties from all AAV-DJ parents, resulting in the enhancement of multiple steps in AAV-DJ transduction. One likely outcome was the combination of efficient primary receptor binding (from AAV-2, compared to AAV-8 and AAV-9) with rapid virus processing and uncoating (from AAV-8) (73) (Fig.

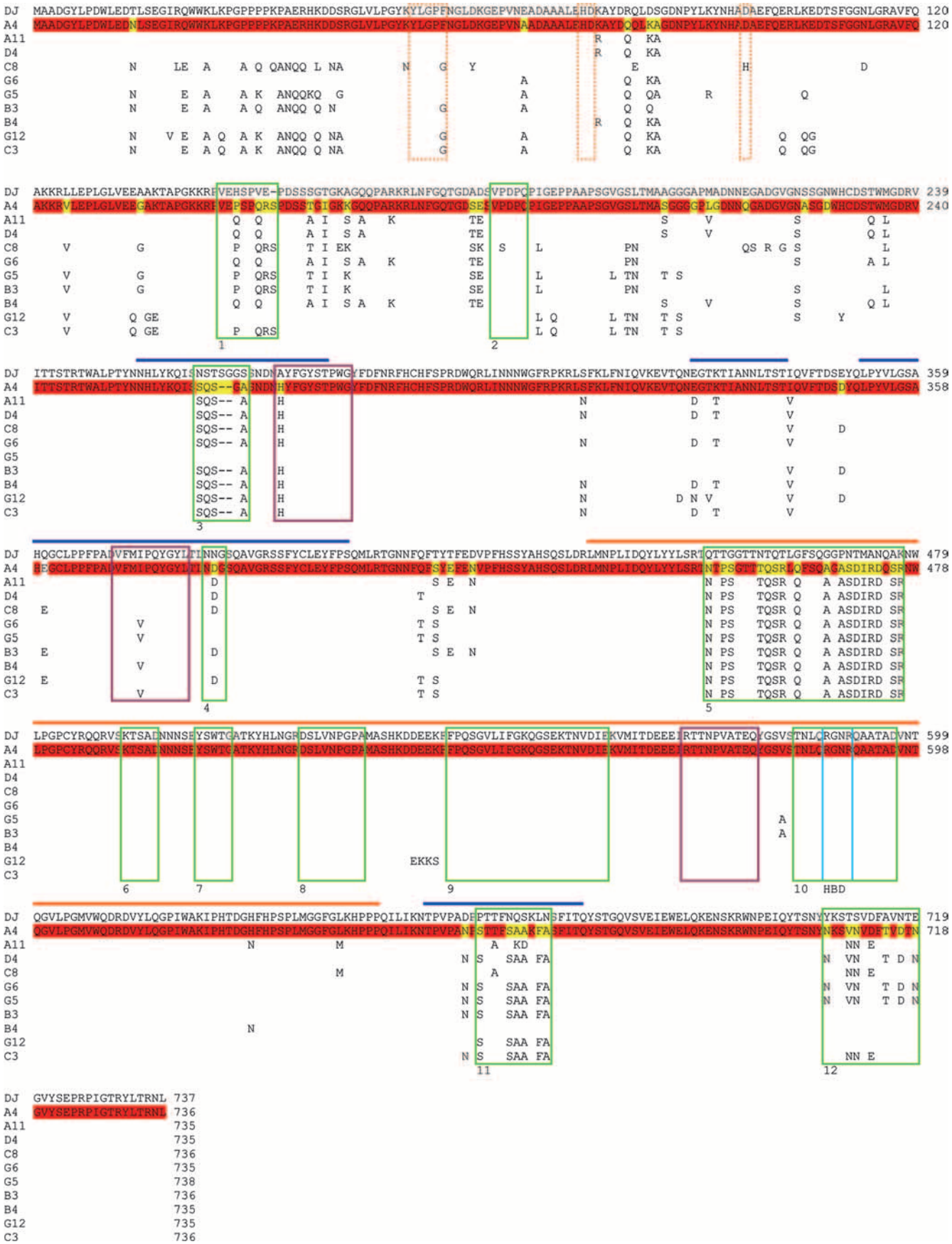

DJ MAADGYLPDWLEDTLSEGIRQWWKLKPGPPPPKPAERHKDDSRGLVLPGYKYLGPFNGLDKGEPVNEADAAALEHDKAYDRQLDSGDNPYLKYNHADAEFQERLKEDTSFGGNLGRAVFQ 120
A4 MAADGYLPDWLEDNLSEGIRQWWKLKPGPPPPKPAERHKDDSRGLVLPGYKYLGPFNGLDKGEPVNAADAAALEHDKAYDQQLKAGDNPYLKYNHADAEFQERLKEDTSFGGNLGRAVFQ 120
A11 R Q KA
D4 R Q KA
C8 N LE A A Q QANQQ L NA N G Y E H D
G6 A Q KA
G5 N E A A K ANQQKQ G A Q QA R Q
B3 N E A A Q ANQQ Q N G A Q Q
B4 R Q KA
G12 N V E A Q A K ANQQ Q NA G A Q KA Q QG
C3 N E A Q A K ANQQ Q NA G A Q KA Q QG
1
2
DJ AKKRLLEPLGLVEEAAKTAPGKKRPVEHSPVE-PDSSSGTGKAGQQPARKRLNFGQTGDADSVPDPQPIGEPPAAPSGVGSLTMAAGGGAPMADNNEGADGVGNSSGNWHCDSTWMGDRV 239
A4 AKKRVLEPLGLVEEGAKTAPGKKRPVEPSPQRSPDSSTGIGKKGQQPARKRLNFGQTGDSESVPDPQPIGEPPAAPSGVGSLTMASGGGGPLGDNNQGADGVGNASGDWHCDSTWMGDRV 240
A11 Q Q A I S A K TE S V S Q L
D4 Q Q A I S A TE S V S Q L
C8 V G P QRS T I EK SK S L PN QS R G S L
G6 Q Q A I S A K TE PN S A L
G5 V G P QRS T I K SE L L TN T S
B3 V G P QRS T I K SE L PN S L
B4 Q Q A I S A K TE S V S Q L
G12 V Q GE L Q L TN T S S Y
C3 V Q GE P QRS L Q L TN T S
3
4
DJ ITTSTRTWALPTYNNHLYKQISSNSTSGGSSNDNAYFGYSTPWGYFDFNRFHCHFSPRDWQRLINNNWGFRPKRLSFKLFNIQVKEVTQNEGTKTIANNLTSTIQVFTDSEYQLPYVLGSA 359
A4 ITTSTRTWALPTYNNHLYKQISSQS--GAGNDNHYFGYSTPWGYFDFNRFHCHFSPRDWQRLINNNWGFRPKRLSFKLFNIQVKEVTQNEGTKTIANNLTSTIQVFTDSDYQLPYVLGSA 358
A11 SQS-- A H N D T V
D4 SQS-- A H N D T V
C8 SQS-- A H V D
G6 SQS-- A H N D T V
G5
B3 SQS-- A H V D
B4 SQS-- A H N D T V
G12 SQS-- A H N D N V V D
C3 SQS-- A H N D T V
5
DJ HQGCLPPFPADVFMIPQYGYLTINNGSQAVGRSSFYCLEYFPSQMLRTGNNFQFTYTFEDVPFHSSYAHSQSLDRLMNPLIDQYLYYLSRTQTTGGTTNTQTLGFSQGGPNTMANQAKNW 479
A4 HEGCLPPFPADVFMIPQYGYLTINNGSQAVGRSSFYCLEYFPSQMLRTGNNFQFSYEFENVPFHSSYAHSQSLDRLMNPLIDQYLYYLSRINTPSGTTTQSRLQFSQAGASDIRDQSRNW 478
A11 D S E N N PS TQSR Q A ASDIRD SR
D4 D T N PS TQSR Q A ASDIRD SR
C8 E D S E N N PS TQSR Q A ASDIRD SR
G6 V T S N PS TQSR Q A ASDIRD SR
G5 V T S N PS TQSR Q A ASDIRD SR
B3 E D S E N N PS TQSR Q A ASDIRD SR
B4 V N PS TQSR Q A ASDIRD SR
G12 E D T S N PS TQSR Q A ASDIRD SR
C3 V T S N PS TQSR Q A ASDIRD SR
6
7
8
9
10
HBD
DJ LPGPCYRQQRVSKTSADNNNSEYSWTGATKYHLNGRDSLVNPGPAMASHKDDEEKFFPQSGVLIFGKQGSEKTNVDIEKVMITDEEEIRTTNPVATEQYGSVSTNLQRGNRQAATADVNT 599
A4 LPGPCYRQQRVSKTSADNNNSEYSWTGATKYHLNGRDSLVNPGPAMASHKDDEEKFFPQSGVLIFGKQGSEKTNVDIEKVMITDEEEIRTTNPVATEQYGSVSTNLQRGNRQAATADVNT 598
A11
D4
C8
G6
G5 A
B3 A
B4
G12 EKKS
C3
DJ QGVLPGMVWQDRDVYLQGPIWAKIPHTDGHFHPSPLMGGFGLKHPPPQILIKNTPVPADPPTTFNQSKLNSFITQYSTGQVSVEIEWELQKENSKRWNPEIQYTSNYYKSTSVDFAVNTE 719
A4 QGVLPGMVWQDRDVYLQGPIWAKIPHTDGHFHPSPLMGGFGLKHPPPQILIKNTPVPANPSTTFSAAKFASFITQYSTGQVSVEIEWELQKENSKRWNPEIQYTSNYNKSVNVDFTVDTN 718
A11 N M A KD NN E
D4 N S SAA FA N VN T D N
C8 M A NN E
G6 N S SAA FA N VN T D N
G5 N S SAA FA N VN T D N
B3 N S SAA FA
B4 N
G12 S SAA FA
C3 N S SAA FA NN E
11
12
DJ GVYSEPRPIGTRYLTRNL 737
A4 GVYSEPRPIGTRYLTRNL 736
A11 735
D4 735
C8 736
G6 735
G5 738
B3 736
B4 735
G12 735
C3 736

TABLE 3. In vitro infectivities of AAV-DJ and wild-type vectors[a]

Cell line	Tissue or cell type	Infectivity of vector:									
		AAV-1	AAV-2	AAV-3	AAV-4	AAV-5	AAV-6	AAV-8	AAV-9	AAV-DJ	AAV-DJ/8
Huh-7	hu liver	4e3	5e2	2e4	2e6	4e5	5e3	7e4	**7e6**	1e2	3e5
293	hu kidney	2e3	5e2	2e4	7e5	4e5	1e4	7e4	**7e5**	1e2	2e5
HeLa	hu cervix	7e4	2e3	1e5	**2e6**	3e4	2e5	1e6	**2e6**	3e2	1e6
HepG2	hu liver	2e6	5e4	3e5	2e7	3e6	1e6	2e7	**ND**	4e3	1e7
Hep1A	mu liver	1e4	2e3	1e6	2e5	2e6	2e5	1e6	**2e7**	5e2	2e6
911	hu retina	6e3	1e3	9e3	5e5	7e5	6e3	1e6	**ND**	2e2	4e5
CHO	ha ovary	1e4	1e4	7e4	7e5	3e3	2e4	1e5	**1e6**	4e1	2e5
COS	si kidney	3e3	1e3	3e3	3e4	2e4	7e3	5e4	**2e5**	2e2	3e5
MeWo	hu skin	2e3	2e2	1e3	7e4	3e3	2e3	2e4	**1e5**	7e0	2e4
NIH3T3	mu fibroblasts	2e5	2e4	7e5	7e5	7e6	2e5	7e6	**ND**	4e3	2e7
A549	hu lung	7e4	1e4	5e4	**ND**	2e6	1e5	2e6	7e6	1e3	2e7
HT1180	hu fibroblasts	5e4	1e4	1e5	7e6	3e6	3e4	2e6	**1e7**	3e3	5e6
Monocytes	hu primary monocytes	9e5	1e7	**ND**	**ND**	8e6	7e5	**ND**	**ND**	1e7	**ND**
Immature DC	hu monocyte-derived DC	8e5	2e7	**ND**	**ND**	9e6	7e5	**ND**	**ND**	1e7	**ND**
Mature DC	hu monocyte-derived DC	9e5	2e7	**ND**	**ND**	6e6	6e5	**ND**	**ND**	2e7	**ND**

[a] Each cell line was infected with 10-fold serial dilutions of each serotype, AAV-DJ, or the mutant AAV-DJ/8 expressing a *gfp* reporter gene. Vector preparations were normalized to contain 2×10^9 total (vector DNA-containing) particles per ml prior to infection. Three days later, green fluorescent protein-expressing cells were counted and infectious titers were determined by taking into account the dilution factor. Numbers shown are average ratios (rounded) of total to infectious AAV particles from at least three independent titrations. Lower numbers indicate higher levels of infectivity. For each cell line, values corresponding to the most efficient AAV are underlined, while boldface indicates the lowest level of efficiency. AAV-DJ vectors showed the highest levels of infectivity on all tested cell lines. hu, human; mu, murine; ha, hamster; si, simian; DC, dendritic cells; ND, not detectable ($>2 \times 10^7$).

6E). A further explanation may be that the juxtaposition of subunits from different parents created a unique property, such as the use of an unidentified coreceptor for faster capsid internalization (see also Discussion and Fig. 12 below). An important role in infectivity was likely also played by the unique AAV-DJ N terminus, which differed from those of all other recovered clones (see above).

AAV-DJ yields robust hFIX expression in mouse liver tissue. Based on the high level of efficacy of the AAV-DJ capsid in vitro, we became interested in evaluating vectors based on this novel chimera in mouse liver tissue in vivo. For this purpose, we produced recombinant AAV-DJ particles expressing the hFIX gene from a robust liver-specific promoter (53). Controls were wild-type capsids of serotypes 2, 8, and 9 and mutants DJ/8, DJ/9, and 2/8 (HBD negative) and 8/2 (HBD positive) (see above and Fig. 6A and D). Immunocompetent C57BL/6 mice were infused via the tail vein with particle doses of each virus ranging over four orders of magnitude (5×10^9 to 1×10^{12} particles), and plasma hFIX levels were monitored for up to 4 months.

We observed dose-dependent expression from the AAV-DJ capsid at levels equivalent to those from AAV-8 and AAV-9, the best two naturally identified AAVs for liver tissue reported thus far (18, 19, 52) (Fig. 7A and data not shown for the 5×10^9 dose). All three viruses readily outperformed the AAV-2 prototype at any dose and expressed over 100% of normal hFIX levels already after the intravenous injection of 5×10^{10} particles (AAV-2 matched these levels only at a dose of 10^{12} particles, i.e., a 20-fold-higher dose). Quantification and analyses of persisting vector DNA confirmed the similarity of AAV-DJ, AAV-8, and AAV-9 and their comparable degrees of superiority over AAV-2 (see Fig. S5 in the supplemental material). These results were verified in analogous experiments using two alternative expression cassettes (data not shown).

Curiously, the two DJ HBD mutants were indistinguishable from AAV-DJ (and serotypes 8 and 9) at these doses, while the corresponding AAV-2 mutant (2/8) was inferior to wild-type AAV-2 (Fig. 7B and C). Different expression levels for AAV-8 and the HBD-positive 8/2 mutant were also noted, albeit here,

FIG. 5. Protein sequence alignments for AAV-DJ and 10 clones from pool A. Shown are full protein alignments for the 10 clones described in the legend to Fig. 3. (The clones correspond to lanes A to J in Fig. 3 and are listed in order; e.g., clone A4 corresponds to lanes A, and clone A11 corresponds to lanes B, etc.). AAV-DJ served as the standard to highlight the different degrees of evolution between pools A and C (in which clones were selected with [pool C] or without [pool A] IVIG [Fig. 2A]). The clone A4 sequence is shown as a full sequence, as clone A4 was recovered twice from pool A. Residues identical in A4 and AAV-DJ are colored in red, while changes are shown in yellow. Only amino acids divergent from AAV-DJ are shown for the other nine clones (for the origin of these residues, see the wild-type sequences in Fig. S4 in the supplemental material and also see the text). The horizontal bars indicate the capsid loops (see Fig. S4 in the supplemental material). Note that many changes in the 10 clones from pool A were clustered in these loops, as could be expected. Moreover, the gene regions corresponding to six of these cluster regions were identical to 6 of the 12 previously reported HVRs (HVRs 1, 3, 4, 5, 11, and 12 among the previously described HVRs 1 to 12, identified by green boxes) in the AAV capsid gene. Intriguingly, our alignments also identified several further regions of sequence diversity not described before, especially in the VP1 and VP2 N termini. The dotted orange lines mark a highly conserved phospholipase 2A domain in the VP1 N terminus; note the unique amino acid change (D97H) in clone C8 (yet the capsid was infectious [see Fig. 3]). The three purple boxes show the A20 epitope; note that almost all clones had fully maintained the respective consensus sequence from AAV-2 (H in the first and V in the second part of the epitope) but that AAV-DJ had not (compare Fig. 4). The blue box shows the location of two of the five residues (two arginines) which constitute the HBD; they were fully conserved in all clones.

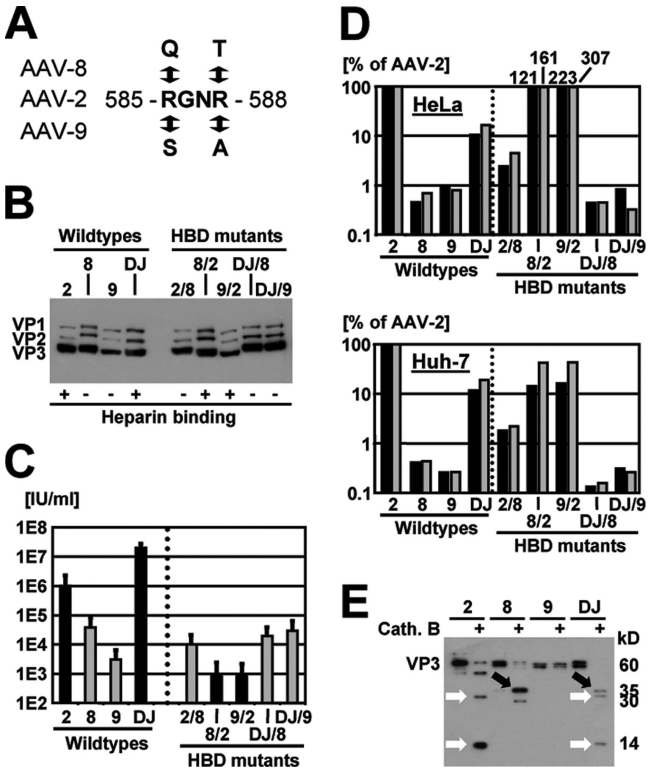


FIG. 6. In vitro analyses of AAV-DJ and HBD mutants. (A) Two arginine residues (numbers refer to positions in AAV-2) in AAV-2, AAV-8, AAV-9, or AAV-DJ were mutagenized to eliminate or introduce an HBD (37). (B) Western blots (using B1 antibody) confirming correct VP protein expression from all HBD mutants. AAV-8 and AAV-DJ (wild types and mutants) expressed proteins more strongly than AAV-2 or AAV-9, for reasons unknown. +, with; −, without. (C) Titration of infectious particles on 293 cells confirmed the role of the HBD in infection in culture. The mutation of the HBD in AAV-2 or AAV-DJ reduced infectivity, measured the ratio of total to infectious AAV particles, by 2 to 3 logs. However, including an HBD in AAV-8 and AAV-9 did not further increase the infectivity of these vectors. (D) Results from cell binding assays confirming the role of the HBD in attachment to cultured cells (HeLa or Huh-7). The drop in binding with the AAV-2 and AAV-DJ mutants correlated well with the transduction data presented in panel C. Surprisingly, the HBD-positive AAV-8 and AAV-9 mutants bound severalfold more efficiently than AAV-2 on HeLa cells and, in all cases, far better than wild types 8 and 9 but transduced much less efficiently. Cell attachment and transduction thus do not necessarily correlate, suggesting that additional intracellular factors and steps contributed to the superior transduction efficiency of AAV-DJ. (E) AAV particle digestion with the endosomal proteinase cathepsin B (cath. B) (2) yielded distinct patterns for the individual serotypes in a Western blot analysis using polyclonal anti-AAV-2 VP serum. AAV-DJ showed a hybrid pattern with bands from AAV-2 and AAV-8 (white and black arrows, respectively), further supporting the idea that its properties resulted from synergistic or additive effects from its parents (cell binding from AAV-2 and rapid uncoating from AAV-8).

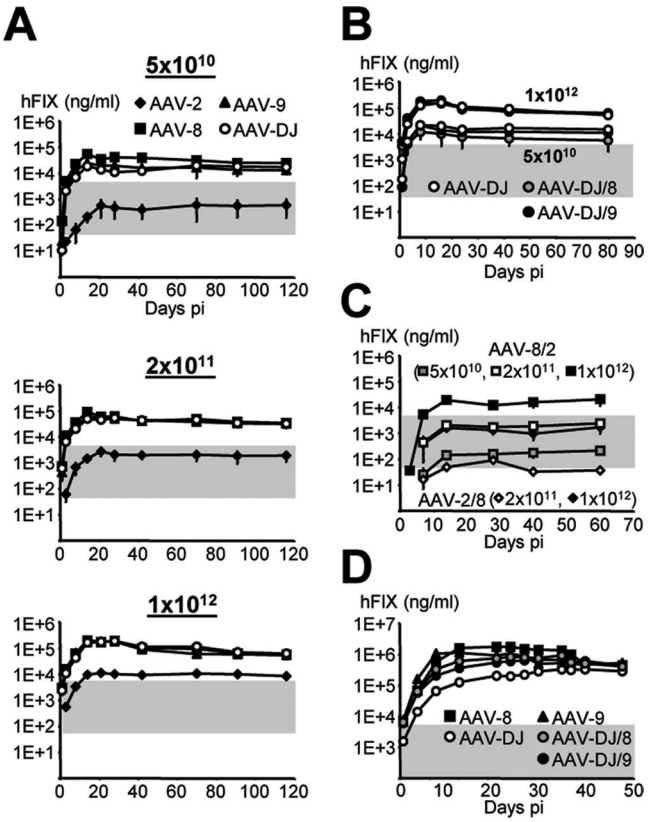


FIG. 7. hFIX expression from AAV-DJ in mice. (A) Dose-dependent and liver-specific hFIX expression. C57BL/6 mice (n = 3 to 8) were infused with all four hFIX-expressing vectors via peripheral tail vein injection. Gray shading indicates the range from 1 to 100% of normal hFIX levels in humans (0.05 to 5 μg/ml). Levels over 1% are considered to be therapeutic in hemophiliacs. Note that AAV-8, AAV-9, and AAV-DJ vectors exceeded the 100% level already at the lowest dose, whereas AAV-2 required a 20-fold-higher dose. (B) hFIX expression from the AAV-DJ HBD mutants (n = 3 per group). Shown are results from two representative doses; there was no significant difference from the results for AAV-DJ. (C) In contrast, the AAV-2 or AAV-8 HBD mutants expressed less hFIX than the corresponding wild types (n = 3 per group). (D) AAV-DJ showed unique transduction kinetics at a maximum dose of 7×10^{12} particles. The onset of gene expression was delayed compared to that from AAV-8 or AAV-9, yet hFIX levels became similar after ~40 days (n = 3 per group). The AAV-DJ HBD mutants showed intermediate kinetics; stable hFIX levels were eventually also similar to those from AAV-8 and AAV-9 (and AAV-DJ). pi, postinjection.

the wild type performed better (Fig. 7C). This finding suggested an essential function of heparin binding for liver gene expression from AAV-2, corroborating previous findings with this serotype (37), but a redundancy for more efficient natural or synthetic capsids (those of AAV-DJ and serotypes 8 and 9). Moreover, together with our data from the in vitro assays (see above), these results exemplified the differential effects of the HBD on AAV transduction in culture and in organisms.

The AAV HBD plays a multifaceted role in vivo. Interestingly, additional studies indicated an even more complex role for the HBD in vivo. At a maximal dose of 7×10^{12} particles, the transduction profiles of the most efficient viruses became unique. All HBD-negative variants showed faster transduction kinetics than AAV-DJ, although all viruses eventually (after ~1.5 months) gave similar expression levels (Fig. 7D). A similarly slow response at extreme particle doses with a resulting lag phase had previously been reported for AAV-2 (53, 67) and was confirmed here (data not shown). The fact that AAV-DJ and AAV-2 share the HBD suggests a common molecular mechanism involving this domain, likely at the level of post-vector entry (e.g., particle trafficking or uncoating). However, this idea warrants further investigation in view of studies re-

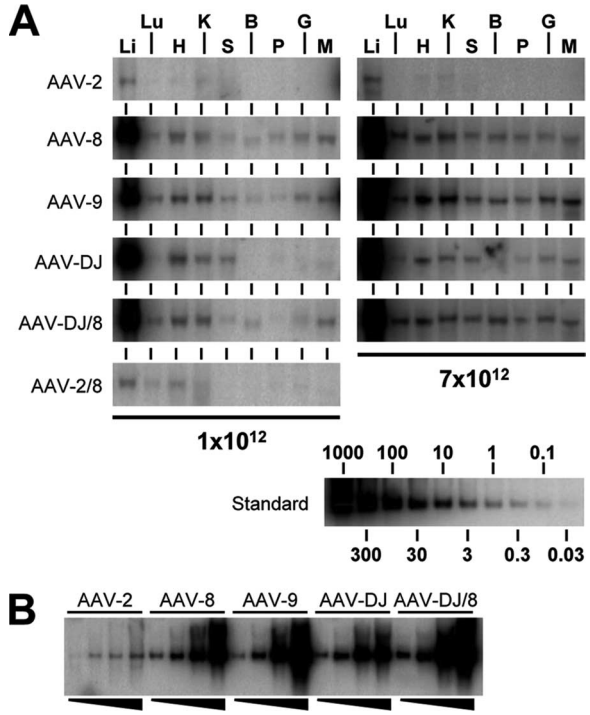


FIG. 8. Vector DNA biodistribution and dose response. (A) Genomic DNA extracted from nine tissue types (li, liver; lu, lung; h, heart; k, kidney; s, spleen; b, brain; p, pancreas; g, gut; and m, muscle) was analyzed for the presence of hFIX-expressing vector DNA. The results and the reference standard shown are representative of data for the two highest doses used here. The AAV-DJ transduction pattern was more restricted to liver, heart, kindey, and spleen tissues than those of AAV-8, AAV-9, and the HBD mutants. At the highest dose (7×10^{12} particles), AAV-DJ spillover into nonhepatic tissues was also less obvious than that of the other vectors. The HBD-negative AAV-2/8 mutant gave increased heart transduction compared to wild-type AAV-2, confirming previous data (37) (an unknown production deficiency prevented evaluation at the highest dose). (B) Comparison of vector DNA levels in liver following transduction with increasing particle doses (from left to right, 5×10^{10}, 2×10^{11}, 1×10^{12}, and 7×10^{12} particles). AAV-DJ showed a blunted response at the highest dose, likely correlating with its slower onset of gene expression (Fig. 7D).

porting blunted dose responses also for AAV-1 and AAV-5, which both lack a consensus HBD (52).

A second function of the HBD became apparent upon analyses of vector DNA biodistribution (Fig. 8A and Table 4). We corroborated previous reports of unrestricted tropism of AAV-8 and AAV-9 (HBD negative) (17, 18, 34, 52, 60), which readily transduced all tested tissues at a dose of 10^{12} particles per mouse. In striking contrast, AAV-2 and likewise AAV-DJ (both HBD positive) were restricted to liver tissue and, to a lesser extent, heart, kidney, and spleen tissues and were near or below the detection limit in all other tissues. In fact, the quantification of double-stranded vector DNA (using liver tissue as an internal standard for each group) showed that AAV-DJ transduced lung, brain, pancreas, and gut tissue about two- to fourfold less efficiently than wild types 8 and 9 (Table 4). The effect of the HBD on viral tropism was best exemplified by comparing AAV-DJ to the DJ/8 mutant: HBD deletion alleviated the liver restriction and expanded transduction to all nonhepatic tissues, including the brain, identical to the transduction patterns of AAV-8 and AAV-9. These findings not only corroborate but also may help explain a series of reports on the wide tissue dissemination of vectors based on HBD-negative natural serotypes (AAV-1 and AAV-4 to AAV-9) in mice, dogs, and monkeys (17, 29, 37, 52, 60), in contrast to that of the HBD-positive AAV-2. Notably, AAV-DJ also transduced nonhepatic tissues at the maximum dose of 7×10^{12} particles but still to a lesser extent than the HBD-negative viruses, in particular AAV-9 (Fig. 8A and Table 4). Importantly, even at this dose, brain and also lung transduction remained marginal.

Additional side-by-side comparison of all liver vector DNA levels showed similar dose responses for the non-AAV-2 viruses at doses between 5×10^{10} and 1×10^{12} particles (Fig. 8B), in agreement with our expression data (see above). However, at 7×10^{12} particles, the HBD-negative viruses persisted at slightly higher copy numbers than AAV-DJ. The data in Fig. 7D, as well as our previous

TABLE 4. Relative levels of transduction of nonhepatic tissues with AAV vectors[a]

Vector	Dose (no. of particles)	Level of AAV DNA in:							
		Lung	Heart	Kidney	Spleen	Brain	Pancreas	Gut	Muscle
AAV-2	1e12	ND	0.7 ± 0.1	0.8 ± 0.1	0.2 ± 0.0	ND	ND	ND	ND
	7e12	ND	1.5 ± 0.03	2.0 ± 0.3	1.0 ± 0.2	ND	ND	ND	ND
AAV-8	1e12	0.5 ± 0.0	1.2 ± 0.2	0.9 ± 0.2	0.3 ± 0.0	0.2 ± 0.0	0.2 ± 0.0	0.3 ± 0.0	0.7 ± 0.1
	7e12	2.5 ± 0.3	2.5 ± 0.2	2.6 ± 0.3	1.5 ± 0.2	1.5 ± 0.2	1.2 ± 0.2	1.2 ± 0.2	1.9 ± 0.2
AAV-9	1e12	0.7 ± 0.1	1.3 ± 0.2	1.1 ± 0.2	0.4 ± 0.0	0.2 ± 0.0	0.2 ± 0.0	0.3 ± 0.0	0.8 ± 0.1
	7e12	2.6 ± 0.3	3.6 ± 0.4	3.8 ± 0.4	1.5 ± 0.2	1.8 ± 0.2	1.3 ± 0.2	1.9 ± 0.2	3.0 ± 0.3
AAV-DJ	1e12	0.2 ± 0.0	1.3 ± 0.2	0.8 ± 0.2	0.5 ± 0.1	ND	0.1 ± 0.0	0.1 ± 0.0	0.2 ± 0.0
	7e12	0.6 ± 0.1	2.3 ± 0.2	2.1 ± 0.2	1.5 ± 0.2	0.4 ± 0.0	0.5 ± 0.0	0.5 ± 0.0	0.8 ± 0.1
AAV-DJ/8	1e12	0.6 ± 0.0	1.3 ± 0.2	0.8 ± 0.2	0.2 ± 0.0	0.2 ± 0.0	0.1 ± 0.0	0.2 ± 0.0	0.7 ± 0.1
	7e12	2.6 ± 0.3	2.5 ± 0.3	2.3 ± 0.3	1.6 ± 0.3	1.8 ± 0.2	1.2 ± 0.2	1.3 ± 0.2	2.0 ± 0.2

[a] Vector copy numbers (per diploid genomic equivalent) were determined via phosphorimager scan analyses of Southern blots as shown in Fig. 8A. At least three independent mice per applied dose were analyzed. Copy numbers are shown as average percentages (rounded to one decimal place) ± standard deviations relative to copy numbers in liver tissue within each group, allowing comparison between vectors and doses. For AAV-2, most signals were below the detection limit of the Southern blot analyses (~0.03 copies of double-stranded AAV DNA per cell), preventing the calculation of relative transduction in these cases (ND, not determined). Underlining highlights values for doses or tissues for which relative AAV-DJ transduction levels differed by at least twofold from those for serotypes 8 and 9, as well as for the AAV-DJ HBD mutant.

findings with AAV-8 (52), imply that this outcome resulted from faster transduction with the HBD-negative viruses than with the HBD-positive viruses. This effect in turn likely increased the steady-state levels of viral DNA. Because the levels of expression from all viruses eventually became similar (Fig. 7D), we further hypothesize that the majority of additional genomes were silenced over time. While the latter conclusion is also supported by the results of our earlier work (52), more detailed studies are needed to prove the ensuing opposite idea, that a higher proportion of vector DNA copies from AAV-DJ transduction than from transduction with HBD-negative viruses remains transcriptionally active in the liver.

AAV-DJ partly escapes humoral neutralization in mice. We next quantified liver transduction in the presence of human serum to assess AAV-DJ's ability to evade neutralization in vivo. Therefore, we passively immunized mice with IVIG prior to the infusion of hFIX-expressing AAV-2, AAV-8, AAV-9, or AAV-DJ. As predicted, AAV-2 expression was nearly completely abolished. In contrast, transduction with AAV-DJ, AAV-8, or AAV-9 was inhibited in a dose-dependent manner, with AAV-DJ showing intermediate resistance at the high IVIG dose and efficient evasion (similar to that by serotypes 8 and 9) at the low IVIG dose (Fig. 9A). These results were essentially confirmed with a second independent IVIG batch from another vendor (Carimune [12%]; Behring AG) (data not shown). Interestingly, the DJ HBD mutants were fully neutralized, comparable to AAV-2 (Fig. 9B). This observation suggested that the HBD affected the display of epitopes on the capsid, thus implying yet another role of this domain for the AAV particle. Alternatively, published data for wild-type AAVs (17), as well as our own preliminary findings (data not shown), indicate that this domain may determine in vivo vector pharmacokinetics by enhancing the clearance of HBD-positive capsids from the blood and, thus, reducing their exposure to neutralizing antibodies.

Lastly, we assessed the feasibility of repeatedly administering the different viruses to mice to evaluate capsid cross-neutralization (Fig. 9C). As expected, we saw no gene expression upon the reinfusion of any of the capsids into animals already treated with the same serotype. However, we noted that AAV-8 and AAV-9 also efficiently blocked each other, substantiating prior data (18). This result may argue against the use of vectors based on these wild types in readministration protocols, although the vectors could be combined with AAV-2. In contrast, primary infusion with AAV-DJ allowed subsequent expression (at up to 18% of the respective PBS control) from AAV-2, AAV-8, or AAV-9, likely due to the fact that AAV-DJ shares only a limited number of epitopes with each wild-type virus. Surprisingly, in the reverse experiment, AAV-DJ vectors were inhibited in animals immunized with AAV-8 or AAV-9 while giving detectable expression in AAV-2-treated mice. This result implied a stronger or broader immune response from primary infusion with serotype 8 or 9 than from that with serotype 2. Intriguingly, AAV-DJ was more resistant to the corresponding mouse sera in culture than in vivo (Fig. 9D), and we also noted less cross-reactivity between AAV-8 and AAV-9 in culture than in vivo. These findings are perhaps due to the display of distinct epitopes in vitro and in vivo. This scenario may likewise explain the different degrees of neutralization of all three viruses with IVIG in cells and in mice.

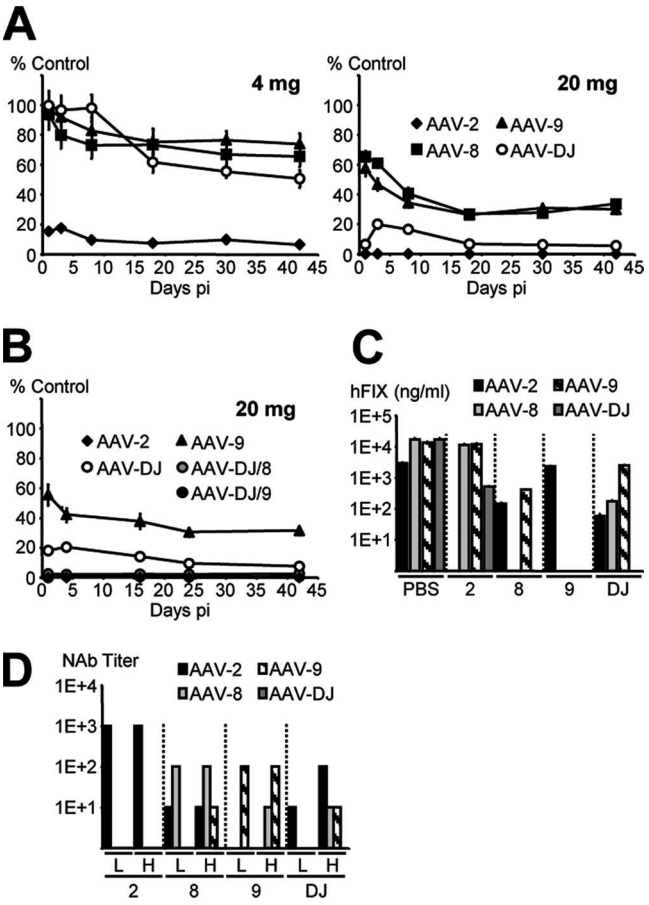


FIG. 9. In vivo and in vitro neutralization of AAV-DJ and wild-type AAVs. (A) Mice ($n = 4$ per group) passively immunized with IVIG (4 or 20 mg) were injected with hFIX-expressing AAV. Plasma hFIX levels per virus and time point are shown as percentages of corresponding levels in control mice (those receiving PBS instead of IVIG). (B) Mice ($n = 4$ per group) immunized with the higher IVIG dose were also injected with the AAV-DJ HBD mutants. AAV-2, AAV-9, and AAV-DJ were included as controls. hFIX expression from the HBD mutants was marginal, comparable to that from AAV-2. (C) Mice ($n = 4$ per group) were injected with PBS or 10^{11} particles of hAAT-expressing AAV-2, AAV-8, AAV-9, or AAV-DJ (x axis), and 3 weeks later, they were reinjected with 10^{11} particles of hFIX-expressing viruses (5×10^{11} for the least efficient AAV-2, due to the enzyme-linked immunosorbent assay detection limit of ~10 ng/ml). Shown are stable hFIX levels for each group as measured 6 weeks after the second injection. (D) Sera were taken from the mice described in the legend to panel C at the time of reinjection (bars H [higher dose]), as well as from a parallel group injected with a lower dose (bars L) of 2×10^{10} particles. Titers of neutralizing antibodies (NAb) against the wild-type AAVs or AAV-DJ were determined as detailed in Materials and Methods. pi, postinjection.

Creation of a viral peptide display library based on AAV-DJ. An intriguing property of the AAV-DJ capsid revealed by our in vitro assays is the inverse correlation of cell binding and transduction efficacies (Fig. 6). Together with the unique endosomal cathepsin B cleavage pattern, this finding suggests that the superior efficacy of the AAV-DJ capsid is due at least partially to faster uptake or enhanced intracellular processing.

Conversely, attachment receptor binding seems less limiting for AAV-DJ transduction (in the presence of a functional HBD) than for transduction with the other vectors, as implied by the consistently high potency of AAV-DJ in multiple distinct cell types. This finding suggested AAV-DJ as a promising candidate for tissue retargeting approaches via viral peptide display, in analogy to prior work with the AAV-2 prototype. Importantly, by using AAV-DJ as a parental virus, we hoped to overcome the two main drawbacks of AAV-2: the high prevalence of neutralizing antibodies and the typically slow intracellular processing limiting transduction efficacy.

In addition to the use of an optimized capsid, we further threefold improved our strategy over those described in the prior reports by Michelfelder et al., Müller et al., Perabo et al., and Waterkamp et al. (48, 50, 58, 76). Firstly, we wanted to ensure that the HBD in AAV-DJ was nonfunctional to increase the likelihood that any new cell tropism was truly mediated by the displayed peptides. Previously, the loss of the heparin binding capability of the AAV-2 capsid had been achieved indirectly and incompletely, through steric hindrance and conformational effects resulting from the peptide insertion. Here, we additionally mutated one of the two critical arginines in this domain (R585) to fully abolish binding to heparin or the heparan sulfate proteoglycan receptor. Secondly, we assembled our random peptide library based on an $(NNB)_7$ oligonucleotide, where B symbolizes the nucleotide C, G, or T. Compared to the $(NNK)_7$ scheme (where K represents G or T) used in three of the four previous studies (48, 50, 76), our design further decreases the statistical risk of the unwanted incorporation of a stop codon (only one, TAG, remains possible among 48 triplets), from 3.1% (NNK) to 2.1% (NNB). Notably, our library still closely mimicks the natural amino acid distribution (see Fig. S6 in the supplemental material). Thirdly and most importantly, we reckoned that using AAV-DJ as a highly efficient parental capsid would permit the biopanning of our library under the physiologically most relevant conditions, i.e., in mice in vivo. This was a critical improvement over all previously reported selection schemes, in which AAV libraries were panned exclusively on cultured cells in vitro. For this goal, we chose the lung as a second target because it offers the extra benefit that it is a natural site of adenovirus infection, implying the feasibility of productively coamplifying AAV and helper virus particles in this organ in vivo.

The AAV-DJ peptide display library was constructed by modifying the basic three-step cloning scheme devised for AAV-2 by Müller et al. (50), with the two mentioned improvements of an additional R585Q mutation and the use of $(NNB)_7$ 21-mers for peptide coding. However, we maintained the concept of displaying the targeting peptide ligands after residue R588, a locale successfully used by many groups. The resulting plasmid library had a diversity of $\sim 3 \times 10^7$ clones, which is well in the range of the four previously described AAV-2 counterparts (with estimated diversities of 1.2×10^7 to 1.7×10^8 clones) (48, 50, 58, 76). Analyses of 24 individual clones confirmed the complete randomization of the inserted oligonucleotides and the absence of repetitive sequences in our library (data not shown). Of the 168 triplets in these clones, only three carried the single possible stop codon TAG, representing a 1.8% frequency in our plasmid library (see Fig. S6 in the supplemental material). This level was even below the theoretical prediction for the $(NNB)_7$ design (2.1%) and also slightly below previous results with an AAV-2 $(NNK)_7$ library (about 2%, with a theoretical possibility of 3.1%) (50, 76). Very similar data (not shown) were obtained for an AAV-2-based library that we generated in parallel, by following the same rules, as a control for the AAV-DJ library. Both plasmid libraries were then packaged into virions (in 2×10^9 cells, to maintain library diversity), resulting in large and complex viral libraries with titers of 5×10^{12} (AAV-2) and 5.8×10^{12} (AAV-DJ) particles/ml, matching or in fact slightly exceeding (in the case of AAV-DJ) the highest numbers reported previously (5.5×10^{12}) (76).

In vivo biopanning of peptide-modified AAV capsids in mouse lung tissue. Critical to the success of AAV capsid evolution is to find an ideal multiplicity of infection giving minimal target cell transduction with a single or only a few particles, which are subsequently amplified by the helper virus. This approach will avoid the uncoupling of genotypes and phenotypes, which can occur if cells are initially infected with excess AAV particles and which will hamper the selection process. Likewise crucial is to find a helper virus dose resulting in efficient yet slow infection, giving the AAVs enough time for productive amplification. To optimize these parameters, we nasally coinfected mouse lungs with various multiplicities of infection of the AAV-2- and AAV-DJ-based libraries, ranging from 10^9 to 10^{11} physical particles, together with escalating volumes (0.2, 1, and 5 μl) of human or murine adenovirus stocks (from the ATCC). Our aim was to find the virus dose combination that would allow PCR detection of amplified AAV particles in helper virus-infected mice but not in controls lacking the adenovirus. The mice were maintained for 4 or 7 days before their lungs were harvested. At the highest dose of murine adenovirus (5 μl of ATCC stock VR-550), all lungs had macroscopic evidence of tissue inflammation. In contrast, mice inoculated with the human adenovirus lacked any gross signs of infection, and their lungs looked normal under all conditions (doses and time points).

A comparison of the results with various AAV doses showed that inoculation with 10^{10} AAV-DJ library particles gave the ideal result, i.e., a clear band for the murine helper virus-treated mice but no or very faint signals in the absence of adenovirus (data not shown). Conversely, we did not obtain bands with the same dose of the AAV-2 library, regardless of the absence or presence of helper virus, and there was also no detectable AAV amplification in any mice infected with the human helper virus. Together, these findings confirmed that the AAV-DJ particles had successfully replicated their genomes in the mouse lungs in the presence of the appropriate murine helper. Moreover, the fact that we observed AAV-2 amplification only from a 10-fold-higher starting dose of 10^{11} particles validated our hypothesis that using AAV-DJ as a parental capsid would increase the in vivo fitness of an AAV library compared to that of a library based on the conventionally used serotype 2.

We next cloned the amplified AAV-DJ genomes from three mice and sequenced 15 to 24 clones per mouse. We were able to read 46 full sequences, whose translation and alignment are shown in Table 5 (for amino acid compositions, see Fig. S6 in the supplemental material). Clearly, the most notable observation was the enrichment with peptides NSSRDLG and ND

TABLE 5. Peptide sequences from in vivo biopanning in murine lungs[a]

Mouse (no. of clones)	Peptide (frequency)	Charge pattern	Hydrophobicity pattern
1 (19)	NSSRDLG (4)	xxx+−yy	−−−−−++
	NDVRAVS (3)	x−y+yyx	−−+−+−−
	NWLLDSG	xyxx−xy	−++−−−+
	NTQDVNK	xxx−yx+	−−−−+−−
	GLEGSSN	yy−yxxx	++−+−−−
	GEQSSFG	y−xxxyy	+−−−−++
	SADRQGP	xy−+xyy	−+−−−++
	DELQGCT	−−yxyxx	−−+−+−−
	VLDGMCR	yy−yyx+	++−++−−
	DNNGLVV	−xxyyyy	−−−++++
	ADWLCRA	y−yyx+y	+−++−−+
	GKEKDTI	y+−+−xy	+−−−−−+
	HCMVRPC	+xyy+yx	−−++−+−
	KMEGIFN	+y−yyyx	−+−+++−
2 (16)	YGGSRSN	xyyx+xx	−++−−−−
	DLRVQGC	−y+xxyx	−+−+−+−
	DFSVSFV	−yxyxyy	−+−+−++
	HDVRWAV	+yy+yyy	−−+−+++
	WVRDVML	yy+−yyy	++−−+++
	ARATDRV	y+yxy+y	+−+−−−+
	VALGRES	yyyy+−x	+++−−−−
	FVLTVGG	yyyxyyy	+++−+++
	SYRVQTS	xx+yxxx	−−−+−−−
	ICEGHSR	yx−y+x+	+−−+−−−
	GLRQPFS	yy+xyyx	++−−++−
	ASSVYWY	yxxyyyy	+−−+−+−
	VIISPTS	yyyxyxx	+++−+−−
	KDIVRKV	+−yy++y	−−+−−−+
	KPGGNQL	+yyyxxy	−+++−−+
	GTGTQSD	yxyxxx-	+−+−−−−
3 (11)	RDVDVGR	+−y−yy+	−−+−++−
	DVGRIRD	−yy+y+−	−+−+−−−
	GDVDSNK	y−y-xx+	+−+−−−−
	GKFGSGP	y+yyxyy	+−++−++
	SMEPRLC	xy−y+yx	−+−+−+−
	DGSTLTR	−yxxyx+	−+−−+−−
	LYKDSGY	yx+−xyy	+−−−−+−
	EAERGRY	−y−+y+x	−+−−+−−
	IDGGWMI	y−yyyyy	+−+++++
	CWWQEYN	xyyx−xx	−++−−−−
	LKASVLW	y+yxyyy	+−+−+++

[a] Shown are 46 peptide sequences from AAV genomes isolated from mouse lungs (from three individual animals) after in vivo biopanning of the AAV-DJ-based peptide display library. The peptides NSSRDLG and NDVRAVS were isolated four and three times, respectively, from the same mouse (all others were isolated once). Residues or short sequence motifs that were enriched in all three animals (see the text) are in bold or underlined. Also shown is the pattern of amino acid side chains, with the following classifications: +, positively charged; −, negatively charged; x, uncharged polar; and y, nonpolar. Moreover, their classification according to hydrophobicity is listed, in which + represents hydrophobic and − represents hydrophilic.

VRAVS in the first mouse. This result was curious, as the identical peptides had previously been isolated independently from an AAV-2-based library after in vitro passaging on two other cell types, coronary arterial and venous endothelial cells (50, 76). Several other findings were also interesting. Firstly, we noted the recurrence of particular peptide motifs composed of the amino acids D-V-R and S-R-D-G in different arrangements among all three mice (Table 5). The two lead peptides from mouse 1 were also enriched with S-R-D(-G-V) residues in distinct permutations. Secondly, we discovered an elevated frequency (~3-fold over that predicted) of arginines (R) in positions 4 of the peptides, especially apparent again in the two lead candidates. Thirdly, the frequency of glycine (G) residues was also markedly increased (from a predicted 6% to 15 to 20%) in multiple positions, particularly 1 and 7 (the start and end points of the peptides), but also 4. As a result of the G/R increase in positions 4, the overall frequency of hydrophilic amino acids in this spot was also elevated (from a predicted 55 to 61%), like that of positively charged residues (from a predicted 15 to 26%). A last remarkable finding was a drop in negatively charged polar amino acid frequency from a predicted 10% to 2 and 4% for positions 6 and 7, respectively, and a concurrent mild increase in the frequency of noncharged polar residues (from 30% to 33 and 35%). Conversely, the frequency of hydrophilic amino acids was lowest (46%, down from a predicted 55%) in positions 6.

Generally, we noted high-level diversity among the peptide sequences from different mice or even among those from the same animal. This finding was not surprising, in light of identical and consistent prior results from in vitro biopannings of AAV-2 libraries on cultured cells (48, 50, 58, 76). As discussed later, there are several possible explanations for this sequence diversity, especially the very complex lung architecture, with multiple cells and receptors. Another important factor was that the sequences in Table 5 were obtained after a single infection round, implying that consecutive in vivo reamplification may result in further enrichment with specific peptides. However, we actually failed to detect AAV DNA signals in new animals infected with whole-lung protein extracts. The most likely reason was the generation of neutralizing antibodies in the primary immunocompetent mice, and this possibility was indeed corroborated by the lack of signs of adenovirus infection in secondary animals, even after prolonged incubation. We therefore pooled the extracts from mice 1 and 2 from the first round and depleted the extracts of murine Igs by using a commercial kit. The cleared eluates were then used for reinfection, together with freshly added murine helper virus. This approach resulted in the expected lung infection and inflammation at day 7 and enabled us to PCR amplify and clone replicated AAV genomes from total lung DNA. Surprisingly, we found all 24 analyzed clones from the second round to be identical and to encode the peptide MVNNFEW. This sequence was unique and had been observed neither in the original unselected library nor in the three primary mice.

Analyses of lung cell tropisms of peptide-modified AAV-DJ vectors. Our next goal was to study whether the isolated peptides would confer new tropism on the AAV-DJ capsid in murine lungs in vivo. We therefore engineered luciferase-expressing recombinant AAV-DJ vectors to display the NSS RDLG peptide (the peptide most frequently recovered in the first round) (Table 5) or the MVNNFEW peptide (the peptide from the second round) and infused them by nasal aspiration at a dose of 10^{11} particles per mouse. As controls, we applied the identical vector genomes corresponding to unmodified DJ capsids, the DJ-2/8 HBD mutant capsid, or the wild-type AAV-8 capsid. In vivo luciferase expression was monitored starting at day 1 and continuing over 4 weeks, before all major tissues including lungs were extracted and imaged separately.

The representative mice shown in Fig. 10A exemplify an approximate twofold variation in overall lung transduction ef-

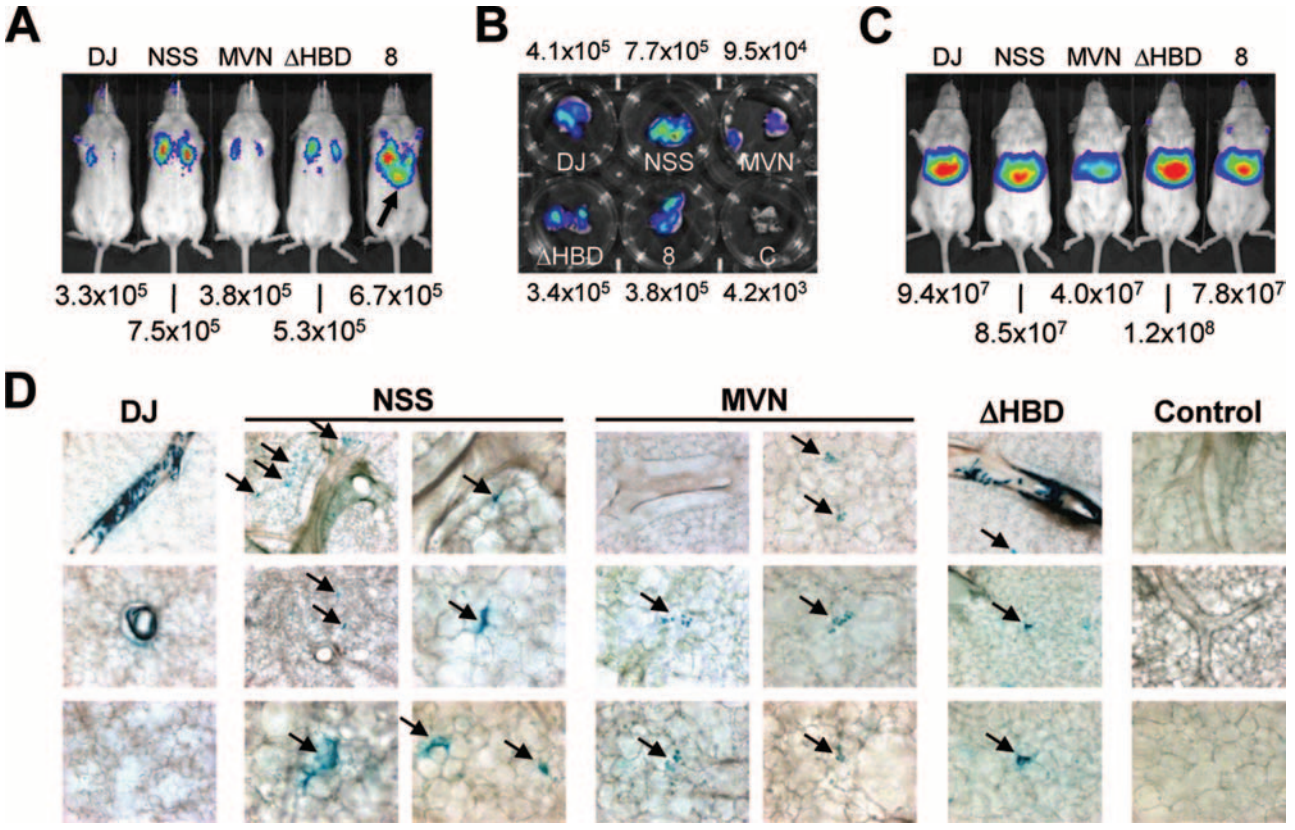


FIG. 10. Analyses of in vivo transduction with peptide-displaying AAV-DJ capsid variants. (A) Wild-type FVB mice were nasally infected with luciferase-expressing AAV vectors as described in the text. Shown are representative examples of lung-directed luciferase expression (numbers below the image are photon counts) 7 days after the inoculation. The black arrow highlights an example of very occasionally observed vector spillover into the stomach (an artifact from the installation procedure). DJ, parental AAV-DJ; NSS, NSSRDLG mutant; MVN, MVNNFEW mutant; ΔHBD, HBD-negative AAV-DJ/8 mutant; 8, wild-type AAV-8. (B) In vitro imaging of isolated lungs confirmed the similarity of luciferase expression levels among all vectors and the mild trend toward higher numbers with the NSSRDLG variant. C, control. (C) Representative examples of results for wild-type FVB mice 7 days after peripheral injection (via the tail vein) with all luciferase-expressing vectors as described in the text. Note the slight (two- to threefold) drop in expression from the MVNNFEW mutant compared to that from the other vectors. (D) Histological analyses (by X-Gal staining) of murine lungs 2 weeks after nasal infection with β-galactosidase-expressing AAV-DJ variants (5×10^{10} particles per mouse). Shown are various representative examples of different sections at different magnifications (×100 or ×200) for each mouse. Black arrows highlight the predominantly transduced cell type for each capsid: (putative) alveolar type II cells for the NSSRDLG variant and alveolar macrophages for the MVNNFEW peptide. The arrows in the images corresponding to the AAV-DJ/8 mutant-infected mouse (labeled ΔHBD) point at occasionally observed positive alveolar cells, while the main transduction target was pulmonary endothelial or smooth muscle cells (top frame), identical to the target of the parental AAV-DJ capsid (the middle frame corresponding to the AAV-DJ-infected mouse shows a vessel cross-section). Sections from an uninfected control mouse (rightmost frames) showed no background signals, with the exception of very faint macrophage staining that was also found in sections from the other mice (not visible here, except in those from the MVNNFEW mutant-infected mouse, which had stronger and more clustered signals than sections from the other mice).

ficacies among the five vectors, with the NSSRDLG mutant peptide (and the AAV-8 capsid) typically yielding slightly be tter results than the other three DJ variant forms. This finding was corroborated by the imaging of isolated lungs (Fig. 10B). Notably, analyses of all other main tissues gave no evidence for vector spillover beyond the lung (data not shown).

In a parallel biodistribution study, we systemically infused all vectors at an intermediate dose of 2×10^{11} particles via peripheral tail vein injection (Fig. 10C). Whole-body imaging revealed comparable levels of liver transduction for most DJ vectors and AAV-8, corroborating our hFIX expression data (see above) (Fig. 7). The only exception was the MVNNFEW mutant vector, which consistently gave two- to threefold-lower luciferase levels than the others. The imaging of all other major tissues gave no clear evidence for the retargeting of the two peptide mutants to a particular organ, including the lungs, from this injection route (data not shown). Intriguingly, this finding seems to contradict the results of a prior study in which the NSSRDLG peptide mediated systemic AAV-2 detargeting from the liver and retargeting to the heart (50). As discussed later, these discrepancies may be due to several crucial differences between the two studies.

The luciferase data had validated lung transduction with all vectors but gave no information on the infected cell types. We thus nasally infused a new set of vectors based on all four DJ variants, expressing β-galactosidase from a CMV promoter. Two weeks later, the lungs were perfused with agarose, sectioned, and X-Gal stained. A number of salient observations are depicted in Fig. 10D. Firstly, both the unmodified DJ and the HBD mutant (a control lacking a peptide insert) strongly

transduced cells of the vasculature (likely pulmonary endothelial cells or smooth muscle cells), whereas these particular cells were entirely negative with the two peptide mutants. Secondly, the HBD mutant but not wild-type DJ additionally infected occasional alveolar cells, which by size, morphology, and location appeared to be type II cells. Thirdly, these specific cells were in fact the main and only distinct target of the NSSRDLG mutant. This obvious contrast to DJ or the HBD mutant highlights the retargeting effect (from endothelial to alveolar cells) mediated by this particular peptide. Yet, both endothelial and alveolar cells in lungs infected with the MVNNFEW mutant were conspicuously negative. Instead, we observed a mild increase in the staining of yet another dispersed cell type, alveolar macrophages. In fact, these cells stained faintly positive in all mice (not visible in Fig. 10D), including an uninfected control (right panels) which was otherwise entirely negative. Even so, the apparent increase in alveolar macrophage transduction with the MVNNFEW mutant may well explain the origin of luciferase expression depicted in Fig. 10A and B, as well as the loss of liver signals (Fig. 10C). Moreover, the evolution of macrophage tropism during AAV passaging in the presence of helper virus would be highly reasonable, as these cells are a main target for adenovirus infection in the lung.

AAV capsid library biopanning in all major organs. Encouraged by the results with lung tissue, we performed a pilot study to assess the potential of our libraries for biopanning in all major tissues of a mouse. We therefore injected two mice each with 5×10^{11} particles from the original shuffled library or the AAV-DJ-derived peptide display library. A week later, we harvested nine major tissue types and screened total genomic DNA for the presence of AAV viral DNA via PCR. As seen in Fig. 11, we could clearly detect AAV *cap* genes in all samples, although we noted differences among the individual tissues and animals (note that the PCR was not quantitative). Strong signals were consistently observed in liver, heart, kidney, and spleen tissues, the typical AAV targets (compare Fig. 8). However, we also obtained good bands for all four brain DNA samples, exemplifying the potential of our unselected libraries to infect tissues that are otherwise inaccessible to the majority of AAVs (in particular, from peripheral virus application).

Our next question was whether we would also be able to enrich optimized capsids or further targeting peptides from these organs. For proof of the concept, we performed the following injections (route and tissue harvested are shown in parentheses): (i) shuffled library (intranasally, lung), (ii) shuffled library (intravenously, liver), and (iii) AAV-2 peptide library (intravenously, liver). We chose the AAV-2-based library since AAV-DJ had already been evolved on liver cells, lowering the chances of recovering hepatotropic peptides. We injected one mouse each for injections i and ii (shuffled libraries) with 5×10^{11} particles, as well as one mouse for injection iii (AAV-2 peptide library) with 2×10^{12} particles. Because of the overall lower level of in vivo fitness of the AAV-2 library, we used a four-times-higher dose than that used before in the biodistribution study with the AAV-DJ counterpart (Fig. 11) in order to permit efficient PCR recovery of viral genomes. All three mice were additionally coinfected with murine adenovirus (5 μl of ATCC stock VR-550) to help AAV genome amplification.

One week after virus installation, the two lungs and the liver

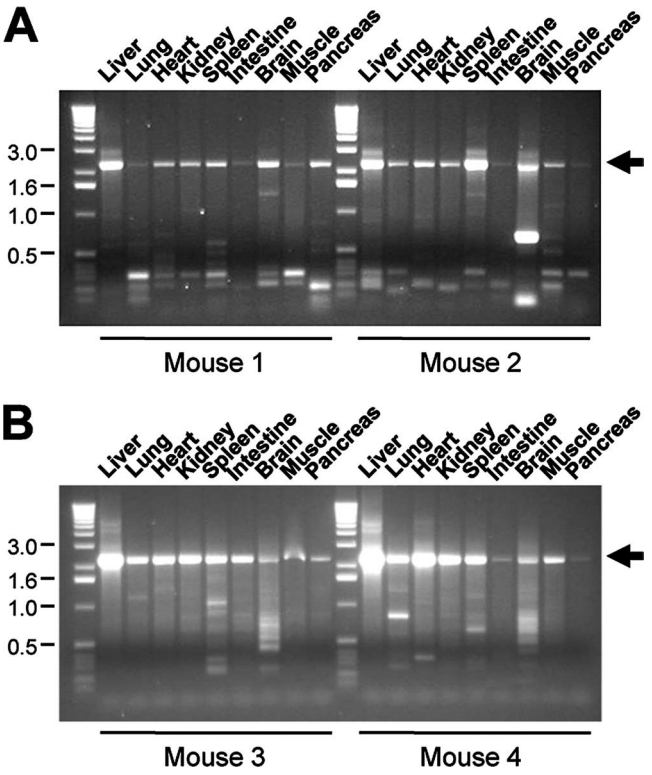


FIG. 11. Biodistribution of AAV capsid libraries following peripheral delivery (via tail vein injection). Wild-type FVB mice were infused with 5×10^{11} particles of the shuffled (A) or AAV-DJ-based peptide display (B) library, and 1 week later, all major organs were harvested for the preparation of total genomic DNA. AAV DNA genomes were detected via PCR using primers flanking the entire *cap* gene (~2.2 kb; arrows). Numbers (in kilobases) on the left refer to a DNA size marker. Shown are results from two representative mice per injection protocol. Note that AAV DNA signals could be detected in all analyzed tissues, including brain tissue, highlighting the potential for the biopanning and evolution of AAV capsids in all major organs in vivo.

from each mouse were harvested, and potentially replicated and enriched AAV genomes were cloned and sequenced (from the 3′ end over ~500 nucleotides, including those corresponding to the HBD and peptide insertion, respectively). Of 20 clones per mouse, we obtained readable sequences for 14 from injection i (shuffled-library particles in lung tissue), 18 from injection ii (shuffled-library particles in liver tissue), and 19 from injection iii (AAV-2 peptide particles in liver tissue). We first performed alignments of the 32 sequences from the shuffled library with the 8 parental viral genomes. Although the numbers of mice and clones per group were too low for comprehensive statistical analyses, we observed markedly different trends between the lung and liver samples. In lung samples, 6 of 14 clones had retained the AAV-2 HBD, whereas the others were homologous in this region to AAV-8 (1 of 14), AAV-9 (1 of 14), or avian AAV (6 of 14) and thus lacked heparin binding capability. Conversely, only 2 of 18 liver clones had the AAV-2 HBD region, while 6 of 18 carried the corresponding sequence from AAV-8, 8 of 18 had that from AAV-9, and 2 of 18 carried the sequence from avian AAV. In summary, ~43% of lung clones contained an HBD, as opposed to only ~11% from the liver tissue. Moreover, it was noteworthy that we unambigu-

TABLE 6. Peptide sequences from in vivo biopanning in murine liver tissue[a]

Peptide (frequency)	Charge pattern	Hydrophobicity pattern
NRGYGAE (2)	x+yxyy−	−−+++++−
NLTSGVY	xyxxyyx	−+−−++−
NSLGSTV	xxyyxxy	−−++−−+
NEARLQG	x−y+yxy	−−+−+−+
NQVGKGT	xxyy+yx	−−++−+−
GPGSYRE	yyyxx+−	++−−−−−
GSPVGQR	yxyyyx+	+−+++−−
GRAPSST	y+yyxxx	+−++−−−
GSDGNMS	yx−yxyx	+−−+−+−
GVGVGGI	yyyyyyy	+++++++
RGGDGSW	+yy−yxy	−++−+−+
DRMVGEG	−+yyy−y	−−+++−+
STVGERV	xxyy−+y	−−+++−+
MDGNHRM	y−yx++y	+−+−−−+
LRIGVAN	y+yyyyx	+−++++−
KNGVNAG	+xyyxyy	−−++−++
FNSAMSL	yxxyyxy	+−−++−+
HIRSQMA	+y+xxyy	−+−−−++

[a] Shown are 19 peptide sequences from AAV genomes isolated from murine liver tissue (from one animal, injected with 2×10^{12} particles of the AAV-2-based peptide display library). The peptide NRGYGAE was isolated twice, and all others were isolated once. Residues or short sequence motifs that were enriched are underlined. See Table 5 for the definition of symbols indicating amino acid classifications.

ously recovered avian AAV sequences in 8 of the 32 clones, although this serotype was lost in our in vitro selection protocols. The opposite was observed for serotypes 4 and 5, which were present in clones after in vitro selection but missing in the 32 (partial) sequences from lung and liver tissues. Finally, it was interesting that in all eight avian AAV sequence-containing clones, the 3′ ends (bases 2069 to 2208) were identical and were from AAV-2.

Curious results were also obtained with the 19 clones from the AAV-2 peptide library from liver tissue (Table 6). As in our prior findings with lung tissue, we recovered a specific sequence twice, NRGYGAE. We also noted a significant increase in glycine but also asparagine residues (G, 22.6% versus 6.3% predicted by the NNB design; N, 9.0% versus 4.2%), as well as enrichment with a G-V motif in half of the clones (9 of 19). The glycine residues accumulated particularly in positions 1 and 3 to 5 of the peptides, whereas positions 1 were enriched with N. This pattern was reminiscent of our lead peptides recovered from lung tissue before and also similar to that of many clones previously isolated by others from various cell types (48, 50, 76), perhaps suggesting a general benefit from asparagine in this spot (see Discussion). Concurrent with the glycine accumulation in the center of the peptide, we found a marked increase in hydrophobic nonpolar residues in positions 3 and 4 to about 80 and 60%, respectively (normal would be 45%).

In analogy to our lung work before, we finally tried to further amplify the potentially enriched and replicated AAV genomes in the liver extract from a second mouse. Yet, this time we consistently failed to detect AAV signals in tissue from the reinfected mouse, regardless of identical attempts to purify anti-AAV and -adenovirus IgGs from the tissue extract. Our most likely explanation is that unlike that in the lung, the adenovirus used for coinfection had not been able to exert the full helper function for the AAV particles in the liver. Interestingly, the mouse had been visibly sick at the time of organ harvesting, and the liver was pale, both observations indicative of successful adenovirus infection. Thus, the inability to reamplify AAVs from the liver but not the lung implies a tissue-specific block in the life cycle of AAV or adenovirus (or both), preventing the production of infectious AAV progeny. Alternatively or in addition, it is possible that the infection conditions for the first mouse (doses, ratios of adenovirus and AAV, and time points) require further fine-tuning to increase the amount of amplified AAV for reinoculation.

DISCUSSION

Our long-standing goal, to optimize the AAV vector system for therapeutic liver transduction, has now led us to devise novel methods for directed AAV diversification from a multispecies set of wild-type viruses. The potent molecular evolution technologies reported here, DNA family shuffling and in vivo biopanning, should significantly complement the current strategies. Indeed, DNA family shuffling provides numerous benefits, as is evident from a comparison of three key parameters: diversity, complexity, and versatility. First and foremost, the diversity in our library, before and after selection, was markedly enhanced over that described in all prior reports. Individual capsids from our unselected library had as little as ~50% homology to the AAV-2 prototype, and our lead candidate (AAV-DJ) differed from its closest natural relative, AAV-2, by 60 residues (of 737 [~8.1%]). This high degree of diversity resulted from the recombination of largely different parental viruses and was further increased by sporadic point mutations. Also, data for wild-type AAVs (11, 18, 44) imply that individual clones can recombine during library growth on cells, further enhancing diversity and explaining the similarity of our pools A and B. In striking contrast, the highest level of diversity achieved before was a difference of only seven residues, in the case of peptide display libraries (50, 58, 76). Moreover, since all insertions occured at the same location, diversification by continuous recombination was unlikely. A maximum of six mutations prior to selection was the upper limit for the second library type, created by error-prone PCR amplification of the AAV-2 capsid gene (46, 59). Postselection, respective lead candidates were ~99.9% identical to wild-type AAV-2, differing by only one or two residues. Hence, the sum of all previous attempts at directed AAV evolution, including four libraries and over 370 mutants from multiple groups (also counting site-directed mutagenesis strategies [42]), did not change more than 1% of capsid residues, at best.

DNA family shuffling also appears to be superior to all nonlibrary strategies for the creation of AAV hybrids, including transcapsidation, marker rescue, and rational domain swapping (8, 30, 62, 64). From therapeutic and technical standpoints, a drawback of the first two approaches is the poor reproducibility, as the genetic templates are not recovered. This problem is solved by the domain-cloning strategy, yet this method can yield hybrids not only identical in phenotype to the parental viruses but also sometimes being noninfectious altogether (64, 85). Rational domain swapping also remains hampered by our limited knowledge of the structure-function re-

lationships for most non-2 serotypes. The same issue continues to restrict the expansion of peptide display into alternative serotypes, with only a few reports of such expansion to date (4, 38). In this respect, a benefit of the AAV-2 HBD in AAV-DJ was that it allowed the straightforward adaptation of peptide display methodology. To our knowledge, we are in fact the first to utilize a synthetic AAV capsid for peptide display and also for library biopanning in vivo. Error-prone PCR is theoretically easier to adapt than peptide-based strategies, as it does not rely on sequence knowledge. Yet, the inherently low level of diversity will pertain as a drawback regardless of the parental virus. Thus, we believe that at this point, DNA family shuffling is the only available method able to yield highly variable libraries whose generation is neither serotype restricted nor limited by our knowledge (or lack thereof) of capsid structures and functions and which truly represent the viral diversity found in nature.

Complexity, i.e., the number of diverse capsids in the library, is a second crucial aspect of evolution methods. A good approximation is the number of bacterial colonies in the plasmid DNA library. Yet, equally important factors that are often ignored in the literature are the degree of interclonal diversity and technical aspects. For example, the simplicity of peptide insertions that require only direct cloning facilitates the creation of large bacterial libraries with up to 10^8 clones (50, 58, 76). This high level of efficacy was readily reproduced with our own peptide libraries and their complexities of $\sim 3 \times 10^7$ clones. PCR randomization is also undemanding, well established, and adaptable, thus easily yielding 10^6 to 10^7 capsid mutants when used for AAV-2 diversification (46, 59). Yet, such numbers may overestimate the true functional complexity, due to contamination with wild-type AAV-2 or phenocopies that falsely raise the library titer. Also, many resulting plasmids do not yield functional virions and are lost during selection. A good measure for vitality is particle yield per transfected cell during viral library production. Our high final titer of 8.2×10^{11} particles/ml, or 3.3×10^{12} total virions, is thus remarkable, as it translates into 3,300 full capsids/cell. These numbers match or exceed the best prior results, indicative of the high degree of vitality of our shuffled library. This vitality was expected, as the principle of DNA family shuffling is homology-based, in-frame recombination of functional sequences. Even so, we cannot technically rule out that our library contained noninfectious clones, similar to observations with domain swapping (64). Notably, our typical AAV-DJ vector yields (including those of all mutants) of $>10^{13}$ particles/ml also exceeded those of earlier chimeras (e.g., reference 76), further supporting the high degrees of vitality and stability of the chimeric AAV sequences in our library. Accordingly, we are pleased with the complexity of our pilot shuffled plasmid library of $\sim 7 \times 10^5$ clones, especially as we had used extreme parameters, i.e., eight parental AAVs with as little as ~50% homology. We can readily anticipate that future libraries based on fewer and/or more-related serotypes will have even higher levels of complexity. It will also always be feasible to increase the titer and complexity by upscaling library production.

Together, diversity and complexity determine a third parameter, versatility. DNA family shuffling also excels here and expands on existing technologies. We define versatility as the sum of viral properties, particularly within a single capsid, that can be molecularly evolved. Peptide display libraries are limited in this regard, as their main purpose is to improve a single parameter, tropism. Some inserts may diminish antibody recognition (33) or affect intracellular processing, but it remains a restriction that only receptor binding is subjected directly to selection. Also, as the capsid gene itself remains unaltered, there is no evolution pressure on the underlying AAV DNA per se. In contrast, error-prone capsid gene mutation via PCR can theoretically alter any residue. Yet, the random and inefficient nature of this method limits library diversity, complexity, and vitality and, thus, versatility. A main drawback is that the technique will typically yield only one or two viable mutations per capsid. Although single residue switches can alter the AAV phenotype (42, 84), such events are probably rare and hard to recap with such libraries. Considering the structure of AAV capsids, with 60 subunits and up to ~735 residues each, it is statistically unlikely that all viral properties can be enhanced by random point mutation. In fact, the only two applications reported to date increased AAV-2 capsid resistance to neutralizing antibodies (46, 58). This result was expected, as prior work had already shown the role of specific residues in antibody recognition (42, 84). Yet, it is unclear how the same technique could be used to improve other properties, or even multiple features at once, especially ones relying on several dispersed residues or domains. The versatility of classical libraries is further restricted if they are derived from AAV-2 (as are almost all to date), as the remaining >99% identity suggests that all capsids will share some of the adverse features that hamper AAV-2 use in humans, including susceptibility to the prevalent immunity.

In conclusion, DNA family shuffling may be the most powerful and potent library-based AAV evolution method to date. With its hallmark of recombination of functional genes, it is an ideal tool to molecularly breed novel viruses merging multiple properties in a single capsid. This capacity is exemplified by our lead candidate, AAV-DJ, which is best characterized as a magnified AAV-2. It merges AAV-2 assets—high-level and broad-range in vitro efficiency, binding to the AAV-2 receptor, and relatively restricted in vivo biodistribution—with those of AAV-8 and AAV-9—superb liver performance, plus the ability to evade preexisting human immunity. By actually surpassing the in vitro efficacy of the best parental wild-type AAVs, AAV-DJ also demonstrates the great potential of DNA family shuffling to create de novo gain-of-function phenotypes. At this point, we are unaware of another synthetic capsid combining a similar extent of valuable assets in a single sequence or any other evolution method providing the same potential to concurrently create high degrees of diversity and versatility (while maintaining reasonable complexity and high-level vitality).

In addition, DNA family shuffling is a potent reverse-genetics tool to study AAV biology. We have provided examples of gain- and loss-of-function phenotypes that it can create and that give insights into diverse viral properties, such as antibody binding and protease cleavage. We also indirectly confirmed key residues constituting the HBD (previously identified via mutagenesis; R484-487-585-588 and K532 [37, 56]), based on conservation in all our selected clones and the critical role of the HBD in vitro. Many dispersed amino acids earlier identified as antigenic determinants in AAV-2 were also recognized in AAV-DJ by alignment with clones evolved without IVIG.

Examples are AAV-2 R471, N705, and V708, which are critical for IVIG resistance (42), and R459, the mutation of which permits escape from anti-AAV-2 antibodies (59). Our alignments also confirmed many of the HVRs in the capsid gene (11, 16) and identified various new areas of diversity. We recently reported the first AAV-8 receptor (LamR) (1), plus an endosomal protease (cathepsin B) involved in intracellular capsid processing (2), and had proposed before that rapid nuclear uncoating is key to potent AAV-8 transduction (73). Future comparisons of shuffled and wild-type capsids will help to further unravel the sequences and mechanisms underlying such viral properties.

Equally crucial for an AAV evolution approach is particle selection and its stringency and clinical relevance, and both were maximized in our study. We particularly consider our use of pooled human antisera (IVIG) for selection an advance in stringency and clinical relevance over approaches described in prior reports, which relied solely on single antisera. These single antisera do not represent the assortment of anti-AAV antibodies in the human population, leaving the usefulness of the evolved particles unclear. The necessity to use pools is validated by a report by Huttner et al., who compared the activities of 65 human serum samples toward AAV-2 mutants (33). Depending on the peptide insertion site, they found substantial differences between individual sera in the ability to bind and/or to neutralize AAV-2 capsids, implying that monoselection is insufficient. As further evidence, AAV-2 variants with point mutations evolved with a single antiserum varied fourfold in their capacities for escape from seven other sera (59).

A second benefit from IVIG was that it forced the evolution of a single hybrid, AAV-DJ, that was not recovered under less stringent conditions. Our key conclusion is that library growth on cells already permissive for one or more parental AAVs is insufficient to select individual capsids. Instead, we obtained pools of related AAVs with homology to AAV-2 and interspersed regions from other AAVs. Notably, we also isolated similarly related derivatives of serotypes 2, 4, 5, 8, and 9 but no single lead candidates from human embryonic kidney cells (293 cells) and mouse fibroblast (NIH 3T3) or liver (Hep1A) cells (data not shown). Most likely key to our success, and likely imperative for future attempts, was to combine stringent positive pressure (growth on cells) and negative pressure (IVIG). Under these conditions, IVIG exerted dual functions. It forced the elimination of immunogenic residues and favored the infectious capsids best able to rapidly escape from neutralization. This conclusion is supported by our result that IVIG was active in culture for >12 h, maintaining pressure on the replicating AAVs. It also explains the superiority of AAV-DJ in vitro, because we inadvertently selected for a capsid that was extremely robust at transducing cells. Some prior evolution attempts also yielded capsids more infectious than that of AAV-2, but usually the increase was lower than that with AAV-DJ (about twofold) (e.g., reference 59). These capsids were also not tested thoroughly and mostly not in vivo. As of now, we do not fully understand all the properties of the AAV-DJ capsid, but most likely, they are determined by synergistic or additive contributions from the parental strains, such as the juxtaposition of multiple peptide motifs potentially involved in cell binding, viral uptake, and subsequent steps (Fig. 12; also see below). Indeed, less-chimeric capsids (obtained without IVIG pressure, e.g., those in pools A and B in Fig. 3) yielded lower levels of gene expression in mice, more like those yielded by AAV-2 (data not shown).

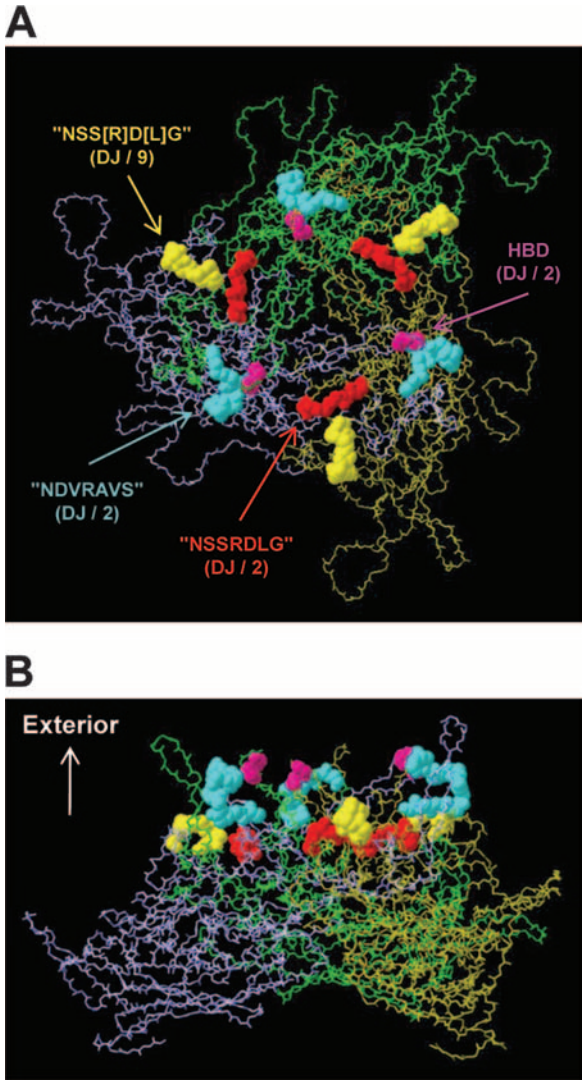


FIG. 12. Model of an AAV VP3 trimer (panel A, top view down the threefold symmetry axis; panel B, side view) created using Swiss-PdbViewer (www.expasy.org/spdbv/text/getpc.htm) and the VIPER oligomer generator (viperdb.scripps.edu/oligomer_multi.php), with the following parameters: T=1 capsid structure; selected matrices A5, A6, and A17; and Protein Data Bank file no. 1LP3 (Fig. 2C) for the AAV-2 sequence. Sequence motifs that may contribute to AAV receptor binding are colored as follows (serotypes with the highest degree of conservation are shown in parentheses): purple, HPD; red, motif with similarity to the NSSRDLG peptide (in AAV-DJ and AAV-2, 534-NGRDSL-539; numbers refer to the AAV-DJ sequence) (compare Fig. 2D); blue, motif with similarity to the NDVRAVS peptide (in AAV-DJ and AAV-2, 505-RV S[KT]SADNNNS-516); and yellow, another motif with (partial) similarity to the NSSRDLG peptide (in AAV-DJ and AAV-9, 277-SGGSSNDN-284). Note how all four motifs are exposed on the capsid surface (B) and how pairs of motifs are located in close proximity to each other (yellow and red motifs or blue and purple motifs), as well as near the HBD (purple), suggesting that they may act cooperatively in receptor binding. Intriguingly, AAV-DJ has the only capsid combining all four motifs in one sequence, perhaps contributing to its high level of efficacy (see the text).

Another key observation was that library growth on cultured cells invariably led to enrichment with the AAV-2 HBD. This bias is likely inherent in any in vitro selection strategy (provided that the library contains AAV-2), considering the role of the HBD in culture. Whether or not its presence is ultimately useful depends on the application. With the liver as our main target, the presence of the HBD was highly rewarding due to the multifaceted role of the HBD in vector biodistribution. Restricted dissemination after intravenous delivery and minimal brain transduction (unlike the transduction patterns occuring with AAV-8 and AAV-9) are significant benefits for human liver gene therapy. More work is needed to elucidate the underlying mechanism(s), but an HBD may affect capsid stability in the blood or the particles' ability to traverse the endothelial cell lining, two prerequisites to transducing remote organs. Notably, a homologous domain was recently associated with capsid-specific T-cell responses in nonhuman primates injected intramuscularly with AAV-2 vectors (74). Yet, it remains unclear whether and to what extent these monkey studies can explain findings in a clinical trial in which one patient injected intraportally with an AAV-2 vector developed cytolytic T cells against capsid-bearing hepatocytes. The authors of the study attributed the incident to two immunogenic peptides in the AAV-2 capsid (47). These are absent in AAV-DJ (Fig. 2D); instead, this capsid part is identical to AAV-8, which did not elicit a T-cell response in the primate study. Yet, recent findings suggest that non-2 serotypes may also be able to elicit T-cell responses, depending on AAV-specific $CD8^+$ memory T cells (49). Clearly, more work and in vivo data are needed to truly understand the anti-AAV cellular immune response and the potential role of the HBD. Importantly, as the constituting residues are known, it is trivial to mutate lead capsids should heparin binding be undesired for an application. Yet, another asset will then also be lost, i.e., the usefulness of the HBD for heparin affinity purification, a scalable and thus superior method to CsCl gradient centrifugation.

Our preliminary data from in vivo biopanning in liver and lung tissues revealed a set of crucial principles which may be broadly applicable to other AAV evolution strategies. Firstly, we noted that the outcomes of in vitro and in vivo evolution can largely differ. For instance, we frequently recovered avian AAV DNA in vivo, despite its absence after in vitro selection, and vice versa for AAV-4 and AAV-5. This result also underscores the diversity and complexity of our initial library, which evidently contained functional capsids derived from all parents. Secondly, the dependencies on heparin binding differed in vitro and in vivo and in distinct tissues. Our pilot data suggest that heparin binding, which is critical for in vitro transduction, may be more important in lung tissue than in liver tissue. This possibility is in line with our results that at higher doses, the HBD-deficient AAV-DJ mutants, as well as AAV-8 and AAV-9, transduced liver tissue better than AAV-DJ. We also noted a much higher proportion of AAV-8 and AAV-9 sequences in liver tissue (14 of 18 sequences; 78%) than in lung tissue (2 of 14 sequences; 14%), corroborating the fact that AAV-8 and AAV-9 are the best-known AAVs for the liver. It is also in line with the high percentage of AAV-8 and AAV-9 sequences in AAV-DJ (Table 2). On the other hand, the inhibition of heparin binding hampered liver transduction with the less efficient AAV-2 (Fig. 7C), and adding an HBD to AAV-8 was also disruptive. Thus, the addition or deletion of an HBD must be considered carefully for each target (cell or tissue type), application (ex or in vivo), and capsid.

A third set of key principles was evident from comparisons to data in the literature. A salient finding was that our two major peptides from lung tissue had previously been selected from an AAV-2 peptide library on arterial or venous endothelial cells (50, 76). Similar sequences were also isolated from acute myeloid leukemia cells in a third study (48). We envision multiple explanations for this phenomenon. One is that identical peptides confer distinct effects, e.g., on tropisms, upon exposure on various AAV backbones. This factor may also explain why in the AAV-DJ context, the NSSRDLG peptide did not alter liver transduction while it detargeted AAV-2 (50). Albeit unlikely, we also cannot technically rule out that our lung sample was marginally contaminated with heart tissue and that the lung tropisms were secondary. Yet, a more probable, captivating possibility is that the NSSRDLG peptide and related motifs bind to a common receptor present on all cells from which these sequences have been isolated to date: alveolar, coronary arterial, venous endothelial, and acute myeloid leukemia cells. Indeed, we noted several conspicuous similarities between our clones and many prior lead peptides, supporting the idea of affinity for the same or related receptors. These similarities include the observation that many peptides were generally enriched with the amino acids A, D, G, L, N, R, S, and V. Likewise, an N in the first position and an R in the fourth position were noted suspiciously frequently in peptides from lung tissue (also in our lead peptide from liver tissue, NRGYGAE) as well as earlier. A third, indirect piece of evidence for binding to widely present receptors is that some prior lead peptides mediated good transduction levels across a panel of cell lines (76).

Curious in this regard is the recent identification of a new integrin $\alpha V\beta 1$ binding motif in AAV-2 and a few other serotypes (5). Intriguingly, this motif (NGR) is part of a larger sequence with striking similarity to the NSSRDLG peptide, i.e., NGRDSL. The latter is fully conserved in AAV-2 and AAV-DJ (and serotypes 3 and 10) and located on the capsid exterior near the HBD, in line with its putative role in integrin binding. Moreover, we identified two further intriguing motifs within AAV-DJ VP, another one similar to NSSRDLG and one resembling the second lead peptide identified in the present study and that by Müller et al., NDVRAVS (50). Both motifs are also displayed on the capsid (Fig. 12B); in fact, all four (including the HBD) are located very close to one another and near the threefold symmetry axis (Fig. 12A). Together with our findings described above, these results make it tempting to speculate that these three additional motifs contribute to the binding of AAV receptors, e.g., integrins. An appealing ensuing idea is that AAV-DJ's superior efficacy on multiple cell types is due in part to the fact that AAV-DJ combines all four motifs in one sequence, unlike any wild-type AAV. The observation that the binding of AAV-DJ to cultured cells is in fact inferior to that of AAV-2 would suggest that the putative additional receptors act as entry, but not attachment, molecules. This idea is in line with the roles of different integrins, which cooperatively act as secondary entry receptors for many viruses, including $\alpha V\beta 1/\alpha V\beta 5$ for AAV-2 (5). The high level of efficacy of AAV-DJ may then indeed result from synergism

from the juxtaposition of multiple parental properties: binding to potent primary attachment and secondary entry receptors and efficient intracellular processing. Further investigations into the true nature of the receptors recognized by selected peptides will certainly be very exciting and important.

In the future, the optimization of in vivo evolution schemes should become a top priority, starting with the AAV helper virus, for multiple reasons. Obvious factors are toxicity and safety issues, but equally critical is the influence of the helper virus on the outcome of selection. AAV libraries can amplify only in coinfected cells, permitting the helper virus to dictate and restrict the tropism of the evolving AAV particles. This property is shown by our findings with lung tissue, in which our lead candidates mimicked adenoviral biodistribution. An intriguing possible solution may be to clone and express the adenoviral helper genes (E1, E2A, E4orf6, and VA genes) from a second AAV library in parallel. Other promising steps toward routine in vivo evolution would be the use of immunodeficient animals or mice with humanized tissues. It remains to be tested whether this approach will help to overcome another hurdle seen in our pilot studies, the block in the AAV or adenoviral life cycle in the liver (and maybe elsewhere). For adenovirus, this problem may also be solved by the expression of the relevant genes from AAV.

Optimized selection schemes will then be useful to resolve many key aspects of AAV vector evolution. For example, parallel in vivo screening of libraries based on different capsids will clarify the role of the hosting virus and the locations and flanking sequences for the displayed peptides. The use of AAV-2-based libraries may be challenging due to the relatively low level of in vivo fitness of the underlying virus, yet our data for liver tissue already show the potential of this approach. Better animal models will also help us to unravel the function of our other lead peptide, MVNNFEW. Thus far, our data imply tropism for alveolar macrophages, albeit this requires validation due to the background staining of alveolar macrophages from even naïve mice. Enrichment with this peptide after IgG depletion suggests an alternative function, i.e., to reduce the recognition of the hosting capsid by neutralizing antibodies. This phenomenon was noted anecdotally before (33) and may be due to sterical or conformational effects, masking immunogenic residues or domains in the capsid. In our case, it is possible that during IgG depletion of our primary lung extract, we also eliminated all capsids still attached to the antibodies, perhaps excluding the MVNNFEW virus which could escape from this procedure. Alternatively, multiple capsids may have evaded depletion but only the MVNNFEW clone could also reamplify in the secondary lung. To distinguish these conceivable possibilites, we will now rescreen our libraries in immunodeficient animals and will purify selected target cells prior to AAV rescue and reamplification.

Finally, essential is the potential clinical usefulness of the AAV clones evolved in this work. For our in vivo-selected capsids, our proof-of-concept data may be too limited to suggest specific uses, as more factors remain to be studied, including biodistribution, doses, time points, delivery routes, and comparisons to more wild-type AAVs. Further in vitro work analogous to and beyond our experiments presented in Fig. 6 will also aim to unravel their mechanisms of transduction. On the other hand, we can envision multiple ex or in vivo gene therapy applications for AAV-DJ vectors. Their high-level efficacy at low doses, from a clinically feasible administration route, implies a use for systemic therapies of hepatodeficiencies such as the hemophilias. The slower kinetics at extreme doses are irrelevant because of the high-level efficiency, with a minimal dose of 5×10^{10} particles per mouse, or 2.5×10^{12} particles/kg of body weight, already sufficing for the expression of 400% of normal hFIX levels. This dose equals the highest particle load in the clinical trial, although the inferior AAV-2 capsid produced only 12% of normal hFIX levels (still in the therapeutic range) (47). Despite the blunted response, the hFIX expression level of ~300 μg/ml from the highest AAV-DJ dose exceeds most reported data for mice. Also, the extreme dose at which AAV-DJ transduction became saturated would correspond to a level of $>2 \times 10^{16}$ particles in humans, which is technically impossible to produce or administer. Finally, combining potent AAV capsids with efficient self-complementary genomes will allow effective particle doses to be lowered further by at least an order of magnitude (20, 26, 28, 54). Hence, we doubt that dosing will ultimately limit therapies in humans and rather assume that issues such as biodistribution will prevail. This conclusion already justifies the further preclinical evaluation of AAV-DJ, despite the strong competition from wild types 8 and 9. It was no surprise that the in vivo efficacy of AAV-DJ did not exceed their in vivo efficacy, considering that they have evolved to outperform most AAVs in mammalian tissues (19, 52). It is still essential to have another similarly efficient AAV at our disposal, due to the escalating evidence that findings with mice are not inevitably predictive for higher species (17, 32, 54, 75). Consequently, the next challenge will be to translate AAV-DJ for use in appropriate large animals and verify our results in a context more relevant to humans.

Of note, AAV-DJ may prove very useful for an emerging new clinical application, liver RNAi to treat hepatocellular carcinoma or infection with hepatitis viruses (25, 28). We recently evaluated AAV-8 vectors for this purpose and observed lethalities in mice, caused by rapid high-level expression of short hairpin RNAs (shRNAs) (28). Due to its more gradual onset of gene expression at high doses, the use of AAV-DJ for shRNA expression may minimize the risk of overloading the cellular RNAi machinery (28) while yielding sufficient shRNAs to achieve therapeutic effects. The reduced vector dissemination would further limit toxicity and enhance safety, especially in combination with our latest liver-specific shRNA expression cassettes (Giering et al., submitted for publication).

The ultimate task remains to engineer AAV capsids to merge specificity with efficiency and safety and tailor them to patient or disease profiles. We anticipate that DNA family shuffling will play a major role in the future, as it is applicable to all natural AAVs and can readily be adapted for directed vector evolution toward many applications. With the rapidly progressing discovery of multispecies AAVs, expanding our repertoire of capsid genes, it should soon be embraced as the most potent technology for AAV diversification. Moreover, our promising pilot efforts toward in vivo biopanning may help to pave the way for future evolution attempts under physiologically and clinically pertinent conditions. The key technologies and principles established here raise optimism that our work will bring us several steps closer to all these critical goals.

ACKNOWLEDGMENTS

We thank Brian Garrison for expert help with the cultivation of the human hepatocytes and Kusum Pandey for excellent technical assistance. We are very grateful to James Wilson for providing AAV-8 and AAV-9 helper plasmids and express our gratitude to Jay Chiorini and Rob Kotin for their kind gifts of plasmids harboring the avian or bovine AAV capsid genes.

This work was supported by NIH grant HL64274 and the California Institute for Regenerative Medicine.

REFERENCES

1. **Akache, B., D. Grimm, K. Pandey, S. R. Yant, H. Xu, and M. A. Kay.** 2006. The 37/67-kilodalton laminin receptor is a receptor for adeno-associated virus serotypes 8, 2, 3, and 9. J. Virol. **80:**9831–9836.
2. **Akache, B., D. Grimm, X. Shen, S. Fuess, S. R. Yant, D. S. Glazer, J. Park, and M. A. Kay.** 2007. A two-hybrid screen identifies cathepsins B and L as uncoating factors for adeno-associated virus 2 and 8. Mol. Ther. **15:**330–339.
3. **Arbetman, A. E., M. Lochrie, S. Zhou, J. Wellman, C. Scallan, M. M. Doroudchi, B. Randlev, S. Patarroyo-White, T. Liu, P. Smith, H. Lehmkuhl, L. A. Hobbs, G. F. Pierce, and P. Colosi.** 2005. Novel caprine adeno-associated virus (AAV) capsid (AAV-Go.1) is closely related to the primate AAV-5 and has unique tropism and neutralization properties. J. Virol. **79:**15238–15245.
4. **Arnold, G. S., A. K. Sasser, M. D. Stachler, and J. S. Bartlett.** 2006. Metabolic biotinylation provides a unique platform for the purification and targeting of multiple AAV vector serotypes. Mol. Ther. **14:**97–106.
5. **Asokan, A., J. B. Hamra, L. Govindasamy, M. Agbandje-McKenna, and R. J. Samulski.** 2006. Adeno-associated virus type 2 contains an integrin $\alpha5\beta1$ binding domain essential for viral cell entry. J. Virol. **80:**8961–8969.
6. **Bartlett, J. S., J. Kleinschmidt, R. C. Boucher, and R. J. Samulski.** 1999. Targeted adeno-associated virus vector transduction of nonpermissive cells mediated by a bispecific $F(ab'\gamma)_2$ antibody. Nat. Biotechnol. **17:**181–186.
7. **Bleker, S., F. Sonntag, and J. A. Kleinschmidt.** 2005. Mutational analysis of narrow pores at the fivefold symmetry axes of adeno-associated virus type 2 capsids reveals a dual role in genome packaging and activation of phospholipase A2 activity. J. Virol. **79:**2528–2540.
8. **Bowles, D. E., J. E. Rabinowitz, and R. J. Samulski.** 2003. Marker rescue of adeno-associated virus (AAV) capsid mutants: a novel approach for chimeric AAV production. J. Virol. **77:**423–432.
9. **Buning, H., M. U. Ried, L. Perabo, F. M. Gerner, N. A. Huttner, J. Enssle, and M. Hallek.** 2003. Receptor targeting of adeno-associated virus vectors. Gene Ther. **10:**1142–1151.
10. **Chang, C. C., T. T. Chen, B. W. Cox, G. N. Dawes, W. P. Stemmer, J. Punnonen, and P. A. Patten.** 1999. Evolution of a cytokine using DNA family shuffling. Nat. Biotechnol. **17:**793–797.
11. **Chen, C. L., R. L. Jensen, B. C. Schnepp, M. J. Connell, R. Shell, T. J. Sferra, J. S. Bartlett, K. R. Clark, and P. R. Johnson.** 2005. Molecular characterization of adeno-associated viruses infecting children. J. Virol. **79:**14781–14792.
12. **Choi, V. W., D. M. McCarty, and R. J. Samulski.** 2005. AAV hybrid serotypes: improved vectors for gene delivery. Curr. Gene Ther. **5:**299–310.
13. **Christians, F. C., L. Scapozza, A. Crameri, G. Folkers, and W. P. Stemmer.** 1999. Directed evolution of thymidine kinase for AZT phosphorylation using DNA family shuffling. Nat. Biotechnol. **17:**259–264.
14. **Crameri, A., S. A. Raillard, E. Bermudez, and W. P. Stemmer.** 1998. DNA shuffling of a family of genes from diverse species accelerates directed evolution. Nature **391:**288–291.
15. **Crameri, A., E. A. Whitehorn, E. Tate, and W. P. Stemmer.** 1996. Improved green fluorescent protein by molecular evolution using DNA shuffling. Nat. Biotechnol. **14:**315–319.
16. **Gao, G., M. R. Alvira, S. Somanathan, Y. Lu, L. H. Vandenberghe, J. J. Rux, R. Calcedo, J. Sanmiguel, Z. Abbas, and J. M. Wilson.** 2003. Adeno-associated viruses undergo substantial evolution in primates during natural infections. Proc. Natl. Acad. Sci. USA **100:**6081–6086.
17. **Gao, G., Y. Lu, R. Calcedo, R. L. Grant, P. Bell, L. Wang, J. Figueredo, M. Lock, and J. M. Wilson.** 2006. Biology of AAV serotype vectors in liver-directed gene transfer to nonhuman primates. Mol. Ther. **13:**77–87.
18. **Gao, G., L. H. Vandenberghe, M. R. Alvira, Y. Lu, R. Calcedo, X. Zhou, and J. M. Wilson.** 2004. Clades of adeno-associated viruses are widely disseminated in human tissues. J. Virol. **78:**6381–6388.
19. **Gao, G. P., M. R. Alvira, L. Wang, R. Calcedo, J. Johnston, and J. M. Wilson.** 2002. Novel adeno-associated viruses from rhesus monkeys as vectors for human gene therapy. Proc. Natl. Acad. Sci. USA **99:**11854–11859.
20. **Gao, G. P., Y. Lu, X. Sun, J. Johnston, R. Calcedo, R. Grant, and J. M. Wilson.** 2006. High-level transgene expression in nonhuman primate liver with novel adeno-associated virus serotypes containing self-complementary genomes. J. Virol. **80:**6192–6194.
21. **Girod, A., M. Ried, C. Wobus, H. Lahm, K. Leike, J. Kleinschmidt, G. Deleage, and M. Hallek.** 1999. Genetic capsid modifications allow efficient re-targeting of adeno-associated virus type 2. Nat. Med. **5:**1052–1056.
22. **Grifman, M., M. Trepel, P. Speece, L. B. Gilbert, W. Arap, R. Pasqualini, and M. D. Weitzman.** 2001. Incorporation of tumor-targeting peptides into recombinant adeno-associated virus capsids. Mol. Ther. **3:**964–975.
23. **Grimm, D.** 2002. Production methods for gene transfer vectors based on adeno-associated virus serotypes. Methods **28:**146–157.
24. **Grimm, D., and M. A. Kay.** 2003. From virus evolution to vector revolution: use of naturally occurring serotypes of adeno-associated virus (AAV) as novel vectors for human gene therapy. Curr. Gene Ther. **3:**281–304.
25. **Grimm, D., and M. A. Kay.** 2006. Therapeutic short hairpin RNA expression in the liver: viral targets and vectors. Gene Ther. **13:**563–575.
26. **Grimm, D., K. Pandey, and M. A. Kay.** 2005. Adeno-associated virus vectors for short hairpin RNA expression. Methods Enzymol. **392:**381–405.
27. **Grimm, D., K. Pandey, H. Nakai, T. A. Storm, and M. A. Kay.** 2006. Liver transduction with recombinant adeno-associated virus is primarily restricted by capsid serotype not vector genotype. J. Virol. **80:**426–439.
28. **Grimm, D., K. L. Streetz, C. L. Jopling, T. A. Storm, K. Pandey, C. R. Davis, P. Marion, F. Salazar, and M. A. Kay.** 2006. Fatality in mice due to oversaturation of cellular microRNA/short hairpin RNA pathways. Nature **441:**537–541.
29. **Grimm, D., S. Zhou, H. Nakai, C. E. Thomas, T. A. Storm, S. Fuess, T. Matsushita, J. Allen, R. Surosky, M. Lochrie, L. Meuse, A. McClelland, P. Colosi, and M. A. Kay.** 2003. Preclinical in vivo evaluation of pseudotyped adeno-associated virus vectors for liver gene therapy. Blood **102:**2412–2419.
30. **Hauck, B., L. Chen, and W. Xiao.** 2003. Generation and characterization of chimeric recombinant AAV vectors. Mol. Ther. **7:**419–425.
31. **Hauck, B., and W. Xiao.** 2003. Characterization of tissue tropism determinants of adeno-associated virus type 1. J. Virol. **77:**2768–2774.
32. **Herzog, R. W.** 2007. Immune responses to AAV capsid: are mice not humans after all? Mol. Ther. **15:**649–650.
33. **Huttner, N. A., A. Girod, L. Perabo, D. Edbauer, J. A. Kleinschmidt, H. Buning, and M. Hallek.** 2003. Genetic modifications of the adeno-associated virus type 2 capsid reduce the affinity and the neutralizing effects of human serum antibodies. Gene Ther. **10:**2139–2147.
34. **Inagaki, K., S. Fuess, T. A. Storm, G. A. Gibson, C. F. McTiernan, M. A. Kay, and H. Nakai.** 2006. Robust systemic transduction with AAV9 vectors in mice: efficient global cardiac gene transfer superior to that of AAV8. Mol. Ther. **14:**45–53.
35. **Jang, J. H., K. I. Lim, and D. V. Schaffer.** 2007. Library selection and directed evolution approaches to engineering targeted viral vectors. Biotechnol. Bioeng. **98:**515–524.
36. **Kay, M. A., C. S. Manno, M. V. Ragni, P. J. Larson, L. B. Couto, A. McClelland, B. Glader, A. J. Chew, S. J. Tai, R. W. Herzog, V. Arruda, F. Johnson, C. Scallan, E. Skarsgard, A. W. Flake, and K. A. High.** 2000. Evidence for gene transfer and expression of factor IX in haemophilia B patients treated with an AAV vector. Nat. Genet. **24:**257–261.
37. **Kern, A., K. Schmidt, C. Leder, O. J. Muller, C. E. Wobus, K. Bettinger, C. W. Von der Lieth, J. A. King, and J. A. Kleinschmidt.** 2003. Identification of a heparin-binding motif on adeno-associated virus type 2 capsids. J. Virol. **77:**11072–11081.
38. **Koerber, J. T., J. H. Jang, J. H. Yu, R. S. Kane, and D. V. Schaffer.** 2007. Engineering adeno-associated virus for one-step purification via immobilized metal affinity chromatography. Hum. Gene Ther. **18:**367–378.
39. **Kolkman, J. A., and W. P. Stemmer.** 2001. Directed evolution of proteins by exon shuffling. Nat. Biotechnol. **19:**423–428.
40. **Kronenberg, S., B. Bottcher, C. W. von der Lieth, S. Bleker, and J. A. Kleinschmidt.** 2005. A conformational change in the adeno-associated virus type 2 capsid leads to the exposure of hidden VP1 N termini. J. Virol. **79:**5296–5303.
41. **Kwon, I., and D. V. Schaffer.** 1 September 2007, posting date. Designer gene delivery vectors: molecular engineering and evolution of adeno-associated viral vectors for enhanced gene transfer. Pharm. Res. doi:10.1007/s11095-007-9431-0.
42. **Lochrie, M. A., G. P. Tatsuno, B. Christie, J. W. McDonnell, S. Zhou, R. Surosky, G. F. Pierce, and P. Colosi.** 2006. Mutations on the external surfaces of adeno-associated virus type 2 capsids that affect transduction and neutralization. J. Virol. **80:**821–834.
43. **Loiler, S. A., T. J. Conlon, S. Song, Q. Tang, K. H. Warrington, A. Agarwal, M. Kapturczak, C. Li, C. Ricordi, M. A. Atkinson, N. Muzyczka, and T. R. Flotte.** 2003. Targeting recombinant adeno-associated virus vectors to enhance gene transfer to pancreatic islets and liver. Gene Ther. **10:**1551–1558.
44. **Lukashov, V. V., and J. Goudsmit.** 2001. Evolutionary relationships among parvoviruses: virus-host coevolution among autonomous primate parvoviruses and links between adeno-associated and avian parvoviruses. J. Virol. **75:**2729–2740.
45. **Lux, K., N. Goerlitz, S. Schlemminger, L. Perabo, D. Goldnau, J. Endell, K. Leike, D. M. Kofler, S. Finke, M. Hallek, and H. Buning.** 2005. Green fluorescent protein-tagged adeno-associated virus particles allow the study of cytosolic and nuclear trafficking. J. Virol. **79:**11776–11787.
46. **Maheshri, N., J. T. Koerber, B. K. Kaspar, and D. V. Schaffer.** 2006. Directed evolution of adeno-associated virus yields enhanced gene delivery vectors. Nat. Biotechnol. **24:**198–204.
47. **Manno, C. S., G. F. Pierce, V. R. Arruda, B. Glader, M. Ragni, J. J. Rasko,**

M. C. Ozelo, K. Hoots, P. Blatt, B. Konkle, M. Dake, R. Kaye, M. Razavi, A. Zajko, J. Zehnder, P. K. Rustagi, H. Nakai, A. Chew, D. Leonard, J. F. Wright, R. R. Lessard, J. M. Sommer, M. Tigges, D. Sabatino, A. Luk, H. Jiang, F. Mingozzi, L. Couto, H. C. Ertl, K. A. High, and M. A. Kay. 2006. Successful transduction of liver in hemophilia by AAV-factor IX and limitations imposed by the host immune response. Nat. Med. **12:**342–347.

48. **Michelfelder, S., M. K. Lee, E. DeLima-Hahn, T. Wilmes, F. Kaul, O. Muller, J. A. Kleinschmidt, and M. Trepel.** 2007. Vectors selected from adeno-associated viral display peptide libraries for leukemia cell-targeted cytotoxic gene therapy. Exp. Hematol. **35:**1766–1776.
49. **Mingozzi, F., and K. A. High.** 2007. Immune responses to AAV in clinical trials. Curr. Gene Ther. **7:**316–324.
50. **Müller, O. J., F. Kaul, M. D. Weitzman, R. Pasqualini, W. Arap, J. A. Kleinschmidt, and M. Trepel.** 2003. Random peptide libraries displayed on adeno-associated virus to select for targeted gene therapy vectors. Nat. Biotechnol. **21:**1040–1046.
51. **Muzyczka, N., and K. H. Warrington, Jr.** 2005. Custom adeno-associated virus capsids: the next generation of recombinant vectors with novel tropism. Hum. Gene Ther. **16:**408–416.
52. **Nakai, H., S. Fuess, T. A. Storm, S. Muramatsu, Y. Nara, and M. A. Kay.** 2005. Unrestricted hepatocyte transduction with adeno-associated virus serotype 8 vectors in mice. J. Virol. **79:**214–224.
53. **Nakai, H., C. E. Thomas, T. A. Storm, S. Fuess, S. Powell, J. F. Wright, and M. A. Kay.** 2002. A limited number of transducible hepatocytes restricts a wide-range linear vector dose response in recombinant adeno-associated virus-mediated liver transduction. J. Virol. **76:**11343–11349.
54. **Nathwani, A. C., J. T. Gray, C. Y. Ng, J. Zhou, Y. Spence, S. N. Waddington, E. G. Tuddenham, G. Kemball-Cook, J. McIntosh, M. Boon-Spijker, K. Mertens, and A. M. Davidoff.** 2006. Self-complementary adeno-associated virus vectors containing a novel liver-specific human factor IX expression cassette enable highly efficient transduction of murine and nonhuman primate liver. Blood **107:**2653–2661.
55. **Nicklin, S. A., H. Buening, K. L. Dishart, M. de Alwis, A. Girod, U. Hacker, A. J. Thrasher, R. R. Ali, M. Hallek, and A. H. Baker.** 2001. Efficient and selective AAV2-mediated gene transfer directed to human vascular endothelial cells. Mol. Ther. **4:**174–181.
56. **Opie, S. R., K. H. Warrington, Jr., M. Agbandje-McKenna, S. Zolotukhin, and N. Muzyczka.** 2003. Identification of amino acid residues in the capsid proteins of adeno-associated virus type 2 that contribute to heparan sulfate proteoglycan binding. J. Virol. **77:**6995–7006.
57. **Pekrun, K., R. Shibata, T. Igarashi, M. Reed, L. Sheppard, P. A. Patten, W. P. Stemmer, M. A. Martin, and N. W. Soong.** 2002. Evolution of a human immunodeficiency virus type 1 variant with enhanced replication in pig-tailed macaque cells by DNA shuffling. J. Virol. **76:**2924–2935.
58. **Perabo, L., H. Buning, D. M. Kofler, M. U. Ried, A. Girod, C. M. Wendtner, J. Enssle, and M. Hallek.** 2003. In vitro selection of viral vectors with modified tropism: the adeno-associated virus display. Mol. Ther. **8:**151–157.
59. **Perabo, L., J. Endell, S. King, K. Lux, D. Goldnau, M. Hallek, and H. Buning.** 2006. Combinatorial engineering of a gene therapy vector: directed evolution of adeno-associated virus. J. Gene Med. **8:**155–162.
60. **Perabo, L., D. Goldnau, K. White, J. Endell, J. Boucas, S. Humme, L. M. Work, H. Janicki, M. Hallek, A. H. Baker, and H. Buning.** 2006. Heparan sulfate proteoglycan binding properties of adeno-associated virus retargeting mutants and consequences for their in vivo tropism. J. Virol. **80:**7265–7269.
61. **Powell, S. K., M. A. Kaloss, A. Pinkstaff, R. McKee, I. Burimski, M. Pensiero, E. Otto, W. P. Stemmer, and N. W. Soong.** 2000. Breeding of retroviruses by DNA shuffling for improved stability and processing yields. Nat. Biotechnol. **18:**1279–1282.
62. **Rabinowitz, J. E., D. E. Bowles, S. M. Faust, J. G. Ledford, S. E. Cunningham, and R. J. Samulski.** 2004. Cross-dressing the virion: the transcapsidation of adeno-associated virus serotypes functionally defines subgroups. J. Virol. **78:**4421–4432.
63. **Scallan, C. D., H. Jiang, T. Liu, S. Patarroyo-White, J. M. Sommer, S. Zhou, L. B. Couto, and G. F. Pierce.** 2006. Human immunoglobulin inhibits liver transduction by AAV vectors at low AAV2 neutralizing titers in SCID mice. Blood **107:**1810–1817.
64. **Shen, X., T. Storm, and M. A. Kay.** 2007. Characterization of the relationship of AAV capsid domain swapping to liver transduction efficiency. Mol. Ther. **15:**1955–1962.
65. **Shi, W., and J. S. Bartlett.** 2003. RGD inclusion in VP3 provides adeno-associated virus type 2 (AAV2)-based vectors with a heparan sulfate-independent cell entry mechanism. Mol. Ther. **7:**515–525.
66. **Shi, W., A. Hemminki, and J. S. Bartlett.** 2006. Capsid modifications overcome low heterogeneous expression of heparan sulfate proteoglycan that limits AAV2-mediated gene transfer and therapeutic efficacy in human ovarian carcinoma. Gynecol. Oncol. **103:**1054–1062.
67. **Snyder, R. O., C. H. Miao, G. A. Patijn, S. K. Spratt, O. Danos, D. Nagy, A. M. Gown, B. Winther, L. Meuse, L. K. Cohen, A. R. Thompson, and M. A. Kay.** 1997. Persistent and therapeutic concentrations of human factor IX in mice after hepatic gene transfer of recombinant AAV vectors. Nat. Genet. **16:**270–276.
68. **Sonntag, F., S. Bleker, B. Leuchs, R. Fischer, and J. A. Kleinschmidt.** 2006. Adeno-associated virus type 2 capsids with externalized VP1/VP2 trafficking domains are generated prior to passage through the cytoplasm and are maintained until uncoating occurs in the nucleus. J. Virol. **80:**11040–11054.
69. **Soong, N. W., L. Nomura, K. Pekrun, M. Reed, L. Sheppard, G. Dawes, and W. P. Stemmer.** 2000. Molecular breeding of viruses. Nat. Genet. **25:**436–439.
70. **Stemmer, W. P.** 1994. DNA shuffling by random fragmentation and reassembly: in vitro recombination for molecular evolution. Proc. Natl. Acad. Sci. USA **91:**10747–10751.
71. **Stemmer, W. P.** 1994. Rapid evolution of a protein in vitro by DNA shuffling. Nature **370:**389–391.
72. **Summerford, C., and R. J. Samulski.** 1998. Membrane-associated heparan sulfate proteoglycan is a receptor for adeno-associated virus type 2 virions. J. Virol. **72:**1438–1445.
73. **Thomas, C. E., T. A. Storm, Z. Huang, and M. A. Kay.** 2004. Rapid uncoating of vector genomes is the key to efficient liver transduction with pseudotyped adeno-associated virus vectors. J. Virol. **78:**3110–3122.
74. **Vandenberghe, L. H., L. Wang, S. Somanathan, Y. Zhi, J. Figueredo, R. Calcedo, J. Sanmiguel, R. A. Desai, C. S. Chen, J. Johnston, R. L. Grant, G. Gao, and J. M. Wilson.** 2006. Heparin binding directs activation of T cells against adeno-associated virus serotype 2 capsid. Nat. Med. **12:**967–971.
75. **Wang, L., R. Calcedo, T. C. Nichols, D. A. Bellinger, A. Dillow, I. M. Verma, and J. M. Wilson.** 2005. Sustained correction of disease in naive and AAV2-pretreated hemophilia B dogs: AAV2/8-mediated, liver-directed gene therapy. Blood **105:**3079–3086.
76. **Waterkamp, D. A., O. J. Muller, Y. Ying, M. Trepel, and J. A. Kleinschmidt.** 2006. Isolation of targeted AAV2 vectors from novel virus display libraries. J. Gene Med. **8:**1307–1319.
77. **White, S. J., S. A. Nicklin, H. Buning, M. J. Brosnan, K. Leike, E. D. Papadakis, M. Hallek, and A. H. Baker.** 2004. Targeted gene delivery to vascular tissue in vivo by tropism-modified adeno-associated virus vectors. Circulation **109:**513–519.
78. **Wistuba, A., A. Kern, S. Weger, D. Grimm, and J. A. Kleinschmidt.** 1997. Subcellular compartmentalization of adeno-associated virus type 2 assembly. J. Virol. **71:**1341–1352.
79. **Wistuba, A., S. Weger, A. Kern, and J. A. Kleinschmidt.** 1995. Intermediates of adeno-associated virus type 2 assembly: identification of soluble complexes containing Rep and Cap proteins. J. Virol. **69:**5311–5319.
80. **Wobus, C. E., B. Hugle-Dorr, A. Girod, G. Petersen, M. Hallek, and J. A. Kleinschmidt.** 2000. Monoclonal antibodies against the adeno-associated virus type 2 (AAV-2) capsid: epitope mapping and identification of capsid domains involved in AAV-2-cell interaction and neutralization of AAV-2 infection. J. Virol. **74:**9281–9293.
81. **Work, L. M., H. Buning, E. Hunt, S. A. Nicklin, L. Denby, N. Britton, K. Leike, M. Odenthal, U. Drebber, M. Hallek, and A. H. Baker.** 2006. Vascular bed-targeted in vivo gene delivery using tropism-modified adeno-associated viruses. Mol. Ther. **13:**683–693.
82. **Work, L. M., S. A. Nicklin, N. J. Brain, K. L. Dishart, D. J. Von Seggern, M. Hallek, H. Buning, and A. H. Baker.** 2004. Development of efficient viral vectors selective for vascular smooth muscle cells. Mol. Ther. **9:**198–208.
83. **Wu, P., W. Xiao, T. Conlon, J. Hughes, M. Agbandje-McKenna, T. Ferkol, T. Flotte, and N. Muzyczka.** 2000. Mutational analysis of the adeno-associated virus type 2 (AAV2) capsid gene and construction of AAV2 vectors with altered tropism. J. Virol. **74:**8635–8647.
84. **Wu, Z., A. Asokan, J. C. Grieger, L. Govindasamy, M. Agbandje-McKenna, and R. J. Samulski.** 2006. Single amino acid changes can influence titer, heparin binding, and tissue tropism in different adeno-associated virus serotypes. J. Virol. **80:**11393–11397.
85. **Wu, Z., A. Asokan, and R. J. Samulski.** 2006. Adeno-associated virus serotypes: vector toolkit for human gene therapy. Mol. Ther. **14:**316–327.
86. **Zadori, Z., J. Szelei, M. C. Lacoste, Y. Li, S. Gariepy, P. Raymond, M. Allaire, I. R. Nabi, and P. Tijssen.** 2001. A viral phospholipase A2 is required for parvovirus infectivity. Dev. Cell **1:**291–302.
87. **Zhong, L., W. Li, Y. Li, W. Zhao, J. Wu, B. Li, N. Maina, D. Bischof, K. Qing, K. A. Weigel-Kelley, I. Zolotukhin, K. H. Warrington, Jr., X. Li, W. B. Slayton, M. C. Yoder, and A. Srivastava.** 2006. Evaluation of primitive murine hematopoietic stem and progenitor cell transduction in vitro and in vivo by recombinant adeno-associated virus vector serotypes 1 through 5. Hum. Gene Ther. **17:**321–333.
88. **Zolotukhin, S., M. Potter, W. W. Hauswirth, J. Guy, and N. Muzyczka.** 1996. A "humanized" green fluorescent protein cDNA adapted for high-level expression in mammalian cells. J. Virol. **70:**4646–4654.

Neutralizing Antibodies Against Adeno-Associated Viral Capsids in Patients with *mut* Methylmalonic Acidemia

Elizabeth A. Harrington,[1,†] Jennifer L. Sloan,[1,†] Irini Manoli,[1] Randy J. Chandler,[1] Mark Schneider,[2] Peter J. McGuire,[3] Roberto Calcedo,[2] James M. Wilson,[2] and Charles P. Venditti[1,*]

[1]Organic Acid Research Section and [3]Metabolism, Infection and Immunity Unit, Medical Genomics and Metabolic Genetics Branch, National Human Genome Research Institute, National Institutes of Health, Bethesda, Maryland; [2]Gene Therapy Program, Department of Pathology and Laboratory Medicine, Perelman School of Medicine, University of Pennsylvania, Philadelphia, Pennsylvania.
[†]Equal contributions as co–first authors.

Isolated methylmalonic acidemia (MMA), a group of autosomal recessive inborn errors of metabolism, is most commonly caused by complete (mut^0) or partial (mut^-) deficiency of the enzyme methylmalonyl-CoA mutase (MUT). The severe metabolic instability and increased mortality experienced by many affected individuals, especially those with mut^0 MMA, has led centers to use elective liver transplantation as a treatment for these patients. We have previously demonstrated the efficacy of systemic adeno-associated viral (AAV) gene delivery as a treatment for MMA in a murine model and therefore sought to survey AAV antibody titers against serotypes 2, 8, and 9 in a group of well-characterized MMA patients, accrued via a dedicated natural history study (clinicaltrials.gov ID: NCT00078078). Plasma samples provided by 42 patients (8 mut^- and 34 mut^0; 10 had received organ transplantation), who ranged in age between 2 and 31 years, were analyzed to examine AAV2 ($n=35$), AAV8 ($n=41$), and AAV9 ($n=42$) antibody titers. In total, the seroprevalence of antibodies against AAV2, AAV8, or AAV9 was 20%, 22%, and 24%, respectively. We observed a lower-than-expected seropositivity rate (titers ≥1:20) in the pediatric MMA patients (2–18 years) for both AAV2 ($p<0.05$) and AAV8 ($p<0.01$) neutralizing antibodies (NAbs) compared with historical controls. Those with positive NAb titers were typically older than 18 years ($p<0.05$ all serotypes) or had received solid organ transplantation ($p<0.01$ AAV8, AAV9). The mut^0 patients who had not been transplanted ($n=24$)—that is, the subset with the greatest need for improved treatments—represented the seronegative majority, with 21 out of 24 patients lacking Abs against all AAV capsids tested. The unexpected lack of NAbs against AAV in this patient population has encouraging implications for systemic gene delivery as a treatment for *mut* MMA.

INTRODUCTION

Methylmalonic acidemia (MMA) is a severe autosomal recessive inborn error of metabolism characterized by lethal metabolic instability and multiorgan pathology. The disorder exhibits genetic heterogeneity and is most commonly caused by complete (mut^0) or partial (mut^-) deficiency of the enzyme methylmalonyl-CoA mutase (MUT), which isomerizes methylmalonyl-CoA into succinyl-CoA for entry into the Krebs cycle[1] (Supplementary Fig. S1; Supplementary Data are available online at www.liebertpub.com/hum). Affected patients are medically fragile and suffer from numerous complications such as recurrent metabolic crises, "metabolic stroke" or infarction of the basal ganglia, pancreatitis, chronic renal failure, impaired growth, osteoporosis, optic nerve atrophy, and intellectual impairment.[2]

Patients with MMA experience significant morbidity and mortality, and the prognosis for long-term survival is poor. This has been established since the first studies were published in the early 1980s, and three decades later the outcomes are still dismal. The mortality of *mut* MMA was 60–88% in the first reports in the 1980s and 1990s[3,4] and has improved somewhat to ~40% by the first

*Correspondence: Dr. Charles P. Venditti, Organic Acid Research Section, National Human Genome Research Institute, National Institutes of Health, Building 49, Room 4A18, Bethesda, MD 20892-4472. E-mail: venditti@mail.nih.gov

© 2016 by Mary Ann Liebert, Inc.
DOI: 10.1089/hum.2015.092

decade in the 2000s.[5,6] This has led centers to pursue elective liver and combined liver–kidney transplantation as a treatment for the metabolic instability that eventually causes death.[7–11] When successful, solid organ transplantation can eliminate the frequent episodes of metabolic acidosis, but has numerous practical limitations that include procedural availability, surgical mortality and morbidity, expense, a finite donor pool, and the need for life-long immune suppression. Alternative approaches to restore enzyme activity to the liver and other tissues in patients with MMA are clearly needed.

We have therefore studied viral gene therapy as treatment for MMA, using preclinical cellular[12,13] and animal models,[14–19] to gather efficacy and safety data. After proof-of-concept experiments using lentiviral[13] and adenoviral delivery,[12,19] we have developed and tested adeno-associated viral (AAV) vectors as gene therapy agents for MMA.[14,16–18] AAV has emerged as an efficacious gene therapy vector for the delivery of small transgenes to somatic tissues *in vivo* and further displays substantial tissue tropism(s) conferred by the capsid.[20] We have used AAVs of serotypes 2, 8, and 9 that express the mouse *Mut* or human *MUT* gene under the control of the enhanced chicken beta-actin promoter (CBA)[16–18,21] or the liver-specific thyroid-binding globulin promoter (TBG)[18] and administered them to $Mut^{-/-}$ mice in the neonatal period. The results of these studies are striking: whereas the untreated $Mut^{-/-}$ mice uniformly perish in early life, the treated $Mut^{-/-}$ mice have near-normal long-term survival and growth parameters, display an ameliorated metabolic phenotype, and demonstrate enzymatic activity longer than one year after a single treatment with an AAV8 or AAV9 vector. Surprisingly, the systemic delivery of an AAV9 vector also resulted in modest transduction of the kidney and long-term preservation of renal function in the treated mutants.[18] Although genotoxicity has been observed in the mouse studies with some vectors, we recently demonstrated that manipulating regulatory elements and AAV dosing could allow for the potential clinical application of systemic AAV gene delivery as a new treatment for *mut* MMA.[21]

Given the well-recognized barrier to *in vivo* gene transfer imposed by preexisting cellular and humoral immunity to AAV capsids,[22–24] we have surveyed a large cohort of well-characterized MMA patients for AAV neutralizing antibody (NAb) titers against serotypes 2, 8, and 9. We anticipate that these data will inform the selection of an optimal serotype to use in a future gene therapy clinical trial. Our results suggest that patients with the most severe forms of isolated MMA display a low prevalence of seropositivity against AAV2, AAV8, and AAV9 capsids during the first two decades of life, and would be suitable candidates for a future AAV gene therapy clinical trial. Whether the low seroprevalence reflects a decreased incidence of exposure to AAV or a generalized impairment in humoral immunity as a consequence of the underlying metabolic block is unknown.

MATERIALS AND METHODS

Patients and samples

The patients were evaluated at the NIH Clinical Center under the protocol "Clinical and Basic Investigations of Methylmalonic Acidemia and Related Disorders" (clinicaltrials.gov identifier: NCT00078078). The study was approved by the National Human Genome Research Institute (NHGRI) Institutional Review Board, and the research adhered to the tenets of the Declaration of Helsinki. Informed consent from patients and/or guardians was obtained. This protocol evaluates clinical and genetic features of patients with MMA and allows for research specimen collection. All patients were clinically characterized, and the subtype of MUT deficiency (mut^0, mut^-) was determined by a combination of propionate incorporation, complementation studies (Dr. David Rosenblatt, McGill University), and molecular genetic analysis of *MUT* (GeneDx, Gaithersburg, MD). Blood samples were drawn in Na heparin tubes and centrifuged at 1000–2000 $\times g$ at 4°C for 10 min. Plasma was removed and aliquoted in 1 ml volumes, and samples were stored at –80°C (mean 4.3 years stored; range 0.5–9.7) until use for this study. Plasma samples were thawed on wet ice. From the thawed samples, one aliquot was removed for AAV8 and 9 NAb analysis. In the subset of patients with remaining serum in the aliquot who were tested for AAV2 NAbs, another freeze–thaw cycle was needed to obtain a third sample for AAV2 NAb testing. NAbs were measured in 41 patients for both AAV8 and AAV9 NAbs, with an additional sample tested only for AAV9 NAbs. Thirty-five samples were also assayed for the presence of AAV2 NAbs, including most of those seropositive against AAV8 and AAV9, as well as an additional subset of clinically severe or older mut^0 patients, aged 2–28. We were unable to measure AAV2 titers in all patients because of limited amounts of plasma.

Cell culture, AAV vectors, and neutralizing antibody assay

The methods have been described previously.[25] In brief, the human hepatoma cell line Huh7 was maintained in Dulbecco's modified Eagle's medium (DMEM; Cellgro) supplemented with 10% fetal bovine serum (FBS; Hyclone). Cells were cultured at 37°C in an atmosphere of 5% CO_2 in air. AAV vectors in the single-strand configuration contained the gene encoding β-galactosidase (LacZ), which was driven by a cytomegalovirus (CMV) promoter (AAV.CMV.LacZ). All AAV.CMV.LacZ vectors used in this study were prepared by the Vector Core of the University of Pennsylvania (Philadelphia, PA) as previously described.[26] Recombinant AAV genomes equipped with AAV2 inverted terminal repeats (ITRs) were packaged by triple transfection of 293 cells with cis-plasmid, adenovirus helper plasmid, and a chimeric packaging construct in which the AAV2 *rep* gene was fused with *cap* genes of different AAV2, AAV8, or AAV9. All recombinant vectors were purified by CsCl sedimentation. Genome copy titers of AAV vectors were determined by TaqMan analysis (Applied Biosystems), using probes and primers targeting a bovine growth hormone polyadenylation signal. Plasma samples were heat inactivated at 56°C for 35 min.

Recombinant AAV.CMV.LacZ (10^9 genomic copies/well) was diluted in serum-free DMEM and incubated with 2-fold serial dilutions (initial dilution, 1:5) of heat-inactivated serum samples on DMEM for 1 hr at 37°C. Subsequently, the serum–vector mixture was added to 96-well plates seeded with 1×10^5 Huh7 cells/well that had been infected 2 hr earlier with wild-type HAdV5 (50 viral particles/cell). After 1 hr, each well was supplemented with an equal volume of 20% FBS DMEM and incubated for 18–22 hr at 37°C and 5% CO_2. Then, cells were washed twice in PBS and lysed, and the lysate was developed with the mammalian β-galactosidase assay kit for bioluminescence, in accordance with manufacturer's protocol (Applied Biosystems), and measured in a microplate luminometer (Clarity; BioTek). The NAb titer was reported as the highest serum dilution that inhibited AAV.CMV .LacZ transduction (β-gal expression) by >50%, compared with the mouse serum control (Sigma S3509). Samples were determined to be positive for antibodies against AAV capsids 2, 8, and 9 when a titer of 1:5 or higher dilution of serum inhibited AAV transduction over 50%.[25,27] Seropositivity for NAbs was defined as titers of ≥1:20 dilution.

Statistics

The sample storage age dependence of the seropositivity was assessed using an unpaired Student's *t*-test. Chi-square statistics were used to compare observed vs. expected seropositivity rates for NAbs against serotype 2 and 8 capsids in the pediatric MMA patients. Fisher's exact test was used to compare number of null alleles, enzymatic subtype, and transplant status.

RESULTS

The salient demographic features of the patient cohort, which lists the age, enzymatic subtype, genotype, and AAV antibodies assayed, are presented in Tables 1 and 2, and Supplementary Table S1. Samples from 42 patients with *mut* MMA between age 2 and 31 years were studied to examine AAV2 ($n=35$), AAV8 ($n=41$), and/or AAV9 ($n=42$) AAV antibody titers. The cohort included 34 mut^0 and 8 mut^- patients; 10 mut^0 patients had previously received a kidney, liver, or combined liver–kidney transplant.

Figure 1A shows the AAV antibody titer distributions among the patients. The seroprevalence in the MMA cohort screened against AAV2, AAV8, or AAV9 was 7/35 (20%), 9/41 (22%), and 10/42 (24%), respectively (Figure 1A and Table 2). Overall, 31/42 (74%) of the collective cohort were seronegative for NAbs against AAV2, AAV8, and AAV9. Furthermore, in those patients who had AAV antibodies, the majority (6/11) were only weakly seropositive (<1:20) for at least one serotype[28] (Fig. 1A). When only the nontransplanted group of mut^0 MMA patients ($n=24$) was considered, the resulting seroprevalence rates were lower and the humoral responses weaker (Fig. 1B).

To assess whether the length of storage might influence the lower-than-expected seroprevalance, we analyzed the age of each sample in the antibody-positive versus antibody-negative groups (Supplementary Fig. S2) for each capsid. There was no difference in the sample age between the groups for

Table 1. *MMA patient demographics*

	AAV2 (n = 35)	*AAV8 (n = 41)*	*AAV9 (n = 42)*
Mean age, years (min, max)	11.91 (2.4, 28.5)	12.27 (2.3, 31.6)	12.09 (2.3, 31.6)
Sex, *n* (%)			
Male	21 (60)	23 (56)	23 (56)
Female	14 (40)	18 (44)	19 (44)
Race, *n* (%)			
White	18 (51)	22 (54)	22 (52)
Other	17 (49)	19 (46)	20 (48)
Type, *n* (%)			
mut^0	28 (80)	33 (80)	34 (81)
mut^-	7 (20)	8 (20)	8 (19)

AAV, adeno-associated viral; MMA, methylmalonic acidemia.

Table 2. *Patient cohort, enzymology, molecular genetics, and anti-AAV antibody status*

Patient	Age (years)	Sex	Subtype	Date of sample	Allele 1	Allele 2	Transplant status	AAV2 Ab titer	AAV8 Ab titer	AAV9 Ab titer
1	2.3	M	*mut*$^-$	12/13/11	c.1846C>T p.R616C	c.1846C>T p.R616C		<1:5	<1:5	<1:5
2	2.4	F	*mut*$^-$	2/28/06	c.91C>T p.R31X	c.323G>A p.R108H		<1:5	<1:5	<1:5
3	2.5	M	*mut*$^-$	12/5/11	c.277C>T p.R93C	c.1106G>A p.R369H		<1:5	<1:5	<1:5
4	3.2	M	*mut*$^-$	12/10/09	c.1207C>T p.R403X	c.2150G>T p.G717V		<1:5	<1:5	<1:5
5	3.3	M	*mut*^{0}	5/12/10	c.1399C>T p.R467X	c.693C>G p.Y231X		ND	<1:5	<1:5
6	3.5	F	*mut*$^-$	8/19/05	c.281G>T p.G94V	c.2150G>T p.G717V		<1:5	<1:5	<1:5
7	4.2	F	*mut*^{0}	8/10/10	c.682C>T p.R228X	c.1106G>A p.R369H	LT	<1:5	1:40	1:40
8	4.4	M	*mut*^{0}	5/20/08	c.91C>T p.R31×	c.1181dupT p.L394FfsX30		<1:5	<1:5	<1:5
9	4.4, 2.3	F	*mut*^{0}	5/9/07, 4/15/05	c.607G>A p.G203R	c.682C>T p.R228X		<1:5	<1:5	<1:5
10	4.5	F	*mut*^{0}	5/9/07	c.1207C>T p.R403X	c.2008G>C p.G670R		ND	<1:5	<1:5
11	4.6	F	*mut*^{0}	12/8/10	c.2080C>T p.R694W	c.643G>T p.G215C		<1:5	ND	1:20
12	5.6	M	*mut*^{0}	6/14/11	c.322C>T p.R108C	c.682C>T p.R228X		<1:5	<1:5	<1:5
13	6.0	F	*mut*^{0}	6/4/07	c.323G>A p.R108H	c.1867G>C p.G623R		ND	<1:5	<1:5
14	6.1	M	*mut*^{0}	2/23/06	c.1741C>T p.R581×	c.753+2T>A p.?		<1:5	<1:5	<1:5
15	6.5	F	*mut*^{0}	5/3/11	c.878A>C p.Q293P	c.878A>C p.Q293P		<1:5	<1:5	<1:5
16	6.6	M	*mut*^{0}	8/4/09	c.2179C>T p.R727X	c.2179C>T p.R727X		<1:5	<1:5	<1:5
17	7.2	M	*mut*^{0}	6/17/09	c.281G>T p.G94V	c.1867G>C p.G623R		<1:5	<1:5	<1:5
18	7.8	M	*mut*^{0}	7/3/06	c.1106G>A p.R369H	c.1778_1782delAAAGT p.S594RfsX11	LT	<1:5	<1:5	<1:5
19	8.6	M	*mut*^{0}	4/20/10	c.1022dupA p.N341KfsX17	c.671_678dup p.V227NfsX16		<1:5	<1:5	<1:5
20	9.4	M	*mut*^{0}	8/26/08	c.1105C>T p.R369C	c.1207C>T p.R403X		<1:5	<1:5	<1:5
21	9.7, 8.2	M	*mut*^{0}	4/17/12, 9/22/10	c.1038_1040delTCT p.347delL	c.349G>T p.E117X	LKT at 8.7	<1:5	<1:5	<1:5
22	10.4	F	*mut*^{0}	11/13/14	c.2179C>T p.R727X	c.2179C>T p.R727X		<1:5	<1:5	<1:5
23	10.6	M	*mut*^{0}	4/17/07	c.670G>T p.E224X	c.682C>T p.R228X	LKT	<1:5	<1:5	<1:5
24	10.9	M	*mut*^{0}	9/8/05	c.322C>T p.R108C	c.322C>T p.R108C		1:5	<1:5	<1:5
25	11.3	M	*mut*^{0}	6/1/08	c.682C>T p.R228X	c.682C>T p.R228X	LKT	<1:5	1:10	1:10
26	11.8, 4.6	F	*mut*^{0}	7/27/10, 6/8/04	c.1942G>C p.G642R	c.1942G>C p.G642R		<1:5	<1:5	<1:5
27	11.9, 8.0	F	*mut*^{0}	6/18/12, 8/25/08	c.927G>A p.W309X	c.983T>C p.L328P		<1:5	<1:5	<1:5
28	13.9, 11.9	M	*mut*^{0}	6/11/09, 6/27/07	c.1106G>A p.R369H	c.1106G>A p.R369H	LT	<1:5	<1:5	<1:5
29	13.2, 8	F	*mut*^{0}	8/10/11, 7/11/06	c.2053dupCTC p.685insL	c.91C>T p.R31X		ND	<1:5	<1:5
30	17, 10.5, 12.6	F	*mut*^{0}	10/19/11, 7/17/07, 6/20/05	c.1658delT p.V553GfsX17	c.29dupT p.L11TfsX38		ND	<1:5	<1:5
31	18.5, 16.4	M	*mut*^{0}	4/3/07, 3/21/05	c.572C>A p.A191E	c.655A>T p.N219Y		<1:5	<1:5	<1:5
32	22.5	M	*mut*^{0}	8/4/05	c.322C>T p.R108C	c.1106G>A p.R369H	KT	ND	1:40	1:80
33	22.7, 24	M	*mut*^{0}	9/12/07, 6/28/06	c.572C>A p.A191E	c.682C>T p.R228X		1:5	1:5	1:5
34	24.7	M	*mut*^{0}	1/27/09	c.655A>T p.N219Y	c.1048C>T p.H350Y		<1:5	<1:5	<1:5
35	26.8, 19.9	F	*mut*^{0}	8/22/11, 8/25/04	c.1106G>A p.R369H	c.1106G>A p.R369H	LKT	1:160	1:40	1:40
36	25.4, 25.4	F	*mut*^{0}	5/9/06, 5/8/06	c.935G>T p.G312V	c.1909G>A p.G637R		<1:5	<1:5	<1:5
37	26.1, 24.2	M	*mut*^{0}	10/1/11, 10/7/09	c.1741C>T p.R581X	c.1741C>T p.R581X	KT	1:160	1:80	1:320
38	26.5, 25.9	M	*mut*$^-$	9/13/10, 12/3/09	c.1760A>C p.Y587S	c.2150G>T p.G717V		1:80	1:10	1:10
39	27.5, 20.6	F	*mut*^{0}	7/27/11, 8/17/04	c.2053dupCTC p.685insL	c.2053dupCTC p.685insL		<1:5	<1:5	<1:5
40	28.5	F	*mut*$^-$	8/22/11	c.2150G>T p.G717V	c.2150G>T p.G717V		1:80	1:5	1:20
41	28.7	F	*mut*$^-$	5/23/07	c.2150G>T p.G717V	unknown		ND	<1:5	<1:5
42	31.6, 27.5	F	*mut*^{0}	10,29/08, 9/17/04	c.826G>T p.E276×	c.1106G>A p.R369H	LKT	1:40	1:10	1:80

Shaded boxes indicate AAV Ab-positive samples. In seropositive patients (33, 35, 37, 38, and 42), the first age listed represents the date of assay for AAV8 and 9 Abs, whereas the later date indicates the age tested for AAV2 Abs.

Ab, antibody; KT, kidney transplant; LKT, combined liver–kidney transplant; LT, liver transplant; ND, not determined because of lack of material.

any serotype ($p=0.77$ AAV2 NAbs and $p=0.83$ AAV8/9 NAbs). This is consistent with the observations from other studies that have documented the stability of antibodies to varied pathogens, such as malaria and adenovirus,[28] as well as a wider range of anti-immunotherapeutic antibodies.[29]

We next compared the seropositivity rate, defined as a titer of ≥1:20, of NAbs AAV2 and 8 in a subset of our MMA cohort, aged 18 and under, to historical data from a reference pediatric population.[27] A lower-than-expected seropositivity rate was observed in the pediatric MMA patients for both AAV2 ($p=0.0066$) and AAV8 ($p=0.0408$) NAbs (Fig. 2A and Supplementary Table S2). Within the MMA cohort, a significant difference in the seroprevalance of all three NAbs was documented between children and adults (AAV2 $p=0.0004$; AAV8 $p=0.0399$; AAV9 $p=0.0054$) (Fig. 2B). In the group of those aged 18 years and less, only 2 patients were seropositive for any AAV serotype, and every patient

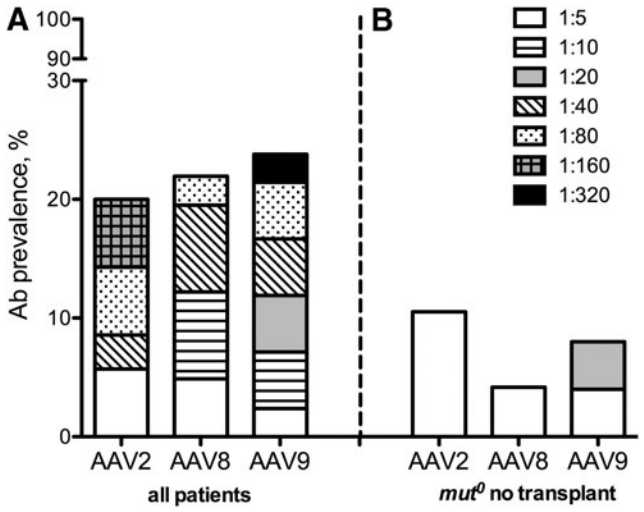


Figure 1. **(A)** AAV antibody seroprevalance within the entire MMA cohort ($n=42$) that includes both nontransplanted and transplanted (liver, kidney, and/or combined liver–kidney; $n=10$) patients. The overall seroprevalance, defined as ≥1:5, is depicted (20–24%) along with the titer distribution of antibodies against AAV2 ($n=35$), AAV8 ($n=41$), and AAV9 ($n=42$) capsids. The seroprevalence is subdivided into titer dilution levels from weak (1:5) NAb titers to strong (1:320). **(B)** AAV antibody seropositivity in the subgroup of patients with mut^0 MMA who were not transplanted ($n=24$), which shows low NAb prevalence (4–10%) for the cohort of severe, nontransplanted patients who would be ideal candidates for gene therapy. AAV, adeno-associated viral; Ab, antibody; MMA, methylmalonic acidemia; NAb, neutralizing antibody.

was seronegative for at least one of the capsids tested (Table 2).

To investigate the clinical characteristics shared by the seropositive group, the cohort was subdivided on the basis of molecular genetics, cellular enzymology, and transplant status (Fig. 3). First, we compared the prevalence of null alleles (nonsense, frameshift, splice mutations) between the AAV NAb-positive and NAb-negative groups and found no statistically significant difference between them (6/16 alleles [38%] vs. 29/68 alleles [42%]; $p=0.7837$). A similar incidence of seropositive titers was noted between enzymatic subtypes, mut^0 and mut^- (AAV2 $p=0.1952$; AAV8 $p=1.0$; AAV9 $p=1.0$) (Fig. 3A). However, when the cohort was stratified based on transplant status, there was a statistically significant difference between the transplanted and nontransplanted groups for NAbs against AAV8 ($p=0.0008$) and AAV9 ($p=0.0016$) but not AAV2 ($p=0.3007$) (Fig. 3B). The 24 nontransplanted mut^0 patients were almost entirely seronegative, with only 1 patient (patient 11) seropositive at a 1:20 dilution against AAV9 (Table 2).

We also examined co-seroprevalance of AAV antibodies (titer ≥1:5), because AAV antibody cross-reactivity can cause neutralization across a range of AAV serotypes.[30] As expected, co-prevalence of antibodies to AAV capsids within individuals was also noted in our cohort. Out of the 11 patients who had AAV antibodies, 9 were tested for all three serotypes and 6 had AAV antibodies against all three capsids (Table 3 and Supplementary Fig. S3). As shown, 100% of individuals who had antibodies against AAV8 capsid ($n=9$) also had antibodies against AAV9 ($n=9$). Three individuals who had antibodies against AAV8 or 9 capsids lacked antibodies against AAV2, and only one individual

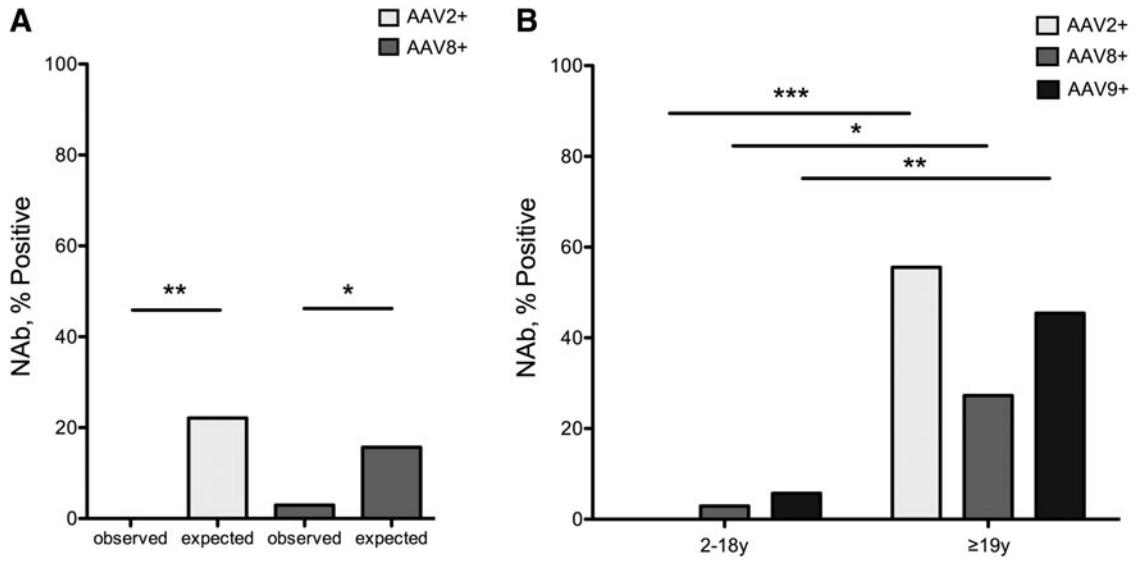


Figure 2. **(A)** Seropositivity, as defined as ≥1:20, in the pediatric MMA cohort compared with historical controls. There was a lower-than-expected AAV2 ($p=0.0066$) and AAV8 ($p=0.0408$) NAb seroprevalance in MMA individuals ≤18 years. **(B)** Neutralizing antibody prevalence to AAV serotypes 2, 8, and 9 by age. The seroprevalance of AAV2, AAV8, and AAV9 NAbs between children and adults was significantly different for all serotypes with a higher incidence of seropositivity in adults (7/11). *$p<0.05$, **$p<0.01$, ***$p<0.001$.

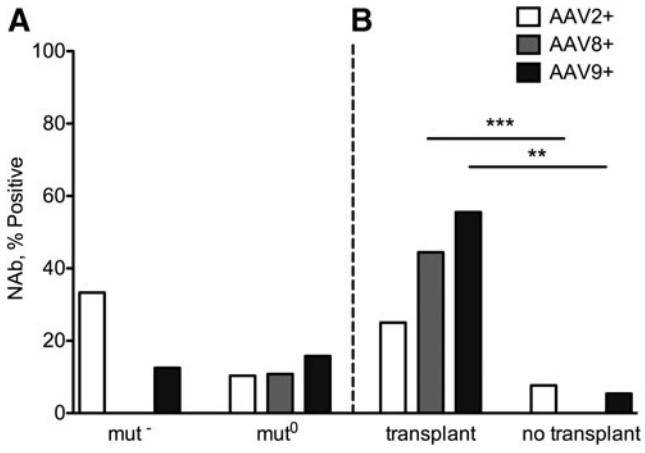


Figure 3. Subgrouping of the MMA cohort by enzymatic subtype **(A)** and transplant status **(B)**. **(A)** The seroprevalance was similar in *mut*$^{-}$ and *mut*^{0} groups (AAV2 $p=0.1952$; AAV8 $p=1.0$; AAV9 $p=1.0$). **(B)** The seroprevalence was significantly different in the transplanted and nontransplanted groups for AAV8 ($p=0.0008$) and AAV9 ($p=0.0016$) but not AAV2 ($p=0.3007$) with 6/10 of the transplanted patients seropositive against AAV2, 8, and/or 9. $^{**}p<0.01$, $^{***}p<0.001$.

showed low titer (1:5) for AAV2 and was negative for AAV8 and AAV9 antibodies (Table 2).

DISCUSSION

Because we envision systemic AAV gene therapy as a potential treatment for MMA patients, we surveyed the presence of AAV antibodies in a large and diverse patient cohort, assembled over a 10-year period at our center through a dedicated natural history study. The current investigation was focused on assessing the humoral immune response to various AAV capsids by retrospectively surveying antibody titers against serotypes that we have previously studied in a preclinical MMA model.[14,16–18] All participants were characterized by molecular genetic analysis and/or enzymology and presented a spectrum of mutations in *MUT*: there were 42 distinct alleles that included 22 missense, 11 nonsense, 6 frameshift, 1 splice, and 2 in-frame insertion/deletion variants. Although cross-reacting material (CRM) status has not been assessed in cell lines from these patients, it is likely to be present in a significant proportion given that 67% of the patients harbored at least one missense or in-frame insertion/deletion mutation ($n=28$).

Table 3. *Coprevalence of antibodies against AAV types 2, 8, and 9 capsids*

	AAV2^{+}	*AAV8*$^{+}$	*AAV9*$^{+}$
AAV2^{+}		88% AAV8+ ($n=8/9$)	90% AAV9+ ($n=9/10$)
AAV8^{+}	66% AAV2+ ($n=6/9$)		100% AAV9+ ($n=9/9$)
AAV9^{+}	70% AAV2+ ($n=7/10$)	100% AAV8+ ($n=9/9$)	

Five different alleles (c.572C>A p.A191E, c.655A>T p.N219Y, c.1106G>A p.R369H, c.2080C>T p.R694W, and c.2150G>T p.G717V) were present in 16 different individuals and all are predicted to produce residual enzyme based on a recent study.[31] The large number of missense mutations is promising for future gene therapy efforts since these individuals would have a lower chance of developing an immune response to MUT encoded by an AAV vector. Although the participants were largely from the United States, and may therefore harbor an environmental and exposure profile distinct from patients in other countries, this cohort reflects a level of molecular and enzymatic heterogeneity similar to what has been previously described.[32–35]

Preexisting immunity against the AAV capsids has emerged as a significant barrier to effective systemic *in vivo* transduction in animal models and human clinical trials.[36–38] More specifically, the presence of low-titer NAbs has been proven to interfere with hepatic transduction in macaques,[37,39] in which significant differences in factor IX (FIX) expression level after AAV8-mediated systemic hepatic gene delivery were noted between control animals with NAb titers <1:5 and animals with preinjection titers of 1:5, 1:10, and >1:10.[39] In an extension of these observations to humans, Nathwani et al. described a blunted response to an AAV8 vector administered to a hemophilia patient who had low-level NAb titers.[40] In this patient, FIX activity was not restored after systemic AAV8 gene delivery, presumably because hepatic transduction was impeded by AAV8 NAbs.

Given the importance of preexisting NAbs as a factor in determining the *in vivo* efficacy of systemic gene therapy, several investigators have surveyed human populations to define the epidemiology of AAV capsid exposure and antibody responses. The seroprevalence data have been largely derived from adult blood donors in whom seropositivity has been defined as NAb titers ≥1:20 dilution. Higher seroprevalence rates were noted against AAV2, 1, and 6 (59%, 50.5%, and 37%) capsids, whereas serotypes AAV5, 8, and 9 were lower (3.2%, 19%, and 33.5%).[31] A study conducted in newborns, children, and adolescents showed that NAb prevalence to AAV2 and AAV8 was moderate at birth, decreased from 7 to 11 months to almost undetectable levels, and then progressively increased through childhood and adolescence.[27] Only a small number of studies have examined NAb prevalence in patient cohorts. Longitudinal studies in the hemophilia population have recognized that after an initial decline from maternal NAbs in the first year of life,[41] the seropositivity rate of NAbs against AAV2 increases over time;

~16% of the tested group presented as seropositive when entering the study, which increased to ~44% by age ≥5 years.[42] Additionally, it has been recognized that reactivity of NAbs to other capsids, such as 5 and 8, paralleled the trend for AAV2 seroconversion. In fact, ~50% of the AAV2 seropositive patients also had NAbs against AAV5 and 8 in a related study.[43] Similarly, surveys of the cystic fibrosis (CF) population have indicated that about 30% of adults were seropositive against AAV2, whereas children with CF had markedly lower rates (~4–15%),[41] and in the case of MPS VI, 42% of children and young adults were seropositive against AAV8.[44]

In the patients studied here, we initially observed an overall seroprevalance of 22–24% against AAV8 or 9 capsids, with 100% co-seropositivity between those who were tested for both AAV8 and AAV9 antibodies. A single patient was seropositive for only AAV9 antibodies, and specimen volume did not allow us to test for AAV8. Although constrained by sample availability, we extended our observations by examining AAV NAbs against serotype 2 in a smaller subset of patients who had an overall seroprevalance of 20%. In total, there were 11 individuals who had detectable AAV antibodies. In these 11 patients, 9 were tested for both AAV2 and AAV8, 10 were tested for AAV2 and AAV9, and 9 were tested for both AAV8 and AAV9. Six of 9 tested for all three were triseropositive (Table 3). Although our numbers are small, the co-seropositivity rates we observe approximate estimates seen in other studies.[30,41,42] It should be noted that most of our patients displayed variable titers when positive, even against AAV2 (Fig. 1).

However, when the patients were stratified based on clinical features (age, molecular genetics, enzymatic subtype [mut^0 vs. mut^-], and transplant status), a striking trend was recognized. The large majority of the seropositive patients were older than 18 years (Fig. 2B) or had received organ transplants (Fig. 3B). Whether this pattern reflects the epidemiology of AAV infection or an improvement in the functional immune status of patients after transplant remains unknown. The latter seems more likely because after transplantation, MMA patients have improved metabolism, lower circulating metabolites, and increased protein tolerance. In contrast, the nontransplanted mut^0 group, which represents the patients most likely to benefit from gene therapy, had only 1 patient out of the total group of 24 tested with a positive AAV NAb titer (≥1:20), against only one capsid (Table 2, patient 11).

When compared with pediatric historical controls,[27] seropositivity rates in our cohort were lower than expected (Fig. 2A and Supplementary Table S2). Whether this is a reflection of an underlying immune disturbance is unknown, but unlikely to be caused by a decreased incidence of exposure to AAV, given the frequent hospitalizations experienced by this group. MMA patients are prone to bone marrow pan-suppression, including neutropenia and thrombocytopenia during periods of stress and infection.[2] In earlier studies, over 50% of mut^0 MMA patients had hematologic abnormalities (leukopenia, thrombocytopenia, and anemia) despite normal serum cobalamin values.[3] Furthermore, there are several reports of MMA patients who experienced atypical infections, including gram-negative or fungal pathogens, and immunological studies have documented complex T- and B-cell defects.[45–47] The immune system dysfunction in MMA warrants further investigation but it is possible that the underlying disorder may impact the ability to mount a robust humoral immune response after exposure to AAV capsids and potentially other antigens.

This report is the first to survey AAV antibody titers of any serotype in patients with MMA. The patterns observed show that patients who have not undergone liver or combined liver–kidney transplantation are very unlikely to harbor NAbs against the AAV capsids that have already been proven to be effective in liver-directed gene therapy in patients with hemophilia[24,40] as well as mice with MMA.[14,15,16–18,21] Furthermore, the very low frequency and titers of NAbs in the younger, severely affected MMA patients, of whom 21 out of 24 tested were seronegative against all 3 capsids, strongly support the application of systemic AAV gene delivery in this population, especially because the complications related to preexisting humoral immunity, as well as the interference with transduction it engenders, should be mitigated.

ACKNOWLEDGMENTS

We thank all patients and their families for their participation, Isa Bernardini and Roxanne Fischer for processing patient samples, and Jean Gagne for assistance with data collection. This work was supported by the Intramural Research Program of the National Human Genome Research Institute.

AUTHOR DISCLOSURE

J.M. Wilson is an advisor to REGENXBIO, Dimension Therapeutics, and Solid Gene Therapy, and is a founder of, holds equity in, and has a sponsored research agreement with REGENXBIO and Dimension Therapeutics; in addition, he is a consultant to several biopharmaceutical companies and is an inventor on patents licensed to various biopharmaceutical companies. No competing financial interests exist for the other authors.

REFERENCES

1. Fenton WA, Gravel RA, Rosenblatt DS. Disorders of propionate and methylmalonate metabolism in the metabolic and molecular bases for inherited disease. In: The Metabolic and Molecular Bases of Inherited Disease (8th edn.). CR Scriver, AL Beaudet, WS Sly, D Valle, eds. McGraw-Hill, New York, NY. 2001; pp. 2165–2192.
2. Manoli I, Sloan JL, Venditti CP. Isolated Methylmalonic Acidemia. In: GeneReviews® [Internet]. Pagon RA, Adam MP, Ardinger HH, et al., eds. University of Washington, Seattle, WA. 2005. Available from: http://www.ncbi.nlm.nih.gov/books/NBK1231/
3. Matsui SM, Mahoney MJ, Rosenberg LE. The natural history of the inherited methylmalonic acidemias. N Engl J Med 1983;308:857–861.
4. van der Meer SB, Poggi F, Spada M, et al. Clinical outcome of long-term management of patients with vitamin B12-unresponsive methylmalonic acidemia. J Pediatr 1994;125:903–908.
5. Horster F, Baumgartner MR, Viardot C, et al. Long-term outcome in methylmalonic acidurias is influenced by the underlying defect (mut0, mut-, cblA, cblB). Pediatr Res 2007;62:225–230.
6. Cosson MA, Benoist JF, Touati G, et al. Long-term outcome in methylmalonic aciduria: A series of 30 French patients. Mol Genet Metab 2009;97:172–178.
7. van't Hoff WG, Dixon M, Taylor J, et al. Combined liver-kidney transplantation in methylmalonic acidemia. J Pediatr 1998;132:1043–1044.
8. Kayler LK, Merion RM, Lee S, et al. Long-term survival after liver transplantation in children with metabolic disorders. Pediatr Transplant 2002;6:295–300.
9. Nagarajan S, Enns GM, Millan MT, et al. Management of methylmalonic acidaemia by combined liver-kidney transplantation. J Inherit Metab Disease 2005;28:517–524.
10. Morioka D, Kasahara M, Takada Y, et al. Living donor liver transplantation for pediatric patients with inheritable metabolic disorders. Am J Transplant 2005;5:2754–2763.
11. Morioka D, Kasahara M, Horikawa R, et al. Efficacy of living donor liver transplantation for patients with methylmalonic acidemia. Am J Transplant 2007;7:2782–2787.
12. Chandler RJ, Tsai MS, Dorko K, et al. Adenoviral-mediated correction of methylmalonyl-CoA mutase deficiency in murine fibroblasts and human hepatocytes. BMC Med Genet 2007;8:24.
13. Chandler RJ, Sloan J, Fu H, et al. Metabolic phenotype of methylmalonic acidemia in mice and humans: The role of skeletal muscle. BMC Med Genet 2007;8:64.
14. Carrillo-Carrasco N, Chandler RJ, Chandrasekaran S, et al. Liver-directed recombinant adeno-associated viral gene delivery rescues a lethal mouse model of methylmalonic acidemia and provides long-term phenotypic correction. Hum Gene Ther 2010;21:1147–1154.
15. Chandler RJ, Chandrasekaran S, Carrillo-Carrasco N, et al. Adeno-associated virus serotype 8 gene transfer rescues a neonatal lethal murine model of propionic acidemia. Hum Gene Ther 2011;22:477–481.
16. Chandler RJ, Venditti CP. Long-term rescue of a lethal murine model of methylmalonic acidemia using adeno-associated viral gene therapy. Mol Ther 2010;18:11–16.
17. Chandler RJ, Venditti CP. Pre-clinical efficacy and dosing of an AAV8 vector expressing human methylmalonyl-CoA mutase in a murine model of methylmalonic acidemia (MMA). Mol Genet Metab 2012;107:617–619.
18. Senac JS, Chandler RJ, Sysol JR, et al. Gene therapy in a murine model of methylmalonic acidemia using rAAV9-mediated gene delivery. Gene Ther 2012;19:385–391.
19. Chandler RJ, Venditti CP. Adenovirus-mediated gene delivery rescues a neonatal lethal murine model of mut(0) methylmalonic acidemia. Hum Gene Ther 2008;19:53–60.
20. Zincarelli C, Soltys S, Rengo G, et al. Analysis of AAV serotypes 1–9 mediated gene expression and tropism in mice after systemic injection. Mol Ther 2008;16:1073–1080.
21. Chandler RJ, LaFave MC, Varshney GK, et al. Vector design influences hepatic genotoxicity after adeno-associated virus gene therapy. J Clin Invest 2015;125:870–880.
22. Janelidze S, Nordstrom U, Kugler S, et al. Pre-existing immunity to adeno-associated virus (AAV)2 limits transgene expression following intracerebral AAV2-based gene delivery in a 6-hydroxydopamine model of Parkinson's disease. J Gene Med 2014;16:300–308.
23. Calcedo R, Wilson JM. Humoral immune response to AAV. Front Immunol 2013;4:341.
24. Manno CS, Pierce GF, Arruda VR, et al. Successful transduction of liver in hemophilia by AAV-Factor IX and limitations imposed by the host immune response. Nat Med 2006;12:342–347.
25. Calcedo R, Vandenberghe LH, Gao G, et al. Worldwide epidemiology of neutralizing antibodies to adeno-associated viruses. J Infect Diseases 2009;199:381–390.
26. Gao GP, Alvira MR, Wang L, et al. Novel adeno-associated viruses from rhesus monkeys as vectors for human gene therapy. Proc Natl Acad Sci U S A 2002;99:11854–11859.
27. Calcedo R, Morizono H, Wang L, et al. Adeno-associated virus antibody profiles in newborns, children, and adolescents. Clin Vaccine Immunol 2011;18:1586–1588.
28. Hendriks J, Stals C, Versteilen A, et al. Stability studies of binding and functional anti-vaccine antibodies. Bioanalysis 2014;6:1385–1393.
29. Michaut L, Laurent N, Kentsch K, et al. Stability of anti-immunotherapeutic antibodies in frozen human serum samples. Bioanalysis 2014;6:1395–1407.
30. Boutin S, Monteilhet V, Veron P, et al. Prevalence of serum IgG and neutralizing factors against adeno-associated virus (AAV) types 1, 2, 5, 6, 8, and 9 in the healthy population: Implications for gene therapy using AAV vectors. Hum Gene Ther 2010;21:704–712.
31. Forny P, Froese DS, Suormala T, et al. Functional characterization and categorization of missense mutations that cause methylmalonyl-CoA mutase (MUT) deficiency. Hum Mutat 2014;35:1449–1458.
32. Worgan LC, Niles K, Tirone JC, et al. Spectrum of mutations in mut methylmalonic acidemia and identification of a common Hispanic mutation and haplotype. Hum Mutat 2006;27:31–43.
33. Lempp TJ, Suormala T, Siegenthaler R, et al. Mutation and biochemical analysis of 19 probands with mut0 and 13 with mut- methylmalonic aciduria: Identification of seven novel mutations. Mol Genet Metab 2007;90:284–290.
34. Merinero B, Perez B, Perez-Cerda C, et al. Methylmalonic acidaemia: Examination of genotype and biochemical data in 32 patients belonging to mut, cblA or cblB complementation group. J Inherit Metab Disease 2008;31:55–66.
35. Acquaviva C, Benoist JF, Pereira S, et al. Molecular basis of methylmalonyl-CoA mutase apoenzyme defect in 40 European patients affected by mut(o) and mut- forms of methylmalonic acidemia: Identification of 29 novel mutations in the MUT gene. Hum Mutat 2005;25:167–176.
36. Nathwani AC, Rosales C, McIntosh J, et al. Long-term safety and efficacy following systemic administration of a self-complementary AAV vector encoding human FIX pseudotyped with serotype 5 and 8 capsid proteins. Mol Ther 2011;19:876–885.
37. Wang L, Calcedo R, Wang H, et al. The pleiotropic effects of natural AAV infections on liver-directed gene transfer in macaques. Mol Ther 2010;18:126–134.
38. Wang L, Wang H, Bell P, et al. Systematic evaluation of AAV vectors for liver directed gene transfer in murine models. Mol Ther 2010;18:118–125.
39. Wang L, Calcedo R, Bell P, et al. Impact of pre-existing immunity on gene transfer to nonhuman primate liver with adeno-associated virus 8 vectors. Hum Gene Ther 2011;22:1389–1401.
40. Nathwani AC, Tuddenham EG, Rangarajan S, et al. Adenovirus-associated virus vector-mediated gene transfer in hemophilia B. N Engl J Med 2011;365:2357–2365.
41. Halbert CL, Miller AD, McNamara S, et al. Prevalence of neutralizing antibodies against adeno-associated virus (AAV) types 2, 5, and 6 in cystic fibrosis and normal populations: Implications for

gene therapy using AAV vectors. Hum Gene Ther 2006;17:440–447.

42. Li C, Narkbunnam N, Samulski RJ, et al. Neutralizing antibodies against adeno-associated virus examined prospectively in pediatric patients with hemophilia. Gene Ther 2012;19:288–294.

43. Mimuro J, Mizukami H, Shima M, et al. The prevalence of neutralizing antibodies against adeno-associated virus capsids is reduced in young Japanese individuals. J Med Virol 2014;86: 1990–1997.

44. Ferla R, Claudiani P, Savarese M, et al. Prevalence of anti-adeno-associated virus serotype 8 neutralizing antibodies and arylsulfatase B cross-reactive immunologic material in mucopolysaccharidosis VI patient candidates for a gene therapy trial. Hum Gene Ther 2015;26:145–152.

45. Church JA, Koch R, Shaw KN, et al. Immune functions in methylmalonic aciduria. J Inherit Metab Disease 1984;7:12–14.

46. Oberholzer VG, Levin B, Burgess EA, et al. Methylmalonic aciduria. An inborn error of metabolism leading to chronic metabolic acidosis. Arch Dis Child 1967;42:492–504.

47. Wong SN, Low LC, Lau YL, et al. Immunodeficiency in methylmalonic acidaemia. J Paediatr Child Health 1992;28:180–183.

Received for publication June 12, 2015;
accepted after revision January 12, 2016.

Published online: January 20, 2016.

© 1999 Nature America Inc. • http://medicine.nature.com

Long-term correction of canine hemophilia B by gene transfer of blood coagulation factor IX mediated by adeno-associated viral vector

ROLAND W. HERZOG[1], EDMUND Y. YANG[2], LINDA B. COUTO[3], J. NATHAN HAGSTROM[1], DAN ELWELL[4], PAUL A. FIELDS[1], MELISSA BURTON[3], DWIGHT A. BELLINGER[4], MARJORIE S. READ[4], KENNETH M. BRINKHOUS[4], GREGORY M. PODSAKOFF[3], TIMOTHY C. NICHOLS[4], GARY J. KURTZMAN[3] & KATHERINE A. HIGH[1,5]

[1]*Departments of Pediatrics and Pathology, University of Pennsylvania Medical Center and The Children's Hospital of Philadelphia, Philadelphia, Pennsylvania 19104, USA*
[2]*Department of Surgery, The Children's Hospital of Philadelphia, Philadelphia, Pennsylvania 19104, USA*
[3]*Avigen Inc., 1201 Harbor Bay Parkway #1000, Alameda, California 94502, USA*
[4]*Department of Pathology and Laboratory Medicine, University of North Carolina at Chapel Hill, Chapel Hill, North Carolina 27599, USA*
[5]*Institute for Human Gene Therapy, University of Pennsylvania, Philadelphia, Pennsylvania 19104, USA*
Correspondence should be addressed to K.A.H.; email: high@email.chop.edu

Hemophilia B is a severe X-linked bleeding diathesis caused by the absence of functional blood coagulation factor IX, and is an excellent candidate for treatment of a genetic disease by gene therapy. Using an adeno-associated viral vector, we demonstrate sustained expression (>17 months) of factor IX in a large-animal model at levels that would have a therapeutic effect in humans (up to 70 ng/ml, adequate to achieve phenotypic correction, in an animal injected with 8.5 $\times$ 10^{12} vector particles/kg). The five hemophilia B dogs treated showed stable, vector dose-dependent partial correction of the whole blood clotting time and, at higher doses, of the activated partial thromboplastin time. In contrast to other viral gene delivery systems, this minimally invasive procedure, consisting of a series of percutaneous intramuscular injections at a single timepoint, was not associated with local or systemic toxicity. Efficient gene transfer to muscle was shown by immunofluorescence staining and DNA analysis of biopsied tissue. Immune responses against factor IX were either absent or transient. These data provide strong support for the feasibility of the approach for therapy of human subjects.

© 1999 Nature America Inc. • http://medicine.nature.com

Hemophilia B is the X-linked bleeding disorder caused by a deficiency of functional coagulation factor IX (F.IX). Current treatment for hemophilia B consists of infusion of clotting factor protein in response to bleeding. Extensive experience with protein concentrates over the last 25 years has established that maintenance of F.IX levels above 1% of normal (>50 ng/ml) in patients with severe hemophilia greatly reduces the frequency of spontaneous bleeding into joints and soft tissues and reduces the risk of fatal intracranial bleeding[1–3]. However, the short half-life of the protein, requiring frequent intravenous infusion, and the expense and other complications associated with this approach have fueled interest in a gene therapy approach for the treatment of hemophilia[4,5]. The introduction of a functional F.IX gene by gene transfer would provide a continuous supply of F.IX. Despite a wealth of data on gene transfer and expression of F.IX in mice, only one study demonstrated sustained expression of F.IX in a large-animal model of the disease, dogs with hemophilia B (ref. 6). However, the plasma levels of F.IX achieved in that study (about 2–4 ng/ml) were far too low to be therapeutic, and also required a number of invasive procedures (surgery, partial hepatectomy and portal vein infusion of the vector) that made the approach unappealing for human trials.

Direct *in vivo* delivery of a human F.IX gene to skeletal muscle with an adeno-associated virus (AAV) vector results in sustained therapeutic levels of F.IX expression in the plasma of mice[7]. AAV vectors are single-stranded DNA viruses with a genome of approximately 4.6 kb. The vector is devoid of viral coding sequences, and efficiently transduces post-mitotic tissues such as muscle (including murine, canine, and primate muscle[8,9,10]). Stable expression of the transgene in transduced fibers of immunocompetent animals[8–10] allowed us to exploit muscle for production of F.IX. F.IX is normally made in liver, but *in vitro* experiments have shown that muscle cells can synthesize biologically active F.IX (ref. 11).

Many gene transfer strategies that have seemed promising in mice have failed to show efficacy in large-animal models. Differences in the transduction characteristics of the target cells, the more robust immune response to the vector and to the transgene product in large animals compared with those in inbred strains of mice, problems related to 'scale-up' of vector production, and efficiency of biosynthesis and secretion from the target cells have all contributed to the dearth of successful gene transfer approaches in large animals (and humans)(refs. 12–17). Here we show that a single administration of a series of intramuscular injections of AAV vector results in stable expres-

© 1999 Nature America Inc. • http://medicine.nature.com

Table Hemophilia B dogs injected intramuscularly with increasing doses of AAV-CMV-cF.IX vector and resulting levels of canine F.IX expression

Dog	Age at time of injection	Weight at time of per site	Sex	Vector dose in particles/kg	Number of injection sites	Injected volume per site	Average WBCT[a] (min)	Average aPTT[a] (sec)	Average cF.IX plasma levels[a] (ng/ml)
1	2 months	5.7 kg	male	1.3×10^{11}	18	250 µl	20 ± 5	61.5 ± 8	2.6 ± 0.7
2	4 months	9.1 kg	male	1.1×10^{12}	8	375 µl	20 ± 2.5	49 ± 6	12 ± 2
3	8 months	20 kg	female	3.4×10^{12}	60	300 µl	16 ± 1.5	40 ± 3	17 ± 2
4	2 months	13.6 kg	male	3×10^{12}	28	500 µl	15 ± 1.5	40 ± 1	21 ± 2
5	2 months	5.9 kg	female	8.5×10^{12}	24	500 µl	17 ± 2	38 ± 1	69 ± 6

[a]Whole blood clotting times (WBCT) and activated thromboplastin times (aPTT) were >60 min and >50 sec, respectively, before injection for all four dogs. Average values after vector administration are given for dog 1 (weeks 16–50 after injection), dog 2 (weeks 6–9 and 13–46), dog 3 (weeks 8–44), dog 4 (weeks 6–11) and dog 5 (weeks 11–23). Weeks 10–12 were omitted in the calculation for dog 2 because values were influenced by plasma infusion in response to two bleeding episodes. Average values for WBCT and aPTT for dog 4 were calculated for weeks 22–27 after injection.

sion (over one year) of functional factor IX in the circulation of a large-animal model of hemophilia B.

AAV-mediated gene transfer of canine F.IX to dog muscle

A recombinant AAV vector was constructed for expression of canine F.IX cDNA from the cytomegalovirus IE promoter by inserting the expression cassette between the AAV inverted terminal repeat sequences. Production of AAV-CMV-cF.IX was achieved by co-transfection of HEK-293 cells with the resulting plasmid pK9 and two helper plasmids in an adenovirus-free system[17]. In a preliminary experiment, 2.8×10^{11} particles of the purified vector were injected in a single intramuscular site of a phenotypically normal dog. The vector suspension contained carbon particles to allow us to locate the injection site in a muscle biopsy 6 weeks after injection. Staining of serial cryosections with antibody against canine F.IX showed expression of F.IX by muscle fibers in areas where carbon particles were localized, and staining with hematoxylin and eosin demonstrated the absence of any inflammatory infiltrate (Fig. 1). No cellular infiltrates were observed in three sets of serial sections from three independently frozen pieces of tissue from the injection site.

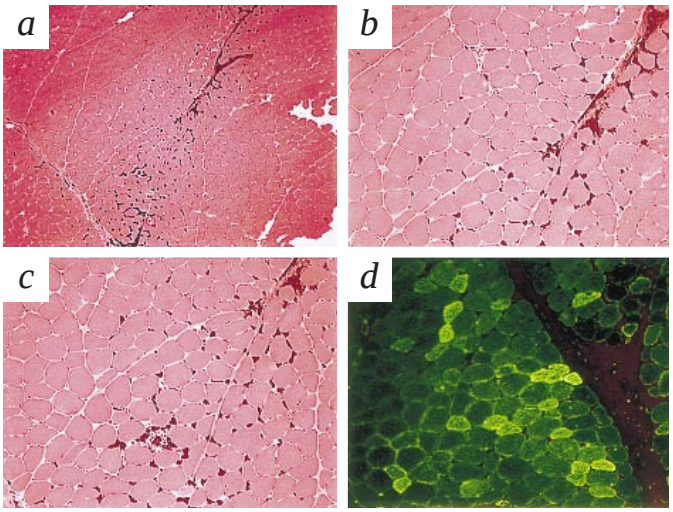


Fig. 1 ***a–c***, Hematoxylin and eosin staining of cross-sections of tibialis anterior muscle of a normal dog injected with 2.8×10^{11} particles of AAV-CMV-cF.IX. The biopsy was obtained 6 weeks after injection. Carbon particles injected along with the vector were used to trace the injection site. There was no inflammation in any section. ***d***, Immunofluorescence staining of canine F.IX produced by muscle fibers. Original magnifications, ×40 (*a*) and ×100 (*b–d*).

The colony of hemophilia B dogs at the University of North Carolina-Chapel Hill at the Francis Owen Blood Research Laboratory are characterized by a point mutation in the sequence encoding the catalytic domain of F.IX, which causes the absence of detectable F.IX levels in plasma[18]. Consequently, these dogs suffer from severe hemophilia B that closely mimics the human disease[19]. In a dose escalation study, four hemophilic dogs received a single administration of an AAV vector expressing canine F.IX delivered intramuscularly at multiple sites (Table). Injections were given to dogs sedated by general anesthesia, but prophylactic infusions of canine plasma were not given. Intramuscular injections were done percutaneously (using ultrasound guidance for the first dog). All dogs recovered well from the procedure and (with one exception) showed no signs of subsequent bleeding at the injection sites. The dogs showed no signs of local (as evidenced by muscle biopsy of an injection site) or systemic (as evidenced by serial measurements of muscle enzymes, complete blood count, liver function tests, electrolytes, and renal function tests, data not shown) toxicity. The dogs had no neutralizing antibodies against AAV before the injections, but developed such antibodies during the first week after injection (data not shown) as described[9,10]. Viral shedding (monitored by PCR) was observed in samples taken 24 hours after injection, but not at any subsequent timepoints (data not shown).

Stable expression of biologically active F.IX

Injection of the first hemophilic dog with a relatively low dose of vector (1.3×10^{11}/kg) resulted in partial clotting of blood samples beginning 2 weeks after injection, and intermittent shortening of the whole blood clotting time (WBCT, >60 minutes for an untreated hemophilic dog and 6–8 minutes for a normal dog) during the first 3 months after injection. (The WBCT is sensitive to low levels of factor IX and begins to shorten at levels of 1–2 ng/ml of plasma.) Subsequently, partial correction of the WBCT stabilized and has been maintained for a period of over 17 months after the administration of vector (Fig. 2*a*). Injection of a second dog with a 700% higher dose caused a persistent shortening of the WBCT, which was first observed 2 weeks after injection and has been maintained for over 13 months, indicating persistent systemic delivery of biologically active F.IX (Fig. 3*b*). The antigen levels of these dogs as measured by ELISA were 2–3 ng canine F.IX per ml plasma for the first dog and about 12 ng/ml for the second dog (Fig. 3*a*). The WBCT of a third dog injected with a dose of 3.4×10^{12} particles/kg was partially corrected during the first week after the injection and decreased

© 1999 Nature America Inc. • http://medicine.nature.com

© 1999 Nature America Inc. • http://medicine.nature.com

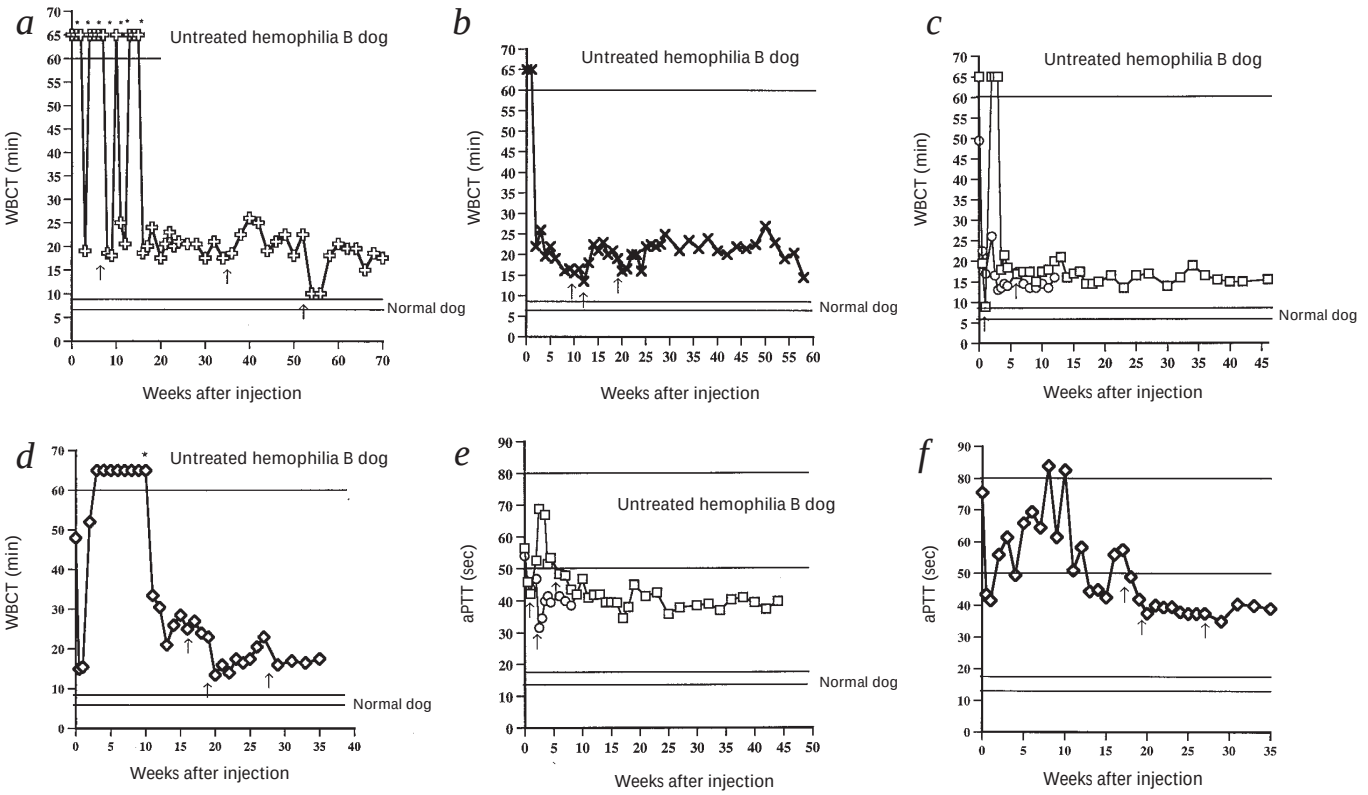


Fig. 2 *a–d*, WBCT of hemophilia B dogs as a function of time after intramuscular injection with AAV-CMV-cF.IX. Horizontal lines indicate the ranges of the WBCT of an untreated hemophilia B dog (>60 min) and a normal dog (6-8 min). Clotting times >60 min are indicated as 65 min. *, Partial clotting (>90%) in less than 60 min. Arrows indicate treatment by plasma infusion after a 'bleed'. ***a***, Dog 1, injected with 1.3×10^{11} particles/kg. Extensive plasma infusion was done during weeks 54–56 after amputation of the dog's tail (necessitated by an injury). ***b***, Dog 2, injected with 1.1×10^{12} particles/kg. ***c***, Dog 3 (□-□) injected with 3.35×10^{12} particles/kg; and dog 4 (○-○), injected with 3×10^{12} particles/kg. Dog 3 had one 'bleed' from an injection site, which was treated by plasma infusion on day 4. (Plasma treatment for dog 4 is not shown in this graph.) ***d***, Dog 5, injected with 8.5×10^{12} particles/kg. ***e*** and ***f***, Activated partial thromboplastin time (aPTT in sec) of plasma samples from dog 3 (*e*, □-□), dog 4 (*e*, ○-○) and dog 5 (*f*) as a function of time after intramuscular injection of AAV-CMV-cF.IX. Clotting times of F.IX-deficient plasma (>50 sec) and normal dog plasma (13.5–18 sec) are indicated by horizontal lines. Dog 4 had trauma-related bleeding from a torn ear lobe that was treated on days 16–18.

© 1999 Nature America Inc. • http://medicine.nature.com

subsequently to 13.5–18 minutes after a short period when no clotting or only partial clotting was observed (days 14–21, Fig. 2*c*). This dog was the first to show sustained partial correction of the activated partial thromboplastin time (aPTT) of plasma samples with an antigen level of about16 ng/ml (Fig. 2*e*). Injection of a fourth dog with an almost identical dose of vector (3×10^{12}/kg) resulted in persistent shortening of the WBCT and aPTT starting at day 4 after injection (Fig. 2*c* and 2*e*), and antigen levels of about 20 ng/ml (Fig. 3*b*). A period of 6–8 weeks was required to reach maximum levels of expression and correction of clotting times in these four dogs. Subsequently, expression levels remained stable. Injection of a fifth dog with a dose of 8.5×10^{12} vector particles/kg also resulted in initial partial correction of the WBCT, followed by a period of no correction that lasted up to week 11 after injection. Partial correction of the WBCT was observed in the following weeks with a steady decrease in clotting times reaching a WBCT as low as 14 minutes, and an aPTT as low as 35 seconds (Fig. 2*d* and *f*). After initial detection of cF.IX antigen in plasma samples (days 4 and 7), factor IX levels fell to undetectable levels by week 2, reappeared during week 8, and reached therapeutic levels (above 50 ng/ml) on day 77 after injection (Fig. 3*c*). Levels of approximately 70 ng/ml have been maintained subsequently (weeks 12–35 after injection). This represents 1.4% of normal human F.IX plasma levels (5 μg/ml). We have summarized the dose-dependent expression of F.IX and improvement of clotting times (Table).

Transient immune responses against canine factor IX

Because this represents a new strategy for treatment of hemophilia, we sought to determine whether antibodies against the transgene product developed. Dogs 1, 2 and 4 were monitored for at least two months after injection by ELISA, western blot, and Bethesda assay (an assay for inhibition of clotting activity) for production of anti-canine F.IX; no evidence for antibodies was obtained. Dog 3, however, showed a weak and transient immune response against cF.IX that affected antigen levels briefly. Although no evidence for an inhibitor was obtained by Bethesda assay, antibody was detectable by western blot on day 14 after injection. The titer of the anti-cF.IX dropped considerably by day 24, and the antibody was undetectable by day 56 even after over-exposure of the blot (Fig. 4*a* and data not shown). After intravenous infusion with normal canine plasma on day 33 after injection (for treatment of bleeding), the dog showed an appropriate clinical response to plasma treatment and did not manifest any increase in antibody level as determined by western blot (Fig. 4*a*). In contrast to this dog, dog 5 developed an inhibitory antibody as measured by Bethesda assay. The Bethesda titer of the inhibitor (which first emerged

© 1999 Nature America Inc. • http://medicine.nature.com

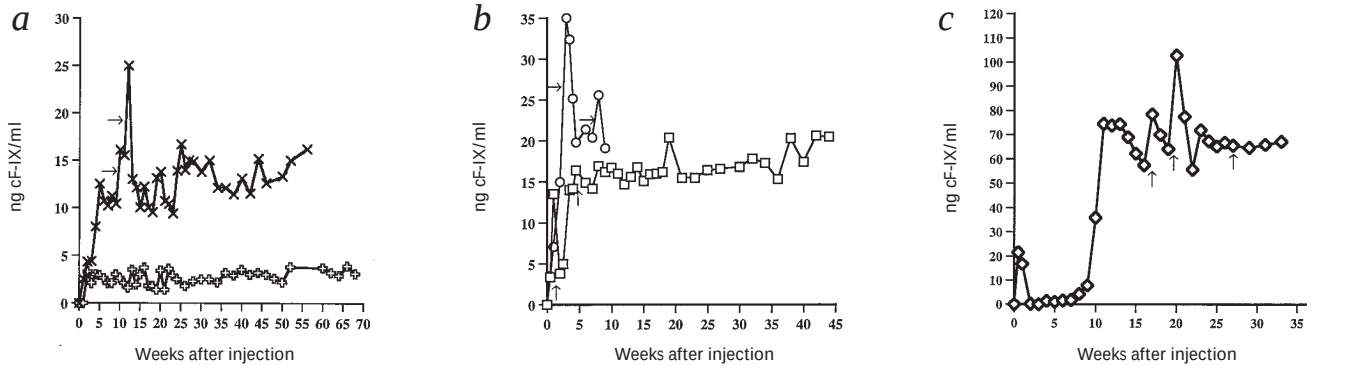


Fig. 3 Canine F.IX levels in plasma samples of hemophilia B dogs (in ng/ml) as a function of time after intramuscular injection of AAV-CMV-cF.IX vector. F.IX concentrations were determined by ELISA. ***a***, Dog 1, injected with 1.3×10^{11} particles/kg (+–+) and dog 2 (×–×) injected with 1.1×10^{12} particles/kg. (Values for dog 1 were omitted for weeks 54–58.) ***b***, Dog 3 (□-□), injected with 3.35×10^{12} particles/kg and dog 4 (○-○), injected with 3×10^{12} particles/kg. ***c***, Dog 5, injected with 8.5×10^{12} particles/kg.

on day 14) gradually rose up through day 35 and fell steadily afterwards to undetectable levels by week 15 after injection (Fig. 4*c*). Western blot analysis correlated well with the data obtained on Bethesda assay, with a peak at day 35 and a subsequent decrease to a faint signal still detectable on day 188 after injection (Fig. 4*b* and data not shown). Transient production of an inhibitory antibody also correlated with the transiently prolonged clotting times and reduced factor IX levels (Figs. 2*d* and *f* and 3*c*). The dog showed an appropriate clinical response to infusion of normal canine plasma on days 110–112 and days 133–134 in response to bleeding. Plasma samples drawn 30 minutes and 24 hours after infusion on day 112 showed no enhanced clearance of cF.IX when compared with data generated in previously untreated hemophilic dogs (data not shown). Dog 5 had a localized skin infection (demodex canis) at the time of injection. This was subsequently treated successfully with amitraz (Upjohn veterinarian preparation).

DNA analyses of introduced vector sequences

Muscle-derived expression of F.IX was confirmed by immunofluorescence staining of a biopsy taken from injected muscle of hemophilia B dog 1 6 weeks after injection with 4.4×10^{10} vector particles per site indicating persistence of vector (Fig. 5). Genomic DNA was isolated from muscle tissue from this injection site as well as from muscle of a normal dog 6 weeks after injection with 2.8×10^{11} particles of AAV-CMV-cF.IX. A Southern blot using a probe specific for the CMV promoter and chimeric intron in the vector was done to analyze the status of the introduced vector DNA (Fig. 6). Uncut DNA showed a high-molecular-weight signal (Fig. 6, lanes 5 and 9; signal partially masked by high molecular weight DNA in lane 5). Restriction digest with an enzyme cutting at a single site within the rAAV genome (*Eco*RV or *Bam*HI) produced an approximately 4.5-kb fragment, which is expected for head-to-tail concatemers of the vector (Fig. 6, lanes 7 and 8). The heavier band (7.5 kb) detected faintly in the *Bam*HI digest and the faint lighter band (3 kb) in the *Eco*RV digest can be explained by a head-to-head arrangement[8]. An additional faint band of 2.5- to 3.0-kb in uncut as well as cut DNA most likely represents single-stranded input vector DNA. Digestion with *Nco*I (which cuts twice within the AAV-CMV-cF.IX genome) releases a 2.5-kb fragment. Comparison of signal strengths obtained from genomic DNA of transduced dog muscle (Fig. 6, lanes 6 and 10) and plasmid controls (Fig. 6, lanes 1 and 2) indicates copy numbers of approximately 1 copy per diploid genome for dog 1, and 6 copies for the normal dog. A potential source of error in determination of copy number is proximity of the muscle biopsy to the center of the site of injection. Thus, estimates of copy number must be regarded as approximate.

Discussion

As noted in the Orkin-Motulsky report (*http://www.nih.gov/od/orda/panelrep.htm*), "confidence in current approaches to somatic gene therapy would rise if a genuine genetic deficiency in an animal were unequivocally corrected." We would add to this statement that correction of a genetic deficiency in a large-animal model is especially convincing, as it has implications for

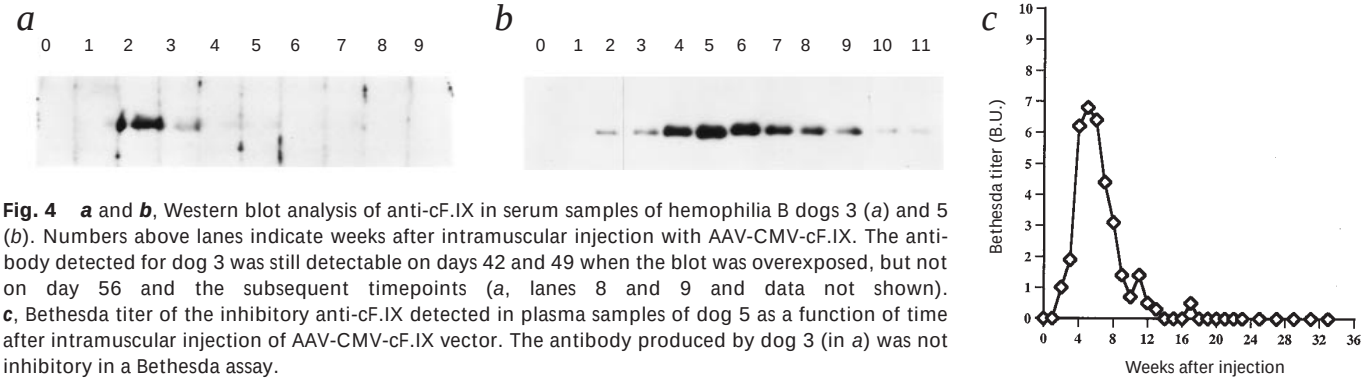


Fig. 4 ***a*** and ***b***, Western blot analysis of anti-cF.IX in serum samples of hemophilia B dogs 3 (*a*) and 5 (*b*). Numbers above lanes indicate weeks after intramuscular injection with AAV-CMV-cF.IX. The antibody detected for dog 3 was still detectable on days 42 and 49 when the blot was overexposed, but not on day 56 and the subsequent timepoints (*a*, lanes 8 and 9 and data not shown). ***c***, Bethesda titer of the inhibitory anti-cF.IX detected in plasma samples of dog 5 as a function of time after intramuscular injection of AAV-CMV-cF.IX vector. The antibody produced by dog 3 (in *a*) was not inhibitory in a Bethesda assay.

© 1999 Nature America Inc. • http://medicine.nature.com

© 1999 Nature America Inc. • http://medicine.nature.com

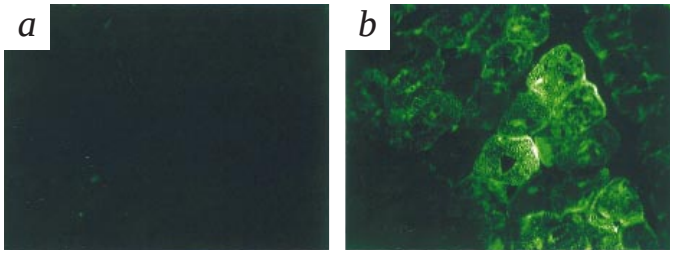


Fig. 5 Immunofluorescence staining of canine F.IX produced by muscle fibers 46 days after intramuscular injection of 4.4×10^{10} particles of AAV-CMV-cF.IX (per site) into the tibialis anterior muscle of hemophilia B dog 1. ***a***, Negative control (muscle from uninjected dog). ***b***, Injected site of dog 1. Original magnification, ×200.

treatment of human disease that cannot be attributed to work in rodents.

Progress towards the goal of sustained production of functional factor IX in a large-animal model at levels that would be therapeutic in humans has been difficult. Work 6 years ago demonstrated sustained expression of low levels of F.IX in hemophilic dogs using a retroviral vector[6]. Until now, there have been no additional reports of sustained expression of F.IX in hemophilic dogs. The advantage of the gene therapy strategy that we report is that the plasma levels of F.IX are 20-fold to 30-fold higher in the highest dose dog (and thus in the therapeutic range) than those in the previous report, and that the procedure required, a series of intramuscular injections, is minimally invasive. Therefore, these experiments provide strong pre-clinical data in support of a clinical trial of gene therapy for hemophilia B.

Efficacy and feasibility for treatment of hemophilia

The shortening of the whole blood clotting time and of the aPTT (a plasma-based clotting assay) provide strong evidence for the functional activity of F.IX expressed *in vivo* in muscle. The close agreement between antigen levels (determined by ELISA) and activity levels (determined by WBCT or aPTT) indicates that most of the muscle-synthesized circulating F.IX is biologically active. Although the WBCT has mostly been designed as a screening test, it allows reasonable assessment of the biological activity of F.IX in blood samples. When dilute normal dog plasma is added to blood samples drawn from untreated F.IX-deficient dogs, a final F.IX concentration of 2 ng/ml (plasma volume) shortens the WBCT to 22 ± 2 minutes, whereas 20 ng/ml shortens the WBCT to 16 ± 1 minutes (T.C.N. *et al.*, University of North Carolina, unpublished data). AAV-injected dog 1 had a WBCT of 17.5–26 minutes with 2–3 ng/ml expression of F.IX; and dog 3, 13.5–18 minutes, with 16 ng/ml. These data are consistent with full biological activity of the circulating F.IX. Comparison of aPTT clotting times of dog 3 with standards of normal dog plasma diluted in F.IX-deficient plasma also indicates full biological activity (data not shown).

The treated dogs continue to experience occasional bleeding episodes (Figs. 2 and 3). Because of the importance of insuring long-term survival of these dogs (to monitor for late-occurring complications of treatment with an AAV vector), the dogs have been closely monitored and promptly treated with plasma if any sign of bleeding developed, whereas the usual approach to managing suspected bleeding is observation. Many of the 'bleeds' in the hemophilic dogs are trauma-related rather than spontaneous; the levels of clotting factor produced in these dogs would not be adequate to prevent bleeding after trauma. The specific activity of canine factor IX is only about one-half that of human F.IX; thus, 70 ng/ml of canine factor IX is less active than the same concentration of human F.IX (ref. 6).

This study also demonstrates that gene transfer and expression are dose-dependent. The results show that a dose of approximately 1×10^{13} particles/kg is required to reach therapeutic levels of expression. This represents on a weight basis an approximate linear 'scale-up' from the mouse model. Linear 'scale-up' from a mouse to a dog (that is, over a range of 250-fold to 800-fold) is a characteristic not shared by most other gene therapy strategies[23]. Successful 'scale-up' over a range of >2 logs provides strong evidence that 'scale-up' will be successful in the threefold to fourfold increase required to go from dogs to humans. The gradual rise of factor IX levels over about 2 months to a stable plateau has been described as a function of slow conversion of the single-stranded input DNA of the vector to a transcriptionally active double-stranded form[10].

Immune responses

Adenoviral vectors are also capable of transducing post-mitotic muscle fibers[24]. However, inflammatory responses to cells ex-

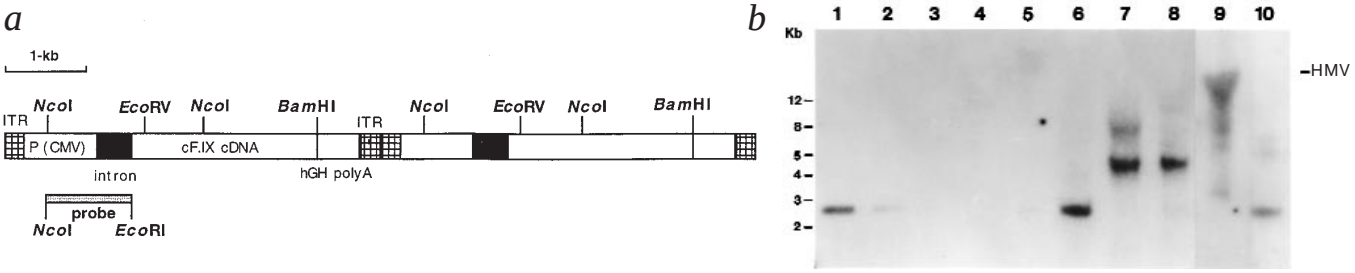


Fig. 6 Southern blot hybridization of genomic DNA isolated from biopsied muscle tissue 6 weeks after injection of AAV-CMV-cF.IX into the tibialis anterior of a normal or hemophilic dog. ***a***, Head-to-tail concatemeric arrangement of two AAV-CMV-cF.IX vector genomes. Indicated are the 0.8-kb *Nco*I–*Eco*RI fragment used as a probe and restriction sites for *Bam*HI, *Eco*RV and *Nco*I. ***b***, Southern blot hybridization results using the *Nco*I–*Eco*RI probe (*a*). Lanes 1 and 2, Plasmid DNA (pK9) cut with *Nco*I (50 pg in lane 1 and 10 pg in lane 2); lanes 3 and 4, Uncut and *Eco*RV-digested genomic DNA from uninjected dog muscle; lanes 5–8, Uncut, *Nco*I-digested, *Bam*HI-digested or *Eco*RV-digested genomic DNA from injection site of tibialis anterior muscle of a normal dog (6 weeks after injection; 2.8×10^{11} vector particles injected); lanes 9–10, Uncut and *Nco*I-digested genomic DNA from muscle biopsy taken from injected tibialis anterior muscle on day 46 after injection (4.4×10^{10} vector particles per site). The 'trail' below the high-molecular-weight (HMW) signal in lane 9 was due to partial shearing of the DNA. For lanes containing genomic DNA, 15 µg of DNA were used. Numbers along right margin indicate fragments of a molecular size marker.

© 1999 Nature America Inc. • http://medicine.nature.com

© 1999 Nature America Inc. • http://medicine.nature.com

pressing adenoviral gene products and to adenoviral coat proteins limit long-term expression[9,10,25]. The lack of inflammation seen after AAV-mediated transduction and the persistence of transgene expression are in agreement with other studies that demonstrate the low immunogenicity of the AAV vector and indicate a lack of CTL responses against transduced fibers[8,10,26]. These data also provide support for the production of AAV vector in an adenovirus-free system[27,28].

Humoral immune responses to the transgene product (F.IX) are an important concern for any proposed gene therapy strategy in hemophilia, as the presence of inhibitors (antibodies that inhibit clotting activity) represents a complication of treatment. The risk of inhibitor formation is influenced by the underlying mutation and the individual's immune response[29]. The most extensive data on the natural history of inhibitor formation in previously untreated patients with hemophilia has been generated in the setting of clinical trials of recombinant F.VIII (refs. 30,31). These data show that, in addition to the patients who develop clinically significant high titer inhibitors, there is a subset of patients (7% of subjects in one study) who develop transient low titer inhibitors. Little is known about the natural history of the antibody response in a gene therapy setting, where the clotting factor is produced continuously rather than infused intermittently.

The transient antibody observed in dog 3 influenced clotting times and F.IX levels only briefly (2 weeks). Because no inhibitory activity was detected, it is likely that the only effect of the antibody was to enhance clearance of F.IX. Such antibodies, detectable by western blot or ELISA but not by Bethesda assay, are not well documented in the hemophilia patient population, as clinical screens for antibodies are usually done by Bethesda assay only[32]. The immune response of dog 4 resulted in a transient and low-titer (<10 Bethesda unit) inhibitor. If testing for antibody response had been confined to measurements now in use in clinical settings (Bethesda assay, recovery study, clinical response to infused plasma), all dogs in our study would now be deemed free of clinically significant antibody response. Using more sensitive testing, however, we have demonstrated that antibody to canine F.IX can be persistently detected in dog 5, although with a declining titer. Further studies, now in progress, will be required to define the natural history of the immune response in AAV-mediated, muscle-directed gene therapy for hemophilia, but our findings seem consistent with other studies in which detailed analysis of the immune response to the clotting factor protein in individuals with hemophilia has shown the presence of antibodies even when no inhibitory activity is detected on Bethesda assay[33]. None of the dogs in this study developed immune responses that limited long-term systemic expression of F.IX.

Analysis of genomic DNA

The presence of high molecular weight head-to-tail concatemers after transduction of mouse muscle is well characterized[7,8,10]. Our data show that the same form of AAV vector DNA is present in transduced canine muscle. Strong evidence has been provided for integration of these concatemers into the chromosomal DNA of mouse hepatocytes transduced *in vivo* with AAV (ref. 34). Integration has also been discussed for transduction of muscle fibers but has not been formally proven[10]. At least a large proportion of the concatemeric AAV vector genome might remain episomal[35]. More detailed analysis of genomic DNA from injected muscle will be necessary to determine the maximum copy number of introduced vector that can be achieved per injection site.

Rescue of infectious recombinant AAV particles from introduced vector DNA has not been addressed in this study. Viral rescue is a very unlikely event even when AAV vector, wild-type AAV, and helper adenovirus are deliberately introduced to the respiratory tract where infection by these viruses normally takes place[36].

The success with this safe and efficient procedure for gene transfer and expression of F.IX in a large-animal model shows that the strategy is likely to be successful in the treatment of humans with hemophilia B. It also indicates potential applications for treatment of other genetic disorders that require systemic delivery of a therapeutic protein.

Methods

AAV vector construction and production. A 2.4-kb canine F.IX cDNA clone including the coding region and 1 kb of the 3' untranslated region[37] was inserted as an *Eco*RI fragment into plasmid p4.1c containing the CMV enhancer/promoter, a chimeric intron composed of a CMV splice donor and a human β-globin splice acceptor site, and the human growth hormone polyadenylation signal. The resulting expression cassette was cloned as a 4.15-kb *Not*I fragment between two AAV inverted terminal repeat sequences contained in plasmid DNA. The resulting plasmid pK9 was used for AAV vector production in an adenovirus-free system[17]. HEK-293 cells were co-transfected with pK9, a second plasmid supplying the AAV *rep* and *cap* gene functions in *trans*, and a third plasmid supplying adenovirus helper functions E2A, E4orf6 and VA. The cells were lysed 72 h after transfection by repeated freeze-thaw cycles, and the released virus was purified by repeated CsCl density gradient centrifugation[17,20]. The titer of the purified AAV-CMV-cF.IX vector was determined by quantitative dot-blot hybridization[38]. Vector stocks were stored at –80 ºC in sterile 1× PBS containing 5% sorbitol. HEK-293 cells were transduced with aliquots of the vector stock (at multiplicities of infection of 10^4–10^5 vector particles/cell), and supernatants were analyzed by ELISA for expression of cF.IX to ensure comparable activity from different preparations.

Animal experiments. A hemostatically normal male dog was injected at the Veterinary School of the University of Pennsylvania with 2.8×10^{11} particles of purified AAV-CMV-cF.IX. The injection was done percutaneously into the tibialis anterior muscle. The dog was killed 6 weeks after injection, and injected muscle was biopsied.

Four outbred hemophilia B dogs kept at the colony of the Department of Pathology and Laboratory Medicine (University of North Carolina-Chapel Hill) were injected at 8–60 intramuscular sites with total doses of 8×10^{11}–6.5×10^{13} particles of AAV-CMV-cF.IX. All injections were done percutaneously with a 25-gauge needle while the dogs were sedated by general anesthesia. No 'coverage' with normal canine plasma was applied before, during or after the procedure. Injections into the first dog were monitored by ultrasound guidance using the Sequoia 512 model from Acuson Corp (Mountain View, California). Dogs 1 and 2 were injected into the tibialis anterior and vastus lateralis muscles of both hind limbs. Additional muscle groups were chosen for 3–5 dogs (which were injected at more sites). For some injections sites, carbon particles (Carbon Black Dispersate No. 8; Eberhard Faber, Bedminster, New Jersey) were included in the vector suspension to allow tracing of the injection site in a muscle biopsy. The dogs were persistently monitored for bleeding, which was generally treated by intravenous infusion of 'pooled' normal canine plasma (10 ml/kg). Analysis of toxicology of the vector administration included complete blood cell counts and biochemical analysis of serum samples including liver and renal function tests, electrolytes, and creatine phosphate kinase levels (a muscle-specific enzyme). Swabs (lacrimal, nasal, rectal, saliva, urogenital) and body fluid samples (serum) were collected for DNA extraction to monitor viral shedding by PCR analysis (days 0, 1, 4, 7, 14, 21 and 28 after injection). Swabs were placed in sterile tissue culture media, and DNA was extracted with the Qiamp Blood Kit from Qiagen (Valencia, California) after concentrating the samples with Centricon tubes (Amicon, Beverly, Massachusetts) to a final volume of 200 μl.

© 1999 Nature America Inc. • http://medicine.nature.com

© 1999 Nature America Inc. • http://medicine.nature.com

Histochemical analysis of muscle biopsies. Muscle biopsies (100–200 mg of tissue) of injected and uninjected tissue were excised with a sterile scalpel from a dog that had been killed or from a live dog sedated by general anesthesia with 'coverage' with normal canine plasma that began after the procedure. Biopsies of injected tissue were taken from areas where carbon particles were localized. Excised tissue was 'snap-frozen' as described[7]. Cryosections (6 μm in thickness) were stained with hematoxylin and eosin or used for immunofluorescence staining and microscopy as described[7]. The primary antibody was a rabbit anti-canine F.IX (Affinity Biologicals, Hamilton, Ontario, Canada) diluted 1:100, and the secondary antibody a FITC-conjugated swine anti-rabbit immunoglobulin diluted 1:30 (Dako, Carpinteria, California).

Clotting assays and F.IX levels. Whole-blood clotting time (WBCT) was measured with the 'two-tube' method using silicone-coated tubes that were tilted every 30 seconds[6,39]. Activated partial thromboplastin time (aPTT) of plasma samples was measured with a fibrometer (Fibrosystem; BBL, Cockeysville, Maryland). Plasma samples and aPTT reagent (Organon Teknika, Durham, North Carolina) were mixed (50 μl each) and incubated at 37 ºC for 3 min before addition of 50 μl of 25 mM $CaCl_2$ and measurement of the clotting time with the fibrometer. Canine F.IX levels in plasma samples were determined by ELISA using a mouse monoclonal anti-human F.IX (Boehringer) as the capture antibody (this antibody cross-reacts with canine F.IX). Plates were coated with 1.5 μg antibody/ml coating buffer. The detecting immunocomplex was a rabbit anti-canine F.IX (Affinity Biologicals, Hamilton, Ontario, Canada) at a 1:1,400 dilution, using a stock of 10 mg/ml (total IgG) and a horseradish peroxidase-conjugated swine anti-rabbit immunoglobulin (with no cross-reactivity with canine or murine immunoglobulins; 1:2,000 dilution; Dako, Carpinteria, California). Buffer conditions and incubation times were as described[40]. Purified plasma-derived canine F.IX (Enzyme Research Laboratories, South Bend, Indiana) was used as a standard. The lower limit of detection with this assay was approximately 1.5 ng/ml.

Antibody assays. Antibodies against canine F.IX were detected by western blot or ELISA as described for human F.IX (ref. 7). For western blots, membrane strips with 1 μg of purified canine F.IX (Enzyme Research Laboratories, South Bend, Indiana) were incubated with canine test serum diluted 1:200. Rabbit anti-canine IgG (with a horseradish peroxidase label) diluted 1:1,000 (Sigma) was used as the antibody for chemiluminescent detection. For detection of anti-cF.IX by ELISA, 96-well plates were coated with canine F.IX (1 μg/ml), and canine test sera was diluted 1:16. The detecting antibody was identical to the one used for western blot detection (diluted 1:2,000). Pre-treatment samples were applied for negative control. Inhibitory antibodies against cF.IX were measured by Bethesda assay. Test plasma samples were mixed with an equal volume of 'pooled' normal dog plasma and incubated at 37 ºC for 2 h, followed by measurement of the aPTT as described above. Controls were pre-treatment samples and serial dilutions of pooled normal dog plasma in F.IX-deficient dog plasma. The Bethesda titer was determined as described[41]. One Bethesda unit equals 50% residual F.IX activity. Neutralizing antibodies against AAV vector were measured by incubating 10-fold serial dilutions of canine serum samples in DMEM media containing 2% fetal bovine serum and AAV-CMV-hF.IX vector[7,20] at room temperature for 1.5 h before transduction of HEK-293(84–31) cells[20] (seeded at a confluency of 80–90% in 96-well plates) with a multiplicity of infection of 1,000 vector particles/cell. Human F.IX levels in supernatants were measured 36 h after transduction using an ELISA specific to human F.IX (ref. 40). The highest dilution with less than 6.25 ng/ml of F.IX production was defined as the neutralizing antibody titer.

DNA Analysis. Isolation of genomic DNA from muscle tissue, restriction enzyme digests, as well as Southern blot transfer and hybridization were done as outlined[42]. Random-primed labeled probes were generated using α-^{32}P-dCTP and the Prime It II kit from Stratagene (La Jolla, California). Intensities of bands on autoradiographs were quantitated by densitometric scanning of the exposed X-ray film. Vector DNA isolated from swabs and body fluids as described above (to monitor viral shedding, 10 μl of sample per reaction) was PCR-amplified with the primer pair 5'–ATAGCAGCTACAATCCAGCTACCATTCTGC–3' and 5'–TGGTATCCCGTAGTACAGGAACAAACCACC–3'. The forward primer is specific to the chimeric intron in the AAV vector, and the reverse primer, to the canine F.IX cDNA. The amplification product is 698 bp. After initial denaturation at 95 ºC for 2 min, 40 cycles were run using the following conditions: 95 ºC for 30 s, 60 ººC for 30 s, and 72 ºC for 1 min. The AmpliTaq kit from Perkin-Elmer (Norwalk, Connecticut) was used for these reactions. No amplification product was obtained from canine DNA from untransduced tissue. The lower limit of detection with this assay was approximately 30 vector genomes per reaction.

Acknowledgments

The authors thank Acuson for supplying the ultrasound equipment, M. Haskins for making the normal dog experiment possible, and J.H. Liu, S.J. Tai, and M.L. McCleland, as well as the Cell Morphology Core of the Institute for Human Gene Therapy at the University of Pennsylvania, for technical assistance. We also acknowledge the work of the staff at the vector production facility at Avigen, and the staff of the Francis Owen Blood Research Laboratory at the University of North Carolina-Chapel Hill. This work was supported by National Institutes of Health Grants R01 HL53668 and P50 HL54500 to K.A.H., and Avigen, a company in which K.A.H. holds equity. P.A.F. is supported by the Katherine Dormandy Trust for Hemophilia, and J.H.H. was supported by NIH grant F32 HL09397

RECEIVED 17 SEPTEMBER; ACCEPTED 30 NOVEMBER 1998

1. Lofqvist, T., Nilsson, I.M., Berntorp, E. & Pettersson, H. Haemophilia prophylaxis in young patients—a long term follow up. *J. Int. Med.* **241**, 395–400 (1997).
2. Eyster, M.E. *et al*. Central nervous system bleeding in hemophiliacs. *Blood* **51**, 1179–1188 (1978).
3. Bray, G.L. & Lubahn, N.L. Hemophilia presenting with–intracranial hemorrhage. An approach to the infant with intracranial bleeding and coagulopathy. *Am. J. Dis. Children* **141**, 1215–1217 (1987).
4. Lusher, J.M. Prophylaxis in children with hemophilia: Is it the optimal treatment? *Thromb. Haemost*. **78**, 726–729 (1997).
5. Ragni, M.V., Hord, J.D. & Blatt, J. Central venous catheter infection in hemophiliacs undergoing prophylaxis or immune tolerance with clotting factor concentrate. *Haemophilia* **3**, 90–95 (1997).
6. Kay, M.A. *et al*. *In vivo* gene therapy of hemophilia B: Sustained partial correction in factor IX-deficient dogs. *Science* **262**, 117–119 (1993).
7. Herzog, R.W. *et al*. Stable gene transfer and expression of human blood coagulation factor IX after intramuscular injection of recombinant adeno-associated virus. *Proc. Nat. Acad. Sci. USA* **94**, 5804–5809 (1997).
8. Xiao, X., Li, J. & Samulski, R.J. Efficient long-term gene transfer into muscle tissue of immunocompetent mice by adeno-associated virus vector. *J. Virol.* **70**, 8098–8108 (1996).
9. Monahan P.E. *et al*. Direct intramuscular injection with recombinant–AAV vectors results in sustained expression in a dog model of hemophilia. *Gene Ther.* **5**, 40–49 (1998).
10. Fisher, K.J. *et al*. Recombinant adeno-associated virus for muscle directed gene therapy. *Nature Med.* **3**:306–312 (1997).
11. Yao, S.-N., Smith, K.J. & Kurachi, K. Primary myoblast-mediated gene transfer: Persistent expression of human factor IX in mice. *Gene Ther*. **1**, 99–107 (1994).
12. Verma, I.M. & Somia, N. Gene therapy - promises, problems and prospects. *Nature* **389**, 239–242 (1997).
13 Kay, M.A. *et al*. *In vivo* hepatic gene therapy: Complete albeit transient correction of factor IX deficiency in hemophilia B dogs. *Proc. Natl. Acad. Sci. USA* **91**, 2353–2357 (1994).
14. Fang, B. *et al*. Lack of persistence of E1$^-$ recombinant adenoviral vectors containing a temperature-sensitive E2A mutation in immunocompetent mice and hemophilia B dogs. *Gene Ther*. **3**, 217–222 (1996).
15. Kohn, D.B. *et al.* T lymphocytes with a normal ADA gene accumulate after transplantation of transduced autologous umbilical cord blood CD34$^+$ cells in ADA-deficient SCID neonates. *Nature Med.* **4**, 775–780 (1998).
16. Nienhuis, A.W., McDonagh, K.T. & Bodine, D.M. Gene transfer into hematopoietic stem cells. *Cancer* **67**, 2700–2704 (1991).
17. Matsushita, T. *et al*. Adeno-associated virus vectors can be efficiently produced without helper virus. *Gene Ther.* **5**, 938–945 (1998).
18. Evans, J.P., Brinkhous, K.M., Brayer, G.D., Reisner. H.W. & High, K.A. Canine hemophilia B resulting from a point mutation with unusual consequences. *Proc. Natl. Acad. Sci. USA* **86**, 10095–10099 (1989).
19. Mitruka, B.M., Rawnsley, H.M. & Vadehra, D.V. in *Animals for Medical Research–Models for the Study of Human Disease*. 216 (John Wiley & Sons, New York, 1976).
20. Nakai, H. *et al*. Adeno-associated viral vector-mediated gene transfer of human blood coagulation factor IX into mouse liver. *Blood* **91**, 4600–4607 (1998).
21. Baskar, J.F. *et al*. The enhancer domain of the human cytomegalovirus major immediate-early promoter determines cell type-specific expression in transgenic mice. *J. Virol.* **70**, 3207 (1996).
22. Kay, M.A. *et al*. Expression of human alpha1-antitrypsin in dogs after autologous

© 1999 Nature America Inc. • http://medicine.nature.com

© 1999 Nature America Inc. • http://medicine.nature.com

trannsplantation of retroviral transduced hepatocytes. *Proc. Natl. Acad. Sci. USA* **89**, 89–93 (1991).
23. Svensson, E.C. *et al*. Long-term erythropoietin expression in rodents and nonhuman primates following intramuscular injection of a replication-defective adenoviral vector. *Hum. Gene Ther.* **8**, 1797–1806 (1997).
24. Yang, Y., Haecker, S.E., Su, Q. & Wilson JM. Immunology of gene therapy with adenoviral vectors in mouse skeletal muscle. *Hum. Molec. Genet*. **5**, 1703–1712 (1996).
25. Dai. Y. *et al*. Cellular and humoral responses to adenoviral vectors containing factor IX gene: Tolerization of factor IX and vector antigens allows for long-term expression. *Proc. Natl. Acad. Sci. USA* **92**, 1401–1405 (1995).
26. Jooss, K., Yang, Y., Fisher, K.J. & Wilson, J.M. Transduction of dentritic cells by DNA viral vectors directs the immune response to transgene products in muscle fibers. *J. Virol*. **72**, 4212–4223 (1998).
27. Xiao, X., Li, J. & Samulski, R.J. Production of high-titer recombinant adeno-associated virus vectors in the absence of helper adenovirus. *J. Virol.* **72**, 2224–2232 (1998).
28. Ferrari, F.K., Xiao, X., McCarty, D. & Samulski, R.J. New developments in the generation of Ad-free, high titer rAAV gene therapy vectors. *Nature Med.* **3**, 1295–1297 (1997).
29. High, K.A. Factor IX: Molecular structure, epitopes, and mutations associated with inhibitor formation. *Adv. Exp. Med. Biol*. **386**, 79–86 (1995).
30. Bray, G.L. *et al*. A Multicenter study of recombinant factor VIII (Recombinate): Safety, efficacy, and inhibitor risk in previously untreated patients with hemophilia A. *Blood* **83**, 2428–2435 (1994).
31. Lusher, J.M., Arkin, S., Abildgaard, C.F. & Schwartz. Recombinant factor VIII for the treatment of previously untreated patients with hemophilia A. *N. Engl. J. Med*. **328**, 453–459 (1993).
32. Gilles, J.G.G., Arnout, J., Vermylen, J. & Saint-Remy, J.-M.R. Anti-factor VIII antibodies of hemophiliac patients are frequently directed towards nonfunctional determinants and do not exhibit isotypic restriction. *Blood* **82**, 2452–2461 (1993).
33. Gilles, J.G., Desqueper, B., Lenk, H., Vermylen, J. & Saint-Remy, J.M. Neutralizing anti-idiotypic antibodies to factor VIII inhibitors after desensitization in patients with hemophilia A. *J. Clin. Invest.* **97**: 1382–1388 (1996).
34. Miao, C.H. *et al*. The kinetics of rAAV integration in the liver. *Nat. Genet.* **19**, 13–15 (1998).
35. Duan, D. *et al*. Circular intermediates of recombinant adeno-associated virus have defined structural characteristics responsible for long-term episomal persistence in muscle tissue. *J. Virol.* **72**, 8568–8577 (1998).
36. Afione, S.A. *et al*. *In vivo* model of adeno-associated virus vector persistence and rescue. *J Virol* **70**, 3235–3241 (1996).
37. Evans, J.P., Watzke, H.H., Ware, J.L., Stafford, D.W. & High, K.A. Molecular cloning of a cDNA encoding canine factor IX. *Blood* **74**, 207–212 (1989).
38. Kessler, P.D. *et al*. Gene delivery to skeletal muscle results in sustained expression and systemic delivery of a therapeutic protein. *Proc. Natl. Acad. Sci. USA* **93**, 14082–14087 (1996).
39. Brinkhous K.M., Landen, C.N. & Read, M.S. Evaluation of sensitivity of whole blood clotting time (WBCT), partial thromboplastin time (PTT), and F.IX one-stage bioassay tests with low plasma F.IX levels observed with transfusion or gene therapy in canine hemophilia B. *Blood* **82**, Suppl.**1**, 592a (1993).
40. Walter, J., You, Q., Hagstrom, N., Sands, M. & High, K.A. Successful expression of human factor IX following repeat administration of an adenoviral vector in mice. *Proc. Natl. Acad. Sci. USA* **93**, 3056–3061 (1996).
41. Kung, S.-H. *et al*. Human factor IX corrects the bleeding diathesis of mice with hemophilia B. *Blood* **91**, 784–790 (1998).
42. Sambrook, J., Fritsch, E.F. & Maniatis, T. in *Molecular Cloning* (ed. Nolan, C.) 9.16–9.19 (Cold Spring Harbor Laboratory Press, Cold Spring Harbor, New York,1989).

© 1999 Nature America Inc. • http://medicine.nature.com

Hu et al. Molecular Neurodegeneration (2015) 10:6
DOI 10.1186/s13024-015-0001-3

MOLECULAR NEURODEGENERATION

RESEARCH ARTICLE Open Access

Opposing effects of viral mediated brain expression of apolipoprotein E2 (apoE2) and apoE4 on apoE lipidation and Aβ metabolism in apoE4-targeted replacement mice

Jin Hu[1†], Chia-Chen Liu[1,2†], Xiao-Fen Chen[1], Yun-wu Zhang[1], Huaxi Xu[1] and Guojun Bu[1,2*]

Abstract

Background: Human apolipoprotein E (apoE) exists in three major isoforms: apoE2, apoE3 and apoE4. In the brain, apoE is produced mostly by astrocytes and transports cholesterol to neurons via apoE receptors. Among the gene alleles encoding the three isoforms, the *APOE4* allele is the strongest genetic risk factor for late-onset Alzheimer's disease (AD), whereas *APOE2* is protective. ApoE4 confers a gain of toxic function, a loss of neuroprotective function or a combination of both in AD pathogenesis. Given that therapeutic impacts of modulating apoE expression may be isoform-dependent, we sought to investigate the relationship between overexpressing apoE isoform and apoE-related functions in apoE-targeted replacement (TR) mice. Specifically, apoE isoform expression driven by the astrocyte-specific glial fibrillary acidic protein (GFAP) promoter was built into an adeno-associated virus serotype 8 (AAV8) vector and injected into the ventricles of postnatal day 2 (P2) apoE3-TR or apoE4-TR mice. Upon confirmation of apoE isoform expression, effects on apoE lipidation and the levels of amyloid-β (Aβ) in the brain were assessed.

Results: AAV8-GFAP-apoE isoforms were specifically expressed in astrocytes throughout all brain regions, which led to overall increased apoE levels in the brain. Viral mediated overexpression of apoE4 in the apoE4-TR background increased poorly-lipidated apoE lipoprotein particles and decreased apoE-associated cholesterol in apoE4-TR mice. Conversely, apoE2 overexpression in apoE4-TR mice enhanced apoE lipidation and associated cholesterol. Furthermore, overexpression of apoE4 elevated the levels of endogenous Aβ, whereas apoE2 overexpression trended to lower endogenous Aβ.

Conclusions: Overexpression of apoE isoforms induces differential effects in the apoE4-TR background: apoE4 decreases apoE lipidation and enhances Aβ accumulation, whereas apoE2 has the opposite effects. Our findings suggest that increasing apoE2 in *APOE4* carriers is a beneficial strategy to treat AD, whereas increasing apoE4 in *APOE4* carriers is likely harmful. We have also established novel methods to express apoE isoforms in mouse brain to study apoE-related pathways in AD and related dementia.

Keywords: Alzheimer's disease, apoE, Lipidation, Aβ, apoE-TR mice

* Correspondence: bu.guojun@mayo.edu
†Equal contributors
[1]Fujian Provincial Key Laboratory of Neurodegenerative Disease and Aging Research, Institute of Neuroscience, School of Pharmaceutical Sciences, College of Medicine, Xiamen University, South Xiangan Road, Xiamen, Fujian 361102, China
[2]Department of Neuroscience, Mayo Clinic, Jacksonville, FL 32224, USA

BioMed Central

© 2015 Hu et al.; licensee BioMed Central. This is an Open Access article distributed under the terms of the Creative Commons Attribution License (http://creativecommons.org/licenses/by/4.0), which permits unrestricted use, distribution, and reproduction in any medium, provided the original work is properly credited. The Creative Commons Public Domain Dedication waiver (http://creativecommons.org/publicdomain/zero/1.0/) applies to the data made available in this article, unless otherwise stated.

Background

Alzheimer's disease (AD) is the leading cause of dementia in the elderly, which accounts for 60 to 80 percent of dementia cases [1]. Brain extracellular amyloid plaques and intracellular neurofibrillary tangles are the two pathological hallmarks of AD. Apolipoprotein E (apoE) is a major apolipoprotein and a cholesterol carrier in the brain [2]. The human *APOE* gene exists as three major polymorphic alleles: ε2, ε3 and ε4. Ample evidence indicates that the ε4 allele of the *APOE* gene is the strongest genetic risk factor for late-onset AD (LOAD), whereas the ε2 allele is protective [2-6].

While the primary function of apoE is to deliver cholesterol and other essential lipids to neurons through binding to cell surface apoE receptors, apoE also regulates brain metabolism of amyloid-β (Aβ) [7], accumulation of which leads to deposition of amyloid and is considered the initiating event in the pathogenesis of AD [8-10]. Previous studies have shown that brain Aβ levels and amyloid plaque loads are apoE isoform-dependent (E4 > E3 > E2) both in humans and in AD transgenic mouse models [11-13]. Several reports showed that the *APOE* genotype strongly affects apoE levels (E4 < E3 < E2) in human cerebrospinal fluid (CSF), brain parenchyma, and in apoE targeted-replacement (apoE-TR) mice [14-16]. Analysis on the levels of apoE and Aβ in different brain regions of non-demented individuals found that apoE levels negatively correlate with Aβ levels both in *APOE4* carriers and non-carriers [17]. ApoE protein levels in human CSF have also been shown to positively associate with CSF Aβ42 levels [14]. In addition, liver X receptors (LXRs) or the retinoid X receptor (RXR) agonists facilitate Aβ clearance and reverse the memory deficits in amyloid model mice by increasing apoE levels and its lipidation [18-20]. These results suggest that apoE levels and lipidation status likely contribute to Aβ clearance; thus, new therapeutic approaches aimed at increasing apoE expression are actively being pursued. However, to better design mechanism-based therapy, it is critical to understand how increasing apoE expression, in particular apoE4 in *APOE4* carriers, impacts apoE lipidation and Aβ metabolism.

Given that apoE is produced predominantly by astrocytes in the brain [21], we investigated the impact of overexpressing different human apoE isoforms in astrocytes in apoE-TR mice, in which the coding region of the mouse endogenous *Apoe* gene was replaced with one of the three human *APOE* alleles without changing the regulatory elements required for modulation of gene expression [22-24]. Thus, apoE-TR mice express human apoE isoforms at the physiological levels and respond to regulatory pathways in a physiological setting [22-25], providing an excellent *in vivo* system to explore the normal function of each *APOE* allele and apoE-associated diseases. Here, we used a gene delivery approach by which adeno-associated viral serotype 8 (AAV8) vectors expressing various human *APOE* alleles under the control of astrocyte-specific glial fibrillary acidic protein (GFAP) promoter were bilaterally injected into the cerebral lateral ventricles of neonatal apoE3-TR or apoE4-TR mice. We demonstrated that apoE isoforms are specifically expressed in astrocytes in the brain three months after injection. Importantly, we found that increasing apoE4 levels in apoE4-TR mice led to decreased apoE lipidation, lower apoE-associated cholesterol, and increased endogenous Aβ. Conversely, increasing apoE2 expression in apoE4-TR mice had the opposite, beneficial effects. Our findings for the first time reveal the consequential effects of overexpressing apoE isoforms in specific isoform background and should help to provide guidance for the designs of apoE-based targeted therapy to treat AD.

Results

Neonatal intracerebroventricular injection of AAV8-GFAP-apoE viruses results in sustained apoE isoform expression in astrocytes in mouse brain

Intracerebroventricular injection of neonatal mice using AAV-based vectors is a relatively easy, fast and efficient way to modulate gene expression in the brain [26,27]. Previous studies have shown that when AAV8 viruses are injected intracranially after P0 of neonatal mice, viral mediated gene expression is detected primarily in astrocytes [27,28]. To specifically express apoE isoforms in astrocytes in mouse brain, we injected AAV8-GFAP viruses carrying cDNAs encoding GFP or one of three apoE isoforms into the cerebral ventricles of P2 neonatal apoE3-TR and apoE4-TR mice. An HA tag was included in apoE constructs to facilitate protein detection. Three months after virus injection, expression of GFP was evaluated in mouse brain. We found that intracranial delivery of AAV8-GFAP-GFP to neonatal mice resulted in an extensive transduction and GFP expression throughout the brain, including the cortex and hippocampus (Figure 1A). To evaluate cell-type specificity of AAV8-GFAP-mediated expression, we evaluated co-expression of GFP or apoE isoforms with cell-type specific markers for astrocytes, microglia, and neurons by immunofluorescence staining. We found that both GFP and apoE isoforms, detected with an HA antibody, were co-localized with GFAP-positive astrocytes, but not with Iba1-positive microglia or NeuN-positive neurons (Figure 1B-E). These results confirm that neonatal injection of AAV8-GFAP-apoE leads to sustained expression of apoE isoforms in astrocytes.

AAV-mediated expression of apoE2 is significantly higher than those of apoE3 and apoE4

We next assessed the mRNA and protein levels of apoE in the cerebral cortex of apoE3-TR and apoE4-TR mice three months after injection with AAV8-GFAP-apoE isoforms or GFP control. Intracerebroventricular injection of AAV8-GFAP-apoE isoforms significantly increased apoE levels in the brains of apoE-TR mice compared with mice injected with GFP control viruses, as detected by real-time PCR

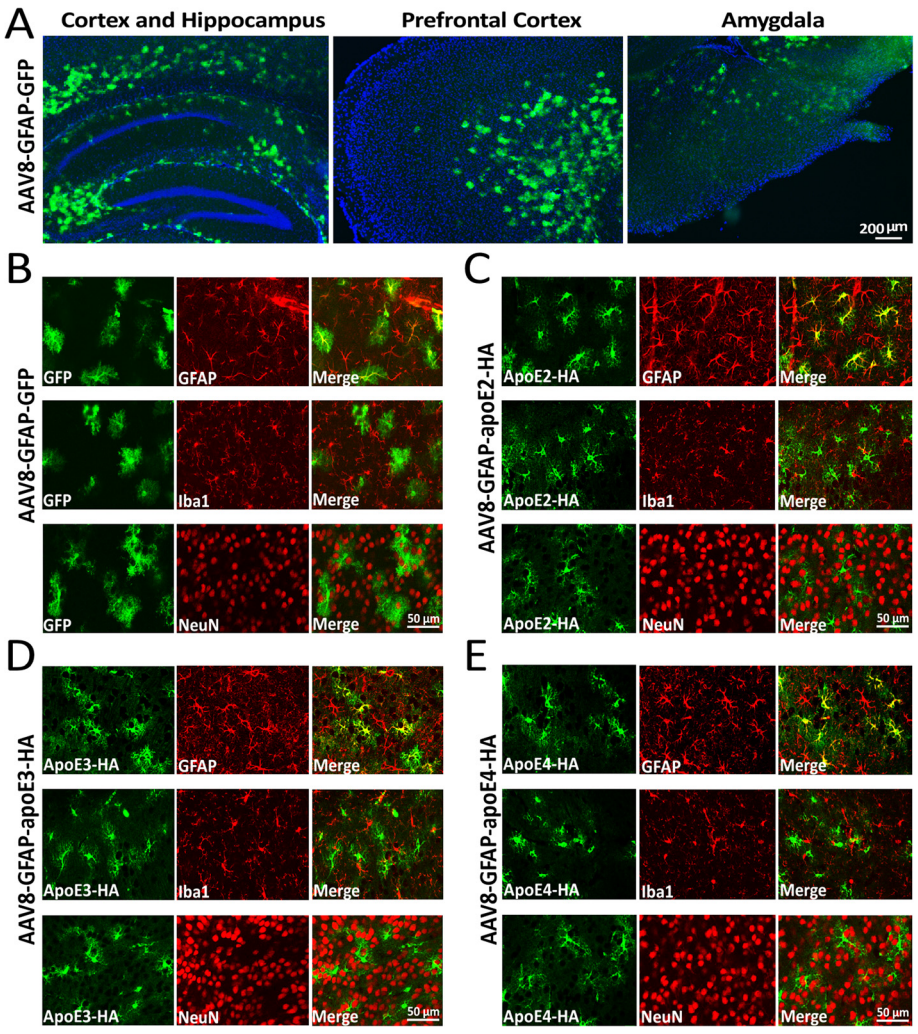


Figure 1 Specific expression of AAV8-GFAP-GFP and AAV8-GFAP-apoE isoforms in astrocytes *in vivo*. Newborn postnatal day 2 (P2) apoE3-TR mice were injected intracerebroventricularly with viruses carrying AAV8-GFAP-GFP or AAV8-GFAP-apoE isoforms. Expression of GFP or apoE isoforms was evaluated 3 months after viral injection. **(A)** GFP expression was detected by green fluorescence and the images from different brain regions are shown. **(B-E)** Mouse brain sections transduced with AAV8-GFAP-GFP (B), AAV8-GFAP-apoE2 **(C)**, AAV8-GFAP-apoE3 **(D)** or AAV8-GFAP-apoE4 **(E)** were co-immunostained with HA antibody for apoE expression and antibodies for cell type-specific markers (GFAP: astrocyte; Iba1: microglia; NeuN: neuron). Note that apoE (HA immunoreactivity) is specifically expressed in GFAP-positive astrocytes.

(Figure 2A and C) and apoE ELISA (Figure 2B and D). While the apoE mRNA levels were not significantly different among apoE isoforms (Figure 2A and C), we found that the apoE protein levels are significantly higher in apoE-TR mice transduced with AAV8-GFAP-apoE2 viruses compared with those transduced with GFP, apoE3 or apoE4 viruses (Figure 2B and D). These results are consistent with a previous study [15] indicating that apoE2 is likely a more stable isoform compared with apoE3 and apoE4.

Increasing apoE4 expression leads to decreased apoE lipidation in apoE4-TR mice

ApoE lipidation is critical for its function in maintaining synapses [2,3,20]. Studies in humans [29] and in apoE-TR mice [30,31] suggest that apoE4 is significantly less lipidated than apoE2 and apoE3. To investigate the lipidation status of apoE in apoE-TR mice transduced with AAV8-GFAP-apoE isoforms, apoE-associated lipoprotein particles in the cortical brain lysates were evaluated by non-denaturing gel electrophoresis, followed by Western blotting (Figure 3). ApoE-immunoreactivity was detected in the molecular sizes between 242 and 1048 kDa. To quantify the distribution of apoE/lipoprotein particles, we defined particle sizes as large, medium and small (Figure 3A). Importantly, we found that the amounts of large apoE/lipoprotein particles were reduced and the small particles were increased in apoE4-TR mice transduced with AAV8-GFAP-apoE4 viruses compared with

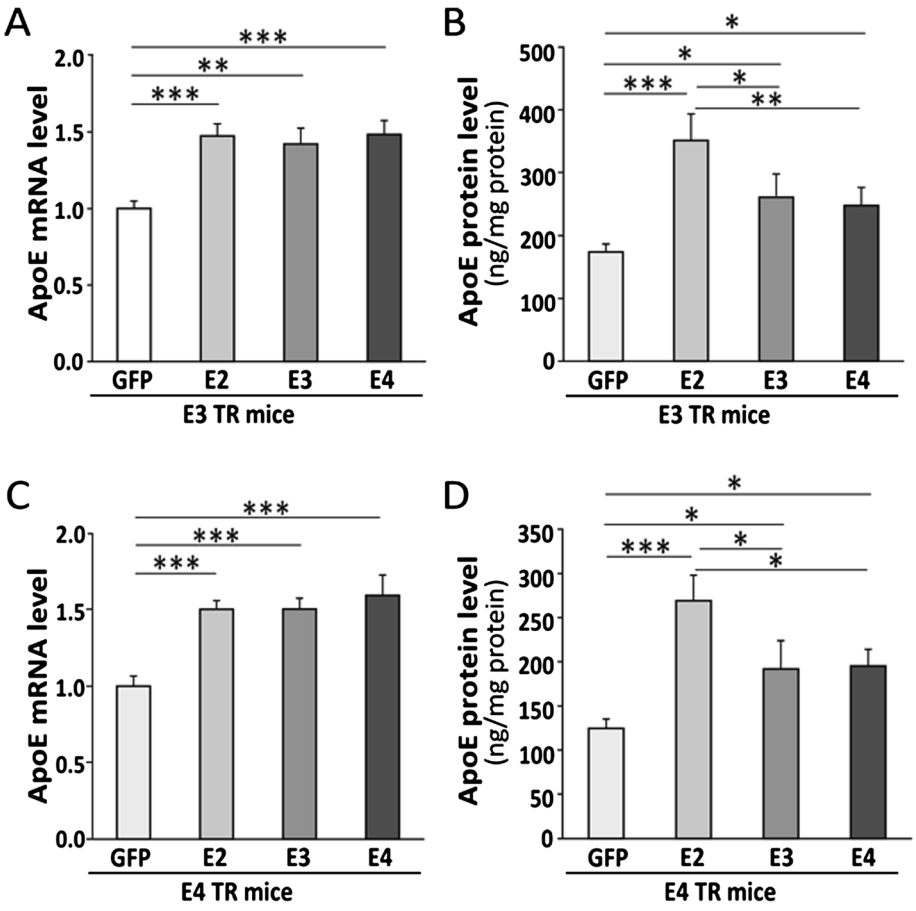


Figure 2 Increased apoE expression in apoE-TR mice following AAV viral mediated expression of apoE isoforms in neonatal mice. Neonatal P2 apoE3-TR or apoE4-TR mice were injected intracerebroventricularly with viruses carrying AAV8-GFAP-GFP or AAV8-GFAP-apoE isoforms, and mouse brains were harvested 3 months after viral injection. **(A** and **B)** Levels of apoE mRNA **(A)** and protein **(B)** in the cortices of apoE3-TR mice transduced with viruses encoding GFP or apoE isoforms were analyzed by real-time PCR or apoE-specific ELISA, respectively. (**C** and **D**) Same as in A and B, except apoE4-TR mice were used. Data are expressed as mean ± SEM (n = 7-8/group). *,$p < 0.05$; **,$p < 0.01$; ***,$p < 0.001$.

those transduced with GFP control (Figure 3B). In contrast, apoE4-TR mice transduced with AAV8-GFAP-apoE2 viruses exhibited increased amounts of large apoE particles and decreased amounts of small particles (Figure 3B). In like manner, transduction of AAV8-GFAP-apoE2 viruses in apoE3-TR mice increased the large particles, whereas transduction of AAV8-GFAP-apoE4 viruses increased the small particles (Additional file 1: Figure S1). These results indicate that apoE4 is associated with poorly and apoE2 abundantly lipidated particles.

To further evaluate apoE lipidation status, we next quantified the amounts of cholesterol associated with apoE isoforms in the buffer/TBS-soluble fractions of apoE3-TR and apoE4-TR mice transduced with different viruses. The apoE-containing particles were immunoprecipitated with a biotinylated apoE antibody and the amounts of cholesterol co-immunoprecipitated with apoE were quantified. Transduction of AAV8-GFAP-apoE isoforms increased the levels of apoE and apoE-associated cholesterol in both apoE3-TR mice (Additional file 1: Figure S2A and B) and apoE4-TR mice compared with those transduced with GFP control (Figure 4A and B). Interestingly, mice transduced with apoE2 had the highest apoE and cholesterol levels (Figure 4A and B; Additional file 1: S2A and B). In addition, the cholesterol-to-apoE ratio was significantly increased in apoE4-TR mice transduced with apoE2, while it was decreased among apoE4-TR mice transduced with apoE4 (Figure 4C). We did not observe a significant difference in the ratio of cholesterol-to-apoE in apoE3-TR mice transduced with AAV8-GFAP-apoE isoforms compared with controls (Additional file 1: Figure S2C). Further, there were no significant differences in the levels of ATP-binding cassette transporters A1 (ABCA1) and ATP-binding cassette transporters G1 (ABCG1), two major cholesterol transporters, in apoE3-TR or apoE4-TR mice transduced with AAV8-GFAP-apoE isoforms compared with controls (Additional file 1: Figure S3). These results indicate that

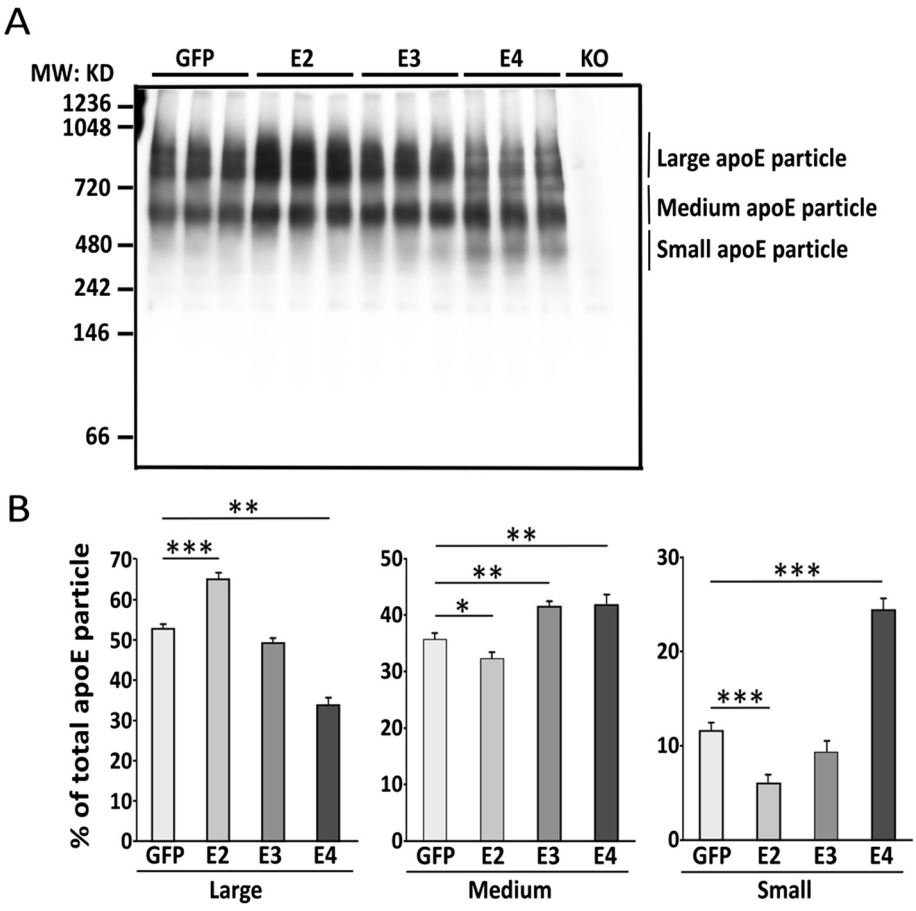


Figure 3 Viral mediated expression of apoE4 in apoE4-TR mice shifts apoE particles to smaller sizes. Neonatal P2 apoE4-TR mice were injected with AAV viruses and brains were harvested as in Figure 2. **(A)** ApoE-associated particles in the TBS fractions of cortical brain tissues were analyzed by native gel electrophoresis. ApoE particle-immunoreactivity was detected at approximately between 242 kDa and 1048 kDa, and defined as three categories of particle sizes: Large particles (>720 kDa); Medium particles (480–720 kDa) and Small particles (<480 kDa). Cortical lysates from age-matched *Apoe* knockout (KO) mice was used as a negative control for apoE immunoreactivity. **(B)** The percentages of apoE particles in different size categories were quantified. Data are expressed as mean ± SEM (n = 3-5). *,$p < 0.05$; **,$p < 0.01$; ***,$p < 0.001$.

AAV8-mediated transduction of apoE in astrocytes increases apoE-associated cholesterol in the brains in an isoform-dependent manner.

ApoE4 overexpression in the brain of apoE4-TR mice results in increased Aβ accumulation

Mounting evidence indicates that apoE regulates Aβ metabolism, aggregation and deposition in an isoform-dependent manner [7,32] and that Aβ clearance is slower in apoE4-TR mice compared with apoE3-TR mice [12]. In addition, many studies suggest that lipid-poor apoE promotes Aβ aggregation while fully lipidated apoE favors Aβ clearance [20,26,27]. In this study, we found that AAV8-mediated transduction of apoE in astrocytes regulated apoE lipidation in an isoform-dependent manner. We thus examined the differential effects of increasing apoE isoforms on Aβ metabolism in the brains of apoE3-TR and apoE4-TR mice. Transduction of various apoE isoforms in apoE3-TR mice did not significantly impact the levels of endogenous Aβ40 in the cortex (Figure 5A). However, when apoE isoforms were overexpressed in the background of apoE4-TR mice, apoE4 significantly increased the levels of endogenous Aβ40 whereas apoE2 trending to the opposite (Figure 5B). We further performed correlation analyses between the levels of apoE and endogenous Aβ40 in apoE4-TR mice transduced with different viruses (Figure 6A-D) and found that the levels of endogenous Aβ40 positively correlated with those of apoE in apoE4-TR mice transduced with AAV8-GFAP-apoE4 viruses (Figure 6D). In contrast, there was a trend of negative correlation between the levels of Aβ40 and apoE in apoE4-TR mice transduced with AAV8-GFAP-apoE2 viruses (Figure 6B). There were no significant correlations between the levels of endogenous Aβ40 and apoE in apoE3-TR mice transduced with viruses expressing different apoE isoforms (Additional file 1: Figures S4A-D). To determine whether transduction of

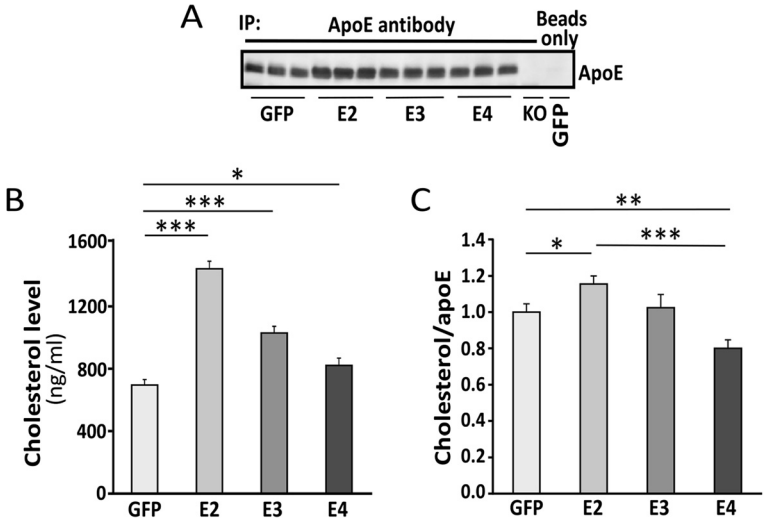


Figure 4 Viral mediated expression of apoE4 in apoE4-TR mice leads to reduced levels of apoE-associated cholesterol. Neonatal P2 apoE4-TR mice were injected with AAV viruses and brains were harvested as in Figure 2. Mouse cortical brain tissues were lysed in TBS and the apoE-associated particles were isolated by immunoprecipitation using a biotinylated-apoE specific antibody. Mice injected with GFP viruses treated with beads only were used as a negative control. **(A)** The immunoprecipitated apoE under different conditions was detected by Western blot. **(B)** ApoE-associated cholesterol was analyzed by Amplex Red Cholesterol Assay. **(C)** The ratios of cholesterol-to-apoE under each condition were calculated. Data are expressed as mean ± SEM (n = 3-5/group). *,p < 0.05; **,p < 0.01; ***,p < 0.001.

AAV8-GFAP-apoE viruses affects the processing of amyloid precursor protein (APP) in mouse brains, we analyzed the levels of full-length APP, APP α- and β-C-terminal fragments (α-CTFs and β-CTFs) in apoE3-TR and apoE4-TR mice. Transduction of AAV8-GFAP-apoE viruses did not significantly affect the levels of full-length APP, APP α-CTF or β-CTFs in apoE3-TR or apoE4-TR mice compared with those transduced with GFP control viruses (Additional file 1: Figure S5A and B), suggesting that overexpression of apoE isoforms does not affect APP expression or processing. Together, these results suggest that increasing the expression level of apoE4 is likely detrimental, while apoE2 is beneficial, in regard to brain Aβ accumulation.

Discussion

The most prevalent genetic risk factor for late-onset AD is the *APOE* genotype with an allele-specific risk profile: *APOE4* > *APOE3* > *APOE2* [33,34]). Despite progress in the past two decades [2,3], it remains unclear how apoE4 increases, and apoE2 decreases, the risk of AD. The amyloid hypothesis proposes that an imbalance between Aβ production and clearance leads to Aβ accumulation

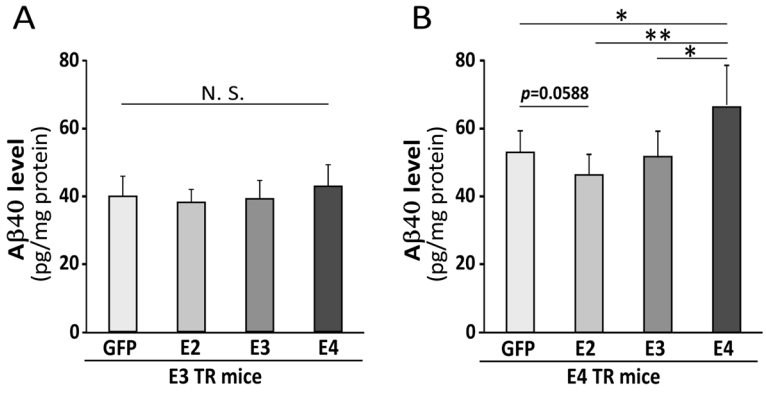


Figure 5 Viral mediated expression of apoE4 in apoE4-TR mice leads to increases of mouse endogenous Aβ. Neonatal P2 apoE3-TR or apoE4-TR mice were injected with AAV viruses and brains were harvested as in Figure 2. **(A** and **B)** Levels of mouse endogenous Aβ in the cortices of apoE3-TR mice **(A)** or apoE4-TR mice **(B)** transduced with AAV viruses encoding GFP or apoE isoforms were quantified by mouse Aβ-specific ELISA. Data are expressed as mean ± SEM (n = 7-8/group). N.S., Not significant; *,p < 0.05; **,p < 0.01.

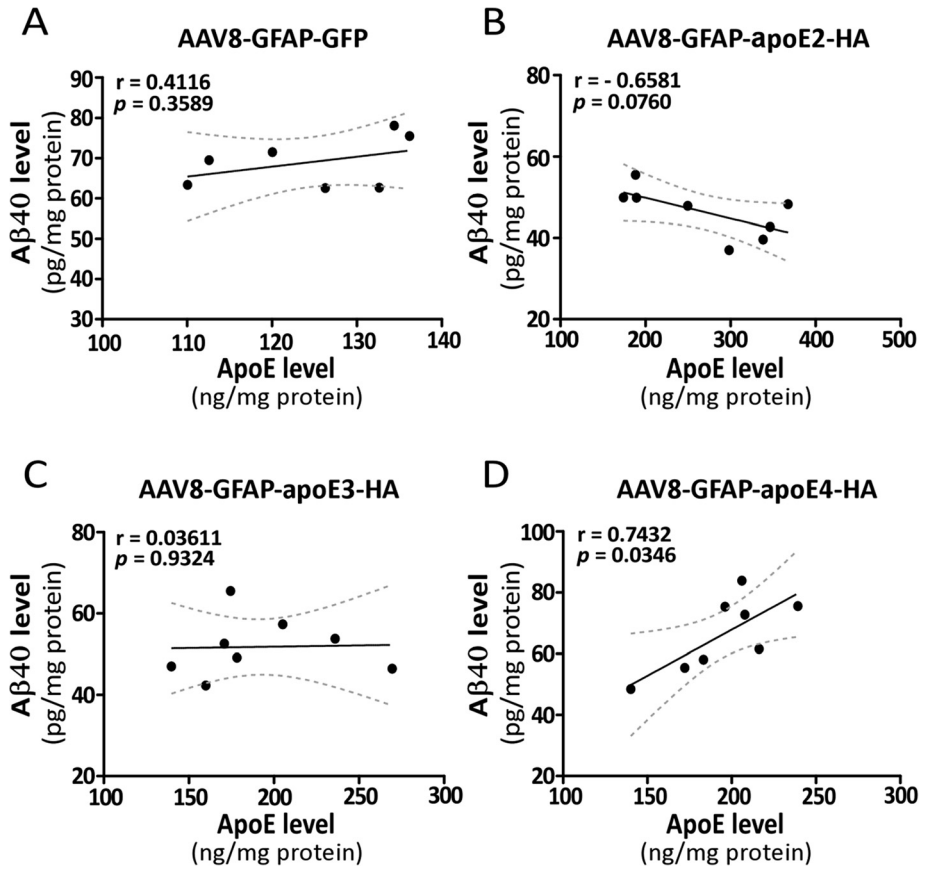


Figure 6 Positive correlations between mouse endogenous Aβ and apoE in apoE4-TR mice transduced with AAV8-GFAP-apoE4 viruses. Three months after intracranial delivery of viruses carrying AAV8-GFAP-GFP or AAV8-GFAP-apoE isoforms, the levels of mouse endogenous Aβ40 and apoE in the cortices of apoE4-TR mice were examined by Aβ40-specific ELISA and apoE-specific ELISA, respectively. **(A-D)** The correlation between levels of Aβ40 and apoE in the cortex of apoE4-TR mice transduced with GFP **(A)**, apoE2 **(B)**, apoE3 **(C)** or apoE4 **(D)** were analyzed and plotted. The Pearson correlation coefficient (r) and p values are shown.

in the brain that initiates AD pathogenesis [8,10]. Multiple lines of evidence demonstrate that apoE isoforms differentially regulate Aβ metabolism in the brain [35-38], likely through modulation of Aβ clearance and aggregation [3,12,32]. These findings suggest that apoE levels, lipidation status and isoform-dependent effects may differently impact Aβ metabolism, thereby contributing to or preventing AD pathogenesis.

In the current study, we used AAV8 constructs driven by an astrocyte-specific GFAP promoter to express three apoE isoforms (AAV8-GFAP-apoE2/3/4) in neonatal apoE3-TR or apoE4-TR mice through intracranial injection. Transduction of AAV8-GFAP-apoE led to sustained expression of apoE isoforms in mouse brain. We found that transduction of apoE4 in apoE4-TR background significantly increased the amounts of small, lipid-poor apoE particles and the levels of endogenous Aβ. Conversely, transduction of apoE2 in the apoE4-TR background led to an increase in the amounts of large, lipid-rich apoE particles and decreased endogenous Aβ. Our findings indicate that modulating the levels of apoE isoforms had differential effects on the lipidation status of apoE and Aβ levels in apoE4-TR, less so in apoE3-TR mice. Specifically, overexpression of apoE2 and apoE4 in apoE4 background leads to opposite effects on the amounts of cholesterol associated with apoE and Aβ accumulation with apoE4 being detrimental and apoE2 beneficial. We did not observe significant changes in APP proteolytic processing products in mice transduced with different apoE isoforms, indicating that APP processing to Aβ is not regulated by the expression levels of apoE isoforms.

A recent study assessed the effects of overexpressing apoE isoforms in the background of amyloid model mice with endogenous murine apoE background [39]. They found that overexpression of apoE4 leads to higher levels of Aβ and enhanced amyloid deposition, whereas overexpression of apoE2 had the opposite effects. Our current study uniquely address how overexpression of apoE isoforms in different human apoE isoform background impact apoE lipidation and Aβ accumulation, events that are critical for the

synaptic functions and the pathogenesis of AD. When combined, these studies should provide mechanism-based guidance on regulating apoE expression and lipidation in the designs of therapeutic approaches to treat AD.

The mechanism underlying the protective effect of apoE2 against AD remains unclear. Our results show that apoE protein levels are significantly higher in mice transduced with apoE2 compared with mice transduced with GFP controls, apoE3 or apoE4 viruses, despite similar mRNA levels. Previous studies have shown that apoE2 may exhibit a more stable conformation [40] and has lower affinity to the low-density lipoprotein (LDL) receptor, which may lead to decreased catabolism [15]. Thus, the higher levels of apoE observed in apoE2-transduced mice may be attributed to its increased stability and decreased turnover. Previous studies suggest that formation of protein complexes between apoE and Aβ may facilitate Aβ clearance [41]. Compared with apoE2 or apoE3, apoE4/Aβ complexes have been shown to be less stable, which is likely attributed to the poor lipidation status of apoE4/lipoprotein particles [7,31,42]. In addition, complex formation between Aβ and apoE isoforms may affect their binding property to their individual or common receptors including the low-density lipoprotein receptor-related protein 1 (LRP1), thereby further affects Aβ clearance [32,43]. Thus, it is possible that overexpression of apoE2 increases and apoE4 decreases apoE/Aβ complex formation and therefore, the clearance of Aβ in the brain.

Emerging evidence indicates that apoE lipidation status directly affects its role in Aβ clearance [20,44,45]. Our current study demonstrates that AAV-mediated transductions of apoE isoforms have different effects on the lipidation status of apoE. Compared with controls, transduction of apoE4 in apoE4-TR mice increased the proportion of poorly-lipidated apoE. Several studies suggest that apoE4 is significantly less lipidated than apoE2 and apoE3 in both human and APP transgenic mice expressing human apoE isoforms [29-31]. ApoE4 more easily self-aggregates, which may affect its lipidation capacity [46]. Hence, it is possible that overexpression of apoE4 in apoE4-TR mice results in apoE4 aggregation, which might impair its lipidation. Consistent with this notion, haploinsufficiency of ABCA1, which mediates apoE lipidation, impairs Aβ clearance and exacerbates amyloid deposition in apoE4-TR mice, but not in apoE3-TR mice [47]. Though we did not observe an alteration in the levels of ABCA1 and ABCG1, boosting apoE4 in apoE4-TR mice may enhance apoE4 aggregation in parallel with an impairment of its lipidation, which in turn decreases Aβ clearance and/or promotes Aβ deposition.

In addition to its effects on Aβ metabolism, apoE mediates neuronal delivery of cholesterol, an essential component for synaptic plasticity required for learning and memory formation [2]. Given the ongoing clinical trial aimed at increasing apoE levels and its lipidation [20], it is imperative to understand the consequences of boosting apoE on cholesterol homeostasis and Aβ metabolism in the background of different apoE isoforms. Our current study directly demonstrates the divergent effects of apoE2 and apoE4 isoforms on Aβ accumulation and apoE lipidation status, effects that are more pronounced in apoE4-TR mice.

Conclusions

Here, we report that increasing apoE4 in the brain of apoE4-TR mice reduces lipid-rich apoE and promotes Aβ accumulation, while increasing apoE2 in the brain leads to opposite effects. To the best of our knowledge, this is the first report demonstrating the impact of boosting different apoE isoforms in astrocytes on cholesterol and Aβ metabolism in the brain of apoE3-TR or apoE4-TR mice. Our findings suggest that astrocyte expression of apoE2 isoforms through AAV-mediated transduction or delivery of apoE2 mimetic into the brain might have therapeutic value, while increasing apoE4 in the brain may be harmful, especially for carriers of the *APOE4* allele.

Materials and methods

Animals

Human apoE3-TR or apoE4-TR mice, which express respective human apoE isoform driven by the endogenous murine *ApoE* promoter, were obtained from Taconic. All animal experiments were conducted in compliance with the protocols of the Institutional Animal Care and Use Committee at Mayo Clinic.

Viral vector construction and production

The AAV8 vector construction and production were performed by the Hope Center Viral Vectors Core at the Washington University School of Medicine. ApoE2, 3, or 4 cDNA in pcDNA3.1 was amplified by PCR with the forward primer containing a BamHI site and the reverse primer containing a SalI site and an influenza hemagglutinin (HA) tag sequence. The PCR products were digested with BamHI and SalI and inserted into an AAV8-GFAP-GFP backbone in which the GFP was replaced with the PCR products. The resulting AAV8-GFAP-aopE2-HA, AAV8-GFAP-aopE3-HA, and AAV8-GFAP-aopE4-HA contain the respective apoE isoforms with a HA tag under the control of a GFAP promoter. The AAV8 viruses were produced as previously described [48]. Briefly, the packaging cell line HEK293 is maintained in Dulbecco's modified Eagles medium (DMEM), supplemented with 5% fetal bovine serum (FBS), 100 units/ml penicillin, 100 μg/ml streptomycin in 37°C incubator with 5% CO_2. The cells were co-transfected with pAAV2/8, pHelper, and rAAV transfer plasmid containing GFP or apoE isoforms using the calcium phosphate precipitation method. The cells were

incubated at 37°C for 3 days before harvesting. Cells were lysed by three freeze/thaw cycles. The cell lysate were treated with 50U/ml of Benzonaze followed by iodixanol gradient centrifugation. The iodixanol gradient fraction is further purified by HiTrap Q column chromatography (GE Healthcare) and concentrated with Vivaspin concentrator (Bohemia, NY). The virus titer was determined by dot blot assay.

Intracranial injections in neonatal mice

AAV8 virus intracranial injection in neonatal mice was performed as previously described with minor modifications [27,28]. Briefly, postnatal day 2 (P2) mice were cryoanesthetized on ice for 5 min and injected intracerebroventricularly with 2 μl (~10^{13} viral particles/ml) of viruses into both hemispheres using a syringe (7642–01, Hamilton) with a 30 gauge needle (7803–07, Hamilton). After injections were complete, pups were placed on a warming pad until they regained normal color and resumed movement. All injected animals were then returned to their mothers for further recovery.

Preparation of mouse brains

Three months post AAV virus injection, mice were anesthetized using isoflurane, perfused with PBS, and their brains were rapidly harvested. The right hemibrains were fixed in 4% paraformaldehyde and used for immunofluorescence analysis, and left hemibrains were dissected and kept frozen at −80°C until further biochemical analysis.

Immunohistochemistry

The immunohistochemistry for the brain sections was performed as previously described [27]. Briefly, brains were fixed overnight at 4°C in fresh 4% paraformaldehyde and then transferred to 30% sucrose for cryoprotection. Brains were frozen on dry ice and then sectioned at 45 μm using a freezing-sliding microtome (LEICA SM2400, Leica). Sections were permeated and blocked with 3% goat serum containing 0.1% Triton-X 100 in Tris-buffered saline (TBS) buffer (25 mM Tris, 0.15 M NaCl, pH 7.4) for 1 h at room temperature. Then, the sections were incubated with mouse anti-HA (1:1000, Covance), rabbit anti-GFAP (1:1000, Millipore), rabbit anti-NeuN (1:1000, Millipore) or rabbit anti-Iba1 (1:1000, Wako Chemicals) antibodies in blocking solution at 4°C overnight. The sections were washed with TBS/0.5% Tween 20 (TBST) and incubated with Alexa Fluor 488-conjugated goat anti-mouse (1:400; Invitrogen) and Alexa Fluor 568-conjugated donkey anti-rabbit (1:400; Invitrogen) secondary antibodies for 2 h at room temperature. Images were obtained by confocal microscope (LSM 510 META, Zeiss) and analyzed by ZEN software.

Quantitative real-time PCR

Total RNAs were extracted from frozen cortical tissues using Trizol (Invitrogen) and Direct-zol RNA MiniPrep kit (Zymo Research). Reverse transcription was performed using SuperScript III First-Strand Synthesis System (Invitrogen). Real-time qPCR was conducted with Universal SYBR Green Supermix (Bio-Rad) using an iCycler thermocycler (Bio-Rad). The following primers were used: Human apoE mRNA forward primer, TGTCTGAGCAGG TGCAGGAG; and reverse primer, TCCAGTTCCGATTT GTAGG. Mouse β-actin forward primer, AGTGTGACGT TGACATCCGTA; and reverse primer, GCCAGAGCAG TAATCTCCTTC Relative mRNA levels were calculated by ΔΔCt method with β-actin used as a reference.

ELISA for human apoE

Cortical tissues were homogenized with a Polytron homogenizer in ice cold TBS buffer containing protease inhibitor and phosphate inhibitor cocktails (Roche). The homogenates were centrifuged at 100,000 g for 30 min at 4°C and the supernatants were collected. ApoE levels were analyzed using an ELISA. Briefly, 96-well plates were coated overnight with an apoE antibody (AB947, Millipore) in carbonate buffer at 4°C overnight. The plates were blocked with 1% Block Ace in PBS, and then washed with PBS 3 times. Recombinant apoE (Fitzgerald) along with samples were diluted and added at a volume of 100 μl/well incubated at 4°C overnight. The plates were washed and incubated with biotin-conjugated goat anti-apoE antibody (Meridian Life Science) for 2 h at room temperature. After incubation with Horseradish Peroxidase Avidin D (Vector Laboratories) for 90 min at room temperature, the plate was developed by adding tetramethylbenzidine Super Slow substrate (Sigma). The reaction was stopped and read at 450 nm with a microplate reader.

ELISA for mouse endogenous Aβ

Mouse endogenous Aβ was extracted from cortical tissues by diethylamine as previously described [49]. The Aβ levels in age-matched APP knockout mice were used as a negative control and subtracted as background. For detection of endogenous mouse Aβ40, 96-well plates were coated at 4°C overnight with 13.1.1 mAb (anti-Aβ35-40) [49,50]. The plates were blocked with 1% Block Ace in PBS, washed with PBS and loaded with samples. Synthetic rodent Aβ40 (AnaSpec) was used as standards. Following overnight incubation at 4°C, the plates were washed, followed by incubation with HRP-conjugated mAb 32.4.1 (rodent Aβ1-16 specific) [49] for detection. The plates were developed with tetramethylbenzidine Supersensitive substrate (Sigma). The reaction was stopped and read at 450 nm with a microplate reader.

Analyses of apoE/lipoprotein particles by Blue Native PAGE and Western blot

Cortical tissues were homogenized with a Polytron homogenizer in ice cold TBS buffer containing protease inhibitor and phosphate inhibitor cocktails (Roche). Proteins were separated by Native PAGE™ Novex 4–16% Bis-Tris gels (Invitrogen) under native conditions following the manufacturer's instructions and transferred to PVDF (Millipore) at 100 V for 1 h using the Trans-Blot Cell (Bio-Rad). Blots were treated with Ponceau S Staining Solution (0.1% (w/v) Ponceau S in 5% (v/v) acetic acid) to visualize the molecular mass markers. The NativeMark Unstained Protein Standard from Invitrogen was used for estimation of particle sizes. After washing in TBS, blots were processed for Western blot. The membrane was incubated with goat anti-apoE antibody (K74180B, Meridian Life Science) overnight at 4°C, followed by peroxidase-labeled donkey anti-goat antibody (Santa Cruz). The membrane was developed with Lumigen ECL Ultra Western Blotting HRP Substrate (Lumigen), and the signals were detected by Fuji film Luminescent Image Analyzer (LAS4000). An antibody that recognizes the C-terminus of APP (18961, IBL-America) was used for detecting APP and its C-terminal fragments. Anti-β-actin (Sigma) was used as a loading control. Western blot bands were quantified by Image J software.

Immunoprecipitation (IP) of apoE particles and cholesterol assay

Streptavidin-conjugated agarose beads (Sigma) were first incubated with biotin-conjugated goat anti-apoE antibody (K74180B, Meridian Life Science) for 2 h at room temperature with shaking. The unbound antibodies were removed by washing with TBS three times. The antibody-bound agarose beads were then mixed with brain lysates in TBS fractions (500 μg total protein) at 4°C overnight. The IP solution was centrifuged for 2 min at 1,000 g to collect agarose beads. The beads were washed with cold TBS three times and re-suspended with TBS/0.1% Triton X-100. The resulting suspension was subjected to Western blot analysis in which equal volumes of samples were loaded. Proteins were separated by 4-20% Mini-PROTEAN TGX Gel (Bio-Rad) and transferred to Immobilon-P PVDF (Millipore). The membranes were incubated with apoE antibody (K74180B, Meridian Life Science), followed by IRDye secondary antibody (LI-COR Biosciences). The results were visualized and quantified by Odyssey infrared imaging system (LI-COR Biosciences). The remaining suspension was used for the detection of apoE particle-associated cholesterol quantified by Amplex Red cholesterol assay (Invitrogen) according to the manufacturer's protocol.

Statistical analysis

All data were analyzed by one-way analysis of variance (ANOVA) with a Tukey's post-hoc test using GraphPad Prism 5. Data were presented as average ± SEM. A p value of < 0.05 was considered statistically significant.

Additional file

Additional file 1: Figure S1. Analysis of apoE-associated lipoprotein particles in apoE3-TR mice transduced with viruses carrying AAV8-GFAP-apoE isoforms. **Figure S2.** ApoE-associated cholesterol levels in apoE3-TR mice transduced with viruses carrying AAV8-GFAP-apoE isoforms. **Figure S3.** Overexpression of apoE isoforms does not affect the levels of ABCA1 and ABCG1 in apoE-TR mice. **Figure S4.** Correlation analysis between mouse endogenous Aβ and apoE in apoE3-TR mice transduced with viruses carrying AAV8-GFAP-apoE isoforms. **Figure S5.** APP expression and processing are not altered in apoE-TR mice upon overexpression of apoE isoforms.

Abbreviations

AD: Alzheimer's disease; ApoE: Apolipoprotein E; AAV8: Adeno-associated virus serotype 8; GFAP: Astrocyte-specific glial fibrillary acidic protein (GFAP); Aβ: Amyloid-β; apoE-TR mice: apoE targeted-replacement mice; RXR: Retinoid X receptor; CSF: Cerebrospinal fluid; APP: Amyloid precursor protein; ABCA1: ATP-binding cassette transporters A1.

Competing interests

The authors declare that they have no competing interests.

Authors' contributions

Experiments were designed and performed by JH, CL, XC, YZ, HX and GB. Manuscript was written by JH, CL and GB and critically reviewed by XC, YZ and HX. All authors read and approved the final manuscript.

Acknowledgements

This work was supported by NIH grants P01NS074969, P01AG030128, P50AG016574, R01AG035355, R01AG027924, R01AG046205, and a grant from the Alzheimer's Association (to G.B.). We thank Drs. Mingjie Li and Joyce Snyder from the Hope Center Viral Vectors Core at the Washington University School of Medicine for producing the AAV viruses. The Hope Center Viral Vectors Core is supported by a Neuroscience Blueprint Core grant (P30NS057105) from NIH to Washington University. We also thank Caroline Stetler for careful reading of this manuscript.

Received: 23 December 2014 Accepted: 26 January 2015
Published online: 05 March 2015

References

1. Thies W, Bleiler L, Alzheimer's A. 2013 Alzheimer's disease facts and figures. Alzheimers Dement: J Alzheimers Assoc. 2013;9:208–45.
2. Liu CC, Kanekiyo T, Xu H, Bu G. Apolipoprotein E and Alzheimer disease: risk, mechanisms and therapy. Nat Rev Neurol. 2013;9:106–18.
3. Bu G. Apolipoprotein E and its receptors in Alzheimer's disease: pathways, pathogenesis and therapy. Nat Rev Neurosci. 2009;10:333–44.
4. Kim J, Basak JM, Holtzman DM. The role of apolipoprotein E in Alzheimer's disease. Neuron. 2009;63:287–303.
5. Corder EH, Saunders AM, Strittmatter WJ, Schmechel DE, Gaskell PC, Small GW, et al. Gene dose of apolipoprotein E type 4 allele and the risk of Alzheimer's disease in late onset families. Science. 1993;261:921–3.
6. Corder EH, Saunders AM, Risch NJ, Strittmatter WJ, Schmechel DE, Gaskell Jr PC, et al. Protective effect of apolipoprotein E type 2 allele for late onset Alzheimer disease. Nat Genet. 1994;7:180–4.
7. Kanekiyo T, Xu H, Bu G. ApoE and Abeta in Alzheimer's disease: accidental encounters or partners? Neuron. 2014;81:740–54.
8. Hardy J, Selkoe DJ. The amyloid hypothesis of Alzheimer's disease: progress and problems on the road to therapeutics. Science. 2002;297:353–6.
9. Selkoe DJ. The molecular pathology of Alzheimer's disease. Neuron. 1991;6:487–98.

10. Mawuenyega KG, Sigurdson W, Ovod V, Munsell L, Kasten T, Morris JC, et al. Decreased clearance of CNS beta-amyloid in Alzheimer's disease. Science. 2010;330:1774.
11. Reiman EM, Chen K, Liu X, Bandy D, Yu M, Lee W, et al. Fibrillar amyloid-beta burden in cognitively normal people at 3 levels of genetic risk for Alzheimer's disease. Proc Natl Acad Sci U S A. 2009;106:6820–5.
12. Castellano JM, Kim J, Stewart FR, Jiang H, DeMattos RB, Patterson BW, et al. Human apoE isoforms differentially regulate brain amyloid-beta peptide clearance. Sci Transl Med. 2011;3:89ra57.
13. Bales KR, Liu F, Wu S, Lin S, Koger D, DeLong C, et al. Human APOE isoform-dependent effects on brain beta-amyloid levels in PDAPP transgenic mice. J Neurosci : Off J Soc Neurosci. 2009;29:6771–9.
14. Cruchaga C, Kauwe JS, Nowotny P, Bales K, Pickering EH, Mayo K, et al. Cerebrospinal fluid APOE levels: an endophenotype for genetic studies for Alzheimer's disease. Hum Mol Genet. 2012;21:4558–71.
15. Riddell DR, Zhou H, Atchison K, Warwick HK, Atkinson PJ, Jefferson J, et al. Impact of apolipoprotein E (ApoE) polymorphism on brain ApoE levels. J Neurosci : Off J Soc Neurosci. 2008;28:11445–53.
16. Sullivan PM, Han B, Liu F, Mace BE, Ervin JF, Wu S, et al. Reduced levels of human apoE4 protein in an animal model of cognitive impairment. Neurobiol Aging. 2011;32:791–801.
17. Shinohara M, Petersen RC, Dickson DW, Bu G. Brain regional correlation of amyloid-beta with synapses and apolipoprotein E in non-demented individuals: potential mechanisms underlying regional vulnerability to amyloid-beta accumulation. Acta Neuropathol. 2013;125:535–47.
18. Riddell DR, Zhou H, Comery TA, Kouranova E, Lo CF, Warwick HK, et al. The LXR agonist TO901317 selectively lowers hippocampal Abeta42 and improves memory in the Tg2576 mouse model of Alzheimer's disease. Mol Cell Neurosci. 2007;34:621–8.
19. Vanmierlo T, Rutten K, Dederen J, Bloks VW, van Vark-van der Zee LC, Kuipers F, et al. Liver X receptor activation restores memory in aged AD mice without reducing amyloid. Neurobiol Aging. 2011;32:1262–72.
20. Cramer PE, Cirrito JR, Wesson DW, Lee CY, Karlo JC, Zinn AE, et al. ApoE-directed therapeutics rapidly clear beta-amyloid and reverse deficits in AD mouse models. Science. 2012;335:1503–6.
21. Pitas RE, Boyles JK, Lee SH, Foss D, Mahley RW. Astrocytes synthesize apolipoprotein E and metabolize apolipoprotein E-containing lipoproteins. Biochim Biophys Acta. 1987;917:148–61.
22. Knouff C, Hinsdale ME, Mezdour H, Altenburg MK, Watanabe M, Quarfordt SH, et al. Apo E structure determines VLDL clearance and atherosclerosis risk in mice. J Clin Invest. 1999;103:1579–86.
23. Sullivan PM, Mezdour H, Aratani Y, Knouff C, Najib J, Reddick RL, et al. Targeted replacement of the mouse apolipoprotein E gene with the common human APOE3 allele enhances diet-induced hypercholesterolemia and atherosclerosis. J Biol Chem. 1997;272:17972–80.
24. Sullivan PM, Mezdour H, Quarfordt SH, Maeda N. Type III hyperlipoproteinemia and spontaneous atherosclerosis in mice resulting from gene replacement of mouse Apoe with human Apoe*2. J Clin Invest. 1998;102:130–5.
25. Xu PT, Schmechel D, Rothrock-Christian T, Burkhart DS, Qiu HL, Popko B, et al. Human apolipoprotein E2, E3, and E4 isoform-specific transgenic mice: human-like pattern of glial and neuronal immunoreactivity in central nervous system not observed in wild-type mice. Neurobiol Dis. 1996;3:229–45.
26. Passini MA, Wolfe JH. Widespread gene delivery and structure-specific patterns of expression in the brain after intraventricular injections of neonatal mice with an adeno-associated virus vector. J Virol. 2001;75:12382–92.
27. Kim JY, Ash RT, Ceballos-Diaz C, Levites Y, Golde TE, Smirnakis SM, et al. Viral transduction of the neonatal brain delivers controllable genetic mosaicism for visualising and manipulating neuronal circuits in vivo. Eur J Neurosci. 2013;37:1203–20.
28. Chakrabarty P, Rosario A, Cruz P, Siemienski Z, Ceballos-Diaz C, Crosby K, et al. Capsid serotype and timing of injection determines AAV transduction in the neonatal mice brain. PLoS One. 2013;8:e67680.
29. Hanson AJ, Bayer-Carter JL, Green PS, Montine TJ, Wilkinson CW, Baker LD, et al. Effect of apolipoprotein E genotype and diet on apolipoprotein E lipidation and amyloid peptides: randomized clinical trial. JAMA Neurol. 2013;70:972–80.
30. Youmans KL, Tai LM, Nwabuisi-Heath E, Jungbauer L, Kanekiyo T, Gan M, et al. APOE4-specific changes in Abeta accumulation in a new transgenic mouse model of Alzheimer disease. J Biol Chem. 2012;287:41774–86.
31. Tai LM, Bilousova T, Jungbauer L, Roeske SK, Youmans KL, Yu C, et al. Levels of soluble apolipoprotein E/amyloid-beta (Abeta) complex are reduced and oligomeric Abeta increased with APOE4 and Alzheimer disease in a transgenic mouse model and human samples. J Biol Chem. 2013;288:5914–26.
32. Deane R, Sagare A, Hamm K, Parisi M, Lane S, Finn MB, et al. apoE isoform-specific disruption of amyloid beta peptide clearance from mouse brain. J Clin Invest. 2008;118:4002–13.
33. Roses AD. Apolipoprotein E alleles as risk factors in Alzheimer's disease. Annu Rev Med. 1996;47:387–400.
34. Bertram L, Tanzi RE. The genetic epidemiology of neurodegenerative disease. J Clin Invest. 2005;115:1449–57.
35. Holtzman DM, Bales KR, Tenkova T, Fagan AM, Parsadanian M, Sartorius LJ, et al. Apolipoprotein E isoform-dependent amyloid deposition and neuritic degeneration in a mouse model of Alzheimer's disease. Proc Natl Acad Sci U S A. 2000;97:2892–7.
36. DeMattos RB, Cirrito JR, Parsadanian M, May PC, O'Dell MA, Taylor JW, et al. ApoE and clusterin cooperatively suppress Abeta levels and deposition: evidence that ApoE regulates extracellular Abeta metabolism in vivo. Neuron. 2004;41:193–202.
37. Holtzman DM, Bales KR, Wu S, Bhat P, Parsadanian M, Fagan AM, et al. Expression of human apolipoprotein E reduces amyloid-beta deposition in a mouse model of Alzheimer's disease. J Clin Invest. 1999;103:R15–21.
38. Fagan AM, Watson M, Parsadanian M, Bales KR, Paul SM, Holtzman DM. Human and murine ApoE markedly alters A beta metabolism before and after plaque formation in a mouse model of Alzheimer's disease. Neurobiol Dis. 2002;9:305–18.
39. Hudry E, Dashkoff J, Roe AD, Takeda S, Koffie RM, Hashimoto T, et al. Gene transfer of human Apoe isoforms results in differential modulation of amyloid deposition and neurotoxicity in mouse brain. Sci Transl Med. 2013;5:212ra161.
40. Hatters DM, Peters-Libeu CA, Weisgraber KH. Apolipoprotein E structure: insights into function. Trends Biochem Sci. 2006;31:445–54.
41. LaDu MJ, Lukens JR, Reardon CA, Getz GS. Association of human, rat, and rabbit apolipoprotein E with beta-amyloid. J Neurosci Res. 1997;49:9–18.
42. Tai LM, Mehra S, Shete V, Estus S, Rebeck GW, Bu G, et al. Soluble apoE/Abeta complex: mechanism and therapeutic target for APOE4-induced AD risk. Mol Neurodegener. 2014;9:2.
43. Bell RD, Sagare AP, Friedman AE, Bedi GS, Holtzman DM, Deane R, et al. Transport pathways for clearance of human Alzheimer's amyloid beta-peptide and apolipoproteins E and J in the mouse central nervous system. J Cereb blood Flow Metab : Off J Int Soc Cereb Blood Flow Metab. 2007;27:909–18.
44. Donkin JJ, Stukas S, Hirsch-Reinshagen V, Namjoshi D, Wilkinson A, May S, et al. ATP-binding cassette transporter A1 mediates the beneficial effects of the liver X receptor agonist GW3965 on object recognition memory and amyloid burden in amyloid precursor protein/presenilin 1 mice. J Biol Chem. 2010;285:34144–54.
45. Jiang Q, Lee CY, Mandrekar S, Wilkinson B, Cramer P, Zelcer N, et al. ApoE promotes the proteolytic degradation of Abeta. Neuron. 2008;58:681–93.
46. Hatters DM, Zhong N, Rutenber E, Weisgraber KH. Amino-terminal domain stability mediates apolipoprotein E aggregation into neurotoxic fibrils. J Mol Biol. 2006;361:932–44.
47. Fitz NF, Cronican AA, Saleem M, Fauq AH, Chapman R, Lefterov I, et al. Abca1 deficiency affects Alzheimer's disease-like phenotype in human ApoE4 but not in ApoE3-targeted replacement mice. J Neurosci : Off J Soc Neurosci. 2012;32:13125–36.
48. Zolotukhin S, Potter M, Zolotukhin I, Sakai Y, Loiler S, Fraites Jr TJ, et al. Production and purification of serotype 1, 2, and 5 recombinant adeno-associated viral vectors. Methods. 2002;28:158–67.
49. Chakrabarty P, Ceballos-Diaz C, Beccard A, Janus C, Dickson D, Golde TE, et al. IFN-gamma promotes complement expression and attenuates amyloid plaque deposition in amyloid beta precursor protein transgenic mice. J Immunol. 2010;184:5333–43.
50. Das P, Verbeeck C, Minter L, Chakrabarty P, Felsenstein K, Kukar T, et al. Transient pharmacologic lowering of Abeta production prior to deposition results in sustained reduction of amyloid plaque pathology. Mol Neurodegener. 2012;7:39.

Molecular Therapy
Methods & Clinical Development
Original Article

Efficient Gene Transfer to the Central Nervous System by Single-Stranded Anc80L65

Eloise Hudry,[1] Eva Andres-Mateos,[2,3] Eli P. Lerner,[1] Adrienn Volak,[4] Olivia Cohen,[1] Bradley T. Hyman,[1] Casey A. Maguire,[4] and Luk H. Vandenberghe[2,3,5,6]

[1]MassGeneral Institute for Neurodegenerative Disease, Massachusetts General Hospital and Harvard Medical School, Charlestown, MA 02129, USA; [2]Grousbeck Gene Therapy Center, Schepens Eye Research Institute and Massachusetts Eye and Ear Infirmary, Boston, MA 02114, USA; [3]Ocular Genomics Institute, Department of Ophthalmology, Harvard Medical School, Boston, MA 02114, USA; [4]Department of Neurology, The Massachusetts General Hospital and NeuroDiscovery Center, Harvard Medical School, Boston, MA 02114, USA; [5]Harvard Stem Cell Institute, Harvard University, Cambridge, MA 02138, USA; [6]The Broad Institute of Harvard and MIT, Cambridge, MA 02142, USA

Adeno-associated viral vectors (AAVs) have demonstrated potential in applications for neurologic disorders, and the discovery that some AAVs can cross the blood-brain barrier (BBB) after intravenous injection has further expanded these opportunities for non-invasive brain delivery. Anc80L65, a novel AAV capsid designed from *in silico* reconstruction of the viral evolutionary lineage, has previously demonstrated robust transduction capabilities after local delivery in various tissues such as liver, retina, or cochlea, compared with conventional AAVs. Here, we compared the transduction efficacy of Anc80L65 with conventional AAV9 in the CNS after intravenous, intracerebroventricular (i.c.v.), or intraparenchymal injections. Anc80L65 was more potent at targeting the brain and spinal cord after intravenous injection than AAV9, and mostly transduced astrocytes and a wide range of neuronal subpopulations. Although the efficacy of Anc80L65 and AAV9 is similar after direct intraparenchymal injection in the striatum, Anc80L65's diffusion throughout the CNS was more extensive than AAV9 after i.c.v. infusion, leading to widespread *EGFP* expression in the cerebellum. These findings demonstrate that Anc80L65 is a highly efficient gene transfer vector for the murine CNS. Systemic injection of Anc80L65 leads to notable expression in the CNS that does not rely on a self-complementary genome. These data warrant further testing in larger animal models.

INTRODUCTION

Adeno-associated viral vectors (AAVs) are considered a vector of choice for *in vivo* gene transfer for various tissues based on an overall attractive safety profile preclinically and clinically. Indeed, AAV is not directly associated with any disease, minimally pro-inflammatory, demonstrates promiscuous tropism for many therapeutic cell and tissue targets, and its genome is stably maintained episomally yet transcriptionally active in the cell nucleus in non-dividing cells.[1–4] These properties have contributed to demonstrations of long-lasting steady-state expression (up to 10 years at least in humans[5]). Data from animal models have shown that AAV can lead to significant therapeutic benefit in inherited,[6–8] acquired,[9–13] and even infectious[14–17] diseases. Excitingly, encouraging results have also been reported in a handful of early-stage clinical trials (phase I/II), such as a dramatically reduced need for protein prophylaxis in hemophilia A and B,[18–20] and remarkable impact on lifespan, motor function, and overall disease in the most severe form of spinal muscular atrophy.[21,22] In January 2018, the first AAV product, voretigene neparvovec, was approved by the Food and Drug Administration (FDA) for the treatment of a form of inherited retinal degeneration.[23]

The ability of AAVs to transduce post-mitotic cells and their strong neuronal tropism has naturally promoted their use in the field of neurosciences, not only for therapeutic purposes, but also as experimental tools to express genetically encoded reporters to interrogate the basic mechanisms underlying neuronal function or brain connectivity.[24–31] In most cases, direct intraparenchymal injection allows to bypass the blood-brain barrier (BBB) and precisely manipulate gene expression with time and spatial resolution, a strategy that has been associated with clinical improvement in many pathological contexts, ranging from neurodevelopmental[32–35] diseases to psychiatric[36,37] or age-related neurodegenerative disorders.[1,38–42] Interestingly, the recent characterization of AAV serotypes able to transduce the CNS after a single intravenous injection in adult mice now offers a non-invasive vector delivery route for the entire neural tissue and the possibility to evaluate the impact of therapeutic candidates for multi-focal neurological disorders.[43–47] Although this approach constitutes a breakthrough for the field, several issues remain when AAV is administered

Received 23 December 2017; accepted 10 July 2018;
https://doi.org/10.1016/j.omtm.2018.07.006.

Correspondence: Luk H. Vandenberghe, PhD, Grousbeck Gene Therapy Center, Schepens Eye Research Institute and Massachusetts Eye and Ear Infirmary, 20 Staniford Street, Boston, MA 02114, USA.
E-mail: luk_vandenberghe@meei.harvard.edu

This is an open access article under the CC BY-NC-ND license (http://creativecommons.org/licenses/by-nc-nd/4.0/).

peripherally for clinical or basic research applications: first, efficient CNS transduction in preclinical models is often conditional to the use of a self-complementary (sc) genome (e.g., AAV9), which greatly limits the insert capacity of the vector (<2.3 kb as opposed to 4.7 kb for single-stranded AAV);[47–51] second, the presence of AAV neutralizing antibodies in human populations where natural AAV infections occur in 30%–90% of individuals can dramatically inhibit the efficacy of gene transfer by systemic delivery;[48,52] and third, ectopic expression of the transgene in peripheral tissues may lead to unwanted side effects (a problem that can be limited by using neural cell-type-specific promoters[53,54]). To overcome those issues, developing novel AAVs that will retain their potential for crossing the BBB, lead to sustained transgene expression from a single-stranded genome, and limit pre-existing immunity is required.

In the present study, we characterized the efficacy and transduction profile of Anc80L65 harboring a single-stranded genome in the CNS, thus preserving the full DNA insert capacity of the vector. As opposed to other AAVs, this relatively novel vector system was designed *in silico* based on ancestral sequence reconstruction with sequence information from natural AAVs, with the primary goal to develop a stable and functional AAV variant, yet serologically and immunologically very distinct from AAVs currently circulating in humans.[55] Anc80L65 had not previously been characterized for CNS targeting, yet has shown remarkable transduction in the anterior segment of the eye,[56] retina,[56,57] and cochlea[58–60] following local injections. We therefore wanted to evaluate Anc80L65 in its ability to target CNS after intravenous, intraparenchymal, and intracerebroventricular routes of delivery. Combining two different reporter approaches by bioluminescence (Firefly luciferase [FLuc]) or fluorescence (EGFP), we demonstrated that a single injection of Anc80L65 into the lateral tail vein of adult immunocompetent mice led to sustained transduction of the entire CNS. Importantly, Anc80L65 largely outperformed the capabilities of AAV9 to target the nervous system and increased the percentage of transduced neurons and astrocytes by a factor 3 and 4.3, respectively. Although this performance remained lower when compared with peripherally delivered AAV9 carrying an sc genome (scAAV9, which is the current configuration used in current clinical trials), the increased transduction capabilities of Anc80L65 will offer novel opportunities to expand the repertoire of therapeutic genes evaluated after systemic delivery. When delivered directly into the brain parenchyma (striatum) or in the lateral cerebral ventricle, less pronounced differences were observed between Anc80L65 and AAV9, even though Anc80L65 further spreads after intracerebroventricular (i.c.v.) injection. Considering the efficient expression of reporter genes in neurons and astrocytes in mice after systemic administration of Anc80L65 carrying a single-stranded genome, this vector is a useful tool for delivery of transgenes in the CNS without the need for packaging an sc genome (which restricts the cloning capacity of the vector by half). These encouraging findings warrant further study of Anc80L65 in larger animal models to evaluate it as a potential candidate for clinical applications.

RESULTS

Bioluminescence Imaging Reveals Higher Signal of Head Region of Mice Systemically Injected with Anc80L65 Encoding FLuc Compared with AAV9-FLuc Vector

To analyze the biodistribution and bodywide transduction pattern of peripherally delivered Anc80L65, we injected in a pilot study BALB/c female mice (n = 5, age 6–8 weeks) via the tail vein with 2×10^{12} genome copies (gc)/kg (5×10^{10} gc/25 g mouse) of Anc80L65 encoding FLuc driven by the cytomegalovirus (CMV) promoter (described in detail in the Materials and Methods). This combination of promoter and transgene allowed for a versatile and highly sensitive evaluation of expression at a moderate dose of vector delivered systemically. For comparison, AAV9 vector carrying the same transgene expression cassette was injected into a separate group of mice (n = 5). Mice were imaged for FLuc-mediated bioluminescence after D-luciferin substrate injection on days 3, 7, 21, and 42 after vector injection (Figures S1 and S2). We observed a remarkably high signal emanating from the liver region at day 3 post-injection in the Anc80L65 group, which was on average 123-fold higher than the AAV9 group at this time point. Signal declined slightly for the Anc80L65 group at day 7 and stabilized for the remaining time points. In contrast, bioluminescent signal from AAV9-FLuc-injected mice increased by 3.7-fold between days 3 and 7 before stabilizing for the remainder of the examined time points (Figure S1A). Interestingly, we also observed a robust bioluminescent signal in the head region of Anc80L65-injected mice (Figure S1B). At day 3, Anc80L65-FLuc-injected mice had an 8.3-fold higher signal from the head region than AAV9-FLuc-injected mice. This enhancement peaked at day 21 with a 34-fold higher signal in the Anc80L65 groups over the AAV9 group. Both groups had an overall slow increase in bioluminescence from days 3 to 42. The bioluminescence data from this pilot study suggested that Anc80L65 might transduce the brain after intravenous (i.v.) delivery; a subsequent study was therefore designed to determine cell-specific transduction properties in the CNS using AAVs that encoded a fluorescent reporter, EGFP, and based on the literature and prior experience, injected at a higher dose in order to obtain sufficient sensitivity to determine cell-intrinsic expression.

Anc80L65 Broadly Transduces the CNS after Systemic Infusion, and Mostly Targets Neurons and Astrocytes in the Brain

In order to get a better understanding of the transduction properties of Anc80L65 in the CNS at a cellular level, another cohort of animals was injected in the lateral tail vein with a vector encoding the EGFP reporter. Due to the relative lack of sensitivity of immunostaining compared with bioluminescence imaging, we infused a higher dose of 4×10^{13} gc/kg (1×10^{12} gc for a 25-g mouse) of Anc80L65-CMV-EGFP and AAV9-CMV-EGFP. We also included a group of mice injected with sc AAV9 (scAAV9) at equal dose as a positive control benchmark because scAAV9 is the current vector of choice used for peripheral approaches in clinical trials[22] and has been previously reported to show a much higher transgene expression as opposed to single-stranded AAV9 via this delivery route.[61,62] The design of the sc and single-stranded (ss) transgene cassettes was

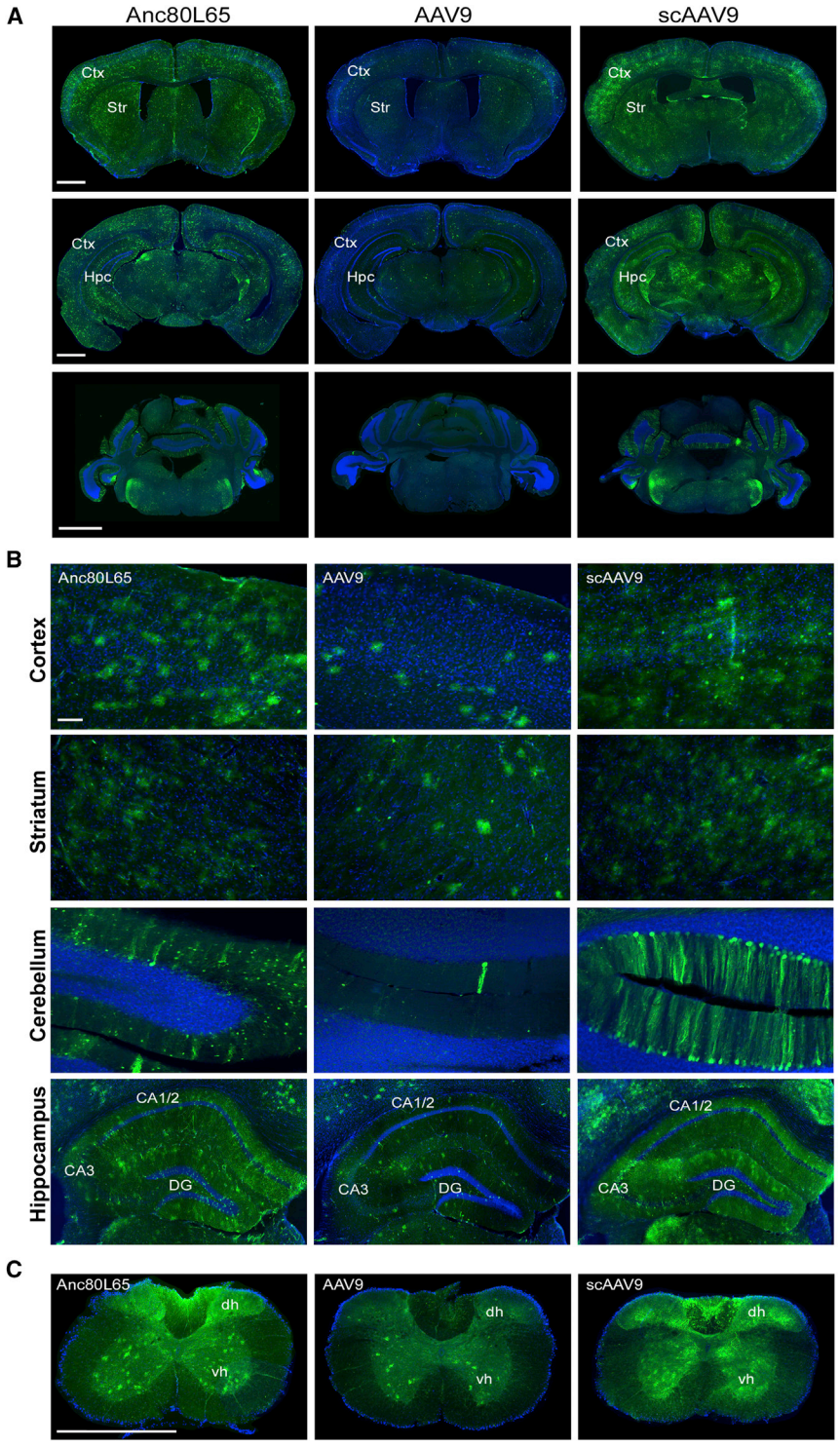


Figure 1. Anc80L65, AAV9, and scAAV9 Transduction Profiles in the CNS after Intravenous Injection

(A) Representative images of EGFP fluorescence signal (and DAPI) across three different coronal sections across the brain: at the level of the striatum (upper panels), hippocampus (middle panels), or cerebellum (bottom panels) after intravenous injection of the same dose of Anc80L65, AAV9, and scAAV9 harboring a self-complementary genome in wild-type mice (4×10^{13} gc/kg). Scale bars: 1,000 μm. (B) A closer view of each section reveals numerous EGFP-positive cells in the cortex (ctx), striatum (str), cerebellum, and hippocampus (hpc) after Anc80L65 infusion. The overall distribution of transduced cells was similar for both AAV9 and scAAV9. Scale bar: 100 μm. (C) Within the spinal cord, AAV transduced cells could be observed in the ventral (vh) and dorsal (dh) horns as well. Scale bar: 500 μm.

made identical to allow for comparability (Figure S6). The number of cells with EGFP signal after Anc80L65 i.v. injection was strikingly higher than AAV9 (lowest EGFP signal), yet lower than scAAV9 (highest EGFP signal), and spread across the entire cerebral tissue (Figure 1A). Cortex, striatum, hippocampus, and cerebellum were homogeneously transduced (Figure 1B), and the distribution of EGFP-positive cells was not significantly different between each vector, even though their overall density varied. Anc80L65 also led to transduction in the spinal cord, again with an intermediate level between single-stranded and sc AAV9 (Figure 1C). These data confirmed our previous observations using the Luciferase reporter system and demonstrated that Anc80L65 can efficiently cross the BBB after peripheral delivery and target the neural tissue. To evaluate the biodistribution of Anc80L65, AAV9, and scAAV9 in peripheral organs after systemic delivery, we determined the number of AAV gc by qPCR in liver, heart, quadriceps, and diaphragm. Anc80L65 led to an intermediate level of vector gc as compared with single-stranded (lowest level of gc/diploid cell) and sc (highest level of gc/diploid cell) AAV9 (Figure S3). Those results suggest that, even though Anc80L65 generally showed a better transduction efficacy as opposed to AAV9, the overall biodistribution of both vectors is not drastically different (as previously reported in our initial characterization of Anc80L65[55]).

In order to characterize which neural cell types were primarily transduced by each AAV after peripheral delivery, we performed co-immunostaining between EGFP and molecular markers of neurons (neuronal nuclei [NeuN]), astrocytes (glutamine synthetase [GS]), microglia (Iba-1), and oligodendrocytes (Olig2). As shown in Figure 2, astrocytes and neurons were transduced by all three AAVs, with different rates of efficacy. Additionally, intraparenchymal

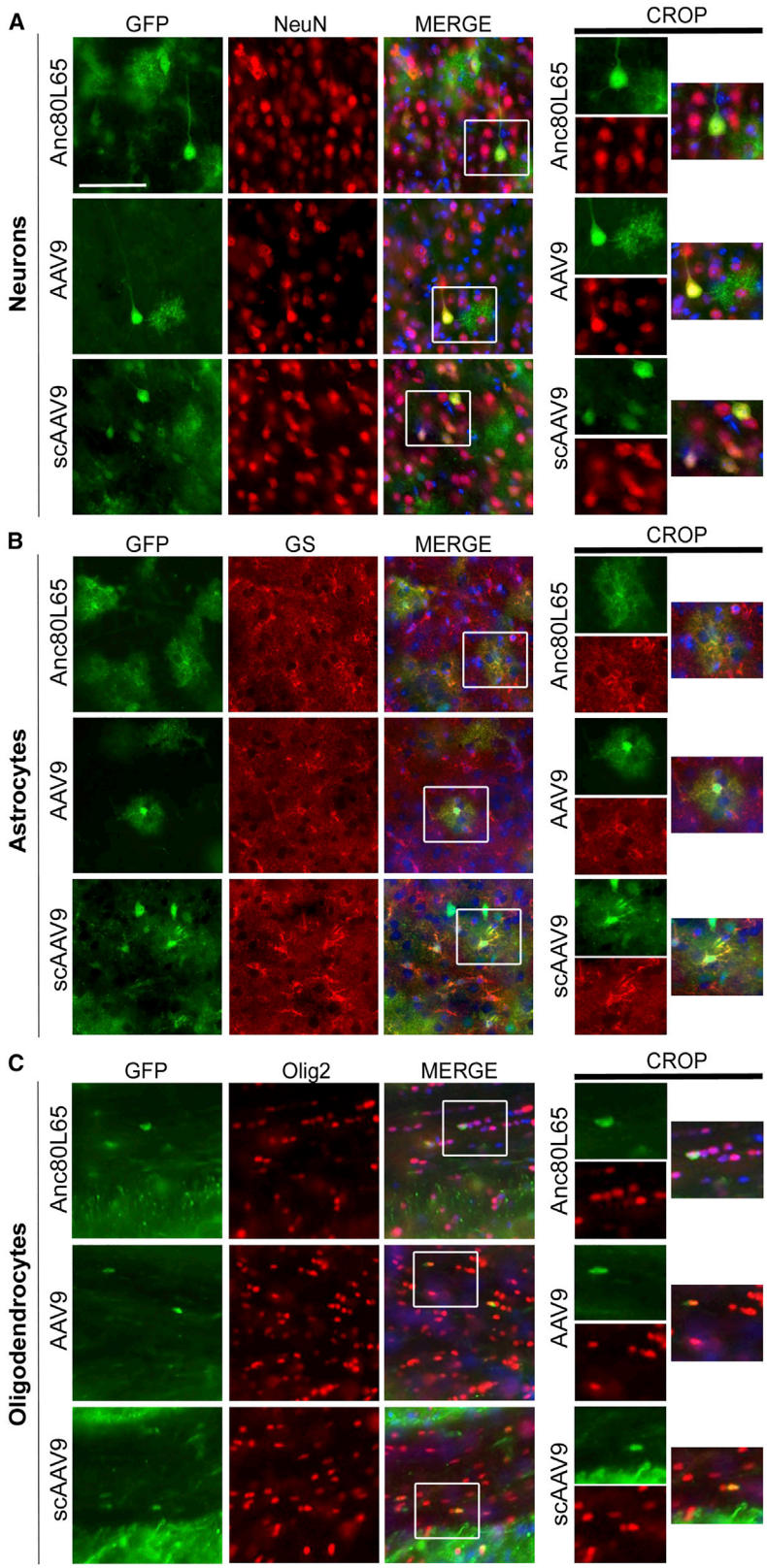


Figure 2. Identification of the Different Neural Cell Types Transduced by Peripherally Administered Anc80L65, AAV9, and scAAV9 Harboring a Self-Complementary Genome

Double immunostainings were performed in order to determine the main neural cell types transduced by each vector. Colocalization between EGFP and NeuN (neuronal nuclei) (A), or EGFP and GS (glutamine synthetase) (B) suggest that neurons and astrocytes are mostly targeted by Anc80L65, AAV9, and scAAV9 delivered intravenously. (C) In the corpus callosum, few oligodendrocytes (identified by the marker Olig2) expressing EGFP were also detected. Higher magnification images of individual cells are presented on the right panels for each cell type. By contrast, no transduced microglial cells (Figure S4) were observed. Scale bar: 50 μm.

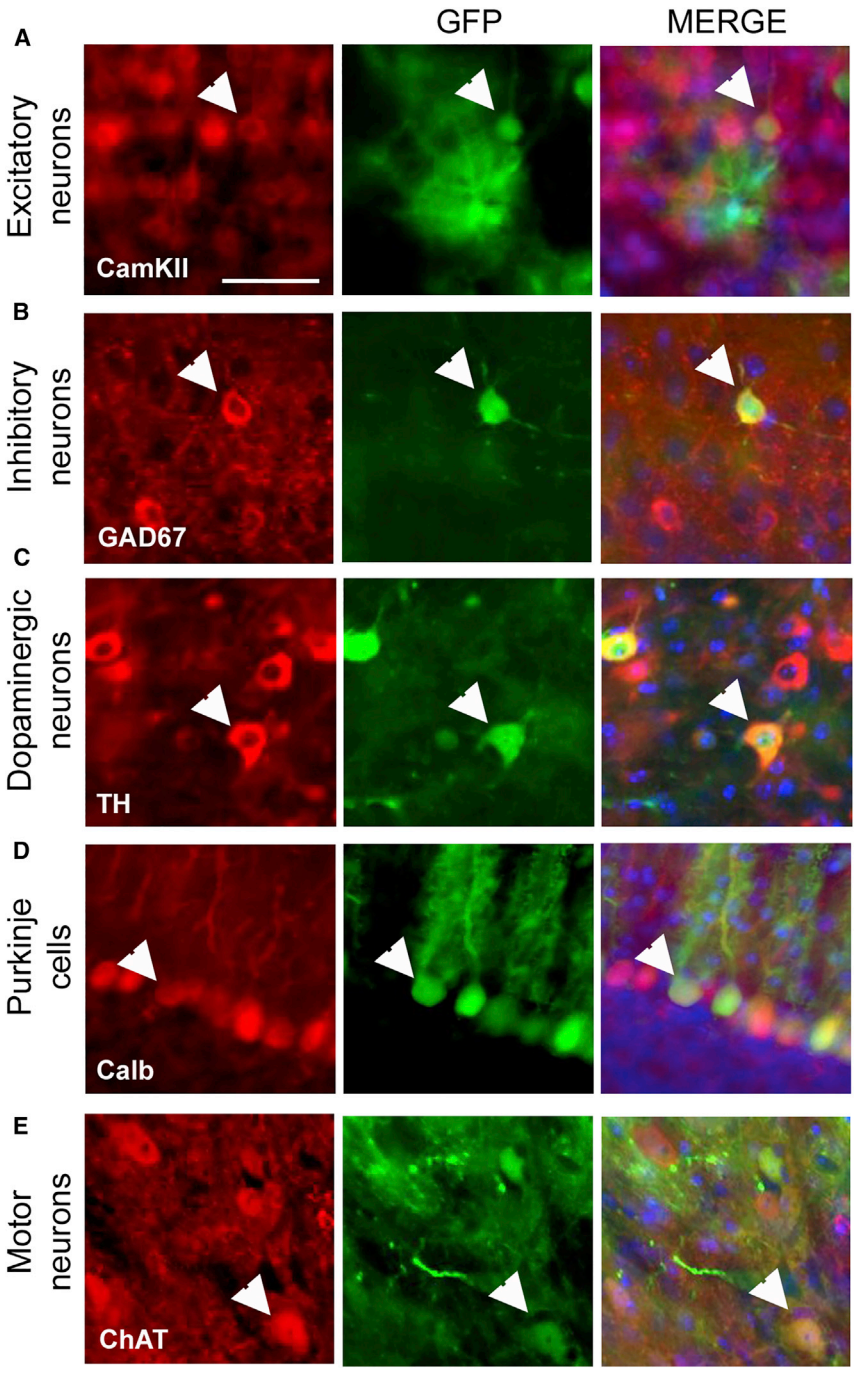


Figure 3. Neuronal Sub-types Targeted by Anc80L65 after Peripheral Injection

Representative images of co-labeling experiments performed to characterize the neuronal sub-types transduced by Anc80L65 (double-positive cells are indicated by white arrows). The colocalization between EGFP with CaMKII (A) or GAD67 (B) markers demonstrates efficient targeting of excitatory and inhibitory neurons, respectively. (C) Interestingly, EGFP/tyrosine hydroxylase (TH)-positive dopaminergic neurons were also observed in the substantia nigra. (D) In the cerebellum, numerous Purkinje cells, identified with the marker Calbindin, express EGFP. (E) In the spinal cord, EGFP-positive motor neurons expressing the choline acetyltransferase (ChAT) were observed. Scale bar: 50 μm.

astrocytes, as well as astrocytic endfeet, were evenly transduced (Figure S4), suggesting that the proximity of astrocytes to blood vessels was not directly correlated with a higher probability of transduction, but that other mechanisms are in play. Seldom EGFP-positive oligodendrocytes were detected, and they were predominantly found in the corpus callosum (Figure 2C). There were virtually no Iba1-positive transduced cells found, indicating that none of the vectors were able to target microglial cells (Figure S5).

To further characterize the neuronal sub-types targeted by Anc80L65-CMV-EGFP after peripheral infusion, we performed additional immunolabeling for specific markers of excitatory neurons (Ca^{2+}/calmodulin-dependent protein kinase II [CaMKII]), inhibitory neurons (glutamate decarboxylase [GAD67]), dopaminergic neurons (tyrosine hydroxylase [TH]), Purkinje cells (calbindin), and motor neurons (choline acetyltransferase [ChAT]), all co-stained for EGFP (Figure 3). In the cortex and hippocampus, a majority of pyramidal excitatory neurons were transduced after i.v. injection of Anc80L65 (Figure 3A), while comparatively fewer inhibitory neurons were detected (Figure 3B). Dopaminergic EGFP-positive neurons in the substantia nigra (Figure 3C), as well as EGFP-positive Purkinje cells in the cerebellum, were numerous (Figure 3D), whereas ChAT/EGFP double-positive cells confirmed that Anc80L65 was also able to target motor neurons (Figure 3E). Overall, those results demonstrate that Anc80L65 efficiently transduces several neuronal sub-types, as well as astrocytes, after systemic injection.

Anc80L65 Transduces Neurons and Astrocytes with a Greater Efficacy Compared with AAV9 after i.v. Delivery When Both Vectors Harbor a Single-Stranded Genome

In order to have a quantitative evaluation of the gene transfer efficacy after i.v. injection of Anc80L65, AAV9, and sc AAV9, we performed in the cortex an unbiased stereological analysis of the percentages of transduced astrocytes and neurons, respectively, identified by the markers GS and NeuN. We quantified the density of EGFP/GS or EGFP/NeuN double-positive cells among the total number of astrocytes or neurons after random sampling of the cortical mantle. We observed that a single injection of Anc80L65 led to the transduction of 6.8% ± 1.3% of neurons and 26.7% ± 5.3% of astrocytes in the cortical mantle, which was significantly higher than AAV9

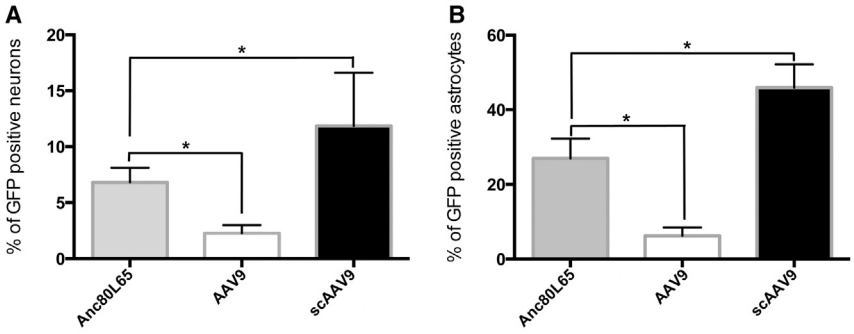


Figure 4. Stereology-Based Quantification of the Percentages of Transduced Neurons and Astrocytes after Peripheral Delivery of Anc80L65, AAV9, and scAAV9 (4×10^{13} gc/kg)

C57BL/6 mice were sacrificed 4 weeks after intravenous injection of Anc80L65, AAV9, or scAAV9. To evaluate the percentage of neuronal transduction, an unbiased stereological analysis of the total number of neurons (identified using the NeuN marker) or astrocytes (identified using the GS marker) and of the total number of NeuN/EGFP and GS/EGFP double-positive cells was achieved by random sampling of the cortex. The percentage of neurons (A) and astrocytes (B) expressing EGFP after transduction by Anc80L65 reached an intermediate level when compared with AAV9 and scAAV9. n = 4 mice per group (two sections analyzed per mouse); non-parametric one-way ANOVA (Kruskal-Wallis test) followed by Dunn's multiple comparison test; *$p < 0.05$. Data are represented as the mean with SD.

(2.3% ± 0.7% and 6.2% ± 2.3%, respectively), but did not reach the levels of sc AAV9 (11.9% ± 4.7% and 45.9% ± 6.2%, respectively; $p < 0.05$, Kruskal-Wallis test followed by a Dunn's multiple comparisons; Figure 4). These results demonstrate that Anc80L65 is advantageous compared with AAV9 when using a single-stranded vector, allowing efficient delivery of transgenes to the CNS after i.v. delivery while preserving the full cloning capacity of AAV.

Direct Intracerebral Injection of Anc80L65 in the Striatum or the Cerebroventricular Space Leads to Widespread Expression of Transgene

While systemic delivery is non-invasive and can lead to transduction of most of the neural tissue at once, targeted intracerebral injections can also offer advantages in certain pathological contexts characterized by focal alteration of the nervous system, achieve clinical efficacy with a much lower dose of vector, and avoid ectopic expression of a specific gene in the periphery. We therefore assessed the performance of Anc80L65 transduction after intrastriatal or intracerebroventricular injections in comparison with conventional AAV9 (both harboring identical single-stranded genomes).

Anc80L65 and AAV9 direct injection profiles in the striatum were rather comparable (Figure 5). Both vectors efficiently transduced the entire region of interest and showed a preferential tropism for neurons as opposed to astrocytes (Figure 5B), in direct contrast with the results observed after i.v. delivery. Injection of Anc80L65 or AAV9 in the lateral ventricle led to more contrasted results (Figure 6), with Anc80L65 showing a higher efficacy at targeting the choroid plexus (Figure 6B) and leading to a much wider transduction pattern as compared with AAV9. In particular, a large number of EGFP-positive Purkinje cells could be detected in the cerebellum, whereas these were seldom detected after AAV9 injection (Figure 6A).

DISCUSSION

Remarkable progress in the field of gene therapy has been made with AAV technologies. Over the past few years, the diversity of the available AAV library has been greatly expanded; initial studies further explored the AAV biodiversity, others modified natural variants rationally, and a third set of strategies that has been a great emphasis of the vector development field has been to leverage methods of library selection via directed evolution.[2,63,64] AAV9 was isolated from a latent viral genome in human tissue by sensitive PCR methods.[65] Anc80L65, on the other hand, was entirely designed *in silico* based on statistical inferences of the putative ancestral sequence state within the primate AAV lineage.[55] Transduction properties in neurosensory targets such as the retina[56] and inner ear[58–60] illustrated its potential for neuronal targeting. Additionally, we observed a low level of cross-reactivity between Anc80L65 and conventional serotypes available, likely because of its significant sequence and structural divergence from the closest AAV sequence rh.10 by 8.6%, an important feature considering that pre-existing immunity against AAV can significantly reduce its efficacy.[66,67]

In order to further characterize this novel variant, the present work specifically studied the transduction capabilities of Anc80L65 in the CNS as compared with AAV9 after i.v., intracerebroventricular, or intrastriatal infusion in adult mice. Of importance, it is conceivable that an sc genome packaged in Anc80L65 would have led to greater performances, because it is the case for conventional AAV9. However, the current study essentially aimed at investigating the transduction capabilities of Anc80L65 based upon the unique characteristics of the capsid of the vector as an ssAAV that preserves the full cloning capacity of AAV, and thereby increases dramatically the number of applications of the technology. In this context, it is important to note that ssAAV genomes at low efficiency are able to package dimeric (analogous to sc) genomes, a phenomenon that is favored for genomes close to or less than 50% of AAV *wild-type* packaging size (Figure S6). While the relative level and contribution in transduction of this dimeric species in the ssAnc80L65 and ssAAV9 is expected to be similar, it was not empirically determined in the current study.

One of the most appealing features of AAV vectors is their ability to transduce non-dividing cells and their excellent neuronal tropism, which make them a tool of choice to study and manipulate brain circuitry or to express therapeutic genes in various neurological contexts.[1,24,25,27–29,31] Often, a strategy by direct intraparenchymal

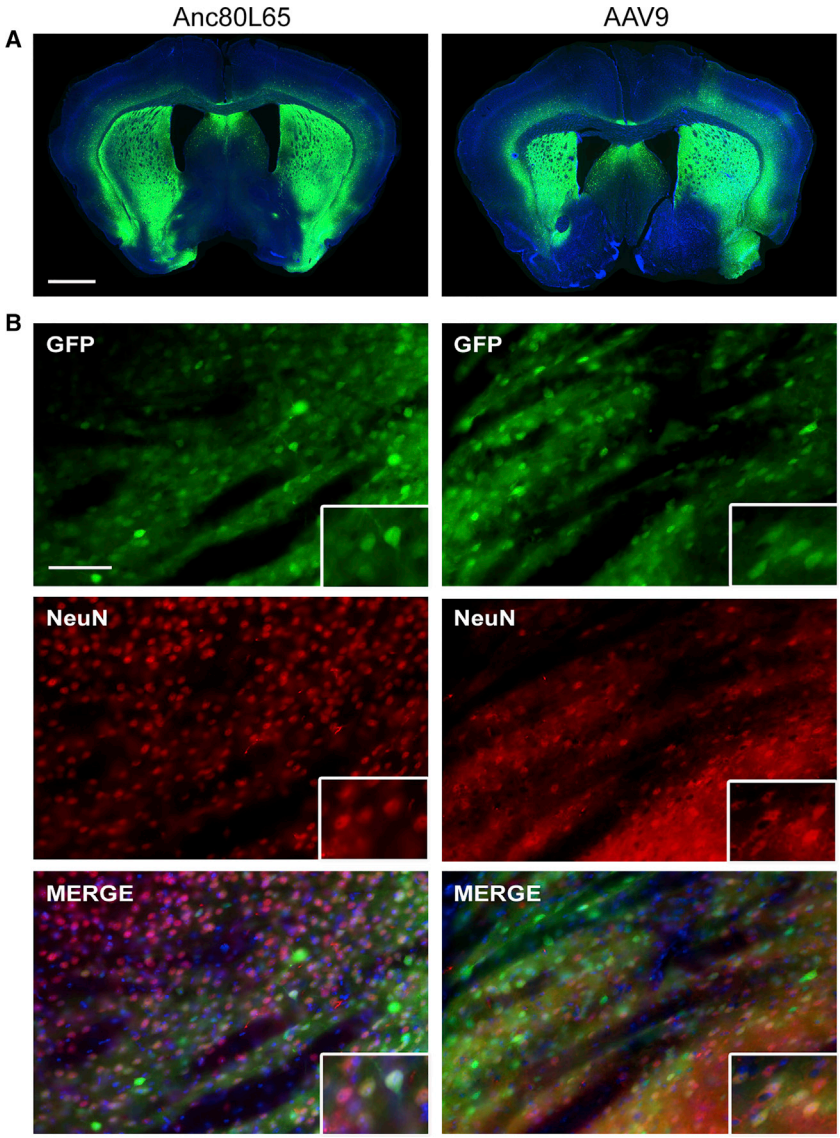


Figure 5. Sustained Neuronal Transduction after Direct Intrastriatal Injection of Anc80L65 and AAV9

(A) Representative images of EGFP fluorescence signal (and DAPI) across the striatum after direct intraparenchymal injection of Anc80L65 or AAV9 (1.5×10^{10} gc/injection site). Scale bar: 1,000 μm. (B) Higher magnification images of the striatum reveal that neurons were mostly transduced with this route of delivery, as demonstrated by the colocalization between EGFP and NeuN. Scale bar: 100 μm.

infusion is chosen to target specific brain regions, and we observed that either direct intraparenchymal or intracerebroventricular injections of Anc80L65 potently transduced neurons and astrocytes in the brain, with similar efficacy as conventional AAV9. Interestingly, i.c.v. delivery of Anc80L65 led to a broader diffusion of the vector than AAV9, extending to the cerebellum. Additionally, a particularly strong tropism for the choroid plexus and the ependymal cells was observed, a feature that may be very valuable for the treatment of specific neurological disorders such as Batten disease[32], spinal muscular atrophy,[68] metachromatic leukodystrophy,[69] mucopolysaccharidosis type IIIA,[70] or Alzheimer's disease.[41] Although strategies by direct intracerebral injection have proven valuable, they still involve moderately invasive surgical procedures that may not become easily translatable to a large number of patients and may not be suitable to impact diffuse neuropathological processes. The discovery that AAV9[47] and several other serotypes (AAVrh.10, AAVrh.39, AAVrh.43, AAV9, and AAV7[46,71]) can cross the blood-brain barrier after systemic infusion and achieve spread transduction of the CNS after minimally invasive surgical procedures has opened novel research avenues in the field of neurosciences. Remarkable benefit has already been demonstrated using i.v. delivery of AAV in multiple animal models,[21,44,72–74] and a first clinical trial has been approved by the FDA to use systemic delivery of AAV9 for the treatment of infantile spinal muscular atrophy type 1.[22] Considering that Anc80L65 is the predicted synthetic ancestor of AAV serotypes 1, 2, 8, and 9, we hypothesized that it may also cross the BBB. Indeed, although the difference in transduction efficacy was minimal after intraparenchymal or intracerebroventricular injections (implying that the steps of receptor-mediated entry, intracellular trafficking, endosomal escape, and intranuclear transport were comparable between Anc80L65 and AAV9), our results demonstrate that peripherally administered Anc80L65 efficiently targets the neural tissue, with an order of magnitude above conventional AAV9. However, the percentages of EGFP-positive cells remained lower when compared with AAV9 harboring an sc genome. The transduction discrepancy between single-stranded and sc AAV administered peripherally has been reported in previous studies,[48,53] an effect potentially related with the rate-limiting conversion of ssDNA to double-stranded genomic DNA, a slow process that relies on host-cell DNA synthesis and delays or impairs transduction.[61,62] By contrast, the increased capacity of Anc80L65 to target the nervous system after peripheral injection as compared with AAV9 necessarily relies on differences of the capsids, which could impact the half-life of the vector within the bloodstream and/or the capacity of the vector to cross vascular endothelial barriers and in particular the BBB. Previous studies have demonstrated that each serotype has a different half-life after systemic infusion, with AAV9 exhibiting a particularly slow blood clearance and sustained infectivity in the bloodstream (up to 24 hr).[75] Additionally, efficient transcytosis of AAV across endothelial cells, which has been demonstrated *in vitro*, could be a determinant factor for CNS gene transfer after peripheral delivery.[76] Indeed,

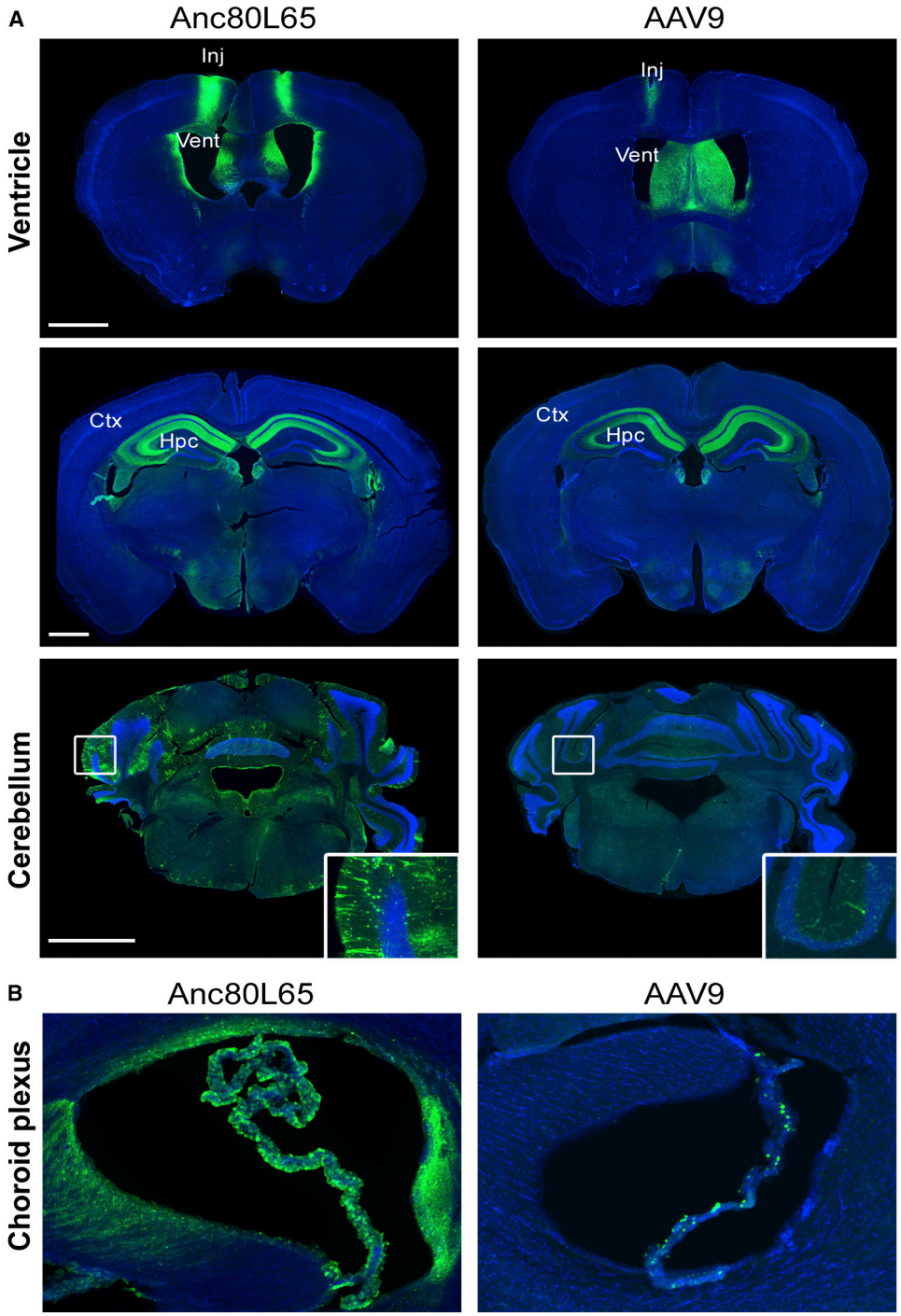


Figure 6. Widespread Diffusion of Anc80L65 as Compared with AAV9 after Intracerebroventricular Injection

(A) Representative images of the EGFP fluorescence intensity detected over three coronal sections after intracerebroventricular infusion of Anc80L65 or AAV9 (4.5×10^{10} gc/injection site). Of interest, although the signal was comparable at the level of the ventricle or in the hippocampus, Anc80L65 appeared to diffuse much more broadly as compared with AAV9, as shown by the increased EGFP fluorescence across the cerebellum. Scale bar: 1,000 μm. (B) Anc80L65 also efficiently targets the choroid plexus, whereas sparse choroid plexus transduction was observed with AAV9.

AAV9 has been shown to shuttle across brain microvascular endothelial cells (BMVECs) more efficiently than AAV2 without compromising the integrity of the BBB. By contrast, AAV2 appears to be directly endocytosed without diffusing through the BMVEC cell layer, resulting in transduction of those cells.[77] Whether those features (blood stability and transcytosis through the BBB) are potentiated with Anc80L65 remains to be determined. In any case, the high efficacy of Anc80L65 harboring a single-stranded genome to transduce the CNS after i.v. infusion makes it a very attractive option for peripheral delivery of a wide variety of genes to the brain and the spinal cord (cloning capacity for a scAAV: ~2.3 kb; for an ssAAV: 4.7kb[78]). Additionally, higher doses of Anc80L65 could be delivered to further increase its transduction efficiency in the nervous system. To date, only a few variants of AAV9 from a library-based selection (AAV-PHP.B, AAV-PHP.eB, and AAV-PHP.S) have been shown to also achieve a high level of transgene expression in the CNS after i.v. administration of recombinant virions carrying a single-stranded genome.[43,45] PHP.B, PHP.eB, and PHP.S, which were not available at the initiation of these studies, are highly potent AAVs that incorporate a peptide in a surface-exposed region of the AAV9 capsid. A library of peptides was successfully selected from a compelling *in vivo* selection strategy in order to identify potent BBB-crossing AAVs, which led to the isolation of AAV.PHP.B and other related variants.[43,45,63,79,80] One concern with orthologous strategies such as the peptide insertion in PHP.B is the risk that a particular technology is active only in the host species it was selected in. Specifically, the inserted peptide may engage a new pathway for transduction as compared with the canonical AAV pathway, which drives the enhanced BBB and CNS biology. Although it is known that the AAV uptake and tropism biology are qualitatively upheld across species (e.g., by the conservation of the AAVR entry receptor), this is not known of these orthologous pathways that AAV normally does not engage, which may impact the ability for vector technologies such as AAVR to translate across species, and eventually to humans. Indeed, a recent study by the group of James M. Wilson[81] demonstrated that AAV.PHP.B's phenotype for enhanced transduction in the CNS following i.v. injection was limited to the C57BL/6 strain in which it was originally derived. By design, Anc80L65 permutates residues on the AAV capsid that were naturally under selective pressure throughout evolution, thereby possibly skewing its transduction biology more toward conserved pathways. Further studies are required, however, to demonstrate whether Anc80L65's findings here do translate to other mouse strains and higher species.

Importantly, although i.v. infusion of Anc80L65 efficiently targeted the brain and spinal cord, very high expression in the liver was also observed (Figures S1 and S2). In fact, at day 3 post-injection, the signal emanating from the liver was 123-fold higher with Anc80L65 than AAV9. This large differential decreased to about 15-fold from day 7 on, due to a slight decrease in expression of Anc80L65 and an increase in expression from days 3 to 7 with AAV9 (Figure S1A). This observation could be partially explained by faster expression kinetics for Anc80L65 versus AAV9, although the mechanism for this is thus far unknown. The decrease of signal between days 3 and 7 in Anc80L65-FLuc-injected mice could be because of transient expression in cells other than hepatocytes (e.g., Kupffer cells, sinusoidal endothelial cells), although future studies will need to address this possibility. The high liver transduction with Anc80L65 raises three concerns when considering translation to the clinic: first, ectopic expression of a foreign protein in an organ that physiologically does not produce it can lead to unpredictable side effects; second, expression of a transgene in the periphery can promote an adverse immune reaction when the protein is initially absent, whereas targeted expression in the neural tissue (referred to as an "immunotolerant" organ) would not lead to such a reaction;[66,82] and third, AAV genotoxicity has occasionally been reported in the liver after infusion of high doses of vector.[83–85] To circumvent those issues and increase the safety of peripherally delivered AAV, strategies to restrict the expression of the transgene specifically in neural cells (using appropriate specific promoters or miRNA)[53,86–88] or to lower Anc80L65 affinity for hepatocytes (approaches known as "liver detargeting"[89]) could be implemented.

Overall, the present study emphasizes the efficacy of ssAnc80L65 as an efficient gene transfer tool to target the CNS after i.v., intracerebroventricular, and i.v. injection. Although those results further investigation of its transduction profile in other species, including non-human primates will warrant its potential as an excellent gene transfer tool.

MATERIALS AND METHODS

AAV Vector Genetic Backbone and Production

A CMV.EGFP.WPRE and CMV.EGFP.T2A.Luciferase.SVPA were cloned into an AAV2 genetic backbone. The expression cassette of the CMV.EGFP.WPRE vector genomes used to produce single-stranded AAV9, Anc80L65, and sc AAV9 (scAAV9) had exactly the same configuration (Figure S6). AAV2/9 and AAV2/Anc80L65 viral stocks were prepared and titered at the Gene Transfer Vector Core (http://vector.meei.harvard.edu) at Massachusetts Eye and Ear. AAV preparations were produced by triple-plasmid transfection as described previously.[90] In brief, large-scale polyethylenimine transfections of AAV *cis*, AAV *trans*, and adenovirus helper plasmid were performed with near-confluent monolayers of HEK293 cells. The downstream purification process was performed following protocols described previously.[90] Viral vectors were resuspended in PBS. DNase I-resistant vector genomes copies were used to titrate AAV preparations by TaqMan qPCR amplification (Applied Biosystems 7500; Life Technologies, Woburn, MA, USA) with primers and probes detecting promoter and transgene of the transgene cassette. The purity was evaluated by SDS-PAGE gel electrophoresis. AAV2/Anc80L65 plasmid reagents are available through http://www.addgene.org/.

Animals and Tail-Vein Injection

All animal experiments were approved by the Institute of Animal Care and Use Committees at the Schepens Eye Research Institute (SERI) and the Massachusetts General Hospital Subcommittee on Research Animal Care following guidelines set forth by the *NIH Guide for the Care and Use of Laboratory Animals*. BALB/c mice or

C57BL/6 females aged 6–8 weeks were purchased from Charles River Laboratories. We used BALB/c mice for *in vivo* bioluminescence imaging because white fur interferes less with the sensitivity of photon detection (compared with black fur). We used C57BL/6 for immunofluorescence detection of EGFP in brain sections because this strain has been used by our laboratory historically for this purpose. For tail-vein injections of AAV vectors, mice were placed into a restrainer (Braintree Scientific, Braintree, MA, USA). The tail was warmed in 40°C water for 30 s before wiping the tail with 70% isopropyl alcohol pads. A 200 μL volume of vector (either 2.0×10^{12} gc/kg for the bioluminescence or 4×10^{13} gc/kg for the EGFP experiments, diluted in PBS) was slowly injected into a lateral tail vein before gently finger-clamping the injection site until bleeding stopped. Animals were euthanized 42 (bioluminescence experiments) or 28 days (immunofluorescence experiments) after injections of Anc80L65/AAV9-Luc or Anc80L65/AAV9-EGFP, respectively. We used a lower dose (5×10^{10} gc/25 g mouse) for the bioluminescence imaging because we were analyzing full-body bioluminescence. At higher AAV doses, the luciferase-induced light emission from the liver is so intense that it can convolute determination of bona fide signal emanating from other body sources.

We used a higher dose (1×10^{12} gc/25 g mouse) in the immunofluorescence experiments, because this is required for detection of EGFP expression in individual cells after i.v. injection.

Stereotactic Intracerebral Injections

Stereotactic intrastriatal and intracerebroventricular injections of AAV9 and Anc80L65 were performed as described previously.[91] Animals were anesthetized by intraperitoneal injection of ketamine/xylazine (100 and 50 mg/kg body weight, respectively) and positioned on a stereotactic frame (Kopf Instruments, Tujunga, CA, USA). Injections of vectors were performed in either the striatum (3 μL of viral suspension/injection site, 1.5×10^{10} gc/mouse) or in the lateral ventricle (5 μL of viral suspension/injection site, 4.5×10^{10} gc/mouse), using a 33G sharp needle attached to a 10-μL Hamilton syringe (Sigma-Aldrich, St. Louis, MO, USA), at a rate of 0.2 μL/min. Stereotactic coordinates of injection sites were calculated from bregma (striatum coordinates: anteroposterior +0.5 mm, mediolateral ±2.5 mm, and dorsoventral −2.5 mm; lateral ventricle coordinates: anteroposterior +0.25 mm, mediolateral ±0.7 mm, and dorsoventral −2 mm).

Immunohistology

Four weeks after injection of Anc80L65, AAV9, and sc AAV9 (scAAV9), mice were given an overdose of anesthesia, transcardially perfused with PBS, and the brain was dissected and post-fixed in 15% glycerol/4% PFA for 48 hr. After cryoprotection in PBS with 30% glycerol for 3 days, 40-μm-thick coronal floating sections were cut using a cryostat microtome for immunohistological analysis. After rinsing off the glycerol in Tris-buffered saline (TBS) buffer, cryosections were permeabilized in 0.5% Triton X-100 (AmericanBio) in TBS for 20 min at room temperature and blocked with 5% normal goat serum (NGS) and 0.5% Triton in TBS for 1 hr at room temperature. Primary antibodies were incubated overnight at 4°C in 2.5% NGS and 0.1% Triton in TBS, whereas Alexa Fluor 488 or Cy3-conjugated secondary antibodies (Jackson Immunoresearch Laboratories, Baltimore, MD, USA) were incubated for 1 hr the next day. Primary antibodies used for this study were chicken anti-GFP (Aves Labs, Tigard, OR, USA), mouse anti-NeuN (EMD Millipore, Burlington, MA, USA), rabbit anti-glutamine synthetase (Abcam, Cambridge, CA, USA), rabbit anti-Olig2 (EMD Millipore, Burlington, MA, USA), rabbit anti-Iba1 (Wako, Japan), rabbit anti-CaMKII (Abcam, Cambridge, MA, USA), mouse anti-GAD67 (EMD Millipore, Burlington, MA, USA), rabbit anti-ChAT (EMD Millipore, Burlington, MA, USA), mouse anti-calbindin (Abcam, Cambridge, MA, USA), rabbit anti-TH (Novus Biologicals, Littleton, CO, USA), and DyLight 594 Lycopersicon Esculentum lectin (Vector Laboratories, Burlingame, CA, USA). Sections were mounted with Vectashield mounting medium with DAPI (Vector Laboratories, Burlingame, CA, USA).

Epifluorescence Microscopy

Tile-scan images were collected on a Zeiss Axio Imager Z epifluorescence microscope equipped with AxioVision software and modified for automated acquisition of entire brain slices, using 5×, 10×, or 20× objectives. Exposure times for each specific immunostaining were set and maintained between each cryosection to preserve consistency.

Stereology-Based Quantitative Analyses

Stereology-based studies were performed as previously described,[92,93] using a motorized stage of an Olympus BX51 epifluorescence microscope equipped with a DP70 digital CCD camera, an X-Cite fluorescent lamp, and the associated CAST stereology software version 2.3.1.5 (Olympus, Tokyo, Japan). The cortex was initially outlined under the 4× objective. Random sampling of the selected area was defined using the optical dissector probe of the CAST software. To evaluate the percentage of Anc80L65, AAV9, and scAAV9 transduced astrocytes or neurons, we performed the stereology-based counts under the 20× objective, with a meander sampling of 10% for the surface of cortex for Anc80L65 and scAAV9, and 30% for AAV9 (the EGFP-positive cells being seldom in this case). For each counting frame, the total number of astrocytes (GS-positive cells) or neurons (NeuN-positive cells) was evaluated, and among each of those populations, the percentages of EGFP-positive cells. Only glial and neuronal cells with a DAPI-positive nucleus within the counting frame were considered. Counts were performed blindly.

Tissue DNA Biodistribution

Snap-frozen tissue was proteinase K digested, and genomic DNA (gDNA) was extracted using the Blood & Cell Culture DNA Mini kit (Qiagen, Germantown, MD, USA) as indicated. Isolated gDNA was quantified using the BioTek plate reading spectrophotometer (BioTek Instruments, Winooski, VT, USA). gc distribution in diploid cells were detected and quantified by qPCR using Applied Biosystems 7500 Real-Time PCR Systems with TaqMan PCR master mix reagents (Applied Biosystems, Woburn, MA, USA) and transgene-specific primer/probes.

Bioluminescence Imaging

Imaging experiments were performed using the IVIS Spectrum imager outfitted with an XGI-8 gas anesthesia system (PerkinElmer, Waltham, MA, USA). Mice were anesthetized and then injected intraperitoneally with 4.5 mg of D-luciferin substrate (Sigma-Aldrich, St. Louis, MO, USA) resuspended in 150 μL of PBS. Five minutes post-substrate injection, mice were imaged for luciferase expression using auto-acquisition. We acquired bioluminescence using the auto-exposure setting. Quantitative analysis of bioluminescence images was performed using Living Image software (Perkin Elmer). Regions of interest were carefully circumscribed around each body area (e.g., liver, head), and the light emission expressed in photons per second in graphical format. In bioluminescence images, the scale is depicted as radiance (photons/s/cm^2/steradian).

Statistics

Statistical analysis of data was performed using GraphPad Prism software (version 5.01). Because of the small number of animals per experimental group, the normality test was not conclusive (D'Agostino-Pearson normality test). A non-parametric one-way ANOVA test (Kruskal-Wallis test) followed by a Dunn's multiple comparisons test was therefore performed. A p value <0.05 was considered to be statistically significant. For statistical analysis of bioluminescence assays, comparison between two groups was performed using an unpaired t test. Data are represented as the mean with SD.

SUPPLEMENTAL INFORMATION

Supplemental Information includes six figures and can be found with this article online at https://doi.org/10.1016/j.omtm.2018.07.006.

AUTHOR CONTRIBUTIONS

L.H.V., E.H., C.A.M., E.A.-M., and B.T.H. designed the study, interpreted the results, and wrote the manuscript. E.H., C.A.M., E.A.-M., E.P.L., A.V., and O.C. performed the experiments.

CONFLICTS OF INTEREST

L.H.V. is an inventor of AAV-Anc and other AAV technologies, which are licensed to various biotechnology and pharmaceutical entities.

ACKNOWLEDGMENTS

This work was supported by NIH/NIA grant 1K99AG047336-01A1 (to E.H.). C.M. received support from the American Brain Tumor Association and the Cure Alzheimer's Fund. L.H.V. was supported by NIH, National Eye Institute Core grant P30EY003790, Giving/Grousbeck, and Lonza Houston.

REFERENCES

1. Choudhury, S.R., Hudry, E., Maguire, C.A., Sena-Esteves, M., Breakefield, X.O., and Grandi, P. (2017). Viral vectors for therapy of neurologic diseases. Neuropharmacology *120*, 63–80.

2. Zinn, E., and Vandenberghe, L.H. (2014). Adeno-associated virus: fit to serve. Curr. Opin. Virol. *8*, 90–97.

3. McCarty, D.M., Young, S.M., Jr., and Samulski, R.J. (2004). Integration of adeno-associated virus (AAV) and recombinant AAV vectors. Annu. Rev. Genet. *38*, 819–845.

4. Bessis, N., GarciaCozar, F.J., and Boissier, M.C. (2004). Immune responses to gene therapy vectors: influence on vector function and effector mechanisms. Gene Ther. *11* (*Suppl 1*), S10–S17.

5. Leone, P., Shera, D., McPhee, S.W., Francis, J.S., Kolodny, E.H., Bilaniuk, L.T., Wang, D.J., Assadi, M., Goldfarb, O., Goldman, H.W., et al. (2012). Long-term follow-up after gene therapy for canavan disease. Sci. Transl. Med. *4*, 165ra163.

6. Chamberlain, J.R., and Chamberlain, J.S. (2017). Progress toward Gene Therapy for Duchenne Muscular Dystrophy. Mol. Ther. *25*, 1125–1131.

7. Ajufo, E., and Cuchel, M. (2016). Recent Developments in Gene Therapy for Homozygous Familial Hypercholesterolemia. Curr. Atheroscler. Rep. *18*, 22.

8. Koo, T., Popplewell, L., Athanasopoulos, T., and Dickson, G. (2014). Triple trans-splicing adeno-associated virus vectors capable of transferring the coding sequence for full-length dystrophin protein into dystrophic mice. Hum. Gene Ther. *25*, 98–108.

9. Mak, K.Y., Rajapaksha, I.G., Angus, P.W., and Herath, C.B. (2017). The adeno-associated virus - a safe and effective vehicle for liver-specific gene therapy of inherited and non-inherited diseases. Curr. Gene Ther. *17*, 4–16.

10. Chamberlain, K., Riyad, J.M., and Weber, T. (2017). Cardiac gene therapy with adeno-associated virus-based vectors. Curr. Opin. Cardiol. *32*, 275–282.

11. Craig, A.J., and Housley, G.D. (2016). Evaluation of gene therapy as an intervention strategy to treat brain injury from stroke. Front. Mol. Neurosci. *9*, 34.

12. Beutler, A.S., and Reinhardt, M. (2009). AAV for pain: steps towards clinical translation. Gene Ther. *16*, 461–469.

13. Park, K., Kim, W.J., Cho, Y.H., Lee, Y.I., Lee, H., Jeong, S., Cho, E.S., Chang, S.I., Moon, S.K., Kang, B.S., et al. (2008). Cancer gene therapy using adeno-associated virus vectors. Front. Biosci. *13*, 2653–2659.

14. Limberis, M.P., Adam, V.S., Wong, G., Gren, J., Kobasa, D., Ross, T.M., Kobinger, G.P., Tretiakova, A., and Wilson, J.M. (2013). Intranasal antibody gene transfer in mice and ferrets elicits broad protection against pandemic influenza. Sci. Transl. Med. *5*, 187ra72.

15. Balazs, A.B., Bloom, J.D., Hong, C.M., Rao, D.S., and Baltimore, D. (2013). Broad protection against influenza infection by vectored immunoprophylaxis in mice. Nat. Biotechnol. *31*, 647–652.

16. Balazs, A.B., Chen, J., Hong, C.M., Rao, D.S., Yang, L., and Baltimore, D. (2011). Antibody-based protection against HIV infection by vectored immunoprophylaxis. Nature *481*, 81–84.

17. Johnson, P.R., Schnepp, B.C., Zhang, J., Connell, M.J., Greene, S.M., Yuste, E., Desrosiers, R.C., and Clark, K.R. (2009). Vector-mediated gene transfer engenders long-lived neutralizing activity and protection against SIV infection in monkeys. Nat. Med. *15*, 901–906.

18. Nathwani, A.C., Reiss, U.M., Tuddenham, E.G., Rosales, C., Chowdary, P., McIntosh, J., Della Peruta, M., Lheriteau, E., Patel, N., Raj, D., et al. (2014). Long-term safety and efficacy of factor IX gene therapy in hemophilia B. N. Engl. J. Med. *371*, 1994–2004.

19. George, L.A., Sullivan, S.K., Giermasz, A., Rasko, J.E.J., Samelson-Jones, B.J., Ducore, J., Cuker, A., Sullivan, L.M., Majumdar, S., Teitel, J., et al. (2017). Hemophilia B gene therapy with a high-specific-activity Factor IX variant. N. Engl. J. Med. *377*, 2215–2227.

20. Rangarajan, S., Walsh, L., Lester, W., Perry, D., Madan, B., Laffan, M., Yu, H., Vettermann, C., Pierce, G.F., Wong, W.Y., and Pasi, K.J. (2017). AAV5-factor VIII gene transfer in severe hemophilia A. N. Engl. J. Med. *377*, 2519–2530.

21. Meyer, K., Ferraiuolo, L., Schmelzer, L., Braun, L., McGovern, V., Likhite, S., Michels, O., Govoni, A., Fitzgerald, J., Morales, P., et al. (2015). Improving single injection CSF delivery of AAV9-mediated gene therapy for SMA: a dose-response study in mice and nonhuman primates. Mol. Ther. *23*, 477–487.

22. Mendell, J.R., Al-Zaidy, S., Shell, R., Arnold, W.D., Rodino-Klapac, L.R., Prior, T.W., Lowes, L., Alfano, L., Berry, K., Church, K., et al. (2017). Single-dose gene-replacement therapy for spinal muscular atrophy. N. Engl. J. Med. *377*, 1713–1722.

23. Russell, S., Bennett, J., Wellman, J.A., Chung, D.C., Yu, Z.F., Tillman, A., Wittes, J., Pappas, J., Elci, O., McCague, S., et al. (2017). Efficacy and safety of voretigene

neparvovec (AAV2-hRPE65v2) in patients with RPE65-mediated inherited retinal dystrophy: a randomised, controlled, open-label, phase 3 trial. Lancet *390*, 849–860.

24. Gaj, T., Epstein, B.E., and Schaffer, D.V. (2016). Genome engineering using adeno-associated virus: basic and clinical research applications. Mol. Ther. *24*, 458–464.
25. Swiech, L., Heidenreich, M., Banerjee, A., Habib, N., Li, Y., Trombetta, J., Sur, M., and Zhang, F. (2015). In vivo interrogation of gene function in the mammalian brain using CRISPR-Cas9. Nat. Biotechnol. *33*, 102–106.
26. Tang, W., Szokol, K., Jensen, V., Enger, R., Trivedi, C.A., Hvalby, Ø., Helm, P.J., Looger, L.L., Sprengel, R., and Nagelhus, E.A. (2015). Stimulation-evoked Ca2+ signals in astrocytic processes at hippocampal CA3-CA1 synapses of adult mice are modulated by glutamate and ATP. J. Neurosci. *35*, 3016–3021.
27. Ekstrand, M.I., Nectow, A.R., Knight, Z.A., Latcha, K.N., Pomeranz, L.E., and Friedman, J.M. (2014). Molecular profiling of neurons based on connectivity. Cell *157*, 1230–1242.
28. Xu, W., and Südhof, T.C. (2013). A neural circuit for memory specificity and generalization. Science *339*, 1290–1295.
29. Cai, D., Cohen, K.B., Luo, T., Lichtman, J.W., and Sanes, J.R. (2013). Improved tools for the Brainbow toolbox. Nat. Methods *10*, 540–547.
30. Shimano, T., Fyk-Kolodziej, B., Mirza, N., Asako, M., Tomoda, K., Bledsoe, S., Pan, Z.H., Molitor, S., and Holt, A.G. (2013). Assessment of the AAV-mediated expression of channelrhodopsin-2 and halorhodopsin in brainstem neurons mediating auditory signaling. Brain Res. *1511*, 138–152.
31. Kaspar, B.K., Vissel, B., Bengoechea, T., Crone, S., Randolph-Moore, L., Muller, R., Brandon, E.P., Schaffer, D., Verma, I.M., Lee, K.F., et al. (2002). Adeno-associated virus effectively mediates conditional gene modification in the brain. Proc. Natl. Acad. Sci. USA *99*, 2320–2325.
32. Katz, M.L., Tecedor, L., Chen, Y., Williamson, B.G., Lysenko, E., Wininger, F.A., Young, W.M., Johnson, G.C., Whiting, R.E., Coates, J.R., and Davidson, B.L. (2015). AAV gene transfer delays disease onset in a TPP1-deficient canine model of the late infantile form of Batten disease. Sci. Transl. Med. *7*, 313ra180.
33. Sargeant, T.J., Wang, S., Bradley, J., Smith, N.J., Raha, A.A., McNair, R., Ziegler, R.J., Cheng, S.H., Cox, T.M., and Cachón-González, M.B. (2011). Adeno-associated virus-mediated expression of β-hexosaminidase prevents neuronal loss in the Sandhoff mouse brain. Hum. Mol. Genet. *20*, 4371–4380.
34. Sevin, C., Benraiss, A., Van Dam, D., Bonnin, D., Nagels, G., Verot, L., Laurendeau, I., Vidaud, M., Gieselmann, V., Vanier, M., et al. (2006). Intracerebral adeno-associated virus-mediated gene transfer in rapidly progressive forms of metachromatic leukodystrophy. Hum. Mol. Genet. *15*, 53–64.
35. Passini, M.A., Macauley, S.L., Huff, M.R., Taksir, T.V., Bu, J., Wu, I.H., Piepenhagen, P.A., Dodge, J.C., Shihabuddin, L.S., O'Riordan, C.R., et al. (2005). AAV vector-mediated correction of brain pathology in a mouse model of Niemann-Pick A disease. Mol. Ther. *11*, 754–762.
36. Gelfand, Y., and Kaplitt, M.G. (2013). Gene therapy for psychiatric disorders. World Neurosurg. *80*, S32.e11–18.
37. Chen, G., Twyman, R., and Manji, H.K. (2010). p11 and gene therapy for severe psychiatric disorders: a practical goal? Sci. Transl. Med. *2*, 54ps51.
38. Liu, W., Zhao, L., Blackman, B., Parmar, M., Wong, M.Y., Woo, T., Yu, F., Chiuchiolo, M.J., Sondhi, D., Kaminsky, S.M., et al. (2016). Vectored intracerebral immunization with the anti-tau monoclonal antibody PHF1 markedly reduces tau pathology in mutant tau transgenic mice. J. Neurosci. *36*, 12425–12435.
39. Zharikov, A.D., Cannon, J.R., Tapias, V., Bai, Q., Horowitz, M.P., Shah, V., El Ayadi, A., Hastings, T.G., Greenamyre, J.T., and Burton, E.A. (2015). shRNA targeting α-synuclein prevents neurodegeneration in a Parkinson's disease model. J. Clin. Invest. *125*, 2721–2735.
40. Foust, K.D., Salazar, D.L., Likhite, S., Ferraiuolo, L., Ditsworth, D., Ilieva, H., Meyer, K., Schmelzer, L., Braun, L., Cleveland, D.W., and Kaspar, B.K. (2013). Therapeutic AAV9-mediated suppression of mutant SOD1 slows disease progression and extends survival in models of inherited ALS. Mol. Ther. *21*, 2148–2159.
41. Hudry, E., Dashkoff, J., Roe, A.D., Takeda, S., Koffie, R.M., Hashimoto, T., Scheel, M., Spires-Jones, T., Arbel-Ornath, M., Betensky, R., et al. (2013). Gene transfer of human Apoe isoforms results in differential modulation of amyloid deposition and neurotoxicity in mouse brain. Sci. Transl. Med. *5*, 212ra161.
42. Hester, M.E., Foust, K.D., Kaspar, R.W., and Kaspar, B.K. (2009). AAV as a gene transfer vector for the treatment of neurological disorders: novel treatment thoughts for ALS. Curr. Gene Ther. *9*, 428–433.
43. Chan, K.Y., Jang, M.J., Yoo, B.B., Greenbaum, A., Ravi, N., Wu, W.L., Sánchez-Guardado, L., Lois, C., Mazmanian, S.K., Deverman, B.E., and Gradinaru, V. (2017). Engineered AAVs for efficient noninvasive gene delivery to the central and peripheral nervous systems. Nat. Neurosci. *20*, 1172–1179.
44. Choudhury, S.R., Harris, A.F., Cabral, D.J., Keeler, A.M., Sapp, E., Ferreira, J.S., Gray-Edwards, H.L., Johnson, J.A., Johnson, A.K., Su, Q., et al. (2016). Widespread central nervous system gene transfer and silencing after systemic delivery of novel AAV-AS vector. Mol. Ther. *24*, 726–735.
45. Deverman, B.E., Pravdo, P.L., Simpson, B.P., Kumar, S.R., Chan, K.Y., Banerjee, A., Wu, W.L., Yang, B., Huber, N., Pasca, S.P., and Gradinaru, V. (2016). Cre-dependent selection yields AAV variants for widespread gene transfer to the adult brain. Nat. Biotechnol. *34*, 204–209.
46. Yang, B., Li, S., Wang, H., Guo, Y., Gessler, D.J., Cao, C., Su, Q., Kramer, J., Zhong, L., Ahmed, S.S., et al. (2014). Global CNS transduction of adult mice by intravenously delivered rAAVrh.8 and rAAVrh.10 and nonhuman primates by rAAVrh.10. Mol. Ther. *22*, 1299–1309.
47. Foust, K.D., Nurre, E., Montgomery, C.L., Hernandez, A., Chan, C.M., and Kaspar, B.K. (2009). Intravascular AAV9 preferentially targets neonatal neurons and adult astrocytes. Nat. Biotechnol. *27*, 59–65.
48. Gray, S.J., Matagne, V., Bachaboina, L., Yadav, S., Ojeda, S.R., and Samulski, R.J. (2011). Preclinical differences of intravascular AAV9 delivery to neurons and glia: a comparative study of adult mice and nonhuman primates. Mol. Ther. *19*, 1058–1069.
49. Fu, H., Dirosario, J., Killedar, S., Zaraspe, K., and McCarty, D.M. (2011). Correction of neurological disease of mucopolysaccharidosis IIIB in adult mice by rAAV9 trans-blood-brain barrier gene delivery. Mol. Ther. *19*, 1025–1033.
50. Bevan, A.K., Duque, S., Foust, K.D., Morales, P.R., Braun, L., Schmelzer, L., Chan, C.M., McCrate, M., Chicoine, L.G., Coley, B.D., et al. (2011). Systemic gene delivery in large species for targeting spinal cord, brain, and peripheral tissues for pediatric disorders. Mol. Ther. *19*, 1971–1980.
51. Duque, S., Joussemet, B., Riviere, C., Marais, T., Dubreil, L., Douar, A.M., Fyfe, J., Moullier, P., Colle, M.A., and Barkats, M. (2009). Intravenous administration of self-complementary AAV9 enables transgene delivery to adult motor neurons. Mol. Ther. *17*, 1187–1196.
52. Samaranch, L., Salegio, E.A., San Sebastian, W., Kells, A.P., Foust, K.D., Bringas, J.R., Lamarre, C., Forsayeth, J., Kaspar, B.K., and Bankiewicz, K.S. (2012). Adeno-associated virus serotype 9 transduction in the central nervous system of nonhuman primates. Hum. Gene Ther. *23*, 382–389.
53. Dashkoff, J., Lerner, E.P., Truong, N., Klickstein, J.A., Fan, Z., Mu, D., Maguire, C.A., Hyman, B.T., and Hudry, E. (2016). Tailored transgene expression to specific cell types in the central nervous system after peripheral injection with AAV9. Mol. Ther. Methods Clin. Dev. *3*, 16081.
54. de Leeuw, C.N., Dyka, F.M., Boye, S.L., Laprise, S., Zhou, M., Chou, A.Y., Borretta, L., McInerny, S.C., Banks, K.G., Portales-Casamar, E., et al. (2014). Targeted CNS delivery using human MiniPromoters and demonstrated compatibility with adeno-associated viral vectors. Mol. Ther. Methods Clin. Dev. *1*, 5.
55. Zinn, E., Pacouret, S., Khaychuk, V., Turunen, H.T., Carvalho, L.S., Andres-Mateos, E., Shah, S., Shelke, R., Maurer, A.C., Plovie, E., et al. (2015). In silico reconstruction of the viral evolutionary lineage yields a potent gene therapy vector. Cell Rep. *12*, 1056–1068.
56. Wang, L., Xiao, R., Andres-Mateos, E., and Vandenberghe, L.H. (2017). Single stranded adeno-associated virus achieves efficient gene transfer to anterior segment in the mouse eye. PLoS ONE *12*, e0182473.
57. Carvalho, L.S., Xiao, R., Wassmer, S.J., Langsdorf, A., Zinn, E., Pacouret, S., Shah, S., Comander, J.I., Kim, L.A., Lim, L., and Vandenberghe, L.H. (2018). Synthetic adeno-associated viral vector efficiently targets mouse and nonhuman primate retina in vivo. Hum. Gene Ther. Published online March 20, 2018. https://doi.org/10.1089/hum.2017.154.
58. Landegger, L.D., Pan, B., Askew, C., Wassmer, S.J., Gluck, S.D., Galvin, A., Taylor, R., Forge, A., Stankovic, K.M., Holt, J.R., and Vandenberghe, L.H. (2017). A synthetic

AAV vector enables safe and efficient gene transfer to the mammalian inner ear. Nat. Biotechnol. *35*, 280–284.

59. Pan, B., Askew, C., Galvin, A., Heman-Ackah, S., Asai, Y., Indzhykulian, A.A., Jodelka, F.M., Hastings, M.L., Lentz, J.J., Vandenberghe, L.H., et al. (2017). Gene therapy restores auditory and vestibular function in a mouse model of Usher syndrome type 1c. Nat. Biotechnol. *35*, 264–272.

60. Suzuki, J., Hashimoto, K., Xiao, R., Vandenberghe, L.H., and Liberman, M.C. (2017). Cochlear gene therapy with ancestral AAV in adult mice: complete transduction of inner hair cells without cochlear dysfunction. Sci. Rep. *7*, 45524.

61. McCarty, D.M. (2008). Self-complementary AAV vectors; advances and applications. Mol. Ther. *16*, 1648–1656.

62. Wang, Z., Ma, H.I., Li, J., Sun, L., Zhang, J., and Xiao, X. (2003). Rapid and highly efficient transduction by double-stranded adeno-associated virus vectors in vitro and in vivo. Gene Ther. *10*, 2105–2111.

63. Davidsson, M., Diaz-Fernandez, P., Schwich, O.D., Torroba, M., Wang, G., and Björklund, T. (2016). A novel process of viral vector barcoding and library preparation enables high-diversity library generation and recombination-free paired-end sequencing. Sci. Rep. *6*, 37563.

64. Gao, G., Vandenberghe, L.H., and Wilson, J.M. (2005). New recombinant serotypes of AAV vectors. Curr. Gene Ther. *5*, 285–297.

65. Gao, G.P., Alvira, M.R., Wang, L., Calcedo, R., Johnston, J., and Wilson, J.M. (2002). Novel adeno-associated viruses from rhesus monkeys as vectors for human gene therapy. Proc. Natl. Acad. Sci. USA *99*, 11854–11859.

66. Mingozzi, F., and High, K.A. (2013). Immune responses to AAV vectors: overcoming barriers to successful gene therapy. Blood *122*, 23–36.

67. Calcedo, R., Vandenberghe, L.H., Gao, G., Lin, J., and Wilson, J.M. (2009). Worldwide epidemiology of neutralizing antibodies to adeno-associated viruses. J. Infect. Dis. *199*, 381–390.

68. Armbruster, N., Lattanzi, A., Jeavons, M., Van Wittenberghe, L., Gjata, B., Marais, T., Martin, S., Vignaud, A., Voit, T., Mavilio, F., et al. (2016). Efficacy and biodistribution analysis of intracerebroventricular administration of an optimized scAAV9-SMN1 vector in a mouse model of spinal muscular atrophy. Mol. Ther. Methods Clin. Dev. *3*, 16060.

69. Hironaka, K., Yamazaki, Y., Hirai, Y., Yamamoto, M., Miyake, N., Miyake, K., Okada, T., Morita, A., and Shimada, T. (2015). Enzyme replacement in the CSF to treat metachromatic leukodystrophy in mouse model using single intracerebroventricular injection of self-complementary AAV1 vector. Sci. Rep. *5*, 13104.

70. Haurigot, V., Marcó, S., Ribera, A., Garcia, M., Ruzo, A., Villacampa, P., Ayuso, E., Añor, S., Andaluz, A., Pineda, M., et al. (2013). Whole body correction of mucopolysaccharidosis IIIA by intracerebrospinal fluid gene therapy. J. Clin. Invest. *123*, 3254–3271.

71. Zhang, H., Yang, B., Mu, X., Ahmed, S.S., Su, Q., He, R., Wang, H., Mueller, C., Sena-Esteves, M., Brown, R., et al. (2011). Several rAAV vectors efficiently cross the blood-brain barrier and transduce neurons and astrocytes in the neonatal mouse central nervous system. Mol. Ther. *19*, 1440–1448.

72. Bosch, M.E., Aldrich, A., Fallet, R., Odvody, J., Burkovetskaya, M., Schuberth, K., Fitzgerald, J.A., Foust, K.D., and Kielian, T. (2016). Self-complementary AAV9 gene delivery partially corrects pathology associated with juvenile neuronal ceroid lipofuscinosis (CLN3). J. Neurosci. *36*, 9669–9682.

73. Crommentuijn, M.H., Kantar, R., Noske, D.P., Vandertop, W.P., Badr, C.E., Würdinger, T., Maguire, C.A., and Tannous, B.A. (2016). Systemically administered AAV9-sTRAIL combats invasive glioblastoma in a patient-derived orthotopic xenograft model. Mol. Ther. Oncolytics *3*, 16017.

74. Gong, Y., Mu, D., Prabhakar, S., Moser, A., Musolino, P., Ren, J., Breakefield, X.O., Maguire, C.A., and Eichler, F.S. (2015). Adenoassociated virus serotype 9-mediated gene therapy for x-linked adrenoleukodystrophy. Mol. Ther. *23*, 824–834.

75. Kotchey, N.M., Adachi, K., Zahid, M., Inagaki, K., Charan, R., Parker, R.S., and Nakai, H. (2011). A potential role of distinctively delayed blood clearance of recombinant adeno-associated virus serotype 9 in robust cardiac transduction. Mol. Ther. *19*, 1079–1089.

76. Di Pasquale, G., and Chiorini, J.A. (2006). AAV transcytosis through barrier epithelia and endothelium. Mol. Ther. *13*, 506–516.

77. Merkel, S.F., Andrews, A.M., Lutton, E.M., Mu, D., Hudry, E., Hyman, B.T., Maguire, C.A., and Ramirez, S.H. (2017). Trafficking of adeno-associated virus vectors across a model of the blood-brain barrier; a comparative study of transcytosis and transduction using primary human brain endothelial cells. J. Neurochem. *140*, 216–230.

78. Wu, J., Zhao, W., Zhong, L., Han, Z., Li, B., Ma, W., Weigel-Kelley, K.A., Warrington, K.H., and Srivastava, A. (2007). Self-complementary recombinant adeno-associated viral vectors: packaging capacity and the role of rep proteins in vector purity. Hum. Gene Ther. *18*, 171–182.

79. Ojala, D.S., Sun, S., Santiago-Ortiz, J.L., Shapiro, M.G., Romero, P.A., and Schaffer, D.V. (2018). In vivo selection of a computationally designed SCHEMA AAV library yields a novel variant for infection of adult neural stem cells in the SVZ. Mol Ther *26*, 304–319.

80. Choudhury, S.R., Fitzpatrick, Z., Harris, A.F., Maitland, S.A., Ferreira, J.S., Zhang, Y., Ma, S., Sharma, R.B., Gray-Edwards, H.L., Johnson, J.A., et al. (2016). In vivo selection yields AAV-B1 capsid for central nervous system and muscle gene therapy. Mol. Ther. *24*, 1247–1257.

81. Hordeaux, J., Wang, Q., Katz, N., Buza, E.L., Bell, P., and Wilson, J.M. (2018). The neurotropic properties of AAV-PHP.B are limited to C57BL/6J mice. Mol. Ther. *26*, 664–668.

82. Zaiss, A.K., and Muruve, D.A. (2005). Immune responses to adeno-associated virus vectors. Curr. Gene Ther. *5*, 323–331.

83. Nault, J.C., Datta, S., Imbeaud, S., Franconi, A., Mallet, M., Couchy, G., Letouzé, E., Pilati, C., Verret, B., Blanc, J.F., et al. (2015). Recurrent AAV2-related insertional mutagenesis in human hepatocellular carcinomas. Nat. Genet. *47*, 1187–1193.

84. Rosas, L.E., Grieves, J.L., Zaraspe, K., La Perle, K.M., Fu, H., and McCarty, D.M. (2012). Patterns of scAAV vector insertion associated with oncogenic events in a mouse model for genotoxicity. Mol. Ther. *20*, 2098–2110.

85. Li, H., Malani, N., Hamilton, S.R., Schlachterman, A., Bussadori, G., Edmonson, S.E., Shah, R., Arruda, V.R., Mingozzi, F., Wright, J.F., et al. (2011). Assessing the potential for AAV vector genotoxicity in a murine model. Blood *117*, 3311–3319.

86. Kügler, S. (2016). Tissue-specific promoters in the CNS. Methods Mol. Biol. *1382*, 81–91.

87. Mudannayake, J.M., Mouravlev, A., Fong, D.M., and Young, D. (2016). Transcriptional activity of novel ALDH1L1 promoters in the rat brain following AAV vector-mediated gene transfer. Mol. Ther. Methods Clin. Dev. *3*, 16075.

88. Malmevik, J., Petri, R., Klussendorf, T., Knauff, P., Åkerblom, M., Johansson, J., Soneji, S., and Jakobsson, J. (2015). Identification of the miRNA targetome in hippocampal neurons using RIP-seq. Sci. Rep. *5*, 12609.

89. Pulicherla, N., Shen, S., Yadav, S., Debbink, K., Govindasamy, L., Agbandje-McKenna, M., and Asokan, A. (2011). Engineering liver-detargeted AAV9 vectors for cardiac and musculoskeletal gene transfer. Mol. Ther. *19*, 1070–1078.

90. Lock, M., Alvira, M., Vandenberghe, L.H., Samanta, A., Toelen, J., Debyser, Z., and Wilson, J.M. (2010). Rapid, simple, and versatile manufacturing of recombinant adeno-associated viral vectors at scale. Hum. Gene Ther. *21*, 1259–1271.

91. Hudry, E., Van Dam, D., Kulik, W., De Deyn, P.P., Stet, F.S., Ahouansou, O., Benraiss, A., Delacourte, A., Bougnères, P., Aubourg, P., and Cartier, N. (2010). Adeno-associated virus gene therapy with cholesterol 24-hydroxylase reduces the amyloid pathology before or after the onset of amyloid plaques in mouse models of Alzheimer's disease. Mol. Ther. *18*, 44–53.

92. Hudry, E., Martin, C., Gandhi, S., György, B., Scheffer, D.I., Mu, D., Merkel, S.F., Mingozzi, F., Fitzpatrick, Z., Dimant, H., et al. (2016). Exosome-associated AAV vector as a robust and convenient neuroscience tool. Gene Ther. *23*, 380–392.

93. Serrano-Pozo, A., Muzikansky, A., Gómez-Isla, T., Growdon, J.H., Betensky, R.A., Frosch, M.P., and Hyman, B.T. (2013). Differential relationships of reactive astrocytes and microglia to fibrillar amyloid deposits in Alzheimer disease. J. Neuropathol. Exp. Neurol. *72*, 462–471.

JAMA Neurology | Original Investigation

Safety and Tolerability of Multiple Ascending Doses of PRX002/RG7935, an Anti–α-Synuclein Monoclonal Antibody, in Patients With Parkinson Disease
A Randomized Clinical Trial

Joseph Jankovic, MD; Ira Goodman, MD; Beth Safirstein, MD; Tonya K. Marmon, DrPH; Dale B. Schenk, PhD; Martin Koller, MD, MPH; Wagner Zago, PhD; Daniel K. Ness, DVM, PhD; Sue G. Griffith, MD, PhD, MRCP; Michael Grundman, MD, MPH; Jay Soto, BS; Susanne Ostrowitzki, MD, PhD; Frank G. Boess, PhD; Meret Martin-Facklam, PhD; Joseph F. Quinn, MD; Stuart H. Isaacson, MD; Omid Omidvar, MD; Aaron Ellenbogen, DO; Gene G. Kinney, PhD

IMPORTANCE Aggregated α-synuclein is believed to be central to the pathogenesis of Parkinson disease (PD). PRX002/RG7935 (PRX002) is a humanized monoclonal antibody designed to target aggregated forms of α-synuclein, thereby inhibiting neuron-to-neuron transfer of presumed pathogenic forms of α-synuclein, potentially resulting in neuronal protection and slowing disease progression.

OBJECTIVE To evaluate the safety and tolerability of multiple intravenous infusions of PRX002 in patients with idiopathic PD.

DESIGN, SETTING, AND PARTICIPANTS Multicenter, randomized, double-blind, placebo-controlled, multiple ascending-dose trial at 8 US study centers from July 2014 to September 2016. Eligible participants were aged 40 to 80 years with mild to moderate idiopathic PD (Hoehn and Yahr stages 1-3).

INTERVENTIONS Participants were enrolled into 6 ascending-dose cohorts and randomly assigned to receive PRX002 (0.3 mg/kg, 1.0 mg/kg, 3.0 mg/kg, 10 mg/kg, 30 mg/kg, or 60 mg/kg) or placebo. Participants received 3 intravenous infusions every 4 weeks of PRX002 or placebo and were monitored during a 24-week observational period.

MAIN OUTCOMES AND MEASURES Safety and tolerability assessments included physical and neurological examinations, laboratory tests, vital signs, and adverse events. Pharmacokinetic parameters included maximum PRX002 concentration, area under the curve, and half-life.

RESULTS Of the 80 participants, most were white (97.5%; n = 78) and male (80%; n = 64); median (SD) age was 58 (8.4) years. PRX002 was generally safe and well tolerated; no serious or severe PRX002-related treatment-emergent adverse events (TEAEs) were reported. The TEAEs experienced by at least 5% of patients receiving PRX002, irrespective of relatedness to study drug, were constipation (9.1%; n = 5), infusion reaction (7.3%; n = 4), diarrhea (5.5%; n = 3), headache (5.5%; n = 3), peripheral edema (5.5%; n = 3), post–lumbar puncture syndrome (5.5%; n = 3), and upper respiratory tract infection (5.5%; n = 3). No antidrug antibodies were detected. Serum PRX002 levels increased in an approximately dose-proportional manner; mean terminal elimination half-life was similar across all doses (10.2 days). Rapid dose- and time-dependent mean reductions from baseline vs placebo in free serum α-synuclein levels of up to 97% were seen after a single infusion at the highest dose ($F_{78,284} = 1.66$; $P = .002$), with similar reductions after 2 additional infusions. Mean cerebrospinal fluid PRX002 concentration increased with PRX002 dose and was approximately 0.3% relative to serum across all dose cohorts.

CONCLUSIONS AND RELEVANCE Single and multiple doses of PRX002 were generally safe and well tolerated and resulted in robust binding of peripheral α-synuclein and dose-dependent increases of PRX002 in cerebrospinal fluid, reaching cerebrospinal fluid concentrations that may be expected to engage extracellular aggregated α-synuclein in the brain. Findings support the design of an ongoing phase 2 clinical study (NCT03100149).

TRIAL REGISTRATION ClinicalTrials.gov Identifier: NCT02157714

JAMA Neurol. 2018;75(10):1206-1214. doi:10.1001/jamaneurol.2018.1487
Published online June 18, 2018.

Editorial page 1180

Supplemental content

Author Affiliations: Author affiliations are listed at the end of this article.

Corresponding Author: Joseph Jankovic, MD, Parkinson's Disease Center and Movement Disorders Clinic, Department of Neurology, Baylor College of Medicine, 7200 Cambridge, Houston, TX 77030-4202 (josephj@bcm.edu).

© 2018 American Medical Association. All rights reserved.

Downloaded From: https://jamanetwork.com/ on 08/13/2020

Parkinson disease (PD) is a chronic, progressive neurological disorder characterized by motor and nonmotor features.[1] Treatments primarily target symptoms but do not slow or halt the underlying neurodegeneration.[2] Eventually, debilitating adverse effects and treatment-resistant symptoms emerge. Therefore, there is a profound unmet need for disease-modifying therapies.

The cause of PD is not fully understood, but genetic, environmental, immune, and other causes contribute to its pathogenesis.[3] Pathologically, PD is typically associated with an accumulation of aggregated α-synuclein protein in the central nervous system (CNS) and the peripheral nervous system. Some forms of soluble aggregated α-synuclein have been proposed as a major extracellular neurotoxic species in the pathogenesis of PD.[4,5] Extracellular aggregated α-synuclein has been implicated in caudal-rostral propagation in the brain (Braak staging)[6] and in host-to-graft transfer of α-synuclein pathology into cells transplanted into the brains of patients with PD.[4,5,7]

Preclinical studies with transgenic mice have shown that overexpression of α-synuclein leads to the development of key PD features, including accumulation of intracellular α-synuclein pathology and motor and cognitive deficits.[8,9] Vaccination (active immunization) and monoclonal antibody (passive immunotherapy) studies in α-synuclein transgenic mice demonstrate that anti–α-synuclein antibodies with high relative affinity to the C-terminus protein region tempered neuronal pathology by decreasing intracellular accumulation of α-synuclein in cell bodies and synapses, protected against synaptic loss and gliosis, and ameliorated motor and cognitive behavior deficits.[9-12] Passive immunization with C-terminal α-synuclein antibodies reduced intracellular α-synuclein pathology, protected neurons, and improved behavior performance in lentiviral[13] and recombinant preformed fibril[14] α-synuclein-transmission models.

PRX002/RG7935 (PRX002) is a humanized IgG 1 monoclonal antibody designed to target the C-terminus of neurotoxic (aggregated) forms of α-synuclein. Preclinical efficacy of the PRX002 murine homologue (9E4) has been demonstrated using multiple in vivo and in vitro α-synucleinopathy models; specifically, 9E4 blocked cell-to-cell transmission of α-synuclein, reduced intracellular α-synuclein pathology, protected against synaptic loss and gliosis, and ameliorated cognitive and motor behavior deficits.[9,11,12,15,16] Sequestration, neutralization, and clearance of toxic α-synuclein species by PRX002 is thought to halt the spreading of pathogenic α-synuclein between neurons, resulting in neuronal protection and potentially slowing disease progression.[15] PRX002 has a substantially higher affinity/avidity for aggregated than monomeric forms of α-synuclein (kinetic affinity constant [K_D], 0.048 nM vs 20 nM, respectively); this attribute, besides targeting an epitope in the C-terminus of α-synuclein, was designed to support antibody efficacy.[15,17]

In a single ascending-dose phase 1 study in healthy volunteers, PRX002 was safe and well tolerated up to the highest tested dose (30 mg/kg) and resulted in dose-dependent reductions in free serum α-synuclein.[18] We report the results of a multiple ascending-dose phase 1b study designed to evaluate the safety and tolerability of PRX002 at doses up to 60 mg/kg in 80 participants with mild to moderate PD. Secondary and exploratory objectives included assessments of the pharmacokinetics, immunogenicity, pharmacodynamics, and clinical efficacy of multiple intravenous infusions of PRX002.

Key Points

Question Is repeated administration of a monoclonal antibody against α-synuclein (PRX002/RG7935) safe and well tolerated in patients with Parkinson disease?

Findings In this randomized clinical trial of 80 patients with Parkinson disease treated with multiple ascending doses of PRX002/RG7935 or placebo, repeated PRX002/RG7935 treatment was generally safe and well tolerated and induced marked reductions in free serum α-synuclein.

Meaning The results of this phase 1b trial provided important safety, pharmacokinetic, and pharmacodynamic information needed to design the ongoing phase 2 trial to assess whether PRX002/RG7935 shows evidence of a treatment benefit during 52 weeks in patients with Parkinson disease.

Methods

Experimental Design

This was a multicenter, randomized, double-blind, placebo-controlled, multiple ascending-dose, phase 1b study in patients with mild to moderate PD at 8 US study centers. The formal trial protocol is available in Supplement 1. Participants were enrolled sequentially into 1 of 6 escalating-dose cohorts and were to receive a total of 3 intravenous infusions of PRX002 (0.3 mg/kg, 1.0 mg/kg, 3.0 mg/kg, 10 mg/kg, 30 mg/kg, or 60 mg/kg) or placebo, administered approximately once every 28 days. Participants returned for pharmacokinetic and pharmacodynamic assessments until 4 weeks after final dosing and for clinical efficacy and safety assessments until 16 weeks after final dosing (24 weeks total). The sample size of 56 active participants was based on detecting an adverse event (AE) of interest occurring at a true rate of 0.04 with a probability of 89.8% and detecting an AE of interest occurring at a true rate of 0.20 with a probability of at least 99%. The study protocol was approved by appropriately constituted institutional review boards. All participants provided written informed consent. The study was conducted according to International Council for Harmonisation Good Clinical Practice guidelines and the principles of the Declaration of Helsinki.

Participants

Key enrollment criteria included mild to moderate idiopathic PD (Hoehn and Yahr stage 1-3) with bradykinesia plus another cardinal PD sign (resting tremor or rigidity); receiving stable (≥90 days) doses of anti-PD medication at baseline if being treated for PD; age 40 to 80 years; body weight 45 to 110 kg; body mass index (calculated as weight in kilograms divided by height in meters squared) 18 to 34; postmenopausal, surgically sterile, or using adequate contraception; and

© 2018 American Medical Association. All rights reserved.

Downloaded From: https://jamanetwork.com/ on 08/13/2020

no history of significant cardiac disorders or abnormal magnetic resonance imaging results.

Randomization

Participants in cohorts 1 through 4 were randomly assigned in blocks of 3, each in a 2 to 1 ratio of PRX002 and placebo (PRX002, n = 8; placebo, n = 4). Participants in cohorts 5 and 6 were randomly assigned in blocks of 4, each in a 3 to 1 ratio of PRX002 and placebo (PRX002, n = 12; placebo, n = 4). Within each cohort, the first block served as a sentinel group (cohorts 1-4, n = 3; cohorts 5-6, n = 4) to assess safety and tolerability before the remaining participants were randomly assigned. Details of blinding procedures are provided in the eMethods in Supplement 2.

Procedures

Lyophilized PRX002 was reconstituted with sterile water for injection and prepared by a nonblinded study pharmacist in normal saline for intravenous infusion for a mean (SD) of 60 (10) minutes for all participants in cohorts 1 through 5 and either 60 (10) minutes or 120 (10) minutes for participants in cohort 6. Premedication was not required. Normal saline was used as placebo. Dose escalation for subsequent cohorts occurred after all participants in the preceding cohort had received at least 1 dose and after review of 6 weeks' safety data from 75% of participants from the preceding cohort. Immunogenicity was assessed before and 4 weeks after each infusion. Serum PRX002 concentrations were assessed at various times before, during, and after each infusion (eMethods in Supplement 2). Free (unbound to PRX002) and total (free plus bound to PRX002) serum α-synuclein concentrations were assessed before and 1 and 4 hours after each of the 3 infusions; 1 and 2 weeks after the first and third infusions; and 4 weeks after the third infusion. Free and total cerebrospinal fluid (CSF) α-synuclein and CSF PRX002 concentrations were determined at screening and 2 to 9 days after the third infusion.

Outcomes

Primary study objectives were to evaluate the safety and tolerability of multiple intravenous infusions of PRX002, and secondary objectives were to assess the pharmacokinetics and immunogenicity of single and multiple infusions of PRX002 in participants with PD. Exploratory objectives were to assess relevant biomarkers and clinical PD progression.

Safety and tolerability were assessed in all patients who received study drug (PRX002 or placebo) and included AEs, laboratory tests, vital signs, electrocardiography, and physical and neurological examinations. Serum and CSF PRX002 were measured using a Prothena-developed quantitative sandwich electrochemiluminescence (ECL) assay.[18] Serum PRX002 pharmacokinetic parameters were generated using noncompartmental analysis; pharmacokinetic variables are described in the eMethods in Supplement 2. Immunogenicity was assessed by measuring anti-PRX002 antibodies using a qualitative dilution-based bridging ECL assay. Total and free α-synuclein were measured in serum and CSF using quantitative sandwich ECL (Intertek Pharmaceutical Services), with free serum α-synuclein values normalized to percentage of total α-synuclein; samples with hemoglobin levels greater than 0.06 g/dL were excluded from analysis because of potential peripheral α-synuclein contamination by lysed red blood cells (to convert to grams per liter, multiply by 10). Total β-amyloid (Aβ) and Aβ42 were measured in CSF using quantitative sandwich ECL. DJ-1 was measured in CSF using enzyme-linked immunosorbent assay.

Exploratory clinical assessments included the Movement Disorder Society–Unified Parkinson's Disease Rating Scale (days 8 and 64), 39-item Parkinson's Disease Questionnaire (day 71), posttreatment Clinical Global Impression of Change (days 8 and 64), 40-item University of Pennsylvania Smell Identification Test (days 15 and 64), 12-item Patient Assessment of Constipation Symptoms (days 15 and 64), bowel movement frequency diaries (days 1, 2, 8, 15, 29, 43, 57, 64, 71, 85, and 169), and DaTscan (cohorts 4-6; day 71). Details of exploratory clinical assessments are listed in eTable 1 in Supplement 2.

Statistical Analysis

Baseline and demographic characteristics, safety, and pharmacokinetic data were summarized using descriptive statistics. All tests were 2-sided, with significance level of .05. No adjustments for multiple comparisons were made. Maximum concentration (C_{max}), area under the concentration-time curve from time-zero extrapolated to infinity for the first infusion, and C_{max} and area under the concentration-time curve from zero to tau for the third infusion were compared across each dose level to assess change in systemic exposure with change in PRX002 dose. Total α-synuclein and free serum α-synuclein percentage changes from baseline were summarized using linear mixed models for repeated measurements. The statistical significance of CSF α-synuclein change from baseline was determined by analysis of covariance.

Results

Study Population

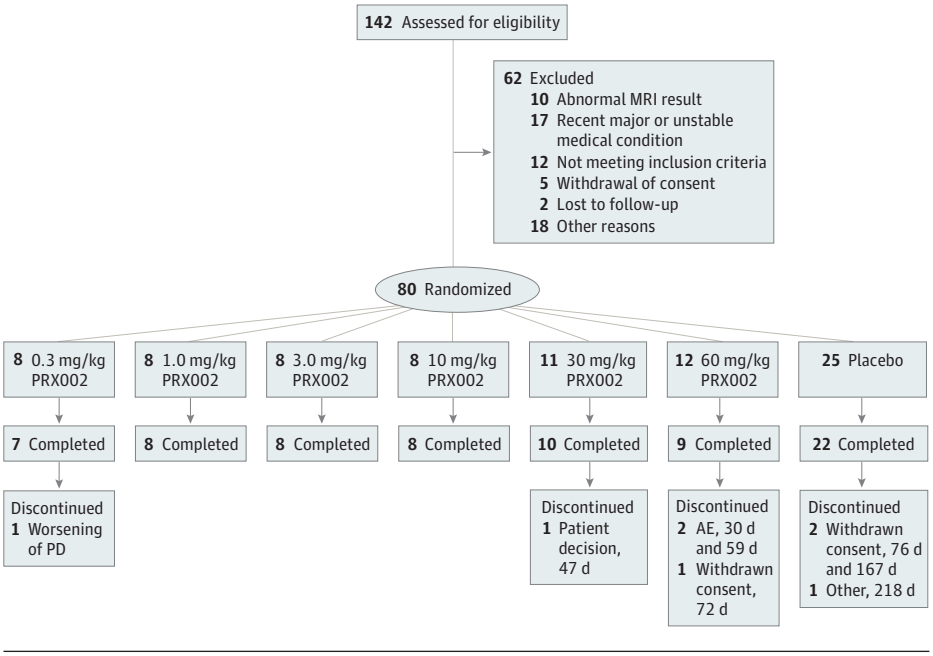
Eighty patients with PD were randomly assigned to receive placebo or PRX002 from July 2014 to September 2016 (**Figure 1**). Demographics and baseline characteristics appeared similar across cohorts (**Table 1**). Median patient age was 58 years. Most participants had Hoehn and Yahr stage 2 (72.0% placebo vs 70.9% PRX002); mean total MDS-UPDRS scores were 48.5 (placebo) vs 47.3 (PRX002). Medical and treatment histories were also similar; most participants across all cohorts used dopaminergic medications before baseline (96.0% placebo vs 80.0% PRX002), did not have a family history of PD (84.0% placebo vs 78.2% PRX002), and did not have a history of rapid eye movement sleep behavioral disorder (88.0% placebo vs 72.7% PRX002).

No significant protocol deviations occurred. One additional patient in cohort 5 was enrolled to replace a patient who was randomly assigned but not treated. All 80 participants (25 placebo and 55 PRX002) were included in the intent-to-treat, pharmacodynamic, and safety analyses; all 55 participants who received PRX002 were included in the pharmacokinetic analysis.

© 2018 American Medical Association. All rights reserved.

Downloaded From: https://jamanetwork.com/ on 08/13/2020

Figure 1. CONSORT Flowchart



Eligibility exclusions were counted more than once for the inclusion/exclusion criteria they did not meet. AE indicates adverse event; MRI, magnetic resonance imaging; PD, Parkinson disease.

Safety and Immunogenicity

Multiple intravenous infusions of PRX002 (range, 0.3-60 mg/kg) were generally safe and well tolerated; no serious or severe treatment-emergent AEs (TEAEs) were reported in PRX002-treated participants. No deaths occurred during the study. Two patients in the 60-mg/kg PRX002 group had AEs leading to study discontinuation (days 30 and 59; both infusion-related reactions [IRRs]).

Fifty-four participants (67.5%) reported TEAEs, most of which were mild. Common TEAEs more frequent in the PRX002 group vs placebo group, irrespective of study drug relatedness, were constipation, IRR, diarrhea, peripheral edema, and post-lumbar puncture syndrome (**Table 2**). The only PRX002-related TEAE experienced by at least 1 participant in any cohort was IRR, reported in 4 participants in the 60-mg/kg PRX002 cohort. Two participants reported moderate IRR. One occurred after the first infusion (acute allergic reaction [skin rash and tongue numbness]) and the other after the second infusion (skin rash); both events resolved with medication, and study drug was discontinued. A third participant reported moderate IRR following the first and second infusions (skin rash) that resolved with medication. This participant was premedicated for the third infusion, which was increased to 120 minutes and was uneventful. A fourth participant reported mild IRRs (dysgeusia and pruritus) with the first infusion that spontaneously resolved; the second and third infusions (no premedication) were uneventful.

All other PRX002-related TEAEs (mild headache, moderate worsening of insomnia, mild nausea, mild diarrhea, mild dizziness, and mild fatigue) occurred in 1 patient each and resolved without treatment. No clinically relevant or treatment-related trends emerged from clinical laboratory data, physical examinations, neurological examinations, vital signs, or electrocardiography after dosing. Exploratory clinical assessments showed no clinically meaningful or dose-dependent PRX002-related treatment differences within any treatment cohort. DaTscan showed statistically significant ($F_{3,31}$ = 2.3; P < .05) increases in DaTscan tracer uptake from baseline to day 71, relative to placebo, but these were not considered clinically meaningful because they occurred only for the 10 mg/kg dose group. No antidrug antibodies were detected.

Pharmacokinetics

Serum mean C_{max} and mean area under the curve increased in an approximately dose-proportional manner across the 6 dose cohorts (eTable 2 in Supplement 2). The mean terminal elimination half-life was similar across all dose cohorts and was approximately 10.2 days (245 hours; range, 206-282; eFigure 1 in Supplement 2). Clearance was similar across dose cohorts and not different between the first and last (third) infusions, with mean clearance at steady state ranging from 0.0185 to 0.0391 L/h. Volume of distribution at steady state was approximately consistent across dose groups, with means ranging from 6.12 to 11.4 L after the third infusion. Accumulation ratios, as measured by C_{max} and area under the concentration-time curve from zero to tau, suggested minimal accumulation of less than 1.5-fold on systemic exposure following the third infusion. Mean CSF PRX002 exposure measured at approximately week 9 increased with PRX002 dose; on average, the concentration of PRX002 in CSF relative to serum was approximately 0.3% across all dose cohorts (**Figure 2**).

Pharmacodynamics

Infusions of PRX002 resulted in statistically significant dose- and time-dependent reductions from baseline in free (unbound) serum α-synuclein (**Figure 3**). The greatest reductions after the first infusion were in the 60-mg/kg dose cohort (96.7%) and were similar after the first, second, and third infusions.

© 2018 American Medical Association. All rights reserved.

Downloaded From: https://jamanetwork.com/ on 08/13/2020

Table 1. Baseline Characteristics of Participants With Parkinson Disease

Characteristic	No. (%)								
		PRX002 Dose Level							
	Placebo (n = 25)	0.3 mg/kg (n = 8)	1 mg/kg (n = 8)	3 mg/kg (n = 8)	10 mg/kg (n = 8)	30 mg/kg (n = 11)	60 mg/kg (n = 12)	Total (n = 55)	All Participants (n = 80)
Age, median (range), y	58.0 (47-77)	56.0 (43-78)	64.0 (48-74)	58.0 (43-73)	59.5 (51-65)	53.0 (43-73)	55.0 (46-73)	57.0 (43-78)	58.0 (43-78)
Sex									
Male	24 (96.0)	6 (75.0)	5 (62.5)	6 (75.0)	7 (87.5)	7 (63.6)	9 (75.0)	40 (72.7)	64 (80.0)
Female	1 (4.0)	2 (25.0)	3 (37.5)	2 (25.0)	1 (12.5)	4 (36.4)	3 (25.0)	15 (27.3)	16 (20.0)
Race									
White	24 (96.0)	7 (87.5)	8 (100)	8 (100)	8 (100)	11 (100)	12 (100)	54 (98.2)	78 (97.5)
Asian	1 (4.0)	0	0	0	0	0	0	0	1 (1.3)
Black or African American	0	1 (12.5)	0	0	0	0	0	1 (1.8)	1 (1.3)
Body weight, median (range), kg	79.4 (59-117)	82.3 (65-96)	70.3 (46-87)	74.7 (63-100)	84.8 (65-106)	73.9 (52-99)	79.5 (59-106)	75.3 (46-106)	78.7 (46-117)
Time since onset of symptoms, median (range), y	7.1 (1-24)	4.2 (2-10)	5.4 (3-18)	4.7 (3-13)	5.0 (2-9)	3.0 (2-8)	4.2 (2-17)	4.2 (2-18)	4.6 (1-24)
Time since diagnosis of PD, median (range), y	3.9 (1-15)	2.8 (0-8)	2.5 (0-12)	2.5 (1-13)	3.5 (0-9)	2.2 (1-6)	3.1 (1-15)	3.0 (0-15)	3.2 (0-15)
Hoehn and Yahr stage									
Stage 1	3 (12.0)	0	1 (12.5)	1 (12.5)	1 (12.5)	3 (27.3)	1 (8.3)	7 (12.7)	10 (12.5)
Stage 2	18 (72.0)	6 (75.0)	3 (37.5)	6 (75.0)	6 (75.0)	7 (63.6)	11 (91.7)	39 (70.9)	57 (71.3)
Stage 3	4 (16.0)	2 (25.0)	4 (50.0)	1 (12.5)	1 (12.5)	1 (9.1)	0	9 (16.4)	13 (16.3)
Total MDS-UPDRS score, mean (range)	48.5 (19-98)	55.8 (41-71)	43.9 (15-71)	52.4 (22-87)	41.5 (11-59)	40.5 (14-57)	50.6 (24-75)	47.3 (11-87)	47.7 (11-98)
Previous use of dopaminergic medications	24 (96.0)	7 (87.5)	5 (62.5)	8 (100)	5 (62.5)	9 (81.8)	10 (83.3)	44 (80.0)	68 (85.0)

Abbreviations: MDS-UPDRS, Movement Disorder Society–Unified Parkinson's Disease Rating Scale; PD, Parkinson disease.

© 2018 American Medical Association. All rights reserved.

Downloaded From: https://jamanetwork.com/ on 08/13/2020

Table 2. Treatment-Emergent Adverse Events Occurring in at Least 5% of Participants

Adverse Event	No. (%)							
		PRX002 Dose Level						
	Placebo (n = 25)	0.3 mg/kg (n = 8)	1 mg/kg (n = 8))	3 mg/kg (n = 8)	10 mg/kg (n = 8)	30 mg/kg (n = 11)	60 mg/kg (n = 12)	Total (n = 55)
AEs[a]	17 (68.0)	4 (50.0)	5 (62.5)	5 (62.5)	4 (50.0)	10 (90.9)	9 (75.0)	37 (67.3)
Treatment-related AEs	3 (12.0)	1 (12.5)	0	1 (12.5)	1 (12.5)	0	4 (33.3)	7 (12.7)
TEAEs								
Constipation	0	0	0	1 (12.5)	2 (25.0)	2 (18.2)	0	5 (9.1)
Infusion-related reaction	0	0	0	0	0	0	4 (33.3)[b,c]	4 (7.3)
Diarrhea	0	0	2 (25.0)	1 (12.5)[b]	0	0	0	3 (5.5)
Headache	2 (8.0)	1 (12.5)[b]	1 (12.5)	0	1 (12.5)	0	0	3 (5.5)
Peripheral edema	0	0	0	0	1 (12.5)	0	2 (16.7)	3 (5.5)
Postlumbar puncture syndrome	0	0	0	1 (12.5)	0	1 (9.1)	1 (8.3)	3 (5.5)
Upper respiratory tract infection	3 (12.0)	0	0	0	0	2 (18.2)	1 (8.3)	3 (5.5)

Abbreviations: AE, adverse events; TEAEs, treatment-emergent adverse events.

[a] Unless indicated, all adverse events were mild and were unrelated to study drug.

[b] Considered related to study drug.

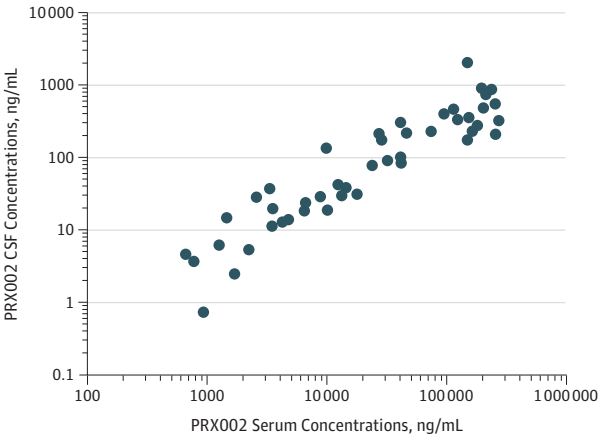
[c] Moderate PRX002-related AEs in 3 participants resulted in the discontinuation of 2 participants from the study.

Statistically significant reductions from baseline vs placebo after the first infusion were seen at 1 and 4 hours for all dose groups, at days 8 and 15 for the 3- to 60-mg/kg PRX002 groups, and at day 29 for the 3-mg/kg, and the 10- to 60-mg/kg PRX002 groups. Statistically significant reductions after the third infusion were seen at 1 and 4 hours for all dose groups, at day 64 for the 1- to 60-mg/kg PRX002 groups, at day 71 for the 1-mg/kg and the 3- to 60-mg/kg PRX002 groups, and at day 85 for the 3- to 60-mg/kg PRX002 groups. Reductions were maintained for longer durations after higher PRX002 doses.

Increases from baseline of total (unbound plus PRX002 bound) serum α-synuclein were also dose and time dependent (eFigure 2 in Supplement 2). The greatest increase was seen 1 week after the third infusion in the 60-mg/kg cohort (least squares mean, 86 µg/mL; increase, 458%). Increases were statistically significant 1 week after the first infusion for the 30- and 60-mg/kg cohorts and 4 weeks after the first infusion for the 10-mg/kg cohort. Increases for the 30- and 60-mg/kg cohorts remained significant until the last sampling (4 weeks after the third infusion) except at 1 hour after the third infusion for the 30-mg/kg cohort, with an upward trend in total serum α-synuclein levels across the 3 infusions.

No statistically significant CSF changes from baseline vs placebo were seen for free α-synuclein, total α-synuclein (except cohort 5 [30 mg/kg PRX002]), total Aβ, Aβ42, or DJ-1 (except cohort 3 [3 mg/kg PRX002]) across the PRX002 dose cohorts, and no dose-dependent trends were observed.

Figure 2. Cerebrospinal Fluid (CSF) and Serum PRX002 Concentrations Approximately 9 Weeks After the First Infusion



Study drug was administered at baseline, week 4, and week 8. The ratio of CSF to serum concentrations was approximately the same across all dose levels.

Discussion

This study demonstrated that PRX002, an immunotherapy designed to preferentially target aggregated α-synuclein, was capable of engaging peripheral α-synuclein in patients with PD. Multiple intravenous infusions of PRX002 were generally safe and well tolerated at all dose levels up to and including 60 mg/kg intravenously every 4 weeks. No deaths, serious AEs, or anti-PRX002 antibodies were noted. Marked reductions in free serum α-synuclein levels were seen within 1 hour of PRX002 administration after each of the 3 infusions. Dose-dependent increases in PRX002 levels were demonstrated in serum and in CSF.

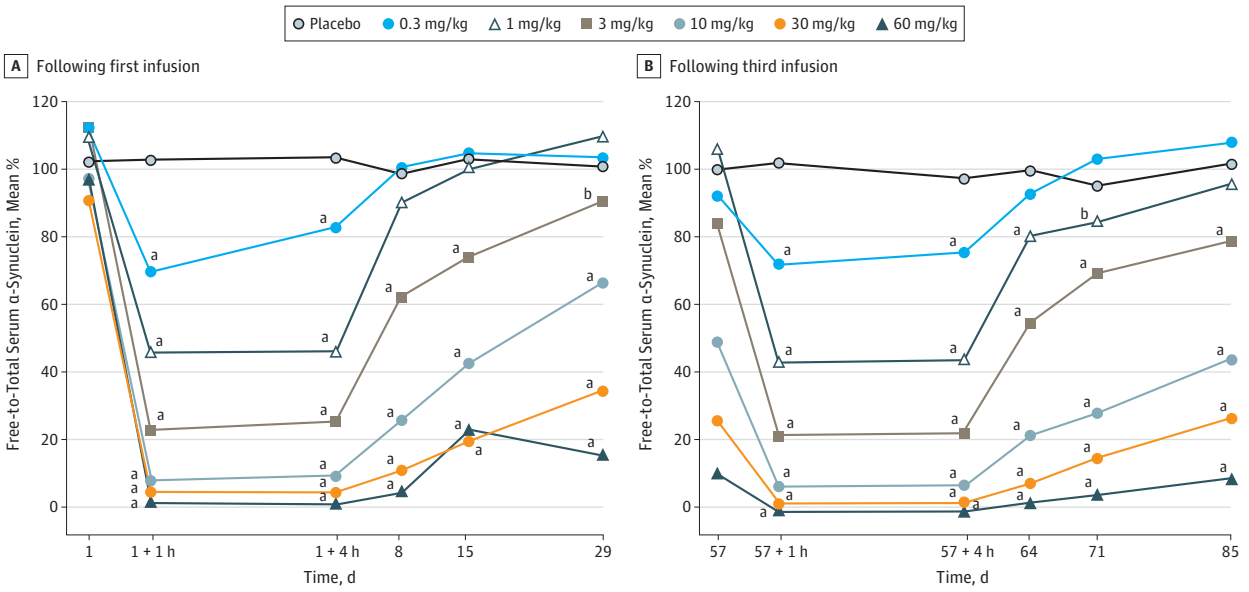
Parkinson disease treatments are aimed chiefly toward attenuating motor symptoms, typically through modulating dopamine pathways,[2] but they do not address the underlying degeneration. Several disease-modifying treatments are being investigated in clinical trials and include but are not limited to growth factors, gene therapy, antiapoptotic agents, immune modulation, stem cell–based neuron replacement therapy, and targeting aggregated protein.[19-21]

The protein α-synuclein performs multiple functions in the body and may be best described as a regulator of vesicular

© 2018 American Medical Association. All rights reserved.

Downloaded From: https://jamanetwork.com/ on 08/13/2020

Figure 3. Pharmacodynamics of Free-to-Total Serum α-Synuclein



Pharmacodynamics after the first (A) and third (B) infusions of PRX002. Data represent free serum α-synuclein levels normalized to total α-synuclein. *P* values represent statistical significance compared with placebo.

[a] $P < .001$.

[b] $P < .05$.

transport and neurotransmitter release in the synaptic terminals of neurons.[22] Multiplications and certain point mutations in *SNCA*, the gene encoding α-synuclein, lead to familial PD, and genome-wide association studies place *SNCA* as the top genetic risk factor for the sporadic form of the disease.[1] In addition, evidence to support targeting α-synuclein as a potential disease-modifying strategy in PD is derived from α-synuclein aggregates in Lewy bodies and neurites in affected brain regions and in nerves innervating peripheral organs in patients with PD and prodromal PD patients.[23-29] Furthermore, neuropathologic staging of PD, as proposed by Braak, points to a neuron-to-neuron propagation of α-synuclein pathology between nervous system regions in patients with PD.[6] Similarly, host-to-graft propagation of α-synuclein pathology was observed post mortem in some nigral transplants.[4,5] Injection of recombinant preformed α-synuclein fibrils into specified brain regions in mice leads to intraneuronal aggregation of α-synuclein and propagation of the pathology, similar to what is observed in PD, indicating that an extracellular form of aggregated α-synuclein may be involved in this pathomechanism.[30-35]

In preclinical studies, the murine homologue of PRX002 reduced intracellular α-synuclein pathology, protected neurons, and ameliorated cognitive and motor behavior deficits in multiple mouse models of α-synucleinopathy.[9,11,12,15,16] Targeting toxic proteins with monoclonal antibodies is also being evaluated as a potential therapeutic strategy in other neurodegenerative diseases.[36-38]

This study demonstrated a favorable safety and tolerability profile and a marked reduction of free (unbound) serum α-synuclein after multiple doses of PRX002. Notably, rapid and robust reductions in free serum α-synuclein levels were achieved without seriously affecting safety, consistent with a previous healthy volunteer PRX002 study.[18] The one PRX002-related TEAE of note in this study was mild to moderate IRR in 4 participants in the highest dose group, which led to study discontinuation in 2 participants; symptoms were rash, pruritus, dysgeusia, and tongue numbness. Infusion-related reactions are the most commonly reported AEs associated with the administration of monoclonal antibodies.[39] In studies with other antibodies, IRR effects have been mitigated by dose fractionation, lower infusion rates, and/or premedication with antihistamines, acetaminophen, or corticosteroids.[40] Premedication of participants for potential IRRs was not required in this study.

Pharmacokinetic profiles were mostly similar to those in an earlier report of single PRX002 infusions in 30 healthy volunteers, with serum concentrations increasing proportionally with PRX002 dose.[18] The terminal half-life in this study was somewhat shorter than that in the single-dose study in healthy volunteers (approximately 10 days vs approximately 18 days, respectively), possibly because of the more prolonged assessment in the single-dose study. Population pharmacokinetic analyses further confirmed a lack of difference in clearance between healthy participants[18] and participants with PD. Data from this study continue to support monthly dosing for further clinical development. In addition, the CSF/serum antibody ratio of 0.3% in this study was in the high range among studies of monoclonal antibodies targeting β-amyloidor α-synuclein in the CNS.[41,42]

Reductions in free serum α-synuclein were rapid, dose dependent, prolonged, and comparable in magnitude and duration after the first and last doses. These findings, along with in vitro data demonstrating a substantially higher

© 2018 American Medical Association. All rights reserved.

Downloaded From: https://jamanetwork.com/ on 08/13/2020

avidity/affinity of PRX002 for aggregated (K_D, 0.048 nM) vs monomeric (K_D, 20 nM) α-synuclein (determined by surface plasmon resonance in kinetic mode; eFigure 3 in Supplement 2)[17] and CSF penetration of PRX002, suggest that target engagement of aggregated α-synuclein in the CNS may be achieved.

Limitations

Limitations of this study were the small number of patients exposed, the short exposure duration, the relatively low demographic diversity, and the possibility that some patients might later be found to have a disorder other than PD. No adjustments were made for multiple comparisons of exploratory efficacy assessments. Further limitations were the lack of validated assay to directly measure aggregated α-synuclein CSF levels and unavailability of imaging methods to monitor intracellular α-synuclein pathology in the brains of patients with PD. Nonetheless, the substantially higher affinity/avidity of PRX002 for aggregated α-synuclein forms,[15,17] along with the high relative CSF concentrations observed in this study (0.3% of blood), indicate that the antibody has the potential to fully engage extracellular aggregated forms of α-synuclein in the CNS within the doses tested in this study.

No effect was seen on free α-synuclein in CSF, which may best be explained by PRX002 concentrations in the CSF, which, in contrast to the periphery, are not sufficiently high to engage the monomeric species (eFigure 3 in Supplement 2). In addition, how much of the toxic protein must be removed to modify disease progression is unknown. This phase 1b safety, tolerability, and pharmacokinetic study involved 3 infusions in a small number of participants and a short duration of observation, limiting clinical assessment of potential treatment effects. Clinical assessments helped rule out any significant untoward investigational drug effects. Despite the limitations, safety and pharmacokinetics findings from this phase 1b trial provide support for further evaluation of doses up to 60 mg/kg in the ongoing phase 2 efficacy study of PRX002. A dose of 60 mg/kg or less is predicted to effectively engage α-synuclein in the brain and is supported by preclinical efficacy models. The absence of serious safety concerns in this study, the accumulating scientific data in support of this approach, and the clear unmet medical need for disease-modifying therapeutics in PD underscore the importance of future trials.

Conclusions

Single and multiple doses of PRX002 resulted in robust binding of peripheral α-synuclein and in dose-dependent increases of PRX002 in CSF and reached CSF concentrations that may be expected to engage extracellular aggregated α-synuclein in the brain. All tested dose levels of PRX002 had acceptable safety and tolerability profiles, supporting the design of an ongoing phase 2 clinical trial, PASADENA (NCT03100149).

ARTICLE INFORMATION

Accepted for Publication: March 8, 2018.

Published Online: June 18, 2018. doi:10.1001/jamaneurol.2018.1487

Open Access: This article is published under the JN-OA license and is free to read on the day of publication.

Author Affiliations: Parkinson's Disease Center and Movement Disorders Clinic, Department of Neurology, Baylor College of Medicine, Houston, Texas (Jankovic); BioClinica, Orlando, Florida (Goodman); MD Clinical, Hallandale Beach, Florida (Safirstein); Prothena Biosciences Inc, South San Francisco, California (Marmon, Schenk, Koller, Zago, Ness, Soto, Kinney); ClinPharma Resources, San Diego, California (Griffith); University of California, San Diego (Grundman); Global R&D Partners, LLC, San Diego, California (Grundman); Genentech Inc, Product Development, Neuroscience, South San Francisco, California (Ostrowitzki); F. Hoffmann-La Roche Ltd, Basel, Switzerland (Boess, Martin-Facklam); Oregon Health & Science University, Portland (Quinn); Portland Veterans Affairs Medical Center, Portland, Oregon (Quinn); Parkinson's Disease and Movement Disorders Center of Boca Raton, Boca Raton, Florida (Isaacson); Collaborative Neuroscience Network LLC, Long Beach, California (Omidvar); QUEST Research Institute, Farmington Hills, Michigan (Ellenbogen).

Author Contributions: Drs Kinney and Koller had full access to all the data in the study and take responsibility for the integrity of the data and the accuracy of the data analysis.

Concept and design: Jankovic, Schenk, Koller, Zago, Ness, Griffith, Grundman, Soto, Ostrowitzki, Kinney.
Acquisition, analysis, or interpretation of data: Jankovic, Goodman, Safirstein, Marmon, Koller, Zago, Ness, Grundman, Soto, Boess, Martin-Facklam, Quinn, Isaacson, Omidvar, Ellenbogen, Kinney.
Drafting of the manuscript: Marmon, Koller, Zago, Ness, Griffith, Soto, Boess.
Critical revision of the manuscript for important intellectual content: Jankovic, Goodman, Safirstein, Marmon, Schenk, Koller, Zago, Ness, Grundman, Ostrowitzki, Boess, Martin-Facklam, Quinn, Isaacson, Omidvar, Ellenbogen, Kinney.
Statistical analysis: Marmon, Koller, Grundman, Ellenbogen.
Obtained funding: Schenk, Kinney.
Administrative, technical, or material support: Koller, Ness, Griffith, Grundman, Quinn, Isaacson, Ellenbogen, Kinney.
Supervision: Schenk, Koller, Grundman, Soto, Ostrowitzki, Boess, Martin-Facklam, Omidvar, Kinney.

Conflict of Interest Disclosures: Dr Jankovic has served as a consultant to Prothena Biosciences Limited and Prothena Biosciences Inc and has received funding from the Parkinson's Foundation to support the Baylor College of Medicine Center of Excellence. Dr Goodman is an employee of Bioclinica. Drs Marmon and Ness and Mr Soto are employees of Prothena Biosciences Inc and shareholders of Prothena Corporation plc. Dr Grundman is a consultant to Prothena Biosciences Limited and a shareholder of Prothena Corporation plc. Dr Schenk was an employee of Prothena Biosciences Inc and an officer and shareholder of Prothena Corporation plc. Dr Koller was an employee of and is a consultant to Prothena Biosciences Inc and was an officer and a shareholder of Prothena Corporation plc. Dr Zago is an employee of Prothena Biosciences Inc and an officer and shareholder of Prothena Corporation plc. Dr Griffith is a consultant to Prothena Biosciences Inc. Dr Ostrowitzki is an employee and stock owner of Genentech Inc, a member of the Roche group. Dr Boess is an employee and stock owner of F. Hoffmann-La Roche Ltd. Dr Martin-Facklam is an employee of F. Hoffmann-La Roche Ltd. Dr Quinn received compensation for serving on a data and safety monitoring board for vTv Therapeutics. Dr Ellenbogen is an employee of the QUEST Research Institute. Dr Kinney is an employee of Prothena Biosciences Inc and an officer and a shareholder of Prothena Corporation plc. No other disclosures were reported.

Funding Support: This study was sponsored by Prothena Biosciences Limited (Dun Laoghaire, Ireland) and F. Hoffmann-La Roche Ltd (Basel, Switzerland).

Role of the Funder/Sponsor: In collaboration with the authors, the study sponsors (Prothena Biosciences Limited and F. Hoffmann-La Roche Ltd) participated in the design and conduct of the study; collection, management, analysis, and interpretation of the data; review and approval of the manuscript; and the decision to submit the manuscript for publication.

Additional Contributions: Medical writing and editorial assistance was provided by ApotheCom

© 2018 American Medical Association. All rights reserved.

Downloaded From: https://jamanetwork.com/ on 08/13/2020

(San Francisco, California) and was funded by Prothena Biosciences Inc and F. Hoffmann-La Roche Ltd.

Additional Information: Dale B. Schenk, PhD, passed away in September 2016.

REFERENCES

1. Poewe W, Seppi K, Tanner CM, et al. Parkinson disease. *Nat Rev Dis Primers*. 2017;3:17013.

2. Tarakad A, Jankovic J. Diagnosis and management of Parkinson's disease. *Semin Neurol*. 2017;37(2):118-126.

3. Rousseaux MWC, Shulman JM, Jankovic J. Progress toward an integrated understanding of Parkinson's disease. *F1000Res*. 2017;6:1121.

4. Kordower JH, Chu Y, Hauser RA, Freeman TB, Olanow CW. Lewy body-like pathology in long-term embryonic nigral transplants in Parkinson's disease. *Nat Med*. 2008;14(5):504-506.

5. Li JY, Englund E, Holton JL, et al. Lewy bodies in grafted neurons in subjects with Parkinson's disease suggest host-to-graft disease propagation. *Nat Med*. 2008;14(5):501-503.

6. Braak H, Del Tredici K, Rüb U, de Vos RA, Jansen Steur EN, Braak E. Staging of brain pathology related to sporadic Parkinson's disease. *Neurobiol Aging*. 2003;24(2):197-211.

7. Forloni G, Artuso V, La Vitola P, Balducci C. Oligomeropathies and pathogenesis of Alzheimer and Parkinson's diseases. *Mov Disord*. 2016;31(6):771-781.

8. Masliah E, Rockenstein E, Veinbergs I, et al. Dopaminergic loss and inclusion body formation in alpha-synuclein mice: implications for neurodegenerative disorders. *Science*. 2000;287(5456):1265-1269.

9. Masliah E, Rockenstein E, Mante M, et al. Passive immunization reduces behavioral and neuropathological deficits in an alpha-synuclein transgenic model of Lewy body disease. *PLoS One*. 2011;6(4):e19338.

10. Bae EJ, Lee HJ, Rockenstein E, et al. Antibody-aided clearance of extracellular α-synuclein prevents cell-to-cell aggregate transmission. *J Neurosci*. 2012;32(39):13454-13469.

11. Spencer B, Valera E, Rockenstein E, et al. Anti-α-synuclein immunotherapy reduces α-synuclein propagation in the axon and degeneration in a combined viral vector and transgenic model of synucleinopathy. *Acta Neuropathol Commun*. 2017;5(1):7.

12. Masliah E, Rockenstein E, Adame A, et al. Effects of alpha-synuclein immunization in a mouse model of Parkinson's disease. *Neuron*. 2005;46(6):857-868.

13. Spencer B, Williams S, Rockenstein E, et al. α-synuclein conformational antibodies fused to penetratin are effective in models of Lewy body disease. *Ann Clin Transl Neurol*. 2016;3(8):588-606.

14. Tran HT, Chung CH, Iba M, et al. A-synuclein immunotherapy blocks uptake and templated propagation of misfolded α-synuclein and neurodegeneration. *Cell Rep*. 2014;7(6):2054-2065.

15. Games D, Valera E, Spencer B, et al. Reducing C-terminal-truncated alpha-synuclein by immunotherapy attenuates neurodegeneration and propagation in Parkinson's disease-like models. *J Neurosci*. 2014;34(28):9441-9454.

16. Games D, Seubert P, Rockenstein E, et al. Axonopathy in an α-synuclein transgenic model of Lewy body disease is associated with extensive accumulation of C-terminal-truncated α-synuclein. *Am J Pathol*. 2013;182(3):940-953.

17. Jankovic J, Goodman I, Safirestein B, et al. Results from a phase 1b multiple ascending-dose study of PRX002, an anti–alpha-synuclein monoclonal antibody, in patients with Parkinson's disease. *Mov Disord*. 2017;32(suppl 2):S560.

18. Schenk DB, Koller M, Ness DK, et al. First-in-human assessment of PRX002, an anti-α-synuclein monoclonal antibody, in healthy volunteers. *Mov Disord*. 2017;32(2):211-218.

19. Lotia M, Jankovic J. New and emerging medical therapies in Parkinson's disease. *Expert Opin Pharmacother*. 2016;17(7):895-909.

20. Tarazi FI, Sahli ZT, Wolny M, Mousa SA. Emerging therapies for Parkinson's disease: from bench to bedside. *Pharmacol Ther*. 2014;144(2):123-133.

21. Jankovic J. Immunologic treatment of Parkinson's disease. *Immunotherapy*. 2018;10(2):81-84.

22. Burré J. The synaptic function of alpha-synuclein. *J Parkinsons Dis*. 2015;5(4):699-713.

23. Breydo L, Wu JW, Uversky VN. A-synuclein misfolding and Parkinson's disease. *Biochim Biophys Acta*. 2012;1822(2):261-285.

24. Spillantini MG, Schmidt ML, Lee VM, Trojanowski JQ, Jakes R, Goedert M. Alpha-synuclein in Lewy bodies. *Nature*. 1997;388(6645):839-840.

25. Stefanis L. α-Synuclein in Parkinson's disease. *Cold Spring Harb Perspect Med*. 2012;2(2):a009399.

26. Goedert M, Spillantini MG, Del Tredici K, Braak H. 100 years of Lewy pathology. *Nat Rev Neurol*. 2013;9(1):13-24.

27. Lee JM, Derkinderen P, Kordower JH, et al. The search for a peripheral biopsy indicator of alpha-synuclein pathology for Parkinson disease. *J Neuropathol Exp Neurol*. 2017;76(1):2-15.

28. Corbillé AG, Letournel F, Kordower JH, et al. Evaluation of alpha-synuclein immunohistochemical methods for the detection of Lewy-type synucleinopathy in gastrointestinal biopsies. *Acta Neuropathol Commun*. 2016;4:35.

29. Stokholm MG, Danielsen EH, Hamilton-Dutoit SJ, Borghammer P. Pathological α-synuclein in gastrointestinal tissues from prodromal Parkinson disease patients. *Ann Neurol*. 2016;79(6):940-949.

30. Luk KC, Kehm VM, Zhang B, O'Brien P, Trojanowski JQ, Lee VM. Intracerebral inoculation of pathological α-synuclein initiates a rapidly progressive neurodegenerative α-synucleinopathy in mice. *J Exp Med*. 2012;209(5):975-986.

31. Masuda-Suzukake M, Nonaka T, Hosokawa M, et al. Pathological alpha-synuclein propagates through neural networks. *Acta Neuropathol Commun*. 2014;2:88.

32. Peelaerts W, Bousset L, Van der Perren A, et al. α-Synuclein strains cause distinct synucleinopathies after local and systemic administration. *Nature*. 2015;522(7556):340-344.

33. Sacino AN, Brooks M, Thomas MA, et al. Intramuscular injection of α-synuclein induces CNS α-synuclein pathology and a rapid-onset motor phenotype in transgenic mice. *Proc Natl Acad Sci U S A*. 2014;111(29):10732-10737.

34. Jones DR, Delenclos M, Baine AT, et al. Transmission of soluble and insoluble alpha-synuclein to mice. *J Neuropathol Exp Neurol*. 2015;74(12):1158-1169.

35. Rey NL, Steiner JA, Maroof N, et al. Widespread transneuronal propagation of α-synucleinopathy triggered in olfactory bulb mimics prodromal Parkinson's disease. *J Exp Med*. 2016;213(9):1759-1778.

36. Dehay B, Decressac M, Bourdenx M, et al. Targeting α-synuclein: Therapeutic options. *Mov Disord*. 2016;31(6):882-888.

37. Valera E, Spencer B, Masliah E. Immunotherapeutic approaches targeting amyloid-beta, alpha-synuclein, and tau for the treatment of neurodegenerative disorders. *Neurotherapeutics*. 2016;13(1):179-189.

38. Bergström AL, Kallunki P, Fog K. Development of passive immunotherapies for synucleinopathies. *Mov Disord*. 2016;31(2):203-213.

39. Ballow M. Safety of IGIV therapy and infusion-related adverse events. *Immunol Res*. 2007;38(1-3):122-132.

40. Chung CH. Managing premedications and the risk for reactions to infusional monoclonal antibody therapy. *Oncologist*. 2008;13(6):725-732.

41. Brys M, Hung S, Fanning L, et al. Randomized, double-blind, placebo-controlled, single ascending dose study of anti-alpha-synuclein antibody BIIBO54 in healthy volunteers. Paper presented at: 13th International Conference on Alzheimer's and Parkinson's Diseases; April 2, 2017; Vienna, Austria.

42. Logovinsky V, Satlin A, Lai R, et al. Safety and tolerability of BAN2401: a clinical study in Alzheimer's disease with a protofibril selective Aβ antibody. *Alzheimers Res Ther*. 2016;8(1):14.

© 2018 American Medical Association. All rights reserved.

Downloaded From: https://jamanetwork.com/ on 08/13/2020

NIH Public Access
Author Manuscript
Acta Neurochir Suppl. Author manuscript; available in PMC 2014 July 21.

Published in final edited form as:
Acta Neurochir Suppl. 2011 ; 109: 21–25. doi:10.1007/978-3-211-99651-5_4.

Intraoperative Imaging in Neurosurgery: Where Will the Future Take Us?

Ferenc A. Jolesz
B. Leonard Holman Professor of Radiology, Division of MRI and Image Guided Therapy Program, Department of Radiology, Brigham and Women's Hospital, Harvard Medical School, 75 Francis Street, Boston, MA 02115, USA

Ferenc A. Jolesz: jolesz@bwh.harvard.edu

Abstract

Intraoperative MRI (ioMRI) dates back to the 1990s and since then has been successfully applied in neurosurgery for three primary reasons with the last one becoming the most significant today: (1) brain shift-corrected navigation, (2) monitoring/controlling thermal ablations, and (3) identifying residual tumor for resection. IoMRI, which today is moving into other applications, including treatment of vasculature and the spine, requires advanced 3 T MRI platforms for faster and more flexible image acquisitions, higher image quality, and better spatial and temporal resolution; functional capabilities including fMRI and DTI; non-rigid registration algorithms to register pre- and intraoperative images; non-MRI imaging improvements to continuously monitor brain shift to identify when a new 3D MRI data set is needed intraoperatively; more integration of imaging and MRI-compatible navigational and robot-assisted systems; and greater computational capabilities to handle the processing of data. The Brigham and Women's Hospital's "AMIGO" suite is described as a setting for progress to continue in ioMRI by incorporating other modalities including molecular imaging. A call to action is made to have other researchers and clinicians in the field of image guided therapy to work together to integrate imaging with therapy delivery systems (such as laser, MRgFUS, endoscopic, and robotic surgery devices).

Keywords

Image guided therapy; Imaging; Interventional; Intraoperative MRI (ioMRI); Magnetic resonance; MR; Neurosurgery

Introduction

Since the early 1990s when we introduced intraoperative MRI (ioMRI) to the field of neurosurgery, it has greatly developed and the number of users and clinical applications have increased [1–10]. It is now important to look back and evaluate the progress of ioMRI to assess what has happened during almost two decades of activity and to identify to the best of our abilities where we are headed.

© Springer-Verlag/Wien 2011

Conflict of interest statement Dr. Jolesz has received cosultant fees from General Electric, who pioneered this system.

NIH-PA Author Manuscript
NIH-PA Author Manuscript
NIH-PA Author Manuscript

NIH-PA Author Manuscript

NIH-PA Author Manuscript

NIH-PA Author Manuscript

The original reasons to develop ioMRI were the following:

1. Brain shift-corrected navigation: The navigational systems used in operating rooms rely on preoperative images that do not reflect changes in brain anatomy due to deformations and shifts during surgery. This situation has caused inaccurate targeting and major limitations for neuronavigation. Today, by updating information on the brain using a 3D image database, navigation is made more accurate throughout the entire surgical procedure [11, 12].
2. Monitoring/controlling thermal ablations: The original idea of MRI-guided interstitial laser brain surgery leveraged the temperature sensitivity of MRI to allow for temperature monitoring during the procedure [13–20]. Today, radio-frequency (RF) and focused ultrasound thermal ablations can similarly be controlled through MRI [21–26].
3. Identifying residual tumor: MRI allows the clinician to verify completeness of tumor removal at the end of surgery and, if needed, to perform an additional tumor resection. The original vision for ioMRI focused on correcting for brain shift and monitoring temperature, while today most users apply to perform ioMRI for the third reason: tumor control [4, 27–29].

Since its introduction, ioMRI, conceptually and in real practice, has grown and changed significantly.

Present Benefits and Capabilities

The original full access open MRI, like the SIGNA SP (General Electric Healthcare Technologies, Waukesha, WI), was replaced with open limited access low and midfield magnets and high (1.5 T) and ultra high field (3 T) closed bore MRI scanners [6, 9, 10, 30–32]. Although, the SIGNA SP represented the best configuration, it is at midfield and, therefore, not optimal for neurosurgery. Today most neurosurgeons want higher field strength and more advanced image acquisition technology that is only available in high field advanced systems to obtain higher image quality and better spatial and temporal resolution.

Advanced 3 T imaging platforms achieve faster and more flexible image acquisitions that improve localization, targeting, monitoring, and therapy control. Advance imaging methods functional MRI (fMRI) and diffusion tensor imaging (DTI) have been introduced into neurosurgery and integrated into intraoperative imaging [33–35].

As far as clinical applications are concerned, ioMRI has been successfully developed and implemented for multiple procedures, including:

- Biopsies and placement of electrodes
- Craniotomies for image-guided resection of benign and malignant intracranial tumors
- Intracranial cyst drainages and
- Thermal ablations for malignant and benign tumors.

NIH-PA Author Manuscript

NIH-PA Author Manuscript

NIH-PA Author Manuscript

Future ioMRI Applications

In the future, this application pool will expand to:

Bening tumors (skull base): MRI-enhanced neuroendoscopy can be faster and safer than conventional neuroendoscopy and minimize the possibility of complications. A strong need exists to develop MRI-compatible flexible endoscopes with position tracking coils. The combination of the two techniques may provide the best surgical guidance. The most promising application is endoscopic transphenoidal surgery for midline skull base and parasellar lesions and transventricular endoscopic removal for extra-ventricular tumors.

Neurovascular abnormalities and stroke: ioMRI provides real-time perfusion and diffusion imaging to intraoperatively diagnose acutely developed vascular occlusion and to monitor the condition of the brain during surgeries and/or endovascular procedures. Intraoperative imaging of vascular anatomy, including feeding arteries and the draining veins of an intracranial arteriovenous malformation (AVM), allows the neurosurgeon to intraoperatively assess vessels and surrounding areas and make decisions about the need to completely and safely resect or obliterate a vascular malformation.

Various diseases of the spine: Spinal surgeries with IMR will include: lumbar discectomies, anterior cervical discectomies with fusion, cervical vertebrectomies, foraminotomies, and laminectomies. Through ioMRI, the accuracy of localization and adequacy of decompression can be assessed. Future applications may also include: resection of spine and spinal cord, tumors, and spinal endoscopy. Temperature sensitive imaging for laser discectomy and vertebroplasty can be performed with ioMRI guidance to prevent the thermal damage of the nerve roots and spinal cord.

ioMRI Approaches

The “tumor control” method of ioMRI is a practical and well accepted use of the technology, though it is best applied, not as a single imaging session at the completion of surgery when the clinician cannot take full advantage of ioMRI, but throughout surgery to provide corrected, brain shift-compensated guidance (with serial imaging and navigation). The goal of more complete and effective tumor resection can only be accomplished if we have better techniques to detect the full extent of infiltrative brain tumors. ioMRI is part of this solution along with other multimodality-based molecular imaging (optical, nuclear, or other). Besides tumor margin detection, we need more detailed information about the functional and structural anatomy of the normal brain tissue that surrounds the tumor (for MRI such detail comes through multiparametric imaging: T1, T2, fMRI, DTI perfusion imaging).

Managing the Brain Shift Challenge

Navigational systems fully integrated with ioMRI are also part of improved image guidance [8, 11, 36–39]. For example, it is necessary to monitor brain shift with a non-MRI technique for continuous monitoring that helps the surgeon/neuroradiologist to decide when a new

NIH-PA Author Manuscript

NIH-PA Author Manuscript

NIH-PA Author Manuscript

MRI 3D dataset should be obtained. Development of an integrated system to improve visualization, navigation, and monitoring is a necessary step in this direction.

Today we know it is possible to create an augmented reality visualization of the intraoperative configuration of the patient's brain merged with high resolution preoperative imaging data, including DTI and fMRI to better localize the tumor and critical healthy tissues. Brain shift-corrected imaging requires the use of non-rigid registration algorithms to compensate for displacements [40–42]. Massive computational needs must support these capabilities that entail online usage in reasonable time frames of less than 5 min. One of the main reasons for this computational load is that, to properly account for ongoing brain shifts, fMRI and DTI must be accurately co-registered and updated.

Methods of monitoring brain shift now include:

Laser Range Scanner (LRS): Devices, mostly used in robotics applications, that emit and receive a laser beam and by measuring difference of phase, time of flight or frequency shift depth is measured.

Stereo camera imaging: Imaging from a type of camera with two or more lenses that can capture three-dimensional images.

Transcranial US (ITUM): A type of device, at the prototype stage, that uses the shear mode of transcranial ultrasound transmission to intraoperatively monitor brain shift. MRI can then be obtained with the device spatially registered to the MRI reference coordinates [43].

Further Development

ioMRI allows for the introduction of new surgical approaches and/or techniques in vascular neurosurgery, spine surgery, and skull base surgery (using image guided and registered neuroendoscopy). Further moving ioMRI forward in neurosurgery is the already-underway integration of ioMRI with image guided robots that provide, through remote manipulation, an alternative solution to limited access. Already, for many types of neurosurgical procedures, companies have developed MRI-compatible robotic systems and manipulators [44–51]. Today most systems still lack the clinical validation that is necessary for the surgical robot to execute not only biopsies but also complex surgical manipulations.

ioMRI today has also moved beyond MRI-guided and controlled thermal ablations for interstitial laser therapy [13, 14, 16, 17, 19] to MRI-guided focused ultrasound surgery (MRgFUS) as well as the targeted ablative treatment of brain tumors via drug delivery through an open blood-brain-barrier (BBB) [23–25, 52–57]. FUS-induced neuromodulation is a complement to functional neurosurgical applications for coagulative lesions [57–59].

Greater progress and expansion for ioMRI requires the development of new, more advanced imaging methods, navigational techniques, surgical instruments and tools; the more efficient use of computing technologies; and the integration of diagnostic and therapy devices with navigational tools (computer-assisted surgery). A need exists for a multi-focused,

NIH-PA Author Manuscript

NIH-PA Author Manuscript

NIH-PA Author Manuscript

multidisciplinary effort involving researchers and clinicians to explore and refine ioMRI to make it as cost-effective and as widely accessible to a multidisciplinary pool of users.

AMIGO: Merging ioMRI and Other Modalities

At the Brigham and Women's Hospital, we are taking a lead in this effort through the development and execution of a multimodality approach to intraoperative imaging by integrating the components of a rich multimodal and translational clinical research environment to carry out open and minimally invasive surgeries and percutaneous interventions. Multimodality IGT provides comprehensive information derived from different physical and biological properties. Combined multimodalities provide anatomical, metabolic, and functional information – a previously stated goal for ioMRI. Images can be complemented with newly developed multiple molecular probes (nuclear, optical, mass spectrometer, etc.). The use of multiple molecular probes improves the sensitivity and specificity of cancer-relevant applications over single mode imaging. To achieve this we must expand our imaging platform for image guided neurosurgery to include all modalities, especially those applicable to molecular imaging (PETCT, MRI, optical imaging).

The validation of imaging tools and molecular imaging agents in a multimodal surgical setting is possible because, during surgeries, multiple tissue samples can be obtained for pathology that can validate imaging findings at the same location. Navigational and registration methods for multimodal registration can be used to compare multiple probes that are measuring exactly the same tissue region.

The BWH's Advanced Multimodality Image Guided Operating (AMIGO) Suite (see Fig. 1), opening in 2010, is uniquely designed to support, alongside routine clinical procedures, the next phase of clinical and research activity in ioMRI that will incorporate multimodal imaging. The logistics of the suite are such that multidisciplinary teams will be in close cooperation with one another during procedures that might involve the use of an array of on-site (i.e., in the suite itself) modalities from 3D ultrasound, fluoroscopy, MRI, and PET/CT to carry out a variety of procedures.

The AMIGO and suites like it are at the forefront by providing settings for practice, refinement, improvement, validation, and innovation. Indeed, the future of intraoperative imaging in neurosurgery depends on such settings and teams and their increased application of advanced technologies and multimodality imaging. Integration of imaging with therapy delivery systems (laser, MRgFUS, endoscopic and robotic surgery devices) will characterize the next phase of this emerging field.

References

1. Black PM, Alexander E 3rd, Martin C, et al. Craniotomy for tumor treatment in an intraoperative magnetic resonance imaging unit. Neurosurgery. 1999; 45(3):423–431. [PubMed: 10493363]
2. Dimaio SP, Archip N, Hata N, et al. Image-guided neurosurgery at Brigham and Women's Hospital. IEEE Eng Med Biol Mag. 2006; 25(5):67–73. [PubMed: 17020201]
3. Hall WA, Martin AJ, Liu H, et al. High-field strength interventional magnetic resonance imaging for pediatric neurosurgery. Pediatr Neurosurg. 1998; 29(5):253–259. [PubMed: 9917543]

NIH-PA Author Manuscript

NIH-PA Author Manuscript

NIH-PA Author Manuscript

4. Jolesz FA, Talos IF, Schwartz RB, et al. Intraoperative magnetic resonance imaging and magnetic resonance imaging-guided therapy for brain tumors. Neuroimaging Clin N Am. 2002; 12 (4):665–683. [PubMed: 12687918]
5. Lewin JS, Metzger AK. Intraoperative MR systems. Low-field approaches. Neuroimaging Clin N Am. 2001; 11(4):611–628. [PubMed: 11995417]
6. Schenck JF, Jolesz FA, Roemer PB, Cline HE, Lorensen WE, Kikinis R, et al. Superconducting open-configuration MR imaging system for image-guided therapy. Radiology. 1995; 195 (3):805–814. [PubMed: 7754014]
7. Schwartz RB, Hsu L, Wong TZ, et al. Intraoperative MR imaging guidance for intracranial neurosurgery: experience with the first 200 cases. Radiology. 1999; 211(2):477–488. [PubMed: 10228532]
8. Schulder M, Liang D, Carmel PW. Cranial surgery navigation aided by a compact intraoperative magnetic resonance imager. J Neurosurg. 2001; 94(6):936–945. [PubMed: 11409523]
9. Steinmeier R, Fahlbusch R, Ganslandt O, et al. Intraoperative magnetic resonance imaging with the magnetom open scanner: concepts, neurosurgical indications, and procedures: a preliminary report. Neurosurgery. 1998; 43(4):739–747. discussion 747–748. [PubMed: 9766299]
10. Sutherland GR, Kaibara T, Louw D, Hoult DI, Tomanek B, Saunders J. A mobile high-field magnetic resonance system for neurosurgery. J Neurosurg. 1999; 91(5):804–813. [PubMed: 10541238]
11. Jolesz FA, Kikinis R, Talos IF. Neuronavigation in interventional MR imaging. Frameless stereotaxy. Neuroimaging Clin N Am. 2001; 11(4):685–689. [PubMed: 11995423]
12. Nabavi A, Black PM, Gering DT, et al. Serial intraoperative magnetic resonance imaging of brain shift. Neurosurgery. 2001; 48 (4):787–797. discussion 797–798. [PubMed: 11322439]
13. Anzai Y, Lufkin R, DeSalles A, Hamilton DR, Farahani K, Black KL. Preliminary experience with MR-guided thermal ablation of brain tumors. AJNR Am J Neuroradiol. 1995; 16(1):39–48. discussion 49–52. [PubMed: 7900601]
14. Ascher PW, Justich E, Schröttner O. Interstitial thermotherapy of central brain tumors with the Nd:YAG laser under real-time monitoring by MRI. J Clin Laser Med Surg. 1991; 9(1):79–83. [PubMed: 10150912]
15. Bettag M, Ulrich F, Schober R, et al. Stereotactic laser therapy in cerebral gliomas. Acta Neurochir Suppl (Wien). 1991; 52:81–83. [PubMed: 1792975]
16. Fan M, Ascher PW, Schröttner O, Ebner F, Germann RH, Kleinert R. Interstitial 1.06 Nd:YAG laser thermotherapy for brain tumors under real-time monitoring of MRI: experimental study and phase I clinical trial. J Clin Laser Med Surg. 1992; 10(5):355–356. [PubMed: 10147968]
17. Kahn T, Bettag M, Ulrich F, et al. MRI-guided laser-induced interstitial thermotherapy of cerebral neoplasms. J Comput Assist Tomogr. 1994; 18:519–532. [PubMed: 8040431]
18. Kettenbach J, Silverman SG, Hata N, et al. Monitoring and visualization techniques for MR-guided laser ablations in an open MR system. J Magn Reson Imaging. 1998; 8(4):933–943. [PubMed: 9702896]
19. McDannold NJ, Jolesz FA. Magnetic resonance image-guided thermal ablations. Top Magn Reson Imaging. 2000; 11(3):191–202. [PubMed: 11145211]
20. Stollberger R, Ascher PW, Huber D, Renhart W, Radner H, Ebner F. Temperature monitoring of interstitial thermal tissue coagulation using MR phase images. J Magn Reson Imaging. 1998; 8(1): 188–196. [PubMed: 9500279]
21. Cline HE, Hynynen K, Watkins RD, et al. Focused US system for MR imaging-guided tumor ablation. Radiology. 1995; 194 (3):731–737. [PubMed: 7862971]
22. Hynynen K, Vykhodtseva NI, Chung AH, Sorrentino V, Colucci V, Jolesz FA. Thermal effects of focused ultrasound on the brain: determination with MR imaging. Radiology. 1997; 204(1):247–253. [PubMed: 9205255]
23. Jolesz FA, Hynynen K. Magnetic resonance image-guided focused ultrasound surgery. Cancer J. 2002; 8(suppl 1):S100–S112. [PubMed: 12075696]
24. Jolesz FA, Hynynen K, McDannold N, Tempany C. MR imaging-controlled focused ultrasound ablation: a noninvasive image-guided surgery. Magn Reson Imaging Clin N Am. 2005; 13(3):545–60. [PubMed: 16084419]

NIH-PA Author Manuscript

NIH-PA Author Manuscript

NIH-PA Author Manuscript

25. Jolesz FA, McDannold N. Current status and future potential of MRI-guided focused ultrasound surgery. J Magn Reson Imaging. 2008; 27(2):391–399. [PubMed: 18219674]
26. McDannold N, Hynynen K, Wolf D, Wolf G, Jolesz F. MRI evaluation of thermal ablation of tumors with focused ultrasound. J Magn Reson Imaging. 1998; 8(1):91–100. [PubMed: 9500266]
27. Claus EB, Horlacher A, Hsu L. Survival rates in patients with low-grade glioma after intraoperative magnetic resonance image guidance. Cancer. 2005; 103(6):1227–1233. [PubMed: 15690327]
28. Mittal S, Black PM. Intraoperative magnetic resonance imaging in neurosurgery: the Brigham concept. Acta Neurochir Suppl. 2006; 98:77–86. [PubMed: 17009704]
29. Nimsky C, Fujita A, Ganslandt O, Von Keller B, Fahlbusch R. Volumetric assessment of glioma removal by intraoperative high-field magnetic resonance imaging. Neurosurgery. 2004; 55(2): 358–370. discussion 370–371. [PubMed: 15271242]
30. Bradley WG. Achieving gross total resection of brain tumors: intraoperative MR imaging can make a big difference. AJNR Am J Neuroradiol. 2002; 23(3):348–349. [PubMed: 11900997]
31. Nimsky C, Ganslandt O, Von Keller B, Romstöck J, Fahlbusch R. Intraoperative high-field-strength MR imaging: implementation and experience in 200 patients. Radiology. 2004; 233(1): 67–78. [PubMed: 15317949]
32. Truwit CL, Hall WA. Intraoperative magnetic resonance imaging-guided neurosurgery at 3-T. Neurosurgery. 2006; 58(4 suppl 2):ONS-338–345. discussion ONS-345–346.
33. Hall WA, Liu H, Truwit CL. Functional magnetic resonance imaging-guided resection of low-grade gliomas. Surg Neurol. 2005; 64(1):20–27. discussion. [PubMed: 15993174]
34. Golby, AJ.; McConnell, KA. Functional brain mapping options for minimally invasive surgery. In: Black, PM.; Proctor, M., editors. Minimally invasive neurosurgery. Humana Press; Totawa, NJ: 2004. p. 87-106.
35. Nimsky C, Ganslandt O, Kober H, et al. Integration of functional magnetic resonance imaging supported by magnetoencephalography in functional neuronavigation. Neurosurgery. 1999; 44 (6): 1249–1255. discussion 1255–1256. [PubMed: 10371623]
36. Gering DT, Nabavi A, Kikinis R, et al. An integrated visualization system for surgical planning and guidance using image fusion and an open MR. J Magn Reson Imaging. 2001; 13(6):967–975. [PubMed: 11382961]
37. Nabavi A, Gering DT, Kacher DF, et al. Surgical navigation in the open MRI. Acta Neurochir Suppl. 2003; 85:121–125. [PubMed: 12570147]
38. Nimsky C, Ganslandt O, Cerny S, Hastreiter P, Greiner G, Fahlbusch R. Quantification of, visualization of, and compensation for brain shift using intraoperative magnetic resonance imaging. Neurosurgery. 2000; 47(5):1070–1079. discussion 1079–1080. [PubMed: 11063099]
39. Nimsky C, Ganslandt O, Hastreiter P, Fahlbusch R. Intraoperative compensation for brain shift. Surg Neurol. 2001; 56(6):357–364. discussion 364–365. [PubMed: 11755962]
40. Clatz O, Delingette H, Talos IF, et al. Hybrid formulation of the model-based non-rigid registration problem to improve accuracy and robustness. Med Image Comput Comput Assist Interv. 2005; 8(Pt 2):295–302. [PubMed: 16685972]
41. Ferrant M, Nabavi A, Macq B, et al. Serial registration of intraoperative MR images of the brain. Med Image Anal. 2002; 6(4):337–359. [PubMed: 12426109]
42. Warfield SK, Haker SJ, Talos IF, et al. Capturing intraoperative deformations: research experience at Brigham and Women's Hospital. Med Image Anal. 2005; 9(2):145–162. [PubMed: 15721230]
43. White PJ, Whalen S, Tang SC, Clement G, Jolesz F, Golby AJ. An intraoperative brain shift monitor using shear mode transcranial ultrasound: preliminary results. J Ultrasound Med. 2009; 28(2):191–203. [PubMed: 19168769]
44. Chinzei K, Miller K. Towards MRI guided surgical manipulator. Med Sci Monit. 2001; 7(1):153–163. [PubMed: 11208513]
45. Chinzei K, Warfield S, Hata N, Tempany C, Jolesz F, Kikinis R. Planning, simulation and assistance with intraoperative MRI. Minim Invasive Ther Allied Technol. 2003; 12(1):59–64. [PubMed: 16754079]

NIH-PA Author Manuscript

NIH-PA Author Manuscript

NIH-PA Author Manuscript

46. DiMaio SP, Pieper S, Chinzei K, et al. Robot-assisted needle placement in open MRI: system architecture, integration and validation. Comput Aided Surg. 2007; 12(1):15–24. [PubMed: 17364655]
47. Elhawary H, Tse ZT, Hamed A, Rea M, Davies BL, Lamperth MU. The case for MR-compatible robotics: a review of the state of the art. Int J Med Robot. 2008; 4(2):105–113. [PubMed: 18481822]
48. Elhawary H, Zivanovic A, Davies B, Lampérth M. A review of magnetic resonance imaging compatible manipulators in surgery. Proc Inst Mech Eng. 2006; 220(3):413–424.
49. Masamune K, Kobayashi E. Development of an MRI-compatible needle insertion manipulator for stereotactic neurosurgery. J Image Guid Surg. 1995; 1(4):242–248. [PubMed: 9079451]
50. Sutherland GR, Latour I, Greer AD. Integrating an image-guided robot with intraoperative MRI: a review of the design and construction of neuroArm. IEEE Eng Med Biol Mag. 2008; 27(3):59–65. [PubMed: 18519183]
51. Sutherland GR, Latour I, Greer AD, Fielding T, Feil G, Newhook P. An image-guided magnetic resonance-compatible surgical robot. Neurosurgery. 2008; 62(2):286–292. discussion 292–293. [PubMed: 18382307]
52. Hynynen K, McDannold N, Vykhodtseva N, Jolesz FA. Noninvasive MR imaging-guided focal opening of the blood–brain barrier in rabbits. Radiology. 2001; 220(3):640–646. [PubMed: 11526261]
53. Kinoshita M, McDannold N, Jolesz FA, Hynynen K. Targeted delivery of antibodies through the blood–brain barrier by MRI-guided focused ultrasound. Biochem Biophys Res Commun. 2006; 340(4):1085–1090. [PubMed: 16403441]
54. Kinoshita M, McDannold N, Jolesz FA, Hynynen K. Non-invasive localized delivery of Herceptin to the mouse brain by MRI-guided focused ultrasound-induced blood–brain barrier disruption. Proc Natl Acad Sci U S A. 2006; 103(31):11719–11723. [PubMed: 16868082]
55. Treat LH, McDannold N, Vykhodtseva N, Zhang Y, Tam K, Hynynen K. Targeted delivery of doxorubicin to the rat brain at therapeutic levels using MRI-guided focused ultrasound. Int J Cancer. 2007; 121(4):901–907. [PubMed: 17437269]
56. Vykhodtseva N, McDannold N, Hynynen K. Induction of apoptosis in vivo in the rabbit brain with focused ultrasound and optison. Ultrasound Med Biol. 2006; 32(12):1923–1929. [PubMed: 17169704]
57. Yoo SS, Lee JH, Zhang Y, et al. FUS-mediated reversible modulation of region-specific brain function. Proc MRgFUS. 2008; 2008:10.
58. Colucci V, Strichartz G, Jolesz F, Vykhodtseva N, Hynynen K. Focused ultrasound effects on nerve action potential in vitro. Ultrasound Med Biol. 2009; 35(10):1737–1747. [PubMed: 19647923]
59. Currier DP, Greathouse D, Swift T. Sensory nerve conduction: effect of ultrasound. Arch Phys Med Rehabil. 1978; 59(4):181–185. [PubMed: 646607]



Fig. 1.

Advanced Multimodality Image Guided OR (AMIGO). The middle room is an operating room with surgical microscope, angiography, ultarsound and optical imaging. The room on the left has a PETCT and on the right a 3T MRI which is seiling mounted and can move into the operating room to image the patient on the operating room table (IMRIS, Winnipeg, Canada)

NIH-PA Author Manuscript NIH-PA Author Manuscript NIH-PA Author Manuscript

JOURNAL OF VIROLOGY, Oct. 2003, p. 11072–11081 Vol. 77, No. 20
0022-538X/03/$08.00+0 DOI: 10.1128/JVI.77.20.11072–11081.2003
Copyright © 2003, American Society for Microbiology. All Rights Reserved.

Identification of a Heparin-Binding Motif on Adeno-Associated Virus Type 2 Capsids†

A. Kern,[1] K. Schmidt,[1] C. Leder,[1] O. J. Müller,[1] C. E. Wobus,[1]‡ K. Bettinger,[2] C. W. Von der Lieth,[2] J. A. King,[1]§ and J. A. Kleinschmidt[1]*

Forschungsschwerpunkt Angewandte Tumorvirologie[1] and Zentrale Spektroskopie,[2] Deutsches Krebsforschungszentrum, 69120 Heidelberg, Germany

Received 8 May 2003/Accepted 15 July 2003

Infection of cells with adeno-associated virus (AAV) type 2 (AAV-2) is mediated by binding to heparan sulfate proteoglycan and can be competed by heparin. Mutational analysis of AAV-2 capsid proteins showed that a group of basic amino acids (arginines 484, 487, 585, and 588 and lysine 532) contribute to heparin and HeLa cell binding. These amino acids are positioned in three clusters at the threefold spike region of the AAV-2 capsid. According to the recently resolved atomic structure for AAV-2, arginines 484 and 487 and lysine 532 on one site and arginines 585 and 588 on the other site belong to different capsid protein subunits. These data suggest that the formation of the heparin-binding motifs depends on the correct assembly of VP trimers or even of capsids. In contrast, arginine 475, which also strongly reduces heparin binding as well as viral infectivity upon mutation to alanine, is located inside the capsid structure at the border of adjacent VP subunits and most likely influences heparin binding indirectly by disturbing correct subunit assembly. Computer simulation of heparin docking to the AAV-2 capsid suggests that heparin associates with the three basic clusters along a channel-like cavity flanked by the basic amino acids. With few exceptions, mutant infectivities correlated with their heparin- and cell-binding properties. The tissue distribution in mice of recombinant AAV-2 mutated in R484 and R585 indicated markedly reduced infection of the liver, compared to infection with wild-type recombinant AAV, but continued infection of the heart. These results suggest that although heparin binding influences the infectivity of AAV-2, it seems not to be necessary.

Attachment of a virus to a host cell requires a specific interaction of the virus shell with cellular receptor molecules. These permit uptake and thus intracellular processing of the virus so that it can successfully infect the cell. For adeno-associated virus (AAV) type 2 (AAV-2), a member of the parvovirus family containing a nonenveloped icosahedral capsid, heparan sulfate proteoglycan has been shown to act as a primary receptor (62). However, the contribution of an additional receptor(s) has been postulated because AAV-2 binding to cells and recombinant AAV-2 transduction did not quantitatively correlate with the amount of heparan sulfate on the surface of different cell types tested (26, 51). After binding to the cell surface, AAV-2 is thought to engage a secondary receptor which mediates cell entry. To date, αVβ5 integrin and human fibroblast growth factor receptor 1 have been proposed (49, 61), but the involvement of other molecules has also been suggested (50, 52).

Heparan sulfate glucosaminoglycans (HSGAGs) are complex polysaccharides with high structural diversity. They consist of repeating disaccharide units each composed of glucuronic acid or iduronic acid linked to glucosamine (17, 48). The immense structural diversity of HSGAGs arises from the modification of individual disaccharide units within the oligosaccharide. This diversity enables these molecules to interact with a wide variety of proteins, such as growth factors, chemokines, morphogens, enzymes, matrix proteins, lipoproteins, and antimicrobial peptides, which are involved in diverse biological processes, such as morphogenesis, tissue repair, energy balance, host defense, cell adhesion, proliferation, and growth factor signaling (3, 40, 48). Numerous viruses, e.g., herpes simplex virus type 1 (HSV-1) and HSV-2 (70), human immunodeficiency virus (46), respiratory syncytial virus (38), dengue virus (9), pseudorabies virus (64), foot-and-mouth disease virus (33), vaccinia virus (11), Sindbis virus (4, 36), several papillomaviuses (34, 58), cytomegalovirus (12), AAV-2 and AAV-3 (26, 62), and others, bind to HSGAGs. HSGAG chains are assembled while attached to a proteoglycan core protein. So far, three major protein families have been characterized: the membrane-spanning syndecans, the glycosylphosphatidylinositol-linked glypicans, and the basement membrane proteoglycans perlecan and agrin (17). The sequence of the HSGAGs does not correlate with the protein family to which they are bound but rather correlates with the cell type in which the HSGAGs have been synthesized.

HSGAGs interact with proteins mainly through electrostatic interactions of basic amino acids with the negatively charged sulfate and carboxyl groups of HSGAG chains (5, 30). However, hydrogen bond formation (18, 31) and, to a lesser extent, hydrophobic interactions can also contribute to such interactions (1). Heparin-binding domains of heparin-binding pro-

* Corresponding author. Mailing address: Angewandte Tumorvirologie, Deutsches Krebsforschungszentrum, Im Neuenheimer Feld 242, 69120 Heidelberg, Germany. Phone: 49 6221 424978. Fax: 49 6221 424962. E-mail: J.Kleinschmidt@dkfz.de.

† This article is dedicated to Harald zur Hausen on the occasion of his retirement as head of the German Cancer Research Center with gratitude and appreciation for 20 years of leadership.

‡ Present address: Department of Pathology, School of Medicine, Washington University, St. Louis, MO 63122.

§ Present address: MRC Centre for Inflammation Research, Edinburgh University Medical School, Edinburgh EH8 9AG, Scotland.

teins have been shown to contain consensus sequence motifs, such as XBBXB and XBBBXXBX, where B is a basic amino acid exposed on one side and X is a neutral or hydrophobic amino acid directed toward the protein interior. Through an analysis of the available experimentally determined heparin-protein complexes, it became obvious that the spatial orientation of basic residues rather than sequence proximity is an important factor in determining heparin-binding affinity (32). Such binding domains are usually located at the protein surface and form a flat pocket with a positive charge (30).

The capsid of AAV-2 is composed of three overlapping capsid proteins (VP1, VP2, and VP3) containing a unique VP1 N terminus, a portion common to VP1 and VP2, and a portion common to VP1, VP2, and VP3 (2, 6, 60, 63). To date, the VP domains involved in binding to heparin have not been studied in detail. Several short basic sequences located in the N-terminal portion of VP1 and VP2 have been proposed as possible candidates for heparin binding (62). However, capsids with mutations in these amino acids (69; unpublished data) and capsids composed only of VP3 molecules (54) showed binding to heparin, suggesting that the heparin-binding domain is located in the portion common to all three VP molecules. Several groups observed that insertions in capsid proteins or clustered charge-to-alanine mutations affected heparin binding (22, 45, 59, 69).

We set out to define precisely, through point mutational analysis, the amino acids of AAV-2 capsid proteins involved in heparin binding. Using information from the recently resolved atomic structure for the AAV-2 capsid (72), we can now describe a heparin-binding motif which is composed of basic amino acids and which is formed by folding into the threefold spike region of the capsid. Infection analysis in vitro and in vivo showed that although heparin binding contributes to AAV-2 infection, it is not a prerequisite.

MATERIALS AND METHODS

Cell cultures. 293T and HeLa cells were maintained in Dulbecco's modified Eagle's medium supplemented with 10% heat-inactivated fetal calf serum (FCS), 2 mM L-glutamine, and 100 μg each of penicillin and streptomycin/ml at 37°C in 5% CO_2.

Transfection and preparation of virus supernatants. 293T cells were plated at 1.5×10^6 cells per 10 ml of Dulbecco's modified Eagle's medium with 10% FCS per 10-cm petri dish 1 day prior to transfection. Transfection was carried out with 12 μg of DNA per dish by the method of Chen and Okayama (8). At 16 to 18 h posttransfection, the medium was replaced with 10 ml of medium containing adenovirus type 5 (multiplicity of infection, 50). The cultures were incubated for 2 days at 37°C in 5% CO_2. Cells were harvested in 10 ml of medium and lysed by three rounds of freezing-thawing (−80 and 37°C) to release the produced virus. Cell debris was removed by centrifugation at $400 \times g$ for 10 min. Prior to cell lysis, an aliquot of 300 μl of harvested cells was taken, washed once with phosphate-buffered saline (PBS), and denatured by being heated at 100°C for 5 min in the presence of sodium dodecyl sulfate sample buffer. After sonication, the samples were analyzed by Western blotting.

Determination of viral titers. Quantitation of AAV-2 capsid titers was carried out by an enzyme-linked immunosorbent assay (ELISA) as described by Grimm et al. (23) with precoated plates supplied by Progen GmbH (Heidelberg, Germany). Infectious and genomic titers were determined as described previously (35). Randomly primed ^{32}P-labeled probes were generated from a *rep* fragment (*Xho*I-*Bam*HI) of plasmid pBSΔTR18 (65).

Plasmids and mutagenesis. Plasmid pTAV2-0 (29) contains the entire AAV-2 genome from pAV-2 (39), including both inverted terminal repeats, cloned into the *Bam*HI site of pBluescript II. Plasmid pJ407, which was used as the template for the site-directed mutagenesis reactions, contains the *Bam*HI-*Not*I fragment of the AAV-2 genome from pTAV2-0 cloned into pUC131. Mutagenesis was performed by using a Stratagene (Amsterdam, The Netherlands) QuikChange site-directed mutagenesis kit according to the manufacturer's protocol. For each mutant, two complementary PCR primers were designed to contain the sequence of the substitution or deletion, respectively, flanked by 15 to 20 homologous base pairs on each side of the mutation. Mutant plasmids were identified by DNA sequencing. The *Bsi*WI-*Xcm*I (*Xcm*I-*Eco*NI, respectively) fragment containing the mutation was then subcloned into the pTAV2-0 backbone. The complete fragment was sequenced to check for additional PCR mutations. Deletion mutant 6 was constructed by inserting a double-stranded oligonucleotide (5′-CGT TAACCCAGGCATGGTCTGGGC-3′ and 5′-CCCAGACCATGCCTGGGTT AACGCATG-3′), providing an additional *Xcm*I site, into the *Sph*I site of mutant 29. The resulting plasmid was digested with *Xcm*I and religated.

Western blot analysis. Western blot analysis and antibodies 303.9 and B1 were described previously (67). Peroxidase-coupled secondary antibodies and an enhanced chemiluminescence kit (NEN, Cologne, Germany) were used according to standard methods.

Cell-binding assay. Cell binding was measured essentially as described previously (68). Briefly, HeLa cells in 100 μl of medium were plated at 10^4 cells/well on microtiter plates (Nunc, Wiesbaden, Germany) 1 day prior to infection. Virus supernatants were diluted in precooled medium without FCS to 10^9 to 10^{10} capsids/well. The cells were incubated with 50 μl of the dilutions/well in triplicate for 60 min at 4°C. After being washed with 200 μl of cooled PBS/well, the cells were fixed with 100 μl of methanol/well, cooled to −20°C for 15 min, and dried at room temperature overnight. After being washed three times with PBS containing 0.05% Tween 20 (wash buffer), the cells were blocked with 200 μl of PBS containing 0.2% casein and 0.05% Tween 20 (blocking buffer)/well for 2 h at 37°C. The blocking buffer was removed and replaced with blocking buffer containing 100 ng of biotinylated antibody A20/well (23), and the cells were incubated for 90 min at room temperature. Unbound A20 was removed by three washes with wash buffer. The cells then were incubated with 100 μl of streptavidin-coupled peroxidase diluted to a final concentration of 0.8 μg/ml in blocking buffer/well for 1 h at room temperature. After three washes with wash buffer, the cells were incubated with 100 μl of tetramethylbenzidine substrate (Devitron, Castrop-Rauxel, Germany). The reaction was stopped by adding 50 μl of 1 M H_2SO_4 to each well. The absorption at 450 nm was measured by using an ELISA reader (MWG, Ebersberg, Germany). Cell binding was expressed as a percentage of absorption measured with the AAV-2 wild-type virus stock by using the same capsid number.

Heparin-binding assay. A 1-ml heparin column (Sigma, Munich, Germany) preequilibrated with 20 ml of PBS containing 1 mM $MgCl_2$ and 2.5 mM KCl (PBS-MK) was loaded with 5 ml of virus supernatants. The column was washed twice with 5 ml of PBS-MK and eluted twice with 5 ml of PBS containing 1 M NaCl. The flowthrough, wash, and eluate fractions were analyzed by using the A20 capsid ELISA as described above. Values were expressed as a percentage of capsids applied to the column.

In vivo analysis of capsid mutants. To analyze the in vivo distribution of double mutant R484E/R585E, recombinant AAV (rAAV) vectors carrying a luciferase reporter gene were generated. The capsid region carrying both mutations (R484E and R585E) was excised with *Xcm*I-*BsiW*I from plasmid pJ407 (R484E/R585E) and inserted into pBSΔTR18, providing *rep* and *cap* genes without inverted terminal repeats (65). Helper plasmid pDG(R484E/R585E) was obtained by excision of the mutated *cap* gene from modified pBSΔTR18 with *Swa*I-*Cla*I and insertion into the corresponding position of pDGΔVP (16). pUFCMV-Luc is a derivative of pUF3 (74) harboring the firefly luciferase sequence from pGL3-basic (Promega, Mannheim, Germany) inserted into the *Hin*dIII site and blunted 3′ *Xho*I site.

rAAV was produced by cotransfection of 293T cells with pUFCMV-Luc and pDG(R484E/585E) or pDG as described by Hauswirth et al. (28). After 2 days, cells were harvested and viruses were purified by using iodixanol gradients (28). Gradient fractions were concentrated by using VIVASPIN columns (Sartorius, Göttingen, Germany), thereby exchanging iodixanol against PBS.

Female immunocompetent NMRI mice (6 to 8 weeks old) were purchased from the German branch of Charles River Laboratories (Wilmington, Mass.). Six mice per group were injected intravenously via the tail vein with concentrated vectors (10^{11} genomic particles) from two independent preparations. After 3 weeks, mice were sacrificed, and representative organs (heart, lungs, liver, spleen, kidneys, skeletal muscle, and brain) were harvested and frozen in liquid nitrogen. All procedures involving the use and care of animals were performed according to the *Guide for the Care and Use of Laboratory Animals* (National Institutes of Health publication no. 85-23, revised 1996) and the German Animal Protection Code.

For the detection of AAV genomes in tissues, genomic DNA was extracted by using a Qiamp tissue kit (Qiagen, Hilden, Germany). Genomic DNA (800 ng)

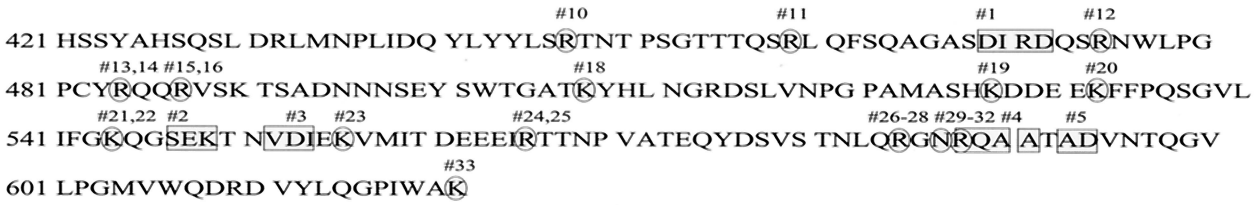


FIG. 1. Amino acids of AAV-2 VPs subjected to site-directed mutagenesis. Blockwise conversions of VP sequences (VP1 numbering) of AAV-2 to those of AAV-3 (mutants 1, 2, 3, 4, and 5) are highlighted by grey rectangles. Single mutated amino acids are highlighted by grey circles. Mutants are numbered as shown in Table 1.

was used for PCR amplification (40 cycles) of a 677-bp fragment of the luciferase gene with primers 5′-GACGCCAAAAACATAAAGAAAG-3′ and 5′-CCAAA AATAGGATCTCTGGC-3′ under standard conditions. The integrity of the DNA was determined by amplifying a 492-bp region of the murine β-actin gene with primers 5′-ATGTTTGAGACCTTCAACAC-3′ and 5′-AACGTCACACT TCATGATGG-3′. PCR products were analyzed by agarose gel electrophoresis.

For the determination of luciferase reporter activities, we used a luciferase assay kit (Promega) according to the manufacturer's recommendations. Frozen tissue samples were homogenized with reporter lysis buffer and centrifuged for 10 min at 10,000 × *g*. Light activities were measured with a Luminometer (Lumat LB9501; Berthold, Bad Wildbad, Germany). A standard curve was generated with luciferin (Roche, Mannheim, Germany). Protein content in tissue homogenates was determined with a NanoOrange kit (Molecular Probes, Leiden, The Netherlands). Luciferase activities were expressed as relative light units per milligram of protein.

Graphics and docking simulation. Pictures were made with Rasmol 2.6 (57) software and Insight2000 (Accelrys Inc.). Starting structures for the protein monomer and the heparin ligand were obtained from the Brookhaven Protein Data Bank (entry 1LP3 for AAV-2 protein [72] and entry 1HPN for the heparin hexamer [44]) and were minimized with the AMBER force field (66). The three-dimensional structure of the AAV-2 capsid was determined (our own software) with the BIOMT information given in the Brookhaven Protein Data Bank file. Potentials and partial charges were derived from the AMBER force field implemented in Insight2000. Partial charges for heparin had to be corrected for the carboxyl and sulfate groups to fit with the net charge of −12 for the heparin hexamer. Docking on the VP trimer was performed with the program AUTODOCK 3.05 (21, 43) with a grid spacing of 0.0375 nm and a rectangular grid box of 4.5 nm.

RESULTS

Search for a heparin-binding motif in the AAV capsid protein sequence. The search for a heparin-binding motif in the AAV-2 capsid proteins was guided by a number of theoretical considerations and previous experimental findings. A sequence comparison of the AAV-2 capsid proteins with the capsid proteins of AAV-1, AAV-4, AAV-5, and AAV-6, which do not bind heparin, revealed major differences between amino acids 443 and 602, which are all located in loop IV, according to the alignment with canine parvovirus (CPV) (7). Several published insertion and charge-to-alanine mutations affecting heparin binding are also located in loop IV (22, 54, 59, 69). In addition, the epitope of monoclonal antibody C37, which effectively blocks the binding of AAV-2 capsids to HeLa cells, maps to two stretches of amino acids at the beginning and at the end of loop IV (68).

Based on the assumption that AAV-2 and AAV-3 bind to different primary receptors (26, 41), we converted short amino acid stretches in the loop IV region of AAV-2 to those of AAV-3 (Fig. 1, mutants 1 to 5, and Table 1) and analyzed the mutant viruses for capsid, genomic, and infectious titers. We observed a significant reduction in infectivity with mutant 4 and a modest reduction with mutant 5. Analysis of cell binding and heparin binding showed that both were reduced in mutant 4 (comprising arginine 588) but not in neighboring mutant 5. These results made us focus on the region surrounding arginine 588, the basic residue missing in mutant 4. An extended deletion from amino acid positions 587 to 601 (mutant 6), as well as short, partially overlapping deletions from amino acids 582 to 586 (mutant 7), from amino acids 584 to 589 (mutant 8), and from amino acids 587 to 590 (mutant 9), all confirmed that the region including arginines 585 and 588 likely is involved in heparin binding. The mutant viruses showed up to 4-log-unit reductions in infectivity, a loss of heparin binding, and a significant reduction in their ability to bind HeLa cells (Table 1). Further support for the involvement of arginine 588 in heparin binding came from double mutant 29 (N587A and R588C), which also resulted in more than a 1,000-fold reduction in infectivity, reduced cell binding, and a loss of heparin binding (Table 1). For all of the mutants analyzed in this report, no significant effect on genome packaging was detected (Table 1). From these results, we hypothesized that the loss of the basic charge of arginines 585 and 588 located in loop IV resulted in reduced cell binding and infectivity.

Two distantly located pairs of arginines (R585-R588 and R484-R487) are involved in heparin binding. In order to substantiate the results obtained so far, we mutated arginines 585 and 588 to the acidic glutamate (E), conservatively to the basic lysine (K), or to neutral methionine or cysteine (M or C). Point mutants were compared to wild-type virus and mutant 8 with respect to infectivity, cell binding, and heparin binding (Fig. 1 and 2a and Table 1). Conversion of arginines 585 and 588 to glutamic acid (R585E and R588E) strongly decreased infectivity, cell binding, and heparin binding, similar to the results obtained with the deletion mutant (mutant 8). In contrast, a conservative exchange of the arginines to lysine (R585K and R588K) had no negative effect on infectivity, cell binding, or heparin binding. The cell binding of R585K was in fact increased. Mutation of arginine 588 to cysteine (R588C) decreased infectivity, cell binding, and heparin binding, whereas mutation of arginine 585 to methionine (R585M) had no significant effect on infectivity, although cell binding was decreased and heparin binding was lost completely. With this exception, heparin binding correlated well with the infectivity of different mutant viruses. Taken together, the results of analyses of these mutants suggest that arginines 585 and 588 participate in the heparin binding of AAV-2 capsids.

Based on the sequence alignment of AAV-2 VP3 and CPV VP3 (7) and the atomic structure of the CPV capsid, we predicted that arginines 484 and 487, as well as two other basic

TABLE 1. Mutant analysis

Mutant	Mutation(s) (amino acid positions)	Infectivity[a]		Packaging[b]		Binding	
		No. of capsids/no. of infectious particles	Phenotype	Capsid/genome ratio	Phenotype	Cell[c]	Heparin[d]
1	DIRD → SMSL (469–472)	10^3	WT	21	WT	ND	ND
2	SEK → TTA (547–549)	10^3	WT	1	WT	ND	ND
3	VDI → AEL (552–554)	10^3	WT	26	WT	ND	ND
4	RQA → TAP (588–590)	2×10^6	LI	42	WT	±	−
5	A; AD → T; GT (591; 593, 594)	7×10^4	RI	5	WT	+	+
6	ΔQ589-V600, L601N, NR → AC (587, 588)	$>10^6$	LI	5	WT	ND	ND
7	ΔN582-G586	8×10^5	LI	2	WT	−	−
8	ΔQ584-Q589	10^6	LI	1	WT	−	−
9	ΔN587-A590	3×10^6	LI	1	WT	−	−
10	R447A	5×10^3	WT	4	WT	+	+
11	R459A	2×10^3	WT	4	WT	±	+
12	R475A	10^7	LI	0.3	WT	−	±
13	R484A	10^7	LI	5	WT	−	−
14	R484E	10^6	LI	6	WT	−	−
15	R487A	4×10^4	RI	7	WT	−	−
16	R487E	3×10^7	LI	5	WT	−	−
17	R484E, R585E	6×10^8	LI	7	WT	−	−
18	K507A	4×10^3	WT	27	WT	±	+
19	K527A	3×10^4	RI	3	WT	±	±
20	K532A	2×10^4	RI	3	WT	−	−
21	K544S	1.3×10^4	RI	1	WT	±	+
22	K544E	1.1×10^4	RI	1	WT	±	+
23	K556A	7×10^2	WT	4	WT	±	+
24	R566A	6×10^3	WT	19	WT	±	+
25	R566E	3×10^3	WT	5	WT	±	+
26	R585E	1.3×10^7	LI	3	WT	−	−
27	R585M	9×10^4	RI	3	WT	−	−
28	R585K	2×10^3	WT	2	WT	+	+
29	NR → AC (587, 588)	2×10^6	LI	5	WT	±	−
30	R588E	2×10^6	LI	3	WT	−	−
31	R588C	10^6	LI	13	WT	±	−
32	R588K	10^3	WT	3	WT	+	+
33	K620A	10^4	WT	9	WT	+	+

[a] Infectious AAV-2 particles were quantified by a dot blot replication assay as described previously (24). The number of assembled capsids was measured by a capsid ELISA (25). Infectivity was expressed as the ratio of the number of capsids to the number of infectious particles. The wild-type (WT) phenotype corresponds to a ratio of $\leq 10^4$; reduced infectivity (RI) corresponds to ratios of $>10^4$ to $<10^6$, and low infectivity (LI) corresponds to ratios of $\geq 10^6$.

[b] Packaging was measured as the ratio of capsids to viral genomes as described previously (23). The WT phenotype indicates a packaging ratio of <50; reduced packaging was indicated by a ratio of >50.

[c] Cell binding was measured as the binding of capsids to HeLa cells by an A20-based ELISA as described in Materials and Methods. It is expressed as the percentage of binding of WT AAV-2: +, more than 80% binding; ±, 40 to 80% binding; −, less than 40% binding. ND, not determined.

[d] Heparin binding was measured as the percentage of viral particles which were applied to a heparin-agarose column and which were recovered after high-salt elution as determined with the A20-based capsid ELISA: +, more than 80% binding; ±, 20 to 80% binding; −, less than 20% binding.

amino acids, lysine 544 and arginine 566, could be spatially very close to arginines 585 and 588 in the folded state. We therefore mutated arginines 484, 487, and 566 to either alanine or glutamic acid and lysine 544 to serine or glutamic acid. All mutants were analyzed for virus infectivity, packaging, cell binding, and heparin binding (Fig. 1 and 2b and Table 1). Both charge-to-alanine mutations (R484A and R487A) and basic-to-acidic mutations (R484E and R487E) of arginines 484 and 487 (mutants 13, 14, 15, and 16) significantly reduced infectivity, cell binding, and heparin binding. This result strongly suggests that these two arginine residues form a basic cluster together with arginines 585 and 588 to strengthen heparin binding. Double mutant 17 (R484E and R585E) showed a similar loss of cell binding and heparin binding and was even more affected in its infectivity than the single mutants, further supporting our interpretation. Two mutations of lysine 544 (K544S and K544E; mutants 21 and 22) showed no reduction in infectivity and a modest reduction in cell binding. Heparin binding was not significantly reduced, although the recovery of the mutant viruses in the high-salt eluate was slightly reduced. Furthermore, mutations of arginine 566 (R566A and R566E; mutants 24 and 25) were not measurably affected in infectivity and heparin binding but, again, cell binding was slightly reduced. These results support the conclusion that, of the four basic amino acids predicted to be potentially located close to R585 and R588, only R484 and R487 are involved in heparin binding.

Further candidate amino acids in loop IV are involved in heparin binding. To analyze whether other basic amino acids in loop IV contribute to the basic cluster around arginines 585 and 588 upon folding and assembly, we mutated all other not-yet-analyzed arginines and lysines between amino acid positions 446 and 620 (Fig. 1). Most residues showed no change in the parameters analyzed (Table 1) (mutants 10, 11, 12, 18, 19, 20, 23, and 33), except for mutations of arginine 475 (mutant 12) and of lysines 532 and 527 (mutants 20 and 19, respectively) (Fig. 2c). Conversion of arginine 475 to alanine (R475A; mutant 12) dramatically reduced the infectivity of the

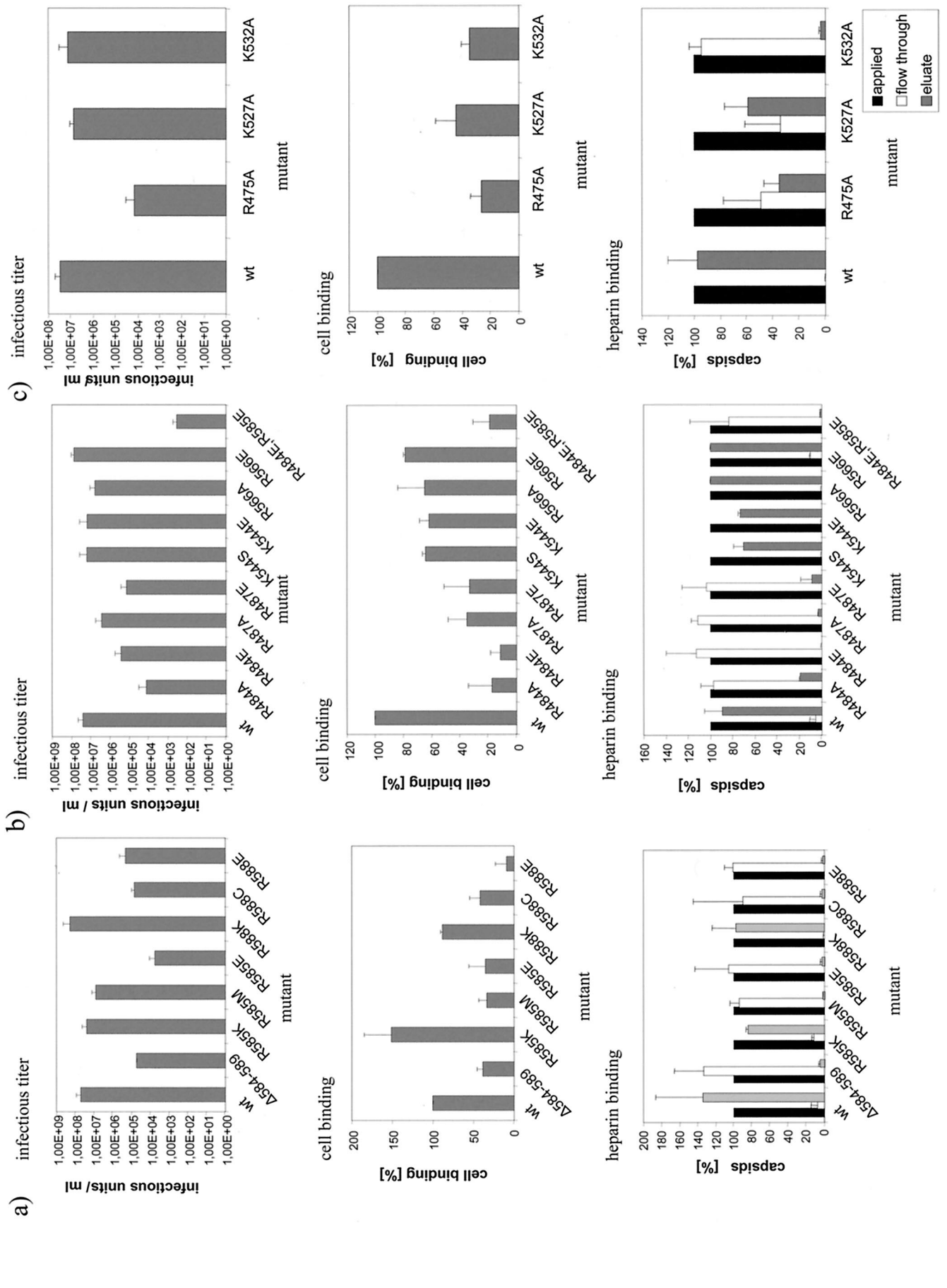

a)
infectious titer
infectious units/ ml
1,00E+09
1,00E+08
1,00E+07
1,00E+06
1,00E+05
1,00E+04
1,00E+03
1,00E+02
1,00E+01
1,00E+00
wt
Δ584-589
R585K
R585M
R585E
R588K
R588C
R588E
mutant
cell binding
cell binding [%]
200
150
100
50
0
wt
Δ584-589
R585K
R585M
R585E
R588K
R588C
R588E
mutant
heparin binding
capsids [%]
200
180
160
140
120
100
80
60
40
20
0
wt
Δ584-589
R585K
R585M
R585E
R588K
R588C
R588E
mutant
applied
flow through
eluate
b)
infectious titer
infectious units / ml
1,00E+09
1,00E+08
1,00E+07
1,00E+06
1,00E+05
1,00E+04
1,00E+03
1,00E+02
1,00E+01
1,00E+00
wt
R484A
R484E
R487A
R487E
K544S
K544E
R566A
R566E
R484E,R585E
mutant
cell binding
cell binding [%]
120
100
80
60
40
20
0
wt
R484A
R484E
R487A
R487E
K544S
K544E
R566A
R566E
R484E,R585E
mutant
heparin binding
capsids [%]
160
140
120
100
80
60
40
20
0
wt
R484A
R484E
R487A
R487E
K544S
K544E
R566A
R566E
R484E,R585E
mutant
c)
infectious titer
infectious units/ ml
1,00E+08
1,00E+07
1,00E+06
1,00E+05
1,00E+04
1,00E+03
1,00E+02
1,00E+01
1,00E+00
wt
R475A
K527A
K532A
mutant
cell binding
cell binding [%]
120
100
80
60
40
20
0
wt
R475A
K527A
K532A
mutant
heparin binding
capsids [%]
140
120
100
80
60
40
20
0
wt
R475A
K527A
K532A
mutant
applied
flow through
eluate

FIG. 2. Influence of mutations of basic amino acids in loop IV on infectivity, cell binding, and heparin binding of AAV-2. Virus stocks were produced by transfection of wild-type (wt) or mutated AAV-2 genomic plasmids into 293T cells and superinfection with adenovirus (multiplicity of infection, 50). (a) Analysis of arginines 585 and 588 for involvement in heparin binding. (b) Analysis of distantly located basic amino acids predicted to possibly contribute to heparin binding. (c) Further loop IV basic amino acids involved in heparin binding. Infectious units were determined as described in Materials and Methods. Capsid titers and genomic titers were not influenced by the mutations (data not shown), implying that they did not affect capsid assembly or genome encapsidation. Virus bound to HeLa cells was measured with monoclonal antibody A20 (68). Heparin binding was assayed by chromatography of virus preparations (freeze-thaw lysates) with heparin-agarose and quantitation of applied, flowthrough, and salt-eluted virus with the A20 capsid ELISA. The amount of applied virus was set to 100%. Error bars indicate standard deviations of at least three independent experiments.

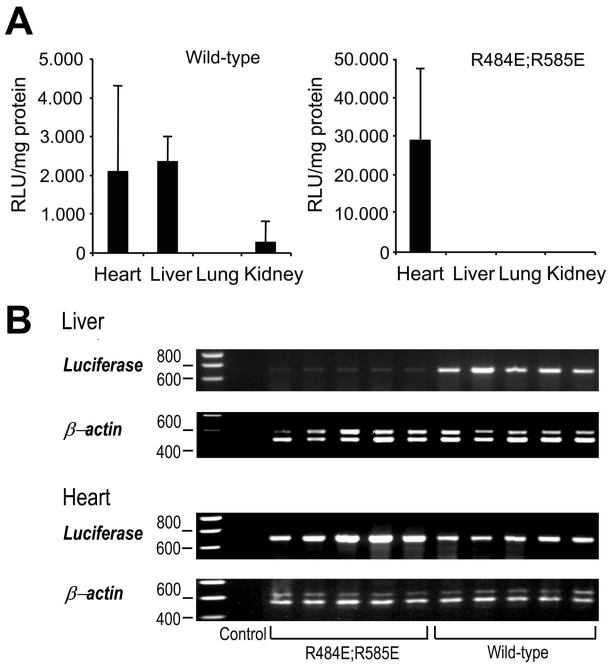


FIG. 3. In vivo distribution of wild-type rAAV and rAAV mutant R484E/R585E in mouse tissues. (A) Luciferase activities in different organs after intravenous injection of 10^{11} wild-type capsids or rAAV mutated in R484E and R585E 3 weeks postinfecion. Luciferase activities are depicted in relative light units (RLU) per milligram of protein. Error bars indicate standard deviations. (B) Detection of luciferase gene transfer by PCR in selected organs 3 weeks after intravenous infusion of 10^{11} vector genomes of rAAV mutant R484E/R585E and wild-type rAAV. Amplification of β-actin was used as a control. The 677-bp luciferase band is barely detectable in liver tissues of mice injected with double mutant R484E/R585E but is clearly visible in mice injected with wild-type rAAV. PCR amplification of tissue samples from heart, lungs (data not shown), and kidneys (data not shown) did not reveal any differences in luciferase gene transduction.

mutant virus as well as cell binding, whereas heparin binding was only partially lost. The opposite was observed for mutation of lysine 532 (K532A; mutant 20): while heparin binding was strongly reduced and cell binding was modestly reduced, infectivity remained nearly unaffected. Mutation of lysine 527 (K527A; mutant 19) to alanine produced similar characterisics, except that heparin binding was only moderately reduced. Based on these results, we concluded that R475 and K532 could be part of the heparin-binding motif together with R588, R585, R487, and R484.

Tissue tropism of AAV-2 heparin-binding mutants in vivo. To test whether mutations in the heparin-binding motif also affect the in vivo tropism of the virus, we injected rAAV with either wild-type or heparin-binding mutant 17 (R484E and R585E) capsids into the tail vein of mice and analyzed vector genome distribution and reporter gene expression in different tissues. The reporter gene activity of rAAV packaged into the wild-type capsid could be detected in the liver and heart muscle after injection of 10^{11} vector genomes (Fig. 3A). Luciferase activity in the lungs and kidneys was close to background levels and could not be detected in the other tissues analyzed. The reporter gene activity of the double mutant was not detectable in the liver; however, it was surprisingly high in the heart

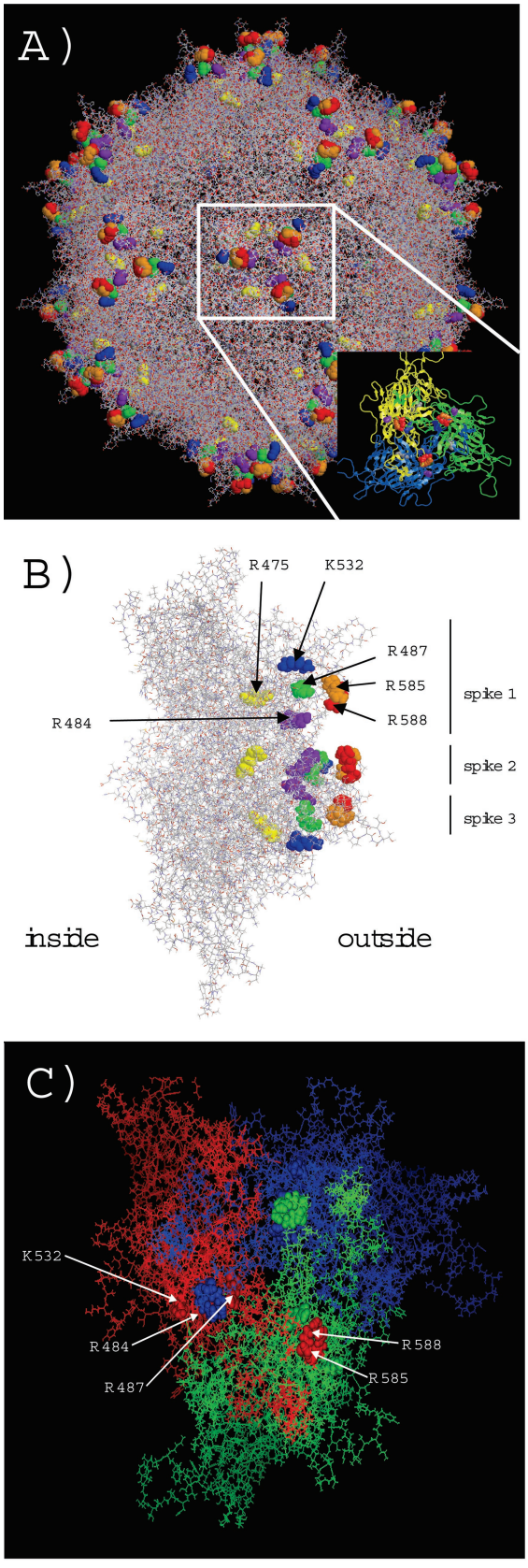


FIG. 4. Localization of amino acids involved in heparin binding on the AAV-2 capsid surface. (A) The amino acids involved in heparin binding—R585 (orange), R588 (red), R484 (purple), R487 (green), K532 (blue), and R475 (yellow)—are grouped in three clusters at the threefold spike region of the capsid. The inset shows a VP trimer which forms the threefold spikes. (B) A side view of a VP trimer shows the surface exposure of the basic clusters at the inner shoulder of the threefold spikes and along a channel-like structure between the threefold spikes. R475 is buried in the capsid wall (at the border of two subunits [not shown]) and likely affects heparin binding indirectly when it is mutated to alanine. The unmarked residues are derived from the second and third spikes. (C) Two different subunits of a VP trimer (indicated in red, blue, and green) contribute to the formation of a basic heparin-binding cluster. R585 and R588 of the red, green, or blue subunit (shown as orbitals, with the red subunit labeled) are surrounded by K532, R484, and R487 of another subunit (orbitals of the red subunit which surround R585 and R588 of the blue subunit are indicated by arrows).

sample, suggesting heparan sulfate-independent transduction of heart tissue in vivo. The difference in reporter gene expression between wild-type and double-mutant vectors was confirmed by PCR analysis of vector genomes in the heart and liver in several independently harvested samples (Fig. 3B). In contrast, vector genomes delivered by wild-type or mutant capsids could be detected by PCR in the lungs and kidneys in similar amounts (data not shown).

DISCUSSION

Our experimental analysis of amino acids potentially involved in heparin binding was performed prior to the atomic structure of AAV-2 capsids being known. The availability of the X-ray structure (72) has allowed us now to analyze our data at the molecular level. The basic residues R484, R487, K532, R585, and R588 all cluster in three basic patches at the threefold rotation axis of the AAV-2 capsid structure (Fig. 4A). A side view of the VP trimer reveals that these basic residues surround the surface of a channel with arginines 484 and 588 located at the border (Fig. 4B). According to this view, the binding motif is not located at the tips of the threefold spikes but at the inwardly oriented shoulders. Arginines 585 and 588 are even partially hidden by asparagine 587 if one looks from outside straight onto the threefold spike (data not shown). This finding suggests that the acidic heparin molecules interact with the basic amino acids along this channel predominantly by electrostatic interactions. Arginine 475, on the other hand, is buried within the capsid protein subunits and cannot have direct contact with heparin at the virus surface. It is therefore most likely that mutation of arginine 475 indirectly influences heparin binding and the infectivity of the virus. Indeed, arginine 475 is located at the border of two adjacent capsid proteins and might distort subunit geometry when mutated. This interpretation is further supported by the fact that basic residues K532, R484, and R487 of one subunit surround R585 and R588 of another subunit, suggesting that formation of the basic heparin-binding motif is a consequence of correct subunit interaction and assembly (Fig. 4C). After this article was submitted, a report in which amino acids in the AAV-2 capsid that contribute to heparan sulfate proteoglycan binding were identified was published (47). The identified amino acids there are essentially identical to those of the motif reported in this article.

Unexpectedly, R585 and R588 of AAV-2 are not conserved

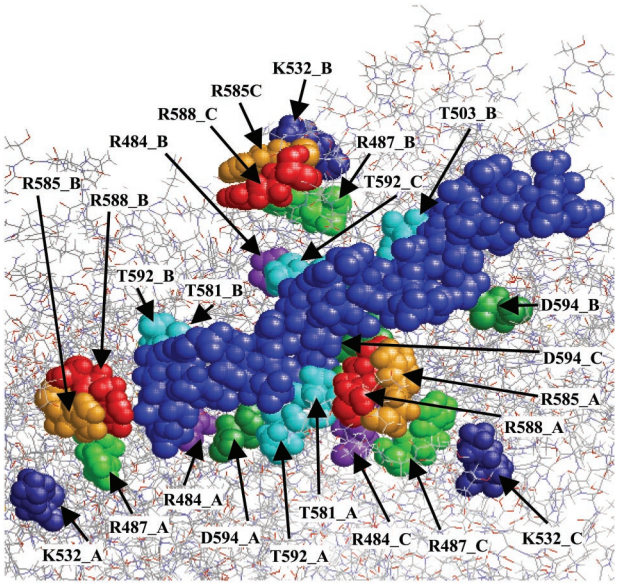


FIG. 5. Computer simulation of heparin docking to the AAV-2 capsid surface. The docking simulation was performed as described in Materials and Methods. The light blue orbitals show the heparin hexamer. Amino acids which are in proximity to the heparin molecule and which might permit electrostatic or hydrogen bond interactions are indicated. Letters A, B, and C indicate the three different VP subunits involved in heparin binding.

in the closely related AAV-3 which also binds to heparin (26, 53). These positions are instead occupied by serine and threonine, respectively. The polar nature of these amino acids could partially substitute for the charged arginines in AAV-2. In addition, they are also able to contribute to heparin binding by hydrogen bond formation. The homologues of arginines 484 and 487 and of lysine 532 are conserved in AAV-3. Together with the observation that AAV-2 and AAV-3 do not compete for binding to HeLa cells (26, 41), this finding may indicate that both viruses bind to different HSGAGs which are both related to and mimicked by heparin but may require slightly different binding sites.

In a computer-simulated heparin-docking experiment involving the AAV-2 capsid surface, the heparin molecule (a heparin hexamer) aligned with the three basic clusters along the channels between the three spikes (Fig. 5). This experiment predicts close contacts (below 3 Å) of several threonines and aspartic acids 269 and 594 with the heparin molecule. While threonines could contribute to heparin binding via hydrogen bond stabilization, the two aspartic acids 269 and 594 may be required for charge neutralization of the basic clusters in the absence of bound heparin molecules. Since this charge neutralization is no longer needed after interaction of the capsid with heparin, a conformational switch might occur upon a capsid-heparin interaction to prevent interference of the acidic amino acids with heparin binding. It will be interesting to test this hypothesis.

Mutational analysis of AAV-2 capsid protein amino acids involved in heparin binding showed a strong correlation with cell binding and virus infectivity, supporting the initial observation that heparin binding is involved in the initiation of an AAV-2 infection (62). Nevertheless, several mutants apparently contradict this interpretation: While heparin binding and cell binding of an R585M mutant (mutant 27) and a K532A mutant (mutant 20) were clearly reduced, the infectivity of these mutants was not affected much. Also, for mutant 12 (R475A) and mutant 19 (K527A), there was no quantitative correlation between infectivity and heparin binding. Mutant 12 had a strong effect on infectivity and only a weak influence on heparin binding, whereas mutant 19 had a very weak effect on infectivity but a moderate influence on heparin binding. In this respect, it should be noted that the infectious titer assay used here to determine infectivity measures more than just infection; it also measures replication and capsid formation. As postbinding events have a strong influence on gene transduction (15, 20, 27, 55, 71, 73), a particular mutation could compensate for a defect in cell binding and entry by improved cytoplasmic and nuclear trafficking or even replication and assembly. Therefore, the lack of a tight correlation between replication titers and heparin binding for these mutants does not necessarily contradict the involvement of AAV-2– HSPAG interactions in the infection process. Furthermore, the heparin-binding assay with a heparin-agarose column might not fully reflect binding to the still unknown HSGAG at the cell surface. There was, however, always a correlation between cell binding and heparin binding, suggesting that binding to heparin-agarose is a reliable measure for the interaction of AAV-2 with its cellular HSGAG.

Alternatively, however, the lack of correlation of heparin binding and infectivity of some heparin-binding mutants could mean that binding to heparan sulfate proteoglycan facilitates and enhances AAV-2 cell interaction but that this interaction is not necessary for infection (51), similar to the situation with adenovirus types 2 and 5, human immunodeficiency virus type 1, and HSV-1 (10, 13, 14, 19, 42, 46, 56, 70). Support for this interpretation comes from the in vivo distribution of wild-type and mutant rAAVs. A double mutation of the heparin-binding motif at R484 and R585 (mutant 17), leading to a loss of heparin binding and to low cell binding on HeLa cells, strongly reduced infection of mouse liver tissue in vivo but had no effect on infection of heart, lung, or kidney tissue. Although in this case the heart would have received a higher amount of virus (due to reduced retention by the liver) than in the wild-type experiment, there must also be a significant permissivity of heart tissue for the mutant virus to explain the observed expression levels. Since heparan sulfate proteoglycans are not internalized upon binding of a ligand when used as receptor molecules, their function in the AAV-2 infection process likely just increases the probability for interaction with a secondary receptor, such as fibroblast growth factor receptor 1 or $\alpha V\beta 5$ integrin. Under this assumption, efficient interaction of the double mutant with one of these or an alternative (secondary) receptor could provide the observed infection of heart tissue with the heparin-binding mutant.

This analysis of a heparin-binding motif in the AAV-2 capsid has focused on basic amino acids in loop IV of the three AAV-2 capsid proteins. Several other basic sequence motifs present in the N-terminal region, unique for VP1 and VP2, were shown to play no role in heparin binding (69) (unpublished data). Nevertheless, Shi et al. (59) reported insertion mutants outside the range of of loop IV which inhibited heparin binding. According to the atomic structure of the AAV-2

capsid, either these positions are not surface exposed like amino acids 312 and 520 and most probably reflect an indirect influence on heparin binding or they are located on the surface of the fivefold symmetry element (V323 and K549), which is less exposed on the capsid surface than the threefold spike (37, 72). Nevertheless, the contribution of further nonbasic residues and a definitive description of all residues involved in an AAV-2– heparin interaction would require the X-ray analysis of heparin-bound capsids.

ACKNOWLEDGMENTS

We thank P. Poberschin for excellent experimental support. We also acknowledge the initial experimental contributions of Niclas Czeloth and Simone Giese.

C.L. was supported by a grant from the HGF, and O.M. is supported by the Deutsche Forschungsgemeinschaft (MU 1654/2-1).

REFERENCES

1. **Bae, J., U. R. Desai, A. Pervin, E. E. Caldwell, J. M. Weiler, and R. J. Linhardt.** 1994. Interaction of heparin with synthetic antithrombin III peptide analogues. Biochem. J. **301:**121–129.
2. **Becerra, S. P., F. Koczot, P. Fabisch, and J. A. Rose.** 1988. Synthesis of adeno-associated virus structural proteins requires both alternative mRNA splicing and alternative initiations from a single transcript. J. Virol. **62:**2745–2754.
3. **Bernfield, M., M. Gotte, P. W. Park, O. Reizes, M. L. Fitzgerald, J. Lincecum, and M. Zako.** 1999. Functions of cell surface heparan sulfate proteoglycans. Annu. Rev. Biochem. **68:**729–777.
4. **Byrnes, A. P., and D. E. Griffin.** 1998. Binding of Sindbis virus to cell surface heparan sulfate. J. Virol. **72:**7349–7356.
5. **Capila, I., and R. J. Linhardt.** 2002. Heparin-protein interactions. Angew. Chem. Int. Ed. Engl. **41:**391–412.
6. **Cassinotti, P., M. Weitz, and J. D. Tratschin.** 1988. Organization of the adeno-associated virus (AAV) capsid gene: mapping of a minor spliced mRNA coding for virus capsid protein 1. Virology **167:**176–184.
7. **Chapman, M. S., and M. G. Rossmann.** 1993. Structure, sequence, and function correlations among parvoviruses. Virology **194:**491–508.
8. **Chen, C. A., and H. Okayama.** 1988. Calcium phosphate-mediated gene transfer: a highly efficient transfection system for stably transforming cells with plasmid DNA. BioTechniques **6:**632–638.
9. **Chen, Y., T. Maguire, R. E. Hileman, J. R. Fromm, J. D. Esko, R. J. Linhardt, and R. M. Marks.** 1997. Dengue virus infectivity depends on envelope protein binding to target cell heparan sulfate. Nat. Med. **3:**866–871.
10. **Choe, H., M. Farzan, Y. Sun, N. Sullivan, B. Rollins, P. D. Ponath, L. Wu, C. R. Mackay, G. LaRosa, W. Newman, N. Gerard, C. Gerard, and J. Sodroski.** 1996. The beta-chemokine receptors CCR3 and CCR5 facilitate infection by primary HIV-1 isolates. Cell **85:**1135–1148.
11. **Chung, C. S., J. C. Hsiao, Y. S. Chang, and W. Chang.** 1998. A27L protein mediates vaccinia virus interaction with cell surface heparan sulfate. J. Virol. **72:**1577–1585.
12. **Compton, T., D. M. Nowlin, and N. R. Cooper.** 1993. Initiation of human cytomegalovirus infection requires initial interaction with cell surface heparan sulfate. Virology **193:**834–841.
13. **Dechecchi, M. C., A. Tamanini, A. Bonizzato, and G. Cabrini.** 2000. Heparan sulfate glycosaminoglycans are involved in adenovirus type 5 and 2-host cell interactions. Virology **268:**382–390.
14. **Deng, H., R. Liu, W. Ellmeier, S. Choe, D. Unutmaz, M. Burkhart, P. Di Marzio, S. Marmon, R. E. Sutton, C. M. Hill, C. B. Davis, S. C. Peiper, T. J. Schall, D. R. Littman, and N. R. Landau.** 1996. Identification of a major co-receptor for primary isolates of HIV-1. Nature **381:**661–666.
15. **Duan, D., Y. Yue, Z. Yan, J. Yang, and J. F. Engelhardt.** 2000. Endosomal processing limits gene transfer to polarized airway epithelia by adeno-associated virus. J. Clin. Investig. **105:**1573–1587.
16. **Dubielzig, R., J. A. King, S. Weger, A. Kern, and J. A. Kleinschmidt.** 1999. Adeno-associated virus type 2 protein interactions: formation of preencapsidation complexes. J. Virol. **73:**8989–8998.
17. **Esko, J. D., and S. B. Selleck.** 2002. Order out of chaos: assembly of ligand binding sites in heparan sulfate. Annu. Rev. Biochem. **71:**435–471.
18. **Fath, M. A., X. Wu, R. E. Hileman, R. J. Linhardt, M. A. Kashem, R. M. Nelson, C. D. Wright, and W. M. Abraham.** 1998. Interaction of secretory leukocyte protease inhibitor with heparin inhibits proteases involved in asthma. J. Biol. Chem. **273:**13563–13569.
19. **Geraghty, R. J., C. Krummenacher, G. H. Cohen, R. J. Eisenberg, and P. G. Spear.** 1998. Entry of alphaherpesviruses mediated by poliovirus receptor-related protein 1 and poliovirus receptor. Science **280:**1618–1620.
20. **Girod, A., C. E. Wobus, Z. Zadori, M. Ried, K. Leike, P. Tijssen, J. A. Kleinschmidt, and M. Hallek.** 2002. The VP1 capsid protein of adeno-associated virus type 2 is carrying a phospholipase A2 domain required for virus infectivity. J. Gen. Virol. **83:**973–978.
21. **Goodsell, D. S., G. M. Morris, and A. J. Olson.** 1996. Automated docking of flexible ligands: applications of AutoDock. J. Mol. Recognit. **9:**1–5.
22. **Grifman, M., M. Trepel, P. Speece, L. B. Gilbert, W. Arap, R. Pasqualini, and M. D. Weitzman.** 2001. Incorporation of tumor-targeting peptides into recombinant adeno-associated virus capsids. Mol. Ther. **3:**964–975.
23. **Grimm, D., A. Kern, M. Pawlita, F. Ferrari, R. Samulski, and J. Kleinschmidt.** 1999. Titration of AAV-2 particles via a novel capsid ELISA: packaging of genomes can limit production of recombinant AAV-2. Gene Ther. **6:**1322–1330.
24. **Grimm, D., A. Kern, K. Rittner, and J. A. Kleinschmidt.** 1998. Novel tools for production and purification of recombinant adenoassociated virus vectors. Hum. Gene Ther. **9:**2745–2760.
25. **Grimm, D., and J. A. Kleinschmidt.** 1999. Progress in adeno-associated virus type 2 vector production: promises and prospects for clinical use. Hum. Gene Ther. **10:**2445–2450.
26. **Handa, A., S. Muramatsu, J. Qiu, H. Mizukami, and K. E. Brown.** 2000. Adeno-associated virus (AAV)-3-based vectors transduce haematopoietic cells not susceptible to transduction with AAV-2-based vectors. J. Gen. Virol. **81:**2077–2084.
27. **Hansen, J., K. Qing, and A. Srivastava.** 2001. Adeno-associated virus type 2-mediated gene transfer: altered endocytic processing enhances transduction efficiency in murine fibroblasts. J. Virol. **75:**4080–4090.
28. **Hauswirth, W. W., A. S. Lewin, S. Zolotukhin, and N. Muzyczka.** 2000. Production and purification of recombinant adeno-associated virus. Methods Enzymol. **316:**743–761.
29. **Heilbronn, R., A. Burkle, S. Stephan, and H. zur Hausen.** 1990. The adeno-associated virus *rep* gene suppresses herpes simplex virus-induced DNA amplification. J. Virol. **64:**3012–3018.
30. **Hileman, R. E., J. R. Fromm, J. M. Weiler, and R. J. Linhardt.** 1998. Glycosaminoglycan-protein interactions: definition of consensus sites in glycosaminoglycan binding proteins. Bioessays **20:**156–167.
31. **Hileman, R. E., R. N. Jennings, and R. J. Linhardt.** 1998. Thermodynamic analysis of the heparin interaction with a basic cyclic peptide using isothermal titration calorimetry. Biochemistry **37:**15231–15237.
32. **Huntington, J. A., S. T. Olson, B. Fan, and P. G. Gettins.** 1996. Mechanism of heparin activation of antithrombin. Evidence for reactive center loop preinsertion with expulsion upon heparin binding. Biochemistry **35:**8495–8503.
33. **Jackson, T., F. M. Ellard, R. A. Ghazaleh, S. M. Brookes, W. E. Blakemore, A. H. Corteyn, D. I. Stuart, J. W. Newman, and A. M. King.** 1996. Efficient infection of cells in culture by type O foot-and-mouth disease virus requires binding to cell surface heparan sulfate. J. Virol. **70:**5282–5287.
34. **Joyce, J. G., J. S. Tung, C. T. Przysiecki, J. C. Cook, E. D. Lehman, J. A. Sands, K. U. Jansen, and P. M. Keller.** 1999. The L1 major capsid protein of human papillomavirus type 11 recombinant virus-like particles interacts with heparin and cell-surface glycosaminoglycans on human keratinocytes. J. Biol. Chem. **274:**5810–5822.
35. **King, J. A., R. Dubielzig, D. Grimm, and J. A. Kleinschmidt.** 2001. DNA helicase-mediated packaging of adeno-associated virus type 2 genomes into preformed capsids. EMBO J. **20:**3282–3291.
36. **Klimstra, W. B., K. D. Ryman, and R. E. Johnston.** 1998. Adaptation of Sindbis virus to BHK cells selects for use of heparan sulfate as an attachment receptor. J. Virol. **72:**7357–7366.
37. **Kronenberg, S., J. A. Kleinschmidt, and B. Bottcher.** 2001. Electron cryomicroscopy and image reconstruction of adeno-associated virus type 2 empty capsids. EMBO Rep. **2:**997–1002.
38. **Krusat, T., and H. J. Streckert.** 1997. Heparin-dependent attachment of respiratory syncytial virus (RSV) to host cells. Arch. Virol. **142:**1247–1254.
39. **Laughlin, C. A., J. D. Tratschin, H. Coon, and B. J. Carter.** 1983. Cloning of infectious adeno-associated virus genomes in bacterial plasmids. Gene **23:**65–73.
40. **Liu, D., Z. Shriver, Y. Qi, G. Venkataraman, and R. Sasisekharan.** 2002. Dynamic regulation of tumor growth and metastasis by heparan sulfate glycosaminoglycans. Semin. Thromb. Hemost. **28:**67–78.
41. **Mizukami, H., N. S. Young, and K. E. Brown.** 1996. Adeno-associated virus type 2 binds to a 150-kilodalton cell membrane glycoprotein. Virology **217:**124–130.
42. **Montgomery, R. I., M. S. Warner, B. J. Lum, and P. G. Spear.** 1996. Herpes simplex virus-1 entry into cells mediated by a novel member of the TNF/NGF receptor family. Cell **87:**427–436.
43. **Morris, G. M., D. S. Goodsell, R. S. Halliday, R. Huey, W. E. Hart, R. K. Belew, and A. Olson.** 1998. Automated docking using a Lamarckian genetic algorithm and empirical binding energy function. J. Comp. Chem. **19:**1639–1662.
44. **Mulloy, B., M. J. Forster, C. Jones, and D. B. Davies.** 1993. N. m. r. and molecular-modelling studies of the solution conformation of heparin. Biochem. J. **293:**849–858.
45. **Nicklin, S. A., H. Buening, K. L. Dishart, M. de Alwis, A. Girod, U. Hacker, A. J. Thrasher, R. R. Ali, M. Hallek, and A. H. Baker.** 2001. Efficient and

selective AAV2-mediated gene transfer directed to human vascular endothelial cells. Mol. Ther. **4:**174–181.
46. **Ohshiro, Y., T. Murakami, K. Matsuda, K. Nishioka, K. Yoshida, and N. Yamamoto.** 1996. Role of cell surface glycosaminoglycans of human T cells in human immunodeficiency virus type-1 (HIV-1) infection. Microbiol. Immunol. **40:**827–835.
47. **Opie, S. R., K. H. Warrington, Jr., M. Agbandje-McKenna, S. Zolotukhin, and N. Muzyczka.** 2003. Identification of amino acid residues in the capsid proteins of adeno-associated virus type 2 that contribute to heparan sulfate proteoglycan binding. J. Virol. **77:**6995–7006.
48. **Park, P. W., O. Reizes, and M. Bernfield.** 2000. Cell surface heparan sulfate proteoglycans: selective regulators of ligand-receptor encounters. J. Biol. Chem. **275:**29923–29926.
49. **Qing, K., C. Mah, J. Hansen, S. Zhou, V. Dwarki, and A. Srivastava.** 1999. Hum. fibroblast growth factor receptor 1 is a co-receptor for infection by adeno-associated virus 2. Nat. Med. **5:**71–77.
50. **Qiu, J., and K. E. Brown.** 1999. Integrin alphaVbeta5 is not involved in adeno-associated virus type 2 (AAV2) infection. Virology **264:**436–440.
51. **Qiu, J., A. Handa, M. Kirby, and K. E. Brown.** 2000. The interaction of heparin sulfate and adeno-associated virus 2. Virology **269:**137–147.
52. **Qiu, J., H. Mizukami, and K. E. Brown.** 1999. Adeno-associated virus 2 co-receptors? Nat. Med. **5:**467–468.
53. **Rabinowitz, J. E., F. Rolling, C. Li, H. Conrath, W. Xiao, X. Xiao, and R. J. Samulski.** 2002. Cross-packaging of a single adeno-associated virus (AAV) type 2 vector genome into multiple AAV serotypes enables transduction with broad specificity. J. Virol. **76:**791–801.
54. **Rabinowitz, J. E., W. Xiao, and R. J. Samulski.** 1999. Insertional mutagenesis of AAV2 capsid and the production of recombinant virus. Virology **265:**274–285.
55. **Sanlioglu, S., P. K. Benson, J. Yang, E. M. Atkinson, T. Reynolds, and J. F. Engelhardt.** 2000. Endocytosis and nuclear trafficking of adeno-associated virus type 2 are controlled by rac1 and phosphatidylinositol-3 kinase activation. J. Virol. **74:**9184–9196.
56. **Sattentau, Q. J., A. G. Dalgleish, R. A. Weiss, and P. C. Beverley.** 1986. Epitopes of the CD4 antigen and HIV infection. Science **234:**1120–1123.
57. **Sayle, R. A., and E. J. Milner-White.** 1995. RASMOL: biomolecular graphics for all. Trends Biochem. Sci. **20:**374.
58. **Selinka, H. C., T. Giroglou, and M. Sapp.** 2002. Analysis of the infectious entry pathway of human papillomavirus type 33 pseudovirions. Virology **299:**279–287.
59. **Shi, W., G. S. Arnold, and J. S. Bartlett.** 2001. Insertional mutagenesis of the adeno-associated virus type 2 (AAV2) capsid gene and generation of AAV2 vectors targeted to alternative cell-surface receptors. Hum. Gene Ther. **12:** 1697–1711.
60. **Srivastava, A., E. W. Lusby, and K. I. Berns.** 1983. Nucleotide sequence and organization of the adeno-associated virus 2 genome. J. Virol. **45:**555–564.
61. **Summerford, C., J. S. Bartlett, and R. J. Samulski.** 1999. AlphaVbeta5 integrin: a co-receptor for adeno-associated virus type 2 infection. Nat. Med. **5:**78–82.
62. **Summerford, C., and R. J. Samulski.** 1998. Membrane-associated heparan sulfate proteoglycan is a receptor for adeno-associated virus type 2 virions. J. Virol. **72:**1438–1445.
63. **Trempe, J. P., and B. J. Carter.** 1988. Alternate mRNA splicing is required for synthesis of adeno-associated virus VP1 capsid protein. J. Virol. **62:**3356–3363.
64. **Trybala, E., T. Bergstrom, D. Spillmann, B. Svennerholm, S. J. Flynn, and P. Ryan.** 1998. Interaction between pseudorabies virus and heparin/heparan sulfate. Pseudorabies virus mutants differ in their interaction with heparin/heparan sulfate when altered for specific glycoprotein C heparin-binding domain. J. Biol. Chem. **273:**5047–5052.
65. **Weger, S., A. Wistuba, D. Grimm, and J. A. Kleinschmidt.** 1997. Control of adeno-associated virus type 2 cap gene expression: relative influence of helper virus, terminal repeats, and Rep proteins. J. Virol. **71:**8437–8447.
66. **Weiner, S. J., P. A. Kollman, D. A. Case, U. C. Singh, C. Ghio, G. Alagona, S. Profeta, and P. Weiner.** 1986. An all atom forcefield for simulations of proteins and nucleic acids. J. Comp. Chem. **7:**230–252.
67. **Wistuba, A., S. Weger, A. Kern, and J. A. Kleinschmidt.** 1995. Intermediates of adeno-associated virus type 2 assembly: identification of soluble complexes containing Rep and Cap proteins. J. Virol. **69:**5311–5319.
68. **Wobus, C. E., B. Hugle-Dorr, A. Girod, G. Petersen, M. Hallek, and J. A. Kleinschmidt.** 2000. Monoclonal antibodies against the adeno-associated virus type 2 (AAV-2) capsid: epitope mapping and identification of capsid domains involved in AAV-2– cell interaction and neutralization of AAV-2 infection. J. Virol. **74:**9281–9293.
69. **Wu, P., W. Xiao, T. Conlon, J. Hughes, M. Agbandje-McKenna, T. Ferkol, T. Flotte, and N. Muzyczka.** 2000. Mutational analysis of the adeno-associated virus type 2 (AAV2) capsid gene and construction of AAV2 vectors with altered tropism. J. Virol. **74:**8635–8647.
70. **WuDunn, D., and P. G. Spear.** 1989. Initial interaction of herpes simplex virus with cells is binding to heparan sulfate. J. Virol. **63:**52–58.
71. **Xiao, W., K. H. Warrington, Jr., P. Hearing, J. Hughes, and N. Muzyczka.** 2002. Adenovirus-facilitated nuclear translocation of adeno-associated virus type 2. J. Virol. **76:**11505–11517.
72. **Xie, Q., W. Bu, S. Bhatia, J. Hare, T. Somasundaram, A. Azzi, and M. S. Chapman.** 2002. The atomic structure of adeno-associated virus (AAV-2), a vector for human gene therapy. Proc. Natl. Acad. Sci. USA **99:**10405–10410.
73. **Yan, Z., R. Zak, G. W. Luxton, T. C. Ritchie, U. Bantel-Schaal, and J. F. Engelhardt.** 2002. Ubiquitination of both adeno-associated virus type 2 and 5 capsid proteins affects the transduction efficiency of recombinant vectors. J. Virol. **76:**2043–2053.
74. **Zolotukhin, S., M. Potter, W. W. Hauswirth, J. Guy, and N. Muzyczka.** 1996. A "humanized" green fluorescent protein cDNA adapted for high-level expression in mammalian cells. J. Virol. **70:**4646–4654.

Author Manuscript

Author Manuscript

Author Manuscript

Author Manuscript

HHS Public Access

Author manuscript

Gene Ther. Author manuscript; available in PMC 2015 April 11.

Published in final edited form as:

Gene Ther. 2015 February ; 22(2): 116–126. doi:10.1038/gt.2014.115.

Antibody Neutralization Poses a Barrier to Intravitreal Adeno-Associated Viral Vector Gene Delivery to Non-Human Primates

Melissa A. Kotterman[1,6], **Lu Yin**[2], **Jennifer M. Strazzeri**[2], **John G. Flannery**[3,4], **William H. Merigan**[2], and **David V. Schaffer**[1,3,4,5,6,*]

[1]Department of Chemical and Biomolecular Engineering, University of California, Berkeley, California, USA

[2]Flaum Eye Institute and Center for Visual Science, University of Rochester, Rochester, NY 14642, USA

[3]The Helen Wills Neuroscience Institute, University of California, Berkeley, California, USA

[4]Department of Molecular and Cellular Biology, University of California, Berkeley, CA 94720–1462, USA

[5]Department of Bioengineering, University of California, Berkeley, California, USA

[6]4D Molecular Therapeutics, San Francisco, California, USA

Abstract

Gene delivery vectors based on adeno-associated viruses (AAV) have exhibited promise in both preclinical disease models and human clinical trials for numerous disease targets, including the retinal degenerative disorders Leber's congenital amaurosis and choroideremia. One general challenge for AAV is that pre-existing immunity, as well as subsequent development of immunity following vector administration, can severely inhibit systemic AAV vector gene delivery. However, the role of neutralizing antibodies (NABs) in AAV transduction of tissues considered to be immune privileged, such as the eye, is unclear in large animals. Intravitreal AAV administration allows for broad retinal delivery, but is more susceptible to interactions with the immune system than subretinal administration. To assess the effects of systemic anti-AAV antibody levels on intravitreal gene delivery, we quantified the anti-AAV antibodies present in sera from non-human primates before and after intravitreal injections with various AAV capsids. Analysis showed that intravitreal administration resulted in an increase in anti-AAV antibodies regardless of the capsid serotype, transgene, or dosage of virus injected. For monkeys injected with wild-type AAV2 and/or an AAV2 mutant, the variable that most significantly affected the production of anti-AAV2 antibodies was the amount of virus delivered. In addition, post-injection antibody titers were highest against the serotype administered, but the antibodies were also cross-reactive against other AAV serotypes. Furthermore, neutralizing antibody levels in serum correlated with those in vitreal fluid, demonstrating both that this route of administration exposes AAV capsid epitopes to the adaptive immune system and that serum measurements are predictive

*Corresponding Author: David V. Schaffer, 274 Stanley Hall, Berkeley, CA 94720-3220, (510) 643-5963, schaffer@berkeley.edu.

Conflict of Interest: M.A.K., J.G.F., and D.V.S. are inventors on patents related to engineering of adeno-associated viruses, and M.A.K. and D.V.S. are associated with a company (4D Molecular Therapeutics) involved in AAV vector engineering.

Author Manuscript Author Manuscript Author Manuscript Author Manuscript

of vitreous fluid NAB titers. Moreover, the presence of pre-existing neutralizing antibody titers in the serum of monkeys correlated strongly (R=0.76) with weak, decaying, or no transgene expression following intravitreal administration of AAV. Investigating anti-AAV antibody development will aid in understanding the interactions between gene therapy vectors and the immune system during ocular administration and can form a basis for future clinical studies applying intravitreal gene delivery.

Introduction

The parvovirus adeno-associated virus (AAV) contains a 4.7 kb single-stranded DNA genome within a non-enveloped protein capsid.[1] The genome is flanked by inverted terminal repeats (ITR) that serve as the viral origin of replication and packaging signal for the genome.[1] The genome contains three open reading frames (ORF). The *rep* ORF encodes four nonstructural proteins that play roles in viral replication, transcriptional regulation, site-specific integration, and virion assembly;[1] the *cap* ORF encodes three structural proteins (VP1-3) that assemble to form a 60-mer viral capsid;[1] and the assembly-activating protein (AAP)[2,3] – which lies in an alternate reading frame within the *cap* gene – localizes AAV capsid proteins to the nucleolus and functions in the capsid assembly process.[2] There are eleven naturally occurring serotypes and over 100 variants of AAV, each of which differs in amino acid sequence, particularly within the hypervariable regions of the capsid proteins, and thus in their gene delivery properties.[4,5] To create recombinant versions of AAV for use in gene delivery, a gene of interest is inserted between the ITRs in place of *rep* and *cap*, which are then provided *in trans* along with helper viral genes during vector production.[6] The resulting AAV vectors can transduce both dividing and non-dividing cells, and delivery can result in stable transgene expression for years in post-mitotic tissue.

As of 2014, there were over 100 completed or ongoing clinical trials that used AAV as the gene delivery vehicle.[7] Among the many characteristics that make AAV an attractive vector for clinical applications, it has not been associated with any human disease.[1] In addition, during Phase I/II clinical trials for Leber's congenital amaurosis (LCA), over 30 patients who received a subretinal injection of AAV2 encoding RPE65, an enzyme responsible for the isomerohydrolase activity of retinal pigment epithelium, showed sustained improvement in both subjective and objective measurements of vision.[8–14] Moreover, a recent phase I trial for choroideremia showed promising signs of efficacy.[15] These trials therefore indicate that AAV may be promising for treating monogenic and complex retinal degenerative diseases, including retinitis pigmentosa, macular degeneration, diabetic retinopathy, and glaucoma.

One potential challenge for the broad application of AAV ocular therapy, however, is its route of administration. Subretinal AAV vector injection, used for the LCA and choroideremia trials, enables efficient gene expression in several retinal cell types, including photoreceptors and retinal pigment epithelial cells.[16,17] This route of administration entails delivery via a needle puncture through the neurosensory retina, which induces a retinal detachment surrounding a bleb of concentrated vector that results in very efficient transduction of the adjacent photoreceptors and retinal pigement epithelia. Although neutralizing antibodies against the AAV capsid do not increase (or prevent readministration)

Author Manuscript Author Manuscript Author Manuscript Author Manuscript

when AAV gene therapy vectors are administered via subretinal injection,[13] delivery is limited to tissues in contact with the bleb(s),[18–20] a suboptimal solution since degeneration occurs across the retina in most diseases. Furthermore, the retinal detachment inherent in subretinal injections can lead to reactive gliosis, retinal disorganization, photoreceptor degeneration, and functional losses in vision,[21,22] risks that may be exacerbated in retinas already weakened by degenerative.[23] In contrast, intravitreal AAV administration, to the vitreous humor of the eye, offers the potential for pan-retinal delivery without the risk of retinal detachment. Recent work has developed AAV variants that are capable of infecting both Muller glia and photoreceptors across the retina following intravitreal administration, making intravitreal injections a promising alternative.[24,25]

However, another challenge to AAV-mediated gene therapy is humoral, anti-AAV antibody mediated immunity, which results from childhood exposure to one or more serotypes or from prior administration of AAV vectors and poses a significant challenge to AAV gene therapy.[26,27] Recent analysis indicated that the prevalence of anti-AAV IgG antibodies in humans was highest for AAV2 (72%) and AAV1 (67%); however, AAV9 (47%), AAV6 (46%), AAV5 (40%), and AAV8 (38%) antibodies were also present in a large portion of the population studied.[28] In non-human primates (NHPs), high concentrations of anti-AAV antibodies significantly reduced the transduction of hepatocytes,[29] and the presence of pre-existing antibodies has been correlated with decreased efficacy of gene therapy in clinical trials where the route of administration exposes vector to serum.[26,30,31]

In addition to antibodies in the blood, antibodies are also present in other bodily fluids, such as human synovial fluid,[32,33] non-human primate cerebrospinal fluid,[34] and NHP vitreal fluid (as we show here), where they can again inhibit vector transduction. For example, the presence of extremely high titers of neutralizing antibodies in serum are accompanied by reduced AAV vector transduction in the rat brain following intracranial injection or in the mouse eye following intravitreal injection.[35,36] Furthermore, AAV administration to immune privileged regions can lead to increases in neutralizing antibody titers, including following intravitreal injection in dogs and non-human primates[37] and following intracranial injections in several clinical trials.[38] While transient immunosuppression may be a promising approach for reducing cellular immune responses to gene therapy,[39–41] it is not effective at mitigating vector neutralization by pre-existing antibodies.

As a result, AAV clinical successes to date have involved delivery either to immune privileged regions or to subjects lacking apparent AAV immunological memory.[8–14,30,42] During the LCA clinical trial, patients were excluded “if immunological studies show presence of neutralizing antibodies to AAV2 above 1:1000.”[11] Recent clinical trials for hemophilia have used even more stringent criteria for patient exclusion, removing patients whose neutralizing antibodies were above 1:4.[31,43] NABs are often the most commonly invoked exclusion criterion for patent enrollment.[30]

As part of a study on the function of optogenetic proteins in the non-human primate retina, we collected serum and intravitreal fluid samples from non-human primates before and after injections with various AAV capsids. As a result, these samples have enabled analysis of the immune response (specifically the presence of anti-AAV antibodies) to AAV vectors, as

Author Manuscript Author Manuscript Author Manuscript Author Manuscript

well as the effects of systemic NAB levels on transgene expression following intravitreal administration. In an effort to provide as much information as possible, AAV injection history for each monkey studied is included in the presentation of the results. Although NHP studies present inherent challenges for larger scale statistical analysis, the trends observed in this study may lend insights to help understand the interactions between AAV vectors and the immune system during ocular administration, and may therefore aid future clinical studies involving intravitreal gene delivery.

Results

Increase of Anti-AAV2 Antibodies Pre-Infection vs. Post-Infection

As part of studies exploring reporter or optogenetic proteins in the non-human primate retina[25,44,45], monkeys were injected with vectors with capsids of one or more of the following: wild-type AAV2 capsid, wild-type AAV5 capsid, wild-type AAV9 capsid, 7m8 (an AAV2-based capsid engineered for murine retinal delivery and containing an insertion of the peptide LGETTRP at amino acid position 588 on the viral capsid)[25], and AAV2 tyrosine 4YF mutant virus (an AAV2-based capsid containing tyrosine to phenylalanine mutations at amino acid positions 272, 444, 500, 704, and 730)[46]. The levels of anti-AAV antibodies present in monkey serum samples obtained before or after intravitreal AAV administration were determined with an *in vitro* neutralization assay in which the inhibition of HEK 293 cell transduction was measured following incubation with a range of serum dilutions. The NAB titers are reported as the reciprocal of the serum dilution at which 50% of transduction is inhibited *in vitro* (Figure 1a). As shown in the representative images for one animal, there was no effect on the level of transduction (measured as GFP positive cells) even in the most concentrated serum dilution (1:10) for a serum sample taken prior to intravitreal administration of 7m8 vector, indicating that this serum did not contain a detectable level of anti-AAV2 antibodies. In contrast, there was a 50% decrease in transduction with a 1:500 dilution of a serum sample taken from the same monkey after intravitreal administration of 7m8 vector, indicating the presence of anti-AAV2 antibodies. Furthermore, even at a 1:10 dilution transduction was fully inhibited, illustrating the neutralization capacity of the anti-AAV2 antibodies found in serum post-viral administration.

Serum samples were obtained before and after intravitreal injections, in one or both eyes, of various AAV capsids in a series of adult macaques. Anti-AAV2 antibody titers increased in all animals following injection regardless of the capsid serotype, transgene, dosage of virus, or unilateral vs. bilateral injection. This finding is consistent with previous reports in rodents indicating that the vitreous is not as immune-privileged a route of administration as subretinal delivery for either AAV or adenovirus delivery.[47,48] However, several variables may change the magnitude of the antibody response. For example, the capsid serotype (AAV2, AAV5, or AAV9) administered may affect the magnitude of increase in anti-AAV2 NAB titers from pre- to post-injection. That is, as expected, monkeys injected with AAV2 generated post-administration antibodies that neutralized AAV2 slightly more potently than monkeys injected with other serotypes (Figure 1b – wild-type AAV2: 10-50 fold increase post-injection vs. Figure 1c – wild-type AAV9 and/or AAV5: 2.5-50 fold increase post-

Author Manuscript Author Manuscript Author Manuscript Author Manuscript

injection). The particular alternative serotype injected may also affect the anti-AAV2 antibody response post-administration. Monkey 108 (injected with both AAV5 and AAV9 – Figure 1c, black circles) had a larger anti-AAV2 response than Monkey 012 (only injected with AAV5 – Figure 1c, gray triangles), which may be due to the larger percentage of sequence similarity between AAV2 and AAV9 capsids, the larger amount of virus administered (since both eyes were injected), or the sequential eye injections in Monkey 108 heightening the immune response to the second injection.

Another anticipated observation is that while the serotype injected (i.e. AAV2, AAV5, or AAV9) appears to modulate the subsequent level of serum neutralization of AAV2, small sequence changes to a serotype (i.e. wild-type AAV2 vs. 7m8) do not significantly affect the antibody response in the seven animals in which these vectors were administered (Figure 1b – wild-type AAV2: 10-50 fold increase in anti-AAV2 NAB titer post-injection vs. Figure 1d – 7m8 capsid: 20-500 fold increase post-injection vs. Figure 1e – double injection of wild-type AAV2 + AAV2 tyrosine mutant 4YF capsid or 7m8 capsid: 50-200 fold increase post-injection; p=0.397). These variants, as anticipated, are not sufficiently different from wild-type AAV2 to disrupt the antibody binding sites on the capsid, so antibodies against a mutant will similarly react to the other mutants or the wild-type capsid (Figure 2). To further support this finding, wild-type AAV2, an AAV2 tyrosine 4YF mutant capsid, and a 7m8 capsid were tested against human intravenous immunoglobulin (IVIG) (Figure 2a) or sera from monkeys that had been exposed to various serotypes and variants (Figure 2 b-d). Although the AAV2 tyrosine 4YF mutant capsid was slightly more infectious to HEK293 cells than wild-type AAV2 at the 1:2500 and 1:5000 serum dilutions, there was no significant difference in the serum dilution at which it was ∼50% neutralized compared to the 7m8 capsid and wild-type AAV2. Since AAV2 and 7m8 are thus equally neutralized by NHP and human antibodies, it to be unlikely that the 7m8 modification results in a different exposure of antibody binding epitopes. The larger NAb titers at the upper range for 7m8 (Figure 1d) may instead be due to the larger viral doses administered, which is discussed below for Figure 1h and 1i.

Analysis was also performed to determine outcomes from injection into one vs. two eyes (for cases where eyes were injected at the same time or within 4 days). Sera samples from Monkeys 002, 109, 110, 906, and 909 (injected in one eye – Figure 1f) and Monkeys 014, 736, and 902 (injected in both eyes– Figure 1g) showed similar magnitudes of anti-AAV2 NAB response (Figure 1f – single eye: 10-500 fold increase post-injection vs. Figure 1g – double eye: 50-250 fold increase post-injection; p=0.996). However, for the seven monkeys injected with wild-type AAV2 and/or an AAV2 mutant, the variable that most significantly affected the production of anti-AAV2 antibodies is the amount of virus delivered (Figure 1h – total virus > 2×10^{12} vg: 200-500 fold increase vs. Figure 1i – total virus < 2×10^{12} vg: 10-50 fold increase; p=0.017). For example, Monkey 902 (50-fold increase post-injection – Figure 1i, gray triangles) had less total virus injected into two eyes (5.4×10^{11} total viral genomes) than Monkey 109 (500-fold increase post-injection – Figure 1h, light gray diamonds) had into only one eye (6.3×10^{12} total viral genomes).

Author Manuscript Author Manuscript Author Manuscript Author Manuscript

Comparison of AAV2 Neutralization by Serum vs. Vitreous Fluid

Determining vitreous fluid antibody titers is challenging for several reasons. First, sampling this fluid in a clinical setting can lead to complications, including retinal detachment, decreased intraocular pressure, intraocular hemorrhaging, or cataracts.[49] These risks are even more concerning in patients whose retinas are already weakened by degenerative disease. Secondly, it is difficult to obtain a sufficiently large volume of vitreous fluid to enable comprehensive analysis of antibodies. In contrast, serum can be readily obtained, making it a more desirable bodily fluid to evaluate. To determine whether serum NAB titers correlate with vitreous fluid titers, matching serum and vitreous fluid samples were obtained at the time of euthanasia from nine monkeys previously administered intravitreally with AAV.

For all nine animals, the anti-AAV2 antibody titers of the vitreous fluid from the right and left eyes were equal (Figure 3). This occurred even though monkeys were injected with various combinations of AAV serotypes and AAV2-based 7m8 or tyrosine 4YF mutant vectors, or were injected in one or both eyes. Similarly, even when one eye received a much larger amount of virus (as is the case with Monkey 108 and Monkey 622), the neutralizing titers in both eyes at the later time were equal. Furthermore, in over half of the samples tested, vitreous fluid and serum samples had the same level of AAV2 neutralization, and in others the levels were within an order of magnitude (Figure 3), indicating that the level of anti-AAV antibodies in the serum is positively correlated with anti-AAV antibody levels in the vitreous fluid ($R=0.30$).

Presence of Anti-AAV2 Antibodies During Long Term Monitoring

For several monkeys, serial serum samples allowed monitoring of anti-AAV2 antibodies over a period of at least 7 months (Figure 4). Naïve, pre-injection samples from Monkey 013 over a year consistently showed low (or undetectable) antibody titers (data not shown). All injected animals showed consistent antibody titers for the initial months post-injection, though most seemed to experience a slight (2-5 fold) decrease in neutralizing antibody titer as early as 3 months post-injection. However, in general long-term data from several animals (Monkeys 002, 012, 013, 014, and 902) – coupled with three year monitoring of Monkey 708 (Figure 4) – demonstrated that antibodies can persist for very long periods after gene therapy administration.

Cross-Reactivity of Antibodies to Various AAV Serotypes Pre-Infection vs. Post-Infection

Several rodent models have reported successful second administrations of AAV gene delivery vectors when different serotypes are used for the first vs. second administrations[50–52]; however, these observations have not been extended to NHPs. Serum samples were evaluated for cross-reactivity of anti-AAV antibodies developed following administration of an initial vector. Consistent with the observation that anti-AAV2 antibody titers increase following injection of other serotypes (Figure 1), anti-AAV5, anti-AAV8, and anti-AAV9 antibody titers also increase following administration of any of the other serotypes (Figure 5a-h). Also consistent with previous observations (Figure 1), the NAB reactivities against AAV5, AAV8, or AAV9 were not significantly different following

Author Manuscript Author Manuscript Author Manuscript Author Manuscript

administration of wild-type AAV2 capsids, AAV2 tyrosine 4YF mutant capsids, or 7m8 capsids (Figure 5a-d).

High pre-injection neutralizing titers trended towards a smaller magnitude of change between pre- and post-injection titers (Figure 5d, f, g), but this was not significant. The trend could be due to a high extent of vector neutralization during the initial administration, leading to less cell transduction and antigen presentation, or to a saturation of the immune response. In 9 of 11 monkeys tested, initial antibody titers against AAV8 and AAV9 were higher than antibody titers against AAV2, most likely due to the high prevalence of natural AAV8 and AAV9 infections in rhesus macaques.[53,54] AAV8 and AAV9 capsids have the highest sequence similarity of any of the four capsids studied (85.7% amino acid sequence identity)[55] and showed consistent magnitudes of anti-AAV8 and anti-AAV9 antibody induction in most monkeys. Furthermore, AAV5 has the most distinct sequence of the capsids (AAV5: 61.2% amino acid sequence identity to AAV2, AAV8: 83.6% amino acid sequence identity to AAV2, AAV9: 82.7% sequence identity to AAV2),[55,56] and consequently had the least predictable antibody response in monkeys administered other serotypes. Finally, as expected from the observation that administration of high vector doses lead to larger anti-AAV2 antibody responses (Figure 1h, i), high doses of AAV2 viral capsids also induce greater anti-AAV5, anti-AAV8, and anti-AAV9 antibody responses in these animals (Figure 6b, c). For example, Monkeys 109 and 110 were injected with the same 7m8 capsid into one eye (Figure 6b, c – first injections). Monkey 109 received an approximately 10-fold higher dose of viral genomes, and developed an antibody response approximately 1-2 orders of magnitude higher towards all serotypes tested compared to Monkey 110.

Progressive Increase of Anti-AAV Antibodies with Sequential Administrations

Due to changes in the injection protocol that required a recovery period between injections into the first and then the second eye of a single animal, serum samples were available at multiple time points for three monkeys that received sequential intravitreal injections of AAV vectors. Monkey 002 (Figure 6a) had a 10-fold increase in anti-AAV2 antibody titer 46 days following injection of AAV2. AAV5 was injected 101 days after AAV2, which led 29 days later to a 2.5-fold increase in anti-AAV2 antibody titer (Figure 6a), once again demonstrating the difference in anti-AAV2 antibody response resulting from administration of AAV2 capsids compared to the administration of capsids from different serotypes. Conversely, a 2-fold increase in anti-AAV5 antibody titer was observed following injection of AAV2, followed by a 100-fold increase in anti-AAV5 antibody titer after injection of AAV5 (Figure 6a). The same trend is observed in Monkey 109, which was injected with a 7m8 capsid, then an AAV5 capsid (Figure 6b). Interestingly, Monkey 110, which was injected with a 7m8 capsid, then an AAV9 capsid, did not follow this trend (Figure 6c).

Effect of Pre-Injection Anti-AAV2 Antibodies on Expression

The observation that pre-existing antibodies inhibit AAV transduction has been broadly documented following mouse, rabbit, non-human primate, and human gene therapy administrations.[31,57–59] In a study monitoring GFP expression in macaque livers following intravenous AAV8 vector administration, neutralizing antibody titers higher than 1:10

Author Manuscript Author Manuscript Author Manuscript Author Manuscript

substantially decreased GFP expression in hepatocytes.[59] We found that for monkeys undergoing intravitreal administrations of vector involving AAV2, 7m8, or AAV2 tyrosine 4YF mutant capsids, the presence of neutralizing antibody titers of 1:10 or greater in the serum resulted in weak or no expression of the transgene (Table 1). Additionally, neutralizing titers in the range of 1:25 to 1:100 occasionally corresponded to weak transgene expression or transgene expression that decayed after initial observation. The presence of transgene expression (although weak) in a few NHP at neutralizing antibody titers in the range of 1:25 to 1:100 when transgene expression was not observed at a neutralizing antibody titer of 1:10 could be explained by an increased vector dosage or the use of an enhanced GFP transgene in these NHP. At any rate, these data suggest that systemic anti-AAV antibodies correlate (R=0.7639) with a loss of vector transduction in other body fluid compartments such as the vitreous.

Discussion

Adeno-associated virus has been successful in clinical gene therapy trials for Leber's congenital amaurosis, hemophilia, familial lipoprotein lipase deficiency, and choroideremia.[8–15,26,27,60,61] However, humoral immunological memory can inhibit or block AAV gene delivery for routes of administrations that expose vector to host antibodies.[57–59] In addition, adaptive immune responses, such as T cell responses to vector proteins or transgene encoded factors,[62] can pose a risk to transduced cells. Intravitreal administration of gene therapy vectors offers the advantages of potentially broader retinal delivery area and less invasive surgery, vectors delivered into the vitreous were more susceptible to neutralizing antibodies than those delivered subretinally in a murine model.[36] We have analogously found that the presence of pre-existing neutralizing antibody titers in the serum of monkeys correlates (R=0.7639) with weak, decaying, or no transgene expression following intravitreal administration of AAV. Furthermore, intravitreal administration resulted in an increase in anti-AAV antibodies in serum, indicating that this route presents AAV capsid antigens to the adaptive immune system. Similar results have been shown for other proteins in rats and rabbits, where intravitreal injection of retinal soluble antigen or human serum albumin resulted in an increase in anti-antigen antibodies in serum.[63,64]

Anti-AAV antibody production following intravitreal injection increased regardless of the capsid serotype, transgene, amount of virus, or number of eyes injected. Antibody titers also further increased following a second AAV administration. As anticipated, the downstream antibody response is stronger against the administered serotype than other AAV serotypes; however, due to the high sequence similarity between AAV2, AAV8, and AAV9, administration of one of these vectors led to increases in antibody titers against all. AAV5 has the least sequence similarity to the other serotypes studied and had the least predictable antibody response in monkeys previously administered with other serotypes. In addition, the initially administered serotype set the antibody response, and small sequence changes to this serotype did not affect or reduce neutralization. For example, 7m8 was neutralized at the same serum dilution as wild-type AAV2 capsid using either pooled human IVIG or individual monkey sera. These minimal differences in neutralizing antibody titer between wtAAV2 and 7m8 are to be expected, given that their capsid proteins differ by <10 amino

Author Manuscript Author Manuscript Author Manuscript Author Manuscript

acids. Although a previous report demonstrated that RGD insertions at amino acid 588 on the AAV2 capsid could disrupt an antibody binding epitope,[65] the insertion of the 7m8 peptide does not appear to have a significant effect on the neutralizing antibody titer, likely due to the polyclonal nature of antibodies in NHP and human serum. The variable that most significantly affected the production of anti-AAV2 antibodies in monkeys injected with wild-type AAV2 and/or an AAV2 mutant was the total amount of virus delivered.

A better understanding of anti-vector antibody responses may aid clinical development as the number of gene therapy clinical trials progressively increases. Weak and decaying transgene expression following intravitreal administration of AAV vectors to monkeys harboring anti-AAV antibodies provides more evidence that pre-existing immunity can challenge transduction of AAV vectors in immune privileged regions, such as the eye and brain.[35] In addition, increases in neutralizing antibody titer were seen in the sera of these monkeys following intravitreal administration of AAV vectors. This observation is consistent with previous reports that subretinal injections of AAV vectors in dogs and non-human primates,[37] as well as some intracranial injections in several clinical trials,[38] led to increased serum anti-AAV antibody titers. Further studies should help to elucidate the full extent to which antibody presence in serum and other bodily fluids, including synovial fluid and vitreal fluid,[32,33] inhibit vector transduction to different organs.

Another important consideration for ocular gene therapy is how AAV neutralization and transduction may differ in patients with advanced retinal degeneration. Previous work has shown that AAV-mediated gene therapy is significantly increased following intravitreal injection in the diseased rat retinal compared to the normal rat retinal.[66] Additionally, in a DP71-null mouse model of retinal degeneration and blood-retinal barrier permeability, gene delivery to Muller cells and photoreceptors via intravitreal injection increased.[67] However, if AAV becomes opsonized by antibodies upon administration to the vitreous fluid, it likely that despite the possibility of increased transduction to degenerated retina, neutralization may well still occur in patients with retinal degeneration. Additionally, if the tissue is already severely degenerated, unfortunately any potential efficacy of gene therapy will likely be substantially decreased.

Knowledge of the antibody response to AAV capsids following intravitreal injections motivates the implementation of strategies to improve the efficacy of gene therapy vectors administered in the presence of neutralizing antibodies. Several approaches that have been applied to the development of gene therapy vectors for systemic delivery in the presence of anti-AAV antibodies may also benefit the ocular gene therapy field. For example, the use of alternative AAV serotypes to which neutralizing antibodies are not as prevalent (for example AAV5) may enable higher gene expression in patients harboring anti-AAV2 antibodies, but cross-reactivity of neutralizing antibodies could still present a challenge. Furthermore, directed evolution has been applied to generate AAV variants capable of evading neutralizing antibodies *in vitro* and *in vivo*.[68–72] New AAV variants created through directed evolution withstood up to 35-fold higher *in vitro* concentrations of pooled human antibodies than AAV2. These antibody neutralization properties also led to enhanced transduction *in vivo*, where AAV variants were capable of significantly higher transduction in the liver, heart and muscle than AAV2 in mice passively immunized with human

Author Manuscript Author Manuscript Author Manuscript Author Manuscript

antibodies. Furthermore, novel AAV vectors have been rationally engineered for increased gene delivery in the presence of neutralizing antibodies. Mapping of linear and conformational epitopes responsible for neutralizing antibody binding and *in silico* structural analysis of potential docking sites for a murine IgG2a antibody have led to the discovery of immunogenic regions of the AAV capsid that could been mutated to develop variants with reduced neutralization by mouse and human antibodies *in vitro*.[73–75] Moreover, a capsid decoy strategy by Mingozzi *et al*. demonstrated that mixing gene therapy vectors with empty AAV2-based capsid particles with mutations that ablate primary cell receptor binding could enhance transduction of the gene therapy vector in the presence of low to moderate levels of neutralizing antibodies.[76] This capsid decoy strategy could be an effective solution to antibody neutralization in the eye, but it would likely have limitations in how high a neutralizing antibody titer the procedure could protect from, and increased capsid antigen load could have implications for overall immune responses.

In conclusion, analysis of sera collected from non-human primates before and after intravitreal injections of various AAV capsids showed clear increases in anti-vector antibodies following intravitreal administration, and in general serum NAB titers correlated well with vitreous fluid titers. Additionally, the presence of these anti-AAV antibodies correlates to weak, degenerating, or no transgene expression in the eye. This study therefore provides information on the interactions between AAV gene therapy vectors and the immune system during ocular administration. Furthermore, these results motivate vector engineering approaches to increase antibody resistance and thereby enhance intravitreal gene delivery.

Materials and Methods

Cell Lines and Adeno-Associated Virus Production

HEK293T cells (American Type Culture Collection, Manassas, VA) were cultured in Dulbecco's modified Eagle's medium supplemented with 10% fetal bovine serum (Gibco, Carlsbad, CA) and 1% penicillin/streptomycin (Invitrogen, Carlsbad, CA) at 37°C and 5% CO_2.

Recombinant AAV vectors were packaged using HEK293T cells with the calcium phosphate transfection method, and the viruses were purified by iodixonal gradient centrifugation.[68,77] AAV vectors for use during *in vivo* injections were further purified by Amicon filtration. DNase-resistant genomic titers were determined via quantitative PCR. 68,77

Intravitreal Injections

Monkeys were anesthetized with ketamine, and the cornea was locally anesthetized with proparacaine drops. The palpebral fissure (eye and lids) was flushed with 50% strength betadine/saline to disinfect the injection site and then flushed out with copious amounts of sterile saline. 40-200 ml of AAV vector was administered through a 30 gauge needle into the posterior chamber of the eye. Finally, ophthalmic steroid ointment and atropine ointment were applied to the cornea post-injection to minimize inflammation. This procedure was

Author Manuscript Author Manuscript Author Manuscript Author Manuscript

conducted according to the ARVO Statement for the Use of Animals and the guidelines of the Office of Laboratory Animal Care at the University of Rochester. At the conclusion of the experiment, euthanasia was achieved by administering an IV overdose of sodium pentobarbital (75 mg/kg), as recommended by the Panel on Euthanasia of the American Veterinary Medical Association. In a certain subset of animals, eyes were injected 4 days apart. The 4 day delay between injections was the result of a change in the animal protocol that required injection-related clouding of the eye to resolve prior to injection in the contralateral eye.

Serum and Vitreal Fluid Extraction

Blood was collected at various time points pre- and post-AAV injection from a peripheral vein using a 22 G Vacuette and a red top Vacutainer. 100-300 μl of vitreous fluid was also collected immediately after animals were euthanized using a 19 G needle and syringe. Once collected, the sample was centrifuged and the serum and vitreous was stored at -80°C.

In Vitro Quantification of Neutralizing Antibody Titers

HEK293T cells were plated at a density of 1.5×10^4 cells per well 24 hours prior to infection. Recombinant AAV serotypes 2, 5, 8, and 9, as well as an AAV2 tyrosine 4YF mutant[46] and an AAV2 7mer insertion variant (7m8),[25] expressing GFP under the control of the CMV promoter were incubated at 37°C for 1 hour with monkey serum, and cells were then infected at a genomic MOI of 2000. The fraction of GFP positive cells were assessed 48 hours post-infection using an ImageXpress Micro Cellular Imaging and Analysis System (Molecular Devices, Sunnyvale, CA) and MetaXpress Image Analysis Software, version 3.1.0, Multi Wavelength Cell Scoring Application Module (Molecular Devices). As a control, infectivity of AAV2, AAV5, AAV8, and AAV9 in the absence of serum was also measured, and these data have been added as Supplemental Figure S1.

Statistical Analysis

The statistical significance of the results was determined using a one way analysis of variance (ANOVA).

Transgene Expression Analysis

Transgene expression was analyzed in previous reports. Imaging methods include fundus imaging with a fluorescent fundus camera, an adaptive optics scanning laser ophthalmoscope, and confocal microscopy of histologically processed tissues.[25,44,45,78] The methods used to determine transgene expression using these imaging methods are described in previous reports. [25,44,45,78]

Supplementary Material

Refer to Web version on PubMed Central for supplementary material.

References

1. Knipe, DM.; Howley, PM. Fields' Virology. Lippincott Williams & Wilkins; Philadelphia, PA, USA: 2007.

Author Manuscript Author Manuscript Author Manuscript Author Manuscript

2. Sonntag F, Schmidt K, Kleinschmidt Ja. A viral assembly factor promotes AAV2 capsid formation in the nucleolus. Proc Natl Acad Sci U S A. 2010; 107:10220–5. [PubMed: 20479244]
3. Sonntag F, Köther K, Schmidt K, Weghofer M, Raupp C, Nieto K, et al. The assembly-activating protein promotes capsid assembly of different adeno-associated virus serotypes. J Virol. 2011; 85:12686–97. [PubMed: 21917944]
4. Schaffer DV, Koerber JT, Lim K. Molecular engineering of viral gene delivery vehicles. Annu Rev Biomed Eng. 2008; 10:169–94. [PubMed: 18647114]
5. Wu Z, Asokan A, Samulski RJ. Adeno-associated virus serotypes: vector toolkit for human gene therapy. Mol Ther. 2006; 14:316–27. [PubMed: 16824801]
6. Flotte TR. Gene therapy progress and prospects: recombinant adeno-associated virus (rAAV) vectors. Gene Ther. 2004; 11:805–10. [PubMed: 15042119]
7. [accessed 18 Mar2014] Gene Therapy Clinical Trials Worldwide. J Gene Med. 2014. http://www.abedia.com/wiley/
8. Hauswirth WW, Aleman TS, Kaushal S, Cideciyan AV, Schwartz SB, Wang L, et al. Treatment of leber congenital amaurosis due to RPE65 mutations by ocular subretinal injection of adeno-associated virus gene vector: short-term results of a phase I trial. Hum Gene Ther. 2008; 19:979–90. [PubMed: 18774912]
9. Cideciyan AV, Hauswirth WW, Aleman TS, Kaushal S, Schwartz SB, Boye SL, et al. Human RPE65 gene therapy for Leber congenital amaurosis: persistence of early visual improvements and safety at 1 year. Hum Gene Ther. 2009; 20:999–1004. [PubMed: 19583479]
10. Bainbridge JWB, Smith AJ, Barker SS, Robbie S, Henderson R, Balaggan K, et al. Effect of gene therapy on visual function in Leber's congenital amaurosis. N Engl J Med. 2008; 358:2231–2239. [PubMed: 18441371]
11. Maguire A, Simonelli F. Safety and efficacy of gene transfer for Leber's congenital amaurosis. N Engl J Med. 2008; 358:2240–2248. [PubMed: 18441370]
12. Maguire AM, High Ka, Auricchio A, Wright JF, Pierce Ea, Testa F, et al. Age-dependent effects of RPE65 gene therapy for Leber's congenital amaurosis: a phase 1 dose-escalation trial. Lancet. 2009; 374:1597–605. [PubMed: 19854499]
13. Bennett J, Ashtari M, Wellman J, Marshall Ka, Cyckowski LL, Chung DC, et al. AAV2 gene therapy readministration in three adults with congenital blindness. Sci Transl Med. 2012; 4:120ra15.
14. Jacobson SG, Cideciyan AV, Ratnakaram R, Heon E, Schwartz SB, Roman AJ, et al. Gene therapy for leber congenital amaurosis caused by RPE65 mutations: safety and efficacy in 15 children and adults followed up to 3 years. Arch Ophthalmol. 2012; 130:9–24. [PubMed: 21911650]
15. MacLaren RE, Groppe M, Barnard AR, Cottriall CL, Tolmachova T, Seymour L, et al. Retinal gene therapy in patients with choroideremia: initial findings from a phase 1/2 clinical trial. Lancet. 2014; 6736:2117–2120.
16. Koerber JT, Klimczak R, Jang JH, Dalkara D, Flannery JG, Schaffer DV. Molecular evolution of adeno-associated virus for enhanced glial gene delivery. Mol Ther. 2009; 17:2088–95. [PubMed: 19672246]
17. Petrs-Silva H, Dinculescu A, Li Q, Min SH, Chiodo V, Pang JJ, et al. High-efficiency transduction of the mouse retina by tyrosine-mutant AAV serotype vectors. Mol Ther. 2009; 17:463–71. [PubMed: 19066593]
18. Aleman TS, Cideciyan AV, Sumaroka A, Windsor EAM, Herrera W, White DA, et al. Retinal laminar architecture in human retinitis pigmentosa caused by Rhodopsin gene mutations. Invest Ophthalmol Vis Sci. 2008; 49:1580–90. [PubMed: 18385078]
19. Jacobson SG, Aleman TS, Cideciyan AV, Roman AJ, Sumaroka A, Windsor EAM, et al. Defining the residual vision in leber congenital amaurosis caused by RPE65 mutations. Invest Ophthalmol Vis Sci. 2009; 50:2368–75. [PubMed: 19117922]
20. Jacobson SG, Aleman TS, Sumaroka A, Cideciyan AV, Roman AJ, Windsor EAM, et al. Disease boundaries in the retina of patients with Usher syndrome caused by MYO7A gene mutations. Invest Ophthalmol Vis Sci. 2009; 50:1886–94. [PubMed: 19074810]
21. Nakazawa T, Matsubara A, Noda K, Hisatomi T, She H, Skondra D, et al. Characterization of cytokine responses to retinal detachment in rats. Mol Vis. 2006; 12:867–78. [PubMed: 16917487]

Author Manuscript Author Manuscript Author Manuscript Author Manuscript

22. Nakazawa T, Takeda M, Lewis GP, Cho KS, Jiao J, Wilhelmsson U, et al. Attenuated glial reactions and photoreceptor degeneration after retinal detachment in mice deficient in glial fibrillary acidic protein and vimentin. Invest Ophthalmol Vis Sci. 2007; 48:2760–8. [PubMed: 17525210]

23. Park TK, Wu Z, Kjellstrom S, Zeng Y, Bush RA, Sieving PA, et al. Intravitreal delivery of AAV8 retinoschisin results in cell type-specific gene expression and retinal rescue in the Rs1-KO mouse. Gene Ther. 2009; 16:916–26. [PubMed: 19458650]

24. Klimczak RR, Koerber JT, Dalkara D, Flannery JG, Schaffer DV. A novel adeno-associated viral variant for efficient and selective intravitreal transduction of rat Müller cells. PLoS One. 2009; 4:e7467. [PubMed: 19826483]

25. Dalkara D, Byrne LC, Klimczak RR, Visel M, Yin L, Merigan WH, et al. In vivo-directed evolution of a new adeno-associated virus for therapeutic outer retinal gene delivery from the vitreous. Sci Transl Med. 2013; 5:189ra76.

26. Manno CS, Pierce GF, Arruda VR, Glader B, Ragni M, Rasko JJ, et al. Successful transduction of liver in hemophilia by AAV-Factor IX and limitations imposed by the host immune response. Nat Med. 2006; 12:342–7. [PubMed: 16474400]

27. Stroes ES, Nierman MC, Meulenberg JJ, Franssen R, Twisk J, Henny CP, et al. Intramuscular administration of AAV1-lipoprotein lipase S447X lowers triglycerides in lipoprotein lipase-deficient patients. Arterioscler Thromb Vasc Biol. 2008; 28:2303–4. [PubMed: 18802015]

28. Boutin S, Monteilhet V, Veron P, Leborgne C, Benveniste O, Montus MF, et al. Prevalence of serum IgG and neutralizing factors against adeno-associated virus (AAV) types 1, 2, 5, 6, 8, and 9 in the healthy population: implications for gene therapy using AAV vectors. Hum Gene Ther. 2010; 21:704–12. [PubMed: 20095819]

29. Wang L, Calcedo R, Wang H, Bell P, Grant R, Vandenberghe LH, et al. The pleiotropic effects of natural AAV infections on liver-directed gene transfer in macaques. Mol Ther. 2010; 18:126–34. [PubMed: 19888196]

30. Nathwani AC, Tuddenham EGD, Rangarajan S, Rosales C, McIntosh J, Linch DC, et al. Adenovirus-Associated Virus Vector–Mediated Gene Transfer in Hemophilia B. N Engl J Med. 2011; 365:2357–2365. [PubMed: 22149959]

31. Jaski BE, Jessup ML, Mancini DM, Cappola TP, Pauly DF, Greenberg B, et al. Calcium upregulation by percutaneous administration of gene therapy in cardiac disease (CUPID Trial), a first-in-human phase 1/2 clinical trial. J Card Fail. 2009; 15:171–81. [PubMed: 19327618]

32. Cottard V, Valvason C, Falgarone G, Lutomski D, Boissier MC, Bessis N. Immune response against gene therapy vectors: influence of synovial fluid on adeno-associated virus mediated gene transfer to chondrocytes. J Clin Immunol. 2004; 24:162–9. [PubMed: 15024183]

33. Boissier MC, Lemeiter D, Clavel C, Valvason C, Laroche L, Begue T, et al. Synoviocyte infection with adeno-associated virus (AAV) is neutralized by human synovial fluid from arthritis patients and depends on AAV serotype. Hum Gene Ther. 2007; 18:525–35. [PubMed: 17532727]

34. Samaranch L, Salegio Ea, San Sebastian W, Kells AP, Bringas JR, Forsayeth J, et al. Strong cortical and spinal cord transduction after AAV7 and AAV9 delivery into the cerebrospinal fluid of nonhuman primates. Hum Gene Ther. 2013; 24:526–32. [PubMed: 23517473]

35. Sanftner LM, Suzuki BM, Doroudchi MM, Feng L, McClelland A, Forsayeth JR, et al. Striatal delivery of rAAV-hAADC to rats with preexisting immunity to AAV. Mol Ther. 2004; 9:403–9. [PubMed: 15006607]

36. Li Q, Miller R, Han PY, Pang J, Dinculescu A, Chiodo V, et al. Intraocular route of AAV2 vector administration defines humoral immune response and therapeutic potential. Mol Vis. 2008; 14:1760–9. [PubMed: 18836574]

37. Amado D, Mingozzi F, Hui D, Bennicelli JL, Wei Z, Chen Y, et al. Safety and efficacy of subretinal readministration of a viral vector in large animals to treat congenital blindness. Sci Transl Med. 2010; 2:21ra16.

38. Mingozzi F, High KA. Immune responses to AAV in clinical trials. Curr Gene Ther. 2011; 11:321–30. [PubMed: 21557723]

Author Manuscript Author Manuscript Author Manuscript Author Manuscript

39. Halbert CL, Standaert TA, Wilson CB, Miller AD. Successful readministration of adeno-associated virus vectors to the mouse lung requires transient immunosuppression during the initial exposure. J Virol. 1998; 72:9795–805. [PubMed: 9811715]
40. Jiang H, Couto LB, Patarroyo-White S, Liu T, Nagy D, Vargas JA, et al. Effects of transient immunosuppression on adenoassociated, virus-mediated, liver-directed gene transfer in rhesus macaques and implications for human gene therapy. Blood. 2006; 108:3321–8. [PubMed: 16868252]
41. Manning WC, Zhou S, Bland MP, Escobedo JA, Dwarki V. Transient immunosuppression allows transgene expression following readministration of adeno-associated viral vectors. Hum Gene Ther. 1998; 9:477–85. [PubMed: 9525309]
42. McPhee SWJ, Janson CG, Li C, Samulski RJ, Camp AS, Francis J, et al. Immune responses to AAV in a phase I study for Canavan disease. J Gene Med. 2006; 8:577–88. [PubMed: 16532510]
43. Jessup M, Greenberg B, Mancini D, Cappola T, Pauly DF, Jaski B, et al. Calcium Upregulation by Percutaneous Administration of Gene Therapy in Cardiac Disease (CUPID): a phase 2 trial of intracoronary gene therapy of sarcoplasmic reticulum Ca2+-ATPase in patients with advanced heart failure. Circulation. 2011; 124:304–13. [PubMed: 21709064]
44. Yin L, Masella B, Dalkara D, Zhang J, Flannery JG, Schaffer DV, et al. Imaging light responses of foveal ganglion cells in the living macaque eye. J Neurosci. 2014; 34:6596–605. [PubMed: 24806684]
45. Yin L, Greenberg K, Hunter JJ, Dalkara D, Kolstad KD, Masella BD, et al. Intravitreal injection of AAV2 transduces macaque inner retina. Invest Ophthalmol Vis Sci. 2011; 52:2775–83. [PubMed: 21310920]
46. Zhong L, Li B, Mah CS, Govindasamy L, Agbandje-McKenna M, Cooper M, et al. Next generation of adeno-associated virus 2 vectors: point mutations in tyrosines lead to high-efficiency transduction at lower doses. Proc Natl Acad Sci U S A. 2008; 105:7827–32. [PubMed: 18511559]
47. Martin KRG, Klein RL, Quigley HA. Gene delivery to the eye using adeno-associated viral vectors. Methods. 2002; 28:267–75. [PubMed: 12413426]
48. Hoffman LM, Maguire AM, Bennett J. Cell-mediated immune response and stability of intraocular transgene expression after adenovirus-mediated delivery. Invest Ophthalmol Vis Sci. 1997; 38:2224–33. [PubMed: 9344345]
49. Benson WE, Brown GC, Tasman W, McNamara JA. Complications of vitrectomy for non-clearing vitreous hemorrhage in diabetic patients. Ophthalmic Surg. 1988; 19:862–4. [PubMed: 3231410]
50. Halbert CL, Rutledge EA, Allen JM, Russell DW, Miller AD. Repeat transduction in the mouse lung by using adeno-associated virus vectors with different serotypes. J Virol. 2000; 74:1524–32. [PubMed: 10627564]
51. Peden CS, Burger C, Muzyczka N, Mandel RJ. Circulating anti-wild-type adeno-associated virus type 2 (AAV2) antibodies inhibit recombinant AAV2 (rAAV2)-mediated, but not rAAV5-mediated, gene transfer in the brain. J Virol. 2004; 78:6344–59. [PubMed: 15163728]
52. Xiao W, Chirmule N, Berta SC, McCullough B, Gao G, Wilson JM. Gene Therapy Vectors Based on Adeno-Associated Virus Type 1. J Virol. 1999; 73:3994–4003. [PubMed: 10196295]
53. Gao GP, Alvira MR, Wang L, Calcedo R, Johnston J, Wilson JM. Novel adeno-associated viruses from rhesus monkeys as vectors for human gene therapy. Proc Natl Acad Sci U S A. 2002; 99:11854–9. [PubMed: 12192090]
54. Nieto K, Stahl-Hennig C, Leuchs B, Müller M, Gissmann L, Kleinschmidt JA. Intranasal vaccination with AAV5 and 9 vectors against human papillomavirus type 16 in rhesus macaques. Hum Gene Ther. 2012; 23:733–41. [PubMed: 22401308]
55. Gao G, Vandenberghe LH, Alvira MR, Lu Y, Calcedo R, Zhou X, et al. Clades of Adeno-associated viruses are widely disseminated in human tissues. J Virol. 2004; 78:6381–8. [PubMed: 15163731]
56. Bantel-Schaal U, Delius H, Schmidt R, zur Hausen H. Human adeno-associated virus type 5 is only distantly related to other known primate helper-dependent parvoviruses. J Virol. 1999; 73:939–47. [PubMed: 9882294]

Author Manuscript Author Manuscript Author Manuscript Author Manuscript

57. Lin J, Calcedo R, Vandenberghe LH, Figueredo JM, Wilson JM. Impact of preexisting vector immunity on the efficacy of adeno-associated virus-based HIV-1 Gag vaccines. Hum Gene Ther. 2008; 19:663–9. [PubMed: 18549307]
58. Halbert CL, Standaert TA, Aitken ML, Alexander IE, Russell DW, Miller AD. Transduction by adeno-associated virus vectors in the rabbit airway: efficiency, persistence, and readministration. J Virol. 1997; 71:5932–41. [PubMed: 9223483]
59. Wang L, Calcedo R, Bell P, Lin J, Grant RL, Siegel DL, et al. Impact of pre-existing immunity on gene transfer to nonhuman primate liver with adeno-associated virus 8 vectors. Hum Gene Ther. 2011; 22:1389–401. [PubMed: 21476868]
60. Gaudet D, de Wal J, Tremblay K, Déry S, van Deventer S, Freidig A, et al. Review of the clinical development of alipogene tiparvovec gene therapy for lipoprotein lipase deficiency. Atheroscler Suppl. 2010; 11:55–60. [PubMed: 20427244]
61. Carpentier AC, Frisch F, Labbé SM, Gagnon R, de Wal J, Greentree S, et al. Effect of alipogene tiparvovec (AAV1-LPL(S447X)) on postprandial chylomicron metabolism in lipoprotein lipase-deficient patients. J Clin Endocrinol Metab. 2012; 97:1635–44. [PubMed: 22438229]
62. Willett K, Bennett J. Immunology of AAV-Mediated Gene Transfer in the Eye. Front Immunol. 2013; 4:261. [PubMed: 24009613]
63. De Kozak Y, Andrieux K, Villarroya H, Klein C, Thillaye-Goldenberg B, Naud MC, et al. Intraocular injection of tamoxifen-loaded nanoparticles: a new treatment of experimental autoimmune uveoretinitis. Eur J Immunol. 2004; 34:3702–12. [PubMed: 15517615]
64. Van der Voet J, Liem A, Otto A, Kijlstra A. Intraocular antibody synthesis during experimental uveitis. Invest Ophthalmol Vis Sci. 1989; 30:316–322. [PubMed: 2914760]
65. Huttner NA, Girod A, Perabo L, Edbauer D, Kleinschmidt JA, Büning H, et al. Genetic modifications of the adeno-associated virus type 2 capsid reduce the affinity and the neutralizing effects of human serum antibodies. Gene Ther. 2003; 10:2139–47. [PubMed: 14625569]
66. Kolstad KD, Dalkara D, Guerin K, Visel M, Hoffmann N, Schaffer DV, et al. Changes in adeno-associated virus-mediated gene delivery in retinal degeneration. Hum Gene Ther. 2010; 21:571–8. [PubMed: 20021232]
67. Vacca O, Darche M, Schaffer DV, Flannery JG, Sahel JA, Rendon A, et al. AAV-mediated gene delivery in Dp71-null mouse model with compromised barriers. Glia. 2014; 62:468–76. [PubMed: 24382652]
68. Maheshri N, Koerber JT, Kaspar BK, Schaffer DV. Directed evolution of adeno-associated virus yields enhanced gene delivery vectors. Nat Biotechnol. 2006; 24:198–204. [PubMed: 16429148]
69. Koerber JT, Jang JH, Schaffer DV. DNA shuffling of adeno-associated virus yields functionally diverse viral progeny. Mol Ther. 2008; 16:1703–9. [PubMed: 18728640]
70. Bartel, MA.; Hwang, BY.; Stone, D.; Koerber, JT.; Couto, L.; Mingozzi, F., et al. Directed Evolution of AAV for Enhanced Evasion of Human Neutralizing Antibodies; American Society of Gene and Cell Therapy's 15th Annual Meeting; Philadelphia, PA. 2012; p. S140
71. Perabo L, Endell J, King S, Lux K, Goldnau D, Hallek M, et al. Combinatorial engineering of a gene therapy vector: directed evolution of adeno-associated virus. J Gene Med. 2006; 8:155–62. [PubMed: 16285001]
72. Grimm D, Lee JS, Wang L, Desai T, Akache B, Storm TA, et al. In vitro and in vivo gene therapy vector evolution via multispecies interbreeding and retargeting of adeno-associated viruses. J Virol. 2008; 82:5887–911. [PubMed: 18400866]
73. Lochrie MA, Tatsuno GP, Christie B, McDonnell JW, Zhou S, Surosky R, et al. Mutations on the external surfaces of adeno-associated virus type 2 capsids that affect transduction and neutralization. J Virol. 2006; 80:821–34. [PubMed: 16378984]
74. Moskalenko M, Chen L, van Roey M, Donahue BA, Snyder RO, McArthur JG, et al. Epitope Mapping of Human Anti-Adeno-Associated Virus Type 2 Neutralizing Antibodies: Implications for Gene Therapy and Virus Structure. J Virol. 2000; 74:1761–1766. [PubMed: 10644347]
75. Wobus CE, Hügle-Dörr B, Girod A, Petersen G, Hallek M, Kleinschmidt JA. Monoclonal antibodies against the adeno-associated virus type 2 (AAV-2) capsid: epitope mapping and identification of capsid domains involved in AAV-2-cell interaction and neutralization of AAV-2 infection. J Virol. 2000; 74:9281–93. [PubMed: 10982375]

Author Manuscript Author Manuscript Author Manuscript Author Manuscript

76. Mingozzi F, Anguela XM, Pavani G, Chen Y, Davidson RJ, Hui DJ, et al. Overcoming preexisting humoral immunity to AAV using capsid decoys. Sci Transl Med. 2013; 5:194ra92.

77. Excoffon KJD, Koerber JT, Dickey DD, Murtha M, Keshavjee S, Kaspar BK, et al. Directed evolution of adeno-associated virus to an infectious respiratory virus. Proc Natl Acad Sci U S A. 2009; 106:3865–70. [PubMed: 19237554]

78. Strazzeri JM, Hunter JJ, Masella BD, Yin L, Fischer WS, DiLoreto DA, et al. Focal damage to macaque photoreceptors produces persistent visual loss. Exp Eye Res. 2014; 119:88–96. [PubMed: 24316158]

Author Manuscript Author Manuscript Author Manuscript Author Manuscript

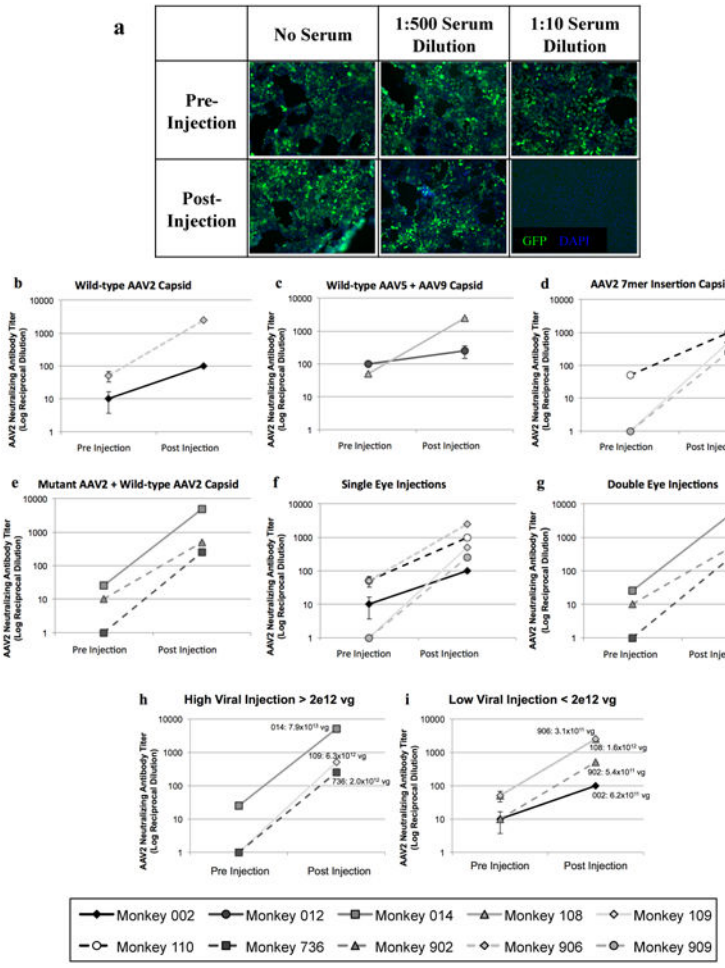


Figure 1.

Increase of Anti-AAV2 Antibodies Pre-Transduction vs. Post-Transduction. (a) Representative sample of fluorescent images taken during *in vitro* neutralization assay and used to determine the amount of viral transduction in the presence of serum dilutions. Top row: conditions of no serum, 1:500 serum dilution, and 1:10 serum dilution from a monkey before injection of a high dose (> 2×10^{12} viral genomes) of 7m8 viruses expressing GFP. Bottom row: same conditions following the injection. (b)-(i) Neutralizing antibody titers in serum pre- and post-injection of monkeys administered with (b) wild-type AAV2 capsid, (c) Alternative wild-type AAV capsids, (d) 7m8 capsid, (e) Mutant (tyrosine mutation or 7m8) AAV2 and wild-type AAV2 capsids, (f) Single eye injections of 7m8 or wild-type AAV2 capsids, (g) Double eye injections of mutant (tyrosine mutant or 7m8) AAV2 or wild-type AAV2 capsids, (h) Injection of high viral titers (> 2×10^{12} viral genomes), or (i) Injection of low viral titers (< 2×10^{12} viral genomes). Error bars indicate standard deviation (SD) (n=3). y-axis: reciprocal of the serum dilution at which 50% of viral transduction is inhibited *in vitro*. vg = viral genomes

Author Manuscript Author Manuscript Author Manuscript Author Manuscript

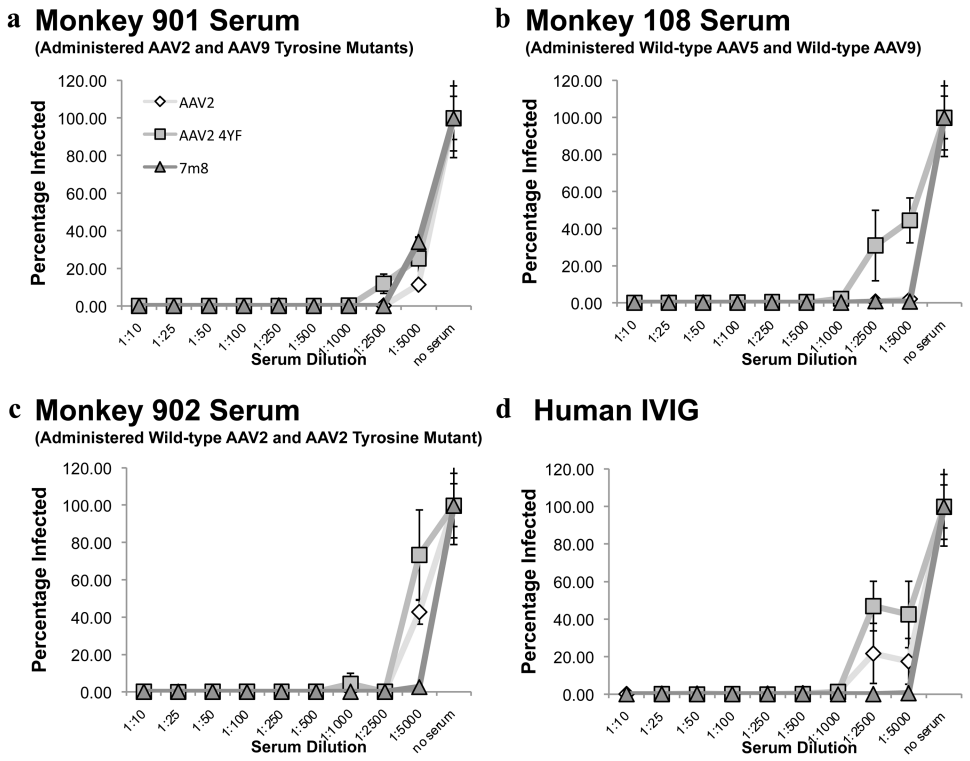


Figure 2.

In Vitro Antibody Evasion of AAV2 Variants. Antibody neutralization curves for wild-type AAV2, AAV2 tyrosine mutant, and 7m8 vectors in the presence of sera from monkeys that had been exposed to (a) Human IVIG, (b) Wild-type AAV2 and AAV2 tyrosine mutant capsids, (c) AAV2 and AAV9 tyrosine mutant capsids, or (d) Wild-type AAV5 and AAV9 capsids. Error bars indicate standard deviation (SD) (n=3).

Author Manuscript Author Manuscript Author Manuscript Author Manuscript

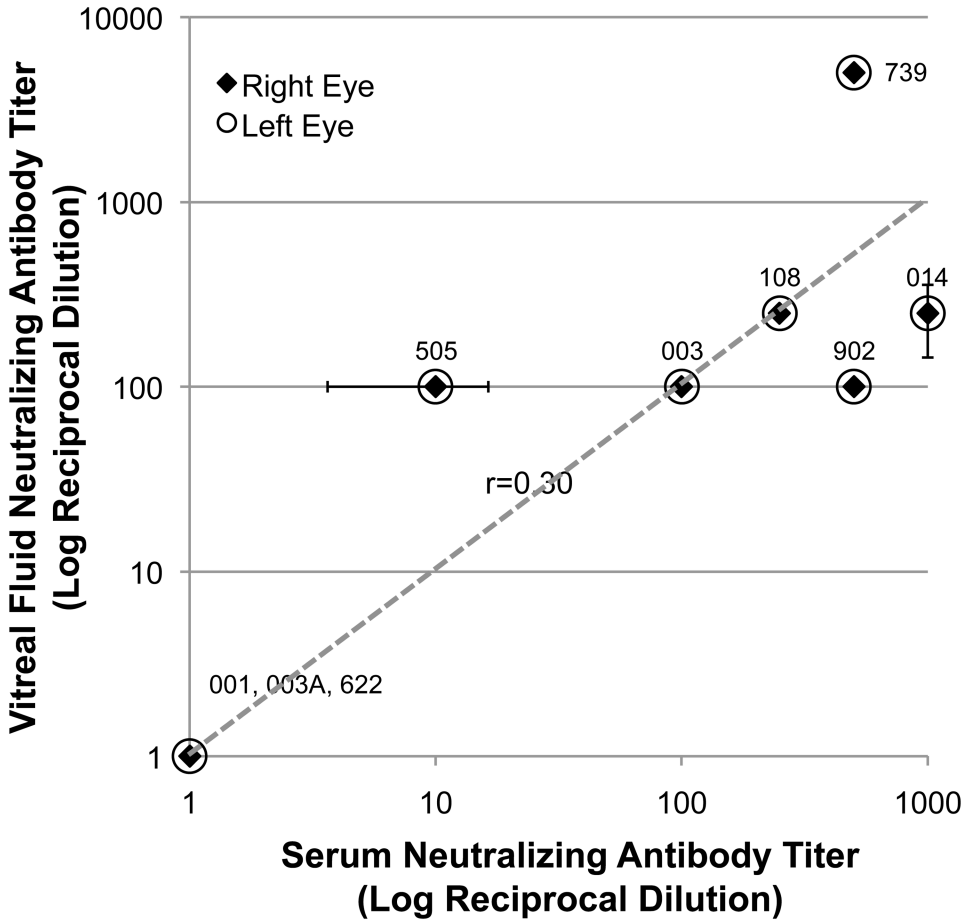


Figure 3.

Presence of Anti-AAV2 Antibodies in Matched Serum and Vitreal Fluid Samples. Neutralizing antibody titers against AAV2 in serum and vitreous fluid samples taken from both the right and left eyes post-administration of mutant (tyrosine mutation or 7m8) AAV2 and wild-type AAV2 capsids (014, 505, 739, and 902), wild-type AAV5 capsids (001 and 622), wild-type AAV2 and wild-type AAV5 capsids (003), mutant AAV8 and wild-type AAV5 capsids (003A), or wild-type AAV5 and wild-type AAV9 capsids (108). Error bars indicate standard deviation (n=3).

Author Manuscript Author Manuscript Author Manuscript Author Manuscript

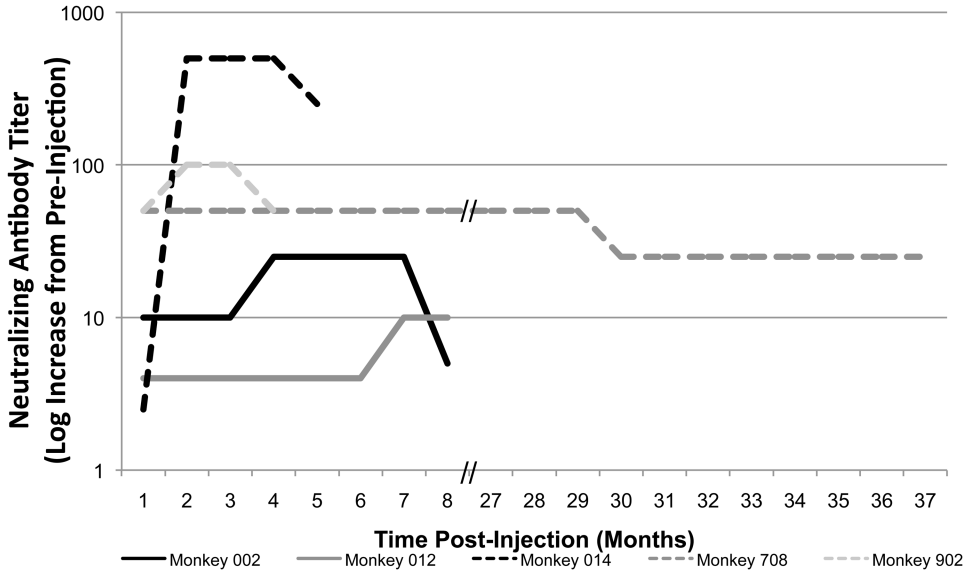


Figure 4.

Presence of Anti-AAV2 Antibodies During Long Term Monitoring. Presence of anti-AAV2 antibodies in the serum of several monkeys at various time points over 2 years. Arrows indicate AAV administration to one or both eyes.

Author Manuscript Author Manuscript Author Manuscript Author Manuscript

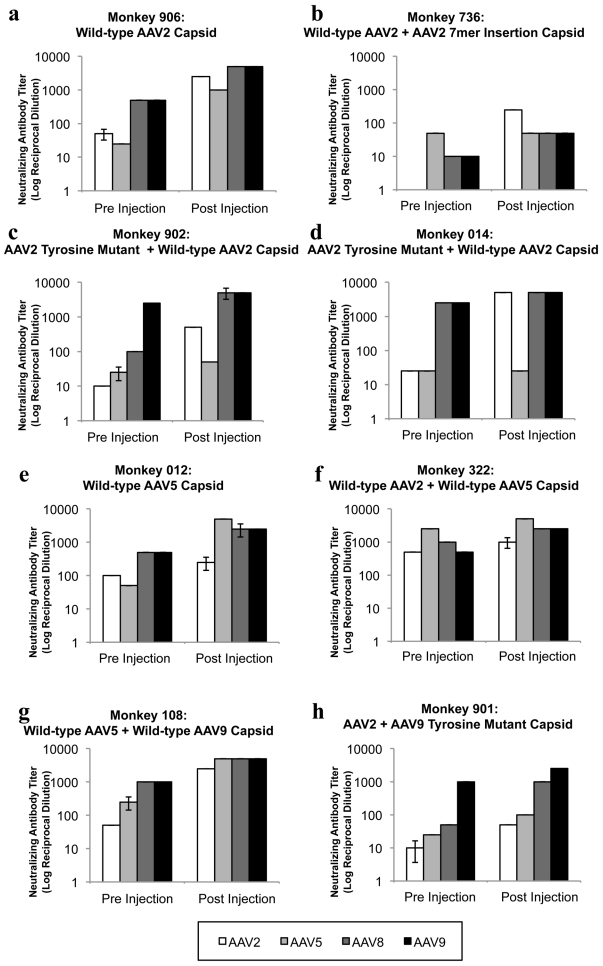


Figure 5.

Cross-Reactivity of Antibodies to Various AAV Serotypes Pre-Infection vs. Post-Infection. Neutralizing antibody titers against AAV2, AAV5, AAV8, and AAV9 in serum pre- and post-injection of monkeys administered (a) Wild-type AAV2 capsid, (b)-(d) Mutant (tyrosine mutation or 7m8) AAV2 and wild-type AAV2 capsids, (e) Wild-type AAV5 capsid, (f) Wild-type AAV2 and AAV5 capsids, (g) Wild-type AAV5 and AAV9 capsids, or (h) AAV2 and AAV9 tyrosine mutant capsids. Error bars indicate standard deviation (n=3).

Author Manuscript Author Manuscript Author Manuscript Author Manuscript

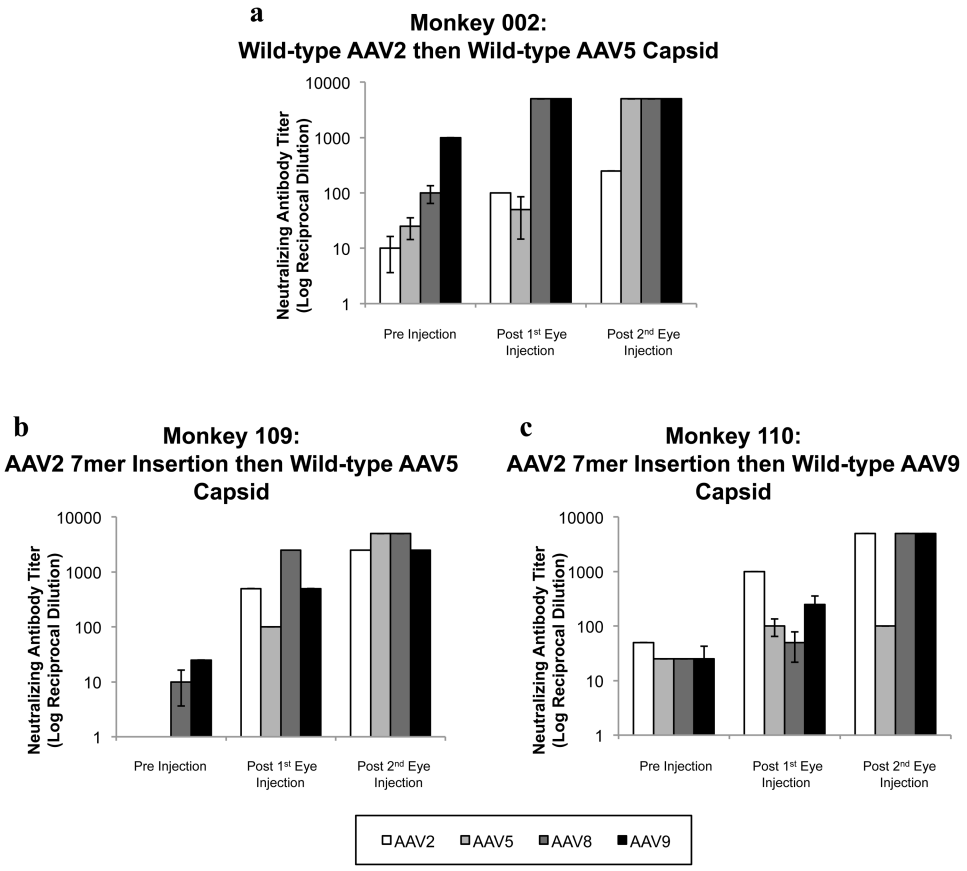


Figure 6.

Increase of Anti-AAV Antibodies Throughout Sequential Infections. Neutralizing antibody titers against AAV2, AAV5, AAV8, and AAV9 in serum pre-injection, post-injection of the first eye, and post-injection of the second eye of monkeys administered (a) Wild-type AAV2 and AAV5 capsids, (b) 7m8 and wild-type AAV5 capsids, or (c) 7m8 and wild-type AAV9 capsids. Error bars indicate standard deviation (n=3).

Author Manuscript Author Manuscript Author Manuscript Author Manuscript

Table 1

Effect of Pre-Injection Anti-AAV2 Antibodies on Expression. The presence of low neutralizing antibody titers in serum pre-intravitreal injection of monkeys administered wild-type AAV2 or AAV2 mutant capsids reduces transgene expression in the eye, while the presence of intermediate to high neutralizing antibody titers completely prevents transgene expression.

Monkey ID	Eye	Capsid	Viral Genomes Injected	Pre-Injection AAV2 Neutralization Titer	Expression?
013	LE	AAV2 7mer insert	10^{13}	no neutralization	yes
109	RE	AAV2 7mer insert	10^{12}	no neutralization	yes
222	RE	AAV2	10^{12}	no neutralization	yes
323	RE	AAV2	10^{11}	no neutralization	weak
507	LE	AAV2	10^{11}	no neutralization	yes
708	LE	AAV2	10^{12}	no neutralization	yes
736	LE	AAV2	10^{12}	no neutralization	yes
736	RE	AAV2 7mer insert	not listed	not available* no serum collected	yes, but degenerated
739	LE	AAV2 tyrosine mutant	10^{12}	no neutralization	yes
739	RE	AAV2 7mer insert	10^{12}	no neutralization	yes
002	RE	AAV2	10^{11}	50% neutralization at 1:10	no
901	RE	AAV2 tyrosine mutant	10^{11}	50% neutralization at 1:10	no
014	LE	AAV2	10^{13}	50% neutralization at 1:25	yes, not typical
014	RE	AAV2 tyrosine mutant	10^{13}	50% neutralization at 1:25	very faint
623	LE	AAV2	10^{11}	50% neutralization between 1:25 and 1:50	no
906	RE	AAV2	10^{11}	50% neutralization between 1:25 and 1:50	weak foveal label
322	RE	AAV2	not listed	50% neutralization between 1:50 and 1:100	bright rim
322	RE	AAV2	10^{12}	not available* no serum collected	no
012	RE	AAV2 7mer insert	10^{13}	50% neutralization at 1:250	**early euth.**
707	LE	AAV2	10^{11}	50% neutralization between 1:500 and 1:1000	no
707	RE	AAV2	10^{12}	not available* no serum collected	no

LE = left eye, RE = right eye,

* = no serum collected.

PAPER

Enlarged perivascular spaces are associated with cognitive function in healthy elderly men

A M J MacLullich, J M Wardlaw, K J Ferguson, J M Starr, J R Seckl, I J Deary

See Editorial Commentary, p 1516

J Neurol Neurosurg Psychiatry 2004;**75**:1519–1523. doi: 10.1136/jnnp.2003.030858

See end of article for authors' affiliations

Correspondence to: A M J MacLullich, Geriatric Medicine Unit, The University of Edinburgh, Room SU220, The Chancellor's Building, 49 Little France Crescent, Edinburgh, EH16 4SB; a.maclullich@ed.ac.uk

Received 22 October 2003
In revised form 19 April 2004
Accepted 29 April 2004

Objectives: Increased white matter (WM) lesions on magnetic resonance imaging (MRI) are associated with worse cognitive function in older people. Enlarged perivascular spaces (EPVS) commonly coexist with and share some risk factors for WM lesions but are not quantified in published scales. It is not known whether the extent of EPVS is also associated with cognitive function. We tested the hypothesis that more EPVS would be associated with worse cognitive function.

Methods: Ninety seven healthy men (65–70 years), not on medications, underwent MRI scanning and comprehensive cognitive testing. EPVS were quantified in both the basal ganglia/centrum semiovale and the hippocampus, and WM lesions were measured.

Results: Scores on published WM lesion rating scales intercorrelated highly significantly and positively ($\rho = 0.61$ to 0.91, $p < 0.0001$). A summary (WML) factor derived from principal components analysis of the WM scales correlated with EPVS in the basal ganglia/centrum semiovale ($\rho = 0.48$, $p < 0.0001$) but not in the hippocampus. EPVS scores in the basal ganglia/centrum semiovale correlated significantly and negatively with non-verbal reasoning ($\rho = -0.21$, $p = 0.038$) and general visuospatial ability ($\rho = -0.22$, $p = 0.032$), adjusted for prior intelligence. The WML factor correlated significantly and negatively with visuospatial ability, as previously reported, and showed an unexpected positive correlation with one test of verbal memory (list-learning).

Conclusions: These findings suggest that increased EPVS are correlated with worse cognitive function. Future studies examining changes in WM with ageing should consider incorporating measures of EPVS and examine the sequence of EPVS and WM lesion development over time. More work is needed to develop valid and reliable measures of EPVS.

Magnetic resonance imaging (MRI) studies have demonstrated that more white matter (WM) lesions are significantly associated with decrements in cognitive function with ageing.[1] However, there remain substantial variations in how the extent and severity of WM lesions are determined.[2]

Enlarged perivascular spaces (EPVS), or Virchow–Robin spaces, appear as punctate or linear hyperintensities, isointense with cerebrospinal fluid (CSF) on T2-weighted images, in the centrum semiovale, basal ganglia, and the hippocampus. In some subjects they may be both numerous and widespread throughout the brain (fig 1). They are thought to correspond with extensions of the subarachnoid space surrounding the penetrating arteries.[3] Like WM lesions, EPVS are not usually present (although a few may be observed) in the brains of healthy young adults, but become increasingly common with ageing.[4] The presence of EPVS has been associated with hypertension,[5] cerebral arteriosclerosis,[6] Parkinson's disease,[7] CADASIL,[8] and diabetes.[9] In some studies the number and size of EPVS correlated with the extent of WM lesions.[4 10] However, EPVS are not explicitly included in most WM lesion scales, including the most recently published scale,[11] and to our knowledge have not been assessed in any published studies of cognitive changes with ageing and WM lesions.

In the present study, we investigated whether EPVS were related to cognitive function in 100 healthy elderly men. We also examined the relations between EPVS, scores on several commonly used WM lesion rating scales, and cognitive function.

METHODS

Subjects

Healthy male volunteers aged 65–70 years, living in Edinburgh, Scotland, were recruited for the study through an invitation letter and interview. The study was approved by the Lothian Region Ethics Committee. All subjects were recruited with the assistance of their local general practitioners and interviewed by a physician (AM) to screen for symptoms suggestive of significant current illness, including dementia, cerebrovascular disease, ischaemic heart disease, and depressive illness. Those with symptoms were excluded. Volunteers with past history of cancer, heart disease, respiratory disease, diabetes, neurological disease, and other significant disease were also excluded. We analysed blood for urea and electrolytes, calcium, liver function tests, thyroid function tests, glucose, glycosylated haemoglobin, haemoglobin, white cell count, platelet count, and B_{12} and folate levels; subjects with abnormalities according to standard clinical criteria were excluded. None of the subjects was on regular medication at the time of cognitive testing or imaging. A total of 100 subjects participated in the study following the screening process.

Magnetic resonance scanning

All MR scanning was performed on a GE Prestige scanner operating at 1.9 T (GE Medical, Haifa, Israel). Structural image acquisition followed a three view localiser and consisted of fast spin echo T2 axial imaging of the whole brain (TR 4000, TE 96, matrix 256×256, 5 mm slice thickness, 1 mm slice gap, 23 cm field of view, 1 NEX, tip angle 160 and acquisition time 1 minute 40 seconds). The subjects also were also scanned for volumetric and spectroscopic analyses, the details and results of which have been published elsewhere.[12 13]

Abbreviations: EPVS, enlarged perivascular spaces; MRI, magnetic resonance imaging; NART, National Adult Reading Test; WM, white matter

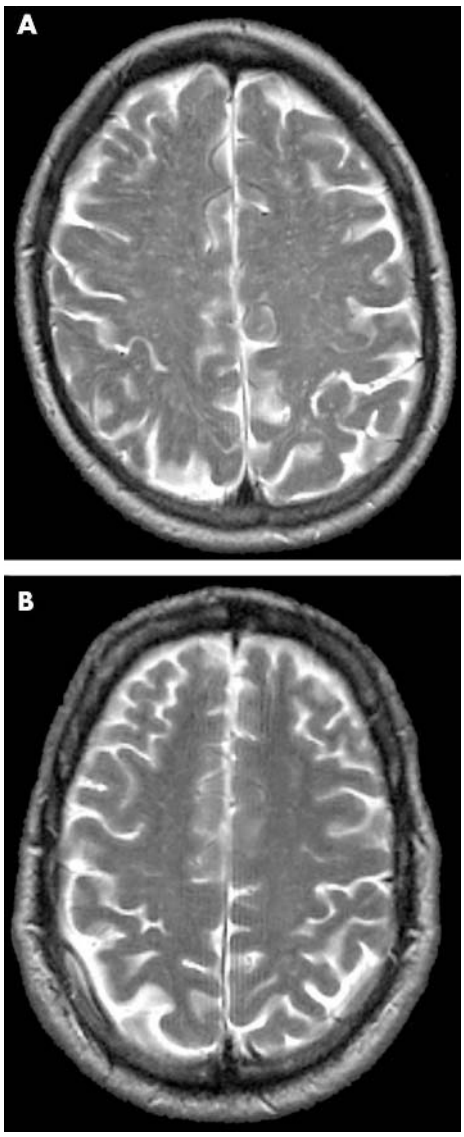


Figure 1 Magnetic resonance scans of enlarged perivascular spaces. (A) Multiple and (B) few enlarged perivascular spaces.

Rating of enlarged perivascular spaces and white matter lesions

The WM rating scales used to score the appearance of the white matter on the T2-weighted axial image were as follows: Longstreth *et al*,[14] Breteler *et al*,[15] van Swieten *et al*,[16] Fazekas *et al*,[17] Shimada *et al*,[18] and Wahlund *et al*.[19] Each was applied according to the published method. For rating, each scan was independently examined by two raters blinded to each other's readings, and all other imaging, cognitive, and biochemical results. One of the raters was a neuroradiologist (JMW) and the other a postdoctoral neuroscientist (KJF). Most scales showed weighted κ of 0.6 or above[20]; in scales with lower κ, JMW's ratings were used. In addition, JMW rated the quantity of EPVS in the hippocampus, and basal ganglia/centrum semiovale (including immediate subcortical white matter) as follows: 0 = no EPVS, 1 = <10 EPVS, 2 = 10–20 EPVS, 3 = 21–40 EPVS, and 4 = >40 EPVS. In each case the most affected hemisphere was rated. EPVS were defined (as in previous publications[4 10]) as small, sharply delineated structures of CSF signal intensity that follow the orientation of the perforating vessels and run perpendicular to the brain surface. Thus they appear round if axially sectioned (as in the basal ganglia) and linear if longitudinally sectioned (as in the peripheral centrum semiovale). They are generally less than 1 mm, at most 2 mm, in diameter. They are of high signal on T2 and low signal on T1 and so are best seen on sequences which show CSF as of bright white signal—that is, on T2-weighted sequences.

Cognitive testing

The subjects underwent tests designed to assess several domains of cognitive functioning; memory was tested in detail. All testing was carried out in the morning by the same tester (AM) who was blind to the results of brain imaging and biochemistry. The order of tests was the same for all subjects; frequent breaks were provided to reduce the effects of fatigue. Fluid, non-verbal reasoning was evaluated with Raven's Standard Progressive Matrices[21] using the number correct in 20 minutes. Verbal memory was evaluated with the Logical Memory (immediate and 30 minute delayed) subtest of the Wechsler Memory Scale[22] and the Rey Auditory-Verbal Learning Test.[23] Visuospatial memory was evaluated with the Visual Reproduction (immediate and 30 minute delayed) subtest of the Wechsler Memory Scale[22] and Administration A of the Benton Visual Retention Test.[24] As the immediate and delayed components of both Logical Memory and Visual Reproduction are highly correlated ($r = 0.83$ and $r = 0.75$, respectively) the summed standardised scores from each component were entered into the analysis. Verbal fluency was assessed with the Controlled Word Association Test using the letters C, F, and S.[23] Attention and processing speed were evaluated with the Digit-Symbol Substitution Test from the Wechsler Adult Intelligence Scale.[25] Prior intelligence was assessed with the National Adult Reading Test.[26] Performance on the National Adult Reading Test (NART) tends not to show decrements early in the process of ageing related cognitive impairment,[27] whereas performance on tests of short term memory and fluid intelligence does show decline with ageing.[28]

Statistical analysis

Descriptive statistics, bivariate correlations and principal components analyses were performed using SPSS for Windows 11.5.

As scores in diverse cognitive tests are substantially positively intercorrelated,[29] the cognitive test data were subjected to principal components analysis, except the NART because it is an estimate of prior intelligence rather than a measure of current ability. Thus NART scores are commonly used to adjust current scores on cognitive tests for prior intelligence. This is done with linear regression, using the saved residuals as the adjusted scores. The adjusted scores therefore are an estimate of ageing related change in cognitive function.[30–33]

EPVS and the various WM lesion scores were correlated with cognitive test performance and also with the factors derived from the principal components analysis of cognitive test scores. Spearman's ρ (rho; rank correlation) was used for these correlations because of the non-normal distribution of many WM scores and the EPVS scores. WM lesion scores were also subjected to principal components analysis to provide a summary score and thus to reduce the number of comparisons. Because of the experimental nature of the EPVS scales, we also used analysis of variance to investigate group differences of scores on cognitive function tests and cognitive factors (with NART entered as a covariate) for subjects with no EPVS versus those with some EPVS. Additionally, we used multiple linear regression to determine whether EPVS scores and WM lesion scales had independent associations with cognitive function.

Table 1 Descriptive statistics for the enlarged perivascular spaces scores and the white matter lesion scales (n = 97)

	Min	Max	Median	Mean	SD
EPVS	0	4	1	1.02	0.89
HC EPVS	0	2	1	1.06	0.81
Longstreth	0	3	1	1.05	0.94
Breteler	0	2	0	0.45	0.61
VS Anterior	0	2	0	0.39	0.55
VS Posterior	0	2	0	0.40	0.61
Fazekas PVH	0	3	1	0.92	0.77
Fazekas DWMH	0	3	1	0.80	0.72
Shimada	1	4	1	1.47	0.74
Wahlund	1	2.5	1.5	1.43	0.44

EPVS, enlarged perivascular spaces; Fazekas PVH, Fazekas periventricular hyperintensities; Fazekas DWMH, Fazekas deep white matter hyperintensities; HC EPVS, hippocampus EPVS; VS anterior/posterior, Van Swieten anterior/posterior.

RESULTS

Of the 100 participants scanned, three were excluded when unexpected pathology was discovered on structural MRI: two because of congenital arachnoid cysts, and one because of a pituitary adenoma (non-secretory). For the correlation analyses, 97 subjects were included for all comparisons except Raven's matrices (n = 95), where two subjects were excluded because of incorrect completion of the answer sheets, logical memory (n = 96), where one subject's score was invalid because of interruption of the testing session, and visual reproduction (n = 96), where another subject's test session was interrupted.

The mean age was 67.8 years (range 65–70). Both EPVS and WM lesion scores ranged from the lowest to the highest possible scores. However, as might be expected in relatively healthy group, the lower scores predominated, resulting in a positive skew. For the basal ganglia/centrum semiovale EPVS scores, the numbers in each category of the scale described above were **0**: 28; **1**: 47; **2**: 15; **3**: 6; **4**: 1. Table 1 shows the descriptive statistics for each scale.

Correlations among EPVS scores and white matter lesion scales

As the EPVS and WM lesion scores were not normally distributed, Spearman's ρ was used for all correlations. Scores on the WM lesion scales were very highly intercorrelated (table 2), with ρ ranging from 0.61 to 0.91. Basal ganglia/centrum semiovale EPVS scores were significantly positively correlated with all the WM lesion scales, although the correlations were clearly lower, ranging from 0.25 ($p = 0.014$) to 0.50 ($p<0.001$). Because of the high intercorrelations between the WM lesion scales we performed a principal components analysis, which yielded a single unrotated component explaining 80.4% of the variance, designated the white matter lesion factor (WML factor). This first component had an eigenvalue of 6.4, with the smaller components having eigenvalues of 0.53 or less. The components' loadings are shown in table 3. The WML factor and EPVS scores were significantly correlated ($\rho = 0.48$, $p<0.0001$). EPVS scores for the hippocampus were significantly positively correlated with the EPVS scores for the basal ganglia/centrum semiovale ($\rho = 0.35$, $p = 0.001$) but were only significantly positively correlated with the individual Longstreth and Fazekas WM lesion scales.

Table 3 Factor loadings of white matter lesion scales

Scale	Component 1*
Longstreth	0.90
Breteler	0.92
VS anterior	0.89
VS posterior	0.92
Fazekas PVH	0.84
Fazekas DWMH	0.87
Shimada	0.93
Wahlund	0.90

*Component 1 refers to the first unrotated principal component.
For abbreviations see table 1.

Correlations between cognitive function, EPVS scores, and white matter scores

EPVS, hippocampus EPVS, and the WML factor correlated with cognitive test scores after controlling for prior intelligence, using the NART. One subject's score for Raven's matrices was excluded as the standardised residual value in the linear regression analysis after controlling for the NART was greater than three standard deviations from the mean. Correlations between the WML factor and EPVS scores with the NART estimate of prior intelligence, and the unadjusted other cognitive tests, were non-significant. NART adjusted Raven's matrices performance correlated significantly and negatively with the basal ganglia/centrum semiovale EPVS ($\rho = -0.21$, $p = 0.038$), indicating that people with fewer EPVS have relatively good non-verbal reasoning after adjusting for prior intelligence. Adjusted Raven's matrices scores also correlated significantly and negatively with the WML factor ($\rho = -0.29$, $p = 0.004$). Adjusted cognitive function scores did not correlate significantly with the hippocampus EPVS scale. Unexpectedly, adjusted Auditory-Verbal Learning Test scores were significantly and positively correlated with the WML factor ($\rho = -0.25$, $p = 0.014$).

As a result of universal significant positive intercorrelations among the cognitive test scores, we carried out data

Table 2 Correlations among the EPVS scores and WM lesion scales

	HC EPVS	Longstreth	Breteler	VS anterior	VS posterior	Fazekas PVH	Fazekas DWMH	Shimada	Wahlund	WML factor
EPVS	0.35**	0.43**	0.32**	0.25*	0.30**	0.50**	0.43**	0.26*	0.48**	0.48**
HC EPVS		0.21*	0.11	0.11	0.10	0.29**	0.03	0.13	0.12	0.09
Longstreth			0.75**	0.74**	0.75**	0.84**	0.71**	0.76**	0.76**	0.90**
Breteler				0.90**	0.90**	0.65**	0.67**	0.85**	0.74**	0.92**
VS anterior					0.91**	0.64**	0.67**	0.85**	0.70**	0.89**
VS posterior						0.65**	0.68**	0.83**	0.70**	0.92**
Fazekas PVH							0.61**	0.67**	0.69**	0.84**
Fazekas DWMH								0.70**	0.84**	0.87**
Shimada									0.76**	0.93**
Wahlund										0.90**

*Correlation significant at the 0.05 level (two tailed).
**Correlation significant at the 0.01 level (two tailed).
For abbreviations see table 1.

Table 4 Factor loadings of cognitive tests

	First unrotated principal component	Obliquely rotated components	
	General cognitive factor	Visuospatial factor	Verbal memory factor
Raven's Standard Progressive Matrices	0.80	0.83	0.41
Benton Visual Retention Test	0.73	0.81	0.29
Visual reproduction	0.79	0.80	0.47
Logical memory	0.66	0.43	0.89
Rey Auditory-Verbal Learning Test	0.62	0.39	0.88
Verbal fluency	0.58	0.64	0.22
Digit-Symbol Substitution Test	0.75	0.74	0.47
Eigenvalues	3.53	3.27	2.30

reduction with principal components analysis, excluding the NART scores. Exclusions because of missing cognitive test data meant that factor scores from 92 participants were available. The first unrotated component accounted for 51% of the variance and had an eigenvalue of 3.53. This was designated the ''general cognitive factor''. Two components had eigenvalues greater than 1. The data were subjected to direct oblimin rotation and the two rotated components were designated the ''visuospatial factor'' (eigenvalue = 3.27) and the ''verbal memory factor'' (eigenvalue = 2.30) as determined from the pattern of loadings of the individual tests. The components' loadings are shown in table 4. The subjects' scores on each of these two rotated factors, and the general cognitive factor, were adjusted for NART estimates of prior intelligence as with the individual cognitive test scores. Adjusted visuospatial factor scores correlated significantly and negatively with the basal ganglia/centrum semiovale EPVS scores ($\rho = -0.22$, $p = 0.032$) and with the WML factor ($\rho = -0.26$, $p = 0.012$), but not with hippocampus EPVS scores. The correlations are shown in table 5.

Using multiple linear regression we found that basal ganglia/centrum EPVS scores did not have a significant independent association with the visuospatial factor scores, whereas the WML factor did have a significant independent association. The regression coefficients were −0.246 ($p = 0.018$) for the WML factor, and −0.176 ($p = 0.102$) for EPVS scores.

Enlarged perivascular spaces: group comparisons

As scales for measuring EPVS have not been published, we also used an alternative method of analysis. We compared cognitive function in the subjects with some EPVS (scores 1 and 2; n = 69) with that of the subjects with no EPVS in the basal ganglia/centrum semiovale (n = 28). Individuals with some EPVS had significantly worse performance compared with those with no EPVS on the visuospatial factor only (adjusted for NART; $F = 4.9$, $p = 0.029$).

Table 5 Correlations between EPVS, WML factor and adjusted cognitive factor scores†

	EPVS	HC EPVS	WML factor
NART	0.12	0.20	0.07
General cognitive factor	−0.16	−0.03	−0.13
Visuospatial factor	**−0.22***	−0.10	**−0.26***
Verbal factor	0.05	0.09	0.18

*Correlation is significant at the 0.05 level (two tailed).
†Cognitive factors are adjusted for NART scores. For NART correlations n = 97; for cognitive factor scores n = 92.
EPVS, enlarged perivascular spaces; HC, hippocampus; NART, National Adult Reading Test; WML, white matter lesion.

DISCUSSION

The novel finding in this study is that increased basal ganglia/centrum semiovale EPVS as measured by MRI in a sample of 97 healthy men aged 65–70 years is associated with worse non-verbal reasoning and, more generally, visuospatial cognitive ability after adjusting for prior intelligence. The correlations were modest but were statistically significant and of similar size to those found between WM lesion scales and cognitive function in published studies.[1] EPVS specific to the hippocampus and cognitive ability were not significantly correlated. We also replicated, using a range of published WM lesion scales, the finding that WM lesions are negatively correlated with cognitive scores (adjusted for prior intelligence) in older people. This is consistent with recent work showing that WM lesions correlate with cognitive ability in older individuals but not with childhood cognitive ability.[33]

The main implication of this finding is that MRI based assessments of changes in WM lesion scales should perhaps add a measure of EPVS. This will allow further exploration of whether EPVS are a form of relatively distinct pathological change seen in the ageing brain and in various disease states, or merely a benign manifestation of ageing, or are part of the sequence of development of WM lesions, whatever the aetiology.

In the present study EPVS scores correlated moderately and significantly with WM lesion scores, but the intercorrelations among the WM lesion scores were higher than the correlations between the EPVS and WM lesion scores, suggesting that EPVS are not directly homologous with MRI derived WM lesions. In the present study, EPVS did not have a statistically significant independent association with cognitive function However, this may not be true for populations with more EPVS and WM lesions, and with more cognitive dysfunction. In addition, despite being reasonably large, our sample size was still insufficient to exclude a modest independent association between WML and EPVS. These questions could be addressed in future studies or by retrospective analyses of existing data. EPVS might have some substantial independent association with respect to brain state.

In addition, current WM lesion scales may not adequately discriminate between different types of WM lesions. Given the wide variation in patterns of WM abnormality in older people—many EPVS but little other WM lesions; increased signal in the immediate periventricular WM but not elsewhere; many confluent WM lesions but few EPVS or periventricular WM lesions; and mixtures of these extremes—it seems likely that different forms of WM lesion

and EPVS may represent different aspects of pathology. Larger studies with subjects with different risk factors, with more WM lesions and EPVS, and follow up to determine the pattern of lesion development over time may help to address this.

In terms of neuroimaging, EPVS are largely distinguishable from other WM lesions, but at the neuropathological level, there may be overlap. For example, Udaka and coworkers[10] found that in 43 aged subjects with known cerebrovascular disease, WM lesions on MRI were associated with subependymal gliosis, myelin pallor and microinfarctions, and also dilatation of the perivascular spaces. From this study it seems as if there is imperfect mapping of neuropathology to neuroimaging. Therefore, an empirical approach, attempting to classify all the WM changes seen on MRI in the ageing brain, seems justified.

Unexpectedly, there was a positive correlation between scores (adjusted for prior intelligence), on one of two measures of verbal memory used here, the Auditory-Verbal Learning Test, and scores on several WM lesion scales and the WML factor. This is difficult to explain, as WM lesions probably represent some form of injury to the brain and one would expect this to affect cognitive function adversely. This finding also contradicts other work which shows that memory is worse in people with more WM lesions. However, the verbal memory factor did not correlate positively with WM lesion scores or the WML Factor. EPVS scores did not show any correlation with scores on the Auditory-Verbal Learning Test.

Some methodological limitations of this study must be noted. The sample consisted only of men and was not randomly selected. Thus the findings may not generalise to the background population. The subjects were also young-elderly and had limited WM disease. Our EPVS scale was developed inhouse and requires further validation and reliability studies.

In conclusion, we found that EPVS were associated with cognitive decline in otherwise healthy men, and replicated previous work showing that WM lesion load is associated with cognitive decline. Future work will help determine if this is a genuine finding, and if so, whether a greater number of EPVS is associated with worse cognitive function. EPVS should be included in assessments of WM change on MRI scans to better characterise their relations with other measures and risk factors of WM disease.

ACKNOWLEDGEMENTS

We thank Ian Marshall, Evelyn Cowie, Annette Blane, and Jim Cannon for technical support.

Authors' affiliations

A M J MacLullich, J M Starr, Geriatric Medicine Unit, University of Edinburgh, Edinburgh, UK
J M Wardlaw, K J Ferguson, Division of Clinical Neurosciences, University of Edinburgh, Western General Hospital, Edinburgh, UK
J R Seckl, Molecular Medicine Centre, University of Edinburgh, Western General Hospital, Edinburgh, UK
I J Deary, Department of Psychology, University of Edinburgh, Edinburgh, UK

This work was funded by a Medical Research Fellowship and a Project Grant from the Scottish Hospital Endowments Research Trust, and a Research Development Grant from the Scottish Higher Education Funding Council.

Competing interests: none declared

I J Deary is the recipient of a Royal Society-Wolfson Research Merit Award.
The brain imaging work was performed in the SHEFC Brain Imaging Research Centre for Scotland (www.dcn.ed.ac.uk/bic).

REFERENCES

1 **Gunning-Dixon FM**, Raz N. The cognitive correlates of white matter abnormalities in normal aging: a quantitative review. *Neuropsychology* 2000;**14**:224–32.
2 **Fazekas F**, Barkhof F, Wahlund LO, *et al*. CT and MRI rating of white matter lesions. *Cerebrovasc Dis* 2002;**13**(suppl):31–6.
3 **Braffman BH**, Zimmerman RA, Trojanowski JQ, *et al*. Brain MR—pathologic correlation with gross and histopathology. 1. Lacunar infarction and Virchow–Robin spaces. *Am J Roentgenol* 1988;**151**:551–8.
4 **Heier LA**, Bauer CJ, Schwartz L, *et al*. Large Virchow–Robin spaces—MR-clinical correlation. *Am J Neuroradiol* 1989;**10**:929–36.
5 **Cole FM**, Yates PO, Path MC. Comparative incidence of cerebrovascular lesions in normotensive and hypertensive patients. *Neurology* 1968;**18**:225–9.
6 **Vanswieten JC**, Vandenhout JHW, Vanketel BA, *et al*. Periventricular lesions in the white matter on magnetic-resonance-imaging in the elderly—a morphometric correlation with arteriolosclerosis and dilated perivascular spaces. *Brain* 1991;**114**:761–74.
7 **Laitinen LV**, Chudy D, Tengvar M, *et al*. Dilated perivascular spaces in the putamen and pallidum in patients with Parkinson's disease scheduled for pallidotomy: a comparison between MRI findings and clinical symptoms and signs. *Mov Disord* 2000;**15**:1139–44.
8 **Coulthard A**, Blank SC, Bushby K, *et al*. Distribution of cranial MRI abnormalities in patients with symptomatic and subclinical CADASIL. *Br J Radiol* 2000;**73**:256–65.
9 **Ferguson SC**, Blane A, Perros P, *et al*. Cognitive ability and brain structure in type 1 diabetes—relation to microangiopathy and preceding severe hypoglycemia. *Diabetes* 2003;**52**:149–56.
10 **Udaka F**, Sawada H, Kameyama M. White matter lesions and dementia—MRI-pathological correlation. *Ann N Y Acad Sci* 2002;**977**:411–15.
11 **Wahlund LO**, Barkhof F, Fazekas F, *et al*. A new rating scale for age-related white matter changes applicable to MRI and CT. *Stroke* 2001;**32**:1318–22.
12 **MacLullich AMJ**, Ferguson KJ, Deary IJ, *et al*. Intracranial capacity and brain volumes are associated with cognition in healthy elderly men. *Neurology* 2002;**59**:169–74.
13 **Ferguson KJ**, MacLullich AMJ, Marshall I, *et al*. Magnetic resonance spectroscopy and cognitive function in healthy elderly men. *Brain* 2002;**125**:2743–9.
14 **Longstreth WT**, Manolio TA, Arnold A, *et al*. Clinical correlates of white matter findings on cranial magnetic resonance imaging of 3301 elderly people—the cardiovascular health study. *Stroke* 1996;**27**:1274–82.
15 **Breteler MMB**, Vanamerongen NM, Vanswieten JC, *et al*. Cognitive correlates of ventricular enlargement and cerebral white-matter lesions on magnetic-resonance-imaging—the Rotterdam Study. *Stroke* 1994;**25**:1109–15.
16 **Van Swieten JC**, Hijdra A, Koudstaal PJ, *et al*. Grading white matter lesions on CT and MRI—a simple scale. *J Neurol Neurosurg Psychiatry* 1990;**53**:1080–3.
17 **Fazekas F**, Chawluk JB, Alavi A, *et al*. MR signal abnormalities at 1.5-T in Alzheimer's dementia and normal aging. *Am J Neuroradiol* 1987;**8**:421–6.
18 **Shimada K**, Kawamoto A, Matsubayashi K, *et al*. Silent cerebrovascular-disease in the elderly—correlation with ambulatory pressure. *Hypertension* 1990;**16**:692–9.
19 **Wahlund LO**, Agartz I, Almqvist O, *et al*. The brain in healthy aged individuals—MR imaging. *Radiology* 1990;**174**:675–9.
20 **Wardlaw JM**, Ferguson KJ, Graham C. White matter hyperintensities and rating scales—observer reliability varies with lesion load. *J Neurol* 2004;**251**:584–90.
21 **Raven JC**, Court JH, Raven J. *Manual for Raven's Progressive Matrices and Vocabulary Scales*. London: HK Lewis & Co, 1977.
22 **Wechsler D**. *Wechsler Memory Scale–Revised (WMS-R)*. New York: Psychological Corporation, 1987.
23 **Lezak M**. *Neuropsychological Assessment*, 3rd edn. Oxford: Oxford University Press, 1995.
24 **Sivan AB**. *Benton Visual Retention Test*, 5th edn. New York: Psychological Corporation, 1992.
25 **Wechsler D**. *Manual of the Wechsler Adult Intelligence Scale–Revised*. New York: Psychological Corporation, 1981.
26 **Nelson HE**, Willison JR. *NART Test Manual (Part II)*. New York: NFER-Nelson, 1991.
27 **Crawford JR**, Deary IJ, Starr J, *et al*. The NART as an index of prior intellectual functioning: a retrospective validity study covering a 66-year interval. *Psychol Med* 2001;**31**:451–8.
28 **Parkin AJ**, Java RI. Deterioration of frontal lobe function in normal aging: Influences of fluid intelligence versus perceptual speed. *Neuropsychology* 1999;**13**:539–45.
29 **Carroll JB**. Human cognitive abilities: A survey of factor analytic studies. New York: Cambridge University Press, 1993.
30 **Crawford JR**, Parker DM, Stewart LE, *et al*. Prediction of WAIS IQ with the National Adult Reading Test: cross-validation and extension. *Br J Clin Psychol* 1989;**28**:267–73.
31 **Deary IJ**, Whalley LJ, Lemmon H, *et al*. The stability of individual differences in mental ability from childhood to old age: follow-up of the 1932 Scottish mental survey. *Intelligence* 2000;**28**:49–55.
32 **Crawford JR**, Deary IJ, Starr J, *et al*. The NART as an index of prior intellectual functioning: a retrospective validity study covering a 66-year interval. *Psychol Med* 2001;**31**:451–8.
33 **Deary IJ**, Leaper SA, Murray AD, *et al*. Cerebral white matter abnormalities and lifetime cognitive change: a 67-year follow-up of the Scottish mental survey of 1932. *Psychology Aging* 2003;**18**:140–8.

Journal of Controlled Release 286 (2018) 114–124

Contents lists available at ScienceDirect

Journal of Controlled Release

journal homepage: www.elsevier.com/locate/jconrel

Cell reprogramming approaches in gene- and cell-based therapies for Parkinson's disease

Jodie H.K. Man[a], Lucianne Groenink[b], Massimiliano Caiazzo[a,*]

[a] Department of Pharmaceutics, Utrecht Institute for Pharmaceutical Sciences (UIPS), Utrecht University, Universiteitsweg 99, 3584, CG, Utrecht, The Netherlands
[b] Department of Pharmacology, Utrecht Institute for Pharmaceutical Sciences (UIPS), Utrecht University, Universiteitsweg 99, 3584, CG, Utrecht, The Netherlands

ARTICLE INFO

Keywords:
Cell therapy
Gene therapy
Parkinson's disease
iPS cells
dopamine neurons
transdifferentiation
astrocytes
microglia

ABSTRACT

Degeneration of dopamine (DA) neurons in the *substantia nigra pars compacta* is the pathological hallmark of Parkinson's disease (PD). In PD multiple pathogenic mechanisms initiate and drive this neurodegenerative process, making the development of effective treatments challenging. To date, PD patients are primarily treated with dopaminergic drugs able to temporarily enhance DA levels, therefore relieving motor symptoms. However, the drawbacks of these therapies including the inability to alter disease progression are constantly supporting the search for alternative treatment approaches. Over the past years efforts have been put into the development of new therapeutic strategies based on the delivery of therapeutic genes using viral vectors or transplantation of DA neurons for cell-based DA replacement. Here, past achievements and recent advances in gene- and cell-based therapies for PD are outlined. We discuss how current gene and cell therapy strategies hold great promise for the treatment of PD and how the use of stem cells and recent developments in cellular reprogramming could contribute to open a new avenue in PD therapy.

1. Introduction

Parkinson's disease (PD) is a neurodegenerative disorder involving genetic defects, exposure to environmental toxins, trauma, and aging in its etiology. These etiological variables cause progressive neuronal damage and formation of α-synuclein-containing Lewy bodies *via* multiple pathogenic mechanisms including intracellular stress, excitotoxicity, altered proteolysis and neuroinflammation. The pathological hallmark of PD is well characterized by the progressive degeneration of dopamine (DA) neurons in the *substantia nigra pars compacta* [1–3]. These subset of DA neurons innervate the striatum and give rise to the nigrostriatal pathway [4], (see also Box 1 and Fig. 1). Degeneration of nigrostriatal DA neurons results into depletion of striatal DA and impaired DA signaling in the basal ganglia, a pivotal neural circuitry involved in the regulation of movement [5]. This in turn eventually causes the primary clinical motor symptoms such as tremor, rigidity and bradykinesia [3].

PD therapeutic approaches should be of neurorestorative as well as neuroprotective nature to slow down, reverse or even prevent disease progression. However, currently available treatment approaches including pharmacological interventions and neurosurgical procedures (*e.g.* levodopa medication, deep brain stimulation) do not alter disease progression [6, 7]. Currently available treatment only provide symptomatic relief to PD patients and it is clear that these are associated with drawbacks and limitations over time [7–10]. For instance, levodopa medication, the mainstay DA replacement treatment for PD, loses efficacy as disease progresses [8, 10]. Over the past two decades promising therapeutic strategies using gene and cell replacement therapies have emerged. Despite this, research in this field has been facing difficult hurdles and none of these treatment approaches have moved forward towards clinical use yet [11, 12]. Recent advances made in cellular reprogramming technology, however, may become a turning point for gene- and cell-based therapy for PD, bringing these therapeutic approaches back to clinical trials. In this review an overview of current gene- and cell-based therapy strategies for PD is outlined, while considering their potential and limitations. We then take the opportunity to discuss recent progresses made in the use of stem cells and cellular reprogramming and their prospects for the treatment of PD.

2. Past achievements in viral vector-based gene therapy for PD

Gene therapy strategies involve the delivery of therapeutic genes using viral vectors into desired target regions. Currently, viruses including adeno-associated viruses (AAVs) and lentiviruses (LVs) are being used for the delivery of therapeutic genes with a relatively acceptable safety profile. Thus far, three major therapeutic strategies

* Corresponding author.
E-mail address: m.caiazzo@uu.nl (M. Caiazzo).

https://doi.org/10.1016/j.jconrel.2018.07.017
Received 10 April 2018; Received in revised form 26 June 2018; Accepted 10 July 2018
Available online 17 July 2018
0168-3659/ © 2018 Elsevier B.V. All rights reserved.

Box 1
The dopaminergic system in the brain

Dopamine is one of the major neurotransmitters in the brain that spreads throughout multiple regions via dopaminergic pathways. The two major dopaminergic pathways are the mesocorticolimbic and nigrostriatal pathways, originating from two distinct regions of the midbrain (Fig. 1). The mesocorticolimbic pathway consists of dopaminergic neurons projecting from the ventral tegmental area to the nucleus accumbens and cortical regions. Conversely, the nigrostriatal pathway comprises of dopaminergic projections from the substantia nigra pars compacta to the striatum (caudate-putamen) [4]. Degeneration of the nigrostriatal neurons is the primary pathological hallmark in PD. This leads to impaired dopaminergic signaling to the striatum, a subcortical nucleus part of the basal ganglia circuitry, and motor dysfunction ([3, 5]).

based on the delivery of genes using viruses have been clinically evaluated in PD patients.In this section, these gene therapy strategies are discussed and their potential as future treatments are weighted.

3. Restoration of striatal DA synthesis

DA biosynthesis is mediated by three major enzymes tyrosine hydroxylase (TH), GTP cyclohydrolase-1 (GCH-1) and dopa decarboxylase (DDC; also known as AADC, aromatic amino acid decarboxylase). Both TH and GCH-1 are crucial for the conversion of tyrosine to levodopa of which the latter is subsequently converted to DA by DDC [13]. In PD, progressive degeneration of nigrostriatal DA neurons disrupts DA production and release in the striatum. Therefore, creating a new DA-producing source in the striatum is an appealing strategy to replace lost striatal DA. This has been attempted by expressing genes encoding the enzymes required for DA synthesis in non-degenerating striatal medium spiny neurons (MSNs). The feasibility of this concept is supported by a number of successful preclinical studies [14–20]. Thus far, four phase I clinical studies have assessed the safety and efficacy of bilateral AAV-DDC delivery to the *putamen* in moderate to advanced PD patients. Viral vector-based gene transfer of DDC was well-tolerated and ameliorated motor complications with improved total and part III motor Unified PD Rating Scale (UPDRS; see Box 2/Table 1) score [21–23]. Furthermore, a long-term follow-up study reported sustained transgene expression for over four years [24]. In line with these results, a phase I/II trial confirmed the safety and efficacy of bilateral LV vector-based intraputaminal delivery of DDC, TH and GCH-1 (ProSavin) in moderate to advanced PD patients. ProSavin improved off-medication part III motor UPDRS scores for up to 12 months in all PD patients [25]. Taken together, the data gathered so far support the therapeutic potential of these strategies for the treatment of PD. Despite this, an overestimation of the beneficial effects due to a 'placebo effect' cannot be excluded because of the open-label design of these clinical studies. Pursuit of randomized placebo-controlled clinical studies would be the next step in order to support current positive findings. However, it remains debatable whether non-degenerating striatal MSNs are the right candidate for targeting. Striatal MSNs lack the ability to store DA in vesicles and to regulate its release. In combination with unregulated and sustained transgene expression, this can lead to continuous high cytosolic and extracellular DA levels, which in turn causes intracellular stress that further induces neurodegeneration [26–28]. This raises concerns for the long-term effect of this gene therapy strategy and the use of viruses for continuous gene expression under unregulated conditions.

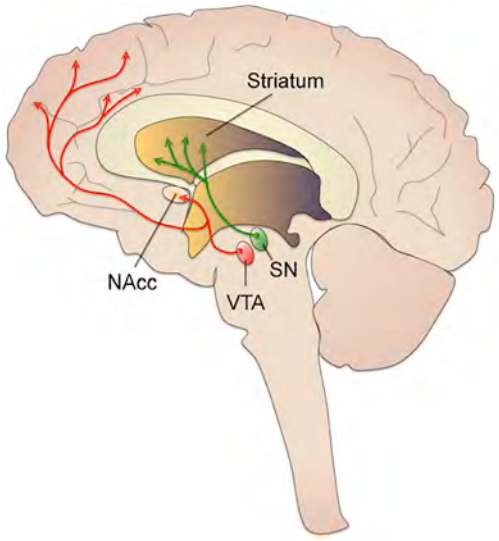


Fig. 1. Sagittal cross-section of the brain showing the two major dopaminergic pathway of the dopamine neuron system. Red arrows: mesocorticolimbic pathway; Green arrows: nigrostriatal pathway (note: the nigrostriatal pathway projects primarily from the *pars compacta* region of the *substantia nigra*). Abbreviations: NAcc = nucleus accumbens; VTA = ventral tegmental area; SN = *substantia nigra*.

4. Modulation of subthalamic nucleus neuronal activity

The basal ganglia circuit comprises of a number of subcortical nuclei including the striatum, the subthalamic nucleus, the *substantia nigra* and the *globus pallidus*. In PD neuronal activity within these subcortical nuclei is altered as described in Box 3 and Fig. 2 [5]. Briefly, striatal DA depletion results in disinhibition of the subthalamic nucleus, subsequently leading to glutamatergic overstimulation of the *globus pallidus interna* and the *substantia nigra pars reticulata* (GPi-SNr), the basal ganglia output nuclei. This further triggers an increased inhibitory drive from GPi-SNr to the thalamus, leading to reduced motor cortex stimulation and subsequently motor impairment. Therefore, controlling neuronal activity within the subthalamic nucleus and its excitatory glutamatergic outflow towards the GPi-SNr could restore lost motor cortex stimulation and improve motor dysfunction in PD. This has been done by viral vector-based gene transfer of glutamate decarboxylase (GAD) into neurons of the subthalamic nucleus. GAD is a key enzyme that exists in two isoforms, GAD65 and GAD67. Both are involved in converting glutamate to GABA (gamma-aminobutyric acid), which are

Box 2
Unified Parkinson's Disease Rating Scale

The Unified Parkinson's Disease Rating Scale (UPDRS) is an extensively used clinical rating scale for Parkinson's disease (PD). In 2007, the Movement Disorder Society published a revised UPDRS (MDS-UPDRS) in effort to overcome the limitations of the original UPDRS [147, 148]. The MDS-UPDRS comprises of four categories (Table 1).

Table 1
MDS-UPDRS.

Categories	Key purpose
Part I Non-Motor Experiences of Daily Living	MDS-UPDRS Part I subscale consists of 13 items designed to assess the presence and severity of non-motor symptoms (*e.g.* sleep, mood disorder, cognitive impairment, apathy, psychosis) in Parkinson's disease patients.
Part II Motor Experiences of Daily Living	MDS-UPDRS part II subscale consists of 13 items designed to assess motor aspects of disability on activities of daily living (*e.g.* speech, eating, handwriting) and quality of life in Parkinson's disease patients.
Part III Motor Examination	MDS-UPDRS part III subscale consists of 18 items designed to assess the presence and severity of motor symptoms (*e.g.* tremor, rigidity) in Parkinson's disease patients.
Part IV Motor Complications	MDS-UPDRS part IV subscale consists of 6 items designed to assess the presence and severity of motor complications related to treatment (*e.g.* motor fluctuations, dyskinesias)

Each part consists of a number of items (*i.e.* questions, clinical assessments) which are scored using a 0–4 rating scale, where 0 = normal, 1 = slight, 2 = mild, 3 = moderate, and 4 = severe.

Box 3
Pathophysiology of motor dysfunction in Parkinson's disease

The striatum is innervated by dopaminergic and glutamatergic neurons of the *substantia nigra pars compacta* and the cortex, respectively. Excitatory glutamatergic input from the cortex results in the stimulation of striatal medium spiny neurons. These are neurons of which neurotransmission involves the release of the primary inhibitory neurotransmitter GABA (gamma-aminobutyric acid). Striatal medium spiny neurons are found in two types that project to different downstream targets, giving rise to the direct and indirect pathway of the basal ganglia. The direct pathway comprises of striatal medium spiny neurons projecting to the main output nuclei *globus pallidus interna* and *substantia nigra pars reticulata* (GPi-SNr). Conversely, in the indirect pathway striatal medium spiny neurons project to the *globus pallidus externa*. Activity of the direct and indirect pathway is modulated by dopaminergic signaling from the *substantia nigra pars compacta*. Importantly, dopamine facilitates and inhibits neuronal activity in the direct and indirect pathway, respectively (Fig. 1) [5].

the primary excitatory and inhibitory neurotransmitters in the brain. Early preclinical studies have demonstrated that AAV-GAD delivery to the subthalamic nucleus facilitated and reduced its local GABAergic neurotransmission and excitatory outflow towards the GPi-SNr, respectively [29, 30]. Following these encouraging preclinical results, two clinical studies have been completed so far. In an open-label phase I study unilateral delivery of AAV-GAD to the subthalamic nucleus in advanced PD patients was well tolerated with improvements in part III motor UPDRS score [31]. A subsequent randomized double-blinded and sham-controlled phase II trial evaluated the therapeutic value of bilateral gene delivery of AAV-GAD but only modest improvement in off-medication part III motor UPDRS score was reported from baseline up to 6 months [32]. Overall, current clinical findings are positive and support the safety of AAV-GAD therapy for PD but the clinical effect found was only modest. We have to take into consideration that this therapeutic strategy solely modulates neuronal activity in the subthalamic nucleus and its downstream targets to a certain extent, while nigrostriatal DA neurons progressively degenerate over time. This illustrates that delivering genes for GAD to the subthalamic nucleus may only provide a modest way to improve motor function in PD.

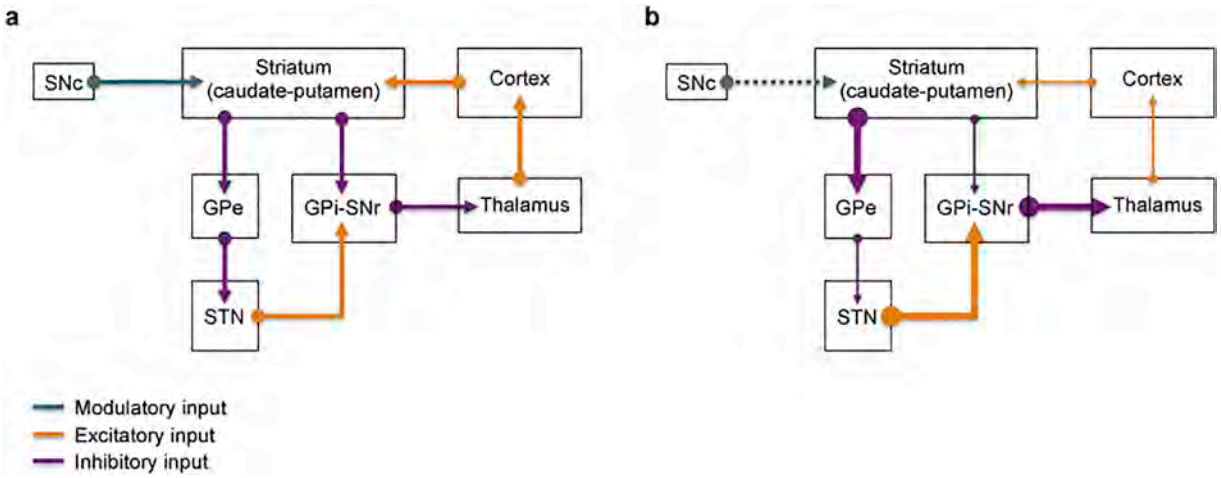


Fig. 2. The basal ganglia circuitry. (a) Under physiological conditions the indirect pathway complements the direct pathway. Activation of striatal medium spiny neurons of the direct pathway suppresses GPi-SNr activity. This in turn reduces the inhibitory outflow from the GPi-SNr to the thalamus, leading to motor cortex stimulation. At the same time, activation of the indirect pathway stimulates neuronal activity within the GPe, leading to the inhibition of the STN. This results in reduced excitatory glutamatergic transmission from the STN to the GPi-SNr, leading to decreased neuronal activity in the GPi-SNr. (b) In PD, progressive degeneration of dopaminergic neurons in the SNc results in striatal dopamine depletion and subsequently loss of the modulatory function of dopamine on the basal ganglia circuitry. Activity of striatal medium spiny neuron is reduced in the direct pathway, while increased in the indirect pathway. The latter causes overstimulation of the GPi-SNr, following increased inhibition of the GPe and disinhibition of the STN. This enhances inhibition of the thalamus, leading to reduced motor cortex stimulation and therefore motor dysfunction. Abbreviations: SNc = *substantia nigra pars compacta*; GPe = *globus pallidus externa*; GPi-SNr = *globus pallidus interna* and *substantia nigra pars reticulata*; STN = subthalamic nucleus.

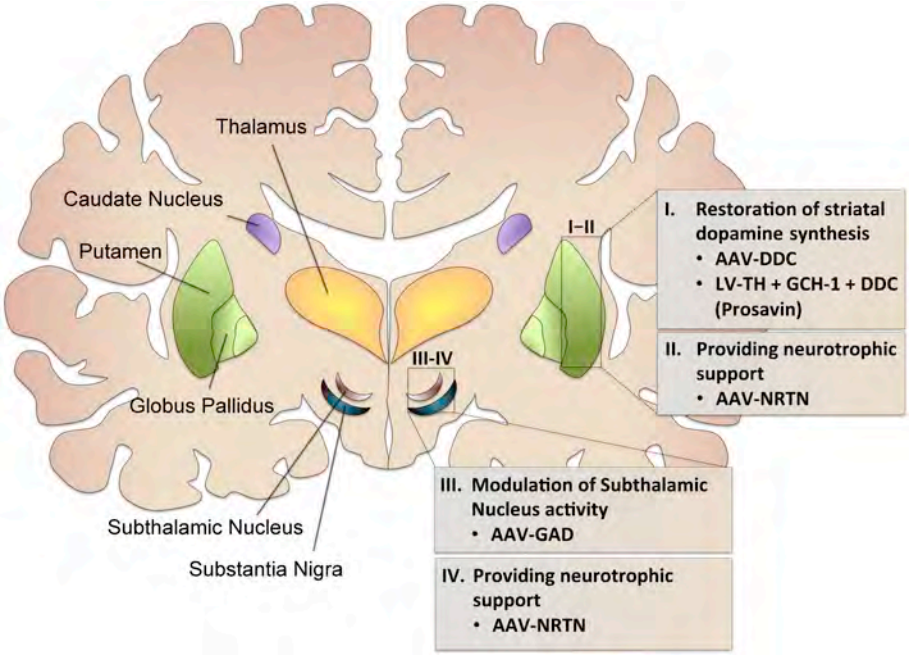


Fig. 3. Current gene therapy strategies for the treatment of PD. Gene therapy strategies to date use viral vectors for target-specific delivery and continuous expression of therapeutic genes. They intend to (I) restore striatal dopamine synthesis, (II and IV) provide neurotrophic support to promote neuronal survival at sites of neurodegeneration or (III) modulate excitatory neuronal activity in the subthalamic nucleus (STN). Abbreviations: AAV = adeno-associated virus; LV = lentivirus; DDC = dopa decarboxylase; TH = tyrosine hydroxylase; GCH-1 = GTP cyclohydrolase-1; GAD = glutamate decarboxylase; NRTN = neurturin.

5. Providing neurotrophic support

Modulating neurodegenerative process in PD is a key strategy to alter disease progression. Neurotrophic factors including glial-cell-line-derived neurotrophic factor (GDNF) and neurturin (NRTN) are pivotal in promoting survival of DA neurons [33]. Based on our current understanding of the pathology of PD, neuroinflammation is associated with loss of neurotrophic support [2]. Therefore, restoring neurotrophic support is an appealing approach to protect and preserve degenerating nigrostriatal DA neurons. Supported by promising results from preclinical studies [34–37], four human clinical trials have now assessed the therapeutic value of viral vector-based gene delivery of NRTN. In an open-label phase I study, bilateral intraputaminal delivery of AAV-NRTN in advanced PD patients improved motor function with reduced off-medication part III motor UPDRS score at 12 months [38]. In contrast to this, a following double-blinded and sham-controlled phase II study, only found substantial improvement after 18 months according to off-mediation part III motor UPDRS scores. Results imply that the delayed clinical effect could be due to defects in axonal transport of the therapeutic gene from the *putamen* to the *substantia nigra* as a consequence of extensive neurodegeneration of the nigrostriatal pathway [39]. Two subsequent clinical studies evaluated the safety and efficacy of AAV-NRTN gene delivery to both the *putamen* and the *substantia nigra* in advanced PD patients [40, 41]. Remarkably, contrary to earlier observation, no significant improvement in motor function was observed in the treatment group in comparison to the control group [40, 41]. These findings suggest that the clinical effects of this gene therapy strategy depends on the extent of degeneration of nigrostriatal DA neurons. Future clinical studies may therefore require strict patient selection in which for instance only 'early stage' PD patients can participate. Nevertheless, PD is often only diagnosed after the occurrence of first motor symptoms when more than half of the nigrostriatal DA neurons are already lost. This underlines the need to identify markers that would allow early diagnosis, as neuroprotective effect may not work in patients with extensively degenerated nigrostriatal pathway. Despite this, it has been stressed that uncontrolled and continuous overexpression of neurotrophic factors could be detrimental resulting in excessive sprouting of DA fibers into other areas such as the *globus pallidus* and the *substantia nigra reticulata* [42–44]. Current gene therapy strategies use viruses to promote long-term gene expression but under unregulated conditions. Alternative delivery strategies including direct neurotrophic factor protein delivery may overcome current limitations of viral vector-based gene therapy. Earlier attempts with direct infusion of recombinant GDNF protein using pumps have achieved little clinical success [45–47] but new drug delivery systems such as intranasal delivery may open a new opportunity for direct and non-invasive delivery of biomolecules including neurotrophic factors [48, 49].

In summary, to date, three viral vector-based gene-based therapeutic strategies have been pursued for PD (Fig. 3) showing a potentially clinical benefit for PD patients. Nevertheless, many open points need to be tackled before gene therapy could be used as alternative treatment for PD. Some of the most crucial points are linked to the use of viral vectors to deliver genes under unregulated conditions.

An alternative therapeutic approach that could overcome gene therapy drawbacks is represented by cell therapy. PD cell-based DA replacement is based on the transplantation of a DA-producing source in the striatum. Several potential DA cell sources have been investigated including human fetal ventral mesencephalic (fVM) tissues (Fig. 4a) [11].

6. Past achievements in cell-based DA replacement therapy for PD

Encouraging results from preclinical animal studies and a series of open-label human studies supported the therapeutic potential of fVM tissue transplantation for PD [11, 50, 51]. However, the prospects for cell-based DA replacement therapy using fVM tissues has dimmed following two randomized sham-controlled phase II clinical trials [52, 53]. Remarkably, in both studies no significant improvement in motor symptoms was observed in PD patients after fVM tissue transplantation in the *putamen*, while significant axonal outgrowth from the graft and increased DA uptake in the striatum was reported after post-mortem examination. Furthermore, patients who received fVM tissue transplantation frequently experienced adverse effects including dyskinesia, which is now referred to as graft-induced dyskinesia (GID) [52–54]. It is now proposed that the occurrence of GID, which may have contributed to the lack of efficacy of fVM tissue transplantation, is attributed to several factors. These factors include imbalanced DA release from the graft [54], pre-existing levodopa-induced dyskinesia [55, 56], placement and capability of graft to reinnervate the target area [57, 58], immunological rejection of graft due to discontinuation of immunosuppressant therapy [52, 53, 59] and the heterogeneity of the graft [60, 61]. Furthermore, it appears that disease progression is a crucial factor as well. Indeed, clinical effect was reported for a subset of younger patients with less severe PD who had no levodopa-induced dyskinesia [52, 53]. However, whether fVM tissue transplantation is a

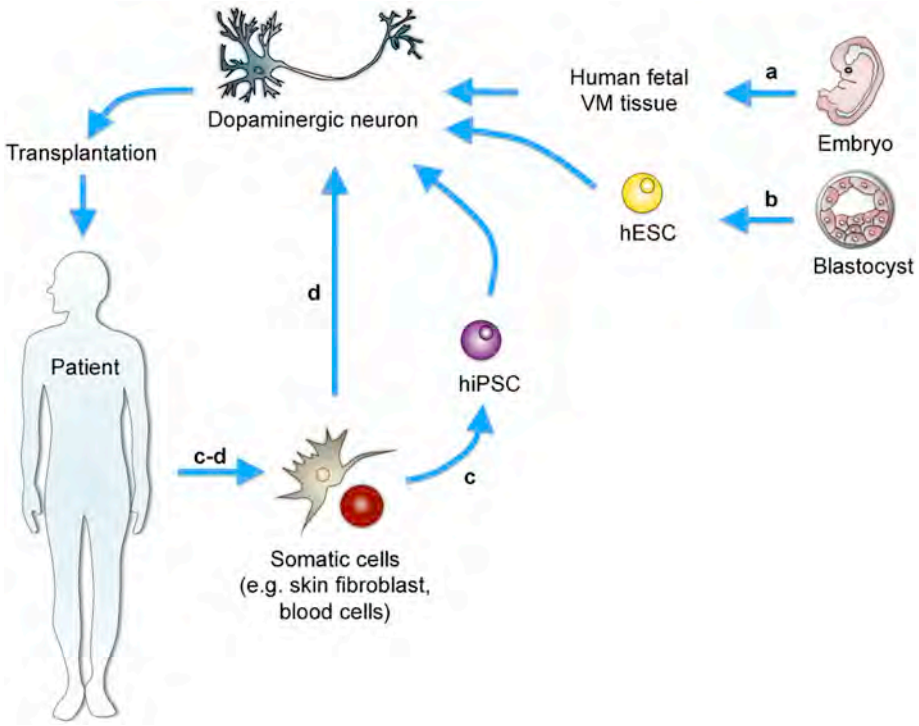


Fig. 4. Sources of dopaminergic neurons for replacement therapy in PD. (a) Human fetal VM have been used as dopaminergic source in transplanted PD patients. (b) hESC are isolated from blastocysts and can be differentiated into functional dopaminergic neurons. (c-d) Patient-specific somatic cells can be (c) reprogrammed into hiPSC and differentiated into dopaminergic neurons or (d) can be directly converted into dopaminergic neurons through direct cell lineage reprogramming. Abbreviation: VM = ventral mesencephalic; hESC = human embryonic stem cell; hiPSC = human induced pluripotent stem cell.

compatible source for cell-based DA replacement therapy in PD is debatable as tissue availability and ethical issues remain an ongoing problem [62]. Recent progress in stem cell technology and cellular reprogramming could overcome at least the issues linked to the limited source of human DA neurons and to the immunological compatibility.

7. DA neurons derived from pluripotent stem cells

The first step towards stem cell-based DA replacement therapy for PD was made after functional midbrain DA neurons were successfully differentiated from mouse embryonic stem cells (ESCs) [63]. Upon transplantation in the striatum of parkinsonian rats, midbrain-specific mouse ESCs-derived DA neurons showed good survival and this was linked to improvement in behavioral motor deficits [64]. Based on this, others have attempted to generate midbrain-specific DA neurons from human ESCs by co-culturing strategies with either stromal feeder cells [65–68] or astrocytes [69]. At first, these approaches successfully produced TH-positive neurons *in vitro* [66–71]. Remarkably, *in vivo* transplantation of these neurons in the striatum of parkinsonian animals have yielded inconsistent results with some experiments resulting in improvement in motor function [67, 69], while others did not [65, 68, 71]. Negative findings were later reported to be linked to poor *in vivo* survival of the cell transplant and 'unstable' human ESC-derived DA neurons with incorrect phenotypic characteristics [65, 68, 71] Furthermore, human ESC-derived cell population contained undifferentiated pluripotent cells, which led to formation of tumors [65, 67, 69]. This underlines a significant safety issue surrounding the use of human ESC-derived DA neurons.

A few years later a new procedure described the successful derivation of stable and functional midbrain-specific DA neurons from human ESCs further exploiting developmental principles (Box 4) [72–75]. In contrast to previous studies, *in vivo* transplantation of these neurons resulted in significant motor improvement without tumor formation as demonstrated in toxin-based animal models of PD [74, 75]. Recent preclinical studies further support the therapeutic potential of human ESC-derived DA neurons as an alterative source for cell replacement therapy for PD [76, 77]. Currently, teams from USA, Europe and Japan (G-Force PD, http://www.gforce-pd.com/) are moving forward to use human ESC-derived DA neurons in new clinical trials for cell-based DA replacement therapy in PD. Several steps need to be taken before understanding the value of this therapeutic approach as widely used clinical solution.To date, G-Force PD teams are focusing on several

Box 4

Current concept in the generation of dopaminergic neurons *in vitro*

Protocols describing the differentiation of dopaminergic neurons from pluripotent stem cells are based on principles derived from embryonic development of DA neurons in mice. First differentiation protocols involved the use of stromal feeder cells or astrocytes and the activation of genes for sonic hedgehog (SHH) and fibroblast growth factor 8 (FGF-8) [65–69]. Remarkably, although TH-positive neurons were generated, they lacked expression of crucial DA neural markers for FOXA2 and LMX1A and showed poor survival upon *in vivo* transplantation [65–71] It is now well accepted that midbrain DA neurons arise from floor plate cells and their further development is regulated by WNT, SHH and FGF signaling pathways [72, 73]. Pluripotent stem cells can be induced to become neural floor plate cells through the dual inhibition of the SMAD signaling pathway at the same time under activation of SHH. Following this, activation of WNT signaling pathway through treatment with GSK3B (glycogen synthase kinase-3 beta) inhibitors facilitate conversion of floor plate cells to dopaminergic neural cell fate. Further differentiation yields stable and functional TH-positive dopaminergic neurons expressing neural markers for FOXA2 and LMX1A [75]. Based on this, similar protocols have been developed by others, resulting also in dopaminergic neurons of correct phenotype [74, 82, 149, 150].

Table 2
Current direct reprogramming approaches to convert somatic cells to functional dopaminergic neurons.

Reference(s)	Cell source	Transcription factor cocktail
Caiazzo et al. [99]	Mouse and human fibroblasts	*Ascl1, Nurr1, Lmx1a*
Kim et al. [100]	Mouse fibroblasts	*Ascl1, Nurr1, Lmx1a, Pitx3*
Pfisterer et al. [102]	Human fibroblasts	*Ascl1, Foxa2, Lmx1a, Brn2, Myt1l*
Liu et al. [101]	Human fibroblasts	*Ascl1, Nurr1, Pitx3, Ngn2, Sox2*
Addis et al. [98]	Mouse Astrocytes	*Ascl1, Nurr1, Lmx1b*
Jiang et al. [103]	Human fibroblasts	*Ascl1, Nurr1, Lmx1a, mir-124*
Rivetti di Val Cervo et al. [111]	Mouse astrocytes (*in vivo*)	*Ascl1, Neurod1, Lmx1a, mir-218*

aspects linked to the definition of a proper immunosuppressive regime, patient selection parameters, patient assessment protocols and trial design. Hopefully, the results of these combined efforts would lead to start clinical trials within 2020 and therefore clinical readouts few years after, [78, 79] (Fig. 4b). However, the use of ESCs still remains an issue of ongoing ethical debate [62] but cell reprogramming technologies couldhelp to overcome this difficulty (Fig. 4c).

The feasibility to promote pluripotency in somatic cells with cellular reprogramming was first reported a 12 years ago [80, 81]. These reprogrammed cells known as induced pluripotent stem cells (iPSCs) share comparable features with ESCs but they are derived from patient-specific somatic cells, eventually overcoming immunological graft rejection upon transplantation and ethical issues. Successful generation of DA neurons from iPSCs and their functional survival as well as therapeutic potential in preclinical models of PD have been reported [82–87]. However, the report of tumor formation upon *in vivo* transplantation of iPSC-derived DA neurons still raises some questions regarding the proposed safety [87].

In order to induce pluripotency in somatic cells, forced overexpression of transcription factors including *Oct3/4*, *Sox2*, *c-Myc* and *Klf4* is required. These are delivered using retroviral or LV vectors which are capable of random integration into the host genome, potentially leading to alteration in genomic structure and unregulated transgenes expression [80, 81]. It has been reported that reactivation of these transgenes, in particular the oncogene *c-Myc*, induced tumor formation [88, 89]. This stresses the need for alternative strategies to transduce transcription factors. A number of new strategies to reprogram somatic cells have been implemented in the last years. These strategies use non-integrating adenoviral vectors [90, 91], direct protein-based delivery [92, 93], DNA- or RNA-based delivery [94–96], or Cre-recombinase-mediated excision of transgenes for cell reprogramming [97].

Another factor that triggers tumor formation is the presence of undifferentiated pluripotent cells in the generated cell populations [85, 93]. These could lead to continuous and extensive outgrowth of the graft upon transplantation. Considerable progress has been made to remove undifferentiated pluripotent cells and other contaminants and enrich iPSC-derived DA neurons using cell sorting strategies including magnetic-activated cell sorting (MACS) or fluorescence-activated cell sorting (FACS) [82, 86]. Thus far, cell sorting using neural markers such as $CORIN^+$ or $NCAM^+/CD29^{low}$ have reduced the number of contaminants and increased the number of TH-positive and midbrain-specific DA neurons in iPSC-derived cell populations [82, 86]. Further optimization of these approaches could refine clinical safety issues surrounding the use of iPSCs as a new cell source for cell replacement therapy for PD (Fig. 3c). However, nowadays, other reprogramming approaches based on direct lineage conversion are also available to generate DA neurons without supporting the risk of tumor generation (Fig. 4d).

8. DA neurons derived from direct cell lineage conversion of somatic cells

Direct cell lineage conversion (also referred to as transdifferentiation) involves fast and direct conversion of somatic cells into functional neurons including midbrain-specific DA neurons skipping any intermediate pluripotent stage. This cellular reprogramming strategy involves viral vector-based delivery of defined combination of transcription factors essential for the direct generation of midbrain DA-specific characteristics in somatic cells (Table 2) [98–103]. Through this way, functional DA neurons with correct phenotype, currently referred to as induced DA (iDA) neurons, were directly derived from somatic cells. iDA neurons share comparable morphological features with resident brain DA neurons and are also capable of producing as well as releasing DA [99, 101, 104].

In vivo transplantation of iDA neurons in the striatum of parkinsonian rats reduced drug-induced rotational motor behavior and were reported to survive and innervate the targeted area [100, 105]. Moreover, Dell'Anno and colleagues showed the *in vivo* functionality of iDA neurons and further proposed the benefits of using the pharmacogenetic tool Designer Receptors Exclusively Activated by Designer Drugs (DREADDs) to advance functional cellular control [105]. DREADDs are engineered G-protein coupled receptors activated by small pharmacological ligands (*e.g.* clozapine-N-oxide (CNO)) that provide reversible and non-invasive manipulation of neuronal activity [106, 107]. The use of DREADDs in iDA neurons provides a novel and efficient way to modulate these neurons for the fine-tuning of their therapeutic efficiency (*i.e.* release of DA) upon transplantation.

The prospect of iDA neurons for cell-based DA replacement therapy are thus far promising. Several issues surrounding the use of pluripotent stem cells including ethical problems, immunological rejection of grafts and potential tumor risk are avoided with direct cell lineage conversion. Although reprogramming strategy still uses viral vectors capable of random genomic integration, alternative transcription factor delivery approaches have been proposed as mentioned earlier. Despite this, current direct conversion strategy using human somatic cells is hindered by low conversion efficiency, implying limitations in scalability which needs to be addressed before translation to therapy [99, 101, 102]. However, advances are being made in improving efficiency of direct conversion [103, 104, 108].A very promising advance in cell reprogramming technology is represented by the implementation of microRNA (miRNA). The first evidence was provided by using the well-known neural miRNAs mir-9/9* and mir-124 to improve the transdifferentiation of fibroblasts into functional neurons [108, 109]. Very interestingly, a recent work showed that mir-34b/c is able to increase the efficiency of transdifferentiation from fibroblasts to induced DA neurons [110] and mir-218 has been proven to improve *in vivo* DA transdifferentiation [111].

These recent advances further contribute to envision a future in

which direct conversion of human somatic cells into compatible DA neurons could provide a safe and unlimited patient-specific source for PD cell-based DA replacement therapy (Fig. 4d).

Taken together, advances made in the use of stem cells and cellular reprogramming opened a new avenue for cell therapy in PD by introducing the possibility of differentiating pluripotent stem cells or somatic cells functional DA neurons. Intriguingly, cell reprogramming technologies are quickly improving in the ability to generate glial neural cell types with neuromodulatory action such as astrocytes and microglia, opening the way for new therapeutic strategies for PD.

9. Glial cells as new key players in cell reprogramming approaches for cell-based gene therapy for PD

Glial cells are the most abundant cell type in the brain and are represented by microglia, astrocytes and oligodendrocytes. Microglia and astrocytes are multifaceted and could be either of neuroprotective or neurodegenerative nature depending on their state of activation. In PD, dysregulated microglia and astrocytes activation enhance neurodegeneration. This is associated with the release of pro-inflammatory and neurotoxic factors as well as loss of beneficial neuroprotective function [112]. Therefore, providing and modulating lost glial cell function is an attractive therapeutic approach as will be outlined below. At the same time, new strategies are arising from the combination of gene- and cell-based therapy such as cell *in vivo* direct reprogramming of resident astrocytes [113].

10. Prospects of microglial cell-based gene therapy for PD

Microglia are resident macrophages of the brain and they play a crucial role in mediating immunological and homeostatic processes by tightly surveying the extracellular environment for pathogenic elements or tissue injury [112]. Under pathological conditions, albeit due to inflammation or tissue damage, microglia are activated and can enter two different phenotypic states defined as M1 and M2. Importantly, microglia of M1 phenotype promote inflammation by releasing pro-inflammatory mediators and cytotoxic factors, while M2 microglia suppress inflammatory response and facilitate tissue repair with the release of anti-inflammatory and trophic factors. Emerging evidence indicate microglia are primarily in their M2 state playing a beneficial role during early stages of inflammation, while over time they switch to a M1 phenotype inducing inflammation [114, 115]. Normally, inflammation ceases upon homeostasis is reached, however, in PD, inflammatory response is uncontrolled with the presence of reactive microglia [116], indicating microgliosis. The continuous production of pro-inflammatory and cytotoxic factors from reactive microglia is detrimental to DA neurons. Subsequently, degenerated DA neurons release aggregated and misfolded proteins as well as reactive oxygen species, which in turn further promote inflammation and drive the vicious cycle of neurodegeneration [112, 115]. Thus, sustained neuroinflammation favoring the activation of pro-inflammatory microglia trigger neurodegenerative process.

An appealing therapeutic strategy could consider to compensate for dysfunctional microglia. Earlier studies revealed that systemically infused bone marrow stem cells (BMSCs) give rise to microglia in the brain. BMSC-derived microglia precursors are recruited and travel to sites of inflammation and neurodegeneration in which they subsequently differentiate into microglia [117, 118]. Many have used this cellular migration and differentiation mechanism to their advantage [119]. For PD, BMSC microglia precursors have been genetically modified *ex vivo* to produce neurotrophic factors and systemic delivery of these engineered BMSCs in parkinsonian mice resulted in preservation of functional nigrostriatal DA neurons with no significant motor dysfunction [120–122]. This experiments support the use of BMSC-derived microglia precursors for cell-based gene therapy for PD. However, it has to be taken in consideration that microglia derives from the embryonic yolk sac leaving doubts on whether BMSC-derived microglia could be defined as 'true microglia'. Moreover, it is uncertain to what extent BMSC-derived microglia contribute to and integrate into the resident microglia population in the brain [117].

In light of this, attempts have been made to generate a new source of microglia from pluripotent stem cells. Only recently microglia cells were successfully derived from yolk sac progenitor cells using human ESCs and iPSCs [123]. This new source of microglia shares similar genetic and molecular patterns with 'true microglia'. Although PSC-derived microglia are primarily of great interest for disease modeling or therapeutic drug screening, they could also be employed as cellular delivery systems for therapeutic genes. In this context, it is of particular interest to use patient-specific microglia derived iPSCs. These could be genetically modified to produce trophic factors or anti-oxidants and compensate for dysfunctional microglia upon transplantation. However, a remaining major drawback of using iPSCs is the risk of tumor formation but implementation of alternative reprogramming approaches and cell sorting may reduce this risk. Future developments in direct cell lineage reprogramming could be an alternative approach but this remains unexplored to date.

11. Prospects of astroglial cell-based gene therapy for PD

Several lines of evidence suggest that astrocytes are involved in neuroinflammation in neurodegenerative diseases [124]. Astrocytes are multifunctional glial cells involved in the regulation of brain homeostasis. They play a pivotal role in supporting neuronal survival and tissue repair by releasing trophic factors and mediating intracellular oxidative stress through the secretion of anti-oxidants. Additionally, astrocytes are capable of uptaking and degrading toxic molecules in the extracellular environment and are vital for ion and nutrient metabolism [124]. Under pathological conditions, astrocytes become reactive and in PD, astrocytes switch to their reactive state once the balance between uptake and degradation of toxic molecules (*e.g.* α-synuclein) is disrupted [125]. Astrocytes are also activated by pro-inflammatory cytokines released from reactive microglia [126]. Reactive astrocytes in turn release pro-inflammatory mediators and reactive oxygen species of which further amplify neuroinflammation and contribute to the vicious cycle of neurodegeneration [112, 125, 126].

Emerging evidence indicates that beneficial astroglial function in providing trophic support and mediating intracellular stress against toxic molecules is reduced during astrogliosis in PD [124, 127]. Therefore, as proposed earlier for microglia, compensating dysfunctional astrocytes is an appealing therapeutic option. Currently functional astrocytes can be generated from embryonic glial restricted precursor cells (GRPCs) [128] and human pluripotent stem cells [129, 130]. Embryonic GRPC-derived astrocytes are capable of releasing trophic factors and anti-oxidants and *in vivo* transplantation in the striatum of parkinsonian rats improved behavioral deficits and restored TH expression [128]. In a similar context, it can be envisioned to genetically modify human PSC-derived astrocytes in order to produce anti-oxidative agents or trophic factors.

Recently, direct cellular lineage conversion has allowed the differentiation of somatic cells into functional induced astrocytes (iAstrocytes) with functional and phenotypic features that are comparable to resident brain astrocytes [131]. Very interestingly, a recent report showed that fibroblasts can be directly converted into astrocytes by treatment with small compounds [132]. Although the therapeutic potential of iAstrocytes for glial cell-based gene therapy remains to be explored *in vivo*, they are of clinical interest as they could contribute as

safe and unlimited patient-specific source to glial cell-based therapy. Recently astrocytes have been proposed also as a potential *in vivo* target for neuronal generation by direct conversion. Direct *in vivo* lineage reprogramming involves the transdifferentiation of resident cells into other cell types through forced gene expression *in vivo*. Thus far, in the brain, functional subtypes of neurons have been directly generated *in vivo* from $NG2^+$ glial cells (oligodendrocyte progenitor cells), astrocytes and other types of neurons [133–140]. For PD, *in vivo* cell reprogramming has great therapeutic potential as it offer the possibility to restore nigrostriatal DA neurons by converting resident cells involved in the neurodegenerative process such as reactive glial cells. Successful reprogramming of these glial cells would have neurorestorative effect, while reducing the presence of reactive glial cells and at the same time altering disease progression. Astrocytes have efficiently been reprogrammed to midbrain DA neurons before *in vitro* [98], but to which extent this *in vitro* cell reprogramming approach can be expanded to *in vivo* reprogramming remains to be determined. *In vivo* reprogramming of microglia has not been done yet and most of the attempts to convert *in vivo* resident astrocytes did not give rise to DA neurons [134, 136, 139]. Very interestingly a recent work showed that mouse brain astrocytes can be converted *in vivo* into DA neurons also providing the first proof-of-principle evidence that this approach can be used to treat a PD animal model [111]. Nevertheless, as research in the field of direct *in vivo* reprogramming is still in its early stages, future developments may soon overcome current challenges to move this approach towards human applications (Fig. 5e).

Taken together, recent advances in cell reprogramming approaches offer a role for glial cells in new treatment strategies for PD (Fig. 5a-c). This opens a new avenue of therapies beyond cell-based DA replacement. As proposed before, *in vitro* reprogrammed microglia and astrocytes could be employed to compensate for dysfunctional glial cells in PD in addition to their role in other biomedical purposes such as disease modeling. This approach would consider to genetically modify *ex-vivo* iAstrocytes in order to secrete anti-oxidants and neurotrophic factors, that would be released, upon brain transplantation (Fig. 5d). Current advances in pharmacogenetics would facilitate the remote modulation of these cells and their therapeutic efficacy upon transplantation using DREADDs [141]. This has previously been demonstrated with *in vivo* transplanted iDA neurons in a rat model of PD [105] and its use could be expanded to astrocytes and microglia. DREADDs have already been used before to selectively and temporarily modulate cellular function of astrocytes and microglia *in vivo* [142, 143], supporting the feasibility to apply this approach (Fig. 5d).

12. Concluding remarks and future perspectives

Current PD treatment approaches primarily address motor dysfunction but are associated with significant drawbacks or decline in effectiveness over time. Over the past decades the focus of attention has been also pointed towards gene therapy strategies. Viral vector-based delivery of therapeutic genes became of great interests as it provides target-specificity as well as long-term transgene expression. Very interestingly viral delivery technology *via* AAVs is fastly improving as shown by the discovery of newly generated AAV9 serotypes with high specificity for the CNS that could allow systemic delivery for PD treatments [144–146].

On the other hand the successes in cellular reprogramming have supported the idea of patient-specific DA neurons directly from somatic cells. However, further developments are necessary to improve reprogramming efficiency of human somatic cells before translation in cell-based DA replacement therapy for PD. Importantly, we have to take into consideration that altering disease progression is of primary interest and that replacement of striatal DA alone does not necessarily have neurorestorative effect. Therefore, future research in this area

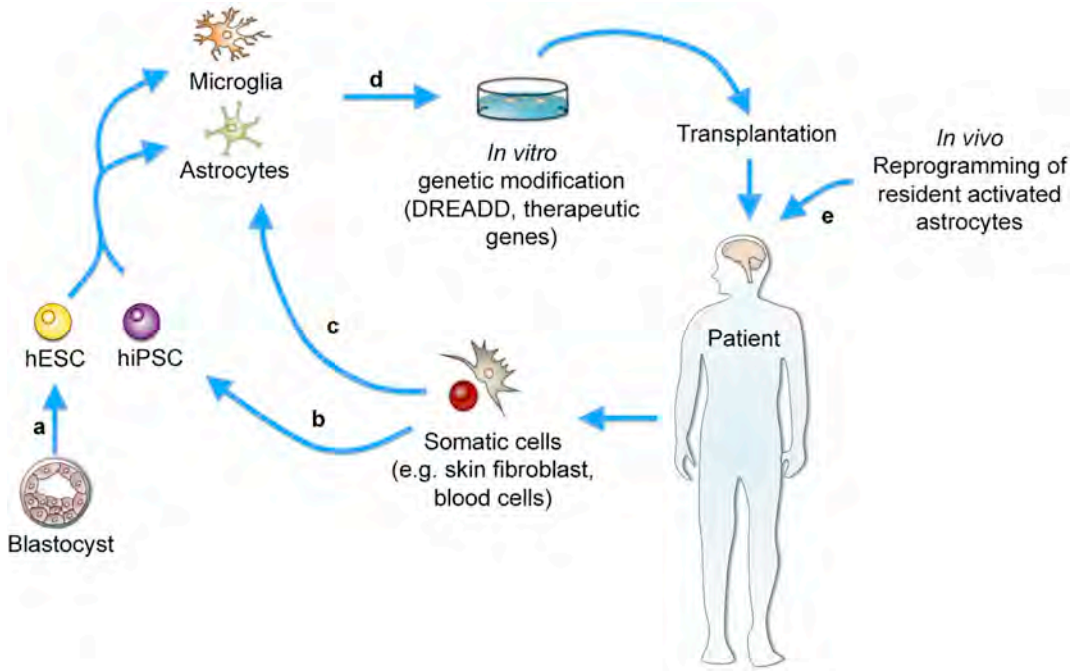


Fig. 5. Microglia and astrocytes as new key players in cell reprogramming approaches for cell-based gene therapy for PD. Reprogrammed microglia and astrocytes can be obtained from (a) hESCs or (b) hiPSCs. (c) An alternative approach to generate reprogrammed astrocytes is *via* direct *in vitro* reprogramming of somatic cells. (d) Reprogrammed glial cells can then be genetically modified *in vitro* to express therapeutic genes of interest (*e.g.* neurotrophic factors, anti-oxidants). Upon transplantation they can compensate for dysfunctional glial cells in PD. Furthermore, inducing the expression of DREADDs at the same time would allow the fine-tuning and remote control of activity and therapeutic effect of these reprogrammed glial cells upon transplantation. (e) Direct reprogramming of resident brain cells *in vivo* could be used to restore dopaminergic neurons at sites of degeneration without the need for transplantation. Resident (activated) glial cells are potential candidates for this therapeutic strategy. Abbreviations: hESC = human embryonic stem cell; hiPSC = human induced pluripotent stem cell.

should focus on how iDA neurons could be used as cell-based treatment for the regeneration of the nigrostriatal pathway in PD patients.

In order to alter disease progression, new therapies should also provide neuroprotection, pointing towards strategies to target pathogenic mechanisms that enhance neurodegeneration such as neuroinflammation. Dysfunctioning microglia and astrocytes remains an unresolved problem and contributes to the vicious cycle of neurodegeneration. With this in mind, we outlined potential cell reprogramming approaches for cell-based gene therapy for PD with glial cells as new key players. Another exciting perspective involving glial cells is the *in vivo* cell reprogramming to convert reactive microglia and astrocytes into functional DA neurons for neurorestorative purposes.

Overall, several efforts are currently put into the development of new PD therapies using our current knowledge in the use of stem cells and cell reprogramming to provide new symptomatic treatments and disease modifying cures to slow down, reverse or even prevent disease progression in PD patients.

References

[1] G.E. Alexander, Biology of Parkinson's disease: Pathogenesis and pathophysiology of a multisystem neurodegenerative disorder, Dialogues Clin. Neurosci. 6 (3) (2004) 259–280.

[2] D.T. Dexter, P. Jenner, Parkinson disease: from pathology to molecular disease mechanisms, Free Radic. Biol. Med. 62 (2013) 132–144.

[3] A.J. Lees, J. Hardy, T. Revesz, Parkinson's disease, Lancet 6736 (09) (2009) 60492-X.

[4] A. Björklund, S.B. Dunnett, Dopamine neuron systems in the brain: an update, Trends Neurosci. 30 (5) (2007) 194–202.

[5] J.L. Lanciego, N. Luquin, J.A. Obeso, Functional Neuroanatomy of the Basal Ganglia, Cold Spring Harbor Perspectives in Medicine 2 (12) (2012) a009621.

[6] M.R. Delong, T. Wichmann, Basal Ganglia Circuits as Targets for Neuromodulation in Parkinson Disease, JAMA Neurology 72 (11) (2015) 1354–1360.

[7] W. Oertel, J.B. Schulz, Current and experimental treatments of Parkinson disease: A guide for neuroscientists, J. Neurochem. 139 (S1) (2016) 1–13.

[8] C.C. Aquino, S.H. Fox, Clinical spectrum of levodopa-induced complications, Mov. Disord. 30 (1) (2015) 80–89.

[9] A.L. Benabid, S. Chabardes, J. Mitrofanis, P. Pollak, Deep brain stimulation of the subthalamic nucleus for the treatment of Parkinson's disease, The Lancet Neurology. 4422 (08) (2009) 70291–70296.

[10] P.A. Lewitt, S. Fahn, Levodopa therapy for Parkinson disease: A look backward and forward, Lippincott Williams & Wilkins, Neurology, 2016.

[11] R.A. Barker, J. Drouin-Ouellet, M. Parmar, Cell-based therapies for Parkinson disease-past insights and future potential. *Nature Reviews*, Neurology 11 (9) (2015) 492–503.

[12] R.T. Bartus, M.S. Weinberg, R.J. Samulski, Parkinson's disease gene therapy: success by design meets failure by efficacy, Mol. Ther. 22 (3) (2014) 487–497.

[13] J. Meiser, D. Weindl, K. Hiller, Complexity of dopamine metabolism, Cell Communication and Signaling 11 (1) (2013) 34.

[14] M. Azzouz, E. Martin-Rendon, R.D. Barber, K.A. Mitrophanous, E.E. Carter, J.B. Rohll, ... N.D. Mazarakis, Multicistronic lentiviral vector-mediated striatal gene transfer of aromatic L-amino acid decarboxylase, tyrosine hydroxylase, and GTP cyclohydrolase I induces sustained transgene expression, dopamine production, and functional improvement in a rat model, J. Neurosci. 22 (23) (2002) 10302–10312.

[15] K.S. Bankiewicz, J. Forsayeth, J.L. Eberling, R. Sanchez-Pernaute, P. Pivirotto, J. Bringas, ... J. Cunningham, Long-Term Clinical Improvement in MPTP-Lesioned Primates after Gene Therapy with AAV-hAADC, Mol. Ther. 14 (4) (2006) 564–570.

[16] M.J. During, R.J. Samulski, J.D. Elsworth, M.G. Kaplitt, P. Leone, X. Xiao, ... D.E. Redmond, In vivo expression of therapeutic human genes for dopamine production in the caudates of MPTP-treated monkeys using an AAV vector, Gene Ther. 5 (6) (1998) 820–827.

[17] D.S. Fan, M. Ogawa, K.I. Fujimoto, K. Ikeguchi, Y. Ogasawara, M. Urabe, ... K. Ozawa, Behavioral recovery in 6-hydroxydopamine-lesioned rats by co-transduction of striatum with tyrosine hydroxylase and aromatic L-amino acid decarboxylase genes using two separate adeno-associated virus vectors, Hum. Gene Ther. 9 (17) (1998) 2527–2535.

[18] J.R. Forsayeth, J.L. Eberling, L.M. Sanftner, Z. Zhen, P. Pivirotto, J. Bringas, ... K.S. Bankiewicz, A Dose-Ranging Study of AAV-hAADC Therapy in Parkinsonian Monkeys, Mol. Ther. 14 (4) (2006) 571–577.

[19] P. Hadaczek, J.L. Eberling, P. Pivirotto, J. Bringas, J. Forsayeth, K.S. Bankiewicz, Eight years of clinical improvement in MPTP-lesioned primates after gene therapy with AAV2-hAADC, Mol. Ther. 18 (8) (2010) 1458–1461.

[20] B. Jarraya, S. Boulet, G.S. Ralph, C. Jan, G. Bonvento, M. Azzouz, ... S. Palfi, Dopamine gene therapy for Parkinson's disease in a nonhuman primate without associated dyskinesia, Sci. Transl. Med. *1* (2) (2009) 2ra4.

[21] C.W. Christine, P.A. Starr, P.S. Larson, J.L. Eberling, W.J. Jagust, R.A. Hawkins, ... M.J. Aminoff, Safety and tolerability of putaminal AADC gene therapy for Parkinson disease, Neurology 73 (20) (2009) 1662–1669.

[22] J.L. Eberling, W.J. Jagust, C.W. Christine, P. Starr, P. Larson, K.S. Bankiewicz, M.J. Aminoff, Results from a phase I safety trial of hAADC gene therapy for Parkinson disease, Neurology 70 (21) (2008) 1980–1983.

[23] S. Muramatsu, K. Fujimoto, S. Kato, H. Mizukami, S. Asari, K. Ikeguchi, ... I. Nakano, A Phase I Study of Aromatic L-Amino Acid Decarboxylase Gene Therapy for Parkinson'ns Disease, Mol. Ther. 18 (9) (2010) 1731–1735.

[24] G. Mittermeyer, C.W. Christine, K.H. Rosenbluth, S.L. Baker, P. Starr, P. Larson, ... K.S. Bankiewicz, Long-term evaluation of a phase 1 study of AADC gene therapy for Parkinson's disease, Hum. Gene Ther. 23 (4) (2012) 377–381.

[25] S. Palfi, J.M. Gurruchaga, G. Scott Ralph, H. Lepetit, S. Lavisse, P.C. Buttery, ... K.A. Mitrophanous, Long-term safety and tolerability of ProSavin, a lentiviral vector-based gene therapy for Parkinson's disease: A dose escalation, open-label, phase 1/2 trial, Lancet 383 (9923) (2014) 1138–1146.

[26] W.M. Caudle, R.E. Colebrooke, P.C. Emson, G.W. Miller, Altered vesicular dopamine storage in Parkinson's disease: a premature demise, Trends Neurosci. 31 (6) (2008) 303–308.

[27] L. Chen, Y. Ding, B. Cagniard, A.D. Van Laar, A. Mortimer, W. Chi, ... X. Zhuang, Unregulated cytosolic dopamine causes neurodegeneration associated with oxidative stress in mice, J. Neurosci. 28 (2) (2008) 425–433.

[28] M. Cyr, J.M. Beaulieu, A. Laakso, T.D. Sotnikova, W.D. Yao, L.M. Bohn, ... M.G. Caron, Sustained elevation of extracellular dopamine causes motor dysfunction and selective degeneration of striatal GABAergic neurons, Proc. Natl. Acad. Sci. U. S. A. 100 (19) (2003) 11035–11040.

[29] M.E. Emborg, M. Carbon, J.E. Holden, M.J. During, Y. Ma, C. Tang, ... D. Eidelberg, Subthalamic glutamic acid decarboxylase gene therapy: changes in motor function and cortical metabolism, J. Cereb. Blood Flow Metab. 27 (3) (2007) 501–509.

[30] J. Luo, M.G. Kaplitt, H.L. Fitzsimons, D.S. Zuzga, Y. Liu, M.L. Oshinsky, M.J. During, Subthalamic GAD gene therapy in a Parkinson's disease rat model, Science (New York, N.Y.) *298* (5592) (2002) 425–429.

[31] M.G. Kaplitt, A. Feigin, C. Tang, H.L. Fitzsimons, P. Mattis, P.A. Lawlor, ... M.J. During, Safety and tolerability of gene therapy with an adeno-associated virus (AAV) borne GAD gene for Parkinson's disease: an open label, phase I trial, Lancet 369 (9579) (2007) 2097–2105.

[32] P.A. Lewitt, A.R. Rezai, M.A. Leehey, S.G. Ojemann, A.W. Flaherty, E.N. Eskandar, ... A. Feigin, AAV2-GAD gene therapy for advanced Parkinson's disease: A double-blind, sham-surgery controlled, randomised trial, Lancet Neurol. 4422 (11) (2011) (70039–4).

[33] K. Krieglstein, Factors promoting survival of mesencephalic dopaminergic neurons, Cell Tissue Res. 318 (1) (2004) 73–80.

[34] M. Gasmi, E.P. Brandon, C.D. Herzog, A. Wilson, K.M. Bishop, E.K. Hofer, ... R.T. Bartus, AAV2-mediated delivery of human neurturin to the rat nigrostriatal system: Long-term efficacy and tolerability of CERE-120 for Parkinson's disease, Neurobiol. Dis. 27 (1) (2007) 67–76.

[35] A.P. Kells, J. Eberling, X. Su, P. Pivirotto, J. Bringas, P. Hadaczek, ... K.S. Bankiewicz, Regeneration of the MPTP-Lesioned Dopaminergic System after Convection-Enhanced Delivery of AAV2-GDNF, J. Neurosci. 30 (28) (2010) 9567–9577.

[36] J.H. Kordower, C.D. Herzog, B. Dass, R.A.E. Bakay, J. Stansell, M. Gasmi, R.T. Bartus, Delivery of neurturin by AAV2 (CERE-120)-mediated gene transfer provides structural and functional neuroprotection and neurorestoration in MPTP-treated monkeys, Ann. Neurol. 60 (6) (2006) 706–715.

[37] L. Wang, S. Muramatsu, Y. Lu, K. Ikeguchi, K. Fujimoto, T. Okada, ... K. Ozawa, Delayed delivery of AAV-GDNF prevents nigral neurodegeneration and promotes functional recovery in a rat model of Parkinson's disease, Gene Ther. 9 (6) (2002) 381–389.

[38] W.J. Marks, J.L. Ostrem, L. Verhagen, P.A. Starr, P.S. Larson, R.A. Bakay, ... R.T. Bartus, Safety and tolerability of intraputaminal delivery of CERE-120 (adeno-associated virus serotype 2-neurturin) to patients with idiopathic Parkinson's disease: an open-label, phase I trial, The Lancet Neurology 4422 (08) (2008) 70065–70066.

[39] W.J. Marks, R.T. Bartus, J. Siffert, C.S. Davis, A. Lozano, N. Boulis, ... C.W. Olanow, Gene delivery of AAV2-neurturin for Parkinson's disease: a double-blind, randomised, controlled trial, The Lancet Neurology 9 (12) (2010) 1164–1172.

[40] R.T. Bartus, T.L. Baumann, J. Siffert, C.D. Herzog, R. Alterman, N. Boulis, ... C. Warren Olanow, Safety/feasibility of targeting the substantia nigra with AAV2-neurturin in Parkinson patients, Neurology 80 (18) (2013) 1698–1701.

[41] C. Warren Olanow, R.T. Bartus, T.L. Baumann, S. Factor, N. Boulis, M. Stacy, ... A.E. Lang, Gene delivery of neurturin to putamen and substantia nigra in Parkinson disease: A double-blind, randomized, controlled trial, Ann. Neurol. 78 (2) (2015) 248–257.

[42] A. Eslamboli, B. Georgievska, R.M. Ridley, H.F. Baker, N. Muzyczka, C. Burger, ... D. Kirik, Continuous Low-Level Glial Cell Line-Derived Neurotrophic Factor Delivery Using Recombinant Adeno-Associated Viral Vectors Provides Neuroprotection and Induces Behavioral Recovery in a Primate Model of Parkinson's Disease, J. Neurosci. 25 (4) (2005) 769–777.

[43] B. Georgievska, D. Kirik, A. Björklund, Aberrant sprouting and downregulation of tyrosine hydroxylase in lesioned nigrostriatal dopamine neurons induced by long-lasting overexpression of glial cell line derived neurotrophic factor in the striatum by lentiviral gene transfer, Exp. Neurol. 177 (2) (2002) 461–474.

[44] D. Kirik, C. Rosenblad, A. Bjorklund, R.J. Mandel, Long-term rAAV-mediated gene transfer of GDNF in the rat Parkinson's model: intrastriatal but not intranigral transduction promotes functional regeneration in the lesioned nigrostriatal system, J. Neurosci. 20 (12) (2000) 4686–4700.

[45] S.S. Gill, N.K. Patel, G.R. Hotton, K. O'Sullivan, R. McCarter, M. Bunnage, ... P. Heywood, Direct brain infusion of glial cell line-derived neurotrophic factor in

Parkinson disease, Nat. Med. 9 (5) (2003) 589–595.
[46] A.E. Lang, S. Gill, N.K. Patel, A. Lozano, J.G. Nutt, R. Penn, ... M. Traub, Randomized controlled trial of intraputamenal glial cell line-derived neurotrophic factor infusion in Parkinson disease, Ann. Neurol. 59 (3) (2006) 459–466.
[47] J.T. Slevin, Gerhardt, G. A, Smith, C. D., Gash, D. M., Kryscio, R., & Young, B., Improvement of bilateral motor functions in patients with Parkinson disease through the unilateral intraputaminal infusion of glial cell line-derived neurotrophic factor, J. Neurosurg. 102 (2) (2005) 216–222.
[48] A.E.-E. Aly, B.L. Waszczak, Intranasal gene delivery for treating Parkinson's disease: overcoming the blood-brain barrier, Expert Opinion on Drug Delivery 5247 (2015) 1–19.
[49] M.M. Migliore, R. Ortiz, S. Dye, R.B. Campbell, M.M. Amiji, B.L. Waszczak, Neurotrophic and neuroprotective efficacy of intranasal GDNF in a rat model of Parkinson's disease, Neuroscience 274 (2014) 11–23.
[50] R.A. Barker, J. Barrett, S.L. Mason, A. Björklund, Fetal dopaminergic transplantation trials and the future of neural grafting in Parkinson's disease, The Lancet Neurology. 4422 (12) (2013) 70295–70298.
[51] O. Lindvall, A. Björklund, Cell therapy in Parkinson's disease, NeuroRx 1 (4) (2004) 382–393.
[52] C.R. Freed, P.E. Greene, R.E. Breeze, W.-Y. Tsai, W. Dumouchel, R. Kao, ... S. Fahn, Transplantation of Embryonic Dopamine Neurons for Severe Parkinson's Disease, N. Engl. J. Med. 344 (10) (2001) 710–719.
[53] C.W. Olanow, J.M. Gracies, C.G. Goetz, A.J. Stoessl, T. Freeman, J.H. Kordower, ... J.A. Obeso, Clinical pattern and risk factors for dyskinesias following fetal nigral transplantation in parkinson's disease: A double blind video-based analysis, Mov. Disord. 24 (3) (2009) 336–343.
[54] Y. Ma, A. Feigin, V. Dhawan, M. Fukuda, Q. Shi, P. Greene, ... D. Eidelberg, Dyskinesia after fetal cell transplantation for parkinsonism: A PET study, Ann. Neurol. 52 (5) (2002) 628–634.
[55] P. Hagell, P. Piccini, A. Björklund, P. Brundin, S. Rehncrona, H. Widner, ... O. Lindvall, Dyskinesias following neural transplantation in Parkinson's disease, Nat. Neurosci. 5 (7) (2002) 627–628.
[56] E.L. Lane, L. Vercammen, M.A. Cenci, P. Brundin, Priming for L-DOPA-induced abnormal involuntary movements increases the severity of amphetamine-induced dyskinesia in grafted rats, Exp. Neurol. 219 (1) (2009) 355–358.
[57] T. Carlsson, C. Winkler, M. Lundblad, M.A. Cenci, A. Björklund, D. Kirik, Graft placement and uneven pattern of reinnervation in the striatum is important for development of graft-induced dyskinesia, Neurobiol. Dis. 21 (3) (2006) 657–668 https://doi.org/10.1016/j.nbd.2005.09.008.
[58] E. Maries, J.H. Kordower, Y. Chu, T.J. Collier, C.E. Sortwell, E. Olaru, ... K. Steece-Collier, Focal not widespread grafts induce novel dyskinetic behavior in parkinsonian rats, Neurobiol. Dis. 21 (1) (2006) 165–180 https://doi.org/10.1016/j.nbd.2005.07.002.
[59] P. Piccini, N. Pavese, P. Hagell, J. Reimer, A. Björklund, W.H. Oertel, ... O. Lindvall, Factors affecting the clinical outcome after neural transplantation in Parkinson's disease, Brain 128 (12) (2005) 2977–2986.
[60] E. Shin, J. Garcia, C. Winkler, A. Björklund, M. Carta, Serotonergic and dopaminergic mechanisms in graft-induced dyskinesia in a rat model of Parkinson's disease, Neurobiol. Dis. 47 (3) (2012) 393–406.
[61] L.H. Thompson, D. Kirik, A. Björklund, Non-dopaminergic neurons in ventral mesencephalic transplants make widespread axonal connections in the host brain, Exp. Neurol. 213 (1) (2008) 220–228.
[62] R.A. Barker, I. de Beaufort, Scientific and ethical issues related to stem cell research and interventions in neurodegenerative disorders of the brain, Prog. Neurobiol. 110 (2013) 63–73.
[63] S.-H. Lee, N. Lumelsky, L. Studer, J.M. Auerbach, R.D. McKay, Efficient generation of midbrain and hindbrain neurons from mouse embryonic stem cells, Nat. Biotechnol. 18 (6) (2000) 675–679.
[64] J.-H. Kim, J.M. Auerbach, J.A. Rodríguez-Gómez, I. Velasco, D. Gavin, N. Lumelsky, R. McKay, Dopamine neurons derived from embryonic stem cells function in an animal model of Parkinson's disease, Nature 418 (6893) (2002) 50–56.
[65] A. Brederlau, A.S. Correia, S.V. Anisimov, M. Elmi, G. Paul, L. Roybon, ... J.-Y. Li, Transplantation of Human Embryonic Stem Cell-Derived Cells to a Rat Model of Parkinson's Disease: Effect of In Vitro Differentiation on Graft Survival and Teratoma Formation, Stem Cells 24 (6) (2006) 1433–1440.
[66] A.L. Perrier, V. Tabar, T. Barberi, M.E. Rubio, J. Bruses, N. Topf, ... L. Studer, Derivation of midbrain dopamine neurons from human embryonic stem cells, Proc. Natl. Acad. Sci. U. S. A. 101 (34) (2004) 12543–12548.
[67] K.-C. Sonntag, J. Pruszak, T. Yoshizaki, J. van Arensbergen, R. Sanchez-Pernaute, O. Isacson, Enhanced Yield of Neuroepithelial Precursors and Midbrain-Like Dopaminergic Neurons from Human Embryonic Stem Cells Using the Bone Morphogenic Protein Antagonist Noggin, Stem Cells 25 (2) (2007) 411–418.
[68] X. Zeng, J. Cai, J. Chen, Y. Luo, Z. You, E. Fotter, ... W.J. Freed, DA differentiation of human embryonic stem cells, Stem Cells 22 (6) (2004) 925–940.
[69] N.S. Roy, C. Cleren, S.K. Singh, L. Yang, M.F. Beal, S.A. Goldman, Functional engraftment of human ES cell–derived dopaminergic neurons enriched by coculture with telomerase-immortalized midbrain astrocytes, Nat. Med. 12 (11) (2006) 1259–1268.
[70] O. Cooper, G. Hargus, M. Deleidi, A. Blak, T. Osborn, E. Marlow, ... O. Isacson, Differentiation of human ES and Parkinson's disease iPS cells into ventral midbrain dopaminergic neurons requires a high activity form of SHH, FGF8a and specific regionalization by retinoic acid, Mol. Cell. Neurosci. 45 (3) (2010) 258–266.
[71] C.-H. Park, Y.-K. Minn, J.-Y. Lee, D.H. Choi, M.-Y. Chang, J.-W. Shim, ... S.-H. Lee, In vitro and in vivo analyses of human embryonic stem cell-derived dopamine neurons, J. Neurochem. 92 (5) (2005) 1265–1276.
[72] E. Arenas, M. Denham, J.C. Villaescusa, How to make a midbrain dopaminergic neuron, Development (Cambridge, England) 142 (11) (2015) 1918–1936.
[73] S.V. Hegarty, A.M. Sullivan, G.W. O'Keeffe, Midbrain dopaminergic neurons: A review of the molecular circuitry that regulates their development, Dev. Biol. 379 (2) (2013) 123–138.
[74] A. Kirkeby, S. Grealish, D.A. Wolf, J. Nelander, J. Wood, M. Lundblad, ... M. Parmar, Generation of Regionally Specified Neural Progenitors and Functional Neurons from Human Embryonic Stem Cells under Defined Conditions, Cell Rep. 1 (6) (2012) 703–714.
[75] S. Kriks, J.-W. Shim, J. Piao, Y.M. Ganat, D.R. Wakeman, Z. Xie, ... L. Studer, Dopamine neurons derived from human ES cells efficiently engraft in animal models of Parkinson's disease, Nature (2011) 480.
[76] S. Grealish, E. Diguet, A. Kirkeby, B. Mattsson, A. Heuer, Y. Bramoulle, ... M. Parmar, Human ESC-derived dopamine neurons show similar preclinical efficacy and potency to fetal neurons when grafted in a rat model of Parkinson's disease, Cell Stem Cell 15 (5) (2014) 653–665 https://doi.org/10.1016/j.stem.2014.09.017.
[77] J.A. Steinbeck, S.J. Choi, A. Mrejeru, Y. Ganat, K. Deisseroth, D. Sulzer, ... L. Studer, Optogenetics enables functional analysis of human embryonic stem cell–derived grafts in a Parkinson's disease model, Nat. Biotechnol. 33 (2) (2015) 204–209.
[78] R.A. Barker, L. Studer, E. Cattaneo, J. Takahashi, G-Force PD: a global initiative in coordinating stem cell-based dopamine treatments for Parkinson's disease, NPJ Parkinsons Dis. 1 (2015) 15017.
[79] R.A. Barker, M. Parmar, L. Studer, J. Takahashi, Human trials of stem cell-derived dopamine neurons for Parkinson's disease: dawn of a new era, Cell Stem Cell 21 (2017) 569–573.
[80] K. Takahashi, S. Yamanaka, Induction of Pluripotent Stem Cells from Mouse Embryonic and Adult Fibroblast Cultures by Defined Factors, Cell 126 (4) (2006) 663–676.
[81] K. Takahashi, K. Okita, M. Nakagawa, S. Yamanaka, Induction of pluripotent stem cells from fibroblast cultures, Nat. Protoc. 2 (12) (2007) 3081–3089.
[82] D. Doi, B. Samata, M. Katsukawa, T. Kikuchi, A. Morizane, Y. Ono, ... J. Takahashi, Isolation of Human Induced Pluripotent Stem Cell-Derived Dopaminergic Progenitors by Cell Sorting for Successful Transplantation, Stem Cell Reports 2 (3) (2014) 337–350.
[83] P.J. Hallett, M. Deleidi, A. Astradsson, G.A. Smith, O. Cooper, T.M. Osborn, ... O. Isacson, Successful Function of Autologous iPSC-Derived Dopamine Neurons following Transplantation in a Non-Human Primate Model of Parkinson's Disease, Cell Stem Cell 16 (2015).
[84] G. Hargus, O. Cooper, M. Deleidi, A. Levy, K. Lee, E. Marlow, ... O. Isacson, Differentiated Parkinson patient-derived induced pluripotent stem cells grow in the adult rodent brain and reduce motor asymmetry in Parkinsonian rats, Proc. Natl. Acad. Sci. U. S. A. 107 (36) (2010) 15921–15926.
[85] T. Kikuchi, A. Morizane, D. Doi, H. Onoe, T. Hayashi, T. Kawasaki, ... J. Takahashi, Survival of human induced pluripotent stem cell-derived midbrain dopaminergic neurons in the brain of a primate model of Parkinson's disease, Journal of Parkinson's Disease 1 (4) (2011) 395–412.
[86] M. Sundberg, H. Bogetofte, T. Lawson, J. Jansson, G. Smith, A. Astradsson, ... O. Isacson, Improved cell therapy protocols for Parkinson's disease based on differentiation efficiency and safety of hESC-, hiPSC-, and non-human primate iPSC-derived dopaminergic neurons, Stem Cells 31 (8) (2013) 1548–1562.
[87] M. Wernig, J.-P. Zhao, J. Pruszak, E. Hedlund, D. Fu, F. Soldner, ... R. Jaenisch, Neurons derived from reprogrammed fibroblasts functionally integrate into the fetal brain and improve symptoms of rats with Parkinson's disease, Proc. Natl. Acad. Sci. U. S. A. 105 (15) (2008) 5856–5861.
[88] S. Markoulaki, J. Hanna, C. Beard, B.W. Carey, A.W. Cheng, C.J. Lengner, ... R. Jaenisch, Transgenic mice with defined combinations of drug-inducible reprogramming factors, Nat. Biotechnol. 27 (2) (2009) 169–171.
[89] K. Okita, T. Ichisaka, S. Yamanaka, Generation of germline-competent induced pluripotent stem cells, Nature 448 (7151) (2007) 313–317.
[90] K. Okita, Generation of mouse induced pluripotent stem cells without viral vectors, Science 322 (2008) 949–953.
[91] M. Stadtfeld, M. Nagaya, J. Utikal, G. Weir, K. Hochedlinger, Induced Pluripotent Stem Cells Generated Without Viral Integration, Science 322 (2008) 945–949.
[92] D. Kim, C.-H. Kim, J.-I. Moon, Y.-G. Chung, M.-Y. Chang, B.-S. Han, ... K.-S. Kim, Generation of human induced pluripotent stem cells by direct delivery of reprogramming proteins, Cell Stem Cell 4 (6) (2009) 472–476.
[93] Y.H. Rhee, J.Y. Ko, M.Y. Chang, S.H. Yi, D. Kim, C.H. Kim, ... S.H. Lee, Protein-based human iPS cells efficiently generate functional dopamine neurons and can treat a rat model of Parkinson disease, J. Clin. Investig. 121 (6) (2011) 2326–2335.
[94] K. Okita, H. Hong, K. Takahashi, S. Yamanaka, Generation of mouse-induced pluripotent stem cells with plasmid vectors, Nat. Protoc. 5 (3) (2010) 418–428.
[95] Y.-D. Sohn, I. Somasuntharam, P.-L. Che, R. Jayswal, N. Murthy, M.E. Davis, Y.-S. Yoon, Induction of pluripotency in bone marrow mononuclear cells via polyketal nanoparticle-mediated delivery of mature microRNAs, Biomaterials 34 (17) (2013) 4235–4241.
[96] L. Warren, P.D. Manos, T. Ahfeldt, Y.-H. Loh, H. Li, F. Lau, ... D.J. Rossi, Highly efficient reprogramming to pluripotency and directed differentiation of human cells using synthetic modified mRNA, Cell Stem Cell Cell Stem Cell 5 (75) (2010) 618–630.
[97] F. Soldner, D. Hockemeyer, C. Beard, Q. Gao, G.W. Bell, E.G. Cook, ... R. Jaenisch, Parkinson's Disease Patient-Derived Induced Pluripotent Stem Cells Free of Viral Reprogramming Factors, Cell 136 (5) (2009) 964–977.
[98] R.C. Addis, F.C. Hsu, R.L. Wright, M.A. Dichter, D.A. Coulter, J.D. Gearhart, Efficient conversion of astrocytes to functional midbrain dopaminergic neurons

using a single polycistronic vector, PLoS One 6 (12) (2011).
[99] M. Caiazzo, M.T. Dell'Anno, E. Dvoretskova, D. Lazarevic, S. Taverna, D. Leo, ... V. Broccoli, Direct generation of functional dopaminergic neurons from mouse and human fibroblasts, Nature 476 (7359) (2011) 224–227.
[100] J. Kim, S.C. Su, H. Wang, A.W. Cheng, J.P. Cassady, M.A. Lodato, ... R. Jaenisch, Functional integration of dopaminergic neurons directly converted from mouse fibroblasts, Cell Stem Cell 9 (5) (2011) 413–419.
[101] X. Liu, F. Li, E.A. Stubblefield, B. Blanchard, T.L. Richards, G.A. Larson, ... C.-Y. Li, Direct reprogramming of human fibroblasts into dopaminergic neuron-like cells, Cell Res. 22 (2) (2012) 321–332.
[102] U. Pfisterer, A. Kirkeby, O. Torper, J. Wood, J. Nelander, A. Dufour, ... M. Parmar, Direct conversion of human fibroblasts to dopaminergic neurons, Proc. Natl. Acad. Sci. U. S. A. 108 (25) (2011) 10343–10348.
[103] H. Jiang, Z. Xu, P. Zhong, Y. Ren, G. Liang, H.A. Schilling, ... J. Feng, Cell cycle and p53 gate the direct conversion of human fibroblasts to dopaminergic neurons, Nat. Commun. 6 (2015) 10100.
[104] X. Liu, Q. Huang, F. Li, C.Y. Li, Enhancing the efficiency of direct reprogramming of human primary fibroblasts into dopaminergic neuron-like cells through p53 suppression, Sci. China Life Sci. 57 (9) (2014) 867–875.
[105] M.T. Dell'Anno, M. Caiazzo, D. Leo, E. Dvoretskova, L. Medrihan, G. Colasante, ... V. Broccoli, Remote control of induced dopaminergic neurons in parkinsonian rats, J. Clin. Investig. 124 (7) (2014) 3215–3229.
[106] B.L. Roth, DREADDs for Neuroscientists, Neuron 89 (4) (2016) 683–694.
[107] D.J. Urban, B.L. Roth, DREADDs (Designer Receptors Exclusively Activated by Designer Drugs): Chemogenetic Tools with Therapeutic Utility, Annu. Rev. Pharmacol. Toxicol. 55 (1) (2015) 399–417.
[108] A.S. Yoo, A.X. Sun, L. Li, A. Shcheglovitov, T. Portmann, Y. Li, C. Lee-Messer, R.E. Dolmetsch, R.W. Tsien, G.R. Crabtree, MicroRNA-mediated conversion of human fibroblasts to neurons, Nature 476 (7359) (2011) 228–231.
[109] J. Drouin-Ouellet, S. Lau, P.L. Brattås, Ottosson D. Rylander, K. Pircs, D.A. Grassi, L.M. Collins, R. Vuono, Sjöland A. Andersson, G. Westergren-Thorsson, C. Graff, L. Minthon, H. Toresson, R.A. Barker, J. Jakobsson, M. Parmar, REST suppression mediates neural conversion of adult human fibroblasts via microRNA-dependent and -independent pathways, EMBO Mol. Med 9 (8) (2017) 1117–1131.
[110] De Gregorio R., Pulcrano S., De Sanctis C., Volpicelli F., Esposito R., Perrone-Capano C., Smidt M., Costa V., Greco D., Di Porzio U., Caiazzo M., Li M., Bellenchi GC. miR-34b/c enhances mesencephalic dopaminergic neuron differentiation by negatively modulating Wnt signaling. Stem Cell Reports, 2018; 0(4):1237–1250.
[111] P. Rivetti Di Val Cervo, R.A. Romanov, G. Spigolon, D. Masini, E. Martín-Montañez, E.M. Toledo, G. La Manno, M. Feyder, C. Pifl, Y.H. Ng, S.P. Sánchez, S. Linnarsson, M. Wernig, T. Harkany, G. Fisone, E. Arenas, Induction of functional dopamine neurons from human astrocytes in vitro and mouse astrocytes in a Parkinson's disease model, Nat. Biotechnol. 35 (5) (2017) 444–452.
[112] C.K. Glass, K. Saijo, B. Winner, M.C. Marchetto, F.H. Gage, Mechanisms Underlying Inflammation in Neurodegeneration, Cell 140 (6) (2010) 918–934.
[113] C. Heinrich, F.M. Spagnoli, B. Berninger, In vivo reprogramming for tissue repair, Nat. Cell Biol. 17 (3) (2015) 204–211.
[114] V. Joers, M.G. Tansey, G. Mulas, A.R. Carta, Microglial phenotypes in Parkinson's disease and animal models of the disease, Prog. Neurobiol. 155 (2015) 57–75.
[115] Q. Wang, Y. Liu, J. Zhou, Neuroinflammation in Parkinson's disease and its potential as therapeutic target, Translational Neurodegeneration 4 (1) (2015) 19.
[116] P.L. McGeer, S. Itagaki, B.E. Boyes, E.G. McGeer, Reactive microglia are positive for HLA-DR in the substantia nigra of Parkinson's and Alzheimer's disease brains, Neurology 38 (8) (1988) 1285–1291.
[117] F. Ginhoux, S. Lim, G. Hoeffel, D. Low, T. Huber, Origin and differentiation of microglia, Front. Cell. Neurosci. 7 (2013) 45.
[118] M. Rodriguez, L. Alvarez-Erviti, F.J. Blesa, M.C. Rodríguez-Oroz, A. Arina, I. Melero, ... J.A. Obeso, Bone-marrow-derived cell differentiation into microglia: A study in a progressive mouse model of Parkinson's disease, Neurobiol. Dis. 28 (3) (2007) 316–325.
[119] N. Cartier, C.A. Lewis, R. Zhang, F.M.V. Rossi, The role of microglia in human disease: Therapeutic tool or target? Acta Neuropathologica, 128 (3) Springer, 2014, pp. 363–380.
[120] K.C. Biju, R.A. Santacruz, C. Chen, Q. Zhou, J. Yao, S.L. Rohrabaugh, ... S. Li, Bone marrow-derived microglia-based neurturin delivery protects against dopaminergic neurodegeneration in a mouse model of Parkinson's disease, Neurosci. Lett. 535 (1) (2013) 24–29.
[121] K.C. Biju, Q. Zhou, G. Li, S.Z. Imam, J.L. Roberts, W.W. Morgan, ... S. Li, Macrophage-mediated GDNF delivery protects against dopaminergic neurodegeneration: a therapeutic strategy for Parkinson's disease, Mol. Ther. 18 (8) (2010) 1536–1544.
[122] K.-W. Park, M.A. Eglitis, M.M. Mouradian, Protection of nigral neurons by GDNF-engineered marrow cell transplantation, Neurosci. Res. 40 (4) (2001) 315–323.
[123] J. Muffat, Y. Li, B. Yuan, M. Mitalipova, A. Omer, S. Corcoran, ... R. Jaenisch, Efficient derivation of microglia-like cells from human pluripotent stem cells, Nat. Med. 22 (11) (2016) 1358–1367.
[124] L. Ben Haim, M.-A. Carrillo-De Sauvage, K. Ceyzériat, C. Escartin, Elusive roles for reactive astrocytes in neurodegenerative diseases, Front. Cell. Neurosci. 9 (2015) 278.
[125] X.-L. Gu, C.-X. Long, L. Sun, C. Xie, X. Lin, H. Cai, Astrocytic expression of Parkinson's disease-related A53T alpha-synuclein causes neurodegeneration in mice, Molecular Brain 3 (2010) 12.
[126] K. Saijo, B. Winner, C.T. Carson, J.G. Collier, L. Boyer, M.G. Rosenfeld, ... C.K. Glass, A Nurr1/CoREST Pathway in Microglia and Astrocytes Protects Dopaminergic Neurons from Inflammation-Induced Death, Cell 137 (1) (2009) 47–59.
[127] P.M. Rappold, K. Tieu, Astrocytes and Therapeutics for Parkinson's Disease, Neurotherapeutics 7 (2010) 413–423.
[128] C. Proschel, J.L. Stripay, C.H. Shih, J.C. Munger, M.D. Noble, Delayed transplantation of precursor cell-derived astrocytes provides multiple benefits in a rat model of Parkinsons, EMBO Molecular Medicine 6 (4) (2014) 504–518.
[129] R. Krencik, J.P. Weick, Y. Liu, Z.-J. Zhang, S.-C. Zhang, Specification of transplantable astroglial subtypes from human pluripotent stem cells, Nat. Biotechnol. 29 (6) (2011) 528–534.
[130] A. Shaltouki, J. Peng, Q. Liu, M.S. Rao, X. Zeng, Efficient generation of astrocytes from human pluripotent stem cells in defined conditions, Stem Cells 31 (5) (2013) 941–952.
[131] M. Caiazzo, S. Giannelli, P. Valente, G. Lignani, A. Carissimo, A. Sessa, ... V. Broccoli, Direct conversion of fibroblasts into functional astrocytes by defined transcription factors, Stem Cell Reports 4 (1) (2015) 25–36.
[132] E. Tian, G. Sun, G. Sun, J. Chao, P. Ye, C. Warden, A.D. Riggs, Y. Shi, Small-molecule-based lineage reprogramming creates functional astrocytes, Cell Rep. 16 (3) (2016) 78–192.
[133] A. De la Rossa, C. Bellone, B. Golding, I. Vitali, J. Moss, N. Toni, ... D. Jabaudon, In vivo reprogramming of circuit connectivity in postmitotic neocortical neurons, Nat. Neurosci. 16 (2) (2013) 193–200.
[134] Z. Guo, L. Zhang, Z. Wu, Y. Chen, F. Wang, G. Chen, In vivo direct reprogramming of reactive glial cells into functional neurons after brain injury and in an Alzheimer's disease model, Cell Stem Cell 14 (2) (2014) 188–202.
[135] C. Heinrich, M. Bergami, S. Gascon, A. Lepier, F. Vigano, L. Dimou, ... M. Gotz, Sox2-mediated conversion of NG2 glia into induced neurons in the injured adult cerebral cortex, Stem Cell Reports 3 (6) (2014) 1000–1014.
[136] W. Niu, T. Zang, Y. Zou, S. Fang, D.K. Smith, R. Bachoo, C.-L. Zhang, In vivo reprogramming of astrocytes to neuroblasts in the adult brain, Nat. Cell Biol. 15 (10) (2013) 1164–1175.
[137] C. Rouaux, P. Arlotta, Direct lineage reprogramming of post-mitotic callosal neurons into corticofugal neurons in vivo, Nat. Cell Biol. 15 (2) (2013) 214–221.
[138] Z. Su, W. Niu, M.L. Liu, Y. Zou, C.L. Zhang, In vivo conversion of astrocytes to neurons in the injured adult spinal cord, Nat. Commun. 5 (2014) 3338.
[139] O. Torper, D.R. Ottosson, M. Pereira, S. Lau, T. Cardoso, S. Grealish, M. Parmar, In Vivo Reprogramming of Striatal NG2 Glia into Functional Neurons that Integrate into Local Host Circuitry, Cell Rep. 12 (3) (2015) 474–481.
[140] O. Torper, U. Pfisterer, D.A. Wolf, M. Pereira, S. Lau, J. Jakobsson, M. Parmar, Generation of induced neurons via direct conversion in vivo, Proc. Natl. Acad. Sci. U. S. A. 110 (17) (2013) 7038–7043.
[141] H. Zhu, B.L. Roth, DREADD: A chemogenetic GPCR signaling platform, Int. J. Neuropsychopharmacol. 18 (1) (2015) (pii: pyu007).
[142] J. Bang, H.Y. Kim, H. Lee, Optogenetic and Chemogenetic Approaches for Studying Astrocytes and Gliotransmitters, Experimental Neurobiology 25 (5) (2016) 205–221.
[143] P.M. Grace, K.A. Strand, E.L. Galer, D.J. Urban, X. Wang, M.V. Baratta, ... L.R. Watkins, Morphine paradoxically prolongs neuropathic pain in rats by amplifying spinal NLRP3 inflammasome activation, Proc. Natl. Acad. Sci. U. S. A. 113 (24) (2016) E3441–E3450.
[144] B.E. Deverman, et al., Cre-dependent selection yields AAV variants for widespread gene transfer to the adult brain, Nat. Biotechnol. 34 (2016) 204–209.
[145] K.Y. Chan, et al., Engineered AAVs for efficient noninvasive gene delivery to the central and peripheral nervous systems 79, Nat. Neurosci. 20 (2017) 1172–1179.
[146] G. Morabito, S.G. Giannelli, G. Ordazzo, S. Bido, V. Castoldi, M. Indrigo, ... A. Sessa, AAV-PHP. B-Mediated Global-Scale Expression in the Mouse Nervous System Enables GBA1 Gene Therapy for Wide Protection from Synucleinopathy, Mol. Ther. 25 (12) (2017) 2727–2742.
[147] C.C. Goetz, The Unified Parkinson's Disease Rating Scale (UPDRS): Status and recommendations, Mov. Disord. 18 (7) (2003) 738–750.
[148] C.G. Goetz, B.C. Tilley, S.R. Shaftman, G.T. Stebbins, S. Fahn, P. Martinez-Martin, ... R.M. Zweig, Movement Disorder Society-Sponsored Revision of the Unified Parkinson's Disease Rating Scale (MDS-UPDRS): Scale presentation and clinimetric testing results, Mov. Disord. 23 (15) (2008) 2129–2170.
[149] M. Denham, C. Bye, J. Leung, B.J. Conley, L.H. Thompson, M. Dottori, Glycogen synthase kinase 3β and activin/nodal inhibition in human embryonic stem cells induces a pre-neuroepithelial state that is required for specification to a floor plate cell lineage, Stem Cells 30 (11) (2012) 2400–2411.
[150] J. Xi, Y. Liu, H. Liu, H. Chen, M.E. Emborg, S.C. Zhang, Specification of midbrain dopamine neurons from primate pluripotent stem cells, Stem Cells 30 (8) (2012) 1655–1663.

Molecular Therapy
Original Article

Extensive Transduction and Enhanced Spread of a Modified AAV2 Capsid in the Non-human Primate CNS

Jerusha Naidoo,[1] Lisa M. Stanek,[2,3] Kousaku Ohno,[1,3] Savanah Trewman,[1] Lluis Samaranch,[1] Piotr Hadaczek,[1] Catherine O'Riordan,[2] Jennifer Sullivan,[2] Waldy San Sebastian,[1] John R. Bringas,[1] Christopher Snieckus,[1] Amin Mahmoodi,[1] Amir Mahmoodi,[1] John Forsayeth,[1] Krystof S. Bankiewicz,[1] and Lamya S. Shihabuddin[2]

[1]Interventional Neuro Center, Department of Neurological Surgery, University of California, San Francisco, San Francisco, CA, USA; [2]CNS Genetic Diseases, Neuroscience Research TA, Sanofi, Framingham, MA, USA

The present study was designed to characterize transduction of non-human primate brain and spinal cord with a modified adeno-associated virus serotype 2, incapable of binding to the heparan sulfate proteoglycan receptor, referred to as AAV2-HBKO. AAV2-HBKO was infused into the thalamus, intracerebroventricularly or via a combination of both intracerebroventricular and thalamic delivery. Thalamic injection of this modified vector encoding GFP resulted in widespread CNS transduction that included neurons in deep cortical layers, deep cerebellar nuclei, several subcortical regions, and motor neuron transduction in the spinal cord indicative of robust bidirectional axonal transport. Intracerebroventricular delivery similarly resulted in widespread cortical transduction, with one striking distinction that oligodendrocytes within superficial layers of the cortex were the primary cell type transduced. Robust motor neuron transduction was also observed in all levels of the spinal cord. The combination of thalamic and intracerebroventricular delivery resulted in transduction of oligodendrocytes in superficial cortical layers and neurons in deeper cortical layers. Several subcortical regions were also transduced. Our data demonstrate that AAV2-HBKO is a powerful vector for the potential treatment of a wide number of neurological disorders, and highlight that delivery route can significantly impact cellular tropism and pattern of CNS transduction.

INTRODUCTION

Adeno-associated viral vector serotype 2 (AAV2) has long been favored for neurological applications because of its neuronal specificity, and numerous studies have demonstrated longevity of transgene expression and clinical safety.[1,2] Despite its advantages, AAV2 has not always translated well from preclinical studies to the clinic for CNS indications largely because of the limited spread and transduction efficiency in large target regions of the brain.[3,4] The incorporation of convection-enhanced delivery (CED), a technique that involves exerting positive pressure to the cannula tip causing bulk flow of macromolecules within brain parenchyma,[5,6] has significantly improved distribution of AAV vectors by enhancing the volume of distribution and creating more uniform drug concentration at the target site.[3,4,7] The function of specific AAV capsid proteins has also been extensively probed in a bid to enhance tissue distribution (reviewed in Bobo et al.,[5] Morrison et al.,[6] Grishagin,[8] and Kotterman and Schaffer[9]). Heparan sulfate proteoglycans (HSPGs) are one such protein. HSPG receptors were long considered the sole receptor for entry of AAV2 into neurons,[3,4,10,11] but recently other receptors have been identified.[5,6,12–15] HSPG and its membrane receptor are abundantly expressed in the brain, possibly to limit distribution of multiple functional proteins such as coagulation cofactors, chemokines, and growth factors,[3,4,7,16,17] and to focus biological activity to anatomically distinct regions. We have previously demonstrated that co-infusion of heparan with therapeutics including AAV2 enhances the area of distribution in the rat striatum likely through competitive blocking of binding sites.[5,6,8,9,18,19] These findings indicate that removal of HSPG binding capability by capsid mutagenesis may not be detrimental to entry of AAV2 into brain cells.

Given that AAV2 has proven extremely valuable for clinical applications, it is important to determine whether removal of the HSPG binding sites allows the vector to retain its ability to safely and efficiently transduce brain cells. Consistent with previous reports, we have found that ablation of heparan sulfate binding enhanced the ability of AAV2 to bind and transduce neurons in the rodent brain and increased the volumetric spread of the vector.[20–22] As highlighted by Wilson and colleagues,[23] AAV transduction patterns in rodents do not always correlate in larger mammals. Studies in larger mammalian brains are therefore critical to establish the potential clinical utility of an AAV2 variant that does not bind HSPGs.

Received 7 April 2018; accepted 3 July 2018;
https://doi.org/10.1016/j.ymthe.2018.07.008.

[3]These authors contributed equally to this work.

Correspondence: Krystof S. Bankiewicz, Interventional Neuro Center, Department of Neurological Surgery, University of California, San Francisco, UCSF Mission Center Building 0555, 1855 Folsom St., Room 226, San Francisco, CA 94103-0555, USA.
E-mail: krystof.bankiewicz@ucsf.edu

The primary goals of the present study were to: (1) evaluate the effect of HSPG receptor binding abrogation on vector distribution and tropism, (2) evaluate the effect of HSPG receptor binding abrogation on axonal transport properties of the vector, and (3) explore the effect of route of administration on vector distribution in the brain and spinal cord of non-human primates (NHPs). Our modified AAV2 vector, referred to as AAV2-HBKO, was evaluated in the NHP brain and spinal cord after either thalamic, intracerebroventricular (ICV), or a combination of both thalamic and ICV delivery. The results indicate that (1) AAV2-HBKO transduces neurons independent of HSPG receptor binding and maintains neuronal tropism following parenchymal delivery, (2) AAV2-HBKO undergoes extensive bidirectional axonal transport when injected into the parenchyma, and (3) the route of administration impacts cellular tropism of AAV2-HBKO. When injected into the thalamus, the vector distributed extensively and neuronal transduction exceeded that previously observed with the parent AAV2 vector.[1,16,24] Neuronal transduction was observed in deep layers of the cortex, deep cerebellar nuclei, and several subcortical regions indicative of robust bidirectional axonal transport. ICV delivery resulted in strong ependymal cell transduction in the ventricular zone, along with widespread cortical transduction. Strikingly, transduction was limited to superficial layers, and GFP expression was observed predominantly in oligodendrocytes. The combination of ICV and thalamic delivery resulted in robust transduction of a majority of cortical layers, with oligodendrocytes primarily transduced in layers 1–3 and neurons transduced in layers 4–6. Motor neuron transduction was observed in all levels of the spinal cord after thalamic delivery, ICV delivery, and the combination of both ICV and thalamic delivery. These findings highlight the potential clinical utility of heparan binding-deficient AAV2 vectors and have important implications for the treatment of neurological diseases requiring widespread and global distribution of gene therapy in the brain and spinal cord, such as motor neuron diseases and lysosomal storage disorders. Others have reported oligodendrocyte transduction in subcortical areas,[25] but this is the first demonstration of oligodendrocyte transduction in the NHP cortex by a modified AAV2 capsid. AAV2-HBKO has possible application for demyelinating diseases, leukodystrophies, and other myelin disorders.

RESULTS

Thalamic AAV2-HBKO Infusion Results in Bidirectional Axonal Transport, Widespread Neuronal Transduction in Deep Cortical Layers, and Spinal Cord Transduction

AAV2-HBKO was delivered under intraoperative MRI guidance bilaterally into the thalamus (n = 3; 1.6–3.4 $\times$ 10^{12} vector genomes [vg]/hemisphere). No adverse effects were observed during infusion in the vasculature or parenchyma. MRI and 3D reconstruction of gadolinium signal revealed that the vector remained primarily within the target site. A small amount of leakage occurred into the subthalamic nucleus (STN), but no infusate was seen in the neighboring putamen or other non-targeted structures (Figure 1A). Tissue analysis of the injection sites revealed that AAV2-HBKO vector carrying a foreign protein (EGFP) triggered an immune reaction after being infused into the parenchyma, a finding consistently observed with expression of EGFP into antigen-presenting cells in the brain.[26–28] H&E staining revealed perivascular cuffing and cellular infiltration in the thalamus, and to a lesser extent in the secondary transduction areas. Astrocytic activation and microglial hyperactivity were also evident from glial fibrillary acidic protein (GFAP) and Iba1 staining in the thalamus, indicating a clear immune reaction (Figure S1). Visual examination of neuronal nuclei (NeuN) staining showed that there was no noteworthy loss of neurons in the thalamus or cortex, and none of the animals presented any gross adverse clinical signs throughout the duration of the study. Thalamic injection of AAV2-HBKO elicited robust anterograde transport to the cortex, with transduction extending from the prefrontal cortex to areas of parietal and temporal cortex just above the brainstem (Figure 1B). Quantification of cortical transduction area revealed that of the total cortical area, 80% of the prefrontal and frontal cortex, 37% of the temporal and parietal cortex, and 14% of the occipital cortex were transduced. Transduced cells were limited to deep cortical layers 4–6 in NHP. Double-immunofluorescent labeling experiments, in which GFP expression was coupled with NeuN, as a marker for neurons, revealed that greater than 90% of transduced cells were neuronal (Figures 1C, 1D, 2A, and 2B).

In addition to anterograde axonal transport to the cortex, AAV2-HBKO underwent retrograde axonal transport to several subcortical regions. GFP staining was evident in the caudate and putamen, globus pallidus (GP), substantia nigra pars reticulata (SNr), substantia nigra pars compacta (SNc), and brainstem (Figure 1E; Table 1).

GFP staining revealed the presence of GFP-positive cells at all levels of the spinal cord (i.e., cervical, thoracic, lumbar, and sacral; Figure 3A) in both the dorsal and ventral horns and the intermediate zone. Double-immunofluorescent labeling with GFP and NeuN revealed that the transduced cells were neurons. Both motor neurons and interneurons were transduced in the ventral horn. Transduced motor neurons in the ventral horn were identified with GFP and NeuN double labeling and morphologically by their large cell bodies (Figure 3B). Quantification of the number of transduced motor neurons revealed 65% motor neuron transduction in the cervical spinal cord, and 33%, 38%, and 33% of motor neurons in the thoracic, lumbar, and sacral regions, respectively (Figure 3C).

ICV AAV2-HBKO Infusion Results in Widespread Oligodendrocyte Transduction in Superficial Cortical Layers and Robust Motor Neuron Transduction in the Spinal Cord

AAV2-HBKO was delivered bilaterally to the lateral ventricle (n = 3; 1.8 $\times$ 10^{13} vg/hemisphere) under MRI guidance. As with the thalamic infusions, we did not observe any adverse effects during infusion. MRI of gadolinium signal revealed that there was no vector leakage into surrounding parenchyma. AAV2-HBKO rapidly distributed through the ventricular system and central canal within 5 min of starting the infusion (Figure 4A). H&E staining revealed a slight increase in cellular infiltration and perivascular cuffing in the cortex. This region also showed signs of mild astrocytic activation and microglial hyperactivity, indicative of a mild immune response (Figure S2). Visual examination revealed that there was no loss of neurons in the

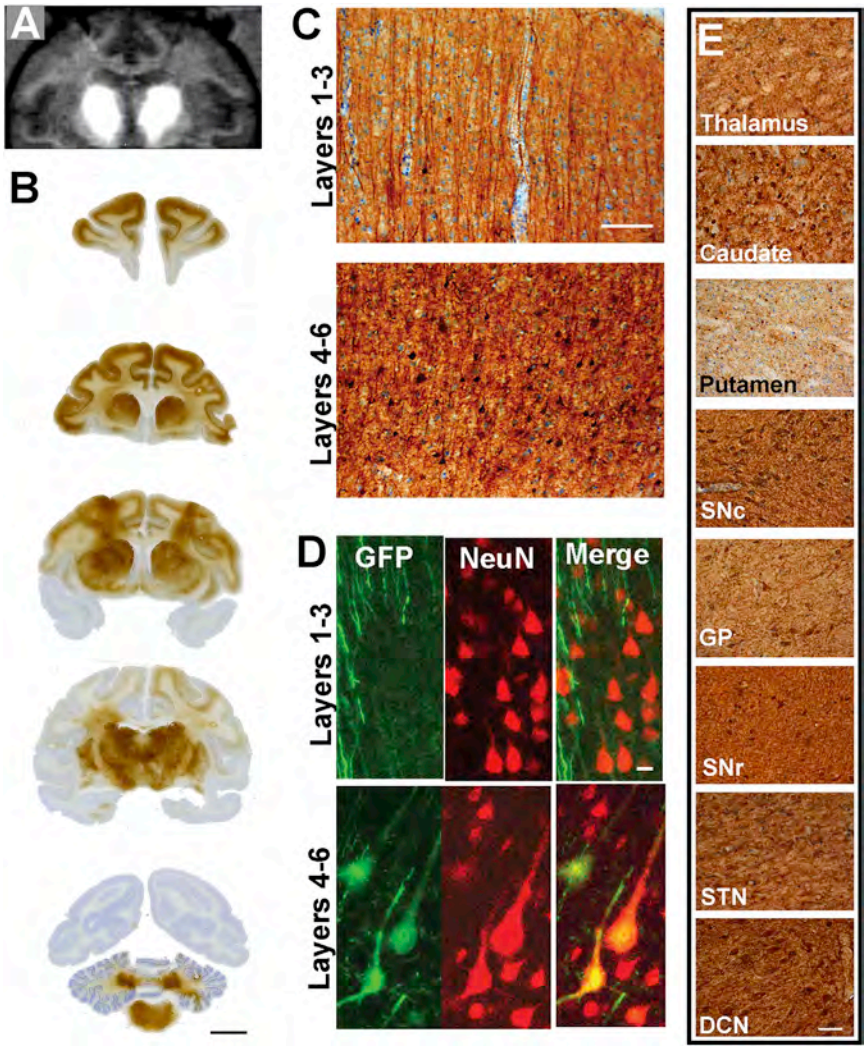


Figure 1. Histological Analysis of the Non-human Primate Brain after MRI-Guided Thalamic Infusion of AAV2-HBKO

(A) Bilateral delivery of AAV2-HBKO-GFP under intraoperative MRI guidance. MRI in the coronal planes showed that gadolinium signal was mostly contained within the thalamus. (B) Low-magnification images showing GFP staining in the prefrontal, frontal, and parietal and temporal cortices, but no GFP expression in the occipital cortex. GFP expression was also evident in several subcortical regions. Scale bar: 1 cm. (C) High-magnification images of 3,3'-diaminobenzidine (DAB) immunohistochemical staining showing primarily fiber transduction in layers 1–3 and cellular transduction in layers 4–6. Scale bar: 50 μm. (D) Double-immunofluorescent staining demonstrated colocalization of GFP and the neuronal nuclei marker NeuN in layers 4–6. Scale bar: 50 μm. (E) Panel of high-magnification images of DAB staining showing GFP expression in the thalamus, caudate, putamen, substantia nigra pars compacta (SNc), globus pallidus (GP), substantia nigra pars reticulata (SNr), subthalamic nucleus (STN), and deep cerebellar nuclei (DCN). Scale bar: 100 μm.

thalamus or cortex, and none of the animals presented any gross adverse clinical signs throughout the duration of the study. ICV infusion of AAV2-HBKO evinced transduction throughout the cerebral cortex (Figure 4B). Quantification of the area of GFP transduction relative to the total cortical area revealed that 65% of the prefrontal and frontal cortex, 60% of the temporal and parietal cortex, and 37% of the occipital cortex were transduced. Strikingly, ICV injections resulted in a cortical transduction pattern that was non-uniform and formed rosettes of oligodendrocytes interspersed with some neurons. The rosettes often surrounded blood vessels. Expression of GFP was mostly localized to superficial cortical layers (layers 1–3), although some patches of expression were observed in deeper layers (Figure 4C). Double-immunofluorescent double-labeling experiments were performed to quantify the phenotype of transduced cells, in which GFP expression was coupled with Olig2, a marker for oligodendrocytes, NeuN, a marker of neurons, or GFAP, a marker of astrocytes (Figure 4D). Of the total population of transduced cells, neurons accounted for 8%–18% of transduced cells in the shallow cortical layers and 13%–29% in the deep cortical layers (Figures 2A and 2B). Oligodendrocytes accounted for 75%–77% of transduced cells in shallow cortical layers and 74%–82% in deep cortical layers (Figures 2C and 2D).

ICV infusion did not result in any subcortical expression, but high levels of ependymal cell transduction lined the lateral ventricle (Figure S2). GFP-positive cells were present in all levels of the spinal cord (i.e., cervical, thoracic, lumbar, and sacral; Figure 3A) in both the dorsal and ventral horns. Quantification of the number of transduced motor neurons revealed that ICV delivery alone resulted in transduction of 93% of motor neurons at the cervical region, 84% in the thoracic, 85% in the lumbar, and 93% in the sacral regions (Figures 3A–3C).

Combination of ICV and Thalamic AAV2-HBKO Infusion Results in Widespread Oligodendrocyte Transduction in Superficial Cortical Layers, Neuronal Transduction in Deep Cortical Layers, and Robust Motor Neuron Transduction in the Spinal Cord

NHPs in this group received a combined bilateral ICV infusion and unilateral thalamic infusion (n = 2) under MRI guidance (1.8×10^{13} vg in ICV hemisphere and 2.0×10^{13} vg in combined ICV plus thalamic hemisphere). As with the other groups, no adverse events were observed during the infusion in the vasculature or parenchyma. AAV2-HBKO was rapidly distributed through the ventricular system and central canal within 5 min of starting the infusion. A small amount of vector leakage occurred into the STN in the hemisphere that received thalamic infusion, but no infusate was observed in

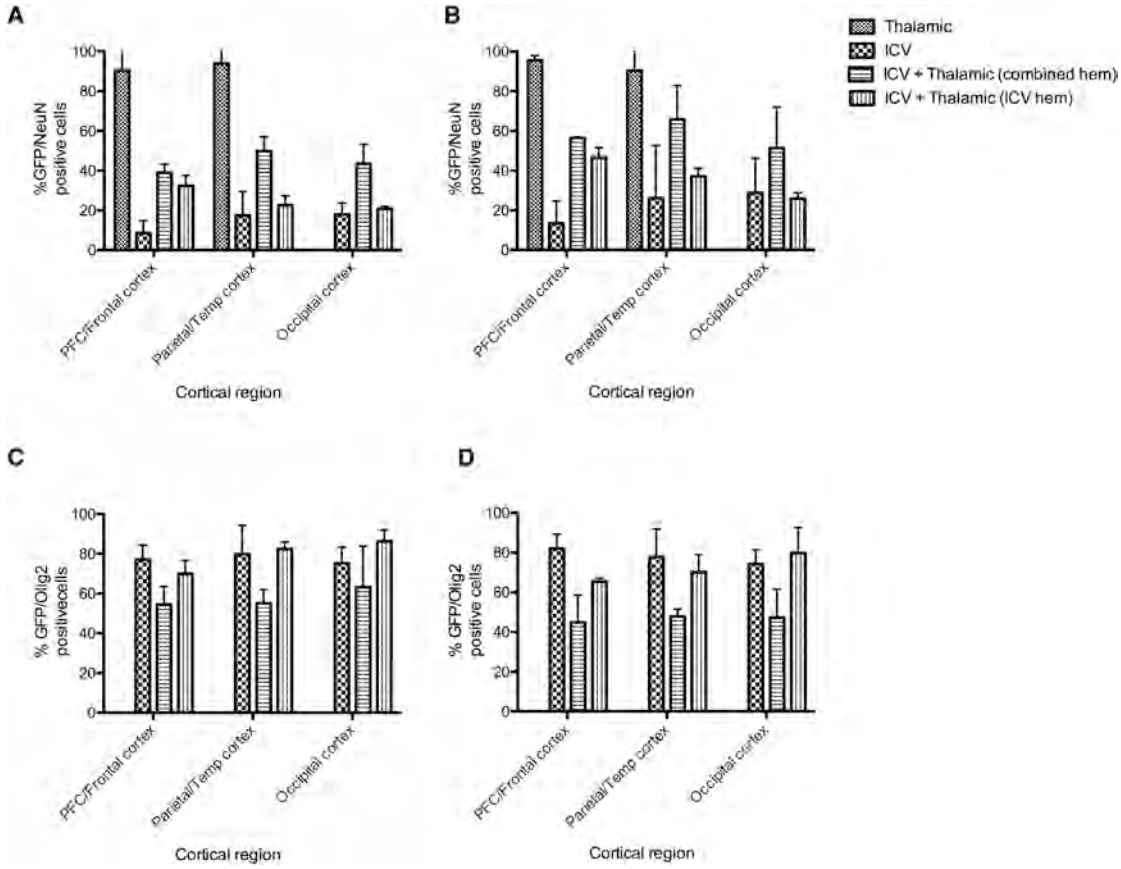


Figure 2. Percentage of Transduction in Each Cortical Region after Different Routes of AAV2-HBKO Delivery

Bar graphs showing that the percentage of GFP-transduced cells that colocalized NeuN was larger after thalamic infusion alone and with combined ICV and thalamic delivery, compared with ICV delivery alone in cortical layers 1–3 (A) and 4–6 (B). By contrast, the percentage of GFP-transduced cells that colocalized with Olig2 was large with ICV delivery and combination of ICV and thalamic, and largely confined to layers 1–3 (C) with minimal transduction of oligodendrocytes observed in layers 4–6 (D). Error bars are expressed as SEM.

neighboring non-target areas (Figure 5A). H&E staining revealed the presence of some perivascular cuffing and cellular infiltration at the injection site in the thalamus in the hemisphere that received the combination of ICV and thalamic delivery, along with an increase in GFAP and Iba1 immunoreactivity indicative of a clear immune response. H&E, GFAP, and Iba1 immunostaining revealed evidence of a mild immune response in the cortex in the hemisphere that received ICV delivery alone (Figure S3). There was no evidence of neuronal loss from visual examination of NeuN staining, and none of the animals presented any gross adverse clinical signs throughout the study.

Cortical transduction was observed in both hemispheres (Figure 5B). In the hemisphere that received combined ICV and thalamic delivery, transduction was observed in 94% of the total prefrontal and frontal cortical area, in 39% of the temporal and parietal cortical area, and in 20% of the occipital cortical area. The hemisphere that received only the ICV injection displayed transduction in 66% of the prefrontal and frontal cortical area, in 56% of the parietal and temporal cortex, and 63% of the occipital cortex. The combination of ICV and thalamic delivery resulted in transduction of primarily oligodendrocytes in superficial layers and neuronal transduction in deeper layers (Figures 5C and 5D). Phenotypic quantification of GFP-transduced cells showed that oligodendrocytes accounted for 54%–63% of the total population of transduced cells in the superficial layers and 45%–48% of transduced cells in deep cortical layers (Figures 2C and 2D). Neuronal transduction was evident in 39%–50% of transduced cells in superficial cortical layers and 51%–66% of transduced cells in deeper cortical layers (Figures 2A and 2B). Interestingly, a lower percentage of neuronal transduction was evident in the hemisphere that received ICV infusion alone (21%–32% of transduced cells in superficial cortical layers and 26%–47% in deep cortical layers) compared with the hemisphere that received both the thalamic and the ICV infusion (Figures 2A and 2B). AAV2-HBKO infusion did not result in astrocytic transduction in any treatment group (data not shown).

Similar to the ICV group, the hemisphere that received combined thalamic and ICV infusion displayed bidirectional axonal transport

Table 1. Summary of Axonal Transport 4 Weeks after Infusion of AAV2-HBKO into the Non-human Primate Thalamus

Structure	Anterograde Transport	Retrograde Transport
Cerebral cortex	√	–
Caudate + putamen	–	√
Globus pallidus	–	√
SNr	–	√
SNc	–	√ (secondary transport[a])

SNc, substantia nigra pars compacta; SNr, substantia nigra pars reticulata.
[a]GFP expression in the SNc occurred via secondary anterograde axonal transport from a primary transduction zone in either the subthalamic nucleus or putamen.

to several subcortical regions. GFP staining was evident in the caudate and putamen, globus pallidus, SNr, and SNc (Figure 5E). High levels of GFP transduction were observed in ependymal cells bilaterally (Figure S2). Quantification of motor neuron transduction revealed 94% transduction at the cervical level, 98% at the thoracic level, 90% transduction at the lumbar level, and 76% in the sacral region (Figure 3C). There were no differences between the left and right spinal cord (data not shown).

DISCUSSION

AAV2 vectors bind HSPGs on the cell surface of neurons and, unlike other vector capsid-receptor interactions, its affinity for HSPGs impedes the spread of the vector beyond the injection site somewhat.[10] AAV serotypes that do not bind to HSPGs (such as AAV1, AAV5, and AAV9) tend to show increased distribution after direct injection into the brain, implicating heparan binding as a barrier to widespread CNS transduction.[12,14,15] Distributing transgenes widely throughout the brain has obvious implications for the treatment of many neurological disorders. In order to establish the potential clinical utility of a non-heparan binding AAV2 vector, we evaluated a novel AAV2-HBKO capsid in a large mammalian brain with the ultimate goal of targeting widespread regions of the human brain with AAV vectors to direct therapeutic transgene expression.

The most notable finding of the present study was the discovery that ICV delivery of AAV2-HBKO resulted in an entirely different cell transduction pattern compared with thalamic delivery. ICV delivery of AAV2-HBKO resulted in transduction of oligodendrocytes in the cortex and motor neuron transduction in the spinal cord. In contrast, thalamic infusion resulted in entirely neuronal transduction in both the brain and spinal cord; no oligodendrocyte transduction was observed in any regions evaluated.

Oligodendrocytes may be preferentially transduced by ICV delivery as a result of vector flow into the perivascular space, which is in direct contact with oligodendrocytes, leaving a smaller proportion of vector particles available to transduce neurons. This idea is consistent with the rosette pattern of transduction we observed surrounding blood vessels. To our knowledge, AAV2 has yet to be assessed by cerebrospinal fluid (CSF) delivery in the NHP, but we observed a similar rosette pattern of transduction with cisterna magna delivery of both AAV7 and AAV9.[29] Astrocytes, which are also in direct contact with CSF, were the primary cell type transduced by AAV7 and AAV9. AAV9 does not bind to HSPGs, indicating that removal of the HSPG receptor binding capability is not in itself sufficient to shift cellular tropism of AAV vectors toward oligodendrocyte transduction. Removal of the HSPG receptor binding site may release steric hindrance allowing other receptor binding sites present on AAV2 vector (that are not present on AAV9) to bind to oligodendrocytes. A direct comparison of AAV2 and AAV2-HBKO by CSF delivery is warranted in order to define clearly the role of HSPG binding on oligodendrocyte transduction. Consistent with what we have described for AAV2,[16] AAV2-HBKO vector maintained the neuronal tropism of the parental AAV2 capsid after thalamic delivery, a characteristic that makes AAV2-HBKO an attractive vector for the treatment of neurodegenerative diseases. Route of delivery has been shown to impact tropism of AAV vectors previously,[30,31] but to our knowledge this is the first time cortical oligodendrocyte transduction has been reported.

The robust spinal cord transduction observed with ICV delivery has important implications for diseases that primarily impact lower motor neuron function. Our finding that AAV2-HBKO transduced primarily oligodendrocytes in the brain, but only motor neurons in the spinal cord, may be explained by the fact that a different subtype of oligodendrocytes is present in the gray matter of the brain, i.e., non-myelinating satellite oligodendrocytes, versus myelinating oligodendrocytes in the spinal cord.[32] Satellite oligodendrocytes in the gray matter of the brain express a different repertoire of cell surface receptors that set them apart from the myelinating oligodendrocytes found in the spinal cord.[32] It is possible that the HSPG receptor binding site sterically hinders binding and internalization of AAV2 vector with other receptors. Abolition of the HSPG binding capabilities may thus allow for binding and internalization by receptors found on satellite oligodendrocytes that are not present on myelinating oligodendrocytes. Basic fibroblast growth factor (bFGF) receptor has been identified as a co-receptor for successful entry of AAV2 vector into host cells,[33] so it is possible that the bFGF receptor was utilized by AAV2-HBKO for entry into either oligodendrocytes or neurons in the present study. Indeed we have previously found that bFGF can act as an adjuvant to enhance distribution of AAV2 in the rat brain,[19] but this hypothesis requires further investigation.

The widespread transduction of cortical oligodendrocytes in the present study is unprecedented for several reasons. First, most widely explored AAV serotypes exhibit a predominantly neuronal tropism. Some AAV serotypes possess a weak tropism for oligodendrocytes when the myelin basic promoter is used, but the overall transduction of oligodendrocytes reported is still low.[34,35] Second, in studies that have reported tropism for oligodendrocytes, transduction has been limited to subcortical areas, and only at the site of parenchymal infusion. For example, we have found that infusion of AAV1 into the corona radiata of NHPs leads to transduction of oligodendrocytes in white matter at the infusion site, but not in any other regions of

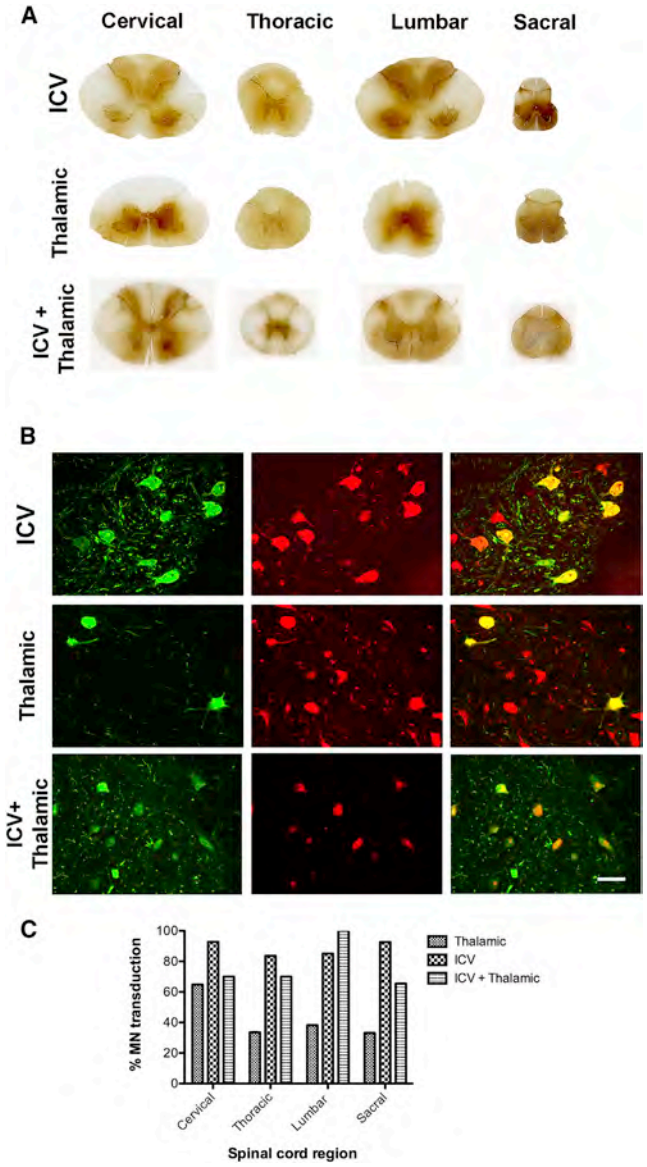


Figure 3. Robust Motor Neuron Transduction in the Spinal Cord after Different Routes of AAV2-HBKO-GFP Delivery

(A) GFP-positive cells were found at cervical, thoracic, lumbar, and sacral spinal regions after chromogenic immunostaining in ICV, thalamic, and combined ICV and thalamic groups. Scale bar: 1 cm. (B) Double-immunofluorescent staining showed GFP and large NeuN-positive motor neurons that colocalized with GFP (merge). Scale bar: 50 μm. (C) Graph showing quantification of motor neuron transduction as a percentage of total motor neurons.

the brain.[30] Similarly, McCown and colleagues[36] described an AAV variant that demonstrated high oligodendrocyte transduction levels in the corpus callosum and striatum but did not report any transduction outside of the infusion site.

Indeed the present study indicates that both vector capsid and route of delivery are key factors in determining tissue distribution and tropism in the brain. To our knowledge, this is the first time ICV delivery of AAV vector has been described in NHP. The total dose administered was higher than with the thalamic infusions to account for dilution of vector particles within the CSF. Intra-operative MRI demonstrates that ICV delivery of AAV vectors is an inherently efficient process that rapidly distributes AAV vector throughout the brain and spinal cord (a total infusion time of 1.5 min). In addition to the pace of CSF flow and compliance of this compartment for large volumes of vector, ICV injection has the added advantage of following the inherent direction of CSF flow. On that basis, one might predict that ICV delivery of AAV vector would be a more efficient distribution modality than the cisterna magna and lumbar injections more commonly used for CSF delivery.

The present study also highlights important distinctions between the axonal transport properties of AAV2-HBKO and AAV2. In our experience, the axonal transport profiles of a particular vector can be impacted by: (1) the neuroanatomical site of infusion, (2) capsid modification, (3) vector purification method, and (4) vector titer. With the exception of one study that is discussed in detail below,[21] AAV2, in our hands and in the hands of other groups, typically undergoes primarily anterograde axonal transport in NHP.[1,16,24]

The thalamus projects primarily to the cerebral cortex, but also sends afferent projections to the striatum, and receives efferent projections from the globus pallidus (internal), the SNr, and the cerebellum. Thalamic infusion of AAV2-HBKO resulted in robust anterograde transport to the cortex, and both anterograde and retrograde axonal transport to transduce several subcortical regions in addition to the site of injection in the thalamus. Anterograde axonal transport of AAV2-HBKO was evident from GFP staining in the striatum via thalamostriatal projections. Robust retrograde transport was discernible from transduction of the globus pallidus, SNr deep cerebellar nuclei, and brainstem. This finding is distinct from what we have previously found with thalamic injection of AAV2 in the primate brain at a comparable titer.[16] In that study we found that AAV2 transduced only the injection site in the thalamus and the cortex, but no other subcortical regions were transduced (Figure S5). This finding suggests that AAV2-HBKO may have a higher propensity for both anterograde and retrograde axonal transport compared with AAV2. In the present study, cortical transduction extended from the prefrontal cortex to areas of parietal and temporal cortex just above the brainstem. The lack of occipital cortex transduction is likely due to inefficient primary transduction of the lateral geniculate nucleus, which projects to the primary visual cortex. The robust brainstem transduction observed after thalamic delivery of AAV2-HBKO is unprecedented, as this area is very difficult to target for gene delivery. All untransduced regions of the brain do not have any direct afferent or efferent connections from the site of injection in the thalamus.

The spinal cord transduction with thalamic delivery indicates that AAV2-HBKO may undergo transsynaptic transport, because there is no direct pathway from the thalamus to the spinal cord. Thalamic

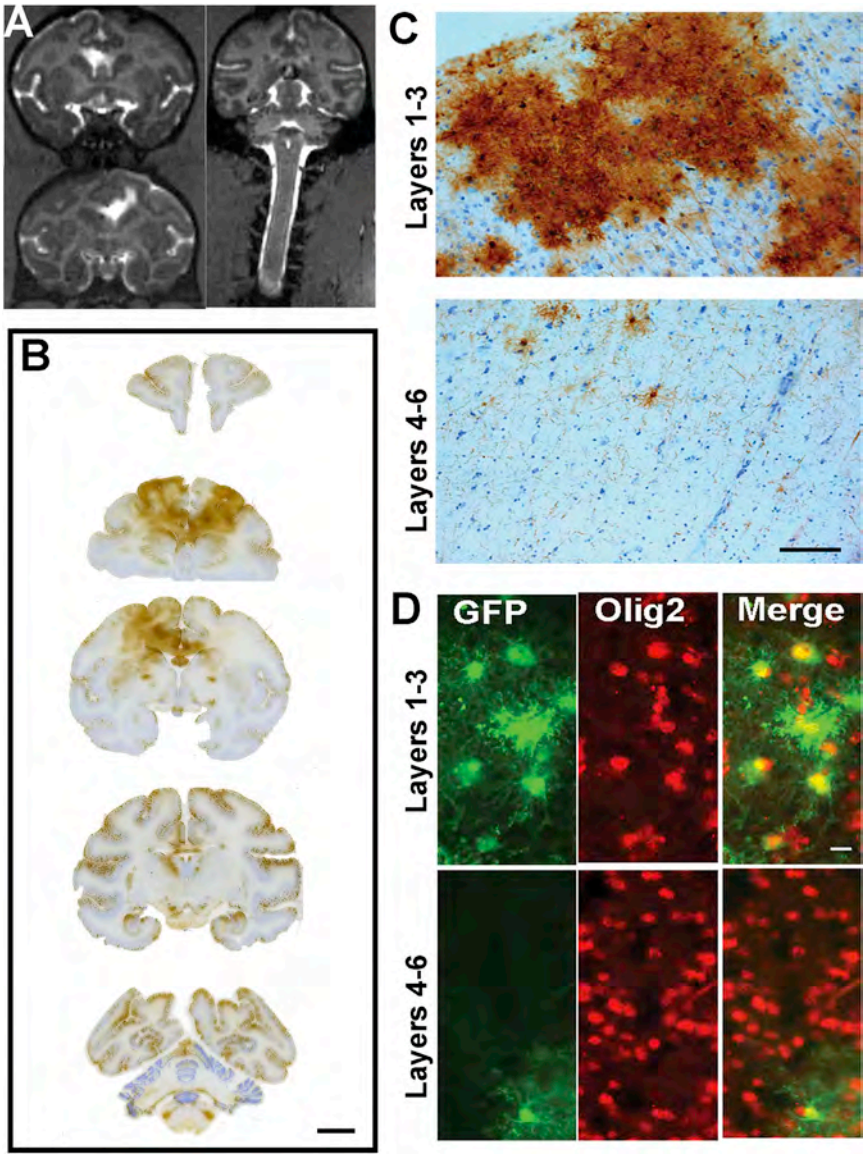


Figure 4. Histological Analysis of the Non-human Primate Brain after MRI-Guided Intracerebroventricular Infusion of AAV2-HBKO

(A) MR image in coronal plane showing gadolinium signal in the CSF at the end of the 1.5-min infusions. Gadolinium signal was mostly contained within the lateral ventricles and was observed following the flow of CSF through the ventricular system and central canal. (B) Low-magnification brain images showing GFP staining throughout the brain in the prefrontal, frontal, parietal and temporal cortex, and occipital cortices. No GFP expression was evident in subcortical regions. Scale bar: 1 cm. (C) High-magnification images of DAB immunohistochemical staining showing robust GFP expression in rosettes in cortical layers 1–3 and very sparse GFP staining in cortical layers 4–6. Scale bar: 50 μm. (D) Double-immunofluorescent staining revealed colocalization of GFP and the oligodendrocyte marker Olig2 in cortical layers 1–3 and 4–6. Scale bar: 50 μm.

infusion of AAV2-HBKO resulted in anterograde axonal transport along the thalamocortical tract to transduce pyramidal cells in layer V of the cortex, then by anterograde transport along the corticospinal tract to transduce interneurons and motor neurons in the ventral horn of the spinal cord. AAV2-HBKO also underwent retrograde axonal transport via the spinothalamic tract to transduce the dorsal spinal cord. This could have occurred either directly along second-order neurons projecting directly from the thalamus to the ventral horn of the spinal cord, or transsynaptically, first via anterograde transport along first-order neurons to the somatosensory cortex, followed by retrograde transport along second-order neurons to the ventral spinal cord. Transsynaptic transport occurred exclusively from the cortex, not all secondary transduction sites. Further studies are required to examine vector particle distribution in secondary and tertiary transduction regions to determine whether this phenomenon is a function of vector particle concentration. Thalamic infusion of AAV2-HBKO could potentially be useful for devastating motor neuron diseases, such as amyotrophic lateral sclerosis (ALS), which affects both upper and lower motor neurons.

Axonal transport properties may also be affected by the vector purification method. As mentioned, to our knowledge, we are the only group to have reported that AAV2 can undergo both anterograde and retrograde transport in the NHP brain,[20] when purified with a column chromatography method different from the more commonly used stringent cesium chloride purification method.[1,24] The present study is similar to the AAV2 described in Hadaczek et al.[21] in the sense that both of the vectors were produced with the same proprietary purification method, were injected at comparable titers, and both preparations had comparable purity, ratio of empty to full, and presence of contaminants. Both studies investigated distribution of the respective vectors after parenchymal delivery, but AAV2 was administered into the putamen by Hadaczek et al.,[21] whereas AAV2-HBKO was delivered into the thalamus in the present study. Bidirectional axonal transport was observed in both studies, but infusion of AAV2 into the putamen resulted in incomplete transduction in some subcortical regions (e.g., the thalamus). AAV2-HBKO, by contrast, resulted in complete transduction of all of the same subcortical regions as with AAV2 in Hadaczek et al.[21] A direct comparison of AAV2 and AAV2-HKO purified by the same method and infused into the same target site in the primate brain would be of interest in future studies in order to further elucidate the full contribution of HSPG binding to vector transport.

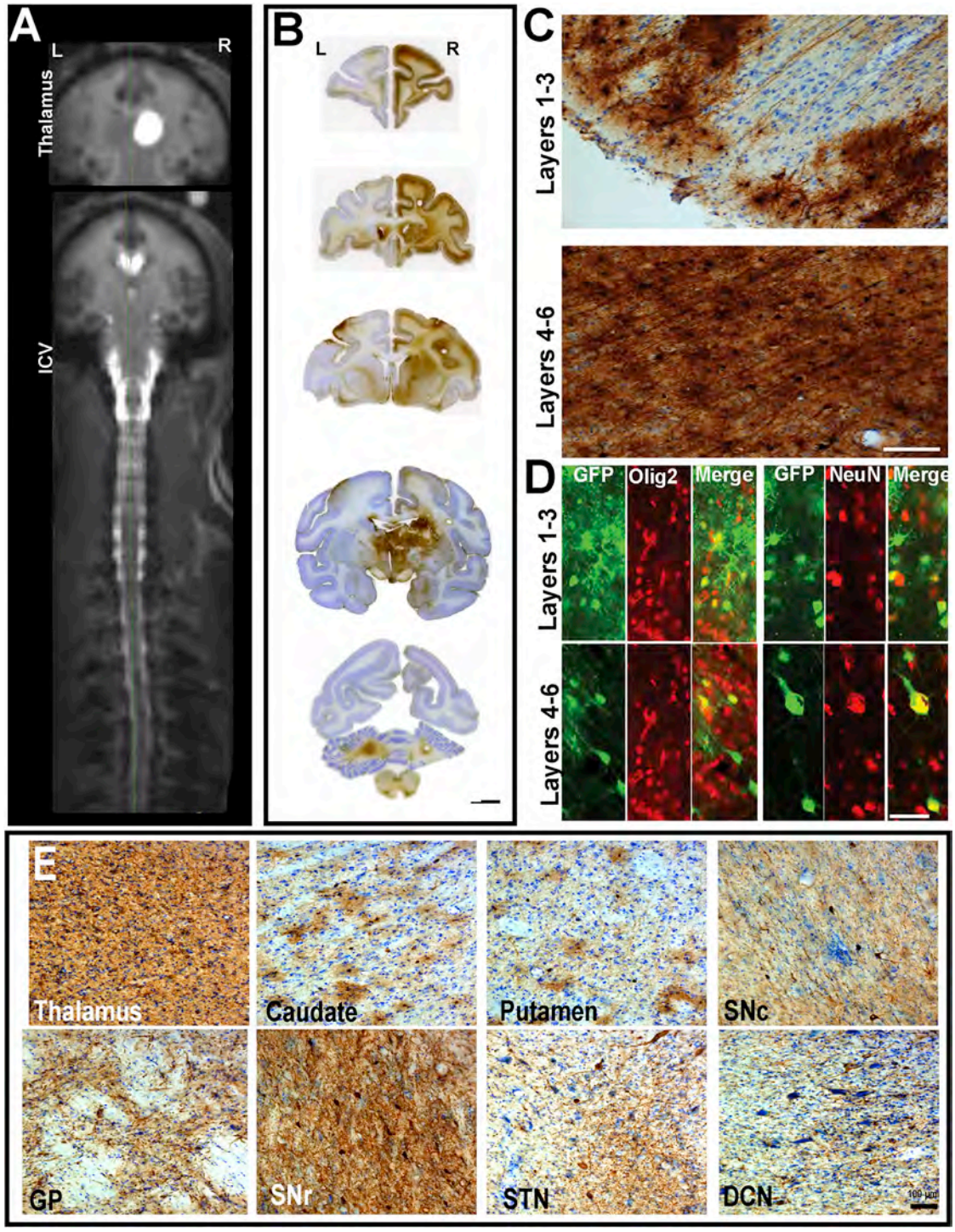


Figure 5. Histological Analysis of the Non-human Primate Brain after MRI-Guided Combined Thalamic and Intracerebroventricular Infusion of AAV2-HBKO
(A) MR images in the coronal plane showing gadolinium signal at the end of the ICV and thalamic infusions. Gadolinium signal was mostly contained within the thalamus in the right hemisphere (top) and with the lateral ventricle. The infusate was observed following the flow of CSF through the ventricular system and central canal (bottom). (B) Low-magnification brain images showing GFP immunostaining. In the ICV hemisphere (left), GFP expression was evident in the prefrontal, frontal, parietal and temporal cortex, and occipital cortices. No GFP expression was evident in subcortical regions. In the ICV and thalamic combination hemisphere (right), GFP expression was evident in the prefrontal, frontal, parietal and temporal cortex, and occipital cortices along with several subcortical regions. Scale bar: 1 cm. (C) High-magnification images of DAB

(legend continued on next page)

Vector dose may also be an important factor influencing axonal transport directionality. In the present study, we injected 1.6–3.4 × 10^{12} vg of AAV2-HBKO per thalamus. We have previously shown strong dose dependency of axonal transport with other serotypes. Notably, retrograde axonal transport triggered with AAV9, at 1.5 × 10^{12} vg,[37] and with AAV5 in the range of 1.0–1.5 × 10^{12} vg.[38] We would argue, therefore, that retrograde transport of AAV2-HBKO may be decreased at lower titers, a hypothesis that requires further investigation.

The results presented here also highlight the important message that rodent data do not always translate to the primate brain. We cannot presume that a route of delivery that produces a particular pattern of distribution and tropism in rodents and other small mammals will reproduce in the NHP or humans. Manfredsson and colleagues[22] have evaluated the impact of AAV2 HSPG binding on transduction in the rat brain, but they have not described axonal transport after intraparenchymal infusion of an analogous AAV2 deficient in HSPG binding into the striatum. AAV2-HBKO, by contrast, underwent robust axonal transport in both NHP and mice.[20] The AAV2 capsid variant described by Manfredsson and colleagues[22] (referred to as T2 3Y +T +dH) had several mutations to the canonical HSPG-binding residues. The AAV2-HBKO-based vector used in our study substituted two positively charged arginine residues (R585A and R588A) for two hydrophobic alanine residues on the surface of the AAV2 capsid, thereby ablating the AAV2 capsid-HSPG interactions. The effect of abrogating HSPG binding was solely evaluated in this study. It is possible that R585A and R588A play important roles in the axonal transport properties of AAV2 vector, and that the substitution with hydrophobic alanine residues resulted in the bidirectional axonal transport observed in the present study. Due to the number of mutations contained in the Manfredsson variant, the contributions of any individual mutation and the contribution of species-specific differences in transduction profiles cannot be fully disentangled.

In rodents, ICV delivery of AAV2 restricts transduction to ependymal cells and offers very little expression outside of the ependymal.[39–41] Both robust ependymal cell transduction and widespread cortical transduction were observed in the present study, indicating that abolition of HSPG binding capability increases the propensity to overcome complete sequestration of all vector particles to ependymal cells, enabling for delivery of remaining vector particles to the cortex. Vector titer differences could also explain some dissimilarities in distribution between rodents injected with parent AAV2, the variant described by Manfredsson and colleagues,[22] and the AAV2-HBKO described in the present study. NHPs were infused with AAV2-HBKO at a titer of 1.2 × 10^{13} vg/mL, whereas Manfredsson and colleagues[22] injected rats with their HSPG binding variant at a lower titer of 1.2 × 10^{12} vg/mL, and parent AAV2 vector was injected at titers as low as 1 × 10^{9} vg/mL.[39–41] Dose-ranging experiments in both rodents and NHPs would enable the effect of titer to be extricated from HSPG binding capability.

The volume of vector relative to CSF volume is another important factor to consider. In the present study, a total of 3 mL of vector was injected, representing approximately 20% of the normal volume of CSF in a normal NHP (~12–15 mL). The volume typically infused into rats is comparatively lower, and typically a 10-μL infusion is administered representing less than 5% of the normal volume of CSF in a rat (~250–350 μL). Due to these differences, in addition to the low number of NHP used in the present study, it is difficult to draw final conclusions about the relationship between dose, volume, and transduction. It is possible that there is a threshold of vector particles in a given volume of CSF that is required to overcome sequestration to ependymal cells, leading to transduction in the cortex. The comparatively lower concentration of vector particles in CSF in the rodent studies may not have exceeded the required number of vector particles to maximally quench ependymal cell transduction and lead to cortical transduction. Another hypothesis to explain this phenomenon is differential binding affinities across species, which might sequester vector to the different cell types more readily in some species.

The concept of paradoxical AAV transduction profiles in rodents versus higher mammals was exemplified recently by Wilson and colleagues,[23] who showed that the AAV9 variant AAV-PHP.B that demonstrated remarkable global transduction of the CNS after intravenous delivery in mice[42] was functional only in the model in which it was selected, i.e., a Cre transgenic mouse in a C57BL/6J background, but resulted in only very low CNS transduction in NHPs and another commonly used mouse strain BALB/cJ. These data serve as a cautionary tale highlighting the importance of assessing biodistribution of viral vectors in large mammals prior to clinical use.

AAV2-HBKO was well tolerated by all subjects regardless of the route of delivery with no gross adverse clinical signs throughout the study. Congruent with previous studies, the high level of GFP expression in primary transduction zones caused some perivascular cuffing, astrocytic activation, and microglial hyperactivity at primary injection sites. We found evidence of mild toxicity in secondary sites, implying that the local inflammatory response was likely due to sequestration of GFP-containing vector particles in the infusion site. Although GFP is valuable when used as a cellular tag to measure gene expression and cell tracking, there is a wealth of evidence to suggest high levels of GFP can produce immunogenicity and toxicity when expressed in antigen-presenting cells over a period of time, i.e., >4 weeks.[26,43] Clinical vectors would not contain the GFP

immunohistochemical staining in the cortex showing robust GFP expression in rosettes in layers 1–3 and nuclei and fiber staining in layers 4–6. Scale bar: 50 μm. (D) Panel shows high-magnification images of double-immunofluorescent staining in the combined ICV and thalamic hemisphere. GFP-positive cells colocalized with Olig2 in layers 1–3. A small proportion of GFP-positive cells colocalized with NeuN in layers 1–3. In layers 4–6, the majority of GFP-positive cells colocalized with NeuN, and a small proportion of GFP-positive cells colocalized with Olig2. Scale bar: 50 μm. (E) DAB staining in the ICV and thalamic hemisphere showing GFP expression in the thalamus, caudate, putamen, substantia nigra pars compacta (SNc), globus pallidus, SNr, subthalamic nucleus (STN), and deep cerebellar nuclei (DCN). Scale bar: 100 μm.

transgene and are thus unlikely to cause the immunogenicity seen at the primary injection sites.

In summary, these findings demonstrate that binding of AAV2 to HSPGs significantly impacts AAV2-mediated transduction in the NHP CNS, and the route of delivery significantly impacts both vector distribution and tropism. We have shown that AAV2-HBKO undergoes extensive bidirectional axonal transport and therefore has considerable potential for the delivery of therapeutic candidate genes, where more global transduction of the brain is required. Further experiments will be needed to obtain a more comprehensive understanding of the axonal transport abilities observed with this vector. Our data demonstrate a valuable example of how modification of capsid-receptor interactions can change transduction profiles of AAV vectors and can be used to tailor AAV gene therapy vectors for clinical application. These findings also underscore the importance of identifying the appropriate vector serotype in conjunction with the optimal route of delivery to selectively deliver transgenes of interest to the CNS for the treatment of neurological disorders.

MATERIALS AND METHODS

Generation of AAV Capsid Mutant Plasmids

Mutagenesis was performed with the QuikChange Lightning Multi Site-Directed Mutagenesis kit following the manufacturer's protocol (Agilent Technologies, Santa Clara, CA, USA). The single-stranded AAV2-HBKO plasmid was generated by a PCR mutagenesis primer designed to introduce two mutations of arginines 585 and 588 to alanines into the parent rep/cap plasmid pIM45BD, a substitution that is repeated 60 times over the capsid surface. These mutations have previously been shown to abolish the HSPG receptor binding capability of AAV2.[44] The sequence of the mutagenesis primer used to introduce the R585A and R588A mutations was 5′-TATCTAC CAACCTCCAGGCAGGCAACGCACAAGCAGCTACCGCAG-3′, and the presence of the mutations was confirmed by sequencing.

AAV Vector Production

AAV vectors carrying the EGFP gene under the control of the chicken β-actin (CBA) promoter were produced by a transient transfection production method as previously described.[45] In brief, HEK293 cells were transfected with polyethyleneimine (PEI) and a 1:1:1 ratio of the three plasmids (ITR vector, AAV rep/cap, and Ad helper plasmid). The Ad helper plasmid used, pHelper, was obtained from (Stratagene/Agilent Technologies, Santa Clara, CA, USA). Purification of the vector was performed by column chromatography as previously described.[46] The vector preparation was substantially free of contaminants, as assessed by SDS-PAGE analysis with SYPRO staining; additionally the fractional content of empty capsids in the vector preparation was low at 13%, as determined by analytical ultracentrifugation (Figure S4).[47]

Non-human Primates

Eight adult male Rhesus macaques (*Macaca mulatta*) were screened for neutralizing antibodies against AAV2 prior to surgery as previously described.[11,24,37] Animals considered seronegative (serum titers < 1:25) were included in the study. Each animal received AAV2-HBKO-CBA-EGFP at a concentration of 1.2×10^{13} vg/ mL bilaterally into either the thalamus (n = 3; 130–280 μL per hemisphere), ICV (n = 3; 1.5 mL per hemisphere), or both ICV and thalamus (n = 2; 1.5 mL per ventricle and 200 μL per thalamus) under MRI-guided CED[48–50] with an adjustable stepped catheter (MRI Interventions, Irvine, CA, USA). The vector was mixed with a gadolinium-based magnetic resonance (MR) contrast agent diluted to 2 mM (ProHance H; Bracco Diagnostics, Princeton, NJ, USA) to enable visualization of the infusion in real time. The animal's head was placed in a MRI-compatible stereotactic frame, and a craniotomy was performed. The NHP was then moved to a 1.5T MRI GE scanner where T1-baseline images were acquired. Trajectory of the cannula relative to the target structures was determined with OsiriX software (Geneva, Switzerland). For the thalamic infusions the vector was infused at 1 μL/min while the cannula was inserted, then at 3–5 μL/min for the remainder of the infusion. ICV infusions involved infusion of vector at 1 μL/min and an increase in the flow rate to 10 μL/min once gadolinium signal was visualized in the target area. A transfrontal trajectory was utilized for both thalamic and ICV infusions.[51]

Tissue Processing

Animals were injected with a lethal dose of sodium pentobarbital 21 days after surgery, followed by transcardial perfusion with 0.1 M PBS and then fixation with 4% paraformaldehyde/PBS. The brains were removed, sliced into 6-mm coronal blocks, and along with the spinal cords, were post-fixed by immersion in 4% paraformaldehyde/PBS overnight. The next day, the brain and spinal cord were transferred to 30% (w/v) sucrose. GFP expression analysis was determined in 40-μm brain sections with a monoclonal antibody against GFP (rabbit anti-GFP, 1:1,000; G10362; Thermo Fisher Scientific, San Francisco, CA, USA). Motor neuron transduction was determined in 15-μm spinal cord sections immunostained with monoclonal antibodies against GFP and NeuN (mouse anti-NeuN, 1:5,000; mab377; Millipore, Temecula, CA, USA) on consecutive sections. A cresyl violet counterstain was performed on all sections to identify brain and spinal cord structures relative to transduced areas as previously described.[28,38,52] Standard H&E staining was performed in all animals in order to assess possible pathological signs. Astrogliosis and microglial hyperactivity were assessed by staining with antibodies directed against a marker of astrocytes (mouse monoclonal anti-GFAP, 1:15,000; mab360; Millipore, Temecula, CA, USA) and a microglial marker (rabbit polyclonal anti-Iba1, 1:1,000; CP290C; Biocare Medical, Pacheco, CA, USA) as previously described.[29,43,52]

Double-Immunofluorescent Staining

The phenotype of GFP-positive cells was examined by double-immunofluorescence staining. Brain sections were washed with 0.1 M PBS + Triton (PBST), blocked for 1 hr in 20% normal horse serum (Jackson ImmunoResearch), and then incubated overnight at 4°C with a mixture of anti-GFP and a specific antibody for oligodendrocytes (anti-Olig 2, mouse monoclonal, 1:100, MAB377; Millipore). After

incubation with primary antibodies, sections were washed in PBST, incubated with a cocktail of the corresponding secondary antibodies in PBS for 2 hr at room temperature, washed in PBS, and mounted on frosted slides. To avoid autofluorescence due to lipofuscin, sections were incubated in 0.3% Sudan Black B solution for 5 min and then washed in PBS followed by distilled water.

Motor Neuron Cell Counting

The number of transduced motor neurons in the spinal cord was determined on sections doubly immunostained with anti-GFP and anti-NeuN antibodies. The number of GFP-positive cells was compared with the total number of motor neurons. Cell transduction was quantified by manual cell counting bilaterally along the rostrocaudal axis of the cervical, thoracic, lumbar, and sacral segments. Large cell bodies located in laminae 8 and 9 (ventral horn) of the spinal cord were considered motor neurons. Approximately 4–6 sections were selected for each spinal cord segment to generate the overall mean number of motor neuron counts transduced per segment for each animal. Care was taken to anatomically match sections between animals.

Quantification of Cortical Transduction

Representative images were captured of representative whole-brain sections from the prefrontal, frontal, parietal, and occipital cortices that had undergone chromogenic anti-GFP staining at 1,200 dots per inch (dpi) with an Epson Perfection V700 Photo Scanner. The region of interest (ROI) tool in ImageJ was used to delineate the transduction area and total cortical area with the ROI manager as previously described.[3] The percentage of cortical transduction was calculated by dividing the area of transduction by the total cortical area. Image processing was undertaken by an observer blinded to treatment group. The average cortical transduction from three sections spaced 480 μm apart was used to determine the "% cortical area" transduced for each cortical region.

Quantification of Cellular Tropism in the Cortex

To determine the percentage of oligodendrocyte and neuronal transduction of the total GFP transduction in the cortex, we selected representative sections from the prefrontal, frontal, parietal, and occipital cortices that had undergone double-immunofluorescent staining against either Olig2 or NeuN and GFP. Images were taken with a Zeiss Axioscope microscope equipped with a Zeiss Mrc5 camera at 40× magnification. Images were captured in 16 randomly selected areas per section (8 images in superficial cortical layers 1–3 and 8 images in the deep cortical layers 4–6) first under blue excitation (to visualize GFP) and then by red excitation (to visualize Olig2 or NeuN). As described previously,[8] ImageJ was used to automatically count the total number of GFP-positive, GFP and NeuN double-labeled, and GFP/Olig2 double-labeled cells with the "Threshold" command used to separate background from the cells, which were then counted with the "Analyze Particles" command. The RGB image was converted to grayscale (8 bit), and the threshold set. The ImageJ analysis algorithm was applied to count the cells with a cutoff area of less than 100 pixels (noise).

Study Approval

All procedures were carried out with the approval of the Institutional Animal Care and Use Committee (IACUC permit: AN 117108) and in accordance with the Standard Operating Procedures protocol at University of California, San Francisco, San Francisco, CA, USA.

SUPPLEMENTAL INFORMATION

Supplemental Information includes five figures and can be found with this article online at https://doi.org/10.1016/j.ymthe.2018.07.008.

AUTHOR CONTRIBUTIONS

J.N. conducted experiments, generated and analyzed data, and wrote the paper; L.M.S. designed the experiment, and wrote and edited the paper; K.O. conducted experiments and analyzed data; S.T. processed tissue and generated data; L.S. conducted experiments and edited the paper; P.H. provided management and oversight; C.O. generated vectors and edited the paper; J.S. conducted experiments; W.S.S. edited the paper; J.R.B. conducted experiments; C.S. processed tissue and managed laboratory resources; Amin Mahmoodi processed tissue; Amir Mahmoodi processed tissue; J.F. reviewed and edited the paper; K.S.B. developed and designed methodology, provided supervision and leadership, and reviewed the paper; L.S.S. conceptualized ideas and edited the paper.

CONFLICTS OF INTEREST

L.M.S., C.O., J.S., and L.S.S. are employees of Sanofi.

ACKNOWLEDGMENTS

This work was supported by Sanofi.

REFERENCES

1. Hadaczek, P., Eberling, J.L., Pivirotto, P., Bringas, J., Forsayeth, J., and Bankiewicz, K.S. (2010). Eight years of clinical improvement in MPTP-lesioned primates after gene therapy with AAV2-hAADC. Mol. Ther. *18*, 1458–1461.

2. Sehara, Y., Fujimoto, K.-I., Ikeguchi, K., Katakai, Y., Ono, F., Takino, N., Ito, M., Ozawa, K., and Muramatsu, S.I. (2017). Persistent expression of dopamine-synthesizing enzymes 15 years after gene transfer in a primate model of Parkinson's disease. Hum. Gene Ther. Clin. Dev. *28*, 74–79.

3. Jensen, E.C. (2013). Quantitative analysis of histological staining and fluorescence using ImageJ. Anat. Rec. (Hoboken) *296*, 378–381.

4. Hocquemiller, M., Giersch, L., Audrain, M., Parker, S., and Cartier, N. (2016). Adeno-associated virus-based gene therapy for CNS diseases. Hum. Gene Ther. *27*, 478–496.

5. Bobo, R.H., Laske, D.W., Akbasak, A., Morrison, P.F., Dedrick, R.L., and Oldfield, E.H. (1994). Convection-enhanced delivery of macromolecules in the brain. Proc. Natl. Acad. Sci. USA *91*, 2076–2080.

6. Morrison, P.F., Laske, D.W., Bobo, H., Oldfield, E.H., and Dedrick, R.L. (1994). High-flow microinfusion: tissue penetration and pharmacodynamics. Am. J. Physiol. *266*, R292–R305.

7. Varenika, V., Kells, A.P., Valles, F., Hadaczek, P., Forsayeth, J., and Bankiewicz, K.S. (2009). Controlled dissemination of AAV vectors in the primate brain. Prog. Brain Res. *175*, 163–172.

8. Grishagin, I.V. (2015). Automatic cell counting with ImageJ. Anal. Biochem. *473*, 63–65.

9. Kotterman, M.A., and Schaffer, D.V. (2014). Engineering adeno-associated viruses for clinical gene therapy. Nat. Rev. Genet. *15*, 445–451.

10. Mastakov, M.Y., Baer, K., Kotin, R.M., and During, M.J. (2002). Recombinant adeno-associated virus serotypes 2- and 5-mediated gene transfer in the mammalian brain: quantitative analysis of heparin co-infusion. Mol. Ther. *5*, 371–380.

11. Summerford, C., and Samulski, R.J. (1998). Membrane-associated heparan sulfate proteoglycan is a receptor for adeno-associated virus type 2 virions. J. Virol. *72*, 1438–1445.

12. Burger, C., Gorbatyuk, O.S., Velardo, M.J., Peden, C.S., Williams, P., Zolotukhin, S., Reier, P.J., Mandel, R.J., and Muzyczka, N. (2004). Recombinant AAV viral vectors pseudotyped with viral capsids from serotypes 1, 2, and 5 display differential efficiency and cell tropism after delivery to different regions of the central nervous system. Mol. Ther. *10*, 302–317.

13. Pillay, S., Meyer, N.L., Puschnik, A.S., Davulcu, O., Diep, J., Ishikawa, Y., Jae, L.T., Wosen, J.E., Nagamine, C.M., Chapman, M.S., and Carette, J.E. (2016). An essential receptor for adeno-associated virus infection. Nature *530*, 108–112.

14. Cearley, C.N., and Wolfe, J.H. (2006). Transduction characteristics of adeno-associated virus vectors expressing cap serotypes 7, 8, 9, and Rh10 in the mouse brain. Mol. Ther. *13*, 528–537.

15. Taymans, J.-M., Vandenberghe, L.H., Haute, C.V.D., Thiry, I., Deroose, C.M., Mortelmans, L., Wilson, J.M., Debyser, Z., and Baekelandt, V. (2007). Comparative analysis of adeno-associated viral vector serotypes 1, 2, 5, 7, and 8 in mouse brain. Hum. Gene Ther. *18*, 195–206.

16. Kells, A.P., Hadaczek, P., Yin, D., Bringas, J., Varenika, V., Forsayeth, J., and Bankiewicz, K.S. (2009). Efficient gene therapy-based method for the delivery of therapeutics to primate cortex. Proc. Natl. Acad. Sci. USA *106*, 2407–2411.

17. Pomin, V.H., and Mulloy, B. (2015). Current structural biology of the heparin interactome. Curr. Opin. Struct. Biol. *34*, 17–25.

18. Hamilton, J.F., Morrison, P.F., Chen, M.Y., Harvey-White, J., Pernaute, R.S., Phillips, H., Oldfield, E., and Bankiewicz, K.S. (2001). Heparin coinfusion during convection-enhanced delivery (CED) increases the distribution of the glial-derived neurotrophic factor (GDNF) ligand family in rat striatum and enhances the pharmacological activity of neurturin. Exp. Neurol. *168*, 155–161.

19. Hadaczek, P., Mirek, H., Bringas, J., Cunningham, J., and Bankiewicz, K. (2004). Basic fibroblast growth factor enhances transduction, distribution, and axonal transport of adeno-associated virus type 2 vector in rat brain. Hum. Gene Ther. *15*, 469–479.

20. Sullivan, J.A., Stanek, L.M., Lukason, M.J., Bu, J., Osmond, S.R., Barry, E.A., O'Riordan, C.R., Shihabuddin, L.S., Cheng, S.H., and Scaria, A. (2018). Rationally designed AAV2 and AAVrh8R capsids provide improved transduction in the retina and brain. Gene Ther. *25*, 205–219.

21. Hadaczek, P., Stanek, L., Ciesielska, A., Sudhakar, V., Samaranch, L., Pivirotto, P., Bringas, J., O'Riordan, C., Mastis, B., San Sebastian, W., et al. (2016). Widespread AAV1- and AAV2-mediated transgene expression in the nonhuman primate brain: implications for Huntington's disease. Mol. Ther. Methods Clin. Dev. *3*, 16037.

22. Kanaan, N.M., Sellnow, R.C., Boye, S.L., Coberly, B., Bennett, A., Agbandje-McKenna, M., Sortwell, C.E., Hauswirth, W.W., Boye, S.E., and Manfredsson, F.P. (2017). Rationally engineered AAV capsids improve transduction and volumetric spread in the CNS. Mol. Ther. Nucleic Acids *8*, 184–197.

23. Hordeaux, J., Wang, Q., Katz, N., Buza, E.L., Bell, P., and Wilson, J.M. (2018). The neurotropic properties of AAV-PHP.B are limited to C57BL/6J mice. Mol. Ther. *26*, 664–668.

24. San Sebastian, W., Kells, A.P., Bringas, J., Samaranch, L., Hadaczek, P., Ciesielska, A., Macayan, M., Pivirotto, P.J., Forsayeth, J., Osborne, S., et al. (2014). Safety and tolerability of MRI-guided infusion of AAV2-hAADC into the mid-brain of non-human primate. Mol. Ther. Methods Clin. Dev. *3*, e14049.

25. Mandel, R.J., Marmion, D.J., Kirik, D., Chu, Y., Heindel, C., McCown, T., Gray, S.J., and Kordower, J.H. (2017). Novel oligodendroglial alpha synuclein viral vector models of multiple system atrophy: studies in rodents and nonhuman primates. Acta Neuropathol. Commun. *5*, 47.

26. Ciesielska, A., Hadaczek, P., Mittermeyer, G., Zhou, S., Wright, J.F., Bankiewicz, K.S., and Forsayeth, J. (2013). Cerebral infusion of AAV9 vector-encoding non-self proteins can elicit cell-mediated immune responses. Mol. Ther. *21*, 158–166.

27. Forsayeth, J., and Bankiewicz, K.S. (2015). Transduction of antigen-presenting cells in the brain by AAV9 warrants caution in preclinical studies. Mol. Ther. *23*, 612.

28. Samaranch, L., Sebastian, W.S., Kells, A.P., Salegio, E.A., Heller, G., Bringas, J.R., Pivirotto, P., DeArmond, S., Forsayeth, J., and Bankiewicz, K.S. (2014). AAV9-mediated expression of a non-self protein in nonhuman primate central nervous system triggers widespread neuroinflammation driven by antigen-presenting cell transduction. Mol. Ther. *22*, 329–337.

29. Samaranch, L., Salegio, E.A., San Sebastian, W., Kells, A.P., Bringas, J.R., Forsayeth, J., and Bankiewicz, K.S. (2013). Strong cortical and spinal cord transduction after AAV7 and AAV9 delivery into the cerebrospinal fluid of nonhuman primates. Hum. Gene Ther. *24*, 526–532.

30. Hadaczek, P., Forsayeth, J., Mirek, H., Munson, K., Bringas, J., Pivirotto, P., McBride, J.L., Davidson, B.L., and Bankiewicz, K.S. (2009). Transduction of nonhuman primate brain with adeno-associated virus serotype 1: vector trafficking and immune response. Hum. Gene Ther. *20*, 225–237.

31. Foust, K.D., Nurre, E., Montgomery, C.L., Hernandez, A., Chan, C.M., and Kaspar, B.K. (2009). Intravascular AAV9 preferentially targets neonatal neurons and adult astrocytes. Nat. Biotechnol. *27*, 59–65.

32. Szuchet, S., Nielsen, J.A., Lovas, G., Domowicz, M.S., de Velasco, J.M., Maric, D., and Hudson, L.D. (2011). The genetic signature of perineuronal oligodendrocytes reveals their unique phenotype. Eur. J. Neurosci. *34*, 1906–1922.

33. Qing, K., Mah, C., Hansen, J., Zhou, S., Dwarki, V., and Srivastava, A. (1999). Human fibroblast growth factor receptor 1 is a co-receptor for infection by adeno-associated virus 2. Nat. Med. *5*, 71–77.

34. Chen, H., McCarty, D.M., Bruce, A.T., Suzuki, K., and Suzuki, K. (1998). Gene transfer and expression in oligodendrocytes under the control of myelin basic protein transcriptional control region mediated by adeno-associated virus. Gene Ther. *5*, 50–58.

35. Lawlor, P.A., Bland, R.J., Mouravlev, A., Young, D., and During, M.J. (2009). Efficient gene delivery and selective transduction of glial cells in the mammalian brain by AAV serotypes isolated from nonhuman primates. Mol. Ther. *17*, 1692–1702.

36. Powell, S.K., Khan, N., Parker, C.L., Samulski, R.J., Matsushima, G., Gray, S.J., and McCown, T.J. (2016). Characterization of a novel adeno-associated viral vector with preferential oligodendrocyte tropism. Gene Ther. *23*, 807–814.

37. Green, F., Samaranch, L., Zhang, H.S., Manning-Bog, A., Meyer, K., Forsayeth, J., and Bankiewicz, K.S. (2016). Axonal transport of AAV9 in nonhuman primate brain. Gene Ther. *23*, 520–526.

38. Samaranch, L., Blits, B., San Sebastian, W., Hadaczek, P., Bringas, J., Sudhakar, V., Macayan, M., Pivirotto, P.J., Petry, H., and Bankiewicz, K.S. (2017). MR-guided parenchymal delivery of adeno-associated viral vector serotype 5 in non-human primate brain. Gene Ther. *24*, 253–261.

39. Davidson, B.L., Stein, C.S., Heth, J.A., Martins, I., Kotin, R.M., Derksen, T.A., Zabner, J., Ghodsi, A., and Chiorini, J.A. (2000). Recombinant adeno-associated virus type 2, 4, and 5 vectors: transduction of variant cell types and regions in the mammalian central nervous system. Proc. Natl. Acad. Sci. USA *97*, 3428–3432.

40. McCown, T.J., Xiao, X., Li, J., Breese, G.R., and Samulski, R.J. (1996). Differential and persistent expression patterns of CNS gene transfer by an adeno-associated virus (AAV) vector. Brain Res. *713*, 99–107.

41. Lo, W.D., Qu, G., Sferra, T.J., Clark, R., Chen, R., and Johnson, P.R. (1999). Adeno-associated virus-mediated gene transfer to the brain: duration and modulation of expression. Hum. Gene Ther. *10*, 201–213.

42. Deverman, B.E., Pravdo, P.L., Simpson, B.P., Kumar, S.R., Chan, K.Y., Banerjee, A., Wu, W.L., Yang, B., Huber, N., Pasca, S.P., and Gradinaru, V. (2016). Cre-dependent selection yields AAV variants for widespread gene transfer to the adult brain. Nat. Biotechnol. *34*, 204–209.

43. Samaranch, L., Sebastian, W.S., Kells, A.P., Salegio, E.A., Heller, G., Bringas, J.R., Pivirotto, P., DeArmond, S., Forsayeth, J., and Bankiewicz, K.S. (2014). AAV9-mediated expression of a non-self protein in nonhuman primate central nervous system triggers widespread neuroinflammation driven by antigen-presenting cell transduction. Mol. Ther. *22*, 329–337.

44. Opie, S.R., Warrington, K.H., Jr., Agbandje-McKenna, M., Zolotukhin, S., and Muzyczka, N. (2003). Identification of amino acid residues in the capsid proteins of adeno-associated virus type 2 that contribute to heparan sulfate proteoglycan binding. J. Virol. *77*, 6995–7006.

45. Xiao, X., Li, J., and Samulski, R.J. (1998). Production of high-titer recombinant adeno-associated virus vectors in the absence of helper adenovirus. J. Virol. *72*, 2224–2232.

46. Nass, S.A., Mattingly, M.A., Woodcock, D.A., Burnham, B.L., Ardinger, J.A., Osmond, S.E., Frederick, A.M., Scaria, A., Cheng, S.H., and O'Riordan, C.R. (2017). Universal method for the purification of recombinant AAV vectors of differing serotypes. Mol. Ther. Methods Clin. Dev. *9*, 33–46.

47. Burnham, B., Nass, S., Kong, E., Mattingly, M., Woodcock, D., Song, A., Wadsworth, S., Cheng, S.H., Scaria, A., and O'Riordan, C.R. (2015). Analytical ultracentrifugation as an approach to characterize recombinant adeno-associated viral vectors. Hum. Gene Ther. Methods *26*, 228–242.

48. Nguyen, J.B., Sánchez-Pernaute, R., Cunningham, J., and Bankiewicz, K.S. (2001). Convection-enhanced delivery of AAV-2 combined with heparin increases TK gene transfer in the rat brain. Neuroreport *12*, 1961–1964.

49. Fiandaca, M.S., Forsayeth, J.R., Dickinson, P.J., and Bankiewicz, K.S. (2008). Image-guided convection-enhanced delivery platform in the treatment of neurological diseases. Neurotherapeutics *5*, 123–127.

50. Su, X., Kells, A.P., Salegio, E.A., Richardson, R.M., Hadaczek, P., Beyer, J., Bringas, J., Pivirotto, P., Forsayeth, J., and Bankiewicz, K.S. (2010). Real-time MR imaging with Gadoteridol predicts distribution of transgenes after convection-enhanced delivery of AAV2 vectors. Mol. Ther. *18*, 1490–1495.

51. Bankiewicz, K.S., Sudhakar, V., Samaranch, L., San Sebastian, W., Bringas, J., and Forsayeth, J. (2016). AAV viral vector delivery to the brain by shape-conforming MR-guided infusions. J. Control. Release *240*, 434–442.

52. Samaranch, L., Salegio, E.A., San Sebastian, W., Kells, A.P., Foust, K.D., Bringas, J.R., Lamarre, C., Forsayeth, J., Kaspar, B.K., and Bankiewicz, K.S. (2012). Adeno-associated virus serotype 9 transduction in the central nervous system of nonhuman primates. Hum. Gene Ther. *23*, 382–389.

Original Paper

Cerebrovascular Diseases

Cerebrovasc Dis 2015;39:224–231
DOI: 10.1159/000375153

Received: August 25, 2014
Accepted: January 12, 2015
Published online: March 19, 2015

Cerebral Perivascular Spaces Visible on Magnetic Resonance Imaging: Development of a Qualitative Rating Scale and its Observer Reliability

Gillian M. Potter Francesca M. Chappell Zoe Morris Joanna M. Wardlaw

Brain Imaging Research Centre, University of Edinburgh, Edinburgh, UK

Key Words

Small vessel disease · Stroke · Leukoaraiosis · Magnetic resonance imaging · Brain infarction · Dilated perivascular spaces

Abstract

Background: Perivascular spaces (PVS) are an important component of cerebral small vessel disease (SVD), several inflammatory disorders, hypertension and blood-brain barrier breakdown, but are difficult to quantify. A recent international collaboration of SVD experts has highlighted the need for a robust, easy-to-use PVS rating scale for the effective investigation of the diagnostic and prognostic significance of PVS. The purpose of the current study was to develop and extend existing PVS scales to provide a more comprehensive scale for the measurement of PVS in the basal ganglia, centrum semiovale and midbrain, and to test its intra- and inter-rater agreement, assessing reasons for discrepancy. ***Methods:*** We reviewed previously published PVS scales, including site of PVS assessed, rating method, and size and morphological criteria. Retaining key features, we devised a more comprehensive scale in order to improve the reliability of PVS rating. Two neuroradiologists tested the new scale in MRI brain scans of 60 patients from two studies (stroke, ageing population), chosen to represent a full range of PVS, and demonstrating concomitant features of SVD such as lacunes and white matter hyperintensities. We rated basal ganglia, centrum semiovale, and midbrain PVS. Basal ganglia and centrum semiovale PVS were rated 0 (none), 1 (1–10), 2 (11–20), 3 (21–40) and 4 (>40), and midbrain PVS were rated 0 (none visible) or 1 (visible). We calculated kappa statistics for rating, assessed consistency in use of PVS categories (Bhapkar test) and reviewed sources of discrepancy. ***Results:*** Intra- and inter-rater kappa statistics were highest for basal ganglia PVS (range 0.76–0.87 and 0.8–0.9, respectively) than for centrum semiovale PVS (range 0.68–0.75 and 0.61–0.8, respectively) or midbrain PVS (inter-rater range 0.51–0.52). Inter-rater consistency was better for basal ganglia compared to centrum semiovale PVS (Bhapkar statistic 2.49–3.72, compared to 6.79–21.08, respectively). Most inter-rater disagreements were due to very faint PVS, coexisting extensive white matter hyperintensities (WMH) or the presence of lacunes. ***Conclusions:*** We developed a more inclusive and robust visual PVS rating scale allowing rating of all grades of PVS severity on structural brain imaging. The revised PVS rating scale has good observer reliability for basal ganglia and centrum semiovale PVS, best for basal ganglia PVS, and moderate reliability for midbrain PVS. Agreement is influenced by PVS severity and the presence of background features of SVD. The current scale can be used in further studies to assess the clinical implications of PVS. © 2015 S. Karger AG, Basel

KARGER 125

E-Mail karger@karger.com
www.karger.com/ced

© 2015 S. Karger AG, Basel
1015–9770/15/0394–0224$0.00/0

Karger Open access

This is an Open Access article licensed under the terms of the Creative Commons Attribution 3.0 Unported license (CC BY 3.0) (www.karger.com/OA-license-WT), applicable to the online version of the article only.

Joanna M. Wardlaw
Division of Neuroimaging Sciences and SINAPSE Collaboration, Brain Imaging Research Centre, University of Edinburgh, Western General Hospital
Crewe Road, Edinburgh EH4 2XU (UK)
E-Mail Joanna.Wardlaw@ed.ac.uk

Introduction

Perivascular spaces (or Virchow-Robin spaces) surround arterioles and venules as they perforate the brain parenchyma [1] and are normally microscopic, but may be visualised on T2- or T1-weighted brain MRI when enlarged (fig. 1). PVS may act as drainage pathways to remove interstitial fluid from the brain [2–4], so, when enlarged, may represent interstitial fluid trapped in the subpial or interpial spaces [5]. The full diagnostic and prognostic significance of PVS are unknown. PVS appear in small numbers in all age groups, but increase in frequency with advancing age [6, 7], and are associated with worse cognition [8–10] and with several disease states, including CADASIL (cerebral autosomal dominant arteriopathy with subcortical infarcts and leukoencephalopathy) [11], depression at older ages [12], active multiple sclerosis during inflammation [13], myotonic dystrophy [14], Parkinson's disease [15] and small vessel disease (SVD) in the form of lacunar stroke [16–20], WMH [18, 20, 21] and vascular dementia [22].

PVS form part of the spectrum of changes seen on MRI in SVD. Until recently, PVS have been somewhat ignored, not being included in any of the existing WMH rating scales [23]. However, a recent international collaboration of experts in SVD has highlighted the need for a robust, easy-to-use PVS rating scale, alongside those in use for WMH and brain microbleeds [24]. Reliable PVS rating scales, whether visual or automated [24] are essential if the diagnostic and prognostic significance of PVS are to be investigated effectively. Several scales have been described (online suppl. table 1; for all online suppl. material, see www.karger.com/doi/10.1159/000375153) [6, 8, 14, 18, 22, 25–28], but may not adequately capture the range of anatomical coverage, frequency or severity; these have not been extensively tested outside their inception studies.

The purpose of this study was to provide a more comprehensive scale and test its observer agreement, assessing whether raters differed in their assessment of none, mild, moderate, frequent, and severe PVS in the presence of common features of aging and SVD.

Methods

We considered PVS to be small, sharply delineated structures of cerebrospinal fluid (CSF) intensity measuring <3 mm in cross-sectional diameter, following the course of perforating vessels, round if in axial and longitudinal if cut in the long axis of the perivascular space [24]. We reported the study according to the STRIVE guidelines.

Development and Extension of Existing PVS Rating Scales

We reviewed previously published scales (online suppl. table 1) [6, 8, 14, 18, 22, 25–28]. A neuroradiologist applied each scale on two occasions to a test set of 20 standard T2-weighted MR scans from a study of aging, and made incremental modifications to one existing scale by carefully noting benefits and drawbacks of each scale as follows:

PVS Sites

We retained basal ganglia and centrum semiovale regions (included in all but one of the previously published scales; online suppl. table 1) and added the midbrain (included in one previous scale), as these are three major sites for PVS [1; fig. 1]. We removed the hippocampus location because of its variable visualisation on axial images and because hippocampal PVS may be confused with hippocampal fissural cysts, currently thought to be normal variants. As most people have PVS in the anterior perforated substance [26], we chose not to add this location to the revised scale, for the basal ganglia, as it would not enhance specificity, although this has been included in a recently developed scale, in which PVS are assessed on a single slice at the level of the anterior commissure [28]. We did not separate PVS into sub-regions in the basal ganglia, as we found this difficult and time-consuming [22]. Similarly, we found subgrouping of PVS in the centrum semiovale [25] did not improve intra-rater variability. We tested the effects on intra-rater variability of using predefined slices and predefined regions, for example, for basal ganglia, using the slice showing the maximal area and for centrum semiovale, regions defined by predefined gyri and sulci, for instance, PVS anterior to the central sulcus. None of these improved consistency.

Method of Rating

We retained the frequency and range of PVS used by Mac Lullich et al. [8] as follows: 0 = none, 1 = 1–10, 2 = 11–20, 3 = 21–40, 4 = >40 PVS per region (fig. 2). These categories are similar to those used by Rouhl et al. [25] and seemed to best reflect the potential frequency and range of PVS in a wide range of normal aging and stroke-related disease subjects; some previous scales had rather restricted range and frequency of PVS grades [18, 22, 27] or required every individual PVS to be counted [14], and therefore, this was impractical for use in large studies and reduced reliability.

Size/Morphology

Unlike two previous studies [14, 27], we did not include size criteria due to difficulties in distinguishing between PVS measuring <2 mm and 2–3 mm on routine images (this could be added in studies with very high-resolution images). We used frequency and range of PVS in preference to morphology. Although excluded in one previous scale [25], we chose to include PVS surrounded by a FLAIR-hyperintense rim, since the exact nature of these is unclear and we saw no reason to exclude them if they met PVS criteria in all other respects.

PVS Rating Scale User Guide

We constructed a user guide with detailed definitions, descriptions and clear examples (http://www.sbirc.ed.ac.uk/documents/epvs-rating-scale-user-guide.pdf) prior to testing the revised scale, providing examples for each category/region with instructions on slice selection.

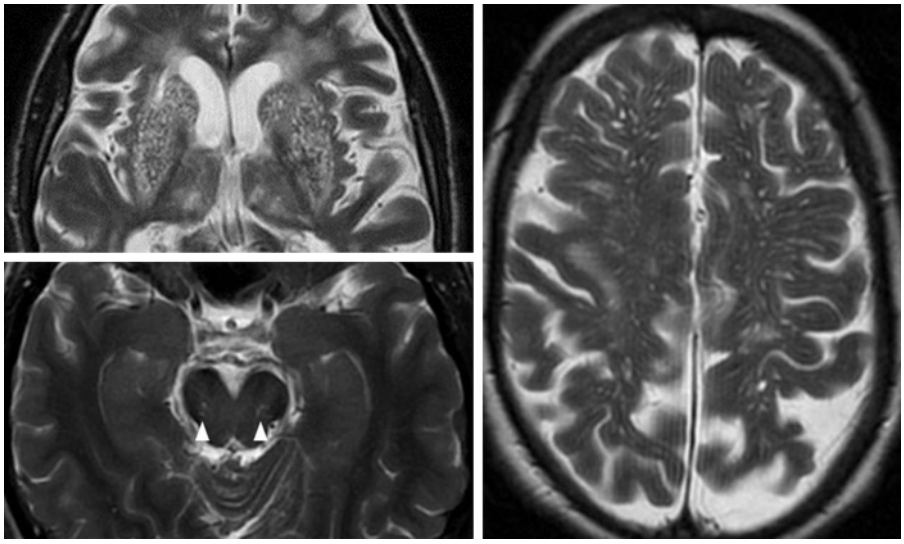
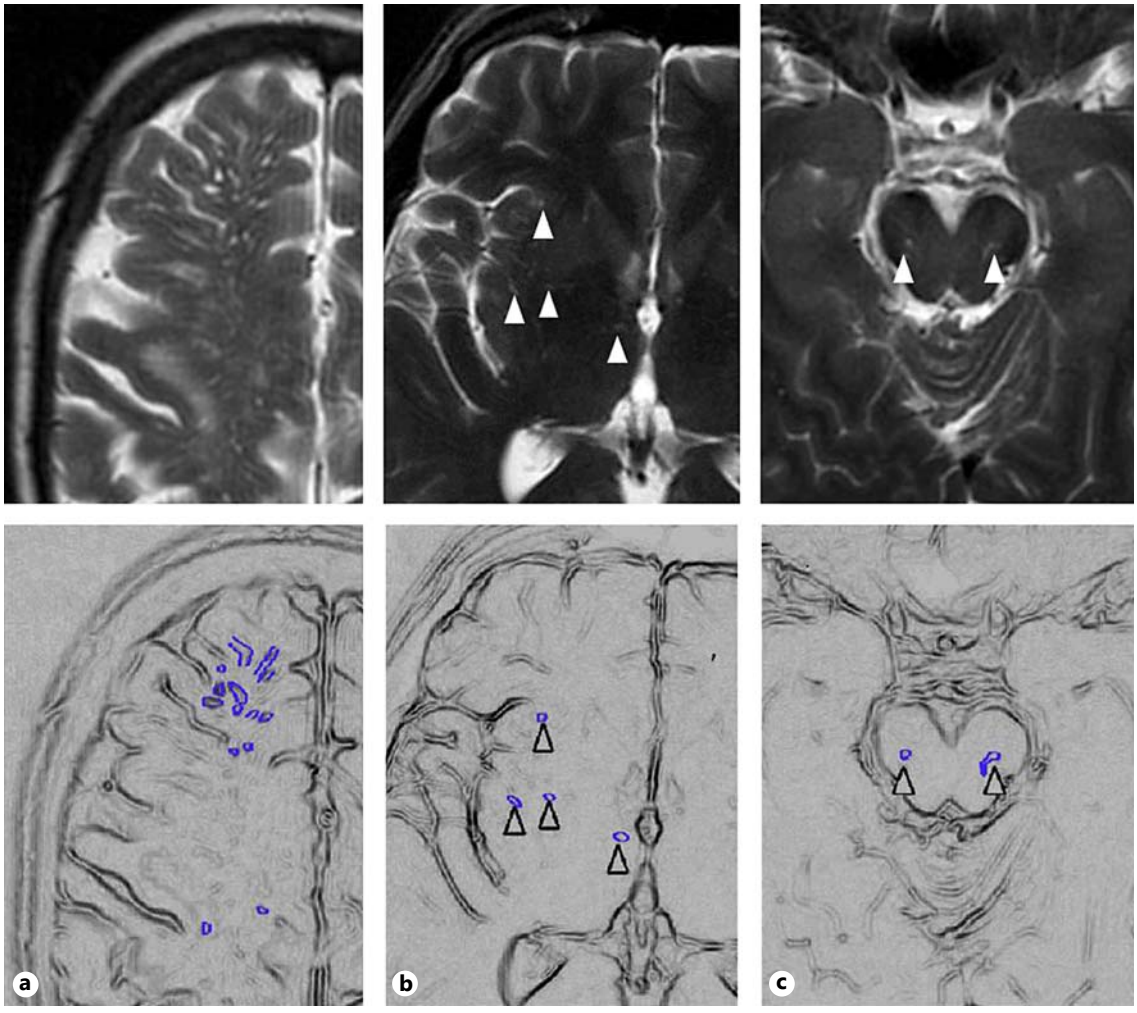


Fig. 1. Severe basal ganglia (top left) and centrum semiovale PVS (right). PVS visible in the midbrain (bottom left, arrowheads).



Color version available online

Fig. 2. a Grade 4 (severe) centrum semiovale PVS (highlighted in schematic). **b** Grade 2 basal ganglia PVS (arrowheads). **c** Visible (grade 1) midbrain PVS (arrowheads).

Table 1. Intra- and inter-rater kappa statistics for PVS rating

Sample	Brain region	Rater	Intra-rater kappa (95% CI)	Inter-rater kappa** (95% CI)
Aging study	Centrum semiovale	1	0.68 (0.34–1.00)	0.61 (0.39–0.81)
		2	0.70 (0.49–0.92)	
	Basal ganglia	1	0.80 (0.66–0.94)	0.80 (0.66–0.94)
		2	0.76 (0.35–1.00)	
	Midbrain	1	0.64 (0.01–1.00)	0.51 (0.06–0.96)
		2	0.58 (0.17–1.00)	
Stroke study	Centrum semiovale	1	0.75 (0.62–0.90)	0.80 (0.67–0.93)
		2	0.74 (0.59–0.86)	
	Basal ganglia	1	0.87 (0.79–0.95)	0.90 (0.84–0.97)
		2	0.80 (0.72–0.89)	
	Midbrain	1	0.60 (0.25–0.96)	0.52 (0.21–0.84)
		2	0.79 (0.56–1.00)	

* Calculated using data from first rating.

** Kappa statistics for centrum semiovale and basal ganglia PVS quadratically weighted; quadratic weighting not possible for midbrain PVS due to only two possible categories for PVS rating.

Assessment of Intra- and Inter-Rater Agreement of Revised PVS Rating Scale

Two experienced neuroradiologists (JMW, ZM), blinded to the other's ratings and not involved in the initial testing of published scales or development of the revised scale, tested the modified PVS rating scale by each rating 60 T2-weighted MR scans (with T1-weighted and FLAIR imaging also available), selected from the archives of the Brain Research Imaging Centre to represent a range of PVS, white matter hyperintensities and atrophy, from studies of ageing and minor stroke, on two separate occasions. For the basal ganglia and centrum semiovale PVS were rated from 0 (none), 1 (1–10), 2 (11–20), 3 (21–40), and 4 (>40), using an overall score for both hemispheres by assessing and scoring each hemisphere separately and then using the hemisphere with the higher score where hemispheres were asymmetric. Midbrain PVS were rated 0 (none visible) or 1 (visible). Images were reviewed by each rater in a random order using a web-based random number service (RANDOM.ORG) on each occasion, at least one week apart. MRI scans were chosen to represent a range of few to many PVS from older subjects scanned in research studies on SVD at the Brain Research Imaging Centre and assessed digitally on a high-definition screen using the National Kodak Picture Archiving and Communication System.

Statistical Analysis

We calculated intra- and inter-observer weighted (quadratic) kappas for agreement beyond that due to chance for the basal ganglia and CS data and simple kappa for the midbrain data. All data were analysed with SAS 9.1 (www.sas.com), R 2.14.2 (cran.r-project.org/), and MH Program 1.2 (www.john-uebersax.com/stat/mh.htm). We also cross-tabulated PVS rating scores and provided the estimates of the overall percentage intra- and inter-rater agreement, calculated by summing the number of times scans were given the same rating and dividing by the total number of scans. We assessed this percentage agreement for the overall score and for basal ganglia, centrum semiovale and midbrain PVS scores.

We also assessed the consistency of rating by whether raters differed in their assessment of PVS severity, both between the first and second scan assessment (intra-rater) and between raters (on the first assessment) using the Bhapkar [29] test of the table obtained by cross-tabulating the scan results.

Results

Observer Agreement, Consistency of Rating and Sources of Discrepancy

Overall kappa statistic measurement of agreement for PVS was moderate to good. There was better agreement for basal ganglia PVS than for centrum semiovale PVS, with basal ganglia PVS intra- and inter-rater agreement ranging from 0.76 to 0.87 and from 0.8 to 0.9, compared to 0.68 to 0.75 and 0.61 to 0.8 for centrum semiovale PVS, respectively; table 1. Agreement was lowest for midbrain PVS, with intra-rater agreement ranging from 0.58 to 0.70 and inter-rater agreement ranging from 0.51 to 0.52 (table 1).

Overall, there was more intra-rater consistency (Bhapkar 0.34 to 18.2) than inter-rater consistency (Bhapkar 2.49 to 21.08), and centrum semiovale PVS were rated less consistently than both basal ganglia and midbrain PVS (online suppl. tables 2, 3).

Table 2. Causes for intra-rater (**a**) and inter-rater (**b**) disagreement

a

PVS site	Description	n (%)
Centrum semiovale (n = 20)	Asymmetric/focally dilated PVS	1 (5)
	WMH present[a]	7 (35)
	No WMH present[b]	11 (55)
	Movement artefact	1 (5)
Basal ganglia (n = 8)	Rating 2 versus 3, no clear cause for disagreement	6 (75)
	Unilateral old large cortical infarct	1 (12.5)
	Multiple possible lacunes bilaterally	1 (12.5)

[a] 1-point different in scale, n = 4; 2-point difference, n = 2; 3-point difference, n = 1. WMH confluent (n = 5) or scattered (n = 2).
[b] 1-point difference in rating in 10/11 cases.

b

PVS site	Description	n (%)
Centrum semiovale (n = 21)	WMH present[a]	9 (42.9)
	No WMH present[b]	11 (52.4)
	Movement artefact	1 (4.8)
Basal ganglia (n = 12)	Rating 2 versus 3, no clear cause for disagreement	5 (41.7)
	Unilateral old large cortical infarct	1 (12.5)
	Multiple possible lacunes[c]	6 (50)

[a] 1-point different in scale, n = 6; 2-point difference, n = 3; WMH confluent (n = 7) or scattered (n = 2).
[b] 1-point difference in rating in 10/11 cases.
[c] Unilateral in 3, bilateral in 3.

Percentage Observer Agreement

For all PVS sites, intra-rater percentage agreement was similar to inter-rater agreement, ranging from 0.54 to 0.96 compared to 0.43 to 0.87, respectively (online suppl. table 4). Percentage agreement for basal ganglia and centrum semiovale categories was similar, with intra- and inter-observer agreement for basal ganglia ranging from 0.54 to 0.68 and from 0.65 to 0.77, respectively and for centrum semiovale, from 0.57 to 0.65 and 0.65 to 0.68, respectively. Higher intra- and inter-rater percentage agreement was seen for midbrain PVS compared to both centrum semiovale and basal ganglia PVS (supplementary table 4).

Discussion

A recent SVD expert collaborative highlights the emerging importance of PVS as an imaging marker for SVD on MRI. We reviewed existing PVS rating scales and developed a more inclusive and robust scale, incorporating all relevant PVS sites and allowing rating of all grades of PVS severity on standard structural brain MR imaging. We found good observer agreement between two experienced neuroradiologists for PVS rating in the centrum semiovale and basal ganglia, and moderate agreement for midbrain PVS. Kappa statistic measurement of agreement and consistency of rating were better for basal ganglia than for centrum semiovale PVS, and lowest for midbrain PVS. Midbrain PVS agreement is likely to be artificially inflated by the limited number of PVS categories to choose from and the fewer number of slices on which midbrain PVS appear. The presence of concomitant WMH and lacunes were the main sources of discrepancy between observers (table 2, figure 3).

The current scale was developed following a comprehensive review of existing PVS scales. We deliberately included MRI scans range of background appearances, including WMH and lacunes, which are more likely to re-

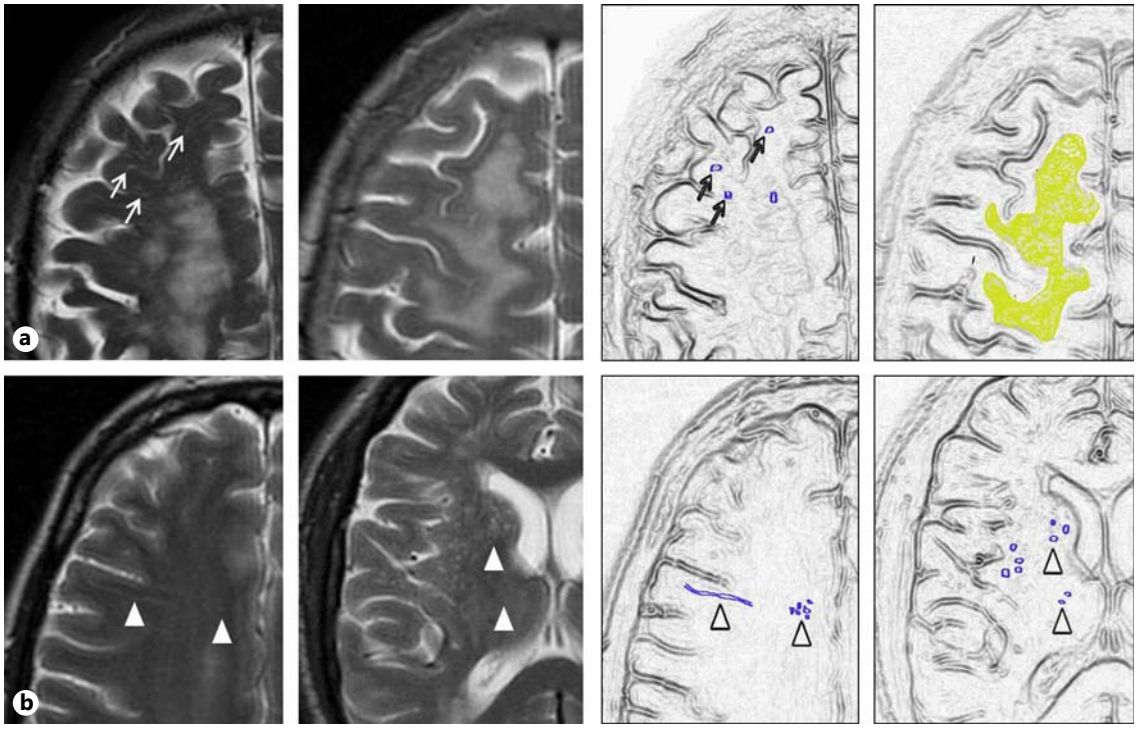


Fig. 3. Main causes for observer variability in PVS rating. **a** WMH in the centrum semiovale, with PVS still visible (left) or obscured (right). **b** Small, poorly visualised PVS in the centrum semiovale (left) and basal ganglia (right).

flect the range of appearances likely to be seen in cohorts of older subjects and stroke patients in whom PVS scales are likely to be used. We included the three main sites where PVS are seen, rather than limiting assessment to restricted brain regions. We assessed PVS on commonly used structural MRI sequences, rather than specialised sequences, helping to increase its general applicability to current research studies of cerebral small vessel disease. We performed extensive, detailed multistatistical analysis of our data.

Our study had limitations. We did not assess atrophy, which may have an influence on PVS severity, but this was not the purpose of this study. The scale was tested by two experienced neuroradiologists, but brain imaging in many research studies is performed by non-radiologists [27] and many raters may be less experienced in reviewing MRI scans and in rating PVS. The use of two raters and experienced raters could have also led to inflated kappa values. Other scales have used multiple observers; however in some cases, the type of rater, and experience in assessing MRI brain images, was unclear; our inclusion of a user guide is designed to help improve observer agreement among observers of difference background and experience. Our revised scale was tested in a cohort of healthy, elderly patients of a similar age and in a stroke cohort; therefore, our results may not be generalisable for all study populations. However, we acknowledge that more studies in larger and different populations are required.

Our finding of lower intra- and inter-rater agreement for centrum semiovale PVS than for basal ganglia PVS confirms previous findings (table 1). Higher overall intra- and inter-observer agreement for all brain regions described by Patankar et al. [22] may reflect the differences in imaging technique or less diseased subjects. We assessed PVS on 5 mm thick contiguous structural brain MR imaging rather than on high-definition 3D sequences, and hence, our data may be more relevant to PVS in other cohorts (table 1). Also high-definition sequences could increase observer disagreement by increasing the visibility of small PVS, which would need to be tested. The overall agreement was higher in all three brain regions in a recently developed PVS scale [28]; however, rating was performed on a single slice for the centrum semiovale and basal ganglia, which, although appearing more accurate, may not be a true or accurate reflection in number or severity of PVS due to individual anatomical variation in the location of PVS, a factor further influenced by differ-

ences in patient positioning. Our inter-rater data for basal ganglia PVS are higher than that described by Rouhl et al. [25], with similar results for centrum semiovale PVS, which may reflect the differences in one or several factors, including type of observer, differences in background MRI brain appearances and method of PVS measurement.

Greater variability in rating of centrum semiovale PVS may be partly due to the higher number of potential slices available for rating, with slices containing more or less PVS depending on the level, or to WMH obscuring PVS; in the current study, concurrent WMH, especially when confluent, led to disagreement. PVS may still remain visible 'through' WMH. Others have selected only one representative slice for the assessment of number of PVS in the hippocampus, basal ganglia, midbrain and centrum semiovale [28]; this may be oversimplification and problematic given the individual variability in position of PVS in the basal ganglia and centrum semiovale, and in our opinion, the assessment of all slices that include PVS in the brain region being assessed is necessary in order to form an overall impression of severity (or visibility, for midbrain).

At the present time, it is unclear whether increased severity of PVS in a particular brain region has more important clinical implications in the context of cerebral SVD [20]; however, until more data are available, assessment of PVS in each site is likely to be beneficial. Depending on future studies, our scale may require further modification, for example, the removal of centrum semiovale and midbrain locations, with a stronger focus on accurate rating of basal ganglia PVS. The clinical relevance of midbrain PVS is unclear at the present time; however, as this is a frequent site of PVS, it seems relevant to include this region.

Although we have developed and tested a visual rating scale, automated PVS measurement methods may be possible with improved image-processing algorithms in future [30], as has already occurred for WMH rating [31, 32], which may further improve consistency in rating.

The clinical relevance of PVS is currently unclear. A recent international collaboration of SVD experts defining the terminology for imaging features of SVD highlights the need for a robust, easy-to-apply PVS rating scale, which can be used in multicenter research studies. We have developed a scale that enables the rating of PVS to a good level of inter-rater agreement for the two major PVS sites in the basal ganglia and centrum semiovale. This scale should be further tested in different patient populations and by raters with different clinical backgrounds and imaging experience. Studies assessing the pathological role of PVS using such scales will need to consider other components of SVD in multivariable analyses to account for the interrelationships between SVD features.

Acknowledgements

We would like to thank the patients and carers, and the doctors, administrators, radiographers, stroke clinical audit and programming staff who contributed to the collection of data. We are grateful for clinical input from Profs. Charles Warlow and Peter Sandercock, neuroradiological input from Dr. Andrew Farrall, programming assistance from Aidan Hutchinson and Mike McDowall, and administrative support from Isabel Jennings. Both studies were approved by the Local Research Ethics Committee and all patients (or their relatives) gave written informed consent.

Disclosure Statement

None declared.

Funding

J.M.W. was funded by the Scottish Funding Council SINAPSE Initiative (Scottish Imaging Network, A Platform for Scientific Excellence). G.M.P. and Z.M. were funded by NHS Lothian Research and Development and the Chief Scientist Office of the Scottish Executive. The Lothian Birth Cohort 1936 Study is funded by Age UK and the UK Medical Research Council. The stroke research register was funded by the Wellcome Trust (grant number 063668).

References

1 Kwee RM, Kwee TC: Virchow-Robin spaces at MR imaging. Radiographics 2007;27:1071–1086.
2 Weller RO, Kida S, Zhang ET: Pathways of fluid drainage from the brain – morphological aspects and immunological significance in rat and man. Brain Pathol 1992;2:277–284.
3 Esiri MM, Gay D: Immunological and neuropathological significance of the Virchow-Robin space. J Neurol Sci 1990;100:3–8.
4 Abbott NJ: Evidence for bulk flow of brain interstitial fluid: significance for physiology and pathology. Neurochem Int 2004;45:545–552.
5 Oztürk MH, Aydingöz U: Comparison of MR signal intensities of cerebral perivascular (Virchow-Robin) and subarachnoid spaces. J Comput Assist Tomogr 2002;26:902–904.
6 Zhu YC, Dufouil C, Mazoyer B, Soumaré A, Ricolfi F, Tzourio C, Chabriat H: Frequency and location of dilated Virchow-Robin spaces in elderly people: a population-based 3D MR imaging study. AJNR Am J Neuroradiol 2011;32:709–713.

7 Satizabal CL, Zhu YC, Dufouil C, Tzourio C: Inflammatory proteins and the severity of dilated Virchow-Robin spaces in the elderly. J Alzheimers Dis 2013;33:323–328.
8 MacLullich AM, Wardlaw JM, Ferguson KJ, Starr JM, Seckl JR, Deary IJ: Enlarged perivascular spaces are associated with cognitive function in healthy elderly men. J Neurol Neurosurg Psychiatry 2004;75:1519–1523.
9 Zhu YC, Dufouil C, Soumaré A, Mazoyer B, Chabriat H, Tzourio C: High degree of dilated Virchow-Robin spaces on MRI is associated with increased risk of dementia. J Alzheimers Dis 2010;22:663–672.
10 Ferguson SC, Blane A, Perros P, McCrimmon RJ, Best JJ, Wardlaw J, Deary IJ, Frier BM: Cognitive ability and brain structure in type 1 diabetes: relation to microangiopathy and preceding severe hypoglycemia. Diabetes 2003;52:149–156.
11 Cumurciuc R, Guichard JP, Reizine D, Gray F, Bousser MG, Chabriat H: Dilation of Virchow-Robin spaces in CADASIL. Eur J Neurol 2006;13:187–190.
12 Patankar TF, Baldwin R, Mitra D, Jeffries S, Sutcliffe C, Burns A, Jackson A: Virchow-Robin space dilatation may predict resistance to antidepressant monotherapy in elderly patients with depression. J Affect Disord 2007; 97:265–270.
13 Wuerfel J, Haertle M, Waiczies H, Tysiak E, Bechmann I, Wernecke KD, Zipp F, Paul F: Perivascular spaces – MRI marker of inflammatory activity in the brain? Brain 2008;131: 2332–2340.
14 Di Costanzo A, Di Salle F, Santoro L, Bonavita V, Tedeschi G: Dilated Virchow-Robin spaces in myotonic dystrophy: frequency, extent and significance. Eur Neurol 2001;46:131–139.
15 Laitinen LV, Chudy D, Tengvar M, Hariz MI, Bergenheim AT: Dilated perivascular spaces in the putamen and pallidum in patients with Parkinson's disease scheduled for pallidotomy: a comparison between MRI findings and clinical symptoms and signs. Mov Disord 2000;15:1139–1144.
16 Zhu YC, Tzourio C, Soumaré A, Mazoyer B, Dufouil C, Chabriat H: Severity of dilated Virchow-Robin spaces is associated with age, blood pressure, and MRI markers of small vessel disease: a population-based study. Stroke 2010;41:2483–2490.
17 Doubal FN, MacLullich AM, Ferguson KJ, Dennis MS, Wardlaw JM: Enlarged perivascular spaces on MRI are a feature of cerebral small vessel disease. Stroke 2010;41:450–454.
18 Adachi T, Kobayashi S, Yamaguchi S, Okada K: MRI findings of small subcortical 'lacunar-like' infarction resulting from large vessel disease. J Neurol 2000;247:280–285.
19 Potter GM, Doubal FN, Jackson CA, Chappell FM, Sudlow CL, Dennis MS, Wardlaw JM: Enlarged perivascular spaces and cerebral small vessel disease. Int J Stroke 2013, DOI 10.1111/ijs.12054.
20 Hurford R, Charidimou A, Fox Z, Cipolotti L, Jager R, Werring DJ: MRI-visible perivascular spaces: relationship to cognition and small vessel disease MRI markers in ischaemic stroke and TIA. J Neurol Neurosurg Psychiatry 2014;85:522–525.
21 Yao M, Hervé D, Jouvent E, Duering M, Reyes S, Godin O, Guichard JP, Dichgans M, Chabriat H: Dilated perivascular spaces in small-vessel disease: a study in CADASIL. Cerebrovasc Dis 2014;37:155–163.
22 Patankar TF, Mitra D, Varma A, Snowden J, Neary D, Jackson A: Dilatation of the Virchow-Robin space is a sensitive indicator of cerebral microvascular disease: study in elderly patients with dementia. AJNR Am J Neuroradiol 2005;26:1512–1520.
23 Fazekas F, Barkhof F, Wahlund LO, Pantoni L, Erkinjuntti T, Scheltens P, Schmidt R: CT and MRI rating of white matter lesions. Cerebrovasc Dis 2002;13(suppl 2):31–36.
24 Wardlaw JM, Smith EE, Biessels GJ, Cordonnier C, Fazekas F, Frayne R, Lindley RI, O'Brien JT, Barkhof F, Benavente OR, Black SE, Brayne C, Breteler M, Chabriat H, DeCarli C, de Leeuw FE, Doubal F, Duering M, Fox NC, Greenberg S, Hachinski V, Kilimann I, Mok V, Oostenbrugge RV, Pantoni L, Speck O, Stephan BC, Teipel S, Viswanathan A, Werring D, Chen C, Smith C, van Buchem M, Norrving B, Gorelick PB, Dichgans M: Neuroimaging standards for research into small vessel disease and its contribution to ageing and neurodegeneration. Lancet Neurol 2013; 12:822–838.
25 Rouhl RP, van Oostenbrugge RJ, Knottnerus IL, Staals JE, Lodder J: Virchow-Robin spaces relate to cerebral small vessel disease severity. J Neurol 2008;255:692–696.
26 Groeschel S, Chong WK, Surtees R, Hanefeld F: Virchow-Robin spaces on magnetic resonance images: normative data, their dilatation, and a review of the literature. Neuroradiology 2006;48:745–754.
27 Heier LA, Bauer CJ, Schwartz L, Zimmerman RD, Morgello S, Deck MD: Large Virchow-Robin spaces: MR-clinical correlation. AJNR Am J Neuroradiol 1989;10:929–936.
28 Adams HH, Cavalieri M, Verhaaren BF, Bos D, van der Lugt A, Enzinger C, Vernooij MW, Schmidt R, Ikram MA: Rating method for dilated Virchow-Robin spaces on magnetic resonance imaging. Stroke 2013;44: 1732–1735.
29 Bhapkar VP: A note on the equivalence of two test criteria for hypotheses in categorical data. J Am Statist Assoc 1966;61:228–235.
30 Hernández Mdel C, Piper RJ, Wang X, Deary IJ, Wardlaw JM: Towards the automatic computational assessment of enlarged perivascular spaces on brain magnetic resonance images: a systematic review. J Magn Reson Imaging 2013;38:774–785.
31 Basile AM, Pantoni L, Pracucci G, Asplund K, Chabriat H, Erkinjuntti T, Fazekas F, Ferro JM, Hennerici M, O'Brien J, Scheltens P, Visser MC, Wahlund LO, Waldemar G, Wallin A, Inzitari D: Age, hypertension, and lacunar stroke are the major determinants of the severity of age-related white matter changes. The LADIS (Leukoaraiosis and Disability in the Elderly) Study. Cerebrovasc Dis 2006;21: 315–322.
32 Jeerakathil T, Wolf PA, Beiser A, Massaro J, Seshadri S, D'Agostino RB, DeCarli C: Stroke risk profile predicts white matter hyperintensity volume: the Framingham Study. Stroke 2004;35:1857–1861.

Human Gene Therapy
© Mary Ann Liebert, Inc.
DOI: 10.1089/hum.2017.062

Systemic Delivery of Dysferlin Overlap Vectors Provides Long-Term Gene Expression and Functional Improvement for Dysferlinopathy

Rachael A. Potter[1*], Danielle A. Griffin[1*], Patricia C. Sondergaard[1], Ryan W. Johnson[1], Eric R. Pozsgai[1,3], Kristin N. Heller[1], Ellyn L. Peterson[1], Kimmo K. Lehtimäki [5], Hillarie P. Windish[4], Plavi J. Mittal[4], Douglas E. Albrecht[4], Jerry R. Mendell[1,2], and Louise R. Rodino-Klapac[1,2,3]

[1] Center for Gene Therapy, The Research Institute at Nationwide Children's Hospital, Columbus, Ohio, USA, [2] Department of Pediatrics and Neurology, The Ohio State University, Columbus, Ohio, USA, [3]Integrated Biomedical Science Graduate Program, College of Medicine, The Ohio State University, Columbus, Ohio, USA, [4]The Jain Foundation, Seattle, WA, [5] Charles River Discovery Services, Kuopio, Finland.

*These authors contributed equally to this work

Correspondence should be addressed to Louise R. Rodino-Klapac, Center for Gene Therapy, The Research Institute at Nationwide Children's Hospital, Room 3016, 700 Childrens Dr., Columbus, Ohio 43205, USA. E-mail: Louise.Rodino-Klapac@nationwidechildrens.org

Human Gene Therapy
Systemic Delivery of Dysferlin Overlap Vectors Provides Long-Term Functional Improvement for Dysferlinopathy (doi: 10.1089/hum.2017.062)
This article has been peer-reviewed and accepted for publication, but has yet to undergo copyediting and proof correction. The final published version may differ from this proof.
Downloaded by Donna Ward from online.liebertpub.com at 07/19/17. For personal use only.

Human Gene Therapy
Systemic Delivery of Dysferlin Overlap Vectors Provides Long-Term Functional Improvement for Dysferlinopathy (DOI: 10.1089/hum.2017.062)
This paper has been peer-reviewed and accepted for publication, but has yet to undergo copyediting and proof correction. The final published version may differ from this proof.

Human Gene Therapy
Systemic Delivery of Dysferlin Overlap Vectors Provides Long-Term Functional Improvement for Dysferlinopathy (doi: 10.1089/hum.2017.062)
This article has been peer-reviewed and accepted for publication, but has yet to undergo copyediting and proof correction. The final published version may differ from this proof.
Downloaded by Donna Ward from online.liebertpub.com at 07/19/17. For personal use only.

Human Gene Therapy
Systemic Delivery of Dysferlin Overlap Vectors Provides Long-Term Functional Improvement for Dysferlinopathy (DOI: 10.1089/hum.2017.062)
This paper has been peer-reviewed and accepted for publication, but has yet to undergo copyediting and proof correction. The final published version may differ from this proof.

Abstract

Dysferlinopathies comprise a family of disorders caused by mutations in the dysferlin (DYSF) gene leading to a progressive dystrophy characterized by chronic muscle fiber loss, fat replacement and fibrosis. To correct the underlying histopathology and function, expression of full-length DYSF is required. We have developed dual adeno-associated virus vectors defined by a region of homology to serve as a substrate for reconstitution of the full 6.5 kb dysferlin cDNA. Our previous work studied the efficacy of this treatment through intramuscular and regional delivery routes. To maximize clinical efficacy, we treated dysferlin-deficient mice systemically to target all muscles through the vasculature for efficacy and safety studies. Mice were evaluated at multiple time points between 4 to 13 months post-treatment for dysferlin expression and functional improvement using MRI and MR-spectroscopy (MRS) and membrane repair. A systemic dose of $6x10^{12}$vg resulted in widespread gene expression in muscle. Treated muscles showed a significant decrease in central nucleation, collagen deposition and improvement of membrane repair to wild-type levels. Treated gluteus muscles were significantly improved compared to placebo treated muscles and were equivalent to wild-type in volume, intramyocellular and extramyocellular lipid accumulation and fat percentage using MRI/MRS. Dual-vector treatment allows for production of full-length functional dysferlin with no toxicity. This confirms previous safety data and validates translation of systemic gene delivery for dysferlinopathy patients.

Human Gene Therapy
Systemic Delivery of Dysferlin Overlap Vectors Provides Long-Term Functional Improvement for Dysferlinopathy (doi: 10.1089/hum.2017.062)
This article has been peer-reviewed and accepted for publication, but has yet to undergo copyediting and proof correction. The final published version may differ from this proof.
Downloaded by Donna Ward from online.liebertpub.com at 07/19/17. For personal use only.

Human Gene Therapy
Systemic Delivery of Dysferlin Overlap Vectors Provides Long-Term Functional Improvement for Dysferlinopathy (DOI: 10.1089/hum.2017.062)
This paper has been peer-reviewed and accepted for publication, but has yet to undergo copyediting and proof correction. The final published version may differ from this proof.

Introduction

There is no cure or treatment for dysferlinopathies, a group of related disorders with varying clinical manifestations caused by absent or mutant dysferlin (*DYSF*). Typically, patients present in their late teens or early twenties with slowly progressive muscle weakness and high serum creatine kinase (CK) [1]. Approximately one-third of patients become wheelchair-dependent within 15 years of onset. There are 2 major clinical presentations of dysferlin deficiency: limb girdle muscular dystrophy type 2B (LGMD2B) is one of the most common LGMDs in the United States with worldwide reports of incidence of 1/100,000-1/200,000 [2], while Miyoshi Myopathy is a more limited distal lower extremity form of dysferlinopathy. Miyoshi myopathy often begins distally with atrophy of the gastrocnemius muscle and then spreads over time to affect proximal muscles [3]. Regardless of where muscle weakness begins, the disease progresses to the majority of muscles in the trunk, all limb muscles, the diaphragm and in some cases the heart [4]; therefore a treatment that targets all muscles is imperative. In most cases, pathogenic *DYSF* mutations lead to absence of dysferlin protein expression, causing a progressive muscular dystrophy with chronic muscle fiber loss, inflammation, fat replacement and fibrosis; all of which are thought to contribute to deteriorating muscle weakness [5].

DYSF is a large gene spanning 55 exons over 150-kb of genomic DNA [6]. The associated 6.2 kb cDNA codes the dysferlin protein which is composed of multiple N-terminal C2 domains with a transmembrane C-terminal region [6-8]. Dysferlin has been implicated in multiple roles within skeletal muscle including sarcolemmal membrane repair [1, 9-11], t-tubule structure and function [12], vesicle trafficking [13] and endocytosis [14]. Although the expression of dysferlin in monocytes may contribute to disease severity [15-17], pathogenesis has been shown to be intrinsically linked to skeletal muscle [18, 19]. Moreover, anti-inflammatory glucocorticoids are ineffective in treating the disease [20], in spite of being standard of care for Duchenne muscular dystrophy and in spite of the characterized inflammation in dysferlinopathy muscle biopsies [21, 22]. The most widely studied DYSF function is membrane repair and is the target of many therapeutics [23, 24]. Collectively, pre-clinical studies that have assessed gene replacement or surrogate gene replacement have shown that multiple strategies exhibit some efficacy in restoring membrane repair [19, 25], but only those that have delivered full-length dysferlin have been able to correct the underlying histopathological [9, 26] and t-tubule formation [27] defects. Thus, there is strong rationale to develop therapies that deliver the entire *DYSF* transcript.

Human Gene Therapy
Systemic Delivery of Dysferlin Overlap Vectors Provides Long-Term Functional Improvement for Dysferlinopathy (doi: 10.1089/hum.2017.062)
This article has been peer-reviewed and accepted for publication, but has yet to undergo copyediting and proof correction. The final published version may differ from this proof.
Downloaded by Donna Ward from online.liebertpub.com at 07/19/17. For personal use only.

Human Gene Therapy
Systemic Delivery of Dysferlin Overlap Vectors Provides Long-Term Functional Improvement for Dysferlinopathy (DOI: 10.1089/hum.2017.062)
This paper has been peer-reviewed and accepted for publication, but has yet to undergo copyediting and proof correction. The final published version may differ from this proof.

Gene transfer as a treatment strategy has undergone profound development in recent years and is particularly applicable for recessive disorders [9, 11, 28-31]. Moreover, the advancement of vector production yield capabilities [32-34] and systemic treatment approaches has revolutionized the opportunities to create truly clinically meaningful therapies [35]. Adeno-associated virus (AAV) is a nonpathogenic vector with serotype dependent tropism for muscle. Serotypes 1, 5, 6, 8, 9, and rh74 have all been shown to efficiently transduce muscle [11, 36, 37]. We have demonstrated that AAVrh74 broadly distributes DYSF to skeletal muscle following vascular delivery [11, 38]. A major limitation of all AAV vector serotypes is their restrictive packaging capacity of ~5kb, which prevents the encapsidation of large genes [39]. Multiple strategies have emerged in the field to address this constraint, including miniaturization of transgenes, concatemermization-splicing and dual vector delivery [11, 27, 32, 40, 41]. Our previous work with a dual vector delivery strategy utilized homologous recombination of a split transgene which allowed for production of full-length protein [11].

Current treatment strategies are limited emphasizing the need for an effective therapeutic approach. Early intervention and systemic delivery of DYSF offers significant advantages including gene restoration to all muscles prior to limitations introduced by fat and fibrosis, and reducing the immune response following multiple intramuscular injections [42, 43]. Here we present delivery of dual vectors carrying the DYSF cDNA systemically in a dysferlin deficient mouse model. This has resulted in long-term widespread expression in skeletal and cardiac muscle with improvement in outcome measures including reduced fibrosis and central nucleation, membrane repair capability and multiple MRI-based measurements including reversal of intramuscular lipids and fat percentage. Additionally, systemic delivery in a non-human primate model confirmed previous indications of vector safety in large animals.

Materials and Methods

Dysferlin Gene Construction

For all gene transfer studies, human dysferlin cDNA (Genbank# NM_003494.3) was used. The dual vector dysferlin cassettes were generated to encompass the 5' or the 3' portion of the full-length dysferlin cassette as previously described [9, 11]. The 5' cassette contains the MHCK7 promoter, the chimeric intron and the first 3370bp of the dysferlin cDNA flanked by AAV2 ITRs. The 3' cassette

Human Gene Therapy
Systemic Delivery of Dysferlin Overlap Vectors Provides Long-Term Functional Improvement for Dysferlinopathy (doi: 10.1089/hum.2017.062)
This article has been peer-reviewed and accepted for publication, but has yet to undergo copyediting and proof correction. The final published version may differ from this proof.
Downloaded by Donna Ward from online.liebertpub.com at 07/19/17. For personal use only.

Human Gene Therapy
Systemic Delivery of Dysferlin Overlap Vectors Provides Long-Term Functional Improvement for Dysferlinopathy (DOI: 10.1089/hum.2017.062)
This paper has been peer-reviewed and accepted for publication, but has yet to undergo copyediting and proof correction. The final published version may differ from this proof.

contains the remaining 3866 bp of the dysferlin cDNA and the native 3'UTR/polyA sequence. The dual vectors result in a 1 kb overlap region that serves as a substrate for recombination to generate the full length dysferlin cDNA. Both constructs were fully sequenced to confirm plasmid fidelity.

AAV Vector Production

pAAV.MHCK7.DYSF5'.PTG and pAAV.DYSF3'.PolyA were packaged into AAV serotype rh74 capsid using the standard triple transfection protocol as previously described [11]. A quantitative PCR-based titration method was used to determine an encapsulated vector genome (vg) titer utilizing a Prism 7500 Fast Taqman detector system (PE Applied Biosystems)[44]. The following primers/probes were used: AAVrh74.MHCK7.DYSF5'.PTG – F primer - CCAACACCTGCTGCCTCTAAA, R primer – GTCCCCCACAGCCTTGTTC, Probe – TGGATCCCCTGCATGCGAAGATC; AAVrh74.DYSF3'.PolyA – F primer – AGATCACCCCACTTCCATCATT, R primer – TGAAATATGTCTGAGCTGATCCAAA, Probe – CCTTCTCCCCCAACCCAACGCT.

Animal Models

Dysferlin Deficient Mouse Strain

Stocks of C57BL/6, 129-*Dysf* ^{tm1Kcam}/J and B6.A-Dysf^{prmd}/GeneJ BlaJ mice were bred and maintained as homozygous animals in standardized conditions in the Animal Resources Core at The Research Institute at Nationwide Children's Hospital. BlaJ mice were maintained in a private colony at the Jackson Laboratories sponsored by the Jain Foundation. The BlaJ mice used for the MRI/MRS analysis were maintained at PsychoGenics labs in Tarrytown, NY. The BLaJ strain were previously backcrossed 10 times onto C57BL/6J mice. Control mice (C57BL/6) were littermates to control for any behavioral variability. In order to undergo MRI/MRS, the mice were transferred at 6 months of age to Charles River Laboratories (CRL), Finland (study number 112314). Mice were maintained on Teklad Global Rodent Diet (3.8z5 fiber, 18.8% protein, 5% fat chow) with a 12:12 h dark:light cycle. Procedures used in experiments were approved by the Institutional Animal Care and Use Committee at Nationwide Children's Hospital (protocol AR08-00017).

Human Gene Therapy
Systemic Delivery of Dysferlin Overlap Vectors Provides Long-Term Functional Improvement for Dysferlinopathy (doi: 10.1089/hum.2017.062)
This article has been peer-reviewed and accepted for publication, but has yet to undergo copyediting and proof correction. The final published version may differ from this proof.
Downloaded by Donna Ward from online.liebertpub.com at 07/19/17. For personal use only.

Human Gene Therapy
Systemic Delivery of Dysferlin Overlap Vectors Provides Long-Term Functional Improvement for Dysferlinopathy (DOI: 10.1089/hum.2017.062)
This paper has been peer-reviewed and accepted for publication, but has yet to undergo copyediting and proof correction. The final published version may differ from this proof.

Non-human Primate

Vendors provided serum from rhesus macaques before animal purchase for determination of AAVrh74 binding antibody titers. Sero-negative animals (categorized by <1:50 total antibody titer dilution via ELISA) were obtained and housed in twos or threes to promote socialization in the Animal Resources Core at the Research Institute at Nationwide Children's Hospital. All procedures were approved by the Institutional Animal Care and Use Committee at Nationwide Children's Hospital (protocol AR06-00116).

In Vivo Gene Delivery

In both primate and mouse studies, vector was delivered in a 1:1 ratio systemically via the vasculature. BlaJ mice were injected in the tail vein at one of two time points, 8 weeks or 6 months with $6x10^{12}$ vector genomes (vg) (total dose $3x10^{12}$ vg of each vector. The 8-week old cohort was necropsied at 28 weeks of age for histological and expression analysis. A separate cohort of mice, also injected at 8 weeks of age, was necropsied at 15 months of age following the final MRI scans. CK levels were determined from serum samples collected at each time point for all mice in the study. The BlaJ mice injected at 6 months of age were necropsied 3 months post-injection. Tibialis anterior muscles from 4-6 week old 129-*Dysf* ^{tm1Kcam}*/J* mice were injected with $2x10^{11}$ vg total of AAVrh74.MHCK7.Dysferlin.DV. A 4 kg rhesus macaque was perfused with $2x10^{14}$ vg total dose ($1x10^{14}$vg of each vector) in 50 mL total volume at a rate of 300 mL/hr in the cephalic vein.

Magnetic Resonance Imaging (MRI & MRS)

The following treatment groups were used: Group 1: 8 wild-type (WT) males treated with saline, Group 2: 8 BlaJ males treated with saline, Group 3: 8 BlaJ males treated with AAVrh74-dysferlin. All study mice from each group were subjected to 11.7T (Bruker BioSpec) MRI and 1H-MRS at age of 7, 9,12, and 15 months to assess longitudinal changes in muscle volumes (3D GRE with water excitation/fat suppression, TE/TR=2.7/25 ms at resolution 81x94x375 μm^3), fat accumulation (same sequence, but with water suppression/fat excitation) and gluteal spectroscopic changes (PRESS, TE/TR=10/2000 ms). At 15 months of age, all mice were evaluated by MRI, but MRS was only performed on control and BlaJ-AAV mice, due to excessive fat infiltration in BlaJ-VEH mice which

Human Gene Therapy
Systemic Delivery of Dysferlin Overlap Vectors Provides Long-Term Functional Improvement for Dysferlinopathy (doi: 10.1089/hum.2017.062)
This article has been peer-reviewed and accepted for publication, but has yet to undergo copyediting and proof correction. The final published version may differ from this proof.
Downloaded by Donna Ward from online.liebertpub.com at 07/19/17. For personal use only.

Human Gene Therapy
Systemic Delivery of Dysferlin Overlap Vectors Provides Long-Term Functional Improvement for Dysferlinopathy (DOI: 10.1089/hum.2017.062)
This paper has been peer-reviewed and accepted for publication, but has yet to undergo copyediting and proof correction. The final published version may differ from this proof.

prevented collection of reliable MRS data. Peak area for major metabolites (creatine, choline, taurine, and components for intra and extramyocellular lipids) were analyzed using the LC Model (Stephen Provencher Inc., Oakville, Canada) and results are given relative to water content in tissue.

Histological Analysis

All muscles and organs, unless used for membrane repair assays, were embedded in 7% gum tragacanth and flash frozen in liquid nitrogen cooled in isopentane. Frozen sections (12 µm) were collected for immunohistochemistry, immunofluorescence and western blot analysis.

Picrosirius Red Stain and Collagen Quantification

Frozen sections placed onto Fisherbrand Superfrost charged microscope slides were fixed in 10% Neutral Buffered Formalin for 5 minutes, then rinsed in distilled water. Slides were then incubated in Solution B (Direct Red 80/2 4 6-Trinitrophenol) from the Picrosirius Red Stain Kit (Polysciences Inc. Catalog # 24901) for 15 minutes. After a thorough rinse in distilled water, the slides were placed in Solution C (0.1N Hydrochloride Acid) for 2 minutes. Slides were counterstained for 3 minutes with 1% Fast Green in 1% Glacial Acetic Acid from Poly Scientific (Catalog #S2114) using a 1:10 dilution in DI water. Finally, the slides were rinsed again in distilled water, dehydrated in graded ethanol, cleared in xylene and mounted with coverslips using Cytoseal 60 media from Thermo-Scientific (Cat#8310). Images were taken using the AxioVision 4.9.1 software. For analysis of Sirius red staining and percent collagen quantification, the contrast between the red and the green colors were enhanced using Adobe Photoshop. The color deconvolution plugin in the ImageJ software program was selected and the RGB color deconvolution option was used. The Red image includes all connective tissue from the Sirius Red stain. The Green image includes all muscle from the Fast Green counterstain. Only the Red image and the original image were used. A threshold was then applied to the images to obtain black and white images with areas positive for collagen in black and negative areas in white. Using the measure function, the area of collagen was calculated. The total tissue area was then determined by converting the originally image to “8-bit” and adjusting the threshold to 254, which will be one unit below completely saturating the image. The total tissue area was then measured as done previously and total area was recorded. The percentage of collagen was calculated by dividing the area of collagen by the total tissue area. The mean percentage for each individual was then calculated.

Human Gene Therapy
Systemic Delivery of Dysferlin Overlap Vectors Provides Long-Term Functional Improvement for Dysferlinopathy (doi: 10.1089/hum.2017.062)
This article has been peer-reviewed and accepted for publication, but has yet to undergo copyediting and proof correction. The final published version may differ from this proof.
Downloaded by Donna Ward from online.liebertpub.com at 07/19/17. For personal use only.

Human Gene Therapy
Systemic Delivery of Dysferlin Overlap Vectors Provides Long-Term Functional Improvement for Dysferlinopathy (DOI: 10.1089/hum.2017.062)
This paper has been peer-reviewed and accepted for publication, but has yet to undergo copyediting and proof correction. The final published version may differ from this proof.

Immunohistochemistry

Immunofluorescence staining for dysferlin was performed on all transduced tissue to assess efficacy of gene transfer. For dysferlin detection, tissue sections (12 µm) were incubated with rabbit anti-human dysferlin monoclonal antibody (Abcam) at 1:100 in blocking solution (10% goat serum, 0.1% Tween-20 in TBS) for one hour at 25°C in a wet chamber. Sections were washed with TBS 3 x 20 minutes, reblocked and then incubated for 45 minutes at 25°C with an Alexa 568 goat anti-rabbit antibody (Invitrogen) at a 1:250 dilution. Sections were washed in PBS for 3 x 20 minutes and mounted with Vectashield mounting medium (Vector Laboratories). Images were captured with a Zeiss Axioskop2 Plus Microscope and Axiocam MRC5 camera. Four random 20x images (each field with an average of 150 muscle fibers) were captured per muscle and the number of fibers with dysferlin labelling was counted and expressed as percent of total number of fibers.

Immunohistochemical staining for CD8a was performed with rat anti-CD8a antibody (Fisher Scientific) and an anti-rat Ig HRP detection kit (BD Biosciences), following kit manufacturer directions. Images were captured with a Zeiss Axioskop2 Plus Microscope and Axiocam MRC5 camera. Four random 20x images (each field with an average of 150 muscle fibers) were captured per muscle and the number of CD8a positive cells were counted and expressed as number of positive cells per square area. Unpaired t-test statistical analysis was performed to compare treatment effect on cells/mm^2.

Morphometrics

Centralized nuclei counts were performed on sections of muscle stained with hematoxylin and eosin (H&E) from treated animals. Four random 20x fields of 12 µm sections for each muscle were captured and the number of fibers with central nuclei counted and expressed as a percentage of the total number of fibers. Two-way ANOVA statistical analysis was performed to compare treatment effect on central nucleation.

Human Gene Therapy
Systemic Delivery of Dysferlin Overlap Vectors Provides Long-Term Functional Improvement for Dysferlinopathy (doi: 10.1089/hum.2017.062)
This article has been peer-reviewed and accepted for publication, but has yet to undergo copyediting and proof correction. The final published version may differ from this proof.
Downloaded by Donna Ward from online.liebertpub.com at 07/19/17. For personal use only.

Human Gene Therapy
Systemic Delivery of Dysferlin Overlap Vectors Provides Long-Term Functional Improvement for Dysferlinopathy (DOI: 10.1089/hum.2017.062)
This paper has been peer-reviewed and accepted for publication, but has yet to undergo copyediting and proof correction. The final published version may differ from this proof.

Western Blot Analysis

From each muscle, fresh-frozen serial tissue sections were taken for protein preparation. Muscle samples harvested from treated and control groups were compared with wild-type tissue for levels of vector-mediated dysferlin compared to endogenous dysferlin. Protein (5 µg for WT lanes and 10 µg for all other lanes) extracted from treated and control samples was separated by SDS-PAGE (3-8% Novex NuPAGE gradient gels, Invitrogen), blotted on PVDF membrane and probed with NCL-Hamlet (Novocastra) primary antibody (for dysferlin) at a dilution of 1:1,000, or γ-tubulin antibody (Sigma) at a dilution of 1:10,000 followed by horseradish-peroxidase (HRP) labeled goat anti-mouse IgG (1:5,000, Millipore) or goat anti-rabbit IgG (1:5,000, Millipore) and signal captured on Hyblot CL autoradiography film (Denville). Densitometry analysis was performed using ImageQuant TL.

Membrane Repair Analysis

6 month old BlaJ mice were injected with $6x10^{12}$vg of AAVrh74.MHCK7.Dysferlin.DV into the tail vein. Muscles were harvested 12 weeks post-injection and subjected to a laser-induced injury. Membrane repair assay was performed on left and right flexor digitorum brevis (FDB) muscles of BlaJ – AAV treated (n=6), BlaJ saline treated mice (n=5) and age-matched C57BL6 (n=5) mice as previously described when the mice were 9 months of age [45]. Briefly, FDB fibers were isolated using a solution containing 2% w/v collagenase type I suspended in Dulbecco's Modified Eagle Medium (DMEM). Following dissociation of the muscle, fibers were placed in a glass bottom dish holding 2.5 µM FM1-43 dye in Dulbecco's PBS (no Ca/Mg) supplemented with 1.5 mM Ca^{2+}. Fibers were subjected to laser injury using a FluoView® FV1000 two-photon confocal laser-scanning microscope (Olympus). Fibers were damaged with an 850 nm laser-guided spot of 4.48µm at 20% power and imaged every 5 sec for 190 s to visualize FM1-43 dye uptake. An average of 7-10 fibers were imaged per muscle per mouse, (total 60 WT, 48 BlaJ, and 69 BlaJ – AAV treated fibers). Fluorescence intensity of dye infiltration surrounding the damage site on the membrane was analyzed with Image J software by measuring integrated density of pixel intensity within the defined area. To do so, under a 2X zoom setting on ImageJ, a rectangular box measuring 7.5 µm by 10 µm region of interest (ROI) is drawn and used to measure the intensity of dye in that region. In the analysis, measured fluorescence intensity at an individual time point was normalized to initial intensity measured at t = -5s (pre-injury) using the equation: $NI = \frac{(\ -\ )}{\quad}$, where NI is the normalized intensity, I is the measured intensity and I_0 is the intensity at t = -5s. When

Human Gene Therapy
Systemic Delivery of Dysferlin Overlap Vectors Provides Long-Term Functional Improvement for Dysferlinopathy (doi: 10.1089/hum.2017.062)
This article has been peer-reviewed and accepted for publication, but has yet to undergo copyediting and proof correction. The final published version may differ from this proof.
Downloaded by Donna Ward from online.liebertpub.com at 07/19/17. For personal use only.

Human Gene Therapy
Systemic Delivery of Dysferlin Overlap Vectors Provides Long-Term Functional Improvement for Dysferlinopathy (DOI: 10.1089/hum.2017.062)
This paper has been peer-reviewed and accepted for publication, but has yet to undergo copyediting and proof correction. The final published version may differ from this proof.

fluorescence intensity was analyzed, values from all fibers from each strain were averaged together. A 2-way ANOVA was performed to determine statistical significance between treated and untreated fibers at each time point ($p<0.001$). BlaJ, WT fibers, and AAVrh74.DYSF.DV treated BlaJ fibers were significantly different at 190 seconds post-injury.

Immunological Assays

For the non-human primate, whole blood samples were collected biweekly and used for enzyme-linked immunosorbent assay (ELISA) and enzyme-linked immunosorbent spot assay (ELISpot) to track immunological response to the viral capsid, AAVrh74, and the dysferlin transgene product. ELISAs were performed in 96-well Nunc Maxisorb ELISA plates coated with $2x10^9$ vg AAVrh74 per well in carbonate buffer. Serum samples were diluted from 1:5 through 1:819,200 in blocking solution (5% non-fat dry milk, 1% normal goat serum (Invitrogen) in $PBS^{-/-}$) and added to wells for 1 hr at room temperature. Sera from previously screened positive and negative NHPs were used for controls. Goat anti-monkey IgG-HRP (Sigma) was used as the secondary antibody for 30 min at room temperature followed by exposure with Ultra TMB-ELISA solution (Thermo Scientific). Absorbance of wells at OD450 was measured and used to calculate titer of positive reaction.

Peripheral blood mononuclear cells (PBMCs) were separated from whole blood samples through density gradient centrifugation, as previously described [46]. Briefly, fresh blood samples were spun in a table-top centrifuge (Sorval Legend RT) and the top plasma layer was removed and stored in -80C freezer. The remaining blood was mixed with $PBS^{-/-}$ (Invitrogen), underlayed with Ficoll-Paque (Fisher) and spun for density gradient separation. The middle layer containing the PBMCs was removed and subjected to various wash/spin cycles before a final resuspension in CellGro RPMI1640 media (Fisher) supplemented with 10% fetal calf serum (Fisher), penicillin and streptomycin. PBMCs were then plated in IP filter plates (Millipore) at a density of $2x10^5$cells/well. IP plate wells were pre-coated with monoclonal antibody provided in monkey interferon-γ ELISpot kit (U-Cytech Biosciences). Three peptide pools were used for the AAVrh74 capsid protein (Genemed Synthesis, San Antonio, TX) containing 34-36 peptides, each 18 amino acids long and overlapping by 11 residues. Ten peptide pools encompassing the dysferlin protein (Genemed Synthesis) containing 48 peptides, each 15 amino acids long and overlapping by 10 residues. Concanavalin A (Sigma, 1μg/mL) served as a positive control and 0.25% dimethylsulfoxide as a

This article has been peer-reviewed and accepted for publication, but has yet to undergo copyediting and proof correction. The final published version may differ from this proof.
Systemic Delivery of Dysferlin Overlap Vectors Provides Long-Term Functional Improvement for Dysferlinopathy (doi: 10.1089/hum.2017.062)
Human Gene Therapy
Downloaded by Donna Ward from online.liebertpub.com at 07/19/17. For personal use only.

Human Gene Therapy
Systemic Delivery of Dysferlin Overlap Vectors Provides Long-Term Functional Improvement for Dysferlinopathy (DOI: 10.1089/hum.2017.062)
This paper has been peer-reviewed and accepted for publication, but has yet to undergo copyediting and proof correction. The final published version may differ from this proof.

negative control. Peptides were added directly to the wells at a final concentration of 1 µg/mL. After the addition of PBMCs and peptides, the plate was incubated at 37°C in 5-7% CO_2 and 100% humidity for 36-48 hours. Following incubation the plate was developed according to the manufacturer's protocol. Interferon-γ spot formation was counted using Immunospot software (Series 3B Analyzer, Cellular Technology, Ltd, Cleveland, OH).

Blood samples from the NHPs were analyzed monthly for chemistry panel and complete blood count (CBC) testing internally.

AAVrh74.DYSF.DV Biodistribution Analysis

Quantitative PCR was performed to quantify the number of vector genome copies present in targeted muscle as well as non-targeted organs according to standard methods [39]. Briefly, DNA was isolated from frozen tissue (20 20 µm sections) according to DNEasy purification kit protocol (Qiagen, Valencia, CA). Absolute quantification for the 5' and 3' vectors were established by creation of standard amplification curves using HindIII-linearized pAAVrh74.MHCK7.DYSF5'.PTG and NotI-linearized pAAV.DYSF3'.POLYA, respectively. Standards ranged from 10^6 to 10^1 copies per reaction. All sample reactions contained 100 ng DNA, and resulting copy numbers were determined according to standard curves performed in parallel. Copy numbers were reported per µg genomic DNA.

Each vector DNA sequence was quantified via the Taqman system (Applied Biosystems, Waltham, MA), using vector-specific primer/probe sets. For AAVrh74.MHCK7.DYSF5'.PTG, the following sequences were used: Forward primer, 5'- CCA ACA CCT GCT GCC TCT AAA -3'; Reverse primer, 5'- GTC CCC CAC AGC CTT GTT C -3'; Probe, 5'- TGG ATC CCC TGC ATG CGA AGA TC -3' with 5' 6-FAM fluorophore, internal ZEN® quencher, and 3' Iowa Black® FQ quencher (IDT, San Jose, CA). For AAV.DYSF3'.POLYA, the following sequences were used: Forward primer, 5'- AGA TCA CCC CAC TTC CAT CAT T -3'; Reverse primer, 5'- TGA AAT ATG TCT GAG CTG ATC CAA A -3'; Probe, 5'- CCT TCT CCC CCA ACC CAA CGC T -3' with 5' 6-FAM fluorophore, internal ZEN® quencher, and 3' Iowa Black® FQ quencher.

Human Gene Therapy
Systemic Delivery of Dysferlin Overlap Vectors Provides Long-Term Functional Improvement for Dysferlinopathy (doi: 10.1089/hum.2017.062)
This article has been peer-reviewed and accepted for publication, but has yet to undergo copyediting and proof correction. The final published version may differ from this proof.
Downloaded by Donna Ward from online.liebertpub.com at 07/19/17. For personal use only.

Human Gene Therapy
Systemic Delivery of Dysferlin Overlap Vectors Provides Long-Term Functional Improvement for Dysferlinopathy (DOI: 10.1089/hum.2017.062)
This paper has been peer-reviewed and accepted for publication, but has yet to undergo copyediting and proof correction. The final published version may differ from this proof.

Statistical Analysis

Data were expressed as the mean ± SEM (error bars) and analyzed using a ONE-WAY ANOVA or TWO-WAY ANOVA with multiple comparisons between groups and statistical significance determined through Tukey's post-hoc analysis test using GraphPad Prism 5 (Graphpad Software, La Jolla, CA) unless otherwise specified. Asterisks in figures and reported data denote level of statistical significance as follows: ns=no significance, *=p<0.05, **=p<0.01, ***=p<0.001, ****=p<0.0001.

Results

Our previous work [11] has shown successful gene transfer in dysferlin-null mice through multiple delivery routes including intramuscular, isolated vascular and systemic injections. As a continuation of that work, we performed a detailed time course following intramuscular delivery over 24 months. Figure 1 demonstrates that disease progression is significantly halted up to 24 months in 129-*Dysf* ^{tm1Kcam}*/J* mice injected intramuscularly with AAVrh74.DYSF.DV at a young age (4 weeks). Treated muscles show a reduction in centralized nuclei to below 5% post gene delivery (Fig 1, Supplementary Fig S1) and high levels of sustained dysferlin expression above 70% through all timepoints (n=3 per group) (Fig 1). We and others have previously noted strong cytoplasmic dysferlin staining post gene transfer[9, 11, 25, 26]. Dysferlin is expressed at both the sarcolemma and intracellular membranes particularly the T-tubules[47]. In addition to sarcolemmal expression, strong cytoplasmic expression of dysferlin is commonly noted in regenerating fibers in dystrophic patient biopsies[3, 48] as well as following gene delivery.

AAVrh74.DYSF.DV systemic gene transfer in young mice

The following work presents an intensive study of systemic (intravenous) delivery of AAVrh74.DYSF.DV with a focus on highly affected muscles in the BlaJ (dysferlin deficient) mouse model: the psoas and the gluteus muscles. We chose to study the BlaJ mouse model as its phenotype more accurately recapitulates the human disease compared to the 129-Dysf model. In a longitudinal study of disease progression and functional deficiencies of the BlaJ model, it has been corroborated that progressive volume loss and fatty infiltration in the gluteal and psoas muscles is the most uniform parameter and identifies consistent disease parameters to human dysferlinopathies [49]. In BlaJ mice, the psoas muscle shows early signs of dystrophic changes

Human Gene Therapy
Systemic Delivery of Dysferlin Overlap Vectors Provides Long-Term Functional Improvement for Dysferlinopathy (doi: 10.1089/hum.2017.062)
This article has been peer-reviewed and accepted for publication, but has yet to undergo copyediting and proof correction. The final published version may differ from this proof.
Downloaded by Donna Ward from online.liebertpub.com at 07/19/17. For personal use only.

Human Gene Therapy
Systemic Delivery of Dysferlin Overlap Vectors Provides Long-Term Functional Improvement for Dysferlinopathy (DOI: 10.1089/hum.2017.062)
This paper has been peer-reviewed and accepted for publication, but has yet to undergo copyediting and proof correction. The final published version may differ from this proof.

including high levels of centralized nuclei, interstitial collagen deposition and infiltration of inflammatory cells (Fig 2A). Following intravenous delivery of $6x10^{12}$ vg of AAVrh74.DYSF.DV via the tail vein in 8 week old BlaJ mice (n= 8), we analyzed the psoas muscle through multiple measures at 7 months of age (following 28 weeks of treatment) and demonstrated widespread gene expression throughout all skeletal muscles with 30.9% ± 5.0 of fibers transduced in the psoas muscle. Figure 2 demonstrates that delivery of dysferlin transgene stabilizes the muscle environment leading to a normalization of fiber size distribution (Fig 2C) where the mean fiber diameter in treated psaos muscles increased from 27.8 µm versus 18.4 µm in saline treated muscle. Significant reductions in centralized nuclei in the treated tibialis anterior, quadriceps, triceps, and psoas muscles were also identified (Fig 2D, Supplementary Fig S1). In addition, a significant reduction of CD8 cells in treated muscles (25.59 cells/mm^2) compared to untreated (62.23 cells/mm^2) was demonstrated. Finally, there was a significant reduction in collagen deposition in treated psoas muscles 9.7% compared to untreated BlaJ psoas muscles 37.0% (Fig 2E).

Long-term benefits from AAVrh74.DYSF.DV systemic gene transfer

In order to evaluate the sustainment of benefit of intravenous gene transfer, additional cohorts of BlaJ mice were injected with $6x10^{12}$ vg of AAVrh74.DYSF.DV via the tail vein at 8 weeks of age (n=8) and evaluated at 15 months post-injection for histopathology (Fig 3A) and fibrosis (Fig 3B). In the gluteus muscle, fiber diameters were normalized (Fig 3C) and reductions in central nuclei were noted to variable degrees with reduction in quadriceps (QD) being significant (Fig 3D, Supplementary Fig S1). Collagen deposition was reduced to wild-type levels in the gluteus muscle (Fig 3D). Additionally, widespread transgene expression was detected at 15 months of age (Fig 4 A-C) and centrally located nuclei were only detected in the dysferlin null fibers (Fig 4D). Less than 0.5% of dysferlin positive fibers had central nuclei, demonstrating that the transgene derived dysferlin confers almost complete protection from degeneration. The presence of full-length dysferlin in treated muscles at 15 months of age was further confirmed by western blot analysis (TA and GAS) (Fig 4E).

As an outcome measure, *in vivo* MRI and MR-spectroscopy were used to evaluate gluteus and psoas muscles (MRS data not collected on the psoas due to inadequate muscle size) and gluteus

Human Gene Therapy
Systemic Delivery of Dysferlin Overlap Vectors Provides Long-Term Functional Improvement for Dysferlinopathy (doi: 10.1089/hum.2017.062)
This article has been peer-reviewed and accepted for publication, but has yet to undergo copyediting and proof correction. The final published version may differ from this proof.
Downloaded by Donna Ward from online.liebertpub.com at 07/19/17. For personal use only.

Human Gene Therapy
Systemic Delivery of Dysferlin Overlap Vectors Provides Long-Term Functional Improvement for Dysferlinopathy (DOI: 10.1089/hum.2017.062)
This paper has been peer-reviewed and accepted for publication, but has yet to undergo copyediting and proof correction. The final published version may differ from this proof.

muscle volumes, fat content, extramyocellular lipid accumulation (EMCL), and metabolite accumulation at 7, 9, 12, and 15 months of age. Figure 5 demonstrates significantly increased gluteus volume (Fig 5A), reduction in fat content and percentage of fat (Fig 5B-D) and a reduction of extramyocellular lipids and creatine accumulation (Fig 5E-F) in the AAV-treated cohort, further supporting normalization of muscle content and functional improvement with long-term gene transfer of AAVrh74.DYSF.DV.

AAVrh74.DYSF.DV systemic gene transfer in aged mice

Clinically, dysferlinopathy is most commonly diagnosed after symptoms and loss of muscle function have begun. To evaluate whether AAVrh74.DYSF.DV can potentially treat established disease, an aged cohort of BlaJ mice with established fibrosis and fiber loss was evaluated. We systemically delivered AAVrh74.DYSF.DV through the tail vein of 6 month old BlaJ mice and animals were sacrificed 3 months post-delivery. Statistically significant reduction of central nucleation (Fig 6A, Supplementary Fig S1) and a slight decrease in fibrosis (Fig 6B) were detected in the psoas of treated animals. Additionally, dysferlin expression resulted in functional improvement in membrane repair of flexor digitorum brevis (FDB) muscle fibers using a laser injury model (Fig 6C). Therefore, AAVrh74.DYSF.DV treatment demonstrates histological and functional benefit to aged muscle with existing fibrosis.

AAVrh74.DYSF.DV non-human primate systemic gene transfer

To further extend the pre-clinical findings in mice toward a clinical paradigm, a rhesus macaque, non-human primate model was treated systemically to confirm safety and efficacy for future clinical trials. Previously, we studied the effect of $5x10^{12}$vg total dose delivered by IM injection to the left TA of rhesus macaques of both AAV5.DYSF (n=3) and AAVrh74.DYSF.DV (n=2) and demonstrated no aberrant responses or toxicity to either the capsid or the transgene [11]. In this study, we evaluated the effect of $2x10^{14}$ vg/kg dose ($1x10^{14}$ vg/kg of each vector) delivered intravenously through the cephalic vein of a rhesus macaque. This dose was proportional (based on animal weight) to the systemic dose given to mice. We collected baseline chemistries and performed immunological studies including IFN-γ enzyme-linked immunosorbent spot assay (ELISpot) analysis to measure T cell responses to AAVrh74 capsid and dysferlin and anti-AAV antibody titers (enzyme-linked immunosorbent assay - ELISA) on enrolled animals. These studies

Human Gene Therapy
Systemic Delivery of Dysferlin Overlap Vectors Provides Long-Term Functional Improvement for Dysferlinopathy (doi: 10.1089/hum.2017.062)
This article has been peer-reviewed and accepted for publication, but has yet to undergo copyediting and proof correction. The final published version may differ from this proof.
Downloaded by Donna Ward from online.liebertpub.com at 07/19/17. For personal use only.

Human Gene Therapy
Systemic Delivery of Dysferlin Overlap Vectors Provides Long-Term Functional Improvement for Dysferlinopathy (DOI: 10.1089/hum.2017.062)
This paper has been peer-reviewed and accepted for publication, but has yet to undergo copyediting and proof correction. The final published version may differ from this proof.

were repeated every two weeks for the duration of the study. Three months following treatment, the animal was euthanized to obtain a full tissue necropsy. Tissues were used for gene expression (Fig 7A) studies including histopathology and biodistribution studies (Fig 7C) on vital organs. Immunological assays did not show any aberrant responses to the capsid or transgene by ELISpot or ELISA (Fig 7B, Supplementary Table 1). In addition, full complete blood count and chemistry panels showed no abnormal values in the macaque (Supplementary Table 2). Systemic gene transfer in the non-human primate thereby established safety and efficacy and validated moving forward to clinical trial with AAVrh74.DYSF.DV gene transfer.

Discussion

Previously, we documented successful dysferlin transgene expression and functional improvement in dysferlin-null mouse models using intramuscular delivery and isolated limb perfusion delivery of AAVrh74.DYSF.DV [11]. Intramuscular delivery to rhesus macaques demonstrated no toxicity and established proof of principle for movement towards the clinic, and a systemic delivery approach with the potential for robust clinical benefit was further pursued. The current study utilized systemic delivery of AAVrh74.DYSF.DV in young and aged mouse models and the rhesus macaque. Our study demonstrates that systemic delivery using AAV-mediated gene delivery results in long-term, widespread transgene expression and functional recovery in both dysferlin-null mouse models and in the rhesus macaque. Treatment with AAVrh74.DYSF.DV at 4 weeks of age demonstrated long-term transgene expression at 6 months of age out to 15 months of age. Furthermore, there were improvements in fiber diameters, centrally located nuclei, and collagen deposition which contributed to stabilization of the muscle environment. As the disease progresses, the lipid content in the muscle typically increases and the volume of infiltrates vary based on the muscle. Understanding this information is important in assessing improvements post gene therapy. Histological improvements were corroborated with functional improvements using MRI/MRS measurements, in which we observed reduced fat infiltration, retained lean muscle volumes, and increased water content to wildtype levels in treated mice aged to 15 months of age.

We found that the timing of treatment administration and duration of treatment impacts the degree of efficacy. However, sustained expression with histological and functional benefit was achieved irrespective of the treatment paradigm. This conclusion is pivotal for predicting the long-

Human Gene Therapy
Systemic Delivery of Dysferlin Overlap Vectors Provides Long-Term Functional Improvement for Dysferlinopathy (doi: 10.1089/hum.2017.062)
This article has been peer-reviewed and accepted for publication, but has yet to undergo copyediting and proof correction. The final published version may differ from this proof.
Downloaded by Donna Ward from online.liebertpub.com at 07/19/17. For personal use only.

Human Gene Therapy
Systemic Delivery of Dysferlin Overlap Vectors Provides Long-Term Functional Improvement for Dysferlinopathy (DOI: 10.1089/hum.2017.062)
This paper has been peer-reviewed and accepted for publication, but has yet to undergo copyediting and proof correction. The final published version may differ from this proof.

term success of systemic AAVrh74.DYSF.DV as a viable treatment for dysferlinopathy patients. The most striking results were realized with young animals treated prior to disease onset, where dysferlin expression persisted for 2 years with no reduction. Moreover, the development of centrally located nuclei, which indicates cycles of degeneration and regeneration, was completely arrested. These findings implore the establishment of newborn/early screening to identify dysferlinopathies during early childhood. This study demonstrates strong evidence that systematic treatment at a young age prior to disease onset has the potential to prevent disease. The results we achieved in an aged cohort were equally intriguing. One of the big questions that is asked universally is whether gene replacement therapy has the potential to help muscular dystrophy patients with advanced disease. When we injected mice at 6 months of age with existing fibrosis and fiber loss, we still achieved functional benefit evidenced by improvement in membrane repair. We also detected reduction in centrally located nuclei and levels of fibrosis along with efficient gene expression. Thus, there is strong rationale that there is the potential for AAVrh74.DYSF.DV delivery to provide clinical benefit regardless of disease status.

We have shown that systemic AAVrh74.DYSF.DV treatment in macaque skeletal muscle can stimulate the overexpression of dysferlin with no apparent toxicity or systemic immune rejection further validating the foundation of preclinical safety. Potential immune responses were carefully monitored through both serum ELISAs and peripheral blood mononuclear cell (PBMCs) ELISpot assays and biodistribution was evaluated for both overlap vectors in all tissues and organs. The lack of immune response shown in the primate is therefore encouraging. Additionally, due to the lack of immune response and transgene overexpression in the rhesus macaque, the dose level utilized will be further translated into the clinic.

In conclusion, systemic delivery of the dual vector approach for dysferlinopathies provides a very promising therapeutic strategy for both younger and older subjects. The results in this study are encouraging in that they establish efficacy of safety and absence of toxicity, as well as improvements histologically and functionally with systemic delivery. Furthermore, the long-term transgene expression and functional improvements are promising as this treatment is moved towards the clinic.

Acknowledgements

We thank the Nationwide Children's Viral Vector Core for Vector Production and Dr. Stephen Hauschka for his gift of the MHCK7 promoter. We would also like to thank Terri Shaffer, MLAS, RLATG, for performing intravenous tail vein injections. This study was funded by the Jain Foundation and the Research Institute at Nationwide Children's Hospital to L.R.R.K.

Author Disclosure Statement

Rachael Potter: No competing financial interest exists

Danielle Griffin: No competing financial interest exists

Patricia Sondergaard: No competing financial interest exists

Ryan Johnson: No competing financial interest exists

Kristin Heller: No competing financial interest exists

Eric Pozsgai: No competing financial interest exists

Ellyn Peterson: No competing financial interest exists

Kimmo K. Lehtimäki: No competing financial interest exists

Hillarie Plessner Windish: No competing financial interest exists

Plavi Mittal: No competing financial interest exists

Douglas E. Albrecht: No competing financial interest exists

Jerry R. Mendell: No competing financial interest exists

Louise R. Rodino-Klapac: Dr. Rodino-Klapac is the inventor of the AAV.dysferlin dual vector technology. This technology has been optioned exclusively to Myonexus Therapeutics, Inc. Dr. Rodino-Klapac is a co-founder and Chief Scientific Officer for Myonexus Therapeutics, Inc.

This article has been peer-reviewed and accepted for publication, but has yet to undergo copyediting and proof correction. The final published version may differ from this proof.
Human Gene Therapy
Systemic Delivery of Dysferlin Overlap Vectors Provides Long-Term Functional Improvement for Dysferlinopathy (doi: 10.1089/hum.2017.062)
Downloaded by Donna Ward from online.liebertpub.com at 07/19/17. For personal use only.

Human Gene Therapy
Systemic Delivery of Dysferlin Overlap Vectors Provides Long-Term Functional Improvement for Dysferlinopathy (DOI: 10.1089/hum.2017.062)
This paper has been peer-reviewed and accepted for publication, but has yet to undergo copyediting and proof correction. The final published version may differ from this proof.

Human Gene Therapy
Systemic Delivery of Dysferlin Overlap Vectors Provides Long-Term Functional Improvement for Dysferlinopathy (doi: 10.1089/hum.2017.062)
This article has been peer-reviewed and accepted for publication, but has yet to undergo copyediting and proof correction. The final published version may differ from this proof.
Downloaded by Donna Ward from online.liebertpub.com at 07/19/17. For personal use only.

Human Gene Therapy
Systemic Delivery of Dysferlin Overlap Vectors Provides Long-Term Functional Improvement for Dysferlinopathy (DOI: 10.1089/hum.2017.062)
This paper has been peer-reviewed and accepted for publication, but has yet to undergo copyediting and proof correction. The final published version may differ from this proof.

References

1. Bansal, D., K. Miyake, S.S. Vogel, et al., Defective membrane repair in dysferlin-deficient muscular dystrophy. Nature 2003;423:168-72.
2. Moore, S.A., C.J. Shilling, S. Westra, et al., Limb-girdle muscular dystrophy in the United States. J Neuropathol Exp Neurol 2006;65:995-1003.
3. Rosales, X.Q., J.M. Gastier-Foster, S. Lewis, et al., Novel diagnostic features of dysferlinopathies. Muscle Nerve 2010;42:14-21.
4. Rosales, X.Q., S.J. Moser, T. Tran, et al., Cardiovascular magnetic resonance of cardiomyopathy in limb girdle muscular dystrophy 2B and 2I. J Cardiovasc Magn Reson 2011;13:39.
5. Emmerling, V.V., S. Fischer, F. Stiefel, et al., Temperature-sensitive miR-483 is a conserved regulator of recombinant protein and viral vector production in mammalian cells. Biotechnol Bioeng 2016;113:830-41.
6. Aoki, M., J. Liu, I. Richard, et al., Genomic organization of the dysferlin gene and novel mutations in Miyoshi myopathy. Neurology 2001;57:271-8.
7. Liu, J., M. Aoki, I. Illa, et al., Dysferlin, a novel skeletal muscle gene, is mutated in Miyoshi myopathy and limb girdle muscular dystrophy. Nat Genet 1998;20:31-6.
8. Liu, J., C. Wu, K. Bossie, et al., Generation of a 3-Mb PAC contig spanning the Miyoshi myopathy/limb-girdle muscular dystrophy (MM/LGMD2B) locus on chromosome 2p13. Genomics 1998;49:23-9.
9. Grose, W.E., K.R. Clark, D. Griffin, et al., Homologous recombination mediates functional recovery of dysferlin deficiency following AAV5 gene transfer. PLoS One 2012;7:e39233.
10. Lennon, N.J., A. Kho, B.J. Bacskai, et al., Dysferlin interacts with annexins A1 and A2 and mediates sarcolemmal wound-healing. J Biol Chem 2003;278:50466-73.
11. Sondergaard, P., D. Griffin, E. Pozsgai, et al., AAV.Dysferlin Overlap Vectors Restore Function in Dysferlinopathy Animal Models. Annals of Clinical and Translational Neurology 2015;2:256-270.
12. Kerr, J., C. Ward, and R. Bloch, Dysferlin at transverse tubules regulates Ca^{2+}

Human Gene Therapy
Systemic Delivery of Dysferlin Overlap Vectors Provides Long-Term Functional Improvement for Dysferlinopathy (doi: 10.1089/hum.2017.062)
This article has been peer-reviewed and accepted for publication, but has yet to undergo copyediting and proof correction. The final published version may differ from this proof.
Downloaded by Donna Ward from online.liebertpub.com at 07/19/17. For personal use only.

Human Gene Therapy
Systemic Delivery of Dysferlin Overlap Vectors Provides Long-Term Functional Improvement for Dysferlinopathy (DOI: 10.1089/hum.2017.062)
This paper has been peer-reviewed and accepted for publication, but has yet to undergo copyediting and proof correction. The final published version may differ from this proof.

homeostasis in skeletal muscle. Frontiers in Physiology 2014;5.

13. Lek, A., F. Evesson, B. Sutton, et al., Ferlins: Regulators of Vesicle Fusion for Auditory Neurotransmission, Receptor Trafficking and Membrane Repair. Traffic 2012;13:185-194.
14. Oulhen, N., T. Onorato, I. Ramos, et al., Dysferlin is essential for endocytosis in the sea star oocyte. Dev Biol 2014;388:94-102.
15. Chiu, Y.H., M.A. Hornsey, L. Klinge, et al., Attenuated muscle regeneration is a key factor in dysferlin-deficient muscular dystrophy. Hum Mol Genet 2009;18:1976-89.
16. de Morree, A., B. Flix, I. Bagaric, et al., Dysferlin regulates cell adhesion in human monocytes. J Biol Chem 2013;288:14147-57.
17. Mariano, A., A. Henning, and R. Han, Dysferlin-deficient muscular dystrophy and innate immune activation. FEBS J 2013;280:4165-76.
18. Millay, D.P., M. Maillet, J.A. Roche, et al., Genetic manipulation of dysferlin expression in skeletal muscle: novel insights into muscular dystrophy. Am J Pathol 2009;175:1817-23.
19. Lostal, W., M. Bartoli, C. Roudaut, et al., Lack of correlation between outcomes of membrane repair assay and correction of dystrophic changes in experimental therapeutic strategy in dysferlinopathy. PLoS One 2012;7:e38036.
20. Walter, M.C., P. Reilich, S. Thiele, et al., Treatment of dysferlinopathy with deflazacort: a double-blind, placebo-controlled clinical trial. Orphanet J Rare Dis 2013;8:26.
21. Gallardo, E., R. Rojas-Garcia, N. de Luna, et al., Inflammation in dysferlin myopathy: immunohistochemical characterization of 13 patients. Neurology 2001;57:2136-8.
22. Fanin, M. and C. Angelini, Muscle pathology in dysferlin deficiency. Neuropathol Appl Neurobiol 2002;28:461-70.
23. Barthelemy, F., N. Wein, M. Krahn, et al., Translational research and therapeutic perspectives in dysferlinopathies. Mol Med 2011;17:875-82.
24. He, B., R.H. Tang, N. Weisleder, et al., Enhancing muscle membrane repair by gene delivery of MG53 ameliorates muscular dystrophy and heart failure in delta-Sarcoglycan-deficient hamsters. Mol Ther 2012;20:727-35.
25. Krahn, M., N. Wein, M. Bartoli, et al., A naturally occurring human minidysferlin

Human Gene Therapy
Systemic Delivery of Dysferlin Overlap Vectors Provides Long-Term Functional Improvement for Dysferlinopathy (doi: 10.1089/hum.2017.062)
This article has been peer-reviewed and accepted for publication, but has yet to undergo copyediting and proof correction. The final published version may differ from this proof.
Downloaded by Donna Ward from online.liebertpub.com at 07/19/17. For personal use only.

Human Gene Therapy
Systemic Delivery of Dysferlin Overlap Vectors Provides Long-Term Functional Improvement for Dysferlinopathy (DOI: 10.1089/hum.2017.062)
This paper has been peer-reviewed and accepted for publication, but has yet to undergo copyediting and proof correction. The final published version may differ from this proof.

protein repairs sarcolemmal lesions in a mouse model of dysferlinopathy. Sci Transl Med 2010;2:50ra69.

26. Lostal, W., M. Bartoli, N. Bourg, et al., Efficient recovery of dysferlin deficiency by dual adeno-associated vector-mediated gene transfer. Hum Mol Genet 2010;19:1897-907.

27. Hofhuis, J., K. Bersch, R. Bussenschutt, et al., Dysferlin mediates membrane tubulation and links T-tubule biogenesis to muscular dystrophy. J Cell Sci 2017.

28. Chicoine, L.G., L.R. Rodino-Klapac, G. Shao, et al., Vascular Delivery of rAAVrh74.MCK.GALGT2 to the Gastrocnemius Muscle of the Rhesus Macaque Stimulates the Expression of Dystrophin and Laminin alpha2 Surrogates. Mol Ther 2014;22:713-24.

29. Gao, G., L.H. Vandenberghe, and J.M. Wilson, New recombinant serotypes of AAV vectors. Curr Gene Ther 2005;5:285-97.

30. Heller, K.N., C.L. Montgomery, P.M. Janssen, et al., AAV-mediated overexpression of human alpha7 integrin leads to histological and functional improvement in dystrophic mice. Mol Ther 2013;21:520-5.

31. Sahenk, Z., G. Galloway, K.R. Clark, et al., AAV1.NT-3 Gene Therapy for Charcot-Marie-Tooth Neuropathy. Mol Ther 2014;22:511-21.

32. Grieger, J.C., S.M. Soltys, and R.J. Samulski, Production of Recombinant Adeno-associated Virus Vectors Using Suspension HEK293 Cells and Continuous Harvest of Vector From the Culture Media for GMP FIX and FLT1 Clinical Vector. Mol Ther 2016;24:287-97.

33. Emmerling, V.V., A. Pegel, E.G. Milian, et al., Rational plasmid design and bioprocess optimization to enhance recombinant adeno-associated virus (AAV) productivity in mammalian cells. Biotechnol J 2016;11:290-7.

34. Qu, W., M. Wang, Y. Wu, et al., Scalable downstream strategies for purification of recombinant adeno- associated virus vectors in light of the properties. Curr Pharm Biotechnol 2015;16:684-95.

35. Foust, K.D., X. Wang, V.L. McGovern, et al., Rescue of the spinal muscular atrophy phenotype in a mouse model by early postnatal delivery of SMN. Nat Biotechnol 2010;28:271-4.

36. Wang, D., L. Zhong, M.A. Nahid, et al., The potential of adeno-associated viral vectors for gene delivery to muscle tissue. Expert Opin Drug Deliv 2014;11:345-64.

37. Rodino-Klapac, L.R., P.M. Janssen, C.L. Montgomery, et al., A translational approach for limb vascular delivery of the micro-dystrophin gene without high volume or high pressure for treatment of Duchenne muscular dystrophy. J Transl Med 2007;5:45.

38. Pozsgai, E.R., D.A. Griffin, K.N. Heller, et al., Systemic AAV-Mediated beta-Sarcoglycan Delivery Targeting Cardiac and Skeletal Muscle Ameliorates Histological and Functional Deficits in LGMD2E Mice. Mol Ther 2017.

39. Clark, K.R., X. Liu, J.P. McGrath, et al., Highly purified recombinant adeno-associated virus vectors are biologically active and free of detectable helper and wild-type viruses. Hum Gene Ther 1999;10:1031-9.

40. Ghosh, A., Y. Yue, C. Long, et al., Efficient whole-body transduction with trans-splicing adeno-associated viral vectors. Mol Ther 2007;15:750-5.

41. Emmerling, V.V., S. Fischer, M. Kleemann, et al., miR-483 is a self-regulating microRNA and can activate its own expression via USF1 in HeLa cells. Int J Biochem Cell Biol 2016;80:81-86.

42. Toromanoff, A., Y. Cherel, M. Guilbaud, et al., Safety and Efficacy of Regional Intravenous (RI) Versus Intramuscular (IM) Delivery of rAAV1 and rAAV8 to Nonhuman Primate Skeletal Muscle. Mol Ther 2008;16:1291-1299.

43. Rodino-Klapac, L.R., C.L. Montgomery, W.G. Bremer, et al., Persistent expression of FLAG-tagged micro dystrophin in nonhuman primates following intramuscular and vascular delivery. Mol Ther 2010;18:109-17.

44. Schnepp, B.C., R.L. Jensen, C.L. Chen, et al., Characterization of adeno-associated virus genomes isolated from human tissues. J Virol 2005;79:14793-803.

45. Sondergaard, P.C., D.A. Griffin, E.R. Pozsgai, et al., AAV.Dysferlin Overlap Vectors Restore Function in Dysferlinopathy Animal Models. Ann Clin Transl Neurol 2015;2:256-70.

46. Labikova, J., J. Vcelakova, T. Ulmannova, et al., The cytokine production of peripheral blood mononuclear cells reflects the autoantibody profile of patients suffering from type 1 diabetes. Cytokine 2014;69:189-195.

47. Roche, J.A., L.W. Ru, A.M. O'Neill, et al., Unmasking potential intracellular roles for

Human Gene Therapy
Systemic Delivery of Dysferlin Overlap Vectors Provides Long-Term Functional Improvement for Dysferlinopathy (doi: 10.1089/hum.2017.062)
This article has been peer-reviewed and accepted for publication, but has yet to undergo copyediting and proof correction. The final published version may differ from this proof.
Downloaded by Donna Ward from online.liebertpub.com at 07/19/17. For personal use only.

Human Gene Therapy
Systemic Delivery of Dysferlin Overlap Vectors Provides Long-Term Functional Improvement for Dysferlinopathy (DOI: 10.1089/hum.2017.062)
This paper has been peer-reviewed and accepted for publication, but has yet to undergo copyediting and proof correction. The final published version may differ from this proof.

dysferlin through improved immunolabeling methods. J Histochem Cytochem 2011;59:964-75.

48. Vontzalidis, A., G. Terzis, and P. Manta, Increased dysferlin expression in Duchenne muscular dystrophy. Anal Quant Cytopathol Histpathol 2014;36:15-22.

49. Nagy, N., R.J. Nonneman, T. Llanga, et al., Hip region muscular dystrophy and emergence of motor deficits in dysferlin-deficient Bla/J mice. Physiol Rep 2017;5.

Human Gene Therapy
Systemic Delivery of Dysferlin Overlap Vectors Provides Long-Term Functional Improvement for Dysferlinopathy (doi: 10.1089/hum.2017.062)
This article has been peer-reviewed and accepted for publication, but has yet to undergo copyediting and proof correction. The final published version may differ from this proof.
Downloaded by Donna Ward from online.liebertpub.com at 07/19/17. For personal use only.

Human Gene Therapy
Systemic Delivery of Dysferlin Overlap Vectors Provides Long-Term Functional Improvement for Dysferlinopathy (DOI: 10.1089/hum.2017.062)
This paper has been peer-reviewed and accepted for publication, but has yet to undergo copyediting and proof correction. The final published version may differ from this proof.

Human Gene Therapy
Systemic Delivery of Dysferlin Overlap Vectors Provides Long-Term Functional Improvement for Dysferlinopathy (doi: 10.1089/hum.2017.062)
This article has been peer-reviewed and accepted for publication, but has yet to undergo copyediting and proof correction. The final published version may differ from this proof.
Downloaded by Donna Ward from online.liebertpub.com at 07/19/17. For personal use only.

Human Gene Therapy
Systemic Delivery of Dysferlin Overlap Vectors Provides Long-Term Functional Improvement for Dysferlinopathy (DOI: 10.1089/hum.2017.062)
This paper has been peer-reviewed and accepted for publication, but has yet to undergo copyediting and proof correction. The final published version may differ from this proof.

Figure Legends

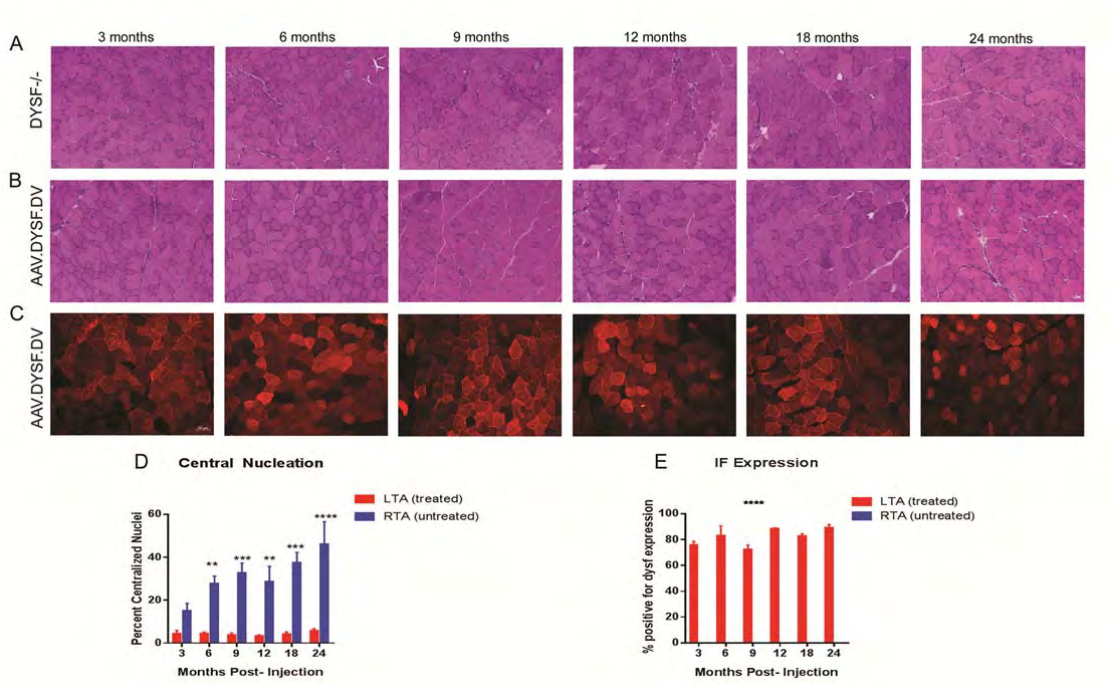


Figure 1. Sustained long-term expression following intramuscular delivery in dysferlin null mice. 4 week old *Dysf* $^{-/-}$ mice were injected with 2 x 10^{11} vg total dose of AAVrh74.MHCK7.DYSF.DV into the left tibialis anterior (TA) muscle and followed for 3-24 months to monitor expression and histology (n=3 per timepoint). (A) Hematoxylin and Eosin staining demonstrates a significant reduction in centrally located nuclei in the treated TA compared to (B) contralateral control TA muscles injected with saline. (C) Anti-dysferlin immunofluorescence staining demonstrates dysferlin transgene expression was sustained throughout all timepoints (3-24 months). (D) At 6, 9, 12, 18 and 24 months post-delivery, there was a significant decrease in central nucleation to below 5%; excluding the 3 month timepoint, all values were significant at or lower than $p \leq 0.01$ for central nucleation quantification. (E) There was no significant decrease in the percentage of dysferlin positive fivers over time and contralateral (right side) muscles demonstrated no dysferlin expression. TWO-WAY ANOVAs were utilized to identify differences in the means between treated and untreated cohorts. Error bars are represented as mean ± SEM ($p<0.05$).

Human Gene Therapy
Systemic Delivery of Dysferlin Overlap Vectors Provides Long-Term Functional Improvement for Dysferlinopathy (doi: 10.1089/hum.2017.062)
This article has been peer-reviewed and accepted for publication, but has yet to undergo copyediting and proof correction. The final published version may differ from this proof.
Downloaded by Donna Ward from online.liebertpub.com at 07/19/17. For personal use only.

Human Gene Therapy
Systemic Delivery of Dysferlin Overlap Vectors Provides Long-Term Functional Improvement for Dysferlinopathy (DOI: 10.1089/hum.2017.062)
This paper has been peer-reviewed and accepted for publication, but has yet to undergo copyediting and proof correction. The final published version may differ from this proof.

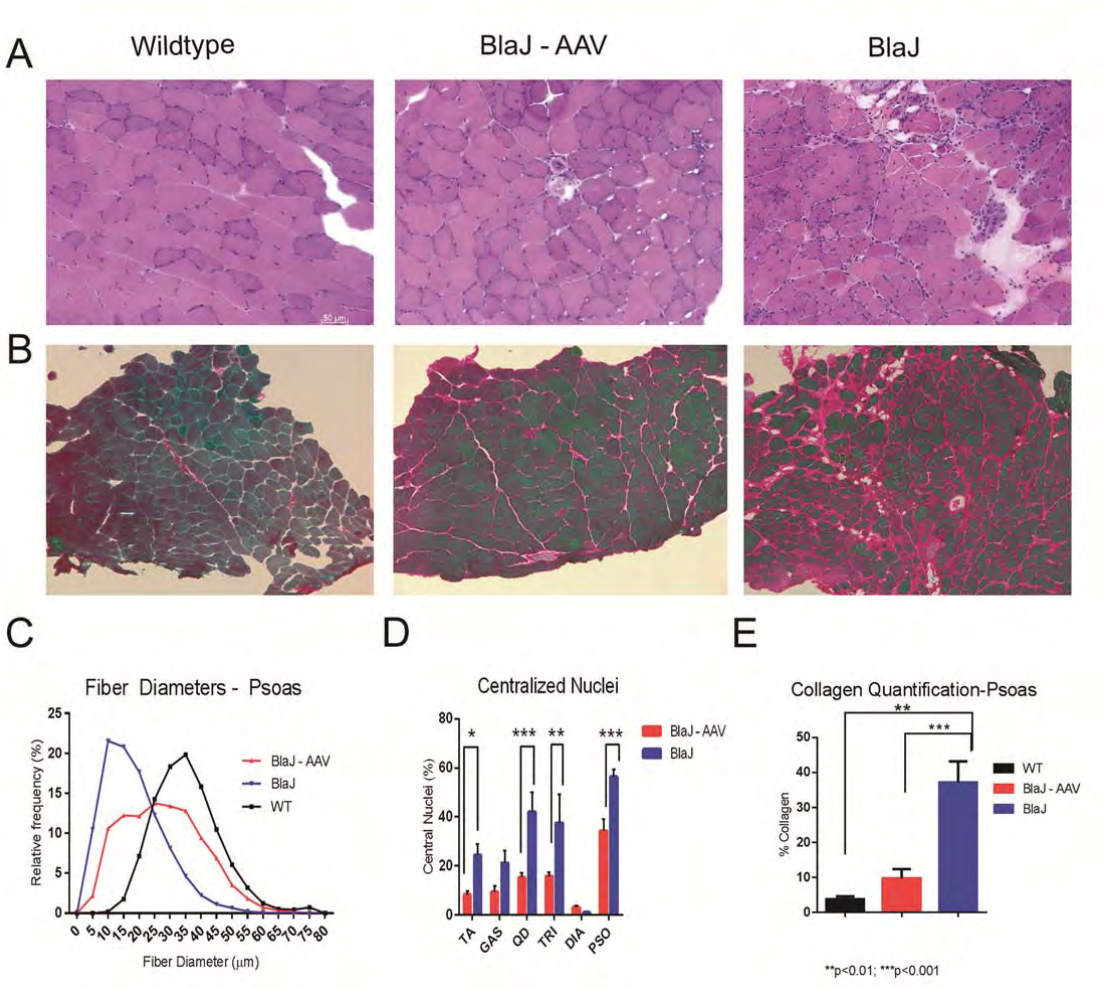


Figure 2. Intravenous delivery of AAVrh74.MHCK7.DYSF.DV improves histological parameters in BlaJ mice. (A) Hematoxylin & eosin staining of the psoas muscle 28 weeks post treatment demonstrated improvement in fiber size distribution and reduced central nuclei following intravenous delivery of 6 x 10^{12} vg total dose of AAVrh74.MHCK7.DYSF.DV in treated BlaJ mice versus and saline treated mice. (B) Picosirius red staining for collagen demonstrated reduction in fibrosis in AAVrh74.MHCK7.DYSF.DV treated psoas muscles. (C) Following AAVrh74.MHCK7.DYSF.DV delivery there was a trend toward normal fiber diameters with a significant increase in mean fiber diameter in treated muscle (27.8µm±0.17) versus control (18.4µm±0.099) , and reduced central nucleation in the tibialis anterior, quadriceps, triceps, and psoas muscles. (E) Additionally, there was a significant decrease from 37.0% to 9.7% collagen deposition in treated mice compared to saline treated mice. TWO-WAY ANOVAs were utilized with post hoc analysis to locate differences in central nucleation and fiber diameters. Error bars are represented as mean ± SEM ($p<0.05$).

Human Gene Therapy
Systemic Delivery of Dysferlin Overlap Vectors Provides Long-Term Functional Improvement for Dysferlinopathy (doi: 10.1089/hum.2017.062)
This article has been peer-reviewed and accepted for publication, but has yet to undergo copyediting and proof correction. The final published version may differ from this proof.
Downloaded by Donna Ward from online.liebertpub.com at 07/19/17. For personal use only.

Human Gene Therapy
Systemic Delivery of Dysferlin Overlap Vectors Provides Long-Term Functional Improvement for Dysferlinopathy (DOI: 10.1089/hum.2017.062)
This paper has been peer-reviewed and accepted for publication, but has yet to undergo copyediting and proof correction. The final published version may differ from this proof.

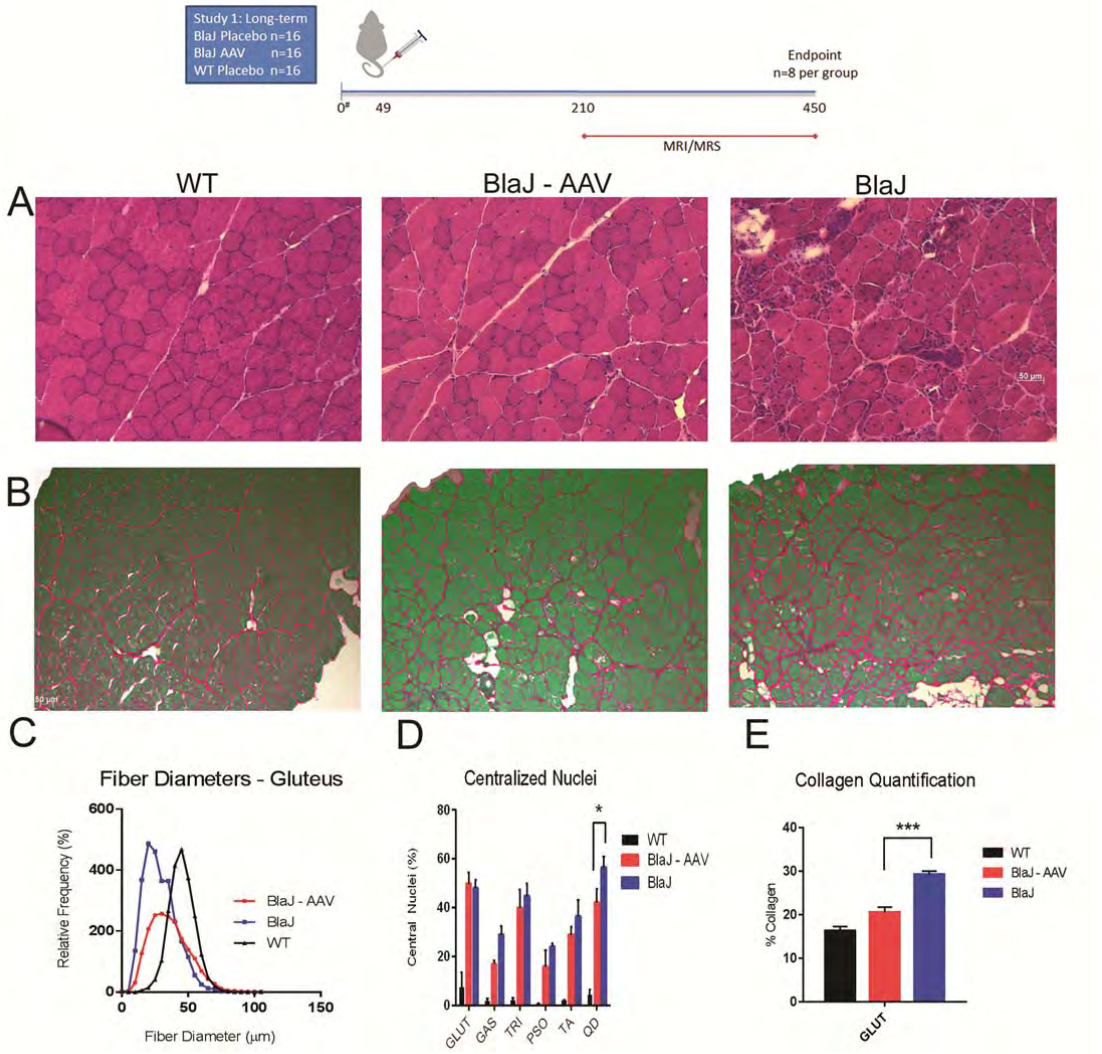


Figure 3. Long term improvement in collagen deposition and immune staining with AAVrh74.MHCK7.DYSF.DV treatment.

(A) At 15 months of age, hematoxylin & eosin staining demonstrated normalization of histology in treated psoas muscles (BlaJ-AAV). (B) Picosirius staining in the gluteus muscle demonstrated a reduction in collagen deposition. (C) Following long term treatment in systemically treated mice, there was a trend toward normalization of fiber diameters and (D) reduced centrally located nuclei in the quadriceps muscle as shown with hematoxylin & eosin staining. (E) Finally, there was a 9.0% reduction in collagen deposition using picosirius staining in the gluteus muscle. ONE-WAY ANOVAs were utilized with post hoc analysis to locate differences in the means. Error bars are represented as mean ± SEM ($p<0.05$).

Human Gene Therapy
Systemic Delivery of Dysferlin Overlap Vectors Provides Long-Term Functional Improvement for Dysferlinopathy (doi: 10.1089/hum.2017.062)
This article has been peer-reviewed and accepted for publication, but has yet to undergo copyediting and proof correction. The final published version may differ from this proof.
Downloaded by Donna Ward from online.liebertpub.com at 07/19/17. For personal use only.

Human Gene Therapy
Systemic Delivery of Dysferlin Overlap Vectors Provides Long-Term Functional Improvement for Dysferlinopathy (DOI: 10.1089/hum.2017.062)
This paper has been peer-reviewed and accepted for publication, but has yet to undergo copyediting and proof correction. The final published version may differ from this proof.

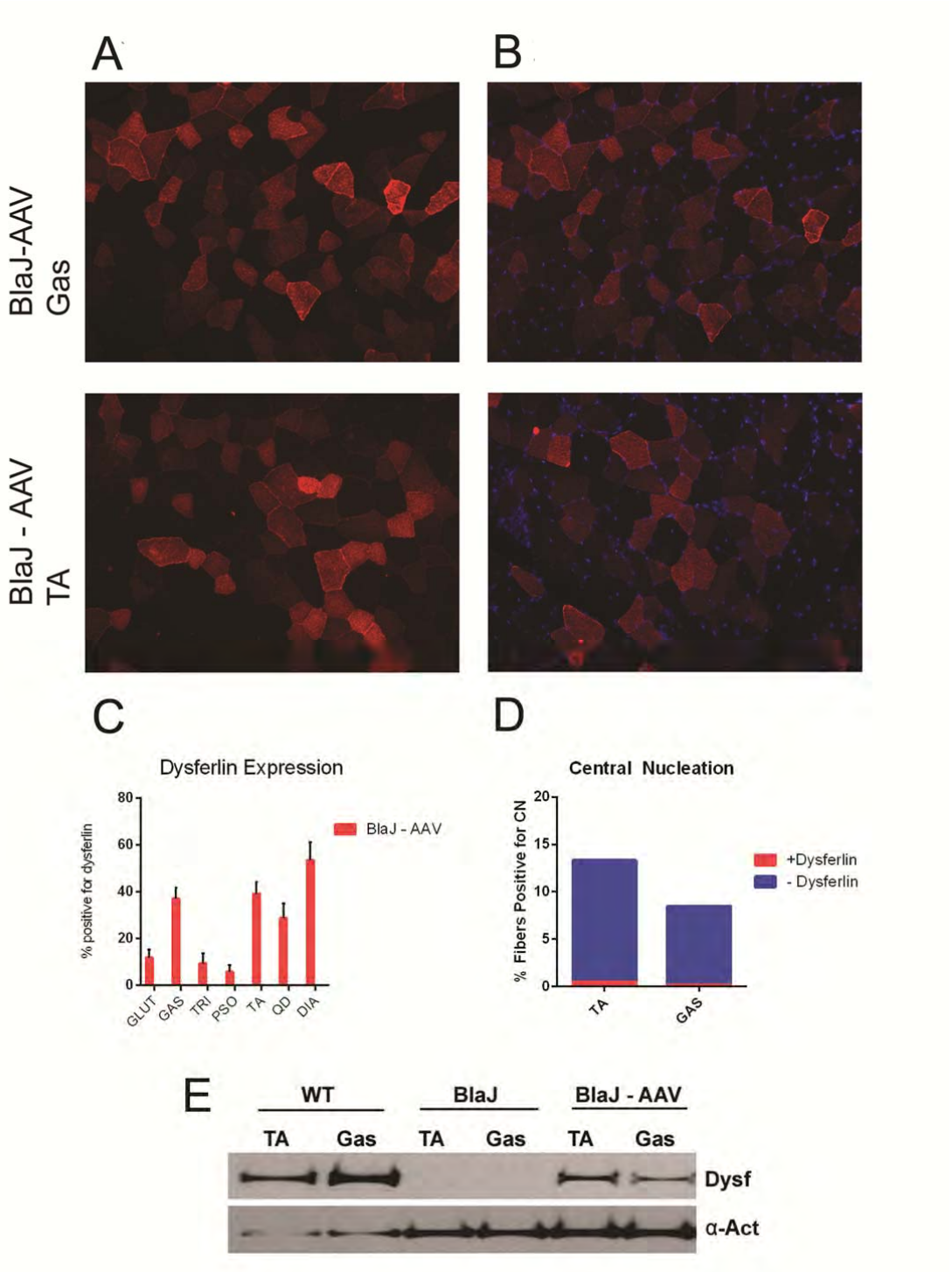


Figure 4. Long term expression and normalization of centrally located nuclei in AAVrh74.MHCK7.DYSF.DV treated mice.

(A) Robust dysferlin expression was seen following systemic delivery ($6x10^{12}$ dose) using anti-dysferlin immune staining with an N-terminal antibody. Gastrocnemius (GAS) and tibialis anterior (TA) muscles are shown for representation. (B) Sections were co-stained with DAPI to quantify dysferlin positive fibers co-localized with centrally located nuclei. (C) There was widespread dysferlin transgene expression at 15 months of age above 5% in all tissues with the diaphragm expressing the highest at 53%. (D) It is demonstrated that the majority of fibers with centrally located nuclei are absent of dysferlin expression (less than 0.5% are positive for dysferlin and centrally located nuclei). (E) Full-length dysferlin in treated muscles at 15 months of age was confirmed by western blot analysis (TA and GAS) compared to wild-type and BlaJ untreated muscle.

Human Gene Therapy
Systemic Delivery of Dysferlin Overlap Vectors Provides Long-Term Functional Improvement for Dysferlinopathy (doi: 10.1089/hum.2017.062)
This paper has been peer-reviewed and accepted for publication, but has yet to undergo copyediting and proof correction. The final published version may differ from this proof.

Human Gene Therapy
Systemic Delivery of Dysferlin Overlap Vectors Provides Long-Term Functional Improvement for Dysferlinopathy (doi: 10.1089/hum.2017.062)
This article has been peer-reviewed and accepted for publication, but has yet to undergo copyediting and proof correction. The final published version may differ from this proof.
Downloaded by Donna Ward from online.liebertpub.com at 07/19/17. For personal use only.

Human Gene Therapy
Systemic Delivery of Dysferlin Overlap Vectors Provides Long-Term Functional Improvement for Dysferlinopathy (doi: 10.1089/hum.2017.062)
This article has been peer-reviewed and accepted for publication, but has yet to undergo copyediting and proof correction. The final published version may differ from this proof.
Downloaded by Donna Ward from online.liebertpub.com at 07/19/17. For personal use only.

Human Gene Therapy
Systemic Delivery of Dysferlin Overlap Vectors Provides Long-Term Functional Improvement for Dysferlinopathy (DOI: 10.1089/hum.2017.062)
This paper has been peer-reviewed and accepted for publication, but has yet to undergo copyediting and proof correction. The final published version may differ from this proof.

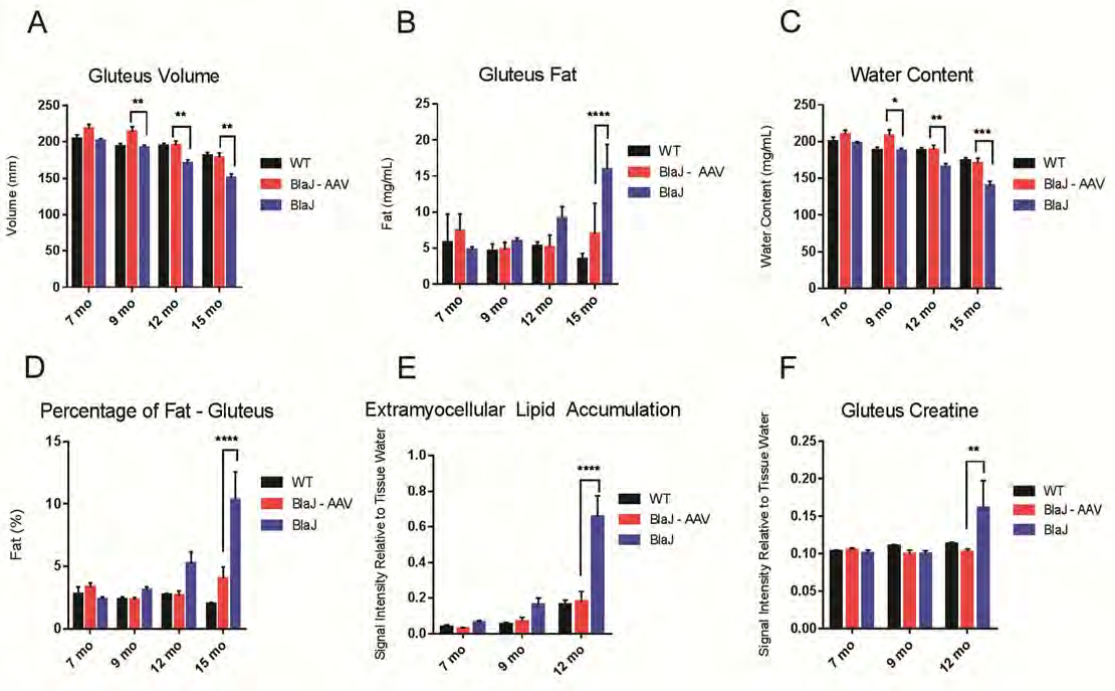


Figure 5. Long term improvements using MRI in systemically treated mice with AAVrh74.MHCK7.DYSF.DV.

(A) Animals underwent MRI after 7, 9, 12 and 15 months of age and demonstrated improvements in gluteus volume ($p<0.001$), (B) decreased gluteus fat ($p<0.0001$), (C) increased water content to wild-type levels ($p=0.223$; $p<0.01$) , and (D) decreased fat percentage significantly at the 15 month timepoints ($p<0.0001$), (E) MR-spectroscopy was used to evaluate metabolite accumulation and decreased extramyocellular lipid accumulation was demonstrated (EMCL) in the gluteus muscle ($p<0.0001$), (F) as well as decreased creatine levels in the muscle to wild-type levels ($p=0.021$). 15 month old BLAJ animals were unable to undergo MR-spectroscopy evaluation due to excessive fat infiltration in the saline treated cohort. TWO-WAY ANOVAs with Tukey post-hoc analysis were utilized to locate differences in the means. Error bars are represented as mean ± SEM ($p<0.05$).

Human Gene Therapy
Systemic Delivery of Dysferlin Overlap Vectors Provides Long-Term Functional Improvement for Dysferlinopathy (doi: 10.1089/hum.2017.062)
This article has been peer-reviewed and accepted for publication, but has yet to undergo copyediting and proof correction. The final published version may differ from this proof.
Downloaded by Donna Ward from online.liebertpub.com at 07/19/17. For personal use only.

Human Gene Therapy
Systemic Delivery of Dysferlin Overlap Vectors Provides Long-Term Functional Improvement for Dysferlinopathy (DOI: 10.1089/hum.2017.062)
This paper has been peer-reviewed and accepted for publication, but has yet to undergo copyediting and proof correction. The final published version may differ from this proof.

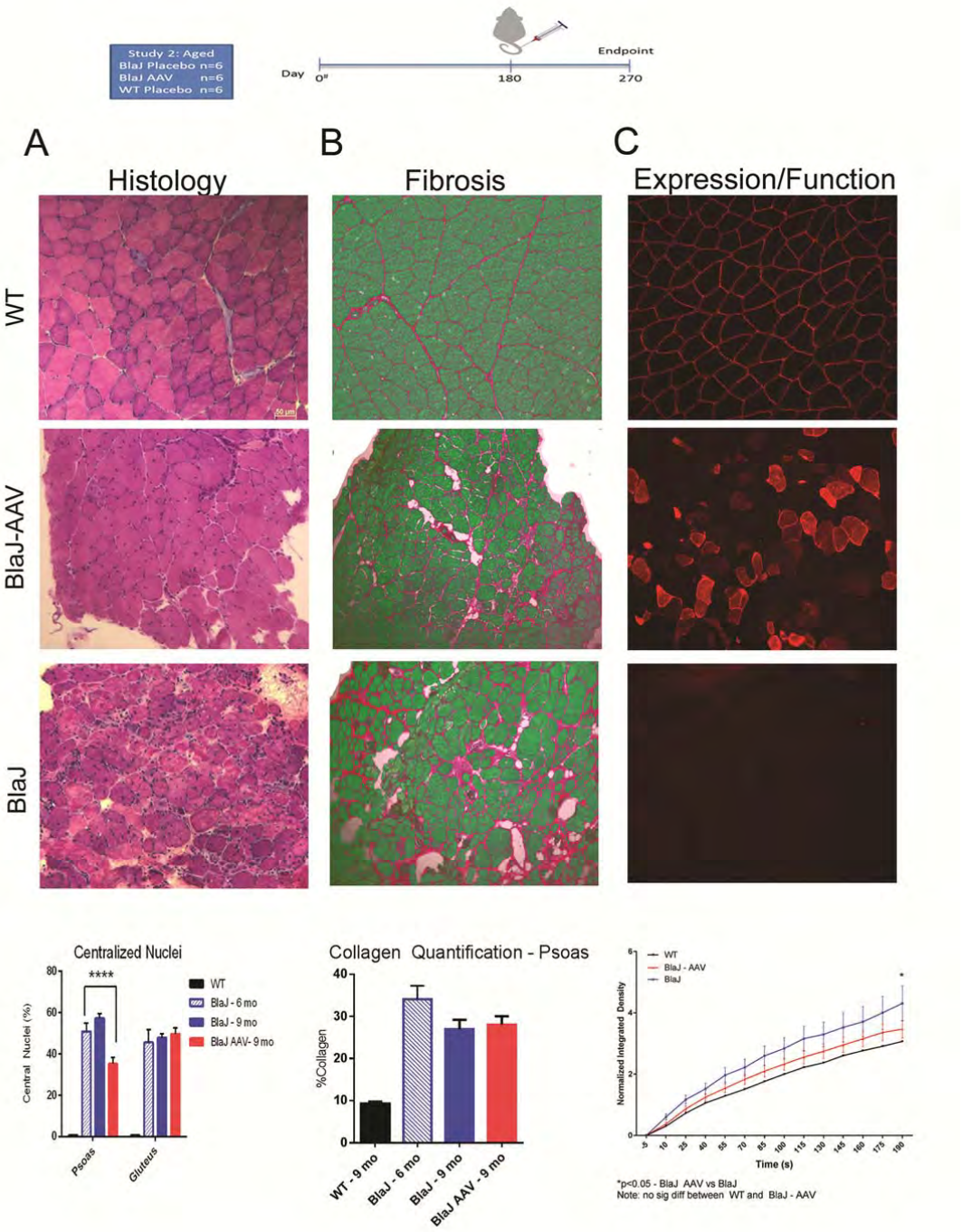


Figure 6. Systemic expression and histological improvements in an aged cohort treated with AAVrh74.MHCK7.DYSF.DV.

(A) Animals treated at 6 month of age and sacrificed at 9 months of age demonstrated reductions in centrally located nuclei in psoas muscle using hematoxylin & eosin staining. (B) There was slightly reduced collagen deposition between 6 months of age and 9 months of age with

treatment. (C) Dysferlin transgene expression was noted across all muscles following AAV treatment in this aged cohort which led to significant improvement in membrane repair capacity in FDB muscles. $p<0.05$ at 190s

Human Gene Therapy
Systemic Delivery of Dysferlin Overlap Vectors Provides Long-Term Functional Improvement for Dysferlinopathy (doi: 10.1089/hum.2017.062)
This article has been peer-reviewed and accepted for publication, but has yet to undergo copyediting and proof correction. The final published version may differ from this proof.
Downloaded by Donna Ward from online.liebertpub.com at 07/19/17. For personal use only.

Human Gene Therapy
Systemic Delivery of Dysferlin Overlap Vectors Provides Long-Term Functional Improvement for Dysferlinopathy (DOI: 10.1089/hum.2017.062)
This paper has been peer-reviewed and accepted for publication, but has yet to undergo copyediting and proof correction. The final published version may differ from this proof.

Human Gene Therapy
Systemic Delivery of Dysferlin Overlap Vectors Provides Long-Term Functional Improvement for Dysferlinopathy (doi: 10.1089/hum.2017.062)
This article has been peer-reviewed and accepted for publication, but has yet to undergo copyediting and proof correction. The final published version may differ from this proof.
Downloaded by Donna Ward from online.liebertpub.com at 07/19/17. For personal use only.

Human Gene Therapy
Systemic Delivery of Dysferlin Overlap Vectors Provides Long-Term Functional Improvement for Dysferlinopathy (DOI: 10.1089/hum.2017.062)
This paper has been peer-reviewed and accepted for publication, but has yet to undergo copyediting and proof correction. The final published version may differ from this proof.

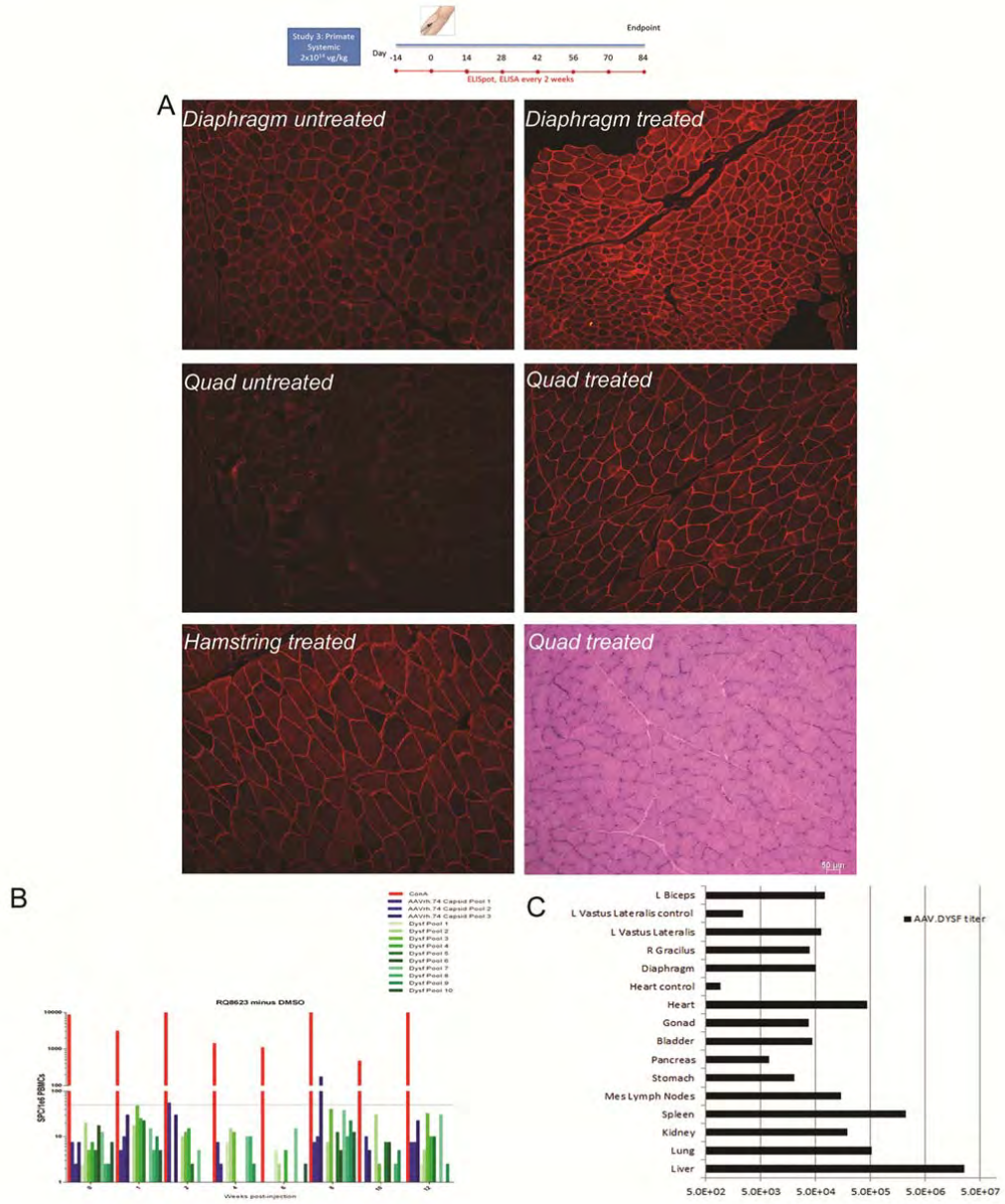


Figure 7. Systemic delivery in rhesus macaque with AAVrh74.MHCK7.DYSF.DV. (A) Anti-dysferlin immunofluorescence staining in untreated naïve rhesus macaque diaphragm and quadriceps muscles (left panel) and systemically treated diaphragm, quadriceps, and hamstring demonstrates robust dysferlin expression. (B) ELISpot analysis of T-cell response to dysferlin and AAV peptide pools demonstrates no adverse T-cell response in the presence of (C) widespread vector genome (vector genomes per ug genomic DNA) biodistribution quantified using qPCR. Vastus lateralis control and heart control in qPCR biodistribution refers to an uninjected male rhesus macaque.

Supplementary Legends:

Supplementary Table 1. ELISA endpoint titers for circulating binding antibodies to AAVrh74 capsid

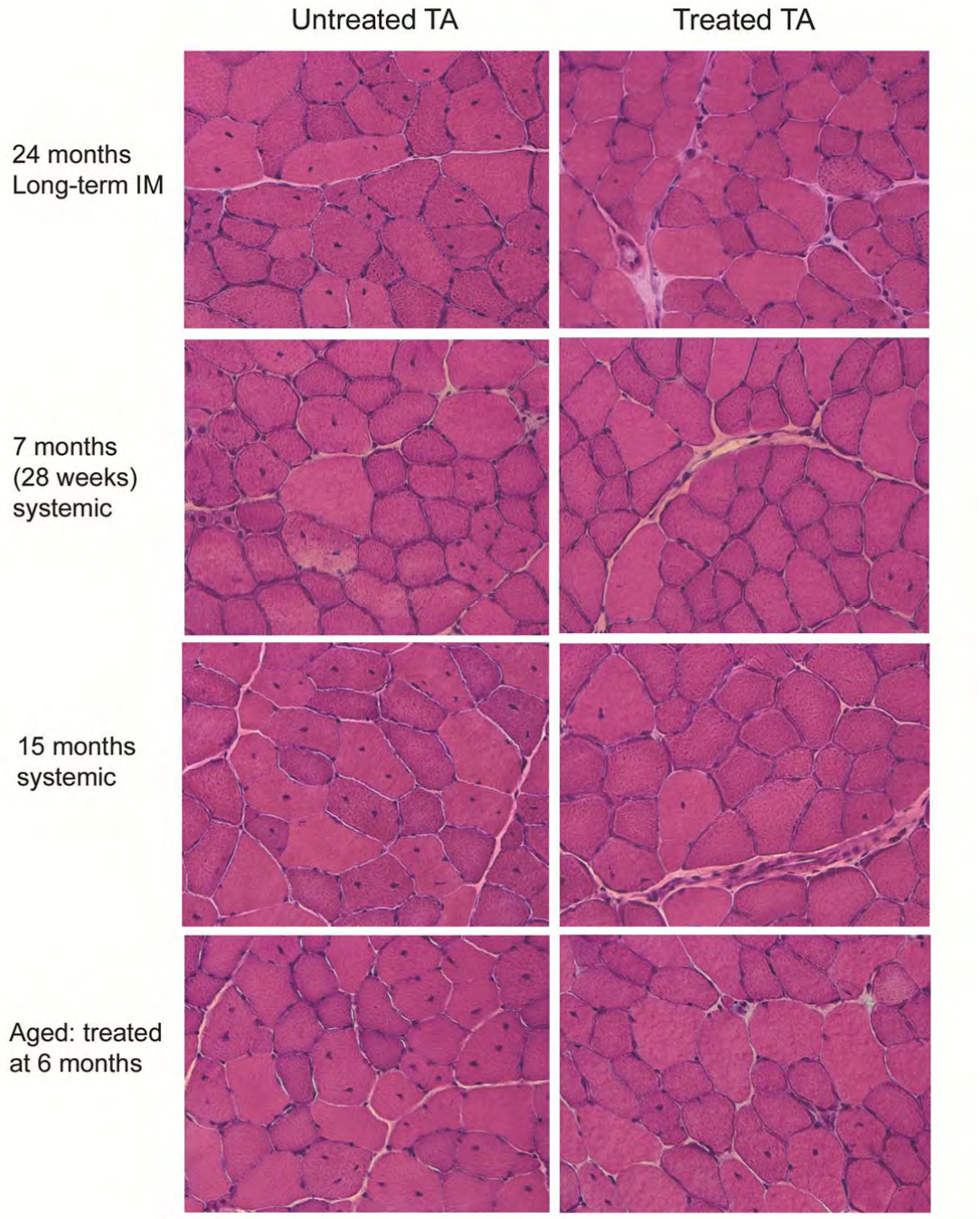
Supplementary Table 2. Non-human primate complete blood counts (CBC) and chemistries following systemic injection with AAVrh74.MHCK7.DV.DYSF

Human Gene Therapy
Systemic Delivery of Dysferlin Overlap Vectors Provides Long-Term Functional Improvement for Dysferlinopathy (doi: 10.1089/hum.2017.062)
This article has been peer-reviewed and accepted for publication, but has yet to undergo copyediting and proof correction. The final published version may differ from this proof.
Downloaded by Donna Ward from online.liebertpub.com at 07/19/17. For personal use only.

Human Gene Therapy
Systemic Delivery of Dysferlin Overlap Vectors Provides Long-Term Functional Improvement for Dysferlinopathy (DOI: 10.1089/hum.2017.062)
This paper has been peer-reviewed and accepted for publication, but has yet to undergo copyediting and proof correction. The final published version may differ from this proof.

Human Gene Therapy
Systemic Delivery of Dysferlin Overlap Vectors Provides Long-Term Functional Improvement for Dysferlinopathy (doi: 10.1089/hum.2017.062)
This article has been peer-reviewed and accepted for publication, but has yet to undergo copyediting and proof correction. The final published version may differ from this proof.
Downloaded by Donna Ward from online.liebertpub.com at 07/19/17. For personal use only.

Human Gene Therapy
Systemic Delivery of Dysferlin Overlap Vectors Provides Long-Term Functional Improvement for Dysferlinopathy (DOI: 10.1089/hum.2017.062)
This paper has been peer-reviewed and accepted for publication, but has yet to undergo copyediting and proof correction. The final published version may differ from this proof.



Supplementary Figure S1. High magnification images (40X) of BlaJ untreated and AAVrh74.MHCK7.DV.DYSF treated tibialis anterior muscles 24 months following IM delivery, 7 months and 15 months following systemic delivery at 8 weeks, and 3 months following systemic delivery of aged mice treated at 6 months of age.

Human Gene Therapy
Systemic Delivery of Dysferlin Overlap Vectors Provides Long-Term Functional Improvement for Dysferlinopathy (doi: 10.1089/hum.2017.062)
This article has been peer-reviewed and accepted for publication, but has yet to undergo copyediting and proof correction. The final published version may differ from this proof.
Downloaded by Donna Ward from online.liebertpub.com at 07/19/17. For personal use only.

Human Gene Therapy
Systemic Delivery of Dysferlin Overlap Vectors Provides Long-Term Functional Improvement for Dysferlinopathy (DOI: 10.1089/hum.2017.062)
This paper has been peer-reviewed and accepted for publication, but has yet to undergo copyediting and proof correction. The final published version may differ from this proof.

Supplementary Tables

Weeks Post Injection	AAVrh74.DYSF.DV RQ8623
0	<5
2	800
4	800
6	204,800
8	409,600
10	204,800
12	204,800

Table 1. ELISA positive titers of circulating binding antibodies to AAVrh74 vector capsid. Serum was isolated from primates biweekly and analyzed for binding antibody titer. Titer reported corresponds to last dilution at which ratio of response ≥2.

Human Gene Therapy
Systemic Delivery of Dysferlin Overlap Vectors Provides Long-Term Functional Improvement for Dysferlinopathy (doi: 10.1089/hum.2017.062)
This article has been peer-reviewed and accepted for publication, but has yet to undergo copyediting and proof correction. The final published version may differ from this proof.
Downloaded by Donna Ward from online.liebertpub.com at 07/19/17. For personal use only.

Human Gene Therapy
Systemic Delivery of Dysferlin Overlap Vectors Provides Long-Term Functional Improvement for Dysferlinopathy (DOI: 10.1089/hum.2017.062)
This paper has been peer-reviewed and accepted for publication, but has yet to undergo copyediting and proof correction. The final published version may differ from this proof.

RQ8623 - AAVrh74.DYSF.DV

Table 2.Complete Blood Count and Chemistries. Serum was isolated from primates biweekly and CBC and chemistries were analyzed. Normal reference ranges for male rhesus macaques are included.

		Baseline	24 Hour Post	1week	2wks	4wks	9wks	10wks	12wks	Reference Values
		value	value	value	value	value	value	value	value	
Albumin	*g/dL*	4.9	4.6	4.7	4.4	4.5	4.2	4.4	4.2	3.64-4.5
Alk Phosphatase	*U/L*	113	105	115	107	118.0	79	90	104.0	495-1415
ALT	*U/L*	28	52	73	36	12.0	87	109	128.0	7.9-63.5
Amylase	*U/L*	377	704	414	504	360.0	333	423	375.0	333-609
AST	*U/L*	57	145	56	56	52.0	59	65	59.0	18-46
BUN	*mg/dL*	18	17	18	14	13.0	15	16	15.0	9-24
Calcium	*mg/dL*	9.5	9.5	9.5	9.4	9.0	9.2	9.4	9.0	7.4-10.6
Cholesterol	*mg/dL*	134	126	172	160	137.0	129	128	108.0	99-154
CK	*U/L*	126	768	91	1045	146.0	269	48	162.0	0-654
Chloride	*mmol/L*	105	104	104	105	105.0	107	107	106.0	103-110
Creatinine	*mg/dL*	0.96	.89	0.95	0.86	0.84	0.72	0.74	0.76	0.5-0.9
GGTP	U/L	82	76	75	66	77	69	75	87	53-92
Glucose	mg/dL	65	71	74	69	76	64	63	75	42-129
Potassium	*mmol/L*	3.5	3.9	3.2	3.7	3.1	3.6	3.4	2.9	3.13-4.01
Lipase	*U/L*	64	362	93	141	62.0	90	103	86.0	18.8-36.2
Magnesium	*mg/dL*	1.5	1.5	1.7	1.7	1.5	1.5	1.6	1.7	1.38-1.6

Human Gene Therapy
Systemic Delivery of Dysferlin Overlap Vectors Provides Long-Term Functional Improvement for Dysferlinopathy (doi: 10.1089/hum.2017.062)
This article has been peer-reviewed and accepted for publication, but has yet to undergo copyediting and proof correction. The final published version may differ from this proof.
Downloaded by Donna Ward from online.liebertpub.com at 07/19/17. For personal use only.

Human Gene Therapy
Systemic Delivery of Dysferlin Overlap Vectors Provides Long-Term Functional Improvement for Dysferlinopathy (DOI: 10.1089/hum.2017.062)
This paper has been peer-reviewed and accepted for publication, but has yet to undergo copyediting and proof correction. The final published version may differ from this proof.

Sodium	*mmol/L*	153	152.0	152	152	149.0	152	150	149.0	141-149
Osmolality	*mosmol/kg*	313	309	314	308	301.0	304	305	304.0	300-315
Phosphorus	*mg/dL*	5.0	4.6	5.2	5.1	5.3	4.6	5.0	3.9	3.9-5.9
Protein, Total	*g/dL*	8.2	8.1	8.4	8.0	7.9	7.8	8.0	7.5	6.0-7.2
Total Bilirubin	*mg/dL*	0.2	0.5	0.1	0.1	0.5	0.0	0.2	0.2	0.29-0.51
Triglycerides	*mg/dL*	81	42	58	55	51.0	76	86	86.0	19.7-113.9
WBC	*K/cu mm*	12.3	6.4	8.2	6.8	6.2	7.0	7.1	6.9	5.3-10.6
RBC	*M/cu mm*	5.65	5.43	5.49	5.0	5.06	5.22	5.19	5.06	4.49-5.51
hemoglobin	g/dL	14.1	13.5	13.7	12.3	12.7	13.0	13.1	12.8	10.5-13.6
Hematocrit	%	43.7	41.6	42.7	39.2	39.8	41.3	41.2	39.9	31.6-39.3
MCV	*fL*	77.3	76.6	77.8	78.4	78.7	79.1	79.4	78.9	66-76
MCH	*pg*	25	24.9	25	24.6	25.1	24.9	25.2	25.3	21.83-26.85
MCHC	*%*	32.3	32.5	32.1	31.4	31.9	31.5	31.8	32.1	31-37
RDW	*%*	12.9	13.1	13.3	13.6	13.7	13.1	13.0	13.2	12.23-13.85
platelet count	*K/cu mm*	261	266	335	283.0	309.0	307	307	305	180.19-415.17
MPV	*fL*		11.2	11.1	11.6	11.6	10.6	10.9	10.7	7.5-11.5
neutrophil	*%*									16.36-36.06
lymphocyte	*%*	26	27.0	51.0	53.0	48.0	33	42	34.0	53-74.3
monocyte	*%*	4.0	6	6	6.0	2.0	9	2	4.0	4.23-10.1
eosinophil	*%*	1.0			4.0	0.0	1			0.2-2.44
basophil	*%*			2.0		0.0				0.28-0.88

Human Gene Therapy
Systemic Delivery of Dysferlin Overlap Vectors Provides Long-Term Functional Improvement for Dysferlinopathy (doi: 10.1089/hum.2017.062)
This article has been peer-reviewed and accepted for publication, but has yet to undergo copyediting and proof correction. The final published version may differ from this proof.
Downloaded by Donna Ward from online.liebertpub.com at 07/19/17. For personal use only.

Human Gene Therapy
Systemic Delivery of Dysferlin Overlap Vectors Provides Long-Term Functional Improvement for Dysferlinopathy (DOI: 10.1089/hum.2017.062)
This paper has been peer-reviewed and accepted for publication, but has yet to undergo copyediting and proof correction. The final published version may differ from this proof.

										37
seg	%	60	67	44	34	50	57	56	63	0-1
stomatocytes										3.64-4.5

NIH Public Access
Author Manuscript
Am J Med Genet B Neuropsychiatr Genet. Author manuscript; available in PMC 2009 February 21.

Published in final edited form as:
Am J Med Genet B Neuropsychiatr Genet. 2006 April 5; 141B(3): 245–249. doi:10.1002/ajmg.b.30293.

[^{18}F]FDOPA PET as an Endophenotype for Parkinson's Disease Linkage Studies

Brad A. Racette, M.D.[1,2], **Laura Good, BA**[1,2], **Jo Ann Antenor, MPH**[1], **Lori McGee-Minnich, BSN**[1,2], **Stephen M. Moerlein, PhD**[3], **Tom O. Videen, PhD**[1,3], and **Joel S. Perlmutter, M.D.**[1,2,3,4,5]

[1] Deptartment of Neurology Washington University School of Medicine

[2] American Parkinson Disease Association Advanced Center for Parkinson Research Washington University School of Medicine

[3] Mallinckrodt Institute of Radiology Washington University School of Medicine

[4] Deptartment of Anatomy & Neurobiology Washington University School of Medicine

[5] Program in Physical Therapy, Washington University School of Medicine

Abstract

Parkinson Disease (PD) is a late onset disorder with age-dependent penetrance that may confound genetic studies since affected individuals may not demonstrate clinical manifestations at the time of evaluation. The use of endophenotypes, biologic surrogates for clinical disease diagnoses, may permit more accurate classification of at-risk subjects. Positron emission tomography (PET) measurements of 6-[^{18}F]fluorodopa ([^{18}F]FDOPA) uptake indicate nigrostriatal neuronal integrity and may provide a useful endophenotype for PD linkage studies. We performed [^{18}F]FDOPA PET in 11 members of a large, multi-incident Amish family with PD, 24 normals and 48 people with clinically definite idiopathic PD (PD controls). Clinical diagnoses in the Amish were clinically definite PD in four, clinically probable in one, clinically possible in five, and normal in one. Abnormal [^{18}F]FDOPA posterior putamen uptake was defined as less than three standard deviations below the normal mean. The criteria were applied to the Amish sample to determine a PET endophenotype for each. We performed genetic simulations using SLINK to model the effect phenoconversion with the PET endophenotype had on logarithm of odds (LOD) scores. PET endophenotype confirmed the status of two clinically definite subjects. Two clinically definite Amish PD subjects had normal PETs. Two possible PD were converted to "PET definite PD". The remainder had normal PETs. The average maximum LOD score with the pre-PET was 6.14±0.84. Simulating phenoconversion of subjects with unknown phenotypes increased the LOD score to 7.36±1.23. The [^{18}F]FDOPA PET endophenotype permits phenoconversion in multi-incident PD families and may increase LOD score accuracy and power of an informative pedigree.

Keywords

Parkinson's disease; Positron Emission Tomography; Linkage; Endophenotype; Amish

Correspondence and reprint requests: Brad A. Racette, M.D. Washington University School of Medicine 660 South Euclid Ave., Box 8111 St. Louis, MO 63110 Telephone-(314)362-6908 Fax-(314)362-0168 email-racetteb@neuro.wustl.edu.

NIH-PA Author Manuscript
NIH-PA Author Manuscript
NIH-PA Author Manuscript

NIH-PA Author Manuscript

NIH-PA Author Manuscript

NIH-PA Author Manuscript

Introduction

The discovery of α-synuclein,(Polymeropoulos et al. 1997) parkin,(Kitada et al. 1998) ubiquitin carboxyterminal hydrolase L1,(Leroy et al. 1998) DJ-1,(Bonifati et al. 2003) genes has provided new insights into the pathophysiology of PD. However, it is not entirely clear what role these genes play in sporadic PD. The search for genetic factors that contribute to late onset neurodegenerative disorders is confounded substantially by age dependent penetrance. Misclassification can falsely increase or decrease LOD scores and can occur due to phenocopies (sporadic cases thought to be genetic) or young age at time of clinical assessment. Age of onset has substantial variability in identical twins with PD.(Dickson et al. 2001) Phenocopies and age dependent penetrance likely confound the search for risk factor genes for PD. Theoretically, identification of a narrow phenotype may reduce the rate of phenocopies, although young onset PD due to parkin can be indistinguishable from sporadic young onset PD.

Neuroimaging biomarkers such as [^{18}F]FDOPA PET may be more sensitive than clinical examination for identification of defects in nigrostriatal pathways associated with PD(Heiss and Hilker 2004) and help identify affected individuals, especially in this age-dependent disease. Previous studies demonstrate that [^{18}F]DOPA PET may detect a nigrostriatal defect several years prior to the onset of clinical manifestations in PD(Brooks 1991) or subclinical lesions in monkeys.(Guttman et al. 1988) We hypothesize that [^{18}F]DOPA PET may provide an endophenotype that will increase the power and accuracy of genetic linkage studies. Patients with PD have reduced [^{18}F]FDOPA uptake in the striatum, especially in posterior putamen, that correlates with loss of neurons in the substantia nigra pars compacta. (Morrish et al. 1996;Morrish et al. 1998) We now use PET-based criteria to segregate research subjects by abnormal, normal or uncertain nigrostriatal neuronal integrity and define this as an endophenotype for PD.

Methods

This study was approved by the Washington University School of Medicine Human Studies Committee and the Radioactive Drug Research Committee.

Subjects

We studied three groups of subjects: people of Amish decent, non-Amish normal controls, and non-Amish people with clinically definite idiopathic PD. Amish subjects were participants in a genetic study of PD.(Racette et al. 2002) Amish subjects' ages ranged from 43-81; seven were men and four were women. They were ascertained by initially contacting (with their permission) relatives of the proband or by identifying subjects with known PD through community volunteers Recruiting from all communities was by word of mouth, local print media, regional Amish weekly newspapers, and through the national Amish newspaper *The Budget*. The pedigree was constructed with the program Cyrillic 2.1(Cherwell Scientific) using family books obtained from subjects and Amish libraries. All known PD genes or loci have been excluded in this pedigree by either direct sequencing of the gene or linkage analysis of markers flanking the known loci.

We obtained relevant PD history with a validated and weighted questionnaire(Duarte et al. 1995) and performed a neurologic examination including a Unified Parkinson's Disease Rating Scale(Fahn et al. 1987) (UPDRS) motor subsection 3 and Mini-Mental State examination (in English)(Folstein et al. 1975) on each subject. Based upon neurological examination, we classify individuals as clinically possible, probable, or definite PD using previously reported criteria.(Racette et al. 1999)

NIH-PA Author Manuscript

NIH-PA Author Manuscript

NIH-PA Author Manuscript

A movement disorders specialist blinded to the subjects' clinical history performed the repeat UPDRS3 examination at the time of the [^{18}F]FDOPA PET studies. Inter-rater reliability between the initial examiner and the repeat examiner was determined by rating a video tape on a group of ten PD subjects followed in the Movement Disorders Center. The intra-class correlation for the total UPDRS3 (without rigidity) was 0.70.

Controls Subjects

We studied 10 male and 14 female non-Amish normal controls. Sixteen of them were age-matched within two years to the Amish (mean age: 58 years old (range: 40-65)). Controls were unrelated, PD patient spouses/caregivers and had normal neurologic examinations. We also studied 48 non-Amish people (mean age: 60 years old (range: 38-80); 29 males and 19 females) with clinically definite PD (as defined above). These people had no neurological abnormality beyond PD.

[^{18}F]FDOPA PET Studies

All PD medications were held for twelve hours prior to the study (when relevant). Subject preparation and PET scans were collected, reconstructed to about 6 mm FWHM, and aligned as previously described (Racette et al. 2001) using a Siemens/CTI 953B scanner in 3D-mode.(Spinks et al. 1993)

A reviewer blinded to the clinical status of the subject outlined an occipital region as well as the entire caudate, anterior and posterior putamen on each side of a magnetic resonance image (3D MPRAGE) for each subject. This MR image was co-registered to the [^{18}F]FDOPA PET image using a validated method.(Black et al. 2001) and this transformation matrix was used to resample the MR-identified regions of interest.

Decay-corrected regional tissue-activity PET measurements were extracted from the dynamic series of PET images, and an influx constant K_i was calculated with the occipital region as the input using data from 24 to 94 minutes after injection(Patlak et al. 1983;Logan et al. 1987)

An Amish subject or non-Amish PD control subject was considered to have an abnormal [^{18}F]FDOPA PET if the K_i for the one of the posterior putamen was more than three standard deviations below the normal mean.

Genetic simulations

Simulated linkage studies were performed with the program SLINK.(Terwilliger et al. 1993) We assumed a rare autosomal recessive, age-dependent penetrant disease locus with a disease gene frequency of 0.0001 based upon the observed population prevalence in this community. The following penetrances were used based upon subjects' age at time of clinical evaluation: 0% ages <35; 10% ages 35-40; 25% ages 41-60; 50% ages 61+. We assumed a marker locus with five equally frequent alleles (gene frequency 0.2). Due to program constraints, we cut all inbreeding loops by duplicating loop breakers. This method of loop breaking is similar to the automatic loops function in FASTLINK.(Cottingham, Jr. et al. 1993) For each permutation we ran 1000 simulated linkage studies and obtained a minimum, maximum and average LOD score and standard deviation. To determine the power of the pedigree with currently available information, markers were simulated and the phenotypes fixed with the pre-PET clinical diagnostic information. Subjects with possible or probable PD were classified as phenotype unknown. This same analysis was performed with the PET endophenotype fixed (when applicable) to determine the effect of PET on the LOD scores. For the post-PET phenotypes, subjects meeting the PET definition of "PET definite" were converted to affected, subjects with clinically definite PD who were "PET normal"

NIH-PA Author Manuscript

NIH-PA Author Manuscript

NIH-PA Author Manuscript

were converted to unknown, subjects with possible or probable PD who were “PET definite” were converted to affected, and subjects with possible or probable PD who were “PET normal” remained unknown for the simulations. To simulate the change in phenotype by phenoconverting more subjects with the PET endophenotype, we simulated the phenotype of living siblings and children under the same assumptions as above. This simulation run permits the SLINK program to assign diagnoses to unknown subjects and provides a very conservative estimate of the overall power of phenoconversion. We also performed a simulated linkage analysis in which we simulated the PET phenoconversion by individually changing possible or probable PD subjects to PET definite.

Results

The pre-PET diagnosis was normal in one Amish subject, possible PD in five, probable PD in one. The mean interval from initial to repeat exam was 2.7±0.8 years. Table 1.The pedigree from which these subjects were taken is in Figure1. Two of the clinically definite subjects have been followed for over five years for clinical management of their PD and have clear response to levodopa, motor fluctuations, and dyskinesias. The other two clinically definite subjects did not desire treatment and were only seen for research clinical assessments and have not been treated for their parkinsonism. Subject # 8 had asymmetric rest tremor, bradykinesia, and rigidity at the initial visit but the tremor seemed to improve with time. Subject # 10 had asymmetric postural tremor, bradykinesia, and rigidity. On one examination she had asymmetric rest tremor but this was not seen on follow-up examination.

Forty-seven of 48 clinically definite control PD subjects were classified as definite by [^{18}F]FDOPA PET critieria. The one PD control that did not meet these criteria had a 6-month history of unilateral, intermittent resting tremor with slight bradykinesia and rigidity in that limb and a Unified Parkinson Disease Rating Scale motor subscore of 4.5.(Figure 2)

The [^{18}F]FDOPA PET confirmed the status of two clinically definite subjects. Two definite PD subjects had normal PETs. Two clinically possible PD subjects were converted to “PET definite PD”. One probable PD, three possible PD and one normal Amish were classified as PET normal. Table 1

Simulation studies

We modeled the effect of using the PET endophenotype in linkage studies in several ways. Table 2. We first studied the power of the pedigree to detect linkage and obtained an average LOD score of 6.14 reflecting the informativeness of this large, complex pedigree. Phenoconversion of the subjects according to their PET diagnosis resulted in no net change in LOD score due to the conversion of two clinically definite subjects to PET normal and conversion of two clinically possible subjects to PET definite. Next, we simulated phenoconversion in subjects with an unknown phenotype by allowing the SLINK program to simulate phenotypes. This provides a conservative approximation of the additional power gained by performing PET in all available subjects and converting some subjects to normal or definite. The average LOD score for the 1000 simulations increased to 7.36±1.23 with the simulated phenotypes. We also calculated the power of converting individual possible or probable PD subjects to PET definite by performing a simulated linkage analysis after phenoconversion of examined possible or probable subjects. Each additional phenoconverted subject added an average .33 to the LOD score. Table 2.

NIH-PA Author Manuscript

NIH-PA Author Manuscript

NIH-PA Author Manuscript

Discussion

This study demonstrates several important findings. First, "[^{18}F]FDOPA may be used to change an equivocal clinical diagnosis of PD to a PET diagnosis of PD for genetic in linkage studies; however, long term follow-up of these patients will determine the accuracy of this PET endophenotype. Although this pilot, feasibility study of eleven subjects was not powered to produce significant changes in the pedigree's power, there was a substantial improvement in the power when we simulated phenoconverting other subjects with unknown phenotypes. It is possible to identify subjects who may be at higher risk of PD and convert them to PET definite PD for linkage. Our findings are likely a conservative estimate of the true power of the PET endophenotype in this pedigree since program limitations in SLINK do not permit inclusion of inbreeding loops. Therefore, the genetic complexity modeled is substantially greater than the program would accept.

A second important finding of this study is that phenocopies of late onset neurodegenerative disorders like PD can have a substantial impact on the LOD score in a linkage study. We found that serial examinations and treatment of subjects resulted in the most stable diagnosis over time. There was no change in diagnosis for those who were treated and followed serially. We have followed and treated the majority of the PD subjects available in this community but treatment information was not available for the two subjects converted from "clinically definite" to "unknown". We suspect that when longitudinal follow-up and response to chronic treatment information is available, the PET endophenotype will be less important. However, in a cross-sectional study, the PET endophenotype may be critical to avoid misclassifying phenocopies and pre-symptomatic subjects.

We do not know the duration of the pre-symptomatic phase during which there is a detectable nigrostriatal defect on [^{18}F]FDOPA PET. Two imaging studies have attempted to measure the pre-symptomatic phase of PD. One study used [^{18}F]FDOPA to estimate the length of time that patients with PD have preclinical abnormalities of the nigrostriatal system prior to the development of clinical symptoms to be 5.2 - 6.5 years.(Morrish et al. 1998) These investigators measured longitudinal [^{18}F]FDOPA uptake and extrapolated backwards from the change in the two PETs in the PD patients to estimate the time that damage to the nigrostriatal system began. Another study used PET and fluorodeoxyglucose (FDG) PET and a completely different method of data analysis to estimate the preclinical period as 4.5 years before symptoms.(Moeller and Eidelberg 1997) However, neither of these studies claim to identify how early one might be able to identify such a preclinical defect.

[^{18}F]FDOPA PET primarily reflects decarboxylase activity(Martin and Perlmutter 1994) and represents just one of several types of PET tracers that can be used to assess integrity of nigrostriatal neurons. Some label presynaptic dopamine transporters, like [^{11}C]CFT(Wullner et al. 1994) or the SPECT tracer beta-CIT, whereas others reflect vesicular monoamine transporter type 2 (VMAT2) sites that occur on presynaptic vesicles that store dopamine for subsequent release.(Marek et al. 2001) VMAT2 sites on presynaptic vesicles are less likely to be regulated than either decarboxylase or DAT(DaSilva et al. 1993;Chan et al. 1999;Lee et al. 2000;Frey et al. 2001). However, it is possible one of these other tracers may be more sensitive for detection of asymptomatic nigrostriatal defects.

Given these caveats, it is certainly possible that we could misclassify subjects who might develop PD in another decade but we believe that the added accuracy of the [^{18}F]FDOPA PET endophenotype may prove to be critical for finding risk factor PD genes in older onset PD pedigrees. Although we anticipate that the [^{18}F]FDOPA PET endophenotype will

NIH-PA Author Manuscript

NIH-PA Author Manuscript

NIH-PA Author Manuscript

facilitate detection of pre-symptomatic PD, the [^{18}F]FDOPA uptake is also age dependent and will likely misclassify younger “at-risk” subjects.

Although the two clinically definite subjects were changed to PET normal, we do not necessarily know the correct clinical diagnosis. In our computer modeling we used the PET diagnosis as a definitive diagnostic procedure; however, there is no consensus on how to categorize parkinsonian subjects with normal [^{18}F]FDOPA or other ligand uptake.(The Parkinson’s Study Group 2004) For the purposes of genetic linkage studies, however, selecting a more homogeneous phenotype (clinical PD with reduced [^{18}F]FDOPA uptake) may increase the likelihood of detecting linkage. Phenocopies have been seen in two longitudinal PD dopamine agonist trials.(Rascol et al. 2000;Parkinson Study Group 2000) Although one study excluded subjects from analysis,(Whone et al. 2003) there is no published data on the longitudinal follow-up of these subjects to guide data analysis. We chose a conservative strategy in our simulation studies of converting those subjects’ diagnoses to PET normal. In fact, these two subjects had persistent UPDRS3 scores performed over time by two movement disorders specialists and cannot be considered “normal”. Since the sensitivity of biomarkers like [^{18}F]FDOPA PET, B-CIT SPECT, and other markers is unknown, only longitudinal clinical and imaging studies of subjects undergoing PET including pathologic study can clarify this issue.

Acknowledgments

This work was supported by NIH grants K23NS43351, NS41509, NS39913, NS041771 the Greater St. Louis Chapter of the American Parkinson Disease Association, the Jack Buck Fund, and the Elliot H. Stein Fund, the Ruth Kopolow Fund.

Reference List

Black KJ, Snyder AZ, Koller JM, Gado MH, Perlmutter JS. Template images for nonhuman primate neuroimaging. 1. Baboon. Neuroimage. 2001; 14:736–743. [PubMed: 11506545]

Bonifati V, Rizzu P, van Baren MJ, Schaap O, Breedveld GJ, Krieger E, Dekker MC, Squitieri F, Ibanez P, Joosse M, van Dongen JW, Vanacore N, van Swieten JC, Brice A, Meco G, van Duijn CM, Oostra BA, Heutink P. Mutations in the DJ-1 gene associated with autosomal recessive early-onset parkinsonism. Science. 2003; 299:256–259. [PubMed: 12446870]

Brooks DJ. Detection of preclinical Parkinson’s disease with PET. Geriatrics. 1991; 46:25–30. [PubMed: 1909983]

Chan GL, Holden JE, Stoessl AJ, Samii A, Doudet DJ, Dobko T, Morrison KS, Adam M, Schulzer M, Calne DB, Ruth TJ. Reproducibility studies with 11C-DTBZ, a monoamine vesicular transporter inhibitor in healthy human subjects. J Nucl Med. 1999; 40:283–289. [PubMed: 10025836]

Cottingham RW Jr. Idury RM, Schaffer AA. Faster sequential genetic linkage computations. Am J Hum Genet. 1993; 53:252–263. [PubMed: 8317490]

DaSilva JN, Kilbourn MR, Mangner TJ, Toorongian SA. Synthesis of [^{11}C]methoxy derivative of α-dihydrotetrabenazine for PET imaging of monoaminergic nerve terminals. J Lab Comp Radiopharm. 1993; 32:257–259.

Dickson D, Farrer M, Lincoln S, Mason RP, Zimmerman TR Jr. Golbe LI, Hardy J. Pathology of PD in monozygotic twins with a 20-year discordance interval. Neurology. 2001; 56:981–982. [PubMed: 11294946]

Duarte J, Claveria LE, de Pedro-Cuesta J, Sempere AP, Coria F, Calne DB. Screening Parkinson’s disease: a validated questionnaire of high specificity and sensitivity. Mov Disord. 1995; 10:643–649. [PubMed: 8552118]

Fahn, S.; Elton, RL.; Members of the UPDRS Development Committee. Unified Parkinson’s disease rating scale. In: Fahn, S.; Marsden, CD.; Goldstein, M.; Calne, DB., editors. Recent developments in Parkinson’s disease. Macmillan; New York: 1987. p. 153-163.

NIH-PA Author Manuscript

NIH-PA Author Manuscript

NIH-PA Author Manuscript

Folstein MF, Folstein SE, McHugh PR. “Mini-mental state”: a practical method for grading the cognitive state of patients for the clinician. J Psychiatr Res. 1975; 12:189–198. [PubMed: 1202204]

Frey KA, Koeppe RA, Kilbourn MR. Imaging the vesicular monoamine transporter. Adv Neurol. 2001; 86:237–247. [PubMed: 11553983]

Guttman M, Yong VW, Kim SU, Calne DB, Martin WR, Adam MJ, Ruth TJ. Asymptomatic striatal dopamine depletion: PET scans in unilateral MPTP monkeys. Synapse. 1988; 2:469–473. [PubMed: 3263709]

Heiss WD, Hilker R. The sensitivity of 18-fluorodopa positron emission tomography and magnetic resonance imaging in Parkinson’s disease. Eur J Neurol. 2004; 11:5–12. [PubMed: 14692881]

Kitada T, Asakawa S, Hattori N, Matsumine H, Yamamura Y, Minoshima S, Yokochi M, Mizuno Y, Shimizu N. Mutations in the parkin gene cause autosomal recessive juvenile parkinsonism. Nature. 1998; 392:605–608. [PubMed: 9560156]

Lee CS, Samii A, Sossi V, Ruth TJ, Schulzer M, Holden JE, Wudel J, Pal PK, Fuente-Fernandez R, Calne DB, Stoessl AJ. In vivo positron emission tomographic evidence for compensatory changes in presynaptic dopaminergic nerve terminals in Parkinson’s disease. Ann Neurol. 2000; 47:493–503. [PubMed: 10762161]

Leroy E, Boyer R, Auburger G, Leube B, Ulm G, Mezey E, Harta G, Brownstein MJ, Jonnalagada S, Chernova T, Dehejia A, Lavedan C, Gasser T, Steinbach PJ, Wilkinson KD, Polymeropoulos MH. The ubiquitin pathway in Parkinson’s disease. Nature. 1998; 395:451–452. [PubMed: 9774100]

Logan J, Wolf AP, Shiue C-Y, Fowler JS. Kinetic modeling of receptor-ligand binding applied to positron emission tomographic studies with neuroleptic tracers. J Neurochem. 1987; 48:73–83. [PubMed: 2432176]

Marek K, Innis R, van Dyck C, Fussell B, Early M, Eberly S, Oakes D, Seibyl J. [123I]beta-CIT SPECT imaging assessment of the rate of Parkinson’s disease progression. Neurology. 2001; 57:2089–2094. [PubMed: 11739831]

Martin WRW, Perlmutter JS. Assessment of fetal tissue transplantation in Parkinson’s disease: does PET play a role? Neurology. 1994; 44:1777–1780. [PubMed: 7936219]

Moeller JR, Eidelberg D. Divergent expression of regional metabolic topographies in Parkinson’s disease and normal ageing. Brain. 1997; 120:2197–2206. [PubMed: 9448575]

Morrish PK, Rakshi JS, Bailey DL, Sawle GV, Brooks DJ. Measuring the rate of progression and estimating the preclinical period of Parkinson’s disease with [^{18}F]dopa PET. J Neurol Neurosurg Psychiatry. 1998; 64:314–319. [PubMed: 9527140]

Morrish PK, Sawle GV, Brooks DJ. An [18F]dopa-PET and clinical study of the rate of the progresssion in Parkinson’s disease. Brain. 1996; 119:585–591. [PubMed: 8800950]

Parkinson Study Group. Pramipexole vs levodopa as initial treatment for Parkinson disease: A randomized controlled trial. J Am Med Assoc. 2000; 284:1931–1938.

Patlak CS, Blasberg RG, Fenstermacher JD. Graphical evaluation of blood-to-brain transfer constants from multiple-time uptake data. J Cereb Blood Flow Metab. 1983; 3:1–7. [PubMed: 6822610]

Polymeropoulos M, Lavedan C, Leroy E, Ide SE, Dehejia A, Dutra A, Pike B, Root H, Rubenstein J, Boyer R, Stenroos ES, Chandrasekharappa S, Athanassiadou A, Papapetropoulos T, Johnson WG, Lazzarini AM, Duvoisin RC, Di Iorio G, Golbe LI, Nussbaum RL. Mutation in the alpha-synuclein gene identified in families with Parkinson’s disease. Science. 1997; 27:2045–2047. [PubMed: 9197268]

Racette BA, McGee-Minnich L, Moerlein SM, Mink JW, Videen TO, Perlmutter JS. Welding-related parkinsonism: clinical features, treatment, and pathophysiology. Neurology. 2001; 56:8–13. [PubMed: 11148228]

Racette BA, Rundle M, Parsian A, Perlmutter JS. Evaluation of a screening questionnaire for genetic studies of Parkinson’s disease. Am J Med Genet. 1999; 88:539–543. [PubMed: 10490713]

Racette BA, Rundle M, Wang JC, Goate A, Saccone NL, Farrer M, Lincoln S, Hussey J, Smemo S, Lin J, Suarez B, Parsian A, Perlmutter JS. A multi-incident, Old-Order Amish family with PD. Neurology. 2002; 58:568–574. [PubMed: 11865134]

NIH-PA Author Manuscript

NIH-PA Author Manuscript

NIH-PA Author Manuscript

Rascol O, Brooks DJ, Korczyn AD, De Deyn PP, Clark CE, Lang AE. A five-year study of the incidence of dyskiensias in patients with early Parkinson's disease who were treated with ropinirole or levodopa. New Engl J Med. 2000; 18:1491.

Spinks TJ, Jones T, Bailey DL, Townsend DW, Grootoonk S, Bloomfield PM, Gilardi M-C, Casey ME, Sipe B, Reed J. Physical performance of a positron tomograph for brain imaging with retractable septa. Phys Med Biol. 1993; 37:1637–1655. [PubMed: 1518905]

Terwilliger JD, Speer M, Ott J. Chromosome-based method for rapid computer simulation in human genetic linkage analysis. Genet Epidemiol. 1993; 10:217–224. [PubMed: 8224802]

The Parkinson's Study Group. Levodopa and the Progression of Parkinson's Disease. New Engl J Med. 2004; 351:2498–2508. [PubMed: 15590952]

Whone AL, Watts RL, Stoessl AJ, Davis M, Reske S, Nahmias C, Lang AE, Rascol O, Ribeiro MJ, Remy P, Poewe WH, Hauser RA, Brooks DJ. Slower progression of Parkinson's disease with ropinirole versus levodopa: The REAL-PET study. Ann Neurol. 2003; 54:93–101. [PubMed: 12838524]

Wullner U, Pakzaban P, Brownell AL, Hantraye P, Burns L, Shoup T, Elmaleh D, Petto AJ, Spealman RD, Brownell GL. Dopamine terminal loss and onset of motor symptoms in MPTP-treated monkeys: a positron emission tomography study with 11CCFT. Exp Neurol. 1994; 126:305–309. [PubMed: 7925829]

NIH-PA Author Manuscript

NIH-PA Author Manuscript

NIH-PA Author Manuscript

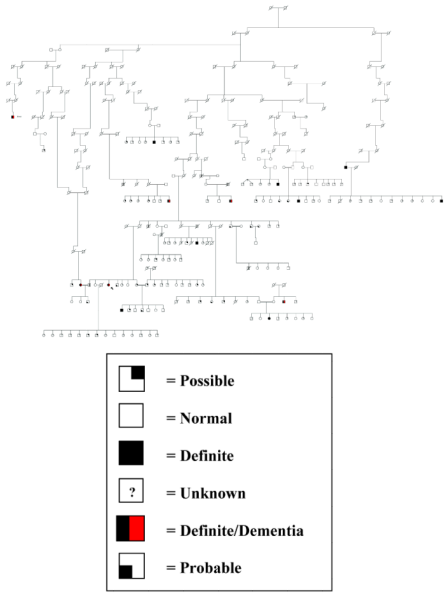


Figure 1.
Amish pedigree demonstrating multiple affected subjects and inbreeding.

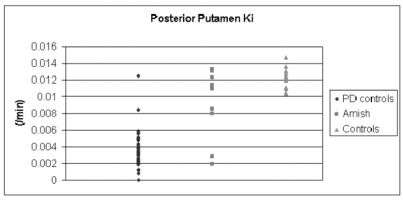


Figure 2.
[18F]FDOPA PET Ki in control subjects and Amish, Forty-seven of 48 PD controls and four Amish met the PET criteria for PD of Ki for one of the posterior putamen more than three standard deviations below the normal mean.

NIH-PA Author Manuscript
NIH-PA Author Manuscript
NIH-PA Author Manuscript

NIH-PA Author Manuscript NIH-PA Author Manuscript NIH-PA Author Manuscript

Table 1

Demographic and Clinical Features of Amish Subjects

Subject	Age*	Gender	Initial UPDRS3	Followup UPDRS3	UPDRS3 Interval (years)	Clinical Diagnosis	Other Neurological Clinical Diagnoses	PET Diagnosis
1	71	M	33.50	43.00	2.85	Definite		Definite
2	70	M	3.00	5.50	0.68	Possible	Essential Tremor	Normal
3	52	M	3.00	2.00	3.02	Possible		Definite
4	72	M	40.00	44.00	3.10	Definite		Definite
5	52	F	11.00	20.50	3.10	Normal	Post-poliomyelitis	Normal
6	81	F	2.00	3.00	2.79	Possible	Essential Tremor/dystonia	Normal
7	43	M	4.00	19.50	3.02	Possible	Essential Tremor	Definite
8	69	M	18.50	22.00	3.23	Definite		Normal
9	73	M	7.00	9.00	1.76	Possible		Normal
10	48	F	13.50	9.00	3.25	Definite		Normal
11	67	F	8.00	5.00	3.25	Probable		Normal

*Age at time of PET scan

NIH-PA Author Manuscript
NIH-PA Author Manuscript
NIH-PA Author Manuscript

Table 2

Phenotype and Genotype Simulations with and without [^{18}F]FDOPA PETEndophenotype

Pedigree	Minimum LOD score	Maximum LOD score	Average LODscore	Standard Deviation
Current Pedigree	2.99	8.25	6.14	0.84
Simulated phenoconversion: 1 possible PD→PET definite	3.23	9.04	6.35	0.85
Simulated phenoconversion: 2 possible PD→PET definite	2.90	9.23	6.82	0.92
Simulated phenoconversion: 2 possible PD→PET definite	3.30	9.78	7.06	1.03

Author Manuscript

Author Manuscript

Author Manuscript

Author Manuscript

HHS Public Access

Author manuscript

Gene Ther. Author manuscript; available in PMC 2016 May 18.

Published in final edited form as:

Gene Ther. 2016 January ; 23(1): 1–9. doi:10.1038/gt.2015.81.

Noninvasive Tracking of Gene Transcript and Neuroprotection after Gene Therapy

Jiaqian Ren[1], **Y. Iris Chen**[1], **Christina H. Liu**[1], **Po-Chih Chen**[2], **Howard Prentice**[2], **Jang-Yen Wu**[2], and **Philip K. Liu**[1,*]

[1]Athinoula A. Martinos Center for Biomedical Imaging, Department of Radiology, Massachusetts General Hospital and the Harvard Medical School, Charlestown, MA

[2]Department of Biomedical Science, Charles E. Schmidt College of Medicine, Florida Atlantic University, Boca Raton, FL

Abstract

Gene therapy holds exceptional potential for translational medicine by improving the products of defective genes in diseases and/or providing necessary biologics from endogenous sources during recovery processes. However, validating methods for the delivery, distribution and expression of the exogenous genes from such therapy can generally not be applicable to monitor effects over the long term because they are invasive. We report here that human granulocyte colony-stimulating factor (hG-CSF) cDNA encoded in scAAV-type 2 adeno-associated virus, as delivered through eye drops at multiple time points after cerebral ischemia using bilateral carotid occlusion for 60 min (BCAO-60) led to significant reduction in mortality rates, cerebral atrophy, and neurological deficits in C57black6 mice. Most importantly, we validated hG-CSF cDNA expression using translatable magnetic resonance imaging (MRI) in living brains. This noninvasive approach for monitoring exogenous gene expression in the brains has potential for great impact in the area of experimental gene therapy in animal models of heart attack, stroke, Alzheimer's dementia, Parkinson's disorder and amyotrophic lateral sclerosis, and the translation of such techniques to emergency medicine.

Keywords

biologic; cardiac arrest; forebrain ischemia; G-CSF; hypothermia; neurogenesis; targeted- delivery

Introduction

Alzheimer's dementia (AD), an age and genetic-related disorder, affects 4.5 million Americans. The risk to develop AD and stroke can be associated in elderly people[1], and a common pathway (p25.cdk5) leads to elevated production of amyloid protein beta in

Users may view, print, copy, and download text and data-mine the content in such documents, for the purposes of academic research, subject always to the full Conditions of use:http://www.nature.com/authors/editorial_policies/license.html#terms

*Address correspondence to: Philip K. Liu, Ph.D., CNY149 13th Street, Charlestown, MA 02129-2020, ; Email: philipl@nmr.mgh.harvard.edu, (617) 724-4563

Conflict of Interests: The authors declare no competing financial interests.

Author Manuscript Author Manuscript Author Manuscript Author Manuscript

individuals with stroke and AD[2]. The granulocyte-colony stimulating factor (G-CSF) in patients diagnosed with AD is found to be significantly lower than age-matched people[3]. G-CSF is a cytokine that stimulates growth and differentiation of myeloid precursors[4]. The expression of G-CSF and its receptor in the microvessels of the CNS suggests that G-CSF provides autocrine neuroprotection in response to brain damage[5]. In pre-clinical tests, G-CSF has been shown to pass through the blood-brain barrier by receptor-mediated endocytosis, leading to a reduction in infarct volume in rat models of acute stroke[6]; G-CSF reduces the level of beta amyloid deposited in excess in the brain and reverses memory impairment in mice genetically altered to develop AD[7]. In addition, studies in different animal models of stroke, Parkinson's disease, and other neurodegenerative disorders have specifically demonstrated that G-CSF may protect neurons, increase blood vessel growth, and improve motor function[8–10]. A phase IIb trial has also tested the safety of G-CSF[11]. On the other hand, a recent clinical study demonstrated that direct injection of exogenous G-CSF protein to the vasculature of 328 acute stroke patients showed a trend to reduce infarct growth, but did not reduce mortality, infarct size or neurological score[12]. The discrepancies between clinical and preclinical responses can partially arise from different approaches used to validate the delivery of exogenous biologics and examine the molecular basis of their therapeutic effects are primarily histology based. These histological methods have limited benefit because they rely on the use of invasive tissue sampling and, because they involve the removal of the very tissue we wish to protect, preclude long-term monitoring. To overcome these limitations we need to re-evaluate the responses using a noninvasive approach to monitor the delivery, expression of exogenous G-CSF genes and its efficacies in the central nervous system of living conditions[1314].

We tested the hypothesis that a neuroprotective biologic encoded in the cDNA carried by a viral vector could be delivered at multiple time points using eye drops to forebrain ischemia model using BCAO-60 in C57blcak6 mice[14–16]. BCAO-60 does not induce significant infarct, although DNA and brain damage can be repaired[17]. By encoding human G-CSF (hG-CSF) in a replication-deficient, self-complementary adeno-associated virus (AAV) vector (scAAV2-CMV-hG-CSF) it may be possible to elicit a continuous supply of endogenous G-CSF[18]. The use of the AAV2 vector, with optimally selected serotype, has proved highly valuable for efficient transduction in the CNS, and for rapid initiation of expression[19]. For example, AAV2 vectors carrying exogenous genes have been employed to examine transduction in brain tissue in vivo in models of AD, amyotrophic lateral sclerosis and Parkinson's disease[16,20,21].

Most significantly, we have developed two noninvasive measurements as alternatives to invasive biopsy procedures. First, we developed MR contrast agents (MR-CAs) to target unique mRNA expression of hG-CSF cDNA in the brains of living mice without biopsy. Second, we established and validated measurements to noninvasively monitor neuroprotection after gene therapy, so that these responses are consistent with hypothermia treatment (34°C, whole-body) during cerebral ischemia, a therapeutic method that has been shown to reduce brain injury after cardiac arrest and traumatic brain injury[22–24]. We demonstrate this approach as an alternative to destructive sampling methods. Such assays would allow long-term monitoring of neuroprotection and continuous expression of exogenous cDNA, as gene therapy becomes translatable to clinical applications. This

Author Manuscript Author Manuscript Author Manuscript Author Manuscript

monitoring system will be central to evaluating the therapeutic efficacy of exogenous cDNA in the CNS.

Results

We first characterized noninvasive measurements of cerebral damage in C57black6 mice. In C57black6 mice, BCAO-60 induces global oxidative stress, DNA damage, apoptosis, but very limited infarction in the brain[14,15,25,26]. Figure 1*a* shows the protocol used for BCAO induction and longitudinal monitoring. This cerebral ischemia model is associated with severe weight loss (Fig. 2) and a mortality rate of 75 ± 10% within the first week. In common with other animal models of cardiac arrest or stroke[27–29], we have reported that BCAO-60 induces regional abnormal water movement (edema), as evidenced by enhanced diffusion-weighted imaging (hDWI), within the first two days (Fig 1*b1*); the regions with hDWI were localized in the forebrain and midbrain (Fig. 3). To overcome the lack of measurable infarct in this BCAO model, we translated the increased hDWI to the reduced apparent diffusion coefficient (rADC), and we quantitatively measured the regions with significant rADC in the brain before and one day after BCAO-60 (Fig 1*b2*). We found VMD is characteristically bi-phasic with a second peak appearing at >10 hours, and the second peak became stable at one to 2 days with pseudo normalization toward the values before cerebral ischemia in the striatum (Fig. 4). We measured DWI and VDM thereafter at one day after BCAO-60 (Fig 3). Without effective treatment, the brains would develop cerebral atrophy and eventual ventriculomegaly by the 4th week (Fig 1*c1*). Indeed, we found that lateral ventricular size (LVS) increased to 4.3% post BCAO-60 significantly ($p = 0.01$, Student *t* test, one tail) from 2.1% in sham-operated mice (Fig. 1*c2*); atrophy measured at 4 weeks and beyond positively correlated with the estimated VMD at one day in living mice post BCAO-60, with a linear coefficient of 0.71.

Unlike mice with brain damage, when normal animals encounter a corner they typically rear forward and upward, then turn back, in either direction, to face away from the corner and toward the open end of the setup (the corner test)[30,31]. We measured the rate of turns when normal mice faced a 30° corner (i.e., turning to either the left or right) to have a rate of 50 ± 8% (symmetric and no bias) before BCAO-60. Mice were measured weekly for at least four weeks after the BCAO-60 procedure (Fig 1*d*). We observed a significant increase in asymmetric turning (~90% to one side) in BCAO-60 mice.

To validate ventriculomegaly and corner tests as robust indicators of the severity of brain damage and treatment responses, we randomly treated a group of the BCAO-60 mice with whole-body hypothermia, whereby the animals were placed on ice immediately after vessel occlusion and returned to room temperature when rectal body temperature measured 34°C during the 60-minute procedure (hypothermia group). Hypothermia treatment was found to significantly improve survival, from 25 ± 10% to 100%, in this group. We found hypothermia significantly reduced lesions and cerebral atrophy in the striatum and cortex (Fig. 1*e* & 1*f*). Furthermore, we found that this neuroprotection involved a reduction in the expression of MMP-9 (Fig. 1*g1* & 1*g2*). Hypothermia therapy was also associated with a significant reduction in asymmetric turning, from 0.9 to 0.58 ($p<0.05$), a rate not significantly different from that seen in the sham operation group; these results were

Author Manuscript Author Manuscript Author Manuscript Author Manuscript

consistent throughout the 4 weeks of weekly tests following BCAO (Fig. 1*d*). Our data thus demonstrated that ventriculomegaly and performance in the corner test served as accurate indicators of the severity of brain damage in this BCAO model.

Genes carried by an AAV vector are delivered as one single-bolus dose in most gene therapies. To evaluate gene therapy using eye drop delivery, we administered a single dose of scAAV2-CMV-hG-CSF (3×10^9 pfu; 1.5 μl to the conjunctival sac of the left eye) at 0.5 (n = 9), 1, 2, 3, 4, or 24 hours (n = 3, each group) after the release of BCAO. Survival rate varied depending on the time of eye drop administration (i.e., 78% for the 0.5 hr group, 66% for the 1 and 3 hr groups, 33% for the 4 hr group and 100% for the 2 and 24 hr groups), but in each instance it was greater than the ~25% survival seen in the group treated with scAAV2-CMV-GFP similarly administered (placebo, n = 15). Moreover, there was no significant reduction in ventriculomegaly compared to the group received scAAV2-CMV-GFP (Fig 5*a*).

When we applied additional scAAV2-CMV-hG-CSF at 0.5 hr, 1, 7 and 14 days after BCAO-60 (n = 7), we observed an exceptionally high survival rate of 100%, compared to ~25% in the BCAO-60 without treatment group (n = 22). The optimal window for multiple scAAV2-CMV-hG-CSF treatments after BCAO coincides with the development of bi-phasic VMD (Fig 4). More importantly, we found that multiple doses of scAAV2-CMV-hG-CSF significantly reduced cerebral atrophy (Fig. 5*a*). Gene therapies with hG-CSF cDNA ameliorated asymmetric turning in the corner test, from 0.9 in the placebo mice (BCAO with scAAV2-CMV-GFP, placebo group) to 0.67 ± 0.1 (Student *t* test, p=0.03, one tail, n ≥ 5 each group), a result not significantly different from that measured before BCAO, i.e., 0.50 ± 0.08. We did not compare the corner tests in single dose groups because variable surviving mice.

To demonstrate positive hG-CSF mRNA expression in vivo, we designed a phosphorothioate-modified oligo DNA with antisense sequence (AS) hG-CSF and Cy3 label (sODN-AS-hG-CSF-Cy3). After transfecting PC-12 cells with scAAV2-CMV-hG-CSF or scAAV2-CMV-GFP DNA we found PC-12 cells expressed exogenous hG-CSF mRNA 6 hours after transfecting using real-time cell imaging for Cy3 or DNA-free RT-PCR (Fig. 6*a* & 6*c*); no hG-SCF mRNA expression was found in the placebo group at any of the time points tested (Fig. 6*b*–6*c*). We successfully showed that secondary GFP^+ transfectants using DNA extracted from primary transfectants of the placebo group exhibit real-time expression of GFP (Fig. 6d & 6e); these data supported a stable scAAV2 vector and its cDNA after gene therapy. Moreover, these data indicate that the sequence in the sODN-AS-hG-CSF-Cy3 will distinguish hG-CSF mRNA from the endogenous rodent mRNA.

We found that hG-CSF mRNA expression was clearly represented as unique ROIs in the R2* map when SPION-AS-hG-CSF and MRI were acquired 3 to 4 weeks after BCAO (arrows, Fig. 5*b1*). However, we observed some enhanced ROIs in the placebo group (Fig. 5*b2*); such noise was mainly near the injured site surrounding the ventricle with ventriculomegaly (asterisk). We used data from target-guided MRI to obtain tissue sample and validated hG-CSF antigen expression to be localized in the non-astroglial population (Fig. 5*c*); the expression of hG-CSF in the placebo group was negligible (Fig 5*d*). We showed that NeuN expressed in most small blood vessels in mice treated with scAAV2-

Author Manuscript Author Manuscript Author Manuscript Author Manuscript

CMV-hG-CSF (arrow, Figure 5*e*); in the control groups (no virus treatment or placebo) the expression of NeuN was found mostly in the nucleus.

To demonstrate the route of scAAV2-CMV-hGCSF or -GFP distribution after eye drop administration, we applied non-targeting Gd-DTPA to the right conjunctival sac (n = 4). Compared to pre-existing signal in fatty tissue (Fig 5f), we noticed a conspicuous elevation of R1 signal in the ipsilateral bulbar and palpebral conjunctiva (ROI near the lens, as denoted by the asterisk) as well as in the naso-lacrimal canal (arrow) 5–10 minutes after application (center panel, Fig 5*f*); enhanced MR-CA distribution becomes apparent in the naso-lacrimal canal on the contralateral side at 30 minutes. We found no MR-CA in the lens and cornea (asterisk), regions where lymphatics are lacking. We then tested the route of distribution after eye drop application in mice (n =3, 14 days after BCAO-60) using targeting Gd-NA-nestin (1 μg Gd-DTPA in 2 μl). This targeting MR-CA binds to nestin mRNA of pericytes in the neovasculature when intraperitoneally injected to mice after BCAO-60[14,15]; we acquired longitudinal MRI (Figs 5g1–5g4). Figure 5g shows enhanced R1 signal in the brain three hours after eye drop application (asterisks, Fig 5g1 vs. Fig 5g3); in addition, we noticed R1 signal in the brain (asterisks) and retina (arrows) where the blood-retina barrier in the choroid might become permeable to MR-CA following BCAO-60. The data we have acquired support the hypothesis that viral vectors for treatment of BCAO-induced brain injuries can be distributed via the orbital lymphatics after delivery through eye drops applied to the conjunctival sac.

Discussion

To the best of our knowledge in the area of theragnostics using gene therapy, this study is the first of its kind to demonstrate effective noninvasive delivery of hG-CSF cDNA in scAAV-type 2 adeno-associated virus via eye drops, and to examine hG-CSF mRNA expression from neural cells in living mouse brains without biopsy. Furthermore, this study is distinct in that it tracked the neurological and histological effects of gene therapy for acute cerebral ischemia. Expression of the exogenous hG-CSF cDNA carried by scAAV2-CMV-hG-CSF and delivered through the eye conjunctiva are found to be effective in reversing neurological symptoms (the corner test) and ventriculomegaly in the brain after ischemia. These data lead us to conclude that repeated administration of hG-CSF cDNA in scAAV-type 2 adeno-associated viruses can protect the brain by supplying endogenous biologic of hG-CSF from neural cells during critical time after BCAO-60, leading to reductions in mortality, cerebral atrophy and the neurological deficits associated with ischemia. In mice that undergo brain repair using gene therapy is mediated by the elevation of neural progenitor cells in the small blood vessels. None of the improvements noted above were observed in mice of the placebo group. We validated noninvasive measurements used in our studies by comparing the results after hypothermia treatment. In normal mice, hypothermia may elevate DWI and reduce ADC. However, we measured rADC one day after hypothermia. Even so the rADC by hypothermia in normal micecould inflate lesion estimation based on the threshold ADC and overestimated the VMD in this hypothermia group (Fig 1*g*). Even so, The finding that hypothermia significantly reduces VMD induces less MMP-9 after BCAO-60 is consistent with our previous using MMP-9 gene knockdown in normal temperature[32].

Author Manuscript Author Manuscript Author Manuscript Author Manuscript

Single doses delivered at various time points within the first 24 hours after injury are found to be less effective in reversing brain damage. Our results from a single application of scAAV2-CMV-hG-CSF confirm the less-than-optimal effect of single-dose delivery of murine G-CSF cDNA in scAAV1/2 to the mouse spinal cord[16]. It is also important to note that for our BCAO model there may be a window immediately after release of vessel occlusion during which uptake and distribution of hG-CSF cDNA are variable. The variability in the reduction of ADC most likely represents the change in the severity of hDWI, elevated MMP-9 expression and/or defective BBB. Therefore, the change in rADC at the second peak supports our rationale to deliver multiple doses of hG-CSF cDNA in scAAV-type 2 adeno-associated viruses. Cerebral damage and disturbance of the BBB were demonstrated by variations in the ADC threshold, which was previously established using power analysis in a project involving 52 normal mice that underwent BCAO at normal temperature[32]. The association of brain damage to the location of lesions with below-threshold ADC was supported by MMP-9 expression (Fig 1*h*); this association is validated by studies, from two different investigators, that used a global ischemia model with potassium chloride and resuscitation[27,28].

The damage that occurs in the brain in the first few hours after cerebral ischemia may reflect reperfusion, and thus exhibit as “normalization” toward the baseline ADC, followed by another elevation of VMD in the secondary ADC drop that continues for at least 48 hours. The lower lesion severity between 3 and 7 hours after BCAO may explain the less-than-optimal efficacy of scAAV2-CMV-hG-CSF treatment we observed at 4 hours. Therefore, although a single dose of scAAV2-CMV-hG-CSF on day one was found to improve survival rate, it did not reduce either cell death or neurological deficits. Indeed, repeated applications of scAAV2-CMV-hG-CSF after the initial 4-hour time point ensure continuous supplies of hG-CSF in our studies. Increased blood vessel growth has been demonstrated in mice treated with G-CSF protein by showing greater numbers of bone marrow neural precursor cells in the vessels[33,34], and we demonstrated the same after repeated treatment. This result suggests that hG-CSF must be present during reperfusion and for at least 7 days for edema-related brain damage and neural cell death to be reversed[35].

We propose that the viral vector is transported through the lymphatic fluid (Fig 5*f–g*) to the vena cava, and then through the blood circulation to the brain, reaching the perivascular space by way of the BBB damaged as a result of cerebral ischemia[14,15]. After the viral particles reach the perivascular space, they may be transported across the cell membrane for intracellular expression[36]. Another distribution route of the viral vector can be via the blood-retina barrier, which will need a retina-specific MR-CA for future evaluation.

Our findings support the hypothesis that G-CSF reduces neurological deficits that develop in the first few days after cerebral ischemia. The corner test is one of more than five sensorimotor tests (including forelimb flexion, forelimb placing, accelerated roared and adhesive removal tests) used to assess neurological deficits in rodents. Among these tests, the corner test is regarded as “more sensitive” in detecting deficits than the other tests because it reflects multiple asymmetries, including forelimb, hind limb, postural and turning bias[37]. It has been established for mice affected by focal cerebral ischemia induced by the middle cerebral artery occlusion model; infract volume is correlated with performance on

Author Manuscript Author Manuscript Author Manuscript Author Manuscript

the corner test for chronic behavioral impairments even as many as 90 days after mild focal cerebral ischemia, and whether with or without treatment[23, 38]. We confirmed here that the corner test can be used in BCAO model that does not induce infarcts. We have demonstrated here that gene delivery and resulting protection of the brain can be validated without removing the brain tissue we hope to preserve. Moreover, the ability to deliver therapeutic agents through eye drops may have important implications for emergency medicine, as lyophilized viral particles can be readily reconstituted in saline and administered to cardiac arrest patients.

Materials and Methods

Cell Culture

We examined the delivery and dynamic uptake of pCMV-hG-CSF and pCMV-GFP transfection in PC12 cells (ATCC, CRL-1721) in a miniature incubator chamber (INU-UK-F1; Tokai Hit Inc., Shizuoka, Japan) on the stage of an upright microscope (Olympus, Lebanon, NH, USA), following published procedure[39]. All cell culture studies were repeated by two separated research staffs.

Expression of hG-CSF cDNA

The scAAV2-CMV-GFP plasmid we used in our study was a gift from Dr. D. McCarty (Ohio State University, Columbus, Ohio) to Dr. JYW. hG-CSF 615 bp cDNA (accession number NM 172219.2) was inserted into the scAAV2-CMV-GFP plasmid by substituting hG-CSF for the GFP cDNA sequence. The new plasmid was thus termed scAAV2-CMV-hG-CSF. The scAAV-type 2 adeno-associated viruses, produced (two separate batches) by the Gene Therapy Vector Core of the University of North Carolina (Chapel, Hill, NC), were generously gifted to Massachusetts General Hospital for explicit research use. Viral titers were determined by dot blot analysis. To test gene expression in vivo, vectors were transiently transfected using lipofectin (Invitrogen) into PC12 cells (50 cells per well) at a total concentration of 1 μg/well in a 6-well dish. At 3, 6, 8, or 24 hours (one dish per time point) after transfection with scAAV2-CMV-hG-CSF plasmid or scAAV2-CMV-GFP plasmid PC12 cells were harvested for RNA isolation using RNA-easy (Qiagen) with the addition of RNase-free DNase before reverse transcription. We generated a primer with antisense (AS) sequence (5’-AACTCGGGGGAGATCCCTTCCA, homemade) to hG-CSF mRNA (AS-hG-CSF) and sense sequence (5”ACTCTCTGGGCATCCCCT, S-hG-CSF). A hG-CSF—specific reverse transcription product using primer AS-hG-CSF was generated using reverse transcriptase, PCR amplification and the DNA product was resolved by agarose gel (1%) electrophoresis, as described previously[40]. To analyze the duration of GFP expression following scAAV2-CMV-GFP plasmid transfection, images were collected by time-lapse optical microscopy (Olympus IX83) from living PC12 cells. A cellSens system (Olympus USA) was used to reconstruct the Z stack image from seven photos (Z dimension +8.82 micron with Z spacing = 1.26 microns; exposure time = 661 ms × 4.22 gain).

Animals and Housing

All procedures were approved by the Massachusetts General Hospital Subcommittee on Research Animal Care, in accordance with the Public Health Service Guide for the Care and

Author Manuscript Author Manuscript Author Manuscript Author Manuscript

Use of Laboratory Animals. At least ten adult C57black6 male mice were ordered from Taconic Farm (Germantown, NY) each time (n ≥ 3 litters at a time), 2–3-months of age (23 ± 2 gm bw), were kept in cages in a room with controlled light cycles (12h/12 h light/dark). All animals had free access to water and standard lab chow. We conducted stratification for baseline values (MRI and corner test) to eliminate abnormal anatomical brains or bias corner test before experimentation. Mice were trained, operated on, and tested in a random manner, with a blinded observer performing all behavioral testing. A numeric identifier for each mouse and was given to the examiner; the treatment was revealed at the completion of testing for data analysis.

Bilateral Carotid Artery Occlusion (BCAO) to Induce Cerebral Ischemia

We used the BCAO model, as described, to for long-term examination of the delivery and dynamics of our therapeutic agents[41]. For each BCAO experiment, we randomly selected 6 mice each day and arbitrarily assigned them to one of three groups (sham operation control, BCAO, or BCAO plus treatment, n = 2 each). The control animals underwent surgical procedures identical to BCAO, except that we did not occlude the arteries (n = 4). For all normothermic animals (n = 22), we maintained body temperature at 36 ± 1°C using a heating blanket, and monitored temperature with a rectal thermos-sensor, throughout BCAO. We analyzed the blood flow of the mid-cerebral artery using Doppler in all animals that underwent surgical procedures, positioning the Doppler probes to the skull during BCAO (n = 4 of 20); these mice were not used for further experimentation. We randomly selected animals and placed them on ice immediately after the completion of vessel occlusion; they were immediately removed from the ice when body temperature dropped to 34°C (the hypothermia group, n = 10). The mice were then kept at room temperature for the remainder of the procedure, before release of vessel occlusion. The average body temperature in the hypothermia group was 34 ± 0.5°C. We applied ScAAV2-CMV-hG-CSF, scAAV2-CMV-GFP (3×10^9 pfu), or saline (1.5 μl) to the eye sac of the left eye after release of BCAO, at single (n = 24) or multiple (n = 7) time points, as indicated. By the third day after cerebral ischemia, all of the surviving post-ischemic mice exhibited spontaneous activity in their home cages, were responsive to handling, and engaged in normal self-grooming behavior.

MRI Protocols for Diffusion-Weighted MRI and Gene-Targeting MRI

Diffusion-Weighted MRI was performed in mice before and after BCAO following previously published procedure[32], using a 9.4 Tesla MRI system (Bruker Avance system, Bruker Biospin MRI, Inc., Billerica, MA). *Ventricular* images were acquired using a T2-weighted spin echo sequence (TR/TE=7000/25ms, $120\times120\mu m^2$ in-plane resolution and 20 slices of 0.5mm thickness, RARE factor 8, NA=4) on a 9.4T system. We segmented the ventricles from the tissue using a threshold of two standard deviations (0.3% confidence interval outside of the mean) above the mean signal intensity of the entire brain slice (including the ventricles).

We have shown T2 MRI to be correlated with volume measured by the threshold ADC[14]. However, BCAO-associated cerebral ischemia does not consistently induce necrosis, and SPION-hG-CSF delivered to measure gene expression may interfere with T2 MRI. Therefore, we applied threshold ADC (ADC values at three standard deviations below the

Author Manuscript Author Manuscript Author Manuscript Author Manuscript

average of n = 6–9 at different dates, and examined different litters of mice). We identified volumes of metabolic disturbance (VMD) as brain lesions where rADC is evident in hyperintense diffusion-weighted images (hDWI) after BCAO, as previously described[32].

To detect hG-CSF cDNA expression *in vivo*, we generated a phosphorothioate-modified oligodeoxynucleotide (sODN) with antisense (AS) sequence (5'-Cy3-sODN-AS-hG-CSF-biotin-3', homemade) to hG-CSF mRNA. Genetic MR-CA was made by conjugating SPION to sODN-AS-hG-CSF at 3 nmol per mg Fe, as described[41]. We examined the expression of hG-CSF cDNA after BCAO by acquiring MR images at 15T (Magnex 130 mm diameter horizontal magnet with a Siemens clinical console) using SPION-AS-hG-CSF or SPION-Ran (4 mg Fe per kg, 0.1 ml, i.p,) injected the night before MRI. SPION was conjugated with Cy3-sODN-AS-hG-CSF or sODN-Ran at 1 mg Fe per 3 nmol sODN for at least 6 hrs before delivery, at 4°C. We measured non-specific R2* changes using non-targeting binding MR contrast agent (SPION-Ran), and evaluated SPION-labeled gene expression in the R2* maps acquired using multi-echo gradient echo sequences: TR 800ms, 6 echoes (TE = 1.94, 3.41, 4.88, 6.35, 7.82, 9.29ms) with spatial resolution of 0.1mm × 0.1mm × 0.25mm. We also obtained the ventricular volume from T2-weighted turbo spin echo images acquired at 15T (TR 3s, effective TE 42ms, Turbo factor 8). The total size of the segmented area (including both lateral ventricles, 3rd and 4th ventricles) was measured, normalized to the total area of the corresponding brain slices, and expressed as the ratio of ventricular volume to brain volume, in percentage.

Corner Tests

The corner test, which determines an animal's asymmetric direction of turning when encountering a corner, is used as an indicator of brain injury. We used an experimental corner setup composed of two boards (with dimensions of 30 × 20 × 1 cm^3) arranged to form a 30° corner; a small opening was left along the joint between the two boards. The mouse was placed 12 cm from the corner and allowed to walk into the corner, so that the vibrissae on both sides of the animal's face made contact with the two boards simultaneously. Before BCAO procedure, we conducted behavior tests (stratification) on all mice to screen for mice with no turning asymmetry ($n \geq 18$). Each mouse took part in ten trials, after which we calculated the percentage of turns to each side, recording only those turns involving full rearing along one of the boards. This stratification procedure excludes mice with 80–100% asymmetric turns (n=4); we included mice that turned in either direction (n=14) with a pretest score of 0.50 ± 0.08. Each mouse took part in ten trials for up to 4 weeks after BCAO.

Immunohistochemistry

Following MR acquisition, the mice ($n \geq 2$, each group) were put under general anesthesia and retrograde-perfused with ice-cold saline. Whole brains were removed from perfused animals and frozen in n-butanol on dry ice. The frozen brain tissue sections (thickness, 20 μm) were prepared and stored at −70°C before staining. The brain samples were fixed in 4% paraformaldehyde (PFA, 50 ml) in 0.1 M phosphate buffer (0.1 M Na_2HPO_4 /NaH_2PO_4 pH 7.4) for 10 min, and then were washed in buffer. For antigen detection, the samples were stained overnight with rabbit polyclonal antibodies against GFAP (Z0334, Dako), G-CSF

Author Manuscript Author Manuscript Author Manuscript Author Manuscript

(NBP1-89894, Novous Biologicals), GFP (Z0334A11122, Life Technologies), or NeuN (MAB337, Millipore); all at 1/1000 dilution at 4°C, followed by fluorescein isothiocyanate (FITC)-goat anti-rabbit IgG (1/1000). Vascular endothelia were stained with Cy3-griffonia simplicifolia lectin I (GSL-I, 1/100 dilution), and nucleic acids were stained with Hoechst dye. All histological images were acquired using the same exposure time and gain, using a cellSens system (Olympus USA).

Statistical Tests

We calculated the minimum number of animals required in each group using power analysis to achieve 85% power for a p value of 0.05, or a minimum of n = 2 viable mice in each comparison. We computed the mean and standard error of the mean (SEM) from the average values in each group of animals. We then compared these values using Student t test, one tail; we used the Mann-Whitney test to assess the corner test results.

Acknowledgements

We thank Dr. Sean I. Savitz (University of Texas Houston Medical School, Houston, TX) for demonstration of the corner tests; Dr. Jarek Aronowski (UTHMS, TX) for sharing the hypothermia treatment protocol; Dr. Charng-Ming Liu for synthesizing all sODN and Dr. JS Yang for conducting RT-PCR. This project was supported by NIH grants R01DA029889 and R01EB013768, as well as by a pilot grant from the Boston Area Diabetes Endocrinology Research Center [P30DK057521-14 (J Avruch)] to PKL, NS045776 to the MGH Neuroscience Center]. The MR systems used for this work were funded by NIH Shared Instrumentation Grants (1S10RR025563) awarded to the Athinoula A. Martinos Center for Biomedical Imaging. The B. Wellcome Trust (No.1012722) to HP, State of Florida (09KW-11) to JYW also supported this research.

Non-standard Abbreviations and Acronyms

ADC	Apparent diffusion coefficient
BBB	blood-brain barrier
BCAO	bilateral carotid artery occlusion
DWI	diffusion-weighted imaging
MMP	matrix metalloproteinase
VMD	volume of metabolic disturbance

References cited

1. Talelli P, Ellul J. Are patients with cognitive impairment after stroke at increased risk for developing Alzheimer disease? Archives of neurology. 2004; 61:983. author reply 983. [PubMed: 15210547]
2. Wen Y, et al. Transcriptional regulation of beta-secretase by p25/cdk5 leads to enhanced amyloidogenic processing. Neuron. 2008; 57:680–690. [PubMed: 18341989]
3. Barber RC, et al. Serum granulocyte colony-stimulating factor and Alzheimer's disease. Dement Geriatr Cogn Dis Extra. 2012; 2:353–360. [PubMed: 23012618]
4. Diederich K, et al. The role of granulocyte-colony stimulating factor (G-CSF) in the healthy brain: a characterization of G-CSF-deficient mice. The Journal of neuroscience : the official journal of the Society for Neuroscience. 2009; 29:11572–11581. [PubMed: 19759304]
5. Demetri GD, Griffin JD. Granulocyte colony-stimulating factor and its receptor. Blood. 1991; 78:2791–2808. [PubMed: 1720034]

Author Manuscript Author Manuscript Author Manuscript Author Manuscript

6. Schneider A, et al. The hematopoietic factor G-CSF is a neuronal ligand that counteracts programmed cell death and drives neurogenesis. The Journal of clinical investigation. 2005; 115:2083–2098. [PubMed: 16007267]
7. Song S, et al. Granulocyte-colony stimulating factor (G-CSF) enhances recovery in mouse model of Parkinson's disease. Neuroscience letters. 2011; 487:153–157. [PubMed: 20951187]
8. Cao XQ, et al. Recombinant human granulocyte colony-stimulating factor protects against MPTP-induced dopaminergic cell death in mice by altering Bcl-2/Bax expression levels. Journal of neurochemistry. 2006; 99:861–867. [PubMed: 17076657]
9. Capoccia BJ, Shepherd RM, Link DC. G-CSF and AMD3100 mobilize monocytes into the blood that stimulate angiogenesis in vivo through a paracrine mechanism. Blood. 2006; 108:2438–2445. [PubMed: 16735597]
10. Gibson CL, Bath PM, Murphy SP. G-CSF reduces infarct volume and improves functional outcome after transient focal cerebral ischemia in mice. Journal of cerebral blood flow and metabolism : official journal of the International Society of Cerebral Blood Flow and Metabolism. 2005; 25:431–439.
11. England TJ, et al. Granulocyte-colony stimulating factor for mobilizing bone marrow stem cells in subacute stroke: the stem cell trial of recovery enhancement after stroke 2 randomized controlled trial. Stroke. 2012; 43:405–411. [PubMed: 22198983]
12. Ringelstein EB, et al. Granulocyte colony-stimulating factor in patients with acute ischemic stroke: results of the AX200 for Ischemic Stroke trial. Stroke. 2013; 44:2681–2687. [PubMed: 23963331]
13. Davis AS, Zhao H, Sun GH, Sapolsky RM, Steinberg GK. Gene therapy using SOD1 protects striatal neurons from experimental stroke. Neuroscience letters. 2007; 411:32–36. [PubMed: 17110031]
14. Liu CH, et al. Noninvasive delivery of gene targeting probes to live brains for transcription MRI. Faseb J. 2008; 22:1193–1203. [PubMed: 18029447]
15. Liu CH, et al. Noninvasive detection of neural progenitor cells in living brains by MRI. FASEB journal : official publication of the Federation of American Societies for Experimental Biology. 2012; 26:1652–1662. [PubMed: 22198388]
16. Henriques A, et al. CNS-targeted viral delivery of G-CSF in an animal model for ALS: improved efficacy and preservation of the neuromuscular unit. Molecular therapy : the journal of the American Society of Gene Therapy. 2011; 19:284–292. [PubMed: 21139572]
17. Liu PK, Grossman RG, Hsu CY, Robertson CS. Ischemic injury and faulty gene transcripts in the brain. Trends Neurosci. 2001; 24:581–588. [PubMed: 11576672]
18. Veldwijk MR, et al. Pseudotyped recombinant adeno-associated viral vectors mediate efficient gene transfer into primary human CD34(+) peripheral blood progenitor cells. Cytotherapy. 2010; 12:107–112. [PubMed: 19929455]
19. Duan D, Yue Y, Yan Z, Engelhardt JF. A new dual-vector approach to enhance recombinant adeno-associated virus-mediated gene expression through intermolecular cis activation. Nature medicine. 2000; 6:595–598.
20. Mandel RJ. CERE-110, an adeno-associated virus-based gene delivery vector expressing human nerve growth factor for the treatment of Alzheimer's disease. Curr Opin Mol Ther. 2010; 12:240–247. [PubMed: 20373268]
21. Theodore S, Cao S, McLean PJ, Standaert DG. Targeted overexpression of human alpha-synuclein triggers microglial activation and an adaptive immune response in a mouse model of Parkinson disease. J Neuropathol Exp Neurol. 2008; 67:1149–1158. [PubMed: 19018246]
22. Whalen MJ, et al. Acute plasmalemma permeability and protracted clearance of injured cells after controlled cortical impact in mice. J Cereb Blood Flow Metab. 2008; 28:490–505. [PubMed: 17713463]
23. Bermpohl D, You Z, Lo EH, Kim HH, Whalen MJ. TNF alpha and Fas mediate tissue damage and functional outcome after traumatic brain injury in mice. J Cereb Blood Flow Metab. 2007; 27:1806–1818. [PubMed: 17406655]
24. Kim F, Bravo PE, Nichol G. What Is the Use of Hypothermia for Neuroprotection After Out-of-Hospital Cardiac Arrest? Stroke. 2015

Author Manuscript Author Manuscript Author Manuscript Author Manuscript

25. Huang D, Shenoy A, Cui J, Huang W, Liu PK. In situ detection of AP sites and DNA strand breaks bearing 3'-phosphate termini in ischemic mouse brain. Faseb J. 2000; 14:407–417. [PubMed: 10657997]
26. Liu CH, Huang S, Kim YR, Rosen BR, Liu PK. Forebrain ischemia-reperfusion simulating cardiac arrest in mice induces edema and DNA fragmentation in the brain. Mol Imaging. 2007; 6:156–170. [PubMed: 17532882]
27. Kida K, et al. Sodium sulfide prevents water diffusion abnormality in the brain and improves long term outcome after cardiac arrest in mice. Resuscitation. 2012; 83:1292–1297. [PubMed: 22370005]
28. Minamishima S, et al. Inhaled nitric oxide improves outcomes after successful cardiopulmonary resuscitation in mice. Circulation. 2011; 124:1645–1653. [PubMed: 21931083]
29. Dijkhuizen RM, et al. Functional magnetic resonance imaging of reorganization in rat brain after stroke. Proceedings of the National Academy of Sciences of the United States of America. 2001; 98:12766–12771. [PubMed: 11606760]
30. Li X, et al. Chronic behavioral testing after focal ischemia in the mouse: functional recovery and the effects of gender. Exp Neurol. 2004; 187:94–104. [PubMed: 15081592]
31. Yli-Hankala A, Edmonds HL Jr, Jiang YD, Higham HE, Zhang PY. Outcome effects of different protective hypothermia levels during cardiac arrest in rats. Acta Anaesthesiol Scand. 1997; 41:511–515. [PubMed: 9150781]
32. Liu CH, et al. Diffusion-weighted magnetic resonance imaging reversal by gene knockdown of matrix metalloproteinase-9 activities in live animal brains. J Neurosci. 2009; 29:3508–3517. [PubMed: 19295156]
33. Pardridge WM, Boado RJ, Kang YS. Vector-mediated delivery of a polyamide ("peptide") nucleic acid analogue through the blood-brain barrier in vivo. Proc Natl Acad Sci U S A. 1995; 92:5592–5596. [PubMed: 7777554]
34. Liu PK, et al. Suppression of ischemia-induced fos expression and AP-1 activity by an antisense oligodeoxynucleotide to c-fos mRNA. Ann Neurol. 1994; 36:566–576. [PubMed: 7944289]
35. Gibson CL, Jones NC, Prior MJ, Bath PM, Murphy SP. G-CSF suppresses edema formation and reduces interleukin-1beta expression after cerebral ischemia in mice. Journal of neuropathology and experimental neurology. 2005; 64:763–769. [PubMed: 16141785]
36. Liu CH, Ren J, Liu CM, Liu PK. Intracellular gene transcription factor protein-guided MRI by DNA aptamers in vivo. FASEB journal : official publication of the Federation of American Societies for Experimental Biology. 2014; 28:464–473. [PubMed: 24115049]
37. Schaar KL, Brenneman MM, Savitz SI. Functional assessments in the rodent stroke model. Exp Transl Stroke Med. 2010; 2:13. [PubMed: 20642841]
38. Zhang L, et al. A test for detecting long-term sensorimotor dysfunction in the mouse after focal cerebral ischemia. Journal of neuroscience methods. 2002; 117:207–214. [PubMed: 12100987]
39. Liu CH, et al. MRI reveals differential effects of amphetamine exposure on neuroglia in vivo. FASEB journal : official publication of the Federation of American Societies for Experimental Biology. 2013; 27:712–724. [PubMed: 23150521]
40. Liu CH, et al. DNA-based MRI probes for Specific Detection of Chronic Exposure to Amphetamine in Living Brains. J Neurosci. 2009; 29:10663–10670. [PubMed: 19710318]
41. Liu CH, et al. MR contrast probes that trace gene transcripts for cerebral ischemia in live animals. Faseb J. 2007; 21:3004–3015. [PubMed: 17478745]

Author Manuscript Author Manuscript Author Manuscript Author Manuscript

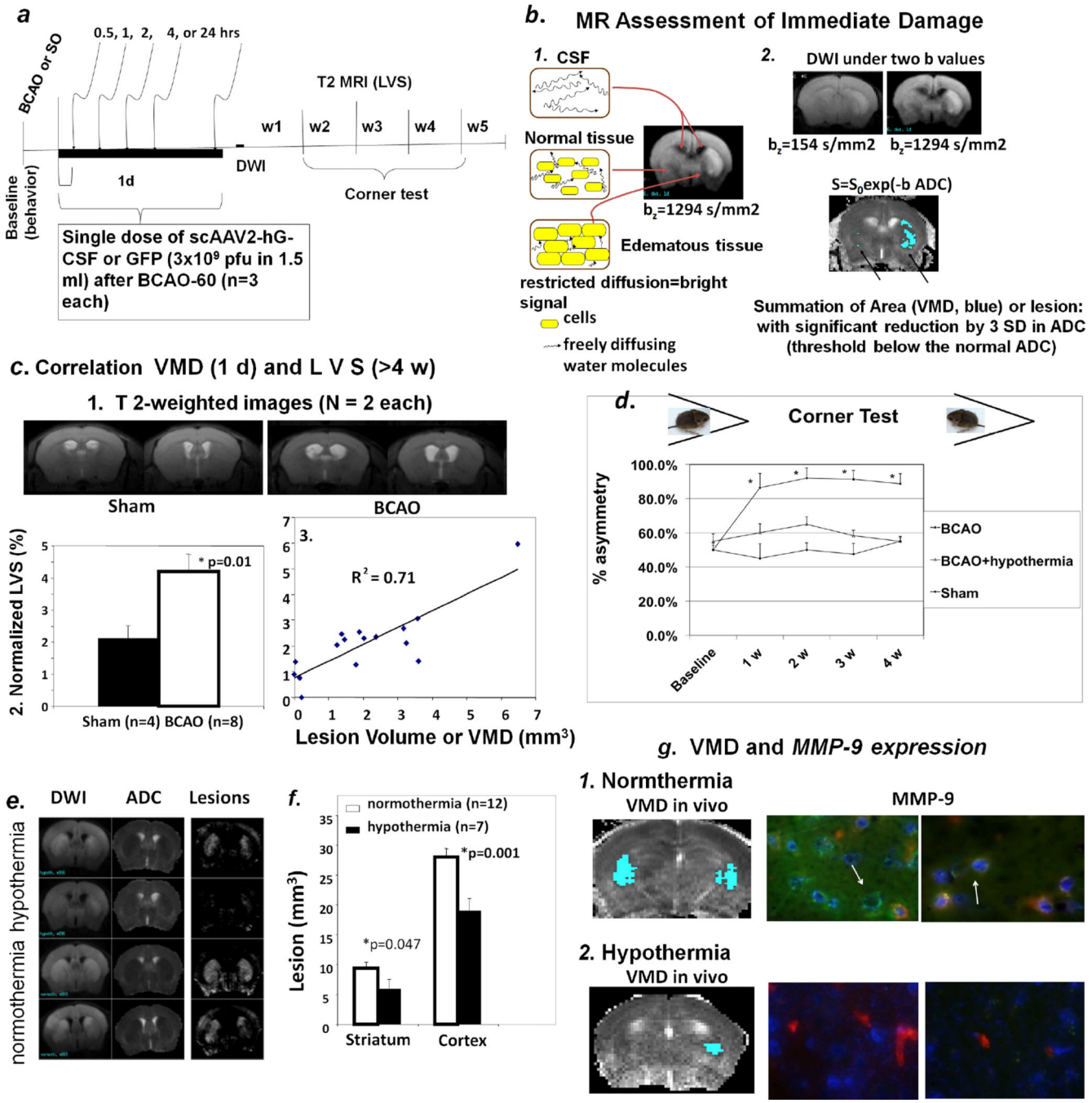


Figure 1.

Panel *a*. Protocol for longitudinal monitoring of brain repair in vivo using MRI in mice with BCAO or sham operation. We made weekly measurements (up to 10 weeks, w10): for cerebral atrophy (ventriculomegaly) without MR-CA at w4 or w5, expression of scAAV2-CMV-hG-CSF, baseline MRI using SPION-Ran studies. The protocol can be extended to 24 weeks in some studies for leakage of the BBB using Gd-DATA. Panel *b*. Abnormal DWI is obvious at high b values; DWIs before and after BCAO are shown (frame 1). High-lighted areas showing significant below-threshold rADC after BCAO-60 represent regions of

Author Manuscript Author Manuscript Author Manuscript Author Manuscript

interest (ROI) for calculating the volume of metabolic disturbance (VMD, summation of all ROI of five MR slices of 1 mm each) as the lesion size (mm^3). The results of BCAO-60, including abnormal water diffusion in the cerebrospinal fluid (CSF) in normal tissue as well as tissue with edema are illustrated, as detected by MRI (frame 2). Panel *c*-1. Representative T2-weighted images (caudal view). Enlarged lateral ventricles show cerebral atrophy without visible abnormal T2 MRI from mice at weeks 4 and 5 following sham operation and BCAO (one of five MR images from each mouse). Panel c-2. Normalized lateral ventricular size (LVS). We measured ventriculomegaly (n = 16) as normalized lateral ventricular size (LVS, or by size ratio of lateral ventricle to corresponding brain volumes in percent, %). Panel c-3. Scatter plot of LSV and VDM from mice before (n = 4) and after (n = 12) BCAO-60. The scatter plot shows the correlation between LVS (%) at w4–w5 post BCAO and lesion volume (VMD) in the same mice. Panel *d*. Corner test results of BCAO mice (normothermia, n = 8 survivors of 32; hypothermia, n = 6; sham-operation, n = 4) when facing a 30° corner. BCAO mice without treatment showed significant asymmetric turning (~90%) beginning one week after the procedure and persisting for at least four weeks. Mice with treatment (BCAO + hypothermia) exhibited behavior not significant differently from that seen in the sham-operated mice. Panels *e*–*h*. Validations of noninvasive measurements. Hypothermia treatment reversed DWI and rADC (e) as well as VMD (f). The expression of MMP-9 antigen one day post-BCAO in postmortem samples (*g*, arrows point to vascular MMP-9, green) validates brain lesion reduction with hypothermia treatment, shown here as normothermia (*g1*) vs. hypothermia (*g2*). (Endothelia = red; Nuclei = Hoechst stain).

Author Manuscript Author Manuscript Author Manuscript Author Manuscript

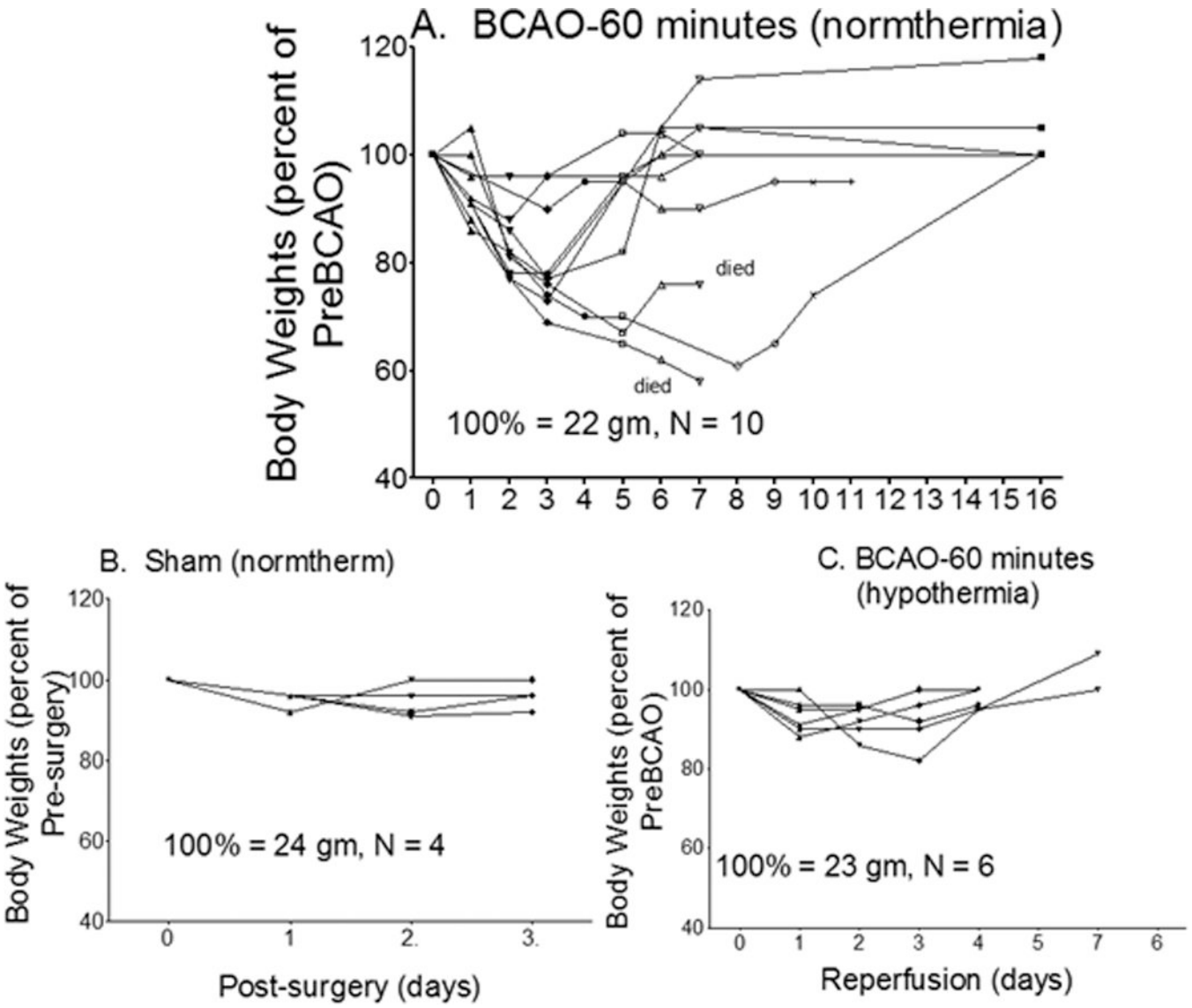


Figure 2.

Changes in body weight before and after BCAO, with and without hypothermia treatment. Body weights of mice after BCAO were measured and recorded daily for at least 7 days after BCAO-60.

Author Manuscript Author Manuscript Author Manuscript Author Manuscript

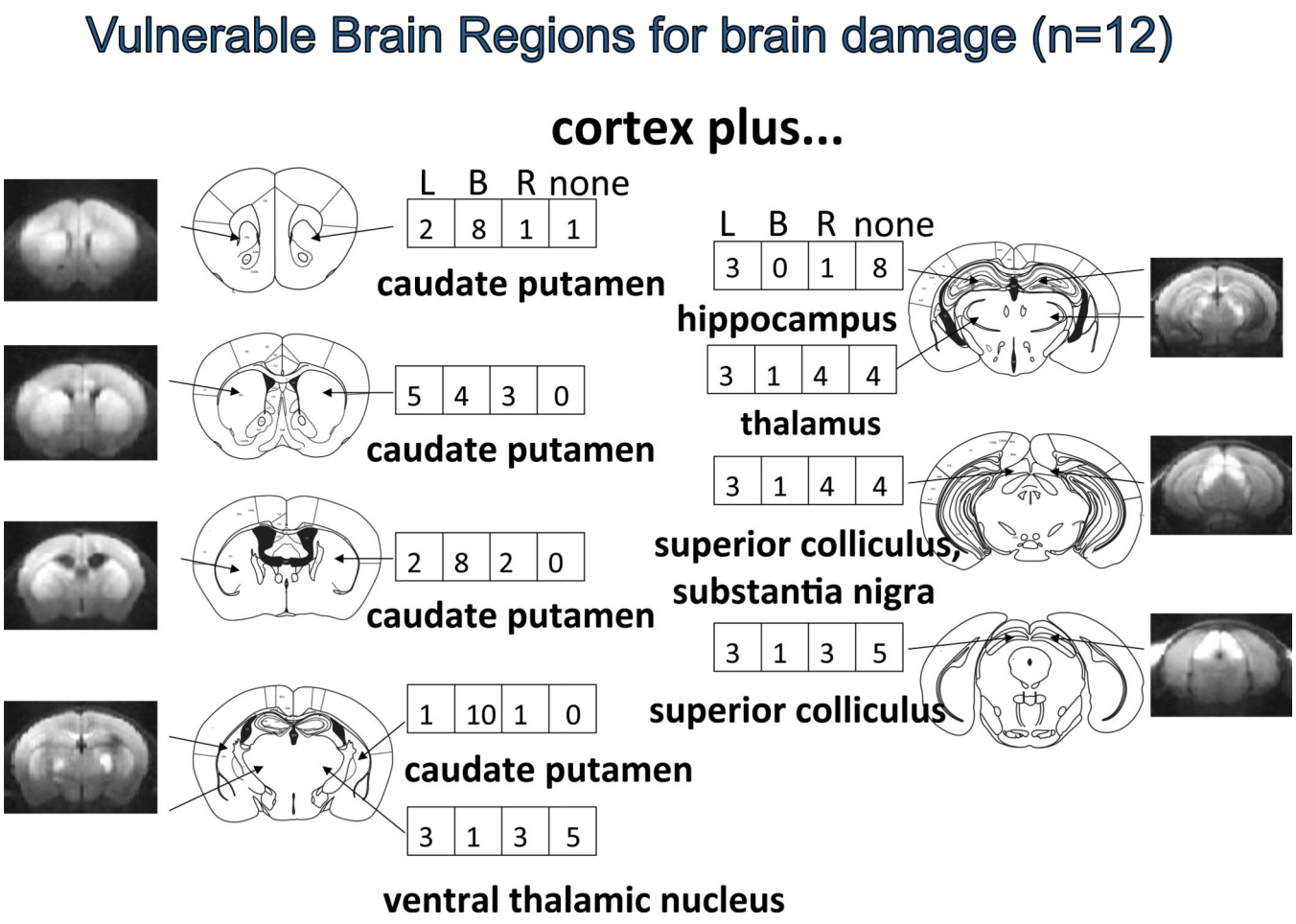


Figure 3.

Summary of potential brain damage (or BBB disruption) measured by MRI at the second peak of DWI or 1 to 2 days after BCAO-60 in C57black6 mice. The number in the box indicates the number of mice exhibiting lesion in the left (L), right (R) both (B) hemispheres [reconstructed from[32]]. The presence of a lesion in the superior colliculus or optic tectum (midbrain) indicates BCAO effects that extend beyond the forebrain; mouse cardiac arrest-resuscitation models also show hyperintense DWI (hDWI) in similar ROI[27,28].

Author Manuscript Author Manuscript Author Manuscript Author Manuscript

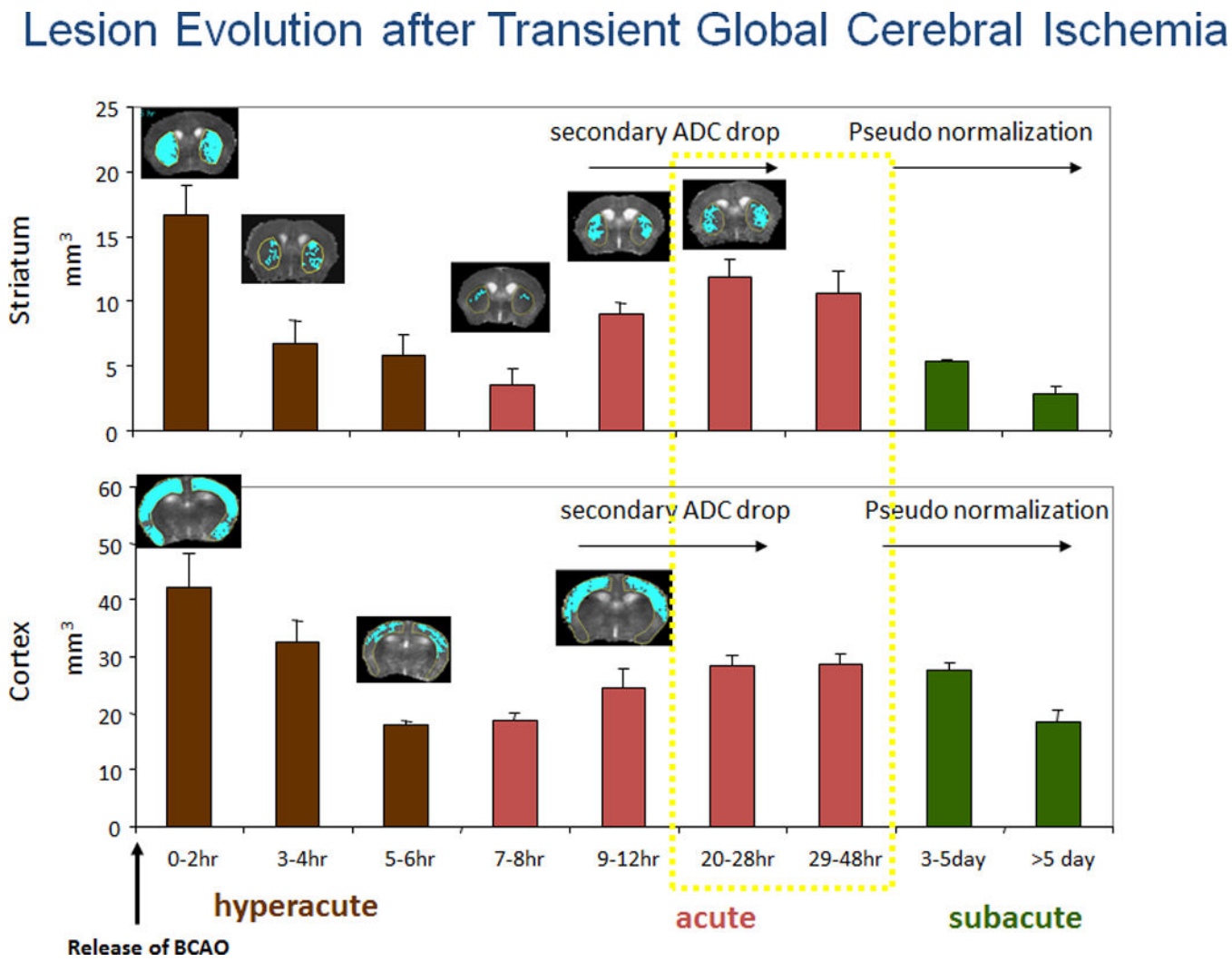


Figure 4.

The time course followed for applying the AAV-CMV vector. Early brain lesions estimated by rADC below the threshold values (see Fig 1c). The tthreshold of ADC in normal mice (n = 6 at different dates and different litters of mice) was established using power analysis after BCAO at normal temperature (Each data point after BAO was obtained from at least n ≥ 4, Data adapted from our previous publication)[32].

Author Manuscript Author Manuscript Author Manuscript Author Manuscript

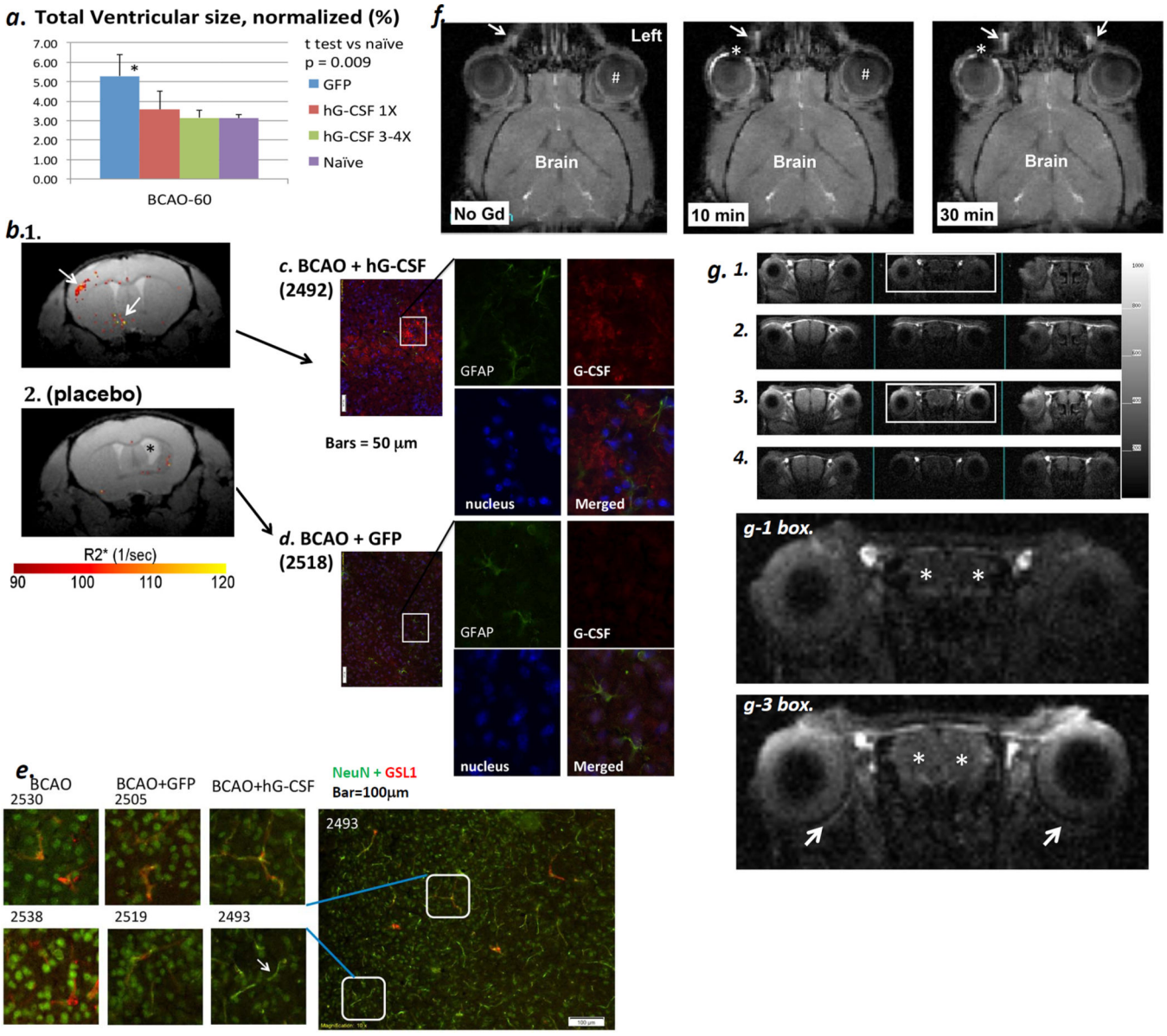


Figure 5.

Panel *a*. Significant reduction in cerebral atrophy (measured during the 4th week after BCAO, purple bar) in the scAAV2-CMV-hG-CSF treatment groups with multiple doses (green bar, n = 5 survivors of 5) compared to the placebo group (blue bar, n = 7 survivors of 28) or BCAO+ single dose hG-CSF (red bar, n = 5 survivors of 8). We validated the expression of hG-CSF antigen using immunohistochemistry in the 11th week (Panels *c* & *d*). Panel *b*. A unique ROI (arrow) using SPION-AS-hG-CSF one week after the final scAAV2-CMV-hG-CSF treatment (the 3rd week). Panel *b1*. The ROI in delta R2* maps from both the multiple treatment (n = 5) and placebo (n = 4 survivors of 16, Panel *b*2) groups of mice. Panels *c & d*. hG-CSF expression in the proximity of the ROI identified in vivo (*b*1), with no expression found in the placebo group (*b2 & d*). Mice with BCAO only did not show elevated hG-CSF expression (n = 2 survivors of 8, data not shown). Panel *e*. NeuN

Author Manuscript Author Manuscript Author Manuscript Author Manuscript

expression in small blood vessels (Cy3-GSL I) in mice with AAV2-CMV-hG-CSF (BCAO +hG-CSF, n = 3) bar = 100 μm. NeuN expression (Cy2, arrow) occurs mostly in the neuronal nuclei of control and placebo groups (BCAO, n = 2 survivors of 8; BCAO+GFP, n = 4 survivors of 16). Panel *f*. T1-weighted MRI of mice (n=4) before and after application of eye drops containing non-targetng MR-CA (Gd-DTPA, 500 mM in 10 μl Magnevist, Scherling, Berlin, Germany) to the conjunctival sac; the distribution of MR-CA is shown in the same mouse. Arrow: the naso-lacrimal canal, #: the vitrous chamber; asterisk: lens. Panel *g*. The distribution of targeted MR-CA (Gd-nestin) in longitudinal MR acquisition (n = 2). T1-weighted MRI was acquired before (*g*1), 10 min (*g*2), 180 min (*g*3) and 41 hr (*g*4) after application of Gd-nestin (50 μg Gd-NA and 30 pmol biotin-sODN-nestin per 2 μl per mouse to one eye) in mice with BCAO-60. Arrows: chorid of the retina; * both hemispheres of the brain. Biotinylated sODN-nestin binds to NeutrAvidin (NA) on SPION or Gd and the MR-CA targets Nestin mRNA of percytes of neovessels after BCAO-60[14,15].

Author Manuscript Author Manuscript Author Manuscript Author Manuscript

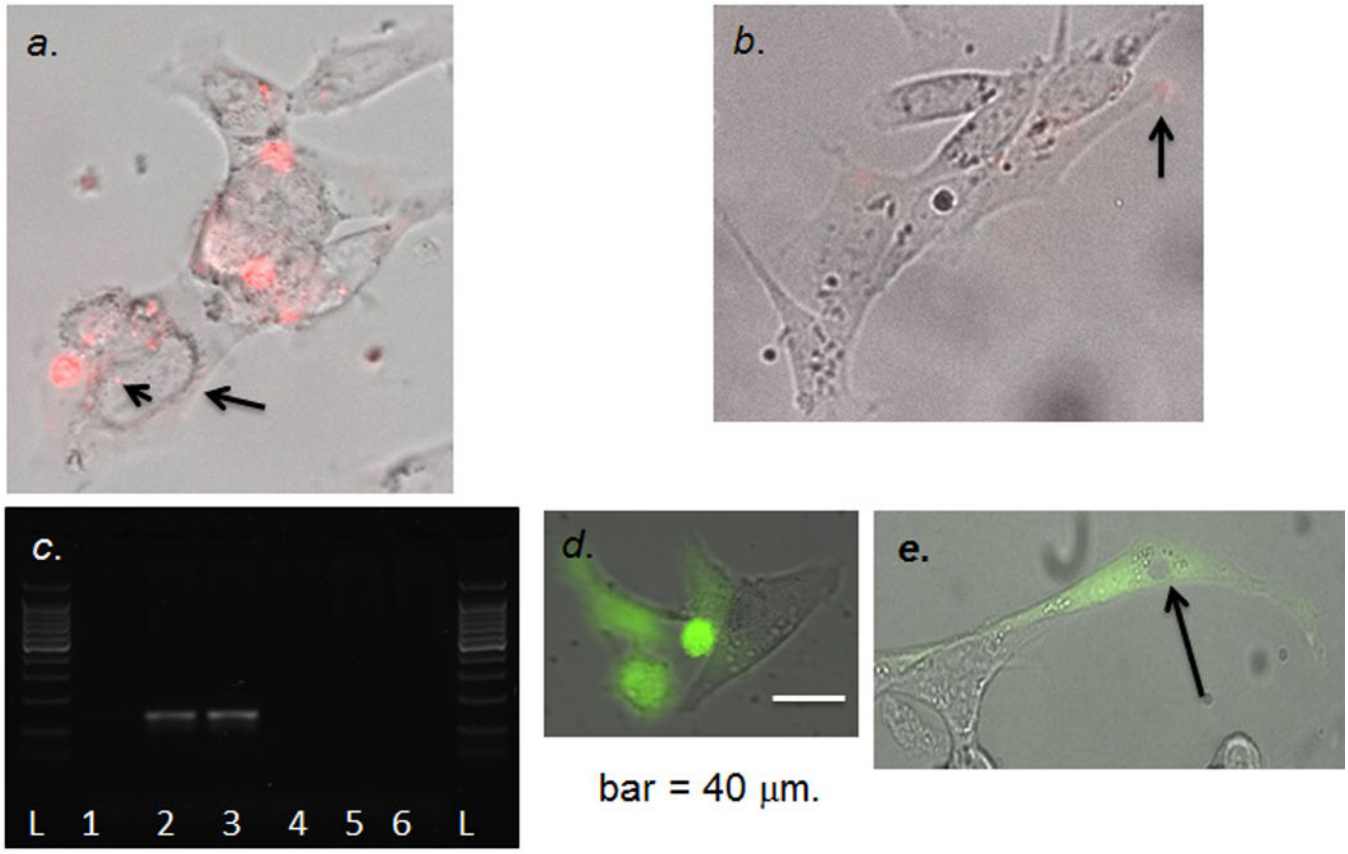


Figure 6.

Panel *a*. hG-CSF cDNA/mRNA expression in PC-12 cells. We transfected Cy3-sODN-AS-hG-CSF to detect hG-CSF mRNA in cells transfected with pCMV-hG-CSF; we observed signal in the nucleus (arrowhead) and peri-nucleus (arrow). Panel *b*. Few Cy3-sODN-AS-hG-CSF (arrow) retention in the cells transfected with pCMV-GFP. Panel *c*. Validation of hG-CSF mRNA expression from transfected PC-12 cells (pCMV-hG-CSF [lanes 1–3] or pCMV-GFP [lanes 4–6] at 3 (lanes1, 4), 6 (Lanes 2, 5) or 8 (lanes 3, 6) hours after transfection. Isolated RNA was treated with DNase before reverse transcription. Panel *d*. Living cells with GFP expression (Z-stack photograph, cellSens, time-lapse optical microscopy, Olympus IX83) >3 hours after transfection with pCMV-GFP. Panel *e*. Stable pCMV-GFP DNA in vivo for 72 hours. We isolated total DNA from PC-12 at 72 hours (Panel d); we then transfected PC-12 again and detected GFP expression at 24 hours after transfection. GFP is in the cytoplasm but there is no nuclear GFP (arrow).

BioDrugs (2018) 32:357–366
https://doi.org/10.1007/s40259-018-0294-1

REVIEW ARTICLE

Regenerative Therapies for Parkinson's Disease: An Update

Thomas B. Stoker[1,2] · **Roger A. Barker**[1,2]

Published online: 19 July 2018
© Springer Nature Switzerland AG 2018

Abstract
Parkinson's disease is the second most common neurodegenerative disorder. It is characterised by a typical movement disorder that occurs in part because of the selective degeneration of the dopaminergic neurons of the substantia nigra pars compacta. Current treatment for the motor disorder of Parkinson's disease consists of dopaminergic medications, but these come with significant adverse effects, themselves an important part of the clinical course of Parkinson's disease, particularly in advanced stages. Therefore, treatment is needed that can restore dopaminergic tone in the striatum in a physiological and targeted manner to avert these side effects. A number of potential regenerative treatments have been developed with a view to achieving this. Following decades of optimisation and development of stem-cell-based treatments and viral gene delivery, clinical trials are on the horizon. For these treatments to be widely useful, they must be clinically effective, cost efficient and safe, and a number of practical aspects regarding storage and delivery of treatment must be optimised. Many barriers have been overcome, and the field of regenerative medicine for Parkinson's disease is now increasingly focussed on how these treatments will be delivered, demonstrating the significant progress that has been made and the optimism surrounding these approaches.

Key Points

Current treatments for Parkinson's disease result in significant adverse effects due to the non-targeted, non-physiological delivery of dopamine.

Cell-based and gene-delivery treatments offer a means of restoring dopamine to the striatum in Parkinson's disease patients in a targeted manner.

Several clinical trials of regenerative therapies are due to commence within the next 2 years.

✉ Thomas B. Stoker
tbs26@cam.ac.uk

[1] John van Geest Centre for Brain Repair, Department of Clinical Neurosciences, University of Cambridge, E.D. Adrian Building, Forvie Site, Robinson Way, Cambridge CB2 0PY, UK

[2] Wellcome Trust - Medical Research Council Stem Cell Institute, University of Cambridge, Cambridge, UK

1 Introduction

Parkinson's disease (PD) is the second most common neurodegenerative disorder after Alzheimer's disease [1]. It results in a typical movement disorder consisting of bradykinesia, rigidity, rest tremor and, as disease progresses, postural instability [1]. A number of non-motor features also occur, such as cognitive impairment and dementia, neuropsychiatric symptoms (e.g. depression and anxiety), fatigue, anosmia and rapid-eye movement (REM)-sleep behaviour disorder [2]. The natural course of PD is one of gradual progression, with functional decline occurring over years [3].

The neuropathological hallmark of PD is the presence of Lewy bodies and Lewy neurites—intra-neuronal protein aggregates consisting largely of abnormal alpha-synuclein [4]. While the non-motor features of PD are due to neurodegeneration in the cerebral cortex and a number of brainstem nuclei, the movement disorder of PD primarily relates to the relatively selective degeneration of the neurons of the substantia nigra pars compacta [1, 5, 6]. These neurons produce the neurotransmitter dopamine and deliver it to the striatum, where it plays a crucial role in control of motor activity and some cognitive processes. Therefore, treatment of the motor features of PD involves restoration of dopamine activity in the striatum. However, current treatment

options result in significant adverse effects that themselves constitute an important part of the illness experienced by the patient, particularly in the advanced stages of disease [1]. There is therefore much interest in the development of novel therapies that can restore dopamine activity without incurring these unwanted side effects. In this review, we discuss progress towards these therapies and their future prospects for the management of PD.

2 Rationale for Regenerative Approaches in Parkinson's Disease

Current treatment of PD motor features generally involves the use of dopaminergic drugs. Most commonly, this involves administration of the dopamine precursor, levodopa, in combination with a peripheral dopa-decarboxylase inhibitor to minimise peripheral side effects. Dopamine agonists or monoamine oxidase B inhibitors may be used in some patients, though the majority require levodopa therapy as disease progresses. In the initial stages of levodopa treatment, most patients experience significant improvement in motor problems and an improvement in function. However, with prolonged treatment, problematic adverse effects can have a significant impact on quality of life. These can include neuropsychiatric features such as hallucinations, thought to be due to delivery of dopamine to extra-striatal brain regions (off-target effects). Patients may also develop disabling levodopa-induced dyskinesias—continuous involuntary movements that may affect the limbs, trunk or face. These motor effects are thought to be due to the manner in which dopamine reaches the striatum following levodopa administration, which is continuous rather than in a physiological pulsatile fashion [7, 8]. Additionally, severe motor fluctuations may occur due to variations in the plasma concentration of levodopa and its transit across the blood–brain barrier [9]. Sudden 'off' spells can be particularly disabling. Therefore, dopamine needs to be delivered specifically to the striatum in a physiological manner that is not achievable with current pharmacological agents.

3 Cell Grafting for Parkinson's Disease

The movement disorder of PD largely results from a decline in the number and functional capacity of dopaminergic neurons in the substantia nigra. The onset of disease probably precedes the development of motor features by several years [2, 10, 11], meaning that significant neuronal loss has already occurred by the time of diagnosis [12]. Restoration of a population of cells delivering dopamine to the striatum could theoretically allow for improvement in motor abnormalities without the development of the off-target and motor side effects associated with prolonged use of dopaminergic medication.

A number of cell sources have been considered as potential options for grafting in PD. The first reports involved the grafting of autologous adrenal medullary cells (which release small amounts of dopamine) into the striatum [13, 14]. The initial positive results in these patients, despite only a short period of follow-up, led to a number of patients receiving this type of graft [15–20]. However, it became clear that the recipients in fact experienced little clinical benefit, with a high incidence of psychiatric complications [21]. Furthermore, post-mortem study of these patients indicated the grafted cells had not survived [22].

Around the same time, there was interest in using foetal midbrains, which contain the developing nigral dopaminergic neurons, derived from terminated pregnancies as an alternative source of dopaminergic cells. Results with the first two patients were disappointing [23], but adjustments to the grafting procedure led to significant clinical benefits in a number of recipients, with some able to come off medication [24–27]. At post mortem, these grafts were shown to have survived for over two decades [28]. This suggested that cell-based approaches could indeed be useful for treating the movement disorder of PD, at least in some patients. However, enthusiasm was dampened following two sham-surgery controlled trials of foetal tissue grafts, in which little clinical benefit was observed, with several recipients developing graft-induced dyskinesias [29, 30]. These trials had several design flaws but did highlight the need for the approach to be optimised, for example, in terms of the delivery method, the age and number of foetal midbrains used, the immunosuppressive regimen, and the identification of a suitable recipient population. After analysis of the outcomes of these foetal grafts, a further trial was set up in Europe using an optimised approach with the aim of showing that cell-based therapies for PD can be effective in appropriately selected patients (https://clinicaltrials.gov/ct2/show/NCT01898390). In total, 11 participants in this trial have now received grafts and are undergoing follow-up. However, even if the approach is proven effective, it will not be a feasible widespread treatment for PD, predominantly because the supply of foetal tissue is inadequate.

A number of other cell sources have been investigated for grafting in PD, including porcine midbrain tissue, autologous carotid body cells and retinal pigment epithelial (RPE) cells bound to microcarriers (Spheramine), with disappointing results (Fig. 1) [31–34]. Carotid body cells were investigated as a means of delivering glial-derived neurotrophic factor (GDNF) to the striatum, which had appeared to be effective in animal models of PD [35]. However, clinical effects were modest in human trials [32, 33]. RPE cells release small amounts of levodopa so have been investigated as a source of cells that could replenish striatal dopamine.

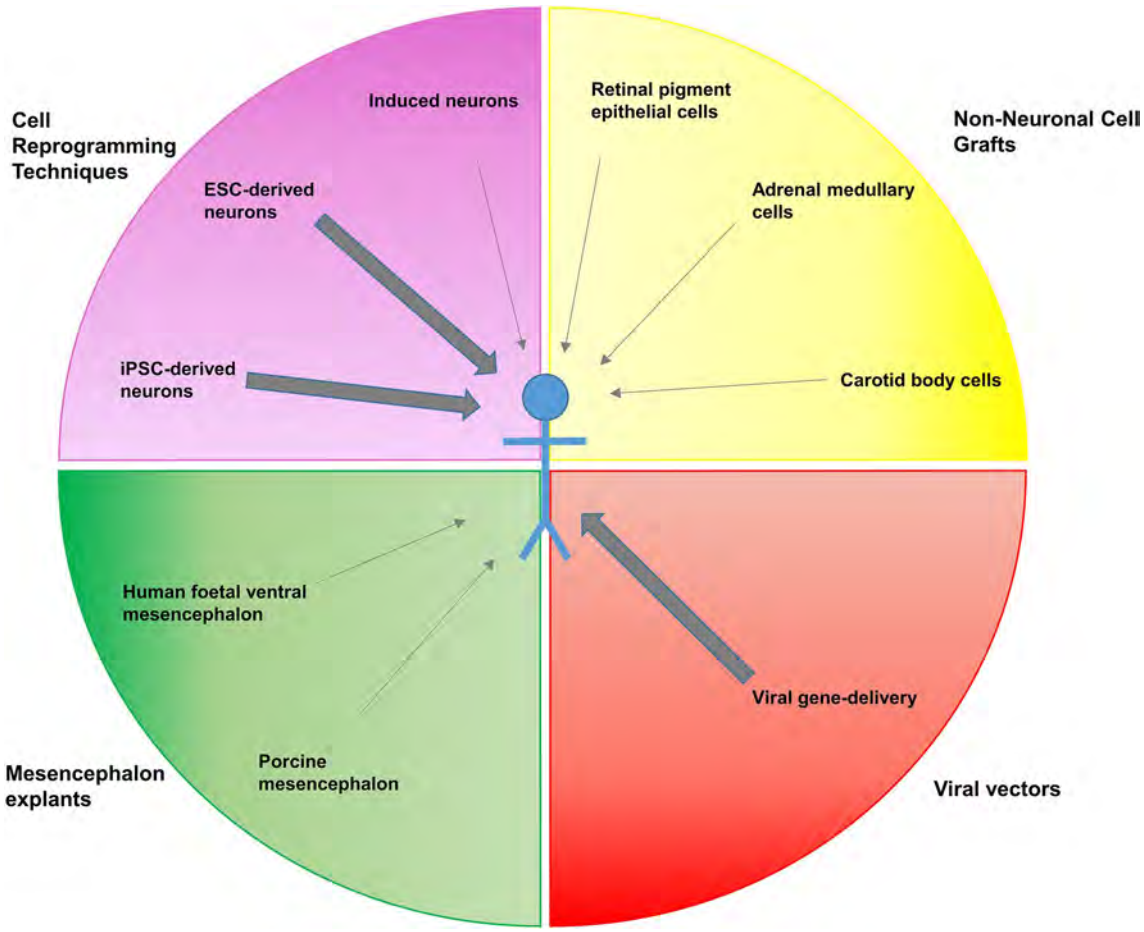


Fig. 1 Sources of potential and previously investigated regenerative treatments for Parkinson's disease. Bold arrows indicate approaches that may offer deliverable treatment options, taking into account ethical, logistical, and regulatory factors. *ESC* embryonic stem cell, *iPSC* induced pluripotent stem cell

However, a sham-surgery controlled phase II trial demonstrated no benefit [31]. These approaches therefore did not offer any advantages over the use of foetal tissue, with which experience was building by this time.

3.1 Stem Cell Treatments for Parkinson's Disease

Though the grafting trials produced mixed results, the significant clinical benefit observed in some of the recipients of human foetal ventral mesencephalon grafts offered proof of concept that dopamine cell-based therapies can be useful in PD. However, particularly given that PD is a common condition, a reliable source of dopaminergic cells is required for this approach to be widely useful—a condition that cannot be met by the unpredictable supply of foetal tissue. In contrast, this is potentially achievable through the use of stem cells to generate dopaminergic neural progenitor cells for grafting. Though other stem cell types have been purported as potential treatment options, two stem cell approaches in particular might offer an effective treatment for the dopaminergic deficits of PD: embryonic stem cell (ESC)-derived and induced pluripotent stem cell (iPSC)-derived dopaminergic neural progenitor cells (Fig. 2) [36].

Human ESCs were first derived in 1998, opening up possibilities for the development of regenerative therapies for a number of conditions, including PD [37]. ESCs are pluripotent cells derived from the inner cell mass of the early blastocyst, harvested from surplus human embryos from in vitro fertilisation procedures [36]. However, the generation of authentic dopaminergic neurons or their precursors has been challenging, and progress has been slow. In particular, while ESCs clearly could produce cells expressing tyrosine hydroxylase (the rate-limiting enzyme in dopamine synthesis) and that these could survive transplantation into rodents, the yield varied widely [38–41]. Subsequent refinements of the differentiation protocols led to reports of ESC products that could not only survive grafting and integrate into the host but also produce a degree of functional recovery in pre-clinical models [38–42].

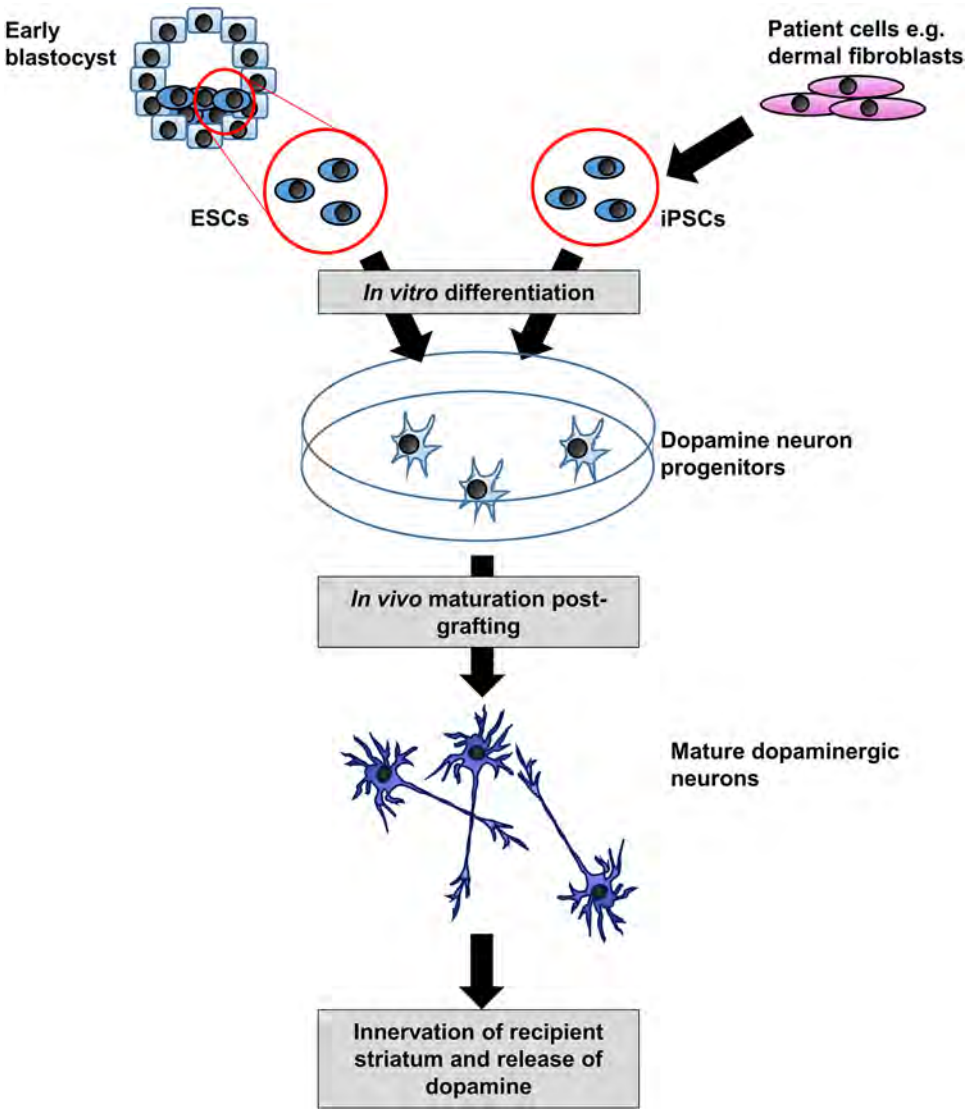


Fig. 2 Stem cell therapies for Parkinson's disease. *ESCs* embryonic stem cells, *iPSCs* induced pluripotent stem cells

A retrospective analysis of over 500 ESC-derived neural progenitor grafts into rats sought to identify factors that determined favourable graft outcome [43]. This study found that a high content of tyrosine hydroxylase-positive cells were obtained in grafts enriched with neural progenitors expressing caudal midbrain markers, such as *EN1* and *CNPY1*. However, the markers that had traditionally been used to signify dopaminergic fate (*LMX1A*, *FOXA2* and *OTX2*) were found to be expressed not only in midbrain nigral progenitors but also in the rostral midbrain subthalamic neuron progenitors, explaining the heterogeneity in graft outcomes [43]. Exposure to FGF8b at the later stages of the reprogramming protocol resulted in a high purity of neuronal progenitors expressing markers of caudal midbrain patterning, which, when grafted, yielded a high level of dopaminergic neurons and functional recovery [43]. This unexpected development in understanding means it is now possible to generate ESC-derived neural progenitors that yield consistently high numbers of tyrosine hydroxylase-positive neurons, which could serve as the basis of a cell-replacement therapy.

In 2007, conversion of human somatic cells to pluripotent stem cells was first reported, offering an alternative renewable source of cells that could serve as the basis of a regenerative therapy for PD [44, 45]. These iPSCs can also be differentiated into dopaminergic neural progenitors through differentiation protocols similar to those used with ESCs, potentially offering an alternative source for a cell-based therapy for PD, as has been shown recently in a primate model [46, 47].

Each of these stem cell approaches has its own merits and drawbacks. Generation of ESC lines results in destruction of a viable human embryo, which of course results in ethical issues, though in most cultures the use of embryonic tissue that would otherwise be discarded is probably more ethically favourable than the use of foetal tissue [48].

ESC-derived grafts would be allogeneic in nature so would require a period of immunosuppression and would carry the associated risk of infection, malignancy and other adverse effects. These ethical implications do not apply to iPSCs, and they can potentially be used to generate autologous grafts, derived from fibroblasts of the recipient, possibly circumventing the need for immunosuppressive treatment. However, heterogeneity in the response to a reprogramming protocol between individuals would mean that the cell product would vary between patients, with each product potentially being subject to regulatory approval and safety testing [36]. The more likely scenario is that investigators will need to prove that their reprogramming and differentiation processes are robust, yielding similar results for each patient, before an iPSC-derived product could be approved for clinical use. Generation of autologous iPSC-derived grafts is probably therefore prohibitively expensive for widespread use, at least in most current regulatory environments. Finally, with respect to autologous grafts, one should also consider the fact that the grafted cells will contain any PD genetic susceptibility factors carried by the patient, so may be at increased risk of themselves succumbing to PD pathology, a situation seen in some long-term surviving human foetal mesencephalon transplants [28].

One proposed option is the generation of haplobanks, in which iPSC lines could be derived from a number of individuals with specific homozygous human leukocyte antigen (HLA) patterns to provide coverage of a whole population. While this is an appealing prospect, such coverage through a haplobank would still require generation of a large number of iPSC lines, all of which would be subject to safety testing and protocol optimisation and the associated costs [36, 49]. Additionally, grafts delivered from haplobanks would probably still warrant a period of immunosuppression, nullifying one of the main advantages of the iPSC approach over ESCs [36]. The use of haplobanks may not be a major advantage for transplantation into immune-privileged sites such as the brain, but they may confer a significant advantage in achieving transplantation of cell products to other organs.

Both iPSC- and ESC-derived grafts involve a theoretical risk of tumour formation, through graft overgrowth, aberrant differentiation of the grafted progenitors or the presence of residual pluripotent cells in the graft, as discussed further in Sect. 5. Though tumours formed in some of the early pre-clinical in vivo studies [40, 41, 50], developments in differentiation protocols have allowed for generation of refined cell products in which there are no residual pluripotent cells, and, at least in animals, no tumour formation.

In addition, bone marrow-derived mesenchymal stem cells have been investigated as a potential therapeutic option for PD. Tyrosine hydroxylase-positive cells have been generated from mesenchymal stem cells [51], but generation of midbrain dopaminergic neurons has not been achieved, so they are unlikely to be useful as a cell-replacement therapy for PD [52]. Alternatively, it has been suggested that these cells may convey a neuroprotective effect through paracrine and anti-inflammatory properties [53, 54]. An open-label trial in a small group of patients with PD demonstrated the short-term safety of the use of these cells, but clinical effectiveness could not be demonstrated [55].

4 Gene-Delivery Therapies for Parkinson's Disease

An alternative approach towards a regenerative treatment for PD involves the use of viral vectors to deliver genes into the striatum. A number of virus-based gene-delivery therapies have now been investigated, some aiming to increase striatal dopamine [56–59], with potentially regenerative potential, and some aiming to convey a neuroprotective, potentially disease-modifying effect [60].

Two phase I trials have investigated the safety of adeno-associated virus (AAV) vectors delivering aromatic amino decarboxylase (AADC; the enzyme responsible for the conversion of levodopa to dopamine) into the putamina of patients with PD [56, 57]. Both of these trials reported improvements in clinical and imaging parameters at 6 months. These procedures were reported to be well-tolerated, though 30% of the subjects in one of the trials developed intracranial haemorrhages along the injection tract [56].

Following these initial trials, a phase I/II trial in France and the UK investigated the safety of a lentivirus gene therapy (ProSavin, Oxford Biomedica, UK) [58]. Lentiviruses have a capacity for a larger genetic cargo than do AAV vectors, meaning it was possible to deliver the genes encoding the other two rate-limiting enzymes in dopamine synthesis, tyrosine hydroxylase and cyclohydrolase-1, in addition to AADC. The treatment was generally well-tolerated, but 73% of recipients experienced an increase in on-medication dyskinesias in the first 12 months, which improved with a reduction in levodopa dose. All patients demonstrated a significant improvement in the off-medication Unified Parkinson's Disease Rating Scale (UPDRS) motor score at 6 months, with continued improvement over 48 months [58].

As well as targeting the dopamine synthesis pathway, AAVs have been used to deliver other genes to patients with PD. A phase I trial in which the GDNF-like growth factor, neurturin, was delivered in an AAV vector demonstrated that this approach was well-tolerated [60], though clinical outcomes in a follow-up sham-surgery controlled double-blind trial showed no benefit [61]. The glutamic acid decarboxylase gene has also been delivered using an AAV vector, with improvement in the UPDRS motor score being reported at

6 months compared with a sham-surgery group [62], which persisted at 12 months [63].

5 Requirements for a Regenerative Therapy

As discussed, the past few decades have seen significant progress towards a clinically useful regenerative therapy for PD. Some of the experimental techniques have shown initial promise in pre-clinical and early clinical trials but have failed to live up to expectations in larger studies. Others, such as foetal midbrain grafts, appear to be effective in appropriately selected patients but are not likely to be clinically useful for logistical and ethical reasons. A number of criteria must therefore be met before a regenerative therapy is to be useful.

First, any potential future regenerative therapy must produce significant clinical benefit in the patient. With the aforementioned cell-based treatments, this relies on delivery of an adequate number of dopaminergic neuron precursors into the striatum. The graft must have a high purity of dopaminergic cells and must receive signals from the host brain so that dopamine is released in a physiological manner. Grafted cells must extend axons across sufficient distances to innervate the recipient striatum. Additionally, the grafted cells must survive for years for the patient to gain maximal benefit during the course of their disease. This includes avoiding rejection from the host immune system and avoiding acquisition of pathology following grafting. Gene-delivery techniques must result in acquisition of dopamine-producing potential in a sufficient number of striatal cells to restore dopaminergic tone. As with potential cell-grafting therapies, the target cells of gene-delivery treatments must avoid acquisition of PD pathology, at least for a number of years, to provide significant clinical benefit. It is also important that these therapies do not result in significant extra-striatal dopamine release, in order to retain the theoretical advantage over levodopa therapy. Finally, the cell transplants must be free of a significant number of cells that could mediate adverse effects, such as the serotonergic neurons that may have been responsible for the graft-induced dyskinesias seen in some recipients of human foetal mesencephalon transplants [64, 65].

The second important consideration with regard to the utility of future regenerative therapies is safety. These experimental treatments not only involve a neurosurgical procedure, which itself conveys risks of intracranial haemorrhage and infection as well as those associated with hospital admission, but are also associated with specific safety concerns that must be addressed before they approach the clinic. With regard to stem-cell-based treatments, the most significant concern is of potential tumour formation. Though tumour formation has not generally been seen in pre-clinical studies involving optimised reprogramming protocols, the risk of tumour formation after grafting into humans, in whom the graft will potentially be in situ for decades instead of the 1 or 2 years in a rodent or non-human primate, is unknown. Unpublished spike-in experiments in which pluripotent cells were intentionally included in the graft have shown that tumour formation from residual pluripotent cells occurs early and with high frequency, so one would perhaps expect that, if tumours are not observed over a 1-year period in a rodent, the risk of tumour formation from residual pluripotent cells would be non-existent.

In addition to the theoretical risk of tumour formation from residual stem cells, there is also potential for increased tumour risk due to acquisition of mutations in the grafted cells during cell culture, in which mutations that favour replication, or prevent apoptosis for example, provide a survival advantage over wild-type cells. For instance, it is clear that mutations in the tumour-suppressor molecule P53 occur during cell culture, albeit with low frequency [66]. The risk that this poses in terms of de novo tumour formation following grafting is unknown, particularly in view of the fact that mutations in these tumour-suppressor genes may require a second hit to herald neoplastic transformation. There is also doubt about the relevance of acquisition of oncogenic mutations that are associated with non-neuronal cancers, for example *BRCA1* mutations, which are strongly associated with breast cancer but are not seen in intracranial tumours. A planned Japanese clinical trial of iPSC-derived RPE cell transplants for age-related macular degeneration was halted after identification of a cancer-associated mutation in the cell product of the second patient [67]. Though there was no evidence of tumour formation with this cell product in animals, the risk that it posed to the potential recipient was difficult to interpret [68]. In view of this significant uncertainty about the implications of finding genetic abnormalities, the ways in which upcoming clinical trials will screen for genetic aberrations in graft products varies, where some may perform whole-genome sequencing, some may test for specific oncogenic mutations and some may test for karyotype anomalies only [69].

Delivery of genes using viral vectors is also associated with specific risks, and safety must be proven before the method can be adopted in the clinic. The use of integrating vectors such as lentiviruses and gammaretroviruses can lead to insertional mutagenesis, with risk of transformation in the transfected cell [70]. Given that lentivirus gene therapies such as ProSavin target post-mitotic cells, the risk of malignant transformation is thought to be low, with no evidence of insertional mutagenesis in pre-clinical studies [58]. Lentiviral vectors are of low immunogenicity, so the impact of an intracranial host inflammatory response against the virus or transfected cells is unlikely to be of clinical significance.

Third, any regenerative therapy must be ethically acceptable if it is to be employed widely [48]. While the use of foetal tissue is particularly ethically contentious, the potential future therapies discussed are generally considered to be less so and are probably acceptable to most societies. Therefore, ethical barriers are unlikely to be a considerable challenge, although issues still exist with the use of human ESC-derived products in some countries.

Additionally, for these regenerative therapies to be widely used, they will need to compete economically with current and other future treatments. In particular, these treatments will need to be comparable, in terms of both efficacy and cost, with deep-brain stimulation and levodopa intestinal gel (Duodopa), both of which target the motor features of PD while minimising motor adverse effects [71, 72]. Furthermore, trials of novel multimodal drugs such as safinamide have demonstrated positive effects on motor function, with no increase in dyskinesia, providing another potential alternative to the regenerative therapies discussed [73]. While the cost of future regenerative therapies will depend on as yet undetermined manufacturing and marketing influences, the ultimate cost is likely to be similar to that of levodopa therapy and deep-brain stimulation and less than the current cost of Duodopa treatment, given the highly efficient differentiation protocols that now exist for making midbrain dopamine neuroblasts.

Finally, a number of technical aspects must be addressed for any of these regenerative therapies to become widely useful. Procedures for freezing, storing and thawing cell-based and virus-based products must be optimised and robust and must not alter the properties of the treatment. Production of biological products must adhere to good manufacturing practice regulations, which may require adjustments to the neurosurgical theatres in which these treatments will be delivered. While many issues remain to be resolved, the focus of the field is now increasingly shifting towards answering questions about the practicalities of how these treatments can be delivered, which highlights the progress made over the past couple of decades.

6 Characteristics of Suitable Patient Populations for Regenerative Therapies

Clinical efficacy will depend on defining an appropriate patient population to target with regenerative therapies. It is becoming increasingly clear that PD encompasses a variety of clinical patterns, with some patients experiencing exclusively motor features and others being at high risk of developing cognitive decline and dementia [3]. Some patients may be more predisposed than others to the development of dyskinesias. The rate of functional decline differs considerably within the PD population. Regenerative therapies designed to increase striatal dopamine, and essentially replace the function of the nigral neurons that have already been lost, will theoretically be effective in patients whose predominant features are bradykinesia and rigidity. However, in patients with or at high risk of developing dementia, in whom the pathological correlate is more widespread Lewy body pathology and loss of extra-nigral neuronal populations [6], replenishing striatal dopamine will have limited effect on their clinical features. Although clinical markers of dementia risk are emerging, including tau haplotype and performance on specific cognitive tasks, the success of regenerative therapies will partly be determined by the ability to accurately determine which patients are likely to benefit from these approaches [74].

One of the safety issues that arose in the randomised clinical trials of human foetal mesencephalon grafting was the high incidence of disabling graft-induced dyskinesias [29, 30]. However, graft recipients with pre-existing drug-induced dyskinesias were not excluded from these trials, and it is felt that appropriate selection of patients for future cell-based therapy trials, along with the use of cell products of increased purity and optimised grafting protocols, will circumvent this risk. However, exclusion of those with established pre-existing drug-induced dyskinesias will prevent the use of these approaches in a significant proportion of patients with PD, and further work will be necessary to determine the population in which regenerative therapies can be used safely. An increase in dyskinesias was also observed in the ProSavin trial, which highlights the need to determine the optimal approach for striatal dopamine delivery before these techniques are used widely [58].

7 Future Perspectives

Since the first reports of the isolation and culturing of human ESCs two decades ago, progress towards a stem-cell-based therapy that could be trialled in PD has been steady. This has warranted extensive in vitro optimisation of reprogramming protocols as well as in vivo pre-clinical studies, which are ongoing. Many challenges have been overcome, including unexpected findings in neurodevelopmental biology, and the first in-human trials of stem cell-derived dopaminergic neuron precursors are now on the horizon.

Trials of ESC-derived dopaminergic neuron precursors are due to commence in the USA and in Europe over the next 2 years [64]. Additionally, a study of ESC-derived neural precursor cells, sponsored by the Chinese Academy of Sciences (https://clinicaltrials.gov/ct2/show/NCT03119636), is currently in the recruitment phase. In Japan, trials of allogenic iPSC-derived neurons and autologous iPSC-derived neurons are expected to commence next year [69]. These trials will provide feasibility and tolerability

data for stem-cell-derived treatments and early data about their clinical effectiveness. A follow-up trial of ProSavin in which an optimised gene-therapy product is to be investigated, is also due to commence in 2018.

Viral-mediated direct conversion of somatic cells (e.g. fibroblasts) to generate induced neurons also offers a potential source of dopaminergic neurons that could serve as a platform for a cell-based treatment for PD. This is a relatively novel technique, first described in 2010, that has a potential advantage over stem-cell-based therapies in that there is no stem cell phase during reprogramming, theoretically reducing the risk of tumour formation [75]. However, it has not yet been possible to generate high purities of dopaminergic neurons, and the potential number of neurons produced is limited by the number of available somatic cells, which is in contrast to the renewable supply of neurons that can be derived from ESCs and iPSCs. Therefore, induced neurons do not currently offer a realistic approach to a useful cell-based therapy. One interesting concept associated with this direct conversion approach is the ability to generate dopaminergic neurons through in vivo reprogramming of host astrocytes [76]. While this technique is a long way from being thought of as a potential therapeutic approach for PD, if safety can be demonstrated and pure dopaminergic neuronal yields can be achieved, it may be considered for further investigation in the future.

In addition to the experimental regenerative approaches discussed, there is also much interest in the development of therapies that could potentially slow or arrest disease progression. These putative treatments are designed to reduce the presence of aggregated alpha-synuclein, for example with novel immunological agents or repurposed drugs that enhance protein clearance mechanisms [77]. With a number of potential treatments currently in trials, the question is where will regenerative therapies fit into the future therapeutic approach to PD? While it is possible that these alpha-synuclein-reducing therapies may slow the progression of the motor and even the cognitive aspects of PD, they will not restore the function of neurons that have already been lost. Given that significant neuronal loss occurs before the clinical diagnosis of PD, even with disease-modifying treatments, many patients will still experience functional impairments due to the neuronal degeneration that occurs in the prodromal and pre-diagnosis stage of disease. The regenerative therapies discussed in this review aim to replace the function of the lost dopaminergic neurons, potentially restoring motor function to the pre-morbid level, without the problematic adverse effects seen with current dopaminergic drugs. One could therefore envisage a landscape in which regenerative therapies are used to restore motor function in patients who have already accrued motor disability, in combination with alpha-synuclein-reduction treatments to prevent disease progression, particularly in individuals at greater risk of cognitive symptoms.

8 Concluding Remarks

Since the early grafting trials for PD in the 1980s, significant progress has now been made towards effective and deliverable cell-based and gene-delivery therapies for the motor disorder of PD. Over the coming decade, these treatments will be investigated in the clinic, and it now seems likely that regenerative therapies will have a role in the management of PD in the medium-term future. Since the introduction of levodopa in the 1960s, significant advances in the treatment of PD have been few, but the regenerative approaches discussed in this review, in combination with the emerging potentially disease-modifying approaches, provide optimism for the future of regenerative treatments for PD.

Acknowledgements The authors acknowledge financial support from the following organisations: Medical Research Council, Wellcome Trust Stem Cell Institute (Cambridge), National Institute for Health Research Biomedical Research Centre and the Cure Parkinson's Trust.

Compliance with Ethical Standards

Funding No funding was received for the preparation of this review.

Conflict of interest TB Stoker and RA Barker have no conflicts of interest.

References

1. Kalia LV, Lang AE. Parkinson's disease. Lancet. 2015;386(9996):896–912.
2. Khoo TK, Yarnall AJ, Duncan GW, Coleman S, O'Brien JT, Brooks DJ, et al. The spectrum of nonmotor symptoms in early Parkinson disease. Neurology. 2013;80(3):276–81.
3. Williams-Gray CH, Mason SL, Evans JR, Foltynie T, Brayne C, Robbins TW, et al. The CamPaIGN study of Parkinson's disease: 10-year outlook in an incident population-based cohort. J Neurol Neurosurg Psychiatry. 2013;84(11):1258–64.
4. Spillantini MG, Schmidt ML, Lee VM, Trojanowski JQ, Jakes R, Goedert M. Alpha-synuclein in Lewy bodies. Nature. 1997;388(6645):839–40.
5. Dickson DW. Parkinson's disease and parkinsonism: neuropathology. Cold Spring Harb Perspect Med. 2012;2(8):a009258.
6. Selikhova M, Williams DR, Kempster PA, Holton JL, Revesz T, Lees AJ. A clinico-pathological study of subtypes in Parkinson's disease. Brain. 2009;132(Pt 11):2947–57.
7. Jenner P. Dopamine agonists, receptor selectivity and dyskinesia induction in Parkinson's disease. Curr Opin Neurol. 2003;16(Suppl 1):S3–7.
8. Huot P, Johnston TH, Koprich JB, Fox SH, Brotchie JM. The pharmacology of L-DOPA-induced dyskinesia in Parkinson's disease. Pharmacol Rev. 2013;65(1):171–222.
9. Nutt JG. On-off phenomenon: relation to levodopa pharmacokinetics and pharmacodynamics. Ann Neurol. 1987;22(4):535–40.

10. Noyce AJ, Bestwick JP, Silveira-Moriyama L, Hawkes CH, Giovannoni G, Lees AJ, et al. Meta-analysis of early nonmotor features and risk factors for Parkinson disease. Ann Neurol. 2012;72(6):893–901.
11. Postuma RB, Aarsland D, Barone P, Burn DJ, Hawkes CH, Oertel W, et al. Identifying prodromal Parkinson's disease: pre-motor disorders in Parkinson's disease. Mov Disord. 2012;27(5):617–26.
12. Kordower JH, Olanow CW, Dodiya HB, Chu Y, Beach TG, Adler CH, et al. Disease duration and the integrity of the nigrostriatal system in Parkinson's disease. Brain. 2013;136(Pt 8):2419–31.
13. Madrazo I, Drucker-Colín R, Díaz V, Martínez-Mata J, Torres C, Becerril JJ. Open microsurgical autograft of adrenal medulla to the right caudate nucleus in two patients with intractable Parkinson's disease. N Engl J Med. 1987;316(14):831–4.
14. Backlund EO, Granberg PO, Hamberger B, Knutsson E, Mårtensson A, Sedvall G, et al. Transplantation of adrenal medullary tissue to striatum in parkinsonism. First clinical trials. J Neurosurg. 1985;62(2):169–73.
15. Allen GS, Burns RS, Tulipan NB, Parker RA. Adrenal medullary transplantation to the caudate nucleus in Parkinson's disease. Initial clinical results in 18 patients. Arch Neurol. 1989;46(5):487–91.
16. Drucker-Colín R, Madrazo I, Ostrosky-Solís F, Shkurovich M, Franco R, Torres C. Adrenal medullary tissue transplants in the caudate nucleus of Parkinson's patients. Prog Brain Res. 1988;78:567–74.
17. Goetz CG, Tanner CM, Penn RD, Stebbins GT, Gilley DW, Shannon KM, et al. Adrenal medullary transplant to the striatum of patients with advanced Parkinson's disease: 1-year motor and psychomotor data. Neurology. 1990;40(2):273–6.
18. Jankovic J, Grossman R, Goodman C, Pirozzolo F, Schneider L, Zhu Z, et al. Clinical, biochemical, and neuropathologic findings following transplantation of adrenal medulla to the caudate nucleus for treatment of Parkinson's disease. Neurology. 1989;39(9):1227–34.
19. Kelly PJ, Ahlskog JE, van Heerden JA, Carmichael SW, Stoddard SL, Bell GN. Adrenal medullary autograft transplantation into the striatum of patients with Parkinson's disease. Mayo Clin Proc. 1989;64(3):282–90.
20. Jiao SS, Zhang WC, Cao JK, Zhang ZM, Wang H, Ding MC, et al. Study of adrenal medullary tissue transplantation to striatum in parkinsonism. Prog Brain Res. 1988;78:575–80.
21. Goetz CG, Stebbins GT, Klawans HL, Koller WC, Grossman RG, Bakay RA, et al. United Parkinson Foundation Neurotransplantation Registry on adrenal medullary transplants: presurgical, and 1- and 2-year follow-up. Neurology. 1991;41(11):1719–22.
22. Waters C, Itabashi HH, Apuzzo ML, Weiner LP. Adrenal to caudate transplantation–postmortem study. Mov Disord. 1990;5(3):248–50.
23. Lindvall O, Rehncrona S, Brundin P, Gustavii B, Astedt B, Widner H, et al. Human fetal dopamine neurons grafted into the striatum in two patients with severe Parkinson's disease. A detailed account of methodology and a 6-month follow-up. Arch Neurol. 1989;46(6):615–31.
24. Lindvall O, Brundin P, Widner H, Rehncrona S, Gustavii B, Frackowiak R, et al. Grafts of fetal dopamine neurons survive and improve motor function in Parkinson's disease. Science. 1990;247(4942):574–7.
25. Wenning GK, Odin P, Morrish P, Rehncrona S, Widner H, Brundin P, et al. Short- and long-term survival and function of unilateral intrastriatal dopaminergic grafts in Parkinson's disease. Ann Neurol. 1997;42(1):95–107.
26. Brundin P, Pogarell O, Hagell P, Piccini P, Widner H, Schrag A, et al. Bilateral caudate and putamen grafts of embryonic mesencephalic tissue treated with lazaroids in Parkinson's disease. Brain. 2000;123(Pt 7):1380–90.
27. Lindvall O, Sawle G, Widner H, Rothwell JC, Björklund A, Brooks D, et al. Evidence for long-term survival and function of dopaminergic grafts in progressive Parkinson's disease. Ann Neurol. 1994;35(2):172–80.
28. Li W, Englund E, Widner H, Mattsson B, van Westen D, Lätt J, et al. Extensive graft-derived dopaminergic innervation is maintained 24 years after transplantation in the degenerating parkinsonian brain. Proc Natl Acad Sci USA. 2016;113(23):6544–9.
29. Freed CR, Greene PE, Breeze RE, Tsai WY, DuMouchel W, Kao R, et al. Transplantation of embryonic dopamine neurons for severe Parkinson's disease. N Engl J Med. 2001;344(10):710–9.
30. Olanow CW, Goetz CG, Kordower JH, Stoessl AJ, Sossi V, Brin MF, et al. A double-blind controlled trial of bilateral fetal nigral transplantation in Parkinson's disease. Ann Neurol. 2003;54(3):403–14.
31. Gross RE, Watts RL, Hauser RA, Bakay RA, Reichmann H, von Kummer R, et al. Intrastriatal transplantation of microcarrier-bound human retinal pigment epithelial cells versus sham surgery in patients with advanced Parkinson's disease: a double-blind, randomised, controlled trial. Lancet Neurol. 2011;10(6):509–19.
32. Arjona V, Mínguez-Castellanos A, Montoro RJ, Ortega A, Escamilla F, Toledo-Aral JJ, et al. Autotransplantation of human carotid body cell aggregates for treatment of Parkinson's disease. Neurosurgery. 2003;53(2):321–8 (discussion 8-30).
33. Mínguez-Castellanos A, Escamilla-Sevilla F, Hotton GR, Toledo-Aral JJ, Ortega-Moreno A, Méndez-Ferrer S, et al. Carotid body autotransplantation in Parkinson disease: a clinical and positron emission tomography study. J Neurol Neurosurg Psychiatry. 2007;78(8):825–31.
34. Schumacher JM, Ellias SA, Palmer EP, Kott HS, Dinsmore J, Dempsey PK, et al. Transplantation of embryonic porcine mesencephalic tissue in patients with PD. Neurology. 2000;54(5):1042–50.
35. Gash DM, Zhang Z, Ovadia A, Cass WA, Yi A, Simmerman L, et al. Functional recovery in parkinsonian monkeys treated with GDNF. Nature. 1996;380(6571):252–5.
36. Stoker TB, Blair NF, Barker RA. Neural grafting for Parkinson's disease: challenges and prospects. Neural Regen Res. 2017;12(3):389–92.
37. Thomson JA, Itskovitz-Eldor J, Shapiro SS, Waknitz MA, Swiergiel JJ, Marshall VS, et al. Embryonic stem cell lines derived from human blastocysts. Science. 1998;282(5391):1145–7.
38. Kriks S, Shim JW, Piao J, Ganat YM, Wakeman DR, Xie Z, et al. Dopamine neurons derived from human ES cells efficiently engraft in animal models of Parkinson's disease. Nature. 2011;480(7378):547–51.
39. Brederlau A, Correia AS, Anisimov SV, Elmi M, Paul G, Roybon L, et al. Transplantation of human embryonic stem cell-derived cells to a rat model of Parkinson's disease: effect of in vitro differentiation on graft survival and teratoma formation. Stem Cells. 2006;24(6):1433–40.
40. Park CH, Minn YK, Lee JY, Choi DH, Chang MY, Shim JW, et al. In vitro and in vivo analyses of human embryonic stem cell-derived dopamine neurons. J Neurochem. 2005;92(5):1265–76.
41. Roy NS, Cleren C, Singh SK, Yang L, Beal MF, Goldman SA. Functional engraftment of human ES cell-derived dopaminergic neurons enriched by coculture with telomerase-immortalized midbrain astrocytes. Nat Med. 2006;12(11):1259–68.
42. Grealish S, Diguet E, Kirkeby A, Mattsson B, Heuer A, Bramoulle Y, et al. Human ESC-derived dopamine neurons show similar preclinical efficacy and potency to fetal neurons when grafted in a rat model of Parkinson's disease. Cell Stem Cell. 2014;15(5):653–65.
43. Kirkeby A, Nolbrant S, Tiklova K, Heuer A, Kee N, Cardoso T, et al. Predictive markers guide differentiation to improve graft outcome in clinical translation of hESC-based therapy for Parkinson's Disease. Cell Stem Cell. 2017;20(1):135–48.

44. Takahashi K, Tanabe K, Ohnuki M, Narita M, Ichisaka T, Tomoda K, et al. Induction of pluripotent stem cells from adult human fibroblasts by defined factors. Cell. 2007;131(5):861–72.
45. Takahashi K, Okita K, Nakagawa M, Yamanaka S. Induction of pluripotent stem cells from fibroblast cultures. Nat Protoc. 2007;2(12):3081–9.
46. Soldner F, Hockemeyer D, Beard C, Gao Q, Bell GW, Cook EG, et al. Parkinson's disease patient-derived induced pluripotent stem cells free of viral reprogramming factors. Cell. 2009;136(5):964–77.
47. Kikuchi T, Morizane A, Doi D, Magotani H, Onoe H, Hayashi T, et al. Human iPS cell-derived dopaminergic neurons function in a primate Parkinson's disease model. Nature. 2017;548(7669):592–6.
48. Barker RA, de Beaufort I. Scientific and ethical issues related to stem cell research and interventions in neurodegenerative disorders of the brain. Prog Neurobiol. 2013;110:63–73.
49. Taylor CJ, Peacock S, Chaudhry AN, Bradley JA, Bolton EM. Generating an iPSC bank for HLA-matched tissue transplantation based on known donor and recipient HLA types. Cell Stem Cell. 2012;11(2):147–52.
50. Sonntag KC, Pruszak J, Yoshizaki T, van Arensbergen J, Sanchez-Pernaute R, Isacson O. Enhanced yield of neuroepithelial precursors and midbrain-like dopaminergic neurons from human embryonic stem cells using the bone morphogenic protein antagonist noggin. Stem Cells. 2007;25(2):411–8.
51. Offen D, Barhum Y, Levy YS, Burshtein A, Panet H, Cherlow T, Melamed E. Intrastriatal transplantation of mouse bone marrow-derived stem cells improves motor behavior in a mouse model of Parkinson's disease. J Neural Transm Suppl. 2007;72:133–43.
52. Barker RA, Drouin-Ouellet J, Parmar M. Cell-based therapies for Parkinson disease—past insights and future potential. Nat Rev Neurol. 2015;11(9):492–503.
53. Delcroix GJ, Garbayo E, Sindji L, Thomas O, Vanpouille-Box C, Schiller PC, et al. The therapeutic potential of human multipotent mesenchymal stromal cells combined with pharmacologically active microcarriers transplanted in hemi-parkinsonian rats. Biomaterials. 2011;32(6):1560–73.
54. Kim YJ, Park HJ, Lee G, Bang OY, Ahn YH, Joe E, Kim HO, Lee PH. Neuroprotective effects of human mesenchymal stem cells on dopaminergic neurons through anti-inflammatory action. Glia. 2009;57(1):13–23.
55. Venkataramana NK, Kumar SK, Balaraju S, Radhakrishnan RC, Bansal A, Dixit A, et al. Open-labeled study of unilateral autologous bone-marrow-derived mesenchymal stem cell transplantation in Parkinson's disease. Transl Res. 2010;155(2):62–70.
56. Christine CW, Starr PA, Larson PS, Eberling JL, Jagust WJ, Hawkins RA, et al. Safety and tolerability of putaminal AADC gene therapy for Parkinson disease. Neurology. 2009;73(20):1662–9.
57. Muramatsu S, Fujimoto K, Kato S, Mizukami H, Asari S, Ikeguchi K, et al. A phase I study of aromatic L-amino acid decarboxylase gene therapy for Parkinson's disease. Mol Ther. 2010;18(9):1731–5.
58. Palfi S, Gurruchaga JM, Ralph GS, Lepetit H, Lavisse S, Buttery PC, et al. Long-term safety and tolerability of ProSavin, a lentiviral vector-based gene therapy for Parkinson's disease: a dose escalation, open-label, phase 1/2 trial. Lancet. 2014;383(9923):1138–46.
59. Kaplitt MG, Feigin A, Tang C, Fitzsimons HL, Mattis P, Lawlor PA, et al. Safety and tolerability of gene therapy with an adeno-associated virus (AAV) borne GAD gene for Parkinson's disease: an open label, phase I trial. Lancet. 2007;369(9579):2097–105.
60. Marks WJ, Ostrem JL, Verhagen L, Starr PA, Larson PS, Bakay RA, et al. Safety and tolerability of intraputaminal delivery of CERE-120 (adeno-associated virus serotype 2-neurturin) to patients with idiopathic Parkinson's disease: an open-label, phase I trial. Lancet Neurol. 2008;7(5):400–8.
61. Marks WJ, Bartus RT, Siffert J, Davis CS, Lozano A, Boulis N, et al. Gene delivery of AAV2-neurturin for Parkinson's disease: a double-blind, randomised, controlled trial. Lancet Neurol. 2010;9(12):1164–72.
62. LeWitt PA, Rezai AR, Leehey MA, Ojemann SG, Flaherty AW, Eskandar EN, et al. AAV2-GAD gene therapy for advanced Parkinson's disease: a double-blind, sham-surgery controlled, randomised trial. Lancet Neurol. 2011;10(4):309–19.
63. Niethammer M, Tang CC, LeWitt PA, Rezai AR, Leehey MA, Ojemann SG, et al. Long-term follow-up of a randomized AAV2-. JCI Insight. 2017;2(7):e90133.
64. Politis M, Wu K, Loane C, Quinn NP, Brooks DJ, Rehncrona S, et al. Serotonergic neurons mediate dyskinesia side effects in Parkinson's patients with neural transplants. Sci Transl Med. 2010;2(38):38ra46.
65. Politis M, Oertel WH, Wu K, Quinn NP, Pogarell O, Brooks DJ, et al. Graft-induced dyskinesias in Parkinson's disease: High striatal serotonin/dopamine transporter ratio. Mov Disord. 2011;26(11):1997–2003.
66. Merkle FT, Ghosh S, Kamitaki N, Mitchell J, Avior Y, Mello C, et al. Human pluripotent stem cells recurrently acquire and expand dominant negative P53 mutations. Nature. 2017;545(7653):229–33.
67. Garber K. RIKEN suspends first clinical trial involving induced pluripotent stem cells. Nat Biotechnol. 2015;33(9):890–1.
68. Blair NF, Barker RA. Making it personal: the prospects for autologous pluripotent stem cell-derived therapies. Regen Med. 2016;11(5):423–5.
69. Barker RA, Parmar M, Studer L, Takahashi J. Human Trials of stem cell-derived dopamine neurons for Parkinson's disease: dawn of a new era. Cell Stem Cell. 2017;21(5):569–73.
70. Mukherjee S, Thrasher AJ. Gene therapy for PIDs: progress, pitfalls and prospects. Gene. 2013;525(2):174–81.
71. Olanow CW, Kieburtz K, Odin P, Espay AJ, Standaert DG, Fernandez HH, et al. Continuous intrajejunal infusion of levodopa-carbidopa intestinal gel for patients with advanced Parkinson's disease: a randomised, controlled, double-blind, double-dummy study. Lancet Neurol. 2014;13(2):141–9.
72. Kalia SK, Sankar T, Lozano AM. Deep brain stimulation for Parkinson's disease and other movement disorders. Curr Opin Neurol. 2013;26(4):374–80.
73. Borgohain R, Szasz J, Stanzione P, Meshram C, Bhatt M, Chirilineau D, et al. Randomized trial of safinamide add-on to levodopa in Parkinson's disease with motor fluctuations. Mov Disord. 2014;29(2):229–37.
74. Evans JR, Mason SL, Williams-Gray CH, Foltynie T, Brayne C, Robbins TW, et al. The natural history of treated Parkinson's disease in an incident, community based cohort. J Neurol Neurosurg Psychiatry. 2011;82(10):1112–8.
75. Vierbuchen T, Ostermeier A, Pang ZP, Kokubu Y, Südhof TC, Wernig M. Direct conversion of fibroblasts to functional neurons by defined factors. Nature. 2010;463(7284):1035–41.
76. di Val Rivetti, Cervo P, Romanov RA, Spigolon G, Masini D, Martín-Montañez E, Toledo EM, et al. Induction of functional dopamine neurons from human astrocytes in vitro and mouse astrocytes in a Parkinson's disease model. Nat Biotechnol. 2017;35(5):444–52.
77. Brundin P, Dave KD, Kordower JH. Therapeutic approaches to target alpha-synuclein pathology. Exp Neurol. 2017;298(Pt B):225–35.

AMERICAN SOCIETY FOR MICROBIOLOGY | Journal of Virology®

STRUCTURE AND ASSEMBLY

Mapping and Engineering Functional Domains of the Assembly-Activating Protein of Adeno-associated Viruses

Longping V. Tse,[a] Sven Moller-Tank,[a] Rita M. Meganck,[a,b] Aravind Asokan[a,b,c]

[a]Gene Therapy Center, The University of North Carolina at Chapel Hill, Chapel Hill, North Carolina, USA
[b]Department of Genetics, The University of North Carolina at Chapel Hill, Chapel Hill, North Carolina, USA
[c]Department of Biochemistry and Biophysics, The University of North Carolina at Chapel Hill, Chapel Hill, North Carolina, USA

ABSTRACT Adeno-associated viruses (AAVs) encode a unique assembly-activating protein (AAP) within their genomes that is essential for capsid assembly. Studies to date have focused on establishing the role of AAP as a chaperone that mediates the stability, nucleolar transport, and assembly of AAV capsid proteins. Here, we map structure-function correlates of AAP using secondary structure analysis, followed by deletion and substitutional mutagenesis of specific domains, namely, the N-terminal hydrophobic region (HR), conserved core (CC), proline-rich region (PRR), threonine/serine-rich region (T/S), and basic region (BR). First, we establish that the centrally located PRR and T/S are flexible linker domains that can either be deleted completely or replaced by heterologous functional domains that enable ancillary functions such as fluorescent imaging or increased AAP stability. We also demonstrate that the C-terminal BR domains can be substituted with heterologous nuclear or nucleolar localization sequences that display various abilities to support AAV capsid assembly. Further, by replacing the BR domain with immunoglobulin (IgG) Fc domains, we assessed AAP complexation with AAV capsid subunits and demonstrate that the hydrophobic region (HR) and the conserved core (CC) in the AAP N terminus are the sole determinants for viral protein (VP) recognition. However, VP recognition alone is not sufficient for capsid assembly. Our study sheds light on the modular structure-function correlates of AAP and provides multiple approaches to engineer AAP that might prove useful toward understanding and controlling AAV capsid assembly.

IMPORTANCE Adeno-associated viruses (AAVs) encode a unique assembly-activating protein (AAP) within their genomes that is essential for capsid assembly. Understanding how AAP acts as a chaperone for viral assembly could help improve efficiency and potentially control this process. Our studies reveal that AAP has a modular architecture, with each module playing a distinct role and can be engineered for carrying out new functions.

KEYWORDS adeno-associated virus, assembly-activating protein, capsid assembly, chaperones, gene therapy, nucleolus, scaffold

Adeno-associated virus (AAV) is a nonenveloped, single-stranded DNA virus belonging to the *Dependoparvovirus* genus within the *Parvoviridae* family (1). The AAV capsid consists of 60 capsid monomers of VP1, VP2, and VP3 at a ratio of 1:1:10 that packages a 4.7-kb single-stranded genome (2, 3). The AAV genome encodes replication (*Rep*), capsid (*Cap*), and assembly-activating protein (*AAP*) open reading frames (ORFs) flanked by inverted terminal repeats (ITRs), which are the sole requirements for genome packaging (4, 5). As such, the majority of the genome can be replaced by exogenous DNA sequences and packaged inside the AAV capsid to create a recombinant vector for DNA delivery both *in vitro* and *in vivo* (6). Unlike other viruses that are replication

Received 7 March 2018 **Accepted** 19 April 2018

Accepted manuscript posted online 25 April 2018

Citation Tse LV, Moller-Tank S, Meganck RM, Asokan A. 2018. Mapping and engineering functional domains of the assembly-activating protein of adeno-associated viruses. J Virol 92:e00393-18. https://doi.org/10.1128/JVI.00393-18.

Editor Lawrence Banks, International Centre for Genetic Engineering and Biotechnology

Copyright © 2018 American Society for Microbiology. All Rights Reserved.

Address correspondence to Aravind Asokan, aravind@med.unc.edu.

competent, AAVs are partially defective since they require a helper virus (such as adenovirus or herpes simplex virus) for replication (7). The lack of pathogenicity and ease of genome manipulation have enabled extensive evaluation of recombinant AAV vectors as candidates for clinical gene therapy (8).

AAV encodes a unique protein, AAP, which is not found in other autonomous parvoviruses and is required for AAV capsid assembly. AAP is predicted to be a 20- to 24-kDa protein, with an actual size ranging from 27 to 34 kDa, which may be due to posttranslational modifications (5, 9). AAP is encoded from a +1 frame within the *Cap* ORF overlapping the junction between VP2 and VP3 (5). Introduction of a stop codon within AAP without affecting the coding frame of VP2/3 prevents capsid assembly and virus/vector production (10). While capsid assembly can be restored by providing AAP *in trans*, overexpression of wild-type (WT) AAP does not increase the vector yield (10). This suggests that AAP is necessary and sufficient for capsid assembly but is not a limiting factor for vector production. Cellular localization of AAPs overlaps with the location of capsid assembly, supporting a direct role for AAP (11). Most AAPs show strong nucleolar localization, while AAP5 and AAP9 are predominantly nuclear and excluded from the nucleolus (9, 12). Although the exact mechanism by which AAP supports AAV assembly is still elusive, several studies have convincingly shown that AAP is important for intracellular capsid expression and localization.

For instance, the steady-state level of capsid is dramatically reduced in the absence of AAP (13). Such regulation must occur at the translational or posttranslational level as *Cap* mRNA expression remains the same regardless of the presence or absence of AAP (10). In addition, the AAV2 VP have been shown to change their cellular localization from cytoplasmic/nuclear to nucleolar in the presence of AAP2 (12). A previous study has shown that the N-terminal region of AAP might interact with the C terminus of the VP, albeit weakly (13). Interaction with AAP2 also appears to alter VP conformation as supported by the lack of binding to several conformational specific antibodies (13). All of the above observations support the notion that AAP2 acts as a chaperone to stabilize and translocate VP to the site of assembly. However, it should be noted that significant differences in cellular localization and cross-complementation have been reported (9).

AAPs encoded by different serotypes are closely related, with sequence identity ranging from 48% (AAV4) to 82% (AAV7) relative to AAP1 (11). Phylogenetic analysis of AAP shows the same relationships as AAV VP, where the serotypes 4, 5, 11, and 12 are distinct from the others (11). The phylogenetic distance is also reflected in the biology of AAP4, -5, -11, and -12, which are unable to complement capsid assembly of other AAV serotypes (9). Furthermore, in the absence of AAP, AAV4, AAV5, and AAV11 are capable of producing 20 to 40% of AAV particles compared to the WT level; these have been termed "AAP independent" (9). At the secondary structure level, using previously defined nomenclature, AAP can be separated into multiple functional regions, N to C terminus: the hydrophobic region (HR), the conserved core (CC), the proline-rich region (PRR), the threonine/serine-rich region (T/S), and the basic region (BR) (13). In the present study, we undertake a systematic dissection of these different domains and generate novel chimeric and artificial AAPs that shed light on the structure-function correlates of this unique viral assembly protein.

RESULTS

The T/S of AAP is a flexible linker that can be replaced by different structures. In order to study AAP independent of the VP ORF, we generated an AAP-null construct by introducing a stop codon early in the AAP ORF without affecting the VP coding sequence and provided different AAP constructs *in-trans* driven by the CMV promoter (Fig. 1A and Table 1). A series of deletion mutants were generated based on AAP domains and tested for the function of AAP using four parameters: steady-state AAP levels, VP levels, vector yield, and transduction efficiency. All AAP constructs have a C9 tag derived from bovine rhodopsin at the C terminus for immunodetection (Fig. 1B). In brief, experiments were performed by transfecting pXX680, pTR-CBA-Luc, pXR1ΔAAP, and a pCDNA3.1-AAP construct into HEK293 cells. All deletion and T/S replacement

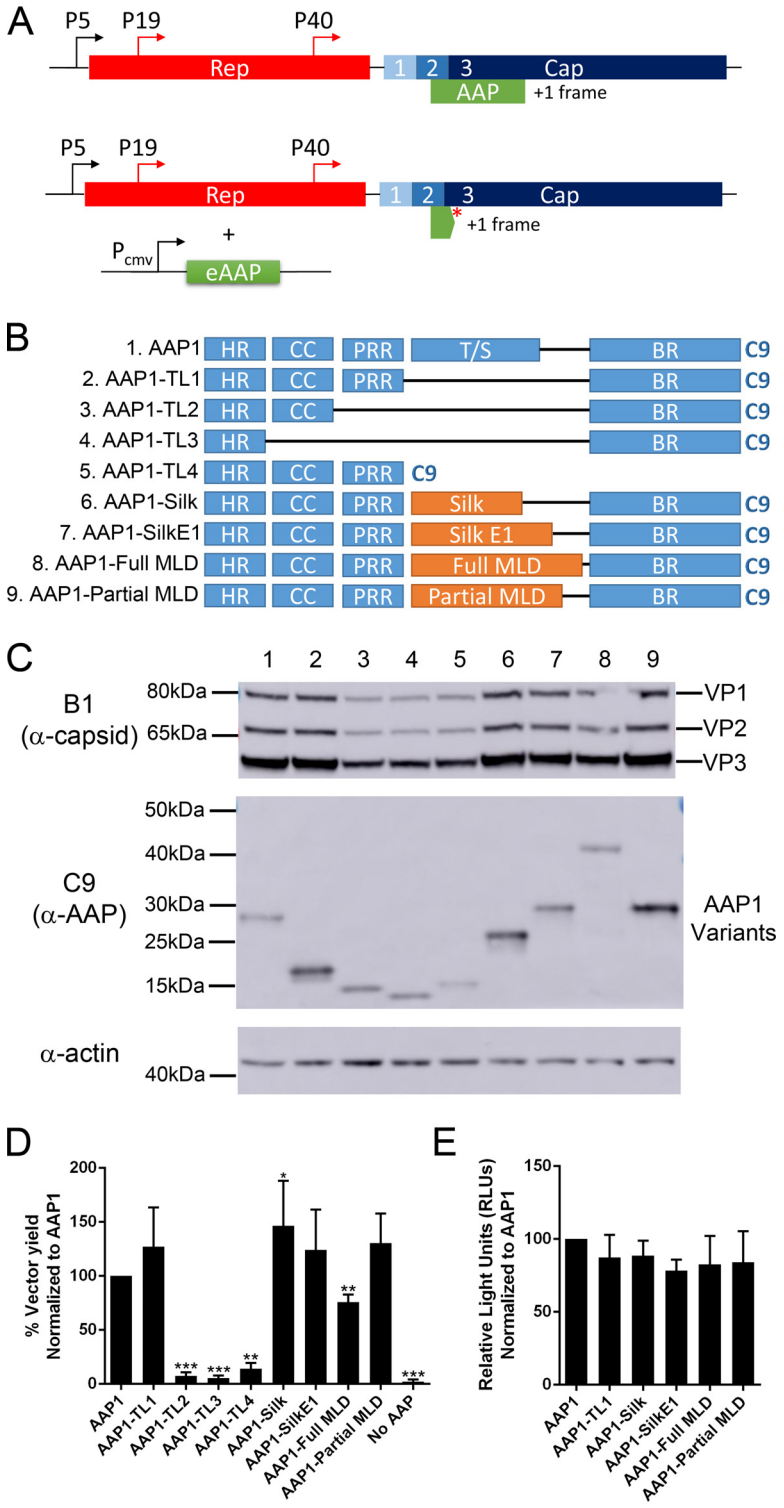


FIG 1 The threonine/serine-rich region (T/S) can be deleted or replaced by heterologous sequences without compromising AAP functions. (A) Original AAV genome showing *Rep* and *Cap* genes with AAP encoded in an alternative reading frame (top) and modified AAV genome with a stop codon that truncates endogenous AAP, with eAAP plasmid provided in *trans* (bottom). (B) Different AAP mutants, truncated linkers 1 to 4 (TL1 to TL4) have different internal regions deleted. For others, the T/S was replaced with *Bombyx mori* silk heavy chain repeats (Silk and SilkE1) or the entire (Full MLD) or partial (Partial MLD) mucin-like domains from murine alpha dystroglycan mucin-like domain. All AAP1 constructs have a C9 epitope tag at the C terminus for immunodetection. (C) Representative Western blot image of VPs, AAPs, and actin expression level in HEK293 cells transfected by quadruple transfection for rAAV production at 3 days posttransfection. (D) Relative vector yield of different AAP mutants normalized

(Continued on next page)

TABLE 1 Amino acid sequences of different T/S and BR module replacement constructs

Construct[a]	Amino acid sequence (5′–3′)
T/S replacements	
Silk (14)	GAGAGAGQGAGAGAGQGAAAGAGAGAGQT
Silk E1 (14)	GAGAGQGAGAGAGQGAAAGAGAGAGQGAGAGAGQGAGAGAGQGAAG AGAGAGQT
Full MLD (15)	PTPVTAIGPPTTAIQEPPSRIVPTPTSPAIAPPTETMAPPVRDPVPGKPTVTIRTR GAIIQTPTLGPIQPTRVSEAGTTVPGQIRPTLTIPGYVEPTAVITPPTTTTKK PRVSTPKPATPSTDSSTTTTRRPTKKPRTPRPVPRVTTK
Partial MLD (15)	TLTIPGYVEPTAVITPPTTTTKKPRVSTPKPATPSTDSSTTTTRRPTKKPRTPRP VPRVTT
Collagen (21)	GSSGVRLWATRQAMLGQVHEVPEGWLIFVAEQEELYVRVQNGFRKVQLE ARTPLPR
Tetramer (22)	AEIEQAKKEIAYLIKKAKEEILEEIKKAKQEIA
WSN	KRMENLNKKVDDGFLDIWTYNAELLVLLENERTLDFHDLNVKNLYEKVKSQLK
BR replacements	
Rpp29 (16)	RHKRKEKKKKAKGLSARQRRELR
AP3D1 (17)	RRHRQKLEKDKRRKKRKEKEERTKGKKKSKK
SV40 (18, 19)	KRTADGSEFESPKKKRKVE
HIV Rev (20)	RQARRNRRRRWRERQR
4BR	STSRSRRSRRRTARQRWLITLPARFRSLRTRRTNCRT
5BR	STFKSKRSRCRTPPPPSPTTSPPPSKCLRTTTTSCPTSSATGPRDACRPSLRRS LRCRSTVTRR
9BR	STFRSKRLRTTMESRPSPITLPARSRSSRTQTISSRTCSGRLTRAASRRSQRTFS

[a]The numbers in parentheses indicate references for the sequences.

constructs produced AAP at different levels. Although truncated linker 2 (TL2), truncated linker 3 (TL3), and the T/S replaced with *Bombyx mori* silk heavy chain repeats (Silk and SilkE1) (14) or the entire mucin-like domain from murine alpha dystroglycan mucin-like domain (Full MLD) (15) showed similar steady levels of AAP, truncated linker 1 (TL1) and T/S replaced by partial mucin-like domain (Partial MLD) produce significantly more AAP. Truncated linker 4 (TL4) shows a reduced level of AAP expression (Fig. 1C and Table 2). Multiple reports have shown that one of the observable functions of AAP is to help stabilize the expression of VP; therefore, we next determined the steady-state VP level in the transfected cells. The level of VP3 correlates proportionally with AAP protein level, except for mutants TL2 and TL3, which have a significant reduction in VP3 level compared to WT AAP, although they produced similar amounts of AAP (Fig. 1C). Despite the production of both AAP and VP proteins in all condition tested, deletion of the HR, CC, or PRR rendered AAP incapable of supporting AAV capsid assembly (Fig. 1D and Table 2). However, deletion of the entire T/S or replacing the region with other flexible protein domains does not affect any tested function of AAP (including capsid assembly), strongly suggesting the T/S is nonessential for the assembly function of AAP (Fig. 1D and Table 2). The transduction efficiency of the recombinant AAV vectors produced using different AAP constructs were similar to control (Fig. 1E). Based on these findings, we concluded that the T/S can potentially be engineered with other heterologous sequences to generate engineered AAPs (eAAPs) with new functions.

The BR of AAP is not serotype specific. We first created a traceable AAP1 protein by replacing the T/S with enhanced green fluorescent protein (EGFP) to create AAP1-EGFP (AAP1E) for fluorescent tracking (Fig. 2A). This newly engineered AAP1E shows the same level of VP expression and capsid assembly, but a higher level of AAP expression compared to AAP1 (Fig. 2B, C, and E; Table 2). Furthermore, the AAP1E mutant localizes within the nucleolus similar to the WT AAP1, suggesting that AAP1E can be useful for

FIG 1 Legend (Continued)
to wild-type AAP1 (AAP1). (E) Transduction of rAAV1 packaging luciferase produced from different AAP1 mutants on HEK293 cells at 10,000 vg/cell. Relative light units (RLUs) were normalized to AAP1. Error bars represent one standard deviation from at least three independent experiments. The data were analyzed by a two-tailed Student *t* test compared to AAP1 (*, $P \leq 0.05$; **, $P \leq 0.01$; ***, $P \leq 0.001$; ****, $P \leq 0.0001$).

TABLE 2 Summary of biological properties of T/S and N-terminal constructs[a]

Construct[b]	AAP level	VP level	Vector yield	Interaction with VP
T/S region				
AAP1 WT	WT	WT	WT	Yes
TL1	++	WT	+	NA
TL2	WT	−	−−−	NA
TL3	WT	−	−−−	NA
TL4	−	−	−−−	NA
Silk	++	WT	+	NA
SilkE1	+	WT	+	NA
Full MLD	WT	−	WT	NA
Partial MLD	+++	WT	+	NA
AAP1E	++++	+	WT	Yes
AAP1-Collagen (21)	++++++	++	+++	NA
AAP1-Tetra (22)	+++++	+	+	NA
AAP1-WSN	++	WT	−	NA
N terminus				
AAP1 WT	WT	WT	WT	Yes
AAP1E	++++	+	WT	Yes
AAP5E	++++	− −	−−−	Yes
ΔHR	++++++	− −	−−−	No
5HR	++++	− −	−−−	Yes
ΔCC	++++	− −	−−−	No
5CC	+	−	− −	Yes
ΔPRR	++++	WT	− −	Yes
5PRR	WT	WT	WT	Yes

[a]WT represents similar properties, "−" represents reduced levels, and "+" represents increased levels compared to AAP1 WT. The numbers of "+" and "−" are proportional to the increase or decrease in expression levels or titer. NA, not applicable.
[b]The numbers in parentheses indicate references for the sequences.

further mechanistic studies (Fig. 2D). Using the AAP1E construct, we swapped the BR of AAP1E with the BR from AAP4, -5, and -9 (Fig. 2A and Table 1). The VP and AAP expression profiles of the BR substitution mutants are generally similar to AAP1E. However, 5BR and 9BR show a slight decrease in VP expression and 9BR shows a slight decrease in AAP expression (Fig. 2B and C; Table 3). Notably, BR1 and BR4 strongly localized to the nucleolus, while BR5 and BR9 only shows partial nucleolus localization as reported earlier (Fig. 2D and Table 3) (9). Intracellular localization appears to correlate with vector titers; for instance, BR5 and BR9 only restore about 50% of assembly (Fig. 2F and Table 3). In contrast, BR4 is able to restore AAP1 function to 120% compared to WT AAP1. The transduction efficiency of the rAAVs generated using different AAPs was not affected (Fig. 2F). Since it is known that AAP4 cannot rescue AAV1 capsid assembly, our data suggest that serotype-specific transcomplementation is not due to the BR but rather to other regions of AAP.

The BR of AAP1 can be replaced by other nucleolar localization signals (NoLS) without disrupting function. Based on the results presented above, we hypothesized that the BR can be replaced completely by other NoLS without affecting AAP function. Therefore, we engineered AAP1E by replacing the BR with other known nuclear or nucleolar localization signals (NLS/NoLS). The amino acid sequences and annotation of each NLS/NoLS are described in Table 1. In brief, we picked four different NLS/NoLS peptides from the RNase P subunit NoLS (Rpp29) (16), adaptor protein in AP-3 complex (AP3D1) (17), virus-derived simian virus 40 NLS (SV40) (18, 19), and HIV Rev NoLS domain (HIV Rev) (20) (Fig. 3A). Although AAP expression levels are comparable to AAP1E from all the BR replacement mutants, VP expression was moderately reduced for some (Fig. 3B and Table 3). This decrease correlates with assembly based on vector yield, where the various BR mutants show a spectrum of activity. SV40 is unable to restore AAP assembly function, while Rpp29, HIV-Rev, and AP3D1 restore AAP assembly function at 40, 50, and 80%, respectively (Fig. 3C and Table 3). All rAAVs generated with these constructs show similar transduction efficiencies (Fig. 3D). Since the NoLS/NLS

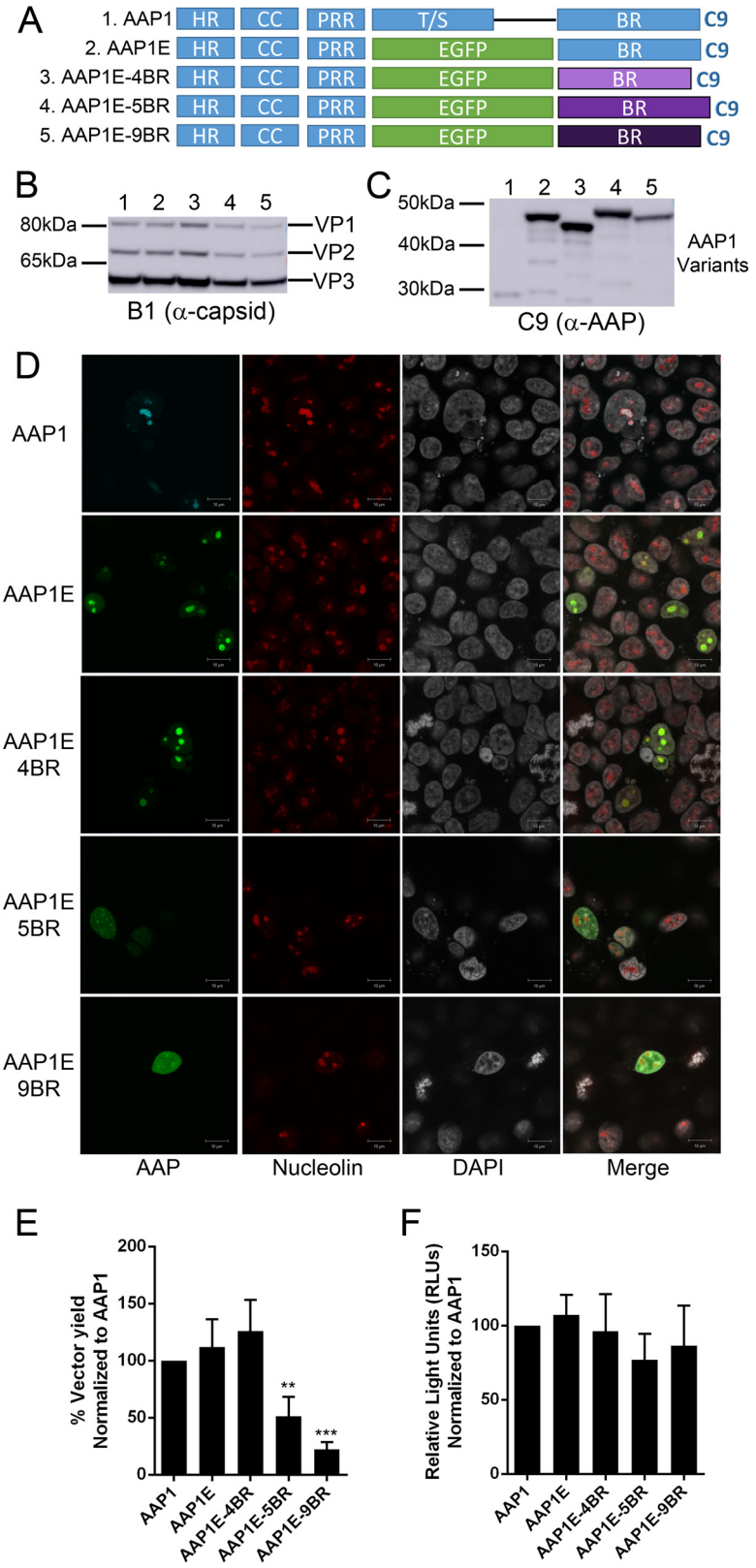


FIG 2 The BR is not the determinant for serotype specificity of AAV capsid assembly. (A) Schematic of different AAP mutants. The T/S of AAP1 was replaced by EGFP (AAP1E). The BR was replaced with those of other serotypes, including AAP4 (4BR), AAP5 (5BR), and AAP9 (9BR). (B and C) Representative Western blot images of VP (B) and AAP (C) expression as described in Fig. 1B. (D) Confocal microscopy of different AAP1E derivatives. AAP1E derivatives (pCDNA3.1-AAPs) were transfected as described in Materials and

(Continued on next page)

TABLE 3 Summary of biological properties of BR constructs[a]

BR construct	AAP level	VP level	Vector yield	AAP localization
AAP1 WT	WT	WT	WT	Nucleolus
DBR	++++	WT	− −	Cytoplasmic
4BR	+++++	+	+	Nucleolus
5BR	+++++	WT	−	Nucleus
9BR	+++	−	− −	Nucleus
Rpp29	++++	−	−	Nucleus/nucleolus
AP3D1	++++	WT	WT	Nucleolus
SV40	++++	+	− −	Nucleus
HIV Rev	++++	−	−	Nucleolus

[a]WT represents similar properties, "−" represents reduced levels, and "+" represents increased levels compared to AAP1 WT. The numbers of "+" and "−" are proportional to the increase or decrease in expression level or titer.

mutants showed a spectrum of AAP function, we performed confocal microscopy to investigate trafficking efficiency compared to AAP. AAP1E shows clear colocalization with the nucleolar marker CD23 (Fig. 4). AAP1E-ΔBR shows cytoplasmic localization, as expected, and is not able to restore function (Fig. 3C and 4). AAP1E-SV40 shows nuclear localization, which only partially rescues AAV assembly. AAP1E-Rpp29 shows moderate (40%) rescue of AAV assembly and has partial nucleolar localization (Fig. 3C and 4). HIV-Rev and AP3D1 show nucleolar localization, and AP3D1 restores assembly function completely (Fig. 3C and 4). Therefore, the ability of AAP to drive AAV1 assembly correlates with its nuclear/nucleolar localization, and the BR region can be replaced by other NoLS without affecting AAP function.

Functionally mapping the structural domains at the N terminus of AAP1E. Currently, there is no structural information on AAP. Based on a modular homology modeling, the N-terminal HR is the only region that can be modeled among all AAP tested and CC from AAP1, -6, -7, and -9 can be modeled. The HR is modeled as an alpha-helix, and the CC region is modeled as either a loop or a beta-strand. Deletion or point mutations in these regions completely abolish the ability of AAP to activate capsid assembly, suggesting that these secondary structures play an important role in AAP function. Furthermore, previous reports have shown that AAP5 is unable to support capsid assembly of AAV1, despite the sequence similarity between the PRR, the T/S, and the BR (9). We investigated the function of each subdomain by deletion analysis and by replacement with the corresponding domain of AAP5 (Fig. 5A). While all the constructs were able to produce AAP, the functional efficiencies were varied. The expression level of the AAP1EΔHR construct is higher than that of AAP1E; however, the level of VP is significantly reduced (Fig. 5B and Table 2). In addition, capsid formation is completely abrogated to background levels (Fig. 5C and Table 2). Replacing the AAP1 HR domain with the AAP5 HR domain shows a similar effect as the deletion, although the AAP expression level is only slightly increased compared to AAP1E (Fig. 5B and C; Table 2). Deletion of the CC region resulted in a similar phenotype, where the expression level of AAP was normal, but VP expression and capsid formation were reduced to the background level (Fig. 5B and C; Table 2). Replacing 1CC with 5CC domains restored the level of VP expression and 50% viral titer, suggesting a link between the CC region and capsid protein stability that is not serotype specific (Fig. 5B and C; Table 2). Deletion of the PRR shows a moderate effect on capsid expression and assembly. Replacing 1PRR with 5PRR only slightly affects AAP function and allows 75% viral yield (Fig. 5B and C; Table 2). All rAAVs generated with AAP show similar transduction efficiencies (Fig. 5D). Confocal microcopy studies further confirmed that the N-terminal modules localized at

FIG 2 Legend (Continued)
Methods and visualized by their native EGFP fluorescence. AAP1 was immunostained with α-C9 antibody, and nucleoli were immunostained with C23 antibody. Nuclei were stained with DAPI. (E) Relative vector yields using different AAP constructs normalized to wild-type AAP1 (AAP1). (F) Transduction of rAAV1 packaging luciferase produced from different AAP1 constructs as described above. RLUs were normalized to AAP1. Error bars were determined and statistical analyses were performed as described above.

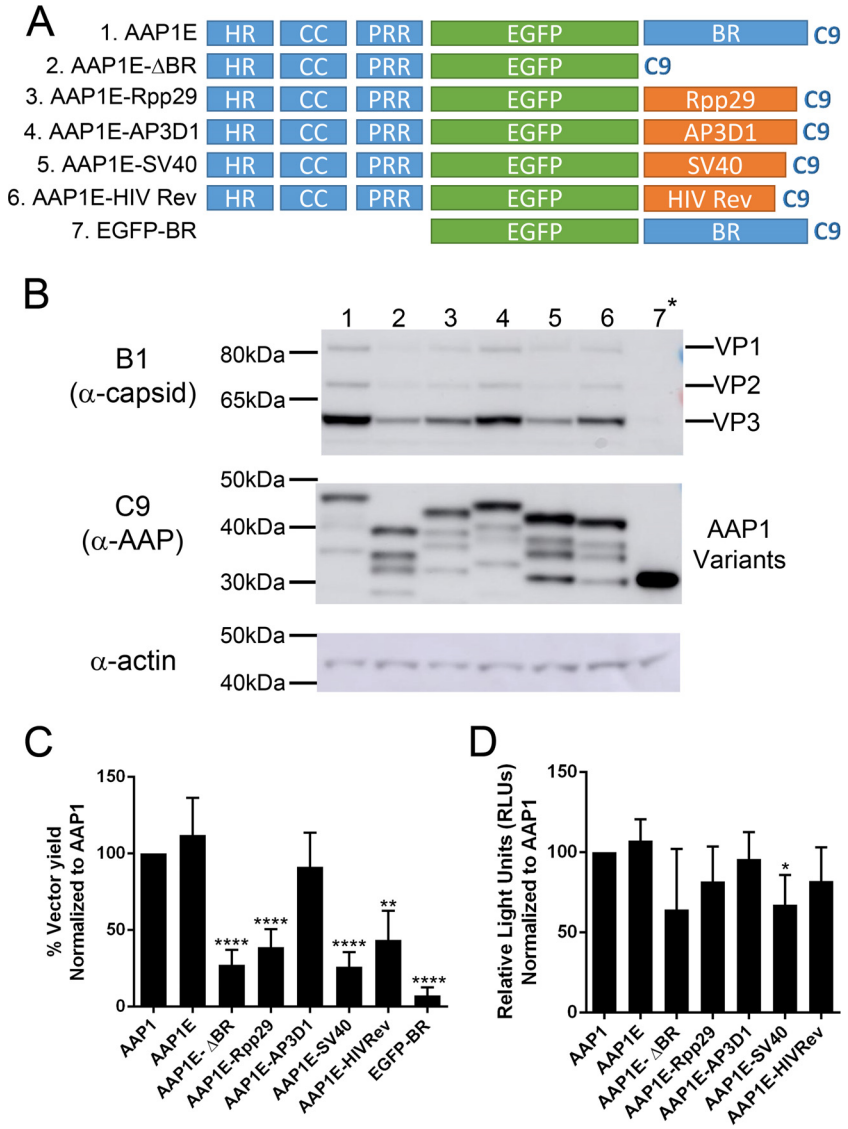


FIG 3 The C-terminal BR is important for AAP1 function but can be replaced by heterologous NoLS. (A) Schematic of different AAP mutants. The T/S of AAP1 was replacing by EGFP (AAP1E). The BR was replaced by RNase P subunit 29 NoLS (Rpp29), adaptor protein in AP-3 complex NoLS (AP3D1), virus-derived SV40 NLS (SV40), and HIV Rev NoLS domain (HIV Rev). (B) Representative Western blot images of VP and AAP expression as described in Fig. 1B. (C) Relative vector yields using different AAP constructs normalized to wild-type AAP1 (AAP1). (D) Transduction of rAAV1 packaging luciferase produced from different AAP1 constructs as described above. RLUs were normalized to AAP1. Error bars were determined and statistical analyses were performed as described above.

the nucleolus, similar to the AAP1E control (Fig. 6). These results corroborate the notion that the HR and CC domains are essential for VP interactions and maintaining stability.

The HR and CC domains are the major structural determinants driving AAP-capsid interactions. Based on deletion and AAP1/5 chimera analysis, we established that capsid assembly and VP expression levels are tightly correlated. We utilized the same deletion and replacement constructs as above and replaced the BR with a human Fc domain to facilitate VP complexation and immunoprecipitation studies (Fig. 7A). The expression level of both VP and AAP varies between constructs. For instance, EGFP, ΔHR, 5HR, ΔCC, and 5CC show a reduced level of AAP expression, while AAP5E and ΔHR show an increase in AAP expression (Fig. 7C and Table 2). To verify our system, we first showed that AAP1E can pull down the AAV1 VP. Surprisingly, although AAP5E was unable to support AAV1 capsid assembly (Fig. 6C), this protein was able to pull down

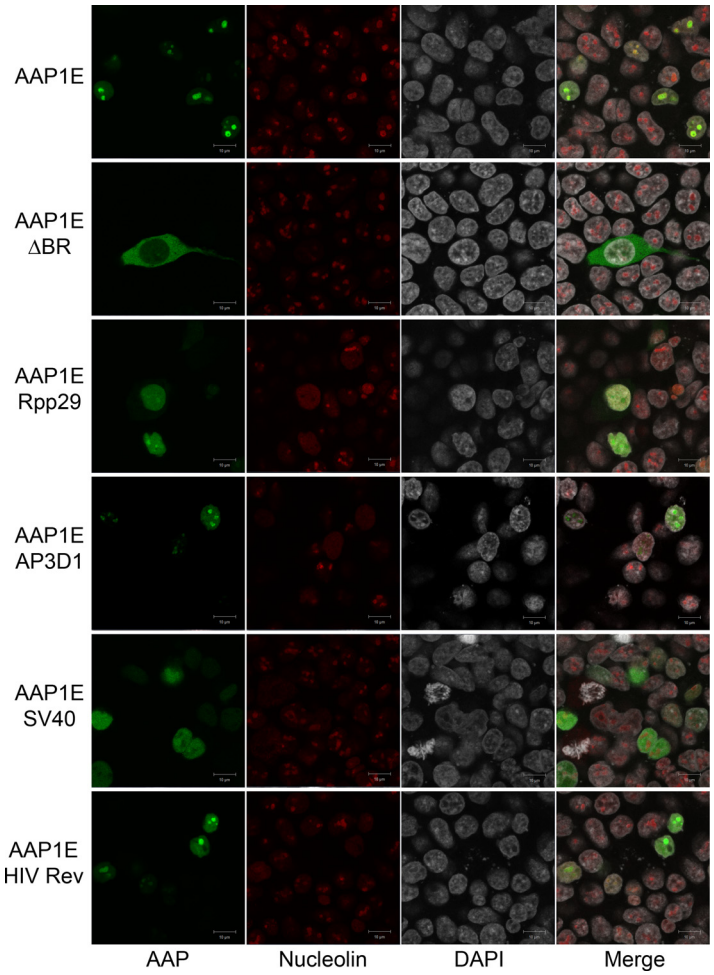


FIG 4 Confocal microscopy of different AAP1E derivatives. AAP1E derivatives (pCDNA3.1-AAPs) are transfected as described in Materials and Methods. The AAP1E derivatives were visualized by their native EGFP fluorescence, the nucleoli were immunostained with C23 antibody, and the nuclei were stained with DAPI.

AAV1 VP similar to AAP1E (Fig. 7B and Table 2). Deletion of the HR or CC regions abolishes the ability of AAP to pull down VP. Replacing the HR and CC regions with AAP5 restores the ability of AAP to pull down AAV1 VP (Fig. 7B and Table 2). Deletion of PRR or replacing 1PRR with 5PRR has no significant effect on AAV1 capsid interaction (Fig. 7B and Table 2). It is worth noting that the lack of immunoprecipitation in some of these constructs cannot be explained by expression level differences. For instance, 5HR and 5CC both have low levels of AAP and VP expression but were able to pull down VP in our assay (Fig. 7B and C; Table 2). On the other hand, ΔHR and the EGFP control are unable to pull down any VP protein despite having the highest levels of AAP expression (Fig. 7B and C; Table 2). However, this interaction is either transient or weak, which is further supported by our observation that majority of the capsid protein is still found in the flowthrough fraction of the pulldown (L. V. Tse and A. Asokan, unpublished data). These results demonstrate that the interactions between AAP and VP are driven by the N-terminal modules.

Engineering AAP for increased stability and vector production. We hypothesized that the T/S of AAP is the most amenable to manipulation for imparting novel/improved functionality. By introducing EGFP in place of T/S, steady-state AAP levels were likely increased probably due to increased protein stability (Fig. 2B). Thus, we attempted to further increase the stability of AAP by replacing the T/S with oligomerization domains. We picked three different oligomerization domains, including (i)

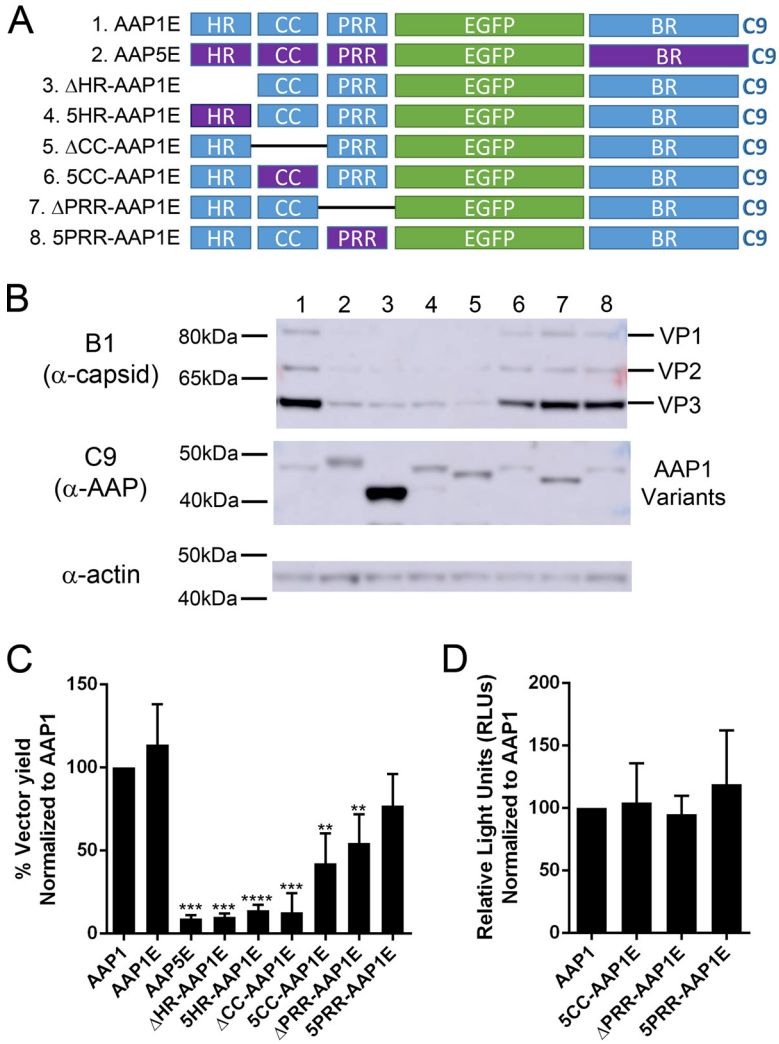


FIG 5 Domain deletion analysis of the N terminus of AAP1 reveals that the HR and CC are important for AAP functions. (A) Schematic of different AAP mutants. The N-terminal domains are either deleted or replaced with their AAP5 counterparts (purple). All AAP mutants have a C9 epitope tag at the C terminus. (B) Representative Western blot image of viral proteins, AAPs, and actin expression of HEK293 cells transfected by quadruple transfection for rAAV production after 3 days posttransfection. (C) Relative vector yields using different AAP constructs normalized to wild-type AAP1 (AAP1). (D) Transduction of rAAV1 packaging luciferase produced from different AAP1 constructs as described above. RLUs were normalized to AAP1. Error bars were determined and statistical analyses were performed as described above.

Collagen (21), which forms trimers, (ii) influenza A/WSN/1933 hemagglutinin (HA), which is a coiled-coil trimerization domain (WSN), and (iii) a synthetic tetramerization domain (Tetra) (22) to replace the T/S of AAP1 (Fig. 8A). Steady-state AAP protein levels were increased among all the AAP variants. The increase was most pronounced in AAP1-Collagen and AAP1-Tetra, while AAP1-WSN shows a moderate increase in AAP level (Fig. 8B and Table 2). VP levels also showed an increase in case of AAP1-Collagen, remained the same in AAP1-Tetra, and were slightly decreased in AAP1-WSN (Fig. 8B and Table 2). Both AAP1-Collagen and AAP1-Tetra increased the rAAV vector yield by 1.5- and 2-fold, respectively, compared to WT AAP1 (Fig. 8C and Table 2). The AAP1-WSN-mediated vector yield is 60% less than that for WT AAP1, suggesting a potential functional incompatibility with AAP1-WSN, despite increased stability (Fig. 8C and Table 2). To further evaluate the impact of engineered AAPs on vector yield, we attempted to establish a dose-response relationship for natural and engineered AAP constructs in supporting rAAV vector production by varying the amount of AAP DNA during trans-

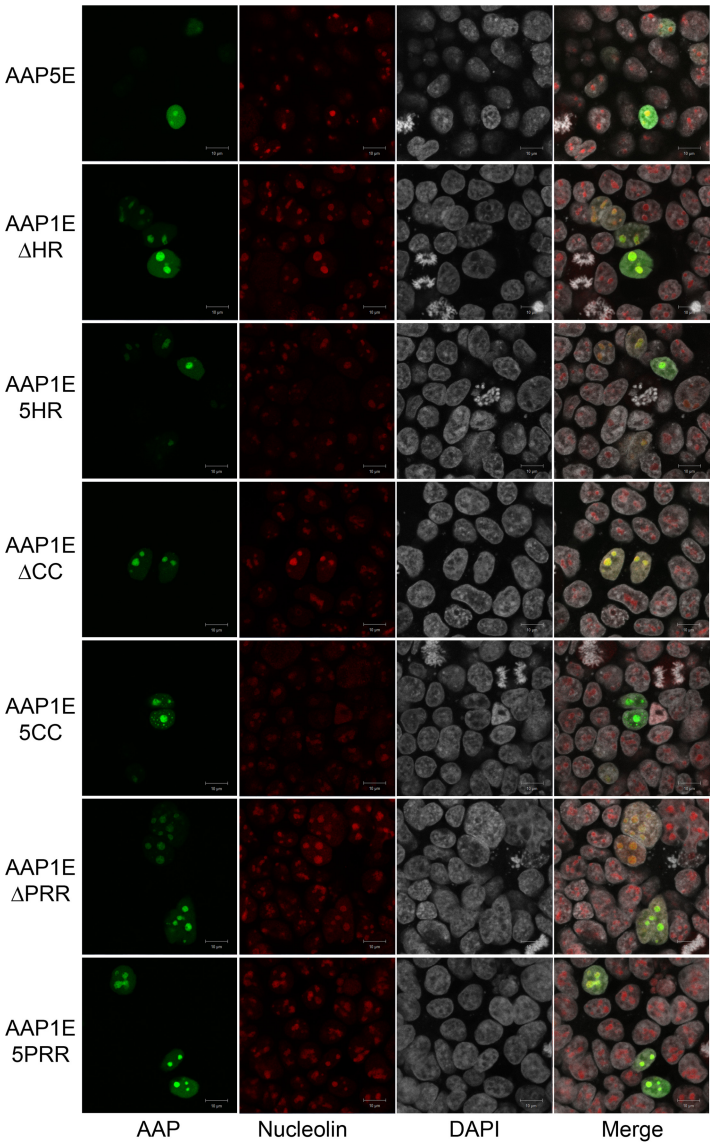


FIG 6 Confocal microscopy of different AAP5E and AAP1E derivatives. AAP5E and AAP1E derivatives were transfected as described in Materials and Methods. AAP5E and AAP1E derivatives were visualized by their native EGFP fluorescence, nucleoli were immunostained with C23 antibody, and nuclei were stained with DAPI.

fection. As expected, the AAP levels increased proportionally to the amount of transfected cDNA. AAP1-Collagen showed a significant increase in AAP levels compared to wild-type AAP1 (Fig. 9A). VP levels were also increased proportional to the amount of AAP DNA, with peak titers observed at 1,000 ng of AAP plasmid transfected. However, it is important to note that titers declined at higher levels potentially due to toxicity of AAP overexpression (Fig. 9A [see also Tse and Asokan, unpublished]).

DISCUSSION

Adeno-associated virus (AAV) encodes different proteins within its 4.7-kb genome using alternative splicing, alternative start codons, and overlapping reading frames (23). AAP is expressed from an alternative reading frame overlapping the VP2/3 sequences (5). We attempted to further understand our observations by calculating the relative conservation of AAP and VP overlapping regions in the *Cap* gene (24). Briefly, we plotted the ratio (AAP/VP) of the conservation scores such that a ratio of >1 denotes higher AAP conservation and a ratio of <1 implies higher VP conservation. Most

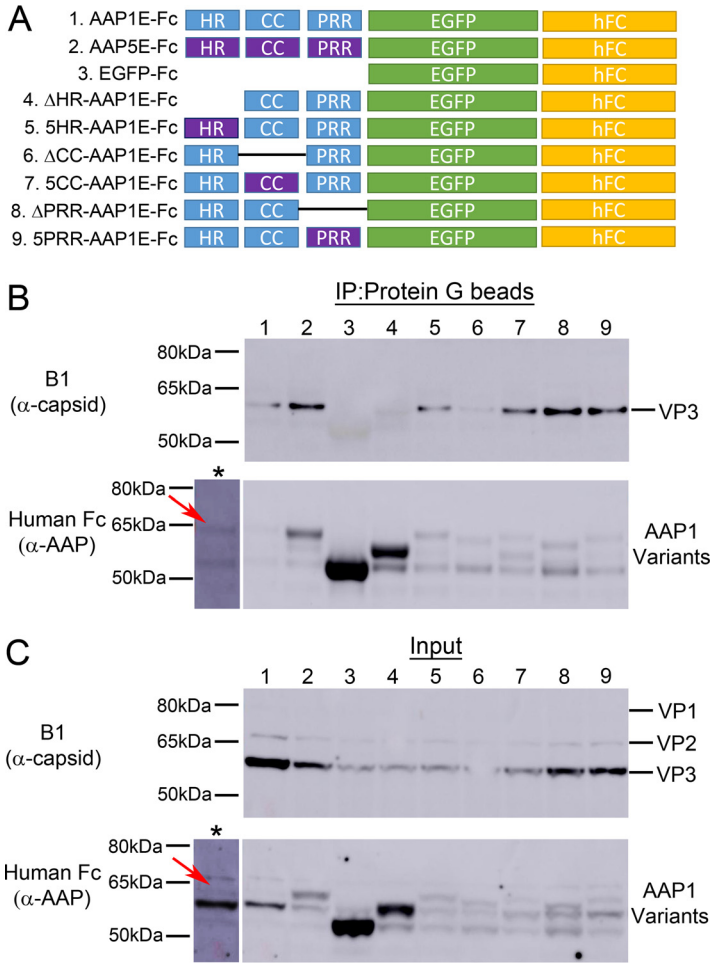


FIG 7 Immunoprecipitation of VPs by different N-terminal mutants of AAP1. (A) Schematic of different AAP mutants. The N-terminal domains are either deleted or replaced with AAP5 counterparts (purple). All AAP constructs have their BRs replaced by the human Fc domain at the C terminus. (B and C) Representative Western blot images of immunoprecipitation (B) and input (C) of VPs by AAP1E mutants. The asterisk (*) lane represents an overexposure of lane 1, and red arrows denote the position of AAP1E-hFc. Samples were collected at 3 days posttransfection of HEK293 cells with pXX680, pXR1ΔAAP1, pCDNA3.1-AAP1E-Fc, and pTR-CBA-Luc. Detailed protocols are described in Materials and Methods. AAP1E-Fc was pulled down using magnetic protein G beads and is immunostained with goat α-human-HRP antibody; VP is stained by mouse α-capsid antibody (B1).

regions show a preference for VP over AAP, with values of <1 (Fig. 10A). For instance, the sequences forming the beta-strand regions that form the jelly roll structure of VP and the highly conserved loop I have AAP/VP conservation ratios ranging from 0.3 to 0.5 due to a higher level of VP sequence conservation. These regions correspond to the nonessential T/S and PRR linker domains of AAP, respectively. Thus, in these regions VP function is favored over that of AAP (Fig. 10A). In contrast, the HR and CC regions show a conservation ratio of >1, indicating a preference for AAP function (Fig. 10A). In corollary, this region corresponds to the VP2 N-terminal domain, which has been shown to be nonessential for AAV capsid infectivity and essentially serves as a linker between the unique VP1 N-terminal phospholipase A2 (PLA2) domain and VP3 major subunit. Further, homology modeling of different AAP modules shows that the HR is the only region that has a strong secondary structure requirement in the form of an alpha-helix. Although AAP4 BR is also modeled as an alpha-helix, no other AAP BR can be modeled. All other domains either form undefined loop structures or are unable to be modeled (Fig. 10B).

The latter theoretical observations corroborate our functional characterization of

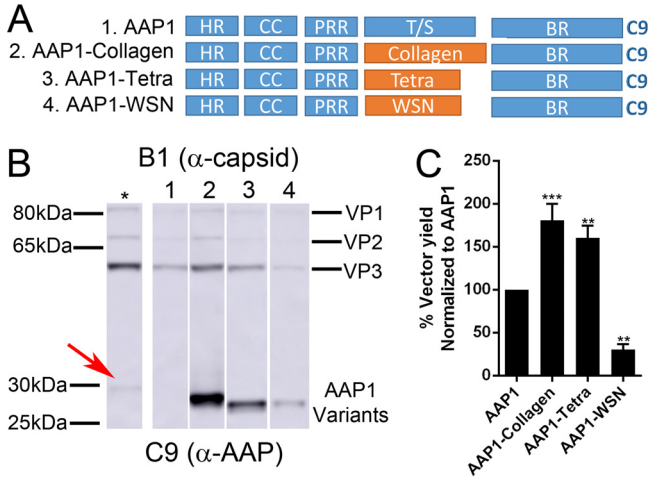


FIG 8 Replacement of T/S with oligomerization domains. (A) Schematic of different AAP mutants. The T/S was replaced by different oligomerization domains: the collagen trimerization domain (Collagen), a synthetic tetramerization domain (Tetra), or the influenza A/WSN/33 HA coiled-coil domain (WSN) and AAP1 as a control. All AAP mutants have a C9 epitope tag at the C terminus. (B) Representative Western blot image of VP and AAP expression as described in Fig. 1B. The asterisk (*) lane is transfected with 2× AAP1 plasmid amount compared to lane 1, and the red arrow denotes the position of AAP1. (C) Relative vector yield using different AAP constructs normalized to wild-type AAP1 (AAP1). Error bars were determined and statistical analyses were performed as described above.

AAP. Indeed, functional analysis showed that the T/S is dispensable and can be replaced by exogenous sequences. All of our T/S deletion or replacement constructs had higher steady-state levels than the WT AAP1. However, we cannot rule out that the T/S could have other potential, regulatory functions. Serine and threonine are the common amino acid substrates for phosphorylation; there are examples showing that multiple phosphorylation events could mark the protein for degradation via phosphodegron modules by the proteasome (25, 26). As previously shown, degradation of AAP can be inhibited by addition of proteasome inhibitor, MG132 (10). Therefore, the increase in the steady level of the T/S deletion constructs could be the result of decreased phosphorylation and, consequently, proteasomal degradation. Among other possible roles for the T/S that we cannot rule out at this writing is transcriptional regulation. These attributes might have been evolved to exploit the host cell machinery to regulate AAP levels and thus influence AAV infection. These latter aspects are the subject of ongoing investigations.

Similar to the T/S, the PRR does not appear to have any assigned function. Deletion

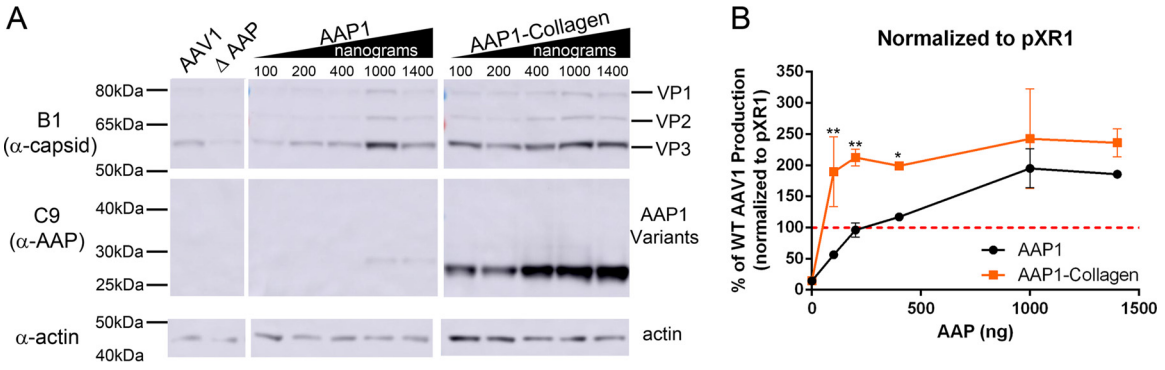


FIG 9 Dose-dependent increase in vector production by AAP1-Collagen. (A) Representative Western blot image of VP, AAP, and actin expression of HEK293 cells at different doses of AAP1 and AAP1-Collagen provided in *trans* at 3 days posttransfection. (B) Relative vector yield of different doses of AAP1 and AAP1-Collagen normalized to standard AAV1 production (pXR1). Error bars represent one standard deviation from at least three independent experiments. The data were analyzed by two-way ANOVA compared to pXR1 standard production (*, $P \leq 0.05$; **, $P \leq 0.01$; ***, $P \leq 0.001$; ****, $P \leq 0.0001$).

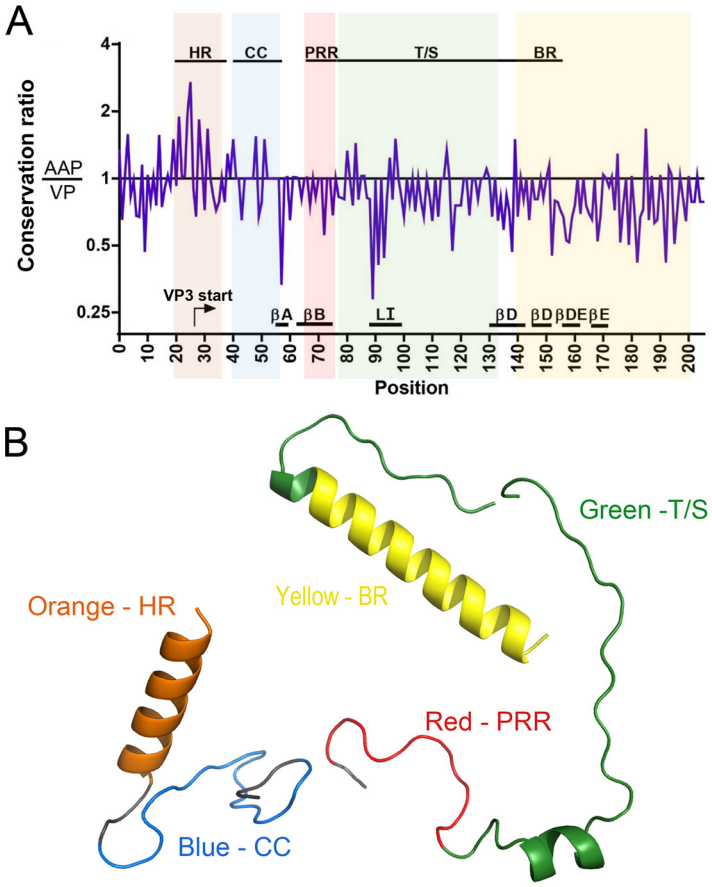


FIG 10 Bioinformatic analysis of AAP and VP conservation and homology modeling of AAP. A multiple-sequence alignment of AAP and the corresponding VP amino acids was performed and used for further analysis. (A) The ratio of AAP conservation to VP conservation was calculated for each amino acid position and plotted along a positional axis (see Materials and Methods for a detailed bioinformatic analysis). Ratios of >1 indicate greater conservation in AAP and vice versa. Overlaid are various regions and structural elements of each protein. The functional groups in VP are the VP3 start site (arrow), beta-strands A, B, D, and E (βA, βB, βD, and βE), and loop I (LI). Functional regions of AAP are highlighted in different colors: orange (HR), blue (CC), red (PRR), green (T/S), and yellow (BR). (B) Homology modeling of AAP1 (HR and CC), AAP2 (T/S), and AAP4 (BR). Detailed modeling parameters are presented in Materials and Methods.

of the PRR and T/S together impairs capsid assembly. However, deletion of the PRR in AAP1E retains 60% of capsid assembly compared to the wild type. Replacement with the PRR from AAP5 further rescues assembly to 80%. These data suggest that the PRR plays a relatively minor role in capsid assembly and serotype specificity but may act as a key structural linker that physically separates the critical HR and CC modules from the T/S. Unlike the PRR and T/S, multiple studies have shown that the BR contains an important NLS/NoLS signal that is responsible for AAP localization and subsequent translocation of the capsid to the assembly site (5, 11, 12). We tested whether other AAP BRs can functionally replace the AAP1 BR for capsid assembly. Surprisingly, only the AAP4 BR is able to support AAV1 capsid assembly function. Since the whole AAP4 protein is unable to rescue AAP1 capsid assembly function (9), our data clearly demonstrate that serotype specificity is independent of the BR. We further corroborate that BR is solely acting as a NoLS in the context of AAP1 by replacing the AAP1 BR with other heterologous NLS/NoLS. Among all of the NLS/NoLS tested, AP3D1, which is supposed to be an endosomal marker as its native form, shows the best nucleolar localization and completely supports capsid assembly. The localization pattern and percent rescue of capsid assembly are highly correlated, where increased nucleolar localization indicates greater restoration of capsid assembly for AAV1. Different BR

sequences have been reported for different AAPs, supporting the notion that AAP exerted a functional, rather structural evolutionary constraint in this region compared to VP.

The HR and the CC are the functional domains for AAV capsid assembly and the determinants of serotype specificity. Deleting the HR or CC led to an inability to pull down VP or support capsid assembly. Replacement of the HR and CC from AAP5 rescued interaction with VP; however, only the 5CC replacement was able to restore capsid assembly (to 50%). Since there are only two residues different between 1CC and 5CC (T44M and Q50R), it is not surprising that the 5CC replacement had relatively little effect on AAV1 capsid assembly compared to other N-terminal mutations. However, the ability of 5HR to pull down AAV1 VP was unexpected, since there are 10 amino acid residue differences between the two serotypes. Furthermore, binding of 5HR is not sufficient for function, since capsid assembly was defective. By replacing the T/S with three different oligomerization domains, our experiments suggest that artificially promoting oligomerization in the linker region of AAP does not correlate with the capsid assembly function. However, we note that the HR has been predicted by homology modeling to form an alpha-helix (Fig. 10B). Since amphipathic helices are often found in oligomerization domains, our data does not rule out the possibility that AAP potentially forms an oligomer. Based on our findings, we speculate that AAP interaction with the capsid is bipartite, where CC binds to a VP structural domain that is conserved among various serotypes (e.g., beta-strand), and HR either binds another site or oligomerizes to facilitate formation of a VP oligomer. Accordingly, capsid assembly only occurs when the two domains act together in a manner similar to a "lock and key" mechanism, where CC is the backbone and HR is the gear of the key which confers serotype specificity. Alternatively, since AAP interaction with the VP subunit is required to be transient, it is also possible that these domains play a role in releasing AAP from VP subunits during capsid assembly.

Using our new knowledge of AAP structure and function, we engineered additional properties onto AAP by replacing the nonessential T/S linker region. The fluorescently traceable AAP1E, which retains the same function as the wild-type counterpart, can potentially be utilized for real-time, live-cell imaging to study intracellular trafficking of AAP and capsid assembly events. Further, we engineered an AAP1-Collagen construct that shows improved stability and, by providing this eAAP in *trans*, we observed a 2-fold increase in vector yield compared to the wild-type counterpart. Such engineered, hyperstable AAPs could also be utilized to solve the structure of this intriguing protein as is or in complex with AAV capsid proteins. These latter observations suggest that with careful dissection of the mechanisms involving AAP biology, we can potentially develop strategies to improve the efficiency of rAAV packaging and rAAV vector yield. Several other questions remain to be addressed. For instance, how are the building blocks for AAV capsid assembly generated: as dimers, trimers, or pentamers? How is AAP involved in facilitating the oligomerization process? Another intriguing question is why do autonomous parvoviruses not appear to require an AAP-like chaperone for capsid assembly? Although these questions provide topics for ongoing and future investigations, the present study constitutes an important step in further understanding and controlling AAV capsid assembly.

MATERIALS AND METHODS

Cells, viruses, and antibodies. HEK293 cells were maintained in Dulbecco modified Eagle medium (DMEM) supplemented with 10% fetal bovine serum (FBS) (Thermo Fisher, Waltham, MA), as well as 100 U/ml of penicillin and 10 μg/ml of streptomycin (P/S; Thermo Fisher), in 5% CO_2 at 37°C. Hybridoma supernatant of anti-AAV monoclonal antibodies B1 and A20 were produced in-house and have been described earlier (27). Mouse anti-rhodopsin (1D4; ab5417) and mouse anti-actin (ab3280) antibodies were purchased from Abcam (Cambridge, United Kingdom). Mouse anti-CD23 antibody (D-6; sc-17826) was purchased from Santa Cruz Biotechnology (Santa Cruz, CA).

Homology modeling of AAP. The amino acid sequences of AAP1 to AAP9 were used in structural prediction using SWISS-MODEL (https://swissmodel.expasy.org/). The templates used for modeling AAP is Arabidopsis G protein-coupled receptor 2, GCR2 (PDB 3T33), for the HR and CC regions. The sequence identity of the modeling region is 12.20%, and the global model quality estimation (GMQE) and QMEAN

Z-score are 0.08 and −1.42, respectively. Different domains of AAP were also predicted individually; the AAP2 PRR and T/S are modeled with cellobiohydrolase (PDB 1Q9H) (28), and the QMEAN Z-score is −2.08. The AAP4 BR is modeled with HIV-Rev (PDB 4PMI) (29), and the QMEAN Z-score is −3.25. The HR domain can also be modeled with bacterial RNase ligase (PDB 4XRU) and *Escherichia coli* topoisomerase (PDB 1YUA), with QMEAN Z-scores of −1.81 and −2.08, respectively (30).

Bioinformatic analysis. Sequences from AAP and VP (only the residues corresponding to those in AAP) were aligned using MUSCLE, followed by manual adjustment. Alignments were done such that residues and gaps directly correspond in AAP and VP. The percent identities and similarities of AAPs from other serotypes compared to AAP1 were calculated with the Sequence Manipulation Suite (31) using the following groups for similarity: GAVLI, FYW, CM, ST, KRH, DENQ, and P. Amino acid conservation scores at each position of AAP and VP were calculated using the prediction tool developed by Capra and Singh (32). Analysis was run using the property entropy scoring method, sequence weighting, the BLOSUM62 background and scoring matrix, and a window size of 0.

Generation of different AAP constructs. All AAP constructs were cloned into pCDNA3.1 using the EcoRI and NotI sites. Chimera constructs were cloned using either overlapping PCR or Gibson Assembly (NEBuilder HiFi; New England BioLabs, Ipswich, MA). Detailed designs for each construct are illustrated in each figure, and the amino acid sequences are given in Table 1.

AAP and capsid expression of different AAP constructs evaluated by Western blotting. HEK293 cells at 60 to 70% confluence on a six-well plate were transfected with 600 ng of pXX680 (adenoviral helper plasmid containing E2A, E4orf6, and VA RNA from human adenovirus 5), 400 ng of pTR-CBA-Luc (AAV packaging plasmid containing CBA-Luciferase flanked by ITRs from AAV2), 600 ng of pXR-AAV1-no AAP (AAV1 Rep and Cap plasmid without ITRs; the AAP ORF is terminated by introducing a stop codon at position 64), and 400 ng of pCDNA3.1 AAP constructs (different AAP substitution, deletion, and fusion constructs driven by a cytomegalovirus promoter) using polyethylenimine (PEI) as the transfection reagent. At 3 days posttransfection, cell pellets were washed two times with 1× Dulbecco-modified phosphate-buffered saline (DPBS) and lysed with 200 μl of 1× passive lysis buffer (Promega, Madison, WI) for 30 min on ice with Halt protease inhibitor (Thermo Fisher). Supernatants were collected after centrifugation at 13,000 × *g* for 5 min at 4°C. The sample were prepared for Western blotting in 1× LDS loading dye (Thermo Fisher) and 100 mM dithiothreitol (DTT), then boiled at 95°C for 5 min, and loaded on a NuPAGE 4 to 12% Bis-Tris SDS-page gel (Thermo Fisher). The protein bands were transferred to nitrocellulose membrane (Thermo Fisher) using a semidry Xcell Surelock module (Thermo Fisher). VP, AAP, and actin proteins were detected by using B1 hybridoma supernatant at a 1:50 dilution, mouse α-rhodopsin antibody (ID4; ab5417) at a 1:2,000 dilution, and α-actin antibodies (ab3280) at a 1:1,000 dilution, respectively; goat α-mouse antibody labeled with horseradish peroxidase (HRP) at a 1:10,000 dilution was used as the secondary antibody. A chemiluminescence reaction was initiated with enhanced chemiluminescent substrate (SuperSignal West Femto maximum sensitivity; Thermo Fisher), and the membrane was developed on an AI600RGB system (Amersham Biosciences, Little Chalfont, United Kingdom).

AAP-dependent capsid assembly/vector production evaluated by qPCR. HEK293 cells at 60 to 70% confluence on a six-well plate were transfected with pXX680 (600 ng), pTR-CBA-Luc (400 ng), pXR-AAV1-no AAP (600 ng), and pCDNA3.1 AAP constructs (400 ng) using PEI. The transfection medium was replaced with fresh media after 24 h, and the supernatant was harvested at 5 days posttransfection. Supernatants were collected after centrifugation at 13,000 × *g* for 2 min. The supernatants were used directly for standard quantitative PCR (qPCR) analysis to determine the vector yield and for transduction assays. Subsequent steps involved the harvesting of media, polyethylene glycol precipitation, iodixanol ultracentrifugation, and buffer exchange. Supernatants were treated with DNase (90 μg/ml) for 1 h at 37°C. DNase was inactivated by the addition of EDTA (13.2 mM), followed by proteinase K (0.53 mg/ml) digestion for 2 h at 55°C. Recombinant AAV vector titers were determined by qPCR with primers that amplify AAV2 inverted terminal repeat (ITR) regions (5′-AACATGCTACGCAGAGAGGGAGTGG-3′ and 5′-CATGAGACAAGGAACCCCTAGTGATGGAG-3′). The relative vector yields from different AAP constructs were normalized to wild-type AAP1 unless specifically indicated otherwise in figure legend.

***In vitro* AAV transduction assays.** AAV vectors produced with different AAP constructs packaging ssCBA-Luc transgenes were prediluted in DMEM plus 5% FBS plus P/S. Portions (50 μl) of recombinant AAV vectors (1,000 to 10,000 vector genomes [vg]/cell) were mixed with 50 μl of 5×10^4 HEK293 cells and added to tissue culture-treated, black, transparent bottom 96-well plates (Corning, Corning, NY). The plates were incubated in 5% CO_2 at 37°C for 48 h. The cells were then lysed with 25 μl of 1× passive lysis buffer (Promega) for 30 min at room temperature. The luciferase activity was measured on a Victor 3 multilabel plate reader (Perkin-Elmer) immediately after the addition of 25 μl of luciferin (Promega). All readouts were normalized to wild-type AAP1 or AAV1 controls.

Immunofluorescence and confocal microscopy. HEK293 cells were seeded on a 12-mm-diameter poly-lysine-treated glass coverslip (GG-12-1.5-PDL; NeoVitro, Vancouver, WA) in a 24-well plate. Cells were transfected at 60 to 70% confluence with pCDNA3.1 AAP alone (250 ng) using PEI as the transfection reagent. At 2 days posttransfection, the cells were fixed with 4% paraformaldehyde in phosphate-buffered saline (PBS) for 15 min and permeabilized with 0.1% Triton X-100 in PBS for 10 min. The nucleolus was stained using α-C23 (D-6) antibody, followed by goat α-mouse IgG H+L Alexa Fluor 594 (Thermo Fisher). The nucleus was stained with DAPI (4′,6′-diamidino-2-phenylindole; Thermo Fisher). Coverslips were mounted onto microscope slides using ProLong Diamond mountant (Invitrogen, Carlsbad, CA). Fluorescence images were taken by using a Zeiss LSM 710 spectral confocal laser scanning microscope at the UNC Microscopy Service Laboratory.

Immunoprecipitation assays. HEK293 cells at 60 to 70% confluence on a 15-cm plate were transfected with pXX680 (3,000 ng), pTR-CBA-Luc (2,500 ng), pXR-AAV1-no AAP (3,000 ng), and pCDNA3.1 AAP constructs (7,500 ng) using PEI as the transfection reagent. At 3 days posttransfection, the cells were harvested from the plate in cold 1× DPBS, followed by more two washes in 1× DPBS. The pellets were resuspended in 400 μl of buffer D (20 mM HEPES/KOH [pH 7.9], 25% glycerol, 0.1 M KCl, 0.2 mM EDTA) and lysed on ice for 30 min with Halt protease inhibitor (Thermo Fisher). Lysates were spun at 13,000 × *g* for 2 min. Then, 5% of the supernatant was retained as input and prepared in 1× LDS buffer and 100 mM DTT. Next, 10 μl of Protein G Mag Sepharose Xtra beads washed three times in buffer D (GE Healthcare, Chicago, IL) was added to the remaining lysate; samples were then placed on a rotator at 4°C for 2 h. Next, the beads were washed twice for 30 min each in buffer D, followed by resuspension in 1× LDS buffer and 100 mM DTT. Samples were denatured at 95°C for 5 min and then loaded onto a precast 10% Bis-Tris gel (Thermo Fisher) and run in MOPS-SDS buffer. The protein was transferred to a 0.45-μm-pore size nitrocellulose membrane (Thermo Fisher) in a wet transfer apparatus. AAP was detected using α-human-HRP at a 1:10,000 dilution and visualized after reaction with Femto Western blot substrate (Thermo Fisher) on an Amersham AI600RGB system (Amersham Biosciences). Membranes were incubated in 30% peroxide for 30 min at room temperature and then reblocked. VP, AAP, and actin proteins were detected by using B1 hybridoma supernatant at a 1:50 dilution and α-actin antibody (ab3280) at a 1:2,000 dilution, respectively; goat anti-mouse-HRP at a 1:20,000 dilution was used as the secondary antibody. The membranes were again visualized as described above.

Statistical analysis. All error bars shown represent one standard deviation. Statistical analysis was carried out in GraphPad Prism software using an unpaired, two-tailed Student *t* test or two-way analysis of variance (ANOVA) in Fig. 9 (*, $P \leq 0.05$; **, $P \leq 0.01$; ***, $P \leq 0.001$; ****, $P \leq 0.0001$).

ACKNOWLEDGMENTS

We acknowledge grant support from the National Institutes of Health (P01HL112761 and R01HL089221; awarded to A.A.).

L.V.T, S.M.-T., and A.A. designed and executed the overall study and carried out data analysis. L.V.T. and A.A. wrote the manuscript. R.M.M. carried out bioinformatic analysis and edited the manuscript.

A.A. is a founder of StrideBio, Inc.

REFERENCES

1. Cotmore SF, Agbandje-McKenna M, Chiorini JA, Mukha DV, Pintel DJ, Qiu J, Soderlund-Venermo M, Tattersall P, Tijssen P, Gatherer D, Davison AJ. 2014. The family *Parvoviridae*. Arch Virol 159:1239–1247. https://doi.org/10.1007/s00705-013-1914-1.
2. Atchison RW, Casto BC, Hammon WM. 1965. Adenovirus-associated defective virus particles. Science 149:754–756. https://doi.org/10.1126/science.149.3685.754.
3. Agbandje-McKenna M, Kleinschmidt J. 2011. AAV capsid structure and cell interactions. Methods Mol Biol 807:47–92. https://doi.org/10.1007/978-1-61779-370-7_3.
4. Xiao X, Xiao W, Li J, Samulski RJ. 1997. A novel 165-base-pair terminal repeat sequence is the sole *cis* requirement for the adeno-associated virus life cycle. J Virol 71:941–948.
5. Sonntag F, Schmidt K, Kleinschmidt JA. 2010. A viral assembly factor promotes AAV2 capsid formation in the nucleolus. Proc Natl Acad Sci U S A 107:10220–10225. https://doi.org/10.1073/pnas.1001673107.
6. Vasileva A, Jessberger R. 2005. Precise hit: adeno-associated virus in gene targeting. Nat Rev 3:837–847.
7. Berns KI. 1990. Parvovirus replication. Microbiol Rev 54:316–329.
8. Daya S, Berns KI. 2008. Gene therapy using adeno-associated virus vectors. Clin Microbiol Rev 21:583–593. https://doi.org/10.1128/CMR.00008-08.
9. Earley LF, Powers JM, Adachi K, Baumgart JT, Meyer NL, Qing X, Chapman MS, Nakai H. 2017. Adeno-associated virus (AAV) assembly-activating protein is not an essential requirement for capsid assembly of AAV serotypes 4, 5, and 11. J Virol 91:1–21. https://doi.org/10.1128/JVI.01980-16.
10. Grosse S, Penaud-Budloo M, Herrmann A-K, Börner K, Fakhiri J, Laketa V, Krämer C, Wiedtke E, Gunkel M, Ménard L, Ayuso E, Grimm D. 2017. Relevance of assembly-activating protein for adeno-associated virus vector production and capsid protein stability in mammalian and insect cells. J Virol https://doi.org/10.1128/JVI.01198-17.
11. Sonntag F, Kother K, Schmidt K, Weghofer M, Raupp C, Nieto K, Kuck A, Gerlach B, Bottcher B, Muller OJ, Lux K, Horer M, Kleinschmidt JA. 2011. The assembly-activating protein promotes capsid assembly of different adeno-associated virus serotypes. J Virol 85:12686–12697. https://doi.org/10.1128/JVI.05359-11.
12. Earley LF, Kawano Y, Adachi K, Sun X-X, Dai M-S, Nakai H. 2015. Identification and characterization of nuclear and nucleolar localization signals in the adeno-associated virus serotype 2 assembly-activating protein. J Virol 89:3038–3048. https://doi.org/10.1128/JVI.03125-14.
13. Naumer M, Sonntag F, Schmidt K, Nieto K, Panke C, Davey NE, Popa-Wagner R, Kleinschmidt JA. 2012. Properties of the adeno-associated virus assembly-activating protein. J Virol 86:13038–13048. https://doi.org/10.1128/JVI.01675-12.
14. Grove TZ, Regan L. 2012. New materials from proteins and peptides. Curr Opin Struct Biol 22:451–456. https://doi.org/10.1016/j.sbi.2012.06.004.
15. Moller-Tank S, Albritton LM, Rennert PD. 2014. Characterizing functional domains for TIM-mediated enveloped virus entry. J Virol 88:6702–6713. https://doi.org/10.1128/JVI.00300-14.
16. Jarrous N, Wolenski JS, Wesolowski D, Lee C, Altman S. 1999. Localization in the nucleolus and coiled bodies of protein subunits of the ribonucleoprotein ribonuclease P. J Cell Biol 146:559–571.
17. Scott MS, Boisvert FM, McDowall MD, Lamond AI, Barton GJ. 2010. Characterization and prediction of protein nucleolar localization sequences. Nucleic Acids Res 38:7388–7399. https://doi.org/10.1093/nar/gkq653.
18. Kalderon D, Roberts BL, Richardson WD, Smith AE, Hill M. 1984. A short amino acid sequence able to specify nuclear location. Cell 39(3 Pt 2):499–509.
19. Lange A, McLane LM, Mills RE, Devine SE, Corbett AH. 2010. Expanding the definition of the classical bipartite nuclear localization signal. Traffic 11:311–323. https://doi.org/10.1111/j.1600-0854.2009.01028.x.
20. Cochrane AW, Perkins A, Rosen CA. 1990. Identification of sequences important in the nucleolar localization of human immunodeficiency virus Rev: relevance of nucleolar localization to function. J Virol 64:881–885.
21. Boudko SP, Sasaki T, Engel J, Lerch TF, Nix J, Chapman MS, Bächinger HP, Sam SW, Park J. 2009. Crystal structure of human collagen XVIII trimerization domain: a novel collagen trimerization fold. J Mol Biol 392:787–802. https://doi.org/10.1016/j.jmb.2009.07.057.
22. Sales M, Plecs JJ, Holton JM, Alber T. 2007. Structure of a designed,

right-handed coiled-coil tetramer containing all biological amino acids. Protein Sci 16:2224–2232.
23. Stutika C, Botschen L, Mietzsch M, Weger S, Feldkamp M, Chen W, Heilbronn R. 2016. A comprehensive RNA sequencing analysis of the adeno-associated virus (AAV) type 2 transcriptome reveals novel AAV transcripts, splice variants, and derived proteins. J Virol 90:1278–1289. https://doi.org/10.1128/JVI.02750-15.
24. Kawano Y, Neeley S, Adachi K, Nakai H. 2013. An experimental and computational evolution-based method to study a mode of co-evolution of overlapping open reading frames in the AAV2 viral genome. PLoS One 8:e66211. https://doi.org/10.1371/journal.pone.0066211.
25. Feldman RMR, Correll CC, Kaplan KB, Deshaies RJ. 1997. A complex of Cdc4p, Skp1p, and Cdc53p/cullin catalyzes ubiquitination of the phosphorylated CDK inhibitor Sic1p. Cell 91:221–230.
26. Skowyra D, Craig KL, Tyers M, Elledge SJ, Harper JW. 1997. F-box proteins are receptors that recruit phosphorylated substrates to the SCF ubiquitin-ligase complex. Cell 91:209–219.
27. Wistuba A, Kern A, Weger S, Grimm D, Kleinschmidt JA. 1997. Subcellular compartmentalization of adeno-associated virus type 2 assembly. J Virol 71:1341–1352.
28. Grassick A, Murray PG, Thompson R, Collins CM, Byrnes L, Birrane G, Higgins TM, Tuohy MG. 2004. Three-dimensional structure of a thermostable native cellobiohydrolase, CBH IB, and molecular characterization of the *cel7* gene from the filamentous fungus, *Talaromyces emersonii*. Eur J Biochem 271:4495–4506. https://doi.org/10.1111/j.1432-1033.2004.04409.x.
29. Jayaraman B, Crosby DC, Homer C, Ribeiro I, Mavor D, Frankel AD. 2014. RNA-directed remodeling of the HIV-1 protein Rev orchestrates assembly of the Rev-Rev response element complex. Elife 3:e04120. https://doi.org/10.7554/eLife.04120.
30. Benkert P, Tosatto SC, Schomburg D. 2008. QMEAN: a comprehensive scoring function for model quality assessment. Proteins 71:261–277. https://doi.org/10.1002/prot.21715.
31. Stothard P. 2000. The sequence manipulation suite: JavaScript programs for analyzing and formatting protein and DNA sequences. Biotechniques 28:1102–1104.
32. Capra JA, Singh M. 2018. Sequence analysis predicting functionally important residues from sequence conservation. Bioinformatics 23:1875–1882.

Molecular Therapy
Methods & Clinical Development
Original Article

A Novel Triple-Mutant AAV6 Capsid Induces Rapid and Potent Transgene Expression in the Muscle and Respiratory Tract of Mice

Laura P. van Lieshout,[1] Jakob M. Domm,[1] Tara N. Rindler,[2,3] Kathy L. Frost,[4] Debra L. Sorensen,[4] Sarah J. Medina,[4] Stephanie A. Booth,[4,5] James P. Bridges,[2,3] and Sarah K. Wootton[1]

[1]Department of Pathobiology, University of Guelph, Guelph, ON N1G 2W1, Canada; [2]Perinatal Institute, Section of Pulmonary Biology, Cincinnati Children's Hospital Medical Center, Cincinnati, OH 45229, USA; [3]Department of Pediatrics, University of Cincinnati School of Medicine, Cincinnati, OH 45229, USA; [4]Molecular Pathobiology, National Microbiology Laboratory (NML), Public Health Agency of Canada, 1015 Arlington Street, Winnipeg, MB R3E 3R2, Canada; [5]Department of Medical Microbiology and Infectious Diseases, University of Manitoba, Winnipeg, MB R3T 2N2, Canada

Gene therapy for the treatment of genetic disorders has demonstrated considerable therapeutic success in clinical trials. Among the most effective and commonly used gene delivery vectors are those based on adeno-associated virus (AAV). Despite these advances in clinical gene therapy, further improvements in AAV vector properties such as rapid intracellular processing and transgene expression, targeted transduction of therapeutically relevant cell types, and longevity of transgene expression, will render extension of such successes to many other human diseases. Engineering of AAV capsids continues to evolve the specificity and efficiency of AAV-mediated gene transfer. Here, we describe a triple AAV6 mutant, termed AAV6.2FF, containing F129L, Y445F, and Y731F mutations. AAV6.2FF yielded 10-fold greater transgene expression in lung than AAV6 after 21 days. Additionally, this novel capsid demonstrated 101-fold and 49-fold increased transgene expression in the muscle and lungs, respectively, 24 hr post vector delivery when compared with the parental AAV6. Furthermore, AAV6.2FF retains heparin sulfate binding capacity and displays a 10-fold increase in resistance to pooled immunoglobulin neutralization *in vitro*. The rapid and potent expression mediated by AAV6.2FF is ideally suited to applications such as vectored immunoprophylaxis, in which rapid transgene expression is vital for use during an outbreak response scenario.

INTRODUCTION

Adeno-associated virus (AAV) is widely regarded as a safe and effective method of gene transfer to a variety of tissues. The *in vitro* and *in vivo* transduction profiles have been well characterized for many AAV serotypes.[1,2] Engineering of AAV capsids by rational design or directed evolution can produce capsid variants with desirable characteristics including altered tissue tropism, enhanced transgene expression in target cells, or the introduction of binding domains to aid in purification, to name a few. A prime example, AAV-DJ, is a product of AAV2 and AAV8 capsid shuffling resulting in a hybrid capsid with beneficial properties of both capsids: heparin binding capacity and *in vitro* transduction capacities from AAV2 and potent *in vivo* liver transduction from AAV8.[3,4]

Alternatively, single-point mutations in an AAV capsid can also yield desirable modifications. AAV6.2, an AAV6 F129L point mutant, was demonstrated by Limberis et al.[5] to be 2-fold more efficient at transducing the nose, airways, and alveolar type II cells of mice than AAV6. Similarly, when delivered intravenously to mice, AAV6.2 mediated 2-fold greater serum concentrations of human alpha-1 antitrypsin (hA1AT) than AAV6.[6] Moreover, intramuscular administration of the same AAV6.2-hA1AT vector mediated higher serum levels of hA1AT than AAV6 or AAV9.[6] Interestingly, F129L is a naturally occurring singleton residue in the majority of over 100 known primate AAV capsid sequences. In fact, AAV5 and AAV6 are the only serotypes that encode a phenylalanine instead of a leucine at this position.[6]

AAV capsids are prone to phosphorylation of tyrosine residues by epidermal growth factor receptor protein tyrosine kinase (EGFR-PTK), leading to alternative cellular trafficking, ubiquitination, and degradation.[7,8] Mutation of various surface-exposed tyrosine residues on AAV capsids has been shown to obstruct ubiquitin-mediated degradation of intracellular vector, thereby leading to more robust transgene expression.[9] Tyrosine-to-phenylalanine mutations introduced at positions 444 and 730 in the AAV2 capsid yielded 9- and 11-fold greater transgene expression *in vitro* and 13- and 29-fold greater hepatocyte transduction in mice, respectively.[9] A double AAV2 Y444F+Y730F mutant generated significantly greater hepatocyte transduction *in vivo* than either of the

Received 27 March 2018; accepted 10 April 2018;
https://doi.org/10.1016/j.omtm.2018.04.005.

Correspondence: Sarah K. Wootton, Department of Pathobiology, PAHL Receiving, Building 89, Room 4814, Ontario Veterinary College, University of Guelph, Guelph, ON N1G 2W1, Canada.
E-mail: kwootton@uoguelph.ca

This is an open access article under the CC BY-NC-ND license (http://creativecommons.org/licenses/by-nc-nd/4.0/).

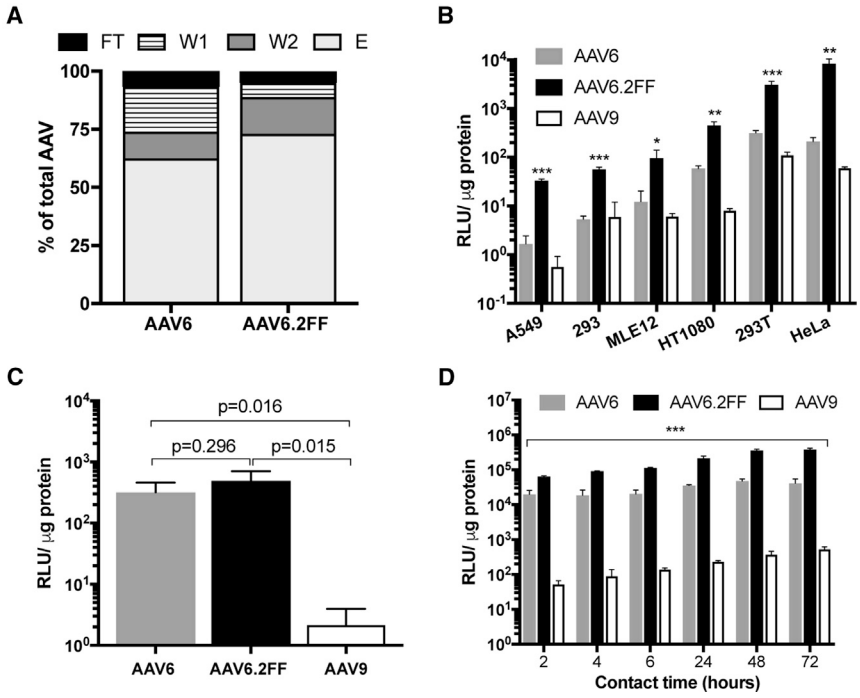


Figure 1. Heparin Binding and Transduction Profiles of AAV6 and AAV6.2FF *In Vitro*

(A) Distribution of AAV vector genomes following heparin binding assay. (B) AAV6-, AAV6.2FF-, or AAV9-Luciferase were added to cells at an MOI of 2,000 and incubated for 72 hr prior to luciferase quantification to determine transduction efficiency. Binding (C) and internalization (D) of AAV vectors in HeLa cells. AAV6.2FF transduction was significantly greater than AAV6 and AAV9 over all time points. All experiments were conducted in triplicate. Values are expressed as means ± SD. Multiple t tests compared AAV6.2FF-mediated luciferase expression with AAV6 and AAV9. *$p < 0.05$; **$p < 0.01$; ***$p < 0.001$. E, elution; FT, flow-through; W1, wash 1; W2, wash 2.

singleton mutants.[10] Similar single-tyrosine mutations have been introduced into corresponding positions in AAV6 (Y445F, Y731F), AAV8 (Y447F, Y733F), and AAV9 (Y731F, Y446F) capsids with success in transducing various tissues; however, to our knowledge, an AAV6 capsid containing Y445F+Y731F has not yet been investigated.[9,10] Alternatively, AAV1 Y445F+Y731F resulted in decreased transgene output *in vitro*, demonstrating that the benefit of mutating surface-exposed tyrosine residues is capsid specific.[11]

Here, we have engineered a triple-mutant AAV6 capsid, termed AAV6.2FF, encoding F129L, Y445F, and Y731F point mutations, which we demonstrate to be superior to the parental capsid in terms of muscle and airway transgene expression kinetics in a mouse model.

RESULTS

F129L, Y445F, and Y731F Mutations Do Not Impede Heparin Sulfate Binding Capacity

The ability of AAV6 to bind heparin sulfate is a favorable characteristic that enables heparin chromatography purification methods; therefore, we sought to determine whether AAV6.2FF retains heparin-binding capacity. In a heparin-binding assay, 62.4% of the input AAV6 vector was found in the elution fraction compared with 72.9% for AAV6.2FF (Figure 1A). Furthermore, less AAV6.2FF vector was located in the flow-through (FT) and wash (W) fractions than AAV6 (AAV6: FT, 6.7%, W1, 19.3%, W2, 11.4%; AAV6.FF: FT, 4.9%, W1, 6.1%, W2, 15.8%), indicating the AAV6.2FF mutations do not negatively impact heparin binding.

AAV6.2FF Mediates Enhanced Transduction *In Vitro*

AAV transduction of a panel of cell lines, including human and murine lung epithelial cells, resulted in significantly increased transgene expression from AAV6.2FF compared with AAV6 and AAV9 (Figure 1B). While AAV9 is known to be relatively poor at transducing cells in culture,[2] AAV6 is considered one of the better serotypes for *in vitro* use[2]; however, AAV6.2FF outperformed AAV6, mediating between a 7- and 39-fold increase in transgene expression, depending on the cell line.

AAV cell binding assays demonstrated similar binding properties for both AAV6 and AAV6.2FF (Figure 1C); however, internalization assays exposed variation in AAV6 and AAV6.2FF luciferase expression (Figure 1D). After 2 hr of contact time, there was a 3.2-fold increase in AAV6.2FF-mediated luciferase expression compared with AAV6, and this trend steadily increased with longer contact times to a 9.1-fold difference at 72 hr. These results indicate that the mechanism of improved AAV6.2FF transduction efficiency is not due to cell binding properties, but rather occurs post-internalization, potentially as increased efficiency in vector trafficking to the nucleus because of reduced capsid ubiquitination at exposed tyrosine residues.

Mutation of Surface-Exposed Tyrosine Residues Reduces IVIG Neutralization

Unexpectedly, the three mutations that generate the AAV6.2FF capsid conferred a 10-fold increase in resistance to pooled intravenous immunoglobulin (IVIG) neutralization. 1 mg/mL IVIG was able to neutralize 97% of AAV6; however, the same concentration was only able to neutralize 20% AAV6.2FF (Figure 2). AAV6.2FF required a minimum of 10 mg/mL to neutralize 100% of the vector.

AAV6.2FF Displays Rapid Early Expression Kinetics in the Muscle and Lung of Mice

Most AAV capsids reach peak transgene expression between 14 and 28 days post-delivery; however, little is known about the early

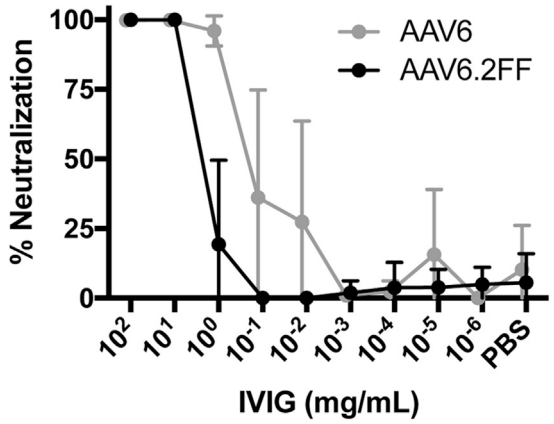


Figure 2. IVIG Neutralization of AAV *In Vitro*

AAV vectors were incubated with 10-fold dilutions of IVIG for 1 hr at 37°C prior to adding to HeLa cells. 72 hr later, luciferase expression was quantified and the data expressed as percent AAV neutralization compared with control virus incubated with PBS only (n = 6). Values are expressed as mean ± SD.

transgene expression kinetics of various capsids. AAV6 and AAV6.2FF vectors expressing firefly luciferase delivered to the muscle or lungs of mice were compared 24 hr following AAV administration using an *in vivo* imaging system (IVIS). Remarkably, in both tissues, AAV6.2FF produced significantly more transgene expression than AAV6 after only 24 hr (Figure 3A). In the muscle, AAV6.2FF yielded 101-fold greater radiance than AAV6 (Figure 3B), while in the lung there was a 49-fold difference favoring AAV6.2FF (Figure 3C).

Long-Term AAV6- and AAV6.2FF-Mediated Expression in the Muscle Is Equivalent

In addition to the 24-hr time point, we also quantified luciferase expression from the muscle on days 3, 7, 14, 21, 28, 56, 112, and 205 post-AAV delivery (Figure 4A). AAV6.2FF-mediated transgene expression was significantly greater than AAV6 on days 3, 7, and 14, with 18.9-fold, 3.5-fold, and 3.0-fold greater signal, respectively (Figure 4B). Beyond 2 wk, there is an insignificant difference in the luciferase expression produced by the AAV6 and AAV6.2FF vectors; however, the luciferase signal from both groups plateaued at a high magnitude and has not begun to decline 16 weeks post-injection.

AAV6.2FF Is Highly Efficient at Transducing the Lung Parenchyma of Mice

Intranasal delivery of AAV6 and AAV6.2FF vectors expressing a heat-stable alkaline phosphatase (AP) reporter gene demonstrated potent transduction of mouse lungs by AAV6.2FF. Although the overall AP staining distribution was consistent between the two vectors, there is a visible difference in the extent of transduction in the nasal cavity and lung lobes when observed grossly (Figures 5A–5H). Microscopic analysis of the lung tissue revealed that both vectors predominantly transduced cells of the distal lung; however, a greater proportion of cells was transduced with the AAV6.2FF vector compared with AAV6 (Figures 5I–5N). Additionally, both vectors were able to transduce epithelial cells of the proximal airway (Figures 5K and 5N).

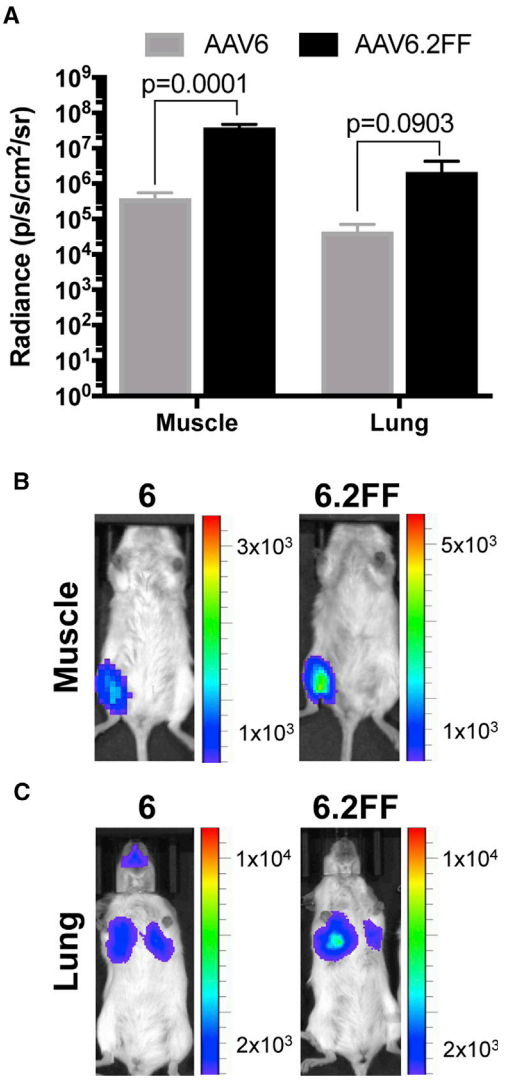


Figure 3. Comparison of AAV6- and AAV6.2FF-Mediated Transgene Expression 24 hr Post-AAV Delivery

Albino C57BL/6 mice (n = 4 mice/group) received 1 × 10^{11} vg by intramuscular injection or intranasal delivery. (A) Quantification of luciferase expression in the muscle and lung 24 hr following intramuscular or intranasal delivery, respectively (n = 4/group). Data are expressed as mean ± SD. Multiple t tests compared AAV6.2FF-mediated luciferase expression with AAV6. Representative images illustrating the pattern and intensity of luciferase expression in the muscle (B) and the lungs (C).

Quantification of the AAV vector genome copy numbers present in lung tissue 3 wk post-vector delivery demonstrates AAV6.2FF transduced the mouse lung 9.6-fold more efficiently than AAV6 (Figure 6A). A secondary quantitative analysis of AP enzymatic activity showed AAV6.2FF transduction yielded a mean of 2.36 ng of AP

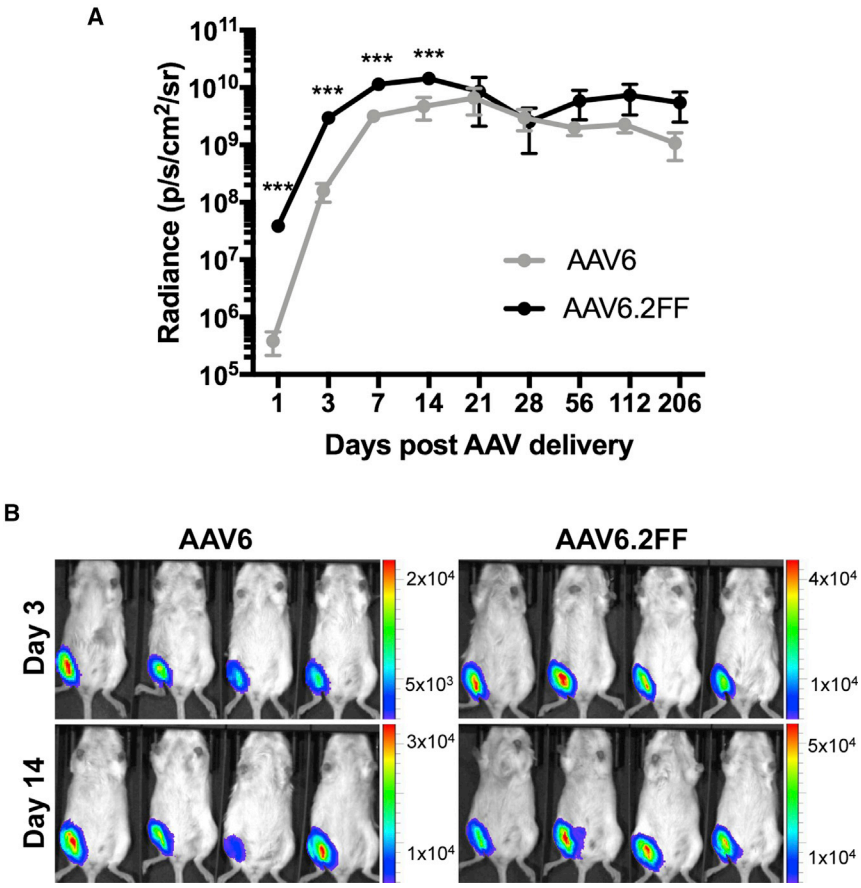


Figure 4. Intramuscular Transgene Expression Kinetics of AAV6 and AAV6.2FF

Albino C57BL/6 mice (n = 4/ group) were injected with 1×10^{11} vg of AAV6- or AAV6.2FF-Luciferase. (A) Quantification of luciferase signal on days 1, 3, 7, 14, 21, 28, 56, 112, and 205 post-AAV delivery from the ventral view. Values are expressed as means ± SD. Paired t tests were used to calculate significance; ***$p < 0.001$. (B) Representative images demonstrating luciferase expression on days 3 and 14 post-AAV delivery to the gastrocnemius muscle.

per microgram of total lung homogenate, while the lungs transduced by AAV6 contained concentrations of AP below the level of detection (Figure 6B).

DISCUSSION

Similar to AAV6.2, AAV6.2FF maintains the heparin sulfate binding properties of AAV6, which is ideal for large-scale production of AAV using heparin column chromatography, as ultracentrifugation is impractical for large volumes.[6,12] AAV6 heparin binding is conferred by a single lysine at position 531, and replacing this residue with a glutamate (K531E) abolishes heparin binding capacity,[13] indicating that F129L, Y445F, or Y731F mutations do not hamper K531 interaction with heparin sulfate.

AAV can be difficult to work with in cell culture, sometimes requiring large MOIs. AAV6 is one of the most amenable serotypes to *in vitro* transduction; however, the mutations introduced to produce AAV6.2FF further improve the *in vitro* transducing property of this capsid. AAV6.2FF mediated the strongest luciferase expression in all cell lines tested, making it a useful tool for cell culture experiments.

Pre-existing immunity to AAV capsids has had detrimental outcomes for some past gene therapy clinical trials.[14] Two separate studies reported the presence of anti-AAV6 neutralizing antibodies in 30%–46% of healthy individuals sampled.[11,13] The increased resistance to IVIG neutralization mediated by AAV6.2FF allows the generation of more effective gene therapies by evading pre-existing immunity while retaining other beneficial properties of AAV6. However, the mechanism of decreased IVIG neutralization against AAV6.2FF is interesting because there are only three amino acid differences between AAV6.2FF and the parental AAV6. F129L is not a surface-exposed residue and only becomes externally available during endosomal trafficking; therefore, its role in antibody neutralization is likely minimal.[15] The surface-exposed tyrosine residues at positions 445 and 731 were replaced with phenylalanine, and although the chemical structures of these amino acids are similar, the mutations resulted in a beneficial reduction in IVIG neutralization.

AAV6.2FF mediated significantly greater transgene expression than AAV6 in the lungs and nasal cavities of mice 3 wk post-AAV administration. AAV6.2 was previously reported to generate an approximately 2-fold increase in transduction of alveolar cells compared with AAV6,[5] whereas AAV6.2FF enhanced transduction 9.6 times over AAV6 in the lung. Conversely, AAV6.2FF did not yield a significant difference compared with AAV6 in the muscle because long-term expression of these vectors beyond 2 wk produced equivalent levels of transgene. However, at 24 hr post-vector administration, transgene expression was significantly stronger from AAV6.2FF in both the muscle and lungs with 101- and 49-fold greater expression, respectively. Therefore, we have engineered an AAV6 variant that enhances the magnitude of early transgene expression without negatively altering the long-term expression kinetics of AAV6. We hypothesize that this increase in 24-hr expression is due to a reduction of ubiquitin-mediated degradation of AAV6.2FF capsid protein due to the absence of tyrosine residues at positions 445 and 731. Consequently, AAV trafficking and entry to the nucleus is more efficient, resulting in greater transgene expression shortly after viral entry.[9]

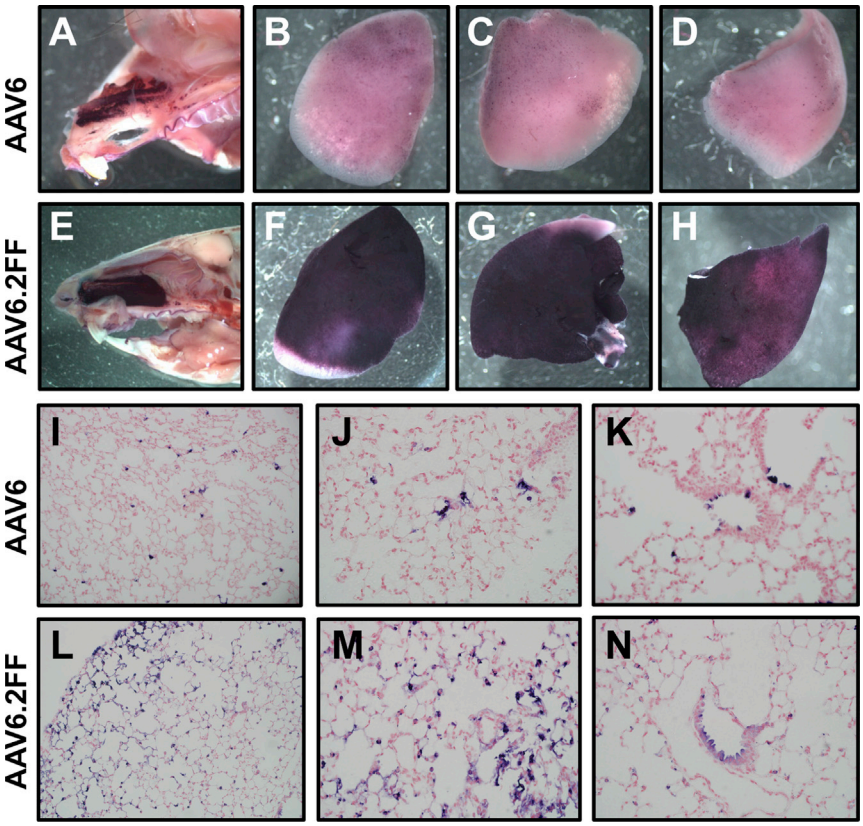


Figure 5. AP Staining of AAV6- and AAV6.2FF-Transduced Nose and Lungs

1×10^{11} vg of AAV6- or AAV6.2FF-AP was delivered intranasally to C57BL/6 mice (n = 4/group), and tissues were harvested and stained after 3 wk. Representative images of (A and E) the nose and (B–D, F–H) lung lobes for both vectors are shown. Lung sections were counter-stained with nuclear fast red, and transduced cells expressing AP appear purple. Representative sections of transduced lung are shown at (I and L) ×20 and (J, K, M, and N) ×40 original magnification for AAV6 and AAV6.2FF.

AAV6.2FF was developed as a dual-purpose capsid for a vectored immunoprophylaxis (VIP) platform to enable muscular and respiratory antibody gene expression, in addition to use as a traditional gene transfer vector to the lung. Using the same AAV capsid for multiple applications will facilitate standardization of vector production both for research use and translation to the clinic. Although early and robust expression of transgenes may not be critical for some traditional gene therapy applications, this advancement may have implications for the use of VIP as a post-exposure treatment option during outbreaks of emerging infectious diseases.

MATERIALS AND METHODS

Cell Culture and Plasmids

Cell lines were maintained in DMEM (HyClone) supplemented with L-glutamine (HyClone) and 7% fetal bovine serum (HyClone) at 37°C and 5% CO_2. The pDGM6 plasmid contains the Rep and AAV6 Cap genes, which was modified to generate a pDGM6.2FF plasmid. The AAV genome plasmids contained firefly luciferase or human placental AP driven by the CASI promoter[16] followed by an SV40 polyA signal and a Woodchuck hepatitis virus (WHP) posttranscriptional regulatory element (WPRE).

AAV Vector Production

AAV vectors were produced by transfection of HEK293 cells as described previously.[17] AAV6 and AAV6.2FF vectors were purified using a GE HiTrap heparin column,[18] while AAV9 was purified by iodixanol gradient.[19] Vector titers were determined using a TaqMan qPCR assay.[20]

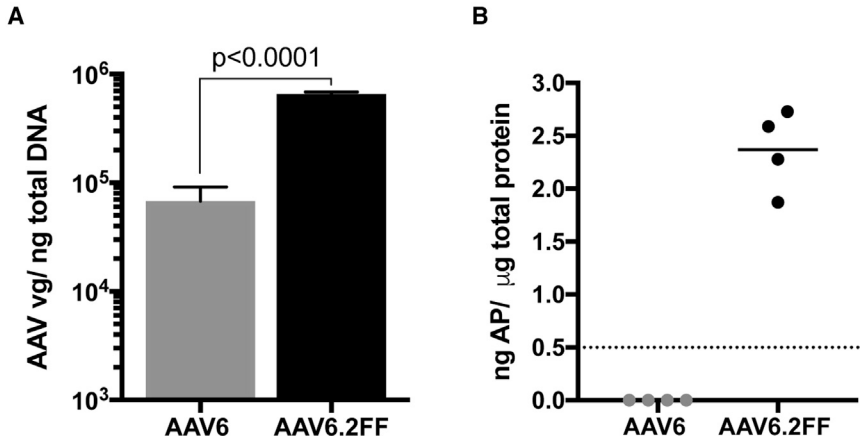


Figure 6. Quantification of AAV Vector Genomes in Transduced Lung Tissue

(A) TaqMan qPCR quantification of AAV genome copy number per nanogram of total DNA extracted from paraffin-embedded lung tissue. Values are expressed as means ± SD. Differences in AAV vg copy number between AAV6 and AAV6.2FF were determined using a Student's t test. (B) Quantification of AP enzymatic activity in unfixed lung tissue. Dashed line indicates the threshold of detection for the assay.

Heparin Binding Assay

Crude lysate from cells transfected with plasmids for production of AAV6 and AAV6.2FF pseudotyped vectors was clarified and 0.22 μm filtered prior to loading onto a 5-mL HiTrap heparin HP column (GE). The column was equilibrated with DMEM prior to loading the vector and subsequently washed first with 25 mL of HBSS without Mg^{2+}/Ca^{2+} (HyClone), again with 25 mL of HBSS with Mg^{2+}/Ca^{2+} and finally eluted with 10 mL of HBSS with Mg^{2+}/Ca^{2+} supplemented with 300 mM NaCl. The proportion of AAV in each fraction was determined by TaqMan qPCR.[21]

AAV Transduction, Binding, and Internalization Assays

1×10^5 cells were seeded into 24-well plates and allowed to adhere overnight. AAV was added the next day at an MOI of 2,000 in triplicate. 72 hr following the addition of AAV vector, cell lysate was harvested for quantification of luciferase expression (Promega) and Bradford analysis to determine the total protein content (Bio-Rad). Transgene expression is reported as relative light units (RLUs) per microgram of total protein.

IVIG Neutralization Assay

Human IVIG (Privigen) was serially diluted in PBS and added to 1×10^8 vector genomes (vg) of AAV in an equal volume, for a total of 25 μL, and incubated for 1 hr at 37°C, then added to HeLa cells in triplicate. After 72 hr, cell lysate was harvested for luciferase quantification according to the manufacturer's instructions (Promega).

In Vivo Imaging of Luciferase Expression

All animal experiments were approved by the Institutional Animal Care Committees of the Canadian Science Centre for Human and Animal Health, the University of Guelph, the Cincinnati Children's Hospital Medical Center, and the National Microbiology Laboratory (NML). Albino C57BL/6 mice (Jackson Labs) received 1×10^{11} vg of AAV6-Luciferase or AAV6.2FF-Luciferase in the gastrocnemius muscle in a 40 μL injection. Luciferase expression was quantified on days 1, 3, 7, 14, 21, 28, 56, 112, and 205 post-AAV delivery using a Xenogen IVIS as previously described.[22] Alternatively, for lung delivery, mice received the same total vector dose, but it was administered in two intranasal instillations of 40 μL each, given 20 min apart (20), and luciferase expression was quantified 24 hr later.

Lung AP Expression

C57BL/6 mice (Jackson Labs) were administered 1×10^{11} vg of AAV6-AP or AAV6.2FF-AP by a modified intranasal technique as described previously.[23] Three weeks following AAV delivery, the lungs and nose were harvested and fixed in 2% paraformaldehyde for 2 or 16 hr, respectively. Tissues were washed three times in PBS and heat-inactivated for 1 hr at 65°C prior to overnight incubation in AP staining buffer (100 mM Tris [pH 8.5], 100 mM NaCl, 50 mM $MgCl_2$) with 100× X-PHOS (10 mg/mL 5-bromo-4-chloro-3-indolyl phosphate; Sigma) and 100× nitro blue tetrazolium chloride (50 mg/mL; Invitrogen). Gross images were acquired prior to paraffin embedding and sectioning for histological staining. Transduction was quantified by analyzing the copy number of AAV vg per 100 ng of genomic DNA extracted from paraffin-embedded tissue by qPCR as previously described.[23] Quantification of AP present in homogenized lung tissue was performed as previously reported.[21]

Statistical Analysis

GraphPad Prism 7 software was used for statistical analyses. Multiple t tests were used unless otherwise stated. Data are expressed as mean ± SD.

AUTHOR CONTRIBUTIONS

L.P.v.L., J.P.B., and S.K.W. designed the experiments. L.P.v.L. and J.M.D. produced the vectors and completed *in vitro* and mouse experiments. J.P.B and S.A.B. oversaw the IVIS experiments, and T.N.R., K.L.F., D.L.S., and S.J.M executed these studies. L.P.v.L. and S.K.W. wrote the manuscript.

CONFLICTS OF INTEREST

The authors declare no conflicts of interest.

ACKNOWLEDGMENTS

We thank Dr. Bernard Thebaud for supplying MLE-12 cells, Dr. David Russell for providing the pDGM6 plasmid, and all those who participated in the care of the mice at all institutions. This work was funded by Cystic Fibrosis Canada (grant numbers 2635 and 3017) and the Ontario Lung Association (grant number 052919).

REFERENCES

1. Zincarelli, C., Soltys, S., Rengo, G., and Rabinowitz, J.E. (2008). Analysis of AAV serotypes 1-9 mediated gene expression and tropism in mice after systemic injection. Mol. Ther. *16*, 1073–1080.

2. Ellis, B.L., Hirsch, M.L., Barker, J.C., Connelly, J.P., Steininger, R.J., 3rd, and Porteus, M.H. (2013). A survey of ex vivo/in vitro transduction efficiency of mammalian primary cells and cell lines with Nine natural adeno-associated virus (AAV1-9) and one engineered adeno-associated virus serotype. Virol. J. *10*, 74.

3. Grimm, D., Lee, J.S., Wang, L., Desai, T., Akache, B., Storm, T.A., and Kay, M.A. (2008). In vitro and in vivo gene therapy vector evolution via multispecies interbreeding and retargeting of adeno-associated viruses. J. Virol. *82*, 5887–5911.

4. Lerch, T.F., O'Donnell, J.K., Meyer, N.L., Xie, Q., Taylor, K.A., Stagg, S.M., and Chapman, M.S. (2012). Structure of AAV-DJ, a retargeted gene therapy vector: cryo-electron microscopy at 4.5 Å resolution. Structure *20*, 1310–1320.

5. Limberis, M.P., Vandenberghe, L.H., Zhang, L., Pickles, R.J., and Wilson, J.M. (2009). Transduction efficiencies of novel AAV vectors in mouse airway epithelium in vivo and human ciliated airway epithelium in vitro. Mol. Ther. *17*, 294–301.

6. Vandenberghe, L.H., Breous, E., Nam, H.J., Gao, G., Xiao, R., Sandhu, A., Johnston, J., Debyser, Z., Agbandje-McKenna, M., and Wilson, J.M. (2009). Naturally occurring singleton residues in AAV capsid impact vector performance and illustrate structural constraints. Gene Ther. *16*, 1416–1428.

7. Yan, Z., Zak, R., Luxton, G.W., Ritchie, T.C., Bantel-Schaal, U., and Engelhardt, J.F. (2002). Ubiquitination of both adeno-associated virus type 2 and 5 capsid proteins affects the transduction efficiency of recombinant vectors. J. Virol. *76*, 2043–2053.

8. Zhong, L., Li, B., Jayandharan, G., Mah, C.S., Govindasamy, L., Agbandje-McKenna, M., Herzog, R.W., Weigel-Van Aken, K.A., Hobbs, J.A., Zolotukhin, S., et al. (2008a). Tyrosine-phosphorylation of AAV2 vectors and its consequences on viral intracellular trafficking and transgene expression. Virology *381*, 194–202.

9. Zhong, L., Li, B., Mah, C.S., Govindasamy, L., Agbandje-McKenna, M., Cooper, M., Herzog, R.W., Zolotukhin, I., Warrington, K.H., Jr., Weigel-Van Aken, K.A., et al. (2008b). Next generation of adeno-associated virus 2 vectors: point mutations in

tyrosines lead to high-efficiency transduction at lower doses. Proc. Natl. Acad. Sci. USA *105*, 7827–7832.

10. Markusic, D.M., Herzog, R.W., Aslanidi, G.V., Hoffman, B.E., Li, B., Li, M., Jayandharan, G.R., Ling, C., Zolotukhin, I., Ma, W., et al. (2010). High-efficiency transduction and correction of murine hemophilia B using AAV2 vectors devoid of multiple surface-exposed tyrosines. Mol. Ther. *18*, 2048–2056.
11. Fuchs, S.P., Martinez-Navio, J.M., Gao, G., and Desrosiers, R.C. (2016). Recombinant AAV vectors for enhanced expression of authentic IgG. PLoS ONE *11*, e0158009.
12. Qiao, C., Zhang, W., Yuan, Z., Shin, J.H., Li, J., Jayandharan, G.R., Zhong, L., Srivastava, A., Xiao, X., and Duan, D. (2010). Adeno-associated virus serotype 6 capsid tyrosine-to-phenylalanine mutations improve gene transfer to skeletal muscle. Hum. Gene Ther. *21*, 1343–1348.
13. Wu, Z., Asokan, A., Grieger, J.C., Govindasamy, L., Agbandje-McKenna, M., and Samulski, R.J. (2006). Single amino acid changes can influence titer, heparin binding, and tissue tropism in different adeno-associated virus serotypes. J. Virol. *80*, 11393–11397.
14. Mingozzi, F., and High, K.A. (2013). Immune responses to AAV vectors: overcoming barriers to successful gene therapy. Blood *122*, 23–36.
15. Ng, R., Govindasamy, L., Gurda, B.L., McKenna, R., Kozyreva, O.G., Samulski, R.J., Parent, K.N., Baker, T.S., and Agbandje-McKenna, M. (2010). Structural characterization of the dual glycan binding adeno-associated virus serotype 6. J. Virol. *84*, 12945–12957.
16. Balazs, A.B., Chen, J., Hong, C.M., Rao, D.S., Yang, L., and Baltimore, D. (2011). Antibody-based protection against HIV infection by vectored immunoprophylaxis. Nature *481*, 81–84.
17. Halbert, C.L., Allen, J.M., and Miller, A.D. (2002). Efficient mouse airway transduction following recombination between AAV vectors carrying parts of a larger gene. Nat. Biotechnol. *20*, 697–701.
18. Halbert, C.L., Allen, J.M., and Chamberlain, J.S. (2018). AAV6 vector production and purification for muscle gene therapy. Methods Mol. Biol. *1687*, 257–266.
19. Khan, I.F., Hirata, R.K., and Russell, D.W. (2011). AAV-mediated gene targeting methods for human cells. Nat. Protoc. *6*, 482–501.
20. Aurnhammer, C., Haase, M., Muether, N., Hausl, M., Rauschhuber, C., Huber, I., Nitschko, H., Busch, U., Sing, A., Ehrhardt, A., and Baiker, A. (2012). Universal real-time PCR for the detection and quantification of adeno-associated virus serotype 2-derived inverted terminal repeat sequences. Hum. Gene Ther. Methods *23*, 18–28.
21. Yu, D.L., Linnerth-Petrik, N.M., Halbert, C.L., Walsh, S.R., Miller, A.D., and Wootton, S.K. (2011). Jaagsiekte sheep retrovirus and enzootic nasal tumor virus promoters drive gene expression in all airway epithelial cells of mice but only induce tumors in the alveolar region of the lungs. J. Virol. *85*, 7535–7545.
22. van Lieshout, L.P., Soule, G., Sorensen, D., Frost, K.L., He, S., Tierney, K., Safronetz, D., Booth, S.A., Kobinger, G.P., Qiu, X., and Wootton, S.K. (2018). Intramuscular adeno-associated virus-mediated expression of monoclonal antibodies provides 100% protection against Ebola virus infection in mice. J. Infect. Dis. *217*, 916–925.
23. Santry, L.A., Ingrao, J.C., Yu, D.L., de Jong, J.G., van Lieshout, L.P., Wood, G.A., and Wootton, S.K. (2017). AAV vector distribution in the mouse respiratory tract following four different methods of administration. BMC Biotechnol. *17*, 43.

OXFORD

Human Molecular Genetics, 2017, Vol. 0, No. 0 1–12

doi: 10.1093/hmg/ddx056
Advance Access Publication Date: 21 February 2017
Original Article

ORIGINAL ARTICLE

AAV9 delivered bispecific nanobody attenuates amyloid burden in the gelsolin amyloidosis mouse model

Adriaan Verhelle[1], Nisha Nair[2], Inge Everaert[3], Wouter Van Overbeke[1], Lynn Supply[4], Olivier Zwaenepoel[1], Cindy Peleman[5], Jo Van Dorpe[4], Tony Lahoutte[5], Nick Devoogdt[5], Wim Derave[3], Marinee K. Chuah[2,6], Thierry Vanden Driessche[2,6] and Jan Gettemans[1,*]

[1]Department of Biochemistry, Faculty of Medicine and Health Sciences, Ghent University, Ghent, Belgium, [2]Department of Gene Therapy & Regenerative Medicine, Free University of Brussels (VUB), Brussels, Belgium, [3]Department of Movement and Sport Sciences, Faculty of Medicine and Health Sciences, Ghent University, Ghent, Belgium, [4]Department of Medical and Forensic Pathology, Faculty of Medicine and Health Sciences, Ghent University, Ghent, Belgium, [5]In Vivo Cellular and Molecular Imaging Laboratory, Free University of Brussels (VUB), Brussels, Belgium and [6]Department of Cardiovascular Sciences, Catholic University of Leuven (KU Leuven), Leuven, Belgium

*To whom correspondence should be addressed at: Faculty of Medicine and Health Sciences, Department of Biochemistry, Ghent University, Albert Baertsoenkaai 3, B-9000 Ghent, Belgium. Tel: +32 9 2649340; Fax: + 32 9 2649490; Email: jan.gettemans@ugent.be

Abstract

Gelsolin amyloidosis is a dominantly inherited, incurable type of amyloidosis. A single point mutation in the gelsolin gene (G654A is most common) results in the loss of a Ca^{2+} binding site in the second gelsolin domain. Consequently, this domain partly unfolds and exposes an otherwise buried furin cleavage site at the surface. During secretion of mutant plasma gelsolin consecutive cleavage by furin and MT1-MMP results in the production of 8 and 5 kDa amyloidogenic peptides. Nanobodies that are able to (partly) inhibit furin or MT1-MMP proteolysis have previously been reported. In this study, the nanobodies have been combined into a single bispecific format able to simultaneously shield mutant plasma gelsolin from intracellular furin and extracellular MT1-MMP activity. We report the successful *in vivo* expression of this bispecific nanobody following adeno-associated virus serotype 9 gene therapy in gelsolin amyloidosis mice. Using SPECT/CT and immunohistochemistry, a reduction in gelsolin amyloid burden was detected which translated into improved muscle contractile properties. We conclude that a nanobody-based gene therapy using adeno-associated viruses shows great potential as a novel strategy in gelsolin amyloidosis and potentially other amyloid diseases.

Introduction

Gelsolin amyloidosis (AGel) is an autosomal dominantly inherited disease caused by a point mutation in the gelsolin (*GSN*) gene (G654A being the most common, D187N) (1,2). The resulting destabilization of the second gelsolin domain (gelsolin consist of 6 domains, G1-G6) results in an aberrant proteolytic

Received: December 21, 2016. **Revised:** February 6, 2017. **Accepted:** February 7, 2017

© The Author 2017. Published by Oxford University Press. All rights reserved. For Permissions, please email: journals.permissions@oup.com

cascade, specifically affecting the plasma variant (3–6). During its transport through the intracellular secretion pathway, mutant plasma gelsolin (PG*), is first cleaved by furin in the trans-Golgi network leading to the formation of a 68 kDa C-terminal fragment (7). When this C68 fragment is secreted, a second proteolytic cleavage by MT1-MMP like proteases results in the release of 8 and 5 kDa amyloidogenic fragments (8). Over time, particularly the 8 kDa peptide will start to aggregate, forming cross-beta-sheet amyloid fibrils and plaques. Patients experience a triad of neurological, ophthalmological and dermatological symptoms (9,10). At the moment, no specific treatments for AGel are available. Instead, patients undergo several symptomatic and aesthetic treatments to improve their quality of life.

Our previous studies have shown that chaperoning nanobodies are able to (partly) inhibit the pathological furin and MT1-MMP cleavages *in vitro* and *in vivo*, resulting in physiological improvements in transgenic mice that recapitulate the proteolytic AGel cascade (11,12). In view of the central roles that furin and MT1-MMP undertake in neuropeptide maturation and connective tissue organization/activation of other metalloproteases, respectively, we argue that these proteases should not be considered as therapeutic targets, particularly since familial amyloidosis is a chronic disease. For this reason we used camelid nanobodies that interact specifically with (mutant) gelsolin and shield the protein either from furin (12) or MT1-MMP degradation (11), thus acting as molecular chaperones.

In the present study, we combined the two nanobodies into a single bispecific format with the aim of providing simultaneous protection against both proteases simultaneously. The nanobodies were separated by an MT1-MMP-sensitive peptide sequence which was used as an MT1-MMP protease decoy. We investigated if this approach affected the binding characteristics of the individual nanobodies and if this format was able to significantly increase the chaperoning capacity *in vitro*.

Because furin is an intracellular protease, our approach required intracellular delivery of the protective bispecific nanobody. We opted for adeno-associated virus serotype 9 (AAV9) gene therapy (13) considering that AAVs are able to infect both dividing and quiescent cells. Moreover, they remain episomally present in the host cell nucleus, thereby preventing the possibility of insertional mutagenesis.

Using a recently developed nanobody based imaging agent (14) and immunohistochemistry, we provide evidence of a significant decrease in gelsolin amyloid buildup in both the skeletal muscle and heart of AGel mice injected with AAV9-Nb11-FAF1 vector during the neonatal period. These results are further supported by improved muscle contractile properties following treatment.

Results

Production of the bispecific nanobody

In a previous study, we have identified a gelsolin nanobody, Nb11, capable of partly inhibiting the production of C68 by furin (12). Nb11 binds (mutant) plasma gelsolin irrespective of calcium, and acts as a molecular chaperone when targeted to the trans-Golgi network where it binds to and protects gelsolin. Further downstream, reduced C68 formation results in a decrease of AGel amyloid buildup. In another study, we followed a different approach and identified three closely related nanobodies, FAF Nb1, 2 and 3, (FAF1-3) capable of binding both C68 and the 8 kDa amyloidogenic gelsolin fragment, thwarting MT1-MMP activity, not furin. *In vivo*, upon binding of C68, these nanobodies once again acted as a chaperone and partly prevented production of the pathological 8 kDa AGel fragment (11). Here our aim was to combine the two in a clinically applicable way.

Nb11 cDNA was amplified through PCR, introducing a HA-tag at the 5' end and the sequence encoding the MT1-MMP sensitive peptide SLAPLGLQRR (15), sandwiched between two Gly-Ser linkers (GS) at the 3' end. This fragment was linked to the 5' end of FAF Nb1-3 cDNA, already present in the pHEN6-V5-His_6 vector, resulting in a final construct where both nanobodies occur in tandem configuration, separated by the MT1-MMP sensitive peptide sequence and GS linker (Fig. 1A).

Bispecific gelsolin nanobodies merge the binding characteristics of their monovalent constituents *in vitro*

The binding characteristics of the bispecific nanobodies were compared to their monovalent counterparts using ELISA. As antigen, PG, PG*, C68 and the 8 kDa AGel fragment were coated. CapG was chosen as a negative control. This protein belongs to the same family as gelsolin and displays 49% similarity (16). Nb11 recognized, in decreasing order of magnitude, PG, PG*, C68 and 8 kDa. The FAF Nbs displayed the opposite binding pattern, as previously described (11,12). The bispecific Nb11-FAF combinations exhibited a merge of the Nb11 and FAF1-3 binding characteristics (Fig. 2A and Supplementary Material, Fig. S1). No significant binding with the negative control was observed. Furthermore, as previously described (11), FAF Nb1-3 can be used in Western blotting as primary antibodies against PG, PG*, C68 and the 8 kDa AGel fragment. Linked to Nb11, this ability remained unaffected (Fig. 2B and C).

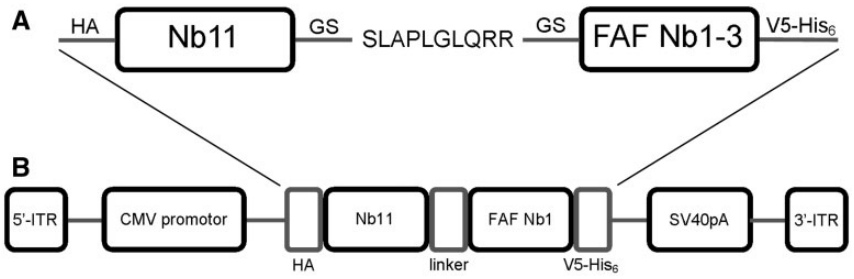


Figure 1. The two nanobodies, Nb11 and FAF Nb1-3, are linked via the MT1-MMP sensitive sequence SLAPGLQRR, flanked between two GS linkers. An N-terminal HA and C-terminal V5-His_6 tag is present (**A**). The expression cassette was cloned in a self-complementary (sc) adeno-associated virus backbone that was packaged using AAV serotype 9 capsids (AAV9). Expression of Nb11-FAF1 is driven by the CMV promoter. The 5' and 3' inverted terminal repeats (ITR) and SV40 polyadenylation site (pA) are indicated (**B**).

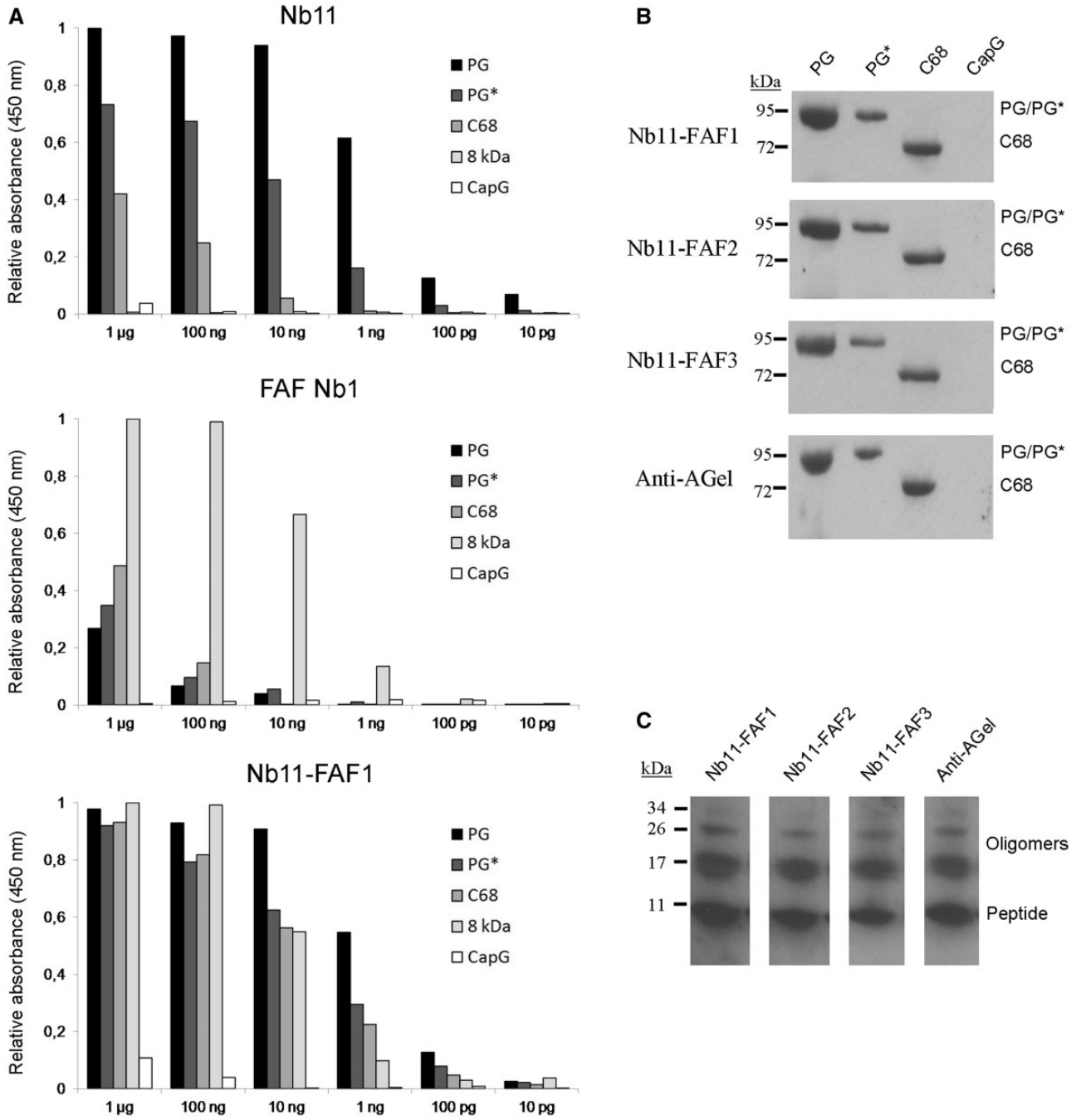


Figure 2. The interaction of monovalent Nb11 and FAF Nb1 with PG, PG*, C68 and the 8 kDa peptide, in an ELISA setup, are merged in the Nb11-FAF1 construct (**A**). Each time a tenfold nanobody dilution series was used, starting from 1 µg up to 10 pg. Signals are represented relative to the highest value, normalized to 1. (**B,C**) 5µg bacterial lysate containing PG, PG*, C68, 8 kDa peptide or CapG was fractionated by SDS-PAGE. Nb11- FAF1-3 can be used as the primary antibody in Western blot analysis (11). Polyclonal anti-AGel antibody was used as a positive control. (**C**) Both the monomeric and oligomeric forms of the 8 kDa peptide are visualized by the nanobodies. Additional bands under the PG/PG* signal (95 kDa marker) and C68 signal (72 kDa marker) represent degradation products.

The MT1-MMP peptide linker is functional in an *in vitro* setup

As mentioned earlier, the linker between Nb11 and FAF Nb1-3 contains the MT1-MMP sensitive peptide SLAPLGLQRR (proteolysis of the GL scissile bond). The purpose of this setup was that, *in vivo*, during secretion, proteolysis of this sequence would release the FAF Nb, enabling it to perform its function without any interference of Nb11. At the same time this mechanism may act as a decoy, luring MT1-MMP away from the (lower amount of) C68 being secreted. This was tested *in vitro* using the recombinant catalytic domain of MT1-MMP. The MT1-MMP sensitive peptide proved to be very efficient in all three bivalent Nb11-FAF constructs and they were readily cleaved upon incubation with MT1-MMP (Fig. 3).

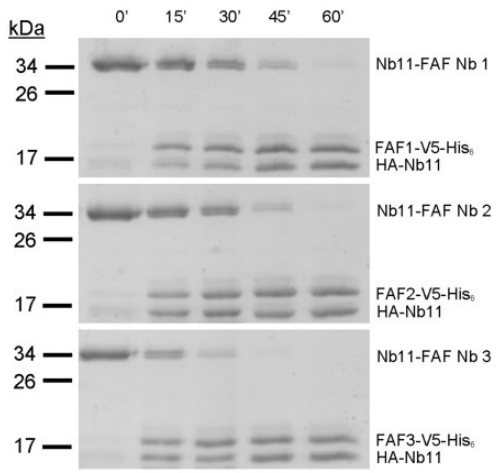


Figure 3. The bispecific Nb11-FAF constructs were incubated *in vitro* with MT1-MMP for 1 h at 37 °C. At distinct time points (0, 15, 30, 45 and 60 min) samples were taken and the reaction was stopped with Laemmli sample buffer. Samples were boiled for 5 min. Visualization was done via Coomassie staining after SDS-PAGE fractionation. MT1-MMP was able to recognize and cleave the SLAPGLQRR sequence, thereby releasing the two individual nanobodies.

Combined furin/MT1-MMP cleavage assay - bivalent Nb11-FAF Nb protects D187N plasma gelsolin against combined furin-MT1-MMP proteolysis

Since Nb11 can inhibit furin proteolysis of PG* whereas FAF1-3 counteract MT1-MMP proteolysis of C68 by shielding the substrate, we hypothesized that bivalent Nb11-FAF formats might be able to combine both traits, leading to a synergetic inhibitory effect on 8 kDa amyloidogenic peptide production. An *in vitro* assay was set up wherein the nanobodies were incubated with PG*, followed consecutively, by furin and MT1-MMP proteolysis. Formation of both C68 and the 8 kDa fragment was assessed by Western blotting (Fig. 4A). Only Nb11-FAF1 could match the inhibitory capacity of Nb11 when looking at C68 formation, the intermediate AGel species formed by furin (Fig. 4B). Quantification of the amyloidogenic 8 kDa fragment showed that all three Nb11-FAF constructs were able to inhibit formation of the 8 kDa AGel peptide more efficiently than their monovalent counterparts (Fig. 4C). Hence, the bivalent format is endowed with a double protective activity, and the formation of the 8 kDa fragment in particular is strongly reduced in comparison to monospecific Nb11 or FAF nanobodies.

Furin assay in HEK293T - bivalent Nb11-FAF Nb inhibit furin proteolysis

In the *in vitro* setup Nb11-FAF1-3 were able to bind their antigen targets and showed a significant protective chaperone activity towards PG* and C68. As we wanted to confirm this in a more complex environment, PG, PG* and the Nb11-FAF constructs were transiently expressed in HEK293T cells. Since the first step in AGel pathogenesis, furin cleavage, takes place in the trans-Golgi network, all constructs were equipped with an N-terminal ER-targeting sequence. Co-staining of the constructs followed by epifluorescence microscopy confirmed their colocalisation along the secretory pathway (Supplementary Material, Figs S2A and S3). After 24 h, we analyzed the cell medium via Western blotting (Supplementary Material, Fig. S2B). Quantification of the C68 signal revealed a similar pattern as in the *in vitro* setup; the bispecific Nb11-FAF nanobodies show an inhibitory effect towards furin proteolysis, however none can outperform monovalent Nb11 in this cell based setup (Supplementary Material, Fig. S2C). We were unable to assess the effect on MT1-MMP proteolysis as no 8 kDa peptide could be detected within the observed timeframe.

Bispecific Nb11-FAF1 gene therapy in AGel mice via AAV9

Since the bispecific nanobodies effectively combined the binding and therapeutic characteristics of its monovalent counterparts, an AGel mouse model intervention study was set up. This mouse model recapitulates the pathological AGel pathway in its muscle tissue, leading to extensive, age related, extracellular amyloidogenic gelsolin buildup (17). Nb11-FAF1 was chosen based on its superior characteristics *in vitro*. Homozygote neonates (2–3 days old) were injected with 4.7 x 10^{10} vg/mouse of AAV9-Nb11-FAF1, AAV9-Luc2 (viral control) (18,19) or PBS (negative control) via the retro-orbital plexus. No adverse effects on the development or behavior of the mice were apparent. Nanobody expression was confirmed at 1, 2 and 3 months of age in the plasma of both WT and AGel mice (Fig. 5). The presence of a band at 34 kDa and two at 17 kDa indicates that the MT1-MMP sensitive linker is functional *in vivo* (Fig. 5). At the age of 3 months Nb11-FAF1 gene therapeutic efficacy was determined via SPECT-CT, immunofluorescence and ex vivo muscle performance.

AAV9-Nb11-FAF1 displays therapeutic properties in AGel mice

SPECT-CT imaging. 3 months post treatment, AGel amyloid burden in skeletal muscle and myocardium was determined using SPECT/CT and a recently developed ^{99m}Tc-FAF Nb1 AGel tracer (14). In the WT control groups, AAV treatment did not significantly alter the background control signal (Fig. 6A and B). In the AGel group however, expression of Nb11-FAF1 resulted in a significantly lower signal (t-test, $p < 0.05$) in the skeletal muscle (25% vs. PBS and 28% vs. AAV9-ctrl) (Fig. 6A) and a significantly lower signal (t-test, $p < 0.05$) in the heart (30% vs. PBS and 36 vs. AAV9-ctrl) (Fig. 6B). This is consistent with a reduction of the characteristic amyloid burden in the AAV9-Nb11-FAF1-treated AGel mice.

Immunofluorescence. The mice were sacrificed three months post AAV injection. AGel amyloidogenic buildup in skeletal muscle and heart tissue was stained and quantified. Laminin was used as an internal control. Nb11-FAF1 expression resulted in a significant reduction (t-test, $p < 0.05$) of AGel amyloidogenic buildup in skeletal muscle (39% vs. PBS and 36% vs. AAV9-ctrl) (Fig. 7C) and in the heart (43% vs. PBS and 55% vs AAV9-ctrl) (Fig. 7D) in AGel mice. In contrast, WT control groups expressing Nb11-FAF1 showed no significantly different staining compared to the WT-PBS or WT-AAV9-Ctrl groups (Fig. 7A).

Ex vivo muscle performance is improved in AAV9-Nb11-FAF1 treated mice. At the end of the trial, mice were anaesthetized, the extensor digitorum longus (EDL) and soleus were dissected and their contractile properties were measured. The expression of Nb11-FAF1 in AGel mice resulted in a specific twitch force indistinguishable from the WT control groups (t-test, $p < 0.05$) and significantly different compared to the untreated (PBS or AAV9-ctrl) AGel groups in EDL muscle (t-test, $p < 0.05$) but not in the soleus (Fig. 8A and B). The amount of force that could be produced for a given frequency (force-frequency) was not affected

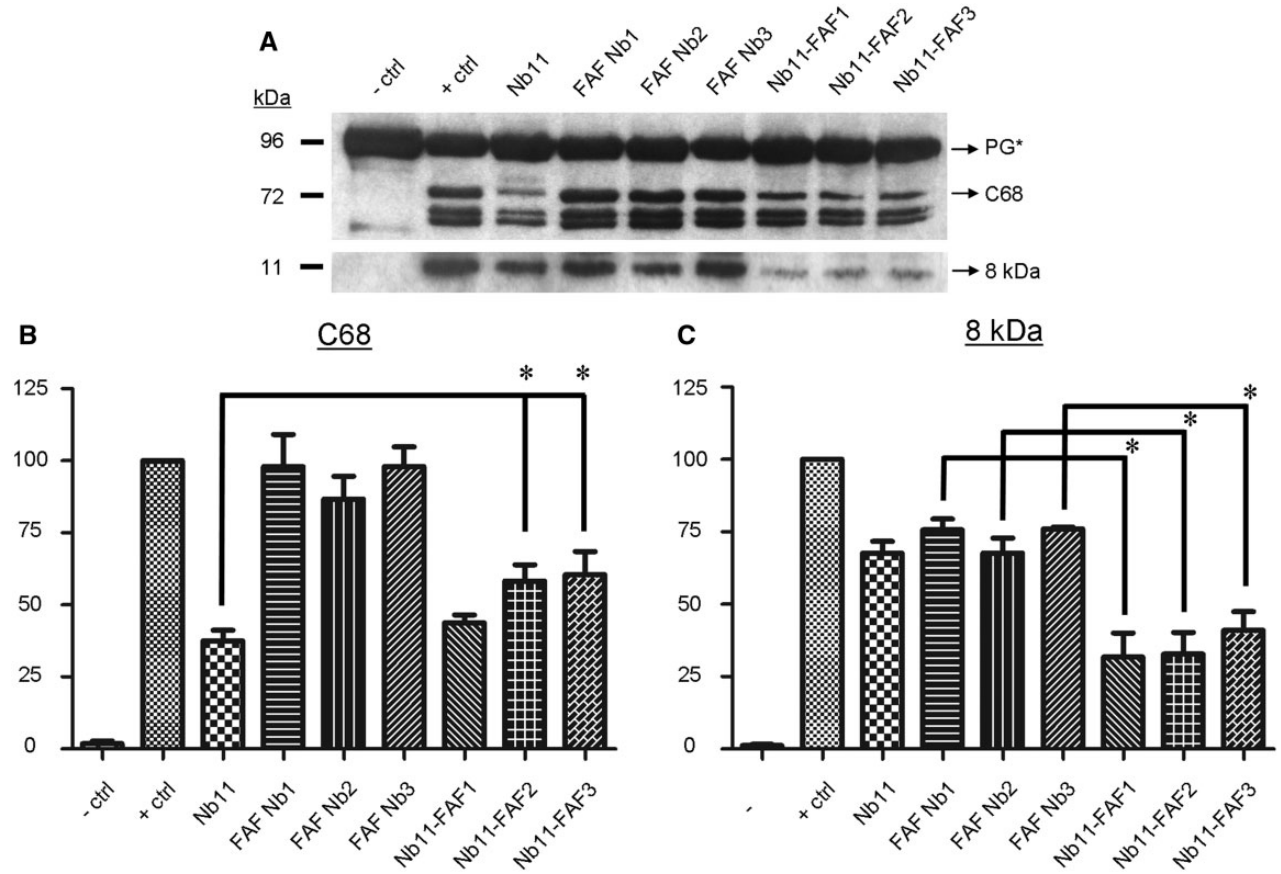


Figure 4. The AGel degradation was recapitulated *in vitro* through consecutive incubation of mutant plasma gelsolin with furin and MT1-MMP. Lane 1: negative control, no furin nor MT1-MMP. Lane 2: positive control, furin and MT1-MMP but no nanobody. Lane 3-9: Furin, MT1-MMP and an equimolar amount of different nanobodies. C68 and the 8 kDa peptide were detected with polyclonal anti-AGel antibody (**A**) and quantified (**B,C**). Based on the amount of C68 formed, only Nb11-FAF1 could match Nb11 (B). Quantification of the 8 kDa peptide (**C**), the end stage of AGel degradation, showed that all three Nb11-FAF constructs performed significantly better than their monovalent counterparts. Data shown are mean of quadruplicates ± SE. $^*P < 0.05$ in a two sided unpaired *t*-test.

by the amyloid burden nor by the treatment. Interestingly, fatigue progression was, both in EDL and soleus, significantly more pronounced in the WT versus the (un)treated FAF mice (data not shown). However, the speed of muscle contraction during fatigue in EDL muscle in the Nb11-FAF1 expressing AGel mice showed, as expected, a similar decline as the WT controls in contrast to the untreated (PBS or AAV9-ctrl) AGel mice (Fig. 8D). The soleus seemed unaffected (Fig. 8C).

Discussion

As is the case in the majority of amyloid diseases, AGel is characterized by a systemic deposition of amyloid fibrils. The amyloidogenic 8 kDa fragment is produced in a two step process; the first intracellular cleavage of PG* by furin is followed by an extracellular cleavage of C68 by MT1-MMP like proteases. Both in the present and previous studies, intra- and extracellularly active chaperoning nanobodies have been investigated regarding their potential to inhibit the formation of the amyloidogenic 8 kDa gelsolin fragment. The *in vivo* success of such chaperone based therapeutics strongly depends on the degree in which they distribute throughout the body. In the case of the extracellularly active FAF Nb1, systemic distribution was achieved by intraperitoneal injection (11). For the intracellularly active Nb11 study, a transgenic mouse model, constitutively expressing Nb11, had to be developed (12). Here our aim was to combine the FAF Nbs and Nb11 into a single format administered in a clinically applicable way; AAV9 based gene therapy.

Three bispecific nanobodies, Nb11-FAF1, Nb11-FAF2 and Nb11-FAF3 (Fig. 1A), were created. ELISA and Western blot analysis (Fig. 2 and Supplementary Material, Fig. S1) showed that, when linked together, the binding characteristics of the constituent nanobodies remained intact. The peptide used to link the two nanobodies was chosen for its susceptibility towards MT1-MMP proteolysis. We envisaged that this approach would result in proteolysis of the amino acid stretch *in vivo* upon secretion of C68, thereby releasing the FAF Nbs, after which they can exert their C68 chaperoning capacity in an unhindered manner. *In vitro*, this peptide sequence performed perfectly; incubation of the bispecific nanobodies with MT1-MMP resulted in the intact release of both constituent nanobodies (Fig. 3).

The chaperone activities of Nb11-FAF constructs were tested *in vitro* in a combined furin/MT1-MMP assay. Quantification of C68 and the 8 kDa peptide revealed that Nb11-FAF1 can rival with Nb11's PG* chaperoning activity. At the level of the 8 kDa peptide, all Nb11-FAF constructs outperformed their monovalent counterparts (Fig. 4).

To address the *in vivo* problem of amyloid buildup in the AGel mouse model we used a therapeutic approach involving on AAV vector-mediated delivery of the cDNA encoding the Nb11-FAF1 nanobody. AAV is a promising vector for gene therapy yielding long-term episomal expression of therapeutic

proteins in clinical trials. The vector tropism is determined by the type of AAV capsid used. We and others had previously demonstrated that AAV serotype 9 is well suited for cardiac and skeletal muscle gene delivery (19–23). Moreover, the first systemic AAV9 clinical therapy was initiated in 2014, in children up to nine months old, suffering from spinal muscular atrophy type 1 (24), resulting in an apparent sustained therapeutic effect. Since the AGel mouse model recapitulates AGel pathology in skeletal muscle and heart, we therefore also opted for AAV9. *In vivo* transduction with AAV9 vectors encoding the Nb11-FAF1 nanobody resulted in long-term expression of Nb11-FAF1, at least for 3 months post vector-injection, the endpoint of the study (Fig. 5). This is consistent with previous studies showing prolonged expression in the muscle after AAV gene therapy with many different serotypes, including AAV9 (19–23).

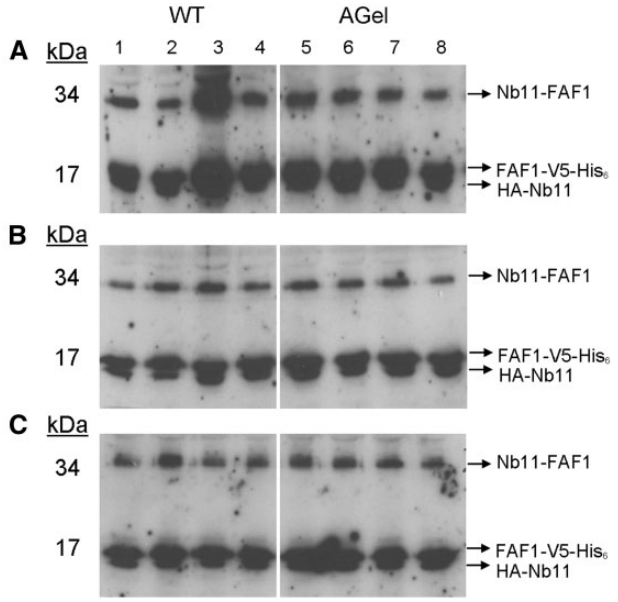


Figure 5. At 1 month of age (**A**), 1 mg of plasma protein was incubated with anti V5-agarose and anti HA-agarose. Bound protein was visualized via Western blotting after SDS-PAGE. Nb11-FAF1 is visible at the 34 kDa marker. The double band at the 17 kDa marker represents the Nb11 and FAF1 fragments, released after *in vivo* MT1-MMP cleavage. No differences in expression could be detected between WT (lane 1-4, 4 littermates) and AGel mice (lane 5-8, 4 littermates) mice. Nanobody expression remained detectable at 2 (**B**) and 3 (**C**) months. At each time point, corresponding lanes represent plasma taken from the same mouse.

Analysis by SPECT/CT and immunohistochemistry revealed a significant decrease in AGel amyloid buildup in both muscle and heart tissue (Figs 7 and 8), consistent with Nb11-FAF1 nanobody expression. The pathological AGel amyloid accumulation could be readily detected using anti-8 kDa antiserum or nanobodies in AGel mice, whereas it was absent in wild-type mice. Most importantly, the observed decrease in AGel buildup translated into improved muscle contractile properties. The EDL showed a specific twitch force indistinguishable from the WT control groups but significantly different from the untreated AGel mice. However, the fact that untreated AGel mice show the highest specific twitch force, and that Nb11-FAF1 treatment reduces this back to the WT base level, is quite counterintuitive. One would expect that the presence of AGel amyloid between the muscle fibers would negatively influence overall muscle performance. At the moment the molecular mechanisms behind this observation are still obscure. One possibility would be that in AGel affected muscle tissue, the fraction of unaffected muscle fibers somehow overcompensates the functional loss of the more affected fibers. EDL from Nb11-FAF1 treated mice also displayed improved relaxation speeds at the onset of fatigue (Fig. 8). The decline in the speed of muscle contraction during fatigue was identical to the one observed in the wild type mice. In contrast, in the untreated AGel control mice, the presence of AGel amyloid around the muscle fibers most likely hinders an efficient exchange of nutrients and metabolites, adversely impacting the relaxation rate. A reduction in AGel deposition, due to Nb11-FAF1 gene therapy, seems to ameliorate this pathological feature. Our results are consistent with our previous studies, showing that intraperitoneal administration of purified monovalent FAF Nbs or transgenic mice expressing Nb11 following insertion in the ROSA26 locus, also resulted in a

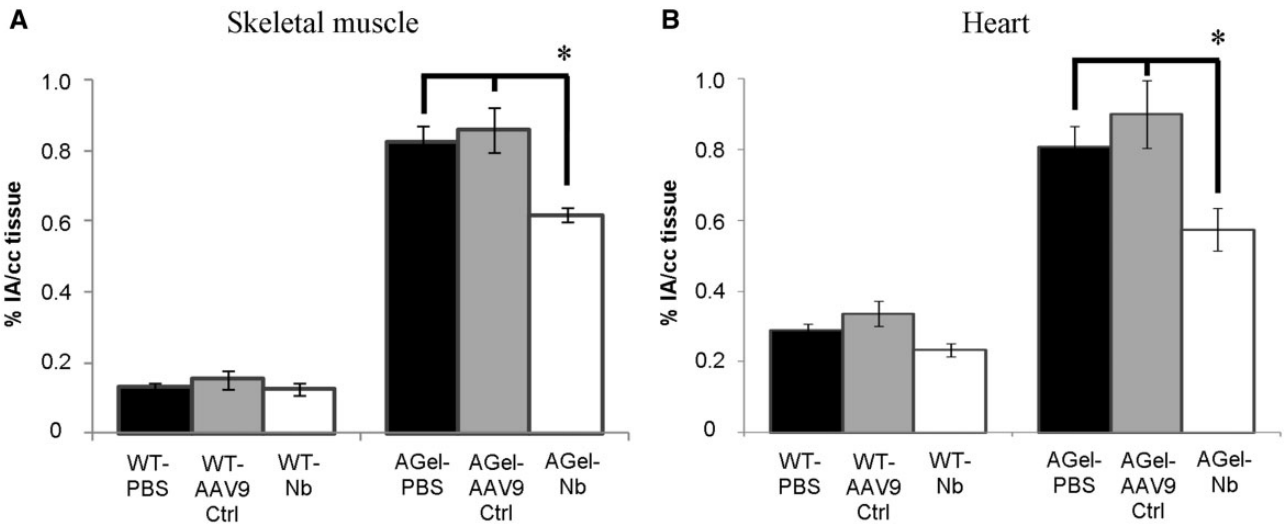


Figure 6. At 3 months of age all mice underwent a SPECT-CT scan with the ^{99m}Tc-FAF Nb1 AGel tracer (14). Identical regions of interest were drawn around hind leg muscles and heart. Signal quantification showed that Nb expression had no effect on WT background signal, neither in skeletal muscle (**A**) nor in heart (**B**). In AGel mice, Nb11-FAF1 expression resulted in a significantly lower signal in skeletal muscle (**A**) and the heart (**B**) compared to PBS and AAV9-control groups. Data shown as mean ± SE. *$P < 0.05$ in a two sided unpaired t-test.

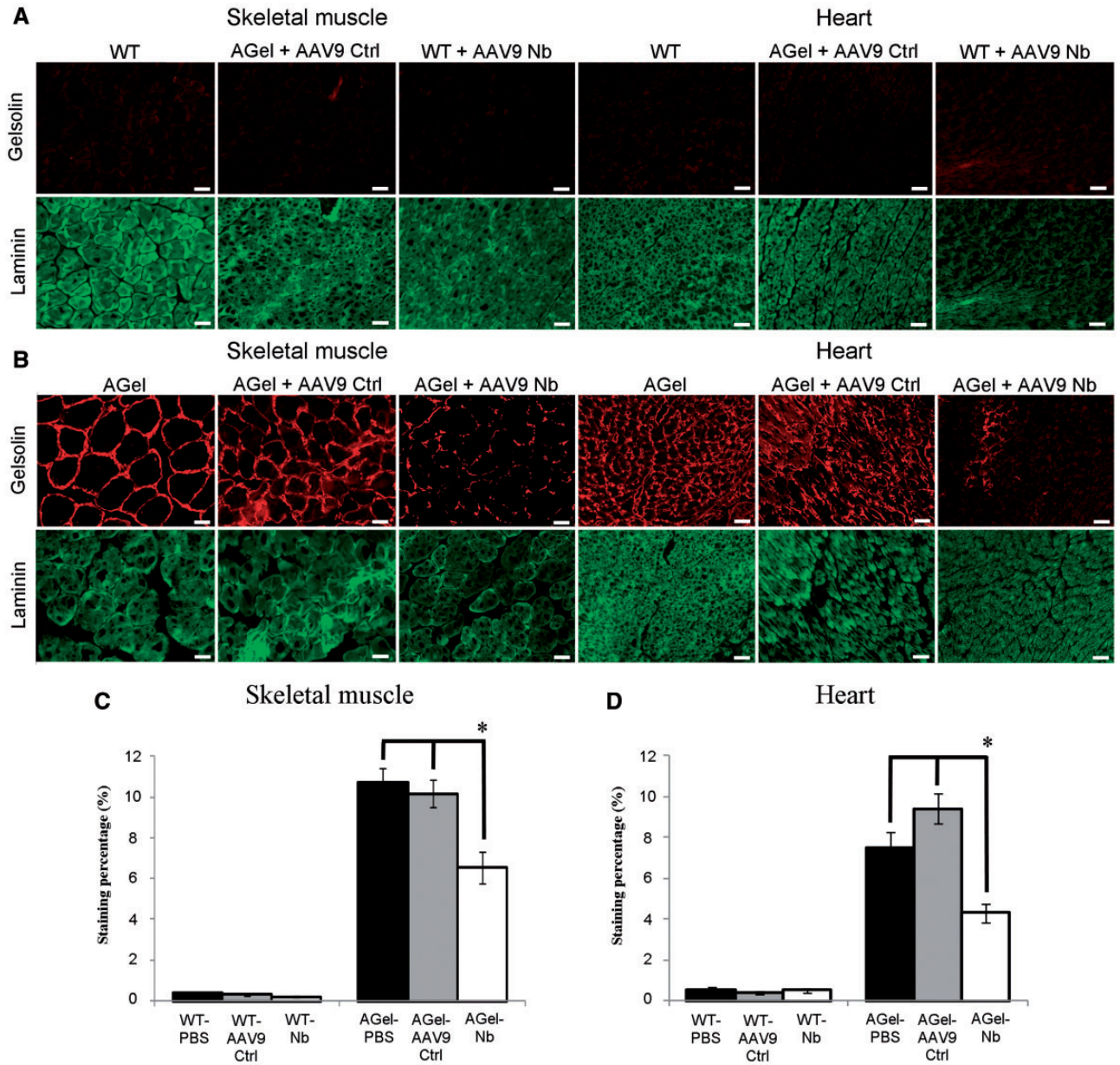


Figure 7. Mice were sacrificed three months post AAV injection. Skeletal muscle and heart tissue was stained for AGel amyloidogenic buildup (**A,B,** red, scale bar = 50 μm) and laminin (**A,B,** green, control, scale bar = 50 μm). The staining pattern was reduced in Nb11-FAF1 expressing AGel mice both in skeletal muscle (**C**) and heart tissue (**D**) compared to PBS and AAV9-control groups.

significant reduction of the AGel amyloid burden. Head to head studies in the same AGel mouse model are required to compare the relative efficiencies of this Nb11-FAF1 nanobody-based gene therapy approach versus injections of purified nanobodies. Nevertheless, the main advantage of the current nanobody-based AAV9-dependent gene therapy approach is that it enabled sustained *in vivo* nanobody expression that is targeted for secretion following passage through the ER and Golgi apparatus where it binds mutant plasma gelsolin. Consequently, the current gene therapy approach is well suited to treat a monogenic disorder like AGel that requires life-long treatment. In contrast, treatment of AGel patients with purified nanobodies, would require life-long, fairly frequent nanobody injections, due to their relatively rapid clearance rates from the circulation. It is particularly encouraging that a long-term therapeutic effect was observed after AAV9-Nb11-FAF1 gene therapy in homozygous AGel mice, which have a more severe phenotype than their heterozygous counterparts (which were used in our earlier studies (11,12)). In particular, homozygosity of the *D187N mutant PG* gene results in an earlier onset and higher degree of AGel amyloid deposition leading to a more significant muscle impairment, as opposed to heterozygous AGel mice (17).

Despite the advantages of AAV, some challenges would still need to be addressed to enable its widespread use in patients afflicted by monogenic disorders like AGel. First, there is a high prevalence of pre-existing immunity in the human population (40–80%) against the known AAV serotypes (25). In time this may be overcome by the discovery of new serotypes against which there is almost no pre-existing immunity or by mutating the antigen epitopes on the AAV capsid. Using directed

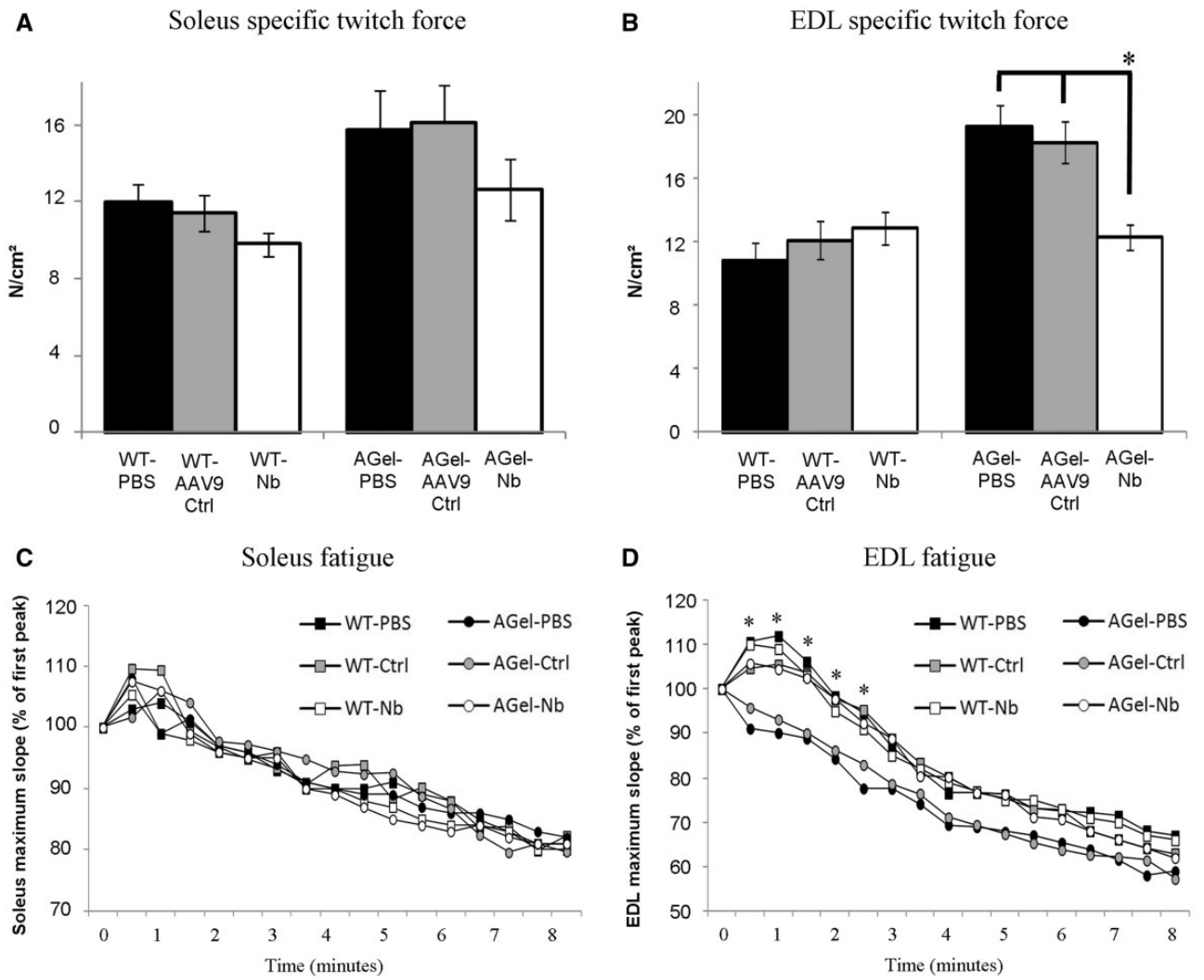


Figure 8. Soleus and EDL muscles were dissected and their *ex vivo* contractile properties measured. Expression of Nb11-FAF1 in AGel mice resulted in a specific twitch force significantly different from AGel control mice (both PBS and AAV9-control) and indistinguishable from the WT-control groups in EDL but not soleus (**A,B,** upper panels, data shown as mean ± SE. *$P < 0.05$ in a two sided unpaired *t*-test). EDL maximum slope (**D**), during the fatigue protocol, in Nb11-FAF1 expressing AGel mice, displayed the same delay as the WT controls. In contrast, AGel PBS and AAV9-control treated mice displayed a significantly faster fatigue onset. The soleus maximum slope during fatigue protocol (**C**) seemed unaffected. *$P < 0.05$ in a two-sided unpaired *t*-test (**A,B**), one way ANOVA (**C,D**).

evolution, the latter has already proven to be at least partly successful (26,27). Secondly, off-target transduction can severely abate the AAV therapeutic efficiency. Any vector taken up by the off-target tissue is essentially lost as it can no longer exert its effect in the desired target tissue. Consequently, this requires higher viral doses, thereby increasing the risk of an immune response. Moreover, since AAV9 also transduces the liver, any nanobody produced in this organ would no longer be able to perform its PG* chaperone activity. Looking forward to applications in patients, such off-target transductions will have to be minimized. Once again mutagenesis of specific capsid proteins can redirect AAVs more specifically to the tissue of interest (28–30). In the case of AGel, and more generally in the case of amyloidosis, this may prove useful as the amyloid precursors are quite often formed in a specific cell type, tissue or organ.

Preventing the formation of amyloid precursors, as was attempted here with nanobodies, would be a major step forward in amyloid research. Currently, administration of (R)-1-[6-[(R)-2-carboxy-pyrrolidin-1-yl]-6-oxo-hexanoyl] pyrrolidine-2-carboxylic acid (CPHPC) followed by anti-SAP antibody is the most promising amyloid removing strategy, as has been proven in patients with AL amyloidosis (31). Obviously, such interventions are only meaningful if, as is the case in AL amyloidosis, one is also able to stop the production of new amyloid precursors. The development of this bispecific, chaperoning, anti-AGel nanobody, may prove to be a fundamental step towards this goal.

Materials and Methods

Antibodies and reagents

Anti-mouse/rabbit IgG HRP conjugate was purchased from VWR (Leuven, Belgium). Polyclonal anti-V5 antibody (1:100 in IHC) was purchased from Sigma-Aldrich (Diegem, Belgium). Alexa fluor 488 goat anti-rat IgG (H + L) and 594 goat anti-rabbit IgG (H + L) were purchased from Life Technologies (Merelbeke, Belgium) (both 1:500 in IHC). Monoclonal anti-laminin antibody (1:500 in IHC) was obtained from Abcam (Cambridge, UK).

Generation of gelsolin-specific nanobodies

Both the anti-gelsolin nanobodies (Nb11 and Nb13) and the anti-8 kDa nanobodies (FAF Nb1-3) were obtained in collaboration with the VIB Nanobody Service Facility as described earlier (11). In short, dromedaries were injected with either cytoplasmic gelsolin or biotinylated human gelsolin 8 kDa AGel peptide and recombinant GST-tagged human D187N gelsolin domain 2. Lymphocytes were collected from the blood, total RNA was extracted and a cDNA library constructed. Phage panning for the anti-gelsolin nanobodies was performed with cytoplasmic gelsolin and resulted in two functional nanobodies; Nb11 and Nb13 (32). Phage panning for the anti-gelsolin nanobodies was performed with the 8 kDa peptide and the mutant G2 domain. Three nanobodies could be identified; FAF Nb1-3.

cDNA cloning

All monovalent nanobodies were available in the pHEN6 vector with a C-terminal V5-His_6 tag. The bispecific nanobodies were constructed as follows: the pHEN6 vector containing the FAF Nb1-3-V5-His_6 constructs was cleaved with NcoI, opening the vector between the pelB signal and nanobody N-terminus. The Nb11 sequence was amplified with a double set of primers to introduce a 5' HA-tag and a 3' linker sequence (Fig. 1A). This sequence encodes a MT1-MMP sensitive peptide (SLAPLGLQRR) flanked by two GS linkers. The Cold Fusion Kit (System Biosciences, Mountain View, CA) was used to ligate the PCR fragment in the opened pHEN6 vector.

Primers used in the first PCR cycle: 5' GGT GGT GGT GGT TCT GGT CAG GTG CAG CTG CAG GAG TCT GG 3' (forward) and 5' GAC GCT GCA GAC CCA GCG GCG CCA GAG AAC CAG AAC CAC CAC CAC CGC TGG AGA CGG TGA CCT GGG TCC C 3' (reverse).

Primers used in the second PCR cycle, using the product of the first cycle as template: 5' CGC GGC CCA GCC GGC CAT GGC CTA CCC ATA CGA TGT TCC AGA TTA CGC TGG TGG TGG TGG TTC TGG TCA GGT G 3' (forward) and 5' CCT CCT CCA GAC TCC TGC AGC TGC ACC TGA CCA GAA CCA CCA CCA CCA CGA CGC TGC AGA CCC AGC GGC GCC AG 3' (reverse).

Purification of recombinant PG*, C68 and nanobodies

Performed as previously described (11).

ELISA

Enzyme-linked immunosorbent assays (ELISA) were performed in Nunc Maxisorp 96-well plates (Roskilde, Denmark). Target protein was coated in coating buffer (100 mM bicarbonate/carbonate, pH 9.6) at 0.2 μg of protein per well. PBS + 1% BSA was used as a blocking buffer, PBS + 0.5% Tween was used as a washing buffer. Nanobodies were added in a ten-fold dilution series ranging from 1 μg to 10^{-5} μg/well. Anti-V5 antibody followed by anti-mouse HRP + TMB substrate kit (3,3',5,5' tetramethylbenzidine, Thermo Scientific, Erembodegem, Belgium) was used for detection.

WB with bispecific Nb11-FAF nanobodies as primary antibody

Bacterial pellets containing PG, PG*, C68, 8 kDa peptide or CapG were resuspended in lysisbuffer + 0.5% NP40. Lysis was performed with 0.2 mg/ml lysozyme for 30 min at room temperature followed by sonication (Vibracell, Sonics and Materials, Newtown, CT). The lysates were collected after 30 min of centrifugation at 29.000 x g, 4 °C. 5 μg bacterial protein extract were fractionated by SDS-PAGE. Western blot analysis was performed with V5-tagged Nb11-FAF1, 2 and 3 as primary antibody. Monoclonal anti-gelsolin antibody was used as a positive control.

In vitro MT1-MMP sensitive linker assay

In vitro MT1-MMP proteolysis of the Nb11-FAF constructs was performed in a total reaction volume of 75 μl. 2.5 μg bispecific Nb11-FAF Nb1-3 was incubated with 100 ng of the catalytic domain of MT1-MMP for 1 h at 37 °C in reaction buffer (50 mM Tris pH 7.5, 5 mM $CaCl_2$, 200 mM NaCl, 20 μM $ZnSO_4$ and 0.05% Brij-35). At 0, 15, 30, 45 and 60 min, samples were taken and the reaction was terminated by adding 5 μl Laemmli sample buffer. Samples were boiled for 5 min, fractionated on a 15% SDS-PAGE gel and stained with Coomassie.

In vitro furin/MT1-MMP assay

The *in vitro* proteolytic furin and MT1-MMP reaction was performed in a total end volume of 20 μl. 3 μM purified recombinant PG* was incubated with an equimolar amount of Nb in furin reaction buffer (250 mM Tris, 20 mM $CaCl_2$, 1 mM β-mercapthoethanol, pH 7.0) for 1 h at 4 °C. Furin was added (0.5 units) and the mixture was incubated for 1 h at 37 °C. Furin Inhibitor I (Merck Millipore, Brussels, Belgium) was added at a final concentration of 100 μM together with 50 ng of the catalytic domain of MT1-MMP. The buffer was supplemented with 200 mM NaCl, 0.05% Brij-35 and 20 μM $ZnSO_4$. After 30 min at 37 °C the reaction was stopped by adding 5 μl of Laemmli sample buffer. The sample was boiled for 5 min and separated on an tricine SDS-PAGE gel. Detection of both the C68 and 8 kDa fragment was done via Western blotting with a polyclonal antiserum raised against the 8 kDa AGel fragment. Quantification was done with the Image J software.

HEK293T cell culture, transfection and microscopy

Cell culture and transfection. HEK293T cells were grown in DMEM medium (Gibco Life Technologies, Grand Island, NY, USA) supplemented with 10% fetal bovine serum (Thermo Scientific, Erembodegem, Belgium), 10 μg/ml streptomycin and 10 IU/ml of penicillin, at 37 °C in a humidified 10% CO_2 incubator. Transient expression of both PG and the nanobodies was achieved with Jetprime (Polyplus Transfection Inc., New York, NY).

Microscopy. Cells were fixed with 3% PFA (paraformaldehyde) and permeabilized with 0.1% Triton. Coverslips were blocked with 1% BSA (bovine serum albumin) and incubated with primary antibodies (1 h at 37 °C). The appropriate Alexa Fluor-conjugated secondary antibodies were incubated at room temperature for 30 min. Nuclei were stained with DAPI (0.4 μg/ml) (Sigma, St. Louis, MO, USA). Cells were mounted with VectaShield (Vector Laboratories, Burlingame, CA, USA) and imaged with a Carl Zeiss Axiovert 200 M Apotome epifluorescence microscope equipped with a cooled CCD Axiocam camera (Zeiss X63 1.4-NA Oil Plan-Apochromat objective; Carl Zeiss, Oberkochen Germany) and Axiovision 4.5 software (Zeiss).

HEK293T medium analysis

HEK293T cells were cultured and transiently transfected as described above. 24 h prior to analysis the cell medium was replaced with a minimum amount of serum free medium. The medium was collected and centrifuged (29.000 x g) for 5 min at 4 °C. The cells were washed 2 times with PBS and disrupted in Tris lysis buffer (20 mM Tris-HCl, pH 7.5, 150 mM NaCl, 1% triton-100, 1 mM PMSF and 200 μg/ml protease inhibitor cocktail) followed by 10 s of sonication. Samples were centrifuged (29.000 x g) for 10 min at 4 °C, the supernatant was collected. 20 μg of the medium was separated on a 10% SDS-PAGE gel followed by Western blot analysis.

AAV9 gene therapy intervention study

The gene encoding the V5-tagged bispecific Nb11-FAF1 nanobody was cloned downstream of a ubiquitously expressed cytomegalovirus (CMV) promoter. This expression cassette was cloned into a self-complementary (sc) AAV backbone (33) to generate the AAV9-Nb11-FAF1 vector (Fig. 1B). As before AAV9-Luc2 vector was chosen as viral control (19). AAV serotype 9 (AAV9) was chosen based on its efficient transduction efficiency in skeletal muscle and heart (19,21,23) . To produce the AAV9-Nb11-FAF1 vector particles, AAV-293 cells were co-transfected by calcium phosphate (Invitrogen Corp, Carlsbad, CA, USA) with the AAV9-Nb11-FAF1 vector along with a chimeric AAV Rep2 Cap9 packaging construct and an adenoviral helper plasmid, as described previously [39]. All plasmids were prepared using Qiagen Maxi kits. Two days after transfection, the cells were harvested and lysed by freeze/thaw cycles and sonication, followed by benzonase (Novagen, Madison, WI, USA) and deoxycholic acid (Sigma-Aldrich, St Louis, MO, USA) treatments. The cognate AAV vector particles were then purified by cesium chloride (Invitrogen Corp, Carlsbad, CA, USA) density gradient ultracentrifugation. Fractions containing the AAV vector particles were collected in phosphate buffered saline (PBS) (Gibco, BRL) containing 1 mM $MgCl_2$. The vector titer was determined using quantitative real-time PCR with SYBR® Green and primers specific for the CMV promoter. The forward primer sequence was 5' CAT GGT GAT GCG GTT TTG G 3'. The reverse primer sequence was 5' TGG AAA TCC CCG TGA GTC A 3'. To generate standard curves, known copy numbers of the corresponding vector plasmid was used.

The intervention study was performed on 2 groups of mice: WT C57BL/6 and AGel mice. Each group consisted of 3 subgroups (6–12 mice): AAV9-Nb11-FAF1 injected (treatment), AAV9-Luc2 injected (viral control) and PBS injected (negative control). Neonatal mice (2–3 days) were injected with $4.7x10^{10}$ vg/mouse (viral genomes/mouse) or PBS in the retro-orbital plexus. Over the course of 3 months blood samples were taken from the tail vein at 4, 8 and 12 weeks. After 4 min of centrifugation at 1700 x g, plasma was collected. 1 mg of plasma was incubated with V5-agarose and HA-agarose. Bound protein was separated on an SDS-PAGE gel. HA- and V5-tagged nanobody was visualized via Western blotting.

Animal experiments were approved by the Animal Experimental Ethics Committee of Ghent University Hospital (ECD 14/62). Animals were housed in individually ventilated cages with food and water ad libitum. Environmental conditions were controlled at 20-23 °C, 50% relative humidity and 12 h light/dark cycles. AGel mice were obtained from the Scripps Research Institute (La Jolla, California, USA). Wild type C57BL/6 mice were obtained from Charles River (L'arbresle Cedex, France).

SPECT-CT imaging

Amyloid burden was visualized using ^{99m}Tc-FAF Nb1 SPECT-CT imaging (14). Mice were intravenously injected with 51–100 MBq of ^{99m}Tc labeled FAF Nb1. One hour post injection, mice were anaesthetized using 18.75 mg/kg ketamine hydrochloride (Ketamine 1000, CEVA) and 10 mg/kg xylazine hydrochloride (Rompun, Bayer). Animals were positioned in a solid holder with two plastic discs containing three ^{57}Co (3.7 MBq) sources. Image acquisition was done using a micro-CT scan for 2 min (60 keV, 615 mA, 360°; Skyscan 1178, Kontich, Belgium) and a dual-headed SPECT camera (e.cam 180, Siemens, USA) equipped with triple pinhole collimators (1.5 mm apertures, focal length of 265.5 mm and a radius of rotation of 20 mm) for 10 s per projection step, 64 projections, and a total scan time of about 10 min. Images were quantified using AMIDE (a Medical Image Data Examiner) software (34). Ellipsoid regions of interest were drawn (ROIs) around the heart and hind leg muscle. The same ROI_{heart} and ROI_{muscle} was used for each individual animal. SPECT signals, acquired from the ROIs, were calculated and expressed as % IA/cc.

Muscle contractile properties

Muscle contractile properties were determined as described before (35). In short, mice were anaesthetized with 80% Ketalar/20% Rompun (3.6 μl/g body weight). The soleus and EDL muscles were dissected, wires were attached to the tendons and the muscles were vertically mounted in an Krebs-Heinseleit medium incubation bath with one tendon attached to a force transducer (PowerLab, ADInstruments, Spechback, Germany) and stimulated with capacitor discharges between platinum electrodes. The Krebs-Henseleit incubation medium (10 ml) was continuously gassed (95% O_2, 5% CO_2) and maintained at 30 °C. After a 15 min stabilization period, optimal muscle length was determined by titanic contractions. Next, the force–frequency relation was determined by stimulating at 10, 20, 35, 50, 75, 100, and 125 Hz with 1 min rest interval for soleus and stimulating at 25, 40 and 55 with 1 min rest followed by 70, 100, 125 and 150 Hz with 2 min rest interval, unless stated otherwise, for EDL. Furthermore, fatigability was evaluated as the percentage decrease in tetanic force, contraction speed (maximum slope) and relaxation rate (minimum slope) values during 8 min of repeated tetanic contractions (train duration, 350 microseconds; soleus, 50 Hz every 5 s; EDL, 100 Hz every 10 s). At the end, mice were euthanized via cervical dislocation.

Immunofluorescence

Musculus gastrocnemius and the heart were dissected and snap frozen in liquid nitrogen. Cryosections were made and thawed for 15 min followed by 10 min incubation in acetone at -20 °C. After 10 min incubation in PBS, the sections were incubated in 50 mM NH_4Cl/PBS for another 10 min followed by an additional PBS washing step. The endogenous peroxidase activity was blocked after 20 min incubation in 0.3% H_2O_2 and then washed in PBS. Sections were incubated with 1% BSA/PBS for 20 min and with the laminin antibody (1:500) at 4 °C overnight, followed by another PBS washing step for 10 min. FAF Nb1-V5 (5 μg/ml) was incubated for 1 h at room temperature followed by 10 min

incubation in PBS. Polyclonal anti-V5 (1:800) was used as secondary antibody. Alexa Fluor antibodies (488 anti-rat and 594 anti-rabbit, both 1:500) were incubated for 1 h at room temperature. Finally, sections were rinsed with PBS, stained with DAPI (1:500) for 2 min and mounted with VectaShield. Imaging was performed at room temperature with a Leica DM6000 B microscope. Two sections were made per tissue and within each section, 3 images from spate regions were taken for quantification with Image J software. From these 6 technical repeats per animal, per tissue, the average was used for further statistical calculations.

Supplementary Material

Supplementary Material is available at *HMG* online.

Acknowledgements

We thank Jeffery.W. Kelly, Lesley J. Page and Carlos A. Guerrero (Scripps Research Institute) for sharing the gelsolin amyloidosis mouse model.

This work was supported by the Queen Elisabeth Medical Foundation (GSKE, Belgium), the 'Stichting Alzheimer Onderzoek' (SAO, Belgium), Ghent University (BOF13/GOA/010), the Research Foundation Flanders (Fonds Wetenschappelijk Onderzoek (FWO) Vlaanderen) and the Interuniversity Attraction Poles Programme of the Belgian State, Federal Office for Scientific, Technical and Cultural Affairs (IUAP P7/13).

Adriaan Verhelle is supported by the Agency for Innovation by Science and Technology in Flanders (IWT).

Thierry VandenDriessche and Marinee K. Chuah were supported by VUB GEAR IOF (GENECURE), VUB SRP "Grower" (GENEFIX) and FWO grants

Conflict of Interest statement. None declared

Funding

Queen Elisabeth Medical Foundation (GSKE, Belgium), 'Stichting Alzheimer Onderzoek' (SAO, Belgium), Ghent University (BOF13/GOA/010), Research Foundation Flanders (Fonds Wetenschappelijk Onderzoek (FWO) Vlaanderen) and Interuniversity Attraction Poles Programme of the Belgian State, Federal Office for Scientific, Technical and Cultural Affairs (IUAP P7/13), Agency for Innovation by Science and Technology in Flanders (IWT), VUB GEAR IOF (GENECURE), VUB SRP Grower (GENEFIX) and FWO grants

Statement of animal rights

All applicable institutional and/or national guidelines for the care and use of animals were followed. Animal experiments were approved by the Animal Experimental Ethics Committee of Ghent University Hospital (ECD 14/62).

References

1. Ghiso, J., Haltia, M., Prelli, F., Novello, J. and Frangione, B. (1990) Gelsolin variant (Asn-187) in familial amyloidosis, Finnish type. *The Biochemical Journal*, **272**, 827–830.
2. Maury, C.P., Alli, K. and Baumann, M. (1990) Finnish hereditary amyloidosis. Amino acid sequence homology between the amyloid fibril protein and human plasma gelsoline. *FEBS Letters*, **260**, 85–87.
3. Kangas, H., Paunio, T., Kalkkinen, N., Jalanko, A. and Peltonen, L. (1996) *In vitro* expression analysis shows that the secretory form of gelsolin is the sole source of amyloid in gelsolin-related amyloidosis. *Hum. Mol. Genet*, **5**, 1237–1243.
4. Burtnick, L.D., Koepf, E.K., Grimes, J., Jones, E.Y., Stuart, D.I., McLaughlin, P.J. and Robinson, R.C. (1997) The crystal structure of plasma gelsolin: implications for actin severing, capping, and nucleation. *Cell*, **90**, 661–670.
5. Nag, S., Ma, Q., Wang, H., Chumnarnsilpa, S., Lee, W.L., Larsson, M., Kannan, B., Hernandez-Valladares, M., Burtnick, L.D. and Robinson, R.C. (2009) Ca2+ binding by domain 2 plays a critical role in the activation and stabilization of gelsolin. *pnas*, **106**, 13713–13718.
6. Burtnick, L.D., Urosev, D., Irobi, E., Narayan, K. and Robinson, R.C. (2004) Structure of the N-terminal half of gelsolin bound to actin: roles in severing, apoptosis and FAF. *embo J*, **23**, 2713–2722.
7. Chen, C.D., Huff, M.E., Matteson, J., Page, L., Phillips, R., Kelly, J.W. and Balch, W.E. (2001) Furin initiates gelsolin familial amyloidosis in the Golgi through a defect in Ca(2+) stabilization. *embo J*, **20**, 6277–6287.
8. Page, L.J., Suk, J.Y., Huff, M.E., Lim, H.J., Venable, J., Yates, J., Kelly, J.W. and Balch, W.E. (2005) Metalloendoprotease cleavage triggers gelsolin amyloidogenesis. *embo J*, **24**, 4124–4132.
9. Pihlamaa, T., Rautio, J., Kiuru-Enari, S. and Suominen, S. (2011) Gelsolin amyloidosis as a cause of early aging and progressive bilateral facial paralysis. *Plast. Reconstr. Surg*, **127**, 2342–2351.
10. Kiuru-Enari, S. and Haltia, M. (2013) Hereditary gelsolin amyloidosis. *Handb. Clin. Neurol*, **115**, 659–681.
11. Van Overbeke, W., Verhelle, A., Everaert, I., Zwaenepoel, O., Vandekerckhove, J., Cuvelier, C., Derave, W. and Gettemans, J. (2014) Chaperone nanobodies protect gelsolin against MT1-MMP degradation and alleviate amyloid burden in the gelsolin amyloidosis mouse model. *Mol. Ther*, **22**, 1768–1778.
12. Van Overbeke, W., Wongsantichon, J., Everaert, I., Verhelle, A., Zwaenepoel, O., Loonchanta, A., Burtnick, L.D., De Ganck, A., Hochepied, T., Haigh, J., *et al*. (2015) An ER-directed gelsolin nanobody targets the first step in amyloid formation in a gelsolin amyloidosis mouse model. *Hum. Mol. Genet*, **24**, 2492–2507.
13. Duan, D. (2016) Systemic delivery of adeno-associated viral vectors. *Curr Opin Virol*, **21**, 16–25.
14. Verhelle, A., Van Overbeke, W., Peleman, C., De Smet, R., Zwaenepoel, O., Lahoutte, T., Van Dorpe, J., Devoogdt, N. and Gettemans, J. (2016) Non-Invasive Imaging of Amyloid Deposits in a Mouse Model of AGel Using 99mTc-Modified Nanobodies and SPECT/CT. *Molecular Imaging and Biology: MIB: The Official Publication of the Academy of Molecular Imaging*, in press.
15. Jabaiah, A. and Daugherty, P.S. (2011) Directed evolution of protease beacons that enable sensitive detection of endogenous MT1-MMP activity in tumor cell lines. *Chemistry & Biology*, **18**, 392–401.
16. de la Chapelle, A., Tolvanen, R., Boysen, G., Santavy, J., Bleeker-Wagemakers, L., Maury, C.P. and Kere, J. (1992) Gelsolin-derived familial amyloidosis caused by asparagine or tyrosine substitution for aspartic acid at residue 187. *Nature Genetics*, **2**, 157–160.
17. Page, L.J., Suk, J.Y., Bazhenova, L., Fleming, S.M., Wood, M., Jiang, Y., Guo, L.T., Mizisin, A.P., Kisilevsky, R., Shelton, G.D., *et al*. (2009) Secretion of amyloidogenic gelsolin progressively compromises protein homeostasis leading to the intracellular aggregation of proteins. *Proc Natl Acad Sci U S A*, **106**, 11125–11130.

18. Rasowo, B., Shilpita, S., Ermira, S., Chuah, M. and VandenDriessche, T. (2014) Development of novel muscle-specific adeno-associated viral vector constructs for gene therapy of duchenne muscular dystrophy. *European Scientific Journal*, **10**, 23–37.
19. Rincon, M.Y., Sarcar, S., Danso-Abeam, D., Keyaerts, M., Matrai, J., Samara-Kuko, E., Acosta-Sanchez, A., Athanasopoulos, T., Dickson, G., Lahoutte, T., *et al.* (2015) Genome-wide computational analysis reveals cardiomyocyte-specific transcriptional Cis-regulatory motifs that enable efficient cardiac gene therapy. *Mol. Ther*, **23**, 43–52.
20. Bish, L.T., Morine, K., Sleeper, M.M., Sanmiguel, J., Wu, D., Gao, G., Wilson, J.M. and Sweeney, H.L. (2008) Adeno-associated virus (AAV) serotype 9 provides global cardiac gene transfer superior to AAV1, AAV6, AAV7, and AAV8 in the mouse and rat. *Human Gene Therapy*, **19**, 1359–1368.
21. Zincarelli, C., Soltys, S., Rengo, G. and Rabinowitz, J.E. (2008) Analysis of AAV serotypes 1-9 mediated gene expression and tropism in mice after systemic injection. *Molecular Therapy: The Journal of the American Society of Gene Therapy*, **16**, 1073–1080.
22. Gao, G.P., Alvira, M.R., Wang, L., Calcedo, R., Johnston, J. and Wilson, J.M. (2002) Novel adeno-associated viruses from rhesus monkeys as vectors for human gene therapy. *Proceedings of the National Academy of Sciences of the United States of America*, **99**, 11854–11859.
23. Vandendriessche, T., Thorrez, L., Acosta-Sanchez, A., Petrus, I., Wang, L., Ma, L., L, D.E.W Iwasaki, Y., Gillijns, V., Wilson, J.M., *et al.* (2007) Efficacy and safety of adeno-associated viral vectors based on serotype 8 and 9 vs. lentiviral vectors for hemophilia B gene therapy. *Journal of Thrombosis and Haemostasis: JTH*, **5**, 16–24.
24. Mendell, J., Al Zaidy, S., Shell, R., Arnold, W., Rodino Klapac, L., Kissel, J., Prior, T., Miranda, C., Lowes, L. and Alfano, L. (2016) Gene therapy for spinal muscular atrophy type 1 shows potential to improve survival and motor functional outcomes. *Molecular Therapy: The Journal of the American Society of Gene Therapy*, **24**,
25. Louis Jeune, V., Joergensen, J.A., Hajjar, R.J. and Weber, T. (2013) Pre-existing anti-adeno-associated virus antibodies as a challenge in AAV gene therapy. *Human Gene Therapy Methods*, **24**, 59–67.
26. Maheshri, N., Koerber, J.T., Kaspar, B.K. and Schaffer, D.V. (2006) Directed evolution of adeno-associated virus yields enhanced gene delivery vectors. *Nature Biotechnology*, **24**, 198–204.
27. Grimm, D., Lee, J.S., Wang, L., Desai, T., Akache, B., Storm, T.A. and Kay, M.A. (2008) *In vitro* and *in vivo* gene therapy vector evolution via multispecies interbreeding and retargeting of adeno-associated viruses. *Journal of Virology*, **82**, 5887–5911.
28. Pulicherla, N., Shen, S., Yadav, S., Debbink, K., Govindasamy, L., Agbandje-McKenna, M. and Asokan, A. (2011) Engineering liver-detargeted AAV9 vectors for cardiac and musculoskeletal gene transfer. *Molecular Therapy: The Journal of the American Society of Gene Therapy*, **19**, 1070–1078.
29. Shen, S., Bryant, K.D., Sun, J., Brown, S.M., Troupes, A., Pulicherla, N. and Asokan, A. (2012) Glycan binding avidity determines the systemic fate of adeno-associated virus type 9. *Journal of Virology*, **86**, 10408–10417.
30. Shen, S., Horowitz, E.D., Troupes, A.N., Brown, S.M., Pulicherla, N., Samulski, R.J., Agbandje-McKenna, M. and Asokan, A. (2013) Engraftment of a galactose receptor footprint onto adeno-associated viral capsids improves transduction efficiency. *The Journal of Biological Chemistry*, **288**, 28814–28823.
31. Pepys, M.B., Cookson, L.M., Barton, S.V., Berges, A.C., Lane, T., Hutt, D., Fontana, M., Moon, J.C., Gillmore, J.D., Wechalekar, A., *et al.* (2015) Dose-Dependent Progressive Immunotherapeutic Clearance of Systemic Amyloid Deposits By Repeated Doses of Antibody to Serum Amyloid P Component (SAP). *Blood*, **126**, 1836–1836.
32. Van den Abbeele, A., De Clercq, S., De Ganck, A., De Corte, V., Van Loo, B., Soror, S.H., Srinivasan, V., Steyaert, J., Vandekerckhove, J. and Gettemans, J. (2010) A llama-derived gelsolin single-domain antibody blocks gelsolin-G-actin interaction. *Cell. Mol. Life Sci*, **67**, 1519–1535.
33. McCarty, D.M., Fu, H., Monahan, P.E., Toulson, C.E., Naik, P. and Samulski, R.J. (2003) Adeno-associated virus terminal repeat (TR) mutant generates self-complementary vectors to overcome the rate-limiting step to transduction *in vivo*. *Gene Therapy*, **10**, 2112–2118.
34. Loening, A.M. and Gambhir, S.S. (2003) AMIDE: a free software tool for multimodality medical image analysis. *Molecular Imaging*, **2**, 131–137.
35. Everaert, I., Stegen, S., Vanheel, B., Taes, Y. and Derave, W. (2013) Effect of beta-alanine and carnosine supplementation on muscle contractility in mice. *Medicine and Science in Sports and Exercise*, **45**, 43–51.



Source: *Voyager Therapeutics, Inc.*

December 07, 2016 16:05 ET

Voyager Therapeutics Announces Positive Interim Results from Phase 1b Trial of VY-AADC01 for Advanced Parkinson's Disease

VY-AADC01 dose-dependently improved measures of motor function and enhanced response to levodopa at six and twelve months; administration of VY-AADC01 was well-tolerated

Program on track to report Cohort 3 data mid-2017 and to begin placebo-controlled trial Q4:17

Conference call scheduled for today at 4:30 p.m. EST

CAMBRIDGE, Mass., Dec. 07, 2016 (GLOBE NEWSWIRE) -- Voyager Therapeutics, Inc. (NASDAQ:VYGR), a clinical-stage gene therapy company developing life-changing treatments for severe diseases of the central nervous system (CNS), today announced positive results from the ongoing Phase 1b trial of VY-AADC01 at six and twelve months of follow-up in patients with advanced Parkinson's disease. The interim data from Cohorts 1 and 2 of this trial demonstrated that accurate MRI-guided delivery of escalating doses of VY-AADC01 were well tolerated and resulted in increased coverage of the putamen, increased AADC enzyme activity, enhanced response to levodopa, and dose-related, clinically meaningful improvements in various measures of patients' motor function. This was especially evident at the higher dose in Cohort 2 with improved UPDRS off medication and on medication scores, and corresponding improvements in patient-reported diary hours, suggesting higher peak effects and a longer duration of action of levodopa. These effects were maintained and in some patients improved at 12 months of follow-up.

"At 12 months in Cohort 2, treatment with VY-AADC01 resulted in a 14-point, or 44%, improvement in UPDRS-III off medication, a 9-point, or 55% improvement in UPDRS-III on medication, and a 2.2 hour, or 48%, decrease in diary off-time from baseline," said Bernard Ravina, M.D., M.S., vice president of clinical development at Voyager Therapeutics. "Very importantly, these improvements in motor function occurred with a substantial 34% reduction in daily doses of oral levodopa and related medications at six months in Cohort 2 that was maintained at 12 months, a magnitude that we find compelling and consistent with the mechanism of action of VY-AADC01. The dose-escalating portion of this trial continues and we plan to complete Cohort 3 enrollment in early 2017, report 6-month data from this Cohort as well as longer-term data from Cohorts 1 and 2 in mid-2017, and present results from this trial at a medical conference in the first half of next year."

About the Phase 1b Trial

In advanced Parkinson's disease, the putamen is depleted of dopamine and of the enzyme aromatic L-amino acid decarboxylase (AADC) that is responsible for converting levodopa to dopamine. VY-AADC01 is Voyager's gene therapy vector that contains the gene that encodes the AADC enzyme. The Phase 1b, open-label trial includes up to 20 patients with advanced Parkinson's disease and disabling motor fluctuations, treated with a single administration of VY-AADC01. The primary objective of the trial is to assess the safety and surgical coverage of ascending doses of VY-AADC01 in the putamen, a region of the brain associated with motor function in Parkinson's disease. The secondary objectives of the trial include the assessment of AADC expression and activity in the putamen measured by positron emission tomography (PET) using [^{18}F] fluorodopa (or ^{18}F-DOPA). In addition, changes in motor responses to levodopa are measured by a

We use cookies to improve your GlobeNewswire experience. By continuing, you agree to our use of cookies.
For more information, please see our Privacy Policy.

Ok

on-time, or time when they have good mobility with or without non-troublesome dyskinesia, off-time when they have poor mobility, and on-time with troublesome dyskinesia when they have uncontrolled movements.

Biomarker and Clinical Results Summary

Today's interim results include data from all 10 patients treated in Cohorts 1 and 2 at six months (five patients in each Cohort), and where indicated, data from five patients in Cohort 1 and three patients in Cohort 2 who have reached 12 months of follow-up. Patients in Cohorts 1 and 2 received a single administration of VY-AADC01 at a total dose of up to 7.5×10^{11} vector genomes (vg) and 1.5×10^{12} vg, respectively. Patients enrolled in Cohorts 1 and 2 were on average 58 years of age with a Parkinson's disease diagnosis for an average of 10 years. Patients were candidates for surgical intervention due to disabling motor complications despite treatment with optimal anti-Parkinsonian medication. At baseline, the average UPDRS III off medication score was 37.2 and 35.8, and the average patient diary off-time was 4.9 and 4.2 hours, for Cohort 1 and 2, respectively. Patients' average amount of Parkinson's disease medications at baseline was 1,468 mg per day for Cohort 1 and 1,636 mg per day for Cohort 2. The results below are reported as mean changes from baseline to six months, or 12 months where indicated.

Putamen Coverage and Biomarker Data

- The use of real-time, intra-operative MRI-guided delivery and increasing infusion volumes resulted in 21% coverage of the volume of the putamen with VY-AADC01 in Cohort 1 and 34% coverage in Cohort 2.
- VY-AADC01 treatment resulted in a 13% increase in putaminal AADC enzyme activity in Cohort 1 and a 56% increase in putaminal AADC enzyme activity in Cohort 2 at six months relative to baseline as measured by ^{18}F-DOPA PET scans.
- Patients reduced their daily oral dose of levodopa and related medications by 14% in Cohort 1 and 34% in Cohort 2 at six months. This reduction in oral medication was generally maintained at twelve months.
- VY-AADC01 treatment prolonged the duration and markedly increased the motor symptom response to levodopa measured following a controlled intravenous infusion of levodopa administered six months after surgery when compared to baseline.

Clinical Data Summary

Treatment with VY-AADC01 resulted in the following:

- 15.6-point and 17.8-point (42% and 50%) improvement (reduction) in UPDRS-III off medication at six months in Cohort 1 and Cohort 2, respectively. These improvements were 16.4-point and 14.3-point (44% and 44%) for Cohorts 1 and 2, respectively, at 12 months.
- 9.6-point (56%) improvement (reduction) in UPDRS-III on medication in Cohort 2 at six months that was sustained at 12 months. Cohort 1 demonstrated a 1.6-point (21%) worsening (increase) at six months that was sustained at 12 months.
- 2.2 hours (20%) increase in diary on-time (with no dyskinesias or non-troublesome dyskinesias) in Cohort 2 at six months that further increased to 4.1 hours (43%) at 12 months. Cohort 1 showed a slight decrease in on-time at six months of 0.3 hours (-3%) and an increase of 1.6 hours (16%) at 12 months.
- 1.1 hour (27%) decrease in diary off-time in Cohort 2 at six months that further decreased to 2.2 hours (48%) at 12 months. Decreases in diary off-time in Cohort 2 also occurred in conjunction with a reduction in troublesome dyskinesias. Cohort 1 showed a decrease in diary off-time of 0.8 hours (16%) at six months and 1.4 hours (27%) at 12 months.

Safety Data from Cohorts 1 and 2

The surgical procedure was successfully completed in all 10 patients and infusions of VY-AADC01 have been well-tolerated with no vector-related serious adverse events (SAEs). Nine of the 10 patients were discharged from the hospital within one to two days following surgery. As previously reported, one patient experienced two SAEs; a pulmonary

We use cookies to improve your GlobeNewswire experience. By continuing, you agree to our use of cookies.
For more information, please see our Privacy Policy.

Ok

putamen," said Paul Larson, M.D., Professor and Vice Chair of Clinical Neurological Surgery, University of California San Francisco, and investigator in the trial. "The increased surgical coverage of the putamen is further validated by the PET data and is translating into motor function improvement in patients with advanced stages of the disease."

Todd Sherer, Ph.D., Chief Executive Officer, The Michael J. Fox Foundation for Parkinson's Research added, "Levodopa has been the gold-standard treatment for Parkinson's for decades, but it has limitations. Enhancing a patient's response to this therapy represents an important development for those who suffer from the advanced stages of this disease, and we are glad to see the continued progress of this program." The Michael J. Fox Foundation funded part of the initial pioneering research for this program in Dr. Krystof Bankiewicz's laboratory at the University of California San Francisco.

Cohort 3 and Posterior Trajectory Trial On Track

To advance the planned dose-escalating portion of the trial, Voyager continues to enroll patients in Cohort 3 (up to five patients) who will receive a single administration of VY-AADC01 at a total dose of up to 4.5×10^{12} vector genomes (vg), representing a three-fold higher total dose than patients in Cohort 2 (1.5×10^{12} vg). To date, four of five patients have been treated in Cohort 3 and Voyager plans to complete Cohort 3 enrollment in early 2017 and remains on track to report six-month data in mid-2017. In preparation for the randomized, placebo-controlled trial, Voyager also plans to initiate a new trial that could enhance the efficiency of the surgical delivery and further increase both coverage and total vector dose. This trial will employ a posterior (i.e., back of the head), or occipital, trajectory which aligns the infusion of VY-AADC01 with the anatomical structure of the putamen. Voyager believes this will result in a higher total volume of coverage of the putamen and therefore a higher total dose (up to 9.4×10^{12} vg, representing a two-fold higher total dose than patients in Cohort 3) and may reduce surgical times. Voyager is activating additional clinical trial sites this quarter and plans to dose the first patient with this trajectory in the first quarter of 2017. Data from Cohorts 1-3 and from this posterior trajectory trial will inform the design of the placebo-controlled trial planned to begin in the fourth quarter of 2017.

Conference Call and Webcast Information

Voyager will host a conference call and webcast today with slides at 4:30 p.m. EST to discuss the results. The conference call may be accessed by dialing (877) 851-3834 for domestic callers or +1 (631) 291-4595 for international callers, and referencing conference ID number 32331935. A live audio webcast of the conference call and replay will be available online from the Investors & Media section of Voyager's website at www.voyagertherapeutics.com. The webcast will be archived for 30 days.

About Parkinson's Disease and VY-AADC01

Parkinson's disease is a chronic, progressive and debilitating neurodegenerative disease that affects approximately 700,000 people in the U.S.[1] and seven to 10 million people worldwide[2]. It is estimated that up to 15% of the prevalent population with Parkinson's disease, or approximately 100,000 patients in the U.S., have motor fluctuations that are refractory, or not well-controlled, with levodopa. While the underlying cause of Parkinson's disease in most patients is unknown, the motor symptoms of the disease arise from a loss of neurons in the midbrain that produce the neurotransmitter dopamine. Declining levels of dopamine in this particular region of the brain leads to the motor symptoms associated with Parkinson's disease including tremors, slow movement or loss of movement, rigidity, and postural instability. Motor symptoms during the advanced stages of the disease include falling, gait freezing, and difficulty with speech and swallowing, with patients often requiring the daily assistance of a caregiver.

There are currently no therapies that effectively slow or reverse the progression of Parkinson's disease. Levodopa remains the standard of care treatment, with its beneficial effects on symptom control having been discovered over 40 years ago[3]. Patients are generally well-controlled with oral levodopa in the early stages of the disease, but become less responsive to treatment as the disease progresses. Patients experience longer periods of reduced mobility and stiffness termed off-time, or the time when medication is no longer providing benefit, and shorter periods of on-time when their medication is effective.

The progressive motor symptoms of Parkinson's disease are largely due to the death of dopamine neurons in the substantia nigra, a part of the midbrain that converts levodopa to dopamine, in a single step catalyzed by the aromatic L-amino acid decarboxylase (AADC) enzyme. Neurons in the substantia nigra release dopamine into the putamen where the receptors for dopamine reside. In advanced Parkinson's disease, neurons in the substantia nigra degenerate and the enzyme AADC is markedly reduced in the putamen, which limits the brain's ability to convert oral levodopa to dopamine[4].

We use cookies to improve your GlobeNewswire experience. By continuing, you agree to our use of cookies.
For more information, please see our Privacy Policy.

Ok

Voyager Therapeutics is a clinical-stage gene therapy company developing life-changing treatments for severe diseases of the CNS. Voyager is committed to advancing the field of adeno-associated virus (AAV) gene therapy through innovation and investment in vector engineering and optimization, manufacturing and dosing and delivery techniques. The Company's pipeline focuses on severe CNS diseases in need of effective new therapies, including advanced Parkinson's disease, a monogenic form of ALS, Friedreich's ataxia, Huntington's disease, frontotemporal dementia, Alzheimer's disease and severe, chronic pain. Voyager has broad strategic collaborations with Sanofi Genzyme, the specialty care global business unit of Sanofi, and the University of Massachusetts Medical School. Founded by scientific and clinical leaders in the fields of AAV gene therapy, expressed RNA interference and neuroscience, Voyager Therapeutics is headquartered in Cambridge, Massachusetts. For more information, please visit www.voyagertherapeutics.com. Follow Voyager on LinkedIn.

Forward-Looking Statements

This press release contains forward-looking statements for the purposes of the safe harbor provisions under The Private Securities Litigation Reform Act of 1995 and other federal securities law. The use of words such as "may," "might," "will," "should," "expect," "plan," "anticipate," "believe," "estimate," "project," "intend," "future," "potential," or "continue," and other similar expressions are intended to identify forward-looking statements. For example, all statements Voyager makes regarding the initiation, timing, progress and reporting of results of its preclinical programs and clinical trials and its research and development programs, its ability to advance its AAV-based gene therapies into, and successfully complete, clinical trials, its ability to continue to develop its product engine, its ability to add new programs to its pipeline, its expected cash, cash equivalents and marketable securities at the end of a fiscal year and anticipation for how long expected cash, cash equivalents and marketable securities will last, and the timing or likelihood of its regulatory filings and approvals, are forward looking. All forward-looking statements are based on estimates and assumptions by Voyager's management that, although Voyager believes to be reasonable, are inherently uncertain. All forward-looking statements are subject to risks and uncertainties that may cause actual results to differ materially from those that Voyager expected. These statements are also subject to a number of material risks and uncertainties that are described in Voyager's most recent Quarterly Report on Form 10-Q filed with the Securities and Exchange Commission, as updated by its future filings with the Securities and Exchange Commission. Any forward-looking statement speaks only as of the date on which it was made. Voyager undertakes no obligation to publicly update or revise any forward-looking statement, whether as a result of new information, future events or otherwise, except as required by law.

[1] Willis et al, *Neuroepidemiology*.2010;34:143–151

[2] www.pdf.org/en/parkinson_statistics

[3] Poewe W, et al, *Clinical Interventions in Aging*.2010;5:229-238.

[4] Lloyd, *J Pharmacol Exp Ther*. 1975;195:453-464, Nagatsu, *J Neural Transm Suppl*.2007

[5] Cold Spring Harb Perspect Med 2012;2:a009258

[6] Braak et al, *Cell Tissue Res*.2004;318:121-134

We use cookies to improve your GlobeNewswire experience. By continuing, you agree to our use of cookies.
For more information, please see our Privacy Policy.

Ok

Author Manuscript

Author Manuscript

Author Manuscript

Author Manuscript

HHS Public Access

Author manuscript

Nat Med. Author manuscript; available in PMC 2018 December 11.

Published in final edited form as:

Nat Med. 2018 July ; 24(7): 931–938. doi:10.1038/s41591-018-0051-5.

Block of A1 astrocyte conversion by microglia is neuroprotective in models of Parkinson's disease

Seung Pil Yun[1,2,15,*], **Tae-In Kam**[1,2,*], **Nikhil Panicker**[1,2], **SangMin Kim**[1,2], **Yumin Oh**[6,7], **Jong-Sung Park**[6,7], **Seung-Hwan Kwon**[1,2], **Yong Joo Park**[6,7], **Senthilkumar S. Karuppagounder**[1,2,15], **Hyejin Park**[1,2], **Sangjune Kim**[1,2], **Nayeon Oh**[1,2], **Nayoung Alice Kim**[1,2], **Saebom Lee**[1,2], **Saurav Brahmachari**[1,2,15], **Xiaobo Mao**[1,2,15], **Jun Hee Lee**[8], **Manoj Kumar**[1,2], **Daniel An**[1,2], **Sung-Ung Kang**[1,2], **Yunjong Lee**[9], **Kang Choon Lee**[10], **Dong Hee Na**[11], **Donghoon Kim**[1,2,3,4], **Sang Hun Lee**[12], **Viktor V. Roschke**[13], **Shane A. Liddelow**[14], **Zoltan Mari**[2], **Ben. A. Barres**[14], **Valina L. Dawson**[1,2,3,4,15], **Seulki Lee**[6,7,#], **Ted M. Dawson**[1,2,4,5,15,16,#], and **Han Seok Ko**[1,2,15,16,#]

[1]Neuroregeneration and Stem Cell Programs, Institute for Cell Engineering, The Johns Hopkins University School of Medicine, Baltimore, MD 21205, USA

[2]Department of Neurology, The Johns Hopkins University School of Medicine, Baltimore, MD 21205, USA

[3]Department of Physiology, The Johns Hopkins University School of Medicine, Baltimore, MD 21205, USA

[4]Solomon H. Snyder Department of Neuroscience, The Johns Hopkins University School of Medicine, Baltimore, MD 21205, USA

[5]Department of Pharmacology and Molecular Sciences, The Johns Hopkins University School of Medicine, Baltimore, MD 21205, USA

[6]The Russell H. Morgan Department of Radiology and Radiological Sciences, Johns Hopkins University School of Medicine, Baltimore, MD 21287, USA

Users may view, print, copy, and download text and data-mine the content in such documents, for the purposes of academic research, subject always to the full Conditions of use: http://www.nature.com/authors/editorial_policies/license.html#terms

Correspondence should be addressed to: **Seulki Lee, Ph.D.**, The Russell H. Morgan Department of Radiology and Radiological Science, Center for Nanomedicine, Johns Hopkins University School of Medicine, 400 North Broadway, Baltimore, MD 21287, USA. slee343@jhmi.edu; **Ted M. Dawson, M.D., Ph.D.**, Neuroregeneration and Stem Cell Programs, Institute for Cell Engineering, Johns Hopkins University School of Medicine, 733 North Broadway, Baltimore, MD 21205, USA. tdawson@jhmi.edu; **Han Seok Ko, Ph.D.**, Neuroregeneration and Stem Cell Programs, Institute for Cell Engineering, Johns Hopkins University School of Medicine, 733 North Broadway, Baltimore, MD 21205, USA, hko3@jhmi.edu.

*These authors contributed equally.

Author Contributions

S.P.Y., and T.-I.K. designed majority of the experiments, performed the experiments, analyzed data, and wrote the manuscript. N.P., S.M.K., Y.O., J.-S.P., S.-H.K., S.-U.K., and D.K. performed experiments, and data interpretation. Y.J.P. injected NLY01 into mice. S.S.K. performed HPLC analysis. H.P., S.K., N.O., N.A.K., S.L., J.H.L., M.K., and D.A., performed sample preparation, and helped experiments. S.B., and X.M. provided and managed mice and PFF, and helped data interpretation. K.C.L., and D.H.N. provided and made NLY01. V.V.R performed mouse PK experiment, and data analysis. Y.L., S.H.L., S.A.L., and B.A.B. preformed manuscript writing, review and editing. Z.M provided human postmortem brain samples. V.L.D., S.L., T.M.D., and H.S.K. supervised project, formulated the hypothesis, designed experiments, analyzed data and wrote the manuscript.

Competing financial Interests Statement

Z.M., V.L.D., S.L., T.M.D., H.S.K are co-founders of Neuraly Inc. and hold ownership equity in the company. This arrangement has been reviewed and approved by the Johns Hopkins University in accordance with its conflict of interest policies. V.V.R. is the CSO of Neuraly Inc.

Author Manuscript Author Manuscript Author Manuscript Author Manuscript

[7]The Center for Nanomedicine at the Wilmer Eye Institute, Johns Hopkins University School of Medicine, Baltimore, MD 21287, USA

[8]Department of Pharmacology and Toxicology, University of Alabama at Birmingham School of Medicine, Birmingham, AL 35294, USA

[9]Division of Pharmacology, Department of Molecular Cell Biology, Sungkyunkwan University School of Medicine, Samsung Biomedical Research Institute, Suwon 16419, Republic of Korea

[10]College of Pharmacy, Sungkyunkwan University, Suwon 16419, Republic of Korea

[11]College of Pharmacy, Chung-Ang University, Seoul 06974, Republic of Korea

[12]Soonchunhyang Medical Science Research Institute, Soonchunhyang University, Seoul Hospital, Seoul 04401, Republic of Korea

[13]Neuraly Inc. Baltimore, MD 21205, USA

[14]Department of Neurobiology, Stanford University, School of Medicine, Stanford, CA 94305, USA

[15]Adrienne Helis Malvin Medical Research Foundation, New Orleans, LA 70130, USA

[16]Diana Helis Henry Medical Research Foundation, New Orleans, LA 70130, USA

Abstract

Activation of microglia by classical inflammatory mediators can convert astrocytes to a neurotoxic A1 phenotype in a variety of neurological diseases[1,2]. Development of agents that could inhibit the formation of A1 reactive astrocytes could be used to treat these diseases for which there are no disease modifying therapies. Glucagon-like peptide-1 receptor (GLP-1R) agonists have been touted as potential neuroprotective agents for neurologic disorders such as Alzheimer's disease (AD) and Parkinson's disease (PD)[3-13]. The mechanisms by which GLP-1R agonists are neuroprotective are not known. Here we show that a potent, brain penetrant long acting GLP-1R agonist NLY01 protects against the loss of dopamine neurons and behavioral deficits in the α-synuclein preformed fibril (α-syn PFF) model of sporadic PD[14,15]. NLY01 also prolongs the life and reduces the behavioral deficits and neuropathological abnormalities in the human A53T α-synuclein (hA53T) transgenic (Tg) model of α-synucleinopathy induced neurodegeneration[16]. We found that NLY01 is a potent GLP-1R agonist with favorable properties that is neuroprotective via the direct prevention of microglial mediated conversion of astrocytes to an A1 neurotoxic phenotype. In light of NLY01 favorable properties it should be evaluated in the treatment of PD and related neurologic disorders characterized by microglial activation.

NLY01 is a pegylated long-acting GLP-1R agonist with an extended half-life and pharmacodynamic profiles in non-human primates (88 hrs versus the 2 hrs half-life of Exendin-4) and in mice (38 hrs) while retaining comparable biologic activity to Exendin-4 *in vitro* (Supplementary Fig. 1, Supplementary Table 1). NLY01 does not increase the risk of hypoglycemia when administered in a normoglycemic state in both WT and hA53T Tg mice (Supplementary Fig. 1g). NLY01 efficiently penetrates the blood-brain barrier (BBB) in wild type (WT) mice and reaches high brain levels in ten-month-old hA53T Tg mice (Supplementary Fig. 2a-c). The high levels in the hA53T Tg mice may be due to the breakdown of the BBB (Supplementary Fig. 2d,e)[5,17,18]. The neuroprotective potential of

Author Manuscript Author Manuscript Author Manuscript Author Manuscript

NLY01 was first evaluated in the α-syn PFF model of sporadic PD[14,15]. Recombinant mouse α-syn was purified and depleted of endotoxin, and α-syn PFF were made and validated via atomic force microscopy (AFM) and transmission electron microscopy (TEM) and the ability to induce phospho-serine 129 α-synuclein (p-α-syn^{ser129}) immunostaining[15,19]. We elected to initiate the treatment of NLY01 one month after the intrastriatal injection of α-syn PFF, since spread and initial manifestation of pathology in this model is beginning to be evident at this time point[14,15]. Six months after the intrastriatal injection of α-syn PFF in which mice received NLY01 for five months, a number of biochemical and behavioral assays were performed and comparisons were made between vehicle (PBS) and 3 mg/kg NLY01 subcutaneously (s.c.) injected mice twice a week (Fig. 1a). As previously described, there is substantial p-α-syn^{ser129} immunoreactivity in the striatum and ventral midbrain (VMB) of α-syn PFF injected mice indicative of pathologic α-syn[15] (Fig. 1b,c and Supplementary Fig. 3a-d). NLY01 significantly reduces p-α-syn^{ser129} immunoreactivity in the striatum, ventral midbrain, and specifically in tyrosine hydroxylase (TH) immunoreactive neurons (Fig. 1b,c and Supplementary Fig. 3a,b). NLY01 also significantly reduces the amount of pathologic Triton X-100 (TX) insoluble α-syn and p-α-syn^{ser129} as determined by western blot (Supplementary Fig. 3c,d). α-Syn PFF injection induces a significant loss of TH and Nissl positive neurons in the SNpc, which is prevented by NLY01 (Fig. 1d-f). Western blot analysis reveals that α-syn PFF mediated reduction in TH and dopamine transporter (DAT) immunoreactivity is restored by NLY01 in the ventral midbrain (Supplementary Fig. 4a, b). In addition, the α-syn PFF induced reduction in striatal TH immunoreactivity (Supplementary Fig. 5a, b) and the striatal levels TH and DAT protein (Supplementary Fig. 5c, d) is rescued by NLY01. α-Syn PFF induced reductions in dopamine (DA) and its metabolites, homovanillic acid (HVA), 3-methoxytyramine (3MT) and 3,4-dihydroxyphenylacetic acid (DOPAC) and the increased DOPAC+HVA DA ratio and the DOPAC+3MT DA ratio are normalized by NLY01 treatment (Fig. 1g and Supplementary Fig. 5e-i). The amphetamine rotation test was utilized to monitor the behavioral consequences of unilateral α-syn PFF injection. There is marked ipsilateral amphetamine induced rotation in the α-syn PFF injected mice, which is prevented by NLY01 (Fig. 1h and Supplementary Fig. 6a). NLY01 also significantly reduces the behavioral deficits elicited by α-syn PFF injected as measured by the accelerating rotarod test (Supplementary Fig. 6b) and the pole test (Fig. 1i and Supplementary Fig. 6c,d). α-Syn PFF injection also reduces contralateral forepaw touches in the cylinder test, which is restored by NLY01 (Supplementary Fig. 6e). There are no defects in the ipsilateral forepaw (Supplementary Fig. 6f). The increase in grooming time and reduction in rearing induced by α-syn PFF is restored by NLY01 (Supplementary Fig. 6g,h).

The effects of NLY01 were further evaluated in a progressive, lethal constitutive α-synucleinopathy model, the hA53T Tg mice[16,20]. This model exhibits hyperactivity and evidence of pathologic α-syn at four to six months of age[16,20]. Accordingly, treatment with NLY01 in the hA53T Tg mice was started at six months of age and the mice were monitored until they were moribund (Supplementary Fig. 7). NLY01 significantly prolongs the lifespan of the hA53T Tg mice by over 100 days (Fig. 2a). Accompanying the prolonged survival is a reduction in p-α-syn^{ser129} immunoreactivity and aggregated α-syn, and a reduction of ubiquitin immunoreactivity in cells (Fig. 2b-h). NLY01 also reduces the accumulation of TX

Author Manuscript Author Manuscript Author Manuscript Author Manuscript

insoluble α-syn and p-α-syn^{ser129} (Fig. 2i-k). These results taken together indicate that NLY01 protects against the degenerative effects of injected α-syn PFF and constitutive expression of the hA53T α-syn.

To determine the potential site of action of NLY01, the expression of GLP-1R was assessed in astrocytes, microglia and neuronal cultures. *Glp1r* mRNA expression is low in the mouse cortex, cerebellum and olfactory bulb, but there are high levels in the striatum, brainstem and ventral midbrain (Fig. 3a). GLP-1R protein is highly expressed in microglia and it is also expressed in astrocytes and neurons with reduced expression (Fig. 3b), which differs from the *in vivo* cortical *Glp1r* mRNA cellular expression profile[21]. This may be due to the regional heterogeneity of *Glp1r* mRNA expression (Fig. 3a). α-syn PFF treatment decreases *Glp1r* mRNA expression in neurons and increases *Glp1r* mRNA expression almost 2-fold in microglia (Fig. 3c). *Glp1r* mRNA expression is elevated greater than 10-fold in the substantia nigra of PD patients compared to controls (Supplementary Fig. 8a and Supplementary Table 2). GLP-1R immunoreactivity is mainly found in ionized calcium-binding adapter molecule (Iba-1) and transmembrane protein 119 (TMEM119) positive microglia in the substantia nigra pars compacta (SNpc) (Supplementary Fig. 8b-d). α-syn PFF treatment increases the immunoreactivity of GLP-1R in microglia, while the GLP-1R immunoreactivity is found at very low levels in neurons (Supplementary Fig. 8c,d) suggesting that the site of action of NLY01 is likely to be predominantly glial, particularly in the non-cortical brain regions. To determine the site of action of NLY01, the effects of NLY01 on microglial, astrocytic and neuronal cultures were assessed after treatment with α-syn PFF (Fig. 3d). In human dopaminergic (DA) neuronal cultures, direct treatment of NLY01 in the DA neurons fails to protect against α-syn PFF induced cell death as assessed by alamarBlue, lactate dehydrogenase (LDH) and trypan blue assays (Supplementary Fig. 9a-c), indicating that the site of action of NLY01 is likely to be upstream in either microglia and/or astrocytes. Previously, we reported that activated microglia convert astrocytes to toxic A1 astrocytes by releasing IL-1α, Tumor necrosis factor (TNF)α and C1q[2]. As such microglia were treated with α-syn PFF for 24 hrs and then the cytokine profile was assessed by an ELISA cytokine screening array. α-syn PFF induces secretion of a variety of cytokines including IL-1α and TNFα. NLY01 reduces the level of a subset of α-syn PFF induced cytokines including IL-1α, TNFα, IL-1ß, IL-6, typical markers of M1 microglia, and leptin (Supplementary Fig. 10a). Since C1q was not present on the ELISA cytokine array, C1q was directly monitored by western blot analysis and compared to TNFα. α-syn PFF induces both C1q and TNFα release into media, which are significantly inhibited by NLY01 (Supplementary Fig. 10b,c). Since NLY01 preferentially blocks microglia derived factors that induce A1 astrocytes, α-syn PFF microglial conditioned media (MCM) was applied to astrocytes for 24 hrs. The astrocyte conditioned media (ACM) was then collected, concentrated and applied to murine primary cortical cultures and human DA neurons in the presence or absence of NLY01 (Fig. 3d). α-syn PFF-ACM kills murine primary cortical cultures in a dose-dependent manner (Supplementary Fig. 11a). NLY01 applied to the α-syn PFF treated microglia significantly prevents α-syn PFF-ACM induced cell death in murine primary cortical cultures (Supplementary Fig. 11b) and human DA neurons (Supplementary Fig. 11c-e). The neuronal cell death of α-syn PFF-MCM is significantly less than that observed in α-syn PFF-ACM treatment (Supplementary Fig. 11f, g), suggesting that α-syn

Author Manuscript Author Manuscript Author Manuscript Author Manuscript

PFF induced A1 astrocytes are likely to be the primary glial culprit that mediates α-syn PFF toxicity. The observations that pretreatment of NLY01 in microglia, but not direct treatment of NLY01 into neurons, significantly reduced the levels of p-α-syn^{ser129} induced by α-syn PFF-ACM provide further support for the microglial action of NLY01 (Supplementary Fig. 12 and Supplementary Fig. 13).

To further investigate the ability of α-syn PFF to activate microglia and the inhibitory effect of NLY01, the levels of IL-1α, TNFα, IL-1ß, IL-6, and C1q were monitored in response to α-syn PFF. α-syn PFF significantly induces mRNA for *Il1a*, *Il1b*, *Tnfa*, *C1qa*, and *Il6* as determined by quantitative RT-PCR (qPCR) in primary microglia, and NLY01 significantly reduces this mRNA induction (Fig. 3e-g and Supplementary Fig. 10d,e). Protein levels for IL-1α, TNFα, IL-1ß, and C1q as determined by ELISA are increased with exposure to α-syn PFF and this induction is reduced by NLY01 (Fig. 3h-j and Supplementary Fig. 10f). To determine whether α-syn PFF induces microglia activation *in vivo*, Iba-1 immunoreactivity was monitored. Intrastriatal injection of α-syn PFF significantly increases Iba-1 immunoreactivity in the SNpc six months post injection and NLY01 significantly reduces the Iba-1 immunoreactivity and microglial density (Fig. 3k-m and Supplementary Fig. 10g). Western blot analysis for Iba-1 confirms the induction by α-syn PFF and the reduction by NLY01 (Fig. 3n,o). Consistent with the primary microglia results, intrastriatal injection of α-syn PFF induces mRNA for *Il1a*, *Il1b*, *Tnfa*, *C1qa*, and *Il6* in the microglia of ventral midbrain. This induction is blocked by NLY01 (Fig. 3p-r and Supplementary Fig. 10h,i). Importantly, the inhibitory effect of NLY01 on α-syn PFF induced A1 microglia activation and α-syn PFF-ACM induced cell death is prevented by depletion of GLP-1R in TMEM119 positive-microglia, indicating that NLY01 exhibits protective effects primarily through microglial GLP-1R (Supplementary Fig. 14). NLY01 does not interfere with the uptake of α-syn PFF in microglia, but instead it inhibits the NF-kB pathway (Supplementary Fig. 15). The further inhibition of α-syn PFF induced microglia activation by NLY01 in TLR2 KO suggest that the effect of NLY01 is independent from TLR2 signaling[22] (Supplementary Fig. 16).

To ascertain whether α-syn PFF treated microglia induces astrocytes, MCM from α-syn PFF treated microglia was applied to astrocytes and 24 hrs later, the expression of glial fibrillary acidic protein (GFAP) was monitored (Fig. 4a). α-syn PFF-MCM induces GFAP and this induction is blocked by NLY01 (Fig. 4b,c). To determine what type of astrocytes are induced by α-syn PFF-MCM, general astrocyte reactive, A1, and A2 specific mRNA levels were assessed by qPCR (Fig. 4d). α-syn PFF-MCM preferentially induces markers of A1 astrocytes, while not perturbing A2 specific transcripts (Fig. 4d and Supplementary Table 3). There is no remaining α-syn PFF in the MCM after 24 hrs treatment, indicating that this is not due to the astrocytes responding to α-syn PFF (Supplementary Fig. 17). Importantly, treatment of α-syn PFF-MCM prior to treatment of astrocytes with neutralizing antibodies to IL-1α, TNFα, and C1q prevents A1 type astrocyte formation (Supplementary Fig. 18a), and there is no neuronal death in primary cortical neurons (Supplementary Fig. 18b,c) and human DA neurons (Supplementary Fig. 18d,e) similar to the effects of NLY01. These results taken together indicate that microglia activated by α-syn PFF specifically convert astrocytes to neurotoxic A1 astrocytes and that NLY01 prevents this conversion. Consistent with the glial enriched expression of GLP-1R and the depletion of microglial GLP-1R

Author Manuscript Author Manuscript Author Manuscript Author Manuscript

(Supplementary Fig. 14), NLY01 treatment of microglia, but not that of astrocytes, prevents the induction of A1 astrocytic specific markers (Fig. 4d and Supplementary Fig. 19). Intrastriatal injection of α-syn PFF induces GFAP immunoreactivity in the ventral midbrain, which is blocked by NLY01 (Fig. 4e,f). Western blot analysis confirms that intrastriatally injected α-syn PFF induction of GFAP level in the ventral midbrain is blocked by NLY01 (Fig. 4g,h). Consistent with the induction of A1 specific transcripts, ventral midbrain C3d immunoreactivity is induced by intrastriatally injected α-syn PFF, which is blocked by NLY01 (Fig. 4g,h). To evaluate A1 astrocyte formation in the intrastriatally injected α-syn PFF model of sporadic PD, C3d immunohistochemistry was assessed in the ventral midbrain. C3d positive astrocytes are increased by α-syn PFF, which are blocked by NLY01 (Fig. 4i,j). NLY01 blocks the induction of *C3* mRNA in isolated astrocytes in the ventral midbrain following intrastriatally injected α-syn PFF as determined by qPCR (Fig. 4k). General astrocyte reactive, A1, and A2 specific mRNA levels were also assessed by qPCR in astrocytes isolated from ventral midbrain. Intrastriatal injection of α-syn PFF primarily induces A1 astrocyte specific transcripts and this is prevented by NLY01 (Fig. 4l and Supplementary Table 4). Microglial and astrocytic activation has been previously described in the hA53T α-syn Tg mice[16,23]. Consistent with these observations, we confirmed both microglial and astrocytic activation as determined by Iba-1 and GFAP immunoreactivity, respectively. NLY01 significantly attenuates both microglial (Supplementary Fig. 20a-c) and astrocytic activation (Supplementary Fig. 20d,e). The mRNA for the A1 astrocyte marker *C3* is markedly increased in ten-month-old hA53T α-syn Tg mice and this increase is prevented by NLY01 (Supplementary Fig. 20f).

The major findings of this paper are the observation that the GLP-1R agonist, NLY01 protects *in vivo* against DA neuronal loss and behavioral deficits in the intrastriatal injection α-syn PFF mouse model of sporadic PD. Furthermore, NLY01 prolongs the survival and reduces the neuropathology of the hA53T α-syn Tg mice, a model of familial α-synucleinopathy. NLY01's protective effects are independent of its potential action on neurons, but appear to primarily involve inhibition of microglia. We show that α-syn PFF induces microglial activation and that the microglia assume a "M1"-phenotype. The "M1"/"M2" macrophage nomenclature is under current refinement because macrophages clearly can display more than two states[24,25]. In any event this "M1" phenotype is consistent with prior reports that aggregated α-syn induces microglial activation and the observations that there are activated microglia in PD postmortem brains[20,26]. This M1 microglial activation then converts astrocytes into toxic A1 astrocytes[1], which contributes to the demise of DA neurons in the α-syn PFF mouse model and in human DA neuronal cultures as well as contributing to the neurodegeneration in hA53T Tg mice. Prior reports are consistent with our findings suggesting that NLY01 site of action is microglia since the GLP-1R agonist, Exendin-4 prevents the activation of microglia both *in vitro* and *in vivo* following a variety of injury paradigms[11,27-32]. There is one report that Exendin-4 does not prevent the activation of microglia *in vitro* and *in vivo* following stimulation with lipopolysaccharide (LPS)[33]. What accounts for the variance of this report with our findings and others is not clear, but it may be due to methodological issues.

GLP-1R agonists are protective in models of stroke, traumatic brain injury (TBI), AD, and the MPTP intoxication model of PD[4,5,8,12,13]. Importantly, the GLP-1R agonist, Exendin-4

Author Manuscript Author Manuscript Author Manuscript Author Manuscript

may have a disease modifying effect in PD[4,13]. The protective effects of GLP-1R agonists have been postulated to involve an insulinotrophic effect, activation of Akt, inhibition of microglial activation, beneficial effects on mitochondrial function through induction of PGC-1α, enhancement of neurogenesis or increased production of trophic factors[30,34,35]. Our results here provide evidence that GLP-1R agonist inhibition of microglia is the primary site of action. Interestingly, in the α-syn PFF model of sporadic PD and in the hA53T Tg mouse model, activated microglia express key factors that are responsible for the conversion of astrocytes to toxic A1 astrocytes[1]. This is consistent with what is observed in human postmortem PD brain[2]. NYL01 blocks the microglial activation and the generation of A1 astrocytes. Because of this, NLY01 may have broad neuroprotective properties in a variety of neurodegenerative disorders and neurologic injuries characterized and involving A1 astrocyte activation[2].

ONLINE METHODS

Detailed information on experimental design and reagents can be found in Life Sciences Reporting Summary that accompanies this paper.

Animal models

All experimental procedures were according to the guidelines of Laboratory Animal Manual of the National Institute of Health Guide to the Care and Use of Animals, which were approved by the Johns Hopkins Medical Institute Animal Care and Use Committee. The PK studies in cynomolgus monkeys were approved by the Institutional Animal Care and Use Committee of Korea Institute of Toxicology (KIT, study plan JN13002) and performed at KIT, Daejeon, Republic of Korea. (1) **Mouse strain for stereotaxic α-syn PFF injection.** C57BL6 mice were obtained from the Jackson Laboratories (ME, USA). The mice do not develop any autoimmune or inflammatory phenotype. NLY01 (3 mg/kg) two times per week was subcutaneously administered one month after α-syn PFF stereotaxic injection until five months. (2) **hA53T α-synuclein transgenic mice.** hA53T α-synuclein transgenic mice were obtained from the Jackson Laboratories (B6; *Prnp-SNCA*A53T*)[16]. NLY01 (3 mg/kg) two times per week was subcutaneously administered to six-months-old hA53T α-synuclein transgenic mice until ten-months of age or until death. (3) **Toll like receptor 2 (TLR-2) knockout mice.** TLR-2 KO mice were obtained from the Jackson Laboratories (B6; *129-Tlr2 ^{tm1kir}/J*).

α-Synuclein purification and α-syn preformed fibril (PFF) preparation

Recombinant mouse α-synuclein proteins were purified as previously described with IPTG independent inducible pRK172 vector system[15,36]. Endotoxin was depleted by ToxinEraser endotoxin removal kit (Genscript). α-Syn PFF (5 mg/ml) was prepared in PBS to by stirring with a magnetic stirrer (1,000 rpm at 37° C). After a week incubation of the α-synuclein protein, aggregates were diluted to 0.1 mg/ml with PBS and sonicated for 30 sec (0.5 sec pulse on/off) at 10% amplitude (Branson Digital sonifier, Danbury, CT, USA). α-Syn PFF was validated via atomic force microscopy (AFM) and transmission electron microscopy (TEM) and the ability to induce phospho-serine 129 α-synuclein (p-α-syn^{ser129}) immunostaining[15,19]. α-Syn PFF was stored at -80˚ C until used.

Author Manuscript Author Manuscript Author Manuscript Author Manuscript

Preparation of NLY01

NLY01 is pegylated [Cys[40]]Exendin-4 and is generously provided by Neuraly Inc. NLY01 was synthesized as described in our previous papers[37,38] and the corresponding amino acid sequence is His-Gly-Glu-Gly-Thr-Phe-Thr-Ser-Asp-Leu-Ser-Lys-Gln-Met-Glu-Glu-Glu-Ala-Val-Arg-Leu-Phe-Ile-Glu-Trp-Leu-Lys-Asn-Gly-Gly-Pro-Ser-Ser-Gly-Ala-Pro-Pro-Pro-Ser-Cys(PEG50K)-NH2.

Characterization of NLY01

(1) HPLC analysis. NLY01 purified by preparative RP-HPLC was analyzed by using a Dionex Ultimate 3000 HPLC system (Sunnyvale, CA, USA) with a Phenomenex Gemini RP-18 column (250 × 4.6 mm, 5 μm) at ambient temperature and a constant flow-rate of 1.0 mL/min under UV monitoring at 280 nm. The mobile phase consisted of 0.1% (trifluoracetic acid (TFA) in deionized water (eluent A) and acetonitrile (AN) containing 0.1% TFA (eluent B), and these were applied as linear gradients from 30% B to 60% B over 20 min. (2) **MALDI-TOF mass spectrometry.** Molecular weight of NLY01 was determined by a Bruker Daltonics Microflex MALDI-TOF mass spectrometer (Bremen, Germany) with a 337 nm nitrogen laser. Mass spectrum was obtained in the linear and positive-ion mode with an acceleration voltage of 20 kV. As a matrix solution, a saturated solution of sinapinic acid in acetonitrile:water (50:50, v:v) containing 0.1% TFA was used. Each analyte was mixed with a matrix solution at a ratio of 1:1 (analyte:matrix, v:v) and 1 μl of the analyte-matrix solution was applied and air-dried on the sample plate.

Stereotaxic α-syn PFF injection

For stereotaxic injection of α-syn PFF, three-month-old male and female mice were anesthetized with xylazene and ketamine. An injection cannula (26.5 gauge) was applied stereotaxically into the striatum (mediolateral, 2.0 mm from bregma; anteroposterior, 0.2 mm; dorsoventral, 2.6 mm) unilaterally (applied into the right hemisphere). The infusion was performed at a rate of 0.2 μl per min, and 2 μl of α-syn PFF (2.5 μg/μl in PBS) or same volume PBS were injected into mouse.

Behavioral tests

To evaluate α-syn PFF-induced behavioral deficits, PBS and α-syn PFF injected mice were assessed by pole test, rotarod test, cylinder test and the amphetamine induced stereotypic rotation test 2 weeks prior to sacrifice. The experimenter was blinded to treatment group for all behavioral studies. All tests were recorded and performed between 10:00-16:00 in the lights-on cycle. (1) **Amphetamine induced stereotypic rotation test.** Six months after mice received the α-syn PFF injection into the right hemisphere with or without NLY01 treatment; 5 mg/kg amphetamine (Sigma-Aldrich) was intraperitoneally administered to the mice. Mice were placed in a white paper cylinder of 20 cm diameter and monitored for 30 min. The behavior of the mice was filmed at three one-minute intervals between 20 and 30 min following amphetamine administration. Full body ipsilateral rotations (clockwise) during the one minute session were counted for each mouse from the video recordings. (2) **Pole test.** Mice were acclimatized in the behavioral procedure room for 30 min. The pole was made of a 75 cm metal rod with a diameter of 9 mm. It was wrapped with bandage

Author Manuscript Author Manuscript Author Manuscript Author Manuscript

gauze[39]. Mice were placed on the top of the pole (7.5 cm from the top of the pole) facing head-up. The total time taken to reach the base of the pole was recorded. Before the actual test, mice were trained for two consecutive days. Each training session consisted of three test trials. On the test day, mice were evaluated in three sessions and the total time was recorded. The maximum cutoff time to stop the test and recording was 60 sec. Results for turn down, climb down, and total time (in sec) were recorded. (3) **Rotarod test.** For the rotarod test, mice were placed on an accelerating rotarod cylinder, and the time the animals remained on the rotarod was measured. The speed was slowly increased from 4 to 40 rpm within 5 min. A trial ended if the animal fell off the rungs or gripped the device and spun around for 2 consecutive revolutions without attempting to walk on the rungs. The animals were trained 3 days before test. Motor test data are presented as the percentage of the mean duration (3 trials) on the rotarod compared with the control. (4) **Cylinder test.** Spontaneous movement was measured by placing animals in a small transparent cylinder (height, 15.5 cm; diameter, 12.7 cm). Spontaneous activity was recorded for 10 min. The number of forepaw touches, rears and grooming were measured. Recorded files were viewed and rated in slow motion by an experimenter blinded to the mouse type and NLY01 treatment.

Immunohistochemistry and quantitative analysis

Immunohistochemistry (IHC) was performed on 30 μm thick serial brain sections. Primary antibodies and working dilutions are detailed in Supplementary Table 5. TH, Nissl, p-α-syn^{ser129} experimental procedures and quantitative analysis were performed as previously described[39,40]. Microglia and astrocytes from the SNpc region were stained with anti-Iba-1 (Wako, St. Louis, MO, USA) or anti-GFAP (Dako, Santa Clara, CA, USA) antibodies, followed by incubation with biotin-conjugated anti-rabbit antibody and ABC reagents. Sections were developed using SigmaFast DAB Peroxidase Substrate (Sigma-Aldrich). The number of microglia and densities of astrocytes in the SNpc region were measured with ImageJ software.

Immunofluorescence analysis

Immunofluorescence was performed on 30 μm thick serial brain sections. Primary antibodies and working dilutions are detailed in Supplementary Table 5. For histological studies, immunofluorescence in tissue sections was performed as described previously[15].

Tissue and cell lysate preparation

Tissue lysates were prepared as described previously with some modifications[15]. Nonionic detergent-soluble and -insoluble fractions were made by homogenization of tissue in brain lysis buffer [10 mM Tris-HCl, pH 7.4, 150 mM NaCl, 5 mM EDTA, 0.5% Nonidet P-40, phosphatase inhibitor cocktail II and III (Sigma-Aldrich), and complete protease inhibitor mixture]. The homogenate was centrifuged at 22,000 x g for 20 min, and the resulting pellet (P1) and supernatant (S1, soluble part) fractions were collected. The P1 was washed once in brain lysis buffer containing nonionic detergent (0.5% Nonidet P-40) and the resulting pellet (P2, nonionic detergent insoluble) was homogenized in brain lysis buffer containing 1% SDS and 0.5% sodiumdeoxycholate. The homogenate was centrifuged and the resulting supernatant (nonionic detergent-insoluble) was collected. Total lysates were prepared by

Author Manuscript Author Manuscript Author Manuscript Author Manuscript

homogenization of tissue in RIPA buffer [50 mM Tris, pH 8.0, 150 mM NaCl, 1% Nonidet P-40, 1% SDS, 0.5% sodium-deoxycholate, phosphatase inhibitor cocktail II and III (Sigma-Aldrich), and complete protease inhibitor mixture]. The homogenate was centrifuged at 22,000 x g for 20 min, and the resulting supernatant (insoluble part) was collected.

Immunoblot analysis

Mouse brain tissues and primary neurons were homogenized and prepared in lysis buffer. Primary antibodies and working dilutions are detailed in Supplementary Table 5. Immunoblots of tissue and neuronal culture was performed as described previously[15]. All raw blot and gel images are available in Supplementary Figures 21 and 22.

Measurement of NLY01 accumulation in brain—The day after the PBS or NLY01 (3 mg/kg) injection in twelve-month-old WT and hA53T α-synuclein Tg mice, the levels of NLY01 in the brain were measured using a Exendin-4 (Heloderma suspectum)–EIA Kit (Phoenix pharmaceuticals, INC, Burlingame, CA, USA), according to the manufacturer's instructions.

Monoamine analysis—High performance liquid chromatography with electrochemical detection (HPLC-ECD) was performed to measure biogenic anime concentrations as described previously[39].

Differentiation of ESC into DA neurons—The H9 human embryonic stem cells (ESCs) were differentiated into DA neurons following a DA neuron induction protocol[41]. All experiments using human stem cells were monitored and approved by the JHU Institutional Stem Cell Research Oversight Committee.

Human postmortem brain tissues—This research uses anonymous autopsy material, substantia nigra from subjects with PD (n=10) and related disorders and controls (n=10) from the Division of Neuropathology, Department of Pathology of Johns Hopkins University School of Medicine. The John Hopkins Medical Institutions (JHMI) Joint Committee on Clinical Investigations decided that these studies are exempt from Human Subjects Approval because of Federal Register 46.101 Exemption Number 4. PD was confirmed by pathological and clinical criteria (Supplementary Table 2). *Glp1r* mRNA levels were monitored in human postmortem substantia nigra brain tissue from Parkinson's disease patients and controls (Supplementary Figure 3a).

Primary neuron, microglia and astrocyte cell cultures—CD1 mice were obtained from Jackson Laboratories (Bar Harbor, ME). Primary cortical neurons were prepared from E15.5 pups and cultured in Neurobasal media (Gibco) supplemented with B-27, 0.5 mM L-glutamine, penicillin and streptomycin (Invitrogen, Grand Island, NY) on tissue culture plates coated with poly-L-lysine. The neurons were maintained by changing medium every 3–4 days. Primary microglial and astrocyte cultures were performed as described previously[42]. Whole brains from mouse pups at postnatal day age 1 (P1) were obtained. After removal of the meninges the brains were washed in DMEM/F12 (Gibco) supplemented with 10% heat-inactivated FBS, 50 U/mL penicillin, 50 μg/mL streptomycin,

Author Manuscript Author Manuscript Author Manuscript Author Manuscript

2 mM L-glutamine, 100 μM non-essential amino acids, and 2 mM sodium pyruvate (DMEM-F12 complete medium) three times. The brains were transferred to 0.25% Trypsin-EDTA followed by 10 min of gentle agitation. DMEM-F12 complete medium was used to stop the trypsinization. The brains were washed three times in this medium again. A single cell suspension was obtained by trituration. Cell debris and aggregates were removed by passing the single cell suspension through a 100 μm nylon mesh. The final single cell suspension thus achieved was cultured in T-75 flasks for 13 days, with a complete medium change on day 6. The mixed glial cell population was separated into astrocyte rich and microglia rich fractions using the EasySep Mouse CD11b Positive Selection Kit (StemCell). The magnetically separated fraction containing microglia and the pour-off fraction containing astrocytes were cultured separately. The conditioned medium from the primary microglia treated with α-syn PFF (α-syn PFF-MCM) with either PBS or NLY01 treatment were collected and applied to primary astrocytes for 24 hrs. The conditioned medium from activated astrocyte by α-syn PFF-MCM, which defined as α-syn PFF-ACM, were collected with complete, Mini, EDTA-free Protease Inhibitor Cocktail (Sigma) and concentrated with Amicon Ultra-15 centrifugal filter unit (10 kDa cutoff) (Millipore) until approximately 50 X concentrated. The total protein concentration was determined using Pierce BCA protein assay kit (Thermo Scientific), and 15 or 50 μg/ml of total protein was added to murine primary neurons or human dopaminergic neuron, respectively, for neuronal cell death assay.

pLentiCRISPR GLP-1R KO microglia—The sgRNAs targeting GLP-1R (KO1, 5′-CCAGGAGTGGCGCTTCCGTG-3′; KO2, 5′-TCGTGAATGTCAGCTGCCCC-3′) were subcloned into a pLentiCRISPR vector (Addgene) and lentivirus was generated as previously described[43]. Microglia were transduced and GLP-1R levels were assessed by immunoblot.

Comparative quantitative real time PCR (qPCR)—Total RNA from cultured cells was extracted with a RNA isolation kit (Qiagen, CA) following the instruction provided by the company. RNA concentration was measured spectrophotometrically using NanoDrop 2000 (Biotek, Winooski, VT). 1-2 μg of total RNA were reverse-transcribed to cDNA using the High-Capacity cDNA Reverse Transcription System (Life Technologies, Grand Island, NY). Comparative quantitative RT-PCR (qPCR) was performed in duplicate or triplicate for each sample using fast SYBR Green Master Mix (Life Technologies) and ViiA 7 Real-Time PCR System (Applied Biosystems, Foster City, CA). The expression levels of target genes were normalized to the expression of β-actin and calculated based on the comparative cycle threshold Ct method ($2^{-\Delta\Delta Ct}$). Name and sequences of primers are summarized in Supplementary Table 6.

Enzyme linked immunosorbent assay (ELISA) analysis—The secreted cytokines from primary microglia 18 hrs after α-syn PFF with either PBS or NLY01 treatment were screened using a mouse cytokine ELISA plate array (Signosis, Santa Clara, CA) according to the manufacturer instructions.

Cell viability analysis—Cell viability was tested via four methods: (1) **Propidium iodide staining.** Primary cultured cortical neurons were treated either with α-syn PFF-ACM or

Author Manuscript Author Manuscript Author Manuscript Author Manuscript

NLY01-α-syn PFF-ACM for 24 h. Cell viability was determined by an unbiased objective computer-assisted cell counting after staining of all nuclei with 7 μM Hoechst 33342 (Invitrogen) and dead cell nuclei with 2 μM propidium iodide (Invitrogen)[44]. The numbers of total and dead cells were counted with the Axiovision 4.3 software (Carl Zeiss). The percentage of cell death was determined as the ratio of live to dead cells as compared with the percentage of cell death in control wells to account for cell death attributed to mechanical stimulation of the cultures. (2-3) **The alamarBlue and LDH assay.** Cell death was assessed through alamarBlue assay (Invitrogen), according to the manufacturer's protocol. LDH (Sigma) activity in culture medium, representing relative cell viability and membrane integrity, was measured using the LDH assay kit spectrophotometrically, following the manufacturer's instructions. (4) **Trypan Blue live cell counting.** Neurons were dissociated into a single-cell suspension using trypsin. Mixtures of suspended cell and the trypan blue solution were (1:1) immediately put in the live cell counter (Countess™, Invitrogen), and the number of living cells and dead cells was measured. Three wells were assayed for each condition.

PK profile of NLY01 in cynomolgus monkeys and mice—The PK studies in cynomolgus monkeys were approved by the Institutional Animal Care and Use Committee of Korea Institute of Toxicology (KIT, study plan JN13002) and performed at KIT, Daejeon, Republic of Korea. Cynomolgus monkeys (Macaca fascicularis), 4-5 years old, male, 3-5 kg. The PK profile of NLY01 was evaluated in cynomolgus monkeys and compared to free [Cys^{40}]Exendin-4. Monkeys were given a single subcutaneous injection of equimolar doses of NLY01 or [Cys^{40}]Exendin-4 (32 μg/kg, n=2). In addition, the PK profile of NLY01 (1 mg/kg, a single subcutaneous injection) was studied in C57BL/6 mice (3 mice were used at each time point). Peptide levels were measured by a exenind-4 EIA kit (Phoenix Pharmaceuticals Inc.) in plasma samples collected at various time points. The PK parameters were calculated by non-compartmental analysis using WinNonlin software (Phasight Corporation, Mountain View, CA, USA).

***In vitro* biological activity of NLY01—**GLP-1R transfected HEK-293/CRE-LUC/GLP1R cells (GenScript, Piscataway, NJ, USA) were treated with serial dilutions of [Cys^{40}]Exendin-4 and NLY01 at the indicated concentrations. After 2 hrs of incubation intracellular cAMP levels were measured. Both GLP-1R transfected cells and cAMP detection reagents are part of the intracellular cAMP human recombinant GLP-1R stable cell line assay (GenScript). Luminescence was measured using SpectraMax M5 plate reader. The data were analyzed using 4 parameter logistic fit model using Prizm software.

Blood glucose level—The hypoglycemic effects of peptides were investigated in age-matched WT and hA53T Tg mice (10-month old). Under non-fasting conditions with free access to food and water, mice were subcutaneously treated with PBS and NLY01 (n=3, 3 mg/kg). A drop of blood was drawn from a tail vein of each animal at predetermined time points and blood glucose levels were measured using a one-touch blood glucose meter (ACCU-CHEK Sensor, Roche Diagnostics Corp., USA).

Author Manuscript Author Manuscript Author Manuscript Author Manuscript

Injection of the Fluorescent Tracers for blood-brain barrier (BBB)—Fluorescein isothiocyanate-labeled dextran (FITC-dextran, molecular weights; 3kD, Sigma) and Rhodamine-labeled dextran (Rh-dextran, molecular weights; 2,000kD, Sigma) were used as gold standard for the evaluation of BBB permeability and disruption. The WT and hA53T α-syn Tg nice were intravenously injected with mixture of FITC-dextran and Rh-dextran in the tail vein, which circulated for 1 hr. After 1 hr, the mice were scarified, their brains were quickly removed.

Statistics—All data were analyzed using GraphPad Prism 6 software. PK parameters were calculated by non-compartmental analysis using WinNonlin software (Phasight Corporation, Mountain View, CA, USA). Statistics Data were presented as mean ± S.E.M. with at least 3 biologically independent experiments. Representative morphological images were taken from at least 3 biologically independent experiments with similar results. An unpaired two-tailed Student's test or a two-way ANOVA test followed by Tukey's multiple comparisons test to assess the statistical significance. Assessments with $p < 0.05$ were considered significant.

Data availability statement

The data that support the findings of this study are available from the corresponding author upon reasonable request.

Supplementary Material

Refer to Web version on PubMed Central for supplementary material.

Acknowledgments

All relevant ethical regulations were followed. This work was supported by grants from the NIH/NINDS NS38377 (H.S.K., V.L.D. and T.M.D.), NIH/NINDS NS082205 and NS098006 (H.S.K.), Maryland Stem Cell Research Foundation 2012-MSCRFE-0059 (H.S.K.), the JPB Foundation (T.M.D.), NIH/National Institute on Aging grant 1K01AG056841-01(X.M.), the American Parkinson Disease Association (APDA) Research Grant Awards (X.M.), and the National Research Foundation of Korea NRF-2016R1D1A1B03934847 (D.H.N). The authors acknowledge the joint participation by the Adrienne Helis Malvin Medical Research Foundation and the Diana Helis Henry Medical Research Foundation through their direct engagement in the continuous active conduct of medical research in conjunction with The Johns Hopkins Hospital and the Johns Hopkins University School of Medicine and the Foundation's Parkinson's Disease Programs M-1 (T.M.D, V.L.D.), M-2 (T.M.D. V.L.D.), H-2014 (T.M.D), M-2014 (H.S.K., T.M.D., V.L.D.), H-1 (H.S.K.), H-2013 (H.S.K.). T.M.D. is the Leonard and Madlyn Abramson Professor in Neurodegenerative Diseases. We thank Neuraly Inc. for providing NLY01.

References

1. Liddelow SA, Barres BA. Reactive Astrocytes: Production, Function, and Therapeutic Potential. Immunity. 2017; 46:957–967. [PubMed: 28636962]
2. Liddelow SA, et al. Neurotoxic reactive astrocytes are induced by activated microglia. Nature. 2017; 541:481–487. [PubMed: 28099414]
3. Athauda D, Foltynie T. The glucagon-like peptide 1 (GLP) receptor as a therapeutic target in Parkinson's disease: mechanisms of action. Drug Discov Today. 2016; 21:802–818. [PubMed: 26851597]
4. Aviles-Olmos I, et al. Exenatide and the treatment of patients with Parkinson's disease. J Clin Invest. 2013; 123:2730–2736. [PubMed: 23728174]

Author Manuscript Author Manuscript Author Manuscript Author Manuscript

5. Chen S, et al. Glucagon-like peptide-1 protects hippocampal neurons against advanced glycation end product-induced tau hyperphosphorylation. Neuroscience. 2014; 256:137–146. [PubMed: 24183963]
6. Harkavyi A, Whitton PS. Glucagon-like peptide 1 receptor stimulation as a means of neuroprotection. Br J Pharmacol. 2010; 159:495–501. [PubMed: 20128800]
7. Li Y, et al. Liraglutide is neurotrophic and neuroprotective in neuronal cultures and mitigates mild traumatic brain injury in mice. J Neurochem. 2015; 135:1203–1217. [PubMed: 25982185]
8. Li Y, et al. GLP-1 receptor stimulation preserves primary cortical and dopaminergic neurons in cellular and rodent models of stroke and Parkinsonism. Proceedings of the National Academy of Sciences of the United States of America. 2009; 106:1285–1290. [PubMed: 19164583]
9. Meier JJ. GLP-1 receptor agonists for individualized treatment of type 2 diabetes mellitus. Nat Rev Endocrinol. 2012; 8:728–742. [PubMed: 22945360]
10. Rachmany L, et al. Exendin-4 induced glucagon-like peptide-1 receptor activation reverses behavioral impairments of mild traumatic brain injury in mice. Age (Dordr). 2013; 35:1621–1636. [PubMed: 22892942]
11. Teramoto S, et al. Exendin-4, a glucagon-like peptide-1 receptor agonist, provides neuroprotection in mice transient focal cerebral ischemia. J Cereb Blood Flow Metab. 2011; 31:1696–1705. [PubMed: 21487412]
12. Tweedie D, et al. Blast traumatic brain injury-induced cognitive deficits are attenuated by preinjury or postinjury treatment with the glucagon-like peptide-1 receptor agonist, exendin-4. Alzheimers Dement. 2016; 12:34–48. [PubMed: 26327236]
13. Athauda D, et al. Exenatide once weekly versus placebo in Parkinson's disease: a randomised, double-blind, placebo-controlled trial. Lancet. 2017; 390:1664–1675. [PubMed: 28781108]
14. Luk KC, et al. Pathological alpha-synuclein transmission initiates Parkinson-like neurodegeneration in nontransgenic mice. Science. 2012; 338:949–953. [PubMed: 23161999]
15. Mao X, et al. Pathological alpha-synuclein transmission initiated by binding lymphocyte-activation gene 3. Science. 2016; 353
16. Lee MK, et al. Human alpha-synuclein-harboring familial Parkinson's disease-linked Ala-53 –> Thr mutation causes neurodegenerative disease with alpha-synuclein aggregation in transgenic mice. Proceedings of the National Academy of Sciences of the United States of America. 2002; 99:8968–8973. [PubMed: 12084935]
17. Cabezas R, et al. Astrocytic modulation of blood brain barrier: perspectives on Parkinson's disease. Front Cell Neurosci. 2014; 8:211. [PubMed: 25136294]
18. Gray MT, Woulfe JM. Striatal blood-brain barrier permeability in Parkinson's disease. J Cereb Blood Flow Metab. 2015; 35:747–750. [PubMed: 25757748]
19. Polinski NK, et al. Best Practices for Generating and Using Alpha-Synuclein Pre-Formed Fibrils to Model Parkinson's Disease in Rodents. J Parkinsons Dis. 2018
20. Brahmachari S, et al. Activation of tyrosine kinase c-Abl contributes to alpha-synuclein-induced neurodegeneration. J Clin Invest. 2016; 126:2970–2988. [PubMed: 27348587]
21. Zhang Y, et al. An RNA-sequencing transcriptome and splicing database of glia, neurons, and vascular cells of the cerebral cortex. J Neurosci. 2014; 34:11929–11947. [PubMed: 25186741]
22. Kim C, Lee HJ, Masliah E, Lee SJ. Non-cell-autonomous Neurotoxicity of alpha-synuclein Through Microglial Toll-like Receptor 2. Exp Neurobiol. 2016; 25:113–119. [PubMed: 27358579]
23. Daher JP, et al. Neurodegenerative phenotypes in an A53T alpha-synuclein transgenic mouse model are independent of LRRK2. Hum Mol Genet. 2012; 21:2420–2431. [PubMed: 22357653]
24. Harms AS, et al. Peripheral monocyte entry is required for alpha-Synuclein induced inflammation and Neurodegeneration in a model of Parkinson disease. Experimental neurology. 2018; 300:179–187. [PubMed: 29155051]
25. Martinez FO, Gordon S. The M1 and M2 paradigm of macrophage activation: time for reassessment. F1000Prime Rep. 2014; 6:13. [PubMed: 24669294]
26. Allen Reish HE, Standaert DG. Role of alpha-synuclein in inducing innate and adaptive immunity in Parkinson disease. J Parkinsons Dis. 2015; 5:1–19. [PubMed: 25588354]

Author Manuscript Author Manuscript Author Manuscript Author Manuscript

27. Goncalves A, et al. Protective Effect of a GLP-1 Analog on Ischemia-Reperfusion Induced Blood-Retinal Barrier Breakdown and Inflammation. Invest Ophthalmol Vis Sci. 2016; 57:2584–2592. [PubMed: 27163772]
28. Gullo F, et al. Plant Polyphenols and Exendin-4 Prevent Hyperactivity and TNF-alpha Release in LPS-Treated In vitro Neuron/Astrocyte/Microglial Networks. Front Neurosci. 2017; 11:500. [PubMed: 28932183]
29. Kim S, Moon M, Park S. Exendin-4 protects dopaminergic neurons by inhibition of microglial activation and matrix metalloproteinase-3 expression in an animal model of Parkinson's disease. J Endocrinol. 2009; 202:431–439. [PubMed: 19570816]
30. Lee CH, et al. Activation of Glucagon-Like Peptide-1 Receptor Promotes Neuroprotection in Experimental Autoimmune Encephalomyelitis by Reducing Neuroinflammatory Responses. Mol Neurobiol. 2017
31. Li Y, et al. Exendin-4 ameliorates motor neuron degeneration in cellular and animal models of amyotrophic lateral sclerosis. PLoS One. 2012; 7:e32008. [PubMed: 22384126]
32. Wu HY, Tang XQ, Liu H, Mao XF, Wang YX. Both classic Gs-cAMP/PKA/CREB and alternative Gs-cAMP/PKA/p38beta/CREB signal pathways mediate exenatide-stimulated expression of M2 microglial markers. J Neuroimmunol. 2017
33. Ventorp F, et al. Exendin-4 Treatment Improves LPS-Induced Depressive-Like Behavior Without Affecting Pro-Inflammatory Cytokines. J Parkinsons Dis. 2017; 7:263–273. [PubMed: 28387682]
34. Ji C, et al. A novel dual GLP-1 and GIP receptor agonist is neuroprotective in the MPTP mouse model of Parkinson's disease by increasing expression of BNDF. Brain Res. 2016; 1634:1–11. [PubMed: 26453833]
35. Salcedo I, Tweedie D, Li Y, Greig NH. Neuroprotective and neurotrophic actions of glucagon-like peptide-1: an emerging opportunity to treat neurodegenerative and cerebrovascular disorders. Br J Pharmacol. 2012; 166:1586–1599. [PubMed: 22519295]
36. Volpicelli-Daley LA, Luk KC, Lee VM. Addition of exogenous alpha-synuclein preformed fibrils to primary neuronal cultures to seed recruitment of endogenous alpha-synuclein to Lewy body and Lewy neurite-like aggregates. Nat Protoc. 2014; 9:2135–2146. [PubMed: 25122523]
37. Kim TH, et al. Mono-PEGylated dimeric exendin-4 as high receptor binding and long-acting conjugates for type 2 anti-diabetes therapeutics. Bioconjug Chem. 2011; 22:625–632. [PubMed: 21401109]
38. Kim TH, et al. Site-specific PEGylated Exendin-4 modified with a high molecular weight trimeric PEG reduces steric hindrance and increases type 2 antidiabetic therapeutic effects. Bioconjug Chem. 2012; 23:2214–2220. [PubMed: 23116483]
39. Karuppagounder SS, et al. The c-Abl inhibitor, nilotinib, protects dopaminergic neurons in a preclinical animal model of Parkinson's disease. Sci Rep. 2014; 4:4874. [PubMed: 24786396]
40. Lee Y, et al. Parthanatos mediates AIMP2-activated age-dependent dopaminergic neuronal loss. Nat Neurosci. 2013; 16:1392–1400. [PubMed: 23974709]
41. Kim S, et al. GBA1 deficiency negatively affects physiological alpha-synuclein tetramers and related multimers. Proceedings of the National Academy of Sciences of the United States of America. 2018; 115:798–803. [PubMed: 29311330]
42. Panicker N, et al. Fyn Kinase Regulates Microglial Neuroinflammatory Responses in Cell Culture and Animal Models of Parkinson's Disease. J Neurosci. 2015; 35:10058–10077. [PubMed: 26157004]
43. Andrabi SA, et al. Iduna protects the brain from glutamate excitotoxicity and stroke by interfering with poly(ADP-ribose) polymer-induced cell death. Nat Med. 2011; 17:692–699. [PubMed: 21602803]
44. Wang Y, et al. A nuclease that mediates cell death induced by DNA damage and poly(ADP-ribose) polymerase-1. Science. 2016; 354

Author Manuscript Author Manuscript Author Manuscript Author Manuscript

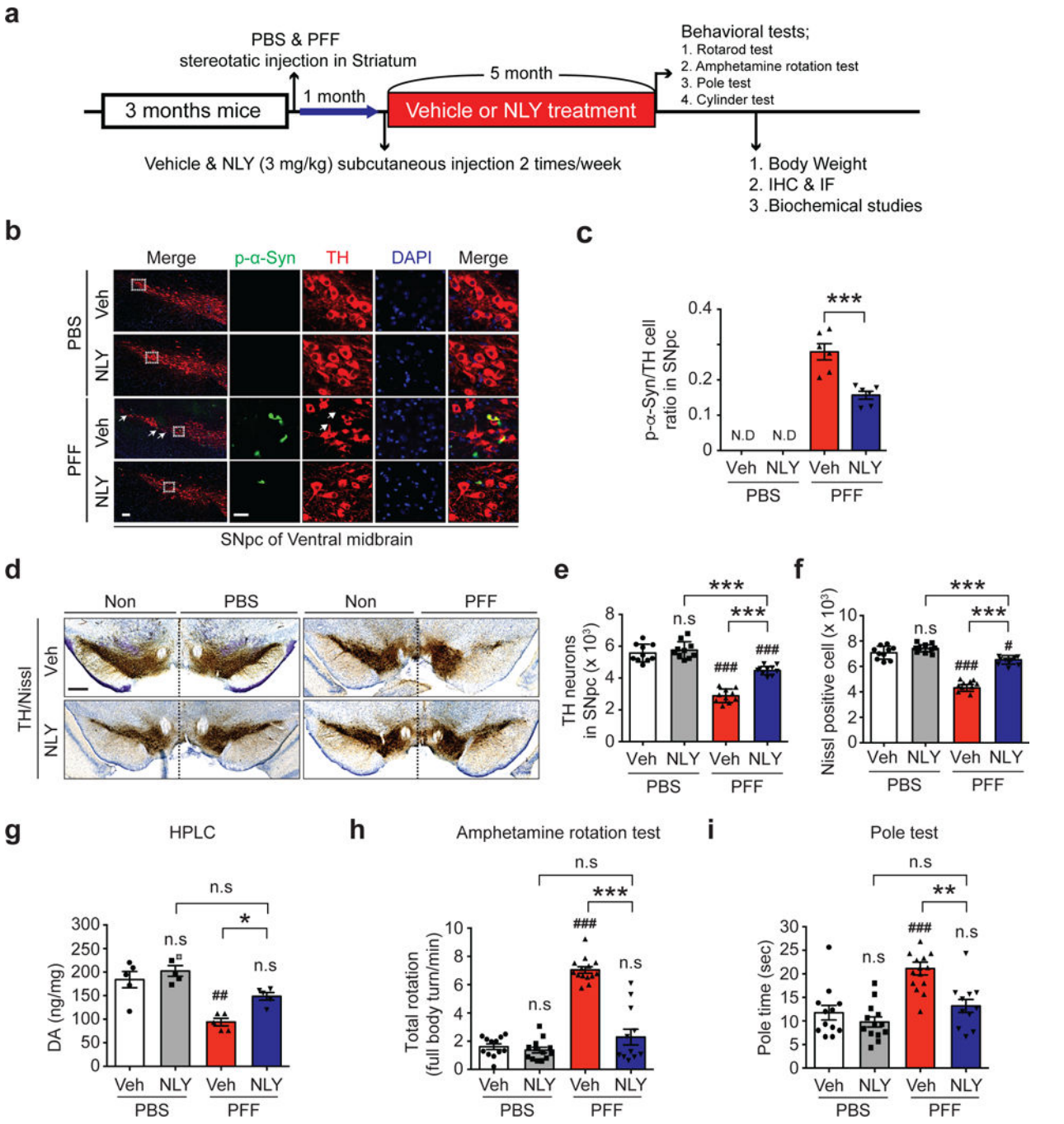


Figure 1.

α-syn PFF-induced PD like pathology is rescued by NLY01. (**a**) Schematic diagram of the α-syn PFF experimental design. (**b**) Representative double-immunostaining for p-α-syn^{ser129} (p-α-syn) (green) and TH (red) in the SNpc. White arrows point to DA neuron loss. Low power images were generated by the tile scan algorithm in the Zen software (n=6, biologically independent animals). Scale bar, 100 μm or 10 μm, respectively. (**c**) Percentage of TH neurons with p-α-syn^{ser129} positive inclusion in the SNpc region. Error bars represent the mean ± S.E.M. (n=6, biologically independent animals, p value = 0.0007). Unpaired

Author Manuscript Author Manuscript Author Manuscript Author Manuscript

two-tailed Student's test were used for statistical analysis. (**d**) Representative photomicrographs from coronal mesencephalon sections containing TH-positive neurons in the SNpc region (n=10, biologically independent animals). Scale bar, 500 μm. (**e**) Unbiased stereologic counts of TH and (**f**) Nissl-positive neurons in the SNpc region. Error bars represent the mean ± S.E.M. (n=10, biologically independent animals). (**g**) HPLC assessment of DA concentrations in the striatum of PBS and α-syn PFF stereotaxic injected mice that were treated with vehicle or NLY01. Error bars represent the mean ± S.E.M. (n=5, biologically independent animals). (**h-i**) Behavioral tests after PBS or α-syn PFF stereotaxic intrastriatal injection at six-months in vehicle or NLY01 treated mice. (**h**) Amphetamine rotation test, and (**i**) pole test. Error bars represent the mean ± S.E.M. (n=12 PBS with vehicle, n=13 PBS with NLY01, n=14 α-syn PFF with vehicle, and n=11 α-syn PFF with NLY01, biologically independent animals). Two-way ANOVA was used for statistical analysis followed by Tukey's multiple comparisons test. $^{\#}P < 0.05$, $^{\#\#}P < 0.01$, $^{\#\#\#}P < 0.001$ vs. PBS stereotaxic injected mice with vehicle; $^{*}P < 0.05$, $^{**}P < 0.01$, $^{***}P < 0.001$ vs. α-syn PFF stereotaxic injected mice with NLY01. Maximum time to climb down the pole was limited to 60 sec.

Author Manuscript Author Manuscript Author Manuscript Author Manuscript

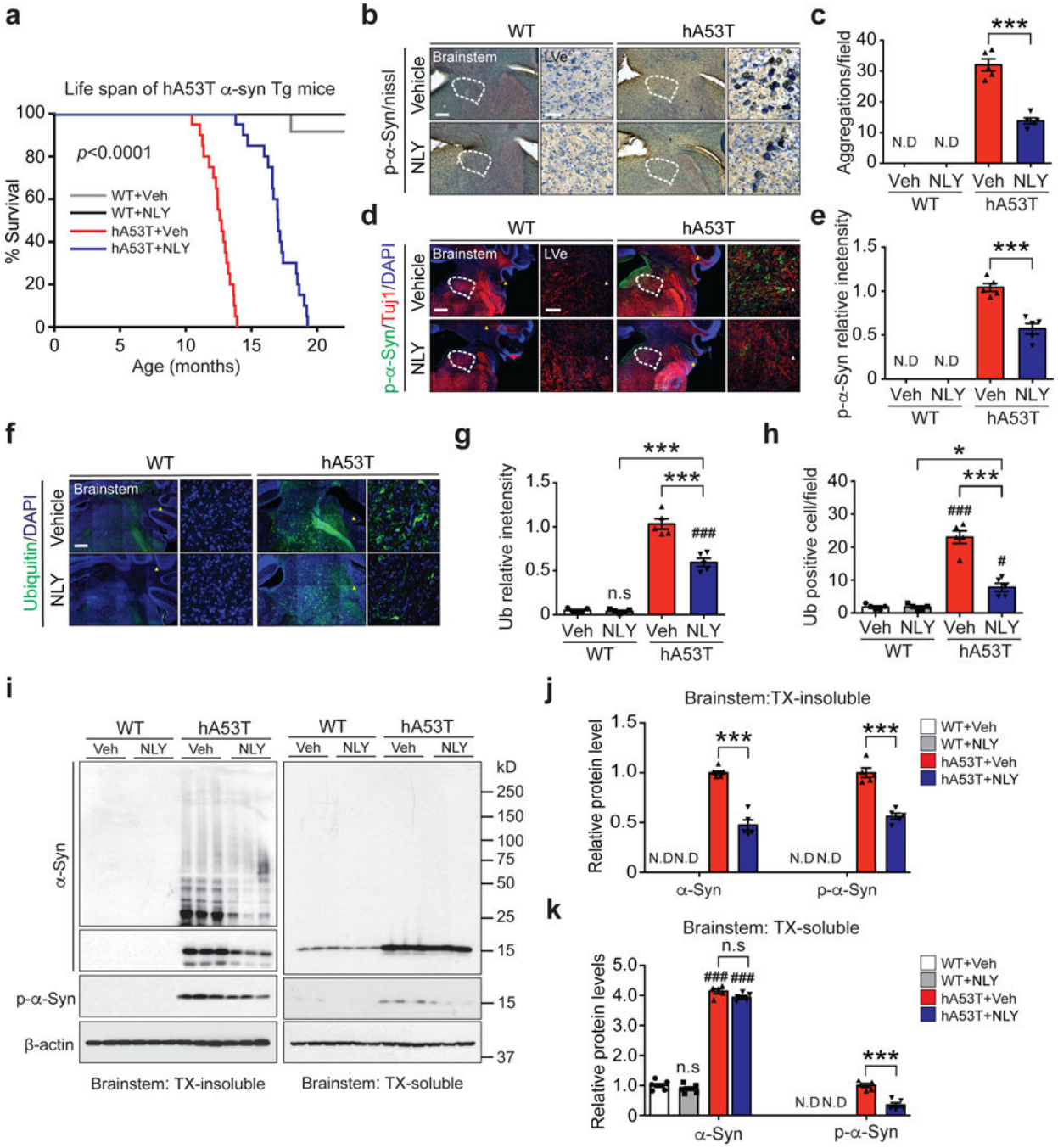


Figure 2.

NLY01 reduces the pathology in the hA53T α-syn transgenic mice. (**a**) Kaplan-Meier survival curves of littermate wild type (WT) and hA53T α-syn Tg mice treated with vehicle or NLY01 (3 mg/kg, n=20, biologically independent animals, p value < 0.0001). Statistical analysis for the survival curves were performed by Log-rank (Mantel-Cox) test. (**b, d**) Representative p-α-syn^{ser129} (p-α-syn) immunohistochemistry and immunostaining (red) in the lateral vestibular nucleus (LVe) of the brainstem (n=5, biologically independent animals). Low power images were generated by the tile scan algorithm in the Zen software. White

Author Manuscript Author Manuscript Author Manuscript Author Manuscript

arrow head (tile image line). Scale bar, 200 μm or 25 μm, respectively. (**c, e**) Quantification of LVe neurons containing p-α-syn^{ser129} positive-immunoreactivity inclusions. Error bars represent the mean ± S.E.M. (n=5, biologically independent animals, p value < 0.0001 for panel c and p value = 0.0003 for panel e). (**f**) Representative ubiquitin immunostaining (green) in the LVe (n=5, biologically independent animals). Scale bar, 200 μm or 25 μm. (**g, h**) Quantification of LVe neurons that are ubiquitin-positive. Error bars represent the mean ± S.E.M (n=5, biologically independent animals). (**i**) Representative immunoblots of α-syn, p-α-syn^{ser129} and β-actin in detergent (Triton-X100) insoluble fractions and detergent soluble fractions of the brainstem from ten-month-old WT and hA53T α-syn Tg mice treated with vehicle or NLY01 for four months (cropped blot images are shown, see Supplementary Fig. 21 for full immunoblots). (**j**) Quantification of α-syn monomer, aggregation, and p-α-syn^{ser129} protein levels in detergent insoluble fractions normalized to β-actin. Error bars represent the mean ± S.E.M. (n=5, biologically independent animals, p value < 0.0001). (**k**) Quantification of α-syn monomer and p-α-syn^{ser129} protein levels in detergent soluble fractions normalized to β-actin. Error bars represent the mean ± S.E.M. (n=5, biologically independent animals, α-syn, p value < 0.0001 and p-α-syn, p value = 0.0002). Unpaired two-tailed Student's test or two-way ANOVA was used for statistical analysis followed by Tukey's multiple comparisons test. $^{\#}P < 0.05$, $^{\#\#\#}P < 0.001$ vs. WT with vehicle; $^{*}P < 0.05$, $^{***}P < 0.001$ vs. hA53T α-syn Tg with NLY01.

Author Manuscript Author Manuscript Author Manuscript Author Manuscript

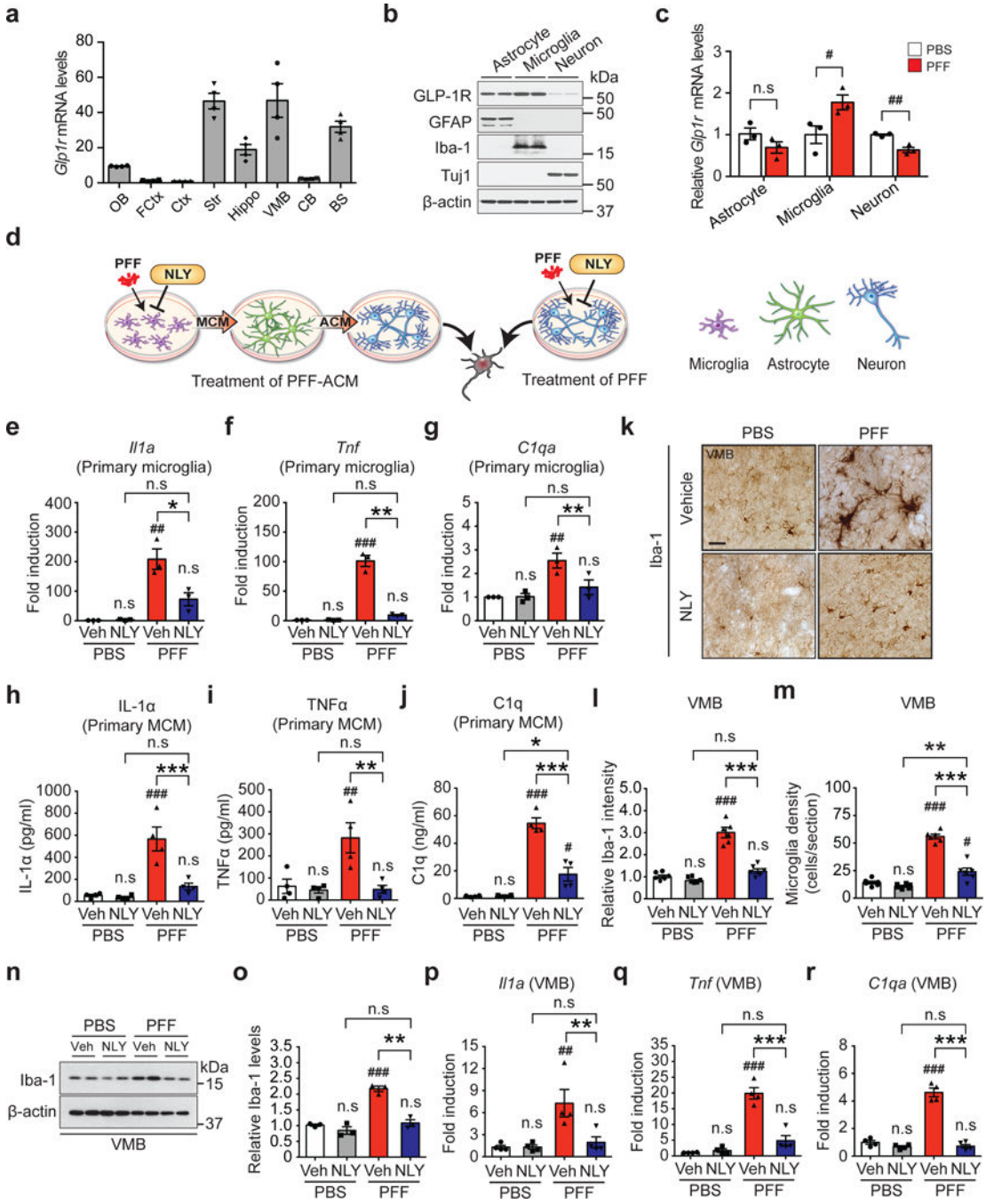


Figure 3.

Inhibition of α-syn PFF-induced microglial activation by NLY01. (**a**) *Glp1r* mRNA expression was analyzed in various mouse brain regions. OB, olfactory bulb; FCtx, frontal cortex; Ctx, cerebral cortex; Str, striatum; Hippo, hippocampus; VMB, ventral midbrain; CB, cerebellum; BS, brainstem. Error bars represent the mean ± S.E.M. (n=4, biologically independent animals). (**b**) Predominant expression of GLP-1R in astrocytes and microglia. Mouse primary astrocytes (GFAP), microglia (Iba-1) and cortical neurons (Tuj1) were subjected to western blotting using GLP-1R antibody (cropped blot images are shown, see

Author Manuscript Author Manuscript Author Manuscript Author Manuscript

Supplementary Fig. 21 for full immunoblots). β-actin is provided as a loading control (n=3, biologically independent primary cells). (**c**) The *Glp1r* mRNA expression in α-syn PFF-activated primary cultured astrocyte, microglia, and neurons was analyzed by real-time RT-PCR. Bars represent the mean ± S.E.M. (n=3, biologically independent primary cells, primary microglia, p value = 0.0475 and primary cortical neuron, p value = 0.0045). (**d**) Schematic diagram showing treatment of α-syn PFF-astrocyte conditioned medium (ACM) or direct treatment of α-syn PFF into neurons. (**e-g**) Quantitative PCR analysis of NLY01 (1 μM) pretreatment on α-syn PFF-induced (1 μg/ml) microglial activation markers, (**e**) *Il1a*, (**f**), *Tnfa*, and (**g**) *C1qa*. Bars represent the mean ± S.E.M. (n=3, biologically independent primary microglia). (**h-j**) Cytokine analysis of α-syn PFF-activated microglia-conditioned medium (MCM) 18 hrs after α-syn PFF treatment by ELISA. NLY01 (1 μM) pretreatment prevented the increase of (**h**) IL-1α, (**i**) TNFα, and (**j**) C1q. Bars represent the mean ± S.E.M. (n=4, biologically independent primary microglia-conditioned medium). (**k-m**) Inhibition of α-syn PFF-induced microglial activation by NLY01 *in vivo*. (**k**) Representative immunohistochemical images of Iba-1. Scale bar, 50 μm. (**l**) Intensity of Iba-1 positive signals in the SNpc, (**m**) Quantification of Iba-1 positive cell number in the SNpc. Bars represent the mean ± S.E.M. (n=6, biologically independent animals). (**n**) Representative immunoblots of Iba-1 and β-actin in the ventral midbrain of PBS and α-syn PFF injected mice treated with vehicle or NLY01 (cropped blot images are shown, see Supplementary Fig. 21 for full immunoblots). (**o**) Quantification of Iba-1 levels in ventral midbrain normalized to β-actin. Bars represent the mean ± S.E.M. (n=3, biologically independent animals). (**p-r**) Quantitative PCR for (**p**) *Il1a* (**q**) *Tnfa*, and (**r**) *C1qa* in the ventral midbrain of α-syn PFF injected mice. Bars represent the mean ± S.E.M. (n=4, biologically independent animals). Unpaired two-tailed Student's test or two-way ANOVA was used for statistical analysis followed by Tukey's multiple comparisons test. $^{\#}P < 0.05$, $^{\#\#}P < 0.01$, $^{\#\#\#}P < 0.001$ vs. PBS with vehicle; $^{*}P < 0.05$, $^{**}P < 0.01$, $^{***}P < 0.001$ vs. or α-syn PFF with NLY01.

Author Manuscript Author Manuscript Author Manuscript Author Manuscript

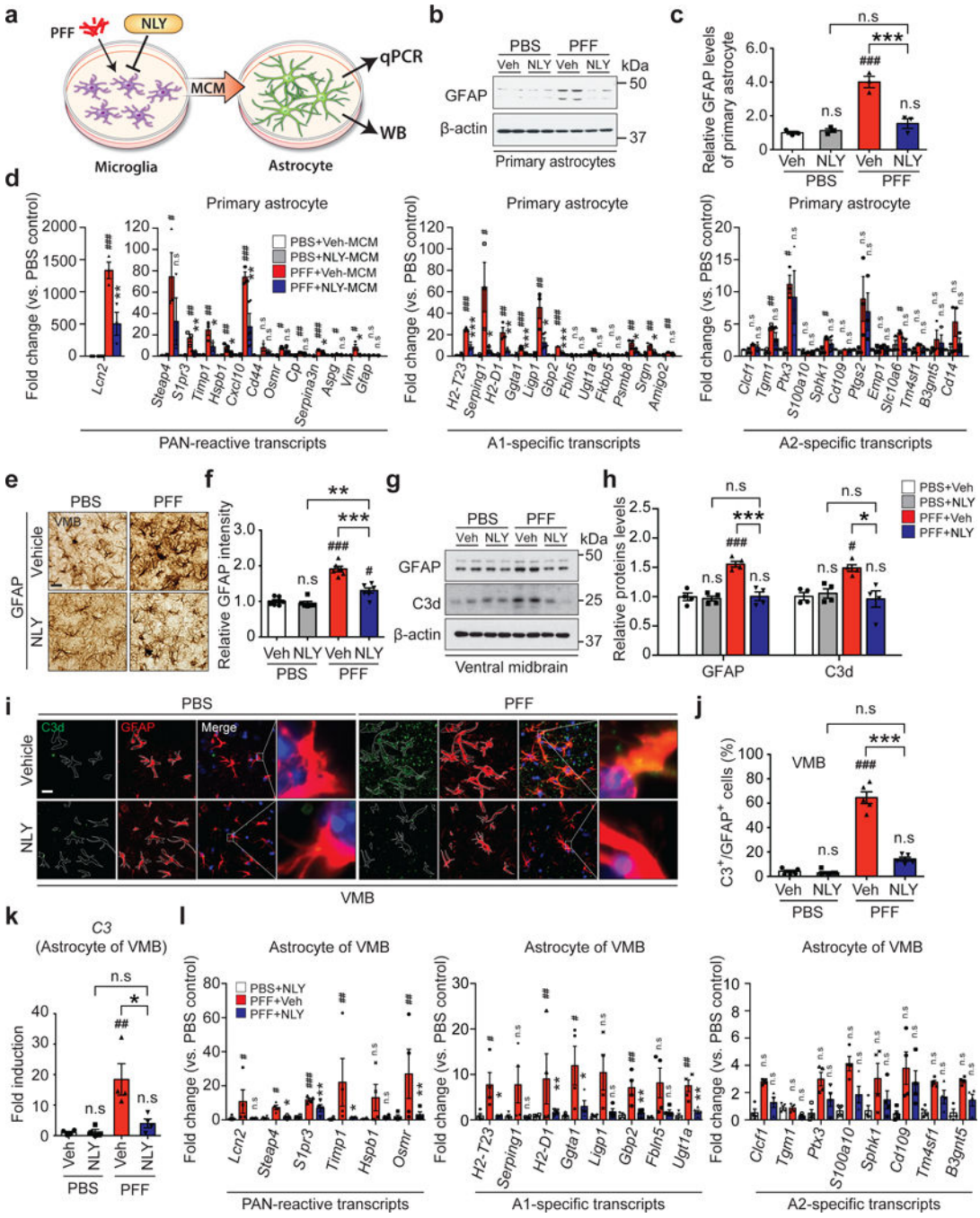


Figure 4.

Inhibition of α-syn PFF-induced A1 reactive astrocytes by NLY01. (**a**) Schematic diagram showing the collection of astrocyte samples after treatment with MCM of α-syn PFF with or without NLY01 treated microglia. (**b**) Representative immunoblots of GFAP in primary astrocytes treated with α-syn PFF-MCM with vehicle or NLY01 (1 μM) (cropped blot images are shown, see Supplementary Fig. 21 for full immunoblots). (**c**) Quantification of GFAP levels. Bars represent the mean ± S.E.M. (n=3, biologically independent primary astrocytes). (**d**) Inhibition of α-syn PFF-induced A1 reactive astrocytes by NLY01 in

Author Manuscript Author Manuscript Author Manuscript Author Manuscript

purified primary astrocytes. Bars represent the mean ± S.E.M. (n=3, biologically independent primary astrocytes). (**e**, **f**) Inhibition of α-syn PFF-induced A1 reactive astrocytes by NLY01 *in vivo*. (**e**) Representative images of immunohistochemistry and (**f**) quantification of GFAP. Bars represent the mean ± S.E.M. (n=6, biologically independent animals). Scale bar, 50 μm. (**g**) Representative immunoblots of GFAP in the ventral midbrain region (cropped blot images are shown, see Supplementary Fig. 21 for full immunoblots). (**h**) Quantification of GFAP levels. Bars represent the mean ± S.E.M (n=4, biologically independent animals). (**i**) Co-localization of C3d and GFAP as assessed by confocal microscopy. Scale bar, 10 μm. (**j**) Percentage of GFAP positive cells that are C3d positive in the SNpc region. Bars represent the mean ± S.E.M. (n=5, biologically independent animals). (**k**) Increase in expression of *C3* transcripts, which is prevented by NLY01 treatment in α-syn PFF injected mice. Bars represent the mean ± S.E.M. (n=4, biologically independent animals). (**l**) Quantitative PCR analysis of purified astrocytes from the ventral midbrain of α-syn PFF injected mice with vehicle or NLY01. Bars represent the mean ± S.E.M. (n=4, biologically independent animals). Two-way ANOVA was used for statistical analysis followed by Tukey's multiple comparisons test. $^{\#}P < 0.05$, $^{\#\#}P < 0.01$, $^{\#\#\#}P < 0.001$ vs. PBS with vehicle; $^{*}P < 0.05$, $^{**}P < 0.01$, $^{***}P < 0.001$ vs. α-syn PFF with NLY01 or with Veh. n.s, not significant.

Neurobiology of Aging 44 (2016) 159–172

Contents lists available at ScienceDirect

Neurobiology of Aging

journal homepage: www.elsevier.com/locate/neuaging

Intracerebral adeno-associated virus gene delivery of *apolipoprotein E2* markedly reduces brain amyloid pathology in Alzheimer's disease mouse models

Lingzhi Zhao [a,*], Andrew J. Gottesdiener [a], Mayur Parmar [a], Mingjie Li [b], Stephen M. Kaminsky [c], Maria J. Chiuchiolo [c], Dolan Sondhi [c], Patrick M. Sullivan [d], David M. Holtzman [e], Ronald G. Crystal [c], Steven M. Paul [a,*]

[a] *Appel Alzheimer's Disease Research Institute, Feil Family Brain and Mind Research Institute, Weill Cornell Medical College of Cornell University, New York, NY, USA*
[b] *Department of Neurology, Hope Center Viral Vector Core, Washington University, St. Louis, MO, USA*
[c] *Department of Genetic Medicine, Weill Cornell Medical College of Cornell University, New York, NY, USA*
[d] *Department of Medicine, Duke University Medical Center, Durham Veterans Health Administration Medical Center's Geriatric Research, Education and Clinical Center, Durham, NC, USA*
[e] *Department of Neurology, Hope Center for Neurological Disorders, Knight Alzheimer's Disease Research Center, Washington University in St. Louis, St. Louis, MO, USA*

ARTICLE INFO

Article history:
Received 5 March 2016
Received in revised form 22 April 2016
Accepted 23 April 2016
Available online 30 April 2016

Keywords:
Adeno-associated virus
Gene delivery
Apolipoprotein E2
Alzheimer's disease
Amyloid pathology

ABSTRACT

The common apolipoprotein E alleles (ε4, ε3, and ε2) are important genetic risk factors for late-onset Alzheimer's disease, with the ε4 allele increasing risk and reducing the age of onset and the ε2 allele decreasing risk and markedly delaying the age of onset. Preclinical and clinical studies have shown that apolipoprotein E (*APOE*) genotype also predicts the timing and amount of brain amyloid-β (Aβ) peptide deposition and amyloid burden (ε4 > ε3 > ε2). Using several administration protocols, we now report that direct intracerebral adeno-associated virus (AAV)–mediated delivery of *APOE2* markedly reduces brain soluble (including oligomeric) and insoluble Aβ levels as well as amyloid burden in 2 mouse models of brain amyloidosis whose pathology is dependent on either the expression of murine Apoe or more importantly on human APOE4. The efficacy of APOE2 to reduce brain Aβ burden in either model, however, was highly dependent on brain APOE2 levels and the amount of pre-existing Aβ and amyloid deposition. We further demonstrate that a widespread reduction of brain Aβ burden can be achieved through a single injection of vector via intrathalamic delivery of AAV expressing *APOE2* gene. Our results demonstrate that AAV gene delivery of *APOE2* using an AAV vector rescues the detrimental effects of *APOE4* on brain amyloid pathology and may represent a viable therapeutic approach for treating or preventing Alzheimer's disease especially if sufficient brain APOE2 levels can be achieved early in the course of the disease.

© 2016 Elsevier Inc. All rights reserved.

1. Introduction

Apolipoprotein E (APOE) is an important central nervous system (CNS) apolipoprotein intimately involved in the pathogenesis of the most common late-onset familial and sporadic forms of Alzheimer's disease (AD; Yu et al., 2014). In the general population, there are 3 common *APOE* alleles (ε4, ε3, and ε2) that encode the 3 APOE isoforms expressed primarily in the liver and brain. *APOE4* carriers have a markedly increased risk of developing AD (3–15 fold for heterozygotes and homozygotes, respectively, compared with *APOE3* homozygotes) and an earlier age-of-onset for developing the disease (approximately 5 years for each ε4 allele; Corder et al., 1993; Farrer et al., 1997; Lambert et al., 2013; Saunders et al., 1993; Strittmatter et al., 1993). The fact that 45% of AD patients carry at least 1 ε4 allele (compared with only 15% of age-matched healthy controls) makes *APOE4* by far the most common genetic risk factor for late-onset AD, the most common form of AD. By contrast, *APOE2* is a protective allele reducing AD risk by approximately 50% and markedly delaying the age-of-onset (Corder et al., 1994; Farrer et al., 1997; Suri et al., 2013; Talbot et al., 1994; Yu et al., 2014). How these

* Corresponding author at: Appel Alzheimer's Disease Research Institute, Feil Family Brain and Mind Research Institute, Weill Cornell Medical College of Cornell University, 413 East 69th Street, New York, NY 10021, USA. Tel.: 646 962 6323; fax: 646 962 0579.
E-mail addresses: liz2010@med.cornell.edu (L. Zhao), stp2015@med.cornell.edu (S.M. Paul).

0197-4580/$ – see front matter © 2016 Elsevier Inc. All rights reserved.
http://dx.doi.org/10.1016/j.neurobiolaging.2016.04.020

2 *APOE* alleles (whose encoded proteins differ by only 2 amino acids) so profoundly alter one's risk of developing AD is one of the most important questions to be answered in contemporary AD research. Several mechanisms have been proposed to explain the effects of *APOE* on AD pathogenesis (Bales et al., 1997, 2009; Holtzman et al., 2012; Kim et al., 2009; Liu et al., 2013; Yu et al., 2014). One potential mechanism appears to involve the differential effects of the APOE isoforms on the accumulation of amyloid β (Aβ)-peptides in the brain in the form of both diffuse and amyloid (senile) plaques (Bales et al., 2009; Holtzman et al., 2012; Kim et al., 2009; Liu et al., 2013; Yu et al., 2014), which are neuropathologic hallmarks of the disease (Hardy and Selkoe, 2002). Studies in both humans and transgenic mice have shown that brain Aβ levels and amyloid plaque burden develop in an APOE isoform-dependent (E4 > E3 > E2) manner (Bales et al., 2009; Castellano et al., 2011; Fagan et al., 2002; Holtzman et al., 2000, 2012; Kim et al., 2009; Liu et al., 2013; Morris et al., 2010; Rebeck et al., 1993; Schmechel et al., 1993), suggesting that APOE isoforms play an important role in determining brain amyloid burden.

The major physiological differences between APOE3, the most common isoform, and APOE2 and APOE4, are due to differences in amino acids at 1 of 2 positions, residues 112 (APOE4) and 158 (APOE2), which are cysteine-arginine interchanges (Hatters et al., 2006). Differences in these 2 amino acids result in differences in protein structure, and the corresponding binding affinities of these APOE isoforms to lipoproteins, lipoprotein receptors, and in regulating Aβ aggregation, degradation, efflux, and phagocytosis (Castellano et al., 2011; Deane et al., 2008; Hashimoto et al., 2012; Hatters et al., 2006; Holtzman et al., 2012; Li et al., 2012; Manelli et al., 2004; Walker et al., 2000; Yu et al., 2014; Zhao et al., 2009). The latter may underlie the reported APOE-isoform–dependent effects on Aβ accumulation observed in both AD patients and animal models of amyloidosis. In addition to these important qualitative differences between the APOE isoforms, recent studies suggest that quantitative differences in their relative levels of expression may also play a role in determining the extent of Aβ accumulation in the brain (Bales et al., 2009; Kim et al., 2011; Sullivan et al., 2011). Earlier work from our laboratory using amyloid precursor protein (APP) transgenic mice demonstrated that a deficiency of murine Apoe (which is more amyloidogenic than human APOE4) is associated with reduced amyloid pathogenesis (Bales et al., 1997), and more recent studies have shown that a decrease in human APOE levels (especially APOE4 and APOE3) is also associated with reduced brain amyloid burden (Kim et al., 2011). In 2005, Dodart et al. (Dodart et al., 2005) reported a bidirectional effect of APOE4 (to increase) and APOE2 (to decrease) brain Aβ/amyloid burden using lentivirus gene delivery of *APOE4* and *APOE2* directly into the hippocampus of mice that overexpress a mutant *APP*. Recently, Hudry et al. (Hudry et al., 2013) extended this finding using an adeno-associated viral vector serotype 4 (AAV4) to deliver either *APOE2* or *APOE4* into the lateral ventricle and cerebrospinal fluid of mice also overexpressing a mutant *APP* transgene. Both these gene delivery studies, however, were carried out in transgenic mice on a background of murine Apoe which differs from the 3 human APOE isoforms. Moreover, although *APOE4* carriers have dramatically increased accumulation and deposition of brain Aβ/amyloid as they age and ≥45% of AD patients are ε4 carriers, there have been no reports examining whether *APOE2* gene delivery impacts APOE4-dependent amyloid pathology. In this study, we assessed the effects of various levels of APOE2 expression, routes of delivery, and the extent of pre-existing amyloid pathology on AAV-APOE2-mediated alteration of amyloid pathology using a widely used mouse model of brain amyloidosis (PDAPP mice) as well as a mouse model that develops APOE4-dependent amyloid deposition (APP.PS1/TRE4 mice; Kim et al., 2011). Our studies show that direct intracerebral gene delivery of *APOE2* via an AAV vector significantly reduces brain Aβ and amyloid deposition in these transgenic mouse models of AD and rescues the detrimental effects of both *APOE4* as well as murine Apoe on brain amyloid pathology. We further show that the "efficacy" of AAV-APOE2 gene delivery to decrease amyloid pathology in these mouse models strongly depends on the level of APOE2 expression and pre-existing amyloid pathology at the time of vector administration, rather than the cellular source of APOE2 or the route of administration. We also show that intrathalamic delivery of *APOE2* using an AAV vector results in widespread brain distribution of APOE2 and a broad reduction of brain Aβ burden following a single injection in APP.PS1/TRE4 mice. Our study provides direct evidence for a qualitative "protective" effect of APOE2 on brain amyloid burden and shows that raising (rather than reducing) brain APOE2 to a sufficient level effectively reduces amyloid pathology in mice where the latter is primarily due to APOE4 expression. Thus, gene delivery of *APOE2* may represent a promising therapeutic strategy especially if used early in the course of the disease.

2. Materials and methods

2.1. Animals and reagents

Three-month-old *Apoe* knockout (EKO) mice and *APOE2* targeted replacement (TRE2) mice were obtained from Taconic Biosciences, Inc (Hudson, NY). PDAPP mice at age 9–10 months were a generous gift of Eli Lilly and Company (Indianapolis, IN). The APP.PS1-21/TRE4 mice (Kim et al., 2011) were generated by crossing APP.PS1-21 mice (a gift of Dr Mathias Jucker at the University of Tübingen, Tübingen, Germany) with *APOE4* knock-in mice (a generous gift of Dr Patrick Sullivan at Duke University, Durham, NC). The mouse colony was maintained and expanded at Weill Cornell Medical College (New York, NY). All animal studies were conducted in compliance with the Weill Cornell Medical College Animal Care and Use Committee and National Institutes of Health guidelines. The AAV9-CAG-APOE2 vector (AAV9-APOE2), the adeno-associated viral vector serotype 9 expressing the APOE2 behind the chicken β actin promoter, and the control vector AAV9-CAG-GFP (AAV9-GFP) were prepared by the Hope Center Viral Vector Core at Washington University (St Louis, MO). The AAVrh.10-CAG-APOE2 vector (AAVrh.10-APOE2), the rhesus adeno-associated viral vector serotype 10 expressing the APOE2 transgene behind the chicken β actin promoter, and the control vector AAVrh.10-CAG-mCherry (AAVrh.10-mCherry) were prepared by the Belfer Gene Therapy Core Facility at Weill Cornell Medical College. Anti-HA was purchased from Roche Applied Science (Indianapolis, IN); anti-GFAP and anti-NeuN antibodies were purchased from Millipore (Billerica, MA); the anti-APOE antibody was purchased from Abcam (Cambridge, MA), and 21F12, 2G3, and 3D6 Aβ antibodies were generous gifts of Eli Lilly and Company. Fluoro-Jade B kits were obtained from Millipore and used as directed. Other reagents were purchased from Sigma-Aldrich (St. Louis, MO) and Thermo Scientific (Rockford, IL).

2.2. AAV vector production

The AAVrh.10 and AAV9 vectors were produced and purified as described previously (Sondhi et al., 2007, 2012; Zolotukhin et al., 2002). Briefly, the vectors were produced by cotransfection of HEK293T cells with an expression cassette plasmid and adenoviral helper plasmids. The packaging cell line, HEK293T, was maintained in Dulbecco's modified Eagles medium, supplemented with 5% fetal bovine serum, 100 U/mL penicillin, 100 μg/mL streptomycin, and maintained at 37 °C with 5% CO_2. The cells were plated at 30%–40%

confluence in CellSTACKS (Corning, Tewksbury, MA) for 24 hours (or when at 70%–80% confluence) followed by transfection with plasmids using the PEIpro procedure. The cells were incubated at 37 °C for 3 days before harvesting and lysed by 5 freeze/thaw cycles. The resulting cell lysate was treated with 50 U/mL of Benzonase at 37 °C for 30 minutes. For AAVrh.10 vectors, the cell lysate was purified by iodixanol density gradient followed by Q-HP ion-exchange chromatography. For AAV9 vectors, the cell lysate was precipitated in PEG (final concentration of PEG: 8%) overnight. After centrifugation, the supernatant was discarded and the pellet was resuspended in 15 mL lysis buffer (150 mM NaCl, 50 mM Tris-HCl, pH 8.5). The sample was purified by centrifugation through 1.37 g/mL CsCl in a 38.5 mL polyallomer tube using an SW28 rotor at 24,000 rpm (182,000*g*), at 20 °C for 24 hours. A 21-gauge needle (Hamilton, Reno, NV) was inserted through the bottom side of the centrifuge tube and 1 mL fractions were collected. Vector-containing fractions were determined by dot blot with a ^{32}P-labeled probe containing the sequence of the vector constructs. The positive fractions were subsequently pooled and diluted with 1.37 g/mL CsCl, and the samples were loaded into a 13.5 mL Quick-Seal tube and centrifuged in an ultracentrifuge (Beckman LE-80K; Beckman Coulter, Fullerton, CA) 90 Ti rotor, at 67,000 rpm (384,000*g*), 20 °C for 16–20 hours. Fractions (0.5 mL) were collected, and the positive fractions were pooled. The purified AAVrh.10 or AAV9 vectors were concentrated in phosphate-buffered saline (PBS). Vector genome titer was determined by TaqMan quantitative polymerase chain reaction. The purified vectors were sterile filtered; tested 14 days for growth on medium supporting the growth of aerobic bacteria, anaerobic bacteria, or fungi; tested for endotoxin; and demonstrated to be mycoplasma free.

2.3. Stereotaxic injections into the hippocampus or thalamus of adult mice

Intracerebral injection of AAV vectors was carried out by stereotaxic surgery as previously described with modifications (Dodart et al., 2005). Briefly, under sterile conditions, mice were anesthetized with isoflurane and secured on a stereotaxic frame (David Kopf Instruments, Tujunga, CA). An incision was made over the skull, the periosteum removed, and burr holes of the size of the injection needle were subsequently drilled using a high-speed drill. The AAV preparation (2 μL, 1.0×10^{10} vg or at the indicated dose) was bilaterally injected into the targeted brain regions using a 33-gauge needle (Hamilton) and a syringe pump (KD Scientific, Holliston, MA) at a rate of 0.2 μL/min. Stereotactic coordinates used for injections were as follows: (1) hippocampus: −1.7 mm anteroposterior from bregma; ±1.2 mm mediolateral from bregma, and −1.7 mm dorsoventral below the dura; (2) thalamus: −2.0 mm anteroposterior, ±1.2 mm mediolateral, and −1.7 mm dorsoventral. After each injection, the needle was left in place for 5 minutes to minimize backflow and then slowly withdrawn. Animals were individually housed and monitored until they regained full consciousness. Eight weeks (or at the indicated time) after injection, the mice were deeply anesthetized with Avertin and transcardially perfused with 0.3% heparinized saline (2500 IU/L). Brains were rapidly collected, and each brain was divided along the sagittal plane with 1 hemibrain processed for histologic and immunohistochemistry (IHC) analyses, and the other hemibrain microdissected into the hippocampus, thalamus, and cortex then rapidly frozen on dry ice and stored at −80 °C for biochemical analyses.

2.4. Tissue preparation and immunohistochemistry

Brains were post-fixed in 4% paraformaldehyde for ≥48 hours, transferred to 30% sucrose for ≥48 hours before freezing, and sectioned using a CM3050-S cryostat (Leica, Buffalo Grove, IL). Serial coronal sections were prepared at 50 μm intervals from the rostral anterior commissure to the caudal hippocampus and kept in a cryoprotectant at −20 °C. IHC analyses were performed as described previously (Bales et al., 1997, 2009; Holtzman et al., 2000). Briefly, free-floating sections were washed and incubated with primary antibodies overnight at 4 °C. Immunoreactivity (IR) was visualized using Alexa Fluor 488 or 594-conjugated secondary antibodies (1:200; Invitrogen, Norwalk, CT) or the Vectastain ABC Elite kit (Vector, Burlingame, CA) and 3, 3-diaminobenzidine solution. The specificity of the primary antibodies staining was verified by the lack of IR signal when the primary antibodies were omitted. The specificity of anti-APOE staining was also verified by the lack of staining in brain sections of EKO mice. Thioflavine-S staining was performed as previously described (Bales et al., 1997, 2009; Holtzman et al., 2000). Fixed brain sections were briefly incubated with 0.1% freshly made thioflavine-S solution (in 50% ethanol) for 8 minutes and then cleared with 80% ethanol for 1 minute followed by washing with H_2O 3 times for 1 minute each before being coverslipped with proper mounting media. Images were taken using an epifluorescence microscope (Nikon H550L; Nikon Instrument Inc, Melville, NY).

2.5. Quantification of amyloid/Aβ burden

Quantification of amyloid/Aβ burden was performed as described previously (Bales et al., 1997, 2009; Holtzman et al., 2000). Briefly, 4 brain sections per mouse, each separated by 300 μm, were selected for quantification. These sections correspond roughly to sections at Bregma −1.4, −1.7, −2.0, and −2.3 mm in the mouse brain atlas (The Mouse Brain In Stereotaxic Coordinates. Franklin and Paxinos, 2007). Quantification of brain Aβ burden was completed after immunostaining with the biotinylated 3D6 antibody as described previously. Images were thresholded to highlight plaques and then analyzed by the "Analyze Particles" function of the ImageJ software (National Institutes of Health, Bethesda, MD). After thresholding, identified objects were individually inspected to confirm that each object quantified was a plaque. The percentage of surface area covered by Aβ IR (Aβ burden) or thioflavine-S (amyloid burden) was determined for specific areas of the hippocampal formation comprising the stratum oriens, pyramidal layer, stratum radiatum, and the dentate gyrus. Aβ or thioflavine-S burden was then represented as a percentage of the total area quantified. An average of 4 tissue sections were used to quantify the plaque load for each mouse. All analyses were performed in a blinded manner, with the examiner unaware of the treatment condition of any animal.

2.6. Amyloid-β enzyme-linked immunosorbent assay

Aβ levels were assayed in brain homogenates from mice using a sandwich enzyme-linked immunosorbent assay (ELISA) as described previously (Bales et al., 2009; Johnson-Wood et al., 1997). Briefly, brain tissue was homogenated serially with RIPA and a 5.5-M guanidine buffer containing a cocktail of protease inhibitors (1:1000; Roche). Aβ measured after the RIPA extraction represented the soluble pool of Aβ, whereas Aβ measured after guanidine extraction represented the insoluble pool. The homogenates were diluted with a cold sample dilution buffer (1% bovine serum albumin in phosphate buffered saline-0.05% tween 20 [PBST]) before measurement of Aβ1–40 or Aβ1–42. Guanidine-solubilized samples were diluted with a cold sample dilution buffer to a final concentration of 0.5 M GuHCl or less. Samples were loaded onto plates coated with an antibody that specifically recognizes the C-terminal domain of Aβ1–42 (21F12), or Aβ1–40 (2G3) as the capture antibody, and biotinylated 3D6 was used for detection. The IR signal after incubation with horseradish peroxidase (HRP)–conjugated streptavidin

(Research Diagnostics, Flanders, NJ) was developed with a TMB substrate (Thermo Scientific) and read on a Synergy H1 Hybrid plate reader (BioTek, Winooski, VT). Levels of Aβ were calculated using a standard curve generated with recombinant human Aβ (American Peptide Company, Sunnyvale, CA). Levels of Aβ in brain homogenates were determined in triplicate, normalized to protein content, and expressed as the amount of Aβ per milligram of protein. Aβ oligomers were quantified with the 3D6/biotin-3D6 sandwich ELISA (Immuno-Biological Laboratories), in which the same N-terminal (residues 1–16) antibodies were used for both capture and detection.

2.7. Apolipoprotein E enzyme-linked immunosorbent assay

APOE levels were measured in brains using a sandwich ELISA as described previously (Bales et al., 2009). Briefly, tissue homogenates were diluted in sample dilution buffer (PBST containing 0.4% glycine). Samples were loaded into 96-well plates coated with an anti-APOE antibody (1:2000; Millipore). After overnight incubation at 4 °C, a biotinylated anti-APOE antibody (1:10,000; Meridian Life Science, Memphis, TN) was used for detection. The IR signal after incubation with HRP–conjugated streptavidin (Research Diagnostics) was developed with a TMB substrate (Thermo Scientific) and read on a Synergy H1 Hybrid plate reader (BioTek). Levels of APOE were calculated using a standard curve generated with recombinant human APOE (Meridian Life Science). Levels of APOE in brain homogenates were determined in triplicate, normalized to protein content, and expressed as the amount of APOE per milligram of protein.

2.8. Electrophoresis and Western blotting

Examination of APOE or other protein levels in mouse brain tissue homogenates was carried out by Western blot as described previously (DeMattos et al., 2001). The total protein concentration in tissue homogenates was determined using a BCA protein assay kit (Thermo Scientific). For sodium dodecyl sulfate polyacrylamide gel electrophoresis, equivalent amounts of protein (25 μg) samples were mixed with loading dye containing 2% SDS and 1% β-mercaptoethanol, incubated for 10 minutes at 90 °C, and resolved on 10% Tris-glycine polyacrylamide gels. For nondenaturing PAGE, equivalent amounts of protein (25 μg) samples were mixed with nondenaturing loading dye to a final concentration of 0.04% bromophenol blue, 4.0% glycerol, and 100 mM Tris (pH 6.8) and resolved on 4%–12% nondenaturing Tris-glycine polyacrylamide gels (Invitrogen). Proteins were transferred onto polyvinylidene difluoride (Millipore) membranes at 100 V. After blocking with Superblock (Thermo Scientific) for 1 hour at room temperature, membranes were probed with primary antibodies overnight at 4 °C followed by species-specific HRP–conjugated secondary antibodies (1:8000; Invitrogen) for 1 hour at room temperature. Enhanced chemiluminescence (GE Healthcare Biosciences, Pittsburgh, PA) was used to identify the bands. Protein molecular weights on denaturing gels were determined by comparison with the kaleidoscope molecular weight marker standard (Bio-Rad, Hercules, CA). Particle diameters on native gels were determined by comparison with a native high molecular weight marker standard (GE Healthcare Biosciences). Signal quantification was done using densitometry analysis of the scanned, autoradiograms with Image Lab software (Bio-Rad). Loading was normalized by stripping blots and reprobing with a β-actin antibody (Sigma-Aldrich).

2.9. Statistical analyses

Quantitative data are presented as mean ± standard deviation. The differences between an AAV-APOE2-treated group and a control group were analyzed by a 2-tailed Student *t* test using GraphPad Prism software (GraphPad Software, La Jolla, CA). When comparisons were being made between ≥3 conditions, 1-way analysis of variance followed by *post hoc* Newman-Keuls analysis were used to identify specific differences between groups. Significance level was set as $p < 0.05$.

3. Results

3.1. Intrahippocampal delivery of AAVrh.10-APOE2 results in abundant and persistent expression of APOE2 in the hippocampus of Apoe knockout (EKO) mice

We first investigated whether human APOE2 could be efficiently expressed in the hippocampus after intrahippocampal delivery of AAVrh.10-APOE2 using mice lacking *Apoe* (*Apoe* knockout mice, EKO mice). AAVrh.10-APOE2 (1.0×10^{10} vg) was bilaterally administered into the hippocampus of EKO mice. APOE2 expression was examined by IHC and biochemically 8 weeks after administration. As shown in Fig. 1A, intrahippocampal administration of AAVrh.10-APOE2 results in abundant APOE2 expression in the hippocampus of EKO mice and the APOE IR was mainly restricted to the hippocampus (Fig. 1A). In the CNS, APOE is a secreted protein and expressed mainly in astrocytes (Boyles et al., 1985). Double staining of brain sections with antibodies recognizing APOE and cell-specific markers demonstrated that the APOE2 IR was observed in ~29% astrocytes and ~67% of neurons in the hippocampus of EKO mice administered AAVrh.10-APOE2 (Fig. 1B and C). No notable microglial APOE2 expression was observed (data not shown). APOE2 levels in the hippocampus of EKO mice administered AAVrh.10-APOE2 for different treatment periods were measured using a human APOE-specific ELISA and compared with those in age-matched targeted replacement APOE2 (TRE2) mice (Sullivan et al., 1997). TRE2 mice are mice that the endogenous murine *Apoe* genes are replaced with the human APOE2 allele and, therefore, produce natural levels and forms of human APOE2. As shown in Fig. 1D, administration of AAVrh.10-APOE2 (1.0×10^{10} vg) results in 5–6 times higher levels of APOE2 in the hippocampus of EKO mice than those observed in TRE2 mice. These expression levels of APOE2 are sustained for up to 6 months (Fig. 1D).

It has been previously shown that lipidated APOE is more stable than nonlipidated APOE and that APOE lipidation is necessary for receptor binding and functional activity (Fan et al., 2009). To examine whether the APOE2 expressed by an AAV vector is lipidated APOE2, nondenaturing gel electrophoresis was used to assess the PBS extracts of the hippocampus from EKO mice injected with AAVrh.10-APOE2 or age-matched TRE2 mice. As shown in Fig. 1E, APOE2 produced from intracerebral administration of AAVrh.10-APOE2 migrated in the same manner as APOE2 isolated from hippocampal extracts of TRE2 mice. The predominant APOE2 species were identical to those present in the extracts from TRE2 mice (8.1–17.0 nm) and similar to those previously reported for lipidated APOE (DeMattos et al., 2001). This result suggests that despite an additional nonastrocytic cellular source of APOE, APOE2 expressed using our AAVrh.10-APOE2 vector is qualitatively very similar to the naturally produced form.

3.2. Gene delivery of APOE2 reduces murine Apoe-dependent amyloid pathology in the PDAPP mouse model of AD

We next examined the ability of APOE2 expressed via AAVrh.10-APOE2 vectors to alter brain amyloid pathology using the PDAPP mouse model of AD. The latter is a well-characterized mouse model of brain amyloidosis that overexpresses a human APP mutation (V717F) under the control of the platelet-derived growth factor

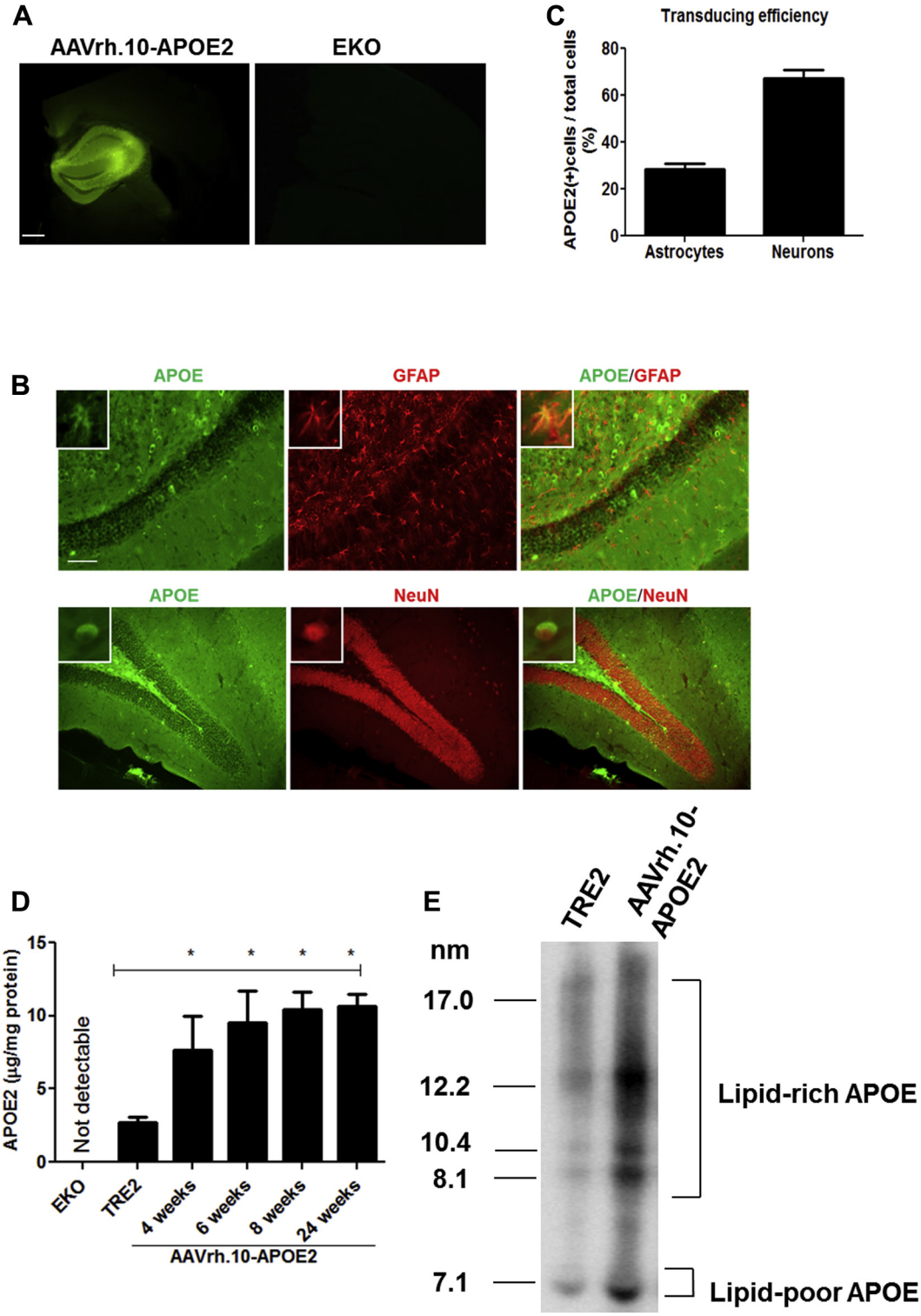


Fig. 1. APOE2 expression in the hippocampus of *Apoe* knockout (EKO) mice intrahippocampally administered with AAVrh.10-APOE2. Representative immunostaining of APOE in the hippocampus of EKO mice injected intrahippocampally with 1.0×10^{10} viral genomes (vg) of AAVrh.10-APOE2 vectors. Mice were killed 8 wk after injection. (A) APOE2 expression was detected by immunostaining with an APOE antibody (left). Brain tissues from naive EKO mice were processed in parallel as a control (right). Scale bar = 200 μm. (B) Representative double immunostaining of APOE and GFAP (an astrocytic marker) or APOE and NeuN (a neuronal marker) in the hippocampus of EKO mice injected intrahippocampally with AAVrh.10-APOE2. Brain sections were double-stained with an anti-APOE (green) and an anti-GFAP (red) antibody or an anti-APOE (green) and anti-NeuN antibody (red). Scale bar = 100 μm. (C) The percentage of cells positive for GFAP and APOE or NeuN and APOE over the total cell numbers in dentate gyrus were calculated. (D) Hippocampal APOE2 levels in the hippocampus of EKO mice injected intrahippocampally with 1.0×10^{10} vg of AAVrh.10-APOE2. Mice were killed 8 weeks after injection or at the indicated time. APOE levels were measured by ELISA. Brain tissue from the *APOE2* targeted replacement (TRE2) mice or EKO mice was processed and the levels were measured in parallel as controls. n = 3–5 animals per group. Data presented as mean ± SD. $^*p < 0.05$ versus the TRE2 group using 1-way ANOVA followed by *post hoc* Newman-Keuls analysis. (E) Representative data of nondenaturing gel electrophoresis of hippocampal extracts from EKO mice injected intrahippocampally with 1.0×10^{10} vg of AAVrh.10-APOE2. Brain tissues were extracted with PBS followed by size-fractionation using native gel electrophoresis (3%–12%). Brain tissue from TRE2 mice was processed in parallel as a control. APOE was visualized using Western analysis. n = 3–5 animals per group. Data presented as mean ± SD. Abbreviations: AAV, adeno-associated virus; ANOVA, analysis of variance; APOE, apolipoprotein E; ELISA, enzyme-linked immunosorbent assay; SD, standard deviation. (For interpretation of the references to color in this figure legend, the reader is referred to the web version of this article.)

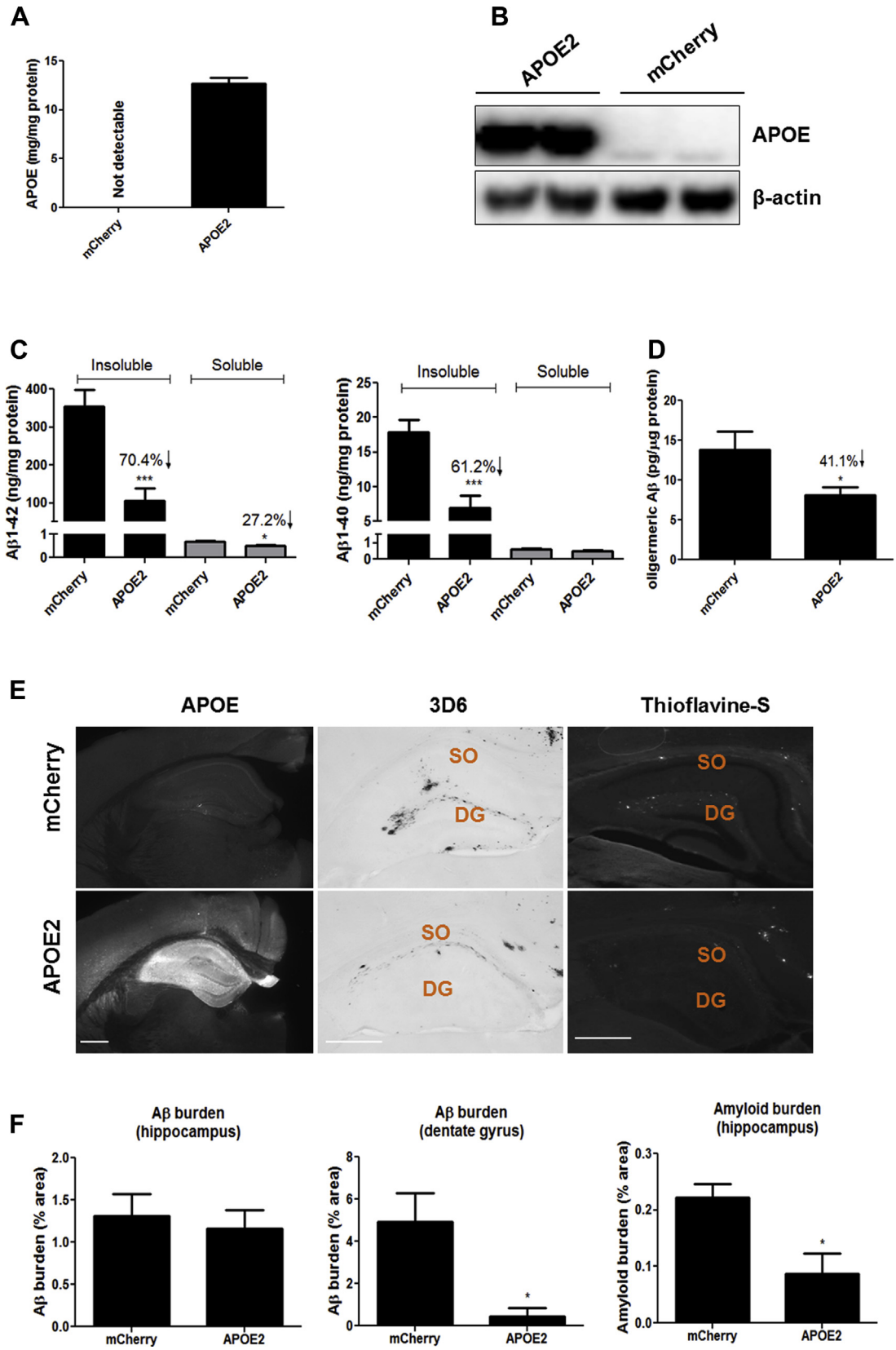


Fig. 2. Effects of intrahippocampal delivery of AAVrh.10-APOE2 on Aβ levels in the hippocampus of brain amyloidosis mouse models whose pathology are dependent on the expression of murine *Apoe* (PDAPP mice). AAVrh.10-APOE2 (APOE2) or AAVrh.10-mCherry (mCherry; 1.0×10^{10} vg) was injected bilaterally into the hippocampus of 9-month-old PDAPP mice. Eight weeks after injection, the mice were killed, and the hippocampus of the left hemisphere was dissected, homogenized, and sequentially extracted with RIPA (representing soluble Aβ) and 5.5 M guanidine (representing insoluble Aβ). APOE, Aβ1–42, and Aβ1–40 levels were determined by ELISA. The right brain hemispheres from each mouse were post-fixed in 4% paraformaldehyde (PFA) for immunohistochemistry (IHC) and histologic analyses. (A) APOE levels in the hippocampus of PDAPP mice.

promoter. PDAPP mice develop abundant age-dependent Aβ and amyloid deposition in the hippocampus and cerebral cortex. At age 9 months, there are abundant Aβ and measurable amyloid plaques in the hippocampus of PDAPP mice (Games et al., 1995). AAVrh.10-APOE2 (1.0×10^{10} vg) was bilaterally injected into the hippocampus of 9-month-old PDAPP mice. AAVrh.10-mCherry was injected in parallel as a control. Hippocampal APOE, Aβ1–42 (the most pathogenic Aβ species in AD brain), or Aβ1–40 (a much less pathogenic Aβ species than Aβ1–42 in AD brain and a most common form of Aβ species in normal human individuals) levels in the left brain hemisphere were quantified by specific ELISAs 8 weeks after injection. As shown in Fig. 2A, APOE levels in the hippocampus of PDAPP mice treated with AAVrh.10-APOE2 are 5–6 times higher than those measured in TRE2 mice, which is consistent with the data from the EKO mice described previously (Fig. 1D). The expression of APOE2 after administration of AAVrh.10-APOE2 was further verified by Western blots (Fig. 2B). Overexpression of APOE2 using the AAVrh.10-APOE2 vector resulted in a marked decrease in insoluble Aβ1–42 (~70.4% reduction. $p < 0.001$ vs. the AAVrh.10-mCherry control) and soluble Aβ1–42 (~27.2% reduction. $p < 0.05$ vs. the AAVrh.10-mCherry control) levels in the hippocampus of PDAPP mice (Fig. 2C, left). Insoluble Aβ1–40 was also dramatically decreased (~61.2% reduction. $p < 0.001$ vs. the AAVrh.10-mCherry control), although the already low levels of soluble Aβ1–40 were not altered (Fig. 2C, right). Since oligomeric Aβ has been reported to be neurotoxic and responsible for cognitive impairment in APP transgenic mice (Haass and Selkoe, 2007), we also assessed whether treatment with AAVrh.10-APOE2 altered the levels of oligomeric Aβ. As shown in Fig. 2D, overexpression of APOE2 using the AAVrh.10-APOE2 vector resulted in a significant decrease in oligomeric Aβ (~41.1% reduction. $p < 0.05$ vs. the AAVrh.10-mCherry control; Fig. 2D).

To further confirm the reduction of brain Aβ levels after gene delivery of AAVrh.10-APOE2, hippocampal APOE (Fig. 2E, left panel), Aβ (Fig. 2E, middle panel), and amyloid deposition (Fig. 2E, right panel) were quantified in the fixed right brain hemisphere using IHC with the biotinylated 3D6 antibody (which recognizes both Aβ1–40 and Aβ1–42) or using thioflavine-S staining (which recognizes amyloid plaques). Brain Aβ and amyloid burden were calculated by determining the percent surface area covered by Aβ IR or thioflavine-S staining over the total area quantified. As shown in Fig. 2F, total hippocampal Aβ burden (3D6-positive staining) in PDAPP mice injected with AAVrh.10-APOE2 was indistinguishable from mice injected with the AAVrh.10-mCherry control vector (Fig. 2F, left). By contrast, hippocampal amyloid burden (thioflavine-S-positive staining) in PDAPP mice injected with AAVrh.10-APOE2 was markedly reduced (>60%) compared with that of PDAPP mice injected with control vector ($p < 0.05$ vs. control; Fig. 2F, right).

Importantly, we found that intrahippocampal delivery of AAVrh.10-APOE2 markedly altered the anatomic distribution of Aβ in the hippocampus. In the PDAPP mouse, Aβ initially and preferentially deposits in the dentate gyrus of the hippocampus (Games et al., 1995). A similar pattern of Aβ distribution was observed in the hippocampus of PDAPP mice treated with the AAVrh.10-mCherry control vector (Fig. 2E, upper panel); however, Aβ and amyloid deposition were detected primarily in the stratum oriens of mice treated with the AAVrh.10-APOE2 vector (Fig. 2E, lower panel). This observation is consistent with several previous reports demonstrating that Aβ IR is redistributed in the hippocampus of PDAPP mice where *APOE2* has been introduced genetically (e.g., PDAPP/TRE2 mice; Fagan et al., 2002). Not surprisingly, quantifying Aβ burden in the dentate gyrus revealed a dramatic reduction (>90%) of Aβ IR in PDAPP mice treated with AAVrh.10-APOE2 compared with the mice treated with the control vector (Fig. 2F, middle).

To examine whether the reduction of hippocampal Aβ burden after gene delivery of *APOE2* was possibly due to neurotoxicity resulting from overexpression of APOE2, brain sections from PDAPP mice injected with AAVrh.10-APOE2 or AAVrh.10-mCherry were stained with Fluoro-Jade B, a fluorochrome that specifically detects dead or degenerating neurons. Wild-type (uninjected mice) or wild-type mice treated with kainic acid were used as negative and positive controls, respectively (Supplementary Fig. 1C). No Fluoro-Jade B positive staining was observed in brain sections from PDAPP mice treated with either AAVrh.10-APOE2 or AAVrh.10-mCherry for 8 weeks (Supplementary Fig. 1C). We also attempted to quantify cell number using cresyl violet staining and did not observe differences in gross hippocampal morphology in mice treated with AAVrh.10-APOE2 or AAVrh.10-mCherry during the 8-week observation (Supplementary Fig. 1A and B). Hippocampal tissue from PDAPP mice treated with AAVrh.10-APOE2 or AAVrh.10-mCherry was also examined for levels of the neuronal protein NeuN by Western blot. As shown in Supplementary Fig. 1D, there was no significant change in NeuN IR in the hippocampus of PDAPP mice treated with AAVrh.10-APOE2 compared with the PDAPP mice treated with AAVrh.10-mCherry.

3.3. *Gene delivery of* APOE2 *reduces* APOE4*-dependent amyloid pathology in the APP.PS1/TRE4 mouse model of AD*

We next assessed whether gene delivery of *APOE2* could counteract or rescue the detrimental effects of APOE4 on Aβ deposition and brain amyloid burden. APP.PS1/TRE4 mice carry both the *APP* Swedish (APPsw) and *PS1* mutations as well as a human *APOE4* transgene. APP.PS1/TRE4 mice develop robust and early age-dependent Aβ and amyloid pathology in multiple brain regions including the cerebral cortex, hippocampus, and thalamus, with the cortex having greater Aβ deposition than the hippocampus and thalamus. Amyloid plaques are observed in the cortex of these mice as early as age 2 months and the brain Aβ/amyloid burden that develops in these mice is largely dependent on APOE4 expression (Kim et al., 2011). AAVrh.10-APOE2 (1.0×10^{10} vg) was bilaterally injected into the hippocampus of 2.5-month-old APP.PS1/TRE4 mice. AAVrh.10-mCherrry (1.0×10^{10} vg) was injected in parallel as a control. Eight weeks after injection, hippocampal APOE and Aβ levels were assessed by ELISA. As shown in Fig. 3, treatment with AAVrh.10-APOE2 (1.0×10^{10} vg) resulted in a 5.7-fold higher level of hippocampal APOE and a marked decrease in insoluble Aβ1–42 (~78.6% reduction. $p < 0.05$ vs. the AAVrh.10-mCherry control) and soluble Aβ1–42 (~52.8% reduction. $p < 0.05$ vs. the AAVrh.10-mCherry control) levels in the hippocampus of APP.PS1/TRE4 mice (Fig. 3B). Insoluble Aβ1–40 was also decreased (~40.2% reduction. $p < 0.05$ vs. the AAVrh.10-mCherry control), although no

(B) Representative Western blots of APOE expression in extracts from the hippocampus of PDAPP mice. (C) Tissue levels of soluble and insoluble Aβ1–42 (left) and Aβ1–40 (right) in the hippocampus of PDAPP mice. (D) Tissue levels of oligomeric Aβ in the hippocampus of PDAPP mice. (E) Representative immunostaining of APOE, Aβ (3D6 anti-Aβ antibody positive staining) or amyloid plaques (thioflavine-S positive staining) in brain sections from PDAPP mice. Dentate gyrus (DG); stratum oriens (SO). Scale bar = 400 μm. (F) Quantitation of hippocampal Aβ burden or amyloid burden in PDAPP mice. The percent surface area covered by Aβ immunoreactivity (IR; Aβ burden) or thioflavine-S (amyloid burden) were quantified by ImageJ. n = 10–12 animals per group. Data presented as mean ± SD. $^{*}p < 0.05$, $^{***}p < 0.001$ versus AAVrh.10-mCherry treatment group using Student *t* test. Abbreviations: Aβ, amyloid-β; AAV, adeno-associated virus; APOE, apolipoprotein E; ELISA, enzyme-linked immunosorbent assay; SD, standard deviation.

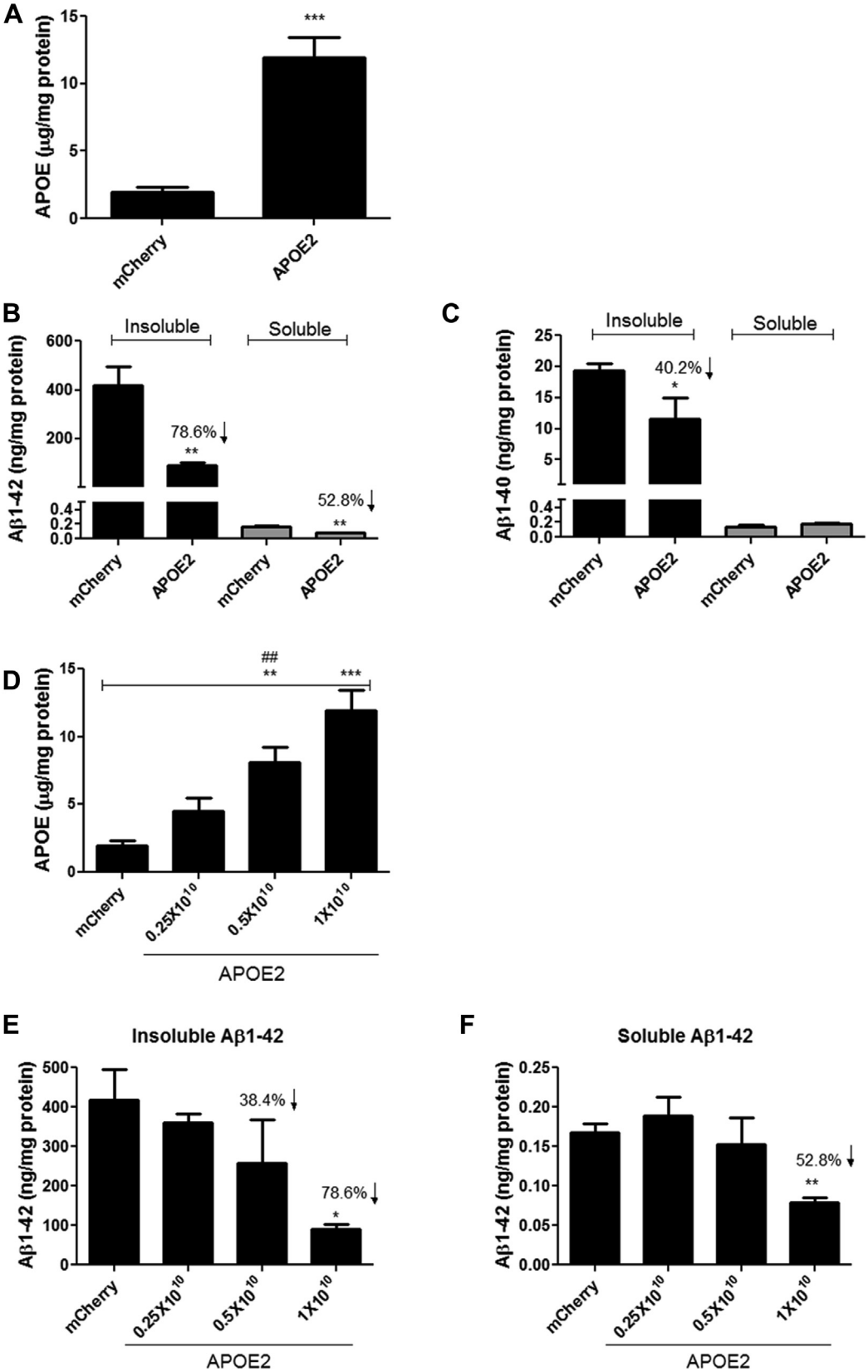


Fig. 3. Effects of intrahippocampal delivery of AAVrh.10-APOE2 on Aβ levels in the hippocampus of brain amyloidosis mouse models whose pathology is dependent on the expression of APOE4 (APP.PS1/TRE4 mice). AAVrh.10-APOE2 (1.0×10^{10} vg, 0.5×10^{10} vg, or 0.25×10^{10} vg), AAVrh.10-mCherry (1.0×10^{10} vg) vectors were injected bilaterally into the hippocampus of 2.5-month-old male APP.PS1/TRE4 mice. Eight weeks after injection, the mice were sacrificed and the hippocampus of the left hemisphere was dissected, homogenized, and extracted with RIPA to assay for soluble Aβ and then with 5.5 M guanidine to assay for insoluble Aβ. APOE, Aβ1–42, and Aβ1–40 levels were determined by ELISA. (A) APOE levels in the hippocampus of mice administered with 1.0×10^{10} vg of AAVrh.10-APOE2 (APOE2) or AAVrh.10-mCherry (mCherry) vectors. (B) Tissue levels of Aβ1–42 in the

significant change of soluble Aβ1–40 was detected after the treatment (Fig. 3C).

3.4. The efficacy of AAV-APOE2-mediated amyloid reduction is dependent on vector dose and the level of APOE2 expression

We found that intracerebral administration of 1×10^{10} vg AAVrh.10-APOE2 dramatically decreases amyloid pathology in both PDAPP mice (Fig. 2) and APP.PS1.TRE4 mice (Fig. 3). To assess whether lower doses of AAVrh.10-APOE2 have the same impact, 0.25×10^{10} vg or 0.5×10^{10} vg of AAVrh.10-APOE2 were bilaterally injected into the hippocampus of 2.5-month-old APP.PS1/TRE4 mice. Eight weeks after injection, hippocampal APOE and Aβ levels were determined and compared with hippocampal APOE and Aβ levels in APP.PS1/TRE4 mice treated with 1.0×10^{10} vg of AAVrh.10-APOE2. As shown in Fig. 3D, intrahippocampal delivery of AAVrh.10-APOE2 results in a dose-dependent increase in hippocampal APOE levels and correspondingly dose-dependent decrease in both insoluble (Fig. 3E) and soluble (Fig. 3F) Aβ1–42 levels in the hippocampus of APP.PS1/TRE4 mice. In contrast to the dramatic decrease in amyloid pathology after treatment with 1.0×10^{10} vg of AAVrh.10-APOE2, lower doses of AAVrh.10-APOE2 led to lower levels of APOE2 expression and correspondingly lower reductions in both soluble and insoluble Aβ1–42 (Fig. 3).

3.5. The efficacy of AAV-APOE2-mediated amyloid reduction is impacted by the extent of pre-existing amyloid pathology

To test whether gene delivery of *APOE2* could reduce Aβ/amyloid deposition in mice with advanced amyloid pathology, 1.0×10^{10} vg of AAVrh.10-APOE2 was administered into the hippocampus of 19-month-old PDAPP mice, where Aβ/amyloid pathology is more advanced and hippocampal Aβ levels are 2–3-fold greater than those measured at age 9 months (Fig. 2). Eight weeks after injection, APOE (Fig. 4A) and Aβ levels (Fig. 4B and C) in the hippocampus of the injected mice were assessed by ELISA. As shown in Fig. 4B, intrahippocampal delivery of AAVrh.10-APOE2 results in an approximately 30.8% reduction ($p < 0.05$ vs. the AAVrh.10-mCherry control) in hippocampal insoluble Aβ1–42 levels (compared with 70.6% in the 9-month-old PDAPP mice, Fig. 2C), whereas the reduction in Aβ1–40 and soluble Aβ1–42 levels observed in PDAPP mice was comparable at both ages. To further confirm the impact of the extent of pre-existing amyloid pathology on the efficacy of AAV-APOE2-mediated Aβ reduction, 1.0×10^{10} vg of AAVrh.10-APOE2 was administered into the hippocampus of 5-month-old APP.PS1/TRE4 mice, where Aβ/amyloid pathology is quite advanced and hippocampal Aβ levels are 8-fold greater than those measured at age 2.5 months (Fig. 3). Eight weeks after injection, APOE (Fig. 4D) and Aβ levels (Fig. 4E and F) in the hippocampus of the injected mice were assessed by ELISA. Despite high levels of APOE expression (Fig. 4D), there was only an approximately 30% reduction in insoluble Aβ1–42 levels in the hippocampus of AAVrh.10-APOE2-treated mice compared with the AAVrh.10-mCherry control and this difference did not reach statistical significance. There were no differences in soluble Aβ1–42, soluble Aβ1–40, or insoluble Aβ1–40 levels between any group (Fig. 4E and F).

3.6. Intrathalamic delivery of AAV9-APOE2 leads to widespread brain distribution of APOE2 and reductions of brain Aβ burden in multiple brain regions

Because AD is a disease that broadly affects the brain, we next attempted to optimize gene delivery of APOE2 to multiple brain regions simultaneously using a single injection of vector. Previous studies have shown that intrathalamic delivery of certain AAV vectors results in widespread brain distribution of payload genes via retrograde and (or) anterograde axonal transport and that AAV9 is a more efficient capsid for axonal transport than are other AAV serotypes (Baek et al., 2010; Cearley and wolfe, 2007; Kells et al., 2009). We, therefore, constructed an APOE2 expressing AAV9 vector (AAV9-CAG-APOE2 or AAV9-APOE2) for intrathalamic delivery of APOE2. When delivered unilaterally into the thalamus of EKO mice, as shown in Supplementary Fig. 2A, this vector resulted in more widespread brain distribution of APOE2 than does intrathalamic administration of AAVrh.10-APOE2 or intrahippocampal delivery of AAV9-APOE2. APOE, detected by IHC, was present throughout the entire brain of EKO mice administered AAV9-APOE2 in the thalamus (Supplementary Fig. 2B). We next examined whether intrathalamic delivery of *APOE2* using AAV9-APOE2 is associated with reduced brain Aβ burden. AAV9-APOE2 (1.0×10^{10} vg) was administered bilaterally into the thalamus of 2.5-month-old APP.PS1/TRE4 mice. Eight weeks after injection, the mice were killed and the thalamus, hippocampus, and cortex were dissected and assayed for both APOE and Aβ. Compared to the same brain regions of mice treated with the control vector (AAV9-GFP), APOE levels in mice treated with AAV9-APOE2 were increased by 7.5-fold in the thalamus, 2.6-fold in the hippocampus, and 1.7-fold in the cortex, respectively (Fig. 5A). Interestingly, Aβ1–42 levels decreased proportionately (i.e., by 70% in the thalamus [$p < 0.001$ vs. the AAV9-GFP control], 50% in the hippocampus [$p < 0.01$ vs. control], and 15% in the cortex [$p =$ n.s.]), respectively (Fig. 5B). The decrease in Aβ deposition in the thalamus was further confirmed by IHC (Fig. 5C). Compared to the control vector–treated mice, Aβ burden in mice treated with AAV9-APOE2 decreased by 54% in the thalamus ($p < 0.05$ vs. the AAV9-GFP control) and 26% in the hippocampus ($p = 0.06$ vs. the AAV9-GFP control; Fig. 5D).

4. Discussion

Although the *APOE* alleles are well-established, quantitatively important genetic risk factors for AD, how these *APOE* alleles contribute so substantially to the pathogenesis of AD is only incompletely understood. Considerable preclinical and clinical data support a pathogenic role for the APOE isoforms as major determinants of the amount, timing, and quality of Aβ-containing plaques in the brain (Bales et al., 1997, 2009; Castellano et al., 2011; Fagan et al., 2002; Holtzman et al., 2000, 2012; Morris et al., 2010). Targeted replacement of murine *Apoe* with human *APOE* in several APP transgenic mouse lines results in an age-dependent (E4 >> E3 > E2)

hippocampus of mice administered with 1.0×10^{10} vg of AAVrh.10-APOE2 (APOE2) or AAVrh.10-mCherry (mCherry) vectors. (C) Tissue levels of Aβ1–40 in the hippocampus of mice administered with 1.0×10^{10} vg of AAVrh.10-APOE2 (APOE2) or AAVrh.10-mCherry (mCherry) vectors. (D) APOE levels in the hippocampus of mice administered with indicated dose of AAVrh.10-APOE2 (APOE2) or 1.0×10^{10} vg of AAVrh.10-mCherry (mCherry). (E) Tissue levels of insoluble Aβ1–42 in the hippocampus of mice administered with indicated doses of AAVrh.10-APOE2 (APOE2) or AAVrh.10-mCherry (mCherry). (E) Tissue levels of soluble Aβ1–42 in the hippocampus of mice administered with indicated doses of AAVrh.10-APOE2 (APOE2) or AAVrh.10-mCherry (mCherry). n = 5–7 animals per group. Data presented as mean ± SD. In (A), (B), (C): $^{*}p < 0.05$, $^{**}p < 0.01$, $^{***}p < 0.001$ versus AAVrh.10-mCherry treatment group using Student *t* test. In (D), (E), (F): $^{*}p < 0.05$, $^{**}p < 0.01$, $^{***}p < 0.001$ versus AAVrh.10-mCherry treatment group; $^{\#\#}p < 0.01$ versus 0.25×10^{10} vg AAVrh.10-APOE2 treatment group using 1-way ANOVA followed by *post hoc* Newman-Keuls analysis. Abbreviations: Aβ, amyloid-β; AAV, adeno-associated virus; ANOVA, analysis of variance; APOE, apolipoprotein E; ELISA, enzyme-linked immunosorbent assay; SD, standard deviation.

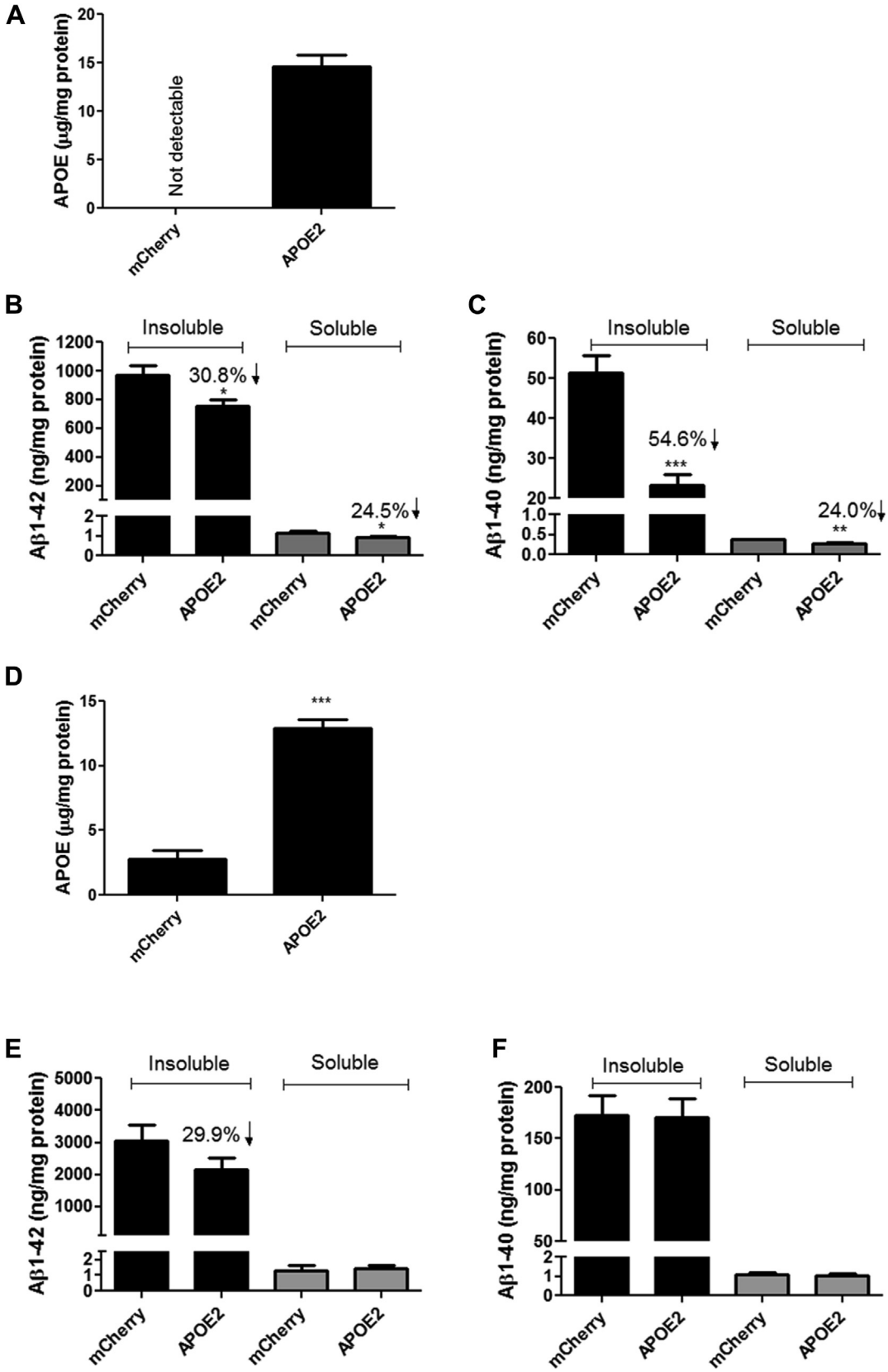


Fig. 4. Effects of the extent of pre-existing amyloid pathology on AAV-APOE2-mediated Aβ reduction. AAVrh.10-APOE2 (APOE2) or AAVrh.10-mCherry (mCherry; 1.0×10^{10} vg) were bilaterally injected into the hippocampus of 19-month-old PDAPP mice or 5-month-old male APP.PS1/TRE4 mice. Eight weeks after injection, the mice were sacrificed. The hippocampus of the left hemisphere was dissected, homogenized, and extracted with RIPA to assay for soluble Aβ and then with 5.5 M guanidine to assay for insoluble Aβ. APOE, Aβ1–42, and Aβ1–40 levels in each extract were determined by ELISA. (A) APOE levels in the hippocampus of PDAPP mice. (B) Aβ1–42 levels in the hippocampus of PDAPP mice. (C) Aβ1–40 levels in the hippocampus of PDAPP mice. (D) APOE levels in the hippocampus of APP.PS1/TRE4 mice. (E) Aβ1–42 levels in the hippocampus of APP.PS1/TRE4 mice. (F) Aβ1–40 levels in the hippocampus of APP.PS1/TRE4 mice. n = 10–12 animals per group. Data presented as mean ± SD. $^{*}p < 0.05$, $^{**}p < 0.01$, $^{***}p < 0.001$ versus AAVrh.10-mCherry treatment group using Student *t* test. Abbreviations: Aβ, amyloid-β; AAV, adeno-associated virus; APOE, apolipoprotein E; ELISA, enzyme-linked immunosorbent assay; SD, standard deviation.

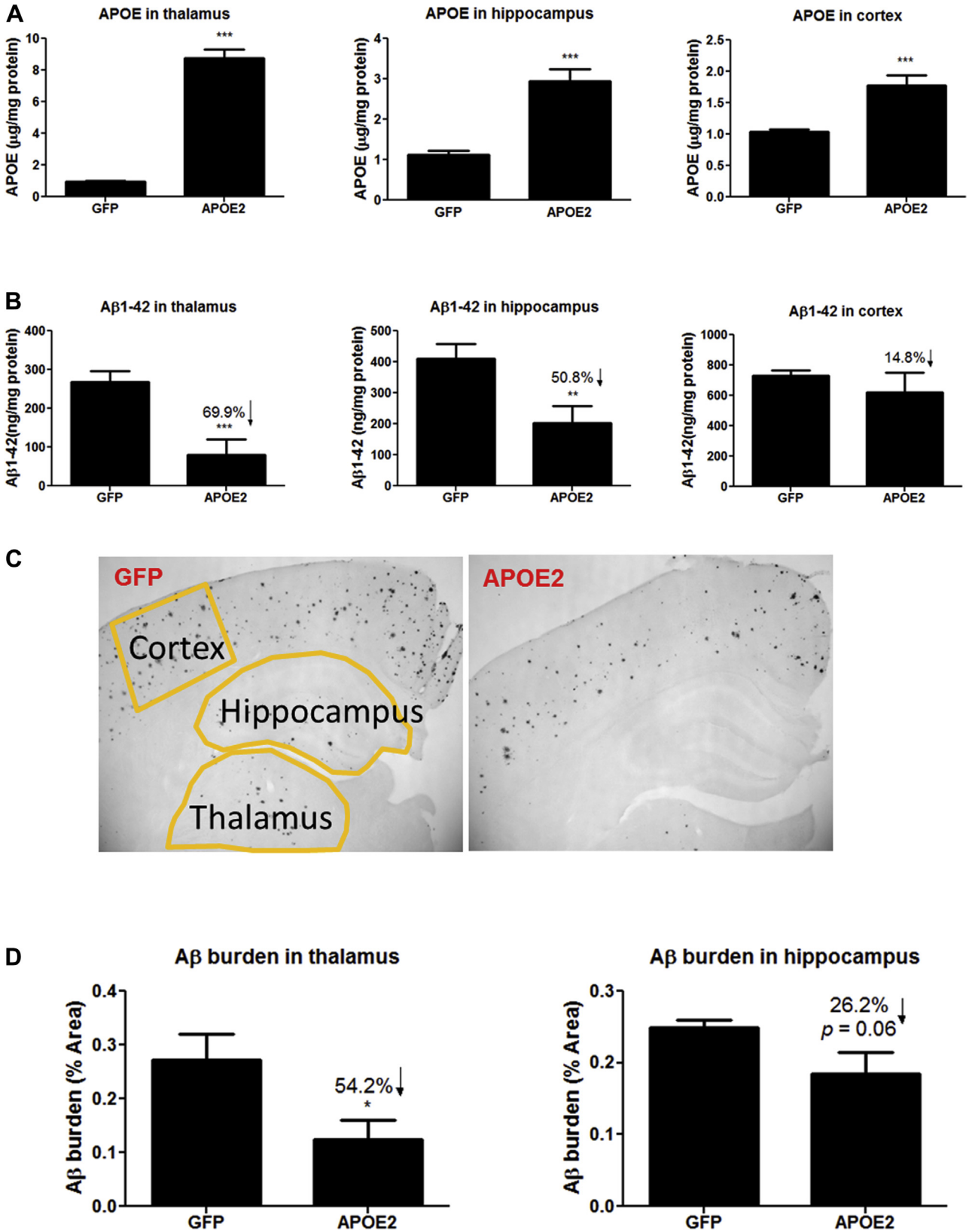


Fig. 5. Effects of intrathalamic delivery of *APOE2* on expression of APOE and Aβ levels in multiple brain regions of APP.PS1/TRE4 mice. AAV9-APOE2 (APOE2) or AAV9-GFP (GFP) (1.0×10^{10} vg) were bilaterally injected into the thalamus of 2.5-month-old male APP.PS1/TRE4 mice. Eight weeks after injection, the mice were killed. The right hemisphere was post-fixed for IHC. The left hemisphere was microdissected into the thalamus, hippocampus, and cerebral cortex. The dissected brain regions were homogenized and sequentially extracted with RIPA (representing soluble Aβ) and 5.5 M guanidine (representing insoluble Aβ). APOE levels (A) and Aβ1–42 levels (B) in each extract of different brain regions were measured by ELISA. (C) Representative immunostaining and quantitation of Aβ in the brains of APP.PS1/TRE4 mice intrathalamically injected with AAV9-APOE2 or AAV9-GFP. Aβ in different brain regions was visualized by IHC with biotin-3D6 anti-Aβ antibody. (D) The percent surface area covered by Aβ IR (Aβ burden) was quantified by ImageJ. The regions selected for ELISA analysis or IHC quantification were shown in (C; left). Scale bar = 400 μm. n = 7 animals per group. Data presented as mean ± SD. $^{*}p < 0.05$, $^{**}p < 0.01$, $^{***}p < 0.001$ versus AAV9-GFP treatment group using Student *t* test. Abbreviations: Aβ, amyloid-β, AAV, adeno-associated virus; APOE, apolipoprotein E; ELISA, enzyme-linked immunosorbent assay; IHC, immunohistochemistry; SD, standard deviation.

accumulation and deposition of Aβ and subsequent amyloid plaque formation (Bales et al., 2009; Castellano et al., 2011; Kim et al., 2011; Youmans et al., 2012). The latter strikingly recapitulates the human clinical data derived from studies of postmortem brain or antemortem biomarkers, including PET neuroimaging (Morris et al., 2010; Ramanan et al., 2013; Rebeck et al., 1993; Reiman et al., 2009; Schmechel et al., 1993). Although APOE undoubtedly has multiple actions in the CNS and possibly in contributing to AD pathogenesis, APOE's role in altering Aβ clearance and, thus, promoting Aβ and amyloid deposition (e.g., plaque initiation and Aβ fibrillization) likely contribute to the strong association of the *APOE* alleles to the age-dependent risk of developing AD.

Gene delivery of the 3 human APOE isoforms was first reported by Dodart et al. (2005) using lentiviral vectors and direct intracerebral (intrahippocampal) administration (Dodart et al., 2005). In this study, direct intrahippocampal administration of lenti-*APOE4* to PDAPP mice lacking *Apoe* (the same strain as used in the present study) resulted in increased insoluble Aβ1–42 and amyloid plaques compared with mice treated with either a lenti-*APOE3* vector or a lenti-*GFP* control vector (Dodart et al., 2005). Remarkably, intrahippocampal administration of lenti-*APOE2* to PDAPP mice expressing murine Apoe and with abundant pre-existing Aβ and amyloid plaques resulted in markedly reduced Aβ/amyloid burden despite much higher levels of total APOE expressed in the hippocampus. These findings are noteworthy since murine Apoe is highly amyloidogenic (Bales et al., 1997; Fagan et al., 2002), prompting the authors to propose that gene delivery of *APOE2* may constitute a promising therapeutic strategy for treating or preventing AD (Dodart et al., 2005). In a recent study, Hudry et al. (Hudry et al., 2013) used AAV4 to deliver *APOE* to the lateral ventricle of APP/PS1 mice. Indeed, like Dodart et al. (2005), these authors also reported isoform-dependent (and bidirectional) effects of APOE on brain Aβ levels and amyloid burden, with the APOE4 and APOE2 isoforms increasing and decreasing brain Aβ/amyloid burden, respectively. Although the reported reductions in brain Aβ and amyloid burden they observed were relatively modest, the brain levels of APOE achieved via intraventricular administration of an AAV4 vector were only 10% of endogenous murine Apoe levels. By contrast, our data suggest that considerably higher brain levels of APOE2 must be achieved to substantially reduce brain Aβ/amyloid burden over a shorter time period (8 weeks in our study vs. 20 weeks in Hudry et al.) especially when pre-existing Aβ/amyloid pathology is already abundant. We underscore, however, that the reductions in brain Aβ/amyloid burden we observed at 8 weeks after intracerebral gene delivery of *APOE2* are quantitatively greater than those reported after passive immunization with several anti-Aβ monoclonal antibodies in the same strain of APP transgenic mice (PDAPP mice; Lemere and Masliah, 2010).

Most importantly, in the present study, we have also shown that gene delivery of *APOE2* markedly reduces Aβ/amyloid pathology when this pathology is dependent on expression of APOE4 (as opposed to murine Apoe). APP.PS1/TRE4 triple transgenic mice develop very early and robust Aβ and amyloid deposition, which is dramatically reduced in the absence of APOE4 (Kim et al., 2011). Here, we show a marked (~80%) reduction in insoluble Aβ1–42 in the hippocampus after intrahippocampal administration of APP.PS1/TRE4 mice 8 weeks after injection of the AAVrh.10-APOE2 vector. These data suggest that APOE2 can essentially counteract or reverse the ability of APOE4 to promote brain Aβ accumulation and deposition/fibrillization. Moreover, this finding strongly suggests a marked qualitative difference between APOE2 and APOE4 in promoting brain amyloidosis since much higher levels of total APOE are associated with much lower levels of brain Aβ/amyloid when the 2 APOE isoforms are expressed together and when APOE2 is expressed in excess. This "protective effect" of APOE2 is potentially important given the role of APOE4 in both the etiology and pathogenesis of AD. Similar results were obtained after intrathalamic administration of the AAV9-APOE2 vector to APP.PS1/TRE4 mice, where the reduction in brain Aβ1–42 and amyloid levels was also correlated to the increased levels of APOE2 not only in the thalamus but also in the hippocampus and cerebral cortex. We note that a 1–2-fold increase in APOE2 levels in the hippocampus resulted in ≥50% reduction in insoluble Aβ1–42 levels. We also observed that intrathalamic administration of AAV9-APOE2 vector resulted in broader and more widespread brain distribution of APOE2 and the reductions in brain Aβ burden were also highly correlated to the regional levels of APOE2. Similar results have been reported for AAV9-mediated intrathalamic delivery of other genes in both mice and nonhuman primates (Baek et al., 2010; Cearley and wolfe, 2007; Kells et al., 2009). This observation is of potential therapeutic significance since AD is a global brain disorder and any successful gene therapy strategy will require widespread brain delivery. While these data are encouraging, we also found that gene delivery of *APOE2* was much less effective when administered to older APP.PS1/TRE4 mice where pre-existing Aβ/amyloid pathology was quite substantial. These data combined with the APOE2 dose-response relationship we observed for APOE expression and reduced Aβ/amyloid pathology after *APOE2* gene delivery strongly suggest that both the gene "dose" (i.e., level of APOE2 expression) and amount of pre-existing brain Aβ/amyloid deposition are important determinants of the "efficacy" of *APOE2* gene delivery, at least in these mouse models.

In addition, we would caution that APOE2 is primarily produced by astrocytes in CNS, and astrocytic APOE2, therefore, may be more beneficial than APOE2 produced by other type of cells especially neurons. Although we have shown that gene delivery of *APOE2* using AAVrh.10 and a ubiquitous promoter (CAG promoter) drives APOE2 expression in astrocytes and abundantly in neurons as well, the APOE2 expressed is well lipidated and results in dramatic Aβ reduction. Our findings, therefore, suggest that the cellular source of APOE2 may not be as critical for the function of APOE2 in altering (i.e., reducing) amyloid pathology and AAV-APOE2 vector may serve as an effective *APOE2* delivery tool for therapeutic intervention.

Taken together, our findings confirm that gene delivery of *APOE2* effectively reduces Aβ/amyloid plaques in 2 transgenic mouse models of CNS amyloidosis. The accumulation of Aβ peptides, especially Aβ1–42, and amyloid plaque deposition/formation is now recognized as very early events in the pathogenesis of AD, that is, these are neuropathologic features that are now known to occur many years before the onset of cognitive impairment and dementia (Hardy and Selkoe, 2002; Holtzman et al., 2012; Kim et al., 2009; Liu et al., 2013; Yu et al., 2014). Importantly, *APOE4* carriers have earlier amyloid deposition and an earlier age of onset of AD than non-carriers (Carrasquillo et al., 2015; Farrer et al., 1997; Lambert et al., 2013; Ramanan et al., 2013; Reiman et al., 2009), suggesting that amyloid deposition is a necessary (but perhaps not sufficient) pathogenic event. If true, CNS gene delivery of *APOE2*, a protective gene which effectively reduces brain Aβ/amyloid burden, could delay or even prevent the onset of disease in a manner similar to that observed in *APOE2* carriers (Corder et al., 1994; Farrer et al., 1997; Suri et al., 2013; Talbot et al., 1994). Our preclinical data clearly suggest that achieving an optimal level of APOE2 expression at a time of modest or minimal pre-existing amyloid pathology might be critical determinants for the success of this strategy.

Disclosure statement

The authors have no actual or potential conflicts of interest.

Acknowledgements

The authors thank Rebecca Cox (Weill Cornell Medical College, New York, NY) for her efforts on APOE immunohistochemistry. The authors thank the Alzheimer's Drug Discovery Foundation (20141209), Robert Belfer, Robert Appel, Burt Resnick, and Dr Howard Fillit for their generous support and encouragement. Special thanks to Dr Ronald DeMattos and Eli Lilly and Company for their gift of PDAPP mice and antibodies used in our ELISAs and for immunohistochemistry. The authors acknowledge support from the Appel Alzheimer's Disease Research Institute and NIH grants 9R01NS090934-19, 5R01NS090934-20, and 1R01AG047644-A1.

Appendix A. Supplementary data

Supplementary data associated with this article can be found, in the online version, at http://dx.doi.org/10.1016/j.neurobiolaging.2016.04.020.

References

Baek, R.C., Broekman, M.L., Leroy, S.G., Tierney, L.A., Sandberg, M.A., D'Azzo, A., Seyfried, T.N., Sena-Esteves, M., 2010. AAV-mediated gene delivery in adult GM1-gangliosidosis mice corrects lysosomal storage in CNS and improves survival. PLoS One 5, e13468.

Bales, K.R., Liu, F., Wu, S., Lin, S., Koger, D., DeLong, C., Hansen, J.C., Sullivan, P.M., Paul, S.M., 2009. Human APOE isoform-dependent effects on brain β-amyloid levels in PDAPP transgenic mice. J. Neurosci. 29, 6771–6779.

Bales, K.R., Verina, T., Dodel, R.C., Du, Y., Altstiel, L., Bender, M., Hyslop, P., Johnstone, E.M., Little, S.P., Cummins, D.J., Piccardo, P., Ghetti, B., Paul, S.M., 1997. Lack of apolipoprotein E dramatically reduces amyloid β-peptide deposition. Nat. Genet. 17, 263–264.

Boyles, J.K., Pitas, R.E., Wilson, E., Mahley, R.W., Taylor, J.M., 1985. Apolipoprotein E associated with astrocytic glia of the central nervous system and with nonmyelinating glia of the peripheral nervous system. J. Clin. Invest. 76, 1501–1513.

Carrasquillo, M.M., Crook, J.E., Pedraza, O., Thomas, C.S., Pankratz, V.S., Allen, M., Nguyen, T., Malphrus, K.G., Ma, L., Bisceglio, G.D., Roberts, R.O., Lucas, J.A., Smith, G.E., Ivnik, R.J., Machulda, M.M., Graff-Radford, N.R., Petersen, R.C., Younkin, S.G., Ertekin-Taner, N., 2015. Late-onset Alzheimer's risk variants in memory decline, incident mild cognitive impairment, and Alzheimer's disease. Neurobiol. Aging 36, 60–67.

Castellano, J.M., Kim, J., Stewart, F.R., Jiang, H., DeMattos, R.B., Patterson, B.W., Fagan, A.M., Morris, J.C., Mawuenyega, K.G., Cruchaga, C., Goate, A.M., Bales, K.R., Paul, S.M., Bateman, R.J., Holtzman, D.M., 2011. Human apoE isoforms differentially regulate brain amyloid-β peptide clearance. Sci. Transl. Med. 3, 89ra57.

Cearley, C.N., Wolfe, J.H., 2007. A single injection of an adeno-associated virus vector into nuclei with divergent connections results in widespread vector distribution in the brain and global correction of a neurogenetic disease. J. Neurosci. 27, 9928–9940.

Corder, E., Saunders, A., Risch, N., Strittmatter, W., Schmechel, D., Gaskell, P., Rimmler, J.B., Locke, P.A., Conneally, P.M., Schmader, K.E., Small, G.W., Roses, A.D., Haines, J.L., Pericak-Vance, M.A., 1994. Protective effect of apolipoprotein E type 2 allele for late onset Alzheimer disease. Nat. Genet. 7, 180–184.

Corder, E.H., Saunders, A.M., Strittmatter, W.J., Schmechel, D.E., Gaskell, P.C., Small, G.W., Roses, A.D., Haines, J.L., Pericak-Vance, M.A., 1993. Gene dose of apolipoprotein E type 4 allele and the risk of Alzheimer's disease in late onset families. Science 261, 921–923.

Deane, R., Sagare, A., Hamm, K., Parisi, M., Lane, S., Finn, M.B., Holtzman, D.M., Zlokovic, B.V., 2008. ApoE isoform-specific disruption of amyloid beta peptide clearance from mouse brain. J. Clin. Invest. 118, 4002–4013.

DeMattos, R.B., Brendza, R.P., Heuser, J.E., Kierson, M., Cirrito, J.R., Fryer, J., Sullivan, P.M., Fagan, A.M., Han, X., Holtzman, D.M., 2001. Purification and characterization of astrocyte-secreted apolipoprotein E and J-containing lipoproteins from wild-type and human apoE transgenic mice. Neurochem. Int. 39, 415–425.

Dodart, J.C., Marr, R.A., Koistinaho, M., Gregersen, B.M., Malkani, S., Verma, I.M., Paul, S.M., 2005. Gene delivery of human apolipoprotein E alters brain Aβ burden in a mouse model of Alzheimer's disease. Proc. Natl. Acad. Sci. U. S. A. 102, 1211–1216.

Fagan, A.M., Watson, M., Parsadanian, M., Bales, K.R., Paul, S.M., Holtzman, D.M., 2002. Human and murine ApoE markedly alters Aβ metabolism before and after plaque formation in a mouse model of Alzheimer's disease. Neurobiol. Dis. 9, 305–318.

Fan, J., Donkin, J., Wellington, C., 2009. Greasing the wheels of Aβ clearance in Alzheimer's disease: the role of lipids and apolipoprotein E. Biofactors 35, 239–248.

Farrer, L.A., Cupples, L.A., Haines, J.L., Hyman, B., Kukull, W.A., Mayeux, R., Myers, R.H., Pericak-Vance, M.A., Risch, N., van Duijn, C.M., 1997. Effects of age, sex, and ethnicity on the association between apolipoprotein E genotype and Alzheimer disease: a meta-analysis. JAMA 278, 1349–1356.

Franklin, K.B.J., Paxinos, G., 2007. The mouse brain in Stereotaxic Coordinates, 3rd edition. Elsevier Inc, New York.

Games, D., Adams, D., Alessandrini, R., Barbour, R., Berthelette, P., Blackwell, C., Carr, T., Clemens, J., Donaldson, T., Gillespie, F., Guido, T., Hagopian, S., Johnson-wood, K., Khan, K., Lee, M., Leibowitz, P., Lieberburg, I., Little, S., Maslian, E., Mcconlogue, L., Montoya-zavala, M., Mucke, L., Paganini, L., Penniman, E., Power, M., Schenk, D., Seubert, P., Snyder, B., Soriano, F., Tan, H., Vitale, J., Wadsworth, S., Wolozin, B., Zhao, J., 1995. Alzheimer-type neuropathology in transgenic mice overexpressing V717F β-amyloid precursor protein. Nature 373, 523–527.

Haass, C., Selkoe, D.J., 2007. Soluble protein oligomers in neurodegeneration: lessons from the Alzheimer's amyloid β-peptide. Nat. Rev. Mol. Cell Biol. 8, 101–112.

Hardy, J., Selkoe, D.J., 2002. The amyloid hypothesis of Alzheimer's disease: progress and problems on the road to therapeutics. Science 297, 353–356.

Hashimoto, T., Serrano-Pozo, A., Hori, Y., Adams, K.W., Takeda, S., Banerji, A.O., Mitani, A., Joyner, D., Thyssen, D.H., Bacskai, B.J., Frosch, M.P., Spires-Jones, T.L., Finn, M.B., Holtzman, D.M., Hyman, B.T., 2012. Apolipoprotein E, especially apolipoprotein E4, increases the oligomerization of amyloid beta peptide. J. Neurosci. 32, 15181–15192.

Hatters, D.M., Peters-Libeu, C.A., Weisgraber, K.H., 2006. Apolipoprotein E structure: insights into function. Trends Biochem. Sci. 31, 445–454.

Holtzman, D.M., Bales, K.R., Tenkova, T., Fagan, A.M., Parsadanian, M., Sartorius, L.J., Mackey, B., Olney, J., McKeel, D., Wozniak, D., Paul, S.M., 2000. Apolipoprotein E isoform-dependent amyloid deposition and neuritic degeneration in a mouse model of Alzheimer's disease. Proc. Natl. Acad. Sci. U. S. A. 97, 2892–2897.

Holtzman, D.M., Herz, J., Bu, G., 2012. Apolipoprotein E and apolipoprotein E receptors: normal biology and roles in Alzheimer disease. Cold Spring Harb. Perspect. Med. 2, a006312.

Hudry, E., Dashkoff, J., Roe, A.D., Takeda, S., Koffie, R.M., Hashimoto, T., Scheel, M., Spires-Jones, T., Arbel-Ornath, M., Betensky, R., Davidson, B.L., Hyman, B.T., 2013. Gene transfer of human Apoe isoforms results in differential modulation of amyloid deposition and neurotoxicity in mouse brain. Sci. Transl. Med. 5, 212ra161.

Johnson-Wood, K., Lee, M., Motter, R., Hu, K., Gordon, G., Barbour, R., Khan, K., Gordon, M., Tan, H., Games, D., Lieberburg, I., Schenk, D., Seubert, P., McConlogue, L., 1997. Amyloid precursor protein processing and Aβ42 deposition in a transgenic mouse model of Alzheimer disease. Proc. Natl. Acad. Sci. U. S. A. 94, 1550–1555.

Kells, A.P., Hadaczek, P., Yin, D., Bringas, J., Varenika, V., Forsayeth, J., Bankiewicz, K.S., 2009. Efficient gene therapy-based method for the delivery of therapeutics to primate cortex. Proc. Natl. Acad. Sci. U. S. A. 106, 2407–2411.

Kim, J., Basak, J.M., Holtzman, D.M., 2009. The role of apolipoprotein E in Alzheimer's disease. Neuron 63, 287–303.

Kim, J., Jiang, H., Park, S., Eltorai, A.E., Stewart, F.R., Yoon, H., Basak, J.M., Finn, M.B., Holtzman, D.M., 2011. Haploinsufficiency of human APOE reduces amyloid deposition in a mouse model of amyloid-β amyloidosis. J. Neurosci. 31, 18007–18012.

Lambert, J., Ibrahim-Verbaas, C.A., Harold, D., Naj, A.C., Sims, R., Bellenguez, C., DeStafano, A.L., Bis, J.C., Beecham, G.W., Grenier-Boley, B., Russo, G., Thorton-Wells, T.A., Jones, N., Smith, A.V., Chouraki, V., Thomas, C., Ikram, M.A., Zelenika, D., Vardarajan, B.N., Kamatani, Y., Lin, C.F., Gerrish, A., Schmidt, H., Kunkle, B., Dunstan, M.L., Ruiz, A., Bihoreau, M.T., Choi, S.H., Reitz, C., Pasquier, F., Cruchaga, C., Craig, D., Amin, N., Berr, C., Lopez, O.L., De Jager, P.L., Deramecourt, V., Johnston, J.A., Evans, D., Lovestone, S., Letenneur, L., Morón, F.J., Rubinsztein, D.C., Eiriksdottir, G., Sleegers, K., Goate, A.M., Fiévet, N., Huentelman, M.W., Gill, M., Brown, K., Kamboh, M.I., Keller, L., Barberger-Gateau, P., McGuiness, B., Larson, E.B., Green, R., Myers, A.J., Dufouil, C., Todd, S., Wallon, D., Love, S., Rogaeva, E., Gallacher, J., St George-Hyslop, P., Clarimon, J., Lleo, A., Bayer, A., Tsuang, D.W., Yu, L., Tsolaki, M., Bossù, P., Spalletta, G., Proitsi, P., Collinge, J., Sorbi, S., Sanchez-Garcia, F., Fox, N.C., Hardy, J., Deniz Naranjo, M.C., Bosco, P., Clarke, R., Brayne, C., Galimberti, D., Mancuso, M., Matthews, F., European Alzheimer's Disease Initiative (EADI); Genetic and Environmental Risk in Alzheimer's Disease; Alzheimer's Disease Genetic Consortium; Cohorts for Heart and Aging Research in Genomic Epidemiology, Moebus, S., Mecocci, P., Del Zompo, M., Maier, W., Hampel, H., Pilotto, A., Bullido, M., Panza, F., Caffarra, P., Nacmias, B., Gilbert, J.R., Mayhaus, M., Lannefelt, L., Hakonarson, H., Pichler, S., Carrasquillo, M.M., Ingelsson, M., Beekly, D., Alvarez, V., Zou, F., Valladares, O., Younkin, S.G., Coto, E., Hamilton-Nelson, K.L., Gu, W., Razquin, C., Pastor, P., Mateo, I., Owen, M.J., Faber, K.M., Jonsson, P.V., Combarros, O., O'Donovan, M.C., Cantwell, L.B., Soininen, H., Blacker, D., Mead, S., Mosley Jr, T.H., Bennett, D.A., Harris, T.B., Fratiglioni, L., Holmes, C., de Bruijn, R.F., Passmore, P., Montine, T.J., Bettens, K., Rotter, J.I., Brice, A., Morgan, K., Foroud, T.M., Kukull, W.A., Hannequin, D., Powell, J.F., Nalls, M.A., Ritchie, K., Lunetta, K.L., Kauwe, J.S., Boerwinkle, E., Riemenschneider, M., Boada, M., Hiltuenen, M., Martin, E.R., Schmidt, R., Rujescu, D., Wang, L.S., Dartigues, J.F., Mayeux, R., Tzourio, C., Hofman, A., Nöthen, M.M., Graff, C., Psaty, B.M., Jones, L., Haines, J.L., Holmans, P.A., Lathrop, M., Pericak-Vance, M.A., Launer, L.J., Farrer, L.A., van Duijn, C.M., Van Broeckhoven, C., Moskvina, V., Seshadri, S., Williams, J., Schellenberg, G.D., Amouyel, P., 2013. Meta-analysis of 74,046 individuals identifies 11 new susceptibility loci for Alzheimer's disease. Nat. Genet. 45, 1452–1458.

Lemere, C.A., Masliah, E., 2010. Can Alzheimer disease be prevented by amyloid-β immunotherapy? Nat. Rev. Neurol. 6, 108–119.
Li, J., Kanekiyo, T., Shinohara, M., Zhang, Y., LaDu, M.J., Xu, H., Bu, G., 2012. Differential regulation of amyloid-beta endocytic trafficking and lysosomal degradation by apolipoprotein E isoforms. J. Biol. Chem. 287, 44593–44601.
Liu, C., Kanekiyo, T., Xu, H., Bu, G., 2013. Apolipoprotein E and Alzheimer disease: risk, mechanisms and therapy. Nat. Rev. Neurol. 9, 106–118.
Manelli, A.M., Stine, W.B., Van Eldik, L.J., LaDu, M.J., 2004. ApoE and Aβ1–42 interactions. J. Mol. Neurosci. 23, 235–246.
Morris, J.C., Roe, C.M., Xiong, C., Fagan, A.M., Goate, A.M., Holtzman, D.M., Mintun, M.A., 2010. APOE predicts amyloid-β but not tau Alzheimer pathology in cognitively normal aging. Ann. Neurol. 67, 122–131.
Ramanan, V., Risacher, S., Nho, K., Kim, S., Swaminathan, S., Shen, L., Foroud, T.M., Hakonarson, H., Huentelman, M.J., Aisen, P.S., Petersen, R.C., Green, R.C., Jack, C.R., Koeppe, R.A., Jagust, W.J., Weiner, M.W., Saykin, A.J., 2013. APOE and BCHE as modulators of cerebral amyloid deposition: a florbetapir PET genome-wide association study. Mol. Psychiatry 19, 351–357.
Rebeck, G.W., Reiter, J.S., Strickland, D.K., Hyman, B.T., 1993. Apolipoprotein E in sporadic Alzheimer's disease: allelic variation and receptor interactions. Neuron 11, 575–580.
Reiman, E.M., Chen, K., Liu, X., Bandy, D., Yu, M., Lee, W., Ayutyanont, N., Keppler, J., Reeder, S.A., Langbaum, J.B., Alexander, G.E., Klunk, W.E., Mathis, C.A., Price, J.C., Aizenstein, H.J., DeKosky, S.T., Caselli, R.J., 2009. Fibrillar amyloid-β burden in cognitively normal people at 3 levels of genetic risk for Alzheimer's disease. Proc. Natl. Acad. Sci. U. S. A. 106, 6820–6825.
Saunders, A.M., Strittmatter, W.J., Schmechel, D., George-Hyslop, P.H., Pericak-Vance, M.A., Joo, S.H., Rosi, B.L., Gusella, J.F., Crapper-MacLachlan, D.R., Alberts, M.J., 1993. Association of apolipoprotein E allele epsilon 4 with late-onset familial and sporadic Alzheimer's disease. Neurology 43, 1467–1472.
Schmechel, D.E., Saunders, A.M., Strittmatter, W.J., Crain, B.J., Hulette, C.M., Joo, S.H., Pericak-Vance, M.A., Goldgaber, D., Roses, A.D., 1993. Increased amyloid β-peptide deposition in cerebral cortex as a consequence of apolipoprotein E genotype in late-onset Alzheimer disease. Proc. Natl. Acad. Sci. U. S. A. 90, 9649–9653.
Sondhi, D., Hackett, N.R., Peterson, D.A., Stratton, J., Baad, M., Travis, K.M., Wilson, J.M., Crystal, R.G., 2007. Enhanced survival of the LINCL mouse following CLN2 gene transfer using the rh.10 rhesus macaque-derived adeno-associated virus vector. Mol. Ther. 15, 481–491.
Sondhi, D., Johnson, L., Purpura, K., Monette, S., Souweidane, M.M., Kaplitt, M.G., Kosofsky, B., Yohay, K., Ballon, D., Dyke, J., Kaminksy, S.M., Hackett, N.R., Crystal, R.G., 2012. Long-term expression and safety of administration of AAVrh.10hCLN2 to the brain of rats and nonhuman primates for the treatment of late infantile neuronal ceroid lipofuscinosis. Hum. Gene Ther. Method 23, 324–335.
Strittmatter, W.J., Saunders, A.M., Schmechel, D., Pericak-Vance, M., Enghild, J., Salvesen, G.S., Roses, A.D., 1993. Apolipoprotein E: high-avidity binding to β-amyloid and increased frequency of type 4 allele in late-onset familial Alzheimer disease. Proc. Natl. Acad. Sci. U. S. A. 90, 1977–1981.
Sullivan, P., Han, B., Liu, F., Mace, B., Ervin, J., Wu, S., Koger, D., Paul, S., Bales, K.R., 2011. Reduced levels of human apoE4 protein in an animal model of cognitive impairment. Neurobiol. Aging 32, 791–801.
Sullivan, P.M., Mezdour, H., Aratani, Y., Knouff, C., Najib, J., Reddick, R.L., Quarfordt, S.H., Maeda, N., 1997. Targeted replacement of the mouse apolipoprotein E gene with the common human APOE3 allele enhances diet-induced hypercholesterolemia and atherosclerosis. J. Biol. Chem. 272, 17972–17980.
Suri, S., Heise, V., Trachtenberg, A.J., Mackay, C.E., 2013. The forgotten APOE allele: a review of the evidence and suggested mechanisms for the protective effect of APOE ε2. Neurosci. Biobehav. Rev. 37, 2878–2886.
Talbot, C., Lendon, C., Craddock, N., Shears, S., Morris, J., Goate, A., 1994. Protection against Alzheimer's disease with apoE epsilon 2. Lancet 343, 1432–1433.
Walker, L., Pahnke, J., Madauss, M., Vogelgesang, S., Pahnke, A., Herbst, E., Stausske, D., Walther, R., Kessler, C., Warzok, R.W., 2000. Apolipoprotein E4 promotes the early deposition of Aβ42 and then Aβ40 in the elderly. Acta Neuropathol. 100, 36–42.
Youmans, K.L., Tai, L.M., Nwabuisi-Heath, E., Jungbauer, L., Kanekiyo, T., Gan, M., Kim, J., Eimer, W.A., Estus, S., Rebeck, G.W., Weeber, E.J., Bu, G., Yu, C., Ladu, M.J., 2012. APOE4-specific changes in Abeta accumulation in a new transgenic mouse model of Alzheimer disease. J. Biol. Chem. 287, 41774–41786.
Yu, J., Tan, L., Hardy, J., 2014. Apolipoprotein E in Alzheimer's disease: an update. Annu. Rev. Neurosci. 37, 79–100.
Zhao, L., Lin, S., Bales, K.R., Gelfanova, V., Koger, D., Delong, C., Hale, J., Liu, F., Hunter, J.M., Paul, S.M., 2009. Macrophage-mediated degradation of β-amyloid via an apolipoprotein E isoform-dependent mechanism. J. Neurosci. 29, 3603–3612.
Zolotukhin, S., Potter, M., Zolotukhin, I., Sakai, Y., Loiler, S., Fraites Jr, T.J., Chiodo, V.A., Phillipsberg, T., Muzyczka, N., Hauswirth, W.W., Flotte, T.R., Byrne, B.J., Snyder, R.O., 2002. Production and purification of serotype 1, 2, and 5 recombinant adeno-associated viral vectors. Methods 28, 158–167.